Technical Digest

Solid-State Sensors, Actuators, and Microsystems Workshop

Editors:
Leland "Chip" Spangler
Thomas W. Kenny

Sponsored by the
Transducer Research Foundation, Inc.

2006

Hilton Head Island, South Carolina
June 4 - 8

Additional support provided by the
Defense Advanced Research Projects Agency

TRF Catalog Number 06TRF-0002
Library of Congress Control Number 2006902128

TRF Catalog Number 06TRF-0002
ISBN Number 0-9640024-6-9
ISSN 1539-2058 (Print)
ISSN 1539-204X (electronic)
Library of Congress Control Number 2006902128

Copies of this volume are available for purchase from the Transducer Research Foundation, 307 Laurel Street, San Diego, California 92101-1630 USA. Please contact the Transducer Research Foundation for ordering information, or consult our website at http://www.transducer-research-foundation.org. Technical digests from previous workshops are also available.

Greetings from the General Chairman

The 2006 Solid State Sensors, Actuators, and Microsystems Workshop is the thirteenth in the biannual series of regional meetings that alternate with the international Transducers Conference. Continuing in a tradition established at the first meeting at Hilton Head in 1984, this meeting will offer an open atmosphere of discussion, collaboration and interaction. We'll see new ideas and new methods, hear about exciting applications, and meet new colleagues. We'll also hear about progress for some older ideas and applications, and renew relationships with old friends. The combination of ideas, opportunities and relationships has always been the objective of this meeting, and we've worked to continue in this tradition.

The conference schedule remains organized around single session oral presentations with several poster presentations. Leland "Chip" Spangler gathered and led a strong and opinionated program committee through a paper selection process that produced the program in this digest. Oral papers were selected on the basis of high quality content and likely broad interest to the meeting audience. Poster papers were selected on the basis of high quality as well, and for their probable high interest to a subset of the meeting audience. The poster papers will be introduced by their authors using a "shotgun" session that was instituted last year. We've also included nine late news oral and four late news poster papers based on a selection process in mid-march. The program committee is to be congratulated for their efforts in reading, ranking, debating, re-ranking, selecting, organizing, and perhaps even understanding all of the more than 270 abstracts submitted in this process. The process may not be perfect, but the combination of so many excellent submissions and the hard work of the committee has produced what we hope is another great technical program for this great meeting.

Another new feature of this year's meeting is appearance of posters representing efforts in MEMS Education. These will be offered in parallel with the Open Poster session on Wednesday Evening, and the corresponding papers are in a supplement to the technical digest. Depending on your feedback, the MEMS Education session may be formally included in the program at future meetings in this series.

As always, significant unscheduled time is available for informal discussions among friends and colleagues. Proposals, job offers, and business plans are the frequent product of these breaks, as are sunburns, lost golf balls, tennis elbows, and sandy navels. There are evening poster sessions, a banquet, and the infamous Rump Session. We hope that you'll make the most of these opportunities for business and pleasure!

The Transducers Research Foundation and DARPA (Thanks John Evans, Dennis Polla and Amit Lal) continued a tradition of providing travel support for presenting author students attending the meeting, enabling the meeting to continue the invigoration of our community with young talent, new ideas, and enthusiasm for the future of our community. We would also like to thank the National Science Foundation for their funding support for the printing of the compilation of educational poster papers.

In addition to thanks to Chip and the technical program committee for their efforts, and to TRF, DARPA, and NSF for significant financial support, it is important also to thank Mark Allen for his continued excellent support of the local arrangements, and Joe Giachino for continuing oversight of our finances. Katharine Cline and her team at Preferred Meeting Management, Inc. have provided all sorts of logistical, administrative, philosophical and psychological support to our organization as always.

Please bring your ideas, recollections, hopes and personalities to the sessions and other events this week.

Thomas W. Kenny
General Chairman

Organizing Committee

General Chairman	**Thomas W. Kenny** Stanford University
Treasurer	**Joseph M. Giachino** University of Michigan
Technical Program Chairman	**Leland "Chip" Spangler** Aspen Technologies
Local Arrangements	**Mark G. Allen** Georgia Institute of Technology

Technical Program Committee

David Arch
Honeywell International

David Arnold
University of Florida

Bernhard E. Boser
University of California at Berkeley

James M. Bustillo
Lawrence Berkeley National Laboratory

Stephen Casalnuovo
Sandia National Laboratory

Gary K. Fedder
Carnegie Mellon University

Storrs Hoen
Agilent Labs

Michael A. Huff
MEMS and Nanotechnology Exchange

Hal Jerman
Coherent, Inc.

Thomas W. Kenny
Stanford University

Sang-Gook Kim
Massachusetts Institute of Technology

Aaron Knobloch
General Electric/Global Research

Mehran Mehrengany
Case Western Reserve University

David Monk
Freescale

Richard S. Payne
Pixtronix, Inc.

Michael Putty
Delphi Research Labs

Antonio J. Ricco
Stanford University

Leland "Chip" Spangler
Aspen Technologies

Svetlana Tatic-Lucic
Lehigh University

William P. Taylor
Allegro Microsystems, Inc.

Kimberly L. Turner
University of California at Santa Barbara

Xin Zhang
Boston University

Technical Program Committee

From left to right, starting in the front

First (Front) Row:
Sang-Gook Kim, Michael Putty, Aaron Knobloch, Xin Zhang,
David Monk, Leland "Chip" Spangler (*Technical Program Chair*), James M. Bustillo, Mehran Mehregany

Second (Middle) Row:
Stephen Casalnuovo, Hal Jerman, Richard S. Payne, Kimberly L. Turner, Svetlana Tatic-Lucic,
Antonio J. Ricco, David Arch

Third (Back) Row:
Gary K. Fedder, Storrs Hoen, William P. Taylor, David Arnold, Thomas W. Kenny (*General Chair*),
Michael A. Huff

Not Pictured: Bernhard E. Boser

Acknowledgements

Special acknowledgement to the Transducer Research Foundation, Inc. and the Microsystems Technology Office (MTO) Program at the Defense Advanced Research Projects Agency (DARPA) for their educational grant funding support of this meeting.

Exhibitors and Benefactors

We gratefully acknowledge the support of this Workshop from the following companies and institutions as of the printing of April 28, 2006:

Coventor

MEMSCAP Inc.

Polytec, Inc.

R&D Newsletter

Sensors Magazine

Texas Instruments/DLP Products

Yole Développement

Program Schedule

Sunday, June 4

6:00 p.m. –
9:00 p.m. **Registration and Welcome Reception**

Monday, June 5

7:30 a.m. **Breakfast**

7:45 a.m. **Welcome and Introduction**
Thomas W. Kenny, *Stanford University* and
Leland "Chip" Spangler, *Aspen Technologies*

Session 1 - Micromirrors and Displays
Session Chair – Hal Jerman, Coherent, Inc.

8:15 a.m. **Invited Speaker**

Mark W. Miles
Qualcomm MEMS Technologies, USA

9:00 a.m.
J.J. Bernstein[1], T.W. Lee[1], F.J. Rogomentich[1], M.G. Bancu[1], K.H. Kim[2],
G. Maguluri[2], B.E. Bouma[2], and J.F. DeBoer[2]
[1]Draper Laboratory and [2]Massachusetts General Hospital

9:25 a.m.
V.A. Aksyuk, D. López, G.P. Watson, M.E. Simon, R.A. Cirelli, F. Pardo,
F. Klemens, A.R. Papazian, C. Bolle, J.E. Bower, E. Ferry, W.M. Mansfield,
J. Miner, T.W. Sorsch, and D. Tennant
Lucent Technologies

9:50 a.m.
B. Winkler[1], D. Elkins[1], A. Tanner[1], V. Ramsey[2], R. Cuff[2], and L. Spangler[2]
[1]Evans & Sutherland Corporation and [2]Aspen Technologies

10:15 a.m. **Break**

Session 2 - Motors
Session Chair – David Arnold, *University of Florida*

11:30 a.m. **Poster/Oral Session Preview Presentations**
Session Chair – Gary K. Fedder, *Carnegie Mellon University*

12:30 p.m. **Lunch**

2:00 p.m. – 5:00 p.m. **Contributed Posters and Late News Poster**
Session Chair – Svetlana Tatic-Lucic, *Lehigh University*

Tuesday, June 6

7:30 a.m. **Breakfast**

Session 3 - Mechanical Structures
Session Chair – David Arch, *Honeywell International*

10:15 a.m. **Break**

Session 4 - Processes
Session Chair – Aaron Knobloch, *General Electric/Global Research*

12:25 p.m. – 1:30 p.m. **Lunch**

7:00 p.m. – 9:00 p.m. **Banquet**

Wednesday, June 7

Thursday, June 8

7:30 a.m. **Breakfast**

Session 7 - Micro Devices
Session Chair – Stephen Casalnuovo, *Sandia National Laboratory*

8:15 a.m. **Invited Speaker**

9:00 a.m.

9:25 a.m.

9:50 a.m.

10:15 a.m. **Break**

Session 8 - Chemical Devices
Session Chair – Storrs Hoen, *Agilent Labs*

12:20 p.m. **Closing Remarks**
Thomas W. Kenny, *Stanford University* and
Leland "Chip" Spangler, *Aspen Technologies*

12:25 p.m. – 2:00 p.m. **Lunch**

Contributed Posters/Oral

Chemical

Physical

Technical

Late News Posters

TECHNICAL PAPERS

Solid-State Sensors, Actuators, and Microsystems
Workshop

2006
Hilton Head Island, South Carolina
June 4 - 8

TOWARD AN iMoD™ ECOSYSTEM

Mark W. Miles
QUALCOMM MEMS Technologies - USA
2581 Junction Ave., San Jose, CA 95134
www.qualcomm.com/qmt

ABSTRACT

The iMoD™ is the basis for a MEMS display that exploits optical interference. QUALCOMM MEMS Technologies (QMT) is engaged in a multi-front effort to commercialize iMoD. This paper will review the history of iMoD development to date, and discuss QMT's strategy, philosophy, and transformation as it addresses the array of issues it must face to succeed.

HISTORY OF iMoD DEVELOPMENT

The iMoD, or interferometric modulator, underwent a rather long gestation not unlike that experienced by similar devices such as the Digital Micromirror Device from Texas Instruments. The device was originally conceived as the "Resonant Membrane Spatial Light Modulator" (RMSLM) in 1989. This period coincided with research activities by a variety of organizations into different MEMS light modulators, exploring the uses of reflection, diffraction, and interference. In the case of the RMSLM, it was thought that interference could provide two very significant advantages. The first was the ability to process light with great efficiency, and the second was the ability to do so with a degree of finesse available only through thin film optics. Applications including optical computing, telecommunications, and adaptive optics were all candidates for ultimate commercialization. However it was flat panel displays that were the original and ongoing focus of the work. The attributes that MEMS brought to this application would become more apparent later in the development.

First funding for the development occurred via the Small Business Administration (SBIR) program that drove the efforts of the author's first company, Etalon Inc. From 1991 to 1997. These resources were used to gain experience with the materials that were suitable for creating MEMS structures, but whose traditional role was in the creation of thin film stacks for static optical devices. All these efforts occurred within a subset of the facilities of MIT's Department of Materials Research where Etalon was an industrial user. It was also during this period that the initial thin film design families, optimized for display applications, were modeled.

The end of this long research phase was marked by the actuation of the first functioning pixels. In typical fashion, these were glass fragments decorated with silver paint, long wires, and barely perceivable pixels. Additionally, a process by which large, full color, bright and vivid static displays could be built was developed. Ironically, or perhaps mercifully, it was conceived in one afternoon and realized the following evening with the help of a laser printer, transparencies, a thermal evaporator, and PECVD. Together, these two accomplishments provided a powerful validation of the technology's potential, and as "sales" tools they enabled significant new funding. It was also during this period that the term "iMoD" was coined, and Iridigm Display Corporation formed. Iridigm's purpose was the commercialization of iMoD technology for display applications. Subsequent, efforts were focused in three main areas. The first was the creation of a functioning macro-pixel array that could be addressed and driven to show basic graphic information. Second was the validation of a manufacturing strategy that would rely on the exploitation of existing TFT LCD facilities. The third was to extend and refine the iMoD family of optical designs.

Iridigm closed its first funding round in 2001, the height of the Internet boom. This process was especially hard-fought due to a combination of circumstances. Venture backed forays into domestic display production were riddled with recent and well publicized failures and technical obstacles. At the same time excitement around the Internet drove capital into web based startups, and startups aimed at fiber-optic infrastructure development. Many MEMS companies dove into the breach of the latter category. Iridigm subsisted with a lean approach that minimally expanded its engineering and management team, and built a small prototype fab. The fab was affectionately known as "New York," a more than passing reference to the song. Costing only $3M and 10 months buildout, it was a completely integrated facility which took 4" glass wafers in, and produced packaged devices. Many similarly purposed facilities cost 10X as much.

A significant array of milestones was achieved. Usable hysteresis, one of the pillars of the iMoD's promise, was realized. This led directly to the fabrication of the first matrix addressable displays. Prototypical static and dynamic displays based on bi-chrome, black and white, and full color families emerged. The manufacturing strategy was also validated by the first successful use of an LCD fab to build iMoD displays.

Iridigm was acquired by QUALCOMM in October of 2004. QUALCOMM MEMS Technologies (QMT) was subsequently formed as fully owned subsidiary focused on the manufacture of displays for portable electronic devices, and the exploitation of iMoD related technology to MEMS in general.

iMoD THEORY AND OPERATION

The theoretical basis for iMoDs has been described in prior publications [1] [2] [3]. Optical interference occurs between the thin film stack and the metallic membrane reflector. Thus the iMoD is viewed through its transparent substrate. The thin film stack comprises a number of dielectrics and highly absorbing metals like chrome or tungsten. Changes in the optical state are produced by the reflection or absorption of light by the iMoD structure, depending on the position of the membrane element shown in Figure 1.

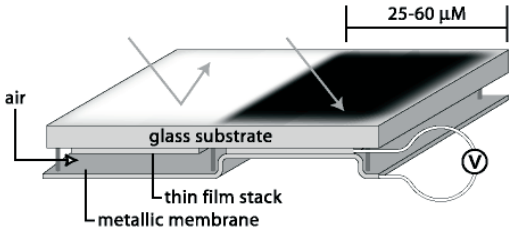

Figure 1. *The iMoD architecture.*

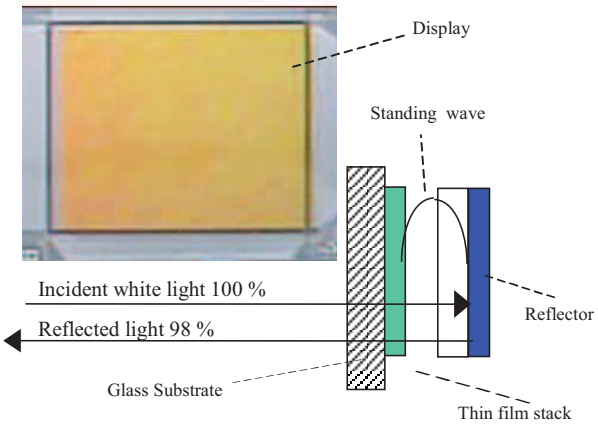

Figure 2. *iMoD in resonant mode.*

Fundamentally the device has a resonant state and an induced absorption state. As in many thin film stacks, a standing wave is produced whose peak position is determined by the position and properties of its constituent films. When the iMoD is in its resonant state, the metallic membrane is not actuated, and the overall design is such that the standing wave peak resides within the airgap. In this state the iMoD behaves as a resonant reflector, reflecting a color peak whose wavelength is determined by the size of the airgap. A diagram of this mode and a micrograph of a corresponding display is shown in Figure 2.

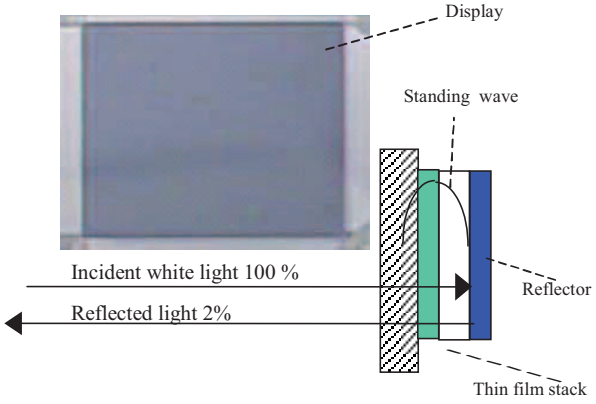

Figure 3. iMoD *in induced absorption mode.*

Actuation of the membrane into contact repositions the standing wave peak so that it coincides with the absorbing film in the thin film stack. The result is a phenomenon known as induced absorption. Light is consequently absorbed with great efficiency producing an effective black state as shown in Figure 3.

From a functional standpoint, the iMoD is very appealing as a display element for two reasons. The first concerns the efficiency of the device as a modulator. Reflective media, like a magazine or a newspaper, must be exceptionally bright to be readable in a variety of ambient conditions. The former generally have a brightness of around 80%, while the latter achieve on average 55%. iMoD pixels routinely achieve reflective peaks in excess of 85%, as shown in Figure 4. The result is an average brightness of 30%, a figure which makes them viewable even in exceptionally dim environments. Overall this attribute minimizes, and in some cases eliminates, the need for some form of supplemental lighting.

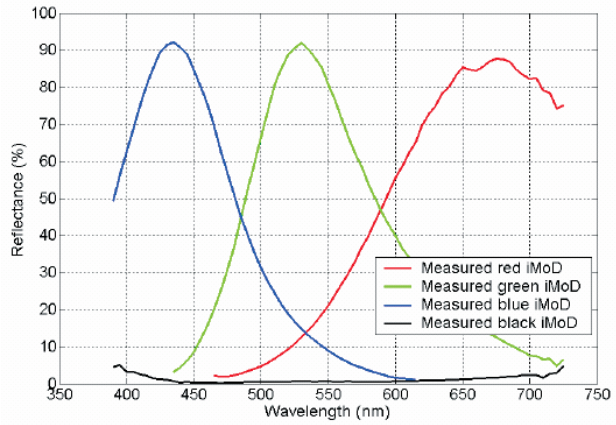

Figure 4. *Typical iMoD reflective peaks.*

Hysteresis is another significant attribute as it allows the elimination of the Thin Film Transistor (TFT) array, a significant component in many matrix addressed displays. The function of the TFT array is to provide memory and a voltage threshold. The combination of memory and threshold allows for the generation of an addressing waveform that can be applied almost independently of the electro-optic behavior of the modulating medium. The downside of the bargain is that the TFT often constitutes one third of the overall cost of a display. Figure 5 illustrates a typical hysteresis curve attained with iMoD. Such curves are easily exploited for they are wide, and have very well defined transitions.

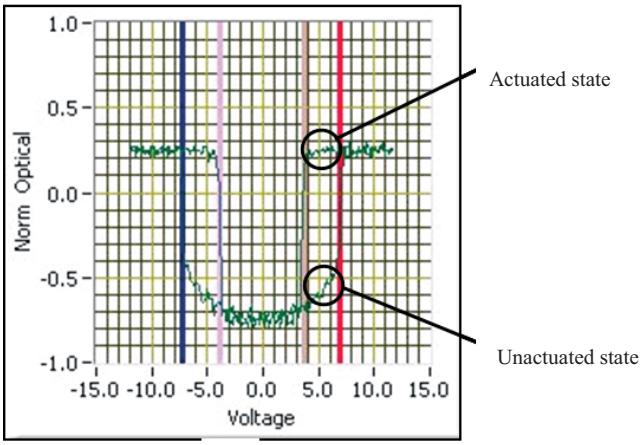

Figure 5 *Typical iMoD hysteresis curve.*

APPLICATIONS AND ECOSYSTEM

Display-centric portable electronic products are engaged in a constant struggle to provide increasing features against a backdrop of decreasing power, size, and cost budgets. The aforementioned qualities of high brightness and inherent hysteresis are two of the cornerstones upon which the iMoD's promise rests. Delivering in these two critical areas makes it an attractive solution for many of these products. However, a discussion of the iMoD's display architecture reveals a broader and more compelling implication.

A comparison between architectures derived from iMoD and LCD solutions is illustrated in Figures 6 and 7. These

figures show that the iMoD solution exhibits a higher degree of functional integration in at least three dimensions. Modulation in the LCD requires a combination of the LC material, and polarizing films vs. a single actuating membrane. LCD color selection relies on a separate color filter component, a component made unnecessary by the iMoD's predefined air gaps. The elimination of the TFT array speaks for itself. Thus it can be seen that the iMoD brings advantages on a broad system wide level as well.

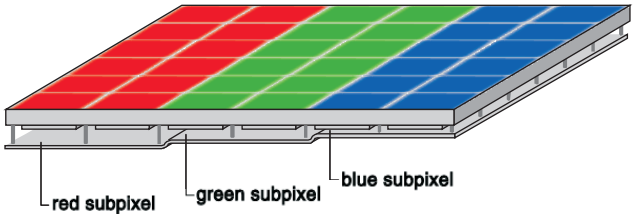

Figure 6. *Full-color iMoD architecture.*

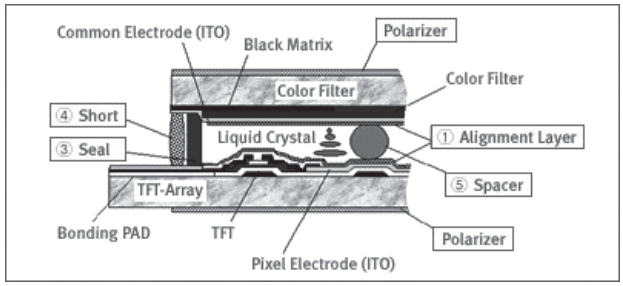

Figure 7. *LCD display system architecture.*

This exercise also serves to bring to light the challenging nature of displays or display subsystems compared to other components comprising a product's BOM (Bill of Materials). Challenging in the sense that the display must "integrate" and "interface" across a wider variety of axes than the other devices in the BOM. Put simply, and by example, IC design must consider standardized silicon layout/fab, packaging, and lead frame options. Display design by default must take equivalent issues into account. However this process is significantly burdened by the need to consider additional complexities. Complexities associated with the physical, electronic, mechanical, and optical coupling of the display to a dizzying array of components and materials. Not to mention that the resulting subsystem must serve as both a compelling visual and frequently tactile transducer. Successful design and deployment of off-the-shelf display technologies depends on the intimate coordination and collaboration between a host of seemingly unrelated industries and disciplines. To achieve a similar result with a technology that is yet to be established requires the almost spontaneous realization of a comparable infrastructure or "ecosystem."

ELEMENTS OF AN iMoD ECOSYSTEM

At last count the author has identified no less than ten separate "niches" which must be filled or otherwise addressed to achieve a functional iMoD ecosystem. Functional in the sense that viable products can result, and mechanisms exist to provide for the evolution and advancement of technology and its application. This is not necessarily an inclusive list. However it should be a fair representation of the general scope, and overlay what QMT has and will establish as part of its larger commercialization strategy. A list and brief descriptions follow.

Basic materials R&D
Materials study and engineering, particularly as it relates to electromechanical behavior and the impact of different oxides.

iMoD architecture development
Fundamental structure design to improve performance and expand the range of iMoD functionality.

iMoD family specific materials R&D
Materials research as it relates to electro-optomechanical behavior. Designs for bi/monochrome, full-color, B&W, etc.

Array manufacturing
Manufacturing process design and toolset specification related to the fabrication of the iMoD array.

Array packaging
Process and tool development for encapsulation of the array, post array fabrication.

Electronic system development
Design and development of drive waveforms, drive/controller electronics, as well as lighting and touch systems.

Lighting system development
R&D of new iMoD specific supplemental lighting systems, and customization and deployment of existing solutions.

Optical film development
Development and customization of organic and inorganic films and coatings for optical performance enhancement.

Module assembly
Adaptation and customization of existing module assembly tools and processes. Development of cost reducing iMoD specific module assembly enhancements.

Advanced Development
iMoD and iMoD derived innovations to support roadmap, and alternative MEMS related opportunities.

CHALLENGES AND STRATEGIES

Each of these niches serves a different purpose or role and is therefore constrained or driven by varying issues or demands. Strategies must be established, or adapted if already existing, that are niche specific but "system aware" (analogous to "think globally, act locally"). In some cases the approach is driven by the availability of resources or the need to control IP. Others are a continuation of strategies put in place years ago, but are challenged by changes in corporate culture and personnel. Yet others must be agile and highly responsive to changing demands from customers and internal processes.

Materials R&D and architecture development represent two separate areas that have almost identical drivers and constraints. Both must respond to the need to continually improve the iMoD, functionally via architecture and electro-dynamically via materials R&D. Both are constrained as they lie at the core of the IP value proposition and as such represent high priority assets. Both have dedicated in-house engineering teams. In the case of materials, this occurs in the form of a relatively new

device physics group. Architecture development of course, has been a central process from the very beginning.

Additionally, one of the legacies of the iMoD's long gestation period is that there has been plenty of time to identify and document a myriad of evolutionary and revolutionary enhancements along material and architecture axes. This plethora of avenues comes with the pressure to explore the most promising ideas quickly, in some cases before another entity does. All these factors helped to drive the decision to establish comprehensive in-house facilities that are fully integrated and capable of small-scale prototyping, as well as exotic R&D. The expense of such a capability is justified by maintaining leadership and control over what is arguably the most critical asset of the company.

On the other hand, there are some areas of R&D that can be "safely" outsourced. One example is the exploration of iMoD family specific materials. Family, in this case, refers to an iMoD design that is defined by the incorporation of a particular material/s, and minor architecture changes. The consequence is that the family exhibits fundamentally different electro-optic behavior. An example of this is shown in Figure 8, where a photograph of a static B&W iMoD is shown.

This outsourcing strategy is palatable because the innovation occurs using software design tools, a resource which can be established and staffed for relatively low cost. The actual development activity involves the deposition of specific materials or materials combinations. The results are then characterized separately or in conjunction with in-house fabricated structures. Since the deposition function can be easily outsourced, burdens on in-house resources are decreased while maintaining control over IP.

Figure 8. Static display based on B&W design family.

The term "niche" is hardly a sufficient label for the resources and energies devoted to array manufacturing. iMoD array manufacturing will occur, in the near term, on existing/modified LCD factories and tools. This strategy was ingrained in the ecosystem at a time when the iMoD design families and associated materials had not been defined. Essentially that decision established a rather rigid catalog of materials that had to be mixed and matched to achieve the iMoD's goals, not the other way around. Figure 9 is one such catalog that derives from a specific LCD factory [4]. The overwhelming benefit has resulted in a relatively mature manufacturing process. The process is exceptionally well adapted to drop-in to an existing TFT LCD fab. This pool is large and increasing in size as existing fabs are supplanted by larger and more efficient replacements.

Material	*Purpose*
Al, Al:Nd	Gate metal, Gate bus line
Ta, Mo-W, MoCr, Mo	Gate metal
ITO	Pixel electrode
SiNx	Passivation, gate dielectric
a-Si	Channel

Figure 9. *Sample "catalog" of materials for iMoD mfg.*

The challenges to this strategy could easily be entitled "The Realities of a 'Drop-in' Process," "Evolution of Staffing From Development to Production," and "Line Balancing: The Act." At its core is the current relationship between QMT and PVI (Prime View International of Taiwan) that provides regular and exclusive foundry access for iMoD manufacture. The particular facility that QMT has access to is well suited for this purpose. Tools and materials can be easily reconfigured, and the production rates are compatible with a cross-section of introductory products. However despite the selection of materials that are already in use and well characterized, production tools rarely deliver the same performance as tools in a development environment. The result is that a technology transfer process begins to resemble a re-development effort. The development team must accept this fact early on and prepare accordingly. Advance sampling and characterization of materials is one approach that can be pursued in parallel [**5**].

Accepting the realities of this process can directly challenge the nature and composition of the development team. In all likelihood an "entire development staff, although well chosen for the creation of a new technology, may not be properly suited for the move to engineering and production" [**5**]. The necessary transformation can sometimes be complicated by "pride of ownership" and a lack of appreciation for the fact that some problems are often more efficiently solved on the manufacturing vs. development side.

From the standpoint of establishing a foundry in an existing factory, the issue of line balancing also emerges. In the case of iMoD, upwards of 90% of the equipment set already exists within a TFT AMLCD fab. However the sequence of process steps for which the factory layout was designed is such that the toolset is not optimized for efficient production. Figure 10 illustrates the iMoD sequence. TFT processes tend to be "heavy" in dielectrics and "light" on the metals side. The resolution of this circumstance is non-trivial for it involves tradeoffs between early incremental equipment changes with potentially large future expenses, versus initial large expenditures with growing savings in the future.

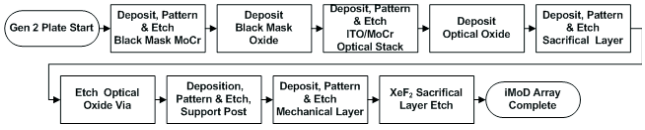

Figure 10. *iMoD array manufacturing sequence.*

Supplemental lighting systems is a niche whose complexity begins to encompass some of the aforementioned "integration and interfacing" issues. It to also subject to pressures which are variable in product space since some apps require lighting and some don't. Variations over time can also occur as the initial product mix along with customer priorities may change, sometimes quite rapidly.

The technical challenge is not unlike that of an LCD where the lighting system is a separately defined component. This is in

contrast to emissive displays, such as plasma, OLED, and FED where light emission is a consequence of the electro-optic effect. This similarity is beneficial in that it creates the potential for adapting existing LCD solutions for application to iMoD. Front lights, as they are called, have existed since the advent of commercially available reflective LCDs. However they have evolved specifically to complement the characteristics of LCDs. LCDs usually accommodate a narrow entry/exit cone, and have an affinity for polarized light.

A typical example is shown in Figure 11, which illustrates the major components and the associated optical path. The general design goal is to minimize losses at each interface, and produce a structure that is robust enough to maintain alignment during everyday use. Effectively homogenizing and coupling the incident light into the display, without producing undue visual artifacts, represents one of the more subtle and difficult design challenges. This approach is sub-optimal given the iMoD's wide viewing angle and polarization insensitivity. It also does not take into account iMoD specific color shift phenomena, as well as characteristics that enable reductions in total system size.

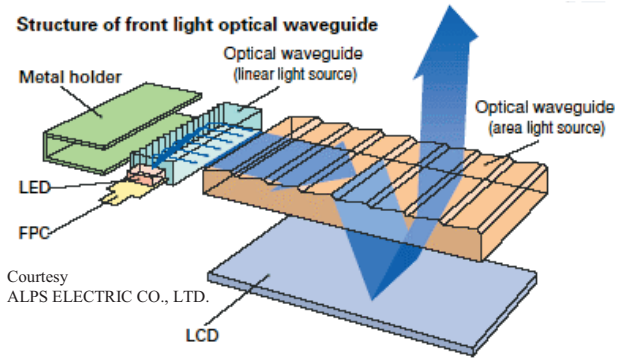

Figure 11 *LCD Frontlight layout.*

Overall, lighting system design must consider the complex interaction of a stack of organic and inorganic films, adhesives, micro structured films, and light sources from an optical, mechanical, visual, and thermal standpoint. Even existing solutions are born and evolve within the framework of yet another industrial infrastructure with different specialty niches. To bring together these resources in-house in a timely fashion is not conceivable. Thus, QMT has established a multi-faceted outsourcing model involving at least four vendors. This model combines both directed efforts to adapt existing solutions, and a "shotgun" approach which allows for a wide variety of advanced solutions to be quickly vetted and, if appropriate, positioned for more targeted development.

BROADER DEVELOPMENT AND APPLICATION

Most of the activities within the ecosystem are guided by a technology roadmap that takes its cues from a product roadmap. The resulting mechanism is highly responsive to customer requirements for introductory products, and for future products that exist along a well defined feature set hierarchy. What this mechanism lacks is the ability to anticipate or, in some cases, define new customer requirements. This is in addition to identifying opportunities that do not exist on the current product roadmap. Consequently QMT has created a Technology Planning Group (TPG) whose areas of responsibility include – a focus on non display applications that lie off the current roadmap, an interest in things that could lie on the current roadmap in the future, and some support of the existing planned product developments.

Existing product development efforts include, for example, the incorporation of MEMS switch arrays to provide a waveform multiplexing function. By capturing this functionality within the array MEMS process, the pin-count and resulting driver cost/complexity is reduced. TPG will support such efforts if supplemental resources or expertise are required within the associated technology development program.

Advanced iMoD architectures illustrate one kind of project that TPG has an interest in. Possible variations include devices which can be addressed with simplified waveforms, and iMoDs which are tunable and therefore can achieve any color with a resulting 3X improvement in brightness. The speculative nature of these thrusts do not necessarily place them on the technology roadmap. TPG's purpose in this case is to drive further exploration of these technology options and their value in enabling future product opportunities. The objective for this work is to reduce uncertainty and fix new points on the technology roadmap for further development.

The iMoD is quite a versatile device in itself. Unlike many display entrants it has the potential to play a role in a more diverse array of display market segments than its competitors. The value and potential are equally manifested in other ways as well. In addition to the large area MEMS process, and manufacturing knowledge and capability, there is the experience being gained in bringing a MEMS based system into a high volume, cost competitive environment.

Thus TPG's third role, its focus, is to explore off-roadmap opportunities that are enabled by the iMoD's functionality, asses and vet non-display applications that are enabled by the growing process and manufacturing expertise, and pursue the development of capabilities that support and benefit all-the-above. Opportunities include television, and large area (kiosk or billboard), but also RF switches, variable capacitors, or telecommunications. Synergistic efforts in the area of ultra low-cost manufacturing range from pre-deposited "starter stacks" and plastic roll-to-roll substrates, to pre-form, or printing like approaches.

CONCLUSIONS

This paper is an attempt to provide insight into the context and intricacies of realizing a new MEMS display technology. It is by no means comprehensive. Commercialization has been and continues to be an exceptionally elaborate and complex undertaking. This is not to suggest that the same cannot be said of any new technology being driven toward the marketplace. However iMoD has come of age from within an industry (MEMS) still recovering from a "boom-bust" cycle and therefore not quite as mature as it might be. At the same time, emerging into an established industry with no precedent for the role of MEMS (flat panel displays). The legacy of Iridigm is a robust, wide IP portfolio, engineering team and manufacturing strategy. The challenge to QMT is broadly developing and commercializing this windfall, while keeping it intact and maintaining control over its future. The product in question is not an individual component to be developed in relative isolation. Rather it is an intricate system whose pieces derive from multiple and disparate industries and disciplines. Getting one's arms around such a project is helped by viewing it as a developing ecosystem. Like all of its natural equivalents, survival depends on the successful positioning and interdependence of the all elements within.

ACKNOWLEDGEMENTS

The author wishes to thank the team at Qualcomm MEMS Technologies for their unabashed enthusiasm and dedication to the pursuit of iMoD displays.

REFERENCES

[1] M.W. Miles, “Digital Paper ™ :Reflective Displays Using Interferometric Modulation”, SID 2000 Digest, p. 32 (2000)
[2] M. Miles, E. Larson, C. Chui, M. Kothari, B. Gally, and J. Batey, “Digital Paper™ for Reflective Displays”, SID Symposium Digest 33, 115 (2002)
[3] Brian J. Gally, “Wide-Gamut Color Reflective Displays Using iMoD™ Interference Technology”, SID Symposium Digest 35, 654 (2004)
[4] P.D. Floyd, D. Heald, B. Arbuckle, et. al, “iMoD™ Display Manufacturing”, SID Symposium (2006)
[5] J.B. Sampsell “Innovation to Production: A Continuum”, SID Symposium (2006)

MAGNETIC TWO-AXIS MICROMIRROR FOR 3D OCT ENDOSCOPY

Jonathan J. Bernstein, Tom W. Lee, Fran J. Rogomentich, and Mirela G. Bancu
The Charles Stark Draper Laboratory
Cambridge, MA USA
Ki H. Kim, Gopi Maguluri, Brett E. Bouma, and Johannes F. DeBoer
Wellman Laboratory of Photomedecine, Massachusetts General Hospital
Boston, MA USA

ABSTRACT

Micromirrors used to steer optical beams at the tip of an endoscope are an active area of research. MEMS mirrors with various actuation mechanisms have been reported including rotating micromotors **[1]**, parallel plate electrostatic **[2]**, electrothermal **[3,4]** and vertical electrostatic combs**[5-8]**. This paper presents for the first time a two-axis magnetically actuated micromirror designed for an OCT (Optical Coherence Tomography) endoscope. We demonstrate also for the first time a free-rotating axis with no spring constraint, combined with an orthogonal resonant drive axis. Magnetic actuation allows large angular deflections (+/- 40 degrees rotation) at low voltage (<1V), a significant advantage relative to electrostatic mirrors for patient safety. Actuation is accomplished with 4 coils (two pairs) in proximity to the moving mirror, which contains a small permanent magnet. The entire endoscope scan engine is contained in a 2.8 mm ID plastic tube. Details of the endoscope design, MEMS fabrication, optical path, scanning, and sample OCT images are presented.

INTRODUCTION

Minimally invasive surgery is an important trend in medicine that leads to reduced trauma and faster patient recovery. Endoscopes are evolving rapidly to smaller sizes and higher functionality, including the ability to image tumors and in some cases treat diseased tissue with radiation or sound.

OCT (Optical Coherence Tomography) has recently evolved from the time-domain systems which sample 2,000 A-lines/sec to spectral domain, **[9]** and Optical Frequency Domain Imaging (OFDI) **[13]** which sample 19,000 to 100,000 A-lines/sec. In contrast, mechanically scanned endoscopes have not kept up with current acquisition speed capabilities of Spectral Domain OCT and Optical Frequency Domain Imaging (OFDI). Rotational scanners suffer non-uniform rotation distortion (NURD) from long, thin cables transmitting torque from the external motor. Linear scan mechanisms are limited to a few Hertz due to the forces needed to translate distally a fiber and lens assembly. Rapidly scanning MEMS micromirrors offer an alternative to mechanical actuation using external motors and mechanical linkages.

MEMS mirrors for endoscopes are an active area of research **[1-8]**. Arguably the most advanced of these use multi-level electrostatic comb actuators. These mirrors offer many advantages such as low mass, absence of exotic materials, and the possibility of built in capacitive feedback. Drawbacks include tiny gaps and high voltages which are potential failure modes and safety concerns. Previous work on magnetic actuation using a film of Permalloy on the mirror **[10],** a coil on the mirror **[11]** or screen-printed magnets **[12]** show that these can achieve large angular or linear scans at low voltages across large gaps, advantages in an endoscope. This work explores a novel design for a two-axis raster scan, using a resonant fast axis and free-rotating slow axis. A large angle raster scan is demonstrated. The entire system fits inside a 2.8 mm ID plastic tube. Preliminary 2-D images taken with both time-domain and spectral domain OCT are shown.

THEORY

OCT is an optical technique for 3D tissue imaging based on back-reflection from the sample. The back-reflected light is detected interferometrically by combining with light from a reference mirror. In time-domain OCT, the back-reflection at various depths is collected sequentially by moving the reference mirror. Newer techniques, such as spectral-domain OCT and OFDI, use Fourier techniques to transform an acquired spectrogram, and are an order of magnitude faster than time-domain OCT **[9, 13]**.

The endoscope design is shown in Fig. 1. The MEMS mirror contains a small NdFeB permanent magnet (0.6 mm X 0.8 mm X 0.2 mm), and is actuated via two pairs of coils: a fast axis pair and a slow axis pair. FEA was used to calculate the torque/mA along each axis (Fig. 3 and Table 1).

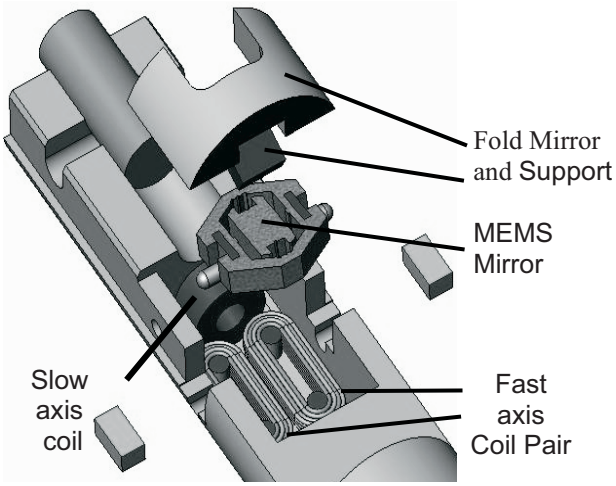

***Figure** 1. Solid model of endoscope system, showing actuation coils, fold mirror and MEMS mirror.*

Endoscope Optical Design

Light from an SMF 28 optical fiber is focused through a GRIN lens, reflected from a fold mirror to the MEMS mirror which steers along two axes (Fig. 2). ZEMAX simulations were used to optimize the optical path for resolution over the 3-dimensional imaging region. Maintaining good focus over large angular deflections is difficult due to cylindrical lensing effects from the plastic sheath of the endoscope. The light beam must avoid normal incidence on the plastic sheath, since this would create a strong back-reflection which would degrade the S/N of

spectral domain image processing. The fold mirror allows the MEMS mirror to steer the optical beam forward towards the endoscope tip.

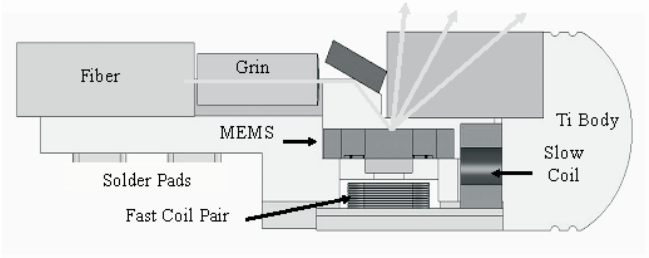

***Figure** 2. Solid model of later version of endoscope system, showing optical path through system and solder pads for strain relief. This version shows only one slow axis coil.*

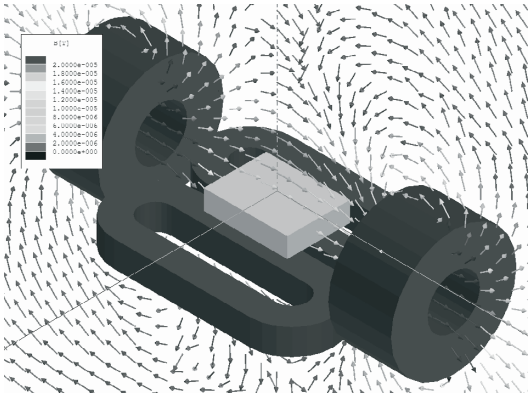

***Figure** 3. FEA model of magnetic field from slow-axis coils used to calculate torque/mA. Similar analysis used for fast axis coils.*

These mirrors have a high Q (600-900) on the resonant axis, therefore driving them off-resonance requires care. For example, driving with a triangle wave is desirable for a raster scan. In this case, the input drive signal must be filtered with a notch or low pass filter to ensure that no high order harmonics are present at the resonant frequency, or ringing will result.

EXPERIMENTAL DETAILS

Fabrication Process: A simple, manufacturable process with only 3 photomask steps was used to fabricate the MEMS mirrors, illustrated in Fig. 4. Photoresist liftoff was used to pattern the metal mirror layer, consisting of Cr/Au on the handle side of an SOI wafer.

The flexures and gimbal were etched using an STS ICP (inductively coupled plasma) etcher running the Bosch process. Folded flexures consisting of 3 beams were either 6 microns wide or 8 microns wide depending on design, and 50 microns thick (set by the device layer of the SOI wafer). Flexures, temporary etch buffers (used to create uniform etch conditions on both sides of each flexure leg) and stops are shown in Fig. 5.

A second ICP etch was used to pattern the handle side of the wafer (350 microns thick), freeing up the mirrors. A final HF etch was used to remove the buried oxide layer. Finally, temporary hold-downs on the SOI layer were snapped to release the mirrors from the wafer. Fig. 6 shows a completed device mirror-side up.

Magnets made from 50 MGOe NdFeB were attached individually using epoxy. Screen printed magnets have been demonstrated previously **[12]**, but to achieve higher magnetic moment per unit mass, a solid rare-earth magnet was selected.

Axles for the slow axis rotation were also inserted manually and attached using epoxy (Figure 7). Axles were packed in Halocarbon stopcock grease for smooth rotation.

The endoscope body, fold mirror support, coil support and axles were machined from bio-compatible titanium using a combination of conventional machining and wire EDM.

a. Metal 1 (Cr/Au) handle side lift-off,

b. ICP etch 50 micron SOI layer to form springs and gimbal

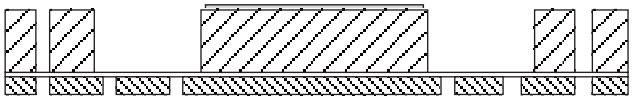

c. ICP etch handle side to release mirror

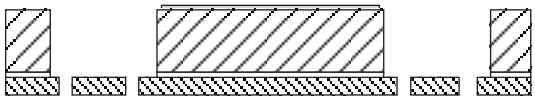

d. HF etch to remove buried oxide.
Break temporary tabs to release mirrors

***Figure** 4. Fabrication sequence used to make mirror chips*

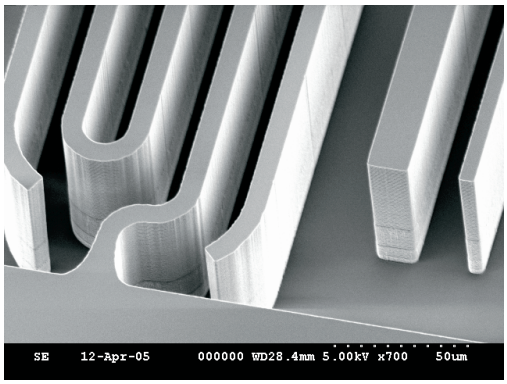

***Figure** 5. ICP etched folded flexure fabricated from single crystal silicon, shown with etch buffers and stops.*

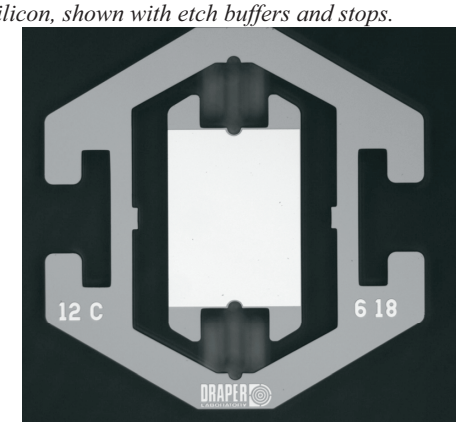

***Figure** 6. MEMS mirror photograph showing Au mirror and side notches (left and right side) for holding axles.*

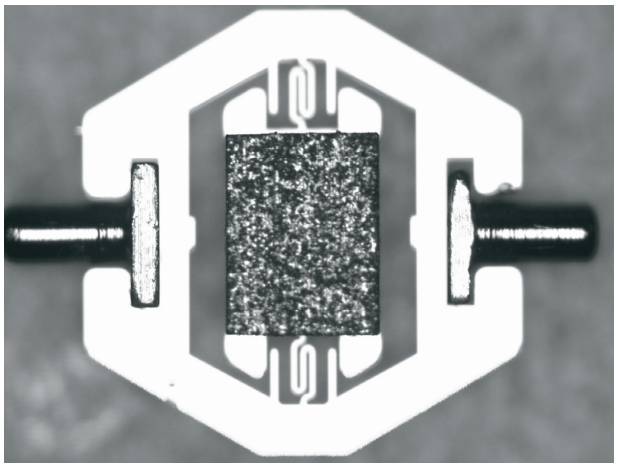

***Figure** 7. MEMS micromirror showing permanent magnet, springs, and axles.*

RESULTS

A completed endoscope scanner is shown in Fig. 8. MEMS mirrors were fabricated with 6 micron and 8 micron wide flexures, giving resonant frequencies near 550 Hz and 800-900 Hz respectively. The measured Q of the fast axis is approximately 600-800, giving a large drive amplification at resonance.

Static angle vs. drive current data for a 6 micron flexure device is shown in Fig. 9. Optical deflection of +/- 8 degrees was achieved at drive currents of 91 mA at 0.73 V drive voltage.

A linear scan at 10 Hz was achieved by driving the fast axis with a triangle wave (Fig. 10). Angle position of a laser spot reflected from the mirror was measured using a Hamamatsu Position Sensing Diode (PSD). Drive signals with harmonic content at the resonant frequency (562 Hz) produced ringing. This could be avoided by several input shaping techniques, such as notch filtering or low-pass filtering the drive signal.

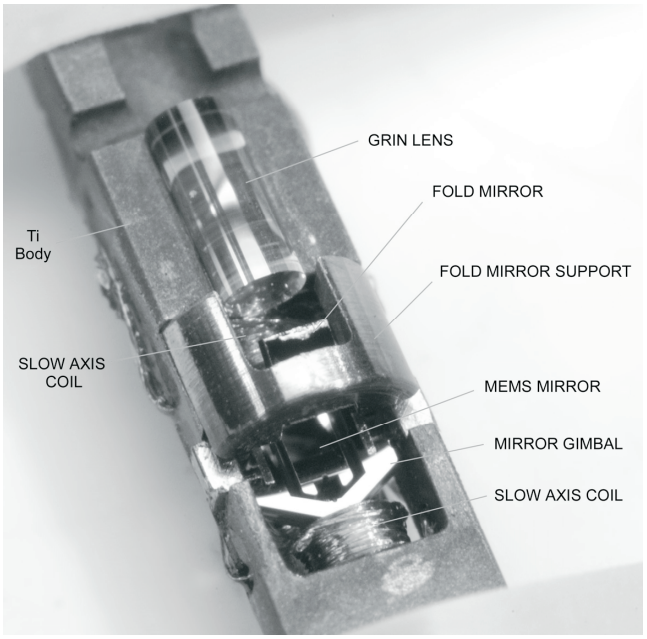

***Figure 8 .** Completely assembled endoscope scan engine with actuation coils fits in a 2.8 mm ID tube.*

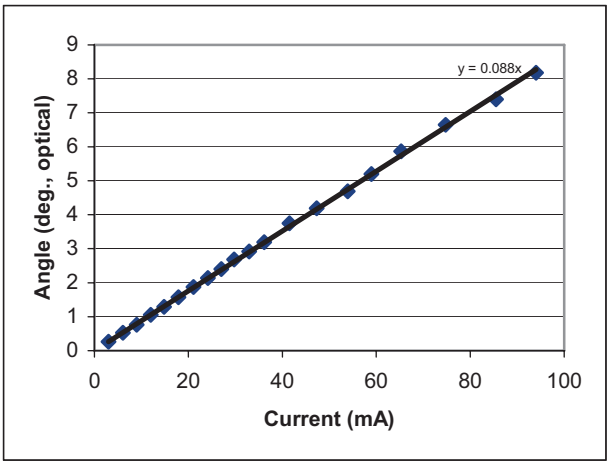

***Figure 9**. Static fast axis angular deflection vs. drive current for mirror with 6 micron wide flexures.*

Table 1. Coil Turns and Torque/A

	Slow Axis	Fast Axis
# turns each coil	300	30
Calc. Torque (N-m/A)	$2.1*10^{-6}$	$1.5*10^{-6}$
Coil Resistance (ohms)	58	8

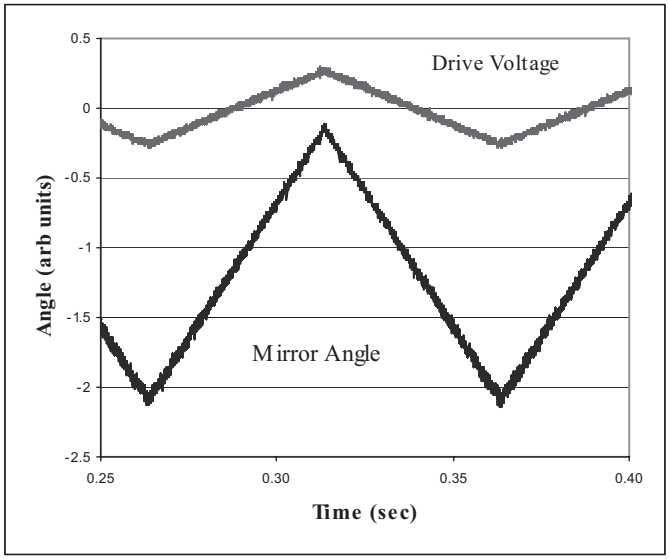

***Figure 10** . Mirror scan following 10 Hz triangle wave.*

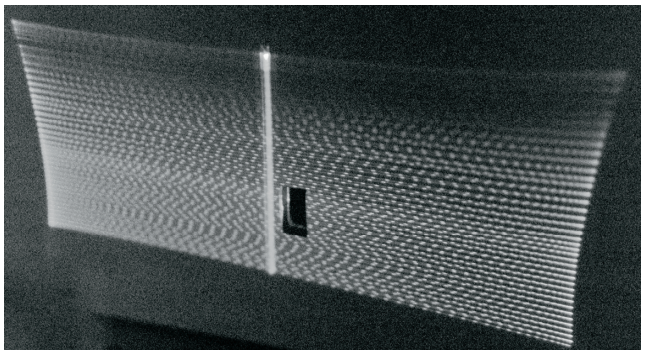

***Figure 11** . Two-axis raster scan produced by MEMS mirror. Laser passes through hole in screen to scanner, mounted on an optical bench. Mirror scans +/- 40 degrees optical both axes.*

Fig. 11 shows a combined fast resonant axis and orthogonal slow triangle wave scan. Fast axis scans were limited by the mirror hitting the gimbal at about +/- 44 degrees optical. Slow axis axle supported scans were limited by the magnet touching the fast axis drive coils, also at +/- 40 degrees depending on the magnet to coil gap.

OCT images: Fig. 12 shows a cross-sectional image of a researcher's finger using spectral domain OCT running at 18.5 frames/s. Fig. 13 shows an image of a finger tip using time-domain OCT at 1 frame/s.

The natural coordinate system for a rotating mirror is spherical, whereas Cartesian coordinates are preferred for imaging. We expect in the future software will be used for this coordinate conversion, and to store successive 2-D images as a 3-D data file.

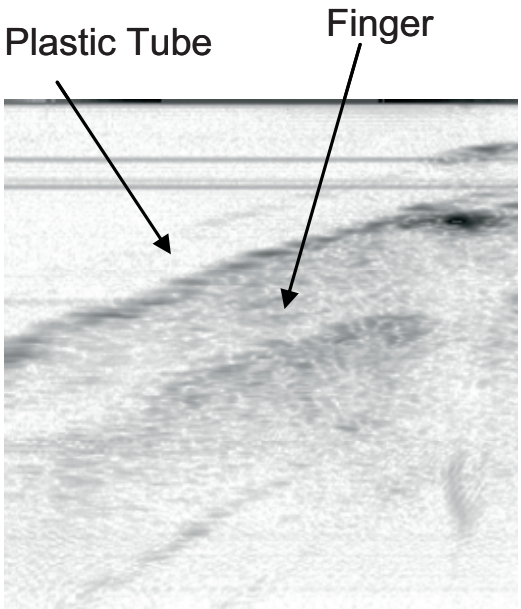

Figure 12 *. Spectral-domain OCT image using slow axis scan of MEMS endoscope.*

CONCLUSIONS

We have designed and demonstrated an endoscope scan engine consisting of a 2-axis MEMS micro-mirror with an attached magnet driven by external copper coils. The resonant axis enables a large scan angle at low drive voltage. A slow axis supported by free-rotating axles was combined with the resonant drive axis to produce a 2-D raster scan. Preliminary OCT images from both Time-Domain OCT and Spectral-Domain OCT are shown.

ACKNOWLEDGEMENTS

The authors gratefully acknowledge the generous financial support for this research from **CIMIT**, the Center for the Integration of Medicine and Innovative Technology.

REFERENCES

1. P. Tran, D. Mukai, M. Brenner, and Z. Chen, "In vivo endoscopic optical coherence tomography by use of a rotational microelectromechanical system probe", Optics Letters, Vol. 29, No. 11, June 1 2004 pp. 1236-1238.
2. J. Yeow, X. Yang, A. Chahwan, M. Gordon, B. Qi, I. Vitkin, B. Wilson and A. Goldenberg, "Micromachined 2-D scanner for 3-D optical coherence tomography", Sensors and Actuators A 117(2005) pp. 331-340.

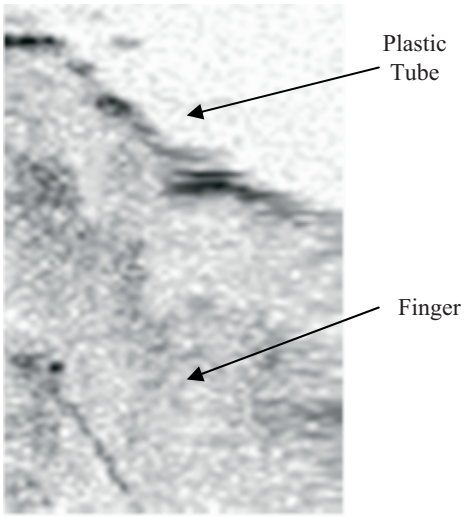

Figure 13. *Time-domain OCT image using slow axis scan of MEMS endoscope.*

3. A Jain, A. Kopa, Y. Pan, G. Fedder, and H. Xie, "A Two Axis Electrothermal Micromirror for Endoscopic Optical Coherence Tomography, IEEE Journal of Selected Topics in Quantum Electronics, Vol. 10, N. 3, May/June 2004 pp. 636-642.
4. T. Xie, H. Xie, G. Fedder and Y. Pan, "Endoscopic optical coherence tomography with new MEMS mirror", Electronics Letters, 16 October 2003, Vol. 39 No. 21, online #20030998.
5. L. Fan, W. Piyawttanametha, M. Wu, A. Aguirre, P. Herz, Y. Chen, and J. Fujimoto, "High Resolution 3D OCT Imaging with a MEMS Scanning Endoscope", MOEMS and Miniaturized Systems V, Proceedings of SPIE Vol. 5719, 2005 pp. 140-143.
6. W. Jung, D. McCormick, J. Zhang, N. Tien, and Z. Chen, Optical coherence tomography based on high-speed scanning MEMS mirror, Proceedings of SPIE Volume 5690, April 2005, pp. 342-348.
7. V. Milanovic, G. Matus and D. McCormick, "Gimbal-Less Monolithic Silicon Actuators for Tip-Tilt-Piston Micromirror Applications, IEEE Journal of Selected Topics in Quantum Electronics, Vol. 10, No. 3, May/June 2004, pp. 462-471.
8. V. Milanovic, Multilevel Beam SOI MEMS Fabrication and Applications, Journal of Microelectromechanical Systems, Vol. 13, No. 1, February 2004, pp. 19-29.
9. S. H. Yun, G. J. Tearney, B. E. Bouma, B. H. Park, and J. F. de Boer, "High-speed spectral-domain optical coherence tomography at 1.3 mm wavelength." Optics Express **11** (26), 3598-3604 (2003).
10. J.W. Judy and R.S. Muller, "Magnetically Actuated, Addressable Microstructures" *IEEE JMEMS*, vol. 6, no. 3, September 1997, pp. 249-256.
11. J. J. Bernstein, W. P. Taylor, J. D. Brazzle, C. J. Corcoran, G. Kirkos, J. E. Odhner, A. Pareek, M. Waelti, and M. Zai, "Electromagnetically Actuated Mirror Arrays for use in 3-D Optical Switching Applications", IEEE JMEMS, Vol. 13. No. 3, June 2004, pp 526-535.
12. L.K. LaGorce, O. Brand, and M.G. Allen, "Magnetic Microactuators Based on Polymer Magnets", IEEE JMEMS, Vol. 8, No. 1, March 1999, pp. 2-8.
13. W. Y. Oh, S. H. Yun, B. J. Vakoc, G. J. Tearney, and B. E. Bouma "Ultrahigh-speed optical frequency domain imaging and application to laser ablation monitoring" APPLIED PHYSICS LETTERS 88, 103902, 2006.

MEMS SPATIAL LIGHT MODULATOR FOR OPTICAL MASKLESS LITHOGRAPHY

V. A. Aksyuk, D. López, G.P. Watson, M.E. Simon, R.A. Cirelli, F. Pardo, F. Klemens, A.R. Papazian, C. Bolle, J.E. Bower, E. Ferry, W.M. Mansfield, J. Miner, T.W. Sorsch and D. Tennant

Bell Labs, Lucent Technologies, Murray Hill, NJ USA

ABSTRACT

128x512 arrays of electrostatically actuated piston micromirrors with 3 μm and 5 μm individual pixels and 90% optical fill factor are realized using a polysilicon surface micromachining process with 5 structural layers and 130nm minimum features. To modulate Deep Ultraviolet (DUV) radiation for Optical Maskless Lithography application, continuously controlled vertical motion of 80nm is achieved at less than 4V. The micromirror response time is less than 10 microseconds. A wiring layer is used to actuate subarrays of up to 128x128 mirrors at the same time in linear gratings, checkerboards and other patterns.

INTRODUCTION

One of the critical technical barriers in the area of Optical Maskless Lithography (OML) for IC fabrication[1,2] is development and implementation of the appropriate beam modulation technology. A MEMS Spatial Light Modulator (SLM) can provide a solution for this challenge, and enable systems to achieve sub 50nm critical dimensions (CD) with throughput of at least one 300mm wafer level per hour.

MEMS SLMs for OML with larger, tilt pixels (16 μm x 16 μm) and up to 1M-pixel size have been previously developed[2] and have found successful commercial application in mask writing. Such devices are built out of Aluminum on top of electronic circuitry supplying ~25V drive signals. However, SLMs with pixels smaller than 5 μm are needed to build the next generation maskless lithography tools capable of 50nm CD[3]. High frame rates (10kHz) and pixel counts (10 Million pixels) are needed to achieve high throughput. Compared to tilt micromirrors, piston micromirrors are easier to reduce in size while maintaining low actuation voltage, and piston-type SLM provides additional capabilities for OML, such as strong phase shifting[4]. Pixels characteristics need to be stable over long times, many cycles of operation and under exposure to UV light. Polysilicon often provides better mechanical performance and stability compared to Aluminum, which may be subject to creep and fatigue. We have built and tested a standalone polysilicon MEMS technology building block, demonstrating performance consistent with these application requirements and scalable to very large pixel counts.

To achieve large pixel counts, electronic drive circuits have to be provided for each mirror. Low voltage operation is absolutely critical, since we have to use high density, low voltage CMOS drivers to fit within the extremely small footprint of our pixels. While the ultimate goal is to hybridly integrate the polysilicon MEMS with drive electronics to address each mirror individually(to be reported elsewhere), to test the MEMS technology we have incorporated a wiring layer to deliver the electrical drive signal without integrated drivers. We have pre-wired our micromirrors and tested them in lines, gratings, checkerboards and other patterns actuated by only a few distinct signals with up to 8192 mirrors connected in parallel to a single wire.

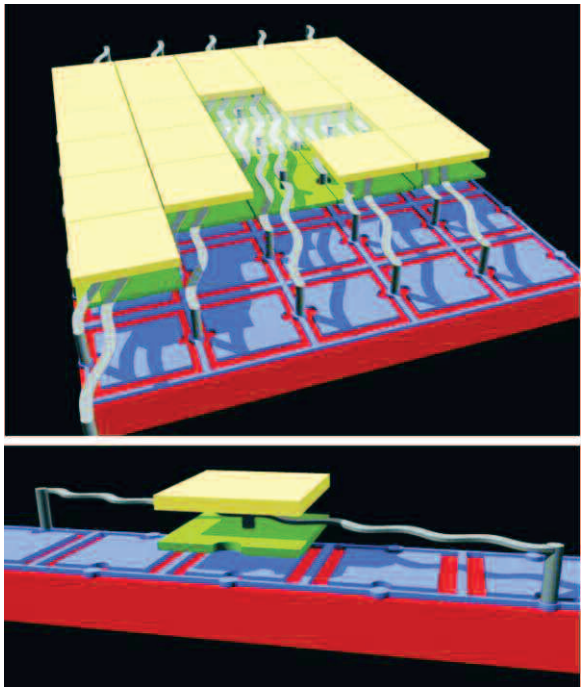

FIGURE 1. Conceptual drawing of the MEMS mirror array and the single mirror. Yellow – reflector, gray – spring, green – movable electrode, blue – fixed electrode and ground.

MICROMIRROR ARRAY DESIGN

Figure 1 shows a conceptual drawing of our MEMS array. Each pixel is actuated electrostatically by applying voltage to a lower fixed electrode, with ground lines in between pixels. The mirror is supported at its center by an elastic, doubly-clamped spring. This spring provides the mechanical restoring force as well as the electrical contact to the ground lines. Even for springs as thin as 100nm, their length has to span over several pixels to provide the required compliance for low voltage operation. Each spring is electrically and mechanically connected to an upper electrode underneath it, which maximizes the force achieved by the actuator by bringing the electrodes closer and increasing the area. It also shields the spring from the electric fields of neighboring electrodes by completely surrounding them with structures at the ground potential. Springs of neighboring pixels are interdigitated in between the upper electrodes and the mirrors; by design there is enough room for the required vertical motion without any of the parts coming in contact. With this approach we achieve the compliant structure needed for very small mirrors without resorting to extremely thin layers or very soft, unconventional materials. Not shown, under the fixed electrodes, a polysilicon wiring layer insulated by the silicon nitride dielectric is used to bring the electrical signals to the lower electrodes from the probe pads on the periphery of the array.

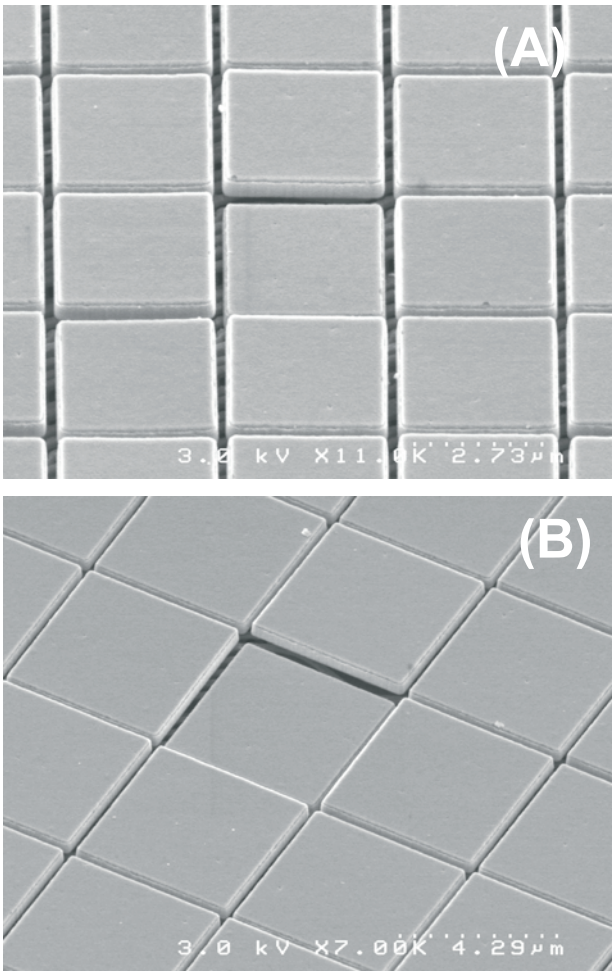

FIGURE 2. Scanning electron micrograph of the (A) 3 μm pitch and (B) 5 μm pitch MEMS mirrors in arrays. One mirror is snapped down for illustration. The top surface is planarized by CMP and coated with evaporated Al for high reflectivity.

To build the MEMS mirrors we use a fabrication process with 3 moving and 2 fixed polysilicon structural layers and 3 sacrificial Silicon dioxide layers. Layer thicknesses are 100 to 500nm for structural layers, and 400 to 700nm for sacrificial layers. Each layer is patterned using a 193nm scanner, achieving CDs of less than 130nm and interlayer alignment better than 50nm. The reflectors are planarized by chemical mechanical polishing (CMP) to produce a smooth, flat top surface. The structures are then freed by etching the sacrificial material (wet etch in 49% HF), and dried using a supercritical point CO_2 dryer. Coating the top surface of the mirrors with 300Å Aluminum reflective layer completes the device (Figure 2).

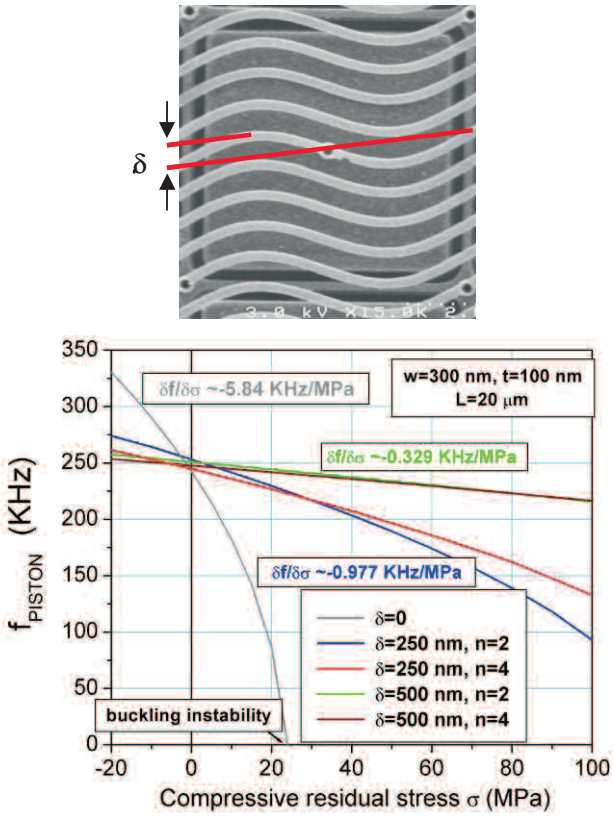

FIGURE 3. Undulating springs (top) reduce sensitivity to residual or induced stress, as illustrated by the FEA analysis (bottom). The pixel size is 5μm and "n" is the undulation frequency.

The lateral undulations ("wiggle") in the springs are designed to provide effective strain relief. In a linear elastic regime, the piston resonance frequency $f_{PISTON} \propto \sqrt{K}$, where is K is the linear stiffness of the spring. Figure 3 shows finite element analysis of the f_{PISTON} as a function of the compressive residual stress for a case of a 5μm mirror with different spring undulations. The springs, 300nm wide, 100nm thick, 20μm long, are clamped at both ends, with the mirror attached in the middle. For straight beams ($\delta = 0$) the frequency shows a strong stress dependence and the buckling instability appears at σ = 23MPa as evident by the frequency going to 0. As the in-plane undulation δ is increased, the effect of the residual stress is reduced and the buckling instability is pushed to larger stress values. For $\delta > w$ the number of periods n of the undulation within the spring length does not significantly affect the stress dependence of the frequency.

Using the same mask set, three lots with different layer thicknesses were fabricated – the spring thickness t and the electrode gap g were (t, g): (100nm, 460nm), (180nm, 690nm), and (110nm, 420nm). Each lot contained 36 design variations, 18 each for 3μm and 5 μm pitch. The spring length for 3μm mirrors varied from 12 to 30μm, the spring length for 5 μm mirrors varied from 20 to 50μm. Nominal spring widths were between 130nm and 460nm. Only small variations of the spring width for each particular length were made, since each spring footprint has to be equal to the mirror area. The longest springs were the narrowest. Other layout variables, such as spring undulation and mirror fill factor, were generally found not to have any significant effect.

All devices were successfully released and dried with all mirrors intact. The deliberate almost 3-decade variation of spring stiffness had a profound effect on actuation voltage and initial mirror height variation, as described below. In particular, the devices in the lowest decade typically showed signs of lateral stiction or had too much height variation after the release to be useful. On the remaining devices we have observed high moving mirror yields with few stuck mirrors, as verified by actuating subarrays of up to 128x128 mirrors. For the devices on the stiff end on the spring design, less than 10 visibly bad mirrors out of 65,000 were typical.

MICROMIRROR ARRAY PERFORMANCE

The piston motion induced by applying a voltage to the lower electrodes was measured by a Wyco NT3300 optical profiler operating in phase shifting interferometry mode, producing height profiles such as shown in the inset in Figure 4. In this case, a device designated A2 with 21μm long, 110nm thick and 150nm wide springs was activated at 3.9 V. The pre-wired pattern was a group of 32 mirrors that form an 8 mirror by 8 mirror alternating line and space array. After baseline removal, vertical position data is extracted from the center of each mirror for a series of voltages. The current at each applied voltage was much less than 1 nA, indicating that essentially no voltage drop should occur except at the electrodes themselves.

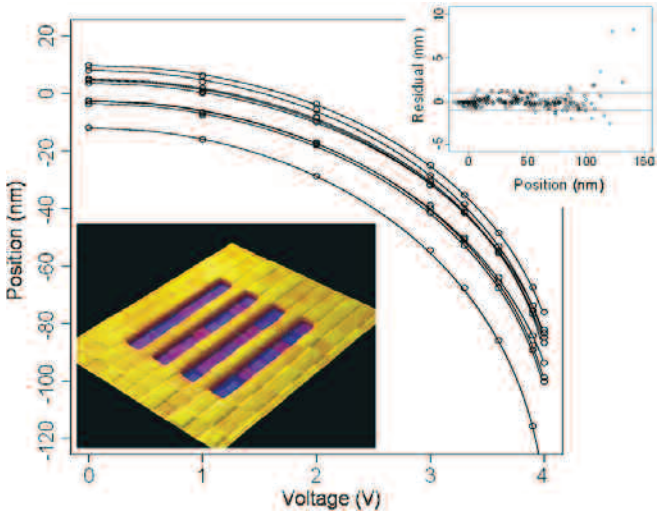

FIGURE 4. Piston motion as a function of applied voltage. Lower inset shows an optical profile of a pattern with 32 actuated mirrors. Top inset shows the fitting residual errors.

To calibrate the mirrors, each position (z) versus voltage (V) data set is fit by a non-linear least squares method to the equation:

$$V \quad \sqrt{(\ -z_0 K\ -z g^2}\ ,$$

where K is a constant that includes the spring stiffness, g is the initial electrode-electrode gap, and z_0 is the measured mirror piston position at 0 V. The parameters K and g are allowed to vary for each mirror. This equation is based on a simple 1-dimensional spring and an idealized parallel plate capacitor models, yet it fits the trends remarkably well; Figure 4 shows a plot of the measured piston motion versus voltage for 10 mirrors from the device A2 and curves representing the data fit. The second inset in Figure 4 is a plot of the difference between the data and the fit position versus piston position for over 300 points taken from device A2. For the majority of data, the difference is less than 1 nm. We went up and down in voltage several times, taking separate measurements, thus low residuals demonstrate high accuracy and repeatability of the mirror motion.

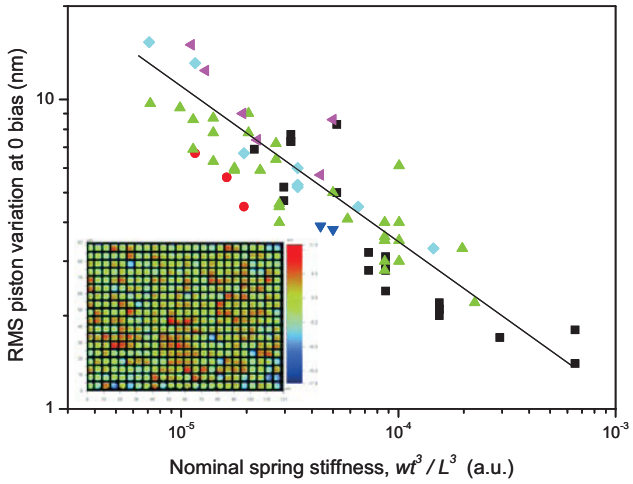

FIGURE 5. Initial mirror position variation as a function of design spring stiffness. Results from 3μm and 5μm mirror pitch designs from 78 die across three lots shown. The line for visual reference shows a square-root relationship. The inset shows an example of optical profiler data.

As evident from the Figure 4, a significant variation in mirror positions exists, affecting their calibration curves and reducing the overall dynamic range of the SLM. This 0V spread was found to have a near-normal distribution for the majority of the devices, except the ones with stuck mirrors. It can be characterized by a single number, the RMS position variation, and was found to vary systematically with the nominal design spring stiffness, Figure 5. Further study is under way to understand and reduce the variation.

Although no detailed quantitative analysis has yet been performed, the piston range and actuation voltage scaled qualitatively in an expected way across multiple designs. The piston range was roughly proportional to the electrode gap, and the voltage increased with both the gap and the spring stiffness, resulting in a large variation, from less than 1V to over 60V, as expected.

In order to study the dynamic response, 405nm laser light was projected onto SLM devices that were actuated with a square wave voltage source. These devices were pre-wired so that 64 alternating rows, each with 128 mirrors moved with the voltage source. The resulting diffraction pattern consisted of a square array of spots with additional spots that formed only when the alternating mirror pattern was activated. A fast Si photodetector was placed in the beam path of such a modulated first diffraction order spot and the photocurrent was recorded. Figure 6 shows the dynamic response of the same A2 mirror devices. The 0-95% ON time, measured at the applied voltage step up from 0 to 3.0 V is less than 10μs, and the 100-5% OFF time, is even shorter at about 2μs. The experiment was performed in air at atmospheric pressure and room temperature. Small oscillations of the curve suggest the piston mode resonance frequency around 300KHz.

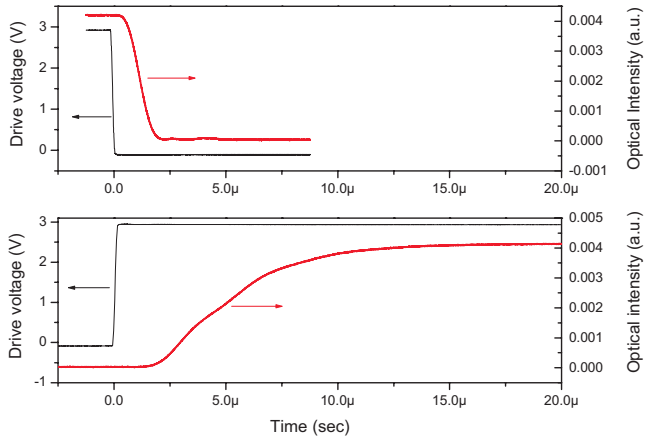

FIGURE 6. Dynamic response. "Off" time 2μs (upper panel),"On" time 10μs (lower panel).

CONCLUSION

We have built and tested a standalone polysilicon MEMS technology building block consistent with OML requirements: arrays of 128x512 pixels with 3 and 5 μm pitch, 90% optical fill factor, Al coating for high reflectivity, accurate and repeatable 80nm stroke at 4V applied voltage, acceptable uniformity, response time of 10μs. Our fabrication process is based on optical lithography and we can scale up to a 10M-pixel array within the tool capability. Future work will focus on improving uniformity and producing a device suitable for hybrid integration with IC drivers. More broadly, while smaller, individual MEMS devices have been built using E-beam lithography, this work demonstrates order-of-magnitude improvement in density for large arrays of multi-layer devices enabled by high-resolution optical lithography.

ACKNOWLEDGEMENTS

This material is based upon work supported by DARPA under SSC SAN DIEGO Contract No. N66001-04-C-8028

REFERENCES

[1] H.Lakner, P.Duerr, U. Dauderstaedt, W. Doleschal, and J. Amelung, Proc. of SPIE vol. 4561 (2001)

[2] T.Sandstrom, T. Fillion, U. Ljungblad, and R. Rosling, Proc. SPIE 4562, 38 (2002)

[3] Y. Shroff, Y. Chen, and W. Oldham, Proc. SPIE 5037, 550 (2003)

[4] G.P. Watson, V. Aksyuk, D.M. Tennant and R.A. Cirelli, J. Vac. Sci. Technol. B 22(6), Nov/Dec 2004

AN OPTICAL MICROSYSTEM FOR DISPLAYS

Bret Winkler, Dennis Elkins, Allen Tanner
Evans & Sutherland Corporation
Salt Lake City, Utah USA

Victor Ramsey, Randy Cuff, Leland "Chip" Spangler
Aspen Technologies
Colorado Springs, Colorado USA

ABSTRACT

This paper describes an optical microsystem for ultra-high pixel count, very large area, laser-illuminated projection displays that address a number of limitations with existing displays. The microsystem consists of CMOS integrated circuits which are flip chip mounted on a surface micromachined MEMS die. This subassembly is mounted into a custom ceramic package and the microstructures are then released using a dry process. Details of the system application, device fabrication, packaging, testing and reliability are presented.

INTRODUCTION

Visual electronic displays are one of the most powerful methods of providing information and entertainment to humans. While most computer displays, televisions and digital theater projectors can create satisfactory images with approximately one million pixels, displays used in applications such as aircraft flight simulators and planetariums must be able to project very high resolution images over very large areas. Some simulation systems require eye-limited resolution. This requires systems that can display 32 million or more, full-color, grey scale pixels at high refresh rates.

Projection displays have been manufactured for a number of years using conventional Cathode Ray Tube (CRT) technology [1]. Up to eight of these CRT-based projectors must be located around the periphery of the display screen to achieve high resolution images over the very large area. These individual projectors must then be spatially, temporally and chromatically synchronized, creating significant image processing requirements along with significant overhead to resynchronize the system on a regular basis. These distributed display systems also create challenges for installation and they are subject to limitations in brightness, contrast ratio and chromatic intensity.

More recently, Liquid Crystal Display (LCD) and MEMS-based projectors using Digital Mirror Device (DMD) technology [2] have been introduced with subsequent improvement in optical performance. High pixel count systems based on these technologies still require several projectors to be placed around the image screen however, and thus are subject to the same synchronization and installation issues that CRT-based systems have. Since CRT, LCD and DMD-based displays are two-dimensional arrays, in order to increase the size of the display and maintain spatial resolution, the number of pixels must increase by a *squared* factor. Projectors that use these technologies thus have practical limitation of a couple million pixels.

To address the limitations inherent in these two-dimensional projectors, a system that uses a *linear* array of pixels combined with a scanning mirror allows pixel counts to be scaled to much higher levels. A MEMS-based scanning projection display system using a reflective mirror array was proposed by Petersen [3] and subsequently systems based on a linear array of diffractive optical elements [4], [5] have been demonstrated. The Grating Light Valve (GLV) is an example of a MEMS device that uses diffraction to modulate the light intensity in display applications.

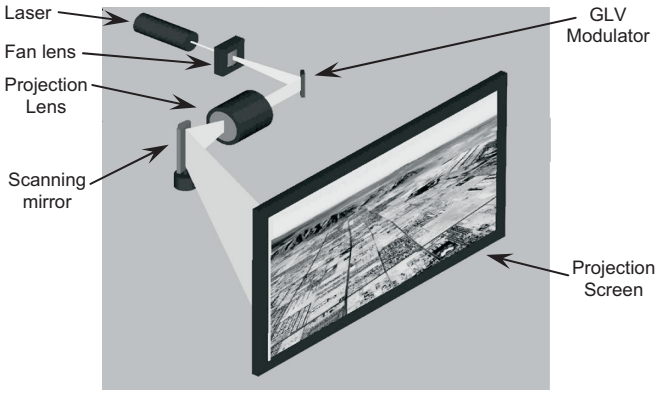

Figure 1. *Projection display system based on a GLV modulator, a laser and a scanning mirror. Actual displays combine signals from a red, green and blue laser and three GLV modulators to create the full color display.*

To create ultra-high resolution, large area, scanned mirror displays, not only does the number of pixels have to increase but the switching speed of the pixels must be increased. The need for high switching speed in these high resolution, scanned projector systems precludes the use of mirror arrays such as the DMD which are generally too slow.

SYSTEM AND DEVICE DESIGN

This paper presents a GLV-based optical microsystem that is a key component in a scanned laser projection display that addresses limitations of existing display technologies while providing greater system flexibility and improved optical performance with higher contrast ratio, brightness and finer resolution. At the same time, the system consumes lower power and offers lower system installation and maintenance costs. The display is designed to project a full-color, 16-bit grey scale, 48 bits per pixel, ~32 million pixel (4,096 rows x 8,192 columns) images at a 60 Hz refresh rate over very large areas.

The system (Figure 1) employs a custom graphics processor and optical projection system along with custom lasers at three different wavelengths, red (448nm), green (532nm) and blue (631nm). The custom lasers each project about 6 to 12 watts of optical power through a lens system that fans the light into a line and focuses it onto one of three GLV modulators at an angle of about 10 degrees to the optical axis. The diffracted light is then

selected and focused onto a scanning mirror and additional lens systems project this light onto the display screen. Data is provided to the GLV modulator synchronously with the scanning mirror to sweep the image over the display screen.

The GLV modulator consists of a linear array of clamped-clamped silicon nitride beams which are suspended over a conductive surface. The beams have a top reflective surface of aluminum and are 3.2 microns wide on a 3.7 micron pitch. The beams are about 200 microns long between the anchors.

Alternate beams are connected to a common "bias" potential while the other beams are individually connected to signal lines. The active beams are deflected by the potential that is applied to them relative to the conducting layer below the beams. When the potential on the bias and active beams is the same, the pixel is in the reflective state and no light is coupled into the projection optics (Figure 2a). When the active beams are brought to ¼ of a wavelength below the bias beams (Figure 2b), all of the light from the both the +1 and -1 diffracted order is captured by the projection optics. Light from the other diffracted orders is blocked and not projected.

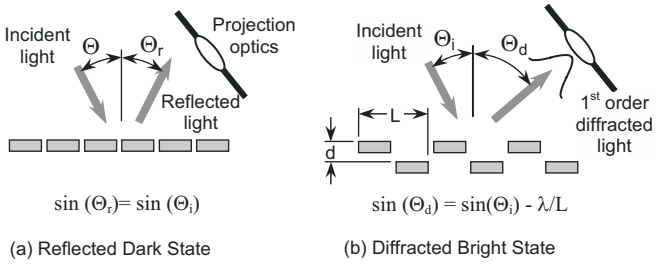

Figure 2. *To project a dark pixel (a), the beams are in the reflective state and the light does not couple into the projection lens. To project a bright pixel (b) the active beams are lowered relative to bias beams so the first order diffractive light couples into the projection optics.*

To achieve grey scale, the active beams are held at a position less than ¼ of the wavelength of the incident light. This acts as a valve that allows some of the light to reflect and some to go into the +1 and -1 orders which means that only a portion of it is coupled into the projection optics. Since 16 bits of grey scale are desired, the active beams in each pixel must be positioned and held with a resolution of 0.002 nm relative to the bias beams in that pixel.

In order to project 8192 columns at a 60 Hz refresh rate, the active beam position must be changed in less than 1 microsecond. Since there are 4096 pixels in the device, the 16-bit analog data must be provided to the microsystem at a rate of over 2 x 10^9 analog data samples (16-bit) per second per color. These specifications were the primary factors in the design of the electrical portion of the device.

Partitioning decisions are important in microsystem design. Size and costs issues make it impractical to use a package that has 4096 input pins to connect to the 4096 pixels. The number of package I/Os can be reduced with time division multiplexing but this requires circuitry to demultiplex the high-speed data prior to applying it to the active beams. A cost/yield analysis has lead to the choice of multiplexing the analog data at a rate of 32:1 which reduces the number of input lines to 128. The partitioning analysis also lead to the decision to divide the multiplexing task over eight separate pretested "driver" die that are flip chip bonded directly onto the GLV modulator die with the beams. This means that each "driver" die has 16 inputs to control 512 pixels.

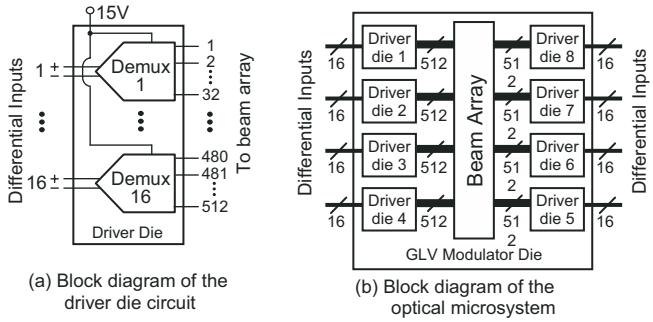

Figure 3. *Block diagram of the driver die circuit (a) and entire GLV modulator assembly (b).*

The 128 analog inputs that are multiplexed into the microsystem are differential signals with a 1 volt swing. A differential input signal path was chosen to help maintain the 16-bit analog precision (~80 microvolts) that is needed to obtain the desired optical grey scale. This analog data must arrive at a rate of nearly 16 x 10^6 samples per second per pixel. Once the differential analog signal is demultiplexed, it is level shifted to a 0 to 15 volt single ended line with 200 microvolt resolution. A sample and hold circuit maintains the potential so that it can be clocked onto the active beams with the proper timing. Given the material properties and internal stress in the nitride beams and their physical geometry, 15 volts is sufficient to pull the beams down at least 210 nm below the bias beams. An analysis of beam mechanics and optical performance is given in [6].

FABRICATION AND PACKAGING

The partitioning decisions require two different wafers to be fabricated and assembled in a custom package with a complex assembly process. The driver die wafers are fabricated in a conventional 0.8 micron CMOS process with two metal layers on 6 inch wafers. After probe testing, they are prepared for solder bumping with an electroless Ni-Au under bump metallization (UBM) process. These pads are then bumped with eutectic Pb-Sn solder to form flip chip interconnections about 80 microns in diameter on a pitch of 200 microns. The bumped wafers are then singulated into die that are 6.9 mm x 5.3 mm in size.

The GLV modulator die is fabricated on 6 inch wafers with a surface micromachining process that uses a sacrificial layer of polysilicon. The wafer fabrication begins by depositing a thin TiN layer that is patterned to be just under the beam array. A polysilicon sacrificial layer is then deposited over the TiN layer and patterned. Subsequently a thin silicon nitride and a thin layer

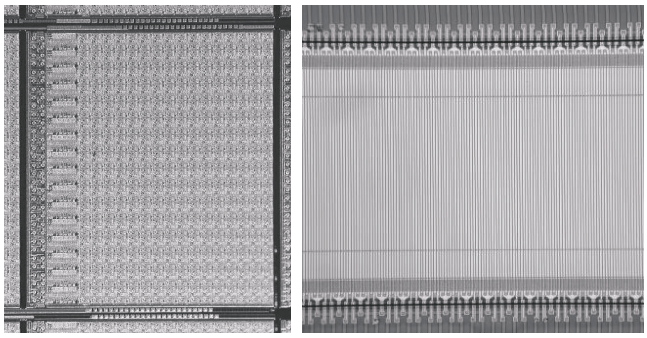

Figure 4. *Photograph of the CMOS driver die (a) and a portion of the beam array on the GLV modulator die (b).*

of aluminum is deposited and patterned to form the beams. Another thicker layer of aluminum is used to connect the aluminum on the beams to the pads that will accept the flipped driver die. This thick aluminum also is used to form the wirebond pads and the interconnection for the driver die inputs.

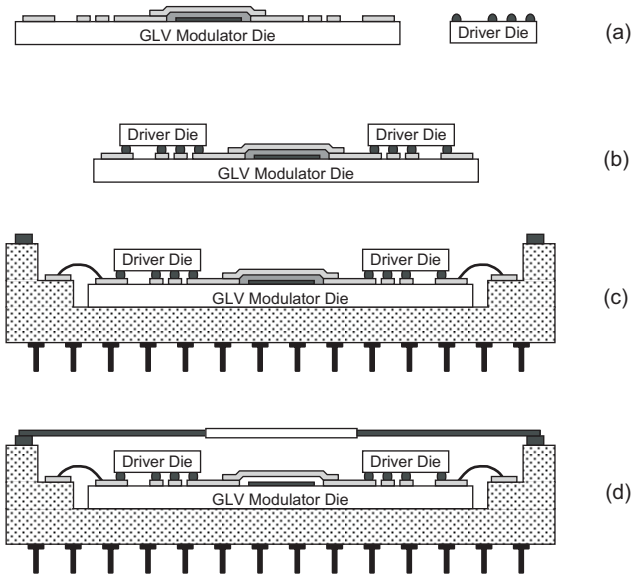

Figure 5. *Fabrication and packaging for the optical microsystem. (a) CMOS driver die fabricated and solder bumped and GLV modulator die fabricated with nitride and aluminum beams over a poly-Si sacrificial layer. (b) Driver die are flipped onto the GLV modulator die. (c) The GLV die assembly is packaged (d) The poly-Si sacrificial layer is etched and the windowed lid attached.*

After wafer fab, a photoresist layer is patterned and hard baked on the wafer to protect the unreleased beams. This final resist layer serves two functions. Another electroless Ni-Au UBM process is needed, this time on the GLV modulator die, to provide a wettable surface for the driver die flip chip bumps. The final resist layer keeps this metal from being plated on the beams and the wirebond pads. This final resist layer also protects the very thin aluminum on the unreleased beams from being damaged during the saw and clean process. After dicing, this final resist layer is stripped from the GLV die individually using a specially formulated wet processing sequence that preserves the optical properties of the aluminum. The final GLV modulator die size is about 31.8mm x 19mm.

To assemble the GLV modulator, the solder bumps on the driver die are coated with a very small amount of solder flux. Eight of these die are aligned and placed on the GLV modulator die. The assembly is then reflowed which allows the solder on the driver die to wet to the adjacent pads on the GLV die forming the desired electrical and mechanical connection. The GLV die assembly is completed by cleaning the flux and underfilling the flipped driver die.

This GLV die assembly is then attached into a custom aluminum nitride (AlN), 470 pin grid array (PGA) package using a "MEMS-grade" adhesive. AlN was chosen for the package because it has much higher thermal conductivity (~200W/mK) and a better CTE match (~4.6 ppm/^{o}C) to silicon than conventional alumina ceramic, despite its higher cost and more difficult manufacturing process. The GLV modulator package (Figure 6) has many internal routing layers to allow the input signals to maintain their differential layout and to allow these signals to be fully shielded by internal metal which is tied to ground potential. This conservative design reduces the chance that noise could be coupled onto the sensitive analog input lines. The package has a recessed die cavity with four wirebond tiers. A Kovar seal ring is brazed on the top of the ceramic for subsequent lid attach.

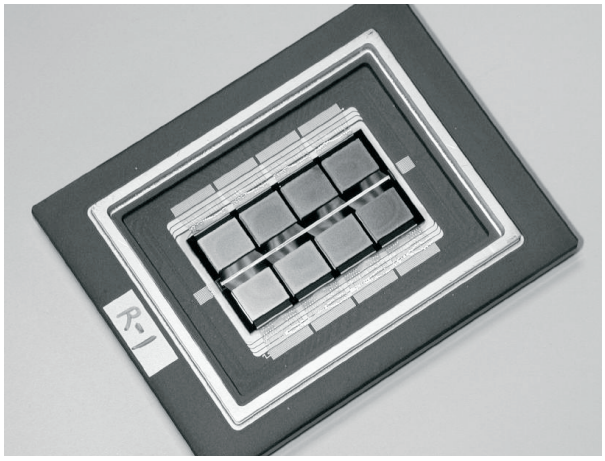

Figure 6. *Photograph of the completed optical microsystem without the seam sealed lid. The strip in the middle of the assembly is the linear beam array.*

After the GLV modulator assembly is die attached into the AlN package, more than 500 wirebonds are placed on two sides of the die to provide electrical interconnection between the package and the pads on the GLV die assembly. The entire GLV assembly is then placed in a xenon difluoride etch system that allows the XeF_2 gas to penetrate the slots between the beams on the GLV modulator die. This releases the beams by selectively etching the underlying polysilicon sacrificial layer (Figure 7). The xenon difluoride does not appreciably attack the other materials used in the assembly. One of the many benefits of this "post-assembly" release process is that there is a reduced chance for microstructure damage during manufacturing.

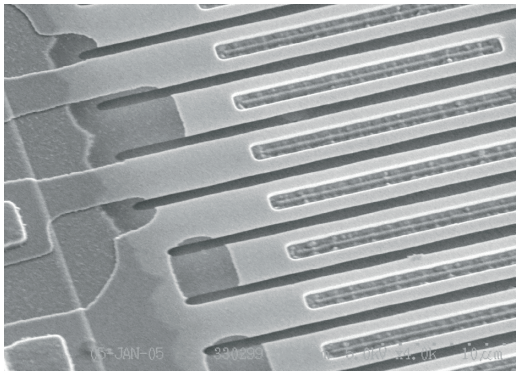

Figure 7. *Photograph of the beam ends after etching the sacrificial polysilicon layer in XeF_2.*

After the beams are released, a Kovar lid with a highly polished glass window is seam sealed onto the seal ring of the PGA package to form a hermetic seal. The glass window has antireflective coatings on both sides. Meeting the detailed optical requirements, including the design of the glass and its installation in the Kovar lid, represented a significant engineering effort to minimize optical distortion.

TESTING

After GLV modulator package assembly, the device is mounted to a heat sink which dissipates the power from the driver die and the incident absorbed optical energy. An interface board provides electrical connection and mechanical mounting so it can be precisely aligned. A variety of different test setups is used to evaluate various aspects of device operation. The most basic test involves using a single color laser on an optical bench with the appropriate lenses and optical filters along with a scanning mirror (Figure 8). Full dynamic testing involves more sophisticated image generators and optical setups.

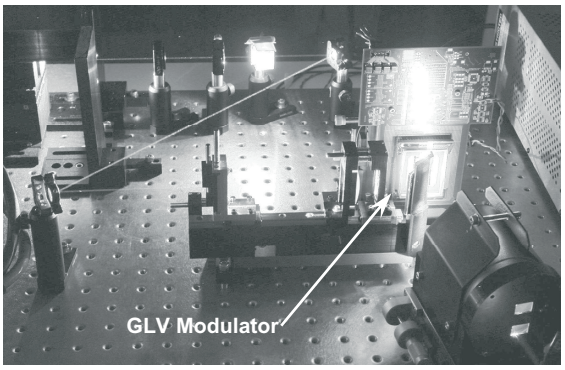

Figure 8. *Photograph of the optical microsystem on a test bench being tested with a green laser.*

With this simpler setup, the pixels can be cycled from an all "on" to all "off" state by actuating all active beams simultaneously. As shown in Figure 9, the amount of light coupled into the first diffracted order increases as predicted with voltage applied to the active beams. The light intensity peaks at around 13 to 14 volts when the "bias" beams and conductive under layer are held at ground potential. A contrast ratio of greater than 3000:1 is obtained which is a factor of 6 better than other projection displays. The non-linear response is compensated for by the image processing system as it applies the appropriate voltages to achieve a linear grey scale. Since one device design is used in all three color channels, each microsystem must be individually aligned and calibrated in the system.

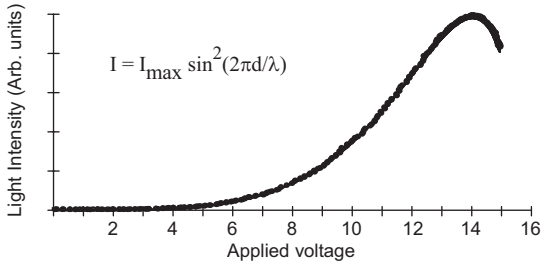

Figure 9. *Measured light intensity diffracted into the first order as a function of voltage applied to the active beams [6].*

Another advantage of the GLV structure is the very fast pixel response time. This speed is what allows a linear array of elements to be used in conjunction with a scanning mirror. Effectively, each GLV pixel is modulated at a speed that allows it to project an entire row of the display during each refresh cycle. The switching speed for a pixel in this device has been measured to be about 150 nsec from the full on or "bright" state to the full off or "dark" state, but similar devices have been made that switch as fast as 20ns.

The reliability of displays for these high pixel count applications is critical. While the operating environment is usually confined to indoor conditions, thermal issues due to system-level power dissipation must be considered. Measurement of the resonant frequency of a microstructure is a good way to observe changes in mechanical properties. Figure 10 shows the resonant frequency of an array of beams before and after stress testing that consists of 110 cycles from 30°C to 150°C and 200 billion actuation cycles on each active beam. The ratio of pre- and post stress resonant frequency is very close to unity suggesting little change over the stress test conditions.

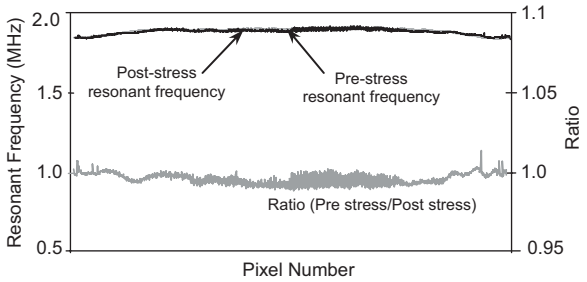

Figure 10. *Reliability data on the linear array of beams as measured by the change in resonant frequency after stress testing.*

CONCLUSIONS

An optical microsystem consisting of a linear array of diffractive pixels and analog signal processing circuitry in a custom package has been designed, fabricated, assembled and tested for ultra-high resolution displays. Partitioning analysis including design and technology tradeoffs, yield and time to market considerations has motivated a multiplexed data input strategy along with a multi-die flip chip assembly process. The design takes advantage of the highly selective nature of a dry XeF_2 release process to allow the microstructures to be released as one of the last steps in device assembly. The optical microsystem is currently in production and is a key component in a full color, scanning mirror, laser illuminated, 32 million pixel display, the highest resolution MEMS-based display ever made.

REFERENCES

[1] Evans & Sutherland Digistar3 laser projector product line (http://www.es.com/products/digital_theater/)

[2] Mignardi, M. A., et. al., "The DMD - An Micro Optical Electromechanical Device for Display Applications," in *MEMS and MOEMS Technology and Applications*, P. Rai-Choudhry, Ed., Bellingham, WA: SPIE Press, 2000, pp.70-208.

[3] Petersen, K. E. "Silicon as a Mechanical Material", *Proc. IEEE*, Vol. 70, No. 5, May 1982, pg 447.

[4] Amm, D.T., Corrigan, R.W., "Grating Light Valve Technology: Update and Novel Applications," *Proc. Society of Information Display Symposium*, Anaheim, CA, May 19, 1998.

[5] Solgaard, O., Sandejas, F.S.A., and Bloom, D.M. , "Deformable Grating Optical Modulator," *Optics Let.*, No.17, pp 688-691, May, 1992.

[6] Trisnadi, J. I., Carlisle, C.B., and Monteverde, R., "Overview and Applications of Grating Light Valve Based Optical Write Engines for High-Speed Digital Imaging," *Proc. Micromachining and Microfabrication Symp., Photonics West 2004*, San Jose, CA, Jan. 26, 2004.

DYNAMIC CHARACTERIZATION OF A LINEAR VARIABLE-CAPACITANCE MICROMOTOR

Nima Ghalichechian[1], Alireza Modafe[1], Alex Frey[1], Jeffery H. Lang[2], and Reza Ghodssi[1]
[1]MEMS Sensors and Actuators Lab (MSAL)
Department of Electrical and Computer Engineering, Institute for Systems Research
University of Maryland, College Park, MD USA
[2]Department of Electrical Engineering and Computer Science
Massachusetts Institute of Technology, Cambridge, MA USA
Email: ghodssi@eng.umd.edu

ABSTRACT

We report, for the first time, the dynamic characterization of a 6-phase, bottom-drive, linear, variable-capacitance micromotor (B-LVCM) supported on microball bearings. The motion of the micromotor was captured using a high-speed video camera, tracked using an image processing software, and analyzed to obtain the instantaneous velocity (11 mm/s), acceleration (1.9 m/s^2), and net force (0.19 mN) (all in amplitude) from the position data. This characterization provides an understanding of the dynamic behavior of both the variable-capacitance micromachines and the microball bearings on which they are supported.

INTRODUCTION

Microball bearing technology in silicon provides a reliable and robust support mechanism for the rotor of micromotors and microgenerators. Design and fabrication of the first-generation device, a 3-phase B-LVCM supported on microball bearings, was demonstrated in our previous work [**1**] . The primary application of the B-LVCM (shown in Figure 1) is long-range, high-speed, linear micropositioning. More important, this device provides a platform to investigate the mechanical properties of roller bearings in MEMS. The initial testing of the linear micromotor was reported in [**2**]. The development of the linear micromotor is based on several studies on the motor core components. An in situ non-contact experimental system was developed to study the frictional behavior of the microballs in the microscale regime. Static and dynamic coefficient of friction of stainless steel microballs and the silicon grooves, fabricated by anisotropic silicon etching using potassium hydroxide (KOH), were measured to be 0.01 and 0.007, respectively [**3**], compared to 0.01-0.08 reported for silicon-silicon structures [**4, 5**]. The dielectric constant and breakdown voltage of benzocyclobutene (BCB) low-k polymer, used as an electrical insulator for reducing parasitic losses, were measured and the effect of humidity on these properties was studied [**6**]. A fabrication process for integration of BCB film with wet etching of silicon using KOH was developed [**7**]. The electrical isolation of the electrodes from the silicon substrate in the previously fabricated device was achieved by a novel fabrication process (Embedded BCB in Silicon, or EBiS) to planarize isolated islands of low-k BCB polymer in silicon [**8**]. While a great deal of research has been conducted on the design and fabrication of micromachines, little work has been done on drive, control, test, and characterization of these machines. The dynamic characterization of the 6-phase micromotor including the measurement results of position, instantaneous velocity, acceleration, and the net force on the slider are presented in this paper.

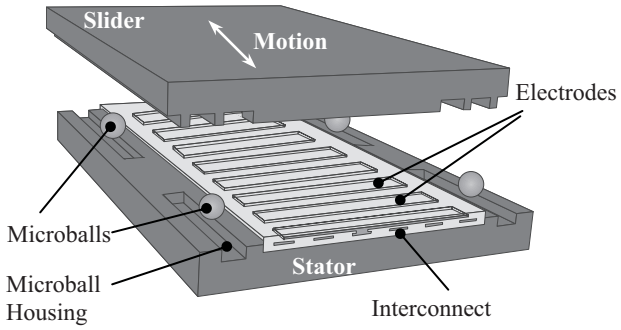

Figure 1: *Schematic 3D view of the bottom-drive, linear, variable-capacitance micromotor [1].*

DESIGN

Figure 1 shows a 3D exploded view of the linear micromotor supported on microball bearings. The micromotor comprises three major components: stator, slider, and microballs. Unlike the (successfully tested) conventional VCMs that were side-drive [**9**], this micromotor has a bottom-drive design which increases the active area and force of the motor. The microball bearing design provides the mechanical support for maintaining a uniform air gap that was not possible in conventional (side-drive or top-drive) VCMs with center-pin or flange designs.

Two new technologies were implemented in the development of the linear micromotor: (1) microball bearing technology in silicon as a support mechanism and (2) BCB low-k polymer as an insulating layer [**1, 2**]. The microball bearing technology results in stable, robust, and reliable mechanical support. The rolling microballs, sandwiched between the rotor and stator, results in less friction and wear than center-pin design and are more reliable and stable than gas-lubricated bearings. A conventional dielectric film of silicon dioxide (SiO_2) was replaced by a low-k (k=2.65) BCB polymer. This results in a reduced parasitic capacitance and an increased efficiency of the motor. BCB also exhibits less residual stress than SiO_2; therefore, the device has less curvature and the air gap is more uniform. The geometry specifications of the tested B-LVCM are shown in Table 1.

FABRICATION

The second-generation B-LVCM was fabricated with some modifications to the process of first-generation device. The fabrication process of the stator comprises the following steps: (1) deposit 3-µm-thick BCB island, (2) fabricate Cr/Au

interconnections and pattern photo-BCB to open vias, (3) fabricate Cr/Au electrodes and pattern photo-BCB passivation layer, and (4) pattern and etch trenches with deep reactive ion etching (DRIE) for housing the microballs. The slider fabrication process comprises a lithography step and a DRIE step to etch both trenches and poles. The yield of the Cr/Au metallization process was increased by replacing the original lift-off process with an etch process. Figures 2 and 3 show the fabricated stator and slider of the 6-phase micromotor, respectively.

Table 1: *Micromotor geometry specifications (electrodes refer to the stator and poles refer to the salient structures on the rotor).*

Parameter	Value
Electrode/pole width, μm	90/90
Electrode/pole pitch, μm	120/180
Electrode/pole number	84/36
Air gap, μm	26-34
Microball diameter, μm	284.5
Trench width, μm	290
Microball material	440C stainless steel

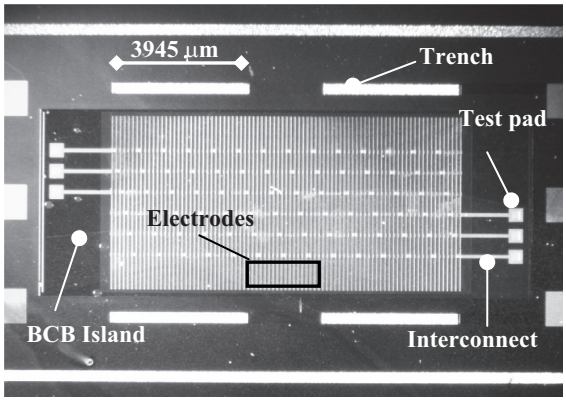

Figure 2: *Optical micrograph (top-view) of the 6-phase stator comprises three BCB layers, two metal layers, and four trenches for housing microballs.*

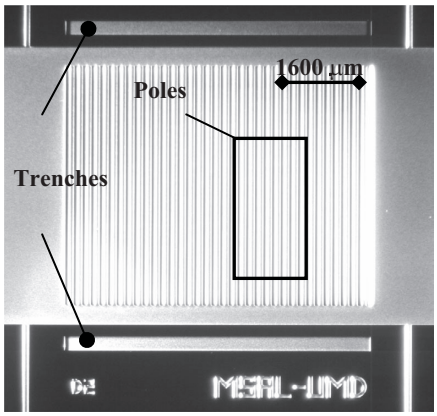

Figure 3: *Optical micrograph (top-view) of the slider showing poles and trenches etched into silicon substrate using DRIE.*

TEST SETUP

A new test-bed for the characterization of the micromotor was developed. Figure 4 shows the block diagram of the test

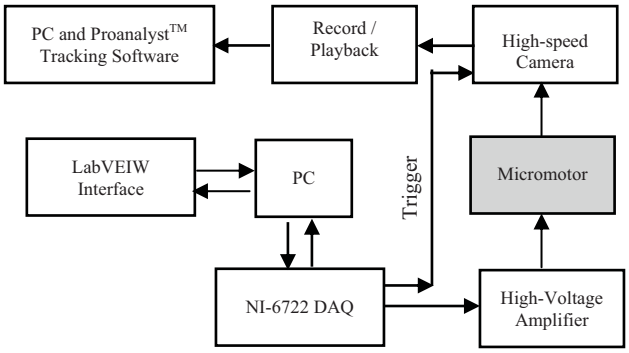

Figure 4: *Block diagram of the micromotor test station.*

station compromised of six-channel high-voltage actuation system, high-speed camera, and image processing division. Initially, the motion of the motor was captured using a 30-frame-per-second (fps) camera. The speed of a standard 30-fps camera was found to be low for capturing the transient response of the micromotor. Therefore, real-time measurement was performed using a low-noise, monochromatic, high-speed (635-1000 fps) video camera (MotionPro HS-3 from Redlake). This real-time measurement was preferred over conventional stroboscopic dynamometry techniques previously used for side-drive micromotors [**10**].

RESULTS

The micromotor is excited with six square-wave pulses. The first three phases are 120° out of phase. The remaining three phases have the inverse amplitude of the first three. This excitation configuration prevents charge build-up on the slider. Figures 5 and 6 show the displacement of the slider measured for an excitation frequency (f_e) of 10 and 20 Hz, respectively, and acquisition rate of 30-fps. Since the range of motion in this design, is limited to 3.4 mm, the direction of motion is changed (forward and backward) with a frequency of 1.5 Hz. This is done by switching the sequence of the phases. The saw-tooth behavior, shown in figures 5 and 6, is a result of the change in the direction of the motion.

The average velocity (V_{avg}) of the slider is given by

$$V_{avg} = 2Wf_e \quad (1)$$

where W is the width of an electrode or pole and f_e is the frequency of excitation voltage. The average velocity can be obtained from

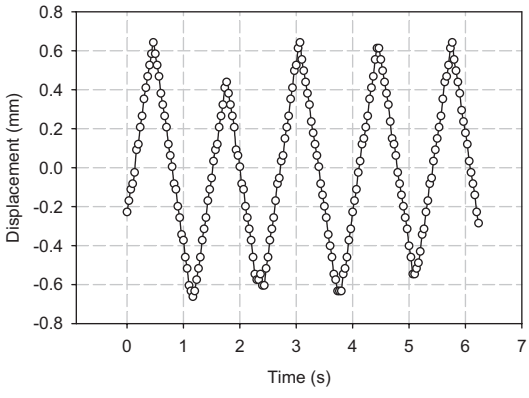

Figure 5: *Displacement of the slider when excited with 120 V, 10 Hz, six-phase, square pulses and measured using a 30-fps camera. The direction of the motion alternates with f_d=1.5 Hz.*

the slopes of the two graphs (Figures 5 and 6). Similar measurements were performed at 40 Hz and 80 Hz excitation. The results, summarized in Table 2, show a good agreement between predicted and measured values of V_{avg} for $f_e \leq 60$ Hz.

The transient response of the micromotor to 120-V square pulses was measured at 1000 fps while the camera's capture sequence was synchronized to the excitation voltage. Figure 7 shows the acceleration of the slider from rest position to a quasi-steady-state in about 20 ms (first region). After this period the machine continues with V_{avg} (second region), however, the instantaneous acceleration is not zero and the velocity changes in a periodic fashion.

Figure 8 shows the oscillation of the rotor position, *X(t)*, in a 130-ms window captured at 635 fps. In order to study the transient response of the machine, the linear component of the displacement signal, $(V_{avg} \times t)$, was filtered from Figure 8 and the remaining component, $(X(t) - V_{avg} \times t))$, was plotted in Figure 9. A damped sinusoidal transient response of the rotor can be seen in this figure. The instantaneous velocity and acceleration were computed from the first and second derivatives of the fitted curve (Figure 9) and are shown in figures 10 and 11, respectively. Figure 11 also demonstrates the instantaneous net force on a 0.1-gram slider (difference between lossless electromechanical and friction force) that is comparable to our models.

The micromotor was modeled as a mass-dashpot-spring system where *m* is the mass of the rotor, *b* is a dashpot coefficient representing the friction of microballs and silicon housing, and *k* is the spring constant of the electrode-pole variable capacitors. Solving the 2nd order differential equation of the system yields an oscillating function with decaying amplitude (underdamped solution). Thus, the dashpot coefficient *(b)* was extracted from the decay envelop of Figure 9 and found to be 6.25×10^{-4} *Kg/s.* This value can be used to characterize the tribological behavior of microball bearings in comparison to macroball bearings.

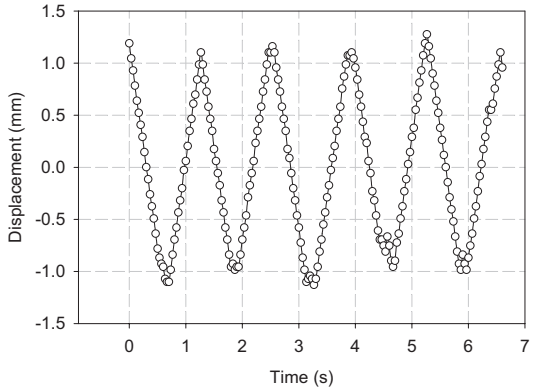

Figure 6: *Displacement of the slider when excited by 120V, 20 Hz, six-phase, square pulses and measured using a 30-fps camera (f_d=1.5 Hz).*

Table 2: *Comparison of predicted and measured average velocity of the micromotor.*

Excitation frequency (Hz)	Predicted average velocity (mm/s)	Measured average velocity (mm/s)
10	1.80	1.94±0.02
20	3.60	3.98±0.02
40	7.20	7.37±0.12
80	14.40	7.21-11.10

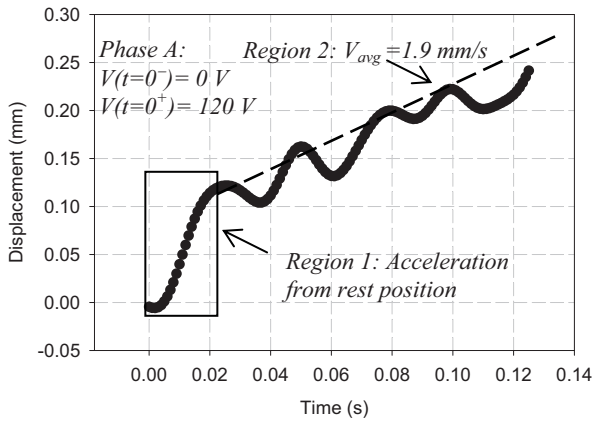

Figure 7: *Startup of the micromotor from rest position captured with a 1000-fps camera showing two regions of operation: (1) acceleration from rest position and (2) quasi-steady-state operation with average velocity of V_{avg} and local oscillations.*

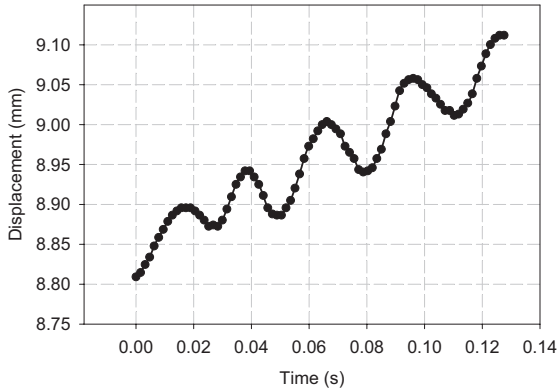

Figure 8: *Position of the slider, X(t), in 130-ms time window captured at 635 fps shows an average speed of 1.8 mm/s at 10 Hz excitation, as well as a sinusoidal oscillation.*

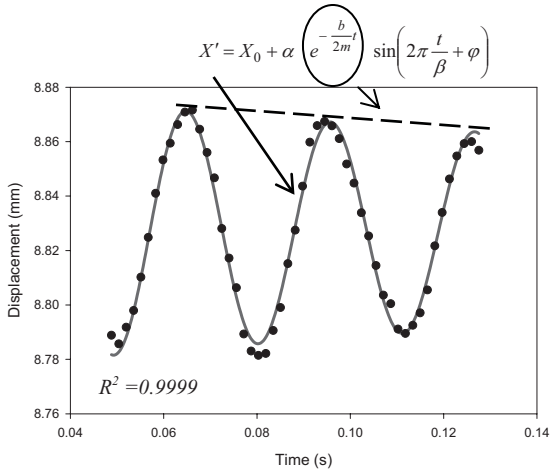

Figure 9: *Local rotor displacement, $(X(t) - (V_{avg} \times t))$, showing damped sinusoidal transient response. The standard coefficient of determination (R^2), describing how well the data points are fitted to the curve, was calculated to be 0.9999.*

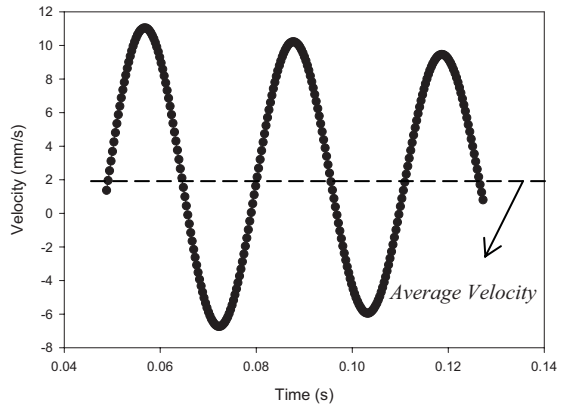

Figure 10: *Instantaneous velocity of the slider with damped sinusoidal form was computed from the curve fit to the position data (Figure 8-9).*

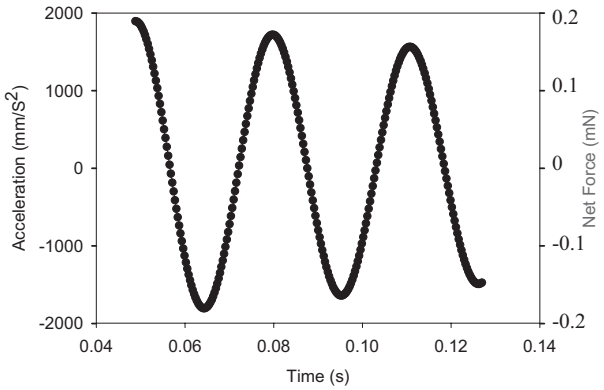

Figure 11: *Instantaneous acceleration and the net force of the slider with damped sinusoidal form were computed from the velocity data shown in Figure 10.*

DISCUSSION

The results from the position measurement using a 30-fps camera, summarized in Table 2, show a good agreement between predicted and measured values of the average velocity for the excitation frequency of $f_e \leq 60$ Hz. The motor does not pull into synchronization at 80 Hz or higher. This is due to a limited range of the linear micromotor (3.4 mm) and the change in the direction of motion. The micromotor does not have enough time to reach the synchronous speed before it reaches the end of the trench.

The period of the oscillations in the transient response measurements (Figures 7-11) was found to be independent of the frequency of excitation voltage. It is believed that this period is the result of the mechanical properties of the slider and the microball bearings support mechanism e.g. mass and damping. The measured net force, shown in Figure 11, is the result of the electromechanical force, produced by the machine, and the frictional force between microball bearings and the silicon housing.

CONCLUSION

The dynamic characterization of a bottom-drive, linear, variable-capacitance micromotor supported on microball bearings was presented. The slider position of the fabricated micromotor was measured using low- and high-speed video cameras; the instantaneous and average velocity, acceleration, net force, and the dashpot coefficient were extracted from the position measurement and are in good agreement with predicted values.

The characterization methodology presented in this paper is applicable to a wide range of micromachines and provides useful information for design, control, and understanding the dynamic behavior of variable-capacitance micromachines.

ACKNOWLEDGMENTS

This work supported by the Army Research Office through MURI Program under Grant No. ARMY-W911NF0410176, with Dr. Tom Doligalski as the technical monitor, the Army Research Lab under Grant No. CA#W911NF-05-2-0026, and the National Science Foundation under Grant No. ECS-0224361. The authors would also like to thank Nitta Haas Company, Japan for providing the CMP supplies.

REFERENCES

[1] A. Modafe, N. Ghalichechian, J. H. Lang, and R. Ghodssi, "A Microball-Bearing-Supported Linear Electrostatic Micromotor with Benzocyclobutene Polymer Insulating Layers," TRANSDUCERS '05, pp. 693-696, Seoul, Korea, 2005.

[2] A. Modafe, N. Ghalichechian, A. Frey, J. H. Lang, and R. Ghodssi, "Microball-Bearing-Supported Electrostatic Micromachines with Polymer Dielectric Films for Electromechanical Power Conversion," Power MEMS '05, pp. 173-176, Tokyo, Japan, 2005.

[3] T. W. Lin, A. Modafe, B. Shapiro, and R. Ghodssi, "Characterization of dynamic friction in MEMS-based microball bearings," *IEEE transactions on Instrumentation and Measurement*, vol. 53, pp. 839-846, 2004.

[4] K. Deng, W. H. Ko, and G. M. Michal, "A preliminary study on friction measurements in MEMS," TRANSDUCERS '91, pp. 213-218, San Francisco, CA, USA, 1991.

[5] K. Noguchi, H. Fujita, M. Suzuki, and N. Yoshimura, "The measurements of friction on micromechatronics elements," MEMS '91, pp. 148-153, Nara, Japan, 1991.

[6] A. Modafe, N. Ghalichechian, B. Kleber, and R. Ghodssi, "Electrical characterization of Benzocyclobutene polymers for electric micro machines," *IEEE Transactions on Device and Materials Reliability*, vol. 4, pp. 495-508, 2004.

[7] N. Ghalichechian, A. Modafe, R. Ghodssi, P. Lazzeri, V. Micheli, and M. Anderle, "Integration of Benzocyclobutene Polymers and Silicon Micromachined Structures Using Anisotropic Wet Etching," *Journal of Vacuum Science & Technology B*, vol. 22, pp. 2439-244, 2004.

[8] A. Modafe, N. Ghalichechian, M. Powers, M. Khbeis, and R. Ghodssi, "Embedded benzocyclobutene in silicon: An integrated fabrication process for electrical and thermal isolation in MEMS," *Microelectronic Engineering*, vol. 82, pp. 154, 2005.

[9] M. Mehregany, S. F. Bart, L. S. Tavrow, J. H. Lang, and S. D. Senturia, "Principles in design and microfabrication of variable-capacitance side-drive motors," *Journal of Vacuum Science & Technology A: Vacuum, Surfaces, and Films*, vol. 8, pp. 3614-3624, 1990.

[10] S. F. Bart, M. Mehregany, L. S. Tavrow, J. H. Lang, and S. D. Senturia, "Electric micromotor dynamics," *IEEE Transactions on Electron Devices*, vol. 39, pp. 566, 1992.

MODELING AND CONTROL OF A 3-DEGREE-OF-FREEDOM WALKING MICROROBOT

Yu-Ming Chen[1], John W. Suh[2], Gregory T. A. Kovacs[2], R. Bruce Darling[1], Karl F. Böhringer[1]
[1] University of Washington, Seattle, Washington, USA
[2] Stanford University, Stanford, CA, USA

ABSTRACT

This paper describes a walking microrobot with 512 thermo-bimorph polyimide actuator legs. Eight groups of unidirectional legs can be separately controlled to produce planar motion with three degrees of freedom. Wave-like gaits propel the robot at speeds of up to 250 μm/sec while consuming approximately 1.6W power. Finite element methods are employed to investigate the force generation and the thermal characteristics of the robot. Results from simulation and experiments lead to a compact model for the relationship between temperature and velocity of the robot.

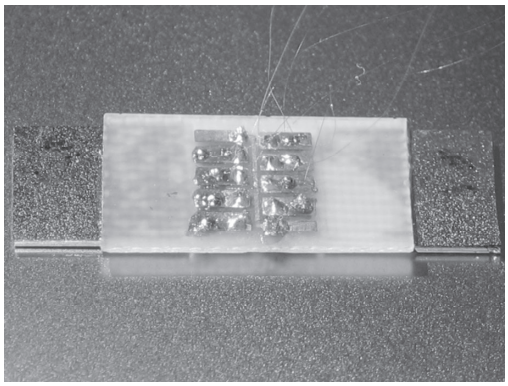

(a)

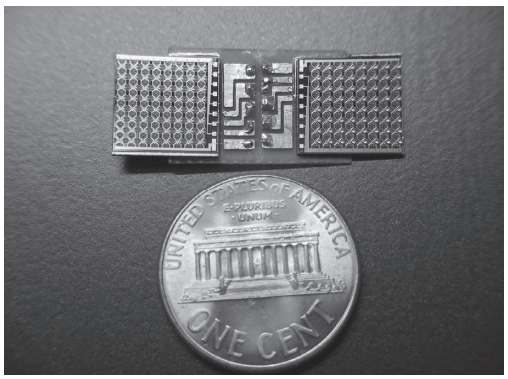

(b)

***Figure 1**. (a) Top and (b) bottom view of the microrobot. The two cilia chips can be seen attached and wire bonded to a PCB backbone. Each chip consists of an 8×8 array of "motion pixels" (i.e., a group of 4 orthogonal cilia). The robot measures approximately 3cm length, 1cm width and 0.5mm thickness.*

INTRODUCTION

Microrobots offer novel solutions for inspection and maintenance of equipment in otherwise inaccessible places, search-and-rescue, reconnaissance, and possibly self-organizing structures. Analogies to ants, grasshoppers, and waterbugs have been invoked in prior work on walking microrobots, e.g. [1-4]. This paper summarizes the experience gathered from an insect-like walking microrobot, including modeling and simulation of its actuators, control strategies for actuator gaits, and several years of experiments under a variety of operating conditions.

SYSTEM ARCHITECTURE

Our system, previously introduced in a preliminary conference abstract [5], consists of two arrays of thermo-bimorph ciliary actuator arrays connected by a small PCB "backbone" (Fig. 1). Each actuator chip measures 1.1mm squared and supports an 8×8 array of "motion pixels" consisting of 4 cilia-like thermo-bimorph actuators capable of generating force with in-plane components in 4 orthogonal directions when activated by an internal resistive heater (Fig. 2). Two layers of polyimide with widely disparate coefficients of thermal expansion (CTE) are the main structural components of the cilia. Since the CTE of the top layer is larger than the CTE of the bottom layer, they curl out of the substrate plane in their cool, inactive state due to internal thermal stress induced by the initial curing at 350°C. As the temperature is increased towards 350°C, the radius of curvature increases and the cilia flatten out towards the substrate surface. Fabrication of the cilia was discussed in detail in [6].

The motion pixels are addressed via 8 control wires and 1 ground wire connected to a PC with LabView interface. The robot is capable of full 3-degree-of-freedom (DOF) motion (i.e., holonomic *x*-*y*-translation and θ-rotation) on a planar surface. It is tracked with a long-working-distance video microscope connected to an automated motion capture system.

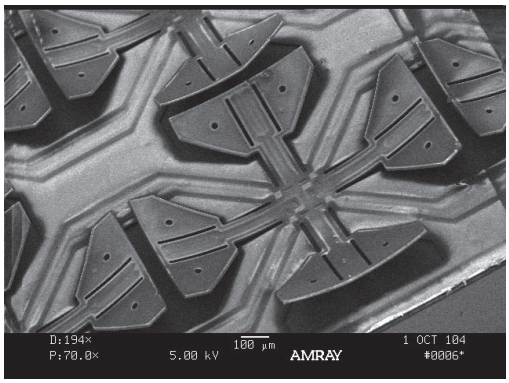

***Figure 2.** Zoomed-in view of cilia chip fabricated by J. Suh [6] in its unheated state. Resistive heating of a thermo-bimorph cilium decreases its curvature. A "motion pixel" consisting of a group of 4 orthogonal cilia is in the center of the image; independent control of the cilia can generate force or motion in 4 orthogonal directions.*

ACTUATOR GAITS

Unlike insect legs, each of the 512 actuators has only one DOF (increase or decrease of curvature) and thus resembles cilia rather than legs. As a consequence, a single cilium or an array of

synchronously acting cilia are not useful for inducing motion. However, several effective locomotion schemes using coordinated, out-of-phase motion of the cilia exist and have been investigated.

We define *gait* in analogy to animal locomotion as a specific sequence of *phases*, which cause controlled motion when executed by the robot. Fig. 3 depicts the principle of 2-phase, 3-phase, and 4-phase gaits with a single motion pixel. Red (dark) triangles symbolize heated actuators with lower cilium curvature. Transitions from phase #2 to #3 and from phase #3 to #4 produce steps towards the right, during which the robot body also moves slightly down and up, respectively.

We define *gait frequency* as the reciprocal of the time to complete one gait cycle. The gait frequency may be different from the frequency at which the cilia activation is changed; this rate is called the *step frequency*. For example, in a 4-phase gait as shown in Fig. 3 the step frequency is 4 times the gait frequency.

A 3-phase gait leaves out one of the phases above; the better choices for omitted phases are #1 or #3. A 2-phase gait uses, e.g., only phases #3 and #4. It has been shown to be a less effective gait.

These gaits can be further refined by varying the relative lengths of each phase, with significant effects on power consumption, operating temperature, and robot speed. For example, the power consumption in phase #1 is 0, in phase #2 and #4 it is 75%, and in phase #3 it is 100%. If all phases have equal length, then the average power consumption is ¼×0 + ½×75% + ¼×100% = 61.5%. By increasing the length of phase #1 and reducing #3 by 10 percentage points, we can reduce the average power consumption to 52.5% while maintaining the same gait frequency.

The gait in Fig. 3 does not effectively utilize the cilia N and S, but they need to be activated during 3 phases so not to obstruct the motion generated by E and W. Instead, if cilium N is operated in sync with E, and S with W, then the robot moves in a diagonal direction towards NE.

Both cilia chips in the robot can be controlled independently, which is useful for rotation. For example, counterclockwise motion is achieved by generating motion towards N in the right chip and motion towards S in the left chip, if seen as depicted at the bottom of Fig. 3.

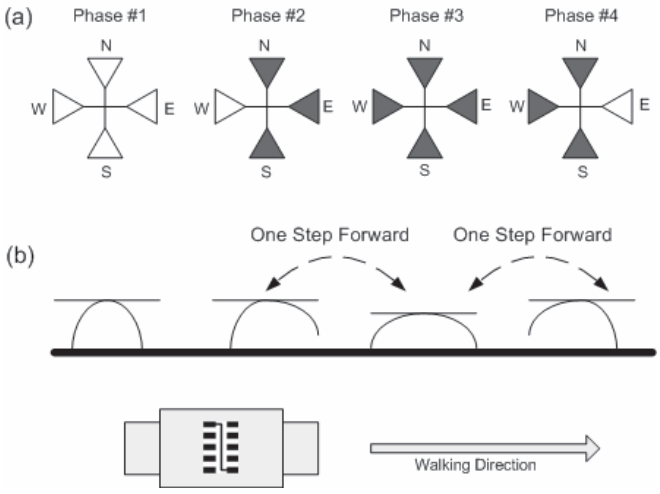

Figure 3. *Schematic of a motion pixel executing a 4-phase gait. Red (dark) triangles symbolize heated actuators with lower cilium curvature. Transitions #2→ #3 and #3→ #4 produce steps towards the right. A 3-phase gait leaves out one of the phases above, e.g., phase #1 or #3. A 2-phase gait uses, e.g., only phases #3 and #4.*

CHARACTERIZATION OF LOCOMOTION

Motion of the robot proceeds in discrete steps produced by the actuation gaits (Fig. 3). Step size depends on control parameters including heating power, frequency, duty cycle, but also system parameters such as robot temperature and load. We hypothesize that the robot velocity v follows a function

$$v(t) = a + be^{-t/\tau} \quad (1)$$

where $a+b$ is its initial velocity at room temperature, and a is its steady state velocity when the robot has heated up. τ describes the time constant of this transition, determined by the robot's thermal mass and heat dissipation. Integrating $v(t)$ leads to an equation for position

$$x(t) = at + \tau b(1 - e^{-t/\tau}) \quad (2)$$

This function has been validated against thermal models using FEM analysis and against large sets of experimental data, as will be described in the following sections.

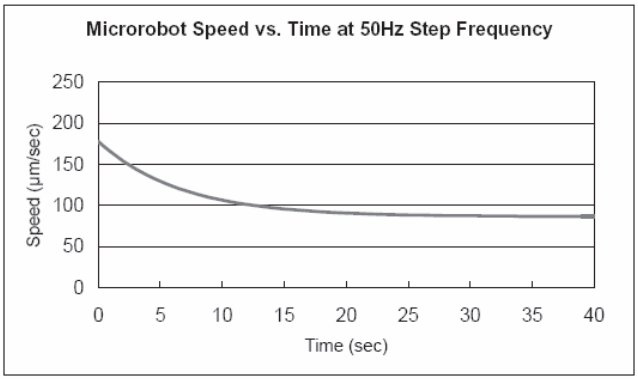

Figure 4. *Robot speed at 50Hz step frequency (12.5Hz gait frequency). Experimental data (>200 sample points) and curve fitting coincide. v(0)=178.3μm/sec, v(∞)=86.6μm/sec.*

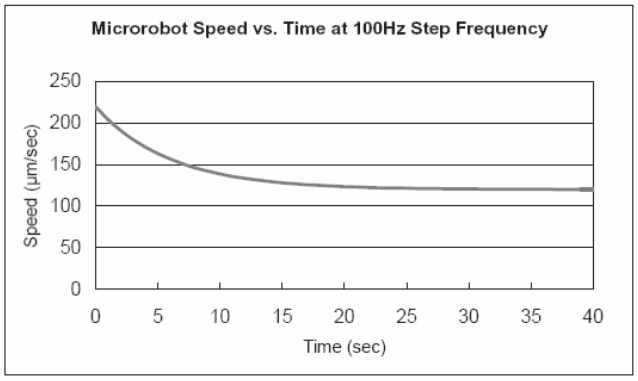

Figure 5. *Robot speed at 100Hz step frequency (25Hz gait frequency). Experimental data (>200 sample points) and curve fitting coincide. v(0)=224.4μm/s, v(∞)=124.5μm/s.*

WALKING EXPERIMENTS

The robot is placed onto a flat, level surface with well-known properties, such as a silicon or glass wafer. The control wires are loosely supported by a stand above the robot such that their weight and stiffness has minimal influence on the robot motion. The control wires are connected to a 60V variable power source and switched by a set of 8 power transistors on a custom-made controller board linked to a personal computer via a NIDAQ

interface card. A custom LabView program allows the user to choose parameters such as step and gait frequency, type and direction of gait. An automated tracking system is used to collect motion data from the experiments at the video frame rate.

Figs. 4 and 5 show velocity data for 4-phase gaits at 12.5Hz and 25Hz gait frequency over a time span of 40sec. The initial and steady state velocities are $v(0) = 178.3\mu m/sec$, $v(\infty) \approx v(40sec) = 86.6\mu m/sec$ for 12.5Hz and $v(0) = 224.4\mu m/sec$, $v(\infty) \approx v(40sec) = 124.5\mu m/sec$ for 25Hz, respectively. The distance traveled during a single gait cycle can be calculated as $d_{gait} = v/f_{gait}$ which is, e.g., approximately 4.5µm at the start of motion with $f_{gait} = 25Hz$.

Fig. 6 summarizes a larger range of such experiments for step frequencies from 50Hz to 200Hz. The slowest speed in steady state is at 50Hz, and frequencies around 90 to 100Hz achieve the highest speeds. Fig. 7 shows the corresponding time constant τ, which was obtained from a least-squares fit between Eq. (2) and the experimental data.

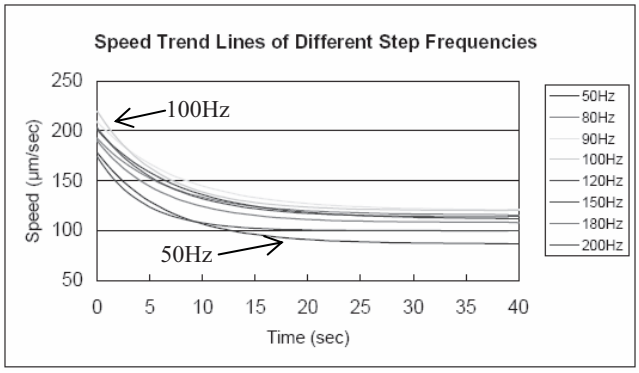

Figure 6. *Robot for different step frequencies (experimental data). The absolute values depend on the step frequency and reach a maximum near 90 - 100Hz. The slow-down trend over time is similar in all experiments and reflects the reduced step size as the robot is heating up.*

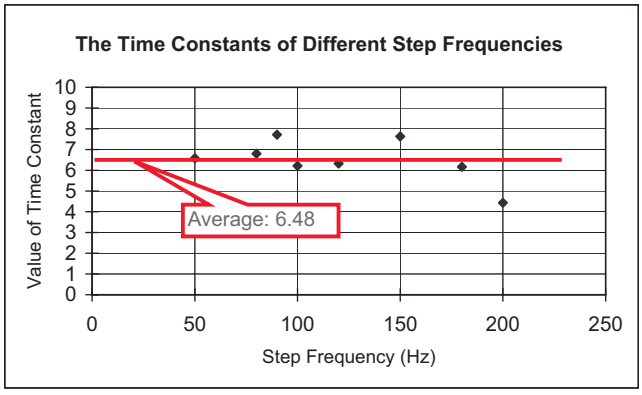

Figure 7. *Time constant τ determined from curve fitting with the experimental data. Similar values are observed for a wide range of control frequencies.*

Discussion: From Figs. 4 and 5 we observe that the speed of the robot is higher for the gait frequency of 25Hz, but it is *not* twice the speed compared to 12.5Hz. This implies that the distance traveled during a single gait cycle d_{gait} decreases with increasing f_{gait}. We believe this decrease is caused by the shorter cooling interval at higher frequencies, which prevents the cilia from reaching their uncooled shape and thus reducing their range of motion. Note, however, that during all of the experiments in Fig. 6 the robot consumes the same amount of electrical power because the duty cycles of the cilia remain unchanged.

MAXIMUM LOAD

To determine the maximal carrying capacity of the microrobot, additional weight is added until it ceases to move. Fig. 8 shows such an experiment with a heavily loaded robot carrying 4 ICs (2.894gr) and 30 metal staples (0.630gr) in addition to its own mass of 0.478gr for a total of 4.002gr. This was the largest load observed that the robot was capable of carrying. During a 4-phase gait, 128 cilia must lift this load during the transition from phase #3 to #4, corresponding to averagely 306µN per cilium.

Fig. 9 shows an ANSYS FEM simulation of the deflection of a heated cilium with two point loads of 153µN at each corner. The simulation illustrates that the cilium is pressed nearly flat against the substrate under this load.

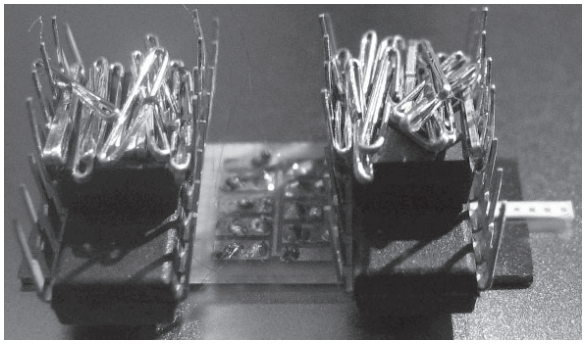

Figure 8. *Microrobot walking under maximal load, carrying 3.524g in addition to its own mass of 0.478g. 128 cilia lift this load during a 4-phase gait, which implies an average of 31mg per cilium (more than 1000 times the cilium mass). Note: the small white strip extending over the right edge of the robot holds the patterns that are recognized by the motion tracking system.*

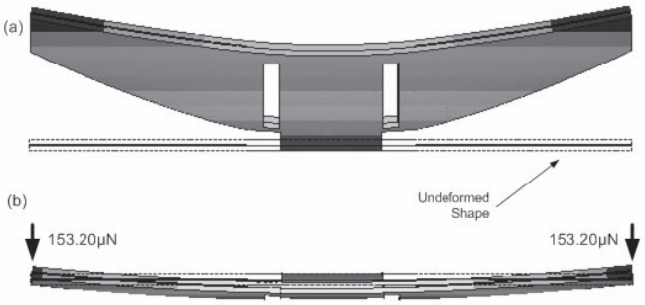

Figure 9. *ANSYS FEM simulation of cilium (a) with curvature due to thermal stress, (b) with mechanical load of 153.2µN applied to each corner, corresponding to a mass load of approximately 4g distributed over 128 cilia.*

SURFACE ROUGHNESS

To investigate the influence of surface roughness on the robot motion, two sets of experiments are performed: (1) Robot motion on the polished and the unpolished side of a silicon wafer. (2) Robot motion on a polished glass wafer and on a glass wafer roughened by a brief dip in hydrofluoric acid, which produces random features with up to 6µm variation (measured by

profilometer). In both cases, the step frequency is varied from 100Hz to 1000Hz. We observe that for lower frequencies, the robot speeds are nearly identical for all surfaces. However, for high frequencies, the robot moves slower and with unsteady velocity on the rough surfaces.

Discussion: As stated earlier, the cilia's range of motion decreases at higher frequencies. If the surface roughness becomes significant compared to the cilia range, then the cilia exhibit a tendency to trip or to get trapped.

THERMAL MODELING

The temperature of the robot body and the walking surface is measured with a small thermocouple (OMEGA HH501BK, 1 sample/sec) by attaching it to the backside of the cilia chip and the backside of the support wafer. Three ANSYS FEM models have been set up to study the thermal characteristics of this system: (1) *Macroscopic model* of the entire system (consisting of cilia chip, cilia immersed in a boundary layer of air, and support substrate) which describes the overall heat dissipation of the robot. (2) *Microscopic model* of an individual cilium, which captures thermal stress and strain due to heating and cooling as well as deformations due to applied loads. (3) *Fluid solid interaction (FSI) model,* which combines structural simulations with computational fluid dynamics to describe the heat transfer between cilia and surrounding air.

Fig. 9 was generated with the "microscopic" model, which recreates a FEM model of the physical cilium shape and materials in great detail. Fig. 10 shows measurements and simulations of the robot temperature in the macroscopic model, which describes cilia chips, support substrate, and air gap as three homogeneous layers.

Discussion: Both the macroscopic and the microscopic model of the robot show excellent agreement with the experimental data. FSI simulation is less successful; so far, no convergence has been achieved between the ANSYS fluid and solid solvers. Likely reasons are the difficulty to accurately model heat conduction and convection in the narrow air gap between cilia chip and support substrate, and the high sensitivity of the cilia to this air flow. A much more detailed discussion of the simulation results can be found in [7].

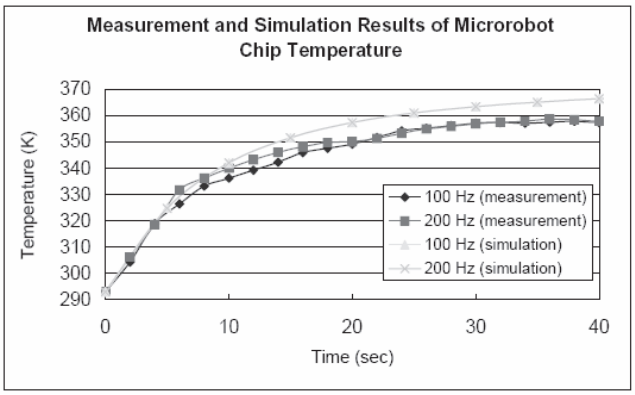

Figure 10. *Simulated and measured robot temperatures during operation at 100Hz and 200Hz step frequency. A "macroscopic" ANSYS FEM model was used to simulate robot body, cilia, walking surface, and air layer in between.*

CONCLUSIONS

A 512-legged walking microrobot capable of full 3-DOF motion across a planar surface has been built and characterized in simulation and experiments. The robot can move at up to 250μm/sec and carry 3.5g load (>7 times its own mass). The robot speed is dependent on its temperature; during operation the robot heats up and slows down accordingly. Its motion can be described by $x(t) = v_\infty t + (v_0 - v_\infty)e^{-t/\tau}$ with v_0 and v_∞ being the robot's initial and steady state velocity (dependent on gait frequency and power supply), respectively, and a thermal time constant $\tau \approx 6.5$sec; this model has been validated by FEM analysis and experiments. The robot has proven extremely reliable during operation in non-cleanroom environments over many years. A more detailed discussion of the robot is provided in [7].

The robot is strong enough to carry additional components such as small sensors, RF elements, or integrated circuits. For a practical autonomous microrobot, the two most significant challenges are power consumption and coping with rough terrain. More efficient thermo-bimorph cilia [8], piezo actuators [4], or electrostatic actuators powered by solar cells [3] are examples to address the first challenge. The small range of cilia motion and the rigid robot body limit the current robot's operation to flat surfaces that are rarely found in uncontrolled environments. Larger range of actuator motion and body compliance would make the robot more widely applicable to rough terrain.

ACKNOWLEDGEMENTS

The authors would like to thank Eric Black, Matt Mohebbi, Anshuman Shukla, Kerwin Wang, Xiaorong Xiong and all the members of the UW MEMS laboratory for their help on this project, and all the staff of the Stanford Nanofabrication Facility (SNF) for their professional and dedicated service. Support for the ciliary array chip research was initially supported by DARPA under contract N001-92-J-1940-P00001 and two additional years were provided by a General Motors Key grant and Kovacs NSF NYI award (ECS-9358289-006). Further support was provided to K. Böhringer by NSF CAREER award ECS-9875367 and by a JSPS fellowship in 2004-2005.

REFERENCES

1. Takeshima, N. and H. Fujita. Polyimide bimorph actuators for a ciliary motion system, in *ASME WAM, Symp. Micromech. Sensors, Actuators, and Systems.* 1991.
2. Ebefors, T., J.U. Mattsson, E. Kèlvesten, and G. Stemme. A robust micro conveyor realized by arrayed polyimide joint actuators, in *IEEE 12th Workshop on Micro Electro Mechanical Systems (MEMS).* 1999. Orlando, FL.
3. Hollar, S., A. Flynn, C. Bellew, K.S.J. Pister. Solar Powered 10mg Silicon Robot, in *IEEE MEMS.* 2003. Kyoto, Japan.
4. Suhr, S.H., S.J. Lee, Y.S. Song, and M. Sitti. Biologically Inspired Miniature Water Strider Robot, in *Robotics: Science and Systems I.* 2005. Cambridge, MA.
5. Mohebbi, M.H., M.L. Terry, K.F. Böhringer, J.W. Suh, and G.T.A. Kovacs. Omnidirectional Walking Microrobot Using MEMS Thermal Cilia Arrays, in *ASME International Mechanical Engineering Congress and Exposition (IMECE'01).* 2001. New York, NY.
6. Suh, J.W., S.F. Glander, R.B. Darling, C.W. Storment, and G.T.A. Kovacs, Organic thermal and electrostatic ciliary microactuator array for object manipulation. *Sensors and Actuators, A: Physical,* 1997. **58**:51-60.
7. Chen, Y.-M., Thermal Model of Microrobot, *Masters Thesis, Electrical Engineering.* 2005, University of Washington, Seattle, WA.
8. Suh, J.W., R.B. Darling, K.F. Böhringer, B.R. Donald, H. Baltes, and G.T.A. Kovacs, CMOS integrated ciliary actuator array as a general-purpose micromanipulation tool for small objects. *ASME/IEEE Journal of Microelectromechanical Systems,* 1999. **8**(4):483-496.

SiSonic™ – THE FIRST COMMERCIALIZED MEMS MICROPHONE

Peter V. Loeppert and Sung B. Lee
Knowles Electronics, LLC
Itasca, Illinois USA

ABSTRACT

The Knowles SiSonic™ MEMS microphone has been successfully commercialized for use in cell phones, cameras, PDA's, and other high volume consumer electronics. One advantage that MEMS microphones have over traditional Electret Condenser Microphones (ECMs) is the ability to be reflow soldered. Cost is a significant driver in the design of a MEMS microphone. SiSonic™ uses a non-integrated approach to MEMS and CMOS while minimizing both die sizes. Key to the small MEMS die size is the use of a simply supported freeplate diaphragm. The CMOS die has been optimized to work with very low input capacitance. A low cost package has been developed utilizing laminated FR4 PCB material. The microphones are 100% tested on a high speed automated acoustic test station.

INTRODUCTION

The Knowles SiSonic™ MEMS microphone is targeted towards high volume consumer electronic products where price is a key factor. In 2005, about 2 billion microphones of all types were produced including about 1 billion for cell phones, cameras, computers, etc. These later products use Electret Condenser Microphones (ECM's) produced by a number of low cost Asian suppliers. For a MEMS microphone to compete effectively in this market, it must at a minimum, meet the performance, reliability, and price expectations set by the ECM suppliers. However MEMS microphones have one distinct advantage over current ECM's; that is the ability to withstand lead-free solder reflow cycles. This ability permits the MEMS microphone to be pick and placed like any other component and thus leads to significantly lower manufacturing costs for the integrator. SiSonic™ is the first MEMS microphone to meet all of these requirements and gain significant market share.

MICROPHONE OVERVIEW

SiSonic™ is a condenser microphone comprising a MEMS die and a CMOS die combined in an acoustic housing. The condenser or variable capacitor consists of a highly compliant diaphragm in close proximity to a perforated, rigid backplate. The perforations permit the air between the diaphragm and backplate to escape. Together, the diaphragm and backplate pair is referred to as the motor. As shown in Figure 1, the motor capacitance couples a voltage source to a high impedance amplifier.

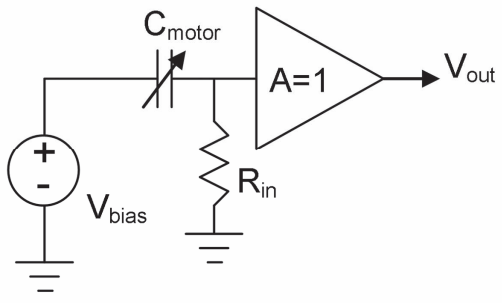

Figure 1. *Condenser microphone schematic diagram.*

The capacitance of the motor in conjunction with the amplifier input resistance forms a high pass filter with a -3dB point well below the audio band. Thus within the audio band the motor is operating in constant charge mode and the sensitivity of the microphone can be represented as follows:

$$S = \frac{\Delta Vout}{\Delta P} = \frac{Vbias}{Cmotor} \cdot \frac{\Delta Cmotor}{\Delta P} \qquad (1)$$

where ΔP is sound pressure

If the distance (gap) between the diaphragm and the backplate is d and the sound pressure causes a change in the gap, Δd, the sensitivity can be approximated as:

$$S = \frac{Vbias}{d} \cdot \frac{\Delta d}{\Delta P} \qquad (2)$$

The first term is the electric field in the gap while the second term is the mechanical compliance of the diaphragm. In an ECM, the bias voltage is typically several hundred volts and comes from a permanently charged electret layer. The gap is usually tens of microns so the resulting electric field is on the order of 10-15 V/μm. The bias voltage in a MEMS microphone is typically derived from the power supply and the gap is much smaller so the resulting electric field is on the order of 2-4V/μm. This means that to achieve a similar sensitivity the diaphragm compliance of the MEMS microphone must be several times larger than that of the ECM diaphragm.

MEMS DESIGN

Since cost is the key factor for SiSonic™, the MEMS die size and hence the diaphragm area must be minimized. At the same time the motor capacitance must be adequate to drive a CMOS amplifier. Achieving consistently high diaphragm compliance has been the major roadblock to developing a successful MEMS microphone. Sessler **[1]** reviewed a number of important development programs throughout the 1980's and early '90s. All used diaphragms with fully clamped edges and most were tensioned by the intrinsic stress in the film from which the diaphragm was formed. It was recognized during this period that controlling the tension was a critical factor and is all the more critical for very small diaphragms **[2]**.

To achieve a consistently high compliance with a small diameter, a diaphragm with a simply supported boundary condition was chosen for SiSonic™. This diaphragm depends on plate bending forces **[3]** rather than tension as the restoring force and is referred to as a free plate diaphragm. Thickness control is essential in this type of diaphragm and fortunately this is routine in thin film deposition. The SiSonic™ freeplate diaphragm has a half millimeter effective diameter and is made of 1 micron thick poly silicon. It is suspended above a through hole in the wafer and separated from the backplate, which is 4 microns above it, by a

series of support posts. Figure 2 shows this schematically. The freeplate design releases all intrinsic stress in the poly silicon. For this diameter a tension as small as 1MPa would reduce the diaphragm compliance by 3dB.

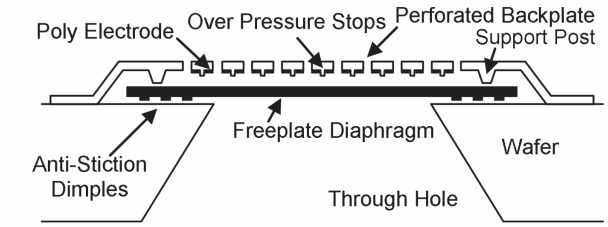

Figure 2. *MEMS microphone cross section.*

Equation 2 indicates a tradeoff between electric field and compliance for a given sensitivity. The limiting factors are dynamic range and electrostatic stability. SiSonic™ operates with an 11V bias across the 4 micron gap. There is no limit to the transient pressure to which a microphone can be exposed. In light of this, the small gap, and the limited non-linear stiffening of a freeplate with deflection, there is a real possibility of electrostatic collapse. SiSonic™ has over pressure stops built into the 1.5 micron thick silicon nitride backplate. These stops make the motor unconditionally stable at the operating bias by limiting the diaphragm travel towards the backplate. Poly silicon on the underside of the backplate serves as the stationary electrode of the capacitor. The perforations in the backplate serve to damp the diaphragm motion. The SiSonic™ MEMS process is a custom 10 mask, dual poly process produced for Knowles primarily by Sony Semiconductor in Japan. Figure 3 shows a plan view of the MEMS die while Figure 4 shows details of the various features. Table 1 summarizes the MEMS design parameters.

MEMS die size	1.651 x 1.651	mm
Diaphragm thickness	1	µm
Effective diaphragm diameter	560	µm
Gap	4	µm
Backplate thickness	1.5	µm
Over pressure stop height	1	µm
Damping hole size	4	µm
Damping hole fraction	22.8	%

Table 1. *MEMS design parameters*

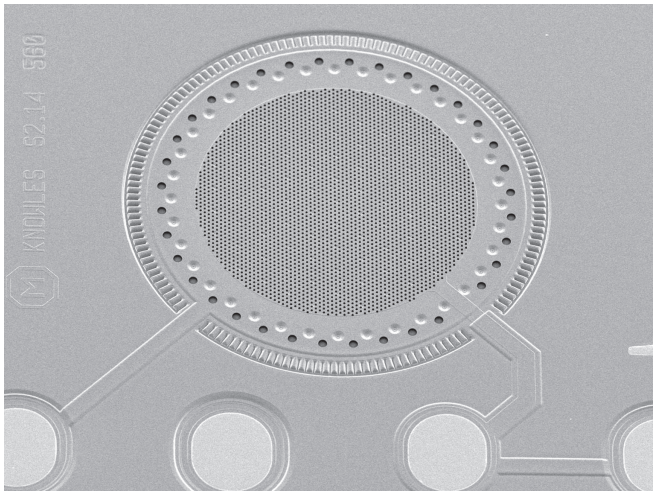

Figure 3. *MEMS motor*

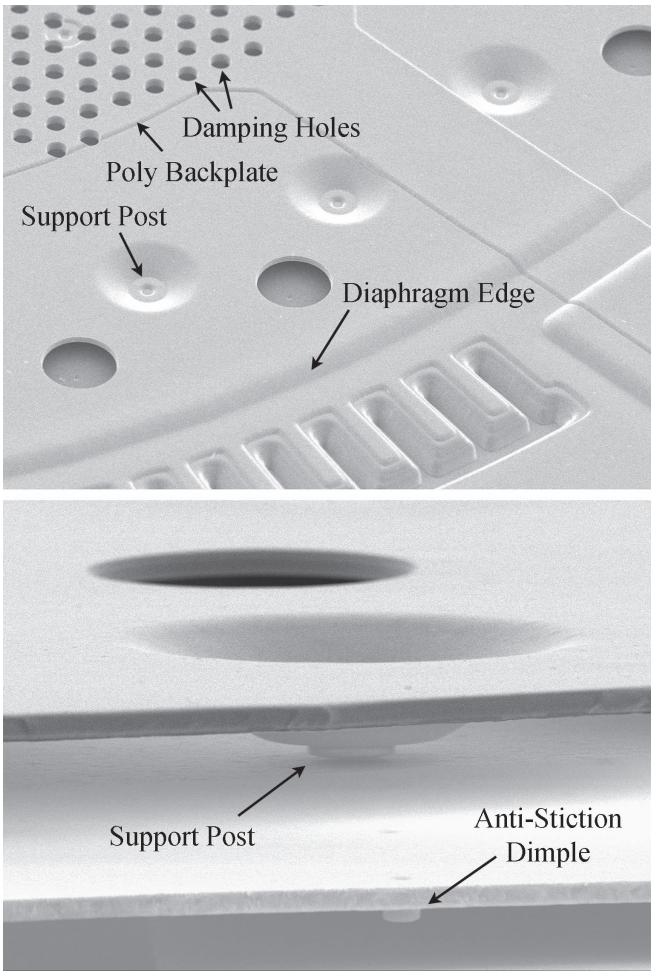

Figure 4. *MEMS motor details*

CMOS DESIGN

The SiSonic™ motor capacitance is only 0.5pF. The CMOS amplifier must be able to accept the millivolt level signal from the MEMS die with minimal loading and buffer the signal to drive the next chip in the audio path. As shown in Figure 5, the SiSonic™ CMOS chip does this in two stages. The first stage is a unity gain buffer with an input capacitance of 0.25pF and an output impedance of several thousand ohms. The second stage is a typical opamp connected in a non-inverting configuration. This stage can be externally configured for 0-20dB of gain. The output of the first stage is fed back to the MEMS die to guard out the approximately 0.2pF of parasitic capacitance associated with the bond pad. Without the guarding, sensitivity drops by 2-3dB.

The CMOS die also must supply the 11V bias supply. Since the microphone presents a purely capacitive load, the charge pump used to generate the bias voltage is quite small. However this does mean that the CMOS process must contain a high voltage option. The SiSonic™ CMOS die is currently being made in both a 0.8 micron and a 0.35 micron process at Austria Micro Systems.

Integration vs. non-integration of MEMS and CMOS is a constant theme in the community. If the cost of a silicon chip in general is related to the product of its complexity, in number of masks, times the chip area, the decision will almost always be not to integrate. This is the case for SiSonic™. The performance improvement attainable through integration is negligible since the

parasitic capacitance is guarded out. The cost of bonding two die instead of one is also small compared to the higher yield achieved individually and the much shorter design cycles possible as separate die.

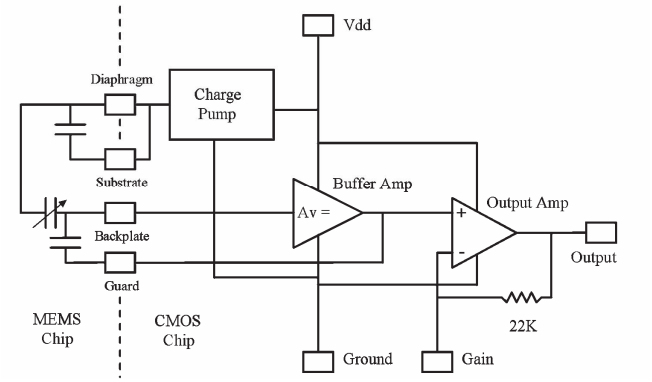

Figure 5. *CMOS block diagram*

PACKAGING

The SiSonic™ package must be extremely low cost, provide open access for the MEMS die to the environment, yet protect the MEMS and CMOS die both physically and from electromagnetic radiation. This has been accomplished, as illustrated in Figure 6. The package consists of a base, a wall, and a lid all made from FR4 PCB material and laminated together. The inside surfaces are plated to provide a Faraday shield again EMI interference.

The two die are adhesively bonded to the base. Gold wire is thermo-sonically bonded between the two die and between the CMOS die and the base. The MEMS die has gold pads so corrosion is no issue however the CMOS die has standard aluminum pads. An opaque silicone encapsulant is used to cover the CMOS die to prevent moisture from entering and causing corrosion on the CMOS pads. The encapsulant also blocks light from reaching certain sensitive nodes in the CMOS circuit. Figure 7 shows a photo of the package with the lid removed.

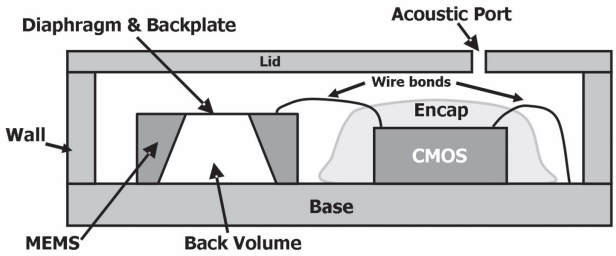

Figure 6. *Microphone package cross section*

The MEMS die is actually a differential pressure sensor and needs a reference pressure against which the tiny acoustic signal can be measured. The back volume under the MEMS die serves this purpose. Pressure equalization is accomplished at sub-audio frequencies by the flow of air around the diaphragm and into the back volume.

The acoustic port is offset from the MEMS die to prevent dirt accumulation or physical damage to the die. The acoustic port in conjunction with the front volume around the two die form an acoustic resonator with a peak frequency around 14KHz. With the lid removed, the frequency response is virtually flat throughout the audio band. Figure 8 shows the frequency response of a microphone with and without its lid.

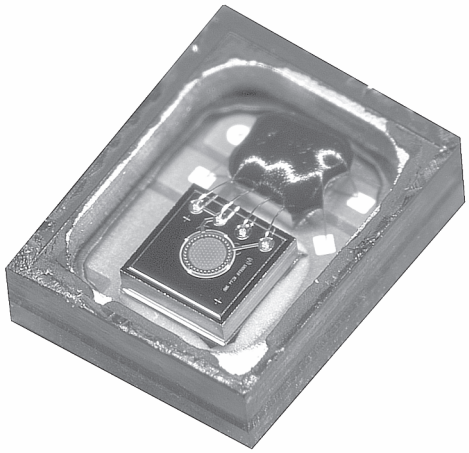

Figure 7. *Photo of microphone package with lid removed*

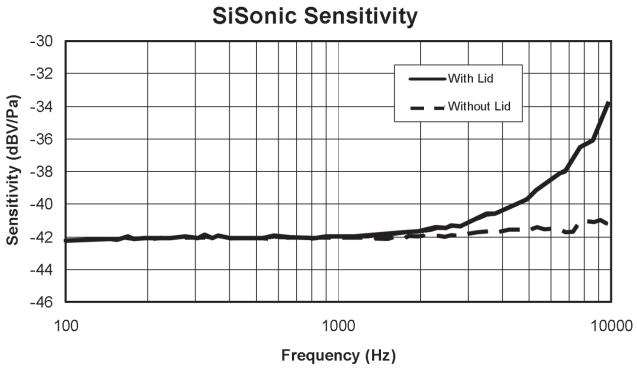

Figure 8. *Frequency response effect of front cavity*

Packaging is performed on 4” by 4” panels containing hundreds of microphones. The panel size is limited by the stage travel limits of typical wire bonders. Only standard semiconductor packaging equipment is used in the assembly of the microphones. When a panel is complete, it is mounted on a dicing frame and the microphones are singulated with a diamond dicing saw. Figure 9 shows a completed panel ready for testing.

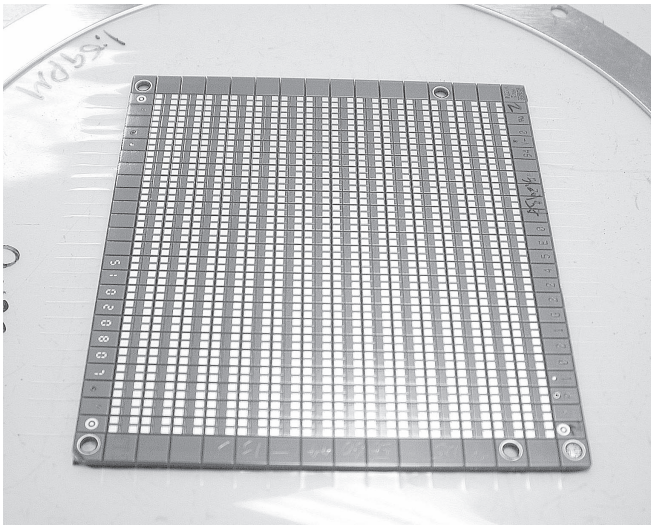

Figure 9. *Panel of microphones ready for testing*

TESTING

The SiSonic™ microphones are 100% tested using a custom test system to determine sensitivity as a function of frequency and self noise level. The system, shown in Figures 10 & 11, tests 12 parts at a time.

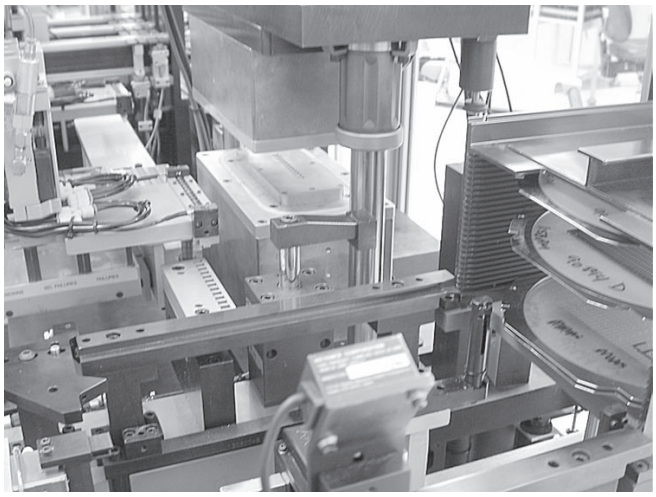

Figure 10. *Test system*

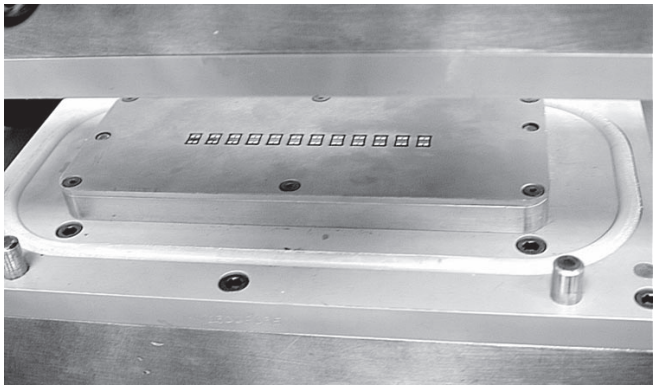

Figure 11. *Close-up of test head with microphones in place*

Each microphone to be tested is placed within a pressure cavity containing a microspeaker and a ¼" B&K reference microphone. The first step of the test is the application of a pseudo random noise signal to the microspeaker and the calculation of an FFT to determine the response of each microphone's output relative to the reference microphone. The second step of the test requires muting the microspeaker and the measurement of the self noise of each microphone. The 12 parts are then removed from the test head and sorted into 3 grades plus a reject bin based on the measured sensitivity and noise. Rejects are categorized to provide feedback to the assembly line. For instance, a high, low frequency roll-off point indicates an acoustic leak at the MEMS die bond site. This is most likely caused by inadequate die bond adhesive. The tester averages one part per second for a capacity of nearly 2.5 million parts per month.

CONCLUSIONS

A MEMS microphone has been successfully developed for high volume consumer applications. Cost has been optimized at every step including minimizing die sizes, making maximum use of automated, batch assembly of the microphone packages, and utilizing standard equipment wherever possible. With careful attention to detail, MEMS technology is once again displacing older, entrenched technology.

REFERENCES

[1] G. M. Sessler, "Silicon Microphones", *J. Audio Eng. Soc., Vol. 44, No. 1/2* (1996).

[2] P. R. Scheeper, "A Silicon Condenser Microphone: Materials and Technology", *Ph.D. Thesis*, University of Twente (1993)

[3] M. Pedersen, "A polymer condenser microphone realized on silicon containing preprocessed integrated circuits", *Ph.D. Thesis*, University of Twente (1997)

A MICROMACHINED PIEZOELECTRIC MICROPHONE FOR AEROACOUSTICS APPLICATIONS

Stephen Horowitz, Toshikazu Nishida, Louis Cattafesta, and Mark Sheplak[†]

Interdisciplinary Microsystems Group, PO Box 116250, University of Florida, Gainesville, Florida 32611-6250
[†] (352) 392-3983, FAX: (352) 392-7303, sheplak@ufl.edu

ABSTRACT

This paper describes the design, fabrication, and characterization of a bulk-micromachined piezoelectric microphone for aeroacoustic applications. The microphone was fabricated by combining a sol-gel lead zirconate-titanate (PZT) deposition process on a silicon-on-insulator (SOI) wafer with deep-reactive ion-etching (DRIE) for the diaphragm release. Experimental characterization indicates a sensitivity of $0.75\ \mu V/Pa$, a dynamic range greater than six orders of magnitude $(47.8-169\ dB, ref.\ 20\ \mu Pa)$, a capacitance of $13.9\ nF$ and a resonant frequency of $50.8\ kHz$.

INTRODUCTION

The goal of this research is to develop a microphone for aeroacoustic wind-tunnel testing **[1]**. Microelectromechanical systems (MEMS)-based microphones have been developed utilizing piezoresistive, optical, capacitive, and piezoelectric transduction techniques **[2-8]**. Most of these designs focused on audio applications that typically require a maximum sound pressure level (SPL) of $\sim 120\ dB$, integrated noise floors of $\leq 35\ dBA$ and bandwidths of $\leq 20\ kHz$. Conversely, aeroacoustics applications may require maximum sound pressure levels in excess of $160\ dB$, bandwidths of $\geq 50\ kHz$, but the noise floor requirements are generally less stringent $\left(< 50\ dB/\sqrt{Hz}\right)$ than audio applications. Each transduction technique has unique advantages and disadvantages for aeroacoustic applications. Piezoelectric transduction offers the potential for a durable, high sensitivity, low noise device that requires no external power to operate. The main drawback is material integration and compatibility with standard micromachining.

A number of authors have developed piezoelectric microphones and have fabricated them using a wide array of piezoelectric materials **[2-6,8,9]**. Thin film, piezoelectric materials include zinc oxide (ZnO), aluminum nitride (AlN), aromatic polyurea, polyvinylidene fluoride (PVDF), and PZT. They each offer different mechanical and electrical properties, as well as transduction capabilities. In addition, some of the materials are CMOS compatible while others are not, which has led to many differing approaches to the implementation of piezoelectric microphones. The ease of integrating the piezoelectric material into a fabrication sequence is an important consideration in the development of a microphone. PZT, for instance, contains lead, barring it from all CMOS facilities, whereas AlN is fully CMOS compatible. ZnO and PVDF, while not fully CMOS compatible, can be integrated more easily with conventional processing. Despite the various microphones that utilize piezoelectric transduction, to date, no piezoelectric microphones have been developed specifically for aeroacoustic applications.

SENSOR DESIGN

This microphone was designed by combining a fundamental piezoelectric composite plate model with a lumped-element, electroacoustic model **[10-11]**. Lumped-element modeling (LEM) was used to estimate the theoretical sensitivity and bandwidth of the device. Finite element modeling was then used to verify the LEM predictions prior to fabrication.

In micromachined piezoelectric devices, thin ferroelectric films are deposited on substrates comprised of a composite of silicon, metals and oxides. Large in-plane residual stresses often result because of the fabrication-induced stresses, different thermal expansion coefficients between the films, and packaging effects. These in-plane stresses can dominate the mechanics of these devices and must be accounted for during design. For this microphone, the electromechanical design employed small-deflection plate theory for the multi-layer piezoelectric diaphragm subjected to in-plane stresses, transverse pressure, and transverse electric field **[11]**.

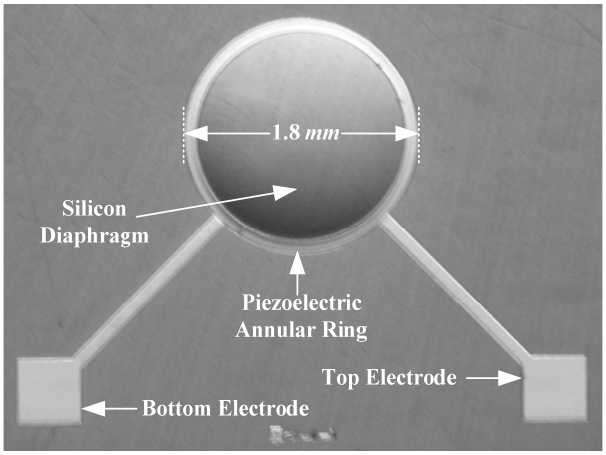

Figure 1: *An optical photograph of the piezoelectric microphone.*

The microphone structure consists of a $1.80\ mm$ diameter, $3\ \mu m$ thick, silicon diaphragm with a thin ring of PZT placed near the boundary of the diaphragm (Figure 1 and Figure **2**). The $1.85\ mm$ diameter, $95\ \mu m$ wide, piezoelectric annular ring was placed near the diaphragm edge to maximize sensitivity due to higher stress concentrations in this region. The placement of the ring near the boundary also eliminates the need to run electrodes across the diaphragm. The $270\ nm$ thick PZT was sandwiched between a $200\ nm$ Ti/Pt layer and a $180\ nm$ Pt layer that serve as bottom and top electrodes, respectively. The entire ring structure is separated from the silicon diaphragm by a $100\ nm$ thick TiO_2 layer that serves as a diffusion barrier for the PZT during processing. Inclusion of this diffusion barrier prevents cracking of the PZT that would otherwise arise from loss of lead via diffusion into the silicon during later processing steps.

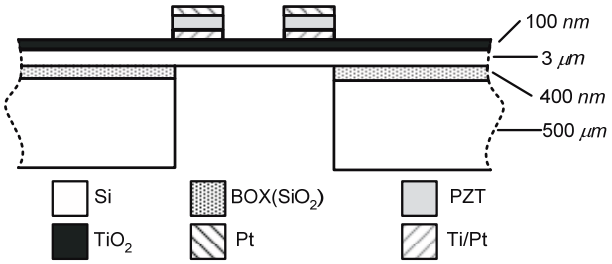

Figure 2: *Cross sectional schematic showing silicon diaphragm with circular piezoelectric composite ring. (Not to scale.)*

The transversely-isotropic composite plate model accounts for material properties of each of the thin-film layers, as shown in Figure 3. These include the mechanical properties of the layers such as Young's Modulus, E, density, ρ, and Poisson's ratio, ν, and electrical properties including the relative permittivity constant, ε_r, and piezoelectric coefficient, d_{31}, of the PZT. The model also accounts for the in-plane compressive stress, σ_0, of each layer. Furthermore, the geometry of the structure is accounted for via the inner PZT radius, R_1, outer PZT radius, R_2, and the various film thicknesses. The material properties used for the electromechanical model are given in Table 1.

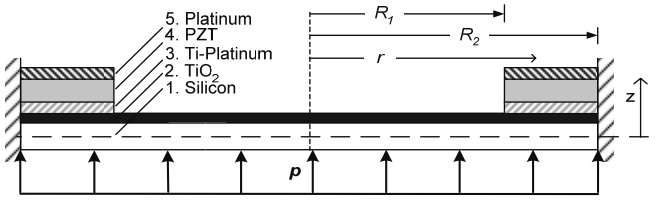

Figure 3: *Cross-sectional schematic of the piezoelectric composite circular plate model.*

Table 1*: Material properties used for design.*

	d_{31} $[pC/N]$	ν	ε_r	E $[GPa]$	ρ $[kg/m^3]$	σ_0 $[MPa]$
silicon	-	0.3	-	169	2.5	0
Pt/Ti	-	0.38	-	170	21.44	-
TiO_2	-	0.28	-	283	2.15	1809
PZT**[12]**	-50	0.3	500	30	7.5	176.0

A lumped element model was then developed to facilitate design of the complete microphone system which involves electrical, mechanical, and acoustical energy domains. In LEM, the coupling between the various energy domains is realized via equivalent two-port models of the physical system **[10]**. An equivalent circuit model is constructed by lumping the distributed energy storage and dissipation into ideal, generalized one-port circuit elements. In an electroacoustic system, differential pressure and voltage are effort variables, while volumetric flow rate and current are flow variables. The lumped elements can then be represented in an equivalent electrical circuit by equating acoustic and mechanical elements to their electrical equivalents. In the electrical domain, a resistor represents dissipation of energy, while inductors and capacitors represent storage of kinetic and potential energy, respectively. Similarly, in the mechanical domain, kinetic and potential energy are stored in mass and compliance (inverse of stiffness), respectively. The same technique of lumping elements and equating them to their electrical equivalent can also be extended to the acoustical energy domain, thereby permitting a single equivalent circuit that represents the dynamics of the entire system. In this paper, an impedance analogy is employed, in which elements that share a common effort are connected in parallel, while those sharing a common flow are connected in series **[10]**.

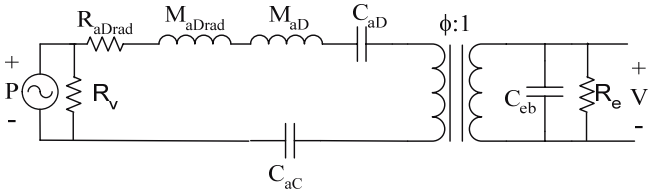

Figure 4*: Equivalent circuit representation of a lumped-element model of a piezoelectric microphone.*

Figure 4 shows a schematic of an equivalent circuit representation of the lumped element model where R_{aDRad}, M_{aDRad}, C_{aD} and M_{aD} are the radiation resistance and mass, and diaphragm compliance and mass, respectively. Also, ϕ, C_{eb} and R_e are the electroacoustic transduction coefficient, blocked electrical capacitance and dielectric loss resistance, respectively. Finally, C_{aC} is the cavity compliance and R_v is the vent resistance. The structure of the equivalent circuit is explained as follows. An acoustic pressure, P, drives the motion of the diaphragm, which in turn generates a voltage, V, across the piezoelectric thin film represented by C_{eb}. This represents a conversion from the acoustical to the electrical domain and is accounted for via a transformer possessing a turns ratio

$$\phi = \frac{-d_A}{C_{as}}; \left[\frac{Pa}{V}\right], \tag{1}$$

where d_A is the piezoelectric coefficient and C_{aD} is the diaphragm acoustic compliance when an electrical short circuit is imposed across the electrodes. The time-harmonic, two-port network equations describing the behavior of the piezoelectric transducer are written in the acoustic domain as

$$\begin{bmatrix} I \\ Q \end{bmatrix} = \begin{bmatrix} j\omega C_{ef} & j\omega d_A \\ j\omega d_A & j\omega C_{aD} \end{bmatrix} \begin{bmatrix} V \\ P \end{bmatrix}, \tag{2}$$

where, $Q = \int \vec{V}(r) \cdot d\vec{S}$ is the volume velocity of the plate, $\vec{V}(r) = \frac{dw(r,t)}{dt}$ is the distributed velocity over the surface, $d\vec{S}$ is normal projection of an infinitesimal element of area, $w(r,t)$ is the transverse deflection, and I is the electrical current **[11]**. The effective acoustic piezoelectric coefficient that relates the volumetric displacement, $\Delta\forall$, to the applied voltage for zero pressure loading is

$$d_A = \left.\frac{\Delta\forall}{V}\right|_{P\to 0} = \frac{\int_0^{R_2} w(r)\big|_{P\to 0} 2\pi r dr}{V}; \left[\frac{m^3}{V}\right], \tag{3}$$

where $\Delta\forall = \int_0^{R_2} 2\pi r w(r) dr = \int Q dt; \left[m^3\right]$. Similiarly, C_{aD} is defined by the volume displaced by the diaphragm for an

applied pressure under zero voltage loading,

$$C_{aD} = \left.\frac{\Delta\forall}{P}\right|_{V\to 0} = \frac{\int_0^{R_2} w(r)\big|_{V\to 0}\, 2\pi r dr}{P}; \left[\frac{m^3}{Pa}\right]. \quad (4)$$

On the electrical side of the transformer, C_{eb} is the blocked electrical capacitance and R_e is the resistance of the piezoelectric ring. The term 'blocked' is used since it is the impedance seen by the source when the diaphragm motion is prevented. At frequencies greater than zero, an equivalent acoustic mass must also be included in the model as

$$M_{aD} = 2\pi \int_0^{R_2} \rho_A \left(\frac{w_{inc}(r)\big|_{V=0}}{\Delta V\big|_{V=0}}\right)^2 r dr; \left[\frac{kg}{m^4}\right], \quad (5)$$

where ρ_A is the areal density of the piezoelectric composite plate given by

$$\rho_A = \int_{z_1}^{z_2} \rho_l dz; \left[\frac{kg}{m^2}\right], \quad (6)$$

and ρ_l is the density of the corresponding layer. Furthermore, this mass must be in series with the compliance as both possess the same motion (i.e., displacement or velocity)

Since the clamped circular plate is vibrating in a medium, the radiation impedance of the plate is also taken into account and consists of a radiation mass, M_{aDrad}, and a radiation resistance, R_{aDrad}, as seen in the circuit of Figure 4. The radiation mass accounts for the inertial mass of the fluid that is vibrating in unison with the plate, while the radiation resistance accounts for the acoustic radiation of energy away from the plate. The radiation impedance can be found by modeling the structure as a piston in an infinite baffle. For $kR_2 << 1$, the radiation resistance and mass can be approximated as **[13]**

$$R_{aDrad} \approx \frac{(kR_2)^2 \rho c}{2A_{eff}}; \left[\frac{kg}{m^4 s}\right] \quad (7)$$

and

$$M_{aDrad} \approx \frac{8kR_2 \rho c}{3\pi\omega A_{eff}}; \left[\frac{kg}{m^4}\right], \quad (8)$$

respectively, where $k = \omega/c$ is the wavenumber, ω is the angular frequency, c is the isentropic speed of sound, and A_{eff} is an effective diaphragm area to maintain continuity of volume velocity. Note the effects of structural damping terms could be added by putting a resistor in series with R_{aDrad}. Additionally, the compliance of the cavity, C_{aC}, formed between the back of the diaphragm and the microphone package will affect the dynamic response and is therefore included in the equivalent circuit. The cavity compliance is defined as

$$C_{aC} = \frac{\forall_c}{\rho c^2}; \left[\frac{m^3}{Pa}\right], \quad (9)$$

where $\forall_c$ is the volume of the cavity. Finally, the resistance, R_v, represents viscous losses incurred in a vent channel that typically connects a microphone cavity to ambient pressure. In the actual device described in this paper, a vent channel was not specifically designed into the structure; however packaging-induced leakage between the cavity and atmospheric pressure provides the same effect.

An important point to note from the equivalent circuit is the effect that the cavity compliance, C_{aC}, can have on the overall sensitivity. If C_{aC} is much larger than the diaphragm compliance, C_{aD}, then the sensitivity will not be noticeably affected. However, if the cavity compliance is the same order of magnitude or smaller than C_{aD}, then it will have a noticeable stiffening effect because C_{aC} and C_{aD} are in series. In order to avoid this generally undesirable effect, the cavity must be made large enough to have a much greater compliance than the diaphragm.

In order to determine most of the lumped element parameters, the distributed deflection, $w(r)$ must be determined. To obtain $w(r)$, an analytical model was developed for the piezoelectric composite circular plate by Wang et al. **[11]**. Analytical modeling was accomplished by dividing the problem of Figure 3 into two portions, an inner circular plate surrounded by an annular composite ring with matching boundary conditions at the interface. The boundary conditions consist of equal moments and forces at the interface as well as equal slope and radial displacement. After solving for the deflection in each region, the deflection equation for each region was then combined into a single equation **[11]**.

FABRICATION

The device fabrication is illustrated in Figures 5-8, highlighting the major steps in the process flow. The devices were fabricated using a sol-gel PZT deposition process on a 4-inch SOI wafer combined with DRIE for the release of the silicon diaphragm. The first step was to deposit a 100 *nm* thick layer of Ti which is then oxidized in a tube furnace to create a TiO_2 layer that serves as a diffusion barrier **[14]** as shown in Figure 5a. A liftoff process was then used to pattern the bottom electrodes with 40 *nm* of evaporated Ti followed by 180 *nm* of evaporated Pt as shown in Figure 5b. The Ti layer served as an adhesion layer in this step.

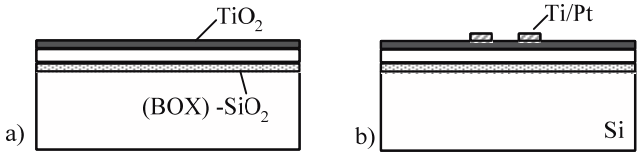

Figure 5: *Initial process steps. a) Deposit 100 nm of Ti and oxidize to form TiO_2. b) Deposit and liftoff Ti/Pt {40/180 nm} to form bottom electrode.*

The next step was the deposition of a previously mixed 52/48 sol-gel solution of PZT as shown in Figure 6a. The solution was spin-cast at 2500 RPM for 30 sec, then pyrolized at 350 ℃ in air for 2 *min* on a hot plate. Repeating the spin and pyrolize step 6 times yielded a total PZT thickness of approximately 400 *nm*. The wafers were then furnace annealed at 650 ℃ for 30 *min* to achieve a perovskite phase of PZT for the piezoelectric properties.

Following the PZT deposition, the top electrodes were deposited and patterned in a liftoff process similar to the bottom electrodes as shown in Figure 6b. The top electrodes also served as a hard etch mask for the PZT etch. The PZT was etched using a 3:1:1 solution of ammonium biflouride ($(NH_4)HF_2$), hydrochloric acid (HCl), and deionized water as shown in Figure 7a. The etchant leaves a residue that then must be removed with a dilute

nitric acid and hydrogen peroxide solution. The next step was to deposit a thick photoresist (PR) on the backside, and pattern the backside release etch as in Figure 7b.

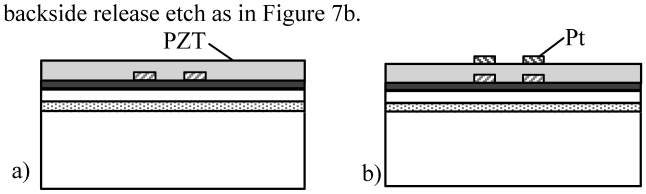

Figure 6: *Continuing process steps. a) Spin PZT 52/48 & pyrolize {4 layers for 267 nm total}. b) Deposit and liftoff Pt {180 nm}.*

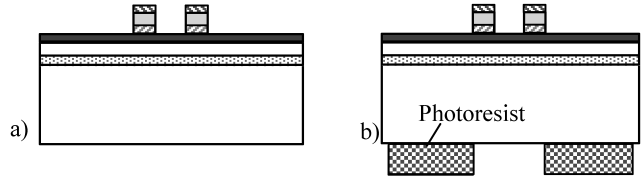

Figure 7: *Continuing process steps. a) Wet etch PZT in 3:1:1 of $(NH_4)HF_2$/HCl/DI water. b) Spin & pattern thick PR on back.*

Then the silicon wafer is backside etched using a DRIE process as shown in Figure 8a, stopping on the buried oxide (BOX) layer. Finally, the resist was ashed and the backside was wet etched in BOE to remove the exposed BOX.

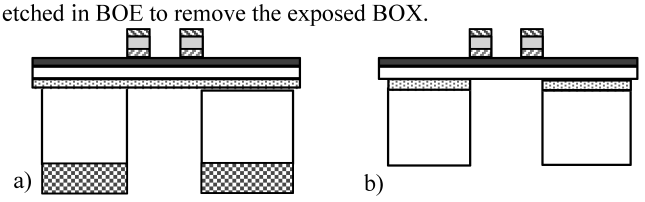

Figure 8: *Final process steps, device release. a) DRIE to BOX. b) Ash resist and wet etch backside to remove the BOX.*

The chip was flush mounted in a Lucite package shown in Figure 9, using epoxy to secure it. The electrical connections to the package leads were accomplished via short lengths of bare wire that were bonded using silver epoxy on the chip bond pads as well as to the copper pads on the package. The completed packaged microphone is shown in the photograph of Figure 10.

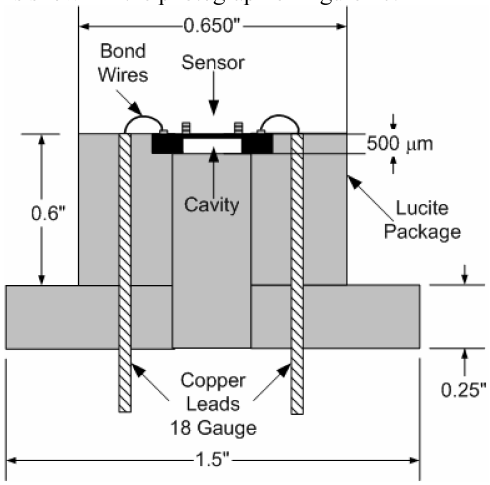

Figure 9: *Lucite package with leads and flush mounted chip.*

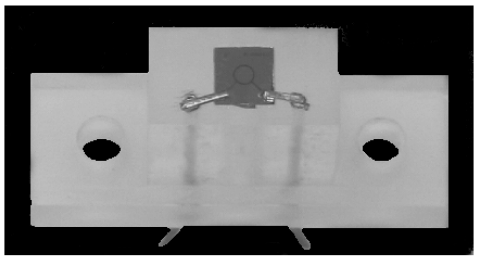

Figure 10: *Optical photograph of packaged microphone.*

EXPERIMENTAL SETUP AND RESULTS

Prior to full characterization of the device, the blocked electrical properties were measured prior to the release of the device using a vector impedance meter (HP Model 4294A) and are shown in Table 2.

Table 2: *Measured blocked electrical properties.*

C_{eb} [nF]	$R_e[M\Omega]$	ε_r	$\tan\delta$
13.9	1.7	809	0.007

Following the electrical characterization, the packaged device was mounted at the end of a $2.54\,cm$ square, normal incidence plane wave tube (Figure 11) to measure the frequency response and device linearity against a reference microphone (Brüel & Kjær (B&K) 1/8" Type 4138). The excitation signal was provided by a B&K PULSE Multi-Analyzer System to a $50.8\,mm$ coaxial compression driver (BMS Model 4590P) via a power amplifier (Techron Model 7540). The B&K PULSE was also used for data acquisition.

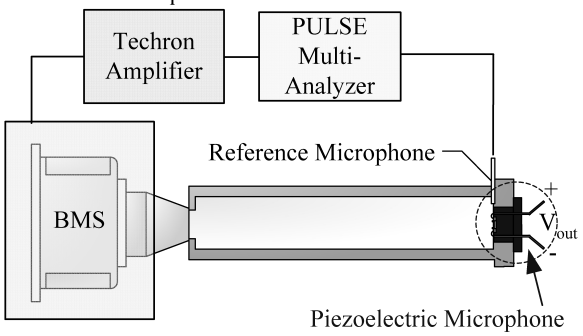

Figure 11: *Experimental setup in a plane-wave tube.*

The frequency response was measured using periodic random noise at $94\,dB$ and 1000 spectral averages over a bandwidth from 0 to $6.4\,kHz$ with a $1\,Hz$ bin width. A representative frequency response function of the sensor is shown in Figure 12 in terms of magnitude and phase. The response is flat over the testable frequency range up to $6.7\,kHz$, except for a low frequency roll-off of approximately $100\,Hz$. This is most likely due to the vent resistance; however, the magnitude of this contribution is unknown, as the value for the vent resistance due to packaging leaks has not been measured.

Representative linearity results, shown in Figure 13, were taken at $1\,kHz$. For each measurement, 100 averages were taken of the rms output voltage from the measured power spectrum using a $1\,Hz$ bin width with a rectangular window centered at $1\,kHz$ to avoid spectral leakage. The device is linear $\left(R^2 = 0.9995\right)$ up to (at least) the maximum testable sound pressure level of $169\,dB$.

The maximum testable level is limited by the output capacity of the compression driver. The measured sensitivity is $0.75\ \mu V/Pa$.

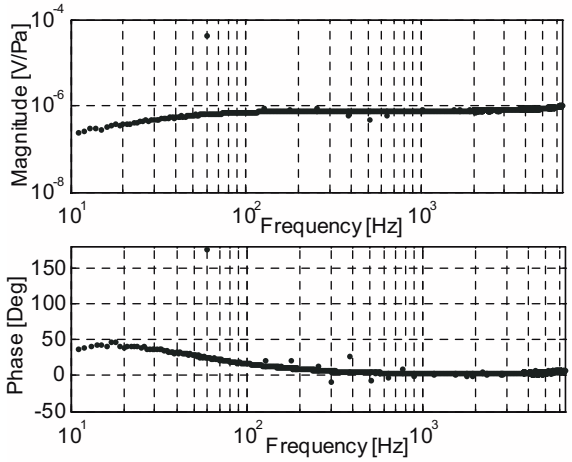

Figure 12: *Measured sensor frequency response.*

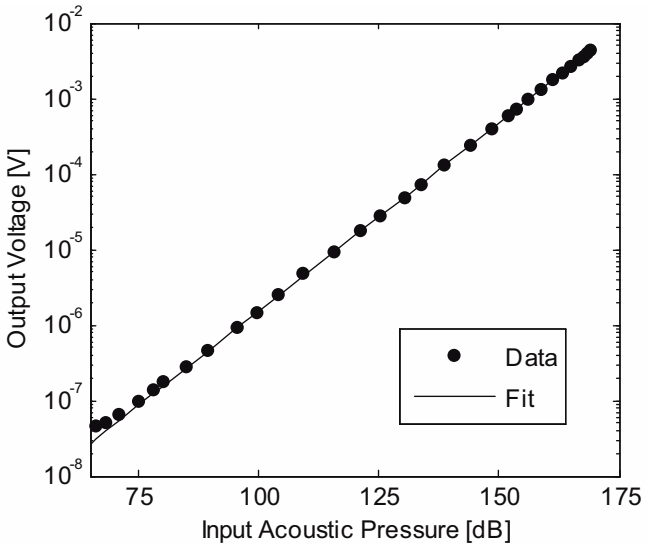

Figure 13: *Measured sensor linearity at 1 kHz.*

To obtain noise floor measurements, the sensor was mounted in a triple Faraday cage along with an SRS 560 low-noise preamplifier, through which the sensor output was routed, to triple-shield the sensor from potential electromagnetic interference. For the measurement, the preamplifier was set to a gain setting of 1000, with a high pass filter cutoff of $0.03\ Hz$ and a low pass filter cutoff of $1\ MHz$. The output of the preamplifier was then routed, via feed-through adapters, out of the Faraday cage to an SRS 785 dynamic signal analyzer.

The noise floor spectrum of the sensor is shown in Figure 14 to $12.8\ kHz$, along with the noise spectrum due to the experimental setup alone. The noise spectrum of the experimental setup alone was obtained by shorting the inputs to the preamplifier and recording the resulting output voltage signal, using the same conditions and setup as the sensor noise floor measurement. This noise power spectral density is characteristic of a resistance shunted by a capacitance. The resistance in this case is the sensor dielectric resistance, R_e, and the capacitance is the blocked electrical capacitance, C_{eb}. The resistance and capacitance form a low-pass transfer function that spectrally shapes the thermal noise. When integrated over an infinite bandwidth, the resulting mean square noise voltage is given by kT/C_{eb}, where k is Boltzmann's constant and T is the ambient temperature. For this device, the low pass filter has a cutoff frequency of $6.7\ Hz$, determined by $1/2\pi R_e C_{eb}$.

There are three characteristic regions in this spectrum. Below $6.7\ Hz$, there exists a relatively flat region where the noise is dominated by the resistance of the sensor. Then, from $6.7\ Hz$ up to approximately $2\ kHz$ a $1/f$ rolloff in the noise is observed that is consistent with a capacitive dominated noise source. Above $2\ kHz$, the noise spectrum flattens out again as the sensor noise approaches the setup noise. For a $1\ Hz$ bin width centered at $1\ kHz$, the output voltage with no acoustic signal applied is $3.69\ nV$, which corresponds to an equivalent acoustic pressure of $4.93\ mPa$ or $47.8\ dB$.

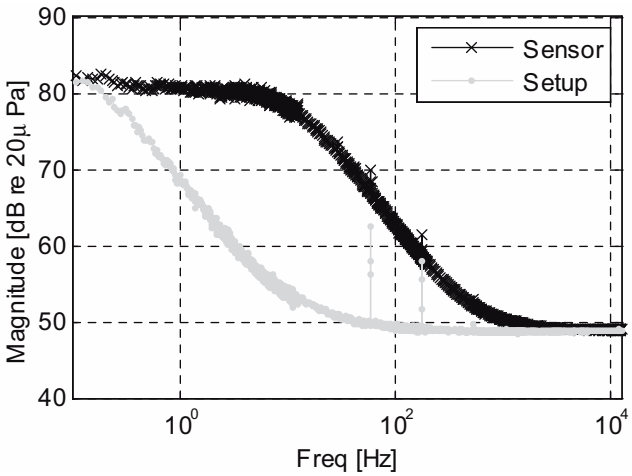

Figure 14*: Measured sensor noise floor spectrum.*

Because the device is a reciprocal transducer, the actuator frequency response can be used to gain additional information about the sensor response, such as the bandwidth **[10]**. In particular, the acoustically actuated frequency response could only be measured up to $6.7\ kHz$ due to testing limitations of the impedance tube. Using reciprocity, the bandwidth can be estimated via use of the electrically actuated frequency response as the piezoelectric microphone.

In order to determine the actuator frequency response, scanning laser vibrometry was performed. The packaged device was mounted under an Olympus BX60 microscope, with a 5x objective lens. The device was excited using white noise from an HP 33120A arbitrary waveform generator. Velocity data were obtained over the surface of the composite diaphragm using a Polytec OFV 3001S laser scanning vibrometer, with a Polytec OFV-074 microscope adapter. Diaphragm displacement was obtained via integration of the measured velocity frequency response. The actuator frequency response is shown in Figure 15 in terms of magnitude and phase. The resonance frequency is $50.8\ kHz$. This resonance provides an estimate of the usable bandwidth as a microphone.

The device characteristics are summarized in Table 3, demonstrating that this microphone has a larger bandwidth and dynamic range than existing piezoelectric microphones.

CONCLUSIONS

A MEMS-based piezoelectric microphone was developed for aeroacoustic measurements and consists of a circular composite

annular ring of PZT for electromechanical transduction. An electroacoustic equivalent circuit model was used to design the device. Experimental characterization yielded a sensitivity of $0.75\ \mu V/Pa$, with a linear dynamic range from $47.8\ dB$ to at least $169\ dB$. The resonant frequency was estimated to be $50.8\ kHz$ by measuring the actuator frequency response. The device characteristics are summarized in Table 3.

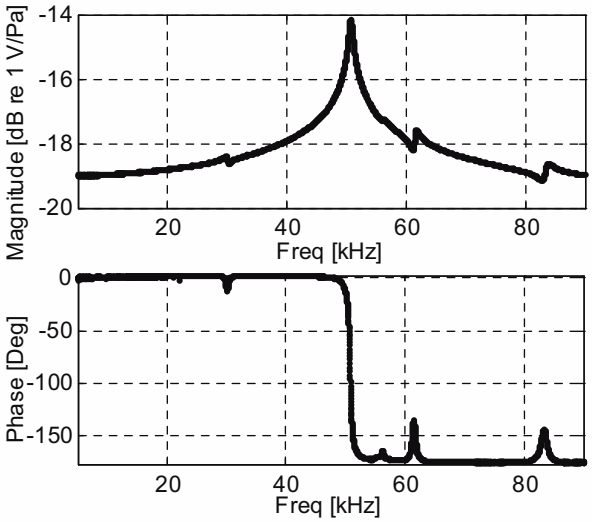

Figure 15: *Measured actuator frequency response.*

Table 3: *Summary of experimental results and comparison to previous work.*

Researcher	**Material**	**Sensitivity** $[mV/Pa]$	f_{res} $[kHz]$	**Noise Floor** $[dB]$
Present Work	PZT	$0.75\ \mu V/Pa$	50.8	47.8
Kim *et al.* **[4]**	ZnO	1	16	50[1]
Ried *et al.* **[5]**	ZnO	0.92	18	57[1]
Lee *et al.* **[2]**	ZnO	30	0.89	N/R
Royer *et al.* **[3]**	ZnO	0.25	10	66.02[2]
Schellin *et al.* **[6]**	polyurea	0.004–0.030	N/R	N/R
Ko *et al.* **[8]**	ZnO	0.51[3]	7.3	N/R

[1] A-weighted,[2] Method not reported,[3] At resonance

The theoretical predictions do not match the experimental results. Specifically, the predicted sensitivity was roughly a factor of three larger than that measured. This discrepancy is due to a combination of factors. First, there tends to be large uncertainties in the thin-film material properties. More importantly, the devices were statically deflected on the order of the diaphragm thickness due to large in-plane compressive stresses from the TiO_2. These large static deflections render the small-deflection assumption in the composite plate theory invalid.

Future work includes the extension of the composite plate model to large deflections. These models will then be validated against the current design and then subsequently used to synthesize an optimal design A new package design is necessary to provide a vent channel to the microphone for a controlled low frequency roll-off. Further characterization of the microphone is needed in order to determine variability from device to device, and to investigate reliability issues such as fatigue and stability of the piezoelectric modulus.

ACKNOWLEDGMENTS

Financial support for this research was provided by Sandia National Laboratories and monitored by Kent Pfeifer. The authors are also grateful for significant fabrication assistance provided by Stephanie Jones of Sandia National Laboratories.

REFERENCES

[1] T. Mueller, ed. *Aeroacoustic Measurements*. 2002, Springer-Verlag: Berlin. 313.

[2] S. Lee, R. Ried, and R. White, "Piezoelectric Cantilever Microphone and Microspeaker". *Journal of Microelectro-mechanical Systems*, 1996. 5,4: p. 238-42.

[3] M. Royer, J. Holmen, M. Wurm, and O. Aadland, "ZnO on Si Integrated Acoustic Sensor". *Sensors and Actuators, A: Physical*, 1983. 4: p. 357-62.

[4] E. Kim, J. Kim, and R. Muller. "Improved IC-Compatible Piezoelectric Microphone and CMOS Process".*Int Conf Solid State Sens Actuators*. San Francisco, CA. IEEE. (1991), p. 270-3.

[5] R. Ried, E. Kim, D. Hong, and R. Muller, "Piezoelectric Microphone with On-Chip CMOS Circuits". *Journal of Microelectromechanical Systems*, 1993. 2,3: p. 111-20.

[6] R. Schellin, G. Hess, W. Kuehnel, G. Sessler, and E. Fukada. "Silicon Subminiature Microphones with Organic Piezoelectric Layers: Fabrication and Acoustical Behaviour".*7th International Symposium on Electrets*. Berlin, IEEE. (1991), pp. 929-34.

[7] P. Scheeper, A. van der Donk, W. Olthuis, and P. Bergveld, "A Review of Silicon Microphones". *Sensors and Actuators A*, 1994. 44,1: p. 1-11.

[8] S. Ko, Y. Kim, S. Lee, S. Choi, and S. Kim, "Micromachined Piezoelectric Membrane Acoustic Device". *Sensors and Actuators, A: Physical*, 2003. 103: p. 130-4.

[9] E. Kim, R. Muller, and P. Gray. "Integrated Microphone with CMOS Circuits on a Single Chip".*International Electron Devices Meeting*. Washington, D.C. IEEE. (1989), p. 880-3.

[10] S.D. Senturia, *Microsystems Design*. 2001, Kluwer Academic Publishers, Inc. Boston, chapter 5.

[11] G. Wang, B. Sankar, L. Cattafesta, and M. Sheplak. "Analysis of a Composite Piezoelectric Circular Plate with Initial Stresses for MEMS".*International Mechanical Engineering Congress & Exposition*. New Orleans, LA. ASME. (2002).

[12] N. Setter, ed. *Piezoelectric Materials in Devices*. 2002, N. Setter, EPFL Swiss Federal Institute of Technology: Lausanne.

[13] D. Blackstock, *Fundamentals of Physical Acoustics*. 2000, John Wiley & Sons, Inc. p. 153-6.

[14] B. Tuttle, J. Voigt, T. Headley, B. Potter, D. Dimos, R. Schwartz, M. Dugger, J. Michael, R. Nasby, T. Garino, and D. Goodnow, "Ferrolectric Thin Film Microstructure Development and Related Property Enhancement". *Ferroelectrics*, 1994. 151: p. 11-20.

FLEXIBLE WIRELESS PASSIVE PRESSURE SENSORS FOR BIOMEDICAL APPLICATONS

Michael A. Fonseca [(1)], Mark G. Allen [(1)], Jason Kroh [(2)] and Jason White [(2)]
(1) School of Electrical and Computer Engineering
Atlanta, GA USA
(2) CardioMEMS, Inc. Atlanta, GA USA

ABSTRACT

Passive resonant sensors have been studied by many groups as an approach to sensing of physical properties in inaccessible locations without the need for incorporating any on-board power sources. In this work, we report two types of **wireless *flexible* micromachined passive pressure sensors**. Since the devices are flexible, they can be rolled or folded into compact shapes suitable for catheter-based delivery into the body. One design is semi-hermetic, intended for acute use. A second design is hermetic, intended for chronic use. Standard flexible and ceramic electronics packaging techniques are used to fabricate the devices. Devices were tested acutely *in vivo* for > 30 days in canine models simulating abdominal aortic aneurysms (AAA) which incorporated a wired reference pressure transducer. The sensor real-time dynamic pressure waveforms were measured and compared to acute devices, with indications for potential extensions to chronic use.

INTRODUCTION

In the measurement of physical parameters within living organisms, passive resonant circuit techniques have been used to create sensors that are wireless, do not require power supplies and can be implanted, both acutely and chronically. Passive resonant circuits used to measure physiological parameters date back to 1957 reported by Mackay [1]. In 1967 Collins reported a miniature "Transensor" ranging in size from 2-6 mm in diameter designed to be implanted in the eye [2]. These devices used two oppositely-wound planar spirals, connected at the periphery, to form an LC circuit with distributed inductance and capacitance. More recently, passive sensors have been developed for continuous measurement of intraocular pressure to monitor glaucoma using two types of sensors: a magnetic sensor and a resonant sensor, reported by [3]. A review of some passive wireless sensing efforts for measurement of physiological parameters was presented in [4]. That work also discussed the development and clinical demonstration in humans of non-flexible passive sensors for monitoring the pressure of abdominal aortic aneurysms (AAA).

Previous work demonstrated a passive wireless scheme used for pressure sensors in high temperature applications [5] and [6]. The concept presented a passive wireless scheme, fabricated from sintered laminated layers of ceramic sheets, indicating use up to 600 ºC. This was achieved through the use of passive resonant circuit structures that were self-packaged and did not incorporate active circuitry or an internal power supply. The fabrication and development began with processing techniques and components from the standard ceramic electronics packaging industry. In a similar lamination-based approach, the work presented in this paper uses standard flex-circuit fabrication techniques to form self-packaged *flexible* wireless passive resonant circuits to measure pressure. Such flexible structures would have the advantage over their non-flexible counterparts that they could be folded into compact shapes during delivery into the body. The devices implement planar spiral inductor coils on flexible polymer film substrates. Similar printed spiral coil structures were developed for transcranial telemetry reported in [7]. Two designs have been studied: a semi-hermetic design using liquid crystal polymers which has high ease of fabrication and is suitable for acute use; and a hermetic design using ceramic-encapsulated pressure references intended for chronic use.

DESIGN AND FABRICATION

The sensors in this work consist of a cavity, bounded on two sides by capacitor plates or distributed capacitive structures, resonantly interconnected with an inductance. If either the top or bottom (or both) sides of the cavity are made of a deflectable diaphragm, the value of this capacitor will change with pressure. The resultant pressure-induced change in the resonant frequency of the distributed passive LC circuit can be measured wirelessly using an external magnetic loop.

Standard flexible electronic packaging techniques are used to fabricate the sensors. Sensors designed for acute use are fabricated from laminated sheets of copper-clad Liquid Crystal Polymer (LCP) and expanded polytetrafluoroethylene (PTFE)-based inner bonding layers. The copper cladding is patterned into the desired inductor structures prior to lamination through standard lithography and wet-chemical etching. This approach results in a self-packaged structure in which only a polymer outer surface is exposed to the environment. The inductor coil layout uses a planar spiral inductor with 12 turns, line width of 60 micron, line spacing of 80 micron, and line thickness of 18 micron; the starting radius for the spiral inductor is 3.8mm. The capacitor plate area for the LCP sensor design is 13.1mm^2. *Figure 1 (a)* illustrates the planar coil design for the LCP design.

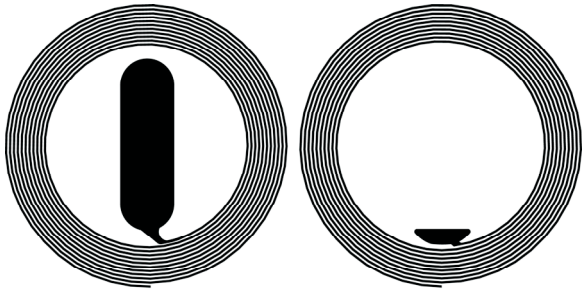

Figure 1 *Planar spiral inductor layout for (a) LCP sensor design and (b) PTFE/ceramic chamber design.*

The inner layer of the LCP sensor, illustrated in *Figure 2 (a)*, is laser-cut using an excimer laser (248 nm wavelength) to achieve accurate dimensions. The span was designed to be 2mm at the ends and 1.4mm at the center with a length of 6.68mm. The cavity was tapered in the center to reduce the deflection and avoid shorting out the capacitor over pressure excursions of interest.

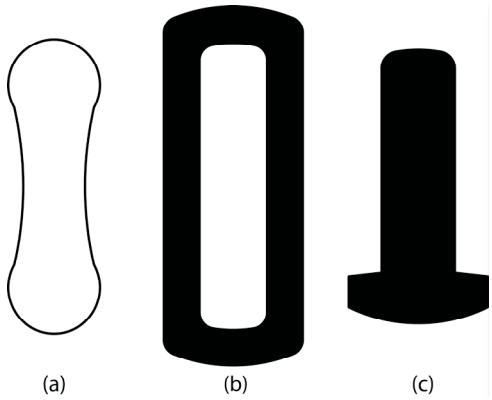

Figure 2 *Inner layer designs for (a) the LCP sensor, (b) ceramic chamber and (c) electrode on the ceramic chamber.*

The layers are aligned via registration pins on platens, assembled and laminated at 180 ºC for 80 minutes with 431 kPa of pressure, illustrated in *Figure 3*. The batch process uses 4 inch sheets with 4 rows and 4 columns, yielding 16 devices per fabrication run. The sensors are individualized using the same excimer laser to achieve various shapes for minimally-invasive delivery. A fabricated sensor is illustrated in *Figure 5 (a)*.

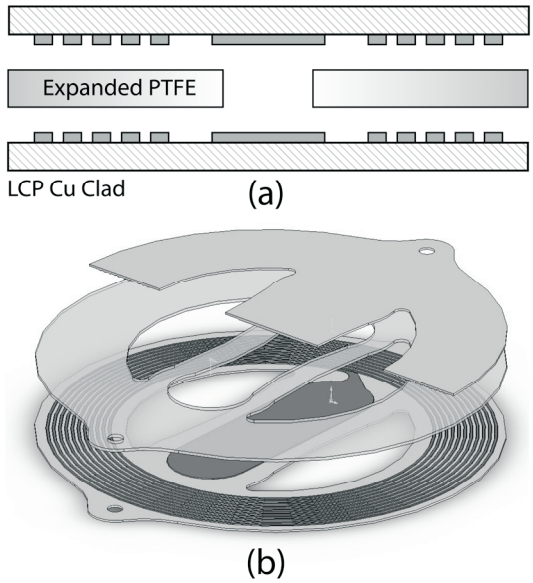

Figure 3 *Sensor lay up for acute use. (a) Cross-sectional view and (b) perspective view of the LCP sensor design.*

Sensors designed for chronic use are fabricated from both copper-clad and non-clad PTFE layers, Fluorinated Ethylene Propylene copolymer (FEP) inner layers, and an encapsulated ceramic chamber (housing the hermetic pressure reference), again resulting in self-packaged structures. Only a PTFE outer surface is exposed to the environment.

The planar inductor coil layout for the PTFE sensor design, illustrated in *Figure 1 (b)*, has the same physical dimensions as the LCP design described above. The chambers are fabricated through the used of sintered layers of zirconia ceramic powders using a standard green-tape approach [6]. The layout design has spans ranging from 1.7- 2.5mm and gaps from 25-50 microns, illustrated in *Figure 2 (b)* and *Figure 4*. The inner layer of the chamber is laser-cut in a green state using a Nd:YLF infrared laser (1 micron wavelength). The sheets are aligned and assembled, three sheets per stack, with thicknesses between 25-35 microns, laminated in a press, and sintered in a box furnace at temperatures between 1300-1500 °C. The ceramic chambers are batch-fabricated with 54 chambers per sheet on a 4 inch sheet. After the ceramic chambers are sintered, they are individualized for assembly into each polymer sensor.

The PTFE and FEP inner layers are laser cut using a CO_2 (10.6 micron wavelength) laser for the solder connection, illustrated in *Figure 4 (a)*, and chamber assembly. The copper clad, inner PTFE and FEP layers, ceramic chambers and solder pellets are aligned and assembled (16 devices per run on 4 inch sheets). The sheets are vacuum laminated in a hot press at 300 °C, for 60 minutes with 431 kPa of pressure. The vacuum eliminates trapped gas between the FEP and ceramic chamber. The sensors are individualized using a CO_2 laser to achieve various shapes for minimally-invasive delivery. A fabricated sensor is illustrated in *Figure 5 (b)*.

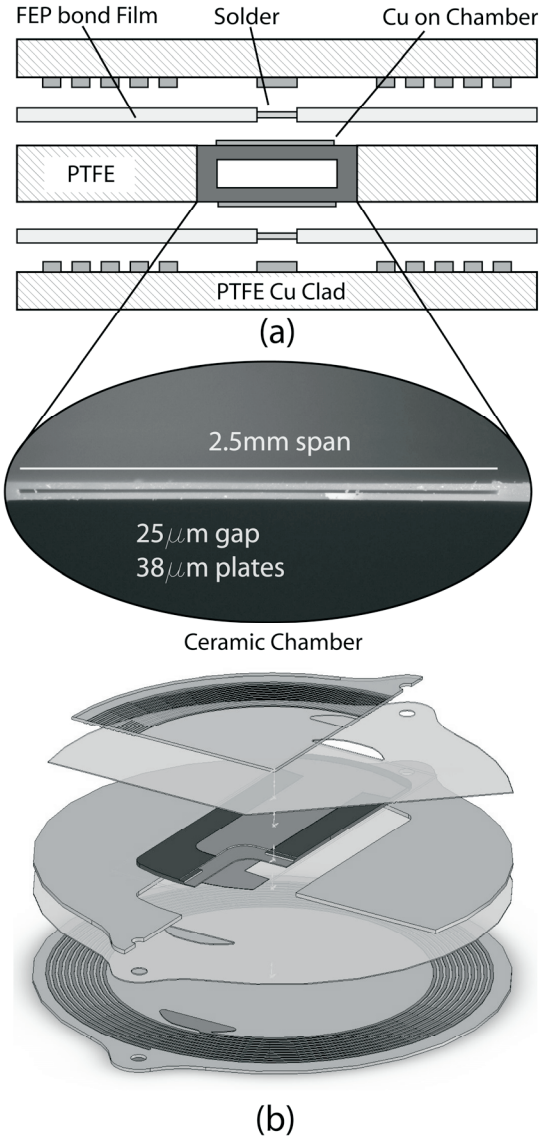

Figure 4 *Sensor lay up for chronic use. (a) Cross-sectional view and (b) perspective view for the PTFE/Ceramic chamber sensor design.*

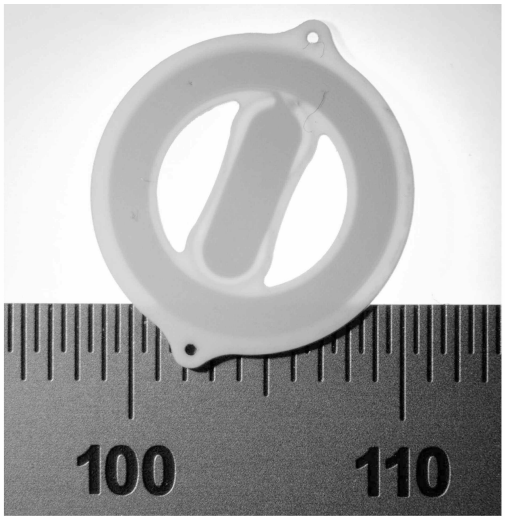

(a)

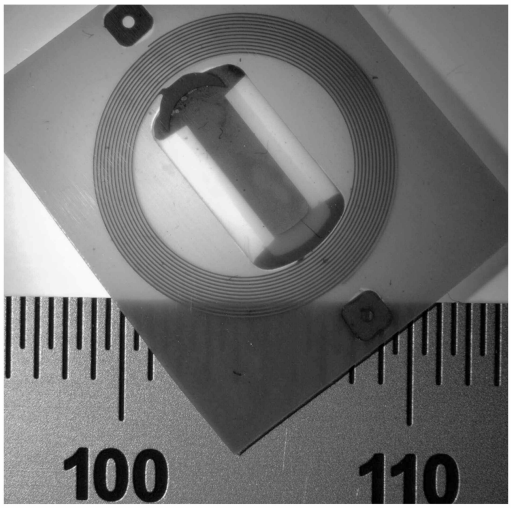

(b)

Figure 5 *Fabricated for (a) acute use using LCP polymer and (b) chronic use using PTFE with ceramic pressure sensitive chamber.*

THEORY AND DEVICE CHARACTERIZATOIN

The development of a circuit model was reported in previous work for passive LC resonant circuits [5] and [6]. The sensors described above can be modeled by a lumped LCR circuit, illustrated in *Figure 6*. Analysis of the circuit results in the input impedance referenced to the terminals of the coupling coil. Substituting into the input impedance $f_o=[2\pi(LC)^{½}]^{-1}$, $k=L_m(L_aL_s)^{-½}$ and $Q=\omega L_sR_s^{-1}$ results in Eq. 1 below.

$$Z_1 = \frac{V_1}{I_1} = j2\pi f L_a \left[1 + k^2 \frac{\left(\frac{f}{f_o}\right)^2}{1-\left(\frac{f}{f_o}\right)^2 + \frac{1}{Q} j \frac{f}{f_o}} \right] \qquad (1)$$

Eq. (1) can be used to fit impedance measurements from a network analyzer and pickup-coil in order to extract the resonance frequency and quality factor, illustrated in *Figure 7*.

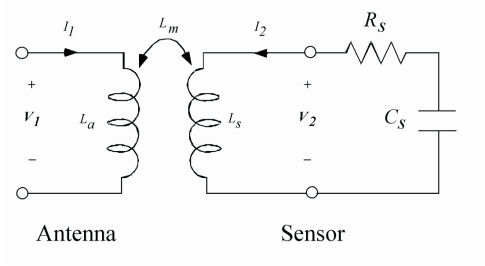

Figure 6 *Equivalent circuit of electrical model for a sensor coupled with an antenna.*

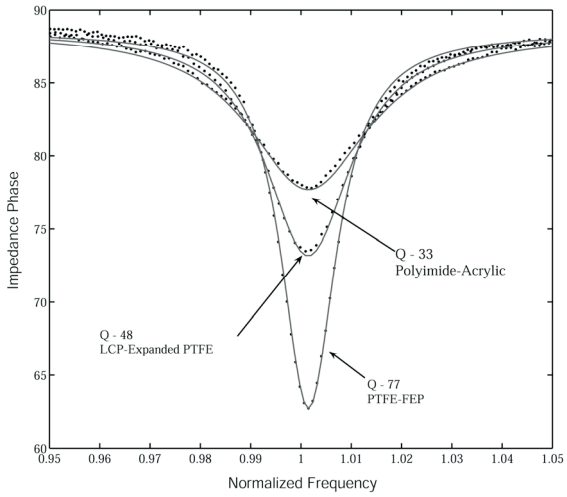

Figure 7 *Impedance Phase data (dots) and model curve fit (line) vs. normalized frequency for three different substrates*

Throughout the development of the two sensors described above, various flexible substrates were tested and characterized. These include polyimide-acrylic, LCP/expanded PTFE, PTFE, PTFE/FEP, and PTFE/FEP/Ceramic. For each progression of substrate material, increasing values of quality factor were achieved; similarly different values of hermeticity were achieved. In order to compare substrates, the layout for the planar spiral inductors were limited to those in *Figure 1*, resulting in resonant frequencies ranging from 30-50 MHz. *Table 1* below lists quality factors achieved vs. substrate materials and electrical characteristics.

Table 1 *Quality factors achieved vs. substrate material and electrical characteristics*

Substrate/Bonding Film	Quality Factors	Dielectric Constant @ ≥ 1 MHz	Dielectric Loss @ ≥ 1 MHz
Polyimide-Acrylic	25-35	(3.7)/(3.6)	(0.0014)/(0.035)
LCP/expanded PTFE	45-55	(2.9)/(2.6)	(0.0025)/(0.004)
PTFE	55-65	2.2	0.0008
PTFE/FEP	65-77	(2.2)/(2.05)	(0.0008)/(0.0006)
PTFE/FEP/Zirconia	60-65	(2.2)/(2.05)/(29)	(0.0008)/(0.0006)/(0.001)

The linear pressure sensitivity of several devices was characterized between -1 to -20 kHz/mmHg for LCP/expanded PTFE devices and -0.5 to -1.5 kHz/mmHg for PTFE/FEP/Ceramic devices. The difference in sensitivities is attributed in part to the increased modulus of the ceramic layer of the pressure sensitive membrane.

The electrical properties were characterized in both deionized (DI) water and saline solution in order to simulate *in vivo* conditions. In both designs, the DI water environment resulted in frequencies lower than those measured in air. In the saline

environment, the measurements resulted in a lowering of quality factor as well as frequency compared to measurements in air. When submerged in saline, both device designs dropped in frequency by ≥ 3 MHz and dropped in quality factor to ≤ 40. These initial changes were followed on the LCP/expanded PTFE design by a gradual decrease in frequency over a timeframe of several days. The PTFE with ceramic pressure sensitive chamber devices showed only the immediate changes, with no significant gradual change.

The initial frequency upon immersion in saline or DI water was attributed to the change in dielectric constant of the surrounding environment (shift from air ε_r ~1 to saline ε_r ~80). The increase in dielectric constant increased parallel paths of electric field through the surrounding media, increasing the total capacitance of the system, leading to a decrease in resonant frequency.

The decrease in quality factor in saline was attributed to the change in loss tangent between air or DI water to saline (from approximately 0 to 0.2); penetration of electromagnetic field lines into this high loss tangent environment increases total losses and reduces the quality factor.

In order to reduce the offsets, losses, and potential drift due to changes in the dielectric environment in which the sensors are embedded, the devices were coated with approximately 0.3 mm thick outer layer of silicone. The addition of this low dielectric constant and low-loss insulating material reduced the fringe electric fields exiting into the surrounding media and reduced this effect. Typical shifts in frequency after silicone coating were < 0.7 MHz, with quality factors dropping between 3-5 points. These offsets could be reduced further for these designs by coating to a greater thickness. Catheter based delivery of the devices limited the total thickness of the sensors.

For LCP based devices, the average normalized frequency drift in saline (under zero applied pressure) was measured to be ≤ -1.75 ±0.32 %, reaching stability after 250 hrs. This is equivalent to -0.612 MHz for a 35 MHz device, and equates to a pressure-equivalent baseline drift of 61.2 mmHg for devices with nominal pressure sensitivities of -10 kHz/mmHg. This baseline drift could be attributed to many factors including moisture absorption into the polymer and/or into the reference pressure chamber of the sensor. For PTFE-ceramic based devices the average normalized frequency drift in saline (under zero applied pressure) was measured < ±0.002% for over 20 hours. This is equivalent to ≤ ±0.7 kHz for a 35 MHz device, and equates to a pressure-equivalent baseline drift of less than 1 mmHg at a nominal pressure sensitivity of 1 kHz/mmHg.

IN VIVO EXPERIMENTAL RESULTS

The devices were tested *in vivo* in canine models simulating abdominal aortic aneurysms, illustrated in *Figure 8*, with LCP based acute devices that were implanted and measured. The aneurysms were created by surgically implanting a graft and wired reference pressure transducer into the aorta. The canine model is described in greater detail in [8]-[10]. After the animal was allowed to heal, the sensors were implanted through catheter delivery, following which a stent graft was used to perform endovascular repair. The following section will describe the catheter and electronics used throughout the test along with measured results.

CATHETER DELIVERABILITY

For minimally invasive implantable devices, catheter based delivery systems are preferable. The flexible sensors could be rolled or folded into catheters that have internal diameters of ≤ 4 mm. The delivery system used for this study consisted of a delivery catheter, sheath, deployment-clip and sensor-tether, illustrated in *Figure 9 (a)*. The sensor is attached to a small diameter (0.020" OD) 'tether tube', *Figure 9 (b)*, by threading a small diameter (0.008") nitinol wire through the length of the tube, and through holes on the top and bottom portion of the sensor, which are shown in *Figure 5 (a)*. The tether tube maintains control over device position in the aneurysm sac by the user, until completion of the endovascular repair with the stent graft. At the time of release, the thin wire is pulled by the user to release the sensor in the desired location within the aneurysm.

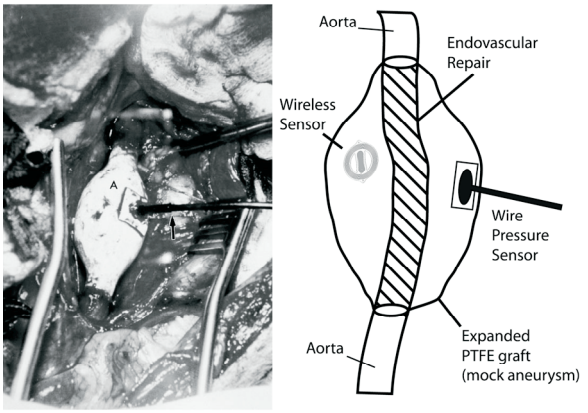

Figure 8 *Creation of mock aneurysm and position of wired and wireless sensor*

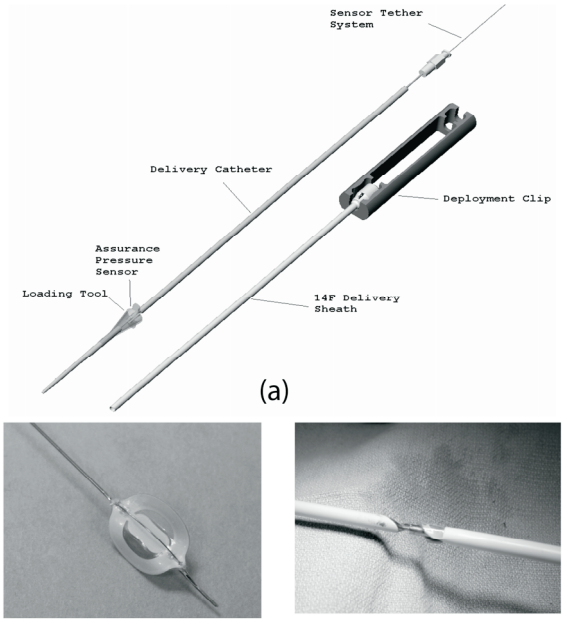

Figure 9 *Sensor delivery system. (a) Schematic of delivery system; (b) sensor on tether; (c) sensor rolled up into sheath prior to implantation*

In order to facilitate folding, additional cut-out features were added to the sensor design in between the planar spiral coils and center pressure-variable capacitor; these are observed in *Figure 5 (a)*. The cut-outs allow for the sensor to be rolled up inside the catheter, illustrated in *Figure 9 (c)*. The delivery procedure introduces the catheter though a cut-down in the femoral artery. The system is advanced into position within the mock aneurysm. The catheter is retracted, exposing the sensor on the tether tube

(a)

(b)

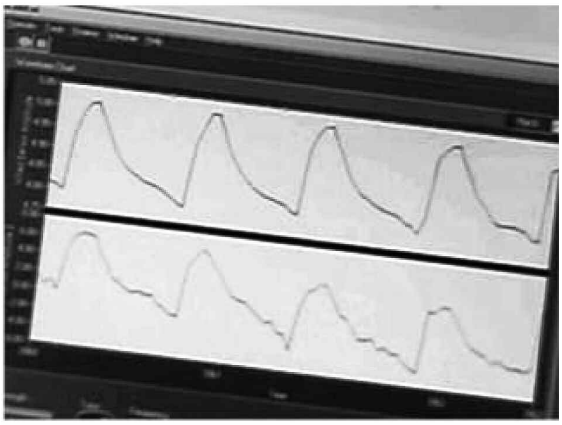

(c)

Figure 10 *Readout telemetry system; (a) system during a measurement while the animal was sedated; (b) antenna on canine during un-sedated measurement; (c) LabVIEW screen-shoot of measurement with the reference signal on the top and wireless pressure sensor on the bottom.*

The sensor is retained on the tether tube until endovascular repair of the aneurysm is completed with a stent graft. Once the sensor is trapped in the space created between the outer surface of the stent graft and the inner surface of the mock aneurysm, the tether wire is pulled, releasing the sensor. The tether tube and delivery catheter are removed, leaving the sensor in the "excluded" portion of the aneurysm sac.

Readout Telemetry

The readout telemetry system consists of switched transmit and receive magnetic loops, a switched RF amplifier and high-sensitivity RF receiver. The system is driven by a microprocessor and phase synchronous oscillator. The system sends a burst of RF energy at the resonant frequency of the devices lasting several microseconds, which is optimized to be long enough to energize the sensor. Soon afterward, the transmit signal is turned off and the receive channel is opened. For a short period of time, based on the sensor quality factor, the sensor will continue to oscillate at the resonant frequency and exponentially decay to zero; this is repeated at the sampling rate of the system. In order to track the sensor real-time frequency response, a phase-locked-loop was implemented. Since the sensors are absolute pressure sensors, a barometric pressure sensor is incorporated into the system to adjust for atmospheric pressure changes in order to report pressure in the aneurysm sac relative to atmospheric pressure. Additional inputs were added to system to be able to readout various catheter based transducers in order to compare to wireless pressure readings. The system is controlled through a LabVIEW software interface, shown in *Figure 10 (c)*. Using this method, devices could be read-out to distances of ≥ 20cm, which was sufficient to achieve measurements in canine models.

Animal Study Results

A total of four devices were implanted into four different animals for a period ranging between 30-60 days. Throughout the study some of the wired reference pressure transducers failed. No failure of the wireless sensors during the study was observed. Also, throughout the study, the telemetry system was improved, which increased the fidelity of the data. The data reported below represents typical results from the four devices. Data was recorded in 60 to 120 second intervals at sampling rates of > 120 Hz, which was sufficient to capture the highest frequency content of interest in the pulse train, illustrated in *Figure 11*. The sensor frequency response to pressure change was determined by pre-implant testing of Fo vs. pressure change in lab testing. At the time of implant, a fluid filled catheter was placed in the aneurysm. The mean (baseline) pressure of this catheter was used as a reference to determine the initial (baseline) mean pressure for the wireless sensor and the wired pressure transducer.

Data was collected beyond 30 days for most of the devices, with pulse pressures ranging between 12 – 37 mmHg and mean pressures ranging from 70 – 120 mmHg. *Figure 12* illustrates the pulse pressure readings over 41 days for both wired and wireless devices. The wireless sensor readings were within the error bars of the reference sensor, indicating low to zero change in response to dynamic pressure changes (pulse pressure). The mean (baseline) frequency drift over the same time is plotted on the secondary axis of *Figure 12*. Over the first six days, the mean frequency drifted by -154 kHz, which is equivalent to an increase in pressure of 28.52 mmHg. Beyond six days the mean frequency continued to drift downward. From the data colleted it is clear that the LCP based sensors are not suitable for applications where an accurate mean pressure reading over time is important. However, this sensor design could be used for long periods of time measuring pulse pressure changes. Improved *in vivo* results are expected from PTFE/ceramic sensors based on results from lab testing.

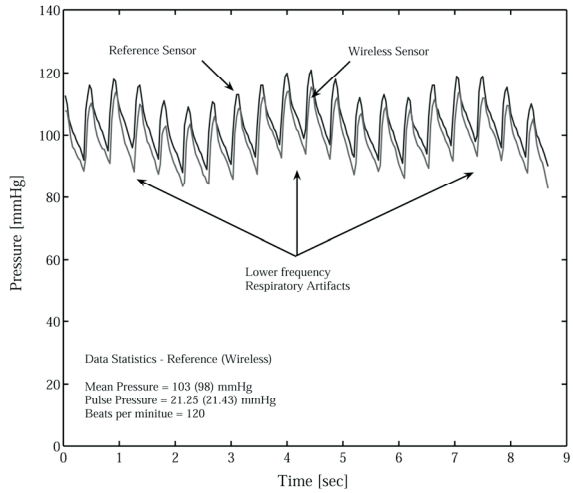

Figure 11 *Continuous pressure waveform of wired and wireless pressure sensor for implanted acute device. Wireless sensor linear sensitivity is -5.76 kHz/mmHg; resonant frequency is 35.675 MHz.*

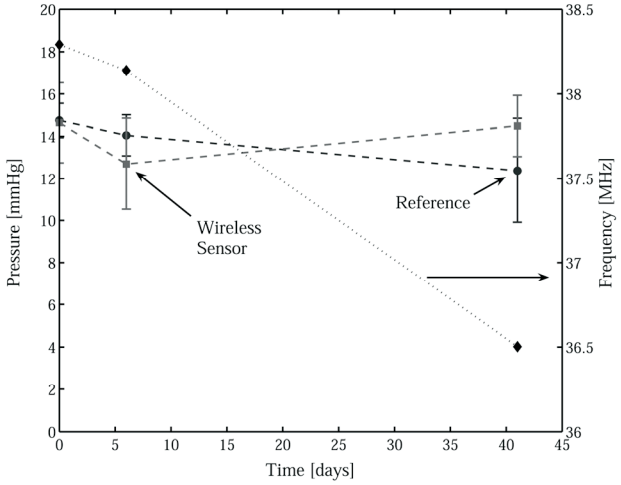

Figure 12 *Pulse pressure vs. time for wired and wireless pressure sensor for acute device (primary axis) and mean resonant frequency vs. time for wireless sensor. Wireless sensor linear sensitivity is -5.4 kHz/mmHg; resonant frequency is 38.293 MHz.*

CONCLUSIONS

The design, modeling, fabrication and characterization for flexible wireless pressure sensors intended for biomedical applications are presented. The devices were fabricated from flexible polymer substrates and optionally-incorporated ceramics, through lamination techniques, in order to implement a passive resonant circuit capable of wireless interrogation. Two sensor designs were presented, one of which is intended for acute use and a second one intended for chronic use. The acute sensor design was implanted, through catheter delivery, into a mock aneurysm in a canine model. Endovascular repair was performed after implantation to exclude the sensor within the aneurysm. Using a telemetry system, measurements of real-time dynamic pressure waveforms were acquired and compared to wired pressure reference transducers. The *in vivo* pulse pressure readings for the wireless acute device showed good correlation to the reference pressure transducer. The acute device drifted in mean (baseline) pressure compared to the reference during the test period. Animal studies on the chronic sensor design have not yet been initiated, but improved baseline drift results are expected based on bench simulated testing. Although neither flexible sensor has yet demonstrated *in-vivo* baseline drift performance of the human-use-approved sensors of [4], both show promise in applications where sensor flexibility is an important factor.

ACKNOWLEDGMENTS

The authors would like gratefully acknowledge Dr. Jay Yadav and Dr. Takao Ohki of the Cleveland Clinic, OH and Montifiore Medical Center, NY, respectively, for their valuable technical input and assistance, as well as the CardioMEMS, Inc. staff, led by CEO David Stern. Also, the authors would like to acknowledge Benjamin King for his assistance in fabrication and characterization, as well as Richard Shafer for his valuable technical discussion.

REFERENCES

[1] R. S. Mackay and B. Jacobson, "Endoradiosonde," *Nature,* vol . 179, pp 1239-1240*,* (June, 1957).

[2] C. C. Collins, "Miniature Passive Pressure Transensor for Implanting in the eye," *IEEE Transactions on Biomedical Engineering*, vol. BME-14, no. 2, (1967).

[3] S. Lizón-Maritinez, R. Giannetti, J. L. Rodrígez-Marrero and B. Tellini, "Design of System for Continuous Intraocular Pressure Monitoring," *IEEE Transaction of Instrumentation and Measurement*, vol. 54, no. 4, (2005).

[4] M. G. Allen, "Micromachined Endovascularly-Implantable Wireless Aneurysm Pressure Sensor: From Concept to Clinic," *Proc. Transducers 2005*, vol 1, pp 275 – 278, (2005).

[5] M. A. Fonseca, J. M. English, M. von Arx, M. G. Allen**,** "High Temperature Characterization of Ceramic Pressure Sensors," *Proc. Transducers 2001*, vol. 1, p 486-489, (2001).

[6] M. A.. Fonseca, J. M. English, M. von Arx, M. G. Allen, "Wireless Micromachined Ceramic Pressure Sensor for High-Temperature Applications," *IEEE/ASME J. Microelectromechanical Systems*, vol. 11, no. 4, p.337-343 (2002)

[7] M. R. Shah, R. P. Phillips and R. A. Normann, "A Study of Printed Spiral Coils for Neuroprosthetic Transcranial Telemetry Applications," *IEEE Transactions on Biomedical Engineering*, vol. 45, no. 7, (1998)

[8] L. A. Sanches et al, "Chronic intraaneurysmal pressure measurement: An experimental method for evaluating the effectiveness of endovascular aortic aneurysm exclusion," *J. Vascular Surgery*, vol. 26, issue 2, pp 222-230, (1997).

[9] P. L. Faries et al, "An Experimental Model for the Acute and Chronic Evaluation of Intra-aneurysmal Pressure," *Valcular Surgery*, pp 290-297, Aug (1997).

[**10]** T. Ohki et al, "Preliminary Results of an Implantable Wireless Aneurysm Pressure Sensor in a Canine Model: Will Surveillance CT Scan Following EVAR Become Obsolete?," *J. Endovascular Therapy*, vol. 10, pp. 1-32, (2003).

A HIERARCHICAL GECKO-INSPIRED SWITCHABLE ADHESIVE

Michael T. Northen
Materials Department
University of California at Santa Barbara
Santa Barbara, CA 93106, USA

Kimberly L. Turner
Mechanical Engineering Department
University of California at Santa Barbara
Santa Barbara, CA 93106, USA

Christian Greiner & Eduard Arzt
Max Planck Institute for Metals Research, Heisenbergstrasse 3
D-70569 Stuttgart, Germany

Abstract

The gecko, as well as other insects and lizards, have a very clever mechanism for reversibly adhering to just about any surface. An integrated multi-scale system enables geckos to run up, down and across vertical or inverted surfaces. Here we report the fabrication of a switchable on/off adhesive. Inspired by the gecko, a hierarchical system composed of aligned vertical polymeric nanorods coating ferromagnetic nickel platforms was fabricated. When subjected to a magnetic field, the nickel platforms undergo a reversible conformational change, reducing the available contact area, and reducing adhesion by 40 fold. Development of such adhesives will lead to a new paradigm in latching systems, and will enable microrobots to climb just about anything, allowing them to enter environments inhospitable to man.

Introduction

The mechanism of adhesion in the gecko dry adhesive has been of scientific interest since Aristotle observed a gecko running up and down a tree (*1*). Recently there has been an intensifying scientific investigation into the fundamental physics of the adhesive isolating van der Waals as the primary interaction (*2, 3*), with some contention that capillarity contributes to the adhesion (*4, 5*). Regardless of the fundamental interactions at the atomic scale, there is clearly a great deal of function contained in the hierarchical structure of the gecko's tarsus (*6-9*). The structure consists of 200 nm spatular termini at the ends of ~100 μm long, ~5 μm diameter setae, which extend from a compliant tarsal pad cushioned by blood sinuses(*10-13*). With each added level of surface compliance there is an increase in the contact area of system, correspondingly increasing adhesion(*6*). Even the toe of the gecko, which can wrap around surface features, serves to increase surface contact area. To better understand this concept, compare the comfort of sitting on a hard wooden bench to that of a cushioned recliner. The recliner is much more comfortable, because the weight of your body is displaced over a larger area. Now imagine they are both coated with an adhesive. Which will be more difficult to get out of? Thus a critical factor in the functionality of an adhesive is the ability of the surface to deform, to evenly displace load, and increase contact area.

There is, however, evidence that the hierarchical structure may serve another purpose – to reduce adhesion (*2, 14, 15*). Just as interesting as the gecko adhesion mechanism is the mechanism by which the gecko is able to release a surface. The specific geometries of the gecko's setae and spatulae allow the gecko to control adhesion through macroscopic movements of its toes. By flexing muscles the toe of gecko peels away from the surface in an inward fashion. This in itself aids in the detachment of the foot, just as peeling a piece of tape off of a surface is easier than trying to pull it off all at once. But there is more to the story. It has been shown theoretically (*16*) and experimentally (*3*) that the magnitude of adhesion of the setae is greatly dependent on the angle of applied pull-off force. Thus when the gecko goes from a squeezing mechanism to a peeling mechanism, the adhesive force goes from a maximum to a minimum (*16*). This can also be seen at the nanoscale as the resolved force on the spatulae changes the interactions from a frictional regime to a peeling regime, greatly reducing the adhesion (*6*). So through clever geometrical design of a hierarchical structure the gecko is able to control the adhesion mechanics from the macro-scale to nano-scale through a macroscopic muscle movement.

Previously, a synthetic system enhancing adhesion through a hierarchical structure was fabricated and tested(*17*). Just as the gecko uses this system to both increase and decrease adhesion, here a hierarchical structure has been fabricated to turn on and off adhesion. However, where the gecko uses muscle to actuate a β-keratin structure, the synthetic system uses a magnetic field to actuate nickel cantilevers. The nickel beams, when placed in a magnetic field, reorient themselves so that the terminal pad of the structure, responsible for adhesion, rotates orthogonally to an adhering surface. This conformational change effectively turns off the adhesion of the structure.

Fabrication

Released 150-500 nm thick and 100 μm long nickel structures, coated with aligned vertical arrays of stiff polymeric nanorods ~200 nm in diameter and ~3 μm tall, were fabricated using a combination of compatible massively parallel fabrication techniques. The fabrication process began by coating blank 4 inch (100) silicon wafers with a 1.4 μm thick layer of image reversal photoresist, AZ 5214. The negative image of the desired platforms was then transferred into the resist across the entire wafer using a Karl Suss MA6 contact aligner. After developing, a 150 nm thick nickel layer was electron beam evaporated onto the entire wafer. The photoresist was then removed, via an ultrasonic acetone bath, lifting off the excess nickel. The wafer was then cleaned and dried and a 7 μm layer of photoresist was spun onto the wafer surface, Shipley SPR 220-7. The positive pattern of the platforms was then transferred into the resist, aligned with the nickel platforms below. The resist and nickel pattern was then transferred into

the exposed silicon alternating between a highly reactive mostly isotropic SF_6 etch and a C_4F_8 passivation deposition, the Bosch process, effectively etching vertically into the silicon. After etching approximately 30 µm into the silicon, a sustained SF_6 etch was performed to undercut the nickel/photoresist platforms. The released platforms were then placed in oxygen plasma with an applied bias between wafer and plasma, creating ~200 nm diameter nanorods, orthogonally on the surface, with an aspect ratio of ~15, Fig. 1.

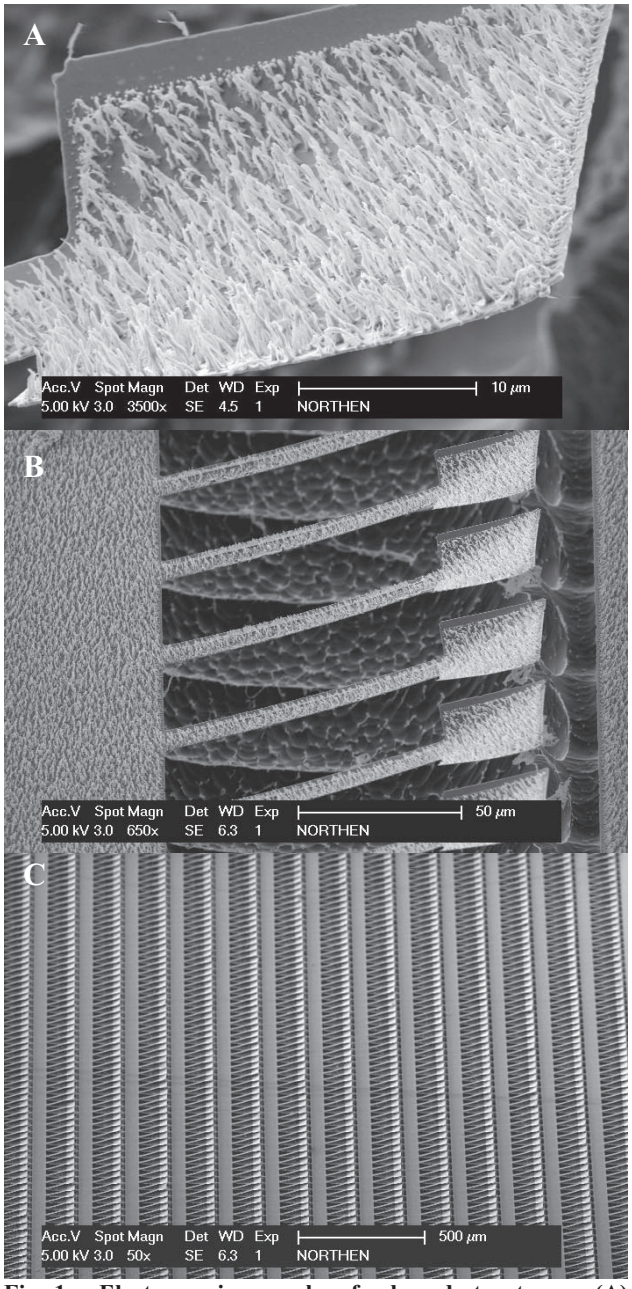

Fig. 1 – Electron micrographs of released structures. (A) Paddle surface coated with evenly spaced uncondensed aligned vertical polymer nanorods, scale bar 10 µm. (B) Freestanding nickel cantilevers and paddles coated with nanorods, scale bar 50 µm. (C) Lower magnification view of a portion of the array, scale bar 500 µm.

Adhesion Testing

The structures were characterized using a home built adhesion test apparatus, Fig. 2. The basic operating principle of the system is very similar to an atomic force microscope, except on a larger scale, where the deflection of a cantilever is monitored, using laser interferometry, to determine the forces applied to a probe tip. In this work, a custom 5 mm flat punch glass probe was manufactured. Proper registration of tip and stage was accomplished by the marriage of probe and cantilever (using high strength glue), with the cantilever secured in the apparatus, and the probe resting flush on the sample stage. Test samples were placed on the micropositioning stage and moved to near contact with the test probe. The probe was then lowered using a piezo electric actuator, and proper probe/sample alignment was observed through a horizontally oriented stereomicroscope. Actuation of the probe and data collection was performed using an automated National Instruments Lab View program. The program simultaneously moved the probe towards the surface and monitored the deflection of the cantilever. Through calibration of the cantilever, spring constant equal to 137.1 N/m, it was possible to determine the interaction forces between the flat punch probe and the test surface. Upon withdrawal from the surface, adhesion would produce a characteristic pull-off event, evident in the negative dip of the force curve, Fig. 4. The reversible adhesive was tested with and without a Neodymium Iron Boron rare earth metal magnet below the silicon chip.

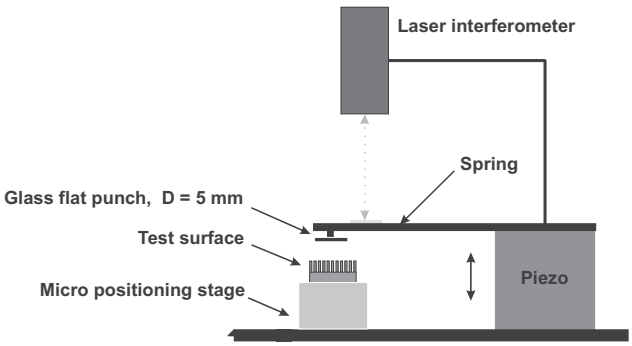

Fig. 2 – Schematic of the adhesion test apparatus. A laser interferometer monitors the deflection of a glass cantilever spring as a piezo actuator moves a 5 mm glass flat punch into and away from the test surface. The interaction forces are calculated by relating the stiffness and deflection of the cantilever upon contact with the surface.

Results and Discussion

Fabrication of the multi-scale structures required the integration of two different processing modalities. The nickel platform microstructures were photolithographically defined and etched using standard microfabrication reactive ion etching. The vertically aligned polymeric nanostructures were created through a stochastic growth method. Both methods employ batch fabrication techniques and scalable for production quantities. So in addition to being the first actuated hierarchical biomimetic adhesive, this system does not present a technological dead end.

The bilayer of the photoresist coating the nickel beams induces a stress mismatch which causes the beams to bend up and out of the device plane, Fig. 1. The upwards bent cantilevers aid in adhesion through enhanced structural compliance, and move the active portion of the adhesive away from the surface. With the active portion of the adhesive isolated the properties of the adhesive could then be controlled by actuating the platforms. High-aspect-ratio ferromagnetic structures have been shown to rotate within a magnetic field to align their long axis with a magnetic field (*18*). When the structures were placed on top of a permanent magnet the platforms were observed to rotate about their long axis, Fig. 3. This rotation is attributed to the preferential alignment of the long axis of the width of the pad in the magnetic field. This rotation reduces the orthogonal contact area, as evident in the stereo-micrograph in figure 3.

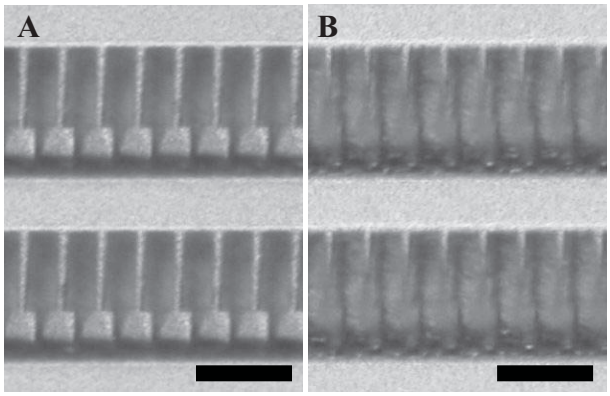

Fig. 3 - Stereomicrographs of the adhesive: (A) in the 'ON' state, no applied magnetic field, with the adhesive paddles facing vertically; and (B) in the 'OFF' state, with an applied magnetic field rotating the paddles sideways, concealing the adhesive faces. Scale bars, 100 µm.

Adhesion testing of the structures, without an applied magnetic field, produced loading and unloading curves with a characteristic pull-off event, Fig. 4. The magnitude of the pull-off force was taken to be the adhesion, and was observed to vary with the maximum applied normal load (due to slight misalignments between the flat punch and the test surface) until a saturation adhesion strength of ~17 Pa was observed (obtained by dividing the adhesion force by the projected area of the pad surfaces), Fig. 4.

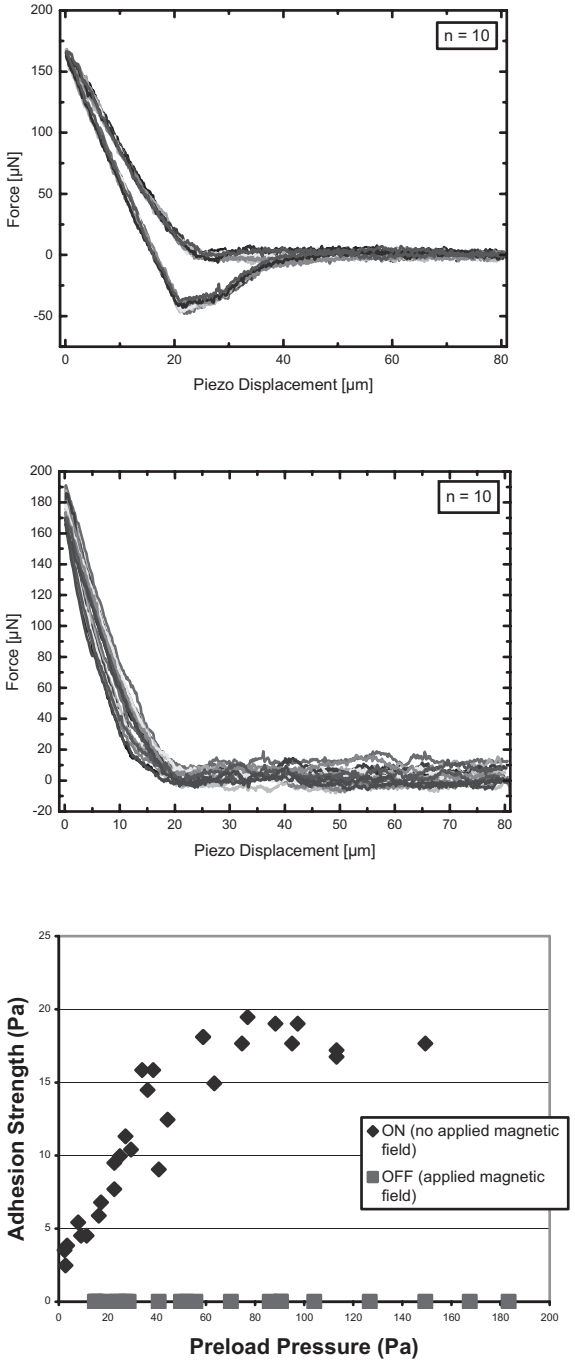

Fig. 4 - Adhesion results showing the on/off behavior of the structures without and with an applied magnetic field, respectively. The plots represent loading and unloading curves during testing, where in the 'ON' state distinctive pull-off events were observed (top) and in the 'OFF' state no pull-off events were observed (bottom). Strength values were obtained by dividing the interaction force by the contact area of the paddles. In the 'ON' state, the devices showed an initial increase in adhesion with preload force, characteristic of increased surface contact with applied load. In the off state there was no detectable adhesion.

Alignment issues, surface inconsistencies and unknown probe geometries have presented difficulties in quantification of non-pressure-sensitive-adhesives. One suggested metric is to simply divide the adhesion force by the maximum preload force, $\mu' = F_{adhesion}/F_{normal}$, thus distinguishing these systems from pressure sensitive adhesives (*19*). In the system described here the maximum μ' value was found to be ~1.5, occurring at the minimum detectable level of adhesion (limited by the noise level of the instrumentation). This value offers a substantial increase from previous synthetic work; where Northen and Turner reported a μ' = 0.125 (*17*), and Geim et al. a μ' = 0.06 (*20*), but still falls short of the gecko with μ' = 8 to 16 (*19*).

In contrast to the adhesion seen in a rest state, the application of magnetic field to the structures produced a catastrophic loss of adhesion, Fig. 4. For no tests performed was any adhesive event observed. This complete reduction in adhesion is attributed to the concealing of the nanorod coated platforms from the test probe. Under an applied magnetic field the platforms tend to rotate about the long axis of the cantilever. This rotation leaves the edge of the platforms facing in the normal direction and the sticky face to the side – turning a cheek to adhesion, if you will.

Additionally, an increase in surface stiffness was seen with an applied magnetic field. The twisting of the cantilevers increases the second moment of area of the structures, relative to the indenting tip, increasing the stiffness and consequently reducing the compliance of the system. Although not a primary factor in the reduction of adhesion, reduction of the compliance of the system serves to lock out one of the hierarchies of this multi-scale adhesive. Ultimately the sideways rotated paddles will contact the underlying substrate and statically inhibit contact between the adhesive and the test substrate, completely turning off the adhesive.

Conclusion

In this paper a novel approach has been presented for micro- and nano-fabricating a synthetic analogue to the gecko adhesive system. The hierarchical system is composed of aligned vertical nanorods coating flexible micron scale cantilever paddles. The paddles, composed of nickel, rotate when subjected to a magnetic field. This rotation conceals the nanostructures on the paddle surface and greatly reduces the available surface area for adhesion. Testing of the system showed reversible adhesion behavior switching from a μ' value ($F_{adhesion}/F_{preload}$) of ~1.5 (largest reported value for a biomimetic system to date (*19*)) to a value less than the noise level in the instrumentation. Thus an active hierarchical structure, inspired by the gecko, has been fabricated and demonstrated to display controlled and reversible adhesion.

References

1. **Aristotle, *Historia animalium translated by Thompson, D'A.W.* (Oxford, The Clarendon Press, 350 B.C.E. (1918)), pp. 584.**
2. **K. Autumn *et al.*, *Nature* 405, 681 (2000).**
3. **K. Autumn *et al.*, *Proc. Natl. Acad. Sci. USA* 99, 12252 (September 17, 2002, 2002).**
4. **G. Huber *et al.*, *PNAS* 102, 16293 (2005).**
5. **W. Sun, P. Neuzil, T. S. Kustandi, S. Oh, V. D. Samper, *Biophys. J.* 89, L14 (2005).**
6. **B. N. J. Persson, S. Gorb, *Journal of Chemical Physics* 119, 11437 (2003).**
7. **C. Y. Hui, N. J. Glassmaker, T. Tang, A. Jagota, *Journal of the Royal Society London Interface* 1, 35 (2004).**
8. **E. Arzt, S. Gorb, R. Spolenak, *Proc. Natl. Acad. Sci USA* 100, 10603 (2003).**
9. **M. Scherge, S. Gorb, *Biological Micro- and Nanotribology: Nature's Solutions* (Springer, Berlin, 2001), pp.**
10. **R. Ruibal, V. Ernst, *Journal of Morphology* 117, 271 (1965).**
11. **U. Hiller, *Z. Morph. Tiere* 62, 307 (1968).**
12. **A. P. Russell, *Journal of Zoology London* 176, 437 (1975).**
13. **E. E. Williams, J. A. Peterson, *Science* 215, 1509 (1982).**
14. **H. J. Gao, X. Wang, H. M. Yao, S. Gorb, E. Arzt, *Mechanics of Materials* 37, 275 (Feb-Mar, 2005).**
15. **R. Spolenak, S. Gorb, E. Arzt, *Acta BIOMATERIALIA* 1, 5 (2005).**
16. **H. Gao, H. Yao, *Proc. Nat. Acad. Sci. U. S. A.* 101, 7851 (2004).**
17. **M. T. Northen, K. L. Turner, *Nanotechnology* 16, 1159 (2005).**
18. **J. Judy, R. Muller, H. H. Zappe, *Journal of Microelectromechanical Systems* 4, 162 (1995).**
19. **K. Autumn, in *Biological Adhesives* A. S. a. J. Callow, Ed. (Springer Verlag, 2006).**
20. **A. K. Geim, S. V. Dubonos, I. V. Grigorieva, K. S. Novoselov, A. A. Zhukov, *Nature Materials* 2, 461 (2003).**

SOI MEMS PROCESS INSENSITIVE TO SACRIFICIAL OXIDE ETCH INDUCED SUBSTRATE ANCHOR PERIMETER VARIATION

G. J. O'Brien [1], D. J. Monk [2] and K. Najafi [3]
[1] Arizona State University, Department of Electrical Engineering, Tempe, AZ 85287
[2] Freescale Semiconductor, Sensor and Analog Products Division, Tempe, AZ 85284
[3] The University of Michigan, Department of Electrical Engineering, Ann Arbor, MI 48109

ABSTRACT

A major challenge of SOI based MEMS transducer design and fabrication has been to provide reliable substrate anchors insensitive to timed sacrificial oxide etch induced perimeter variation. Typically, SOI substrate anchors are designed quite large to account for anchor perimeter variation due to the lack of an etch stop mechanism. This paper describes the use of silicon nitride, as a sacrificial oxide etch stop film, patterned and deposited via a novel trench refill process. Additionally, this trench refill process can be further improved using polysilicon to provide a low electrical resistance substrate contact between the SOI and silicon handle wafer. A process combining both the silicon nitride substrate anchor perimeter etch stop and polysilicon substrate electrical contact is provided with device characterization results.

INTRODUCTION

SOI mechanical substrate anchors are typically fabricated by utilizing the buried oxide layer as a readily available electrical insulator and easily etched sacrificial material via hydrofluoric (HF) acid. A process cross section of a typical SOI timed HF etch defined oxide substrate anchor is shown in Figure 1 where *x* represents the desired lateral undercut dimension.

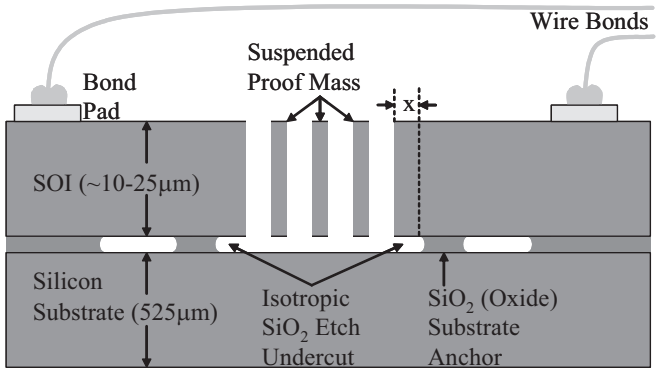

***Figure 1**. Cross section of typical SOI timed HF etch lateral undercut defined oxide substrate anchors.*

This lateral undercut dimension (*x*) is a strong function of time and initial-final HF concentration. A non-exhaustive list of variables contributing to lateral undercut etch variation include trench width, trench depth, buried oxide thickness, and HF concentration as a function of time, temperature, etc. Several of these variables are difficult to control when batch processing high volumes of silicon wafers in a manufacturing environment. MEMS SOI sensor designers typically make the anchors much larger than desirable in order to guarantee device reliability as a function of lateral etch undercut variability as observed across the device, wafer, and lot over time. This increases the design's required area consequently resulting in higher production cost per die. Therefore, an etch-stop based mechanical substrate anchor which allows the designer to use a smaller anchor area insensitive to timed HF lateral undercut variability based on trench refill processing [1] is highly desirable.

SOI DEVICE FABRICATION

A process cross section of silicon nitride trench refill encapsulated oxide substrate anchors insensitive to HF timed etch variation [2, 3] is shown in Figure 2.

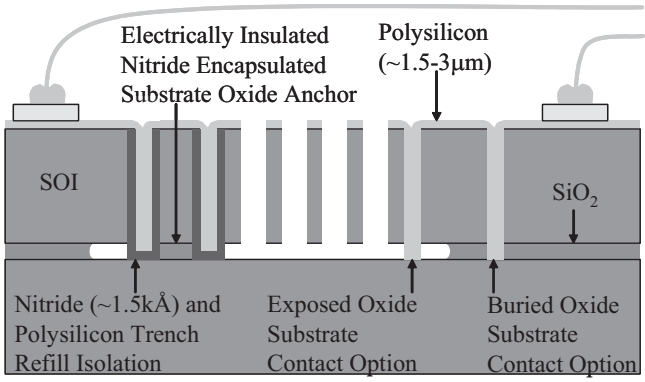

***Figure 2**. Cross section of silicon nitride encapsulated buried oxide substrate anchors insensitive to HF timed etch variation.*

The low pressure vapor phase deposition (LPCVD) silicon nitride film serves as an electrical insulator, HF etch stop, and diffusion barrier. An LPCVD polysilcon flim is used to back fill the trench due to its high degree of as deposited conformality. The nitride film serves as a diffusion barrier between the degenerately doped adjacent SOI and intrinsic LPCVD polysilicon film. A capacitive angular acceleration sensor [4] fabricated in SOI using this process flow [5] is shown in Figure 3.

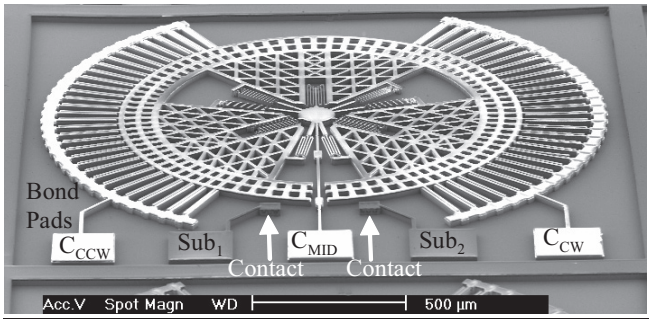

***Figure 3**. Angular accelerometer fabricated w/substrate contacts.*

The silicon nitride film functions as an electrical insulator and HF etch stop surrounding the encapsulated buried oxide anchor perimeter as shown in Figure 4. This silicon nitride encapsulated buried oxide anchor represents a substrate anchor

with the bond strength between the SOI and silicon handle wafer approaching the fracture strength of single crystal silicon [6].

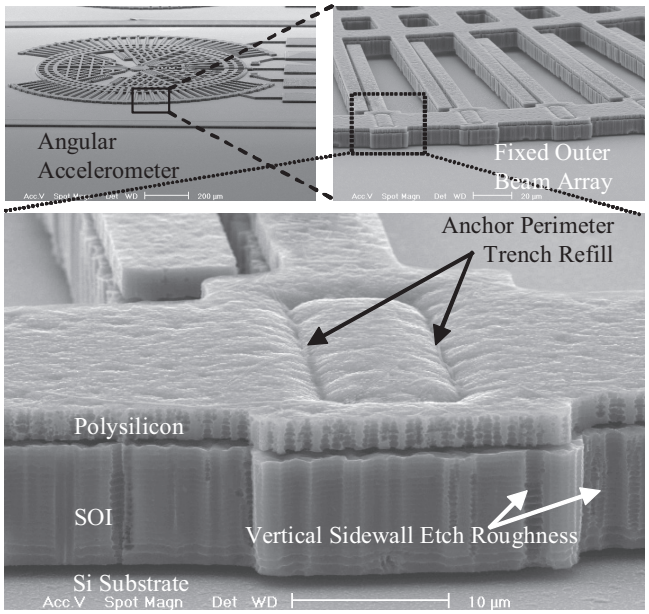

***Figure 4**. SOI trench refill silicon nitride encapsulated buried oxide anchor perimeter.*

Low electrical resistance silicon handle wafer substrate contacts were formed using LPCVD polysilicon refilled trenches without silicon nitride sidewall passivation present. The intrinsic trench refilled polysilicon contacts were autodoped using adjacent degenerately doped SOI as a dopant source via a thermal anneal maintained at 950°C for 30 minutes. The test structure used to characterize the substrate contact resistance is shown in Figure 5.

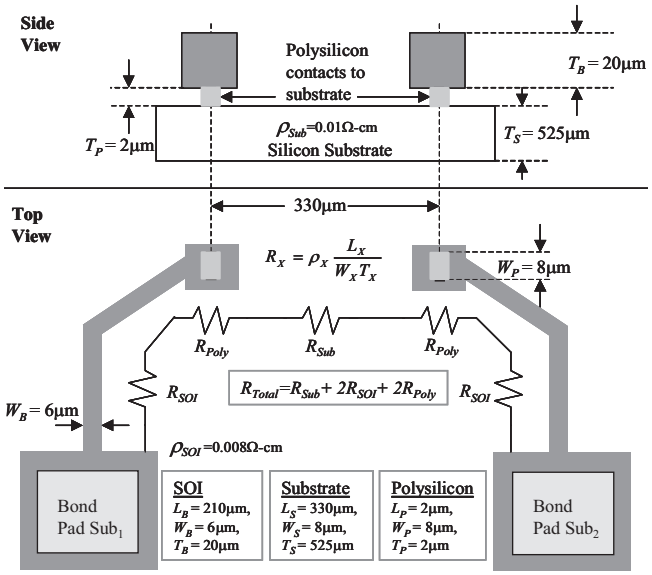

***Figure 5**. Polysilicon trench refill electrical substrate contact bond pad test structure schematic for angular accelerometer.*

A cleaved cross section of a typical polysilicon substrate contact fabricated in 20µm thick SOI is shown in Figure 6. Electrical resistance was measured between the Sub_1 and Sub_2 bond pads via micro-manipulator probes. The pre-anneal concentration of phosphorous dopant atoms in the 20µm thick SOI film sample was $6*10^{18}cm^{-3}$. The post-anneal concentration of phosphorous dopant atoms in the polysilicon substrate contact was calculated as $1.2*10^{16}cm^{-3}$ based on electrical resistance measurements of 528Ω per contact [2]. This represents a polysilicon contact resistivity of 0.42Ω-cm. The SOI and silicon handle wafer bulk film resistivity was 0.008Ω-cm and 0.01Ω-cm respectively. As a result of the large difference between pre-anneal SOI and post-anneal polysilicon contact dopant (phosphorous) concentrations, increasing anneal temperatures and/or time can be used to provide further reduction of polysilicon contact resistance values if desired. The post thermal anneal auto-doped polysilicon film can exhibit a significant stress gradient [7]. This undesirable stress gradient was minimized by removing the polysilicon film from the SOI top-side as shown in Figure 7.

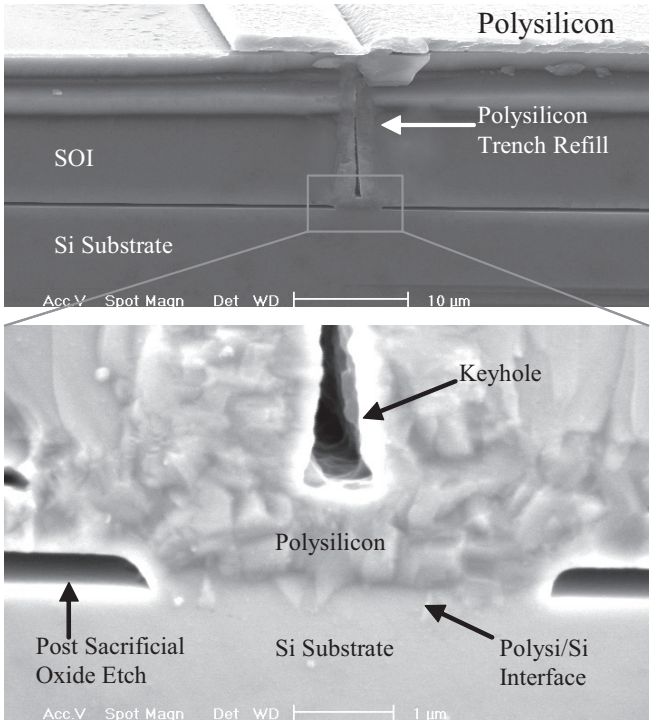

***Figure 6**. Cleaved cross section of autodoped polysilicon substrate contact with detail shown at single crystal silicon substrate interface (using the exposed oxide substrate contact option as described in Figure 2).*

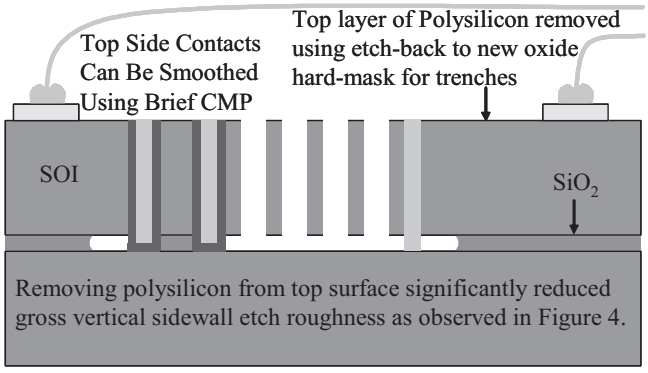

***Figure 7**. Second generation SOI process flow with polysilicon removed from top-side via etch-back process steps.*

While the highly doped polysilicon exhibits a non-zero film stress due to thermal anneal and auto-doping effects, doped

polysilicon is localized to small substrate contact areas isolated relatively far from the suspended sensor proof mass. Additionally, a folded beam electrical interconnect was used to reduce stress transmitted from the substrate contact towards the adjacent bond pad structure (Sub_1) shown in Figure 8. Removing the polysilicon from the SOI top-side also eliminated the vertical sidewall etch roughness observed previously in Figure 4. Sidewall roughness was attributed to laterally etched columnar polysilicon grains shadowing the underlying SOI material.

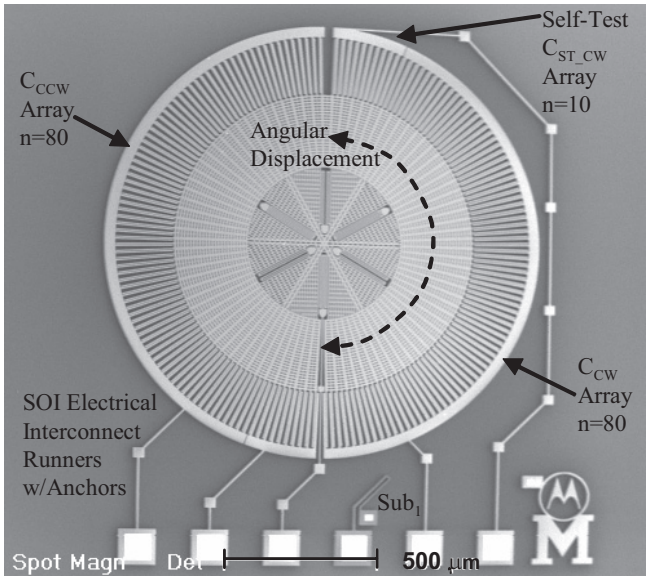

***Figure 8**. Angular accelerometer fabricated with the second generation SOI process flow.*

CHARACTERIZATION RESULTS

Capacitive angular acceleration sensors, fabricated using the second generation SOI process, were mounted in a 16 pin ceramic dual-in-line (DIP) packages. The sensors were wire-bonded to an adjacent sensor interface application specific integrated circuit [2] (ASIC) with 2mil diameter gold wire as shown in Figure 9.

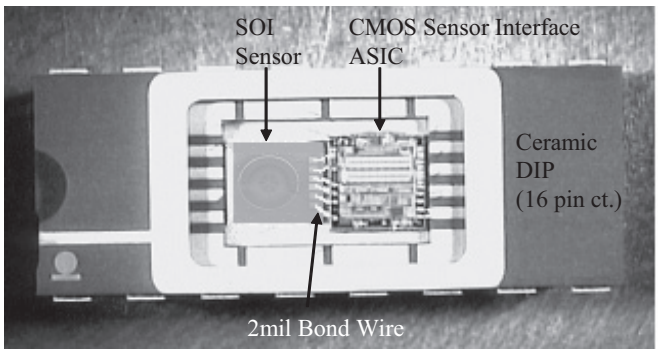

***Figure 9**. SOI sensor integrated with CMOS interface ASIC.*

The ASIC was wire bonded to the ceramic DIP leads using 1mil diameter gold wire. Characterization results for a sinusoidal (2Hz) input angular acceleration of 40r/s^2 is shown in Figure 10. The CMOS ASIC output angular acceleration sensitivity was measured as 1.9mV/r/s^2. Full scale span was calculated as (+/-) 1260r/s^2 using output amplifier high and low rails conservatively estimated at 4.9V and 0.1V respectively. Angular acceleration resolution was calculated as 2.3r/s^2 using the measured noise and sensitivity values [2] for a typical device a shown in Figure 10.

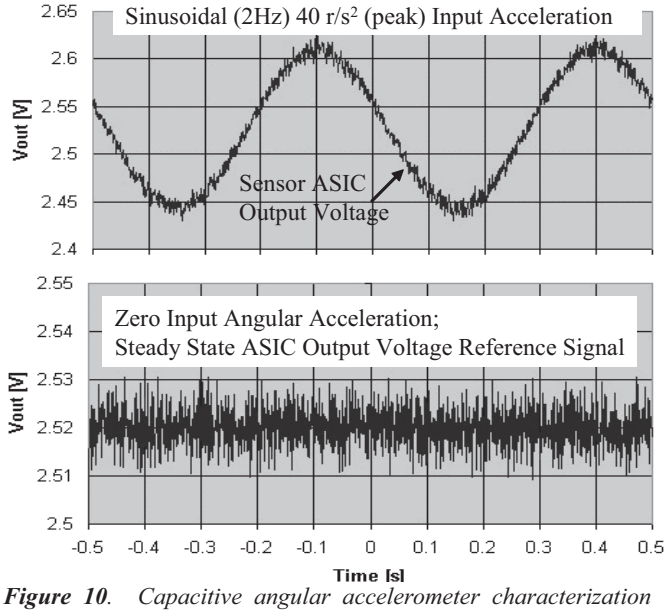

***Figure 10**. Capacitive angular accelerometer characterization measurements.*

SUBSTRATE ANCHOR SIZING

The Si_3N_4 passivated SiO_2 substrate anchor was designed as a direct replacement of a typical timed etch SiO_2 substrate anchor. As a result, minimum anchor dimensions were preserved at 20µm for both anchor schemes as shown in Figure 11.

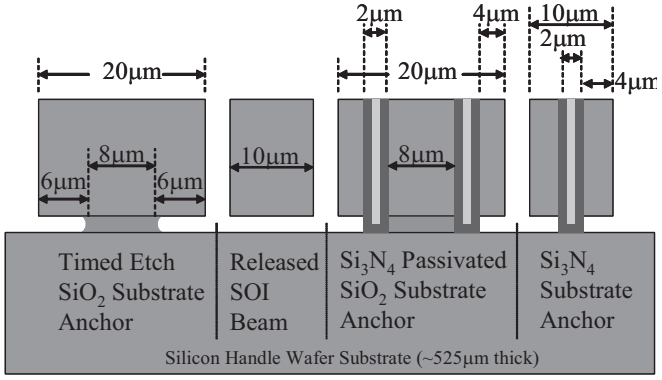

***Figure 11**. Comparison cross section of SOI timed etch SiO_2, Si_3N_4 passivated, and Si_3N_4 substrate anchors.*

The SiO_2 sacrificial etch time was characterized using 6:1 aqueous HF solution (Motorola and Freescale Semiconductor proprietary buffered HF recipe) to fully release SOI beams up to 10µm in width (5µm lateral SiO_2 undercut per side) on wafers with a 2µm thick buried oxide layer. In order to account for SiO_2 etch rate variability across the device (and wafer) a target of 6µm SiO_2 undercut was defined by etch time per previous buried oxide etch rate characterization experiments. A replicated angular acceleration sensor design with both Clear and Dark-Field device perimeters are shown side-by-side in Figure 12. Note that the Dark-Field device can be hermetically sealed using previously described wafer encapsulation techniques [8,9].

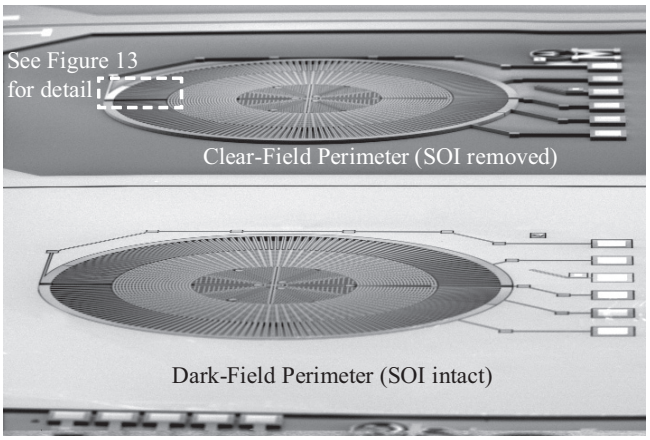

***Figure 12**. Clear and Dark-Field angular accelerometer designs fabricated on 20μm thick SOI wafers.*

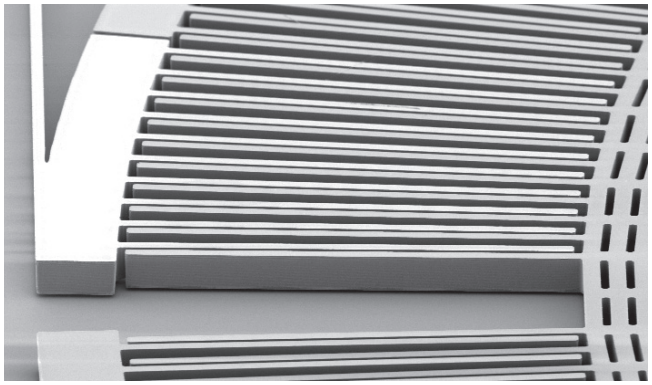

***Figure 13**. Clear-Field capacitive self-test array detail.*

The angular accelerometer device (internal perimeter) is identical for both the Clear and Dark-Field designs. The inertial proof mass is suspended at a central hub using six folded beam springs attached to the silicon handle wafer via substrate anchors as shown in Figure 14.

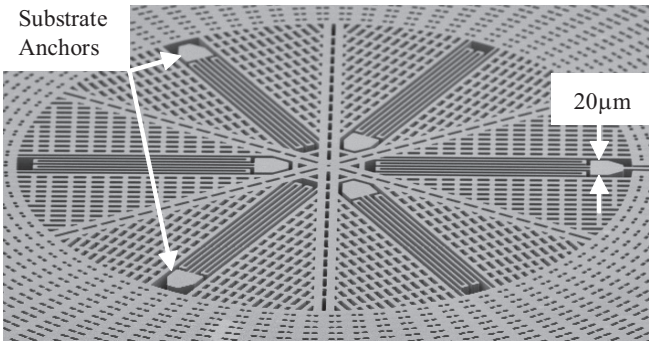

***Figure 14**. Capacitive angular accelerometer central hub folded beam springs with interleaved 20μm wide substrate anchors.*

The 6μm lateral SiO_2 etch exposes the LPCVD Si_3N_4 passivated substrate anchors to 6:1 BHF for approximately 1/3rd of the total etch time. Approximately 19% of the original 1.5kA LPCVD Si_3N_4 film is removed during the 6:1 BHF sacrificial oxide etch step. The encapsulated SiO_2 substrate anchors are protected from etchant exposure using the Si_3N_4 film as an etch stop. Selectivity of buried oxide etch rate to silicon nitride etch rate was measured on blanket wafer tested films in excess of 100:1 using 6:1 BHF as an etchant.

Substrate anchors using only Si_3N_4 have been previously fabricated on SOI based linear accelerometer devices [10] with minimum top and bottom anchor dimensions of 10μm and 2μm respectively as shown in Figure 11. Multiple Si_3N_4 posts can also be applied as single trench anchors [3] limited only by the fabrication facility minimum photolithography dimension, DRIE trench width, and mask-mask maximum misalignment dimensions.

CONCLUSIONS

We have demonstrated SOI substrate anchors defined by a novel trench refill process utilizing LPCVD Si_3N_4 as an etch stop film using standard semiconductor fabrication tools. This process was further modified with a polysilicon trench refill to provide low electrical resistance substrate contact. Characterization results of an angular acceleration sensor fabricated using this novel SOI process was also reported. Smaller lateral dimension anchors can be realized by using smaller minimum trench and buried SiO_2 anchor widths. Using 1.5μm as the minimum trench width, dual trench separation, and mask-to-mask maximum misalignment error, the smallest realizable anchor is 7.5μm wide for dual trench Si_3N_4 anchors and 4.5μm wide for single trench Si_3N_4 anchors.

REFERENCES

[1] A. Selvakumar and K. Najafi, "High Density Vertical Comb Array Microactuators Fabricated Using a Novel Bulk/Polysilicon Trench Refill Technology," presented at IEEE Solid State Sensors and Actuators, Hilton Head, SC, pp. 138-141, 1994.

[2] G. J. O'Brien, "Design and Fabrication of MEMS Angular Rate (Gyroscope) and Angular Acceleration Sensors with CMOS Switched Capacitor Signal Conditioning," Ph.D. Dissertation, University of Michigan, Ann Arbor, MI, 2004.

[3] G. J. O'Brien and D. J. Monk, "SOI Polysilicon Trench Refill Oxide Anchor Perimeter Scheme", U.S. Patent 6,913,941, issued 2005.

[4] T. J. Brosnihan, A. P. Pisano, and R. T. Howe, "Micromachined Angular Accelerometer with Force Feedback," presented at ASME Conference and Expo, pp. 941-947, 1995.

[5] G. J. O'Brien, D. J. Monk, and K. Najafi, "Capacitive Angular Accelerometer with Dual Anchor Support," presented at IEEE Transducers, Boston, MA, pp. 1371-1374, 2003.

[6] M. A. Schmidt, "Silicon Wafer Bonding for Micromechanical Devices", presented at IEEE Solid State Sensors and Actuators Workshop, Hilton Head, SC, pp. 127-130, 1994.

[7] H. Guckel et. al, "Processing Conditions for Polysilicon Films with Tensile Strain for Large Aspect Ratio Microstructures", presented at IEEE Solid State Sensors and Actuators, Hilton Head, SC, pp. 51-56, 1988.

[8] L. J. Ristic, "Sensor Technology and Devices", Artech House Publishing, Norwood, MA, pp. 208-209, 1994

[9] R. N. Candler, W. T. Park, H. Li, G. Yama, A. Partridge, M. Lutz, and T. W. Kenny, "Single Wafer Encapsulation of MEMS Devices", IEEE Transactions on Advanced Packaging, vol. 26, No. 3, pp. 227-232, 2003.

[10] G. J. O'Brien, J. Hammond, G. Li, D. Koury, and D. J. Monk, "Outrigger; A Solid Outer Frame Lateral Accelerometer Design," presented at IEEE Transducers, Seoul, Korea, pp. 176-179 , 2005.

A PLANAR GLASS/SI MICROMACHINING PROCESS FOR THE HEAT EXCHANGER IN A J-T CRYOSURGICAL PROBE

Weibin Zhu[1], Daniel W. Hoch[2], Gregory F. Nellis[2], Sanford A. Klein[2], Yogesh B. Gianchandani[1]
[1]*Department of Electrical Engineering and Computer Science, University of Michigan, Ann Arbor*
[2]*Department of Mechanical Engineering, University of Wisconsin, Madison*

ABSTRACT

This paper reports a lithography-based microfabrication process and the preliminary experiments for a recuperative heat exchanger intended for use in a Joule-Thomson (J-T) cryosurgical probe. The heat exchanger must maintain high stream-to-stream thermal conductance while restricting parasitic stream-wise (axial) conduction losses. Rows of fins composed of high conductivity silicon are bonded onto a 100 μm thick base plate composed of low conductivity Pyrex glass. The heat exchanger has a footprint of 6×1.5 cm^2 and 2.5 mm thickness, and is fabricated using a 5-mask process. The fabrication process involves anodic bonding, deep reactive ion dry etching, glass frit bonding, electrochemical discharge drilling and several other steps, along with special features that compensate for manufacturing tolerances. Preliminary experiments include measurement of the thermal effectiveness in an ice-water bath, as well as evaluation of self-cooling with butane. The data suggest an optimal area of 0.2 mm^2 for the expansion orifice. The primary performance constraint is imposed by the compromise between mechanical robustness and transverse conductance of the thin glass plate that separate the high pressure and low pressure sides.

I. INTRODUCTION

Cryosurgery has been used to treat several types of cancers including prostate cancer and liver cancer in the past three decades. In this medical procedure, cancerous tumors are locally destroyed by exposing pathological tissues to repeated freeze/thaw cycles [1]. The ablated tissue is subsequently absorbed or sloughed by the body. By avoiding excision, operative blood loss and discomfort are minimized. Even in the cases where excision is required, the growth of tumor cells that might escape during resection can be prevented by a pre-treatment on the tumors with the cryotherapy.

Cryosurgery, which is competitive with other therapies, has been a standard treatment for cancerous tumors located in easily accessible areas of the body. Recent development of miniature cryoprobes with large refrigeration capacity [2-4] and techniques for real-time monitoring using ultrasound or magnetic resonant imaging [5-7] is allowing cryosurgical techniques to be extended to the treatment of cancers in areas that are not readily accessible [8]. In fact, this effort, which examines the possibility of fabricating cryoprobes with micromachining technologies, is motivated in part by the need of miniaturizing cryoprobes to a size that permits them to be inserted through a small incision. However, the performance of the cyroprobe must not be compromised in this scaling effort because the freeze region that surrounds the cold end of the probe is controlled by the refrigeration power and surface temperature attainable by the tip of the probe. It is known, for example, that temperatures below -50°C are always necrotic for pathological tissue [9-11]. In addition, a rapid cool-down rate [1, 12] between 25-50 °C/min. and multiple freeze-thaw cycles [13] are preferred to decrease the likelihood of cell survival.

The ultimate goal of this research effort is to develop a fully integrated micromachined cryosurgical probe that has significant advantages over the conventional cryosurgical probe in terms of thermal performance, size, flexibility and cost. The Joule-Thomson cooling cycle (Fig. 1) can meet these requirements [14]. In this cycle, cold, high-pressure fluid leaving a recuperative heat exchanger expands through a valve, resulting in a temperature drop through the valve if the state of the fluid lies below the inversion curve before expansion. This paper describes the fabrication and preliminary experiments of one possible approach to the micromachined recuperative heat exchanger which utilizes a planar design and 5 wafers in a 5-mask process (Fig. 2).

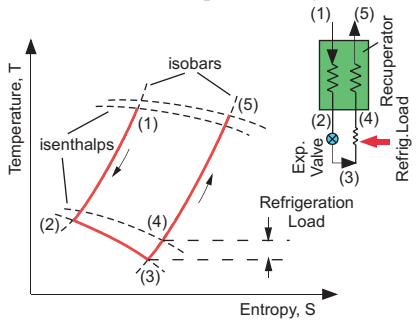

Fig. 1: Joule-Thomson refrigeration cycle. High pressure fluid at state (1) passes through a counter flow recuperative heat exchanger, where it is pre-cooled by the low-pressure fluid returning from the refrigeration load. The cold high-pressure fluid leaving the heat exchanger at state (2) expands through a valve to state (3). The cold, low-pressure fluid is directed through the load heat exchanger where it is warmed by the refrigeration load to state (4) and then is fed back into the heat exchanger.

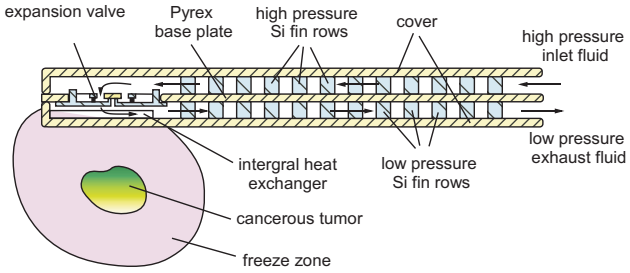

Fig. 2: Schematic diagram of micromachined Joule-Thomson cryosurgical probe. High pressure inlet fluid is obtained from external compressor.

II. DESIGN AND FABRICATION

One of the critical challenges in developing a micromachined J-T cooler is that the recuperative heat exchanger must maintain good stream-to-stream heat conductance while restricting parasitic stream-wise conduction losses. This requirement is necessary in order to have a large enthalpy difference between the two streams and thus achieve high cooling performance for the probe. The planar, micromachined recuperative heat exchanger uses rows of fins that are composed of high conductivity silicon that is anodically bonded onto a very thin base plate composed of low

Corresponding author: Weibin Zhu, 1301 Beal Ave., Ann Arbor, MI, 48109, USA; Tel: (734) 763-5914, Fax: (734) 763-9324, Email: zhuwb@umich.edu

conductivity Pyrex (Fig. 3). This design is in contrast to conventional cryogenic heat exchangers that use either perforated plate designs with oxygen-free high conductivity (OFHC) copper plates interleaved with stainless steel spacers or finned tube designs that use one or more finned tubes wound on a mandrel. Silicon has thermal conductivity that is similar to OFHC copper, and Pyrex has thermal conductivity that is an order of magnitude less than stainless steel; this combination of very high and low thermal conductivity suggests that a silicon and Pyrex composite heat exchanger will be attractive. In order to allow adequate thermal communication between the streams, preliminary modeling [15] and simulation of an optimized design [16] suggest that for a working pressure of 20 bar, the Pyrex base plate between the high pressure channel and low pressure channel can be no thicker than about 100 μm in order to provide adequate refrigeration power.

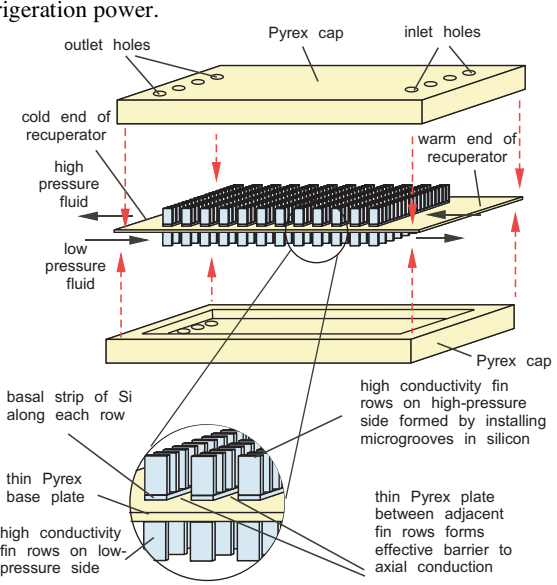

Fig. 3: Fin rows structure of the micro heat exchanger.

There are five masks required for this process (Fig. 4):

1) Two Si wafers of 200 μm thickness are bonded to a glass wafer of 100 μm thickness. The entire stack is loaded simultaneously into the bonding apparatus and heated to 400°C, before a 500 V bonding voltage is applied. By sequentially reversing the polarity of the voltage source, both Si-Pyrex interfaces are bonded one-by-one.

2) A 2 μm-thick layer of silicon dioxide is deposited on both sides of the Si surface using plasma enhanced chemical vapor deposition (PECVD). This layer and a subsequent layer of photoresist will serve as masks in a two-step DRIE process.

3, 4) The oxide layers on both sides are then patterned by reactive ion etching (RIE).

5) A 10 μm thick layer of photoresist is then coated and patterned on the top side. A conformal thick resist layer is used to protect the oxide pattern in the next DRIE step. On the top side of the wafer, Si channels between each fin row are etched down 20 μm by DRIE before the photoresist is stripped. This etch will ultimately lead to the creation of the basal strip along each row that is illustrated in the magnified part of Fig. 3. It is needed in part to compensate for a DRIE artifact that is explained below, but also has the added benefit of strengthening the attachment of the fins to the glass base plate.

6) A 10 μm photoresist layer is coated and patterned on the bottom side. On the bottom side of the wafer, Si channels between each fin row are etched down 20 μm by DRIE. The photoresist is then stripped.

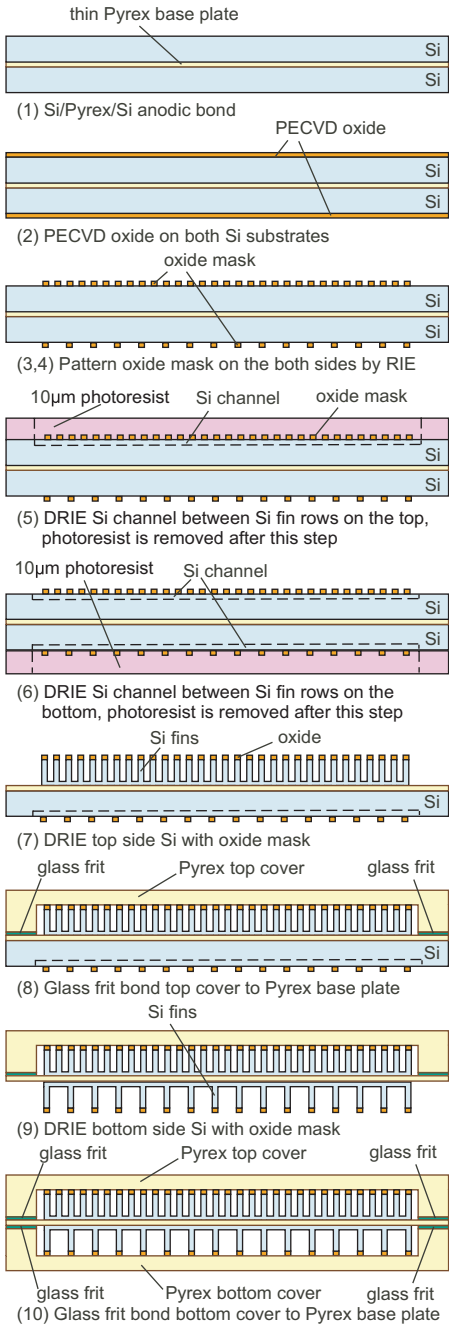

Fig. 4: Fabrication process flow of micro heat exchanger.

7) Fin rows on the top side are etched and defined by DRIE with an oxide mask. This is a high aspect ratio etch of 180 μm depth. The etch must clear the narrow regions between rows, etch between the tightly packed fins, and also clear the perimeter of the device, which has no masked features, and etches faster.

Optimizing the DRIE chemistry is one of the significant challenges of the process for three reasons: (a) the relatively large size of the device and the narrow widths of the fins demands high uniformity over a large area; (b) the DRIE step must clear the narrow openings between rows and the wide spaces of the perimeter simultaneously; and (c) the termination of the etch on the glass layer sandwiched between the two Si layers causes a problem known as "footing," which is the lateral spread of the etch profile once the insulating glass is exposed at the bottom of the trench [17]. The two-step DRIE (in steps 5 and 7) is necessary to fabricate separated grooves on the high-pressure side, shown in Fig. 3, and

compensate for the non-uniform etch rate due to the varying density of the features. Due to micro loading [18, 19], the areas between fins and fin rows with small openings are usually etched more slowly than the area around the device with large openings. Since each fin row must be thermally isolated along the flow direction, the Si in the gap between fin rows must be completely etched away while the over-etch in the area around the device must be minimized to prevent the footing effect from damaging nearby fins. In step 5, the area between each fin row is etched down 20 μm, allowing this densely packed region to be etched through fully during the DRIE in step 7.

8) A glass cap (the fabrication of which is described separately, below) is bonded to the base plate with commercial glass frit tape (G1017, from Vitta Corp.) at 500°C so as to construct a sealed chamber on the high pressure side. A significant challenge in this step is patterning of the tape, which cannot be done lithographically. In this effort, because of the large bonding area, the tape was cut and placed on the die manually.

9) A similar DRIE process is completed on the low-pressure side afterward.

10) Another glass cap is bonded onto the bottom side of the base plate using glass frit.

The glass caps are fabricated from 1.1 mm thick Pyrex wafers. The Pyrex wafer is coated with 500 Å/5000 Å Cr/Au layer and then patterned with photoresist. Using the metal layer as a mask, the wafer is immersed in the HF:HNO_3 solution to create a recess that is 100 μm deep. The photoresist and Cr/Au layer are removed after the wet etching. Inlet and outlet holes are drilled with an electrochemical discharge drilling method [20]. This method provides a smooth and debris-free surface, but is a serial method, and is not performed lithographically. An electrode needle is positioned in the proximity of the glass wafer while both are immersed in NaOH 30% wt. solution at room temperature. A bias of 33 V permits a 1100 μm thick glass plate to the perforated in about 10 s. Figure 5 shows a fabricated micro recuperative heat exchanger. The size of this device is 6×1.5 cm^2 with 2.5 mm total thickness.

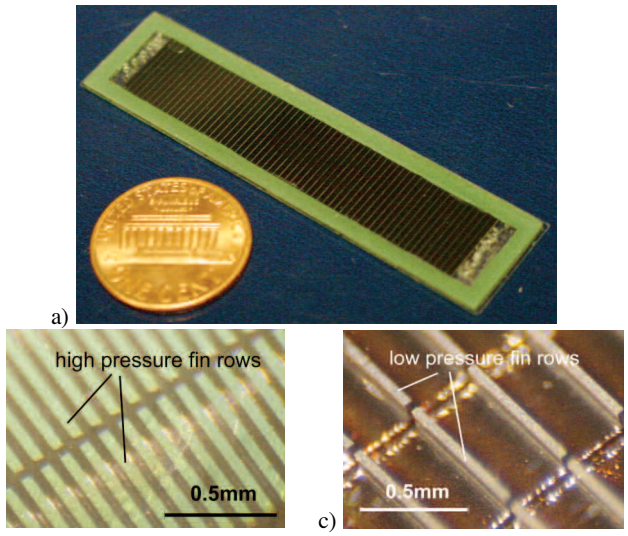

Fig. 5: a) The size of micro recuperator is 6×1.5 cm^2 with total 2.5 mm thickness. Gap between each fin row is 51 μm. b) High pressure fin rows with 50 μm gap, fin size is 50×782 μm^2, 200 μm high. c) Low pressure fin rows with 345 μm gap. Fin size is the same as high pressure fins.

III. MEASURED RESULTS

Two types of preliminary tests were performed. The micro heat exchanger was first tested in an ice bath (Fig. 6), with helium gas flowing through one side of the micro heat exchanger and ice water flowing through the other side. At the beginning of the test, the ice water inlet pressure was increased in order to match the helium inlet pressure, so that the pressures on either side of the heat exchanger were approximately balanced. This configuration provided essentially a constant, 0°C heat sink on one side so that the thermal effectiveness could be evaluated in this simple limit and compared with the numerical model of the device.

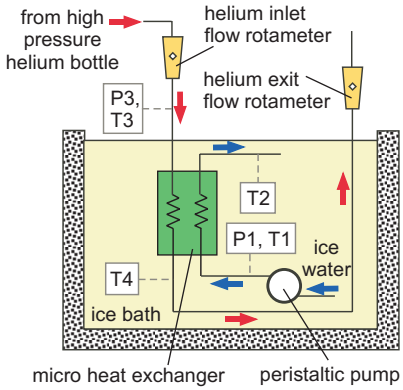

Fig. 6: Ice bath test setup of the micro heat exchanger. The temperature measurements use Type E thermocouples.

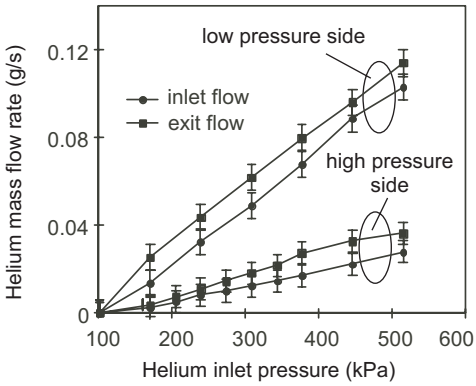

Fig. 7: Helium flow rate measured by the inlet and exit flow meters as a function of the helium inlet pressure for the high and low pressure sides.

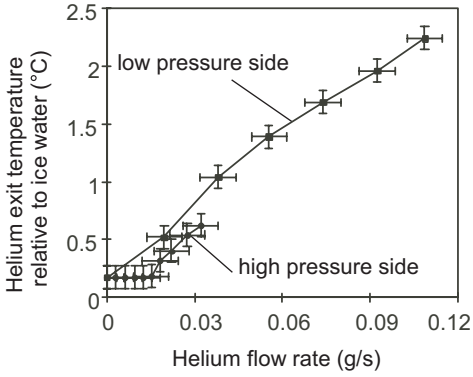

Fig. 8: Helium exit temperature, relative to measured ice water temperature, as a function of flow rate (average measured by the inlet and exit flow meters) for the high and low pressure sides.

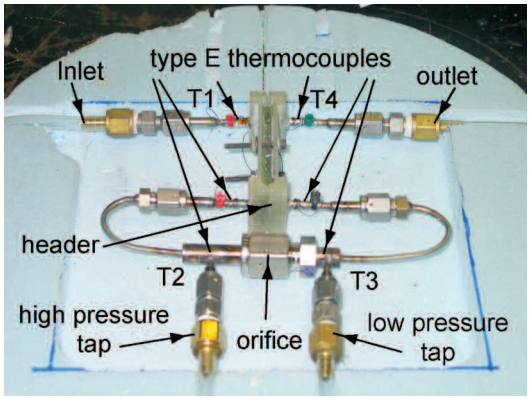

Fig. 9: Self-cooling setup. Butane gas with regulated pressure is introduced from the inlet. The micro recuperative heat exchanger is mounted inside the header. The type E thermocouples are inserted into the high and low pressure taps to measure the gas temperature inside the tube.

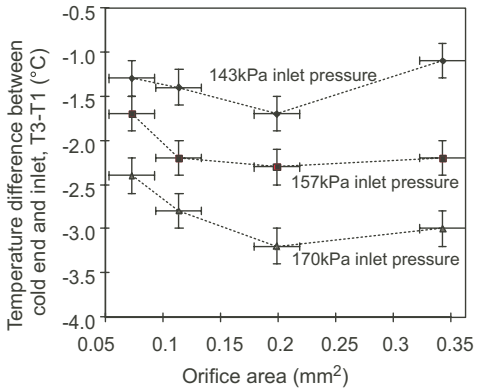

Fig. 10: Temperature difference between cold end and inlet as a function of orifice area for three different inlet pressures.

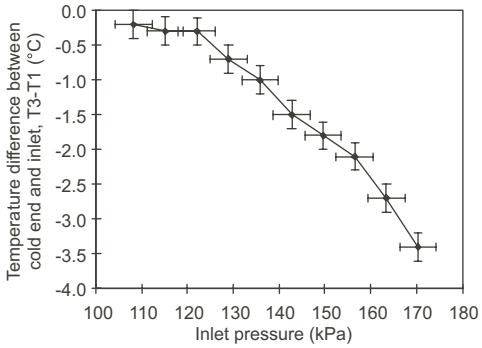

Fig. 11: Temperature difference between cold end and inlet as a function of the inlet pressure for 0.2mm^2 orifice area.

Figure 7 illustrates the inlet and outlet flow rate measured for the high and low pressure sides of the device. Note that the low pressure side of the micro heat exchanger allows much more flow for a given pressure difference due to the larger channels on the low pressure side. The inlet and exit flow rates should be the same as there was no leakage observed during the testing; however, the difference is nominally within the uncertainty of the rotameters that were used.

Figure 8 illustrates the helium exit temperature (relative to the ice water temperature) as a function of the helium flow rate (the average measured by the inlet and exit rotameters) for the two sides. The helium inlet temperature was between 17-19°C for all tests and therefore the helium exit temperature is an indicator of the thermal performance of the heat exchanger: a lower helium exit represents better performance. As expected, the high pressure side showed better performance than the low pressure side because the fin structure is more dense (Fig. 5). However, this difference is relatively slight because the dominant thermal resistance in the heat exchanger is the Pyrex plate.

For the second test, the device was installed into a macro-scale self-cooling system (Fig. 9). In this experiment, the heat exchanger is placed in a cavity within a piece of Styrofoam insulation and surrounded by fiberglass insulation. The hot inlet is provided with a flow of butane from a high pressure bottle at room temperature. The pressure, flow rate, and temperature (T_1) of this flow are measured. The high pressure butane passes through the heat exchanger where it is pre-cooled by the low pressure butane returning from the cold end. The butane is expanded through an orifice (a precision jewel installed in a blank gasket) located at the cold end of the system; by varying the size of the orifice it is possible to control the flow rate through the heat exchanger. The temperatures on either side of the orifice (T_2 and T_3) are measured using thermocouples that penetrate the butane stream. Figure 10 illustrates the temperature difference between the cold end and the inlet as a function of orifice area for three different inlet pressures. The optimal orifice size is 0.2 mm^2. The temperature difference as a function of inlet pressure for this optimal orifice is shown in Fig. 11; the measured temperature difference matches the theoretical model assuming a parasitic heat loss of 40 mW.

IV. DISCUSSION

In addition to the challenges in the various steps identified in the design and fabrication section, the development of the fabrication process has yielded a number of important lessons. At a very basic level, the fragility of the 100 μm thick glass plate requires it to be bonded to at least one Si wafer as early as possible in the process. Another general challenge is the footprint of the device, which is so large that the possibility of a defect or non-uniformity is high. In the processing steps, as already discussed, the primary challenges include the double-sided bonding of the glass wafer; the DRIE sequence and its limitations related to overall uniformity, micro loading, and footing; the frit glass bonding; and the electrochemical etching. However, reasonable solutions exist for each of these challenges, and a feasible process for manufacturing heat exchangers in this manner has been developed.

The self-cooling data is limited to very small temperature differences relative to a practical device that is useful for cryosurgery. This is due to the following reasons:

1) The difference between the high and low pressures in the heat exchanger is limited by the structural integrity of the base plate. The pressure difference anticipated for a cryosurgical probe may be as high as 1400 kPa (200 psi) whereas the testing was limited to 70 kPa (10 psi) in order to avoid fracturing the base plate. Theoretically, this thickness of the base plate should be able to sustain larger pressure differences, but in practice this is not true. A thicker base plate would provide greater structural integrity, but the increased transverse thermal resistance would further reduce cooling power. This design concept is not ideal if the base plate is made of Pyrex and an alternative material with a higher conductivity (optimal value is about 30 W/m-K) must be found to make this concept practical.

2) The fin height of 200 μm is much smaller than the initial target of 500 μm. This modification was required by manufacturing constraints, but results in both a 2.5× reduction in heat transfer area as well as a 5× increase in the pressure drop.

3) The structural integrity and hermeticity restrictions prevent installation in a thermal vacuum facility. Therefore, there is a substantial parasitic heat load on the device that prevents it from achieving very low temperature.

The predicted and measured effectiveness as a function of mass flow rate (based on the hot side energy balance) is illustrated in Fig. 12. The effectiveness of the heat exchanger (ε) is defined as the ratio of the heat transferred within the heat exchanger to the maximum possible amount of heat that could have been transferred had the heat exchanger been perfect (i.e., the heat transferred if T_4 was equal to T_1). The effectiveness can be computed based on either the hot- or cold-side balance (ε_h or ε_c, respectively):

$$\varepsilon_h = \frac{\dot{q}_{HX,h}}{\dot{q}_{HX,max}} \text{ or } \varepsilon_c = \frac{\dot{q}_{HX,c}}{\dot{q}_{HX,max}},$$

where $\dot{q}_{HX}$ is the actual heat transfer and $\dot{q}_{HX,max}$ is the ideal heat transfer in perfect conditions. The error bars are theoretical errors based on the uncertainty in the thermocouple temperature measurements. Note that the error increases as the mass flow rate drops due to the smaller temperature differences that are required to compute the effectiveness. This measured result properly matches the theoretical model.

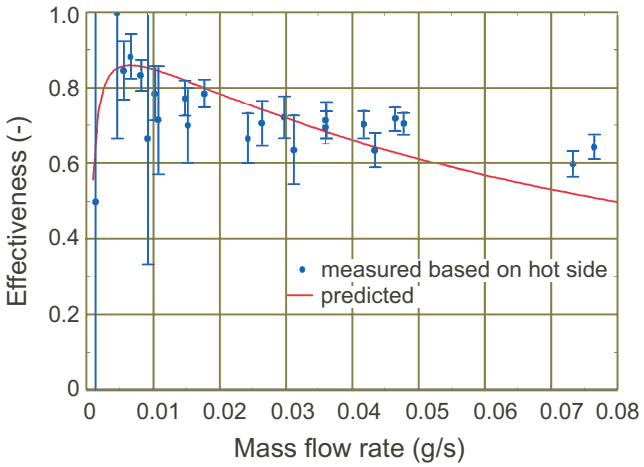

Fig. 12: Measured effectiveness based on hot side energy balance and the predicted effectiveness using the micro heat exchanger model as a function of the mass flow rate.

V. SUMMARY

A planar micro heat exchanger with a footprint of 6×1.5 cm^2 and 2.5 mm thickness was fabricated in a 5-mask process using 3 glass wafers and 2 Si wafers. In our tests, the self-cooling performance of the micro heat exchanger was mainly limited by (i) mechanical robustness of the glass base plate and (ii) Si fin height that was constrained by the uniformity of DRIE. However, the effectiveness of the heat exchanger varied from 0.8 at a mass flow rate of about 0.01 g/s to 0.6 at 0.075 g/s, which matched the developed theoretical model. We are presently developing a new structure to avoid fracturing the base plate. If successful, the robustness, flexibility and performance associated with the micromachined device may result in the application of cryosurgery to new biomedical areas.

ACKNOWLEDGEMENT

This work was funded in part by a grant from the US National Institutes of Health (R21 EB003349-02).

REFERENCES

[1] J. Dobak, "A Review of Cryobiology and Cryosurgery," *Advances in Cryogenic Engineering*, 43, pp. 889-896, 1998

[2] Z. H. Chang, J. J. Finkelstein, J. G. Baust, "Optimization of Cryosurgical Instrumentation for use in Minimally Invasive Prostate Surgery," *ASME Heat Transfer Div Publ HTD*, v 267, pp. 45-55, 1993

[3] B. Z. Maytal, "Fast Joule-Thomson Cryocycling Device for cryosurgical Applications," *Advances in Cryogenic Engineering*, 43, pp. 911-917, 1998

[4] J. Dobak, X. Yu, and K. Ghaerzadeh, "A Novel Closed Loop Cryosurgical Device," *Advances in Cryogenic Engineering*, 43, pp. 897-902, 1998

[5] R. Masumoto, K. Oshio, F. A. Jolesz, "Monitoring of Laser and Freezing-Induced of the Liver with Tl-Weighted MR Imaging," *Journal of Magnetic Resonance Imaging*, 2, pp. 555, 1992

[6] B. Rubinsky, J. C. Gilbert, G.M. Onik, M.S. Roos, S.T. Wong, K.M. Brennan, "Monitoring Cryosurgery in the Brian and Prostate with Proton NMR," *Cryobiology*, 30, pp. 191-199, 1993.

[7] G.R. Pease, S.T. Wong, M.S. Roos, B. Rubinsky, "MR Image-Guided Control of Cryosurgery," *Journal of Magnetic Resonance Imaging*, 5, pp. 753-760, 1995

[8] J. K. Cohen, R. J. Miller, "Thermal Protection of Urethra during Cryosurgery of the Prostate," *Cryobiology*, 31, pp. 313-316, 1994

[9] A. Gage, "Five-year Survival Following Cryosurgery for Oral Cancer," *Archives of Surgery*, 111, pp. 990-994, 1976

[10] A.A. Gage, J.A. Caruana and M. Montes, "Critical Temperature for Skin Necrosis in Experimental Cryosurgery," *Cryobiology*, 19, pp. 273-282, 1982

[11] J. Bischoff, K. Christov, B.A. Rubinsky, "Morphological Study of Cooling Response in Normal and Neoplastic Human Liver Tissue: Cryosurgical Implications," *Cryobiology*, 30, pp. 482-492, 1993

[12] A. A. Gage, K. Guest, M. Montes, J.A. Caruana, D. A. Whalen, Jr., "Effect of Varying Freezing and Thawing Rates in Experimental Cryosurgery," *Cryobiology*, 22, pp. 175-182, 1985

[13] A. A. Gage, "Cryosurgery in the Treatment of Cancer," *Surgery, Gynecology & Obstetrics*, 174, pp. 73-92, 1992

[14] E. D. Marquardt, R. Radebaugh, J. Dobak, "A cryogenic Catheter for Treating Heart Arrhythmia," *Advances in Cryogenic Engineering*, 43, pp. 903-910, 1998.

[15] G. F. Nellis, "A Heat Exchanger Model that Includes Axial Conduction, Parasitic Heat Load, and Property Variations," *Cryogenics*, vol. 43, no. 9, pp. 523-538, 2003

[16] M. Frank, M, *Recuperative Heat Exchanger for a MEMS Cryoprobe*, M.S. Thesis, Univ. Wisconsin, Dept. of Mechanical Engineering, 2004

[17] K. Ishihara, C. F. Tung, A. A. Ayón, "An Intertial Sensor Technology Using DRIE and Wafer Bonding with Interconnecting Capability," *J. Micromech. Sys.*, 8 (4), pp. 403-408, 1999

[18] K. Kühl, S. Vogel, U. Schaber, R. Schafflik, B. Hillerich, "Advanced Silicon Trench Etching in MEMS Applications," *SPIE*, vol. 3511, Santa Clara, California, pp. 97-105, 1998

[19] M. Chabloz, J. Jiao, Y. Yoshida, T. Matsuura, K. Tsutsumi, "A Method to Evade Microloading Effect in Deep Reactive Ion Etching for Anodically Bonded Glass-silicon Structures," *IEEE Intl. Conf. on Micro Electro Mechanical Systems (MEMS'00)*, Miyazaki, Japan, pp. 283-287, 2000

[20] V. Fascio, R. Wüthrich, D. Viquerat, H. Langen, "3D Microstructuring of Glass Using Electrochemical Discharge Machining (ECDM)," *International Symposium on Micromechatronics and Human Science*, pp. 179-183, 1999

LIGHT-ACTUATED AC ELECTROOSMOSIS FOR OPTICAL MANIPULATION OF NANOSCALE PARTICLES

Pei-Yu Chiou, Aaron T. Ohta, Arash Jamshidi, Hsan-Yin Hsu, Jeffery B. Chou, and Ming C. Wu
Department of Electrical Engineering and Computer Sciences, University of California at Berkeley, Berkeley, California, USA

ABSTRACT

We report on a novel light actuated ac electroosmosis (LACE) mechanism enabling optical manipulation of nanoscale particles on a featureless photoconductive surface using direct optical images. This mechanism applied optically patterned microfluidic vortices to circulate the nanoscopic particles onto the surface of light patterned virtual electrodes and trap them via the strong electrokinetic forces near the surface. For particles larger than 1 μm, we are able to achieve 31,000 individually addressable particle traps across a 1.3×1 mm^2 area. Each trap is created by one micromirror pixel of the digital-micromirror-devices (DMD) spatial light modulator used for patterning the optical images. For nanoscale particles, we have demonstrated optically guided concentration and transportation of 200 nm fluorescent nanoparticles.

INTRODUCTION

Tools for manipulating cells and particles in micro- and nano-scale play important roles in the biological and colloid fields. Manipulation functions such as trapping, concentrating, sorting, and transporting are highly sought after. Several mechanisms have been employed. For example, optical tweezers can precisely trap and transport a cell or a particle in a three-dimensional space[1]. Multiple traps can be generated using holography optical tweezers [2]. However, the optical power requirement and the small field of view of the high-N.A. objective lens limit its capability for parallel manipulation. Another commonly used mechanism is dielectrophoresis (DEP), which is produced by a non-uniform electric field[3]. Using microfabrication techniques, a large number of electrodes can be integrated for parallel manipulation. However, the size of the trap is limited by the electrodes, and its resolution is lower than that of optical tweezers. Parallel manipulation of a large number of single cells is even more challenging. It requires integrated "active matrix" circuits to individually address the electrodes, which increases the fabrication complexity and cost[4]. Magnetic tweezers and acoustic traps have also been reported[5, 6], however, it is difficult to trap and independently manipulate a large number of single cells.

To overcome this limitation, Chiou *et al.* have proposed a new mechanism called "optoelectronic tweezers (OET)," which allows optically patterned virtual electrodes on a photoconductive surface to address dielectrophoretic forces for massively parallel single cell manipulation using direct optical images[7]. By integrating a digital-micromirror-device (DMD) spatial light modulator, this technology allows a million light patterned virtual electrodes to be individually addressed on a low cost, disposable, plain amorphous silicon-coated glass for parallel control of a large number of single cells.

The DEP force is proportional to the volume and dielectric constant of the manipulated particles. Thus, a mixture of different particles can be sorted by DEP according to the characteristics of each particle because each particle may respond differently to the same electric field. However, manipulating nanoscale particles would require a very strong electric field gradient to overcome the thermal force. Alternatively, one can use fluidic flow to trap nanoparticles since the viscous force is only proportional to the linear dimension of the particles. As a result, manipulating particles using fluidic flow is much less dependent on the characteristics of the individual particles. Such a technique may be useful when it is desirable to manipulate each member of a mixture of particles in a substantially similar way.

In this paper, we present a novel mechanism called light-actuated ac electroosmosis (LACE) for manipulating micro- and nanoscale particles using light patterned microfluidic vortices. Unlike DEP, LACE uses fluidic flow to manipulate particles. Individually addressable traps for 2-μm particles and concentration of 200-nm particles have been demonstrated.

THEORY

Electroosmosis has been widely employed in the microfluidic systems for pumping liquids. The tangential electric field in the fluidic channel interacts with the charged ions in the double layer and generates a body force to drive the boundary fluidic layer. The velocity of the fluids at the edge of the double layer, called slip velocity, can be calculated by Helmholtz-Smoluchowski equation[8]

$$v_{slip} = -\frac{\varepsilon \varsigma E_t}{\eta} \qquad (1)$$

where v_{slip} is the slip velocity, ε is the dielectric constant of the liquid, ζ is the zeta potential at the interface between the liquid and the channel, E_t is the tangential component of the electric field, and η is the fluidic viscosity. Electroosmosis has generally been shown in the dc electric field. Recently, the ac electroosmosis has also been demonstrated as an effective mechanism in pumping fluidic flow by coupling the tangential electric field component with the field induced double layer charges on the electrode[9].

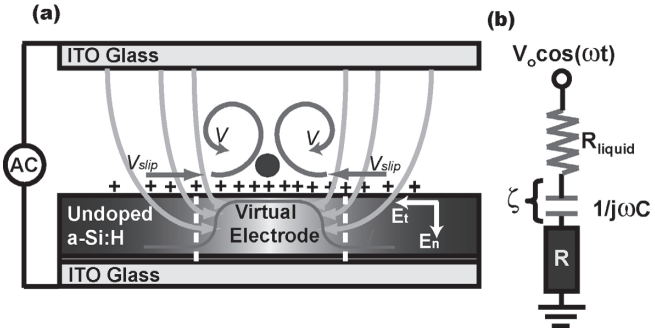

Fig.1 *(a) Schematic illustrating the operating principle of LACE.. (b) The equivalent circuit model along one of the electric field lines.*

Figure 1(a) illustrates the device structure and the working principle of LACE. The liquid solution containing nanoparticles are sandwiched between an indium tin oxide (ITO) glass and a photoconductive surface consisting of multiple featureless layers

including an ITO glass, a 50-nm n+ a-Si:H layer, and an 1-μm-thick undoped a-Si:H layer. An ac bias is applied between the top and the bottom ITO glass. In the dark area, the electric impedance of the amorphous silicon layer is high, and only a small portion of the total voltage drops across the liquid layer. In the illuminated area, the increased photoconductivity creates a virtual electrode on amorphous silicon and causes the applied bias to drop across the interface double layer capacitor C and the liquid resistor, as shown in Fig. 1(b). By using light patterning to create virtual electrodes, electrode patterns can be changed quickly and efficiently, rendering fixed physical or chemical pattering of the electrodes unnecessary.

Since creating the boundary slip velocity requires both the tangential electric field and the charged ions at the interface, there exists an optimal ac frequency $f_{opt}=1/2\pi RC$ at which the product of the electric field and the interface zeta potential in Eq. (1) reaches maximum. For frequency much high than f_{opt}, the capacitor has low electrical impedance and the bulk liquid resistor dominates. This results in a small zeta potential and a small slip velocity. For frequency much lower than f_{opt}, the impedance of the capacitor is much larger than the bulk liquid layer. The electric field that can penetrate through the double layer is small, resulting in a small tangential electric field. This also yields a small slip velocity. It can be shown that the optimal frequency of the device structure shown in Fig.1 (a) is

$$f_{opt} = \frac{1}{2\pi}\frac{\sigma}{\varepsilon}\frac{\lambda_d}{L} \qquad (2)$$

where σ is the conductivity of the liquid medium, ε is the dielectric constant of the liquid, λ_d is the double layer thickness, and L is the gap spacing of the liquid layer. For a LACE device with a 100 μm gap spacing, a KCL electrolyte with a liquid conductivity of 10 mS/m and a double layer thickness around 10 nm, the estimated f_{opt} is equal to 229 Hz. The actually f_{opt} is slightly higher when considering geometry factor due to the diverging electric field pattern in the liquid layer. In current LACE device, the ac frequencies are usually between 1 kHz ~ 10 kHz, while DEP operates at much higher frequencies, above 20 kHz to 10 MHz, to decouple the ac electroosmosis effect. The liquid conductivity is between 3 mS/m ~ 10 mS/m.

The microfluidic vortex created by the light induced ac electroosmosis near the virtual electrode is illustrated in Fig.1 (a). The charged ions accumulated at the interface are attracted towards the center by the tangential field, carrying the surrounding fluids with them. This results in a slip velocity pointing towards the center of the virtual electrode. By projecting a symmetrical optical pattern, a balanced microfluidic vortex is generated at the virtual electrode.

Trapping of nanoscopic particles using LACE involves two processes. First, the circulating fluid brings the nanoscopic particles via viscous forces to the center of the virtual electrode, where a minimum speed of the flow pattern exists since there is no tangential electric field due to symmetry. Second, although there is no tangential electric field in the center of the virtual electrode, the normal component of the electric field is strong. This results in the trapping of nanoparticles on the surface by the strong electrokinetic forces in the vertical direction, either through particle induced electrohydrodynamic flow or DEP forces.

SIMULATION

The LACE mechanism is simulated by combining the electrostatic model with the incompressible Navior Stoke's fluidic model. A dc electrostatic model in FEMLAB 3.0 is used to calculate the zeta potential, the tangential component of the electric field, and the slip velocity at the surface of the photoconductive layer. To facilitate computation, the double layer capacitor is replaced by a conductive layer with the same magnitude of frequency dependent resistance. Fig. 2 shows the vertical and the tangential components of the electric field distribution in the liquid layer using the following parameters, double layer thickness: 10 nm, liquid conductivity: 10 mS/m, applied bias: 2 V. The equivalent resistance of the capacitor is calculated at 8 kHz. The photoconductivity in the a-Si:H layer is a gaussian distribution with a full-width-at-half-maximum (FWHW) size of 30 μm and a peak conductivity 0.2 mS/m. Fig. 2(a) shows the vertical electric field is symmetric with respect to the center of the illumination spot and has a strong gradient near the surface. This provides the strong electrokinetic forces to trap nanoparticles at the surface. The tangential electric field on the surface is anti-symmetric, as shown in Fig. 2(b). The zeta potential can be extracted out from the voltage across the capacitor layer and the slip velocity at the interface is calculated using Eq. (1) along the radial direction. This slip velocity is used as the boundary condition to solve the incompressible Navior Stoke's equations for the flow pattern shown in Fig. 3.

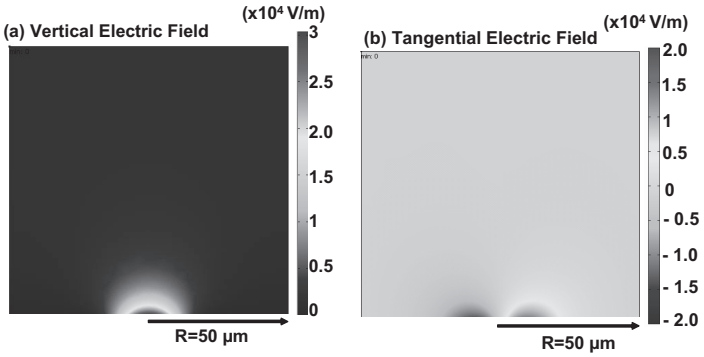

Fig.2 *(a) Vertical and (b) tangential electric field distributions in the liquid layer.*

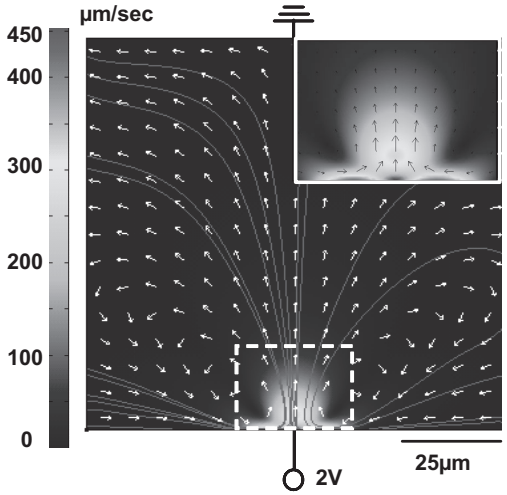

Fig.3 *Light induced fluidic flow near the virtual electrode. The inset shows the enlarged flow pattern in the center. There exists a dead zone in the middle where nanoparticles are trapped.*

In Fig. 3, this light induced flow circulates around the illumination spot with the highest speed at the edge of the virtual electrode. In the center surface of the virtual electrode, there exists a dead zone where the flow speed reaches minimum, as shown in

the inset in Fig. 3. The nanoparticles are circulated and swept into the dead zone where the electrokinetic forces dominate over the fluidic viscous forces and trap the nanoparticles at the center surface of the virtual electrode.

DEVICE FABRICATION AND EXPERIMENTAL SETUP

Figure 4 shows the pictures of the fabricated device. Fig. 4(a) is the photoconductive glass with multiple featureless layers as described in Fig. 1(a). The a-Si:H near one edge is removed by reactive ion etching (RIE) ($CF_4 + O_2$) to expose the bottom ITO layer for electrical contact. Fig. 4(b) is the commercial available transparent ITO glass.

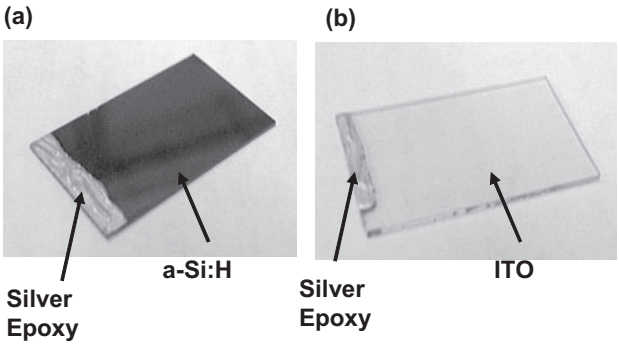

Fig.4 *Pictures of the LACE device. (a) The a-Si:H-coated ITO glass. The a-Si:H layers at the edge is removed for electrical contact. (b) The commercial available ITO glass.*

Figure 5 shows the experimental setup constructed on a Nikon TE-2000E inverted microscope. The LACE device is placed on the observation stage. We can operate the LACE device with the photoconductive side either up or down. For fluorescent observation, the photoconductive surface is placed on top of the ITO glass to prevent absorption of the excitation and the emission signals by amorphous silicon. This configuration is used for nanoparticle experiments since a fluorescent signal is used to observe particles smaller than the optical diffraction limit.

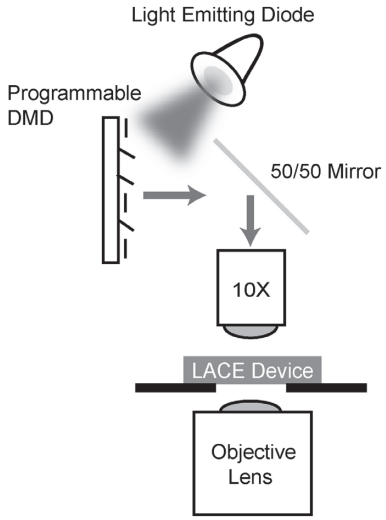

Fig.5 *The experimental setup for nanoparticle manipulation using LACE.*

The optical patterns are projected from the top side to minimize the interference with observation microscope. In this paper, we used two kinds of optical sources. The first is a single light-emitting diode (LED) with a wavelength of 625 nm (Lumileds, Luxeon Star/O). The light is expanded and spatially modulated by a DMD with 769×1024 mirror pixels. Each pixel has a size of 13.68 × 13.68 μm^2. The optical image is projected onto the LACE device using a 10× objective lens, generating a 1.5 × 1.5 μm^2 optical pixel on the imaging plane and an optical power of 25 nW/pixel. In some experiments, the background fluorescent excitation intensity is too strong, the LED does not provide sufficient contrast. In that case, a 5-mW, 632-nm laser beam is directly focused on the LACE surface by the 10× objective lens.

EXPERIMENTAL RESULTS

We have created 31,000 optical traps across a 1.3 × 1 mm^2 area for trapping and transporting 2-μm beads in parallel. Fig. 6 shows a small part of the trap array. Each optical trap is produced by a single DMD pixel. In Fig. 6(a), the particles are randomly distributed and not trapped by LACE yet. Within a second, these particles are swept into the bright spots by the microfluid vortices induced around the virtual electrodes. The spot size of the virtual electrode is small enough that each trap can only accommodate one particle. The un-trapped particles keep moving in the dark area until they are captured by an empty trap, as shown in Fig. 6(b). The applied ac frequency is 1 kHz and the bias is 4 V_{pp}. The process from Fig. 6(a) to (c) takes less than 10 seconds. The same optical patterns can also be used to trap 1 μm beads individually. For particles with size smaller than 1 μm, multiple particles will be trapped in one optical spot.

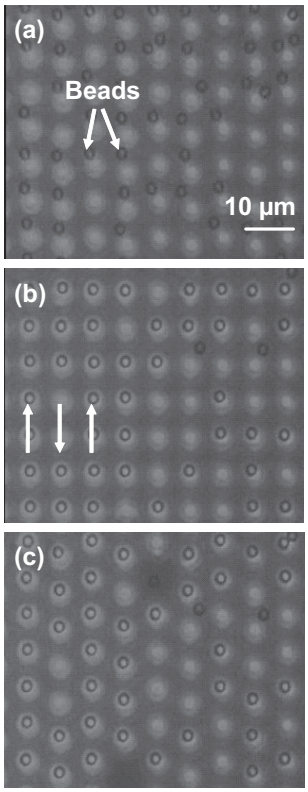

Fig.6 *Parallel trapping and transport of single 2 μm polystyrene beads. Each trap is produced a single DMD mirror pixel and the pitch is 5 pixels.*

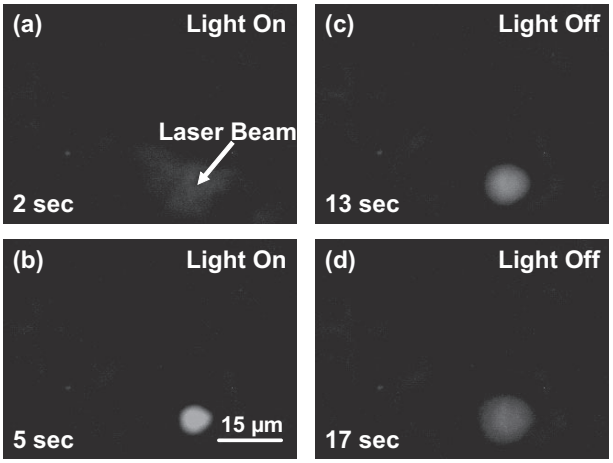

Fig.7 The snapshots of the captured video showing the concentration and release of 200-nm fluorescent particles using LACE activated by a 5-mW, 632 nm laser beam focused by a 10× objective lens.

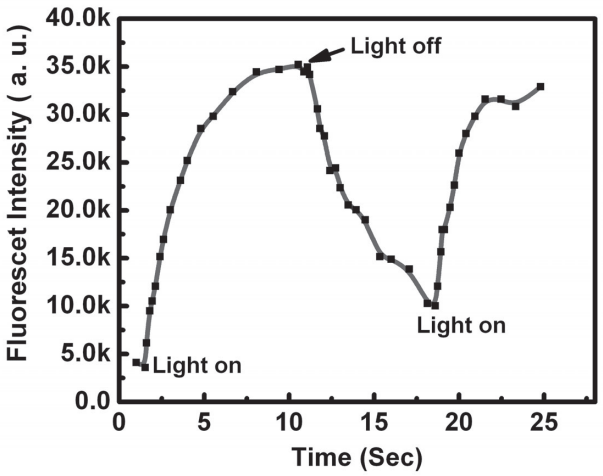

Fig.8 The fluorescent intensity at the center of the illumination spot. The concentration and releasing process of nanoscopic particles is repeatable.

Figure 7 shows the trapping and releasing of a group of 200 nm green fluorescent particles using a 5 mW, 632 nm laser beam and a 8.3 V_{pp}, 1.6 kHz ac bias. In Fig. 7(a), the particles are dispersed in the solution and the fluorescent signals are very weak. In Fig. 7(b), we turn on the focused laser beam near the lower right corner. The particles are concentrated to the center of the illuminated spot and produce a strong fluorescent signal. The fluorescent intensity saturated after few seconds, indicating the number of trapped particles has reached the maximum. The laser beam is turned off after the intensity saturated. These concentrated particles start to diffuse away due to the Brownian motion and the intensity of the fluorescent signal goes back to the background intensity after a few seconds, as shown in Fig. 7(c) and (d). This concentration and releasing process is repeatable. Fig. 8 shows the temporal response of the fluorescent signal at the center of the illumination spot.

CONCLUSIONS

This paper presents a novel light-induced ac electroosmosis (LACE) mechanism that enables optically patterned microfluidic flow to manipulate particles ranging from 2 μm to 200 nm on a featureless photoconductive glass. In contrast to DEP, which uses electric field to exert forces directly on particles according to their dielectric constant, LACE uses electric field to cause fluidic flow, which can then be used to trap particles, essentially independent of their dielectric constants. Using a DMD spatial light modulator, the high-resolution virtual electrodes generated 31,000 individually addressable microfluidic vortices to trap and transport 2 μm and 1 μm particles. For particles smaller than 1 μm, we have achieved light activated nanoparticle concentration using the LACE mechanism. This light-activated concentration and releasing process is controllable and repeatable. These experimental results show that LACE is potentially a powerful technique to manipulate nanoscale particles optically in real time.

ACKNOWLEDGEMENT

This project is supported by Center for Cell Mimetic Space Exploration (CMISE), a NASA University Research, Engineering and Technology Institute (URETI). P.Y. Chiou is partially supported by UC GREAT Fellowship.

REFERENCES

[1] A. Ashkin, J. M. Dziedzic, J. E. Bjorkholm, and S. Chu, "Observation Of A Single-Beam Gradient Force Optical Trap For Dielectric Particles," *Optics Letters*, vol. 11, pp. 288-290, 1986.

[2] J. E. Curtis, B. A. Koss, and D. G. Grier, "Dynamic holographic optical tweezers," *Optics Communications*, vol. 207, pp. 169-175, 2002.

[3] M. P. Hughes, "Strategies for dielectrophoretic separation in laboratory-on-a-chip systems," *Electrophoresis*, vol. 23, pp. 2569-2582, 2002.

[4] N. Manaresi, A. Romani, G. Medoro, L. Altomare, A. Leonardi, M. Tartagni, and R. Guerrieri, "A CMOS chip for individual cell manipulation and detection," *IEEE Journal Of Solid-State Circuits*, vol. 38, pp. 2297-2305, 2003.

[5] H. Lee, A. M. Purdon, and R. M. Westervelt, "Manipulation of biological cells using a microelectromagnet matrix," *Applied Physics Letters*, vol. 85, pp. 1063-1065, 2004.

[6] H. M. Hertz, "Standing-Wave Acoustic Trap For Nonintrusive Positioning Of Microparticles," *Journal Of Applied Physics*, vol. 78, pp. 4845-4849, 1995.

[7] P. Y. Chiou, A. T. Ohta, and M. C. Wu, "Massively parallel manipulation of single cells and microparticles using optical images," *Nature*, vol. 436, pp. 370-372, 2005.

[8] J. Lyklema, *Fundamentals of Interface and Colloid Science*, vol. 2. London: Academic Press, 1991.

[9] A. Ramos, H. Morgan, N. G. Green, A. Gonzalez, and A. Castellanos, "Pumping of liquids with traveling-wave electroosmosis," *Journal Of Applied Physics*, vol. 97, 2005.

800 MHZ LOW MOTIONAL RESISTANCE CONTOUR-EXTENSIONAL ALUMINUM NITRIDE MICROMECHANICAL RESONATORS

Philip J. Stephanou and Albert P. Pisano
Berkeley Sensor & Actuator Center (BSAC)
The University of California at Berkeley, Berkeley, CA 94720

ABSTRACT

This work introduces novel contour-extensional mode piezoelectric Aluminum Nitride micro-mechanical resonators that enable breakthrough increases in operating frequency and reductions in motional resistance. By selectively patterning the transduction electrodes and routing the excitation waveform, the resonant frequency of the device is effectively uncoupled from the overall dimensions of the AlN plate. Consequently, the motional resistance of a resonator with a given frequency can be significantly reduced by scaling up the lateral dimensions of the structural layer. The design has been validated by demonstrating an 803 MHz resonator with 24 Ω motional resistance and a *Q* factor over 1,000 when tested in air.

INTRODUCTION

The demand for highly-integrated analog filtering and frequency reference elements has spurred rapid innovation in the area of vibrating RF MEMS **[1]**. To date however, no single technology has emerged that can simultaneously deliver monolithic, post-CMOS integration of IF and RF components that can readily interface with 50 Ω RF systems. Thickness-extensional FBAR resonators have proven the technical feasibility and commercial viability of thin film piezoelectric Aluminum Nitride (AlN) based processing technology for RF applications, but the designs are practically limited to a single frequency per AlN deposition and not scaleable to IF **[2]**. Air and solid dielectric gap electrostatic contour mode resonators inherently do not suffer either of the aforementioned limitations, but despite monumental improvements have yet to demonstrate low motional resistance, fundamental mode resonators suitable for RF filter synthesis **[3,4]**. AlN contour mode MEMS resonators have emerged as the premier technology for realizing multi-frequency per chip, CMOS-compatible, low-loss filters, but heretofore have been limited to operating frequencies between 10 and 500 MHz **[5,6]**.

The present work introduces a novel design for piezoelectric contour mode MEMS plate resonators that effectively uncouples the resonant frequency of the devices from their overall dimensions by selectively patterning the transduction electrodes and routing the excitation waveform as seen in Figure 1. The ability to scale the lateral dimensions of the structural material enables more mechanically robust devices that are capable of attaining higher frequencies (803 MHz demonstrated) with reduced motional resistances (24 Ω) and relaxed fabrication tolerances (structural plate measures 51x100 μm). The electrode configuration also suppresses the appearance of any lower or sub-harmonic modes in the frequency response of the device.

THEORY

Piezoelectric and electrostatic contour mode MEMS resonators based on rectangular or annular plates offer the ability to prescribe frequency and motional resistance independently within a limited design space, but are ultimately precluded from reaching GHz fundamental modes by the need to define half-wavelength features (on the order of several microns) in whatever structural material is being used **[3,7]**. Theoretical designs for low motional resistance, GHz rectangular or annular plate resonators are marked by extreme length to width or average radius to annular width, respectively, which in practice result in unacceptable mechanical compliance, inefficient use of layout area, and the need for exacting fabrication tolerances.

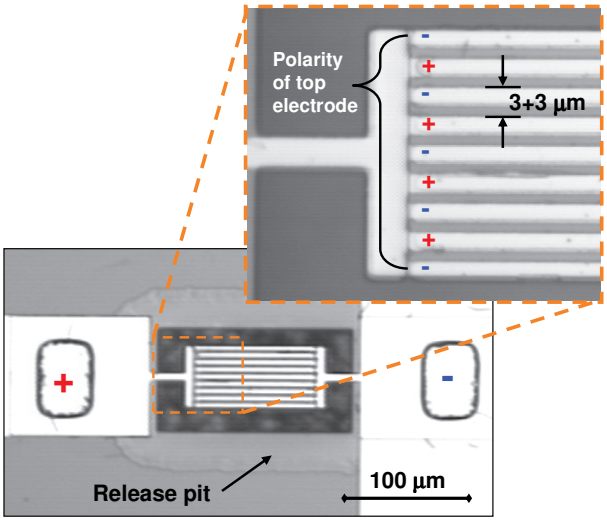

Figure 1: *Optical micrograph of micromechanical resonator with selectively patterned half-wavelength period electrodes. The polarity of the electric excitation signal alternates between adjacent top and bottom electrode pairs. The effective characteristic lengths for determining frequency and motional resistance are 6 and 900 μm, respectively.*

In the present design, the frequency determining dimension is effectively uncoupled from the overall dimensions of the AlN plate by patterning the transduction electrodes such that the polarity of the excitation electric field alternates at half-wavelength intervals in the direction of wave propagation as seen in Figure 2. The polarity of the electrodes uniquely matches that of the strain field for a specific bulk mode of vibration of the plate. Moreover, the number of half-wavelength electrodes can be scaled to engineer a proportional decrease in motional resistance (the motional resistance also depends on the length of the plate).

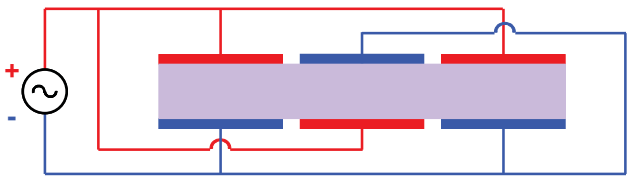

Figure 2: *Schematic of resonator cross-section showing selective electrode patterning and signal routing. The polarity of each top and bottom electrode pair alternates at half-wavelength intervals. The period of the electrode pairs determines the operating frequency of the resonator while the number of periods affects its motional resistance.*

The practical implication of the design is that half-wavelength features need only be defined in the thin metal electrodes, and the feasibility of fabricating such features in a production environment has essentially been proven by SAW device manufacturers (in fact SAW devices have more demanding fabrication requirements due to their lower acoustic wavespeed). As with SAW devices, the nominal frequency of the resonator depends not only on the absolute dimensions but also the periodicity of the electrodes.

FABRICATION PROCESS

The resonators under investigation are fabricated using a variation of a previously published four-mask, low-temperature process **[7]**. The device consists of a thin film piezoelectric AlN structural layer sandwiched between Pt bottom and top electrodes. The approximate thicknesses of the AlN and Pt layers are 1.5 µm and 200 nm, respectively. A 300 nm low-stress silicon nitride layer is deposited between the silicon substrate and bottom electrode for electrical isolation. The AlN films are deposited using a single-module AMS Inc. sputtering tool.

EXPERIMENTAL DETAILS

The fabricated MEMS filters are tested in a Janis RF probe station with micro-manipulated ground-signal-ground (GSG) probes. All testing is performed in air at atmospheric pressure and ambient temperature. The S_{11} parameter of the devices is extracted by an Agilent E5071B vector network analyzer with 0 dBm of signal power following a short-open-load calibration on a ceramic reference substrate. The admittance transformation is calculated by the network analyzer.

Figure 3 shows a plot of the admittance response of a piezoelectric contour mode MEMS resonator over a 200 to 1,000 MHz frequency range. The AlN plate in this instance measures 51x100 µm and has 9 pairs of Pt top and bottom electrodes with 3 µm line width and spacing. Notice the effective suppression of spurious modes achieved by the electrode configuration.

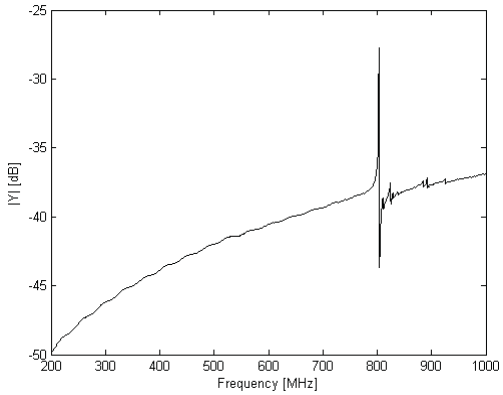

Figure 3: *Admittance response of a micromechanical resonator with 9 half-wavelength top and bottom electrode pairs showing effective suppression of spurious modes from 200 MHz to 1 GHz.*

Figure 4 shows the admittance response of the same resonator in the vicinity of its 803 MHz series resonance exhibiting 24 Ω motional resistance and a *Q* factor of 1,300 when tested in air. A similar resonator with 7 pairs of 3 µm line and space electrodes displayed an 828 MHz resonant frequency with 58 Ω motional resistance and a *Q* of 1,000 when tested in air.

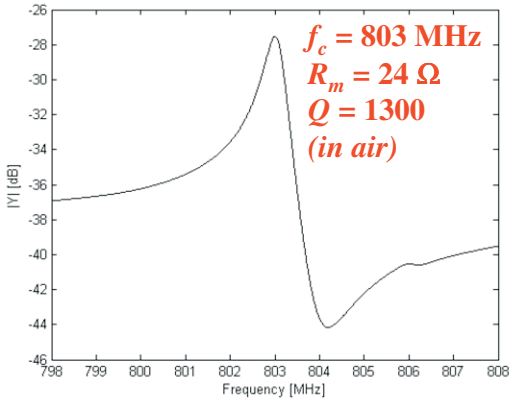

Figure 4: *Admittance response of same resonator as Figure 3 showing resonant behavior. Testing is done in air with 0 dBm signal power. Data are measured directly on network analyzer.*

CONCLUSIONS

Novel piezoelectric contour mode MEMS resonators have been demonstrated that enable breakthrough increases in frequency and reductions in motional resistance. The performance gains stem from a technique for selectively patterning the transduction electrodes and routing the excitation waveform. An AlN resonator measuring 51x100 µm overall with 9 pairs of 3 µm line and space Pt electrodes has been tested at 803 MHz with 24 Ω motional resistance and a *Q* of 1,300 in air. This technology promises to for the first time permit monolithic integration of post-CMOS compatible, low-loss filters spanning IF to RF that can readily be interfaced with existing 50 Ω RF systems.

ACKNOWLEDGEMENTS

This work was supported by DARPA grant No. NBCH1020005. The authors offer special thanks to AMS Inc. for their assistance with AlN deposition and tool installation, and to the UC Berkeley Microfabrication Laboratory staff for their support.

REFERENCES

[1] K.M. Lakin *et al.*, "Development of Miniature Filters for Wireless Applications," *IEEE Trans. on Microwave Theory and Tech.*, vol. 43, no. 12, pp. 2933-2939, 1995.

[2] R. Ruby, *et al.*, Y. Oshmyansky, "PCS 1900 MHz duplexer using thin film bulk acoustic resonators (FBARs)," *Electronics Lett.* 35, pp. 794, 1999.

[3] J. Wang, C.T.-C. Nguyen, *et al.*, "1.156-GHz Self-Aligned Vibrating Micromechanical Disk Resonator," *IEEE Trans. on UFFC*, vol. 51, no. 12, pp. 1607-1628, 2004.

[4] Y.-W. Lin, .T.-C. Nguyen, *et al.*, **"**Vibrating micromechanical resonators with solid dielectric capacitive transducer gaps," *IEEE Proc. Freq. Cont. Symposium and Exhibition*, pp. 128-134, 2005.

[5] G. Piazza, *et al.*, "Single-chip multiple-frequency filters based on contour-mode aluminum nitride piezoelectric micromechanical resonators," *TRANSDUCERS 2005*, pp. 2065-2068, 2005.

[6] P.J. Stephanou, *et al.*, "Mechanically Coupled Contour Mode Piezoelectric Aluminum Nitride MEMS Filters," *IEEE MEMS 2006*, pp. 906-909, 2006.

[7] G. Piazza, *et al.*, "Low motional resistance ring-shaped contour-mode aluminum nitride piezoelectric micromechanical resonators for UHF applications," *IEEE MEMS 2005*, pp.20-3, 2005.

COMPOSITE FLEXURAL MODE RESONATOR WITH REDUCED TEMPERATURE COEFFICIENT OF FREQUENCY

R. Melamud, B. Kim, M. A. Hopcroft, S. Chandorkar, M. Agarwal, C.Jha, S. Bhat, K. K. Park, and T. W. Kenny
Departments of Mechanical and Electrical Engineering, Stanford University
Stanford, CA, USA

ABSTRACT

This paper reports a method to passively reduce the native temperature coefficient of frequency (TCF) by creating a Silicon - Silicon Dioxide (Si-SiO_2) composite resonator whose bending stiffness has reduced sensitivity to temperature. Silicon exhibits softening with increasing temperature. Amorphous silicon dioxide exhibits an anomalous hardening with increasing temperature. An optimal combination of Si-SiO_2 in flexural mode resonators is determined that would yield zero TCF. Composite single anchor, double ended tuning forks (DETF) where fabricated and show a greater than 10x reduction in TCF in the 15°C to 70°C temperature range. The composite beam resonators were fabricated in our wafer-scale encapsulation process, which is described by [1] and is being commercialized.

INTRODUCTION

To become a viable replacement for the ubiquitous quartz crystal technology, silicon resonators must have a frequency stability of under 100 ppm in the 0°C to 70°C temperature range. Silicon resonators exhibit a native temperature coefficient of frequency (TCF) of –30 ppm/°C that is dominated by the decrease of the resonator stiffness due to the material softening of Silicon.

Current compensation methods can be classified as either active or passive. Active compensation techniques such as ovenization [2] and electrostatic tuning [3] require power in order to reduce the TCF into the desirable range. Passive compensation methods attempt to reduce the native TCF without application of power. Previous passive compensation techniques [4,5] have used axial stress induction in flexural mode resonators to shift the natural frequency. This was accomplished by using materials with different coefficients of thermal expansion (CTE) that would induce thermal stresses with changes in temperature. Although these methods demonstrated the ability to reduce TCF, introducing materials with mismatched CTE's can cause stress induced hysteresis, processing difficulties due to large thermal stresses, restrictions on material selection for clean processes, and undesirable sensitivity to package stress.

This paper reports a method to passively reduce the native TCF by creating a Silicon - Silicon Dioxide composite resonator whose bending stiffness can be insensitive to temperature variation. Silicon dioxide exhibits an anomalous temperature coefficient of Young's Modulus (TCE) that is positive [6]. By combining it with Silicon, which has a negative TCE, it is possible to reduce the temperature dependence of the stiffness of the resonator. Furthermore, this method does not use stress induction as the means to compensate frequency.

THEORY

Flexural mode beam-type resonators, such as the double end tuning forks used in this paper (Fig. 1), that are fabricated from a single material and are single anchored have a frequency and

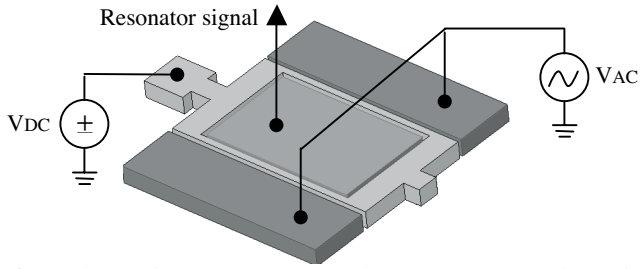

Figure 1. *Single anchor, DETF with outer excitation electrodes and an inner sense electrode.*

TCF described in Equation 1. Equation 1.b ignores the smaller effect of dimensional changes with temperature and assumes linear material properties.

$$f = \frac{\beta^2}{2\pi L^2}\sqrt{\frac{B}{\rho A}} = \frac{\beta^2}{2\pi L^2}\sqrt{\frac{EI}{\rho A}} \qquad 1.a$$

$$TCF = \frac{1}{f_o}\frac{\partial f}{\partial T} \approx \frac{1}{2}\frac{\partial f}{\partial B}\frac{\partial B}{\partial T} \approx \frac{TCE}{2} \qquad 1.b$$

In the above equations, β is the mode constant, E is the Young's Modulus, ρ is the density of the material, I is the flexural rigidity, L is the length of the beam, A is the cross sectional area of the beam, $B = EI$ is defined as the bending stiffness of the beam, f_o is a reference frequency, and TCE is the temperature coefficient of Young's modulus of the beam's material. The TCE of Silicon is approximately -60 ppm/°C which results in a TCF of -30 ppm/°C for Silicon resonators.

For a composite beam of N materials, the above equations are modified such that the bending stiffness takes into account the geometric composition of the beam (Eq. 2a).

$$B = \sum_{j=1}^{N} E_j I_j \qquad 2.a$$

$$TCF \approx \frac{1}{2}\left[\sum_{j=1}^{N} E_j I_j TCE_j \Big/ \sum_{j=1}^{N} E_j I_j\right] \qquad 2.b$$

The resulting modified TCF is a function of the TCE of each of the materials in the composite. By using amorphous SiO_2, which has a positive temperature coefficient of Young's Modulus (TCE) of +195 ppm/°C, in combination with Silicon, it is possible to design an ideal composite beam whose bending stiffness does not change with temperature yielding a zero TCF resonator.

From the above equation, the only design parameter that can be controlled is the flexural rigidity of each material. For a Si-SiO_2 composite, the optimal configuration requires the minimal amount of SiO_2 growth in order to achieve zero TCF. Several configurations have been considered (Fig 2). A laminate type structure (Fig 2.a) has a flexural rigidity that is linearly related to the thickness of the SiO_2. However, an encapsulated structure (Fig 2.b) has a quartic dependence on thickness of the SiO_2. The latter configuration was chosen since it is most sensitive to SiO_2 thickness and can be easily achieved by oxidizing all exposed Silicon surfaces. Figure 3 shows the result of evaluating the composite beam TCF equation (Eq. 2.b) for the optimal

configuration (Fig 2.b). The target thickness necessary to achieve zero TCF depends on the width of the beam. The model also took into account the orientation dependent oxidation of the beam surfaces as well as the consumption of Silicon during oxidation (0.46µm of Si for 1µm of SiO_2) [7].

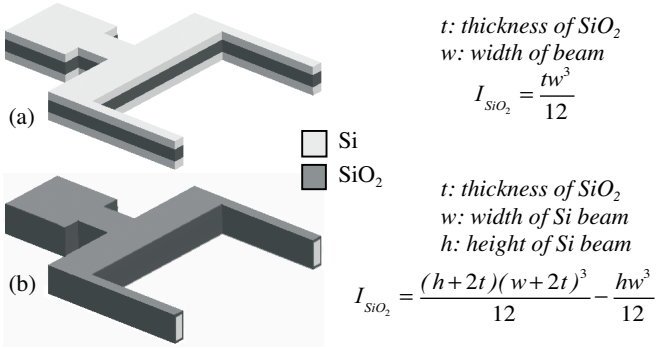

t: thickness of SiO_2
w: width of beam

$$I_{SiO_2} = \frac{tw^3}{12}$$

t: thickness of SiO_2
w: width of Si beam
h: height of Si beam

$$I_{SiO_2} = \frac{(h+2t)(w+2t)^3}{12} - \frac{hw^3}{12}$$

Figure 2. *Cross-section of the DETF through the beams of the resonator. The TCF of the composites will depend on the thickness of the SiO_2 layers. (a) Laminate construction with SiO_2 sandwiched between Si layers. (b) SiO_2 coated Si by oxidation of all Si surfaces. The oxidized configuration is optimal since the flexural rigidity, I, of the SiO_2 is most sensitive to the thickness of SiO_2*

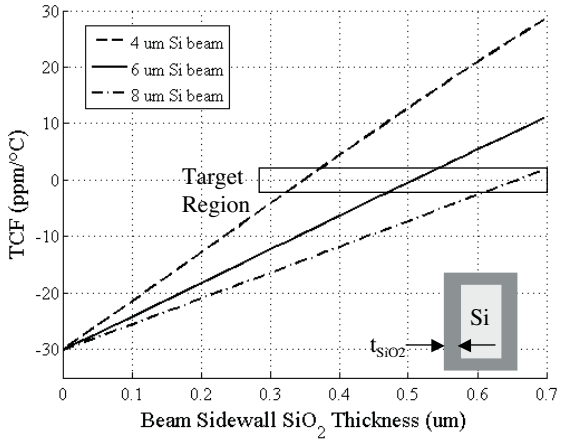

Figure 3. *SiO_2 thickness on sidewall of beam versus TCF for oxidized silicon resonator configuration (Fig 2.b). This model takes into account orientation dependent oxidation rates and consumption of silicon during oxidation. The target oxidation depends on the initial width of the Si beam. The constants used in this model are: TCE_{Si}=-60 ppm/°C, TCE_{SiO2}=+195 ppm/°C, E_{Si}=168 GPa, E_{SiO2}=70G Pa, h=20µm.*

FABRICATION AND EXPERIMENTS

Si-SiO_2 composite resonators were fabricated using a wafer scale polysilicon encapsulation with oxide seal processes described in [1]. The only modification was a 30 minute wet oxidation at 1100°C to oxidize the surfaces of the resonator beams. The oxidation occurred after the resonator was released by HF vapor etching of the sacrificial oxide. The thickness of the oxidation was approximated by measuring the SiO_2 thickness (0.44 µm) on the surface of the encapsulation. The oxidized resonators, with 7.5µm beam widths, were measured at 40°C and over a 15°C to 70°C temperature range using a temperature controlled oven.

The oxide seal process used for these preliminary experiments in not as clean as our high temperature epi-polysilicon seal. Devices sealed in this process were operated at a fixed 40°C temperature for 3 hours and showed a positive frequency drift of ~11 ppm / hr. This drift is attributed to migration of absorbents off of the resonators. The drift is slow enough to allow our first experiments on the temperature dependence of frequency for oxide/silicon composite beams.

Frequency versus temperature data was taken for five cycles over a temperature variation from 15°C to 70°C. The experiment took place over a continuous 15 hr time span and a +9.9 ppm/hr drift was observed. The total frequency excursion during this time span was 260 ppm. However, approximately 150 ppm is attributed to a linear frequency drift over time. Figure 4 shows the frequency versus temperature data for the five cycles as well as a comparison to the native TCF of a silicon DETF.

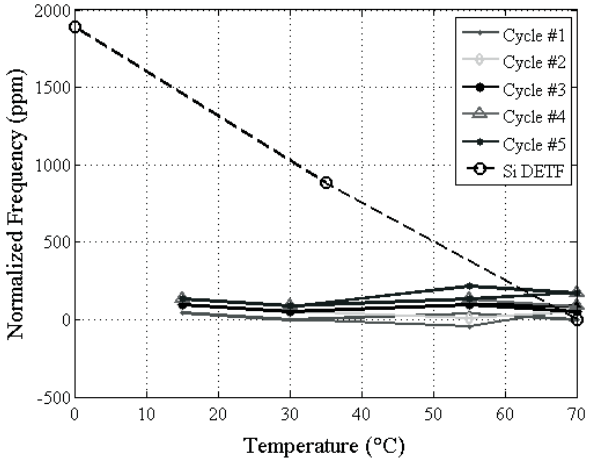

Figure 4*. Frequency vs. temperature variation of an oxidized DETF over five cycles from 15°C to 70°C. The total frequency excursion, over a 15 hr span, was 260 ppm. However, approximately 150 ppm could be attributed to a ~10ppm/hr drift.*

CONCLUSION

Preliminary results show that it is possible to passively reduce the TCF of silicon resonators by incorporating Silicon Dioxide into the structure of the resonator. A relation for the TCF of a composite beam is developed and it is shown that the optimal composite configuration is achieved by oxidation of the surfaces of the silicon resonator. Devices were fabricated in a wafer-scale oxide seal processes and show a 10x reduction in the native TCF compared to single material Silicon resonators. In future work, a combination of passive and active compensation will be used to achieve a TCF less than 1 ppm over this same range.

ACKNOWLEDGEMENTS

This work was supported by DARPA HERMIT (ONR N66001-0-18942), The National Nanofabrication Users Network facilities funded by NSF (ECS-9731294), The National Science Foundation Instrumentation for Materials Research Program (DMR 9504099), and the Stanford Graduate Fellow support for R. Melamud. The authors would like to thank Gary Yama and Eric Peroziello for their invaluable help and guidance.

REFERENCES

[1] W.-T. Park, *et al. Technical Digest of Transducers (2003)*
[2] M.A. Hopcroft, *et.al. Technical Digest Hilton Head* (2004)
[3] W-T. Hsu, *et.al. Technical Digest of MEMS* (2002)
[4] W-T. Hsu, *et.al. Technical Digest IEDM.* (2000)
[5] Melamud, *et.al. Technical Digest Transducers (2005)*
[6] McSkimmin, *Journal of Applied Physics.* 24 (8), (1953)
[7] Plummer, *et.al.* "Silicon VLSI Tecnology", (2000)

SUB-NANOMETER POSITION CONTROL USING SECOND STAGE ACTUATORS IN HARD DISC DRIVES

Dallas W. Meyer[1], Neal F. Gunderson[1], Kevin J. Schulz[2], Todd A. Bordson[2], Rick A. Budde[2], Marsha A. Huha[2], Mingxiao Jiang[1], David A. Sluzewski[2], John S. Wright[2] and Lowell J. Berg[1]

[1]Seagate Technology
1280 Disc Drive
Shakopee, MN 55379
dallas.w.meyer@seagate.com

[2]Seagate Technology
7801 Computer Avenue South
Bloomington, MN 55435
kevin.j.schulz@seagate.com

Introduction

Secondary actuation to improve tracking capability in disc drives has been proposed for many generations and in multiple forms. Disc drives have increased in areal density by more than 50% per year over the past 15 years. This density has been accompanied by an increase in track density (defined as the inverse of track pitch) of nearly 100 times over that same time period, as shown in Figure 1 (the other primary contributor to the areal density increase is increasing bit density). In fact, track density has been increasing at a disproportional rate with respect to areal density, stressing the tracking system even further. Until recently, successive increases in tracking density have been accomplished with continued technology scaling, i.e., shrinking tolerances and improving capability of the main actuator in the disc drive (main actuator is defined as the "first stage" or coarse control actuator in this paper).

The rationale for continued scaling of the technology is primarily cost. As an illustrative point related to cost, consider the trends of drive unit storage. The cost per unit of storage has declined by more than 2000 times in a 15-year period (>$1 per MB in 1991 vs. $0.50 per GB in 2006)! Additional componentry for dual stage tracking has been considered an unacceptable cost detractor and therefore has been avoided. Rather, the intellectual and development focus with the storage industry has been towards techniques allowing for the avoidance of secondary actuation. Many other very creative solutions with lower cost have been developed and deployed in disc drives, in the form of improved mechanical structures (stiffness, damping, etc.), airflow management features (reduced excitation during tracking), and drive level acceleration sensors for measuring and actively compensating for external disturbances. Figure 2 shows an example of plates used to decrease the level of turbulent flow in the drive. Many of these improvements are now reaching their scaling limits, and are forcing the industry to move into the age of secondary micro-actuation, as much as fifteen years after the first proclamations were made about the need! This paper will discuss additional details on the deployment of a dual stage actuator, now used by Seagate in enterprise drive- level applications.

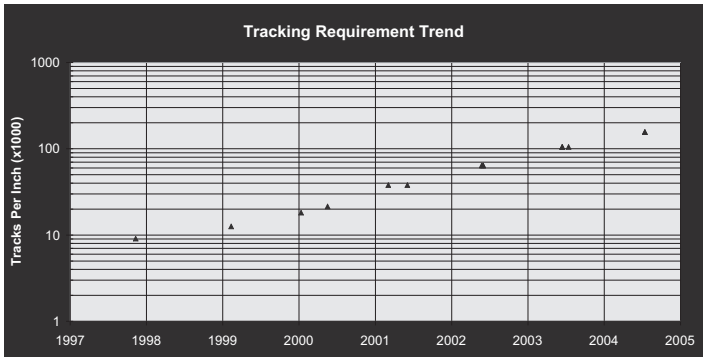

Figure 1. Track density trend over time

One critical factor to consider with any tracking scheme is the reliability of the disc drive under multiple environmental extremes. During this time of tremendous cost reduction, the reliability of the disc

drive has improved more than 10 times, with current disc drives supporting a mean time between failures of 1.4 million hours. Much of this improvement has been in the areas of head and media tracking, and redundancy checks. As an example, consider an event where a drive was bumped when writing. If you were listening to music from an MP3 player, you potentially will hear a skip in the music, depending on the depth of buffering. However, consider this same scenario when your bank account information is being recorded in a data center - a potentially life-impacting event! Without sufficient tracking stiffness to respond with sufficient bandwidth, the information during this critical write could be placed "off-track," creating an error. Obviously, the drive and system must possess sufficient intelligence and redundancy (data integrity checks) to monitor and correct for such events. However, the example helps to illustrate drive requirements in today's demanding applications, and why the reliability focus is so critical for deployment of any technology into the disc drive unit.

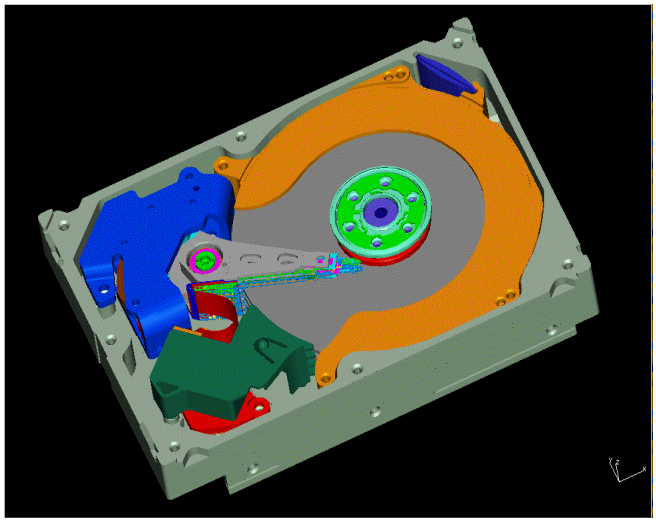

Figure 2. A disc drive using air diverter plates, reducing the level of air turbulence and allowing improved tracking

A closely associated requirement to reliability is that of drive performance. Unlike with many other high speed communication technologies, an advantage for storage is that the information requested will be "available" again as the disc completes a rotation, therefore retries are often used to improve the overall error rate capability of the drive. Unfortunately, these retries degrade system performance, especially in RAID configured systems (redundant arrays of inexpensive discs). Figure 3 illustrates an example comparing desktop to enterprise drives showing the influence of external system performance (normalized to the quiescence state) vs. disturbance (rotational acceleration). For systems with poor tracking capability or overlapping resonance peaks, system performance will be quickly degraded as multiple drives are put into operation in adjacent storage cabinets (in systems, most of the external excitation is generated from adjacent drive actuators).

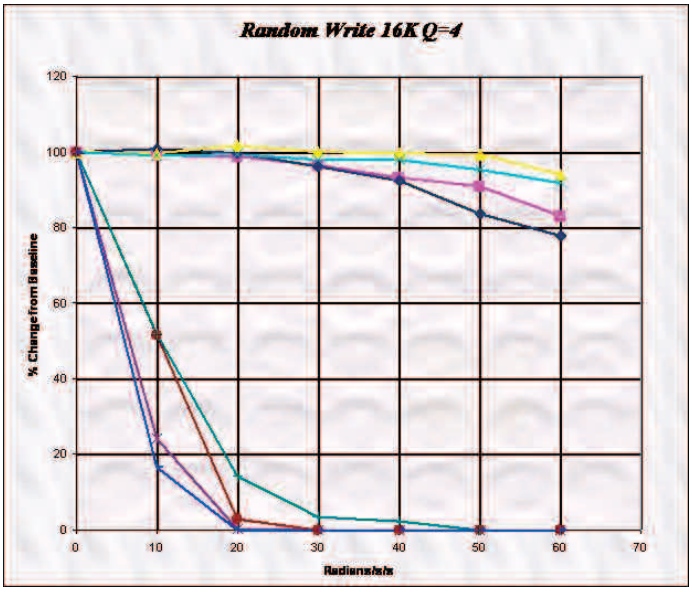

Figure 3. Performance as a function of external rotational vibration, enterprise (upper grouping) vs. desktop (lower)

Methods

Secondary actuation (putting a secondary active control unit between the coarse position and the recording head) can be accomplished using several different technologies, and can be incorporated at several levels within the system. Figure 4 illustrates a device where the second stage actuator is inserted at the base of the suspension, just beyond the actuator. The device uses two bulk piezoelectric elements spaced across a deformable metal hinge, allowing the suspension to undergo an in-plane rotation with applied voltage. This rotation allows the recording head to move to an adjacent track without moving the primary actuator. Because this device is built into the suspension, it has been termed a milli-actuator (however given the positioning and stroke requirements – this reference to "milli" is not an accurate depiction of the device). Other options, such as shown in Figure 5, are to build multi-layer piezoelectric elements around the recording head slider allowing the system to actuate at the slider

level (multi-layer elements are required for sufficient stroke). Because this is housed at the recording head, slider level, it has previously been referred to as a micro-actuator.
Still other configurations have been developed, using other principles for generating forces. Electrostatic and electromechanical devices have been proposed, but not yet deployed in commercial storage devices. A quick review of the patent literature illustrates multiple concepts. Piezoelectric driven concepts appear to be the continuing preferred choice for drive deployment.

As noted previously, piezoelectric secondary actuators have been in volume production in Seagate 10 krpm enterprise disc drives since July 2004, and will be discussed in more detail in later sections of this paper. This design, shown in Figure 4, has enabled non-repeatable run out reduction and improved drive performance under rotational vibration. The suspension actuator design was engineered to meet a challenging set of requirements for stroke, tracking, reliability and low-cost assembly.

Integration

A key aspect to any actuation structure is the tracking frequencies. The second stage actuator of Figure 4 has the advantage of a large multiplier of length based on small hinge movements, and can therefore be made very stiff. The downside is that disturbances generated in the suspension cannot be compensated with the actuator, given the suspension is after the first and second stages of actuation.

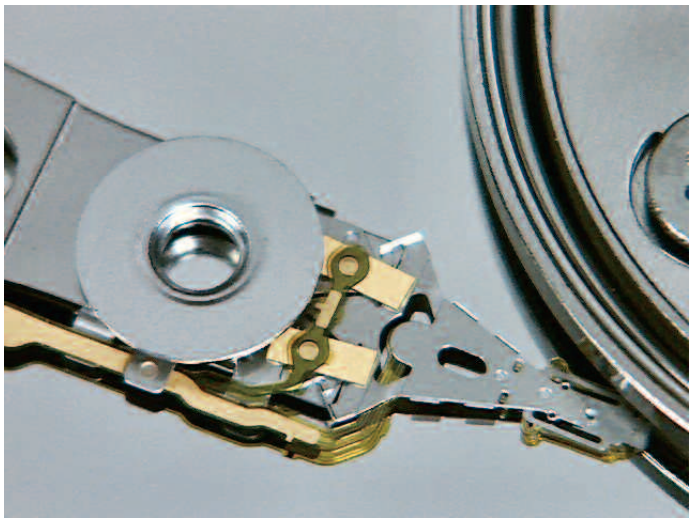

Figure 4. A commercially deployed microactuated suspension

The placement of the microactuator of Figure 5 has the advantage of being beyond the main suspension, and can therefore compensate for motions generated in the suspension. The deficiency of this location is the complexity of the integration. The air-bearing surface, as shown in Figure 5 as part of the actuator, is a photolithographically defined pattern on the slider surface, and is designed to "fly" over the surface at a spacing of 20-30 angstroms. These "fly" characteristics are developed numerically and validated empirically using modified forms of the Reynolds equation. Due to the small spacings involved, and the limited length and width of the slider, the part is extremely sensitive to perturbations in both the gimbal biasing (torque variances arising from static angular variations of the suspension holding the slider), and the overall flatness of the bearing surface. As an example, the surface of the slider must be maintained to less than 10A of flatness difference, over temperature extremes of zero to nearly 100^{o}C. The incorporation of these elements directly onto the slider body, and the required interconnect, make this an extremely challenging manufacturing process.

A further observation to note in any disc drive, including those with secondary actuation is that the transducer, which is what is actually reading and writing information from the disc surface, is very localized to the trailing edge of the slider (a characteristic length of 10-20 microns). The remainder of the slider (characteristic lengths of hundreds of microns) provides a mechanically stabilized platform for holding the transducer. To achieve very high actuation bandwidths in future systems, one should not consider the slider body mass as a fixed requirement for actuation. Actuation of the isolated transducer unit satisfies the requirements for track-to-track actuation. Given the reduced masses and sizes involved, techniques using lower forces can be employed. Multiple concepts have been disclosed in the patent literature, however no commercial device has been deployed.

The integration complexities are very severe at the transducer level. For a device where the transducer is now presented with a degree of freedom separate from the slider body, the spacing control from the media dictates that the actuator translate track-to-track with virtually no head-to-disc spacing change (less than a few Angstroms). Another option proposed is a bi-directional actuator, where the spacing in both track-to-track and head-media are

actively controlled, thereby compensating for unwanted head-media spacing changes during track-to-track actuation. Actively controlling head-media spacing is also very advantageous for improving overall drive reliability and recording performance. The challenge is to actively control spacing in one direction to an Angstrom level, while ensuring sufficient track-to-track stroke exceeding a 1000 Angstroms.

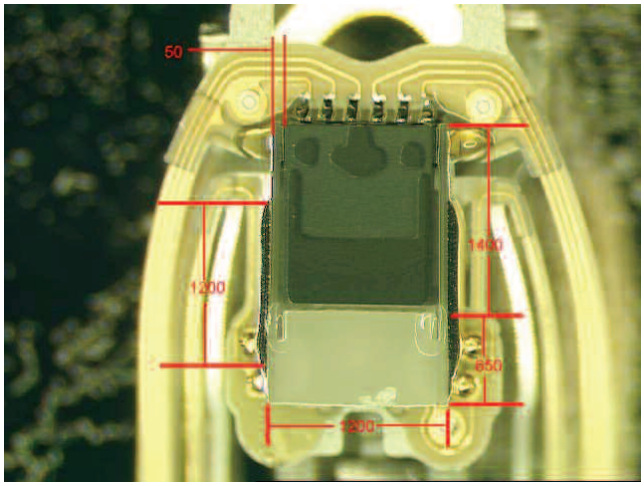

Figure 5. A commercially deployed slider level microactuator

Concepts for transducer level actuation, including bi-directional, are detailed in several patents by various authors, and differ substantially in prime mover technology and construction.

Suspension Based Design

We now discuss in detail the suspension-based actuator of Figure 4. The device utilizes PZT (lead zirconate titanate) for the motor, and has been documented in (head gimbal assembly) several key patents [1]. A suspension actuated HGA design introduces several important trade-offs. The most important are the stroke of the micro motor, the primary resonance mode of the micro motor, and the degree to which the PZT motors act as structural members to carry the pre-load of the HGA. The HGA design productized for this drive successfully managed these trade-offs to arrive at an optimal design point. Performance is summarized in Table I with a typical frequency response function shown in Figure 6. A key enabler was the use of a laminated steel/polyimide/steel material to fabricate the load beam of the HGA. The laminated material allowed more flexibility in the construction of the load beam to incorporate the PZT elements and to tune the stiffness to optimize the resonance performance. The design introduced has a very high primary resonance mode of 18 kHz while still achieving 20 nm/V of micro motor stroke. By limiting the structural load carrying function of the PZT motors, this design is very robust to damage against shock and handling concerns. A planar assembly process using solder reflow for the PZT interconnect resulted in a design that is simpler and lower in cost to produce than many other micro actuator HGA designs proposed previously.

HGA PERFORMANCE CHART	
1st Bending (Hz)	4500
1st Torsion (Hz)	9000
Sway/Microactuator Mode (Hz)	17500
Motor Stroke (Nm/V)	20
Mass (mgr)	76

Table I. HGA Performance

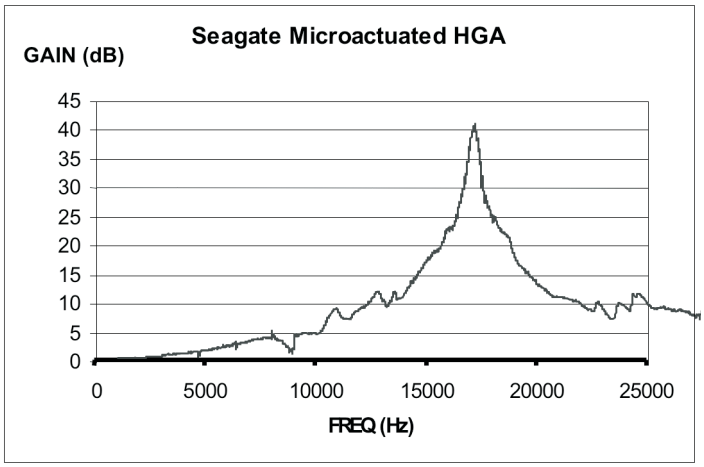

Figure 6. Frequency Response Function

PZT Motor

Selection of PZT Navy type VI was made to provide a balance between thermal and voltage stability and high piezoelectric coefficient. PZT types with higher piezoelectric coefficients are available, however, lower Curie temperatures result in greater depoling from assembly thermal exposure (epoxy cure cycles, solder electrical interconnect, etc.). Electrode heterostructure provides adequate adhesion to the PZT and provide a surface suitable for a solder

electrical interconnect. Solder reflow process experiments were conducted to develop a process that minimized thermal depoling of the PZT while providing adequate adhesion.

PZT particle counts on the suspension assembly were kept within specification of a single stage suspension assembly by optimization of PZT dicing and cleaning processes. Several experiments were run that looked at key input variables such as wheel type, cutting speed, and cleaning surfactant. Edge condition is shown in Figure 7. Wheel type decreased edge roughness, which correlated to lower liquid particle counts on PZT. This enabled suspension counts to go from >30,000 particles/cm^2 to <13,000 particles/cm^2.

The optimized PZTs were used to investigate the generation of PZT particles in the HDA and whether those particles posed any substantial risk to the HDI with longitudinal media. Suspensions actuated at extreme drive operating conditions showed a maximum of eight particles generated over three days (Figure 8). PZT particle generation was shown to stabilize after four hours of actuation. PZT particles were found to be a relatively soft ceramic (~5.5 MOHS hardness) that did not impart significant high DPPM of scratches in component and drive level particle testing. Drive level injections of very large numbers of PZT particles showed recoverable errors with no defects detected upon teardown as compared to alumina injections, which exhibited severe HDI occurrences (Table II). Other particle reduction techniques such as encapsulant coatings were also investigated but are not discussed here.

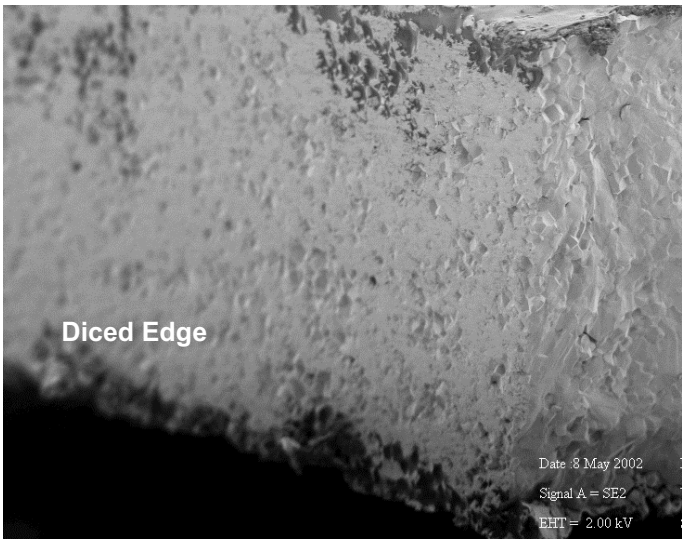

Figure 7. Scanning electron micrograph of diced PZT edge

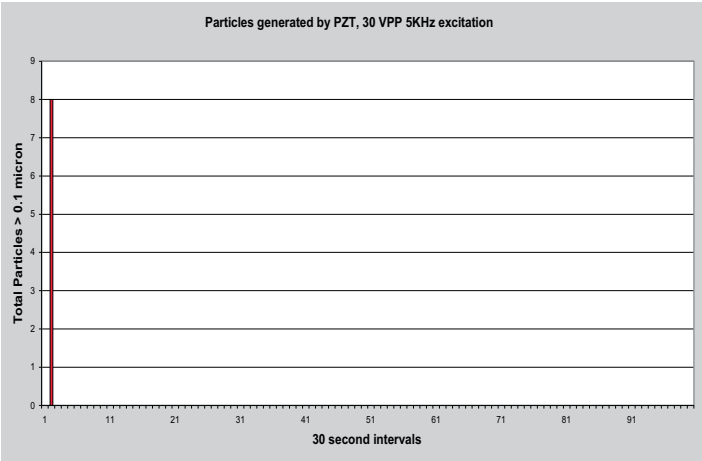

Figure 8. Component particle generation test results

Carbon Thickness	Particle	Point Defects	Scratches > 1.2 mm	Scratches, 0.1-1.2 mm	Total Defects/ Opportunity	Total scratches / Opportunity
Low	PZT	0.28%	**0.00%**	**0.00%**	0.28%	0.00%
Low	PZT	0.36%	**0.00%**	**0.00%**	0.36%	0.00%
Medium	PZT	0.41%	**0.00%**	**0.00%**	0.41%	0.00%
High	PZT	0.25%	**0.00%**	**0.00%**	0.25%	0.00%
High	PZT	0.32%	**0.00%**	**0.00%**	0.32%	0.00%
Low	Alumina	0.22%	0.89%	0.30%	1.41%	1.19%
Low	Alumina	0.21%	0.17%	0.08%	0.46%	0.25%
Medium	Alumina	0.71%	0.11%	0.23%	1.05%	0.34%
High	Alumina	0.40%	0.12%	0.15%	0.68%	0.28%
High	Alumina	0.27%	0.00%	0.15%	0.42%	0.15%

Table II. Summary of drive particle injection tests

Reliability

Seagate conducted a degradation Accelerated Life Test (ALT) under multiple stress levels of two stressors: temperature and AC (at 3kHz) voltage. Each stressor has three levels (temperature: 60^{o}C, 80^{o}C, 100^{o}C; AC voltage: 0 to 20V, 0 to 35V, 0 to 50V). The combination generates nine test conditions. The test is conducted with 10 HGA units at each test condition. Units are to be "aged" for one week at room temperature and zero volts after each stress exposure. The test units are measured (stroke level, in nm/V) at zero days, one day, three days, one week, two weeks and three weeks. "Failure" is defined as performance degradation with 20% stroke loss.

An ALT model was built using thermal-nonthermal life-stress equations and maximum likelihood estimation methods (MLE). We also conducted a prediction of micro-actuator long-term reliability under normal usage condition (random process of AC voltage) by employing Palgrem-Miner's damage accumulation rule. The results show that the Seagate

designed micro-actuator demonstrates very high long-term reliability (Figure 9).

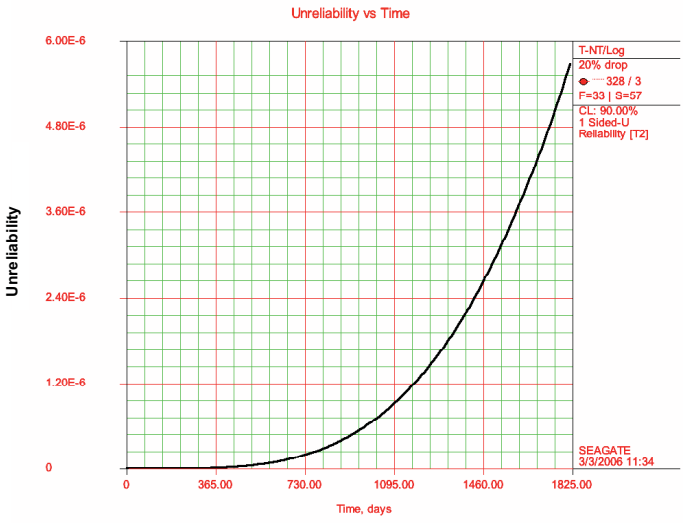

Figure 9. Device level unreliability as function time under usage condition. The unreliability under usage condition is less than 5.8E-6 after five-year usage at 90% confidence level.

Besides the ALT, Seagate also conducted drive-level long-term reliability tests for microactuators under accelerated drive operation at elevated temperatures. No degradation in stoke is observed after nine months of operation (Figure 10). Recent production drive-level micro-actuator stroke was continuously monitored for nine months with identical results.

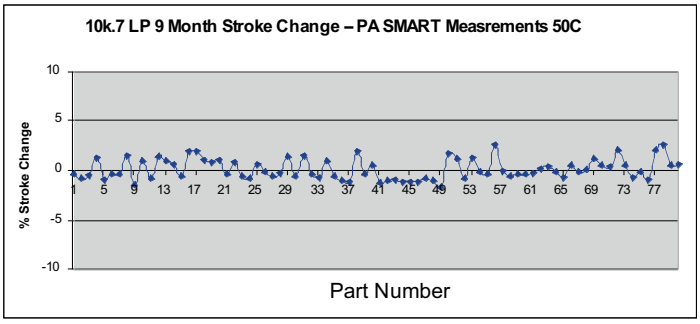

Figure 10. Stroke change over 9 month reliability test

References

[1] US Patents 6157522, 6522624

[2] Z. He, H. Loh, and E. Ong, A Probalistic Approach to Evaluate the Reliability of Piezoelectric Micro-Actuators, IEEE Trans. On Rel., Vol. 54, No. 1, March 2005, pp. 83-91

[3] H. Kuwajima, H. Uchiyama, Y. Ogawa, H. Kita, and K. Matsuoka, Manufacturing Process of Piezoelectric Thin-Film Dual-Stage Actuator and Its Reliability for HDD, IEEE Trans on Magnetics, Vol. 38, No. 5, September 2002

[4] Yang Jing, Jianbin Luo, Wenyan Yang, and Guoxian Ju, Fabrication of Piezoelectric Ceramic Micro-Actuator and Its Reliability for Hard Disk Drives, IEE Trans. on Ultrasonics, Ferroelectrics, and Frequency Control, Vol. 51, No. 11, November 2004

AUTOMATED OPTICAL FIBER ALIGNMENT IN 2-AXES USING 3D SHAPED ACTUATORS

Brian Morgan and Reza Ghodssi

MEMS Sensors and Actuators Lab (MSAL)
Department of Electrical and Computer Engineering, Institute for Systems Research
University of Maryland, College Park, MD USA
Email: ghodssi@eng.umd.edu

ABSTRACT

We report the development and characterization of an automated on-chip 2-axis optical fiber alignment system using 3D shaped actuators. Gray-scale technology was used to integrate sloped silicon wedges with electrostatic comb-drive actuators to deflect an optical fiber cantilever in- and out- of the plane of the wafer. Automated fiber alignment to Indium-phosphide (InP) waveguides with an accuracy of 1.6μm or better is demonstrated for the first time. The influences of alignment target location, actuation parameters, and alignment algorithms on total alignment time are also presented.

INTRODUCTION

Alignment of an optical fiber within an optoelectronic package is an on-going challenge and often dominates optoelectronic module cost. Passive fiber alignment techniques would be preferred for their simplicity where passive systems utilizing silicon waferboards have reported alignment accuracies of 1-2μm **[1]**. Yet, as alignment requirements approach 0.2μm for many applications **[2]**, active alignment is necessary to achieve sufficient coupling. Thus, to alleviate the expensive, slow macro actuators currently required to achieve sub-micron alignment, multi-axis on-chip methods for final alignment of the optical fiber are attractive.

Previous MEMS fiber actuators have required complicated fabrication (LIGA **[3]**) and/or specialized fiber preparation (e.g. permanent magnets **[4]**). In contrast, the actuator discussed here requires neither, instead exploiting the coupled motion of opposing in-plane actuators with integrated 3D wedges. This device creates a dynamic v-groove controlled via simple MEMS in-plane actuators to modify the horizontal and vertical position of the optical fiber, as shown in Figure 1 **[5]**.

This paper characterizes the performance of fabricated optical fiber actuators and demonstrates their potential for automated in-package alignment. Results regarding the alignment range, resolution, and speed of current devices are reported. The influences of alignment target location, actuation parameters, and alignment algorithm on total alignment time are also evaluated.

DESIGN AND FABRICATION

The optical fiber aligner discussed here is composed of three primary components, as shown in the top view schematic of Figure 2: a static trench, two sets of opposing sloped alignment wedges, and an in-plane actuation mechanism. An optical fiber is placed in the static trench and secured using UV-curing epoxy. This static trench provides approximate passive alignment of the fiber cantilever so that its free end rests between the sloped alignment wedges. The actuation mechanism can be made using any number of in-plane MEMS actuation techniques, but in this case electrostatic comb-drives were chosen for simplicity.

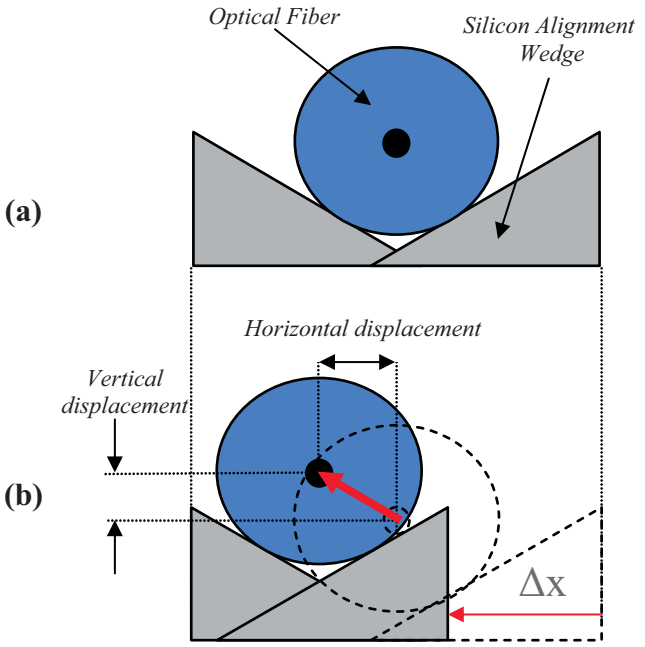

Figure 1: *Optical fiber (a) at rest and (b) after actuating single wedge, causing horizontal and vertical displacement* ***[5]****.*

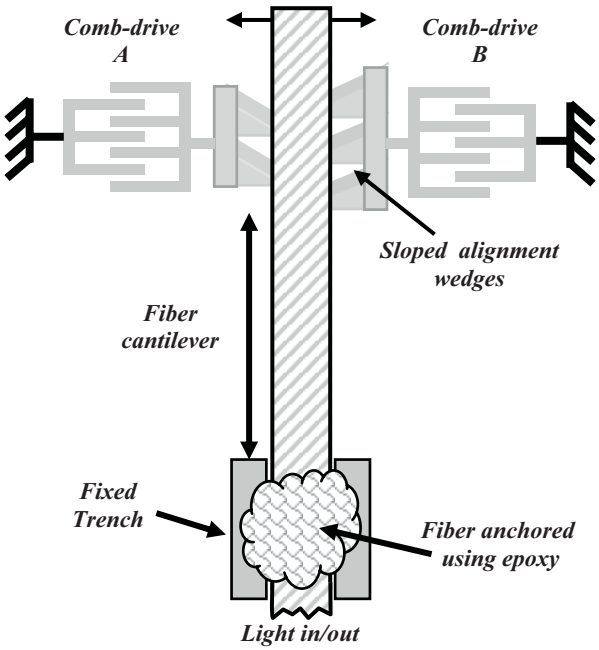

Figure 2: *Top view schematic of the 2-axis optical fiber actuator.*

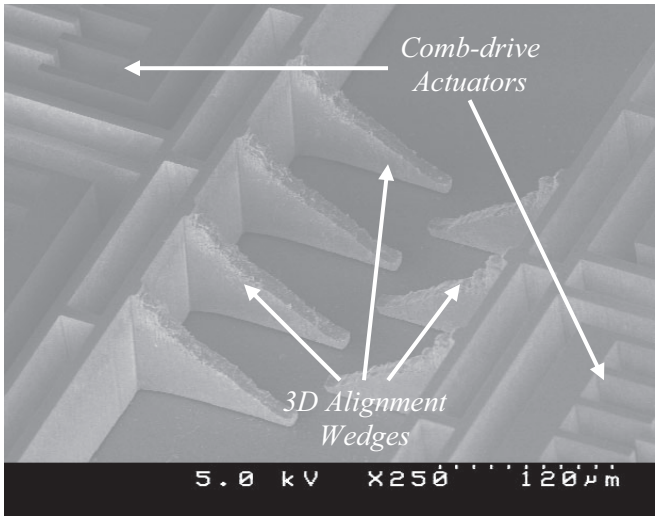

Figure 3: *3D alignment wedges before fiber attachment.*

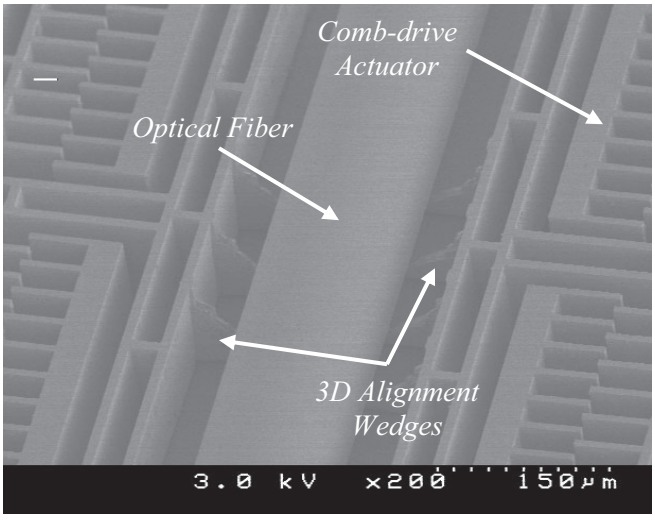

Figure 4: *SEM of the device after fiber attachment.*

The 3D silicon wedges were fabricated using gray-scale technology, where a single variable intensity exposure creates a 3D photoresist mask that is transferred into the underlying substrate using deep reactive ion etching (DRIE) **[6]**. The gray-scale process was integrated with an electrostatic actuator process using SOI wafers, thus creating the suspended 3D wedges that are shown in Figure 3 **[5]**. Of particular importance is the design and fabrication of the wedges themselves, which must be smooth compared to the size of the optical fiber (diameter=125µm). A set of 50 gray-levels was created in photoresist to define the slope. Specifically developed DRIE recipes were then used to control the etch selectivity of silicon to photoresist to define the final vertical dimensions of the 3D structure in silicon. SEM's such as Figure 3 show that micron-level roughness has been achieved over the majority of the slope. Quantitative roughness measurements are difficult on such sloped, high aspect ratio structures.

For final assembly, a single mode optical fiber (SMF-28) was manually stripped and cleaved. The cleaved free end of the fiber was placed between the two wedges that are attached to the comb-drives. The bulk fiber was then secured in the static trench with UV-curing epoxy (Norland Products, Inc.) to create a flexible cantilever. A device after fiber attachment is shown in Figure 4. Since this fiber attachment process is entirely manual, it is difficult to ensure that the fiber touches both wedges in its resting state. Reliable operation can be achieved with small gaps between the wedge and fiber, but result in a voltage offset before the fiber actually moves which can slightly complicate fiber control.

STATIC TESTING

The extents of fiber movement were investigated by applying four voltage combinations to the two actuators. The fiber tip location was measured using the peak coupling to an opposing electrostrictively controlled fiber. These four points are shown in Figure 5, representing the extreme movements of each alignment wedge. Fiber positions within the diamond-shaped bounds of these measurements (37µm tall, 48µm wide) should be achievable given the appropriate set of applied voltages. If one wedge is kept stationary and the other moved, the fiber tip will trace out an angled trajectory parallel to one side of the diamond-shaped alignment area shown in Figure 5.

Since this actuator relies on multiple surfaces sliding together, an important characteristic to investigate is hysteresis of the fiber motion, primarily caused by the morphology of the gray-scale wedges. Thus, a sequence of increasing then decreasing identical voltages was applied to each side of the actuator to create purely vertical fiber deflection. The coupled power to a fixed output fiber (which should be Gaussian in nature for cleaved fiber-fiber coupling) was then measured as the MEMS-actuated fiber moved 'Up' and 'Down' over multiple cycles. As shown in Figure 6, there is a definite hysteresis between the 'Up' and 'Down' actuation paths, amounting to a 'lag' of approximately 4µm between the peaks. We believe that frictional forces between the wedges and optical fiber, increases the force required from each actuator to move the fiber "Up." On the way back "Down," the

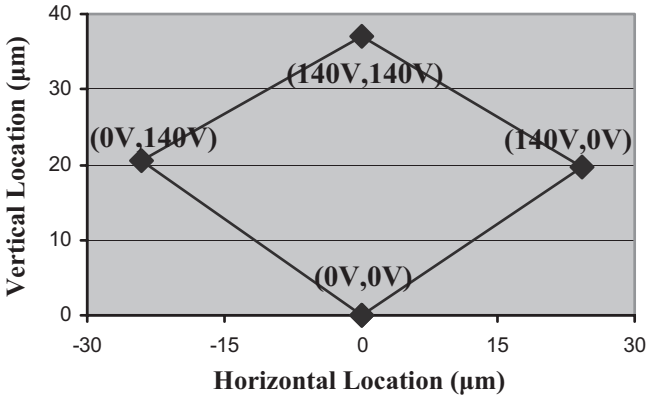

Figure 5: *Measured fiber location for extreme actuation voltages, which form a diamond-shaped alignment area.*

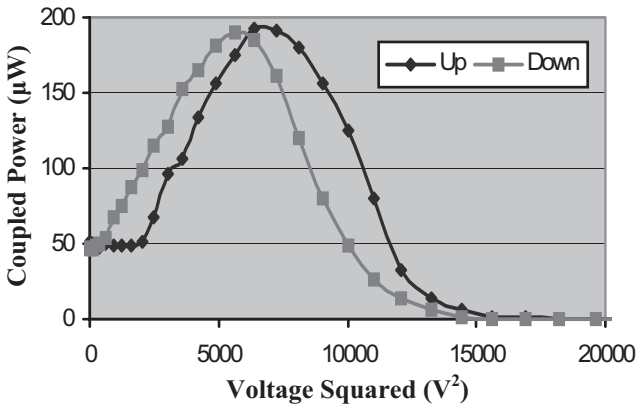

Figure 6: *Actuating both sides identically creates a vertical up/down motion that exhibits noticeable hysteresis (~4µm).*

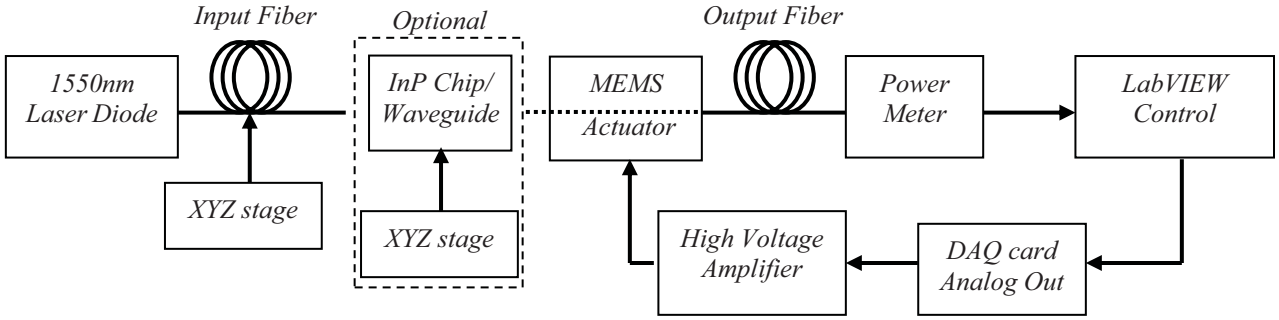

Figure 7: *Optical test setup for auto-alignment of MEMS-actuated fiber to cleaved fibers or InP waveguides.*

frictional force acts in the opposite direction and delays the fiber's return "Down" to its new state. This hysteresis effect should be reduced by improving the wedge design and/or fabrication. However, fiber alignment using closed-loop control has proven robust with the current structures. Single devices have been actuated $>10^5$ times in numerous testing configurations without any observed change in performance.

AUTOMATED ALIGNMENT

The optical setup used for automated alignment characterization is shown in Figure 7. A 1550nm laser diode is coupled to a fiber located on an electrostrictively-controlled XYZ stage. The MEMS aligner sits on the output stage, with its fiber coupled to an optical power meter to measure the coupled power. Depending on the configuration, an InP waveguide **[7]** is placed between the two fibers and misaligned by approximately ~20μm with the MEMS aligner. The setup is controlled via LabVIEW.

Alignment algorithms typically contain an initial coarse alignment step to achieve an intermediate threshold power (to avoid noise/secondary peaks), followed by a fine alignment step to optimize the alignment. The simplest coarse alignment routine is that of a raster scan, where the voltage on the 1st actuator is held fixed, while the voltage on the 2nd actuator is swept. The voltage on the 1st actuator is then incremented, and the process repeated. Using a raster scan, Figure 8 shows the time required to achieve coarse alignment as a function of input fiber position. The sloped wedges cause the contour lines to be tilted with respect to the X-Y axes. Note that times >36sec indicate failure to achieve threshold, illustrating the diamond-shaped alignment area of the device.

A hill-climbing algorithm **[8]** was then modified to serve as the fine alignment step. Inserting an InP ribbed waveguide to our setup, Figure 9 shows the total alignment time for different coarse threshold powers and settling times (the pause between discrete fiber movements and power measurements). The final alignment threshold used for this test (92% peak) corresponds to ~3.5μm misalignment (calibrated using the electrostrictive XYZ stages). We observed that the total alignment time was reduced from 34.2 to 8.5 seconds by decreasing both the settling time (from 1000ms to 300ms) and coarse threshold level (from 75% to 50% peak). Further decreasing the settling time did not allow sufficient time for the power meter to read accurately, while smaller threshold powers would leave the system susceptible to false peaks. However, in all cases of Figure 9, the coarse algorithm dominates total alignment time and the alignment accuracy (3.5μm) was much larger than desired.

A spiral search algorithm was developed for our actuator to replace the raster scan to decrease coarse alignment time. A 2μm square InP waveguide (tighter optical confinement than ribbed) was also used to decrease the alignment threshold to 1.6μm (in conjunction with increasing the ultimate threshold power to 95% of the peak). Rather than begin at the rest location of the MEMS aligner like the raster scan, the spiral algorithm begins in the center of the achievable motion, presumably the most likely location for the alignment target (in this case the square InP waveguide). The fiber then proceeds to spiral outward to progressively less-likely positions until the coarse alignment threshold is reached. Figure 10 shows the measured coarse alignment time for different input fiber positions, confirming that the coarse threshold is reached most quickly for targets located near the center. Note that the total

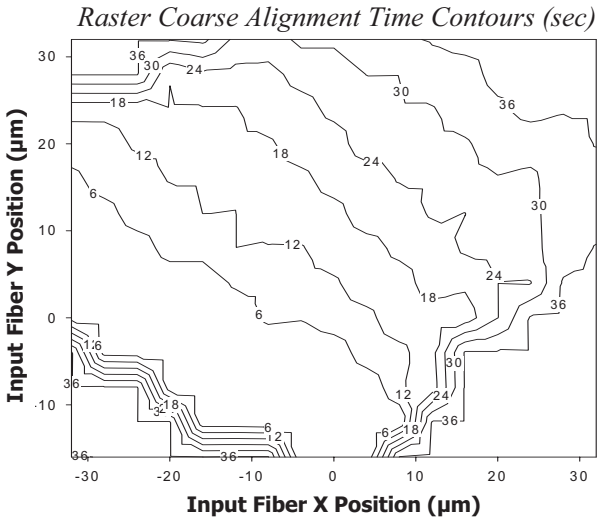

Figure 8: *Coarse alignment time contours using a raster algorithm for different locations of the input fiber.*

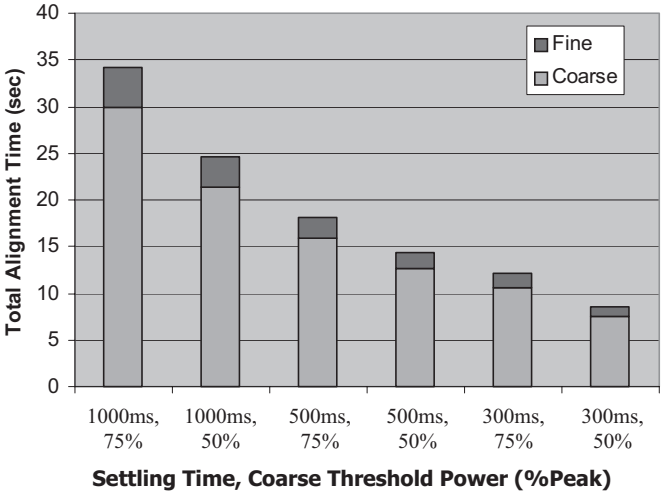

Figure 9: *Alignment times to an InP waveguide for different settling times and coarse threshold power (% peak).*

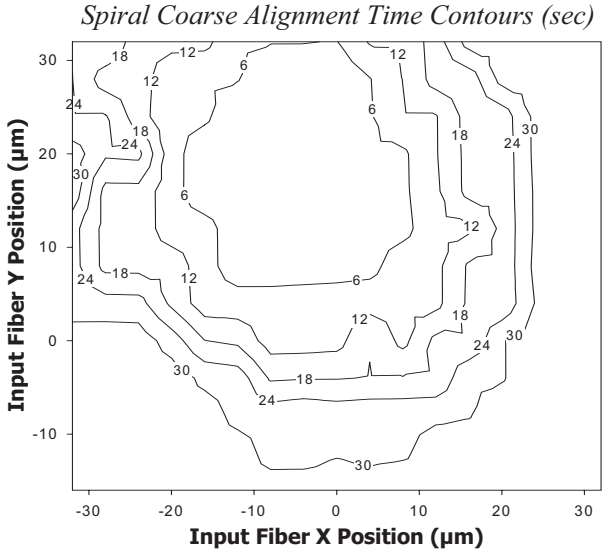

Figure 10: *Coarse alignment time contours using a spiral algorithm as a function of input fiber location.*

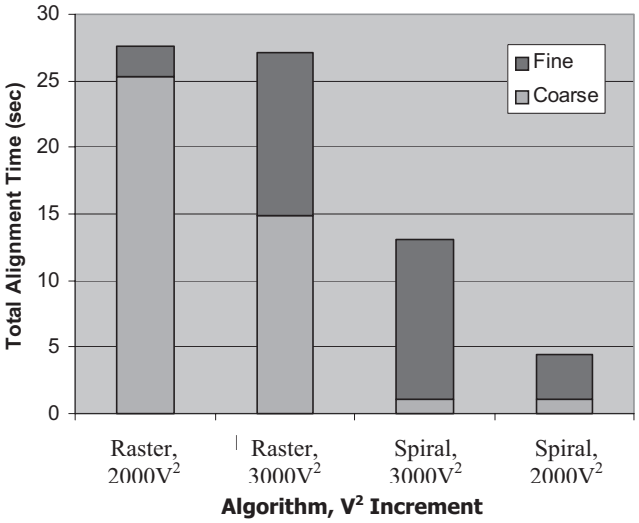

Figure 11: *Time to align within <1.6µm (95% peak power) to an InP waveguide, as a function of coarse search algorithm and Voltage² increment setting.*

time required to scan the entire alignment area is approximately the same (>30sec) for both raster and spiral algorithms, with the primary difference between them being the location where they start their search.

Figure 11 compares the total alignment time required to align within 1.6µm of the square InP waveguide using raster or spiral algorithms and different incremental actuator step sizes (Voltage^2 applied to comb-drive). As expected, using the spiral algorithm dramatically decreased the coarse alignment time for an InP waveguide located towards the center of the range. In addition, we observed that the longer fine alignment time for large V^2 increments was caused by often overshooting the optimal position due to the tighter alignment tolerance. Ultimately, an accuracy of <1.6µm (>95% of peak coupled power) was routinely achieved in 5-10 seconds to InP waveguides initially misaligned by ~20µm.

CONCLUSION

The alignment results reported here compare favorably to active alignment times reported using external actuators **[8]** while approaching the desired micron-level resolution. The device design, fabrication, and algorithms discussed provide numerous avenues for optimizing active alignment time and accuracy for optoelectronics packaging. Alternative search algorithms could also be adapted to work with this actuator design.

Future work will concentrate on miniaturizing the actuator to enable alignment of fiber arrays in a compact footprint and within optoelectronic packaging modules. Methods for further improving the alignment accuracy of these devices will also be pursued.

ACKNOWLEDGEMENTS

This research was funded in part by the U.S. Army Research Laboratory under the Collaborative Technology Alliance Power and Energy Program (Cooperative Agreement DAAD-19-01-2-0010), NASA-Goddard Space Flight Center (Grant APRA04-0000-0087), and an NSF-CAREER award (Ghodssi). The authors would like to thank the staff of both the Army Research Lab (ARL) and the Laboratory for Physical Sciences (LPS) for access to their cleanroom facilities, Northrop Grumman for optical mask fabrication, and Jonathan McGee of UMD for instrumentation assistance. Brian Morgan is the recipient of the Achievement Rewards for College Scientists (ARCS) Fellowship (Metropolitan Washington Chapter) for 2004-2005 and 2005-2006.

REFERENCES

[1] C. A. Armiento, A. J. Negri, M. J. Tabasky, R. A. Boudreau, M. A. Rothman, T. W. Fitzgerald, and P. O. Haugsjaa, "Gigabit transmitter array modules on silicon waferboard," *IEEE Transactions on Components, Hybrids, and Manufacturing Technology*, vol. 15, pp. 1072, 1992.

[2] W. J. Shakespeare, R. A. Pearson, J. L. Grenestedt, P. Hutapea, and V. Gupta, "MEMS integrated submount alignment for optoelectronics," *Journal of Lightwave Technology*, vol. 23, pp. 504, 2005.

[3] J. M. Haake, R. L. Wood, and V. R. Dhuler, "In-package active fiber optic micro-aligner," *Proceedings of the SPIE*, vol. 3276, pp. 207, 1998.

[4] T. Frank, "Development and manufacturing of a two-dimensional microactuator for moving of an optical fibre," *Proceedings of the SPIE - The International Society for Optical Engineering*, vol. 2882, pp. 226, 1996.

[5] B. Morgan, and R. Ghodssi, "On-chip 2-Axis Optical Fiber Actuator using Gray-scale Technology," *Proceedings of IEEE MEMS 2006, Istanbul, Turkey*, pp. 266-269, 2006.

[6] B. Morgan, C. M. Waits, J. Krizmanic, and R. Ghodssi, "Development of a deep silicon phase Fresnel lens using Gray-scale lithography and deep reactive ion etching," *J. of Microelectromechanical Systems*, vol. 13, pp. 113, 2004.

[7] D. P. Kelly, M. W. Pruessner, K. Amarnath, M. Datta, S. Kanakaraju, L. C. Calhoun, and R. Ghodssi, "Monolithic suspended optical waveguides for InP MEMS," *Photonics Technology Letters, IEEE*, vol. 16, pp. 1298, 2004.

[8] J. Guo and R. Heyler, "Fast active alignment in photonics device packaging," *2004 Proceedings. 54th Electronic Components and Technology Conf*, vol. Vol.1, pp. 813, 2004.

HALF-MILLIMETER-RANGE VERTICALLY SCANNING MICROLENSES FOR MICROSCOPIC FOCUSING APPLICATIONS

Ankur Jain and Huikai Xie
Department of Electrical & Computer Engineering, University of Florida
Gainesville, Florida 32611-6200, USA

ABSTRACT

This paper presents the design, fabrication and operation of a new class of microlens scanners that can generate large vertical piston motion at low actuation voltages. These scanners are needed by endoscopic bio-imaging applications such as optical coherence microscopy (OCM) which require microlenses to axially scan their focal planes by 0.5 to 2 mm. Photoresist reflow technique was used to form microlenses on lens holders that are integrated with large-vertical-displacement (LVD) microactuators. The lens holders are fabricated using a modified post-CMOS micromachining process which can provide additional thermal isolation to the polymer microlens and form a transparent oxide mesh within the hollow lens-holders to enable formation of larger polymer microlenses. These scanners have demonstrated a maximum vertical displacement of 0.71 mm at an actuation voltage of 23 V.

INTRODUCTION

Microlenses have been widely used for numerous optical-beam focusing applications, which vary from optical communication to biomedical applications. Microlens scanners have been developed for lateral laser-beam scanning in optical switching systems **[1]**, while vertically scanning microlenses have been used for biomedical imaging **[2]**, and optical data storage applications **[3]**. Stationary microlenses with tunable focal lengths have been demonstrated for miniature cameras **[4]**, microfluidic systems **[5]**, and other microscopic focusing applications **[6]**.

Another promising application for vertically-scanning microlenses is optical coherence microscopy (OCM), which is a biomedical imaging technology that combines the imaging capabilities of optical coherence tomography (OCT) and confocal microscopy to achieve high resolutions in both axial and transverse directions **[7]**. However, OCM achieves high transverse resolution at an expense of small imaging depth. In order to increase OCM's imaging depth, a lens scanner must be used to scan along the optical axis. OCM imaging requires vertical scanners that can provide an axial scanning depth of 0.5 to 2 mm. The vertical scanning range of microlens scanners demonstrated by other research groups is far less than 0.1 mm, and high driving voltages are often required **[2,3]**.

This paper presents microlens scanners that use large-vertical-displacement (LVD) microactuators to generate half-millimeter-range vertical scans at low actuation voltages; and these devices are also small enough to be packaged inside slender catheters for endoscopic OCM imaging. At Hilton Head 2004, the LVD microactuation mechanism was introduced for the first time **[8]**, and then a prototype LVD microlens scanner with a vertical scan range of 0.28 mm was presented at MEMS 2005 **[9]**. In this paper, we report new LVD microlens scanners with vertical displacements up to 0.71 mm at 23 V. These newly designed scanners provide better thermal isolation for the polymer microlens using two different approaches. Another innovation is the addition of a transparent oxide mesh within the hollow lens-holder to enable formation of larger polymer microlenses.

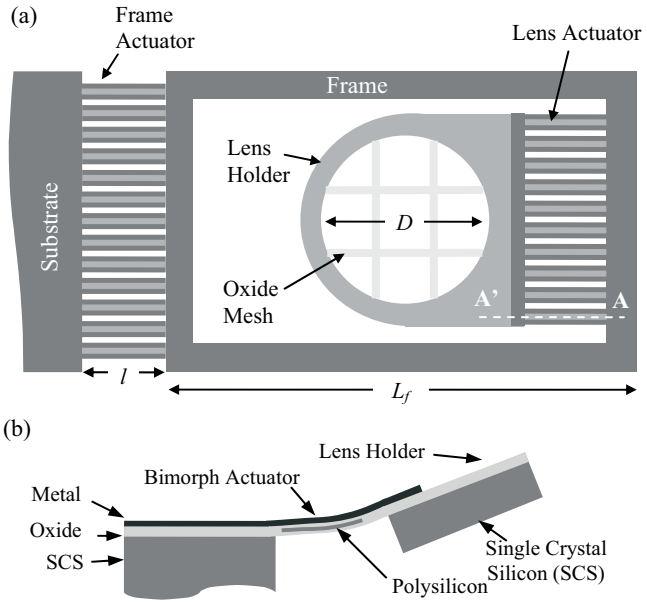

Figure 1. *(a) Top-view design schematic of the LVD scanner. Actuator length, l = 200 μm; Frame length, L_f = 1.6mm; Lens-opening diameter, D = 0.6mm. (b) Cross-sectional view of A-A'.*

SCANNER DESIGN & FABRICATION

The structure of this scanner consists of a polymer microlens integrated on a MEMS lens-holder, which is thermally-actuated using the LVD mechanism. The schematic drawing of the LVD scanner is illustrated in Fig. 1, where the lens-holder is attached to a rigid silicon frame by a set of aluminum/silicon-dioxide bimorph beams (lens actuator). A 0.6-mm diameter circular opening in the center of the lens-holder allows light to pass through, and it also contains a transparent silicon-dioxide mesh structure. This mesh structure is designed to hold the polymer microlens, and it also prevents smaller polymer droplets from falling through during the microlens formation process step. The structural rigidity of the lens-holder plate and the frame are maintained by a 30 to 40-μm-thick single-crystal-silicon (SCS) layer. The 1.6-mm long frame is attached to the substrate by another set of identical bimorph beams (frame actuator). These actuators together form an LVD microactuator set, in which the curls of the two sets of bimorph beams compensate each other resulting in zero initial tilt of the lens-holder. The polysilicon resistors embedded in the bimorph beams are used for electrothermal actuation. The LVD microactuator provides large piston motion by simultaneously applying voltage to both actuators, so that equal angular rotation by both actuators results in pure vertical displacement of the microlens. Further details about the LVD actuation principle have been previously reported in **[8-10]**.

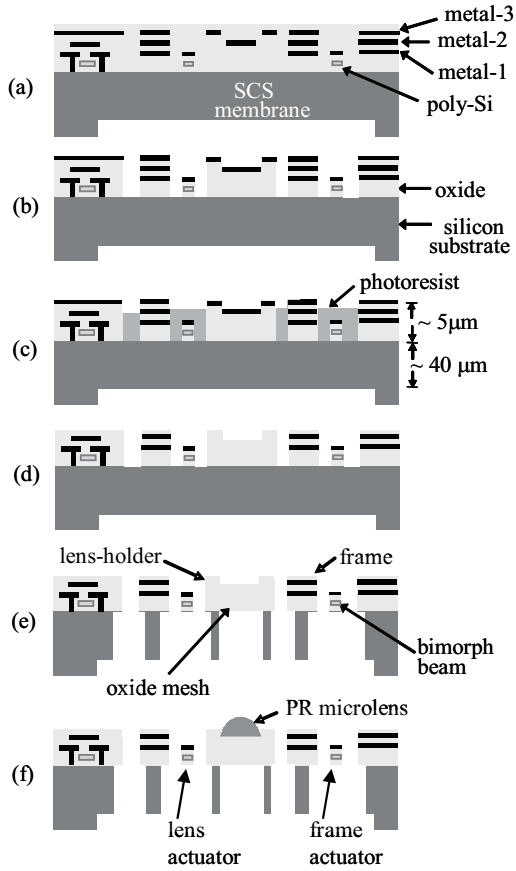

Figure 2. *Modified CMOS-MEMS fabrication process. (a) Backside Si etch. (b) Frontside oxide etch. (c) PR spun-on and etched to protect Metal-1. (d) Wet etch of exposed layers of Metal's 2 & 3. (e) Deep Si trench etch, followed by Si undercut. (f) Microlens formation.*

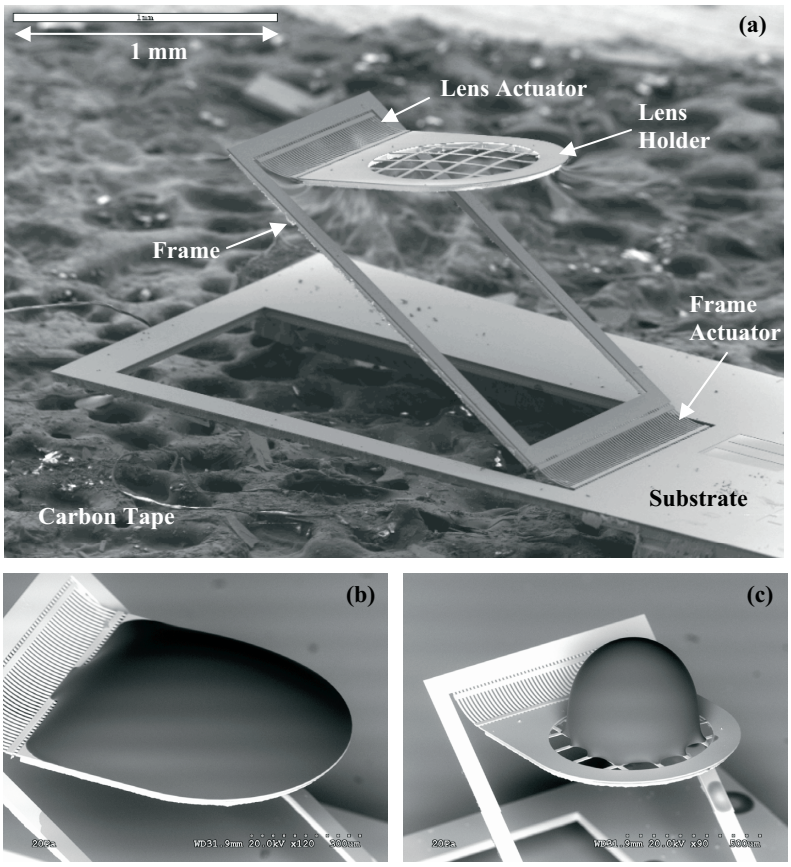

Figure 3. *SEM images of: (a) Fabricated device before microlens formation. (b) 3mm focal length convex PR microlens formed on entire lens holder plate. (c) 0.5mm focal length PR ball-lens formed on the mesh area only. These PR lenses were imaged using a variable-pressure environmental SEM.*

In order to form a transparent oxide mesh within the 600-μm diameter opening of the lens-holder, the post-CMOS-MEMS fabrication process used in **[9]** was modified to include two additional etch steps, as illustrated in Fig. 2. After the backside Si and frontside oxide etch steps [Figs. 2(a) and 2(b)], a planar photoresist (PR) layer is spun on and dry-etched to expose the metal-3 and metal-2 layers only[1] [Fig. 2(c)]. Next, the exposed metal layers are completely removed using a wet aluminum etchant, and the remaining PR layer is stripped off [Fig. 2(d)]. The device is then released using a deep Si trench etch, followed by an isotropic Si undercut to etch the SCS from beneath the bimorph beams to form the thin-film actuators [Fig. 2(e)]. Finally, PR droplets are precisely dispensed on the lens-holder to form the polymer microlens due to surface tension [Fig. 2(f)]. The process modifications allow the use of the metal-2 layer to define the structure for the 3-μm thick oxide mesh within the lens holder. Also, the PR microlens is now formed on a layer of insulating oxide instead of a more thermally-conductive Al metal layer, resulting in better thermal isolation from the electrically-heated lens-actuator. Thermally isolating PR microlenses from heating sources prevents the situations in **[11]**, where the focal length of a polymer microlens changed significantly with increasing heat. Thermal isolation also prevents carbonization of the PR microlens, which tends to occur at temperatures greater than 200°C **[12]**.

The initial rest position of a fabricated microlens [Fig. 3(a)] is 1.2 mm above the substrate surface. In order to form a polymer microlens on the elevated lens-holder, droplets of PR are first dispensed using a nanoliter-injection system and then baked in an oven to form a microlens due to surface tension **[12]**. Focal length can be controlled by varying the quantity and/or volume of the dispensed dropets. PR microlenses with focal lengths between 0.5 to 3 mm with numerical apertures (NA) ranging from 0.1 to 0.35 have been successfully fabricated. Figs. 3(b) and 3(c) show two fabricated PR microlenses with different focal lengths and lens sizes. To test the imaging quality of these microlenses, a chrome

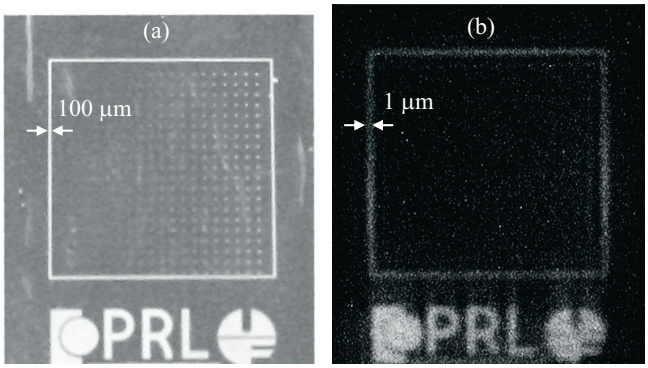

Figure 4. *Imaging using the PR microlens. (a) Photo of the test pattern on a chrome mask. (b) Corresponding image of the test pattern as seen at the focal plane of the PR microlens.*

[1] For die level fabrication, lithographic techniques can be used to expose the metal-2 and metal-3 layers on the lens-holder only.

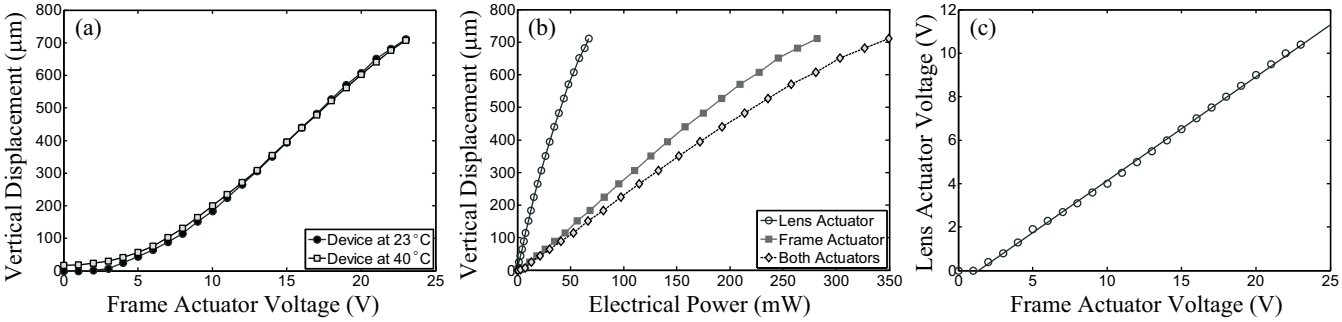

Figure 5. *Plots of the vertical displacement of the microlens as a function of: (a) frame actuator voltage, and (b) applied electrical power. (c) Corresponding plot of the actuation voltages applied to the two actuators to obtain the vertical displacement in (a) and (b).*

test mask was placed ~100 mm away from the ball-type microlens, and the image at its focal plane (which is de-magnified by about 100×) was captured using a CCD microscope camera. The test pattern image obtained by a PR microlens with a numerical aperture of 0.35 is shown in Fig. 4, where features as small as 1 μm can be resolved.

EXPERIMENTAL RESULTS

Vertical displacement of the PR microlens was achieved by simultaneously exciting both actuators and tuning the actuation voltages such that the opposite angular rotations of the two actuators offset any net tilting of the microlens. The static displacements of the microlens and its corresponding driving voltage plots are shown in Fig. 5, where the vertical displacements of the microlens were observed to within an accuracy of ±2 μm by using a 40× objective lens (0.65 NA). Fig. 5(a) shows that a maximum vertical displacement of 0.71 mm was obtained at a dc voltage of 23 V applied to the frame actuator. Fig. 5(b) displays the same vertical displacement data, but with respect to the electrical power supplied to the two actuators. The plot of the two driving voltages that are required to obtain this vertical displacement is shown in Fig. 5(c). The slope of this linear plot yields the driving voltage ratio for the two actuators for LVD actuation. The driving voltage applied to the lens actuator is 43% of the frame actuator voltage, which is provided by a voltage divider. Using this constant voltage ratio, the maximum tilt of the microlens in the entire 0.71mm travel range is less than 0.4°.

There is significant lateral shifting of the microlens during vertical actuation, as shown in Fig. 6(a). A maximum lateral shift of 425 μm is observed for the entire vertical scan range. This lateral shift is mainly due to the rotational displacement of the frame actuator, and is amplified by the long length of the silicon frame. This lateral shift will be accounted for and corrected during the OCM image formation stage.

The initial elevations of the microlens at different operating temperatures were also documented, and the results are presented in Fig. 6(b). The initial lens-holder elevation of a fabricated microlens is 1.2 mm at a room temperature (23°C), and it decreases with increasing temperature. Since this device will be packaged inside an endoscope for *in vivo* OCM imaging, the maximum ambient temperature shall not exceed 40°C. Therefore, the vertical scan range of the device will, in the worst case, be reduced by up to 20 μm, which is less than 3% of the entire scan range. This can be seen in the plots of Fig. 5(a) where an increase in ambient temperature to 40°C reduced the vertical scan range by ~17 μm.

The resistances of the polysilicon heaters embedded in both actuators increase significantly with applied voltage due to Joule heating. Joule heating raises the temperature of the bimorphs, which in turn increases the heater resistances due to the thermal coefficient of resistivity of polysilicon. The open-circuit, room-temperature electrical resistances of the lens and frame actuators are 1.17 kΩ and 1.35 kΩ, respectively. A linear correlation between the vertical displacement of the microlens and the heater resistance of the two actuators was observed, as shown in Fig. 6(c). This experimentally determined linear relationship between the resistors allows for closed-loop feedback control of the vertical position of the microlens by monitoring the polysilicon resistance change of each actuator.

MICROLENS SCANNER DESIGN 2

Another LVD microlens scanner (design illustrated in Fig. 7(a)) that uses thin-film isolation beams to thermally isolate the PR microlens was fabricated using the unmodified CMOS-MEMS process used in **[9]**. This design also provides thermal conduction metal lines that preferentially conduct heat away from the two frames and towards the substrate. The SEM of a fabricated device with the lens-holder elevated 0.5 mm above the substrate

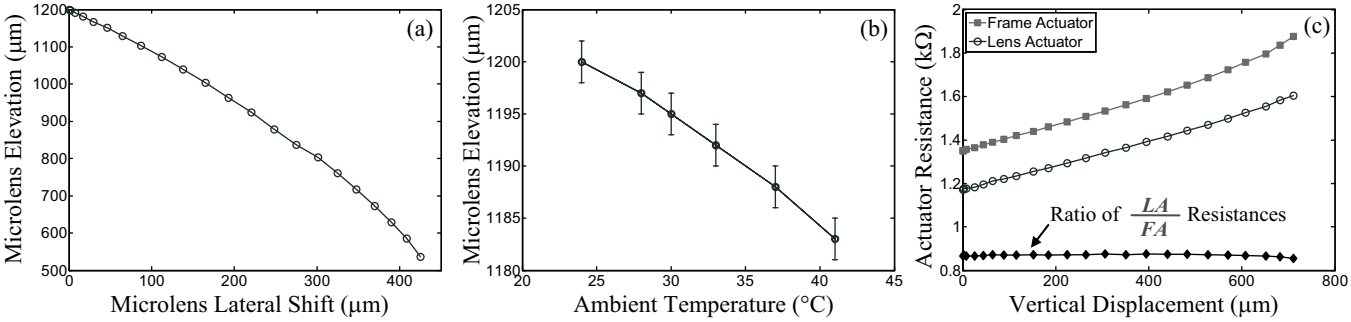

Figure 6. *(a) Plot of the observed lateral shift of the microlens during LVD actuation. (b) Initial elevation of the microlens as a function of the ambient temperature. (c) Plot showing the linear increase in polysilicon heater resistance of the two actuators during LVD actuation of the microlens.*

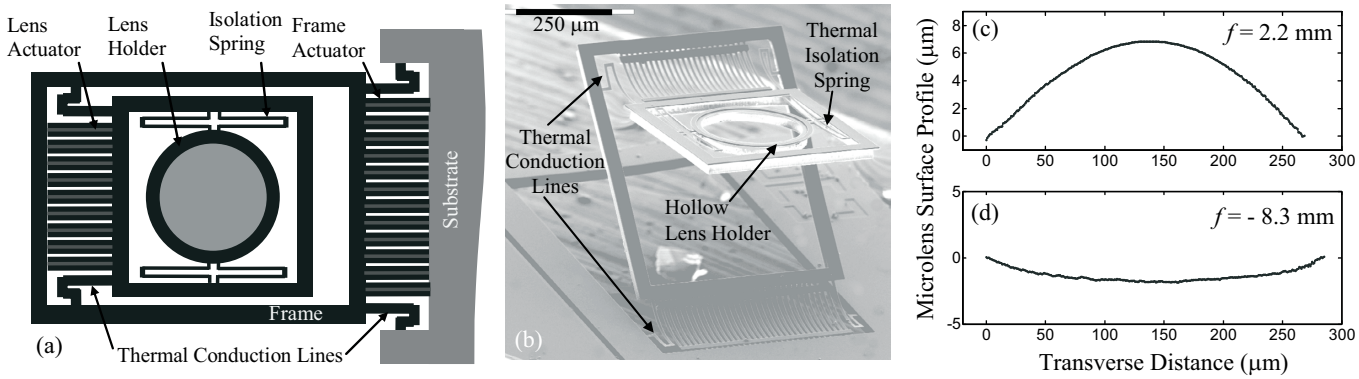

Figure 7. *Microlens Scanner Design 2. (a) Schematic showing the thermal isolation spring and thermal conduction lines. (b) SEM of a fabricated scanner showing that the initial elevation of the lens holder is 0.5 mm above the substrate plane. Surface profiles of the (c) convex and (d) concave PR microlenses formed within the lens holder of Design 2.*

plane is shown in Fig. 7(b). Microlenses were formed by dispensing a PR droplet into the hollow 280-μm diameter lens-holder. Depending on the volume of the PR droplet dispensed, it is possible to obtain convex or concave microlenses. The profiles of convex and concave microlenses, as obtained using a white-light optical profilometer, are shown in Figs. 7(c) and 7(d). The maximum microlens displacement is 0.32 mm at a frame actuator voltage of 21 V, as shown in Fig. 8. The same voltage divider was used to drive this device.

The increase in thermal isolation to the PR microlens due to the isolation springs, and the thermal effectiveness of adding thermal conduction lines are still under investigation.

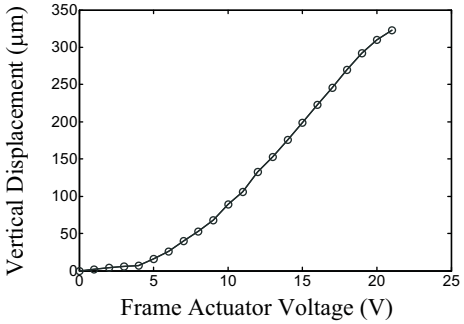

Figure 8. *Vertical displacement of the microlens of Design 2.*

CONCLUSIONS

Half-millimeter-range vertically scanning microlenses have been successfully demonstrated. The CMOS-MEMS fabrication process was modified in order to allow the formation of a transparent silicon-dioxide mesh within the hollow microlens holder. This mesh allowed the formation of larger PR microlenses, and it also provided additional thermal isolation to the polymer lenses from the electrically-heated LVD actuators. A fabricated microlens scanner demonstrated a maximum vertical displacement of 0.71 mm at an actuation voltage of 23 V. The large actuation range and small device footprint make this LVD microlens scanner very suitable for use in endoscopic OCM and other microscopic focusing applications.

ACKNOWLEDGEMENTS

The authors would like to thank T. Riedhammer for the VP-SEM images. This project is supported by the National Science Foundation Biophotonics Program under award BES-0423557.

REFERENCES

[1]. H. Toshiyoshi, G. –D. J. Su, J. LaCosse, and M. C. Wu, "A surface micromachined optical scanner array using photoresist lenses fabricated by a thermal reflow process," *Journal of Lightwave Technology* ***21***, pp. 1700-1708 (2003).

[2]. S. Kwon, V. Milanovic, and L. P. Lee, "Vertical microlens scanner for 3D imaging," *2002 Solid State Sensor and Actuator Workshop*, Hilton Head, SC, June 2002, pp. 227-230.

[3]. S.–H. Kim, Y. Yee, J. Choi, H. Kwon, M.–H. Ha, C. Oh, and J. U. Bu, "Integrated micro optical flying head with lens positioning actuator for small form factor data storage," *Transducers 2003*, Boston, MA, June 2003, pp. 607-610.

[4]. S. Kuiper and B. H. W. Hendriks, "Variable-focus liquid lens for miniature cameras," *Applied Physics Letters* ***85***, pp. 1128-1130 (2004).

[5]. N. Chronis, G. L. Liu, K. –H. Jeong, and L. P. Lee, "Tunable liquid-filled microlens array integrated with microfluidic network," *Optics Express* ***11***, pp. 2370-2378, (2003).

[6]. W. Wang, J. Fang, and K. Varahramyan, "Compact variable-focusing microlens with integrated thermal actuator and sensor," *IEEE Photonics Technology Letters* ***17***, pp. 2643-2645 (2005).

[7]. A. D. Aguirre, P. Hsiung, T. H. Ko, I. Hartl, and J. G. Fujimoto, "High-resolution optical coherence microscopy for high-speed, in vivo cellular imaging," *Optics Letters* ***28***, pp. 2064-2066, (2003).

[8]. A. Jain, H. Qu, S. Todd, G. K. Fedder, and H. Xie, "Electrothermal SCS micromirror with large-vertical-displacement actuation," *2004 Solid State Sensor, Actuator and Microsystems Workshop*, Hilton Head, SC, June 2004, pp. 228-231.

[9]. A. Jain and H. Xie, "A tunable microlens scanner with large-vertical-displacement actuation," *IEEE MEMS 2005*, Miami Beach, FL, January 2005, pp. 92-95.

[10]. A. Jain, S. Todd, and H. Xie, "An electrothermally-actuated, dual-mode micromirror for large bi-directional scanning," *IEDM 2004*, San Francisco, CA, December 2004, pp. 47-50.

[11]. A. L. Glebov, L. Huang, S. Aoki, M. Lee, and K. Yokouchi, "Planar hybrid polymer-silica microlenses with tunable beamwidth and focal length," *IEEE Photonics Technology Letters* ***16***, pp. 1107-1109 (2004).

[12]. D. Daly, *Microlens Arrays*, Taylor & Francis: London, 2001.

BILLION-CYCLE ULV ELECTROSTATIC RF MEMS SWITCH

Tsung-Kuan A. Chou, Hanan Bar, John Heck, Qing Ma, Joseph B. Melki, Quan Tran, Shlomy Tubul, Boaz Weinfeld, Nataly Ziharev
Intel Corporation
SC9-09, 2200 Mission College Blvd., Santa Clara, CA 95052, USA.

ABSTRACT

An ultra-low-voltage (ULV) electrostatic RF MEMS switch has been demonstrated with actuation voltage as low as ~1.5V, the lowest reported. The switch is designed to collapse on to actuation electrode with zipping action. The device consists of multiple spring constants, which maximizes the open force while reducing the pull-in voltage to <3V. Physical stopper design eliminates the usage of dielectric between electrodes so that actuation charging problem is minimized. The device is fabricated using a low-stress-gradient polysilicon as beam structure to realize ULV actuation. The ULV switch has achieved cold-switching lifetime of $\sim 1\times10^9$ cycles with close speed of ~50μs at 3.2V and open speed of ~25μs.

INTRODUCTION

The RF MEMS switch provides disruptive technology to wireless communications due to its high linearity and low insertion loss. Resistive contact switch is most suitable for frequency in the range of 0 to 6GHz. Different actuation approaches have been used in contact switches, such as electrostatic, electromagnetic, and thermal actuations [1]-[4]. Electrostatic RF MEMS switch is the best candidate for its low powder consumption, and integration compatibility with LC filters and CMOS circuitries. Fig.1 illustrates one of the conventional RF MEMS contact switches. It consists of a thick metal cantilever beam with a bottom actuation electrode. A contact tip is located at front end of the cantilever, corresponding to a RF trace underneath. The pull-in voltage of the switch can be expressed in Eq. 1, where k_1 is the cantilever spring constant, g is the gap between electrodes, and A is the actuation area. When a DC voltage of >Vp is applied on the actuation electrode, the top beam is pulled down electro-statically. The cantilever tip makes contact on bottom RF trace so that electric signal can pass through. When actuation voltage is removed, the cantilever's restoring force opens the switch contact.

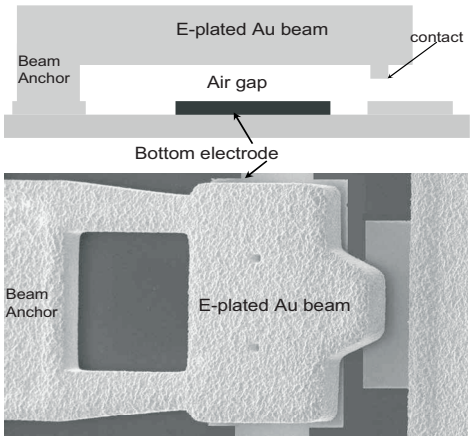

Figure 1. *Schematic of conventional electrostatic contact switch with electroplated gold cantilever beam and SEM of a fabricated 40V RF MEMS switch.*

$$Vp = \sqrt{\frac{8k_1 g^3}{27\varepsilon_o A}} \quad (1)$$

A 40V RF MEMS switch was fabricated as shown in Fig 1. It has achieved insertion loss of <0.3dB, isolation of ~32dB at 2GHz, and lifetime of $>300\times10^6$ cycles. Similar switch with lifetime of $>1\times10^9$ cycles is also reported by other researchers with actuation voltage of >80V [5]. However, such switches require an expensive high-voltage (HV) driver, which can cost significantly more than the switch itself. As a result, there is a strong demand on the development of ULV MEMS switch which can be actuated at 3.3V. Electro-statically actuated MEMS switch with actuation voltage of 6V has been reported [6]. However, the switch has very limited lifetime obtained. Meanwhile, switch with lifetime of >100M cycles and actuation voltage of <5V have not been demonstrated to-date. This research work attempts to develop an electrostatic contact switch with actuation voltage of <3.3V and lifetime of $\sim 1\times10^9$ cycles.

DESIGN OF ULV MEMS SWITCH

In order to achieve ultra low pull-in voltage, one needs to either reduce spring constant k_1, reduce the gap g between electrodes, or increase the actuation area A. Most favorable approach is to reduce the air gap and increase the actuation area. Some reduction on the spring constant is also necessary in order to reach 3V actuation. However, the beam's curving amount from stress gradient increases drastically when the cantilever or electrode area increases. The final air gap between electrodes is dominated by the stress gradient curving, which prevents Vp reduction. Peroulis *et. al*. have achieved 6V actuation voltage by making the structure highly compliant. The cantilever spring constant k_1 has been reduced down to ~0.5N/m with serpentine clamp-beam structure. However, since the cantilever's restoring force is also used to open the switch, such ultra compliant device can easily suffer from contact stiction failure with open force of only about 1μN.

Figure 2 illustrates the top view (Fig.2a) and cross-section (Fig.2b) view of zipper polysilicon switch structure with back contact design. The top beam is composed by a low stress gradient (LSG) polysilicon. This polysilicon cantilever serves as the main switch actuation structure, and carries the metal conductor to open and close the switch contact for RF signal transmission. LSG poly silicon is used for its material robustness. Meanwhile, the consistent stress control of the polysilicon film also makes small air gap feasible for ultra low voltage actuation. The polysilicon beam consists of two parts, short polysilicon arms with stiff spring constant k_2 and a large electrode plate attached to the stiff arms. A bottom

2a) Top view schematic of ULV poly switch

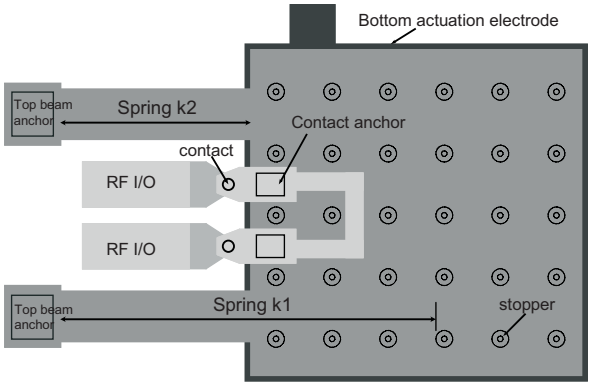

2b) Cross-section view of zipper poly switch

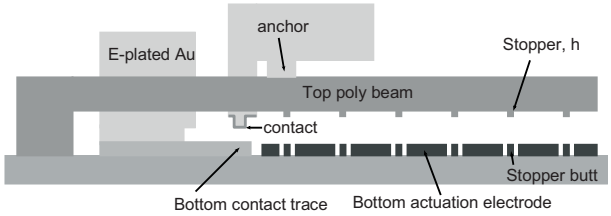

2c) Pull-in of top beam with ultra low Vp

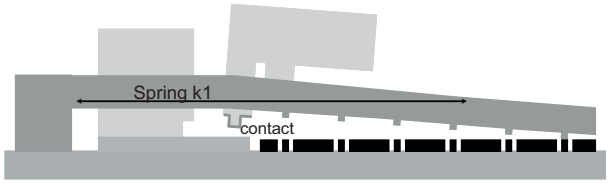

2d) Collapsing of top beam with zipping action and contact made

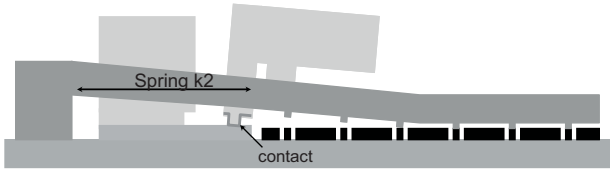

Figure 2. *Design and operation of ULV collapsing zipper switch.*

electrode is located directly underneath the top electrode. This actuation electrode will experience a much longer cantilever beam and much more compliant spring constant k_1. The bottom side of LSG beam contains many stopper bumps. Meanwhile, there are electrically isolated butts distributed within actuation electrode in corresponding to the stopper bumps above. These stopper pairs are functioning as insulator layer between two electrodes, which allow the top beam collapsing onto bottom electrode without suffering from any electrical short. Since no actual dielectric layer is used, it significantly reduces actuation charging problem as commonly observed in uni-polar electrostatic actuation [7].

The switch RF contact metal is located on the LSG polysilicon close to cantilever anchor in corresponding to the short arms with spring constant k_2. The thick metal provides low trace resistance for RF signal transmission and the robust poly beam structure provides ultra low voltage switch actuation. Such design configuration has separated the very compliant spring k_1 for ultra low Vp and stiff k_2 for large open force. The ULV switch open force at contact is expressed in Eq. 2, where Δz is the contact tip displacement.

$$F_{open} = k_2 \Delta z \tag{2}$$

When DC voltage is applied to the actuation electrode, top beam collapses toward the actuation electrode with spring k_1 as shown in Fig.2c. Pull-in voltage is determined by k_1, air gap and the electrode dimension as depicted in Eq. 1. The spring k_1 is in the range of 10N/m based on the cantilever and electrode dimension design. Vp is expected to be <3V for air gap of <1μm. When the top electrode collapses, electrostatic force increases drastically due to very small gap between electrodes. The electrostatic force depends on the stopper height design (40nm to 100nm). Top beam continues collapsing with zipping action towards the beam anchor until contact is made as shown in Fig.2d. Meanwhile, the cantilever restoring force increases with the zipping action until the stiff spring k_2 (100N/m to 250N/m) is reached. Larger open force with spring k_2 can reduce contact stiction failure when actuation is removed. Spring force of >10μN is required to overcome the contact stiction based on nano-indenter and actual switch contact tests with contact force of 50μN to 100μN. Contact and open forces are optimized in the range of 30μN to 50μN for 3.3V in the design. The zipping action design in this structure reduces the large impact force directly on contact. Less contact bouncing, deformation, and stiction is expected. Meanwhile, the switch opens with zipping action, which reduces the stiction on electrodes as well. Note that this initial ULV switch development is focusing on the switch's functionality and electro-mechanical responses. RF performance was not optimized in this work.

FABRICATION OF ULV LOW STRESS GRADIENT POLYSILICON SWITCH

A low stress gradient LPCVD polysilicon film has been developed. The surface profile of polysilicon cantilevers at open state is shown in Fig 3. The stress-uncompensated polysilicon film shows a large internal stress gradient with >9μm tip displacement on 350μm long beam as seen in Fig 3a. Despite the large stress gradient, these polysilicon beams have consistent stress bending across wafer. After deposition process tuning and stress compensation, low stress gradient polysilicon was obtained as shown in Fig. 3b. These LSG poly beams showed reproducible stress gradient bending of ~50nm over 350μm beam with deviation of ~22nm, significantly less than the electroplated Au beam.

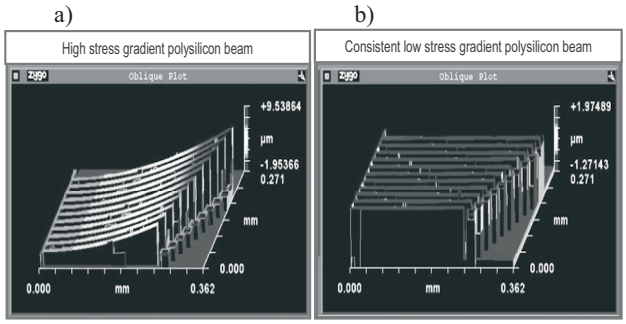

Figure 3. *a) Uniform high stress gradient polysilicon with Δz>9μm on 350μm poly beam. b) Consistent low stress gradient poly silicon with Δz~0.05μm on 350μm beam for ULV switch.*

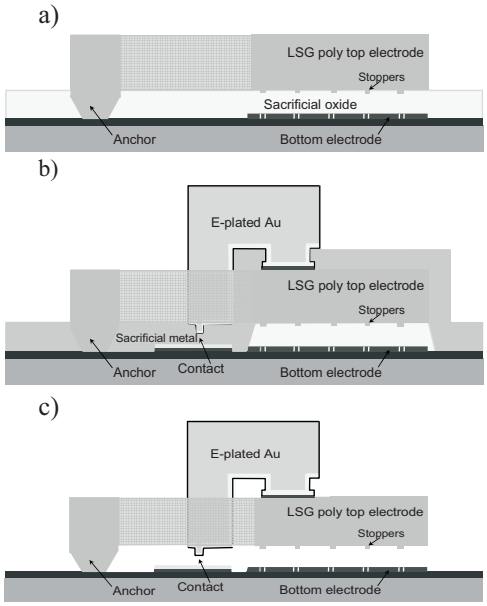

Figure 4. *Process illustration of ULV polysilicon switch*

The basic process of ULV polysilicion switch starts with isolation nitride on high-resistivity silicon substrate (>5k Ω-cm). A thin polysilicon bottom electrode (0.1μm~0.2μm) was deposited and patterned to form the actuation pad and resistor. LPCVD sacrificial oxide was deposited to define the air gap. Polysilicon stopper bump formation and anchor via etch were performed and followed by the deposition of LSG polysilicon (1.5μm ~2.5μm). Polysilicon beam and top electrode were then pattern as seen in Fig 4a. Bottom contact metal were then deposited and patterned. Sacrificial material was then deposited to define the gap between bottom metal and top contact. Anchor etch was then performed and the contact metal was deposited followed by thick gold layer electroplating to construct the switch RF I/Os as shown in Fig. 4b. The sacrificial layers were then etched away. And the device was finally released by supercritical CO_2 drying method to prevent "stiction" (Fig. 4c).

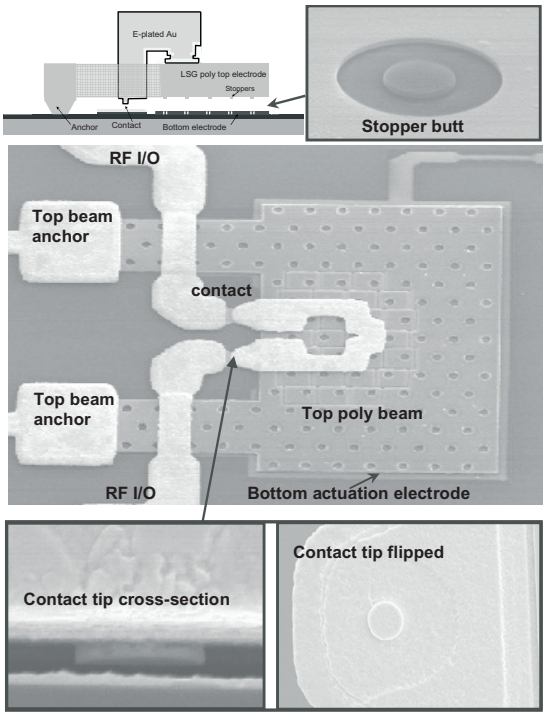

Figure 5. *SEM views of fabricated ULV polysilicon switch.*

Fig.5 shows the fabricated ULV switch with two contacts in series. SEMs of the stopper and contact are also illustrated. The RF I/O traces reach to the switch contact with air bridges over the cantilever arms as seen in the photo. This approach provides more flexibility in the routing. However, one should take into account the capacitive coupling issue while design such type of air bridge. RF optimization is needed but is beyond the scope of this paper focus.

DETAILED TEST RESULTS

The fabricated ULV polysilicon switches were first screened for Vp uniformity. Figure 6 shows the wafer-level uniformity of the pull-in voltage obtained from laser scanning vibrometer (LSV) measurement. LSV in-situ monitored the cantilever mechanical closing velocity and captured both the applied voltage at the moment when the top beam collapsed. The fabricated switches have an average Vp of ~2.5V, higher than expected of 1.5V to 2V. Functional switch with lowest Vp of ~1.5V has been demonstrated, the lowest voltage for electrostatic switch actuation to author's knowledge. The variation of Vp was due to the stress mismatch of the electroplated gold anchoring on the polysilicon beam. It resulted in slight upward bending of the polysilicon beam. Due to variation of the gold stress, the gap variation between ULV switches leads to Vp differences across the wafer.

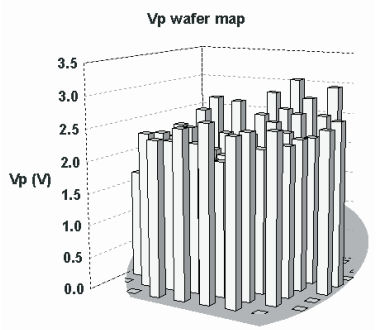

Figure 6. *Wafer-lever uniformity of pull-in voltage.*

The switching speed of the ULV switch was evaluated by applying a prompt -3.2V at actuation electrode. Hot switching measurement was used to obtained the close and open speed, t_{on} and t_{off}. Figure 7a illustrates the schematic of test setup for hot switching. Oscilloscope was used to capture the actuation voltage and the signal through switch contact simultaneously. A 500kHz AC signal was imposed on one of the switch RF trace I/Os while the oscilloscope monitored the signal on the other RF I/O with 50Ω load. When switch was closed by the applied voltage (~-3.2V), switch contact was made and formed a conduction loop. The AC signal then passed through the contacts and was detected by the OSC. It can be seen from Fig. 7b that the switch has close speed t_{on} of ~50μs. No contact bounce was observed in the measurements. When the actuation voltage was removed (0V), the switch broke the contact. AC signal was not able to pass onto the 50Ω load terminal after ~25μs, corresponding to the switch open speed t_{off}.

The ULV switch has achieved contact resistance of Rc<=1Ω/contact. Each switch contains two contacts in series and

2Ω trace resistance in design, resulting in total trace resistance of ~4Ω. Although the ULV switch design was not optimized for RF performance, it exhibited <0.4dB insertion loss up to 6GHz. The device isolation is ~-20dB at 2GHz. The current RF trace structure has known capacitive coupling between RF I/Os, which can be improved by design modification. A single-contact ULV polysilicon is also developed to future improve. It was observed that the contact cleanliness is crucial to ULV switch for its relatively low contact force (25μN~50μN). Clean contact surface is the key to reliable switch operation. Contact failure due to drastic Rc increase often occurred much faster if the contact was not clean (higher initial Rc). An improved switch cleaning process was used to achieve low initial contact resistance. However, as the fabrication process improves to cleaner surface, the probability of contact stiction increases as well. Experiment result showed that Au contact can suffer from contact stiction within 100×10^6 cycles even without RF signal passing through the contact. It is suspected that the contact tip has deformed during cycling and contact stiction force becomes too high to be overcome by the switch's open force (<=50μN). Hard metals showed less contact deformation and stiction after persistent contact impact cycling.

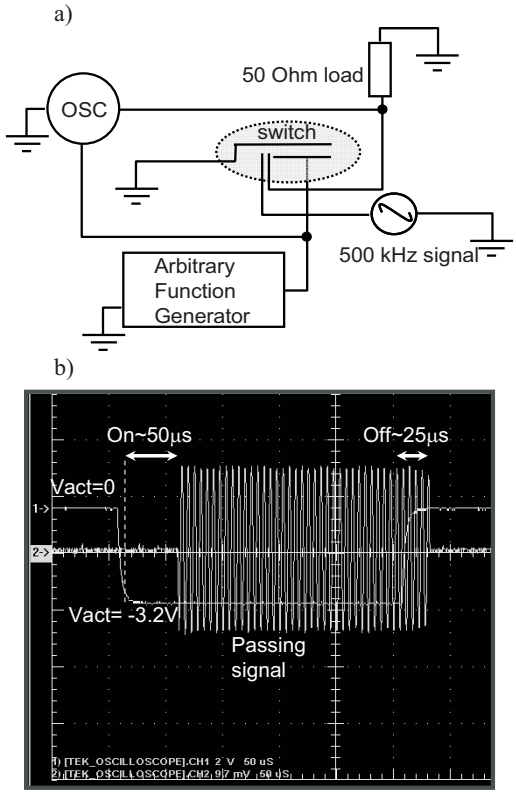

Figure 7. *Measured switching speed of ULV MEMS switch. t_{on} ~ 50μs and t_{off} ~ 25μs.*

The ULV polysilicon switch is intended for reconfigurable RF receiver in this work. The RF signal power strength is expected to be less than 0dBm. Test result showed that the main switch failure was due to increase of contact resistance at such power level. Preliminary analysis indicated that there was organic built up at contact surface. Higher input power (>0dBm) could breakdown this layer and prolong the switch's low contact resistance. However, to mimic the low RF power in reconfigurable receiver, the ULV switch was cold-switched with input powder of -10dBm to 0dBm range. Figure 8 shows the cold-switching lifetime of the fabricated ULV switch. The trace resistance (~2Ω) is included in the insertion loss result. The switch reached ~1.15×10^9 cycles before drastic increase on the insertion loss. The device switching lifetime was strongly affected by the surface and environment cleanliness as discussed previously. Hermetic encapsulation is necessary to ensure reliable switch lifetime.

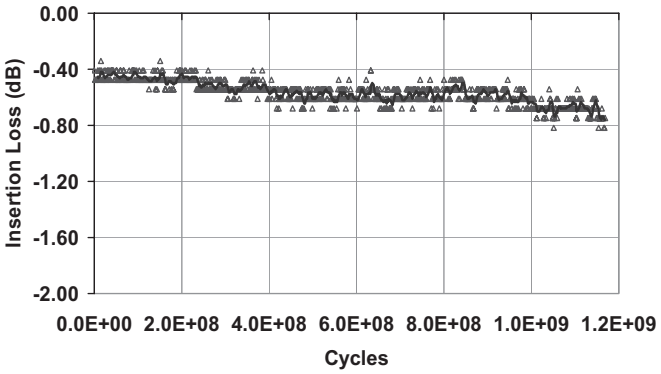

Figure 8. *Cold-switching lifetime of ULV switch. Insertion loss includes 2Ω trace resistance.*

CONCLUSIONS

A 3.3V ultra low voltage electrostatic MEMS switch has been developed. The device structure design separates the spring constants for Vp and open force. Contact resistance of <1Ω/contact has been achieved with improved process cleanliness. The ULV switch demonstrated cold-switching lifetime of >1B cycles with close speed of ~50μs and open speed of ~25μs. The development results suggest that ultra-low-voltage electrostatic switch with 3.3V can be realized without using HV driver.

ACKNOWLEGEMENT

The authors wish to thank all the contributing members, TMG, WNG, and NBI at Intel Corporation for the support of this work.

REFERENCES

[1] R. Mihailovich, *et. al.*, "MEMS Relay for Reconfigurable RF Circuits," *IEEE Microwave Comp. Lett.,* Vol. 11, No.2, Feb. 2001, pp. 53-55.

[2] P. Zavracky, *et. al.,* "Microswitches and Microrelays with a View toward Microwave Applications," *Int. J. RF Microwave CAE*, Vol. 9, No. 4, 1999, pp. 338-347.

[3] P. Blondy, *et. al.*, " Packaged mm-Wave Thermal MEMS Switches," *31st European Microwave Conference*, Vol. 1, Sep. 2001, pp. 283-286.

[4] M. Ruan, *et. al.*, " Latching Micromagnetic Relays," *IEEE J. Microelectromech. Systems*, Vol. 10, Dec. 2001, pp. 511-517.

[5] S. Majumder, *et.al.*, "A Packaged, High-Lifetime Ohmic MEMS RF Switch," *IEEE MTT-S Intl. Microwave Symp. Dig.*, June 2003, pp. 1935-1938.

[6] D. Peroulis, *et. al.*, "Electromechanical Considerations in Developing Low-Voltage RF MEMS Switches," *IEEE Trans. Microwave Theory Tech*., Vol. 51, No. 1, Jan. 2003, pp 259-270.

[7] X. Yuan, *et. al.,* "Modeling and Characterization of Dielectric-Charging Effects in RF MEMS Capacitive Switches," *IEEE MTT-S Intl. Microwave Symp. Dig.*, June 2005, pp 753-756.

COUPLED TORSIONAL CANTILEVERS FOR LABEL-FREE SINGLE MOLECULAR LEVEL BIO-DETECTION AND NANOMATERIALS CHARACTERIZATION

Ozgur Sahin
Rowland Institute at Harvard, Cambridge, MA USA

Henrik H. J. Persson
Stanford Genome Technology Center, Palo Alto, CA USA

Calvin F. Quate, and Olav Solgaard
E. L. Ginzton Laboratory, Stanford, CA

ABSTRACT

We have developed a micromachined atomic force microscope cantilever with an integrated force sensor that enables time-resolved measurement of forces between the vibrating tip and the sample in tapping-mode atomic force microscopy. These tip-sample interaction forces depend on the elastic, viscoelastic, and adhesive properties of the sample and are determined by the chemical and structural composition of the material. With this technique we are able to detect bio-molecular associations on the molecular level and map chemical compositional variations and physical changes within materials at the nanoscale.

INTRODUCTION

Mechanical properties of nanoscale objects highly depend on their chemical composition. Measurement of nanomechanical properties of materials and macromolecules will allow us to map chemical compositional variations and detect biomolecular reactions. Tapping-mode atomic force microscopy provides a framework to interact with nanoscale objects mechanically and non-destructively. In this mode of atomic force microscopy the cantilever with the sharp tip is vibrating on resonance in the vicinity of the sample surface so that the tip intermittently interacts with the surface. Dynamic forces between the tip and the sample carry information on the local mechanical properties with nanoscale spatial resolution. Unfortunately, in conventional tapping mode, measurement of these dynamic forces with temporal resolution is not possible as the cantilever oscillation depends only on the time average value of tip sample forces [1,2]. Recently, measurement of higher harmonics of tip-sample forces has been demonstrated [3-6]. These harmonic forces carry information on the time variation of tip-sample forces, however, they have limited signal to noise ratios. Enhancement of a particular higher harmonic signal has been demonstrated with the use of special micromachined cantilevers [5], however that technique recovers only one higher harmonic.

Here we present a micromachined atomic force microscope cantilever, the coupled torsional cantilever, which allows us to simultaneously measure higher harmonics of tip-sample forces up to the 20th harmonic.

THE COUPLED TORSIONAL CANTILEVER

The coupled torsional cantilever has a tip that is offset from the longitudinal axis (Fig. 1 (a)). When the cantilever is tapping on a sample while vibrating in its first flexural mode, offset tip couples the tip-sample forces to the first torsional mode (Fig. 1(b)). The first torsional vibration mode has a much larger bandwidth and mechanical response at high frequencies than the first flexural vibration mode (Fig. 2(a)). The coupling to the torsional mode therefore provide the high-bandwidth force sensor that is required to detect the tip-sample interaction forces that are of short duration compared to the fundamental vibration frequency. The quadrant position sensitive detectors used in commercial atomic force microscopes allow us to measure torsional and flexural deflections of the cantilever simultaneously. The simultaneously obtained flexural and torsional vibration spectra of a cantilever tapping on a polystyrene sample (Fig. 2(b)) show that the torsional vibrations enhance the signal levels at higher harmonics by 20 to 40 dB. It is these higher harmonics that contain information about the high speed variation of tip-sample forces within a period of cantilever oscillation. Therefore, coupled torsional cantilevers recover the information on time-resolved tip-sample forces.

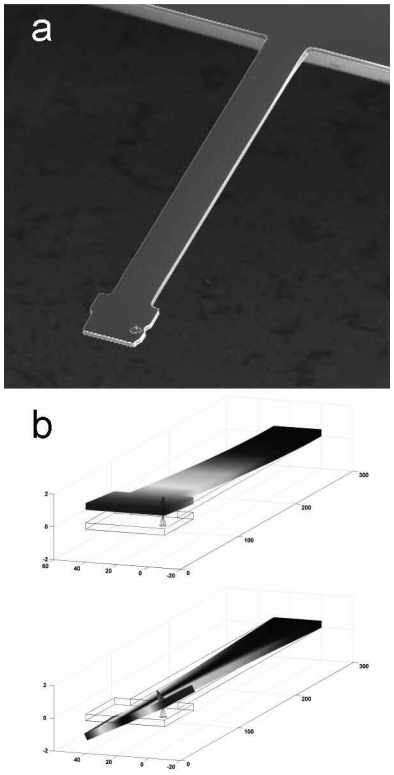

Figure 1. *(a) SEM micrograph of a coupled torsional cantilever. The cantilever is 300 um long, 30 um wide, and 3 um thick. Note the offset location of the sharp tip. (b) Simulated mode shapes of first flexural and torsional resonances.*

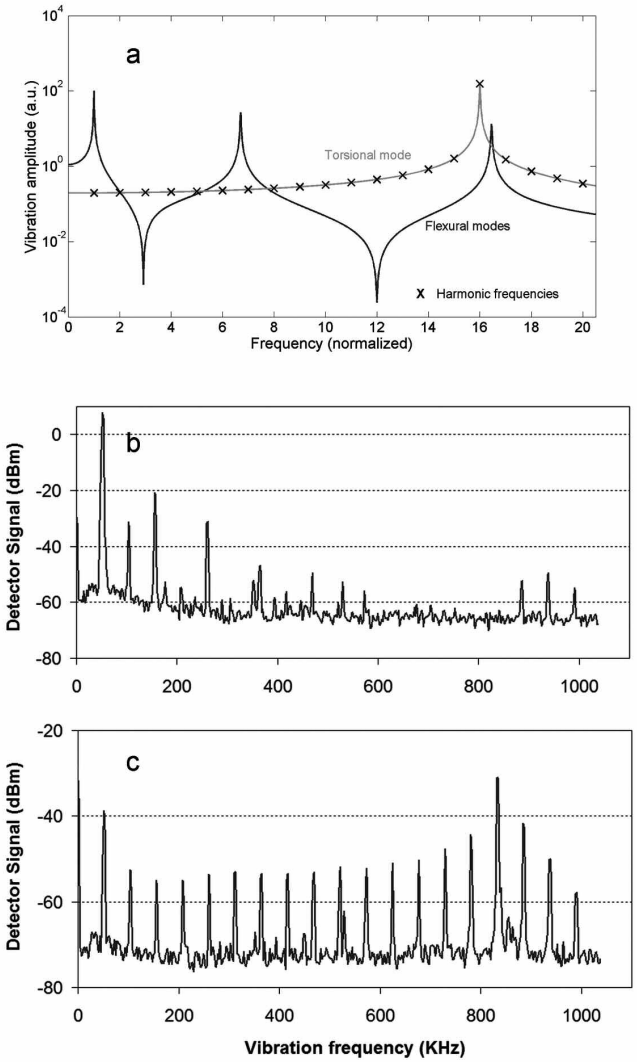

Figure 2. *(a) Frequency response of the flexural and torsional vibrations of a typical rectangular cantilever. Measured flexural (b) and torsional (c) vibration spectra of a coupled torsional cantilever tapping on a polystyrene sample.*

TIME RESOLVED INTERACTION FORCE MEASUREMENTS

The ability to measure higher harmonics of tip-sample forces allows us to reconstruct the periodic tip-sample force waveform. Those frequency components of tip-sample forces that are close to the torsional resonance frequency get enhanced by the resonance. This is seen in the torsional vibrations given in Fig. 2(b). The harmonics that are close to 850 KHz have larger magnitudes. We are interested in the actual magnitude of the forces. Therefore, we correct for the resonance enhancement of the first torsional mode. This is done by sampling the torsional deflection signal at a high sampling rate (with a digital oscilloscope) and then passing it through a linear filter that has a transfer function equal to the inverse of the first torsional mode. We recorded torsional oscillations on three different materials (high density polyethylene, low density polyethylene, and highly oriented pyrolytic graphite) and calculated time resolved tip-sample forces. The resulting waveforms are given in figure 3(a). These measurements are recorded under the same drive force and tapping amplitude, and with the same tip. These waveforms show that tip-sample interaction forces are different for different materials. Interpretation of the differences is difficult, however. The interpretation is simplified when the the forces are plotted against tip-sample separation (Fig. 3 (b)). Note that the tip is approaching and retracting from the surface in a sinusoidal orbit and the peak forces are obtained when the tip is at the bottom of its trajectory. The slopes of the curves in Figure 3(b) at negative separations (sample indentation) are proportional to the stiffness of the sample. As expected, the slope on graphite is higher than the polymers and the slope on the high density polyethylene is higher than the low density polyethylene. An interesting feature of these plots is the hysteresis they exhibit. Hysteresis in the force vs. distance plots is a measure of adhesiveness. As a result of attractive forces, compliant materials can be pulled above its equilibrium surface level.

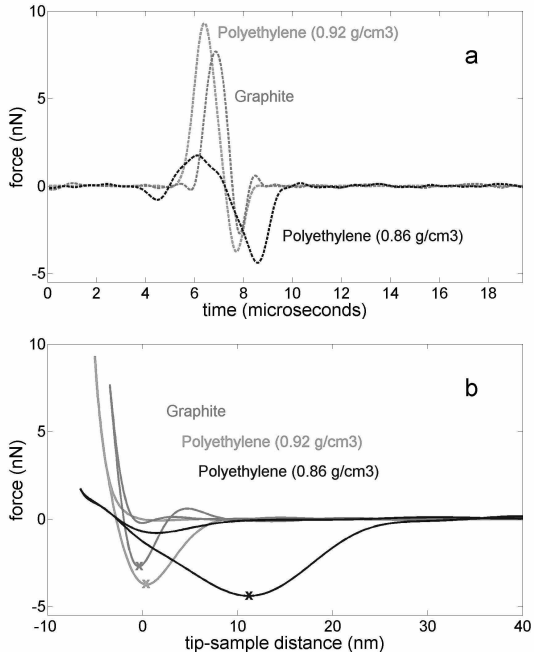

Figure 3. *(a) Time-resolved tip-sample forces measured with coupled torsional cantilever on three materials. (b) The same measurements in (a) are plotted against tip-sample separation. Negative separation corresponds to sample indentation. The slopes depend on material stiffness. Hysteresis and maximum negative forces depend on the adhesiveness of the sample.*

OBSERVING PHASE TRANSITIONS OF COMPOSITE POLYMERS

We studied thermal characteristics of an ultra-thin binary polymer blend film with sub-micron features. The polymer is composed of polystyrene and PMMA. The latter has a higher

glass transition temperature. We imaged mechanical properties at the surface at elevated temperatures with our torsional harmonic technique (Fig. 4 (a)). In this technique, we scan the surface in tapping mode and simultaneously record a particular higher harmonic signal in the torsional spectrum. Higher harmonic imaging has been previously demonstrated with the use of harmonic signals in the flexural response with lower signal to noise levels [3-5]. The advantage of using torsional harmonics is that one can lock onto any higher harmonic, because all the harmonics provide good signal levels. Note that the information in each harmonic is not the same [7].

At lower temperatures, the two polymers have similar characteristics. However, as the glass transition temperature of polystyrene is exceeded, we observed a drastic change in the contrast indicating softening in the polystyrene regions. Detailed understanding of the changes is obtained with the measurement of time resolved forces on both materials. Figure 4 (b) shows the time-resolved force measurements plotted against tip-sample separation on polystyrene and PMMA. These plots show that polystyrene is softening significantly as the temperature is increased, while PMMA does not exhibit detectable changes. These measurements show that polystyrene regions are going through glass transition. To our knowledge, this is the first observation of glass transition in polymers at the nanoscale.

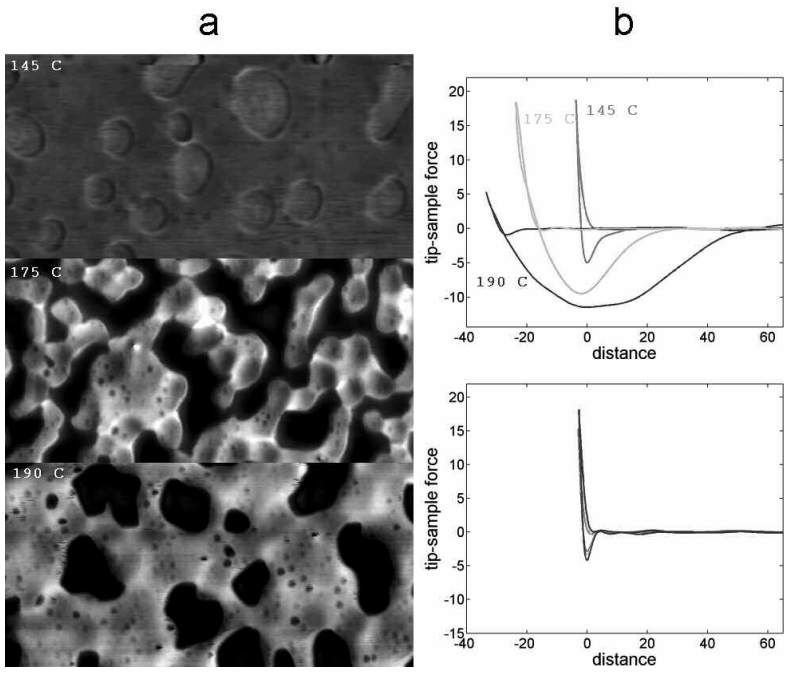

Figure 4. *(a) Harmonic force images of a thin blended binary polymer film at three temperatures obtained at the 16th harmonic. Increasing contrast suggests that one polymer component has gone through glass transition. Scan area is 2.5 x 5 microns at 145 °C and 5 by 10 microns at 175 °C and 190 °C. (b) Time-resolved tip-sample force measurements on the two material components reveal the nature of the changes. One material is softening drastically and becoming adhesive. The other material is nearly intact.*

DISCRIMINATION OF SINGLE HYBRIDIZED DNA MOLECULES

An application of timeresolved AFM technology is to detect biomolecular associations through mechanical changes in molecules. We studied mechanical changes in the hybridized DNA-oligonucleotides versus single stranded DNA. A mixture of hybridized and single stranded molecules are immobilized on a gold surface with thiol linkers [8] and imaged in air with our technique. We employed different mixture rates to obtain control groups in the experiments. In the first sample only single stranded DNA molecules are immobilized. In the second sample 0.1% of the molecules in the mixture were double stranded. In the third sample all the molecules were double stranded. We recorded harmonic images with the use of a resonantly enhanced 16th flexural harmonic. These images are given in figure 5. The images show good contrast between the fully hybridized and fully single stranded samples. Furthermore, on the sample with 0.1% hybridization we observe features with approximately 40 nm in diameter that we believe correspond to individual hybridized DNA molecules. The increased radii of these features are due to tip convolution. This hypothesis is supported by the comparison of signal levels measured on these features. On the right side of each harmonic image, we give actual harmonic signal levels measured at a section of the image. The signal level observed on the fully single stranded sample (~0.9 mV) is also observed on the 0.1% percent hybridized sample as the background signal levels. On the bright features in this image, the harmonic signal drops to 0.45 mV. This signal level is also recorded on the bright features of the fully hybridized sample. These results indicate that bright features with signal levels around 0.45 mV correspond to hybridized molecules.

Furthermore, the hybridization of a single DNA molecule results in a contrast that provides approximately 30dB signal to noise ratio. The high resolution of the AFM tip allows us to see individual hybridized molecules, and makes it possible to count the number of molecules. Our results show that with this technique, it is possible to quantitatively measure hybridization reactions with large dynamic range and detect very low concentrations of molecules. Alternative technologies like nanowire based electrical sensors, or fluorescence and plasmon based optical sensors do not provide this level of sensitivity, and neither do they provide the spatial resolution to identify individual molecules. Another advantage of this technique is that the measurements are performed on label-free DNA molecules and the recorded signal levels are specific to the chemical species. Other label-free techniques, such as resonant mass sensors, do not provide chemical specificity, since any attachment of a foreign body on the resonating device will result in a shift in resonance frequency.

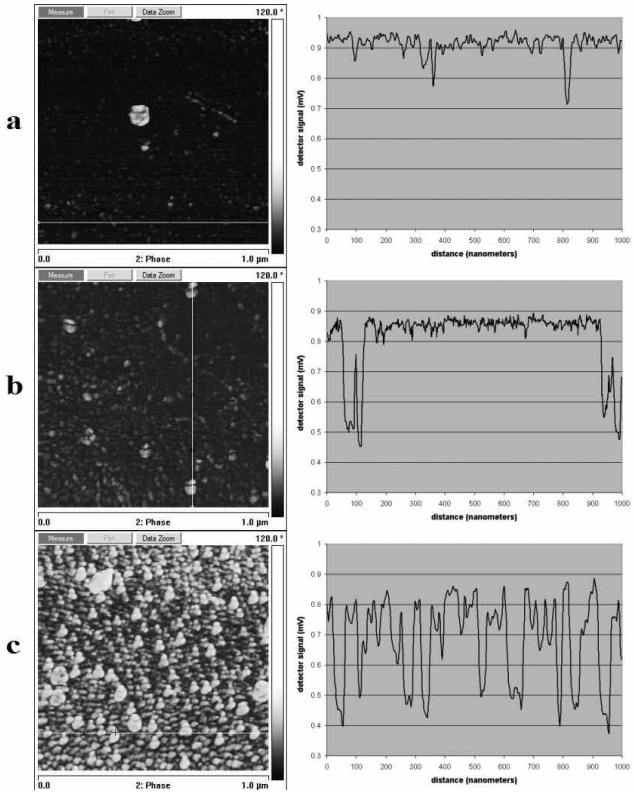

Figure 5. *Harmonic force images obtained on self assembled DNA oligo-nucleotides on atomically flat gold. Scan areas are 1 um by 1um. Signal levels recorded on a section of the images are given to the right of the corresponding image. The three samples are prepared by immobilizing a mixture of 20 nucleotide long single and double stranded DNA molecules. Percentage of the double stranded molecules in the mixture are 0 % in (a), 0.1 % in (b), and 100% in (c). The signal levels given to the right of each image show that single stranded molecules result in a signal level of 0.9 mV and double stranded molecules result in 0.45 mV. The widths of the features in (b) suggest that these belong to individual hybridized DNA molecules, since our tips are typically 20-50 nm wide.*

CONCLUSIONS

We presented the coupled torsional cantilever to measure the mechanical interaction between the sharp tip of the atomic force microscope and the sample. Mechanical properties of materials and individual molecules highly depend on the physical and chemical properties. We used this fact to study phase transitions of composite polymers with nanometer level spatial resolution and observed the glass transition of submicron polystyrene domains within the composite. Then we studied the effects of hybridization of DNA molecules on the mechanical properties of the surface and used this phenomenon to detect and quantify hybridized DNA molecules. This technology shows promise for nanomaterials characterization and highly sensitive and quantitative biomolecular analysis.

REFERENCES

[1] A. S. Paulo and R. Garcia, "Unifying theory of tapping-mode atomic force microscope" *Phys. Rev B.* 66, 041406(R) (2002).

[2] J. P. Cleveland, B. Anczykowski, A. E. Schmid, and V. B. Elings, "Energy dissipation in tapping-mode atomic force microscopy." *Appl. Phys. Lett.* 72, 2613-2615 (1998).

[3] R. Hillenbrand, M. Stark, and R. Guckenberger, "Higher-harmonics generation in tapping-mode atomic force microscopy: Insights into tip-sample interaction." *Appl. Phys. Lett.* 76, 3478-3480 (2000).

[4] R. W. Stark and W. M. Heckl "Higher harmonics imaging in tapping-mode atomic-force microscopy." *Rev. Sci. Instrum*. 74, 5111-5114 (2003).

[5] O. Sahin, G. Yaralioglu, R. Grow, S. F. Zappe, A. Atalar, C. F. Quate and O. Solgaard, "High resolution imaging of elastic properties using harmonic cantilevers." *Sensors and Actuators A,* 114, 183-190 (2004).

[6] M. Stark, R. W. Stark, W. M. Heckl and R. Guckenberger, "Inverting dynamic force microscopy: from signals to time resolved forces." PNAS, 99, 8473-8478 (2002).

[7] O. Sahin, A. Atalar, C. F. Quate, and O. Solgaard, "Resonant harmonic response in tapping-mode atomic force microscopy." *Phys. Rev. B.* 69 165416 (2004)

[8] T. M. Herne and M. J. Tarlov: Characterization of DNA probes immobilized on gold surfaces. *J. Am. Chem. Soc.* 119, 8916-8920 (1997)

DISSIPATION IN SINGLE-CRYSTAL 3C-SIC ULTRA-HIGH FREQUENCY NANOMECHANICAL RESONATORS

X. L. Feng,[1] C. A. Zorman,[2] M. Mehregany,[2] and M. L. Roukes[1]
[1]Kavli Nanoscience Institute, California Institute of Technology, 114-36
Pasadena, CA 91125, USA
[2]Electrical Engineering & Computer Science Department, Case Western Reserve University
Cleveland, OH 44106, USA

ABSTRACT

The energy dissipation Q^{-1} (where Q is the quality factor) and resonance frequency characteristics of single-crystal 3C-SiC ultra-high frequency (UHF) nanomechanical resonators are measured, for a family of UHF resonators with resonance frequencies of 295MHz, 395MHz, 411MHz, 420MHz, 428MHz, and 482MHz. A temperature dependence of dissipation, $Q^{-1} \propto T^{0.3}$ has been identified in these 3C-SiC devices. Possible mechanisms that contribute to dissipation in typical doubly-clamped beam UHF resonators are analyzed. Device size and dimensional effects on the dissipation are also examined. Clamping losses are found to be particularly important in these UHF resonators. The resonance frequency decreases as the temperature is increased, and the average frequency temperature coefficient is about -45ppm/K.

INTRODUCTION

Nanoelectromechanical systems (NEMS) [**1**] have attracted considerable research attention and NEMS based resonators offer immense potential for applications such as ultra-sensitive force detection [**2**], single-molecule mass sensing [**3**], and mechanical computation [**4**] and signal processing [**5**]. In most of these applications, operating at high frequencies provides a key advantage allowing NEMS to surpass conventional solutions. Hence, nanoscale devices and materials with large elastic modulus-to-density ratio (E/ρ) are being pursued. Using single-crystal 3C-SiC as a structural material, beam-structured resonators operating in the VHF, UHF, and microwave frequency bands have been demonstrated [**6**], which are of particular interest for resonant nanomechanical sensing applications. However, one known trade-off is that the quality factor decreases as the resonance frequency increases (*i.e.*, as the devices dimensions are reduced in order to increase the frequency) [**6**] — thus "Q-engineering" is crucial for retaining high Q while scaling up the frequency. Although the practical performance of these resonators very strongly depends upon quality factors, the mechanisms of dissipation affecting Q's of nanomechanical resonators are still not well understood. It has been qualitatively identified that surface roughness of SiC structural layer can play an important role [**6**]. With recent advances in ultrahigh quality large SiC crystal growth [**7**] and surface roughness control [**8**], SiC promises to be one of the most promising and practical materials for high-performance VHF/UHF/Microwave NEMS. In this work, we report the first systematic measurements and analyses of the dissipation characteristics in several successive generations of single-crystal 3C-SiC UHF NEMS resonators.

EXPERIMENTAL DETAILS

By following a process specifically suitable for UHF SiC NEMS [**6**], doubly-clamped beam resonators are nanofabricated from a single-crystal 3C-SiC epitaxial layer grown on a single-crystal silicon substrate by atmospheric pressure chemical vapor deposition (APCVD), supported by newly developed surface roughness control and improvement techniques [**8**]. Shown in Figure 1 are SEM images of a typical UHF 3C-SiC resonator. The doubly-clamped beam design simplifies understanding of device size and dimensional effects, and also minimizes the influence of complexities in, and variations from, the fabrication processes. Metallization consisting of 10nm Titanium atop a 30nm Aluminum layer is deposited onto the SiC structural material. This enables patterning devices read out by magnetomotive excitation and detection [**6**] of the beam resonance from the in-plane flexural fundamental mode. Measurements are performed in a strong magnetic field up to B = 8T, within a low-temperature cryostat where the device is also secured in high vacuum ($\leq 10^{-7}$ Torr). Typical device dimensions are w=120nm, t=80nm (excluding metallization layers), and l=1.55~2.65μm.

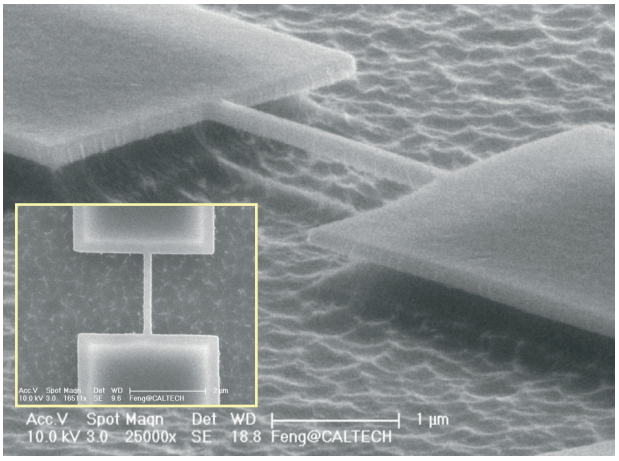

Figure 1. *Scanning electron micrographs of a typical single-crystal 3C-SiC UHF NEMS resonator. (**main**) Oblique view (scale bar: 1μm) and (**inset**) Top view (scale bar: 2μm).*

Network analysis techniques for two-port systems are used to detect the magnetomotively-transduced signals from the devices and to measure the resonance frequencies and quality factors. Resonance signals of these UHF devices are diminutive and are often easily overwhelmed by the embedding parasitic background response arising from the detection system. It has been a challenge to extract large and clean resonance signals out of the electrical background response. We employ a balanced-bridge detection scheme involving the use of pairs of impedance-matched devices [**6**]. We further incorporate high-resolution bridge-balancing and background-nulling techniques into the circuitry for UHF NEMS resonance readout. These techniques typically allow us to attain signal-to-background ratios (on-resonance to off-resonance ratio) of 5~10dB (whereas previously only 0.1~0.5dB were routinely obtained for UHF NEMS). Quality factors are then reliably extracted from the clean resonance signals of the network analysis measurements for each device under controlled

experimental conditions. We note that the same quality factor can also be extracted from time-domain ring-down process of a resonator, albeit somewhat less conveniently than from the frequency-domain power spectrum obtained by network analysis.

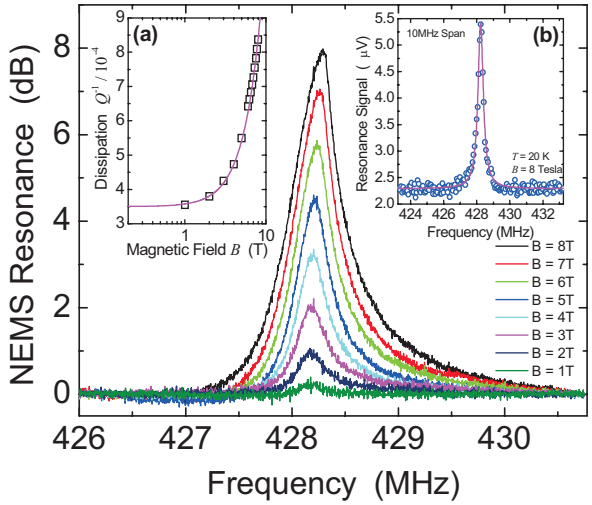

Figure 2. *Resonance signal of a 428MHz NEMS resonator, at various magnetic field conditions, as measured by a microwave network analyzer, utilizing detailed balancing and nulling techniques with a bridge circuitry scheme.* ***(inset (a))*** *The magnetomotive damping effect.* ***(inset (b))*** *A typical UHF resonance signal over a 10MHz wide frequency span.*

RESULTS AND DISCUSSIONS

Figure 2 shows the measured resonance signal of a 428MHz device, with the background response nulled out, as the magnetic field is ramped up from 0T to 8T. The resonance curves clearly indicate an effective Q decrease with increasing magnetic field (as the resonance is getting broadened). The measured dissipation Q^{-1} versus magnetic field is shown in the inset (a) of Figure 2 with the quadratic fit in dashed line. At B = 8T, the signal-to-background ratio is 8dB at the resonance peak. The inset (b) of Figure 2 shows the resonance signal referred to the input of the preamplifier, in which both the background signal and the resonance amplitudes are shown in linear scale (in μVolts, 8dB at peak if converted into dB, exactly corresponding to the dB plot in Figure 2; but here in the linear scale plot the absolute level of the flat background, ~2.25μV, *i.e.*, -100dBm, is clearly indicated). The solid line from a Lorentzian fit matches the resonance data over a 10MHz wide span. This readily observed magnetomotive damping effect originates from the fact that the electromagnetomotive force (emf) voltage generated by the vibrating NEMS device in the B field, creates a current as the device is in a closed circuit (with the resistive elements of both the device itself and the measurement system), and in the B field this current induces a force which intends to *oppose* or *damp* the resonating device. This effect can be modelled by a *loaded* Q due to the impedances forming a closed circuit with the emf voltage in the detection system [**9**],

$$\frac{1}{Q} = \frac{1}{Q_{device}}\left(1 + R_m \frac{\mathrm{Re}(Z_{ext})}{|Z_{ext}|^2}\right), \qquad (1)$$

in which Q_{device} is the *unloaded* Q of the device itself; $R_m = Q_{device}\eta B^2 l^2/(2\pi f_0 m)$ is the electromechanical resistance of the device, with m the device mass and mode shape coefficient η=0.83086 for the fundamental mode; and Z_{ext} (seen by the emf voltage in its closed circuit) is the impedance in series to R_m, consisting of the DC resistance of the device, the impedance of the coaxial cable and the input impedance of the preamplifier. Shown in Figure 2 inset (a), the measured Q decrease versus B field, fitting with *Eq.* (1), leads to an estimation of the *unloaded* Q of $Q_{device} \approx 2860$ at ~20K.

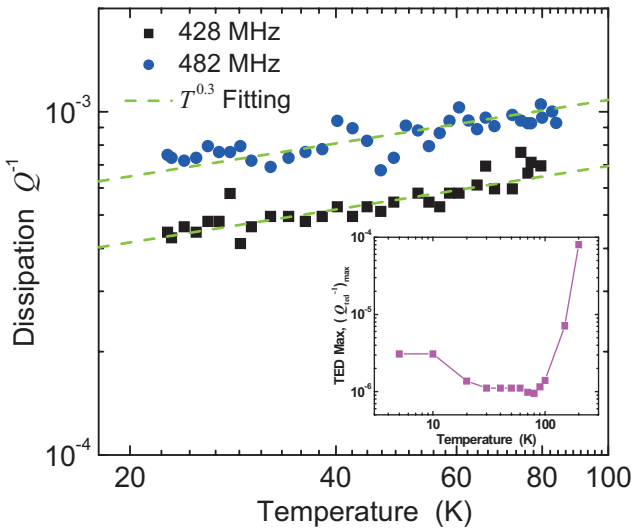

Figure 3. *Measured dissipation as a function of temperature for the selected 428MHz and 482MHz NEMS resonators. The dashed lines show the $Q^{-1} \propto T^{0.3}$ approximation to guide the eyes.* ***(inset)*** *Theoretical estimation of maximum possible thermoelastic dissipation as a function of temperature.*

To identify the temperature dependence of device dissipation, feedback control of sample temperature is applied and for each measurement, temperature fluctuation is limited to ≤1 mK, in order to minimize the instantaneous resonance frequency variation due to the temperature fluctuation. Figure 3 shows the measured dissipation versus temperature for the 428MHz and 482MHz devices, with all other parameters and settings kept the same and leaving temperature the only variable. RF driving power (-33dBm) with suitable bias field (B = 6T) is calibrated and applied to attain large enough signals within the dynamic range in all the temperature dependence measurements. The measured dissipation increases with increasing temperature, with a power-law dependence of roughly $Q^{-1} \propto T^{0.3}$. Note that the data are taken in the range of T = 20~100K, which is limited solely by practical limitations of our existing measurement system. Dissipation in resonant nanodevices is complicated and associated with various energy loss mechanisms. Hence, to understand the data requires examinations of all dominant dissipation processes. Assuming that the dissipation from different origins are uncorrelated, the possible important mechanisms that may contribute to the measured dissipation include the 3C-SiC structure layer's intrinsic dissipation Q_0^{-1}, magnetomotive damping Q_{mag}^{-1}, thermoelastic damping Q_{ted}^{-1}, clamping losses Q_{clamp}^{-1}, metallization layer dissipation Q_{metal}^{-1}, surface losses Q_{surf}^{-1}, *etc.*,

$$\frac{1}{Q} = \frac{1}{Q_0} + \frac{1}{Q_{mag}} + \frac{1}{Q_{ted}} + \frac{1}{Q_{clamp}} + \frac{1}{Q_{metal}} + \frac{1}{Q_{surf}} \cdots \qquad (2)$$

Here we neglect the effect of viscous damping in air since all our measurements are performed with devices in high vacuum. The aforementioned, easily observed magnetomotive damping effect can be non-negligible but is readily modelled and identified.

The thermoelastic damping effect arises from the fact that when the beam is deformed and is vibrating, the strain field is coupled to local temperature field and vibratory mechanical energy

is dissipated through phonon relaxation processes to the environment. Based on the theory and modelling of thermoelastic damping in doubly-clamped beam resonators [**10**], we estimate the upper limit of thermoelsatic damping in 3C-SiC devices to be

$$\left(\frac{1}{Q_{ted}}\right)_{\max} = \max\left\{\frac{E\alpha^2 T}{\rho C_P}\left[\frac{6}{\xi^2} - \frac{6}{\xi^3}\frac{\sinh\xi + \sin\xi}{\cosh\xi + \cos\xi}\right]\right\}, \quad (3)$$

where E, α, ρ, C_P are the Young's modulus, thermal expansion coefficient, mass density, and heat capacity (per unit mass), respectively. Here ξ is a dimensionless variable representing the relative magnitude of the characteristic size of the device (*e.g.*, device width) versus the characteristic thermal relaxation length (*e.g.*, phonon mean free path). The upper limit of thermoelastic damping, $(1/Q_{ted})_{max}$, independent of the device dimensions, occurs for a system operating at ξ=2.225. As plotted in the inset of Figure 3, thermoelastic damping effect in the 3C-SiC NEMS devices is not strong and could be neglected (still more than 2 orders of magnitude smaller than the measured dissipation). We note that this estimation is based on the conventional view in which thermoelastic damping is considered to be a *bulk* effect, and the estimation relies on the available material properties.

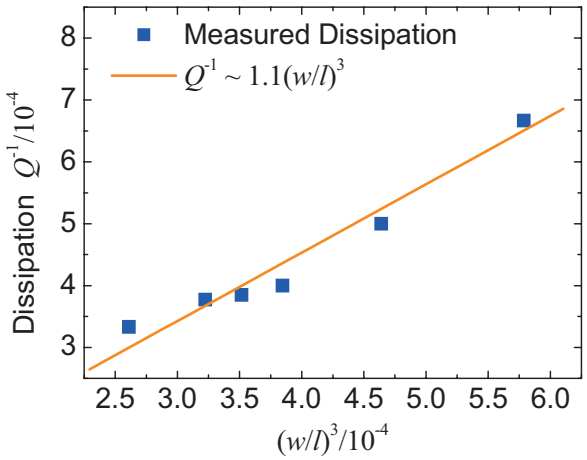

Figure 4. *Experimental results of dissipation in several generations of UHF NEMS resonators with dimensions and operating frequencies scaled, all measured under the same experimental conditions (the individual device characteristics are listed in Table 1). The solid line is the approximate theoretical fit based on the theory of elastic energy transmission from the vibrating NEMS device to its clamping and supporting pads.*

Table 1. *Specifications of several 3C-SiC UHF NEMS resonators.*

Resonant Frequency (MHz)	Device Dimension l (μm)	w (nm)	t (nm)	Aspect Ratio (l/w)	Measured Q^{-1}
295	2.65	170	80	15.65	3.33×10^{-4}
395	1.75	120	80	14.58	3.77×10^{-4}
411	1.70	120	80	14.17	3.85×10^{-4}
420	1.80	150	100	12.00	6.67×10^{-4}
428	1.65	120	80	13.75	4.00×10^{-4}
482	1.55	120	80	12.92	5.00×10^{-4}

Scaling resonance frequency up to UHF range brings the doubly-clamped beam length down to only 1~2 μm (*e.g.*, for a SiC layer thickness ~100nm, and a lithography-process-determined width which is typically 100nm~150nm), thus the clamping loss can become important. Theoretical analyses predict that for the in-plane flexural mode of doubly-clamped beams, dissipation into the supports follows $Q_{clamp}^{-1} \approx \beta(w/l)^3$, where the coefficient β is not readily modelled [**11**]. The experimental data from a family of UHF NEMS achieve quite sound agreement with the theoretical prediction, as shown in Figure 4 (with the device characteristics listed in Table 1). The close fit to $Q_{clamp}^{-1} \approx \beta(w/l)^3$ not only indicates that the clamping loss plays an important role that increases with shrinking device dimensions (scaling up frequency); but also suggests that relative role of the clamping loss to the total dissipation, Q_{clamp}^{-1}/Q^{-1}, is about the same in these devices. It is thus clear that the offset between the two data traces in Figure 3 is due to the larger clamping loss in the 482MHz device than that in the 428MHz device.

Metallization layers made by evaporation, are not ideal and always possess internal friction, and thus also contribute to the device dissipation. We analyze this by using the general definition $Q^{-1}=\Delta W/(2\pi W)$, where W is the energy stored in the resonator and ΔW the dissipated energy per cycle, assuming that the energy stored and dissipated can be split into corresponding portions in the structural layer and metallization layers. For our flexural mode doubly-clamped beams, we then obtain

$$\frac{1}{Q} = \sum_{j,k\neq i}^{i=SiC,Al,Ti}\left(1 + \frac{t_j E_j}{t_i E_i} + \frac{t_k E_k}{t_i E_i}\right)^{-1} \cdot \frac{1}{Q_i}, \quad (4)$$

in which t_i, E_i are thickness, Young's modulus of the layers (including SiC, Al, Ti), and Q_i^{-1} are the phenomenological dissipation in each layer, respectively. The coefficients for the dissipation in metallization layers are very small, 0.0543 and 0.0293, respectively. With the measured dissipation in deposited submicron Al and Ti films from [**12**] (each having a plateau in the interested temperature range), the estimated dissipation in metallization layers is $5\sim6\times10^{-6}$ (as listed in Table 2), still ≤1% of the measured dissipation.

Table 2. *Estimation of the dissipation contributed by the metallization layers (Al and Ti) with the internal friction in these evaporated metal layers.*

Metal Layer	Thickness (nm)	Young's Modulus (GPa)	Q_{film}^{-1}	Calculated Dissipation
Al	30	68	1.0×10^{-4}	5.43×10^{-6}
Ti	10	110	2.0×10^{-4}	5.86×10^{-6}

Surface loss arises from the fact that surface atoms are different than those of the "bulk" and can therefore cause energy dissipation — presumably through forming an additional energy reservoir, or by mediating anharmonic mode coupling, or both. Surface stress, adsorbates and crystal defects on the device surface all may enhance such dissipation. Exact theoretical analyses and models capturing the mesoscopic surface loss mechanisms have yet to be clearly established and are likely often sample-specific and dependent upon *quasi*-random surface conditions. Nonetheless, intuitively one expects larger dissipation (lower Q's) when the device surface-to-volume ratio is increased. Experiments show that for ultra-thin (t<<w) cantilevers, Q's are roughly proportional to the device thickness (in the regime where surface losses are dominant, *i.e.,* when the cantilevers are long enough). This can be qualitatively explained by conventional macroscopic theory based on the concept of a complex modulus ($E=E_1+iE_2$, where E_2 is the dissipative part) [**13**]. For the UHF NEMS devices of very short beams, as shown in Table 1, the surface-to-volume ratio $2(w+t)/(wt)$ does not change much (or almost remains the same) because of fabrication process consistency and the maintenance of relatively constant values for w and t. Thus, surface losses in these devices should be approximately the same,

and the Q differences measured from these devices are still found to be dominated by clamping losses. To estimate or determine the absolute amount of surface loss, annealing and other surface treatment techniques could, in future, be applied to test how much dissipation might be reduced.

The above analyses show that the observed dissipation temperature dependence $Q^{-1}\sim T^{0.3}$ within the temperature range of these measurements can be ascribed to intrinsic dissipation within the 3C-SiC material itself. Other important mechanisms (*e.g.,* clamping loss) add to this intrinsic dissipation, without markedly changing the temperature dependence. In principle, it may be possible to develop an accurate model describing this temperature dependence with a more detailed, atomistic understanding of the mesoscopic energy dissipation nature within the single-crystal 3C-SiC. The measurements of the temperature-dependent dissipation in 3C-SiC shown herein may provide new insight into this intriguing open question.

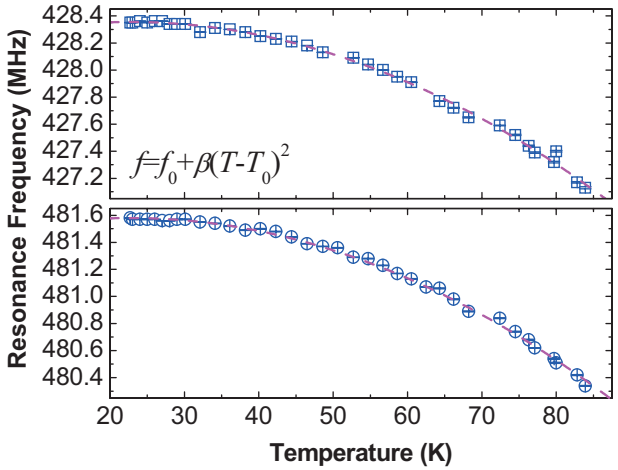

Figure 5. *Measured resonance frequency as a function of temperature for selected 3C-SiC UHF NEMS resonators (at carefully controlled and stabilized temperatures).*

The dependence of resonance frequency upon temperature is measured and is plotted in Figure 5. As shown, the resonance frequency decreases as the temperature is increased. A polynomial fit to the data shows that a quadratic dependence $f = f_0+\beta(T-T_0)^2$ matches the heating-induced ($T \geq T_0$) frequency tuning data quite well, with $\beta \approx$ -320Hz/K^2 for both data traces of Figure 5. We attribute this primarily to the effect of thermal expansion: the frequency changes as both the beam length and its tension are altered with temperature. The results imply that the tensile stress increases monotonically when the devices are cooled down from 85K to 20K. Another observation is that the fractional frequency change does not show dependence upon device size (the two devices shown have different lengths), and both devices exhibit average resonance frequency temperature coefficients of about -45ppm/K in the range T = 20~85K. This effect, once calibrated over wider temperature range, can be employed to study the basic properties of SiC material, and can be further engineered for sensing applications.

CONCLUSIONS

We have investigated the dissipation in single-crystal 3C-SiC nanomechanical resonators operating at ultra-high frequencies, to gain understanding and develop engineering solutions that make optimal trade-offs between scaling up resonance frequency and attaining high-Q's for UHF NEMS resonators. It is found that the temperature dependence of the dissipation in the 3C-SiC NEMS resonators studied follows $Q^{-1} \propto T^{\alpha}$, with $\alpha \approx 0.3$. It is clear that in-depth theoretical models and analyses are needed to reveal the underlying microscopic mechanisms. The magnetomotive damping effect can be appreciable, but it is relatively well understood and (to some extent) controlled. Thermoelastic dissipation is found to be negligible for the devices of this study. The losses from metallization layers contribute ≤1% of the observed total dissipation. However, a major source of the dissipation is clamping losses through the supports for these doubly-clamped beam UHF resonators. The measured data show that the theoretical prediction $Q_{clamp}^{-1} \propto (w/l)^3$ provides a rough but reasonable model for these clamping losses. Verifying and understanding the dominant clamping losses can lead to new designs and optimization guidelines for UHF NEMS enabling attainment of high Q's. Moreover, because SiC can be deposited both in polycrystalline form as well as in several single-crystal polytypes with excellent properties (including 3C-SiC, 6H-SiC, 4H-SiC and 2H-SiC), it represents a particularly promising material for NEMS applications. Future collective studies of dissipation in SiC NEMS with all these SiC variations would be beneficial.

ACKNOWLEDGEMENT

This work is supported by the DARPA MTO under grant DABT63-98-1-0012, DARPA/SPAWAR under grant N66001-02-1-8914, and the NSF under grant ECS-0089061.

REFERENCES

[1] M.L. Roukes, "Nanoelectromechanical Systems Face the Future", *Physics World, 14*, 25 (2001).

[2] J.L. Arlett, J.R. Maloney, B. Gudlewski, M. Muluneh, M.L. Roukes, "Self-Sensing Micro- and Nanocantilevers with Attonewton-Scale Force Resolution", *Nano Lett., 6*, xxxx (*in press*) (2006).

[3] Y.T. Yang, C. Callegari, X.L. Feng, K.L. Ekinci, M.L. Roukes, "Zeptogram-Scale Nanomechanical Mass Sensing", *Nano Lett., 6*, xxxx (*in press*) (2006).

[4] M.L. Roukes, "Mechanical Computation, Redux?", *Tech. Digest, IEEE IEDM 2004*, San Francisco, CA, 12/13-15/04, 539 (2004).

[5] C.T.-C. Nguyen, "Vibrating RF MEMS Overview: Applications to Wireless Communications", *Proc. Photonics West: MOEMS-MEMS 2005,* San Jose, CA, 1/22-27/05, Paper No. 5715-201 (2005).

[6] X.M.H. Huang, X.L. Feng, C.A. Zorman, M.Mehregany, M.L. Roukes, "VHF, UHF and Microwave Nanomechanical Resonators", *New J. Phys., 7*, 247 (2005).

[7] D. Nakamura, I. Gunjishima, S. Yamaguchi, T. Ito, A. Okamoto, H. Kondo, S. Onda, K. Takatoir, "Ultrahigh-Quality Silicon Carbide Single Crystal", *Nature, 430*, 1009 (2004).

[8] X.A. Fu, C.A. Zorman, M. Mehregany, "Surface Roughness Control of 3C-SiC Films during the Epitaxial Growth Process", *J. Electrochem. Society, 151*, G910 (2004).

[9] A.N. Cleland, M.L. Roukes, "External Control of Dissipation in a Nanometer-Scale Radiofrequency Mechanical Resonator", *Sensors and Actuators, 72*, 256 (1999).

[10] R. Lifshitz, M.L. Roukes, "Thermoelastic Damping in Micro- and Nanomechanical Systems", *Phys. Rev. B, 61*, 5600 (2000).

[11] M.C. Cross, R. Lifshitz, "Elastic Wave Transmission at an Abrupt Junction in a Thin Plate with Application to Heat Transport and Vibrations in Mesoscopic Systems", *Phys. Rev. B, 64*, 085324 (2001).

[12] X. Liu, E. Thompson, B.E. White Jr., R.O. Pohl, "Low-Temperature Internal Friction in Metal Films and in Plastically Deformed Bulk Aluminum", *Phys. Rev. B, 59*, 11767 (1999).

[13] K.Y. Yasumura, T.D. Stowe, E.M. Chow, T. Pfafman, T.W. Kenny, B.C. Stipe, D. Rugar, "Quality Factors in Micron- and Submicron-Thick Cantilevers", *J. MEMS, 9*, 117 (2000).

AMPLITUDE NOISE INDUCED PHASE NOISE IN ELECTROSTATIC MEMS RESONATORS

Manu Agarwal, Kwan K. Park, Bongsang Kim, Matthew A. Hopcroft, Saurabh A. Chandorkar, Rob N. Candler[1], Chandra M. Jha, Renata Melamud, Thomas W. Kenny, Boris Murmann
Departments of Electrical and Mechanical Engineering, Stanford University,
Stanford, California USA

ABSTRACT

This work investigates the effects of amplitude perturbations on the frequency stability of Electrostatic MEMS resonators. As in quartz, the activity limit, or maximum sustainable drive current depends on the nonlinearities of the resonator and its quality factor (Q). We find that at high activity the random amplitude fluctuations get mixed into the phase noise of the oscillator, causing frequency instability (phase noise). Using a Double-Ended-Tuning-Fork (DETF) structure we verify the presence of *A-f* (Amplitude frequency dependence) effect in MEMS resonators. We find that the *A-f* coefficient in our low frequency test structure is orders of magnitude higher when compared to quartz crystal resonators.

INTRODUCTION

Electrostatically coupled micromechanical devices have become a promising solution for frequency references and signal processing applications in recent times [1]. Integration of these micromechanical structures with on-chip CMOS circuitry potentially leads to considerable size and cost reduction, making them a commercially attractive and viable replacement for quartz crystal technology.

Several efforts to commercialize electrostatic MEMS resonator technology are currently underway. One of the most promising applications of commercial interest is probably the cellular communication business. MEMS resonator based oscillators with frequency stability that satisfies the GSM standard requirements have already been reported in [2, 3]. Other important applications include networking and timekeeping. While some of these applications focus on higher frequency resonators, low frequency and flexural type resonators appear in a wide assortment of resonant sensing applications including acceleration sensors, mass sensors, etc.

For these applications, nonlinearities in the resonators limit the ultimate frequency stability (or phase noise performance) that can be achieved. In sensors, this stability is a measure of the achievable resolution. Nonlinearities in quartz have been studied and their impact on frequency stability of oscillators has been discussed [4]. Perhaps the most important limitation on frequency stability is dictated by the limitation on the 'activity' or power handling, which is a measure of the useful signal strength that can be sustained by these devices. At high amplitudes of oscillation the nonlinearities can become considerable and cause *Duffing* type effects. The broader term used for this effect in quartz literature is *A-f* (Amplitude-frequency) effect. The generating mechanisms for nonlinearities that can cause this effect in MEMS and a mathematical description for power handling have been developed previously [3, 5]. Nonlinear multiplication of low frequency electronics noise into the close-to-carrier noise have also been studied [6-8].

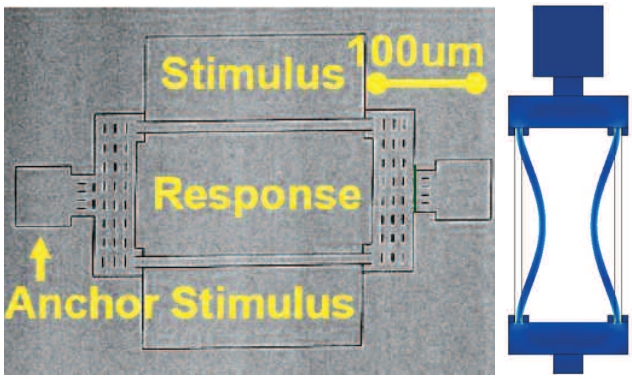

(a) (b)

Figure 1. a) *Scanning electron micrograph of the top view of the DETF resonator used in our experiments. The beam dimensions used were L = 220 μm, w = 8 μm and t = 20 μm. The resonant frequency of this resonator is ~1.3 MHz. b) FEMLAB simulation showing the resonant mode shape of the structure.*

In this work we focus primarily on the *A-f* effect, which converts the amplitude noise into frequency noise, and at higher amplitudes can even cause bifurcation instability [3, 5]. Analytical models for the effect of this nonlinearity on the noise performance of these oscillators will be presented, along with experimental verification using a double-ended tuning fork resonator, schematically shown in Figure 1. Methods for measurement and quantification of nonlinearities and comparison with quartz will also be presented.

AMPLITUDE NOISE vs. PHASE NOISE

In this section we describe the two kinds of noise in an oscillator output, namely amplitude noise and phase noise. The output voltage of an oscillator can be represented by

$$V_{out}(t) = \left(A_0 + a_N(t)\right)\cos\left(2\pi f_0 t + \varphi_N(t)\right) \quad (1)$$

Here A_0 is the average amplitude of the output signal and f_0 is nominal frequency of oscillation. $a_N(t)$ and $\varphi_N(t)$ represent the time varying components of the amplitude and phase, respectively. These components are considered as noise, because an ideal oscillator would have constant amplitude A_0 and phase varying at a constant rate $2\pi f_0$. It can be shown that white noise power of the amplifier electronics is equally partitioned into amplitude and phase noise components [9].

The low frequency noise components, at $f_N << f_0$, of $a_N(t)$ and $\varphi_N(t)$ are most important because they appear at $f_0 \pm f_N$ in the output spectrum of the oscillator, and form the "close to carrier" noise.

In most commercial applications where these devices are used as timing or frequency references, the amplitude noise $a_N(t)$ can be ignored. As can be seen from (1), the amplitude noise by itself does not affect the temporal position of the zero crossings of the

[1] Current address – BOSCH Research and Technology Centre, Palo Alto, CA

signal where all the useful timing information is situated. Phase noise $\varphi_N(t)$, on the other hand, affects only the zero crossings and is hence a measure for the frequency stability of the oscillator. Therefore, it is hence more relevant for timing and frequency reference applications. Additionally, amplitude noise can be removed, if needed, using simple amplitude saturation or hard limiting of the oscillator output to remove amplitude fluctuations, followed by filtering to remove the harmonics. Such a practical method is not available for removing phase noise.

Because MEMS resonators have low intrinsic power handling compared to quartz they almost always need to be operated close to their nonlinear limits [3, 5, 6]. At such high amplitudes the *A-f* effect becomes even more important. It is hence important to design the sustaining circuit with stable amplitude at the input of the resonator. In most cases this can be achieved by limiting the amplitude of the AC voltage using a feedback loop and a variable gain amplifier (VGA) or hard limiting with something similar to a comparator.

AMPLITUDE-FREQUENCY DEPENDENCE OR *A-f* EFFECT

It is widely mentioned in quartz literature that the *A-f* and related effects limit the usable amplitude of resonator vibration [4, 10], defining the maximum signal strength available. In this section, we give a mathematical description of this effect in MEMS resonators. These models quantitatively describe the nonlinear distortion of the resonator response [3, 5], thereby providing an important design objective.

Since the dominant nonlinearities in these devices are of 2nd and 3rd order in the restoring force, the amplitude-frequency relationship will exhibit a parabolic dependence for high *Q* resonators [11]. Ignoring thermal effects this can be represented by

$$\frac{\Delta f}{f_0} = \kappa I_d^{\,2} \tag{2}$$

where I_d is the r.m.s. drive current through the resonator and κ is called the *A-f* coefficient, consistent with quartz terminology.

MEMS resonators exhibit two kinds of nonlinearities – electrical softening and mechanical stiffening [3, 5]. Quartz exhibits only stiffening type nonlinearities. At low DC bias voltages, the capacitive forces are weaker and the dominant nonlinearities occur due to geometrical and material effects at large displacements/strains. This causes mechanically induced stiffening type *A-f* effect. At higher bias voltages the capacitive forces become stronger and hence the electrostatic nonlinearities become dominant. This causes electrically induced softening *A-f* effect.

Mechanical nonlinearities are similar to the kind seen in quartz [4], where the resonator response *bends* toward the higher frequency side. This is caused by mechanical stiffening of the effective spring constant at higher amplitudes. This effect is shown in Figure 2(a). The device used for this measurement was fabricated using the epi-seal encapsulation process as discussed in [12].

We can express the mechanical nonlinearity terms in the system by looking at the higher order components in the mechanical restoring (or spring) force, given by

$$F_{spring} = -k_1 x - k_3 x^3 \tag{3}$$

where k_1 is the linear spring constant, k_3 is the 3rd order force nonlinearity component and x is the beam displacement. The 2nd order nonlinearity component has been ignored due to symmetry of the structure. The negative sign here indicates the restoring nature of the force. For this system the mechanical *A-f* coefficient is given by [5, 11]

$$\kappa_m = \frac{3k_3 d^4}{4m\omega_0^4 \varepsilon^2 A^2 V_{Bias}^2} \tag{4}$$

where d is the electrostatic gap size, m is the effective mass of the structure, ω_0 is the angular frequency, A is the area of transduction capacitance, and V_{Bias} is the DC bias voltage on the structure. This effect may not be observed in devices with low *Q* or very small gap size. This is because under these conditions the amplitude of oscillation required for getting an amplitude based frequency shift comparable to the bandwidth of the resonator becomes a larger fraction of the electrostatic gap size. The system cannot be modeled with 2nd and 3rd order nonlinearities alone in this case, and higher electrostatic nonlinearities start to have an impact. These electrostatic nonlinearities are always of the softening type, making the mechanical stiffening effect impossible to observe.

Electrical nonlinearities make the effective stiffness of the device smaller at high amplitudes, leading to a resonator response that progressively bends towards the lower frequency side as we increase the drive current. Figure 2(b) illustrates this effect. The nonlinearities in the electrostatic forces are due to the change in the gap size as the resonator vibrates. This can be accurately modeled by looking at the higher order Taylor coefficients of the expression for the force between the plates of a capacitor. Using the third order nonlinearity term, the electrical *A-f* coefficient becomes [5, 11]

$$\kappa_e = -\frac{1}{2m\omega_0^4 \varepsilon A d} \tag{5}$$

In this regime, κ is independent of the bias voltage. This effect should be observed at high bias voltages in almost every electrostatic MEMS resonator. It is also to be noted that the models presented up to this point are not specific to flexural designs but are valid for all types of electrostatic resonators.

STATIC MEASUREMENT OF *A-f* EFFECT

To measure the *A-f* coefficient using this method, we need to measure the frequency shift as a function of the drive current level, and extract the parabolic dependence coefficient. Figure 3 shows the peak frequency plotted against the peak activity for different regimes of operation in the resonators. The inset in this figure shows the distortion in the response as we change the drive level for this resonator. The device in this measurement is the same design as specified before, but fabricated using the oxide seal encapsulation process [13]. The device layer thickness was *20 μm* with an electrostatic gap size of *~ 2 μm*.

DYNAMIC MEASUREMENT OF *A-f* EFFECT

An alternative way of measuring the *A-f* coefficient is using dynamic measurements, a technique also used in quartz crystal resonators [14]. In this method we connect the resonator in a self oscillating circuit and modulate the amplitude of the voltage input to the resonator at several test frequencies ($f_N << f_0$), looking for phase perturbations in the oscillator output.

This technique has several advantages. First, it can be used to isolate the thermally induced frequency shift effect from the nonlinear effect to make a more accurate measurement of the nonlinear properties. Second, since this is a small perturbation experiment, we can verify whether the impact of random amplitude perturbations in the real system can be completely explained from this nonlinear effect. This is so, because these forced small amplitude perturbations emulate the random amplitude perturbations that would be present in a real oscillator more accurately. Finally, since this measurement is done on an oscillator

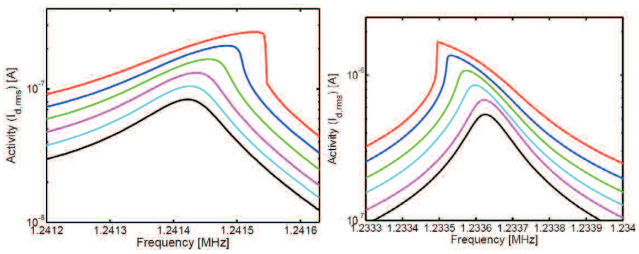

***Figure 2**. Measured A-f effect in a DETF MEMS resonator. The plots show activity (I_{drive}) as a function of frequency at a) low bias voltage (13V) showing mechanical nonlinearities and b) at high bias voltage (60V), showing electrical nonlinearities.*

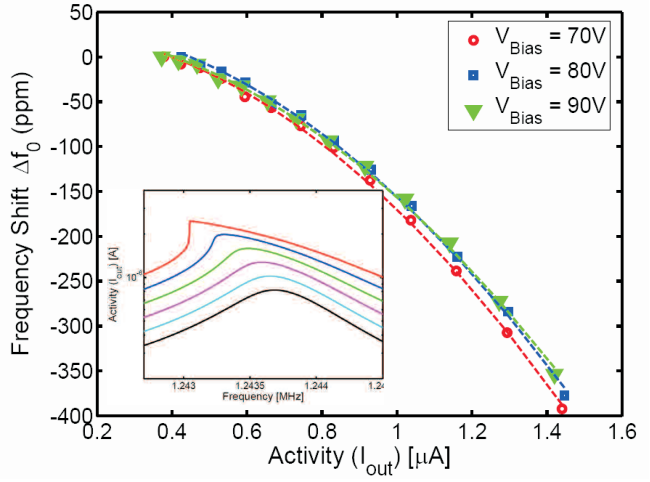

***Figure 3**. Static measurement of the electrical A-f coefficient. The plot shows the peak frequency as a function of the peak output current at different bias voltages. The dashed lines are parabolic fits. It can be seen that a very good match of dependence is observed with the model developed in equation (2). Also, as predicted by equation (5), we find that the κ for the resonator remains independent of bias voltage. The inset shows resonator frequency responses with different activity levels at V_{Bias}=70V.*

rather than a resonator, the measurement includes the effects of any circuit non-idealities (like phase error) that may be present. Hence it can be used to provide a figure of merit for the complete oscillator circuit. Figure 4 shows a schematic of the oscillator circuit used for this measurement and a picture of the PCB fabricated for this circuit.

Without amplitude modulation at the input, the output frequency spectrum of the oscillator would be a single peak at the resonant frequency. However, when we introduce amplitude modulation at the input at a frequency f_N we see side-peaks at $f_0 \pm f_N$ as shown in Figure 5.

The phase information of the sidepeak is not available in this measurement. This means that the "Amplitude Noise (AN) – Phase Noise (PN)" sidepeak could also be "PN – AN" depending on the relative magnitudes. Hence, in order to extract the phase perturbation component we look at both, the sum and difference of the side-peak levels. A more precise method to do this is to use a phase bridge as described in [14]. An extracted phase perturbation level plot is shown in figure 6. It should be noted that this graph does not plot the inherent random phase noise level of the oscillator. This is the phase perturbation level due to the controlled

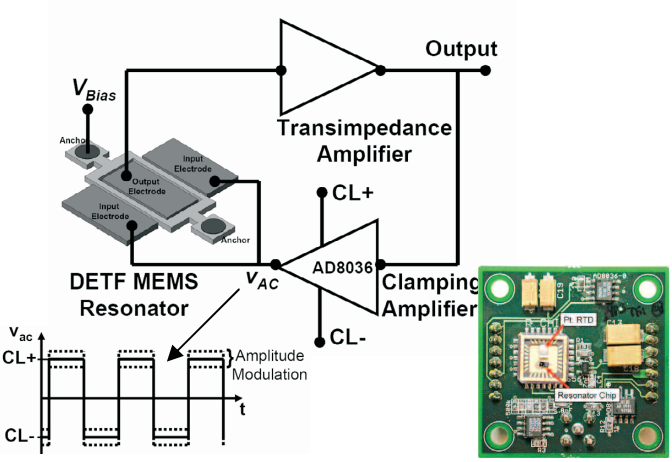

***Figure 4**. Circuit schematic and PCB of the oscillator. The AD8036 is a clamping amplifier that limits the peak levels of v_{AC} to CL+ and CL-. Amplitude modulation of the resonator driving current was achieved by superposing a small sinusoidal signal on the CL+ and CL- voltage levels using simple bias tees.*

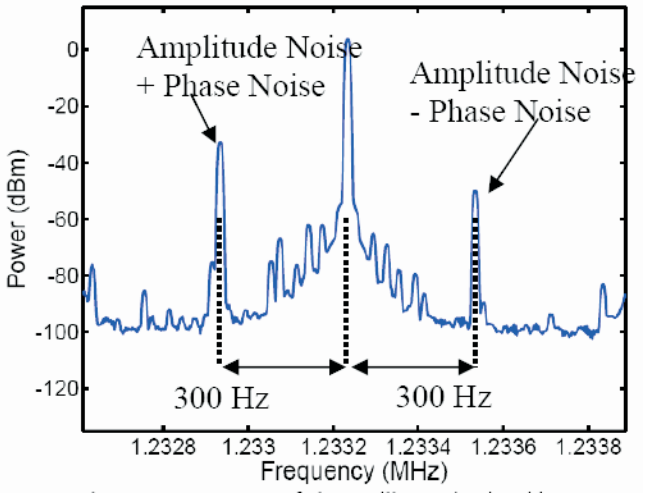

***Figure 5**. Output spectrum of the oscillator with the resonator input having amplitude modulation at 300 Hz. In this case where κ is negative, the low frequency sideband can be shown to be the sum of amplitude and phase perturbations and the higher frequency sideband is the difference of amplitude and phase perturbations. The inequality of sidebands confirms that amplitude perturbations in the input cause phase perturbations, or that amplitude noise is converted to phase noise due to the A-f effect.*

amplitude modulation at the input, which is much higher than the inherent random phase noise of the oscillator. Close-to-carrier perturbation exhibits $1/f^2$ behavior which represents a constant frequency perturbation at the modulation frequency. We can estimate the κ of the device from the relative strength of the side-peak level $L(f_m)$ in *dBc*, by

$$L(f_m) = 20\log\left(\frac{f_0 \kappa I_d \Delta I_d}{f_m}\right) \qquad (6)$$

where f_m is the amplitude modulation frequency. In this equation, if ΔI_d is replaced by the random amplitude noise in the drive current, we will obtain the phase random noise in the system. The extracted value of κ from the dynamic measurements and comparison with static measurements are shown in Figure 7.

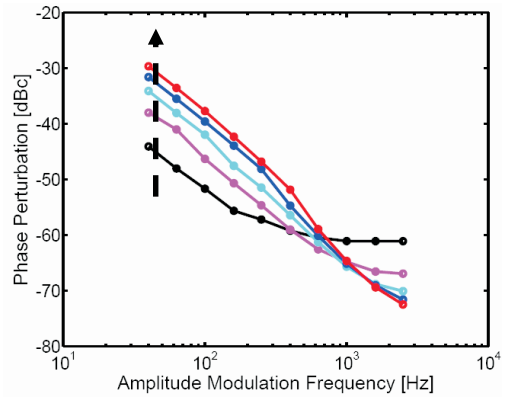

Figure 6. *Phase perturbation levels extracted from the sidepeak levels in the output spectrum (Figure. 5). The $1/f^2$ behavior close to the carrier can be observed from this plot, consistent with the model, as shown in (6). The different curves represent the phase perturbation levels at different input AC voltages from 0.1 V_p to 0.5 V_p with a constant modulation voltage of 9 mV superposed on it. The arrow points in the direction of measurements obtained for increasing input AC voltages.*

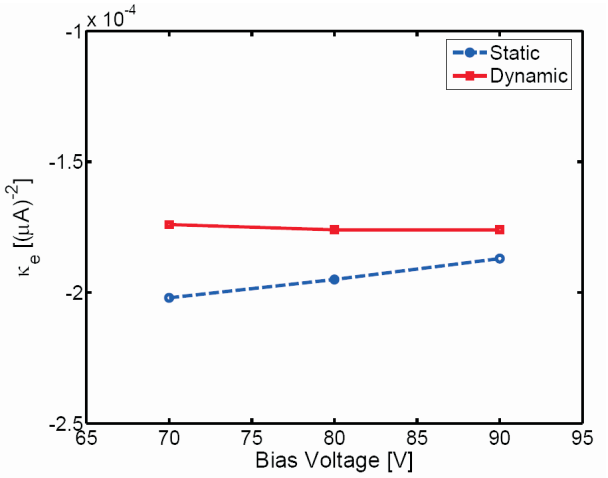

Figure 7. *Comparison of κ from different measurements.*

DISCUSSION

We found that the *A-f* coefficient of the DETF MEMS resonator considered here is very large. This is representative of its power handling capability, and such high numbers suggest that the sustainable drive current is merely on the order of μA, even with a Q of the order or 10^4, as found in [5]. By comparison, a 5-MHz quartz AT cut crystal has $\kappa \sim 10^{-13}/(\mu A)^2$ [4] which is about 9 orders of magnitude lower than MEMS ($\kappa \sim 10^{-4}/(\mu A)^2$). Hence, quartz crystals can sustain drive currents of several mA even though the quality factor is comparatively high, about 10^6.

As can be seen in equations (4) and (5), the κ coefficient in MEMS resonators should decrease considerably as we go to higher frequencies (ω_0). For instance, a 100-MHz resonator built on a similar process could have its *A-f* coefficient within approximately an order of magnitude of quartz ($\kappa \sim 10^{-13}/(\mu A)^2$ for a 100-MHz, AT cut quartz [4]). However, higher frequency structures tend to be stiffer and need smaller gap sizes for their operation, which would mildly counteract the benefit from higher ω_0.

CONCLUSIONS

In this work, we demonstrated that amplitude noise in the studied oscillator induces phase noise in presence of the nonlinear *A-f* effect. A model for the *A-f* effect was derived and both static and dynamic measurements on a double ended tuning fork resonator were presented for verification.

It was also observed that the *A-f* effect in our MEMS test structure was much stronger than in quartz crystals. We conjecture that this disadvantage will be less pronounced in higher frequency resonators.

ACKNOWLEDGEMENTS

This work was supported by DARPA HERMIT (ONR N66001-03-1-8942), and The National Nanofabrication Users Network facilities funded by the National Science Foundation under award ECS-9731294, and The National Science Foundation Instrumentation for Materials Research Program (DMR 9504099).

We also thank Dr. John R. Vig, Dr. David A. Howe and Prof. David B. Leeson for their useful inputs on the subject of nonlinearities in oscillators.

REFERENCES

[1] C. T.-C. Nguyen, "Vibrating RF MEMS technology: fuel for an integrated micromechanical circuit revolution?," presented at TRANSDUCERS, 2005.

[2] Y.-W. Lin et al., "Low phase noise array-composite micromechanical wine-glass disk oscillator," presented at IEDM, 2005.

[3] V. Kaajakari et al., "Nonlinear limits for single-crystal silicon microresonators," *JMEMS,* vol. 13, pp. 715-724, 2004.

[4] J. J. Gagnepain, "Nonlinear Properties of Quartz Crystal and Quartz Resonators: A Review," presented at the Frequency Control Symposium, 1981.

[5] M. Agarwal et al., "Non-Linearity Cancellation in MEMS Resonators for Improved Power-Handling," presented at IEDM'05.

[6] S. Lee et al., "Influence of automatic level control on micromechanical resonator oscillator phase noise," presented at the Frequency Control Symposium, 2003.

[7] S. Lee et al., "Phase noise amplitude dependence in self limiting wine-glass disk oscillators.," presented at Hilton Head, 2004.

[8] V. Kaajakari et al., "Phase noise in capacitively coupled micromechanical oscillators," *IEEE Trans. Ultrasonics, Ferro-electrics and Frequency Control*, vol. 52, pp. 2322-2331, 2005.

[9] T. H. Lee, *The Design of CMOS Radio Frequency Integrated Circuits*, 2nd ed. New York, USA: Cambridge University Press, 2004, pp. 664-667.

[10] M. Planat et al., "Nonlinear Characteristics of SAW Grooved Resonators," presented at the Ultrasonics Symposium, 1980.

[11] L. D. Landau and E. M. Lifshitz, "Resonance in non-linear oscillations," in *Mechanics*, vol. 1, *Course of Theoretical Physics*, 3 ed. Reading, MA: Butterworth-Heinemann, 1982, pp. 87-92.

[12] R. N. Candler et al., "Hydrogen diffusion and pressure control of encapsulated MEMS resonators," presented at TRANSDUCERS, 2005.

[13] R. N. Candler et al., "Single wafer encapsulation of MEMS devices," *IEEE Trans. Advanced Packaging*, vol. 26, pp. 227-232, 2003.

[14] M. Planat et al., "Non-linear Propagation of Surface Acoustic Waves on Quartz," presented at Frequency Control Symposium, 1980.

FAST, MEMS-BASED, PHASE-SHIFTING INTERFEROMETER

Hyuck Choo[1], Rishi Kant[2], David Garmire[1], James Demmel[1], and Richard S. Muller[1]
[1]*Berkeley Sensor & Actuator Center, University of California, Berkeley, CA USA*
[2]*Department of Electrical Engineering, Stanford University, Stanford, CA USA*

ABSTRACT

We demonstrate a MEMS-based, phase-shifting interferometer (MBPSI) that is much faster than conventional phase-shifting interferometers (PSI). For phase shifting, our system employs a comb-driven vertically resonating micromachined mirror illuminated by synchronized laser pulses (λ=660nm). Our MBPSI employs a four-frame phase-shifting technique (four CMOS-imager frames per one profile measurement), at a rate of 23 profile measurements-per-second (23Hz, 43.5msec per measurement). At this rate, the MBPSI can continuously capture more than 500 profile measurements of a transient phenomenon over 21.7 seconds. The MBPSI in Twyman-Green configuration has accurately tracked in real time the fast-changing, transient motion of a PZT actuator, within ±λ/110 (±6nm).

INTRODUCTION

PSIs are desired for precision measurements of moving objects, and increasing the PSI data-collection rate makes it possible to observe faster motions. Our MBPSI system can capture 500 or more profile measurements of a transient phenomenon continuously at a rate of 23 Hz. Besides sizably expanding the range of PSI applications (for example, to transient optical phenomena such as chemical diffusion, crystal growth, and measurements of rapidly varying object temperatures [**1-2**]), the MBPSI's rapid measurement rate reduces the data noisiness caused by low-frequency vibrations. Batch-fabricated, MEMS phase-shifting components are not only faster, but also much more cost-effective to fabricate and operate than are the piezoelectric actuators that are now typical in PSI systems.

FAST PHASE-SHIFTING METHOD

Our phase-shifting technique (illustrated in Figure 1) is, in principle, similar to that used to obtain a stroboscopic movie of a periodically moving object.

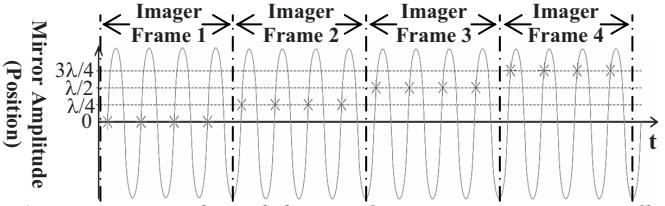

Figure 1. *Fast phase-shifting technique using our vertically resonating micromirror and a pulsed laser diode: '✳' indicates when the laser pulse is flashed. In this example, there are four phase steps; each frame of the CMOS imager integrates images generated by four laser pulses flashed for each phase step.*

In the MBPSI, we obtain stable interference patterns using a periodically moving mirror and synchronized laser pulses. The interference patterns corresponding to 0, λ/4, λ/2, and 3λ/4 phase shifts are captured in the CMOS-imager frames 1, 2, 3, and 4, respectively [**3**]. In each frame, while driving a MEMS mirror at its resonant frequency, we pulse the laser diode when the mirror is displaced by the desired fraction of the illuminating wavelength from its initial position. Because the integrating-bucket technique for CMOS imagers requires that the movement of the phase shifter be linear [**3**], we use the linear region of the mirror's resonant motion, which is in the beginning of each period, as shown in Figures 1 and 5. When using this technique, the maximum profile-measurement rate is equal to the CMOS-imager frame rate (fps) divided by the number of phase steps required.

MEMS PHASE-SHIFTING MIRROR: FABRICATION AND CHARACTERIZATION

The phase-shifting mirror measures 5 by 5 by 0.05 mm and is micromachined using a fabrication method that we have described earlier [**4**] and applied to produce high-precision torsional microscanners (Figure 2).

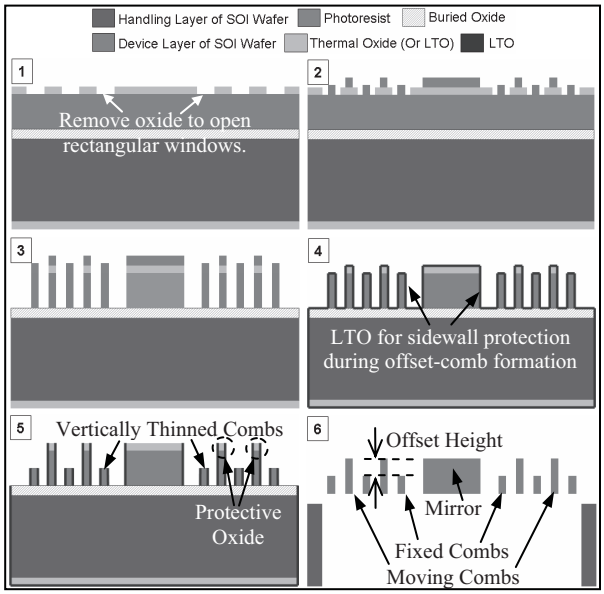

Figure 2. *Fabrication Process: The left column shows top views while the right column shows cross-sectional views along the dotted lines in our CMOS-compatible mirror-fabrication process.* ***1.*** *Grow 0.5-μm thermal or low-temperature oxide (LTO). Using the photolithography mask #1, pattern and remove the thermal oxide selectively where fixed combs will be later fabricated;* ***2.*** *Using mask #2, create patterns of micromirror including moving and fixed combs, flexures, and mirrors;* ***3.*** *Use deep-reactive-ion-etch (DRIE) to define the micromirror in the device layer;* ***4.*** *Remove the photoresist layer and deposit a very thin layer (~0.2 μm) of LTO;* ***5.*** *Use timed-anisotropic-plasma etch to remove 0.2-μm thick LTO from the top-facing surfaces. Then use timed-anisotropic or isotropic silicon-etch to create a set of vertically thinned combs; and* ***6.*** *Using mask #3, pattern and open the backside of the micromirror. Release the devices in HF and perform critical-point drying.*

A new feature of our mirror design for the MBPSI is the incorporation of stress-relieving beams which improve the flatness of the mirror (Figures 3 and 4). We have measured the surface profile of a representative mirror (of more than 100 that we have produced) using a WYKO NT3300 (Figure 3) and determined that its radius of curvature exceeds 20m, and its surface-roughness values do not exceed 20nm. In order to time the laser pulses precisely, the mirror resonance has been analyzed using a piezo-based, calibrated stroboscopic interferometer (Figure 5) [**5**]. The

measured resonant frequency and mechanical quality factor of the mirror are 3.55 kHz and 63, respectively. When the mirror achieves a resonant amplitude of 1.5μm (actuation voltage=18$V_{ac_p\text{-}to\text{-}p}$), the pulses (1-μsec duration) for 0, λ/4, λ/2, and 3λ/4 (λ=660nm) occur at intervals of 0, 10, 20, and 30μsec (Figure 5). Dynamic deformation of the mirror, between the center and the four corners of the mirror, within this linear region of operation, is less than 6nm (λ/110) (Figure 5).

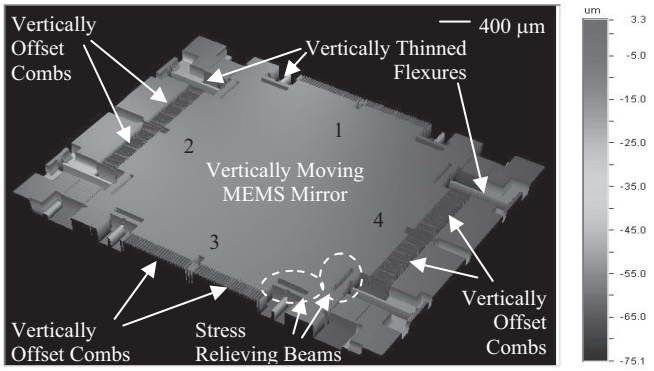

Figure 3. *WYKO profile measurement of fabricated MEMS mirror*

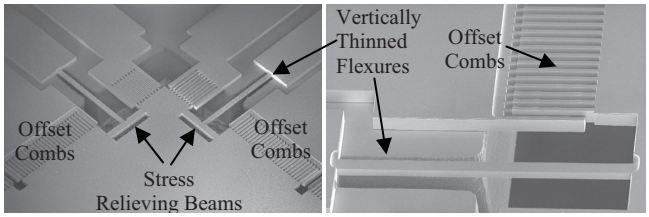

Figure 4. *SEM images showing the key sections of the phase-shifting MEMS mirror*

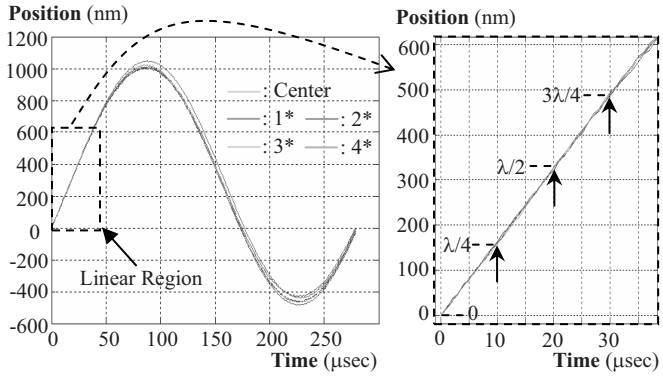

Figure 5 *Resonant-motion analysis for our phase-shifting MEMS mirror using calibrated laboratory Stroboscopic Interferometer – Left: One full period of resonant motion, with the linear region indicated by the red rectangle, Right: Linear region used for phase-shifting (peak-to-peak deviation in position: < 6 nm) (*1-4: Please refer to Figure 3.)*

OPTICAL MEASUREMENT RESULTS OF MBPSI

The MBPSI in Twyman-Green configuration (Figure 6) has tracked in real time the fast-changing, transient motion of a PZT actuator [**6**]. The actuator was stepped at intervals of 100 nm every 0.5sec over a 6.478-sec period (150 profile measurements, Figure 7). The maximum frame rate of our CMOS-imager is 100 fps. We ran the imager at a conservative 92 fps, reflecting a 23 Hz profile-measurement rate. The transient measurement was precise to within ±6nm (±λ/110), lower than the 10nm-accuracy limit of the PZT-actuator movement (from the readings of the PZT's built-in feedback position sensor), as shown in Figure 7.

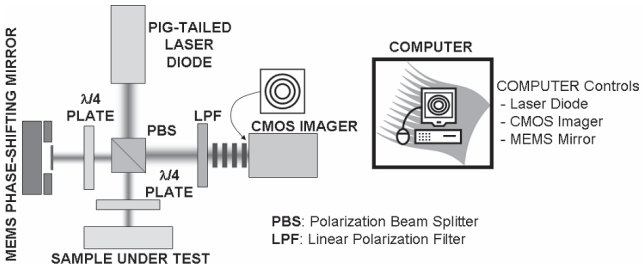

Figure 6 *MBPSI optical test setup (Twyman-Green configuration)*

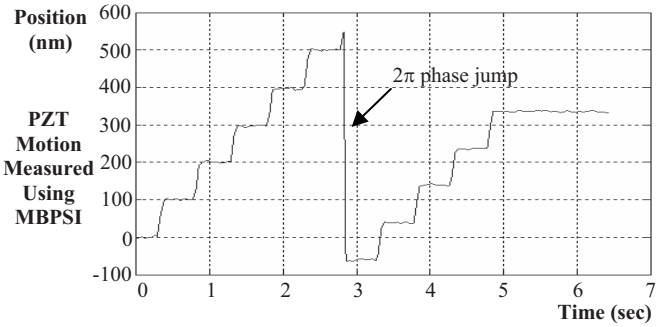

Figure 7 *Section of a total 150 measurements made with our MBPSI system showing a PZT actuator moving at a step of 100nm every 0.5 seconds during the 6.478-second period (PZT movement resolution: <±10nm from the readings of the PZT built-in feedback position sensor)*

CONCLUSIONS

We have demonstrated a fast, accurate, MEMS-based PSI, which can continuously measure transient optical phenomena at 23Hz. We plan to report long-term repeatability, analysis for the effects of various error/noise sources, performance in the presence of mechanical vibrations, and new application(s) in our presentation.

ACKNOWLEDGEMENT

The authors thank Prof. J. Bokor of UC Berkeley and Prof. C. R. Pollock of Cornell University for helpful discussions on interferometry techniques and optical fiber properties. We also thank the National Science Foundation for generously funding our research (NSF EEC0318642 and CITRIS NSF TR22325).

REFERENCES

[1] K. Onuma, K. Tsukamoto, and S. Nakadate, "Application of real-time phase shift interferometer to the measurement of concentration field," J. of Crystal Growth, vol. 129, 1993, pp. 706-718

[2] P. V. Farrell, G. S. Springer, and C. M. Vest, "Heterodyne holographic interferometry- Concentration and temperature measurements in gas mixtures," Applied Optics, vol. 21, no. 9, May 1982, pp.1624-7, USA

[3] D. Malacara, Ed., "Optical Shop Testing," 2nd Edition, Chap. 14, New York: Wiley, 1992, USA

[4] H. Choo, D. Garmire, J. Demmel, and R. S. Muller, "A Simple Process to Fabricate Self-Aligned, High-Performance Torsional Microscanners: Demonstrated Use in a Two-Dimensional Scanner," 2005 IEEE/LEOS International Conference on Optical MEMS and Their Applications, August 1-4, 2005, pp.21-22, Oulu, Finland

[5] M. R. Hart, R. A. Conant, K. Y. Lau, and R. S. Muller, "Stroboscopic Interferometer System for Dynamic MEMS Characterization," J. MEMS, vol. 9, no. 4, December 2000, pp. 409-418, USA

[6] PZT Actuator: PI P-753 LISA, PZT Controller: PI E-501

ADVANCED MEMS SPATIAL LIGHT MODULATOR FOR COMMUNICATIONS, IMAGING, AND TARGETING

Flavio Pardo, M.E. Simon, V.A. Aksyuk, W.Y-C. Lai, C.S. Pai, F.P. Klemens, J.F. Miner, R.A. Cirelli, E.J. Ferry, J.E. Bower, W.M. Mansfield, A. Kornblit, T.W. Sorsch, J.A. Taylor, M.R. Baker, R. Fullowan, H. Dyson, A. Gasparyan, and S. Arney

Bell Labs Lucent Technologies, Murray Hill, NJ USA

ABSTRACT

64x64 arrays of electrostatically actuated piston-tip-tilt micromirrors are realized using a surface micromachining, 3-structural-layer polysilicon process. Flat mirrors (λ/30 @1550nm wavelength) 120µm in size and fill factor exceeding 98% have mechanical resonance frequencies of 30KHz for both tip-tilt and piston motion, with +/- 4 deg. mechanical tip and tilt and 5µm piston continuous, controllable range under 110V. The design implements four dual, rotational, in-plane, deep comb drives under each mirror, with 0.5 µm critical features.

INTRODUCTION

High speed and high-resolution, ASIC-integrated spatial light modulators (SLM) based on optical MEMS are enabling components for communications, imaging and targeting applications which require precise real-time control of the optical beam's wavefront to achieve maximal, aberration-free performance. State-of-the-art segmented SLMs are currently limited to about 32x32-mirror fast piston-only arrays [**1-2**], lower pixel count piston-tip-tilt [**3**], or lower range piston or tilt, 200x240 metal mirror arrays [**4**]. The combination of piston-tip-tilt in each mirror would improve considerably the phase-reconstruction fidelity [**5**]. The ultimate specs for such SLMs include high-pixel-count arrays of flat mirrors with 3 degrees of freedom -piston, tip and tilt- with continuous, large displacements and fast response time. The combination of all these characteristics makes the MEMS design and process implementation a formidable challenge. Furthermore, the scalable integration (64x64 and larger arrays) with driving electronics puts a severe limit to the maximum available driving voltage and hence, to the maximum mechanical power that could be achieved in simple, parallel-plate actuators, thus limiting the speed and the range of motion.

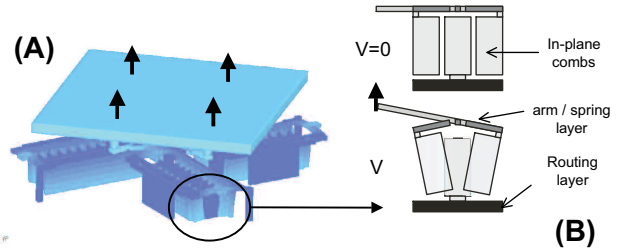

FIGURE 1. Simulation image showing all four dual rotational in-plane comb-drives actuated to produce upward piston motion (A) Schematic of the actuation principle (B).

MICROMIRROR DESIGN AND PERFORMANCE

The design solution to the parallel-plate actuator limitations is to exploit the third dimension: deep, dense, in-plane comb-drive actuators. Our basic design is presented in Figure **1**. It consists of four dual, rotational, in-plane comb drives, each attached to an arm that rotates out of plane. A flexible joint at the end of each arm attaches to the mirror, allowing 3 independent degrees of freedom of motion: bi-directional tip-tilt, and upward piston. The actuators are densely packed under a high fill factor mirror array.

Figure **2** shows a SEM picture of the finished device characteristics, e.g., the actuators under the mirrosr, back of the

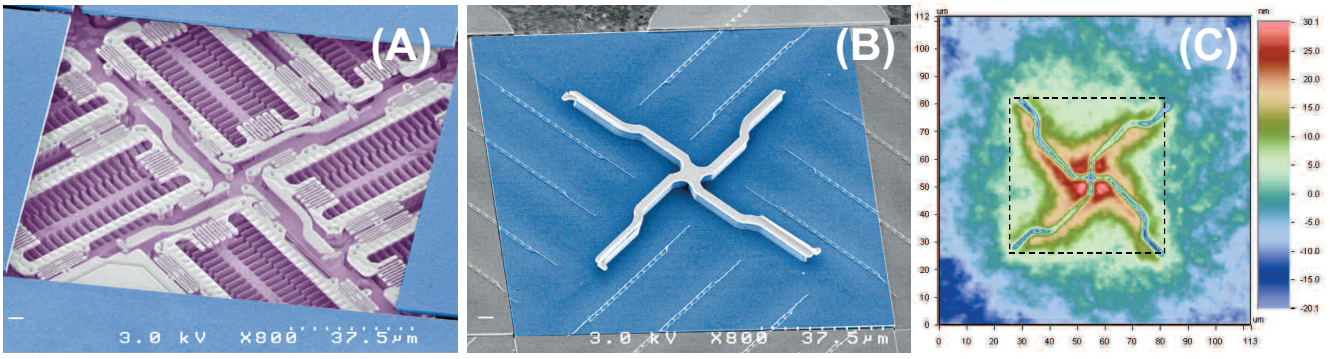

FIGURE 2. SEM image of a finished device (A) showing the four actuators under the mirror and (B) back of the monolithic mirror showing the 4µm thick X-shaped strengthening member created by a trench in the sacrificial silicon oxide under it. (C) Interferometer data showing mirror planarity and roughness. Most of the 50nm peak-to-peak topography comes from the non-optimized trench filling process within the central region. The RMS roughness is 8nm including the strut print-through and less than 2nm without it. The 1.5µm-thick mirror has been metalized with 40Å Ti / 400Å Au

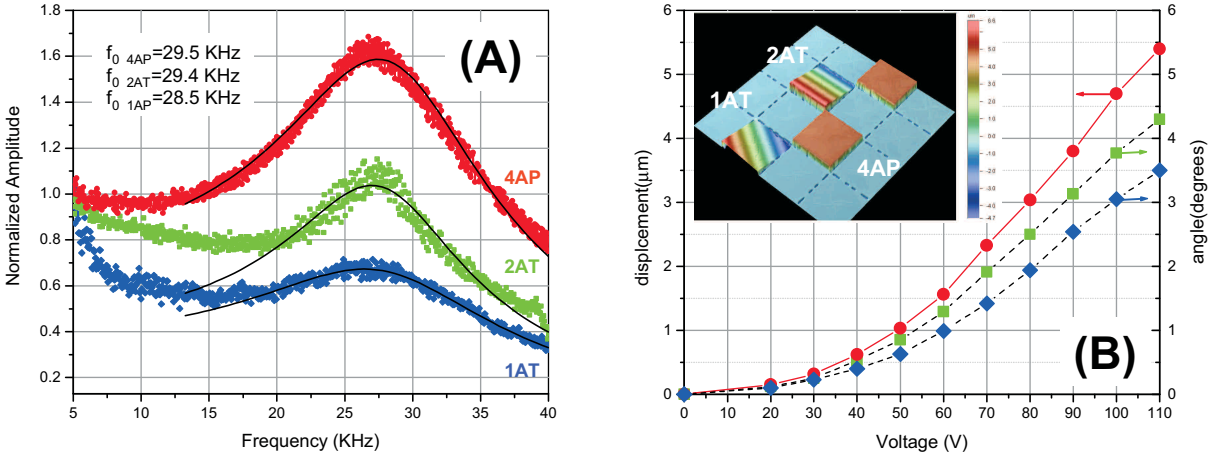

FIGURE 3. (A) Mechanical response of individual mirrors for 60-90V-amplitude tip and piston motion. Experimental data and fitting to driven harmonic system behavior. From the fitting natural frequencies at about 30kHz are extracted. The responses have a quality factor Q~2 at atmospheric pressure, with roll-offs at around 27KHz. (B) Piston and angular displacement versus voltage. Piston is achieved by actuation of all 4 actuators (4AP ●). Diagonal tilt (1AT ◆) is a one-actuator motion, horizontal or vertical tilt is a two-actuator motion (2AT ■).The inset shows interferometer data for all three actuation modes.

mirror, and front-of-mirror planarity.

Typical dimensions for the most relevant surface-micromachined polysilicon structural layers are: combs 6μm tall with 0.5μm wide fingers, spring-arm layer thickness of 1-1.5μm with 0.5μm features, and a 1-2μm thick mirror with 0.5-2μm lateral gaps. Low stress silicon dioxide with thickness ranging from 2 to 4μm forms the sacrificial layers between structural layers, for a combined film stack of up to 17μm. A critical step in the fabrication is the silicon dioxide filling and planarization of the high-aspect-ratio combs, achieved by a controlled etch-back, re-deposition step and chemical-mechanical polishing (CMP). The final polysilicon layer forming the mirror is also partially planarized by a CMP touch-up to achieve a flat, smooth surface. The structures are released in vapor-phase-HF or in liquid HF (49%) and subsequently dried in a supercritical point CO_2 system. A blanket 40Å Ti / 400Å Au reflective layer evaporation completes the device. After these steps typically only 1 or 2 mirrors have been observed optically to be stuck or damaged, out of the 4096 in early implementation of the process.

This novel design has been implemented for both 64x64 and 256x256 array sizes in a 10-mask process using 248nm stepper optical lithography, which provides uniform exposure of sub-micron features across the array. Special care has been taken in the design of alignment features throughout the process flow to guarantee alignment accuracy better than 100nm between all layers.

This structure is currently being monolithically fabricated on a wafer with Through-Wafer-Vias (TWV) to provide electrical connection to the driving electronics chip (to be presented elsewhere). Results presented here were obtained in a hard-wired system, with an extra wiring layer replacing the TWVs and grouping the mirrors in clusters of up to 64 elements.

Figure **3** shows the mechanical response of fabricated devices. The resonance curves were fitted to a driven oscillator model in the peak region to extract resonance frequencies of about 30kHz and Q~2 for all three degrees of freedom, very close to the FEA simulated values of 29.6KHz for tilt and 30.9 KHz for piston. The lower frequency roll-offs are due to frequency-dependent damping processes and will require further analysis. Note also the slight inflection point in the angle/displacement versus voltage curves showing a sub-quadratic behavior, a result of the onset of partial disengagement in the rotational comb-drives.

CONCLUSIONS

We have presented an integration-ready, scalable MEMS SLM mirror array. This work demonstrates a level of complexity never achieved before in terms of the combination of the number of degrees of freedom per chip, pixel speed, controlled motion range and optical quality. Within this MEMS process platform, simulations show that we can achieve 256x256 arrays with a spec of 10μs response time by increasing the spring stiffness (spring layer ~2μm) and increasing the actuator comb force by fabricating deeper combs of 12μm, both well within our fabrication capabilities.

AKNOWLEDGMENTS

This material is based on work supported by DARPA's CCIT program under contract Number HR0011-04-C-0048 and approved for Public Release, Distribution Unlimited.

REFERENCES

[1] "High Resolution Wavefront Control Using Micromirror Arrays", *Technical Digest of the 2004 Solid-State Sensor, Actuator and Microsystems Workshop, Hilton Head Island, SC, June 6-10, 2004*

[2] T. G. Bifano and J. B. Stewart, "High-speed wavefront control using MEMS micromirrors" *Proceedings SPIE*, 5895 (2005)

[3] J. B. Stewart, T. G. Bifano, P. Bierden, S. Corneliss, T. Cook, B. M. Levine, "Design and development of a 329-segment tip-tilt piston mirror array for space-based adaptive optics" *presented at Photonics West, San Jose, CA, January, 2006*

[4] A. Gehner, M. Wildenhain, H. Neumann, A. Elgner and H. Schenk. "MEMS Phase Former Kit for High-Resolution Wavefront Control", *Proceedings SPIE 5894 (2005).*

[5] F. Roddier, "Adaptive Optics in Astronomy" Cambridge University Press, 1999.

PROXIMITY MODE INCLINED UV LITHOGRAPHY

Yong-Kyu Yoon and Mark G. Allen
School of Electrical and Computer Engineering
Georgia Institute of Technology
Atlanta, GA 30332

ABSTRACT

Proximity mode inclined UV lithography is a fabrication approach enabling the single-mask realization of solid and hollow three-dimensional microstructures of unusual shapes. Expanding upon previous inclined exposure approaches, a defined gap between the photomask and the substrate adds an additional degree of freedom to generate different ray trace patterns in the photoresist layer. The proximity approach can be used with both front-side and reverse-side exposure approaches: the air gap is controlled by spacers with different thicknesses between the photomask and the substrate for front-side exposure, while UV transparent glass of known thickness on the substrate prior to photoresist deposition enables proximity reverse-side exposure. With continuously varying air gap spacing, nozzles with various orifice sizes of 0 μm to 255 μm, a height of 250 μm, a side wall tilting angle of 25°, a wall thickness of approximately 60 μm have been successfully fabricated using front-side exposure with an incident angle of 45° and 50 μm-diameter of clear circle mask patterns. A horn shape has been achieved by reverse-side inclined exposure using the same photomask patterns used in nozzle fabrication.

INTRODUCTION

Placement of photomasks in proximity to, rather than in contact with, the substrate has been widely used in standard UV lithography to prevent contamination or damage of the mask or the substrate **[1,2]** and for photoresist patterning on an uneven substrate **[3]**. In conventional proximity patterning, since the UV source is incident normal to the substrate, the transferred patterns follow the photomask image in shape, potentially with reduced resolution due to light diffraction at the edge of the pattern.

Recently, advanced UV lithography processes using SU-8 such as inclined exposure and reverse-side exposure have been reported for complex three-dimensional (3-D) fabrication **[4]**. When the inclined exposure technique is utilized in a rotational fashion, e.g. the substrate stage rotating during exposure, various patterns of revolution can be produced.

In this paper, the inclined rotational exposure process has been further advanced by exploiting the proximity scheme to generate unusual 3-D patterns, which are different from the original mask patterns. Since the proximity gap between the mask and the photoresist plays an essential role to determine the resultant 3-D image, the gap effects for 3-D patterning have been investigated. To demonstrate its versatility, tapered micronozzles and conical microhorns have been fabricated from front-side exposure and reverse-side exposure, respectively. Mathematical equations for resultant dimension as a function of gap and incident angle have been provided and compared with the fabricated results.

PROXIMITY MODE INCLINED UV LITHOGRAPHY

Two types of proximity modes are illustrated in Figure 1. Figure 1a shows an air gap inserted between the mask and the substrate for front-side exposure. The gap can be controlled by placing spacers of known thickness. A ray trace through a clear window with a diameter of d_m in the optical mask can generate a 3-D nozzle latent pattern of revolution in the SU-8 layer after inclined rotational exposure, while its geometrical dimensions can be determined by the incident angle θ_i, the refractive index of SU-8 $n_{SU\text{-}8}$($\cong$1.67 **[4]**), the thickness of the photoresist layer t, and the gap between the photomask and the substrate g, and are described as follows:

$$d_{oti}: \text{inner diameter of orifice tip} = 2*g/\tan\theta_i - d_m \quad (1)$$
$$d_{oto}: \text{outer diameter of orifice tip} = 2*g/\tan\theta_i + d_m \quad (2)$$
$$d_{ori}: \text{inner diameter of orifice root} = 2*g/\tan\theta_i - d_m + 2*t*\tan\theta_r \quad (3)$$
$$d_{oro}: \text{outer diameter of orifice root} = 2*g/\tan\theta_i + d_m + 2*t*\tan\theta_r \quad (4)$$
$$\theta_r: \text{refracted angle} = \sin^{-1}(\sin\theta_i * n_{air}/n_{SU\text{-}8}) \quad (5)$$

Proximity patterning can be implemented for reverse-side exposure by adding a known-thickness gap layer prior to SU-8 deposition as shown in Figure 1b, where both the substrate and the gap layer are UV transparent, e.g. glass. However, the gap layer is not limited to glass but can be UV-transparent polymer or ceramic. The substrate has a prepatterned metal layer for a photomask, having a clear open window. The resultant pattern after reverse-side inclined rotational exposure will produce a horn shape.

Figure 2 shows structures fabricated from the same photomask with 50 μm diameter clear window patterns: (a) a nozzle from front-side exposure, (b) a horn array with the lower portion truncated by the gap layer from reverse-side exposure, (c) a horn with a central column fabricated from additional vertical exposure after reverse-side inclined rotational exposure using the same mask.

As a reference, the contact mode structures are shown in Figure 3: (a) a closed top conical shape from front exposure, (b) a horn from reverse-side exposure, and (c) a multi-layer horn with various exposure angles from reverse-side exposure. The tips of the microcones or microhorns are the same size as the mask pattern.

MICRONOZZLE ARRAY

By implementing continuously varying air gaps between the photomask and the substrate, a micronozzle array with different orifice sizes can be simultaneously formed as shown in Figure 4. The gap of the leftmost side is set to zero and that of the rightmost side has a spacer with a thickness of approximately 500 μm. The gap g is a function of the distance x from the leftmost side. Since the mask width is 1" (=25.4mm), the gap is described as a function of the distance:

$$g = 0.5x/25.4 \cong 0.02x \quad (6)$$

The mask tilting angle θ_m is approximately 2° and therefore the overall nozzle shape is not noticeably asymmetric due to the tilting gap. Figure 5 shows a fabricated micronozzle array with various orifice sizes. The inner and outer orifice diameters of the fabricated nozzles are calculated using Eq. (1) and (2), respectively and compared with the measured ones as shown in Figure 6. In the calculation, the nozzle width has been assumed to be the same as the original opening diameter d_m (50 μm) in the mask. Taking into account diffraction through the air gap, the resultant wall thickness could be widened as much as 1 ~ 30 μm in the air gap range utilized **[1]**, showing good agreement with the measurement results.

CONCLUSION

We demonstrate that incorporated with inclined rotational UV exposure, proximity lithography could produce solid and hollow structures of revolution such as a nozzle or horn structure from a single mask pattern. The proximity approach provides an additional process parameter, i.e. gap, in addition to inclined angle, refractive index of photoresist, and thickness of the photoresist of inclined rotational exposure, for the fabrication of 3-D microstructures. Both front-side and reverse-side exposure could exploit the gap effects by changing the air gap between the photomask and the substrate or by adding a gap layer between the mask layer and the photoresist. A nozzle array with various orifice sizes has been simultaneously obtained using a continuously varying gap. The fabricated micronozzles or microhorns may have potential for microfluidic, biomedical, or RF antenna applications.

ACKNOWLEDGEMENT

The authors would like to thank Mr. Seong-O Choi, Dr. Jung-Hwan Park, and Dr. Mark Prausnitz at Georgia Tech for their valuable discussion.

REFERENCES

1. C.G. Wilson, "Organic Resist Materials," *in Introduction to Microlithography, L.F. Thompson, C.G. Wilson, and M.J. Bowden, Eds.* Washington D.C.; American Chemical Society, 1994.
2. W. Henke, M. Weiss, R. Schwalm, and J. Pelka, "Simulation of proximity printing," *Microelectron. Eng.* vol. 10, pp 127-52, 1990.
3. Y.-K. Yoon, M.G. Allen, et al. "Surface Micromachined Electromagnetically Radiating RF MEMS," Solid State Sensor, Actuator, and Microsystems Workshop 2004, Hilton Head Island SC, pp. 328-331.
4. Y.-K. Yoon, J.-H. Park, and M.G. Allen, "Multidirectional UV lithography for complex 3-D MEMS Structures," *IEEE Journal of MEMS* (in press)

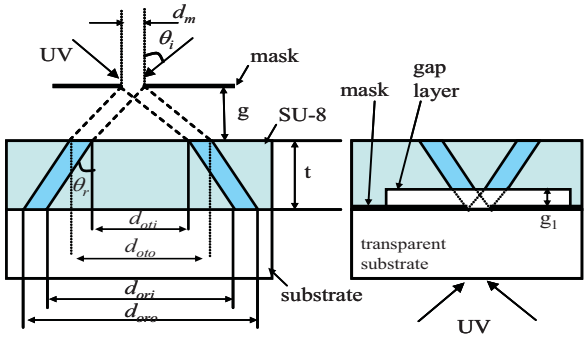

(a) (b)

Figure 1. *Proximity mode inclined UV lithography: (a) front-side exposure, (b) reverse-side exposure through a transparent substrate and a gap layer.*

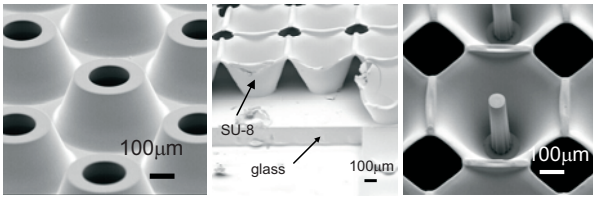

(a) (b) (c)

Figure 2. *Proximity mode inclined rotational UV lithography: (a) front-side exposure, (b) reverse-side exposure with a 200 μm thick glass gap, and (c) reverse-side exposure with a 200 μm glass gap and an additional vertical exposure for the central column*

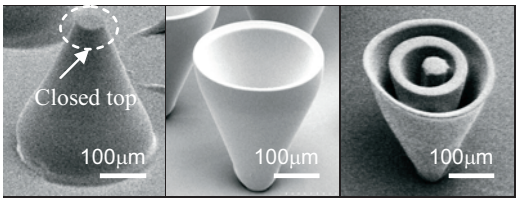

(a) (b) (c)

Figure 3. *Contact mode inclined rotational UV lithography: (a) front-side exposure, (b) reverse-side exposure, and (c) reverse-side exposure with multiple inclined angles*

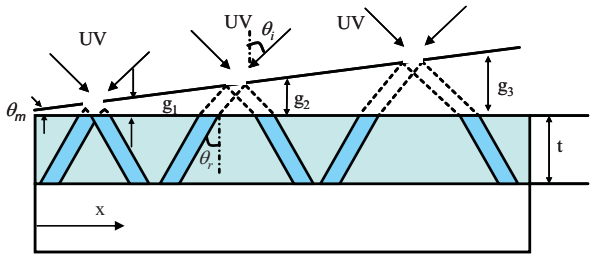

Figure 4. *Nozzles fabricated using proximity mode inclined rotational exposure with a continuously varying gap*

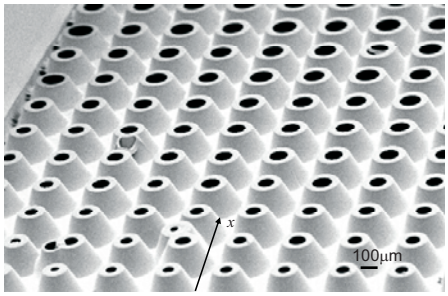

Figure 5. *Fabricated micronozzle array with various orifice sizes resulting from continuously varying gap*

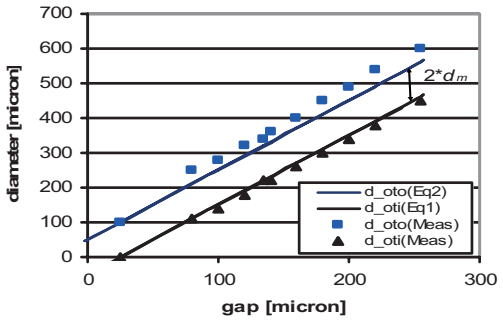

Figure 6. *Outer diameter of orifice tip (d_{oto}) and inner diameter (d_{oti}) as a function of gap*

SILICON-ON-SILICON (SOS): A NEW CMOS COMPATIBLE LOW-TEMPERATURE MEMS PROCESS USING PLASMA ACTIVATED FUSION BONDING

Tzeno Galchev, Warren C. Welch III, and Khalil Najafi
Center for Wireless Integrated Microsystems (WIMS)
University of Michigan, Ann Arbor, Michigan USA, 48109-2122

ABSTRACT

This paper explores the use of dielectric barrier discharge (DBD) surface activated low-temperature wafer bonding in MEMS device fabrication. A new high aspect-ratio MEMS technology based on bonding two silicon wafers with an intermediate silicon dioxide layer at 400°C is presented. This Silicon-On-Silicon (SOS) process requires three masks and provides several advantages compared with Silicon-on-Glass (SOG) and Silicon-on-Insulator (SOI) processes, including better dimensional and etch profile control of narrow and slender MEMS structures. This is demonstrated by fabricating a 5 µm wide 30 mm long beam. Additionally, by patterning the intermediate SiO_2 insulation layer before bonding, footing is reduced without any extra processing, as compared to both SOG and SOI. All SOS process steps are CMOS compatible.

INTRODUCTION

Deep Reactive Ion Etch (DRIE) is a proven technology for creating high aspect-ratio structures. Silicon-On-Glass (SOG) [1] and Silicon-On-Insulator (SOI) are widely used processes which have been developed around DRIE [1,2]. In the case of SOG, a glass substrate is recessed, a silicon device wafer is anodicaly bonded to it, and MEMS devices are formed using DRIE from this silicon wafer. However, glass causes problems during DRIE, namely "footing" or "notching," and overheating. Although footing can be dealt with using shield metals [1], at the expense of process complexity, there is no effective way of removing the heat created during the etch because glass is a poor thermal conductor. This problem is compounded by the fact that a backing wafer must always be used because the glass is not strong enough to survive the pressurized helium cooling in a typical ICP chamber. In the case of SOI, already processed substrates, consisting of a silicon film separated from a silicon wafer using an intermediate buried oxide layer, are etched using DRIE and then released using an isotropic etch of the buried oxide layer. Although overheating is no longer a problem, the oxide creates the same footing problem as glass. Additional processing can be used to solve this by etching first from the back and removing the oxide layer underneath the devices before DRIE [3]. Alternatively, footing can be reduced by limiting the layout to having uniform width and varying the DRIE process parameters [4].

This paper presents a new process for high aspect-ratio MEMS devices based on low-temperature plasma activated fusion bonding. An oxidized silicon wafer is patterned to form silicon dioxide islands, and a second device wafer is bonded to it. DRIE is used to form and release the mechanical structures. Silicon-On-Silicon (SOS) processing has several advantages, when compared to SOG and SOI. Because the oxide is patterned before DRIE, footing problems can be minimized without additional fabrication steps, and the need for wet etching of the oxide after DRIE is removed; so the MEMS devices will not see any wet processing after release. Additionally, when the carrier wafer is silicon, not only is a backing wafer not needed, but also heating during etching is reduced. Third, the carrier wafer can undergo standard micro-fabrication technologies before bonding. Fourth, the thermal mismatch between silicon and glass in the SOG process, which can add a temperature component to precision sensors, is eliminated in the SOS process where the carrier wafer is silicon. Fifth, the low-temperature process allows the formation of buried feedthroughs using a variety of materials, including metals. Finally, SOS does offer the opportunity of achieving full integration because all process steps are CMOS compatible.

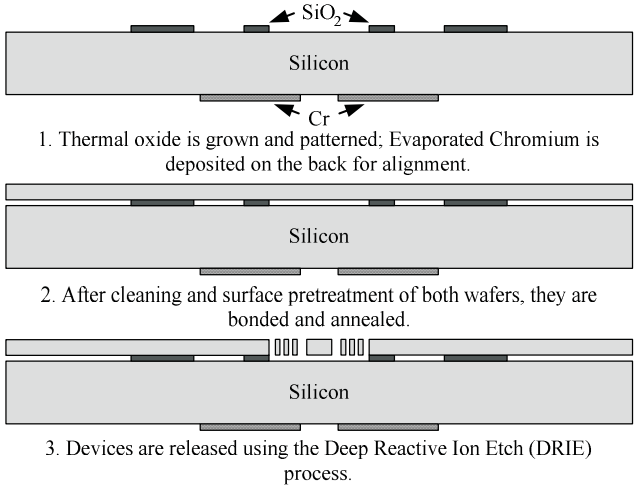

Figure 1. *SOS process flow*

FABRICATION AND RESULTS

In its simplest form the SOS process consists of three masking steps. The process flow is shown in Figure 1. First, a 1µm wet thermal oxide is grown and patterned using RIE. The oxide serves as electrical insulation and bond sites for the device wafer. Alignment patterns made from 250Å of evaporated chromium are patterned on the back using lift-off. A thin 100µm electrically conductive p^{++} silicon wafer is used for eventual creation of the MEMS devices. This wafer is dipped in BHF and rinsed in DI water. Both wafers are then pretreated using dielectric barrier discharge (DBD) atmospheric pressure N_2 plasma in a SÛSS MicroTec nanoPREP 200 system. The DBD method is described in Figure 2. The plasma is created with a 400W AC bias and scanned across the wafers at a gap of 300 µm, while 50 slpm N_2 flows between the electrodes. Plasma treatment creates molecular level surface modifications which increase the surface tension and make silicon hydrophilic [5]. The carrier wafer is megasonically cleaned and dried in a SÛSS MicroTec CL200 cleaner, while the more fragile device wafer, which is only 100µm thick, is hydrated in DI water for 5 minutes and blown dry with nitrogen. The two wafers are bonded in a SÛSS MicroTec SB6e substrate bonder and annealed at 400°C for 4 hrs while applying a pressure of 300 Torr. The devices are released using DRIE in a Surface Technology Systems ICP-RIE chamber.

A SEM of a fabricated die, consisting of two comb-drive resonators and two Pirani gauges, is shown in Figure 3. The same

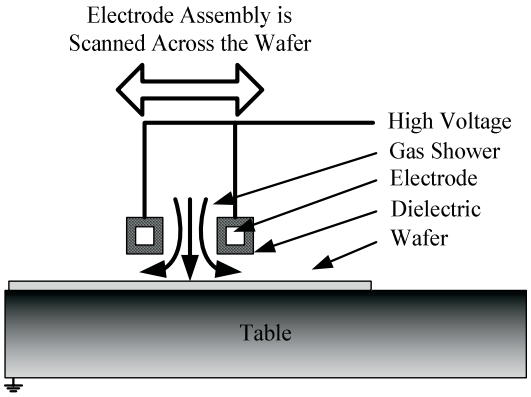

Figure 2. *Dielectric Barrier Discharge creates a uniform plasma discharge due to a high frequency AC voltage applied between two electrodes. The discharge is scanned across the wafer surface. This process does not affect sensitive substrates.*

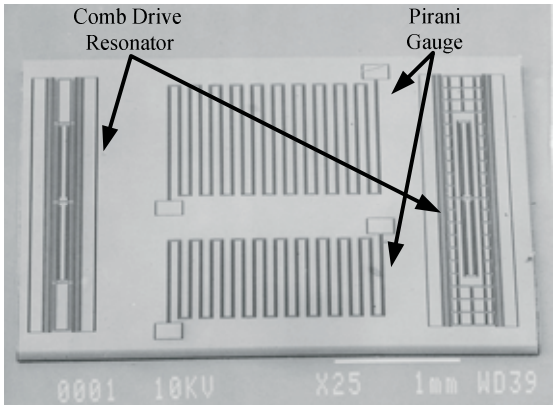

Figure 3. *SEM of the fabricated SOS die. It consists of two comb dive resonators and two Pirani gauges.*

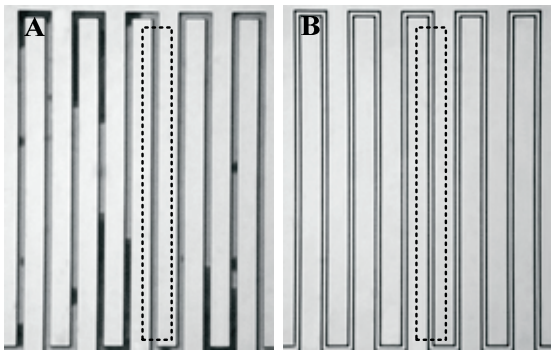

Figure 4. *Close up photograph of one of the Pirani gauges made using SOG (a) and SOS (b). Devices made with SOS survive whereas the devices made with SOG are over etched due to the trapped heat during DRIE. The dark spots in A constitute areas where the underlying shield metal has been burned due to the intense heat.*

mask set was used to make the same devices with the SOG process. The glass was recessed by 8µm before bonding. Additionally, both processes used the same DRIE recipe. The glass substrate was mounted on a silicon wafer for structural support during DRIE with thermally conductive grease. A close-up photo of one of the Pirani gauges is shown in Figure 4a SOG and Figure 4b SOS. The Pirani gauge, which consists of 30mm long 10x100µm beams with a 5µm gap, did not survive the SOG process, which produced a yield of zero. The heat generated during

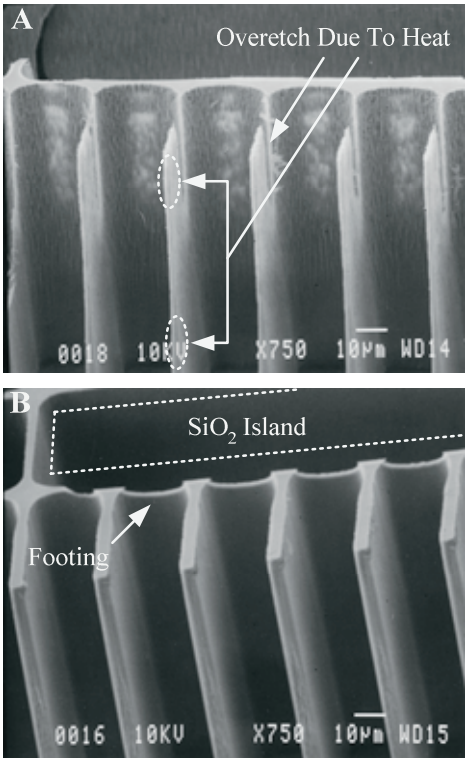

Figure 5. *SEM of the bottom of comb fingers made using SOG (a) and SOS (b) The device made using SOG is severely over-etched, while the SOS device shows a nice etch profile with mild footing.*

DRIE causes the thin long beams of the Pirani gauge to be completely undercut and etched away.

Adhesive tape was used to break off the released resonators to expose the bottom for inspection. A SEM close-up of the bottom of the comb fingers is shown in Figure 5a SOG and Figure 5b SOS. The comb-fingers made using SOS show very mild signs of footing due to a nearby oxide island. However their etch profile turned out as expected, while the SOG comb fingers have been severely consumed by the uncontrollable etch due to overheating.

ACKNOWLEDGEMENTS

The authors thank Dr. Sangwoo Lee for his assistance. This project is partially supported by the Engineering Research Centers Program of the National Science Foundation under Award Number EEC-9986866.

REFERENCES

[1] J. Chae, H. Kulah, and K. Najafi, "A hybrid Silicon-On-Glass (SOG) lateral micro-accelerometer with CMOS readout circuitry," *MEMS'02*, Las Vegas, NV, (2002).

[2] N. Belov and N. Khe, "Using deep RIE for micromachining SOI wafers," *52nd Electr. Comp. & Tech. Conference*, San Diego, CA, (2002).

[3] A. Sharma, F. M. Zaman, B. V. Amini, and F. Ayazi, "A high-Q in-plane SOI tuning fork gyroscope," *IEEE Sensors*, p. 467-70,Vienna, Austria, (2004).

[4] K. Ishihara, Y. Chi-Fan, A. A. Ayon, and M. A. Schmidt, "Inertial sensor technology using DRIE and wafer bonding with connecting capability," *JMEMS* vol. 8, pp. 403, (1999).

[5] Q. Y. Tong and U. Gosele, "Semiconductor Wafer Bonding," *John Wiley & Sons Inc*, (1999).

A MICROFABRICATED IMPEDANCE SENSOR FOR IONIC TRANSPORT IN NANOPORES

Shaurya Prakash, Junghoon Yeom, and Mark A. Shannon
Department of Mechanical and Industrial Engineering, University of Illinois at Urbana-Champaign
Urbana, Illinois USA

ABSTRACT

This paper reports on a multilayer micro-electrochemical impedance spectroscopic (μ-EIS) sensor with an integrated planar Ag/AgCl reference electrode that has been fabricated using MEMS technologies. The μ-EIS sensor is used to detect and characterize ionic transport across nanoporous membranes. The microfabricated multilayer μ-EIS system consists of integrated nanoporous membranes, working, counter, and reference electrodes. The μ-EIS sensor is tested for ionic flow through nuclear track-etched polycarbonate nanoporous membranes with pore diameters of 800, 220, 50, and 10 nm. For validation, the μ-EIS performance is compared to a macroscale 3-electrode electrochemical cell. The electrolyte is an aqueous solution of potassium phosphate (KH_2PO_4) of varying concentrations. Equivalent circuit modelling results are reported and these capture the trends displayed by the experimental results. Use of a Warburg impedance and the constant phase element (CPE) in modelling helps predict the mass transport limit for these sensors and accounts for the non-ideal capacitive behavior observed for these membranes.

INTRODUCTION

The ability to monitor ionic transport across nanopores is important for a variety of scientific and technological reasons, including the development of synthetic constructs mimicking ion-transport in biological channels **[1]**, single molecule detection **[2]**, and the development of molecular gates controlling separation of attomolar concentrations **[3]**. Macroscale electrochemical impedance spectroscopy (EIS) typically uses samples and electrodes with several cm^2 of area and cannot have electrodes placed near the nanopores. Thus, detecting and characterizing ionic transport across a few nanopores at a known transmembrane potential is difficult, often yielding extremely poor signal to noise (S/N) ratio for systems such as molecular gates **[3]**. In μ-EIS, the electrodes can be located relatively close to the nanoporous membrane. Also, with greatly reduced sensor size, small changes in ionic current can be detected with a reasonable S/N ratio. However, device integration challenges such as incorporating ideally polarized working and counter electrodes with an ideally non-polarized on-chip reference electrode must be addressed. Also, the relative location and dimensions of the electrodes must allow for accurate transmembrane potential measurements. Thus, a μ-EIS sensor needed to be developed that can provide rapid and direct characterization of translocating ionic species through nanoporous membranes without the need for amplification, chemical modification, surface adsorption, or binding agents. The μ-EIS impedance data gives magnitude and phase information along with I-V characteristics, thus also providing insight into the interaction between the translocating ions and the electric double layer (EDL) within nanopores due to the interplay between the surface zeta potential and the ionic charge of the electrolyte. Developing a system in which nanopore impedance can be measured accurately will help develop *in-situ* monitoring of nanopore electrokinetic flows.

EXPERIMENTAL DETAILS

A microfabricated multilayer μ-EIS system consisting of integrated nanoporous membranes, and working, counter, and reference electrodes is shown in Fig. 1. The schematic represents an assembled device. A 1000 Å thick sputtered Au layer, serving as the cell electrodes, is patterned on a 100 mm Si wafer, and a polyimide layer is spin-coated to serve the dual role of providing electrical isolation for electroplating the Ag layer and adhesion between the die stack. Double-sided photolithography and DRIE yields four 18 x 16 mm Si dies that are used to assemble the multi-layer stack with the nanoporous membrane sandwiched in between. Device assembly requires several alignment and bonding steps. The various layers are bonded using a commercial adhesive and the process for applying and curing the adhesives has been reported previously **[4]**. The electrodes are located ~500 μm from the membrane for accurate measurements of voltage drop across the membrane. A planar Ag/AgCl reference electrode **[5]** is incorporated to provide on-chip reference. The formation of the reference electrode with the appropriate chemical structure is verified by XPS (Fig. 2).

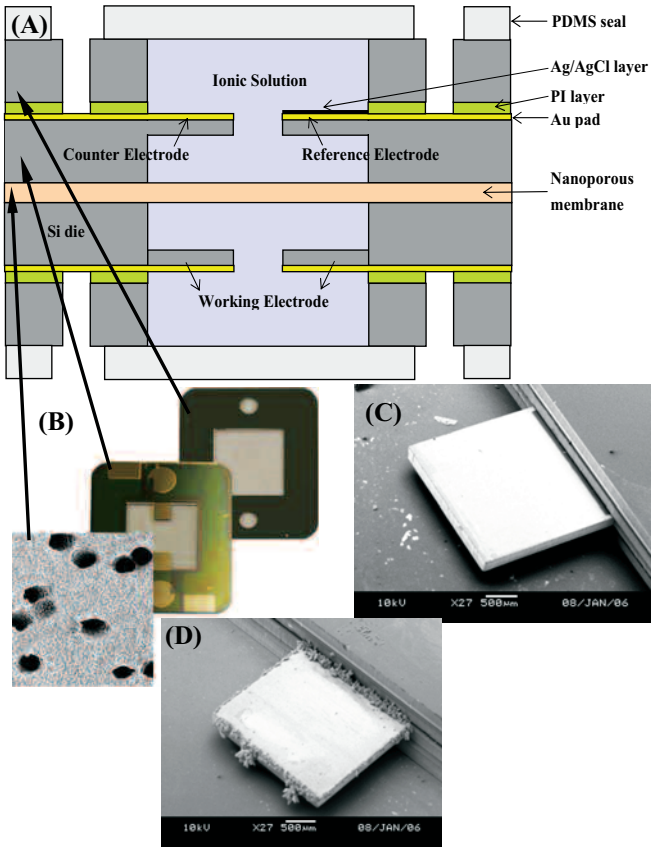

Figure 1: ***(A)*** Schematic of an assembled μ-EIS system showing the working, counter and reference electrodes, and the sandwiched nanoporous membrane. ***(B)*** An SEM image of the nanoporous membrane is shown along with digital photographs of individual dies in (A). ***(C-D)*** SEM images of Au and Ag/AgCl electrodes.

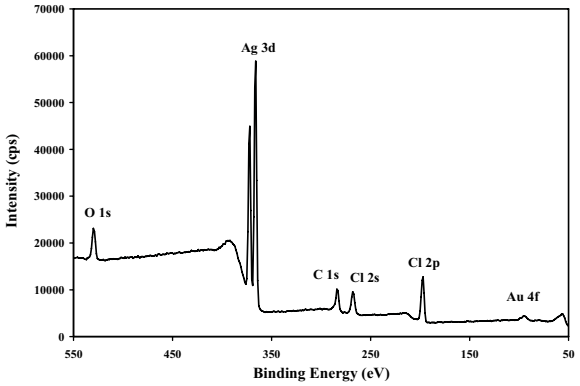

Figure 2: XPS spectra for the electroplated Ag/AgCl layer after treatment in $FeCl_3$. The key peaks are shown in the spectra above including the characteristic double peak structure for Ag (3d) indicative of AgCl formation. The Ag/AgCl layer is used as the reference electrode.

RESULTS AND DISCUSSION

Impedance data is collected for varying salt concentrations of monobasic potassium dihydrogen phosphate (KH_2PO_4) in an aqueous solution. The thickness of the EDL can be estimated by using equation 1, which is valid for dilute solutions **[6]**.

$$\lambda_D^{-1} = .329 \times 10^7 z\sqrt{c} \qquad (1)$$

where, λ^{-1}_D is the inverse Debye length (~ the thickness of the EDL) predicted by the Gouy-Chapman model, z is the valence of the ion and c the bulk concentration of electrolyte solution. Equation (1) shows that with decreasing concentration the EDL thickness increases. For validation of the μ-EIS measurement, impedance measurements are conducted on a macroscale 3-electrode electrochemical cell with 800 nm pores in polycarbonate track etched (PCTE) membranes. Figure 3 shows the comparison between the macroscale EIS measurement and the μ-EIS system. It is seen from Fig. 3 that impedance data matches well from about 100 kHz to approximately 5 Hz. At low frequencies the magnitude of the measured impedance for the μ-EIS is about 3 times lower. The observed large differences seen at low frequencies can be possibly attributed to leakage current through the Si substrate. Figure 4 shows a comparative Nyquist plot for the 10 nm and the 800 nm pore diameter PCTE membranes at 100 mM salt

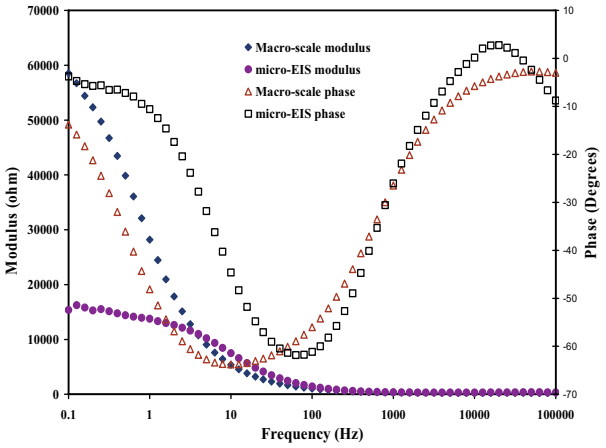

Figure 3: A Bode plot showing a comparison between the impedance data for the macroscale EIS measurement and the μ-EIS collected from 0.1 Hz to 100 kHz for a 800 nm PCTE membrane at 100 mM salt concentration.

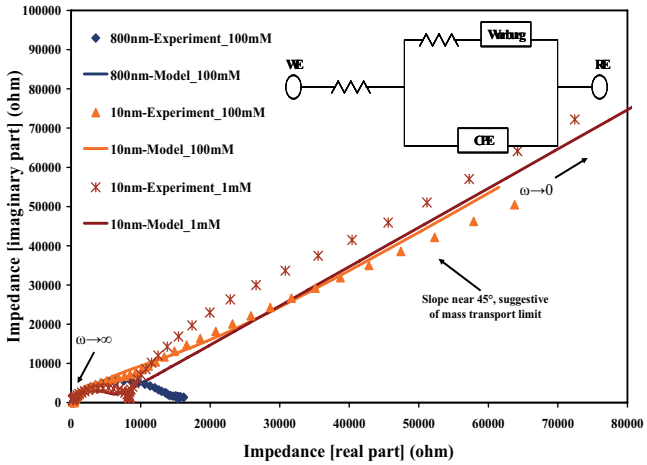

Figure 4: A Nyquist plot showing comparison between impedance data for the μ-EIS collected from 0.1 Hz to 100 kHz for a 800 and 10 nm PCTE membrane at 100 mM salt concentration. The model used is shown as the inset.

concentration. The 10 nm pores display a mass transport limit indicated by the 45° line at low frequencies. At 1 mM salt with overlapping EDLs, the concentration impedance for the 10 nm pores increases by almost 2.4 times at low frequency (<1 Hz) and the imaginary part of impedance shows an increase of about 31% in comparison to the 100 mM case. Equivalent circuit modelling is carried out to estimate a possible electrical circuit that would better elucidate the physics of nanopore ionic transport. The presence of a Warburg impedance indicates that hindered ionic transport occurs in the 10 nm pore, and its absence till about 0.1 Hz for the 800 nm at 100 mM indicates normal electrokinetic flows without interacting EDL's.

This paper demonstrates the fabrication and preliminary testing results for a μ-EIS sensor, and that such a sensor can be used to evaluate electrokinetic ionic transport across nanopores.

ACKNOWLEDGEMENTS

The authors thank the National Science Foundation for financial support for the current research through the WaterCAMPWS under the agreement number CTS-0120978. The authors thank CMM, University of Illinois, which is partially supported by the U.S. Department of Energy under grant DEFG02-91-ER45439.

REFERENCES

[1] M. Nishizawa, V.P. Menon, C.R. Martin, "Metal nanotubule membranes with electrochemically switchable ion-transport selectivity", *Science*, *268* 700 (1995).

[2] H. Wang, D. Branton, "Nanopores with a spark for single-molecule detection", *Nature Biotechnology, 19,* 622 (2001).

[3] J.J. Tulock, M.A. Shannon, P.W. Bohn, J.V. Sweedler, "Microfluidic separation and gateable fraction collection for mass-limited samples", *Analytical Chemistry*, *76,* 6419 (2004).

[4] B.R. Flachsbart, K. Wong, J.M. Iannacone, E.N. Abante, R. Vlach, P.A. Rauchfuss, P.W. Bohn, J.V. Sweedler, M.A. Shannon, "Design and fabrication of a multilayered polymer microfluidic chip with nanofluidic interconnects via adhesive contact printing", *Lab on a Chip* (In Press).

[5] B.J. Polk, A. Stelzenmuller, G. Mijares, W. MacCrehan, and M. Gaitan, "Ag/AgCl microelectrodes with improved stability for microfluidics" *Sensors and Actuators B* (In Press).

[6] P.J. Kemery, J.K. Steehler, P.W. Bohn, "Electric field mediated transport in nanometer diameter channels", *Langmuir*, *14*, 2884 (1998).

PASSIVE MICROFLOW REGULATION USING THERMALLY RESPONSIVE POLYMERS

Boris Stoeber
Departments of Mechanical and Electrical & Computer Engineering, University of British Columbia
Vancouver, BC, CANADA

Dorian Liepmann
Department of Bioengineering
University of California
Berkeley, CA, U.S.A.

Susan J. Muller
Department of Chemical Engineering
University of California
Berkeley, CA, U.S.A.

ABSTRACT

Thermally responsive polymer solutions have previously been used in microchannels with integrated heaters for active valving. In addition, passive flow regulation based on viscous heating in microchannels can be achieved under constant flow rate and constant pressure drop conditions. In the case of pressure-driven flow through a microchannel, we demonstrate for the first time that viscous heating can cause periodic gel formation leading to pulsatile flow with no need for moving parts or active components. This is a unique concept for passive microflow regulation showing such a performance.

INTRODUCTION

Microflow control is an important field of research driven by the demands of microfluidic applications such as ink-jet printing and lab-on-a-chip devices for biochemical analysis and DNA sequencing. While ink-jet print heads require very fast acting valve mechanisms that operate at the order of 1 kHz, the flow control requirements of Micro Total Analysis Systems can be very diverse. In addition to fast and reliable valve actuation, passive flow control or flow control in response to changing environmental variables can be very attractive for such systems in order to efficiently manage biological and chemical samples.

For this purpose, Fréchet, [1], Beebe [2], and others have synthesized temperature, pH, or glucose sensitive polymer structures that are anchored inside microchannels; these materials swell and block the channel in response to changes in the environment. We demonstrate a fundamentally different concept for automatic flow rate control based on the reversible phase change of a thermally responsive polymer present in the flow. Valving occurs in a straight section of a flow channel, where viscous heating triggers the heat-induced gelation of the fluid, which can lead to total blockage of the flow passage or to periodic velocity fluctuations.

RESULTS AND DISCUSSION

The viscosity η of dilute (~10%) aqueous solutions of the biocompatible polymer Pluronic F127 (BASF) increases with temperature until the solutions reversibly solidify. This phase change occurs over a temperature change of only 0.5ºC. The gel formation temperature is a function of polymer type and concentration. We previously demonstrated an active microvalve for Pluronic solutions using integrated heaters in microchannels [3]. Here, we demonstrate and explain passive flow control using dilute Pluronic solutions. These mechanisms allow self-regulating valves or valves that respond to changes in ambient temperature.

The simple flow channels (cross section: 100 µm x 100 µm) used for passive valving were etched into silicon using DRIE and were covered with glass. The high shear rate $\dot{\gamma} = \mathrm{d}v/\mathrm{d}x$ regions along the channel walls can produce significant viscous heating $\Phi = \eta\,\dot{\gamma}^2$. In cases where the ambient temperature is close to the gelation temperature of the Pluronic solution, viscous heating can cause local gel formation on the channel wall. The subsequent flow regime, either channel blockage or velocity fluctuations, depends on the mechanism that drives the flow, controlled flow rate or controlled pressure drop respectively.

In the case of controlled flow rate, gel formation on the channel wall reduces the cross sectional area of the flow channel, which increases the shear rate in the flow. This leads to more viscous heating and to more gel formation until the entire channel is blocked as mentioned in [3].

However, a different mechanism occurs if a controlled pressure drives the flow. Here, the presence of gel on the channel wall increases the flow resistance of the channel, which reduces the flow rate and therefore the shear rate in the flow as shown in Fig. 1. This leads to less viscous heating so that the heat can dissipate into the substrate and the gel becomes liquid again, which can result in flow fluctuations. Figure 2 shows video frames of an 18 % Pluronic solution driven through a microchannel at controlled pressure. The flow gels periodically on the walls and becomes liquid with a time period of 2.2 s.

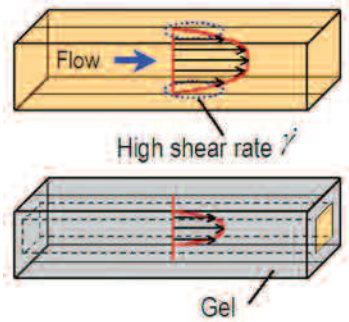

Figure 1. *Schematic of gel formation in the channel due to shear-induced viscous heating.*

Digital particle image velocimetry (DPIV) results for pressure driven flow (Figs. 3 and 4) show that the flow fluctuations are more pronounced slightly below the gelation temperature (22°C), while the shear thinning properties of the fluid can lead to a different kind of flow instability above the gel point. The time period of velocity fluctuations from all 18 experiments was $\tau_p = 2.0 \pm 0.4$ s.

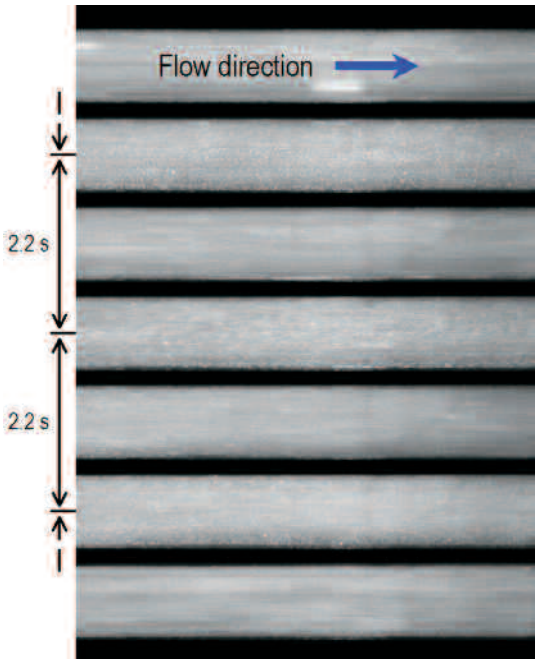

Figure 2. *Video frames of seed particles in a Pluronic solution, driven through a microchannel at constant pressure.*

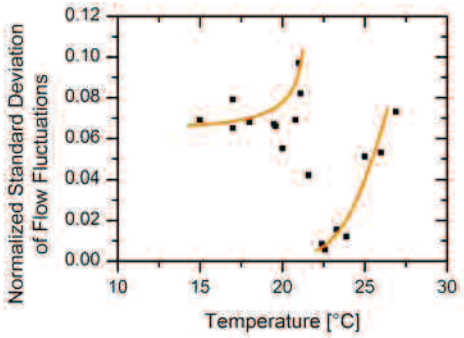

Figure 3. *Velocity fluctuations for pressure-driven flow of a Pluronic solution in a microchannel at different temperatures.*

This new flow control mechanism is possible because of the particular rheology of Pluronic solutions that are shear-thinning and thermo thickening. In particular, it can be shown that at controlled pressure, the amount of viscous heating as a function of the diameter of the open channel D and the fluid viscosity η scales as $\Phi \sim D^2/\eta$, while at controlled flow rate viscous heating goes as $\Phi \sim \eta/D^6$. A related but fundamentally different kind of shear-induced flow instabilities has been observed previously for the more conventional case of thermo thinning fluids [4].

The velocity profiles in Fig. 4 show the effects of the particular properties of the Pluronic solutions. Below or at the gel formation temperature (15.0°C and 21.0°C) the velocity profile is parabolic suggesting that the solution is still behaving primarily as a Newtonian fluid. Above the gel temperature (22.0°C) the velocity profile is flattened and appears plug-like showing the effects of shear-thinning along the channel walls. However, at still higher temperatures some seed particles assemble into extended strings of particles on the walls oriented along the channel axis.

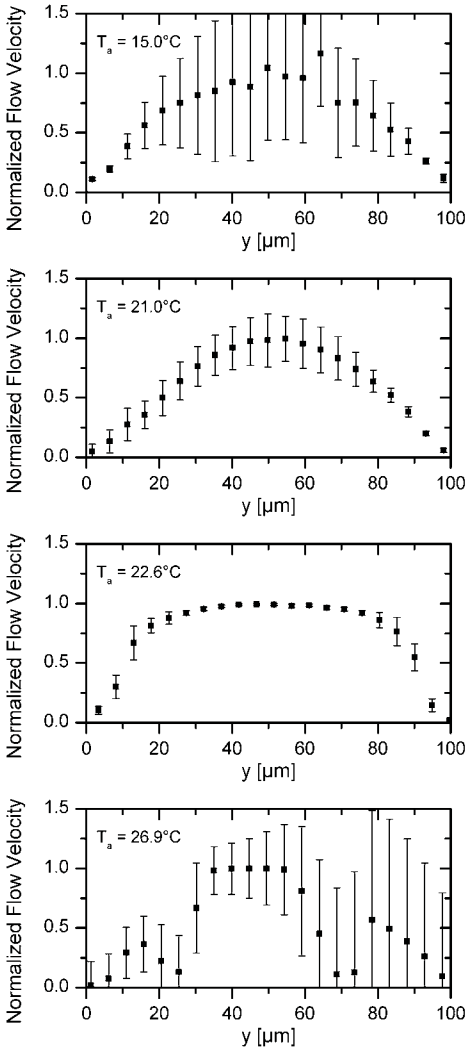

Figure 4. *Velocity profiles from DPIV of a Pluronic solution through a microchannel at different ambient temperatures.*

CONCLUSIONS

We demonstrated a new concept for passive microflow regulation that leads to a unique pulsatile flow rate. This can be very useful for Micro Total Analysis Systems in order to effectively manage biological and chemical samples. This concept is mechanically robust because it does not include movable parts. At a fixed temperature, the automatically generated flow fluctuations can be used for controlled dosage of chemical compounds or biological samples transported with the Pluronic solutions. In addition, microflow regulation can be achieved in response to temperature variations, which can be useful to control the flow rate of a reagent in response to heat production in an on-chip reaction chamber.

REFERENCES

[1] E.C. Peters, F. Svec, J.M.J. Frechet, Advanced Materials, vol.9, no.8, pp.630-633, 1997.

[2] R.H. Liu, Q. Yu, and D.J. Beebe, JMEMS, vol. 11, no. 1, pp. 45-53, 2002.

[3] B. Stoeber, Z. Yang, D. Liepmann, S. J. Muller, JMEMS, vol. 14, no. 2, pp. 207-213, 2005.

[4] D. D. Joseph, Physics of Fluids, vol. 8, no. 12, pp. 2195-2200, 1965.

CONTROLLED DROPLET COALESCENCE IN AIR AND ITS APPLICATION TO MICROMIXING

Chuang-Yuan Lee, Hongyu Yu, and Eun Sok Kim
Department of Electrical Engineering-Electrophysics,
University of Southern California, Los Angeles, CA 90089-0271, USA

ABSTRACT

This paper describes the controlled coalescence of liquid droplets in air by acoustic directional ejections and its application to micromixing. We intentionally created an asymmetrical electric field within the piezoelectric transducer to produce lopsided acoustic waves, which were focused on the liquid surface to obliquely eject nanoliter droplets. Effective micromixing was carried out in air through the continuous flight and rotations (16,000 rad/s) of the coalesced droplet. This digital fluid manipulation by directional droplet ejections allows complex analyses at high throughput and is practicable to versatile life-science applications.

INTRODUCTION

The interest in on-chip biochemical analysis systems is growing rapidly, because they offer a fast, efficient and low cost assay. Rapid and homogenous mixing of two or more fluidic species is essential for these micro total analysis systems (μTAS). However, in a conventional microfluidic system, laminar flow occurs due to a low Reynolds number. Diffusion, dominant at the microscale, can take a relatively long time and decrease the overall system efficiency. In order to enhance the mixing performance, several passive micromixing methods have been developed by inducing chaotic advection and creating laminar shear, which require relatively long channels to lead the flow to a chaotic state [1].

Here we report the coalescence of liquid droplets in air resulting from acoustic directional ejections and its application to active mixing. This digital fluid manipulation by directional droplet ejections will be useful not only for micromixing but also for deoxyribonucleic acid and protein microarrays and other microfluidic applications.

DESIGN AND FABRICATION

A single directional ejector consists of an acoustic transducer and a lens [2]. By focusing acoustic energy on the liquid surface, acoustic radiation pressure acts to overcome the restraining force of surface tension and expels the droplets from an open space without any nozzle. To generate directional ejections, an asymmetrical electric field was intentionally created within the piezoelectric layer to produce lopsided acoustic waves (Fig. 1). A lead zirconate titanate (PZT) transducer with both top and bottom electrodes patterned into a sector shape was used in our design. Acoustic waves were only produced from the regions covered with patterned electrodes, resulting in uneven acoustic pressure distributions on the liquid surface.

Among the various patterns investigated, it was found that sectors with larger angles would incur lesser tilting for directional ejections, while smaller angles would suffer from severe electric fringing fields and consequent unstable ejections. There existed a tradeoff between directionality and stability, and a 90° sector was observed to be the optimal design. Four ejectors were coordinately arrayed on a single chip to target one spot in the center with multiple liquids.

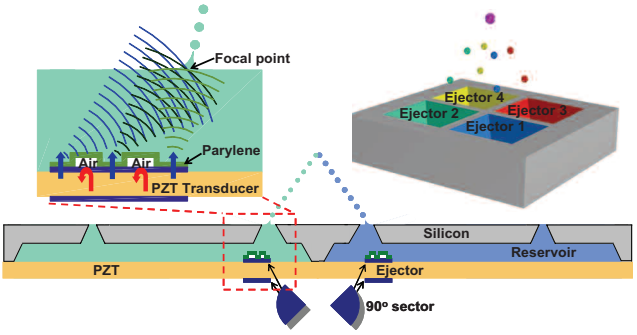

Figure 1. *Schematic diagram of directional acoustic ejector array.*

To fabricate the device, we first sectored top and bottom nickel electrodes on a 127-μm-thick PZT. Parylene was then deposited and patterned as the lens structure with photoresist as the sacrificial layer. After release, we adhesively bonded the PZT substrate to silicon wafers on which the 800-μm-deep (matching the lens focal length) reservoirs were microfabricated. Fig. 2 shows the photos of the fabricated PZT ejectors and silicon chambers before they were adhesively bonded together, and Fig. 3 shows the finished device in a dual-in-line package.

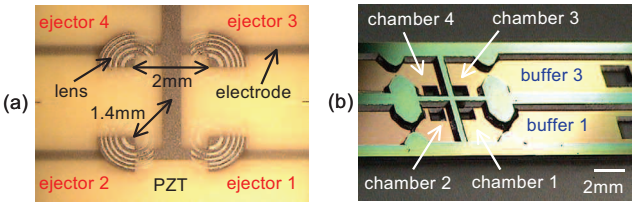

Figure 2. *Photos of (a) ejector array and (b) chamber array.*

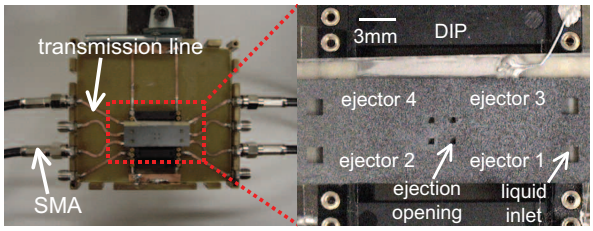

Figure 3. *Fabricated device in a DIP package connected to transmission lines and SMA connectors.*

RESULTS AND DISCUSSION

We first tested the performance of two ejectors (Ejectors 1 and 2) using water as the medium (Fig. 4). Two droplets (80 μm in diameter) broke off simultaneously from their own bulk liquids 200 μs after the rising edge of an applied pulse. They then approached each other at a speed of 2.3 m/s. At around 1100 μs, they arrived at the same place in air at the same time and coalesced into one larger droplet. The coalesced droplet kept on traveling with no velocity along the *x* direction. Although the droplet size (80 μm) is much smaller than the distance between the two ejectors

(2 mm), the two droplets still meet in a three-dimensional space because of the same ejection speed and precise directionality.

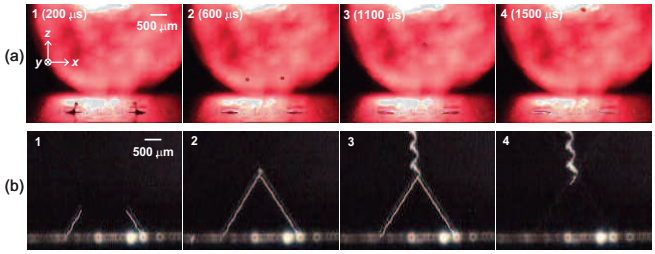

Figure 4. *Droplet ejection process captured (a) with and (b) without strobe (Ejectors 1 and 2 activated). Ejectors were driven with ±80-$V_{peak\text{-}to\text{-}peak}$ pulses of 16-μs pulsewidth with 60-Hz pulse repetition frequency (PRF).*

The ejection sequences of Ejectors 2 and 4 show the coalescence from another angle (Fig. 5). Coalescence was achieved by the sufficient collision kinetic energy to expel the air layer between the two colliding surfaces. The coalesced droplet continued to travel in air with the following characteristics. First, its gross traveling trajectory is in the additive direction of its composing droplets. Because the two composing droplets have the same density and size, this phenomenon is a consequence of the conservation of momentum. Second, as its airborne travel continues, the coalesced droplet rotates repeatedly with a periodicity of 400 μs and a rotation velocity of 16,000 rad/s.

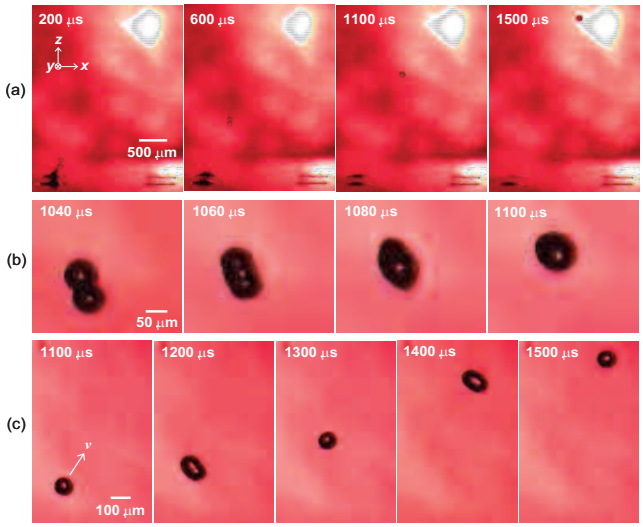

Figure 5. *Droplets ejection process (Ejectors 2 and 4 activated). (a) Overview pictures of the ejection process. (b) Detailed droplets coalescence sequence around 1100 μs. (c) Rotations of the traveling coalesced droplet with a periodicity of 400 μs.*

To demonstrate that more than two droplets can be merged in air, we actuated the four ejectors on a chip. The four droplets were created simultaneously, moved toward the center along the matched directions, and joined together in air to form a single coalesced droplet (Fig. 6).

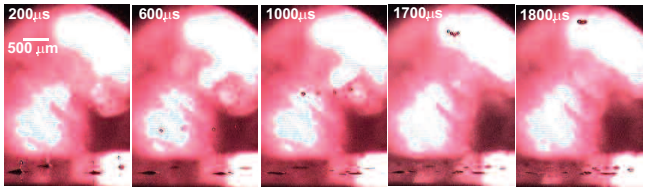

Figure 6. *Optical micrographs of the droplets ejection process (all four ejectors activated). Ejectors were driven with ±80-$V_{peak\text{-}to\text{-}peak}$ pulses of 30-μs pulsewidth with 60-Hz PRF.*

The rotating characteristics of the coalesced droplet can be applied to micromixing for the following benefits. First, by mixing reagents in air without long channels on a substrate, the lab-on-a-chip real estate is greatly reduced. Second, through the active rotations after the coalescence, mixing is achieved more efficiently than by passive diffusion. To illustrate the mixing effect, two different mediums (water and red ink) were ejected by two separate directional ejectors. Because it was relatively difficult to perform mixing analysis for airborne droplets from the side-view micrographs, we examined the droplets collected on a glass slide placed 2-cm above the device (Fig. 7). With a rotation velocity of 16,000 rad/s, the airborne droplet (containing the two liquids after the coalescence) was vigorously mingled through rotations of about 30 rounds before it was collected on the glass slide. The droplet homogeneity exhibited the excellent mixing by the precise directional ejections and the continuous flight and rotations after the coalescence.

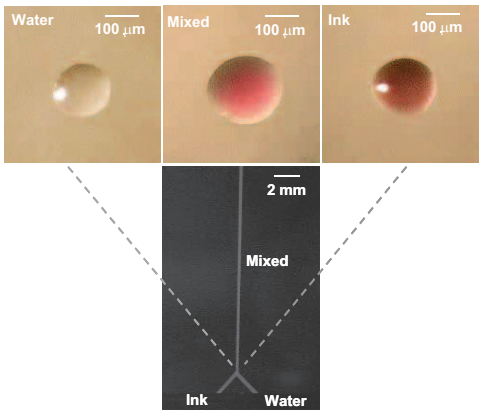

Figure 7. *The water, ink, and mixed droplets ejected onto a glass slide by directional ejections. For comparison, one water droplet (~0.27 nl) was first ejected and collected, and then one ink droplet (~0.27 nl) was ejected and collected. Finally, one water and one ink droplet were simultaneously ejected and coalesced in air. The coalesced droplet continued traveling until it was collected.*

CONCLUSIONS

We have demonstrated the controlled coalescence of liquid droplets in air and its applications to micromixing. Not only can the directional ejectors dispense nanoliter droplets of aqueous and non-aqueous fluids, it can also eject fluids with solid particles in various oblique angles for droplet coalescence and micromixing in air. This droplet dispensing method is capable of targeting a same spot in air with combinations of different reagents either concurrently or sequentially. A more flexible microfluidic system can be further constructed with arrays of multi-directional ejector having a set of electrically-tunable sector electrodes. Because of its high throughput, positional accuracy, and repeatability, directional acoustic ejection is suitable for many other applications, ranging from drug discovery to combinatorial chemistry.

REFERENCES

[1] H. Suzuki, C.-M. Ho, and N. Kasagi, "A Chaotic Mixer for Magnetic Bead-Based Micro Cell Sorter," *Journal of Microelectromechanical Systems, 13,* 779 (2004).

[2] C. Lee, H. Yu, and E.S. Kim, "Acoustic Ejector with Novel Lens Employing Air-Reflectors," *IEEE MEMS Conference*, Istanbul, Turkey, 1/22–26/06, pp. 170-173.

CHIP-SCALE ATOMIC DEVICES

John Kitching, Svenja Knappe, Peter D. D. Schwindt, Ying-Ju Wang, Hugh Robinson and Leo Hollberg
Time and Frequency Division, National Institute of Standards and Technology
Boulder, CO USA

Li-Anne Liew, John Moreland
Electromagnetics Division,
National Institute of Standards and Technology
Boulder, CO USA

Alan Brannon, Jason Breitbarth, Brad Lindseth and Zoya Popovic
Department of Electrical and Computer Engineering, The University of Colorado
Boulder, CO USA

Vishal Shah
Department of Physics, The University of Colorado
Boulder, CO USA

Vladislav Gerginov
Department of Physics, University of Notre Dame
Notre Dame, IN USA

Matthew Eardley
Department of Physics, The State University of New York,
Stony Brook, NY USA

ABSTRACT

We present an overview of recent work to develop chip-scale atomic devices such as frequency references and magnetometers. These devices take advantage of advances over the last ten years in the fields of micro electro mechanical systems (MEMS), precision atomic spectroscopy and semiconductor lasers. The convergence of processes and techniques from these three disparate areas allows for highly compact, low-power sensors with exceptional sensitivity and stability. We will discuss in detail several important ongoing activities in our laboratory including recent advances in alkali cell fabrication and new physics package designs for chip-scale atomic clocks and magnetometers. Finally, we discuss opportunities related to the coupling of resonant, magnetic microstructures to atoms for highly compact, low power sensor applications.

INTRODUCTION

Instruments based on precisely measured transitions in atoms include clocks [1], magnetometers [2, 3], gyroscopes [4, 5], accelerometers [6] and RF power meters [7]. Many of these instruments provide, or have the potential to provide, the most sensitive measurements of basic quantities (time, magnetic field, angular rotation rate, linear acceleration) available. However, in their most precise form, they are typically large and complex, and require several person-years of effort to construct. A key challenge in moving these instruments into widespread use in applications is miniaturization, and the associated gains in power consumption and cost. MEMS micromachining appears to provide an excellent avenue for achieving this miniaturization and enabling precision instrumentation in the increasing spectrum of portable, battery-operated systems.

The development of chip-scale atomic clocks, for example, has progressed rapidly from concept [8] to component-level demonstration [9] to subsystem demonstration [10, 11] to prototype [12]. Physics packages for chip-scale atomic magnetometers have also been demonstrated [13] and it is anticipated that even more atom-based sensors and instruments could be miniaturized using MEMS technology. We describe here one possible approach that may find general use in achieving these goals.

ATOMIC SPECTROSCOPY

Atoms in the gas phase hold a somewhat unique position in the world of precision measurement because of several important properties. First they are fairly simple quantum mechanical systems, with energy spectra composed of a few well-separated states rather than a continuum found in many solid-state systems. Particularly important for spectroscopic purposes are alkali atoms, which have a single valence electron. Because high interaction energies are required to perturb a closed electron shell, almost all properties of the atoms are determined by the position and orientation of the valence electron with respect to the nucleus.

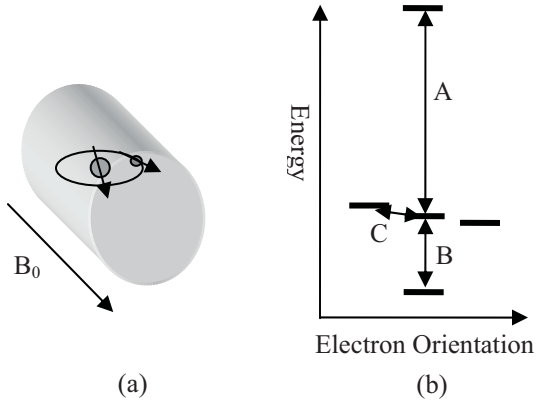

Figure 1. *(a) The internal state of the atom and orientation in an external magnetic field (B_0) determine its energy. (b) Transitions between energy levels (not to scale in the figure) may be induced by optical (A), microwave (B) and RF (C) electromagnetic fields.*

We may consider a somewhat generic situation in which atoms at room temperature are confined in an otherwise evacuated volume and subjected to an external magnetic field (see Figure 1). In this case, four properties of the valence electron in the atom almost completely determine the energy spectrum: the mean distance of the electron from the nucleus, its orbital angular momentum about the nucleus, the orientation of the electron spin with respect to the nuclear spin and the orientation of the electron spin with respect to the external magnetic field. Transitions between these electron states can be excited by electromagnetic

fields with a frequency equal to the energy difference between the states divided by Planck's constant, *h*. Typically, transitions between states involving the electron-nucleus distance and orbital angular momentum are excited by optical fields with frequencies above 100 THz. Transitions between orientations of the electron spin with respect to the nuclear spin are excited with microwave fields in the 1-10 GHz range. And transitions between orientations of the electron spin with the external magnetic field are induced with RF fields below 1 MHz, for magnetic fields less than 100 μT.

Alkali atoms in the gas phase can be made to interact only weakly with their surroundings; the random perturbations of the atomic energy levels in this case are rather small. As a result, the level energies are very well defined, as are the frequencies of the electromagnetic fields that connect any two levels. It is therefore possible to obtain detailed information about the internal state of the atom by measuring the frequency of the transition precisely. Alternatively, the universal and long-lived nature of the internal states can be used to stabilize the frequency of an external oscillator and make a precise and/or accurate frequency standard.

MEMS ALKALI CELL FABRICATION

Perhaps the most significant technological advances so far in enabling MEMS-based atomic devices are methods for fabricating highly miniaturized evacuated cells containing vapors of alkali atoms. The difficulty here is in maintaining a very pure environment inside the cell. This is required to prevent contaminants from reacting with the alkali atoms and from perturbing their energy levels. Traditionally, vapor cells for almost all atom-based instruments have been fabricated either with ultra-high vacuum technology or by using glass-blowing techniques, in which discrete glass elements are fused and shaped by heating the material to near its softening point. The difficulties with this process are that the resulting cells tend to be fairly large, difficult to integrate with other components, and are usually made one-by-one resulting in high cost.

MEMS-based assembly processes promise to revolutionize the way in which alkali atom cells are fabricated and used. Perhaps the simplest design [9], is shown in Figure 2. In this design, a hole is etched in a Silicon wafer and glass wafers are bonded to the top and bottom surfaces, forming an empty cavity. Alkali atoms are then confined in this sealed volume, along with a controlled environment such as a pure buffer gas, which lengthens the coherence time of the alkali oscillating moment by preventing frequency collisions with the cell walls.

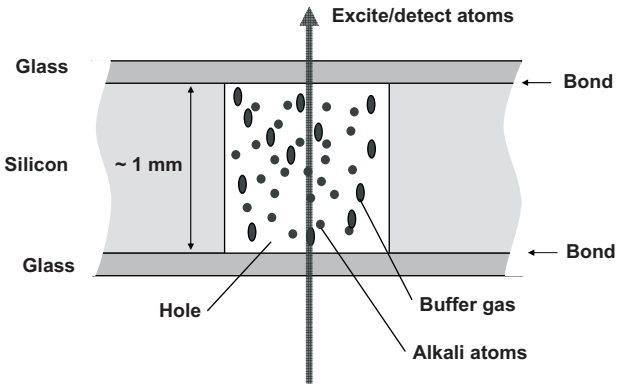

Figure 2. *Design of a MEMS-based alkali atom vapor cell for chip-scale atomic devices.*

The processes by which alkali atoms are introduced into the cell vary substantially. Pure alkali elements are metallic substances for which a vapor phase coexists with either a solid or liquid phase at room temperature. The atoms in the vapor phase are those that have the properties necessary for precision spectroscopy. But since the vapor phase is present whenever the solid or liquid exists, Alkali material can be directly deposited into cell as a solid or liquid under a controlled environment such as that produced inside a glove box or anaerobic chamber [9, 11, 14].

It is also possible to fill the cells in a manner similar to conventional glass-blowing, in which a filling tube is connected to the cell interior through a hole in one of the glass surfaces [15, 16]. The cell can then be evacuated with a vacuum pump and alkali atoms distilled into the cell with thermal gradients. A third method involves a chemical reaction to produce the pure alkali metal. This reaction can be carried out either inside the cell before it is bonded [9] or in an external ampoule with an opening placed near the cell opening [17]. Waxes have also been used to seal cells closed once the alkali atoms have been distilled into the interior volume [18]. Compact systems for confining laser cooled atoms at microKelvin temperatures are also under development [19].

A new technique being developed at NIST that shows considerable promise for wafer-level batch fabrication is the evaporative deposition of CsN_3 into the cell preform, followed by ultra-violet dissociation of the azide material into Cs and N_2 after sealing [20]. This technique allows a careful control of the final buffer gas (N_2, in this case) pressure in the cell through the adjustment of the time the cell is subject to the UV light. This could be used to advantage in fabricating temperature-compensated cells with two or more buffer gases. Finally, a technique based on diffusion of alkali atoms through the glass windows at high temperature has is also under development [21], which may enable very low-cost cell production.

A common advantage of all of these schemes, in addition to the capability for small sizes, is the possibility of fabricating large numbers of vapor cells with the same process sequence on a single wafer. A conceptual view of how a final wafer of cells might look in shown in Figure 3.

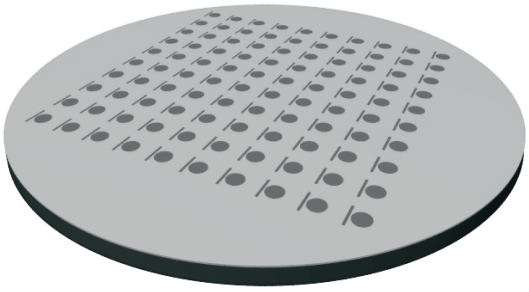

Figure 3. *Conceptual implementation of wafer-level cell fabrication.*

PHYSICS PACKAGE DESIGNS

The integration of the MEMS vapor cells with miniature optical components provides an interface that connects the atomic states and coherent oscillation with the outside world. Transitions in the atoms are excited with a modulated laser field [22], which can be decomposed into components of an optical spectrum that differ in frequency by the modulation frequency. This combination of spectral components allows a wide range of atomic transitions to be excited. A single spectral component, tuned into resonance with an optical transition in the atoms, will excite transitions between atomic energy levels with different electron-nucleus

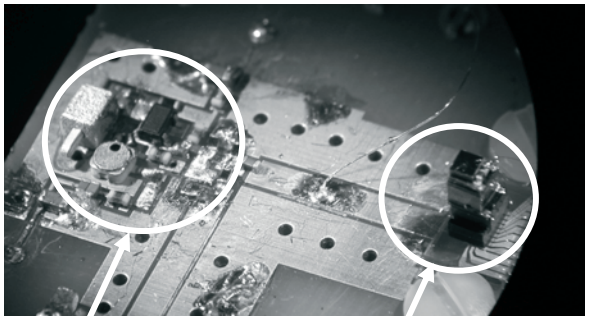

(a)

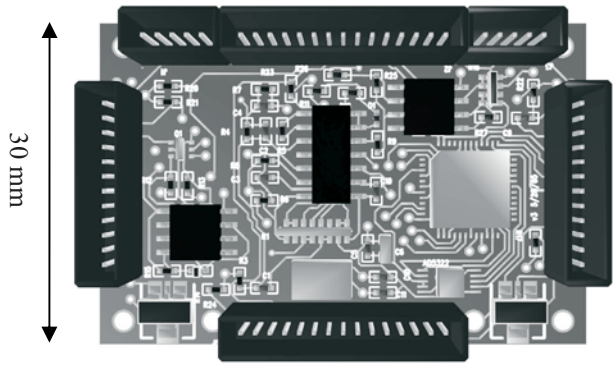

(b)

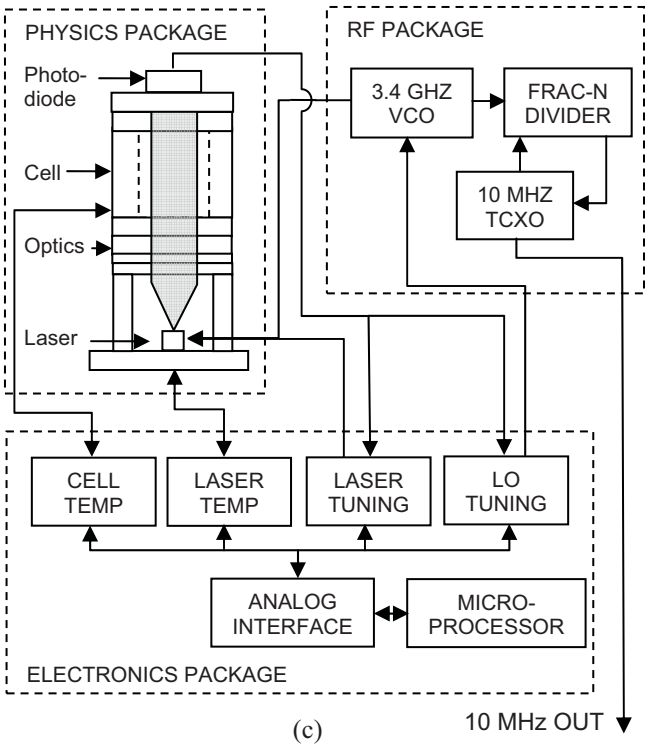

(c)

Figure 4. *(a) Chip-scale atomic clock physics package and local oscillator integrated on a single substrate. (b) Control electronics design. (c) Schematic indicating major CSAC subsystems and interconnections.*

separation and/or orbital angular momentum. A combination of two spectral components can excite microwave and RF transitions in atoms through the fundamental nonlinearity of atomic systems [23]. A nonlinear resonator, driven by two fields with differing frequencies, can be made to oscillate at the sum or difference of those frequencies. Parametric amplification is one example of this process. When atoms are illuminated by two optical fields therefore, a coherent oscillation can be excited at the difference between the frequencies of those fields; the amplitude of this oscillation is particularly large if the difference frequency corresponds to a natural resonance in the atoms.

A typical physics package, therefore, consists of a modulated diode laser, some optics to adjust the light intensity, polarization and divergence to suitable values, a vapor cell, and a photodetector, that detects the transmitted optical power [10, 13]. A geometry typical of most of NIST's physics packages is shown in Figure 4(c). The physics package in this case is a passive device: it takes as its input a signal from an external oscillator and generates an output that depends on the difference between the frequency of the input signal and that of the atomic resonance.

NIST has recently demonstrated a chip-scale atomic clock physics package integrated with a compact, low-power oscillator based on a micro-coaxial resonator. Both the physics package [10] and local oscillator [24] are similar in structure to ones described previously. The integrated subsystems are shown schematically in Figure 4(a). The atomic resonance, as measured by the modulated diode laser, is shown in Figure 5(a) and the stability of the compact local oscillator, both when it is free running and when it is locked to the physics package, is shown in Figure 5(b). A compact control system has also been designed; the layout is shown in Figure 4(b). It is based on a microprocessor, which implements the four main servo systems required to run the clock. These servo systems actively stabilize the laser temperature, the cell temperature, the laser frequency (optical tuning) and the LO frequency. The microprocessor is interfaced with the physics package and local oscillator through an analog interface circuit. The main electrical connections between the different subsystems are shown in Figure 4(c).

Complete chip-scale atomic clock prototypes, which include not only the physics package and local oscillator but also compact implementations of the control system needed to run them have been demonstrated recently [12]. These devices have a volume near 10 cm^3, require approximately 200 mW of electrical power to operate and achieve a short-term fractional frequency instability of a few parts in 10^{10} at one second of integration. While the long-term frequency instability has not been well characterized in these systems, a recent experiment has demonstrated that MEMS-based alkali vapor cells are capable of supporting an instability below 10^{-11} at one hour of integration and 10^{-10} at one day [17]. It appears likely that commercial systems with the specifications above and with steerable 10 MHz output will be available in the 1-2 year timeframe. This will represent an improvement by an order of magnitude in size and by over an order of magnitude in power dissipation from the current state of the art in compact atomic clocks.

Further miniaturization to 1 cm^3 and power reduction to near 30 mW also seems feasible. Physics packages dissipating less than 10 mW of power [11] and local oscillators dissipating below 5 mW have already been demonstrated [24]. It remains to develop a suitable compact, low-power control system and integrate all subsystems together.

Chip-scale atomic magnetometers have recently emerged as another type of sensor enabled by MEMS-based alkali cell fabrication. While atomic clocks are based on atomic transitions

that are first-order insensitive to magnetic fields, chip-scale magnetometers use transitions whose frequencies depend on magnetic field. The first chip-scale magnetometer, demonstrated at

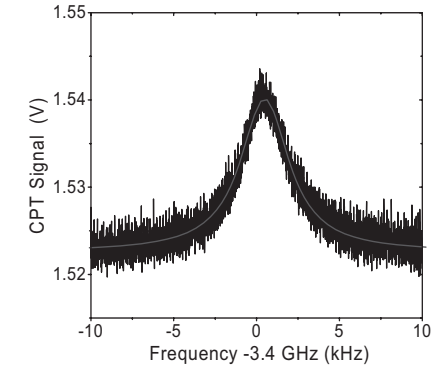

(a)

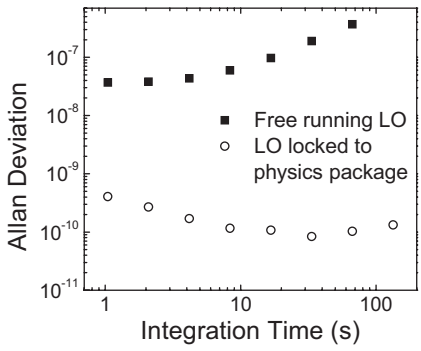

(b)

Figure 5. *(a) Atomic resonance excited with a modulated diode laser. The resonance width is 3 kHz FWHM based on the modulation frequency of 3.4 GHz (b) The fractional frequency instability, as measured by the Alan deviation, as a function of integration time for the free-running local oscillator and one locked to the chip-scale physics package.*

NIST in 2004 [13], achieved a sensitivity of 40 pT/√Hz at a frequency of 10 Hz. Subsequent table-top experiments have shown that magnetic sensors incorporating MEMS-based vapor cells can achieve a sensitivity near 1 pT/√Hz at 10 Hz. This sensitivity is comparable to that achieved by fluxgate sensors but the atom-based device offers the advantages of being non-magnetic and of measuring the magnitude of the field, rather than the component along a single axis. The scalar nature of atomic magnetometers makes them largely insensitive to rotation and therefore suitable for use on moving or vibrating platforms.

The magnetometer described in Ref. [13] had a bandwidth of approximately 20 Hz that was limited by magnetic fields produced by the thin-film resistive heaters used to heat the cell to its operating temperature. The current running through the heaters was modulated at 40 Hz to move the effects of the associated magnetic field out of the low-frequency band where the sensor operated. However, considerable improvement in the bandwidth could be obtained with a MEMS-based cell heater that generated a magnetic field below 1 pT while producing 50 mW of heat from a 3.3 V supply.

DIRECTLY COUPLED ATOM-MEMS SYSTEMS

In the work described above, MEMS techniques are used primarily for confining the atoms to a small volume. However, it is also conceivable that the quantum states of atoms in a vapor could be altered or probed with a MEMS device directly. Consider, for example, the experimental arrangement shown in Figure 6. Here a mechanically resonant microcantilever with a magnetic tip is coupled to an ensemble of atomic spins in an external magnetic field through their collective magnetic moment. Both the cantilever and the atoms have independent resonant frequencies: the cantilever's is determined by its geometry and material and the atoms' is determined by their magnetic moment and the applied DC magnetic field. If the cantilever is caused to oscillate at its resonant frequency, the motion of the cantilever tip causes an oscillating magnetic field at the location of the atoms. If the DC magnetic field is such that the atomic precession frequency (typically ~ 10 GHz/T for alkali atoms) is equal to the frequency of the cantilever motion, this oscillating magnetic field can excite a coherent spin precession in the atoms. Alternatively, if the atoms are caused to precess by some other means, the cantilever can act as a very sensitive detector for the atomic motion. It may even be possible for the coupled resonator/atom system to oscillate on its own if the coupling could be made strong enough. Such a possibility was investigated theoretically Bargatin and Roukes in Ref. [25].

In some ways this idea is similar to recent work on the detection of single atomic spins embedded in solids using magnetic resonance force microscopy [26]. While the spatial resolution of this type of detection is superior in solid-state systems due to the highly localized nature of the spin, it may be that longer coherence times can be attained in atomic vapors due to the very weak interaction of atoms in the vapor phase with their surroundings. We anticipate that a device such as that shown in Figure 6 could be used as a very compact, sensitive magnetometer by comparing the atomic precession frequency, which is proportional to the magnetic field, to the cantilever resonant frequency.

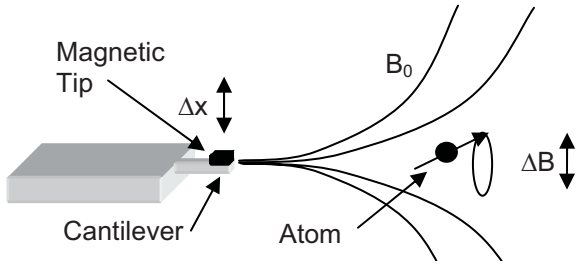

Figure 6. *Atomic spins coupled directly to the motion of a micro-cantilever with a magnetic tip through their magnetic moment.*

CONCLUSIONS

We have described in this paper an overview of some recent efforts to develop MEMS-based devices based on precise atomic transitions. The use of MEMS fabrication techniques offers the potential for small size, low power dissipation and parallel processing of many units for low cost production. Chip-scale atomic clocks are well under development. Most of the underlying physics and fabrication issues have been addressed and commercial devices are expected to appear soon. Physics packages for chip-scale atomic magnetometers, utilizing the same cell fabrication technology and with sensitivities in the range of 1 pT/√ Hz also seem feasible. Initial demonstration devices have yielded promising results. Finally, a scheme for the direct excitation and/or detection of atomic spins with a magnetic, mechanically resonant microstructure is proposed.

ACKNOWLEDGEMENTS

This work is a contribution of NIST, an agency of the US Government, and is not subject to copyright. This work was supported by NIST and the Microsystems Technology Office of the Defense Advanced Research Projects Agency (DARPA).

REFERENCES

[1] J. Vanier and C. Audoin, *The Quantum Physics of Atomic Frequency Standards*. Bristol: Adam Hilger, 1992, and references therein.

[2] A. Bloom, "Principals of Operation of the Rubidium Vapor Magnetometer", *Applied Optics*, *1*, 61 (1962).

[3] J. C. Allred, R. N. Lyman, T. W. Kornack, and M. V. Romalis, "High-Sensitivity Atomic Magnetometer Unaffected by Spin-Exchange Relaxation", *Physical Review Letters*, *89* (2002).

[4] J. T. Fraser, "Optically Pumped Magnetic Resonance Gyroscope and Direction Sensor," US Patent #3,103,621, 1963.

[5] T. L. Gustavson, P. Bouyer, and M. A. Kasevich, "Precision Rotation Measurements with an Atom Interferometer Gyroscope", *Physical Review Letters*, *78*, 2046 (1997).

[6] M. J. Snadden, J. M. McGuirk, P. Bouyer, K. G. Haritos, and M. A. Kasevich, "Measurement of the Earth's Gravity Gradient with an Atom Interferometer-Based Gravity Gradiometer", *Physical Review Letters*, *81*, 971 (1998).

[7] J. C. Camparo, "Atomic Stabilization of Electromagnetic Field Strength Using Rabi Resonances", *Physical Review Letters*, *80*, 222 (1998).

[8] J. Kitching, S. Knappe, and L. Hollberg, "Miniature Vapor-Cell Atomic-Frequency References", *Applied Physics Letters*, *81*, 553 (2002).

[9] L. A. Liew, S. Knappe, J. Moreland, H. Robinson, L. Hollberg, and J. Kitching, "Microfabricated Alkali Atom Vapor Cells", *Applied Physics Letters*, *84*, 2694 (2004).

[10] S. Knappe, V. Shah, P. D. D. Schwindt, L. Hollberg, J. Kitching, L. A. Liew, and J. Moreland, "A Microfabricated Atomic Clock", *Applied Physics Letters*, *85*, 1460 (2004).

[11] R. Lutwak, J. Deng, W. Riley, M. Varghese, J. Leblanc, G. Tepolt, M.Mescher, D. K. Serkland, K. M. Geib, and G. M. Peake, "The Chip-Scale Atomic Clock - Low-Power Physics Package," *Technical Digest of 36th Annual Precise Time and Time Interval (PTTI) Meeting*, Washington, DC, December 7-9 (2004), pp. 339.

[12] R. Lutwak, P. Vlitas, M. Varghese, M. Mescher, D. K. Serkland, and G. M. Peake, "The Mac - a Miniature Atomic Clock," *Technical Digest of Joint IEEE International Frequency Control Symposium and Precise Time and Time Interval (PTTI) Systems and Applications Meeting* Vancouver, Canada, August 29-31 (2005), pp. 752.

[13] P. D. D. Schwindt, S. Knappe, V. Shah, L. Hollberg, J. Kitching, L. A. Liew, and J. Moreland, "Chip-Scale Atomic Magnetometer", *Applied Physics Letters*, *85*, 6409 (2004).

[14] M. H. Kwakernaak, S. Lipp, S. McBride, P. Zanzucchi, W. K. Chan, V. B. Khalfin, H. An, J. R. D. Whaley, B. I. Willner, A. Ulmer, J. Z. Li, T. Davis, A. M. Braun, J. H. Abeles, A. Post, Y.-Y. Jau, N. N. Kuzma, and W. Happer, "Components for Batch-Fabricated Chip-Scale Atomic Clocks," *Technical Digest of 36th Annual Precise Time and Time Interval (PTTI) Meeting*, Washington, DC, December 7-9 (2004), pp. 355.

[15] R. Lutwak, D. Emmons, T. English, W. Riley, A. Duwel, M. Varghese, D. K. Serkland, and G. M. Peake, "The Chip-Scale Atomic Clock - Recent Development Progress," *Technical Digest of 35th Annual Precise Time and Time Interval (PTTI) Meeting*, San Diego, CA, December 2-4 (2003), pp. 467.

[16] M. Zhu, L. S. Cutler, J. E. Berberian, J. F. DeNatale, P. A. Stupar, and C. Tsai, "Narrow-Linewidth Cpt Signal in Small Vapor Cells for Chip Scale Atomic Clocks," *Technical Digest of IEEE International Frequency Control Symposium*, Montreal, PQ, August 23-27 (2004), pp. 100.

[17] S. Knappe, V. Gerginov, P. D. D. Schwindt, V. Shah, H. G. Robinson, L. Hollberg, and J. Kitching, "Atomic Vapor Cells for Chip-Scale Atomic Clocks with Improved Long-Term Frequency Stability", *Optics Letters*, *30*, 2351 (2005).

[18] C.-H. Lee, H. Guo, S. Radhakrishnam, A. Lal, C. Szekely, T. Mcclelland, and A. P. Pisano, "A Batch Fabricated Rubidium-Vapor Resonance Cell for Chip-Scale Atomic Clocks," *Technical Digest of Solid-State Sensor, Actuator and Microsystems Workshop*, Hilton Head Island, SC, June 6-10 (2004).

[19] S. W. Du, M. B. Squires, Y. Imai, L. Czaia, R. A. Saravanan, V. Bright, J. Reichel, T. W. Hansch, and D. Z. Anderson, "Atom-Chip Bose-Einstein Condensation in a Portable Vacuum Cell", *Physical Review A*, *70*, 053606 (2004).

[20] L.-A. Liew, J. Moreland, V. Gerginov, and J. Kitching, *To be published.*

[21] Y.-Y. Jau, A. Post, E. Miron, N. Kuzma, and W. Happer, "Physics and Cell Manufacturing of Miniature Atomic Clocks," *Workshop on Chip Scale Atomic Clock: Status and Potentiality*, Koganei, Tokyo, Japan, March 9-10 (2006).

[22] N. Cyr, M. Tetu, and M. Breton, "All-Optical Microwave Frequency Standard - a Proposal", *IEEE Transactions on Instrumentation and Measurement*, *42*, 640 (1993).

[23] W. E. Bell and A. L. Bloom, "Optically Driven Spin Precession", *Physical Review Letters*, *6*, 280 (1961).

[24] A. Brannon, J. Breitbarth, and Z. Popovic, "A Low-Power, Low Phase Noise Local Oscillator for Chip-Scale Atomic Clocks", *IEEE Microwave Theory and Techniques Symposium, in press* (2005).

[25] I. Bargatin and M. L. Roukes, "Nanomechanical Analog of a Laser: Amplification of Mechanical Oscillations by Stimulated Zeeman Transitions", *Physical Review Letters*, *91*, 138302 (2003).

[26] D. Rugar, R. Budakian, H. J. Mamin, and B. W. Chui, "Single Spin Detection by Magnetic Resonance Force Microscopy", *Nature*, *430*, 329 (2004).

A MEMS SINGLET OXYGEN GENERATOR

Tyrone F. Hill, Luis F. Velásquez-García, Benjamin A. Wilhite[†], Klavs F. Jensen, Alan H. Epstein, and Carol Livermore[1]

Massachusetts Institute of Technology, Cambridge, MA 02139 USA

[†]Department of Chemical Engineering, University of Connecticut, Storrs, CT 06269 USA

ABSTRACT

Abstract— The design, creation, and demonstration of a singlet oxygen generator (SOG) that operates on the microscale are presented. The micro singlet oxygen generator (μSOG) chip creates singlet delta oxygen ($O_2(^1\Delta)$) in an array of packed bed reaction channels fed by inlets with pressure drop channels to equalize flow. An integrated capillary array separates the liquid and gas byproducts, and microscale cooling channels remove excess heat of reaction. The fabrication process and package are designed to minimize collisional and wall deactivation of $O_2(^1\Delta)$. Flow behavior and capillary separation are characterized over a range of plenum (gas outlet) pressures and feed rates. The testing setup enables measurement of $O_2(^1\Delta)$ via optical emission measurements and mass spectrometry. Spontaneous decay of the $O_2(^1\Delta)$ molecule into its triplet state is observed, confirming the production of $O_2(^1\Delta)$.

Index Terms— singlet oxygen, Chemical Oxygen Iodine Laser (COIL), MEMS

INTRODUCTION

Singlet delta oxygen, $O_2(^1\Delta)$ or spin-excited molecular oxygen, is valuable as a reactant for organic synthesis and as an energy carrier for the Chemical Oxygen-Iodine Laser (COIL). COIL is attractive for applications requiring very high average powers, light weight, and overall system compactness. COIL provides a promising alternative to CO_2 lasers for industrial machining. A lower emission wavelength (1.315μm vs. 10.6 μm for CO_2) results in more efficient coupling to metals, reducing the power needed for welding and cutting. The lower wavelength also results in smaller spot size, so COIL systems offer higher machining resolution, and enables fiber-optic beam delivery for greater flexibility. In a flowing gas laser such as COIL, the waste heat flows out with the reactant exhaust gas stream so the laser average power is not limited by cooling, as are most high energy solid state lasers. The COIL system is scalable to average power output in excess of 1 MW.

COIL systems are chemical lasers in which iodine acts as the lasing species [1]. Population inversion of the gain medium is sustained by collisions between ground state iodine atoms ($I(^2P_{3/2})$) and $O_2(^1\Delta)$. $O_2(^1\Delta)$ is a metastable molecule which may be synthesized through the highly exothermic multiphase chemical reaction of gaseous Cl_2 with an aqueous mixture of concentrated H_2O_2 and KOH, commonly referred to as basic hydrogen peroxide (BHP). The laser application of $O_2(^1\Delta)$ generation requires a high yield to sustain laser emission, where yield is defined as the fraction of product oxygen in the $O_2(^1\Delta)$ state. High conversion of Cl_2 to $O_2(^1\Delta)$ is achieved by effective mixing of the gas and liquid reagents. Once produced, singlet-oxygen may deactivate into ground-state oxygen by gas-phase collisions with water vapor, other oxygen or helium diluent molecules, and by heterogeneous collisions with either solid- or fluid surfaces. Thus, the reactor design must provide large surface areas for initial $O_2(^1\Delta)$ generation, balanced by subsequent rapid separation of gas and liquid phases, while maintaining low pressures (~50-250 torr) to minimize homogeneous deactivation and low temperatures (< 0°C) to minimize water vaporization and subsequent deactivation. The present work shows that the challenges of high yield, thermal management, and product separation can be successfully addressed by a MEMS-based approach to $O_2(^1\Delta)$ generation.

Before continuing the discussion of μSOG development, it is useful to define the excitation states of molecular oxygen discussed. An oxygen molecule has four electrons in its outer p-subshell. The $O_2(^3\Sigma)$ state ("triplet" or ground state oxygen) has three electrons in one spin state and the fourth in the other, while the $O_2(^1\Delta)$ state has two electrons in each of the 'spin up' and 'spin down' configurations [2]. The near resonance between $O_2(^1\Delta)$ state and the $I(^2P_{1/2})$ state of atomic iodine makes $O_2(^1\Delta)$ an ideal pumping source for laser emission.

Generation of $O_2(^1\Delta)$ for COIL was first demonstrated by McDermott et al. in 1978[1]. Cl_2 gas was bubbled through an aqueous solution of 90% wt H_2O_2 and 6M NaOH in a sparger at a flow rate of 6000 sccm, producing singlet delta oxygen. After passing through a cold trap to remove moisture and unreacted chlorine, the product gas was injected into a mixture of I_2 and Ar. The yield obtained was approximately 40%. The system was cooled by a combination of dry ice and ethanol. McDermott's method was successful, but it is limited by significant deactivation of $O_2(^1\Delta)$ gas before separation from the liquid phase. Subsequent SOG configurations have employed either jets of BHP droplets mixed with Cl_2 [3] or rotary SOG configurations [4]. In rotary SOGs a film of BHP on the surface of a rotating wheel is exposed to a Cl_2 stream, resulting in $O_2(^1\Delta)$ production at the interface. However, these configurations have their limitations: a small gas – liquid contact area for rotary SOGs, and a large volume for the jet configuration. The present work demonstrates that arrays of

[1] Sponsored by Defense Advanced Research Projects Agency, Tactical Technlogy Office (TTO); Micro Chemical Oxygen-Iodine Laser (COIL) Program; ARPA Order No. T171/00, Program Code: 4G10; Issued by DARPA/CMO under Contract No. MDA972-04-C-0140.

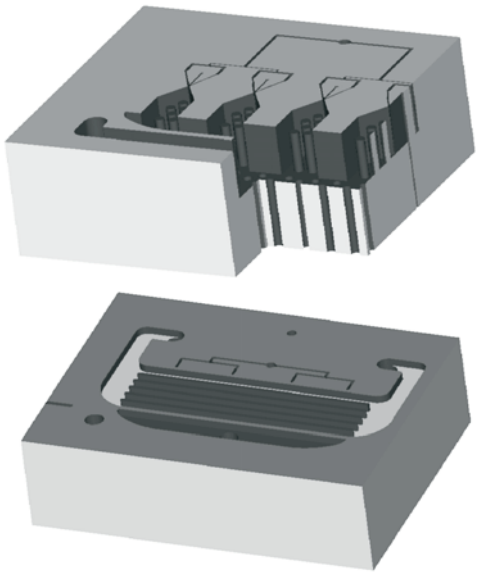

Figure 1. *(Top) A simplified 3D cutaway of the SOG device, showing bifurcated inlets, pressure drop channels, reaction channels, and capillary separator array. (Bottom) The lower wafer contains gas bifurcations, cooling channels, and inlet/outlet ports.*

MEMS-based SOGs can address the shortcomings of these previous designs, thus providing greater $O_2(^1\Delta)$ flow per unit volume.

This paper first presents a conceptual discussion of SOG operation and details of the device design. The packaging scheme and testing rig are then summarized. Flow functionality of the chip was demonstrated for a variety of gas and liquid feed rates. Experimental results that confirm the production of singlet delta oxygen are presented, and comparisons with macro-scale SOGs are made.

SOG CONCEPT

SOGs typically produce $O_2(^1\Delta)$ by mixing gaseous chlorine and BHP, according to the chemical equation

$$H_{22} \quad KOH\Theta + Cl_2 \quad 2H_2 \quad 2KCl\Theta + {}_2{}^1\Delta)(O \qquad (1)$$

Often the Cl_2 is mixed with a buffer gas (He or N_2) in order to raise the total pressure of the stream. After generation, $O_2(^1\Delta)$ may be deactivated by several mechanisms, the most prominent being collisions between $O_2(^1\Delta)$ molecules,

$${}_2{}^1\Delta)(O \quad {}_2{}^1\Delta)(O\Theta + {}_2(O\Sigma) + \quad {}_2(O\Sigma)\,, \qquad (2)$$

and wall interactions

$${}_2(O\Delta) + \quad 1 \rightarrow \quad {}_2(O\Sigma)\text{val} \qquad (3)$$

Because reactants are distributed between two different phases, maximizing the contact area between gas and liquid phases is critical to obtain high yields. Previous studies have shown that microreactors offer advantages with respect to mass and thermal transfer characteristics [5]. The µSOG maximizes contact area between phases by conducting the reaction in an array of packed bed reaction channels. Pressure-drop channels located upstream of each packed bed aid in equalizing gas and liquid flow throughout the microdevice.

A previous analytical study evaluated the feasibility of microscale $O_2(^1\Delta)$ generation [6]. Using standard MATLAB numerical simulation techniques and estimates of physical parameters, key SOG dimensions and operating points were optimized. The optimum device dimensions (with respect to the estimated parameters) included a reaction channel length of 0.516 cm, 0.25 cm long pressure drop channels, a 1 cm section for gas and liquid flow distribution, and an optimal $He:Cl_2$ flow rate of 175 sccm. The dimensions employed in the present µSOG mask design were largely based on the results and conclusions of this study.

DEVICE DESIGN AND FABRICATION

The µSOG consists of a two-wafer silicon stack capped by a Pyrex layer. The upper silicon layer contains symmetrically bifurcated BHP inlets and pressure drop channels to distribute the reactants evenly across the chip, an array of 32 reaction channels to enable the multiphase reaction of BHP and Cl_2, and a capillary separator array to remove spent BHP and waste products. The pressure drop channels have a width of 25 µm and a depth of approximately 20 µm. The reaction channels are each 6.1 mm long, 630 µm wide, and 300 µm high. They contain posts of diameter 70 µm and pitch 90 µm, which increase the contact area between gas and liquid phases. This post-bed configuration is a two-dimensional approximation of a conventional packed-bed, providing reduced pressure drops while alleviating the need for subsequent packing of reaction channels. The separator contains approximately 10,000 20 µm holes which remove the liquid effluent via capillary forces [7].

The lower silicon layer contains cooling channels to remove heat generated during the reaction, enabling low-temperature operation, along with supporting structures: inlets, outlets, and bifurcated gas distribution. The 19 cooling channels are of width 300 µm and height 300 µm. The BHP and Cl_2 inlets are 1 mm in diameter; all other inlet and outlet connections are 2 mm in diameter. Finally, the chip contains a thermocouple port for *in situ* temperature monitoring. The die size was set at 3.6 cm x 2.8 cm to accommodate packaging. The features on both layers were created using a deep reactive ion etch (DRIE) process.

Starting materials for the SOG were two 625 µm thick <100> DSP silicon wafers purchased from Silicon Quest (San Jose, CA) and one 625 µm thick Pyrex wafer obtained from Bullen Ultrasonics of Eaton, OH. First, a 0.5 µm silicon dioxide protection layer was grown on each wafer by thermal oxidation. A nested mask was used to create 20 µm deep pressure drop channels, 350 µm high posts, and the separator bed on the reaction chamber wafer. Next, a wet oxidation step was used to grow a 0.5 µm protective oxide layer over the posts. This layer prevented erosion of the posts during subsequent long DRIE steps. The capillary holes were formed by lithographically patterning the wafer backside and DRIE. Finally, all remaining thin films were removed from both sides.

The first step in creating the lower wafer was the deposition of a 4 µm PECVD oxide hard mask on both surfaces. Photoresist was spun onto both sides of the wafer, and cooling channel and inlet/outlet patterns were patterned in the films on the top and bottom surfaces, respectively. DRIE was used to form the cooling

TABLE I
EXPERIMENTAL CONDITIONS

Parameter	Value
He Flowrate	37 sccm
Cl_2 Flowrate	13 sccm
BHP Flowrate	1 ml/min
BHP Delivery Pressure	40 psig
Plenum Pressure	100 torr
Separator Pressure	20 torr
Chip Temperature	3 C
BHP Supply Temperature	-10 C

channels and liquid waste collection area on the top surface. Finally, flow inlets and outlets were etched in the backside by DRIE. Selected fabrication cross sections for both wafers are given in Fig. 2.

After removing the remaining films from the cooling wafer, the stack was fusion bonded. Following bonding, the stack was annealed in N_2, and 0.4 μm PECVD Si-rich nitride was deposited on it. The nitride forms a protective layer over the reaction wafer surface as well as the sidewalls of the capillary separator features and inlets, preventing the BHP from attacking the silicon during operation. Finally, the Pyrex wafer was anodically bonded to the stack and the chips diced.

PACKAGING

The finished chips were packaged using teflon tubing and fiberglass-reinforced epoxy. Teflon connections were chosen to give the setup flexibility and to minimize alignment issues. Stainless steel Swagelok ferrules were used to hold the tubing in place prior to gluing. The BHP inlet was connected to 1/16" tubing. All other connections were made with 1/8" teflon with the exception of the gas outlet, which was connected directly to a quartz optical cell for $O_2(^1\Delta)$ detection.

A significant issue when selecting packaging materials was minimizing deactivation of $O_2(^1\Delta)$. Glass surfaces are particularly attractive for the gas outlet, owing to a wall deactivation coefficient that is half that for the best metals and an order of magnitude lower than teflon [8].

EXPERIMENTAL SETUP

Because of the toxic and corrosive nature of chlorine gas and hydrogen peroxide, all experiments are performed inside a ventilated cabinet. As shown schematically in Figure 4, mass flow controllers regulate both helium and chlorine supply to the μSOG. A second helium flow is employed to pump BHP from a thermostated reservoir to the μSOG. The helium pressure (and thus the BHP flow rate) is regulated by a pressure controller. After flowing through the chip and separator, the BHP is collected in a second thermostated reservoir. Both reservoirs were maintained at temperatures of $^{-}10^{o}$C - $^{-}20^{o}$C to minimize BHP decomposition. Ensuring that the BHP is properly cooled is critical for safety; at temperatures above 50C, H_2O_2 decomposition is accelerated and the solution can be explosive. Before reaching the vacuum pump, both lines pass through liquid nitrogen cooling traps in order to condense water vapor and unreacted chlorine. The gas outlet is also connected to a mass spectrometer through a 189 μm diameter

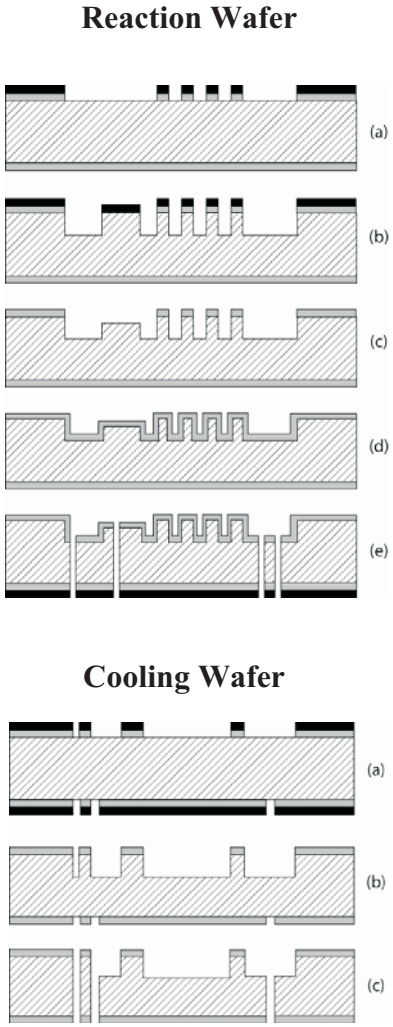

Figure 2. *μSOG fabrication process: (gray denotes SiO_2, black denotes resist) Reaction wafer— (a) reaction channels are patterned in SiO_2 and resist layers, (b) & (c) nested mask process creates pressure drop and reaction channels, (d) SiO_2 protection layer grown over features, (e) separator holes and inlets are pattern and etched from the backside. Cooling wafer— (a) front and backside features patterned with resist and SiO_2, (b) & (c) a silicon dioxide layer is used as a hard mask to etch features on both surfaces.*

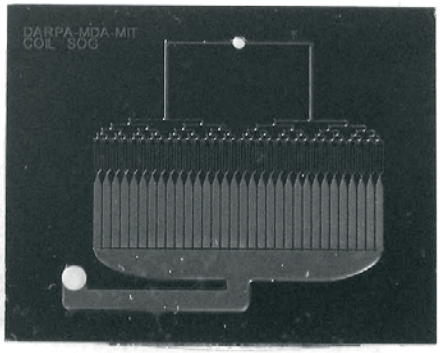

Figure 3. *Photograph of a completed chip*

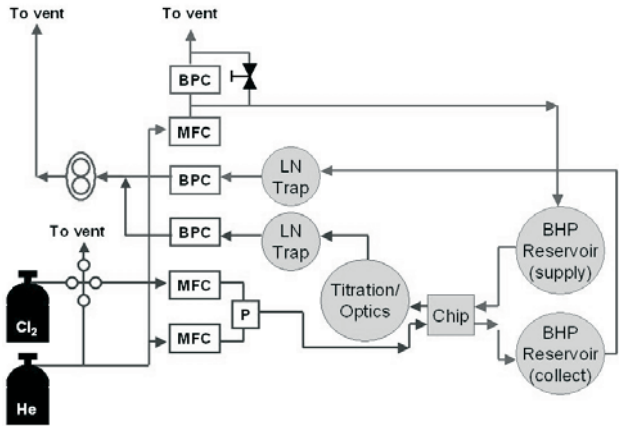

***Figure 4**. Schematic of experimental apparatus*

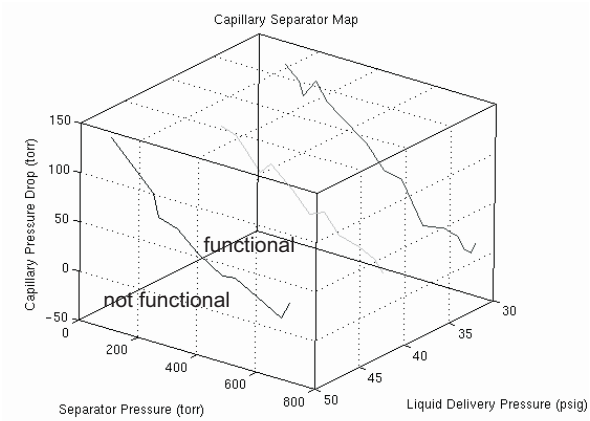

***Figure 5**. Map of capillary separator performance*

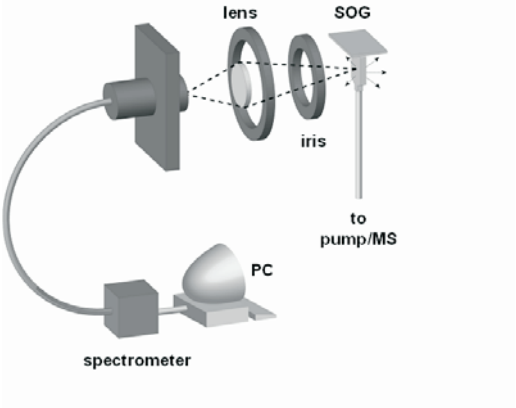

***Figure 6**. Illustration of emission measurement concept*

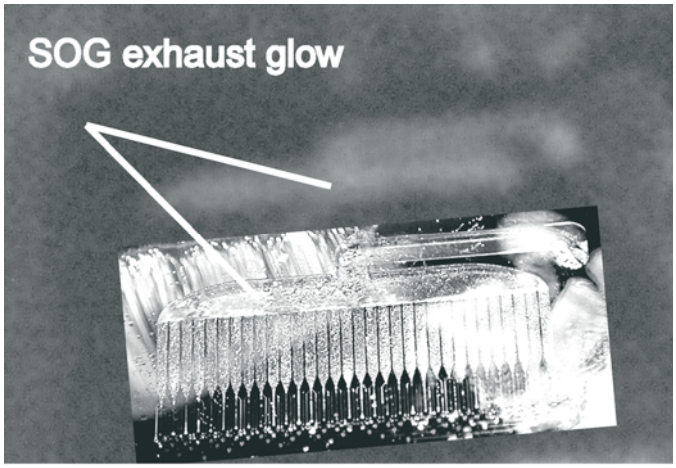

***Figure 7**. (Background) pink glow from $O_2(^1\Delta)$ dimer emission. (Foreground) Superimposed image of μSOG.*

glass capillary line, allowing sampling of a portion of the plenum stream. The entire setup is served by an external chiller (Julabo, Allentown, PA), which circulated a silicone-based cooling fluid through the chip and both the BHP supply and collection reservoirs.

Prior to operation with Cl_2 and BHP reagents, the μSOG flow functionality was investigated using inert He and distilled (DI) water. The two functionalities of primary importance are (i) gas-liquid hydrodynamics in the packed-bed reaction channels, and (ii) extent of liquid removal by the capillary separator. Both are critical to device performance, as the former directly effects the rate of $O_2(^1\Delta)$ generation, and the latter impacts $O_2(^1\Delta)$ yield.

Two unique modes of gas-liquid flow were observed in the present device. At low to moderate gas and liquid flows, a steady flow pattern is observed, in which the liquid flows continuously as a wetted film along both the channel walls and partially wets the posts, while the gas flows through the remaining voids. Once developed, gas-liquid interfaces remained stationary with the majority of reactor volume being gas, resulting in limited interaction of the two phases. At high gas and liquid flow rates, the gas-liquid interface begins to fluctuate rapidly, resulting in an unsteady liquid flow which may enhance gas-liquid mixing. The former, steady flow, was observed under all reacting conditions investigated.

The capillary separator performance was also investigated using He and H_2O. The separator operates on the basis of liquid capillary pressure; during operation the 20 μm holes are filled with liquid, which is driven through the holes and out of the chip by an imposed pressure drop. The capillary pressure of the liquid film resists flow of gas through these same holes, thus effectively separating the two phases. It was observed (shown in Figure 5) that as the liquid flow increases, the necessary capillary pressure drop likewise increases. As separator pressure decreases, the required pressure drop across the separator also increases.

Although it is relatively straightforward to confirm $O_2(^1\Delta)$ generation, quantitatively measuring the yield is a significant challenge. Typically SOG performance is determined in the context of a complete COIL system; heuristics are used to estimate yield from output power along with various losses and efficiencies in the system [9]. Out of the array of methods of measuring and quantifying yield [4,10,11], one of the simpler options was chosen. Production was confirmed by observing the $O_2(^1\Delta)$ dimer emission, which appears as a pink glow. The number of $O_2(^1\Delta)$ molecules in a given volume can be calculated by measuring the spontaneous emission produced by the $O_2(^1\Delta)$ - $O_2(^3\Sigma)$ transition at a wavelength of 1268 nm. The chlorine utilization, or percentage of chlorine converted to oxygen, can be determined via mass spectrometry. These two measurements were used together to calculate $O_2(^1\Delta)$ yield.

The emission measurement was done on a 4 cm x 1 cm quartz

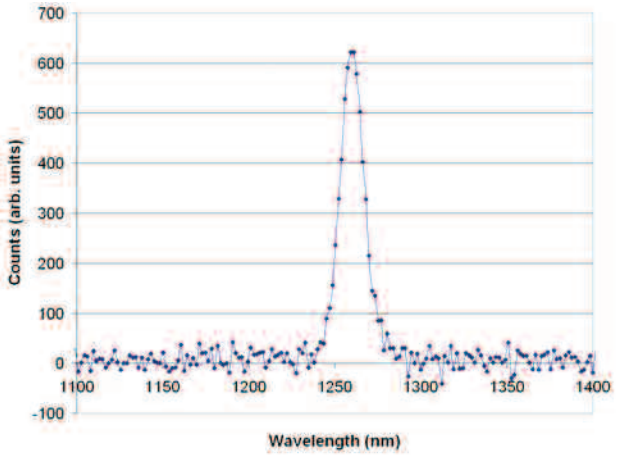

Figure 8. *IR Spectra from μSOG showing peak from $O_2(^1\Delta)$- $O_2(^3\Sigma)$ transition*

CONSTANTS FOR EQUATIONS 4-8

Symbol	Quantity	Units
I	LED current (used in calibration)	Amperes
V	LED voltage (used in calibration)	Volts
η_{LED}	LED efficiency	dimensionless
X	Fraction of illumination captured by optics (calibration)	dimensionless
γ	Spectrometer efficiency correction factor	dimensionless
Δt	Integration time	seconds
θ_{samp}	Solid angle sampled by optics (experiment)	steradians
y_x	Mole fraction of species x	dimensions
P_{oxygen}	Partial pressure of oxygen	torr
V_{optics}	Column of cuvette sampled by optics	cm^3
C_m	Measured counts	Arbitrary units
τ	Singlet oxygen lifetime	seconds

cuvette (Starna, Atascadero, CA), which was connected directly to the μSOG gas outlet. An Ocean Optics (Dunedin, FL) NIR512 InGaAs array spectrometer was used to analyze photons from the spontaneous emission. Light was relayed from the cuvette to the spectrometer by focusing optics. A lens (f/# 1.9) was placed 13.1 cm from the cuvette and 8.1 cm from the spectrometer's fiber input. The emission setup, described in Figure 8, was calibrated using an infrared LED. Sample gas for the mass spectrometer was collected through a glass capillary connected to the plenum line. The signal was calibrated using an 80%:20% He:O_2 tank, with other conditions matching those of the experimental run.

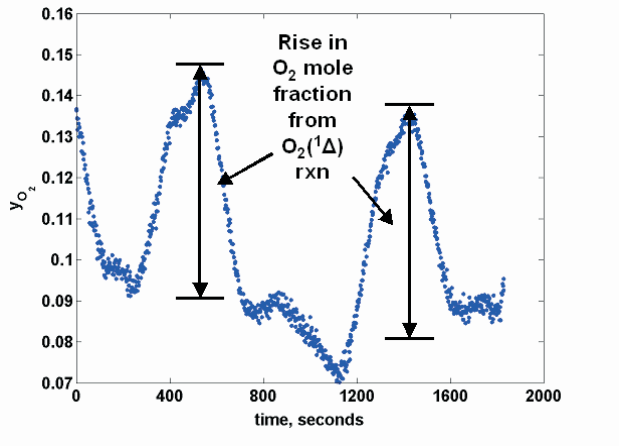

Figure 9. *Mass spectrometer signal showing oxygen mole fraction as a function of time during the experimental run*

TABLE II
COMPARISONS WITH OTHER SOGS

SOG type	$O_2(^1\Delta)$ FLOW RATE PER UNIT VOLUME ($X10^{-4}$ MOL/S/L
Sparger	2.3
Jet-type	23
Disk-type	87
μSOG (this work)	90

TESTING

Prior to testing, the BHP solution is prepared within the supply reservoir as follows. First 20 ml of a 50 wt% aqueous H_2O_2 solution (Aldrich) is chilled to ¯20°C in the jacketed reservoir. Then, 20 ml of a 50 wt% aqueous KOH solution is slowly added, such that the mixture temperature never exceeds 10°C. Significant heat is released upon mixing of KOH and H_2O_2, and thus care must be taken to avoid overheating of the BHP solution. When complete, the BHP reservoir is sealed and pressurized with He to initiate BHP flow through the μSOG. He flow is then initiated through the chip, and the separator and plenum pressures are slowly lowered to 100 and 80 torr respectively. When the pressures are stable and the separator is working properly, the chlorine flow is introduced in pulses of several minutes duration each. Table 1 summarizes the test conditions. A visible pink glow from the dimer emission, shown in Figure 7, is observed in the chip's capillary separator. The emission measurement was made 2.5 cm below the SOG gas outlet. Spectra from the $O_2(^1\Delta)$ - $O_2(^3\Sigma)$ transition are shown in Figure 8. The oxygen mole fraction of the output stream, given in Figure 9, shows an increase in O_2 content with the Cl_2 pulses.

DISCUSSION

In order to determine $O_2(^1\Delta)$ yield, concentrations of both $O_2(^1\Delta)$ and total oxygen must be calculated for the volume interrogated by the optics. The calibration factor β, defined as

$$\beta = \frac{I \quad \eta_{LED} **** \gamma * \Delta t X V}{counts} \qquad (4)$$

relates energy from the $O_2(^1\Delta)$ - $O_2(^3\Sigma)$ transition to spectrometer counts. Because the calibration and experiment involve two different wavelengths (940 and 1268 nm respectively), the correction factor γ is needed to account for variations in spectrometer sensitivity. The efficiency of the calibration LED, η_{LED}, was calculated as approximately 15% using the half angle of emission and assuming a Gaussian intensity profile. The number of $O_2(^1\Delta)$ photons collected by the optics is

$$N_{SD} = \frac{C_m \quad \beta \quad 4\pi^{**}\tau}{h\upsilon * \Delta t_{\exp} * \theta_{samp}} . \qquad (5)$$

The isotropic nature of the $O_2(^1\Delta)$ emission is reflected by the solid angle correction factor ($4\pi/\theta_{samp}$). The oxygen mole fraction of the output stream was calculated from the mass spectrometry data and shows an increase in O_2 content as a function of the Cl_2 pulses

$$r_{Cl} = \frac{\Delta y_{O_2}}{y_{Cl}} . \qquad (6)$$

Considering the rise in O_2 mole fraction and the original Cl_2 mole fraction of 25%, r_{Cl} was determined to be 24%. After using r_{Cl} to determine P_{oxygen}, the total number of O_2 molecules is calculated as

$$N_{tot} = \frac{P_{oxygen} V_{optics}}{RT} . \qquad (7)$$

The yield,

$$Y = \frac{N_{SD}}{N_{tot}} , \qquad (8)$$

at the measurement point is between 77-100%. The uncertainty in the yield measurement is primarily due to 4% error in the distance of the focusing optics from the cuvette. This uncertainty is reflected in both the calculation of V_{optics} and in the final yield number.

The analytical model described in [6] predicts a yield of 86% at the gas outlet for these flow conditions and for a chlorine utilization of 24%, which is consistent with the experimental data obtained. The high yield of the μSOG makes it competitive with the existing COIL technologies [3, 4, 12]. Table 2 offers a comparison between the performance of the μSOG and published macroscale SOGs. The $O_2(^1\Delta)$ molar flow rate per unit reaction volume is 90×10^{-4} mol/l/s, which is comparable to the most efficient $O_2(^1\Delta)$ flow rates reported for macro-scale SOGs.

These results were obtained for flow rates near the minimums of the parameter space (gas and liquid flowrates) explored in the previous theoretical study [6]. Results from that study predict higher yields at increased throughputs, owing to higher chlorine conversions. Further improvements in performance are possible via improved gas-liquid mixing at higher flows. Present results were obtained under steady-flow patterns in which gas and liquid contact area comprised a small portion of the available reaction channel surface. As a result, chlorine utilization was significantly lower than expected theoretically, and therefore less $O_2(^1\Delta)$ was created. At increased gas and liquid flows, unsteady-flow patterns develop, resulting in improved gas-liquid interaction.

CONCLUSIONS

We have demonstrated the first production of $O_2(^1\Delta)$ in a microscale device for COIL applications. The yield was determined through a combination of emission and mass spectrometry measurements. Using the metrics of $O_2(^1\Delta)$ yield and molar flow rate per unit reaction volume, the μSOG performs better than its macro scale counterparts. Future increases are possible, dependent on flow regime and chlorine utilization. The results obtained are very promising for COIL applications.

ACKNOWLEDGEMENTS

The authors acknowledge J. Letendre for his expertise in building the experimental apparatus and D. Park for help with images of the SOG and optics. Additionally, the microfabrication expertise of Dr. Hanqing Li was critical to the success of the project. The Missile Defense Agency (MDA) and the Tactical Technology Office at DARPA generously provided funding for this research. The views and conclusions contained in this document are those of the authors and should not be interpreted as representing the official policies, either expressed or implied, of the Defense Advanced Research Projects Agency or the U.S. Government.

REFERENCES

[1] W. E. McDermott et al., "An electronic transition chemical laser," *Appl. Phys. Lett*., vol. 32(8), 1975.

[2] H. H. Wasserman and R. W. Murray, *Singlet Oxygen*. New York, New York: Academic Press Inc., 1979, p. 25.

[3] S. Yoshida, H. Saito, and T. Fujioka, "New singlet oxygen generator for chemical oxygen-iodine lasers," Appl. Phys. Lett., 49 (18), 1986.

[4] K. R. Kendrick et al., "Determination of Singlet-Oxygen Generator Efficiency on a 10-kW Class Supersonic Chemical Oxygen-Iodine Laser (RADICL)" *IEEE J. Quantum Electronics*, vol. 35(12), pp. 1759-1764, 1999.

[5] M. W. Losey et al., "Microfabricated Multiphase Packed-Bed Reactors: Characterization of Mass Transfer and Reactions," *Ind. Eng. Chem. Res*. 2001, vol. 40, pp. 2555-2562.

[6] B. A. Wilhite et al., "Design of a MEMS-Based microChemical Oxygen-Iodine Laser (μCOIL) System," *IEEE J. Quantum Electronics*, vol. 40 (8), pp. 1041-1055, 2004.

[7] A. Günther, et al., "Micromixing of Miscible Liquids in Segmented Gas-Liquid Flow," Langmuir, vol. 21, pp.1547-1555, 2005.

[8] K. A. Truesdell, S. E. Lamberson, G. D. Hager, "Phillips Laboratory COIL Technology Overview," AIAA 92-3003.

[9] J. F. Hon et al., "A Heuristic Method for Evaluating COIL Performance," AIAA 94-2422.

[10] W. T. Rawlins et al., "Spectroscopic Studies of a Prototype Electrically Pumped COIL System," SPIE Photonics West (2004), San Jose, CA.

[11] W. Zhao et al., "Measures of the yield and chlorine utilization of singlet oxygen generator by uses of Raman spectroscopy," *Applied Optics*, vol. 42 (18), 2003.

[12] M. V. Zaguidullin et al., "The sub- and supersonic COILs driven by jet type singlet oxygen generator," *SPIE*, vol. 3574, pp. 246-252.

A MICRO DIRECT METHANOL FUEL CELL WITH SELF-PUMPING OF LIQUID FUEL

Dennis Desheng Meng* **and Chang-Jin "CJ" Kim**
Mechanical and Aerospace Engineering Department, University of California, Los Angeles (UCLA)
Los Angeles, CA, U.S.A.

ABSTRACT

This paper introduces a micro direct methanol fuel cell (μDMFC) with an imbedded self-pumping mechanism to deliver liquid fuel. The fuel is propelled without any power consuming component (e.g., a pump), while removing the CO_2 bubbles generated by the fuel-cell electrochemical reaction of the system. Furthermore, the pumping rate is self-regulated by the reaction, i.e., by the load. By eliminating the need for a pump and gas/liquid separator, our design allows much simpler systems, which is especially beneficial for miniaturization. Although we test with μDMFC in this paper, the mechanism applies to other hydrocarbon liquid fuels as well.

INTRODUCTION

Due to its much higher energy density than traditional batteries, micro direct methanol fuel cell (μDMFC) has been widely considered as the next generation power source for portable electronic devices. μDMFC has been anticipated to be one of the first fuel cells to fully enter the consumer market in the near future [1], with a few products already announced [2-4]. However, several technical hurdles still need to be cleared to make the μDMFC mature and finally accepted by the consumer market, including the cost, the performance of membrane electrode assembly (MEA), and the complexity compared with traditional batteries.

The working principle of μDMFC is illustrated in Fig. 1. The aqueous methanol solution is fed into the anodic channel while air flows through the cathodal channel. A series of electrochemical reactions are enabled by the proton exchange membrane (PEM) and the catalyst layers. Protons migrate from anode to cathode through the PEM, while electrons are collected by the anodic electrode and consumed in the cathodal electrode. The accumulated electrons provide the continuous current for the external circuit. An external pump is usually used to provide a continuous flow of methanol fuel to the anode and maintain the fuel concentration there.

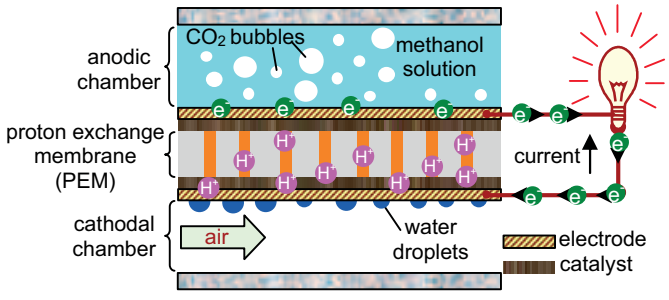

Figure 1. *Working principle of direct methanol fuel cell*

In the fuel stack of a DMFC, the electrochemical reactions are:

$$CH_3OH + H_2O \rightarrow 6e^- + 6H^+ + CO_2\uparrow, \quad \text{(anode side)}$$
$$1.5O_2 + 6e^- + 6H^+ \rightarrow 3H_2O, \quad \text{(cathode side)}$$
$$CH_3OH + 1.5O_2 \rightarrow 2H_2O + CO\uparrow. \quad \text{(overall reaction)}$$

According to this reaction, μDMFCs intrinsically generate CO_2 gas bubbles. If not promptly removed, these bubbles will clog the anodic microchannels and aggravate the deleterious methanol crossover. The current common practice is to use an external pump to deliver the fuel and push the gas bubbles to downstream at the same time. Then an open tank (gas/liquid separator) can be used to release CO_2 gas [5]. This approach is impractical in a portable device because of the danger of fuel leakage. Meanwhile, using an external pump to deliver fuel not only takes up a space and complicates the microsystem, but also claims a significant portion of the power output of μDMFC. Since most reported micropumps require 100 mW or higher of power input, about 10% of the fuel cell total power output (usually ~1 W) has to be consumed by pumping. This percentage can be even higher if the fuel cell is not working at the maximum power capability.

We have previously proved that nanoporous membrane can remove gas bubbles while holding liquid with satisfactory pressure tolerance [6]. Combined with virtual check valves, the venting mechanism has also enabled a new bubble-driven pumping mechanism. The gas bubbles generated by electrolysis were employed to circulate Na_2SO_4 aqueous solution in a microfluidic loop [7].

In this paper, a similar pumping mechanism is applied to a μDMFC, with the intrinsically generated CO_2 gas bubbles as the gas source. Therefore, the fuel delivery requires no power input at all. The design solves the bubble clogging and fuel delivery problems at the same time. Both the gas/liquid separator and external pump are eliminated from the system, allowing an integrated, simply and economic design of μDMFC system.

HYDROPHOBIC VENTING

The gas removal approach is implemented by microscopic hydrophobic (or lyophobic for methanol) venting holes, which allow the gas to pass through relatively undeterred while the liquid menisci blocks the liquid from flowing out. Fig. 2 represents an idealized model to illustrate how liquid can be restricted from leaking by its own meniscus. On the sharp corner of the venting hole's entrance, this meniscus can assume a range of curvatures, so as to balance with the varying pressure across the meniscus (transmeniscus pressure) according to the Laplace-Young equation:

$$P_l - P_o = 2\sigma_l \cdot \cos(\pi - \alpha)/r, \quad (1)$$

where P_l is the pressure of the liquid fuel, P_o is the ambient pressure, σ_l is the surface tension of the liquid fuel, α is the angle

* Corresponding author: Dennis Desheng Meng, 37-129 Engr. IV, UCLA, CA 90095, Tel: (310)825-3977, Email: desheng@seas.ucla.edu

between meniscus and the capillary, and *r* is the radius of the capillary.

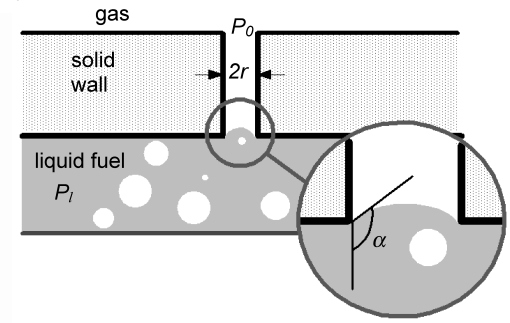

Figure 2. *Hydrophobic venting by a microscopic venting hole*

The maximum transmeniscus pressure that can be withstood without leakage (leakage onset pressure) is determined by the size of the venting hole as well as the surface properties associated with the hydrophobic material. Due to their intrinsic hydrophobicity and small pore size, hydrophobic nanoporous membranes can provide very high leakage onset pressure. Successful venting of gas bubbles has been achieved for both pure water and methanol fuel with a concentration as high as 10 M, by employing porous polypropylene membrane with a nominal pore radius of 0.1 μm (from Chemplex®). The fuel is proven to be contained without leakage under the over-pressures as high as 200 kPa for both pure water and 10 M methanol, fulfilling the requirement of the current- as well as next-generation μDMFC [8].

PUMPING BY HYDROPHOBIC VENTING

A new bubble-driven pumping mechanism [9] has been developed utilizing hydrophobic venting, as Fig. 3 illustrates. A group of small hydrophilic capillaries are fabricated on the left side of the bubble source to serve as a virtual check valve for gas bubbles. When a bubble grows at a location close to this virtual check valve (as Fig. 3-a shows), expansion of the left menisci of the bubble is hindered due to its capability to provide higher capillary pressure than the right meniscus does. Consequently, the bubble only grows to the right and pushes the liquid rightward. The bubbles generated in the middle of the microchannel can be pushed by the leftmost one to the right. This rightward bubble motion can also be promoted by proper design of the channel shape, e.g., a diverging hydrophilic shape [10]. By making the microchannel hydrophilic (e.g., SiO_2), a surface energy difference between its hydrophilic surface and the hydrophobic membrane can make the latter a "bubble trap" [11]. Once a bubble reaches the hydrophobic nanoporous membrane, it will be drawn into the membrane region (Fig. 3-b). Through the venting holes in the membrane, the bubble is vented out without liquid loss. The liquid then fills into the section symmetrically to replace the vacancy left by the gas bubble. A pumping cycle is thus completed and a net pumping to the right is achieved.

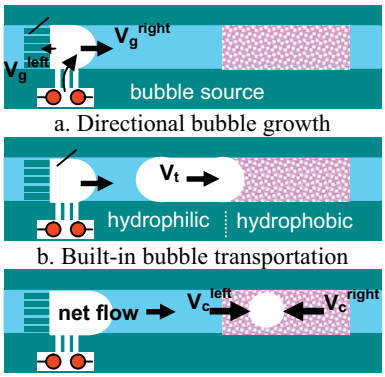

Figure 3. *Micropumping by directional growth and hydrophobic venting of bubbles*

By using this self-pumping method, liquid circulation in a sealed closed-loop microchannel has been demonstrated by using electrolytic gas bubbles (H_2 and O_2). By applying 2-85 mW power input, the liquid is circulated at a volumetric flow rate of 4.5-13.5 nL/s in the particular pump loop. Compared with the similar thermal-bubble-driven pump, the electrochemical-bubble-driven micropump exhibits better controllability and biocompatibility with 10-100 times higher power efficiency.

FABRICATION AND ACTIVATION OF μDMFC

In this paper, a similar pumping mechanism is applied to a μDMFC, with the intrinsically generated CO_2 gas bubbles as the gas source. Therefore, the fuel delivery requires no power input.

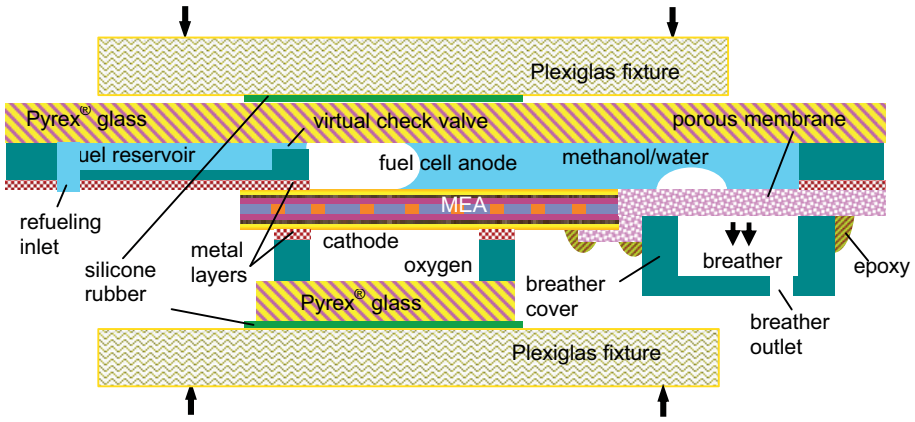

Figure 4. *The cross-section of assembled self-pumping μDMFC*

The cross-section of the assembled self-pumping μDMFC is shown in Fig. 4. Microchannels of the anode, the cathode and the breather cover are fabricated by DRIE, followed by metal evaporation (0.01 μm Cr, 3 μm Cu and 0.5 μm Au). The anode and

the cathode are then anodically bonded to two pieces of Pyrex® glass. A Plexiglas fixture is used to sandwich MEA (E-TEK®) between the anode and the cathode. Silicone rubber sheets are added between the Plexiglas fixture and the µDMFC device to ensure uniform clamping pressure. A piece of nanoporous polypropylene film (Chemplex®) is glued between the anode and the breather cover by epoxy to remove CO_2 gas bubbles during operation. The breather outlet is connected to a valve via tubing. The venting can be stopped by closing the valve to perform the control experiment. The layout of the anode microchannels, the return loop and the reservoir is shown in Fig. 5.

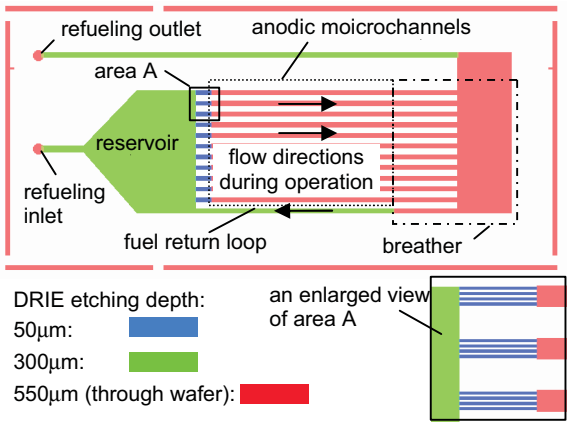

Figure 5. *Layout of anodic microfluidic loop*

After assembly, the MEA of the fuel cell is activated according to the procedure provided by the manufacturer. Hot DI water at 90 °C is first flowed through the anode microchannels with a flow rate of 5 mL/min for 1.5 hours to activate the proton exchange membrane. Then, 2 M methanol at 90 °C is flowed through the anode microchannels with a flow rate of 5 mL/min for 3 hours. Meanwhile, oxygen is flown through the cathode channel at ~100 mL/min. The cell voltage is controlled at ~0.25 V by connecting it to a variable resistor. This second step activates the catalyst. During activation, an external pump is used to deliver the anodic liquid from the "refueling inlet" to the "refueling outlet" in Fig. 5. A pressurized gas tank is used to provide the cathodal gas flow. The measured polarization and power density curves of the µDMFC after activation are shown in Fig. 6. This test has been performed with 5 ml/min 2 M methanol flow at anode, ~ 100 ml/min oxygen flow at cathode and 80 °C cell temperature.

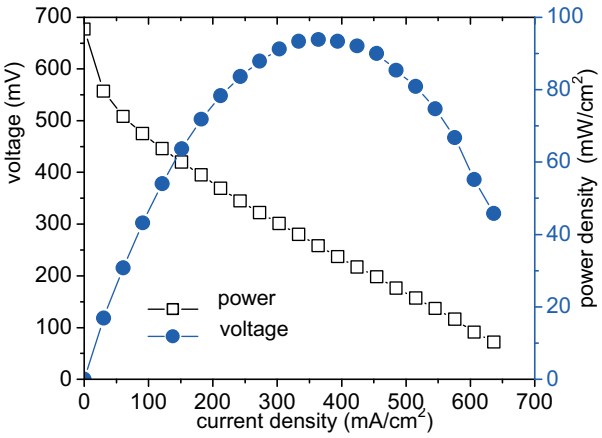

Figure 6. *Polarization and power density curves of the assembled µDMFC after MEA activation*

VERIFICATION OF FUEL CIRCULATION

After activation, the fuel cell can be brought to operation condition with both the "refueling inlet" and the "refueling outlet" closed. They can be used to refuel the fuel cell if the fuel in the reservoir is used up. The gas bubbles generated by the electrochemical reaction are used as the gas source in a self-pumping mechanism to circulate the fuel, as Fig. 5 indicated. This fuel circulation mechanism does not require any external power input. Similar bubble motion pattern as in [7] has been observed throughout the flow field. Fig. 7 demonstrates the bubble motion at the end of an anodic microchannel, as well as the successful bubble removal.

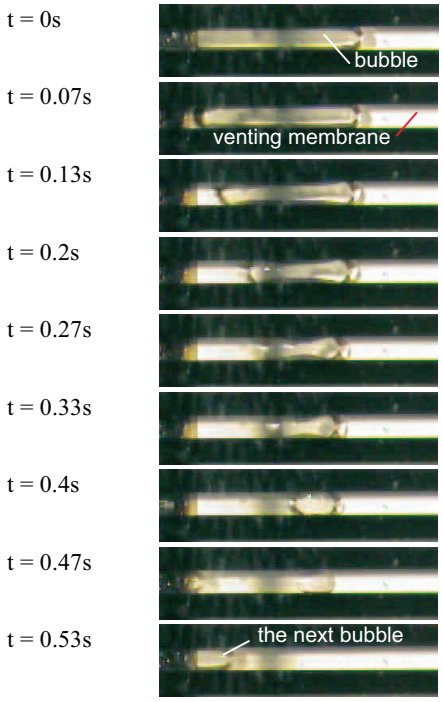

Figure 7. *Bubble removal by the breather*

In order to further verify the fuel circulation, the self-sustainability of the µDMFC is tested by loading the fuel cell with a 1.3 Ω resister and measuring the power output over time, as shown in Fig.-8. The self-sustainability experiments were performed under 80 °C, with 2 M methanol in the anode and ~ 100 ml/min oxygen flow in the cathode. The operation time span (~ 8 min) confirmed the sufficient fuel delivery, because the given reservoir is theoretically supposed to support an operation time of ~ 9 min at the peak power output of this electrical load. As a reference, a control experiment was performed by closing the valve connected to the breather outlet, i.e., blocking CO_2 venting and disabling the self-pumping mechanism. In the control experiment, gas bubbles were observed to grow and fill the entire anodic microchannel, and power output dropped rapidly after about 2.5 mins. Furthermore, fuel leakage was eventually observed, leading to the failure of the µDMFC device.

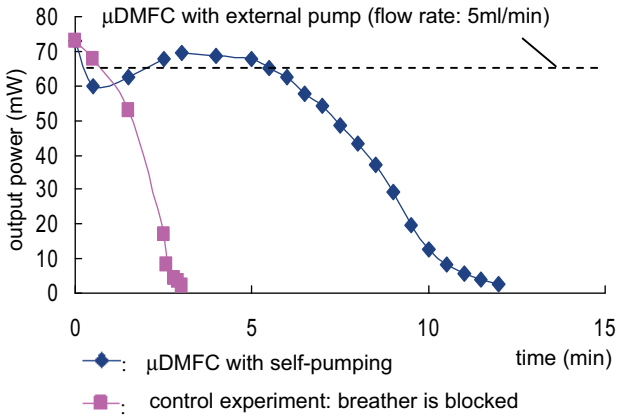

Figure 8. *Self-sustainability of the self-pumping µDMFC*

An interesting feature of the self-pumping is that it can be self-regulated by the reaction of µDMFC. Since the bubble generation rate is directly connected to the electrochemical reaction rate, the pumping rate will increase with a faster reaction to supply fuel faster, when the external load is larger, and the pumping rate will decrease when the load is smaller.

CONCLUSIONS

A self-pumping mechanism was integrated into a µDMFC to circulate liquid fuel in the anode microchannel without any power input. By employing the directional growth of CO_2 gas bubbles by the intrinsic electrochemical reaction and removing them by hydrophobic venting, a compact design of µDMFC was implemented. The complexity and cost of the system can be reduced by eliminating the gas/liquid separator and the external pump. Without the external fuel pump, significant portion of power consumption on fuel delivery (estimated to be more than 10%) can be saved. The fuel circulation has been verified both visually and by confirming the self-sustainability of the fuel cell.

ACKNOWLEDGEMENT

The authors would like to thank Professor C.-M. Ho, Dr. T. Cubaud and Dr. T. J. Yen for their discussions and suggestions, as well as Mr. J. Jenkins and Ms. A. Lee for the help with the manuscript.

REFERENCES

[1] E. Sakaue, "Micromachining/Nanotechnology in Direct Methanol Fuel Cell," *Proc. IEEE Int. Conf. Micro Electro Mechanical Systems,* Miami, FL, 2005, pp. 600-5.

[2] MTI micro fuel cell: "http://www.mtimicrofuelcells.com/".

[3] IBM & Sanyo's µDMFC: "http://www.ibm.com/news/be/en/2005/04/11.html".

[4] Toshiba's µDMFC: "http://www.toshiba.co.jp/about/press/2004_06/pr2401.htm".

[5] K. Yoshida, Y. Hagihara, S. Tanaka, and M. Esashi, "Normally-Closed Electrostatic Micro Valve with Pressure Balance Mechanism for Portable Fuel Cell Application," *Proc. IEEE Int. Conf. Micro Electro Mechanical Systems,* Istanbul, Turkey, Jan. 2006, pp. 722-5.

[6] D. D. Meng, J. Kim, and C.-J. Kim, "A degassing plate with hydrophobic bubble capture and distributed venting for microfluidic devices," *Journal of Micromechanics and Microengineering (to appear)*, 2006.

[7] D. D. Meng and C.-J. Kim, "Micropumping by Directional Growth and Hydrophobic Venting of Bubbles," *Proc. IEEE Int. Conf. Micro Electro Mechanical Systems,* Miami, FL, Jan. 2005, pp. 423-6.

[8] D. D. Meng, T. Cubaud, C.-M. Ho, and C.-J. Kim, "A Membrane Breather for Micro Fuel Cell with High Concentration Methanol," *Tech. Dig. Solid State Sensor, Actuator and Microsystems Workshop,* Hilton Head Island, SC, Jun. 2004, pp. 141-4.

[9] D. D. Meng and C.-J. Kim, "Method and Apparatus for Pumping Liquids Using Directional Growth and Elimination of Bubbles." U.S. Patent pending: 60/647,139, 2006.

[10] U.-C. Yi and C.-J. C. Kim, "Soft Printing of Droplets Pre-Metered by Electrowetting," *Sensors and Actuators A*, 2004, vol. **114**, pp. 347-54.

[11] D. D. Meng and C.-J. Kim, "Self-aligned Micro Bubble Arrays by Using Surface Tension," *2004 ASME Int. Mechanical Engineering Congress and Exposition,* Anaheim, CA, Nov. 2004, CD: IMECE 2004-62182.

AN IMPROVED SILICON DIRECT FORMIC ACID FUEL CELL FOR PORTABLE POWER GENERATION

Kuan-Lun Chu, Richard I. Masel
Department of Chemical and Biomolecular Engineering, University of Illinois at Urbana-Champaign
Urbana, Illinois, 61801, USA

Mark A. Shannon
Department of Mechanical and Industrial Engineering,
University of Illinois at Urbana-Champaign
Urbana, Illinois, 61801, USA

ABSTRACT

The formation of various nanoporous silicon membranes, their usage for the solid electrolyte in silicon-based direct formic acid fuel cells compatible with silicon micro-fabrication technology, and an improved fuel cell design for higher power output is reported in this presentation.

INTRODUCTION

Recently there has been considerable interest in the development of micro fuel cells for portable electronic devices due to their advantages over conventional batteries, including rapid recharging and much higher stored energy density. Micro-fabricated fuel cells using silicon are particularly promising for power generation for MEMS and IC devices. Among many options of fuel, pioneering work in our research group has demonstrated that direct formic acid fuel cells with novel electro-catalysis are interesting for micro power generation [1].

A solid electrolyte membrane that is compatible with standard silicon processing is crucial. Although perfluorinated polymer membranes like Nafion® are widely used in proton exchange membrane fuel cells, they are not compatible with standard silicon microfabrication techniques. One can fabricate silicon-based miniature fuel cells by sandwiching a Nafion® membrane between two silicon chips [2], but the Nafion® membrane will shrink and swell in response to their environment. This drawback can fail practical operation of silicon devices with Nafion® membranes. Previous work in our research group has shown that nanoporous silicon membranes exhibit properties comparable to Nafion® membranes for usage as solid electrolyte membranes [3]. Primitive micro fuel cell models based on nanoporous silicon membranes have been designed, fabricated, and tested [4]. However, the power output of the devices in our previous work was limited to below the useful range. Similar concept for nanoporous silicon based micro fuel cells was proved to work independently by another research group [5], but the reported performance also left significant room for improvement. This paper presents further improvement and investigation of microfabricated direct formic acid fuel cells based on nanoporous silicon compared to our previous work reported in [4].

EXPERIMENTAL DETAILS

The fabrication process for porous silicon membranes is illustrated in Figure 1. Starting with n-type, highly antimony doped silicon wafer, silicon nitride film was deposited by LPCVD and patterned as mask for both KOH etching (Figure 1, A to D) and nanopore formation (Figure 1, E). Nanopores were formed by electrochemical etching of silicon substrate in ethanolic hydrofluoric acid solution using three different anodic current densities. Reactive ion etching on silicon substrate backside was applied to open up nanopores on the backside (Figure 1, F). Micro fuel cells with structure illustrated in Figure 2 were fabricated as follows. Cathode electrode was formed by painting one side of nanoporous silicon surface with a catalyst ink consisting of w.t. 5% Nafion solution, millipore water, and platinum nanoparticles. Anode electrode was formed by painting the other side with a similar catalyst ink consisting of same solvent but with palladium nanoparticles. Current collector was formed by sputtering a gold-palladium alloy thin film on top of the catalyst film and painting gold ink at the edge of catalyst film. Performance tests were carried out in ambient air without pumping neither fuel to anode or gas to cathode.

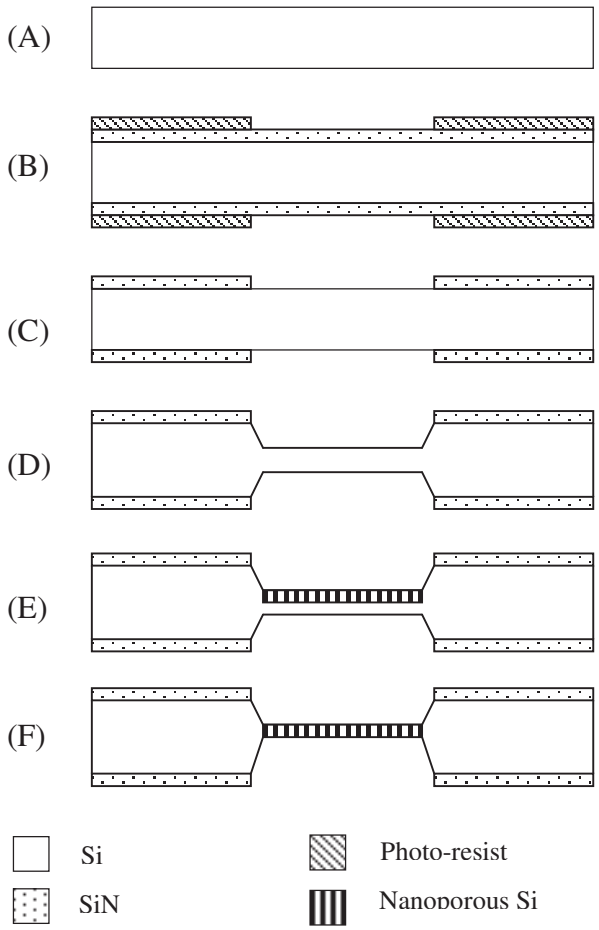

Figure 1. *Fabrication process of nanoporous silicon membrane.*

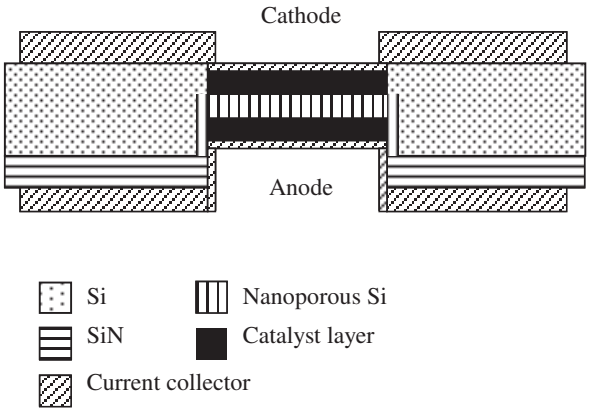

Figure 2. *Micro fuel cell structure.*

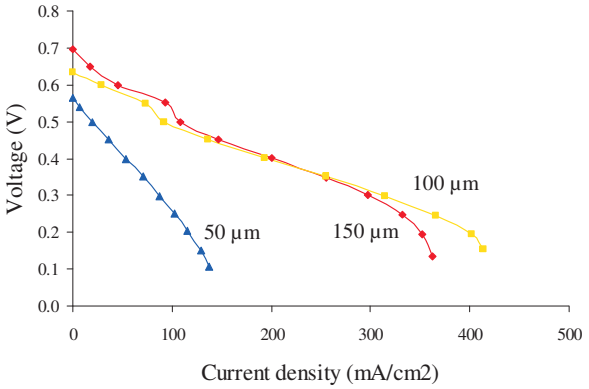

Figure 4. *Fuel cell polarization curves with three different nanoporous silicon thickness.*

RESULTS AND DISCUSSIONS

Figure 3 is the picture of a micro fuel cell based on nanoporous silicon membrane compared to a penny coin. The effects of nanoporous silicon thickness, nanopore size (depending on the pore formation current density), and formic acid concentration on micro fuel cell performance were studied, as shown in Figures 4 to 9.

Using 5 M formic acid with 0.5 M sulfuric acid as the fuel, polarization curves (in Figure. 4) show that micro fuel cell with 150 µm thick nanoporous silicon produced higher open cell voltage of 0.7 V than those with the other two thickness (50 µm and 100 µm). It can be seen that the thinner nanoporous silicon was used, the lower open cell voltage was obtained. It is possible that fuel crossover from anode to cathode increased as nanoporous silicon thickness decreased, and lowered the open cell voltage. Figure 5 shows the power density curves of the three micro fuel cells and the one with 100 µm thick nanoporous silicon produced the highest peak power density among the three.

It has been reported that for nanoporous silicon produced from n-type silicon substrate, pore size increases with current density used to form the pores [6]. To investigate the pore size effect on the miniature fuel cell performance, three different current densities of 20, 40, and 80 mA/cm^2 were used to produce various nanoporous silicon with same thickness of 100 µm.

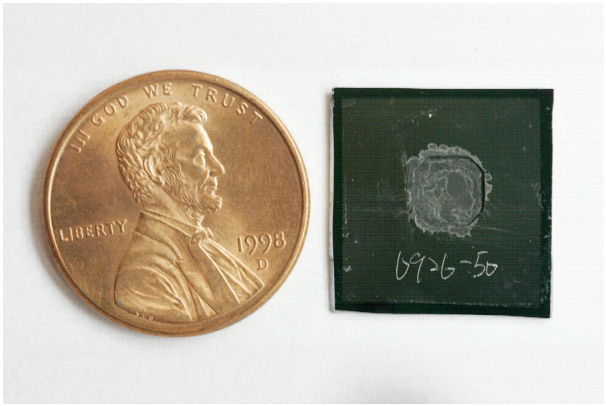

Figure 3. *Picture of a miniature fuel cell based on nanoporous silicon.*

SEM (scanning electron microscopy) images of nanoporous silicon prepared using different current densities are shown in Figures 10 and 11. In nanoporous silicon made using current density of 20 mA/cm^2 or 40 mA/cm^2, a spongelike structure was observed throughout the substrate. But in nanoporous silicon made using 80 mA/cm^2, nanopore structure changed from spongelike (near the top region) to treelike (near the bottom region), as can be seen from Figure 11. This structural change was possibly due to electrolyte concentration gradient along the nanopores during pore formation. It can be seen that nanopore size in treelike structure was larger than that in spongelike structure.

The effect of nanopore size on fuel cell performance can be seen in Figures 6 and 7. Micro fuel cell with nanoporous silicon made using 40 mA/cm^2 produced higher open cell voltage than the other two. Under the same operation voltage, micro fuel cell with nanoporous silicon made using 80 mA/cm^2 produced higher current density and also higher peak power density.

For miniature fuel cells with 100 µm thick nanoporous silicon, three fuel solutions with different formic acid concentrations of 1 M, 5 M, and 9 M were used to test the fuel cell performance. All the fuel solutions contain 0.5 M sulfuric acid. The results are shown in Figures 8 and 9.

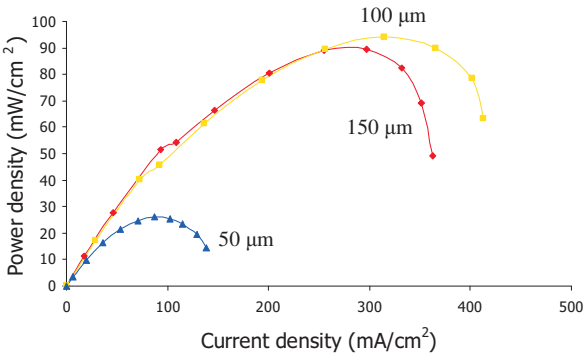

Figure 5. *Fuel cell power density curves with three different nanoporous silicone thickness.*

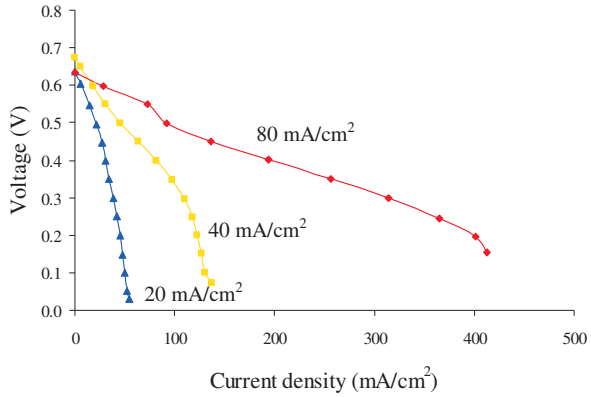

Figure 6. *Fuel cell polarization curves with three different nanopore formation current densities*

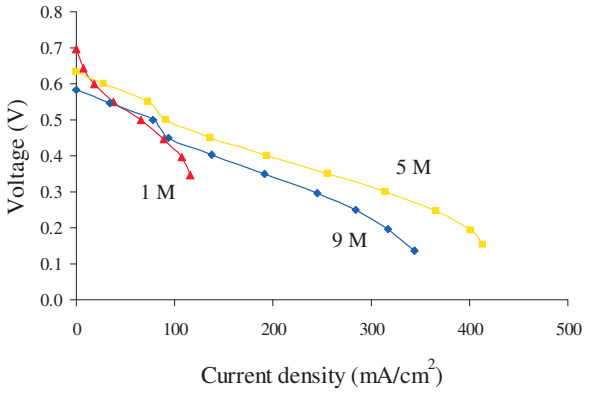

Figure 8. *Fuel cell polarization curves with three different formic acid concentrations (100 µm thick nanoporous silicon)*

From Figure 8, it can be seen that open cell voltage decreased as formic acid concentration increased. It was possibly caused by increase in fuel crossover to cathode side. Micro fuel cell performance suffered fuel transport limit more significantly when using 1 M formic acid than when using 5 M and 9 M, as can be seen from the more rapid drop of current density output. And this rapid drop of current density output contributed to lower power density output when using 1 M formic acid than the other two fuel concentrations, as shown in Figure 9.

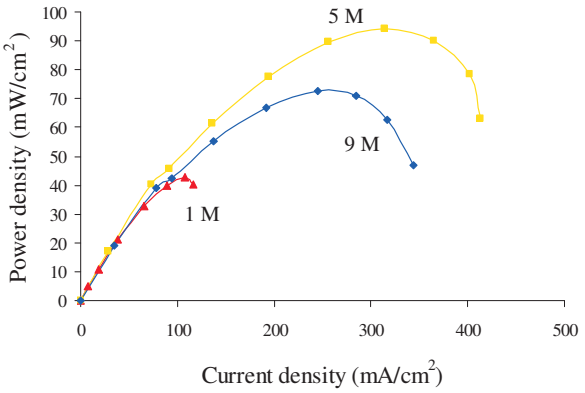

Figure 9. *Fuel cell power density curves with three different formic acid concentrations (100 µm thick nanoporous silicon)*

CONCLUSIONS

From the above results, using 5 M formic acid with 0.5 M sulfuric acid as fuel, 100 µm thick nanoporous silicon produced using the highest current density in this study (80 mA/cm^2) gave the best micro fuel cell performance in general. Factors such as fuel crossover, proton conductivity, and fuel transport limit were proposed to explain these observations. The fuel cell peak power density reached 94 mW/cm^2 at current density level of 314 mA/cm^2 when fuel cell voltage being 0.3 V. This power output is three times of that reported in our previous work [4].

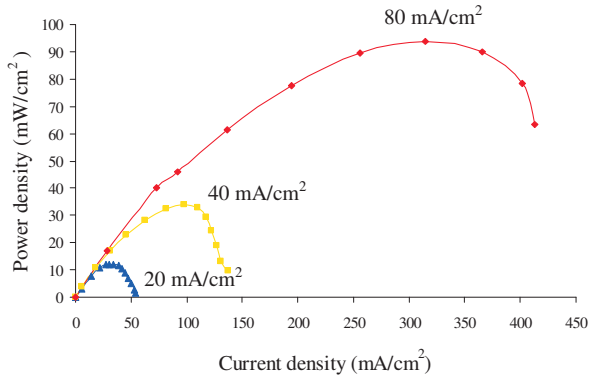

Figure 7. *Fuel cell power density curves with three different nanopore formation current densities*

REFERENCES

[1] C. Rice, S. Ha, R. I. Masel, P. Waszczuk, A. Wieckowski, T. Barnard, "Direct Formic Acid Fuel Cells", *Journal of Power Sources, 111*, 83 (2002).

[2] G. Q. Lu, C. Y. Wang, T. J. Yen, and X. Zhang, "Development and Characterization of a Silicon-based Micro Direct Methanol Fuel Cell," *Electrochimica Acta, 49*, 821 (2004).

[3] S. Gold, K.-L. Chu, C. Lu, M. A. Shannon, R. I. Masel, "Acid Loaded Porous Silicon as a Proton Exchange Membrane for Micro Fuel Cells," *Journal of Power Sources, 135*, 198 (2004).

[4] K.-L. Chu, S. Gold, R. Subramanian, M. A. Shannon, R. I. Masel, "A Nanoporous Silicon Membrane Electrode Assembly for On-Chip Micro Fuel Cell Applications", *IEEE Journal of Micro-Electro-Mechanical Systems*, in press.

[5] T. Pichonat, B. Gauthier-Manuel, "Development of Porous Silicon-based Miniature Fuel Cells", *Journal of Micromechanics and Microengineering, 15*, S179 (2005).

[6] V. Lehmann, R. Stengl, A. Luigart, "On the Morphology and the Electrochemical Formation Mechanism of Mesoporous Silicon", *Materials Science and Engineering B, 69*, 11 (2000).

(a)

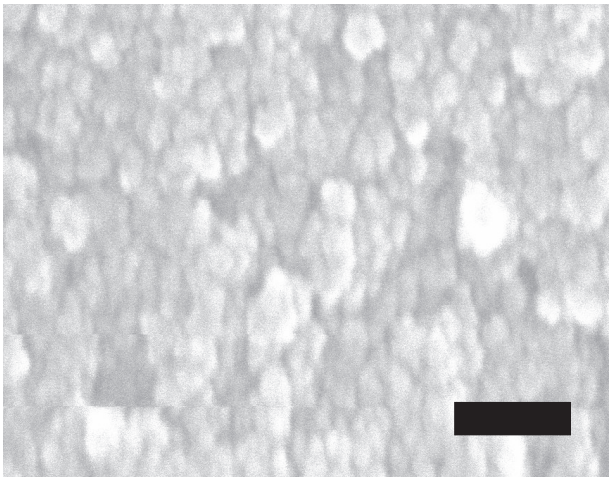

(b)

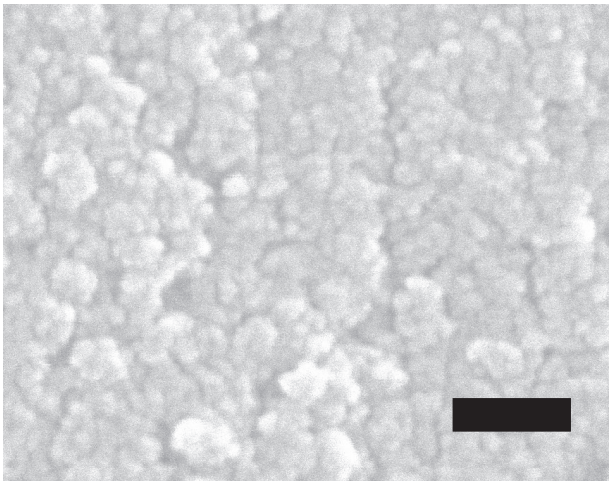

Figure. 10. *SEM pictures of nanoporous silicon made using (a) 20 mA/cm^2 and (b) 40 mA/cm^2 (scale bar length: 90 nm).*

(a)

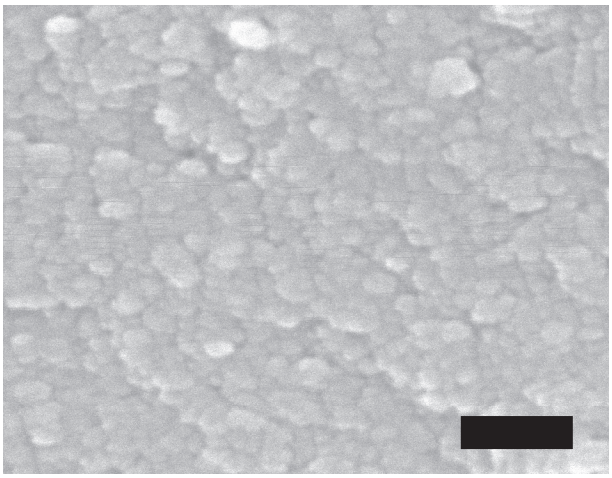

(b)

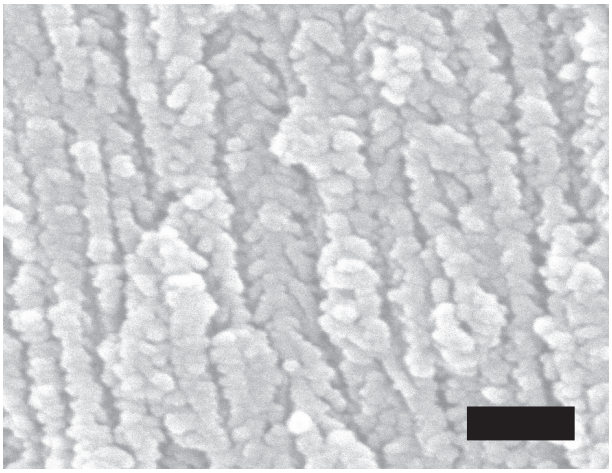

Figure. 11. *SEM pictures of nanoporous silicon made using 80 mA/cm^2 (a) top region, (b) bottom region (scale bar length: 120 nm for (a) and 150 nm for (b)).*

CHANNEL-TO-DROPLET EXTRACTIONS FOR ON-CHIP SAMPLE PREPARATION

Ui-Chong Yi, Wayne Liu, Peter-Patrick de Guzman, and Chang-Jin "CJ" Kim
Core Microsolutions, Inc.
Los Angeles, California USA

ABSTRACT

We report a new capability in on-chip sample preparation for digital microfluidic lab-on-chip systems: "channel-to-droplet" sample extraction by integrating proven capillary electrophoretic (CE) separation and electrowetting-on-dielectric (EWOD) droplet manipulation. This sample preparation approach consists of: a) separating particles within a channel using conventional in-channel CE methods and then b) extracting the concentrated particle bands from a channel opening in a mobile droplet form using EWOD actuations. The extraction enables the concentrated sample droplet to be further processed on chip or presented to ancillary devices for amplifications or sensing. The concept is successfully demonstrated by separating two types of bead particles by CE separations in a channel and extracting particles from a channel opening in droplet form with EWOD. Integration of proven CE technology with new droplet-based EWOD digital microfluidics will enable highly flexible sample separation and transport options while minimizing sample and reagent consumptions.

INTRODUCTION

While high performance liquid chromatography (HPLC) dominates capillary electrophoresis (CE) in analytical practice, CE is also popular to implement on microfluidic analysis and sensing chips due to simple fabrication methods and a low reliance on high pressure fluidics. Since early 1990's [1], there have been numerous reports on microfabricated on-chip CE devices including demonstration and performance improvement. [2, 3] However, conventional CE separation methods typically require sample analysis to be conducted within or about the CE channel to minimize transport-driven diffusion/mixing of concentrated sample/solute bands; this imposes certain limitations on the choice and interchangeability of sensing mechanisms. If the purified samples can be transferred to off-channel and user-selected analytical sites without undergoing diffusion or pressure-driven dispersion, highly flexible and multi-staged sample preparation and analysis processes can be devised, opening the door for many powerful and cost effective analytical or immuno-sensing devices.

To enable transport of channel-concentrated samples to off-channel analysis or extraction points with little or no reduction in sample concentration, we have developed novel "channel-to-droplet" sample extraction capabilities that combine well-proven on-chip CE separation methods [1] with electrowetting-on-dielectric (EWOD) based droplet transport [4]. In our approach (Fig. 1):

- unconcentrated samples can be pipetted or driven in a droplet form by EWOD transport into a channel,
- then separated and purified in the channel by CE (Fig. 1 (a)),
- and finally extracted out of a channel side opening in droplet form by EWOD (Fig. 1 (b)).

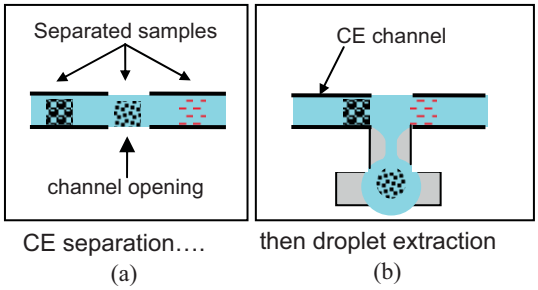

Figure 1. *"Channel-to-droplet" sample extraction and purification is achieved by integrating channel based CE separation and EWOD droplet extraction.*

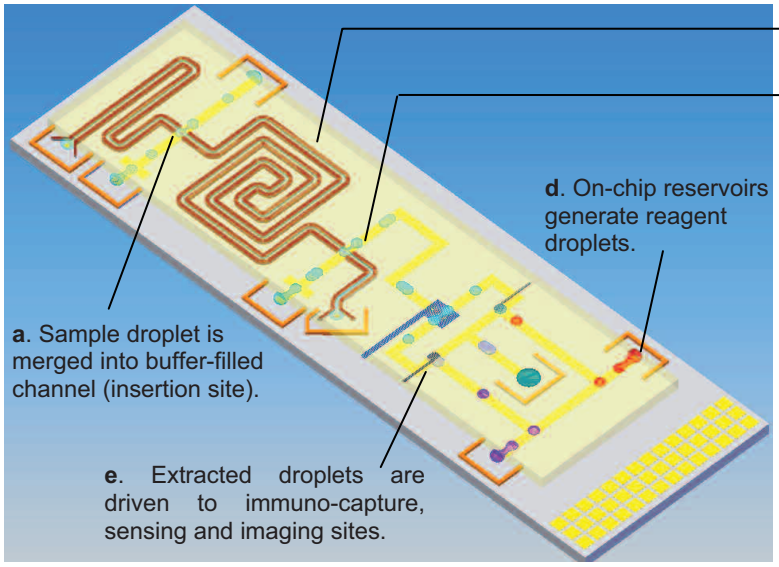

Figure 2. *Conceptual lab-on-chip system combines proven CE separation methods with EWOD-based digital microfluidics to achieve channel-to-droplet sample extraction for: 1) routing of concentrated sample droplets to on-chip sensing sites (shown in the figure) or 2) off-chip transfer to ancillary analytical devices (not shown in the figure). Since the concentrated sample bands are isolated as discrete droplets, the concentration is not compromised by dispersion or diffusion during sample handling downstream.*

The concentrated sample droplet (sub-µl) can then be routed to other downstream processes (Fig. 2) or extracted for off-chip analysis. Figure 2 shows a conceptual EWOD digital microfluidic system with an integrated CE channel. Transportations of sample droplets and down stream processes are also illustrated.

EWOD based digital microfluidics enables the unique extraction and transport of sample droplets out of the CE channel, but also achieves: a) a reduction in sample and reagent consumption from more conventional continuous microfluidics, and b) a simplification of device design and fabrication since no pumps, channel structures or high pressure valve elements are needed.

To demonstrate the concept, CE separation of bead particles and extraction of sample with droplet by EWOD transport are designed and carried out. Two types of bead particles (i.e. ~10 µm red carboxyl modified aatex (CML) beads and white amino-sulfate coated latex beads from Interfacial Dynamics Corp.) were selected in the tests to simulate biological particles.

DESIGN AND FABRICATION

A key for complete and repeatable EWOD droplet extractions from a channel side opening lies in the mitigation of the high pull-back forces within a channel (caused by hydrophilic channel interiors) that resist fluid extraction (Fig. 3(a)). This competition between inherent capillary forces and active EWOD wetting effects yields inconsistent, if not failed, droplet extraction. We found this pull-back can be mitigated by inserting an additional fluid volume (refill droplet) into one side of the extraction opening when a concentrated sample droplet is extracted out the opposite side. By merging a refill droplet into the channel just prior to or during droplet extraction, the resistive tension of the capillary forces was temporarily neutralized, enabling a successful and repeatable droplet extraction. This simultaneous insertion and extraction can be achieved with a column of EWOD drive pads positioned to pass through the channel opening (Fig. 3(b)).

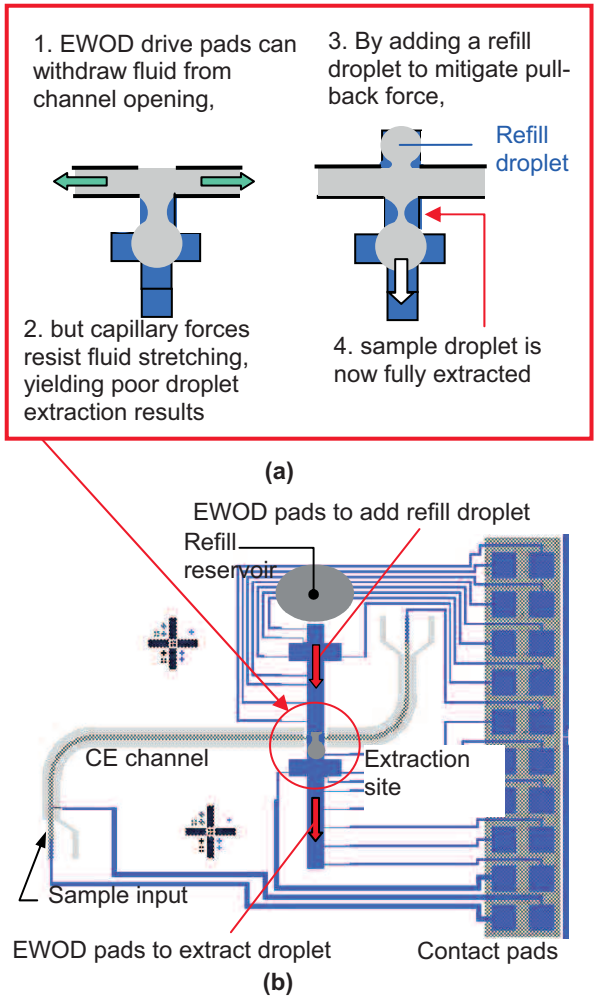

Figure 3. *Chip design for channel-to-droplet extraction. (a) Refill droplet is introduced to mitigate channel capillary forces and enable full droplet extraction from channel opening. (b) Mask layouts, showing EWOD drive pads merge refill droplet to CE channel and extract sample droplet from it*

Test chips (Fig. 4) consisting of top/bottom plates and ~1.25"x2.0" in dimensions were fabricated for concept demonstration. The bottom plate contained EWOD and CE electrodes patterned and passivated with SiO_2. Additionally, a 100µm-wide and 60mm-long CE channel was constructed with photoreist (PR) walls. For sample extraction from the channel, the constructed channel has side openings or breaks to allow pass-through of the EWOD driving electrodes. The top plate is coated with ITO and SiO_2 and provides electrical referencing during EWOD operation. A Cytop® layer is spin-coated onto both plates to achieve hydrophobic surface conditions (inner channel surfaces were not exposed to Cytop® to enable capillary loading of buffer). The extraction site is shown magnified in the photo inset.

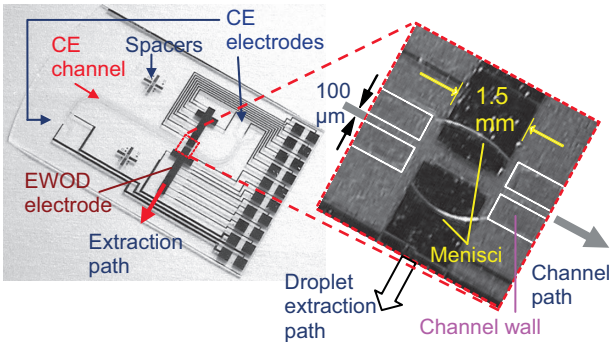

Figure 4. *Testing chip. Top plate is removed for a better picture quality. The inset magnifies the extraction site (with top plate in place), showing the open section of the channel.*

EXPERIMENT AND RESULT

To demonstrate the concept, we have tested CE separation and sample extraction by EWOD separately with the devices described above. The fabricated chips were evaluated on a testing stage, which provided the connections for programmed electrical signals from our control circuit for EWOD and microscope based imaging. For the separation tests, a DC power supply was connected to the test stage instead of EWOD control circuit connectors.

For CE separation, the microchannel was first filled with water or buffer solutions by capillary force to provide filling medium in the channel before loading sample solutions. Since inner surfaces of the channel are hydrophilic, an introduction of

liquid at any end of the channel fills the channel. However, it is important to ensure that water column is connected throughout the channel (including the channel break for extraction) between two CE electrodes. Once the channel was filled, a drop of solution containing mixtures of two bead particles (i.e. red CML and white Amino-Sulfate beads) was added at the sample input reservoir (Fig. 3 (b)) and a voltage (~75 V_{DC}) was applied across two CE electrodes located at the ends of the channel to initiate the separation.

Figure 5 illustrates the result of successful separation of bead particles. During the separation, the red CML beads move faster than white amino-sulfate beads due to mobility difference and become concentrated in band while moving to the extraction point (Fig. 5(a)). A concentrated band of white beads is also formed in the channel (Fig. 5(b)) as they became separated.

The two separated bands of particles then enter the extraction site, with the red beads entering first (Fig. 5(c)) and then followed by the white beads (Fig. 5(d)).

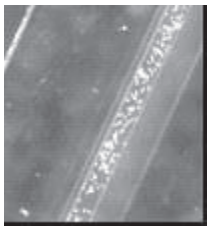

(a) Red beads are separated along the CE channel and are concentrated in a band while moving to the extraction site

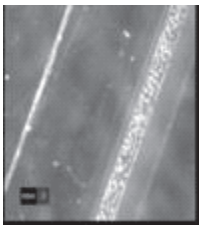

(b) White beads are also concentrated in a band-like formation while moving through the CE channel to the extraction site

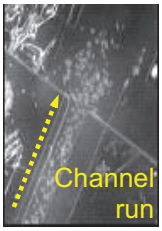

(c) Red beads arrive first at extraction site.

(d) White beads arrive later at extraction site

Figure 5. *CE separation of two bead types and collection of the separated beads at the extraction site.*

For the droplet extraction test, a water droplet (~2 µl) was pipetted onto the bottom chip and pushed down with top cover plate during the assembly of the device. A solution with two types of beads particles was also preloaded in the channel. Successful sample extraction by EWOD is illustrated in Fig. 6.

A refill droplet was moved into the left side of the channel opening, just as droplet extraction was initiated to the right by EWOD actuation (~60 V_{rms} (@1kHz)). Refill droplet insertion and sample droplet extraction were performed simultaneously to neutralize the channel pull-back force. (Figs. 6(c)–6(f)) Based on visual inspection, more than 90% of particles were extracted from the channel break into a separated and mobile droplet. (Figs. 6(g)–6(h))

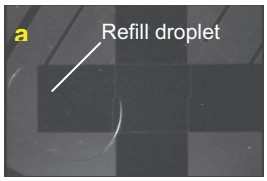

Refill droplet at rest before moving right to the extraction site.

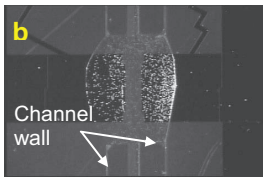

Extraction site (channel break) with bead solution.

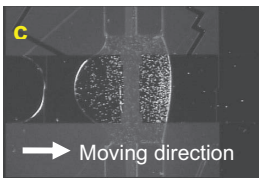

Refill droplet approaches extraction site from left

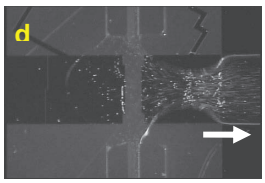

and merges during sample extraction.

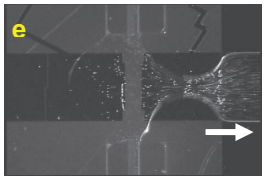

Sample droplet drives right to neck down fluid

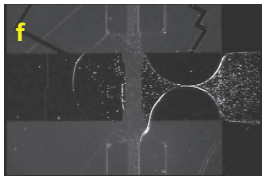

Just before full extraction of sample droplet.

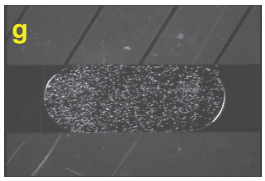

Extracted sample droplet is filled with beads

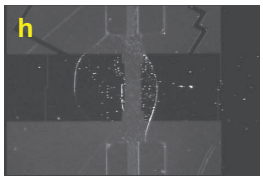

Fewer particles in channel break after extraction

Figure 6. *Photos show merging of refill droplet and extraction of sample droplet from channel break (opening). Channel and EWOD drive pad dimensions are annotated in extraction site close-up on Fig. 4.*

CONCLUSIONS

The concept of "channel-to-droplet sample preparation" utilizing well-established capillary electrophoresis and EWOD digital microfluidics has been introduced and demonstrated with micromachined devices. We have successfully introduced and separated a mixture of red CML and white amino-sulfate bead particles in a CE channel. We also have successfully extracted samples from a channel in droplet form using EWOD actuations and established the proposed functionalities.

ACKNOWLEDGEMENT

This work was funded by Department of Homeland Security (HSARPA SBIR NBCHC050123). The authors would like to thank Professor Sungkwon Cho in University of Pittsburgh for valuable discussions on general EWOD principles.

REFERENCES

[1] D. Harrison, A. Manz, Z. Fan, H. Ludi, and H. M. Widmer, “Capillary electrophoresis and sample injection systems integrated on a planar glass chip,” *Anal. Chem.,* **64**: p. 1926. (1992)

[2] R. Bharadwaj, J. G. Santiago and B. Mohammadi, “Design and optimization of on-chip capillary electrophoresis,” *Electrophoresis*, **23**: p. 2729-2744 (2002)

[3] A. Wainright, U. T. Nguyen, T. Bjornson and T. D. Boone, “Preconcentration and separation of double-stranded DNA fragments by electrophoresis in plastic microfluidic devices,” *Electrophoresis*, **24:**p. 3784-3792 (2003)

[4] S. K. Cho, H. Moon, and C.-J Kim, “Creating, transporting, cutting, and merging liquid droplets by electrowetting-based actuation for digital microfluidic circuits," *J. MEMS*, **12**, p. 70 (2003)

ENGINEERING SURFACE MICRO-STRUCTURE TO CONTROL FOULING AND HYSTERESIS IN DROPLET BASED MICROFLUIDIC BIOANALYTICAL SYSTEMS

Ashutosh Shastry, Sidhartha Goyal, Aziel Epilepsia, Marianne J. Case, Shaghayegh Abbasi, Buddy Ratner[±] and Karl F. Böhringer

Department of Electrical Engineering, [±]Department of Bioengineering, University of Washington
Seattle, WA USA

ABSTRACT

This paper presents the principle, fabricated structure, characterization and experimental results obtained for a new class of surfaces—"hydrophobic non-fouling surfaces"—for droplet-based microfluidics. Building on the theory of wetting of rough surfaces, we have developed novel surfaces which are chemically hydrophilic, i.e., the droplet is in contact with a non-fouling hydrophilic material but has high contact angle as a result of thermodynamically stabilized air traps beneath the droplet. This paper also presents the experimental characterization of rough super-hydrophobic surfaces, dynamic measurements of sliding angles of water droplets, and a modeling approach to estimate bounds on contact angle hysteresis—a major dissipative mechanism in droplet based microfluidic systems. A comprehensive study of the dependence of hysteresis on texture parameters is presented to evaluate the current model, propose a modification, and show that the two models—original and modified—provide useful bounds on the hysteresis of the surface.

INTRODUCTION

Microscale bioanalysis offers assay possibilities useful for diagnostic applications and as research tools for biologists. The promise to enable spatially and temporally resolved chemistries [**1**] has fuelled the emergence of droplet-based "digital" microfluidics. Electrowetting, the electrical approach to droplet manipulation, involves voltage-controlled actuation of droplets on a "hydrophobic" surface. Proteins are ubiquitous components of bioassays. Past studies have confirmed, however, that hydrophobic interactions are involved in protein adsorption [**2**, **3**]. Also, most non-fouling materials are hydrophilic [**3**]. The use of hydrophobic surfaces therefore presents a challenge. It is important to devise a strategy to minimize protein adsorption on the surface to not only guard against the system being rendered defunct but also to minimize protein loss from the limited quantity present in a droplet.

While minimizing bio-fouling is one worthwhile pursuit, developing low energy schemes of moving droplets is another. Low energy schemes are particularly interesting as they can enable microfluidic platforms with integrated electronics. While drag and contact angle hysteresis are the two energy dissipative mechanisms at work, it is the latter that decides the actuation voltages [**4**]. Bringing actuation voltages down to the sub-CMOS regime is critical to the development of integrated microfluidic platforms. One route to lower actuation voltages and to reduce energy dissipation involves employing low hysteresis, low drag rough hydrophobic surfaces [**5**, **6**]. Understanding the quantitative relationship between the impeding force of contact angle hysteresis and surface parameters is an important milestone in this pursuit.

We first review the theory of wetting of rough surfaces and then explain the principle of our hydrophobic non-fouling surfaces. Next we detail the fabrication of rough hydrophobic surfaces and the non-fouling hydrophobic surfaces. Experimental work, results and discussion follow. We conclude by summarizing the on-going efforts to complete these studies.

THEORY AND PRINCIPLE

Consider a rough surface realized by creating pillars of controlled geometry on a smooth surface. Here the roughness is characterized by *r*, the ratio of rough to planar surface area, as explained in Fig. 1. The basic effect of surface roughness on wetting is modeled by Wenzel's relation (Eq. 1), which relates the apparent contact angle θ_W of a droplet on a rough surface with $r \geq 1$ to Young's intrinsic contact angle θ_i [7].

$$\cos\theta_W = r\cos\theta_i \qquad (1)$$

In the Wenzel state the droplet is conformal with the topography, as seen in Fig. 2(b). The droplet can also sit on the pillar tops with air pockets trapped beneath it, as shown in Fig. 2(a). This configuration is referred to as the "Fakir" state. In the Fakir state, the base of the droplet essentially contacts a composite surface of pillar tops and air. The apparent contact angle θ_{CB} on a composite surface is determined using the Cassie-Baxter relation given in Eq. 2.

$$\cos\theta_{CB} = \sum_j \phi_j \cos\theta_i \qquad (2)$$

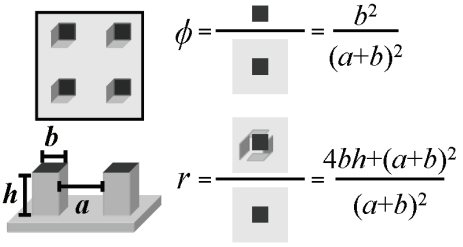

Figure 1: The texture parameters ϕ and r are expressed in terms of the design parameters a (gap length), b (pillar size) and h (pillar height), where ϕ is the fraction of pillar top area over total horizontal surface area and r is the fraction of total surface area over total horizontal surface area.

Here, ϕ_j is the surface area fraction and θ_j is the intrinsic contact angle of water with material *j*. For a sessile Fakir droplet, a surface area fraction ϕ (Fig. 1) of its base rests on pillar tops that have an intrinsic contact angle of θ_i; the remaining surface area fraction of $(1-\phi)$ suspends freely, contacting air with a contact angle of 180°. Substituting these values, the apparent contact angle in the Fakir state—a special case of Cassie-Baxter contact—is readily computed [7,8] to yield Eq. 3.

$$\cos\theta_F = \phi(\cos\theta_i + 1) - 1 \qquad (3)$$

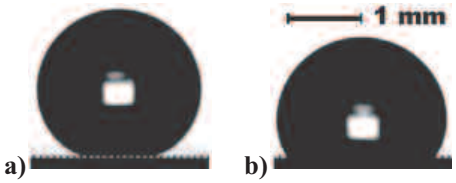

Figure 2: Droplets of volume 5 μl, on a Teflon-coated silicon surface with $\phi = 0.05$ and $r = 1.4$ in a) Fakir state with a footprint diameter of 1 mm, $\theta_F = 156.6^o$ (expected: 164.5^o) and b) Wenzel state with a footprint diameter of 1.96 mm, $\theta_W = 118^o$ (expected: 112.8^o). Air pockets are visible between pillars under the Fakir state droplet. Pinning of the droplet edge causes significant deviations from the predicted equilibrium value.

The angles θ_F from Eq. 3 and θ_W from Eq. 1 are equilibrium values of the apparent contact angle in the two states. Equilibrium angles of the droplet are expected when there is no impending movement. When there is impending movement, the difference between the cosines of maximum advancing and minimum receding angles that a droplet makes with a surface is defined as contact angle hysteresis. Hysteresis results from the pinning of the three-phase contact line to the solid surface and is attributed to physical and chemical inhomogeneities [**6**]. At equilibrium, we notice by comparing θ_F from Eq. 3 and θ_W from Eq. 1 that the Fakir state has a lower energy relative to the Wenzel state (i.e., $\cos\theta_W < \cos\theta_F$) if the following inequality proposed by Bico et al. [**8**] (Eq. 4) holds true.

$$\cos\theta_i < \frac{\phi - 1}{r - \phi} \qquad (4)$$

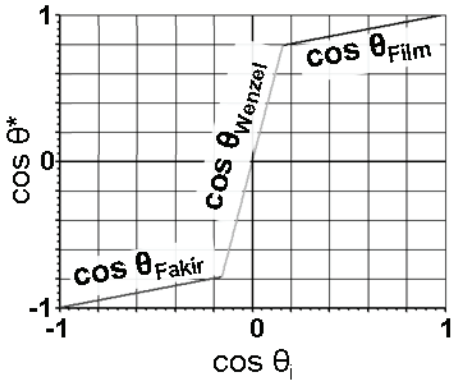

Figure 3: Fakir, Wenzel and Film regimes are shown for a typical rough surface with r =5 and ϕ =.25.

A droplet at a given location on a surface does not spontaneously transit from one state to the other because of the presence of an energy barrier. This energy barrier is analogous to the activation energy of a chemical reaction that prevents spontaneous conversion to products (Fig. 4). This energy barrier is easily estimated [**9**]. In situations where Eq. 4 does not hold, the energy barrier gives a useful bound on the energy that needs to be coupled to a "metastable" Fakir droplet before risking its transition to the Wenzel state.

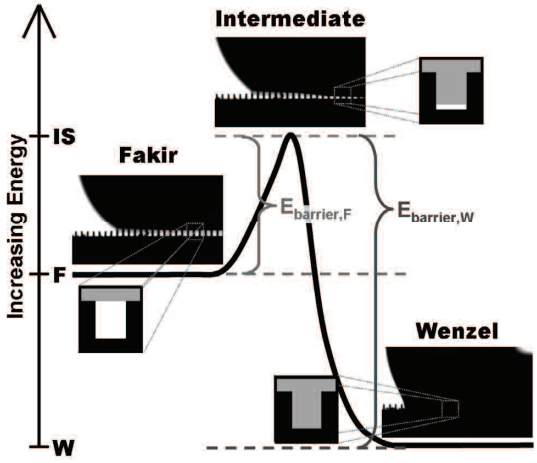

Figure 4: A schematic showing energy levels of the Fakir and Wenzel states. The choice of texture parameters makes the Fakir state metastable in this case. The energy of the intermediate state is calculated by assuming nearly complete penetration of the droplet; only a thin film of air separates the liquid-air and solid-air interfaces at the bottom of the valleys. A Fakir droplet needs to overcome the energy barrier $E_{barrier,F} = E_{IS} - E_F$ to transit to the Wenzel state.

From this analysis, we realize that the contact angle depends only on ϕ and θ_i—it is independent of the coating on the sidewall. But the energy barrier depends only on the coating of the sidewalls—it is independent of the θ_i of the pillar tops. A Fakir droplet can exist with hydrophilic, non-fouling pillar tops pillar tops but hydrophobic side walls.

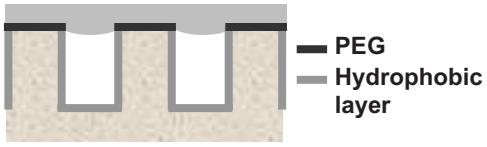

Figure 5: Schematic diagram of liquid deposited on physically and chemically patterned surface. The top surface is hydrophilic non-fouling polyethylene glycol (PEG). The trough and side-walls are hydrophobic. Although the liquid-vapor surface may be curved, the large size of the droplet relative to the spacing between pillars allows the profile to be approximated as spanning straight across surfaces in the derivation.

We therefore proposed composite micro-textured surfaces with hydrophobic troughs and side walls of the pillars and a hydrophilic non-fouling material polyethylene glycol (PEG) on the pillar tops (Fig. 5).

FABRICATION AND EXPERIMENT

The fabrication process employed for the hydrophobic-non – fouling surfaces is detailed in Fig. 6. A thiol-ending molecule formed a self assembled monolayer to provide the hydrophobic coating on gold. Contact angles of the droplets were measured on these surfaces to test the hypothesis.

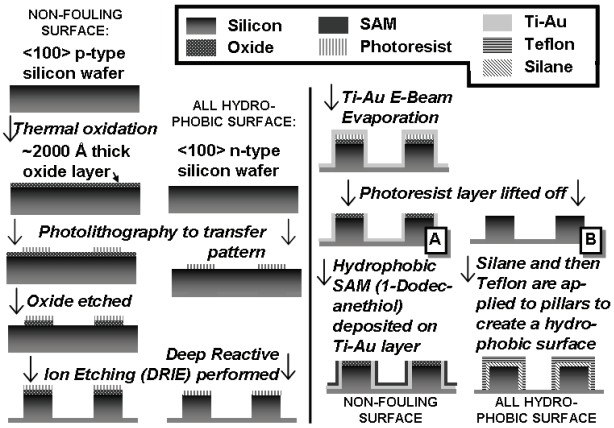

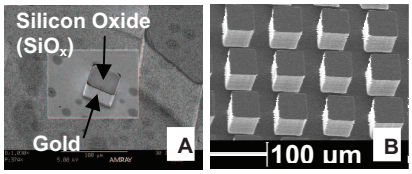

Figure 4: Fabrication steps for the non fouling hydrophobic surface and the all-hydrophobic surface (SEM micrograph B), are shown. In SEM micrograph A, the non-conducting oxide shows up dark while conducting metal film (Ti-Au) on the sidewalls of the pillars and on the trough shows up bright.

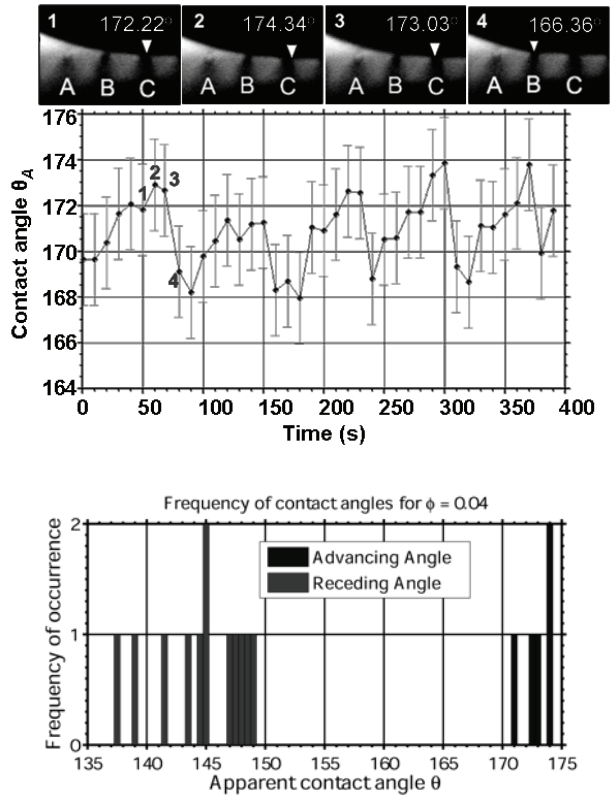

Figure 6: a) The advancing contact angle is plotted as a function of time for a sessile droplet (on a surface with $\phi = 0.04$) b) Contact angle values in the entire video for the advancing angle measurements were used to create the histogram shown.

We built another set of test surfaces with similar physical texture but uniformly covered with a hydrophobic coating of Teflon AF 1600 as detailed in Fig. 5. These test surfaces were used for hysteresis characterization. Sessile droplets on these surfaces were expanded and contracted by adding and removing water using the syringe pump while a video was recorded at 60 fps; contact angles were measured on each frame. As seen in Fig. 6a, the contact angle increases as the advancing edge expands forward but drops precipitously as it eventually lands on the next pillar. For the contracting droplet, the receding angle jumps to a high value as the receding edge snaps off a pillar. Each landing (or snapping) is an experiment and the mode value is reported (Fig. 6b) as the advancing or the receding angle for a surface. Movies were made for surfaces of varying texture (ϕ ranging from 0.025 to 1), data plotted, and trends analyzed.

RESULTS AND DISCUSSION

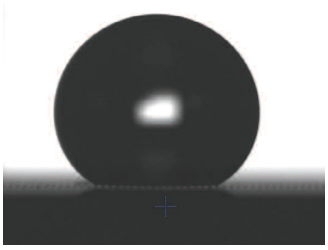

Figure 7: A droplet of volume 7.68 µl in Fakir regime with θ_F = 137°. Light below the droplet confirms that it is the Fakir regime.

For the droplet placed on the hydrophobic surface with hydrophilic pillar tops, its contact angle was measured using a goniometer. The light filtering through the air traps beneath the droplet established that it rested as expected, in the Fakir state, contacting only the hydrophilic oxide layer on the pillar tops. It therefore made a high contact angle as seen in Fig. 7. The measurements were repeated over several test surfaces—with a range of pillar widths and gaps—as summed up in Fig. 8.

For the hysteresis experiments, the cosines of advancing and receding angles were observed to decrease linearly with ϕ —for both the Teflon AF 1600 and FOTS coated surfaces—as evident from Fig. 9. The advancing angle model is $\cos\theta_A = -1 + \phi(1 + \cos\theta_{i,A})$, a heuristic relation proposed by He et al. [11] —obtained by replacing the intrinsic equilibrium contact angle θ_i with the intrinsic advancing angle $\theta_{i,A}$.

These results provide the first experimental validation of this relation. The current model for the receding angle in the Fakir state, $\cos\theta_R = 2\phi - 1$, is obtained assuming a trailing film remains on the pillar tops [**11**]. As seen in Fig. 8a, this assumption, originally proposed for hydrophilic surfaces [**10**], overestimates hysteresis—providing an upper bound (for ϕ >0.1). We re-derived the relation from first principles, heuristically replacing "1" (=cos0) by cosθ_I in the coefficient of ϕ to obtain $\cos\theta_R = \phi(1 + \cos\theta_{i,R}) - 1$. This model accounts for partial coverage of pillars by the trailing film—as expected for a hydrophobic coating. Our model provides the lower bound to hysteresis (Fig. 9c).

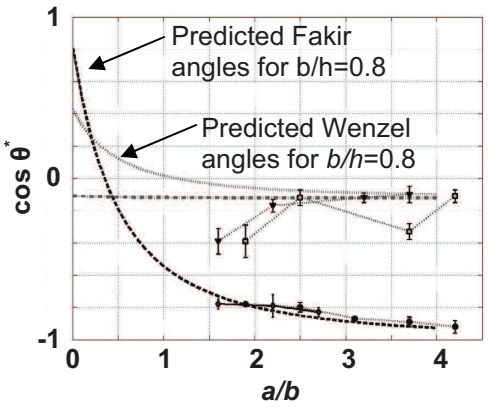

Figure 8: Measured contact angle values for Wenzel and Fakir are plotted along with the predicted angles based on the measured pillar dimension b and spacing a. Predicted values for Fakir, Wenzel with h/b = 0.8, and Wenzel with h/b = 1.9 .

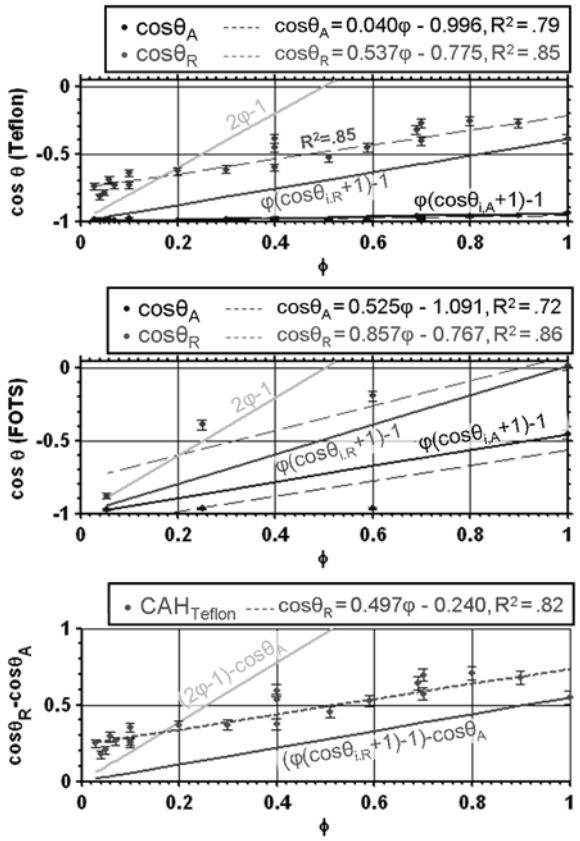

Figure 9: Mode values of advancing and receding contact angles obtained on a) Teflon coated surfaces and b) FOTS coated surfaces are plotted as a function of ϕ along with the linear fit lines and model predictions. c) The contact angle hysteresis (CAH) is plotted as a function of ϕ for Teflon, as well as model lines and a fit line.

CONCLUSIONS

We have introduced a new class of non-fouling surfaces and have obtained the "proof-of-concept" results demonstrating hydrophobic surfaces where droplets contact only the in the "hydrophilic" portions of rough surfaces. The ongoing effort entails quantifying their fouling behavior using radio-labeled protein adsorption on a well characterized PEG layer deposited on the oxide.

For very low ϕ (ϕ <0.1), study is under way to evaluate our hypothesis that the perimeter per unit area, and not ϕ, controls the hysteresis behavior. The non-fouling hydrophobic surfaces and bounds on contact angle hysteresis thus mark two important steps towards droplet based open microfluidic systems for bioanalytical applications.

ACKNOWLEDGEMENTS

This work is funded by NIH Center of Excellence in Genomic Science and Technology grant 1-P50-HG002360-01.

REFERENCES

[1] A. A. Darhuber and S. M. Troian, "Microfluidic actuation by modulation of surface stresses," *Ann. Rev. Fluid. Mech.*, vol. 37, pp. 425–455, January 2005.

[2] V. Tangpasuthodal, N. Pongchaisirikul, and V. P. Hoven, "Surface modification of chitosan films. Effects of hydrophobicity on protein adsorption," *Reviews of Modern Physics*, vol. 338, pp. 937–942, 2003.

[3] D. G. Caster and B. D. Ratner, "Biomedical surface science: Foundation to frontiers," *Surf. Sci.*, vol. 500, pp. 28–60, 2002.

[4] F. Mugele and J.-C. Baret, "Electrowetting: from basics to applications," *Journal of Physics: Condensed Matter*, vol. 17, pp. R705–R774, 2005.

[5] C. Cottin-Bizonne, J.-L. Barrat, L. Bocquet, and E. Charlaix, "Low-friction flows of liquid at nanopatterned interfaces," *Nature Materials*, vol. 2, p. 237240, April 2003.

[6] D. Quéré, A. Lafuma, and J. Bico, "Slippy and sticky microtextured solids," *Nanotechnology*, vol. 1, pp. 14–15, 2003.

[7] J. Bico, C. Marzolin, and D. Quéré, "Pearl Drops", *Europhysics Letters*, vol. 47, pp. 220–226, 1999.

[8] J. Bico, U. Thiele, and D. Quéré, "Wetting of textured surfaces", *Colloids and Surfaces A: Physiochemical and Engineering Aspects*, vol. 206, pp. 41–46, 2002.

[9] N.A. Patankar, "Transition between Superhydrophobic States on Rough Surfaces", *Langmuir*, vol.20, pp.7097-7102, 2004.

[10] P. Roura and J. Fort, "Equilibrium of drops on inclined hydrophilic surfaces," *Physical Review E*, vol.64, no.011601, pp. 1–5, 2001.

[11] B. He, J. Lee, and N. A. Patankar, "Contact angle hysteresis on rough hydrophobic surfaces," *Colloid and Surfaces A: Physicochem. Eng. Aspects*, vol. 248, pp. 101–104, 2004.

A NOVEL BENZOCYCLOBUTENE-BASED DEVICE FOR STUDYING THE PHYSICS OF THE EBULLITION PROCESS

Saeed Moghaddam[1], Kenneth T. Kiger[1], Alireza Modafe[2], and Reza Ghodssi[2]
[1]Department of Mechanical Engineering
[2]MEMS Sensors and Actuators Lab (MSAL)
Department of Electrical and Computer Engineering, Institute for Systems Research
University of Maryland, College Park, MD USA

ABSTRACT

We report, for the first time, simultaneous measurement of temperature and heat flux with a resolution of about 35 μm underneath/around a bubble. This was achieved by fabrication of a multilayer Silicon/Benzocyclobutene (BCB) structure with embedded temperature sensors. The sensors are radially distributed around a cavity, with energy input by a thin film heater microfabricated on the backside of the membrane structure. Single bubbles were generated from the cavity while the temperatures and the bubble images were recorded with a sampling frequency of 8 kHz. Analysis of the results revealed unique details of the nucleation dynamics and its associated heat transfer processes.

INTRODUCTION

Boiling heat transfer has been considered one of the most efficient mechanisms of heat transfer, and as such, has been implemented in wide variety of applications ranging from nuclear reactors to electronic cooling. Over the past 50 years, scientists have developed several competing mechanistic models to describe the boiling heat transfer process. Although the developed models are intended to predict the heat transfer coefficient at macroscales, their fundamental assumptions lie on complex microscale sub-processes that remain to be experimentally verified. Two main unresolved issues regarding these sub-processes are: 1) dynamics of bubble growth and associated heat transfer processes and 2) the bubble's role in surface heat transfer during the boiling process.

Although it is common knowledge that bubble growth in heterogeneous boiling is due to liquid evaporation at the bubble/liquid interface, the mechanism of heat transfer during this process is yet unknown. The two main competing views on the mechanism of heat transfer to a bubble are typified by the models of Mikic and Rohsenow [1] and Cooper [2]. Mikic and Rohsenow [1] suggested that energy transfer into a bubble predominately comes from the superheated liquid that covers the bubble dome. In contrast, Cooper [2] suggested that evaporation of a thin liquid layer (the so called microlayer) underneath the bubble (i.e. at the bubble/surface contact area) is the main contributing factor into the bubble growth. Numerous studies (e.g. Mei et al. [3] and Robinson and Judd [4]) have been conducted to evaluate the accuracy of the two proposed models. Unfortunately, the lack of experimental data at microscales, where the phenomenon takes place, hasn't allowed a full examination/verification of the two models and their fundamental assumptions.

The second unresolved issue in the boiling process is how a bubble affects the heat transfer around the nucleation site, or in a broader sense how the individual bubbles contribute to the net energy flux from the heated surface. In general, boiling models can be classified into two following categories: 1) single phase convection models and 2) combined single phase convection and latent heat transfer models. The first group of models suggests that surface heat transfer is mainly due to liquid motion induced by bubbles. The exact nature of this convection process is still unknown. Different analogies have suggested convection at macro- and micro-scales. The macro-scale models suggest that heat transfer to the liquid is the result of local agitation generated by the wake of departing bubbles from the heat transfer surface [5]. The micro-scale models suggest that bubbles act as micropumps and continuously pump the hot liquid away from the surface [6]. The second group of studies (e.g. Judd et al. [7]) accounts for latent heat transfer from the surface along with the single-phase convection. To the best of our knowledge, the accuracy of the fundamental assumptions of these heat transfer models hasn't been experimentally verified.

Motivated by a need to develop an advanced two-phase microcooler for electronics thermal management, we have conducted a comprehensive study to understand the nucleation dynamics and mechanism of heat transfer during the boiling process. This was achieved through fabrication of a composite wall with embedded Resistance Temperature Detectors (RTDs) that can measure the surface temperature and heat flux distribution near the nucleation site. The device consists of an array of temperature sensors embedded in an 10.5-μm thick multilayer Benzocyclobutene (BCB) structure on a 60-μm thick, 3.6×3.6 mm^2 square-shape silicon membrane. The 60-μm thick silicon membrane was designed to keep the lower surface of the BCB structure at a constant temperature level during the bubbling process. BCB was selected among several other low-conductivity polymers such as SU-8, polyimide, and PDMS, because of its microfabrication properties and its stability at high temperatures. The thickness of the BCB layers and the sensor geometry were determined in a design trade off between the heat flux measurement accuracy and interference with the nucleation process.

The surface is heated by a thin film resistor microfabricated on the backside of the membrane. Bubbles are generated at a dedicated nucleation site at the center of the sensor array. The surface temperature and heat flux underneath/around a bubble along with the images of the bubbles were recorded at a frequency of 8 kHz. Results provided the necessary data to explain nucleation dynamics and

different mechanisms of heat transfer involved in the boiling process. This paper describes the fabrication and testing of the device.

FABRICATION PROCESS

The device was fabricated on a 300-μm thick n-type <100> silicon wafer with silicon oxide and silicon nitride layers on both sides. The nitride and oxide layers were patterned and etched using the RIE process over a 3.6×3.6 mm^2 square-shape area on the backside of the wafer. The silicon was then etched through KOH anisotropic etching to make a 60-μm thick membrane. Temperature sensor T_1 (see Figure 1) was fabricated on the silicon nitride layer, followed by a 7.5-μm thick BCB layer that was spin-coated and fixed by a soft bake. The T_2 sensor was then fabricated on the preceding BCB layer, with its sensing element centered and aligned to the T_1 sensor, but the two sensor's leads rotated to the opposite side. Note that the temperature difference between sensors T_1 and T_2 determines the spatially averaged heat flux in the boiling site region. The structure was subsequently covered with a second BCB layer (2.5 μm thick), and the sensor array was then fabricated on the resulting surface. Note that the temperature difference between each element of the sensor array (T_i) and T_1 determines the spatially resolved heat flux. The sensor array was subsequently covered with a 0.5-μm thick BCB layer and was hard baked. The BCB layer over all the bond pads was then etched. Initial trials determined that the Cr/Ni/Au bond pads constructed during the sensor fabrication were not stiff enough to allow direct wire bonding. The original pads were etched and 0.5 μm Ti/1.5 μm Al bond pads were fabricated at their place. Figures 2 and 3 show the top view of the device. A 0.3-μm thick alumina layer was then deposited on the backside of the membrane and a chromium heater with Au leads was subsequently fabricated on the alumina layer. In the last fabrication stage, three cavities (shown in Figure 4) were fabricated at the center of the sensor array using Focused Ion Beam (FIB).

EXPERIMENTAL APPARATUS

The device was attached and wire bonded to a custom made Pin Grid Array (PGA). The PGA was then installed on the bottom cap of a chamber that contains the test liquid. FC-72 (developed by 3M company) was used for the tests, as it is a strong candidate for electronic cooling applications. The chamber pressure was controlled via a connecting bellows and a pressure regulating system (see Figure 5). A hot water line was connected to the external jacket of the test chamber to control the test liquid temperature. The PGA was connected from below to a custom signal conditioning board, and routed to an A/D card installed in a PC. All sensors were sampled with a frequency of 8kHz. Also, a CCD camera, synchronized with the A/D board, was used to capture the bubble images with a rate of 8000 frames/sec.

DATA REDUCTION AND ANALYSIS

Temperature of the test liquid was set at different levels by adjusting the temperature of the hot water supplied to the chamber jacket. Data was collected at different surface temperatures by varying the power applied to the thin film heater on the backside of the membrane. An example set of data at a liquid temperature of 52.7 °C under 1 atm pressure is presented and analyzed in the following.

Figure 6 shows a typical bubbling event with its corresponding temperature data shown in Figure 7. An approximate value for the heat flux could be calculated using $q = k_{BCB}(T_1 - T_i)$. This assumes, however, essential a perfect material with zero heat capacity. To properly account for transient thermal energy stored in the BCB, a numerical model of the BCB layer was built using Icepak (a numerical software developed by Fluent Corporation) to accurately determine the surface heat flux. The experimental temperature profiles were applied to the model and surface heat flux at the area covered by each sensor was determined. Figure 8 shows the numerically calculated heat flux profiles. The temperature and heat flux results and the images of the bubbles have been used to analyze different aspects of the nucleation dynamics and the boiling heat transfer sub-processes. A detailed interpretation and analysis of the experimental results is far beyond the scope of this paper and will be presented in future publications. Only a brief analysis of the results, limited to the broad overview of the phenomena presented in the introduction section, will be discussed in the following.

As can be seen in Figure 8, formation of a bubble is associated with a sudden spike in surface heat flux at the bubble/surface contact area. This indicates a rapid cool down of the surface due to microlayer evaporation. Comparison of the microlayer evaporation energy with the total bubble energy (calculated using the bubble volume) indicated that microlayer accounts only for 12.8% of the total energy transferred into the bubble for this particular case. The rest of the bubble energy came from the superheated liquid surrounding the bubble dome. This indicates that neither of the bubble growth models [1,2] accurately represents the actual bubble growth mechanism observed in this study.

The results also revealed the details of the heat transfer process from the surface. As can be seen in Figure 8, after the initial heat flux spike at the contact area caused by microlayer evaporation, the heat flux at the contact area approached to zero due to surface dry-out. This trend continued until the contact line started to recede shortly after it reached a radius of 225 μm, near the middle of the S-5 sensor. The liquid front started to cool the surface in a process commonly known as transient conduction heat transfer mode. Contrary to what has been commonly assumed in classical boiling models, transient conduction mode occurred mainly before, and not after, the bubble departure. Calculating the total heat transfer during this process suggested that transient conduction accounts for 24% of the total heat transfer from the sensor area. Also, comparison of the heat transferred by the microlayer with the total heat transfer from the sensor area suggested that latent heat transfer (i.e. microlayer evaporation) accounts for about 13% of the total heat transfer. The rest of the heat transfer from the sensor area (63%) occurred outside the contact area. As can be seen in Figure 8, temperature of this region didn't change during the bubble growth and departure and the steady state heat flux in this region can be reasonably calculated using $q = k_{BCB}(T_1 - T_i)$. An additional test in natural convection mode (in the absence of the bubbles) showed that although heat flux at this region didn't change with the frequency of the bubbling event, it was approximately 3 times higher than the natural convection heat flux at the same wall temperature.

CONCLUSIONS

A novel device for direct measurement of the temperature and heat flux fields around a bubble nucleation site with an unprecedented spatial resolution of 35 μm was developed. Capability of the device in revealing some aspects of the processes involved in the boiling heat transfer was demonstrated. Results of this study enhance the understanding of the physics of heat transfer process in boiling that is the building block for development of more efficient microcooling devices for electronics cooling applications.

REFERENCES

[1] B. B. Mikic and W. M. Rohsenow, "Bubble Growth Rates in Non-Uniform Temperature Field", *Prog. Heat Mass Transfer*, 2, 283 (1969).

[2] M. G. Cooper, "The Microlayer and Bubble Growth in Nucleate Pool Boiling", *Int. J. Heat Mass Transfer*, 12, 915 (1969).

[3] M. R. Mei, W. Chen, and J. F. Klausner, "Vapor bubble growth in heterogeneous boiling-I & II", *Int. J. Heat Mass Transfer*, 38, 909 (1995).

[4] A. J. Robinson and R. L. Judd, "Bubble Growth in a Uniform and Spatially Distributed Temperature Field", *Int. J. Heat Mass Transfer*, 44, 2699 (2001).

[5] W. M. Rohsenow, "A Method of Correlating Heat Transfer Data for Surface Boiling of Liquids", *ASME J. Heat Transfer*, 74, 969 (1951).

[6] H. K. Forster and R. Greif, "Heat Transfer to a Boiling Liquid-Mechanism and Correlations", ASME *J. Heat Transfer*, 81, 43 (1959).

[7] R. L. Judd and K. S. Hwang, "A Comprehensive Model for Nucleate Pool Boiling Heat Transfer Including Microlayer Evaporation", ASME *J. Heat Transfer*, 98, 623 (1976).

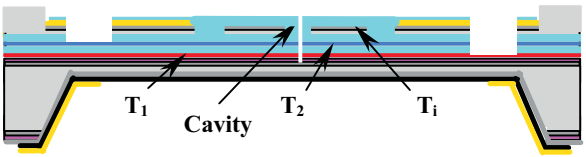

Figure 1. Cross section of the device.

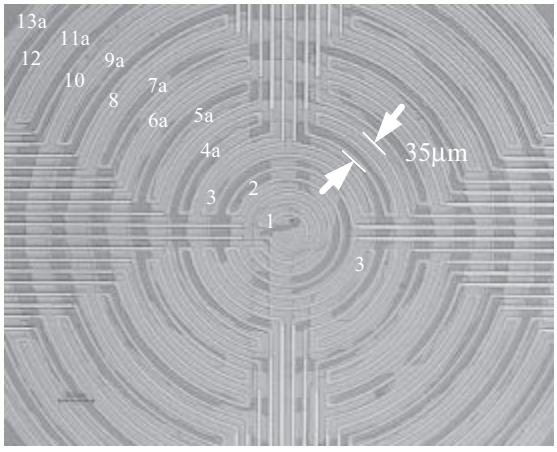

Figure 2. Top view of the device showing sensor array on top of sensors T_1 and T_2. Sensor array covers a 1mm in diameter circular area

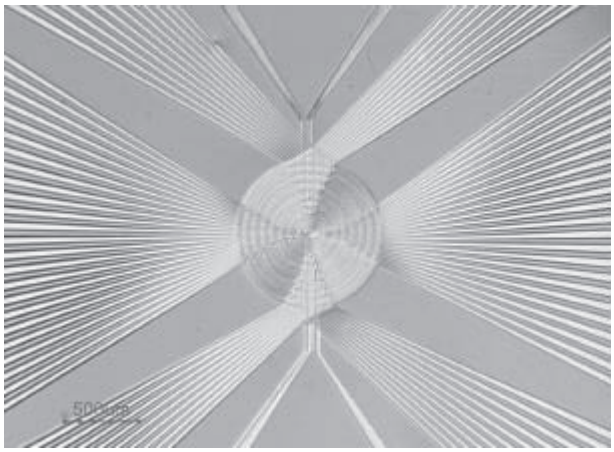

Figure 3. Wide view of the device showing leads of the sensor array and two pairs of leads for sensors T_1 and T_2.

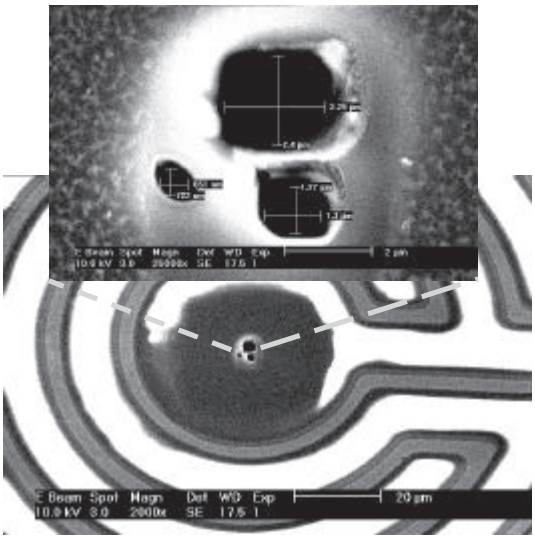

Figure 4. SEM view of the central sensor with cavities about 0.7, 1.3, 2.4 μm in diameter at the center. Each cavity is active in a certain temperature range.

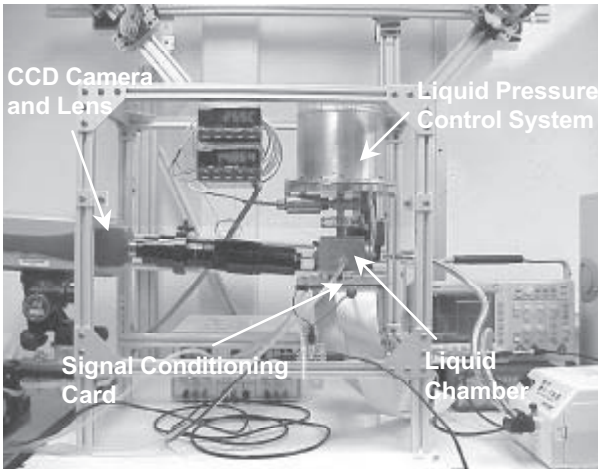

Figure 5. Experimental setup

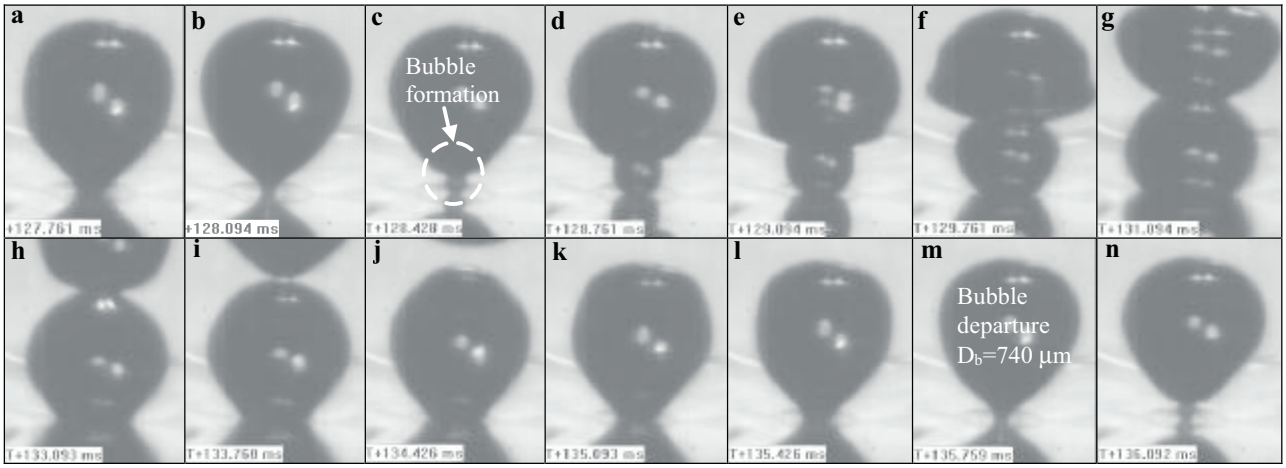

Figure 6. Images of a sample bubbling event. Note that the particular bubble for which the temperature and the heat flux variations are shown in Figures 8&9, forms at t=128.428 ms (image "c") and departs at t=135.749 ms (image "m").

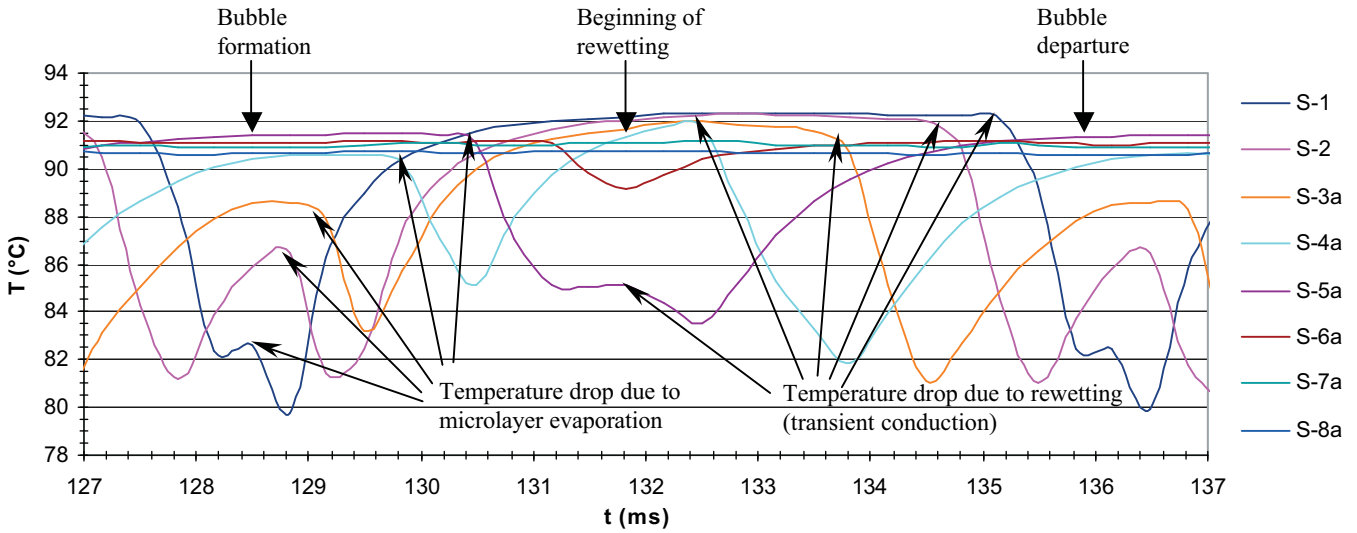

Figure 7. Surface temperature variations under the bubble shown in Figure 7 (see Figure 1 for positions of sensors S-1 to S-8a). Temperature of sensors 9a to 13a is equal to sensor 8a. Temperatures are symmetric at the four sensor array quadrants.

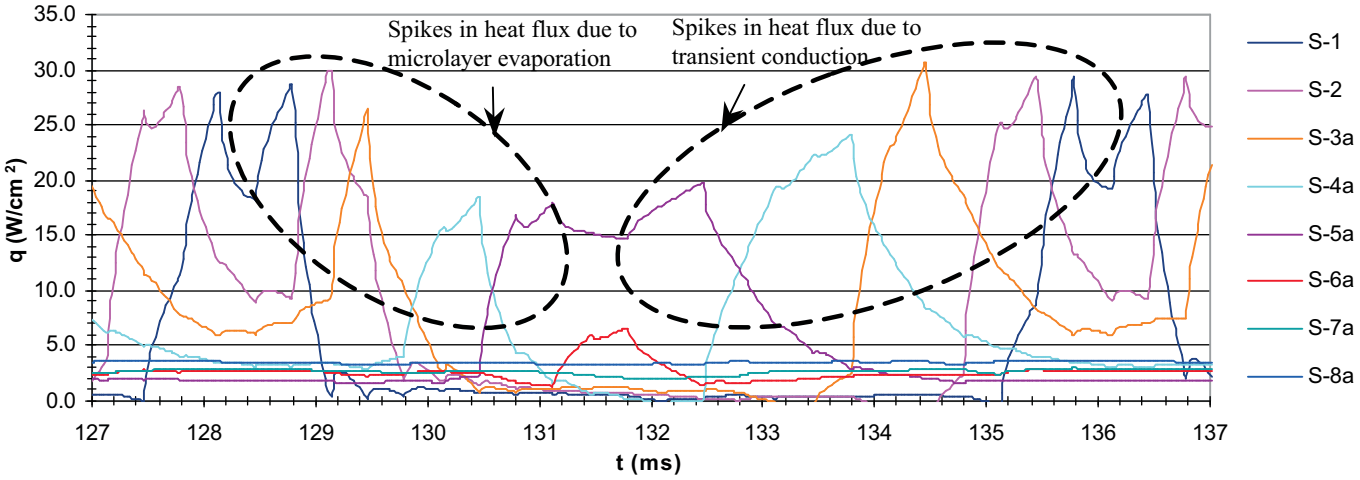

Figure 8. Heat flux variations at the surface for the bubble shown in Figure 7. The area under each curve shows the total heat transfer. These results are numerically modified to account for sensor thermal cross talk and some very fast transient events.

STREAMLINE BASED DESIGN OF A MEMS DEVICE FOR CONTINUOUS BLOOD CELL SEPARATION

Siyang Zheng, Yu-Chong Tai
Electrical Engineering, California Institute of Technology
Pasadena, California 91125, USA

ABSTRACT

We report a new MEMS device for continuous separation of particles based on size. Unlike previous passive fluidic devices for particle separation, fluidic streamline design based on local geometry and fluidic resistance of side channels are used. The filtering effect is achieved not by physical device boundaries, but by the collection zones established by fluidic field. The separation region of the device has a small footprint of 1.5mm by 0.8mm for separation of particles in micron range. The particles are automatically collected in different exit channels after they are separated, which facilitate further sensing and processing. Like crossflow filters, particles are separated perpendicular to flow direction. The minimal feature size of the device is designed to be larger than the diameter of the largest particles, so clogging can be minimized. Solvent exchange can be accomplished for larger particles. We demonstrate separation of 5μm and 10μm polystyrene beads, as well as erythrocytes and leukocytes of human blood with better than 96% efficiency.

INTRODUCTION

Size based particle separation is a basic technique in chemical and biological analysis. Centrifugation, traditional filtration and size exclusion chromatography are incorporated into various sample preparation procedures. As devices are miniaturized to micron scale, there are efforts on separation of cell size particles, for examples, field-flow fractionation [1-3], dielectrophoretic force separation [4], magnetic separator [5], micro-fabricated filtration [6] and microstep [7]. Recently, there are a group of passive, continuous flow devices that utilizes the flow properties in micro domain, for example pinched flow fractionation [8], pillar structure based deterministic lateral displacement separation [9, 10] and channel based hydrodynamic separation [11]. Unlike active separation, these devices only require simple flow control without moving parts, signal sensing and actuation. Unlike traditional filtration plagued with membrane clogging and fouling, malfunction of devices due to clogging can be minimized.

	Erythrocyte	Leukocyte
Cell shape	Biconcave disc	Sphere
Diameter range (μm)	5-8	7-20
Height (μm)	1.5-3.5	7-20
Volume (μm^3)	80 - 100	160 - 450
Count (10^9/L)	4,200 – 5,800	4.5 – 11.0

Table 1. *Comparison of erythrocytes and leukocytes [12, 13].*

One good application for size based particle separation is to separate erythrocytes (red blood cells, RBCs) and leukocytes (white blood cells, WBCs). As shown in table 1, erythrocytes are smaller than leukocytes with a diameter overlap. But because of their shape, erythrocytes have a significant smaller height and volume. The challenge is to design microfluidic system that utilizes this difference and achieve separation with high efficiency. Successful separation of erythrocytes and leukocytes can facilitate leukocyte purification or downstream cell sensing and counting in a lab-on-a-chip application.

PRINCIPLE

The principle of the device under discussion is based on *separation streamline theory*. For low Reynolds number laminar flow, the centers of particles follow streamlines if there are no interactions between particles and device walls. When obstacles, such as device walls or pillar structures inside channels, are introduced into the flow, there are special streamlines that ended at the stagnation points of these obstacle structures. We call these special streamlines as *separation streamlines*, for example the labeled streamline in figure 1. The special property about the separation streamlines is that it sets up asymmetry for particle flow. Particles with centers lying on one side of the separation streamline will always stay that side if there is no particle to obstacle direct interaction. As the flow is separated by an obstacle into two flows so are the particles. The region between a separation streamline and the boundaries of the obstacles (device walls in the case of figure 1) defines a *collection zone*. The minimal width of a collection zone is the *critical separation size R*. For a particle with radius larger than R (for example the large white one in figure 1), if at upstream its center is inside one collection zone, because of particle and obstacle interaction, the center of the particle is forced to shift out of the collection zone downstream at the place where R is measured. On the other hand, a particle with radius smaller than R (for example the small grey one in figure 1), it always stay in the same collection zone. As a result, particles originally flowing in the same collection zone are physically separated based on the critical separation size R after they pass the obstacle.

DESIGN AND FABRICATION

A streamline based design is applied to the separation region. For this device, perpendicular side channels with shifted downstream edges serve as obstacles. Inside the device (figure 2), the particle flow is first pinched against main channel wall by the buffer flow so that all the particles flow in the collection zones of downstream side channels. Then they enter a separation region with an array of side channels perpendicular to main channel. Particles with radiuses smaller than the critical separation size R exit from these side channels, while larger particles are displaced by main channel wall so much that they continue to flow along it. The collection zones are defined by the channel walls and the streamlines ended at stagnation points on the downstream edges of side channels.

The critical separation size R measures the minimal distance between the separation streamline ended at a stagnation point and the upstream edge of the same side channel. R can be controlled

by local geometry of separation region and the flow resistance of the side channels. The flow pattern inside the device is simulated by solving 2D incompressible Navier-Stokes equation with FEMLAB. No-slip boundary conditions are used for the device walls. Also assumed are parallel velocity field profile at the inlet and zero pressure at the outlet. As shown in figure 3, R increases exponentially as the distance of upstream and downstream edge $\Delta\lambda$ of the same exit channel increases linearly. On the other hand, R decreases linearly as the length of side exit channels increases exponentially (figure 4).

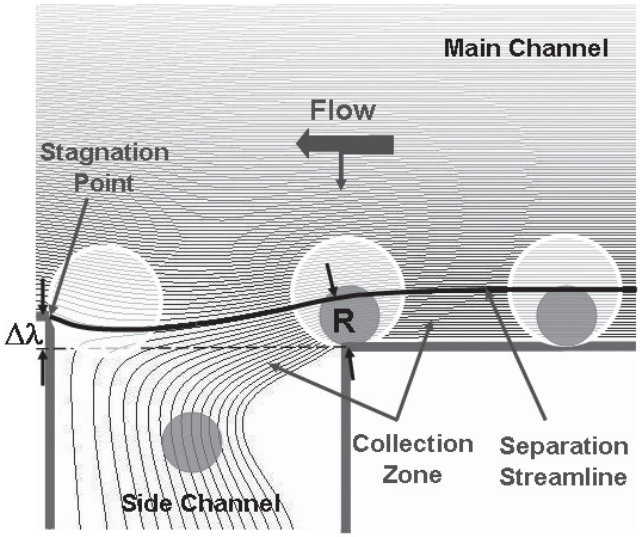

***Figure 1**: Principle of device operation. Particles with diameter smaller than the critical separation size R (grey) exit from side channel. Larger particles (white) are displaced by the main channel wall so much that they can not flow into side channel. Grey scaled lines are streamlines from FEMLAB simulation. The separation streamline ended at the stagnation point is labeled.*

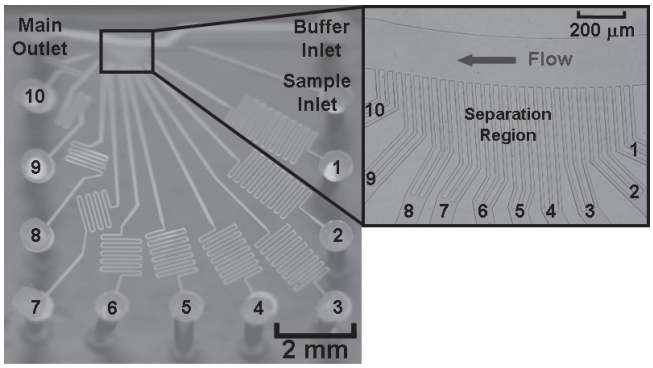

***Figure 2**. Device layout: Two inlets are labeled as sample inlet and buffer inlet. Outlets are labeled as main outlet and side channel outlets from 1 to 10. Particles are pinched against main channel wall before entering the separation region. The critical separation size is controlled by side channel lengths (as shown left) and the distance between upstream and downstream edges of the same side exit channel (as shown right).*

From the separation streamline theory, it's clear that the separation is binary for one geometry design, meaning there is a fixed single critical separation size and the particles are separated into two groups. To separate particles with a wide size range into more groups, geometries have to be changed. In our current design for blood cell separation, there are ten groups of side channels and each group consists of three individual channels. For different groups, from upstream to downstream, $\Delta\lambda$ increases linearly from 0μm to 9μm and the length of the exit channels decreases linearly from 22,000μm to 2,200μm. The width of the side exit channels is kept at 40μm.

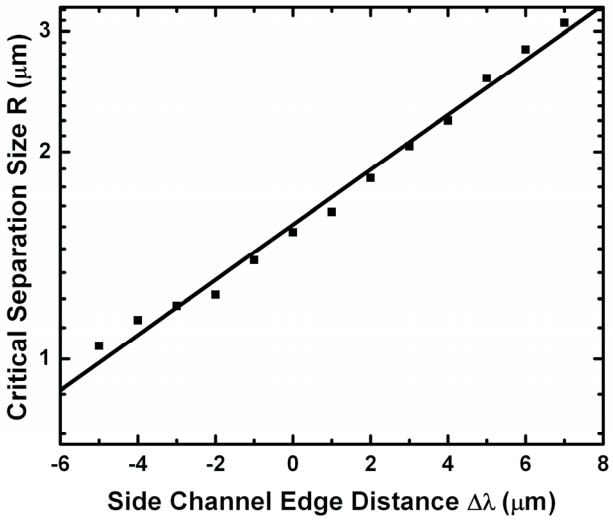

***Figure 3**. Effect of side channel edge distance $\Delta\lambda$ on minimal separation lane width R. Simulation results are based on a T shape channel structure.*

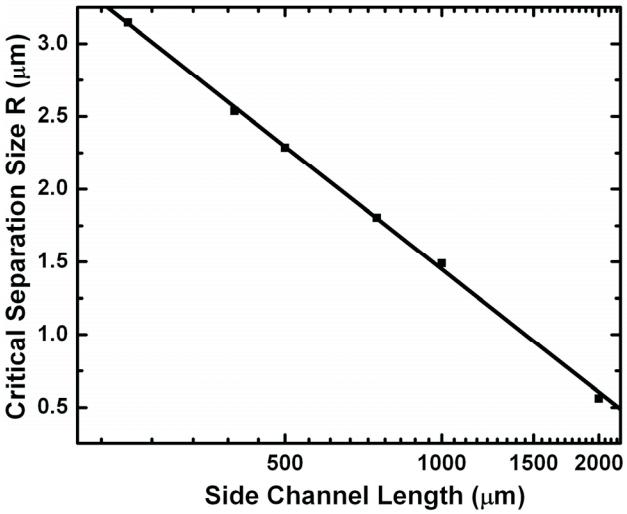

***Figure 4**. Effect of side channel length on critical separation size R. Simulation results are based on a T shape channel structure.*

The critical separation size increases from upstream to downstream as predicted by FEMLAB (table 1). Each side channel group works like a bucket to collect particles of a certain range. From side channel group number one to ten, the critical separation size R increase exponentially, which means the collection range of the bucket is fine for small particles and coarse for large particles. This is good for erythrocyte/leukocyte separation because the ratio of small erythrocytes to large leukocytes is on the order of one thousand to one.

Devices are fabricated with DRIE etched silicon molds and mounted on a glass slide by overnight baking at 80 degree Celsius. We chose PDMS (Sylgard 184, Dow Corning, MI) for the device

because of its blood compatibility and ease of use. The channel height is 20μm.

Side Channel Group Number	*Side Channel Length L (μm)*	*Edge Distance $\Delta\lambda$ (μm)*	*Critical Separation Size R (μm)*
1	22000	0	2.28
2	19800	1	2.57
3	17600	2	2.88
4	15400	3	3.08
5	13200	4	3.54
6	11000	5	4.12
7	8800	6	4.79
8	6600	7	5.76
9	4400	8	7.39
10	2200	9	10.75

Table 2. *Prediction of critical separation size R by simulation of 2D incompressible Navier-Stokes equation with FEMLAB.*

RESULTS AND DISCUSSION

Calibration is accomplished with fluorescent polystyrene beads (Duke Scientific, CA). Flows were pumped into devices by syringe pumps (Pico Plus, Harvard Apparatus, MA) with volume flow rate of buffer flow to sample flow about ten to one.

5μm green beads exit mainly from side channel groups one and two and 10μm red ones exit mainly from side channel groups nine and ten (figure 5 and 6). Under microscope, we observed the 10μm beads flow in a "jumping" mode in separation region, meaning they move towards the stagnation points of side exit channels and slow down. After passing these stagnation points, they quickly flow to the next side exit channel. Assuming 5μm beads exit from side channel groups one to three and 10μm beads exit form four to ten, after normalization statistics analysis shows the separation has a high efficiency of 96% (figure 7).

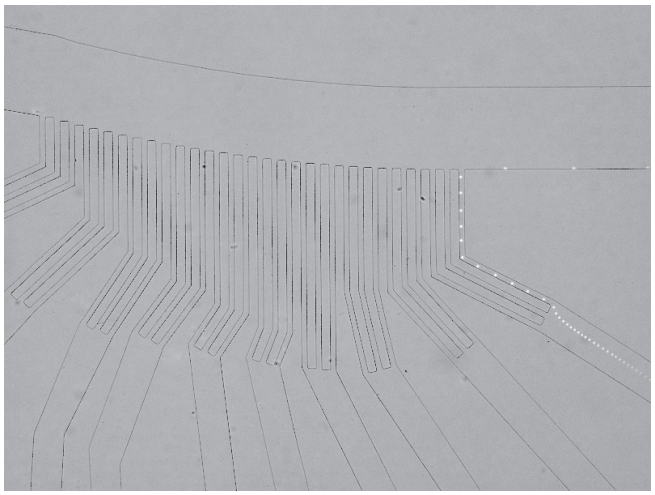

Figure 5. *Typical trace of 5μm fluorescent polystyrene beads.*

Human blood cells are obtained from healthy donors and used within 48 hours. Human blood cells are prepared by sedimentation based Wintrobe method. The erythrocyte portion is diluted 1500 times with Ficoll-Paque Plus (Amersham Biosciences, Sweden). Ficoll-Paque Plus is a mixture of diatrizoate sodium and Ficoll 400. Ficoll 400 is a neutral, highly branched, hydrophilic polymer of sucrose. Traditionally it has been used as a reagent to purify lymphocytes from human peripheral blood based on density gradient centrifugation. Its density is 1.077 g/ml, which is more close to blood cell density than aqueous saline. Diluting blood with Ficoll-Paque Plus enables us to run experiment over one hour without severe sedimentation.

Erythrocytes exit mainly from exit channel groups two and three (figure 8). To study leukocytes flow inside the device, leukocyte rich plasma is stained with fluorescent cell nucleus dye Aridine orange. Erythrocytes, which have no nucleus, do not fluoresce. Only leukocytes are stained and fluoresce. As shown in figure 9, leukocytes demonstrate a different separation profile from erythrocytes. Assuming erythrocytes exit from side channel group one to three and leukocytes exit from side channel group four to ten, a separation efficiency of 97% can be achieve after data normalization (figure 10).

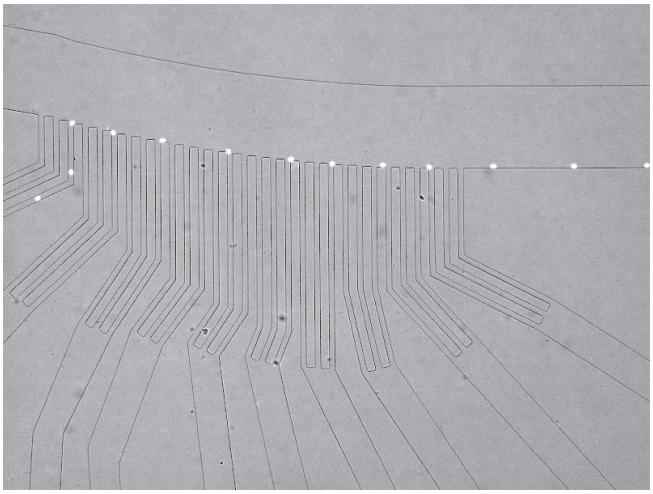

Figure 6. *Typical trace of 10μm fluorescent polystyrene beads.*

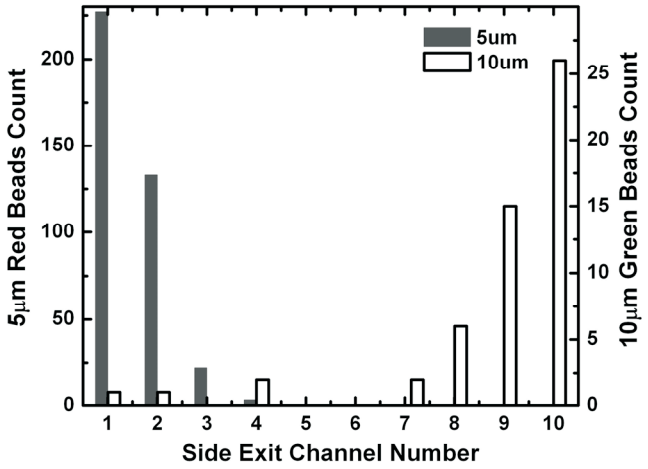

Figure 7. Statistics of 5μm and 10μm polystyrene beads separation.

For the flow rate ratio used during testing, the solvent in the sample flow is observed to exit from the side channel groups one and two. So all the larger particles exit from side channel groups three and above are flow in the solvent of the buffer flow. Although in our testing, there is no difference between the solvent in the sample flow and that in the buffer flow, this can be a unique and useful property when solvent exchange for larger particles is desirable.

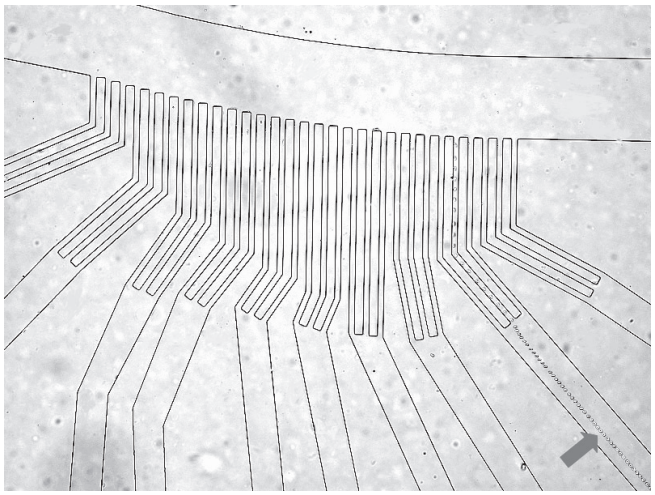

Figure 8. Typical trace of erythrocytes as pointed by arrow under bright field of microscope.

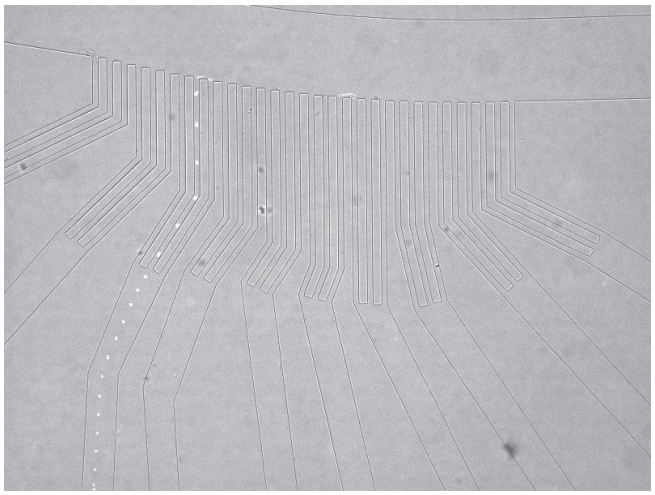

Figure 9. Typical trace of Acridine Orange labeled leukocytes.

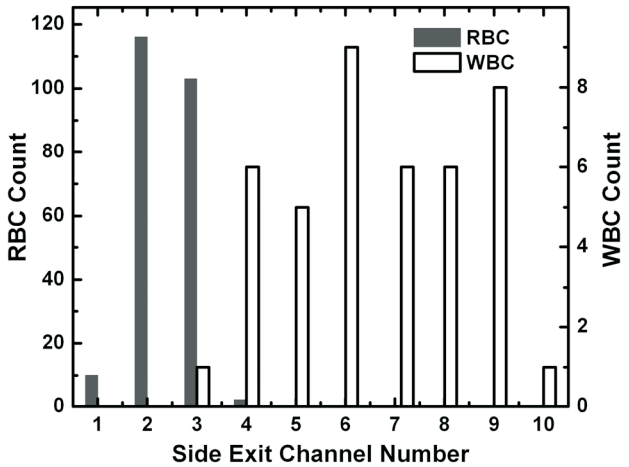

Figure 10. Statistics of erythrocytes (RBCs) and leukocytes (WBCs) separation.

CONCLUSION

We have produced a MEMS device for erythrocytes and leukocytes separation. Based on the separation streamline theory, streamline based design is applied. Local geometry and fluidic channel resistance are shown to change the critical separation size by simulation. The fabricated MEMS device demonstrates separation of 5μm/10μm beads and erythrocytes/leukocytes with high efficiency. The advantages of the device include high efficiency, small footprint, continuous flow, particle collection in channels after separation, minimized clogging and solvent exchange for larger particles. Further work should integrate the device into lab-on-a-chip systems.

ACKNOWLEDEG

This work is supported by NASA through National Space Biomedical Research Institute (NSBRI). The co-operative agreement number is NCC 9-58-317.

REFERENCES

[1] J. C. Giddings, "Field-Flow Fractionation - Analysis Of Macromolecular, Colloidal, And Particulate Materials," *Science*, vol. 260, pp. 1456-1465, 1993.

[2] Y. Jiang, M. N. Myers, and J. C. Giddings, "Separation behavior of blood cells in sedimentation field-flow fractionation," *Journal Of Liquid Chromatography & Related Technologies*, vol. 22, pp. 1213-1234, 1999.

[3] J. Yang, Y. Huang, X. B. Wang, F. F. Becker, and P. R. C. Gascoyne, "Cell separation on microfabricated electrodes using dielectrophoretic/gravitational field flow fractionation," *Analytical Chemistry*, vol. 71, pp. 911-918, 1999.

[4] J. Cheng, E. L. Sheldon, L. Wu, A. Uribe, L. O. Gerrue, J. Carrino, M. J. Heller, and J. P. O'Connell, "Preparation and hybridization analysis of DNA/RNA from E-coli on microfabricated bioelectronic chips," *Nature Biotechnology*, vol. 16, pp. 541-546, 1998.

[5] M. Berger, J. Castelino, R. Huang, M. Shah, and R. H. Austin, "Design of a microfabricated magnetic cell separator," *Electrophoresis*, vol. 22, pp. 3883-3892, 2001.

[6] S. Zheng, Y. C. Tai, H. Lin, M. Balic, R. Datar, and R. J. Cote, "Circulating Tumor Cell Capture from Whole Blood by Parylene Filter Devices," presented at microTAS2005, Boston, Massachusetts, USA, 2005.

[7] S. Vankrunkelsven, D. Clicq, K. Pappaert, G. V. Baron, and G. Desmet, "A novel microstep device for the size separation of cells," presented at microTAS 2004, Malmö, Sweden, 2004.

[8] M. Yamada, M. Nakashima, and M. Seki, "Pinched flow fractionation: Continuous size separation of particles utilizing a laminar flow profile in a pinched microchannel," *Analytical chemistry*, vol. 76, pp. 5465, 2004.

[9] L. R. Huang, E. C. Cox, R. H. Austin, and J. C. Sturm, "Continuous particle separation through deterministic lateral displacement," *Science*, vol. 304, pp. 987, 2004.

[10] S. Zheng, R. Yung, Y. C. Tai, and H. Kasdan, "Deterministic lateral displacement MEMS device for continuous blood cell separation," presented at 18th IEEE International Conference on Micro Electro Mechanical Systems (MEMS '05), Miami Beach, Florida, USA, 2005.

[11] M. T. Yamada and M. Seki, "Hydrodynamic filtration for on-chip particle concentration and classification utilizing microfluidics," *Lab on a chip*, vol. 5, pp. 1233, 2005.

[12] H. L. Kasdan, personal communication, 2004.

[13] S. B. McKenzie, *Clinical Laboratory Hematology*: Prentice Hall, 2004.

A LOW-POWER PRESSURE- AND TEMPERATURE-PROGRAMMABLE μGC COLUMN

Joseph A. Potkay, Gordon R. Lambertus, Richard D. Sacks, and Kensall D. Wise
Engineering Research Center for Wireless Integrated MicroSystems (WIMS ERC)
The University of Michigan, Ann Arbor, MI 48109-2101

ABSTRACT

This paper presents the theory, fabrication and experimental results for the highest performance, low-power micro gas chromatography (μGC) column realized to date. The suspended-dielectric 1m-long column is split into two sections, permitting pressure programming. Furthermore, each section is individually temperature programmable. The integrated heaters have a mean resistance of 6.8 kΩ and a TCR of 1439 ppm/ºC. A single heater in the fully suspended column requires 6 mW to raise the local column temperature by 100 ºC in vacuum (10 μTorr). The column has separated 10 alkanes in 52 s and four chemical warfare agent simulants and an explosive simulant in 60s.

INTRODUCTION

Accurate chemical (gas) sensing is critically needed for a wide variety of applications, including those in industrial process control, food processing/monitoring, environmental monitoring, pharmaceutical screenings, health care, and homeland security. However, past devices have often lacked speed, sensitivity, stability, and, in particular, selectivity. A miniaturized gas chromatograph (GC) potentially provides a solution to all of these problems, especially selectivity, since it is able to separate components in space and time.

In a typical gas chromatography system, the separation process begins when a gaseous sample is injected into a separation channel (column). The column is usually coated with a thin film, known as the stationary phase, which enhances the separation ability of the column and can be chosen based on the targeted compounds. As a carrier gas transports the sample through the column, the individual components in the mixture spend different amounts of time adsorbed in the stationary phase on the wall of the column. This adsorption process is dependent on several variables, including the component vapor pressures and their polarities, the column temperature, the carrier gas velocity, the stationary phase characteristics, and the component retention factors. In general, compounds that spend less time in the stationary phase exit the end of the column first, where they are detected. Thus, the elution time can be used to identify the compound, and the magnitude of the detector signal can be used to determine its concentration.

Commercial GC systems exist, but are inconvenient in field use due to their size and power. In some cases, gas samples are collected in the field and analyzed in the laboratory using a conventional GC, but this process is inefficient at best. By miniaturizing such systems, lower power levels may be achieved, facilitating analysis directly in the field. The addition of integrated pre-concentrators to such miniaturized microsystems could also aid in reducing analysis time relative to commercial systems.

The first efforts to produce a μGC began in 1970 at Stanford University [1], with more recent efforts at Lawrence Livermore [2] and Sandia National Laboratories [3]. Various column structures have been explored, including anodically-bonded glass-silicon columns [2,3,4], silicon/silicon dioxide fusion-bonded columns [5], metal LIGA-based columns [5], and parylene columns [6]. Although these efforts have yielded important progress, they have not yet provided the high performance and low-power operation needed for many applications. In addition, none of the systems developed to date have been completely miniaturized or fully integrated.

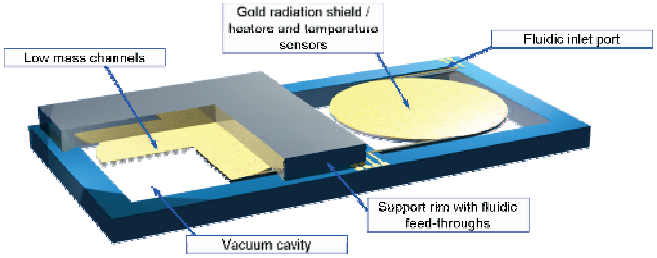

Figure 1. *Drawing of the CVD column structure.*

The column described here is aimed at substantially lower power, smaller size, and higher performance than anything reported in the past. It leverages previous work at Michigan on column design [4], coating and testing [8], and process technology [9]. It forms the heart of a μGC intended for an environment monitoring system that is currently under development as part of the NSF-funded Engineering Center for Wireless Integrated MicroSystems (NSF WIMS ERC). This microsystem, which will monitor temperature, pressure, humidity, and gas composition with part-per-billion sensitivity, is targeted at less than 5cc with an average power of less than 1mW. The finished system will analyze 30+ volatile organic compounds (VOC's) in less than 5 mins. The following sections describe the theory, fabrication, and experimental results for the column portion of this microsystem.

THEORY AND DESIGN

The column structure is shown in Fig. 1 and is designed to minimize power and maximize performance. As shown, the column is suspended and vacuum-sealed to reduce conductive and convective heat losses, etched back to improve the thermal response time, and coated with metal to decrease radiation losses and improve temperature uniformity across the column. The structure consists of two individually-suspended and heated columns so that the first column may be bypassed (in order to increase flow in the second column) using integrated microvalves. Thus, the column has two zones, both temperature and pressure programmable. As μGC columns decrease in size, their resolution also decreases; temperature and pressure programming provide a powerful means to increase performance. The column is made up of semi-circular channels, which were chosen for ease in processing and to minimize stationary phase pooling. In general, circular-cross-section channels perform well over a larger range of flow than other column shapes, permitting increased system design flexibility.

The performance of gas chromatography columns is conventionally measured in terms of the total number of theoretical plates (N) (a measure of the resolving power of the column) and in terms of the height equivalent to a theoretical plate (H) (a measure of the efficiency of the column). Golay performed the first analytical modeling of gas chromatography channels in 1958 [10]. The H of a column with a circular cross section is given by:

$$H = 2\frac{D_g}{u} + \frac{1+6k+11k^2}{96(1+k)^2}\frac{ud^2}{D_g} + \frac{2h^2ku}{3D_l(1+k)^2}, \qquad (1)$$

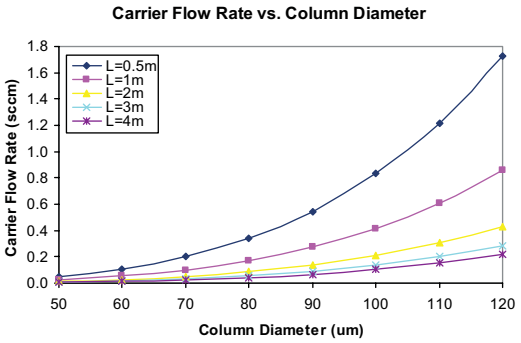

Figure 2. *Effect of the channel diameter and length on the theoretical flow rate of the column.*

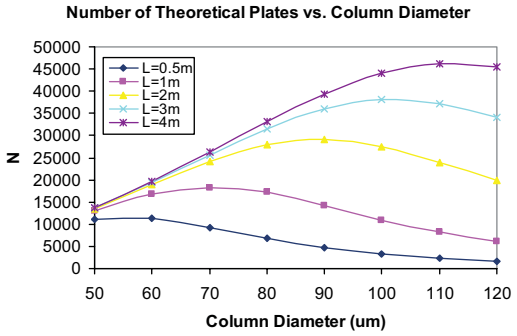

Figure 3. *Effect of the channel diameter and length on the theoretical resolving power of the column.*

where D_g and D_l are the diffusion coefficients in the gas and liquid phases, respectively, k is the retention factor, h is the thickness of the liquid phase, and d is the channel diameter. The average carrier gas velocity, u, is given by (2), where u_o is the outlet gas velocity, f_2 is the Martin-James gas compression correction factor, given in (3), p_o is the outlet pressure, p_i is the inlet pressure, and L is the column length.

$$u = u_o f_2 = \frac{d^2 p_o \left(\left(\frac{p_i}{p_o}\right)^2 - 1\right)}{64\eta L} f_2 \tag{2}$$

$$f_2 = \frac{3\left(\left(\frac{p_i}{p_o}\right)^2 - 1\right)}{2\left(\left(\frac{p_i}{p_o}\right)^3 - 1\right)} \tag{3}$$

To determine the total resolving power of a column, the total number of plates, N, is calculated as

$$N = \frac{L}{H}, \tag{4}$$

where L is the total length of the column. Finally, the holdup time, t_m, is the time it takes for an unretained component to be injected into the system and travel through the column to the detector. It is calculated as in (5):

$$t_m = \frac{L}{u} \tag{5}$$

For the μGC under development, many factors constrain the design and performance of the column. Integration with a MEMS vacuum pump further facilitates miniaturization and low-power operation, but hinders the ability to increase the performance of the column by increasing its inlet pressure as is conventionally done. The use of air as a carrier gas eliminates the need for gas storage and facilitates miniaturization. However, air has a higher viscosity and smaller diffusion constant than conventional carrier gases such as hydrogen, resulting in a diminished flow rate in (2) and decreased resolving power in (4). In addition, the total analysis time was limited to less than 10min, and because of fabrication and power issues, the diameter of the low-mass columns was limited to between 50μm and 120μm. Total length was limited to 4m.

The plots shown in Figs. 2 and 3 were generated using (1-5) and show the tradeoff between various design parameters. Figure 2 shows the column flow rate for various channel dimensions. Although a low flow rate is preferable for the MEMS vacuum pump (less than 2sccm at 0.5atm of pressure), a high flow rate is favorable for sweeping components out of the preconcentrator and across the detector. However, other techniques can also be applied, such as split flow injection to improve the gas flow rate over the preconcentrator and detector. Thus, flow should be maximized while remaining within the requirements of the vacuum pump.

Figure 3 displays the relationship between the resolving power of the column and its diameter and length. There is an optimum column diameter for each length (for a fixed differential pressure). Based on fabrication and power considerations, it is desirable to keep the column diameter and length small. However, a high resolving power is required to be able to separation all of the components in a complex mixture of 30+ VOC's. Thus, a column diameter of around 90μm and lengths of 0.5m, 1m, and 2m were chosen as a compromise among all of the system requirements. Nearly all of the data points of interest correspond to a total analysis time of less than 5 minutes, assuming a maximum retention factor of 10.

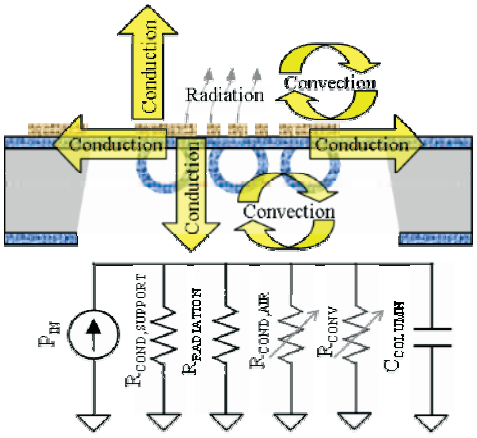

Figure 4. *Thermal model and the equivalent circuit for the suspended CVD column.*

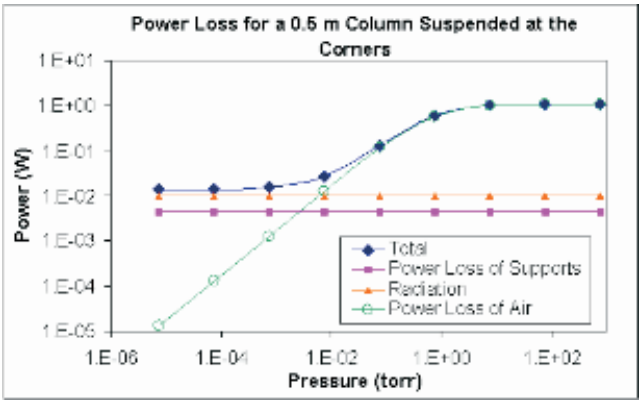

Figure 5. *Power loss as a function of pressure for a 0.5 m column suspended at 4 points using the model in Fig. 4. The model predicts a power consumption of 14 mW in vacuum.*

Next, a thermal model of the device was developed to optimize the device speed and power and predict its behavior. The model in Fig. 4 considers the effects of conduction (through the supports and air), convection and radiation. Conduction occurs both through the oxynitride supports and through the air above and below the column. Conduction through the supports was modeled assuming a thermal conductivity of 1.4 W/mK for the oxynitride. The thermal conductivity of air between two enclosed plates is a function of pressure, approximated in [11] by:

$$k_{air} = k_{air,0} \times \frac{1}{1 + \frac{7.6x10^{-5}}{P \times d / T}} \quad (6)$$

where $k_{air,o}$ is the thermal conductivity of air at room temperature and pressure (0.0284 W/mK), P is the pressure, d is the distance between the plates and T is the average temperature of the plates. Due to the transparency of the dielectric column, radiation occurs from both the column top and bottom in an enclosed space. In both cases, heat loss can be modeled as [12]:

$$Q_{rad} = \frac{\sigma_{SB} A (T_{S1}^4 - T_{S2}^4)}{\varepsilon_{S1}^{-1} + \varepsilon_S^{-1} - 1} \quad (7)$$

where σ_{SB} is the Boltzmann constant, A is the area, and T_{S1} and T_{S2} and ε_{S1} and ε_{S2} are the temperatures and emissivities of the two surfaces, respectively. Due to the size of the cavity, viscous forces in the air are much larger than buoyancy forces and no fluid motion occurs. Thus, the Rayleigh number is very small and convection can be neglected [13].

The plot in Fig. 5 was generated using (6), (7) and Fig. 4. It predicts the heat loss as a function of pressure for the column. In vacuum, the model predicts a heat loss of 14mW at a temperature rise of 100 ºC.

FABRICATION

Fabrication of the column (Fig. 6) requires 6 masks. First, a grid is anisotropically etched in a 2µm-thick PECVD oxynitride dielectric layer using a reactive ion etch (RIE). A vertical sidewall is necessary in order to prevent voids when the channel is later sealed and, thus, improve the strength of the column. The grid is then undercut using a 25 minute long dry isotropic etch and sealed using a 12µm-thick PECVD oxynitride layer (Fig. 7). Both oxynitride layers are designed to be stress free and require less than 15min for deposition.

Next, a 200/400Å Ti/Pt metal layer is deposited and patterned to form the heaters and temperature sensors. The Ti/Pt layer is also used to reduce radiation losses and increase temperature uniformity across the column. Next, the Ti/Pt layer is protected with another 2µm-thick oxynitride layer and then a 300/1000/5000Å Ti/Pt/Au bond ring is deposited via evaporation. The intermediate platinum layer serves as a diffusion barrier during the later bonding step. Finally, the oxynitride is wet etched for device isolation and to open metal contacts. The cap wafer requires 3 additional masks. Two DRIE etches form a recess and low-dead-volume fluidic connectors, and a 300Å/4µm Cr/Au bond ring is plated. Finally, the two wafers are bonded together utilizing Si/Au eutectic formation, and a dry etch is used to release the device (Fig. 8). Stress minimization of both the metal and oxynitride films is critical to device release. In addition, low-dead-volume fluidic interconnects are crucial in preventing band broadening. It should be noted that the structure in Fig. 5(d) contains a dielectric layer connecting the column to the substrate. This layer is used for structural support; however, it may optionally be etched away to fully suspend the device and reduce its power consumption. The process can also be extended by bonding a second cap wafer to the bottom of the device and, thus, vacuum encapsulating the column.

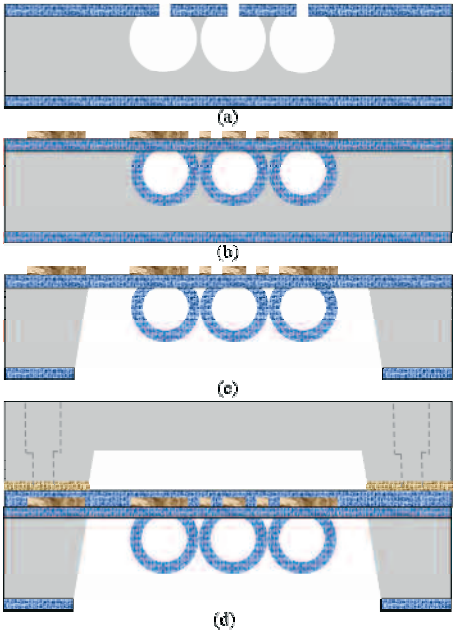

***Figure 6**. Process flow for the released dielectric columns.*

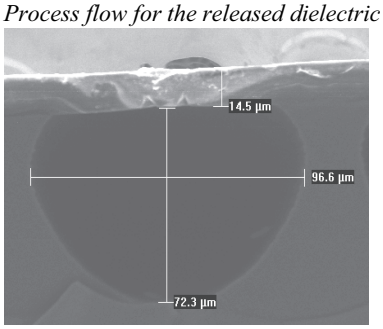

***Figure 7**. Cross section of a sealed buried channel with a height of 72µm, width of 97µm, and ceiling thickness of 15µm.*

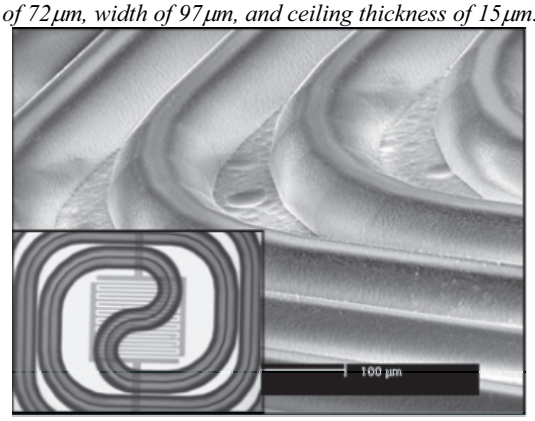

***Figure 8**. SEM of the bottom side of a released column. A picture of the backside of the transparent dielectric column is shown (inset). The heater is visible through the column.*

RESULTS

A fabricated 1m column is shown in Fig. 9. The three low-dead-volume fluidic interconnections are visible on the top substrate and permit individual coating of the two column segments and pressure programming. The electrical interconnects can be seen on the shelf along the bottom of the column and provide contacts to the heaters, temperature sensors and substrate.

After fabrication, initial tests were done to examine the strength of the eutectic bond and its hermeticity. First, a gross bond strength test was completed by prying apart the two wafers using a razor blade. The bond area was extremely hard to break, and when it did, the breaking occurred in the substrate and not along the bond interface. Next, capillary tubing was epoxied into the fluidic connectors and fluidic pressure of up to 0.5atm was applied to the input. The device was immersed in acetone and no leaks were visible, verifying the gross hermeticity of the bond and viability of the fluidic interconnections. Complete characterization of a similar bond technology can be found elsewehere [14]. The current bond technology differs from [14] in that it utilizes metal feedthroughs and a PECVD isolation layer.

Next, the device was placed in an environmental oven and the temperature was varied from 25ºC to 125ºC. The resistances of the temperature sensors were found to have a mean resistance of 6.88 kΩ and a TCR of 1439 ppm/ºC. The devices were then placed in a custom vacuum chamber at 10μTorr. Power was applied to a single heater in a fully suspended column and only 6 mW was required to raise the local column temperature by 100ºC. The devices were then coated with a PDMS stationary phase. During coating, the devices withstand an inlet pressure of 25psi without damage. Next, the device was hooked up to an injection system and flame ionization detector (FID). The separation of 10 alkanes in 52s is shown in Fig. 10. The separation of four chemical warfare agent simulants and an explosive simulant in 60s is shown in Fig. 11. Both separations utilized a temperature ramp from of 30 to 100ºC at 50 ºC/min.

CONCLUSION

This paper presented a high-performance low-power μGC column operating at milliwatt power levels and capable of separating 10 alkanes in under 52 s. Such columns are critically needed for remote chemical monitoring systems for homeland security, environmental monitoring and health care.

ACKNOWLEDGEMENTS

The authors would like to thank Mr. Jay Mitchell for his advice and help with the design of the Au-Si eutectic bond technology and help with the vacuum testing of the devices. This work was supported by the Engineering Research Centers Program of the National Science Foundation under Award Number EEC-9986866.

REFERENCES

[1] S. Terry, J. Jerman, and J. Angell, "A gas chromatographic air analyzer fabricated on a silicon wafer," *IEEE Trans. ED.*, vol. 26, pp. 1880-1886, December 1979.

[2] E. Kolesar, R. Reston, "Silicon micromachined gas chromatography system," *IEEE Conf. on Innovative Syst. in Silicon*, pp. 117-125, Oct. 1997.

[3] G. Frye-Mason, et. al., "Integrated chemical analysis systems for gas phase CW agent detection," *μTAS*, pp. 477-480, 1998.

[4] J. Potkay, J. Driscoll, M. Agah, R. Sacks, and K. Wise, "A high-performance microfabricated gas chromatography column," *IEEE Conf. on MEMS*, pp. 395-398, January 2003.

[5] A. Bhushan, D. Yemane, J. Goettert, E. Overton, and M. Murphy, "Fabrication and testing of high aspect ratio metal micro-gas chromatograph columns," *ASME IMECE*, pp 321-4, November 2004.

[6] H.-S. Noh, P. Hesketh, and G. Frye-Mason, "Heating element embedded parylene microcolumn for miniature gas chromatograph," *IEEE Conf. on MEMS*, pp. 73-76, Jan. 2002.

[7] C. Yu, M. Lucas, J. Koo, P. Stratton, T. DeLima, and E. Behymer, "A high performance hand-held gas chromatograph," *Proc. IEEE Conf. on MEMS*, pp. 481-486, Nov.1998.

Figure 9. *Picture of a finished 1 m column next to a dime.*

[8] G. R. Lambertus, A. Elstro, K. Sensenig, J. A. Potkay, M. Agah, K. D. Wise, F. Dorman and R. D. Sacks, "Design, Fabrication, and Evaluation of Microfabricated Columns for Gas Chromatography," *Analytical Chemistry*, v 76, n 9, pp. 2629-2637, 2004.

[9] M. Agah and K. D. Wise, "A Fully-Dry PECVD-Oxynitride Process for MicroGC Column Fabrication," *Proceedings of the 18th IEEE Conference on MEMS*, pp. 774-777, 2005.

[10] M. J. E. Golay, *Gas Chromatography*, New York: Academic Press, 1958, pp. 36-55.

[11] *Fluid Flow Databook*, General Electric, Genium Publishing, Section 410.2, May 1982.

[12] M. Kaviany, *Principles of Heat Transfer*, New York: Wiley, 2002.

[13] D. Pitts, and L. Sissom, *Schaum's Outline of Theory and Problems of Heat Transfer*, New York: McGraw Hill, 1998.

[14] J. S. Mitchell, G. R. Lahiji, and K. Najafi, "Encapsulation of Vacuum Sensors in a Wafer Level Package Using a Gold-Silicon Eutectic," *Transducers '05*, pp. 928-931, 2005.

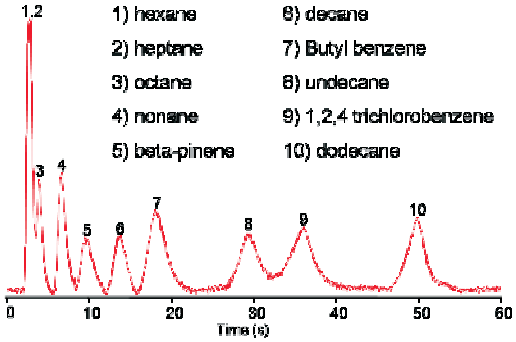

Figure 10. *Separation 10 components in 52s using the 1 m column. A temperature program of 30-100°C at 50°C/min was used in conjunction with a flame ionization detector.*

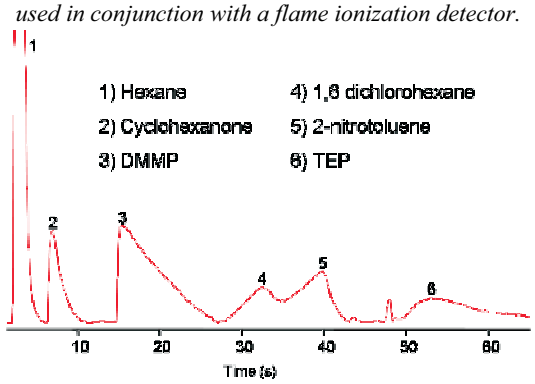

Figure 11. *Separation of 4 CWA simulants and an explosive simulant in 60s utilizing the 1 m column. A temperature program of 30-100°C at 50°C/min was used in conjunction with a flame ionization detector.*

A NANO INTERDIGITATED ELECTRODES ARRAY ON POLYMER FOR DISPOSABLE IMPEDIMETRIC BIOSENSORS

Zhiwei Zou[1], Junhai Kai[1], Michael J. Rust[1], and Chong H. Ahn[1,2]
Microsystems and BioMEMS Laboratory
[1] Department of Electrical & Computer Engineering & Computer Science
[2] Department of Biomedical Engineering
University of Cincinnati
Cincinnati, OH 45221-0030, USA

ABSTRACT

This paper presents an integrated nano interdigitated electrodes array (IDA) on polymer substrate with microfluidic system. It can be used as a miniaturized, sensitive, and easy-to-use impedimetric sensor for genomics, proteomics, and cellular analysis. A gold (Au) nano IDA has been successfully patterned on polymer (Cyclic olefin copolymer, COC) substrate, which can be widely used for disposable lab-on-a-chip applications. The fabricated device has been characterized in KCl salt solution using electrochemical impedimetric spectroscopy (EIS). The preliminary result of monitoring protein binding is demonstrated as well, which insures the potential of this device to be used for protein immunosensors.

INTRODUCTION AND MOTIVATION

Electrochemical impedance spectroscopy (EIS) shows detailed information on capacitance and resistance changes from the biorecognition events occurring at the electrode or substrate surface directly, thus, allowing for label-free biosensing [**1**]. When target DNA hybridizes to oligonucleotide probes or when antibodies bind to antigens, the change in electric properties results in a change of impedance, enabling the measurement of a direct electrical signal. The nanoscale interdigitated electrodes array (nanoIDA) can be introduced to improve the sensitivity since the generated electric field between a gap of 100 nm matches the region of interest (i.e. on the order of 10-100 nm for protein immobilization and up to 200 nm for DNA binding) [**2**]. In addition, the space confinement of the nanogap minimizes the noise from the electrical double layer [**3**].

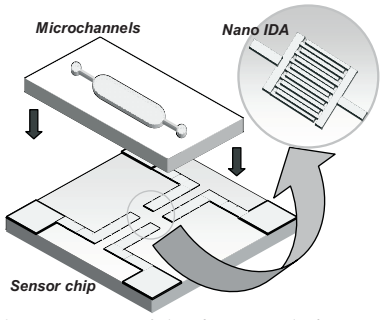

Figure 1. *Schematic view of the device including an Au nano IDA on polymer substrate and a polymer microfluidics chip.*

High density IDA has been used as a sensing surface to analyze cellular and biomolecular activities in solution using EIS. A small AC voltage is applied to the electrode pairs, thus different concentrations of cells or biomolecules bound to the surface will yield different changes in electrical impedance between the electrodes. This effect has been theoretically analyzed by calculating the electric field between the interdigitated electrodes, and the result is shown and discussed in [**2**,**4**]. The sensitivity of biomolecular analysis has been improved by shrinking the electrodes array size down to the nanoscale due to the electric field being confined much closer to the binding surface. The theoretical calculation indicates that 80% of the electric field and current flow between two electrodes is in a layer which has thickness less than *L/2*, where L is the sum of the electrode width and spacing as shown in Figure 2a. Because the DNA and protein molecular binding layer is less than 200 nm, by applying voltage on one pair of electrodes, most electric field and current flow are limited in this region for nanoscaled electrodes while most parts of the electric field are out of this region for conventional microelectrodes.

Most reported nano IDA structures were fabricated on Si or glass substrate whereas recently polymer has been considered as one of the most suitable substrate materials for low cost lab-on-a-chip devices. Patterning metal nano IDA on polymer provide a direct way to integrate the high sensitivity nano biosensor into polymer biochips to utilize both benefits of high sensitivity and low cost. In this work, the nano IDA is patterned on polymer substrates (Cyclic Olefin Copolymer, COC) since COC offers excellent material properties for nano biosensors and is very suitable for disposable polymer lab-on-a-chips [5].

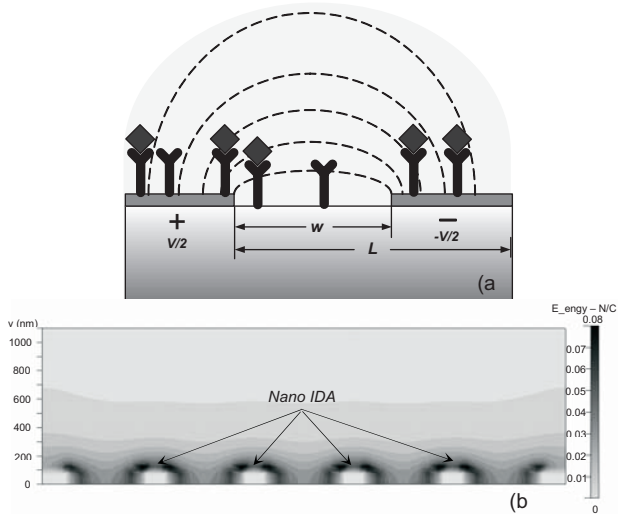

Figure 2. *NanoIDA: (a) Design of an Au nano IDA protein binding impedimetric sensor on polymer and (b) FEA simulation of the electrostatic energy distribution of nano IDA in water. (L= 700 nm, W= 200 nm, and V= ±25 mV).*

DESIGN AND FABRICATION

A schematic illustration of the Au nano IDA on polymer with integrated microfluidic system is shown in Figure 1. By using polymer microfluidic chips, the analyte consumption and the total sensing time are significantly reduced.

FEA simulation is used to analyze the electric field energy around the Au nanoIDA in water. Three pairs of Au electrodes are modeled with 100 nm height, 200 nm width, and 500 nm spacing in water medium as shown in Figure 2. The simulation result clearly indicates that all the electric filed is concentrated within 600 nm of the sensor surface where protein binding occurs.

The fabrication processes is summarized in Figure 3. A 3-inch blank COC wafer with very good surface smoothness is prepared by plastic injection molding techniques using a highly polished, mirror face Ni mold-disk. A Cr layer of 10 nm is first evaporated on the COC to make the substrate compatible with e-beam lithography. Electron resist Polymethylmethacrylate (PMMA) is spin-coated and the pre-baking condition is adjusted due to the relatively low melting point of COC. E-beam lithography is performed by Raith-150 system, exposing the PMMA. The nano pattern is defined after developing and Cr etching. Subsequently, a Au layer of 100 nm is evaporated on the patterned substrate by e-beam metal evaporator. The sample is then placed in acetone for lift-off; the Au nanoIDA is created in this step. After nanofabrication, photolithography techniques are used for nano-micro interface patterning and integration of Au nanoIDA with electrical connection pads. A second Au layer (200 nm) is evaporated, covering the existing contact pads achieved by the nano fabrication. The sample is then dipped in acetone for lift-off. Finally, all the redundant Cr is etched out.

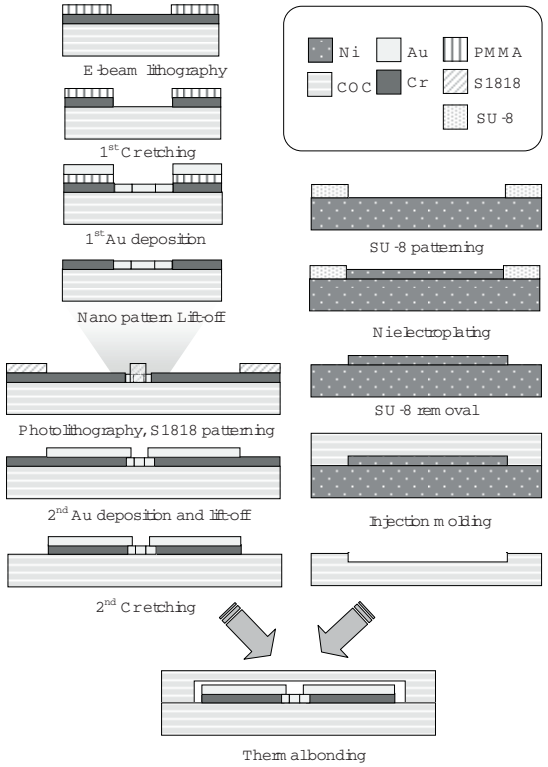

Figure 3. *Fabrication processing for the nanoIDA with polymer microfluidic channels.*

In order to fabricate the polymer microfluidic system, the plastic injection molding and thermal bonding techniques have been developed [**6**]. The SU-8 2035 photoresist is spin-coated on the 3-inch nickel disk to achieve 100 um thickness. Then, a pre-bake process is performed. After the photoresist layer is exposed with UV source, it is baked again for the cross-linking. After developing the SU-8 photoresist, the electroplating is performed in a nickel plating bath, using a two-electrode system with a nickel anode and a nickel disk cathode with SU-8 patterns. Finally, a nickel mold with a plating microstructure is attained after removal of the residual SU-8 photoresist. The microfluidic chip was replicated from this mold over a plastic substrate of COC by injection molding. After drilling holes for fluidic interconnection at inlets and outlets, the microfluidic chip is bonded with the sensor chip using thermal fusion bonding technique to make the final device.

Photographs of the fabricated device are shown in Figure 4. Figure 4a and 4b illustrate the configuration of Au nanoIDA, electrical connections and microchannel. The images of nanofabricated IDAs on polymer by SEM and AFM are shown in Figure 4c, 4d, and 4e. The nanoIDA consists of 100 electrode fingers with 100 μm length, 200 nm width, 100 nm thickness and 500 nm spacing in the 0.01 mm2 sensing area.

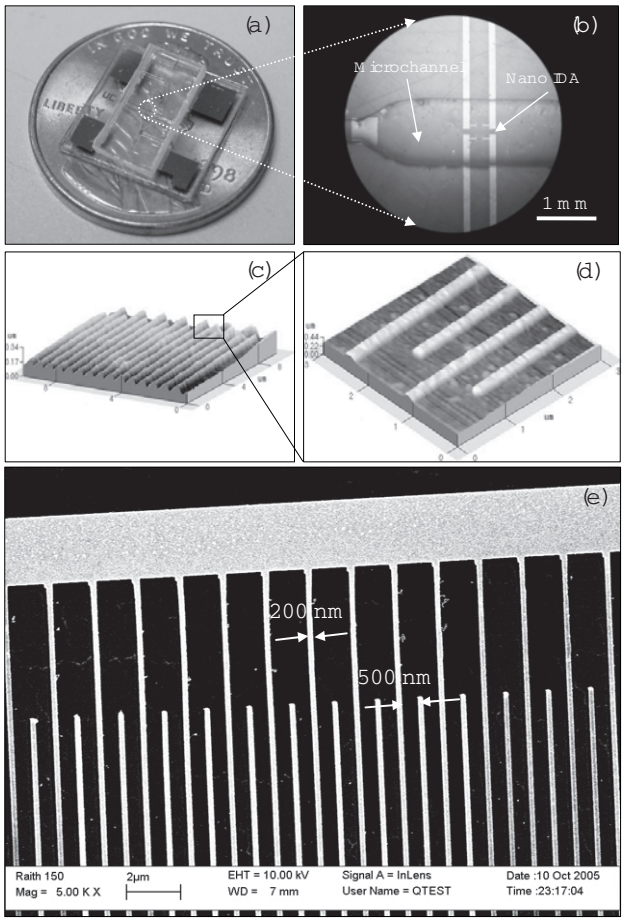

Figure 4. *Photographs of the nanodevice: (a) the entire chip; (b) microscope image of nano IDA, electrical connections and microchannel; (c), (d) AFM; and (e) SEM images of the nano IDA array on polymer substrate.*

RESULTS AND DISCUSSION

The nano device is electrically characterized in KCl solution with various concentrations using HP 4284A LCR meter (Figure 5). The EIS is performed at 50 mV with the frequency range 20 Hz to 1MHz after the sample solution is injected into the sensing channel. The DI water and KCl solutions are measured from low to high concentration using the same method. By analyzing a typical impedance response of the nano IDA in 10^{-3} M KCl solution, three regions can be subdivided as shown in Figure 6a.

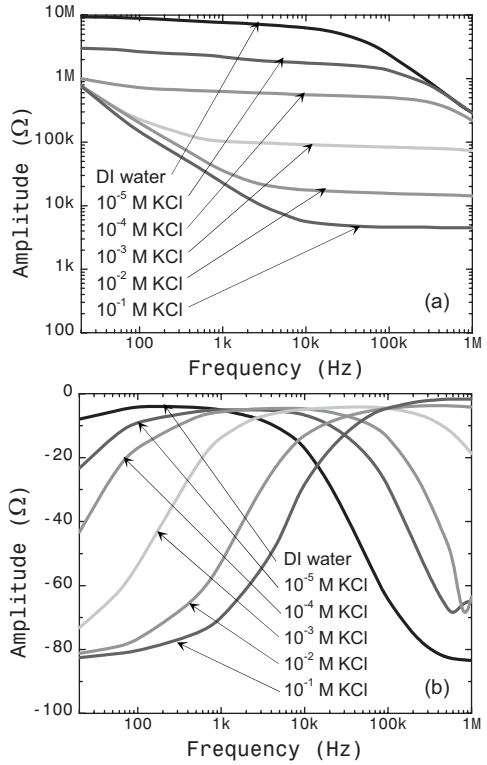

Figure 5. *EIS of a nanoIDA under KCl electrolyte with different concentrations: a) amplitude response and (b) phase response.*

A simplified electrical model [**2**] (Figure 6a) can be used to explain these three regions. They correspond to three major electrical components: the serial double layer capacitance C_{dl}, the serial electrolyte resistance R_{sol}, and the parallel solution capacitance C_{di}. At the low frequency range, C_{dl} determines the signal. Phenomena occurring in the neighborhood of the electrode are measured in this region, thus surface related processes influence this capacitance. At intermediate frequencies, R_{sol} governs the signal, and the conduction of ions in the solution determines the signal. At the high frequency end, the dielectric behavior can be observed. The dielectric behavior of solution C_{di} dominates the signal in this region. Further measurement and analysis of this simplified model is presented in Figure 6. In the range from 20 Hz to 100 KHz, the capacitance of 10^{-2} M KCl solution C_{di} can be neglected. The agreement of the fitting curve coming from the model and the measurement data is shown in Figure 6.

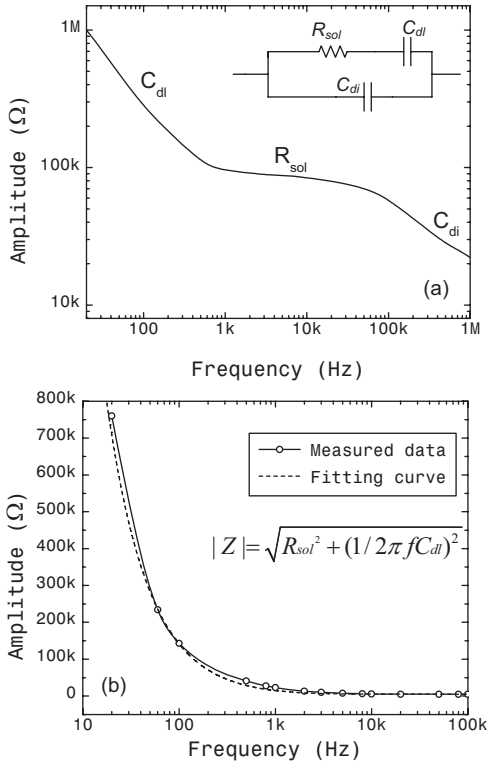

Figure 6. *Electrical modeling for the nanoIDA in the electrolyte: (a) impedance amplitude spectrum in the 10^{-3} M KCl solution and the three different impedimetric response regions which can be explained by the (inset) simplified electrical model and (b) Impedimetric response in a 10^{-2} M KCl solution in the frequency range from 20 Hz to 100 KHz. The fitting curve coming from the simplified electrical model is also given with C_{dl}= 15 nF and R_{sol}= 5 KΩ.*

One of possible applications for an integrated microchannel/EIS system is the investigation into the dielectric properties and bio-affinity interaction of proteins, which includes the protein binding to functionalized electrode surface and the antibody-antigen specific binding. These interactions create a new charged layer as a capacitance that is serial to the C_{dl}; hence decrease the C_{dl} and increasing the impedance at the low frequency range. This analysis has been verified by the preliminary test. Figure 7 gives the result of impedance change when proteins (Mouse monoclonal anti-rabbit immunoglobulin, mouse anti-rabbit IgG) are immobilized. The immobilization of proteins is based on the formation of based self-assembled monolayer (SAM) of alkanethiols group on Au electrodes surface. The sensor chip is preconditioned in a 11-Mercaptounadecanoic acid (MUA) and 3-Mercaptopropionic acid (MPA) mixing solution and activated with 1-(3-Dimethylaminopropyl)-3-ethylcarbodiimide (EDAC) and N-hydroxysuccinimide (NHS) before testing [**7**]. The sample solutions with different concentrations of mouse anti-rabbit IgG are injected into the sensing microchannel and held for 5 minutes for incubation. After completely washing out the samples, the EIS is performed in the same PBS buffer solution. As shown in Figure 7a, impedance change occurs at the low frequency range in which C_{dl} dominates as we expected. Accordingly, the relative impedance increase at

100 Hz with varying protein concentrations are recorded (Figure 7b).

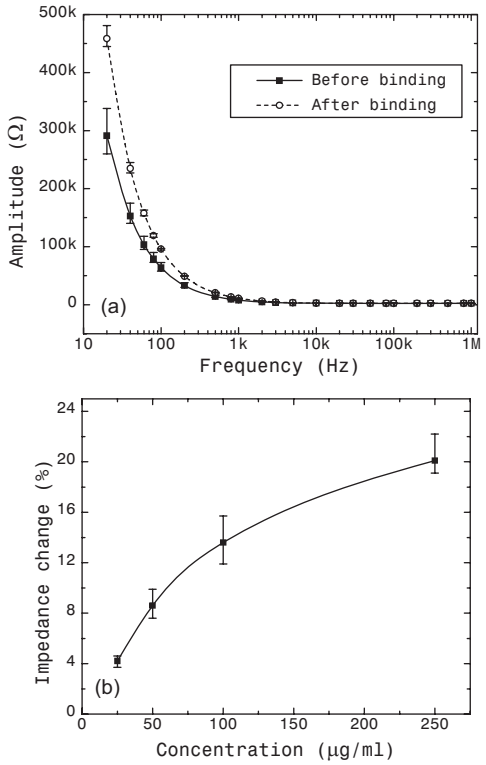

Figure 7. *(a) Impedimetric response: (a) Before and after protein binding (0.25 mg/ml mouse anti-rabbit IgG) and (b) Calibration curve of relative impedance change versus different mouse anti-rabbit IgG concentrations at 100 Hz.*

As proof of concept, this preliminary results show a potential of the device as an immunosensor with high sensitivity. Further investigation is under progress to improve the sensor's performance such as the sensitivity and specificity. Specificity of the target protein could be achieved by utilizing the antibody-antigen specific binding and Bovine serum albumin (BSA) surface pre-blocking. Moreover, COC shows the natural property to absorb protein molecule by hydrophobic force for an excellent specific binding [8]. Thus, future investigation can be employed to monitor the impedance change caused by the COC surface absorbed protein between the electrodes pair, which would greatly shorten the sensor preparation by eliminating the SAM formation step.

CONCLUSIONS

In this work, a novel nanoIDA on polymer has been nanofabricated and successfully characterized as EIS biosensors. Using KCl solution, the measured impedance spectra has shown a good matching to the theoretically predicted impedance spectra. Preliminary testing results for the EIS nano biosensor indicate that this nano biosensor has a high potential for rapid, direct, and label-free biomolecular and cellular analysis. In addition, the nanosensor can be easily integrated with disposable polymer lab-on-a-chip.

ACKNOWLEGEMENTS

The authors gratefully thank Mr. Ron Flenniken, Mr. Robert Jones, and Mr. Jeff Simkins in the Institute of Nanotechnology at the University of Cincinnati for their technical support. This work has been partially supported from NSF-P921-L856 and NIH-P021-L684. The Raith e-beam lithography system is supported from NSF Grant #0216374.

REFERENCES

[1] E. Katz and I. Willner, "Probing Biomolecular Interactions at Conductive and Semiconductive Surfaces by Impedance Spectroscopy Routes to Impedimetric Immunosensors, DNA-Sensors, and Enzyme Biosensors", *Electroanalysis,* 15, 11 (2003), pp. 913 - 947.

[2] P. Van Gerwen, W. Laureyn, W. Laureys, G. Huyberechts, M. O. D. Beeck, K. Baert, J. Suls, W. Sansen, P. Jacobs, L. Hermans, and R. Mertens, "Nanoscaled Interdigitated Electrodes Array for Biochemical Sensors", *Sensors and Actuators B,* 49 (1998), pp. 73 - 80.

[3] M. Yi, K. H. Jeong, and L. P. Lee, "Theoretical and Experimental Study towards a Nanogap Dielectric Biosensor", *Biosensor and Bioelectronics*, 20 (2005), pp. 1320 - 1326.

[4] M. W. den Otter, "Approximate Expressions for the Capacitance and Electrostatic Potential of Interdigitated Electrodes", Sensor and Actuators A, 96 (2002), pp. 140 - 144.

[5] C. H. Ahn, J. W. Choi, G. Beaucage, J. H. Nevin, J. B. Lee, A. Puntambekar, and J, Y. Lee, "Disposable *Smart* Lab on a Chip for Point-of-Care Clinical Diagnostics", *Proceedings of the IEEE*, 92 (2004), pp. 154 - 173.

[6] J. W. Choi, S. Kim, R. Trichur, H. J. Cho, A. Puntambekar, R. L. Cole, J. R. Simkins, S. Murugesan, K. S. Kim, J. B. Lee, G. Beaucage, J. H. Nevin, and C. H. Ahn, "A Plastic Micro Injection Molding Technique Using Replaceable Mold-Disks for Disposable Microfluidic Systems and Biochips", *Proceedings of the 5th International Conference on Micro Total Analysis Systems (micro-TAS 2001),* Monterey, CA, Oct. 21 - 25, (2001), pp. 411 - 412.

[7] M. Veish, Y. Zhang, K. Hinkley, and M. Zhang, "Two-Dimensional Protein Micropatterning for Sensor Applications through Chemical Selectivity Technique," *Biomedical Microdevices*, 3 (2001), pp. 45 - 51.

[8] J. Kai, Y. S. Sohn and C. H. Ahn, "Protein Microarray on Cyclic Olefin Copolymer (COC) for Disposable Protein Lab-on-a-Chip," *Proceedings of the 7th International Conference on Micro Total Analysis Systems (micro-TAS 2003)*, Squaw Valley, CA, Oct. 5-9, (2003), pp.1101-1104.

A MICROMACHINED INKING CHIP FOR SCANNING PROBE NANOLITHOGRAPHY USING LOCAL THERMAL VAPOR INKING METHOD

Shifeng Li, Kashan A Shaikh, Sandra Szegedi, Edgar Goluch and Chang Liu
Micro and Nanotechnology Laboratory, University of Illinois at Urbana and Champaign
208 North Wright Street, Urbana, IL, USA

ABSTRACT

A new method for inking scanning probes, based on local thermal evaporative inking transfer, has been demonstrated in this paper. The new method results in low loss and rapid parallel inking action. The scanning probes are accommodated at the opening of each ink reservoir. A underneath resistive heater is provided local heating to initiate vaporization of inks to uniformly coat individual probe. 1mM 16-Mercaptohexadecanoic acid (MHA) in the ethanol solution is used to characterize this inking chip. After 2 minutes heating and following 2 minutes cooling, MHA patterns are successfully written on the fresh gold-coated silicon substrate at 25 ºC room temperature and 30 % relative humidity environment. The minimum feature is less than 60 nm. Moreover, the different ink channels can be loaded different inks so this chip has multiple inking capabilities potential. Also, due to special design of ink reservoirs, each probe is completely sealed inside individual reservoir so the ink cross contamination is limited
Keywords: Scanning Probe Nanolithography, Micromachining, Surface Tension and Reservoir Array

INTRODUCTION

Scanning Probe Nanolithography (SPL) has been widely used to generate nanometer scale pattern on the various substrates **[1-3]**. The chemicals (inks) need deposit on scanning probe tips for subsequent writing onto a substrate [**4,5**]. The inking is a very critical and challenging step. Ideally, the inking procedure should be fast, highly efficient, and paralleled ink transfer onto an array of SPL probes. Existing methods of inking face severe limitations. The liquid phase dip inking is simple and popular, but it provides non-uniform, uncontrollable inking. It also suffers from high rate of evaporative ink loss from reservoirs and cross-contamination **[6]**. Inkpad based probe inking method is proposed to overcome this issue. It employs a porous membrane (e.g., PDMS) for containing/capping the inking solution. However, it takes long time (> 6 hours) for thiol molecules to diffuse through the thin membrane from ink-delivery channels **[7]**. Vapor-phase inking is uniform, reliable, and much faster than liquid phase inking. Traditionally, vapor phase inking is conducted by placing probes in a container filled with liquid chemical solutions or crystallized chemical compounds. Unfortunately, this method does not support multi-probe and multi-ink delivery **[8]**.

We report a new method for inking scanning probes, including the design, fabrication, and testing of the new chip and the validation of performance. The new method, based on local thermal evaporative inking transfer, results in low loss and rapid parallel inking action (minutes). The inks are delivered to the closely spaced ink sites that provide local, on-demand vaporization and ink transfer to the scanning probes.

DESIGN AND FABRICATION

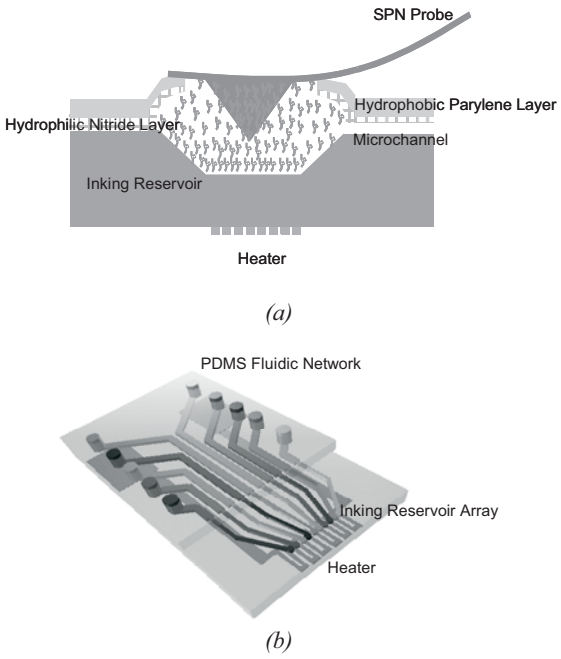

***Figure 1**. (a) Mechanism of local thermal vapor inking for SPL (b) Schematic of local thermal vapor inking based inking chip for SPL*

This novel inking chip consists of two parts: PDMS fluidic network and silicon inking reservoir array. The ink loading channels are made inside PDMS layer using softlithogrpahy. The inking channels are made of hydrophilic silicon nitride using the standard micromachining techniques. Also, in order to keep ink solution from overflowing the reservoirs, a 2-μm thick highly hydrophobic Parylene layer is deposited on the top of silicon nitride layer. Each ink reservoir is designed to accommodate each SPL probe. A thin film heater is fabricated underneath the silicon chip to locally heat up thiol molecules inside reservoirs (Fig. 1a). At first, the specific ink is delivered into the specific inking channel through PDMS fluidic network. Due to the dominant surface tension force inside hydrophilic silicon nitride microchannels, the thiol solution would be automatically pumped into individual ink reservoirs. After the probes are located on the right inking reservoirs, the temperature is locally increased by applying the current to the underneath thin film heater. When the temperature is up to the certain melting point (> 60 ^{o}C), the deposited thiol molecules inside each ink reservoir are evaporated and uniformly coated on the tip of SPL probe (Fig. 1b).

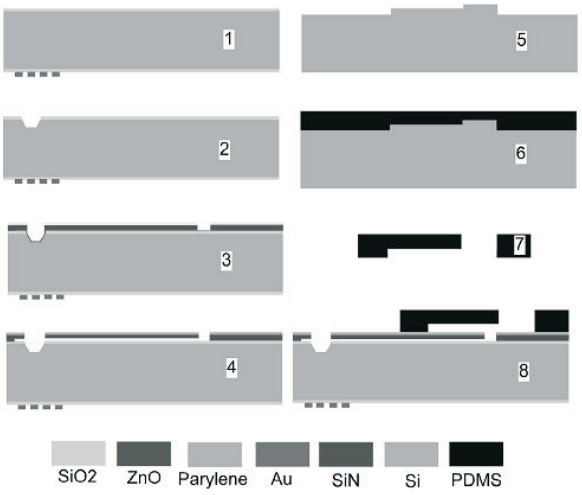

Figure 2. *Inking chip fabrication flow: (1) Au thin film heater fabrication on oxide wafer; (2) flat bottom cavity array EDP etching; (3) scarification layer ZnO deposition and patterning and function layers PECVD nitride / Parylene deposition, then RIE etching windows;(4) hydrochloride acid solution chip releasing; (5) Silicon molding surface treatment;(6) PDMS liquid polymer heat curing; (7) loading hole punching and cutting; (8) PDMS layer alignment with silicon chip*

Many advantages are associated with this novel inking chip: (1) no active pumping or vavling is required to transport ink solution and inks transport in the microchannel is mainly due to automatically surface tension force, (2) it is low loss and rapid parallel uniform inking, (3) the cross contamination of adjacent ink reservoir is limited because of the special inking reservoir design, (4) it is scalable to high density parallel inking, (5) it has multiple ink coating capability due to the fact that the different microchannels can be filled different inks.

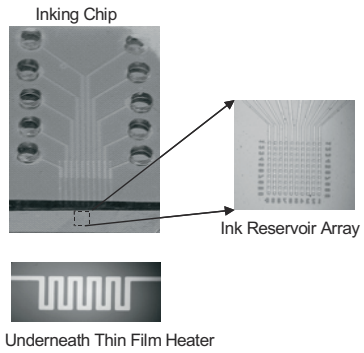

Figure 3. *The assembled thermal vapor-inking chip*

The fabrication process to realize the novel-inking chip is shown in Fig. 2. (1) First, a 2600-A thick silicon dioxide layer is thermally grown on the 2" <100>-orientation silicon wafer (International Wafer Service, Portola Valley, CA, USA). A Cr/Au thin film resistive heater is deposited on the substrate using thermal evaporation (Cr / Au = 50 A / 5000 A). (2) Using the photolithography with backside alignment, the SiO_2 layer at the front side is wet etched to open square windows to etch 5 μm depth reservoir cavities using EDP silicon etchant. (3) A 1 μm thick ZnO is sputtered on the substrate as sacrificial layer, then the ink channels are photolithographically patterned. A 2-μm thick silicon nitride layer and a 2-μm Parylene layer are deposited to cover the ink microchannels, respectively. A 1200-A thick Al thin film is deposited as etching mask for subsequent reactive ion etching to etch inking loading holes and ink reservoir windows. (4) The whole chip is released using diluted HCL solution (38 % HCl: H_2O = 2 ml: 400 ml) for 48 hours shaking on an orbit shaker. The rotation speed of the shaker is set as 60 RPM. (5) The silicon mold is etched using deep reactive ion etching. The depth of mold pattern is 60 μm. (6) Before the molding, the silicon mold was deposited a thin carbon layer to enhance PDMS layer releasing, then PDMS prepolymer (10:1 mixing ratio with curing agent, Dow Corning Sylgard 184, Midland, MI, USA) is poured on the silicon mold. (7) After 30 minutes curing at 90 ^{o}C, PDMS layer is peel off and punch the access holes using a sharpened needle. The blade cuts the PDMS layer into final dimensions: 30 mm wide and 40 mm long. (8) Finally, the PDMS layer is aligned and assembled with silicon chip. Fig.3 is an optical picture of the final assembled inking chip.

TEST RESULTS

Thiol chemical MHA is used to characterize this inking chip. At first, 1mM ethanolic MHA is filled into PDMS channels. Once the ink solution reaches the loading holes at the beginning of the silicon nitride microchannels. Due to dominant surface tension force inside hydrophilic silicon nitride microchannels, the ink solution is automatically pumped to individual ink reservoir. Finally, due to quickly evaporation nature of ethanol, MHA ink is deposited inside ink reservoirs (Fig. 4). The measured resistance of the thin film heater is around 150 Ω. After applied 20 DC voltages using a power supply (E3612A, Agilent, CA, USA), we found the local temperature at the ink reservoirs quickly reached MHA melting point (64 ^{o}C) within 2 minutes. The inking chip subsequently cooled down for another 2 minutes to make sure uniform coating on the scanning probe tips (Fig. 5). After 2 minutes heating and following 2 minutes cooling, the inked probe (type A, NanoInk Inc. Chicago, USA) is loaded on Nscriptor (Nanoink Inc, Chicago, USA). MHA patterns are successfully written on the fresh gold-coated silicon substrate (Au / Cr = 30 nm / 5 nm) at 25 ºC room temperature and 30 % relative humidity environment (Fig. 6a and 6b). The minimum feature is less than 60 nm. In order to prove that the ink transfer is mainly due to the thermal evaporation, the tip of the scanning probe was sealed inside the ink reservoir and the thin film heater did not turn on. After 15 mins inking, the probe was loaded on Nscriptor to write the pattern on the fresh gold-coated substrate under the same working temperature and humidity. It was found the same patterns written on the substrate at the least 10 times slower even after 15 minutes inking.

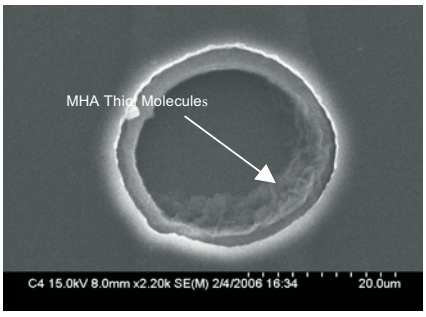

Figure 4. *The chemical thiol was deposited inside individual ink reservoir*

The ink reservoir is specially designed as Fig. 1(a) and the tip of each SPL probe was sealed inside individual reservoir, so the ink cross contamination is expected to be limited. A cross-contamination test was performed by filled the ink solution in the specific ink channel as shown in Fig. 3 and leave the adjoined ink channels were empty. After using the aforementioned method to finish inking, we perform writing on fresh gold substrates. But only the probe, which is inked from the filled channel, can write the patterns on the substrate. For other probes, no MHA patterns were detected. We can conclude that no appreciable cross contamination occurs during the local thermal vapor inking.

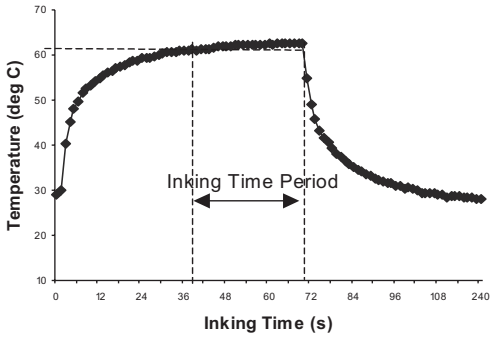

Figure 5*. Transient temperature measurement during local thermal vapor inking using IR microscope*

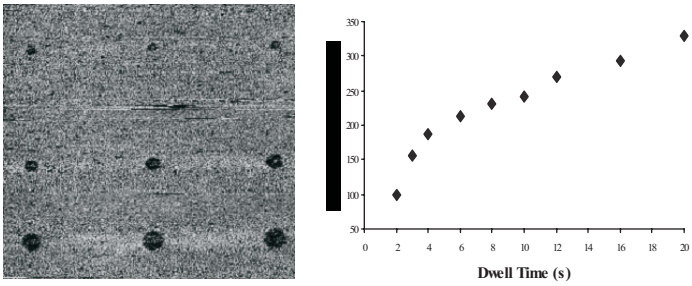

(a)

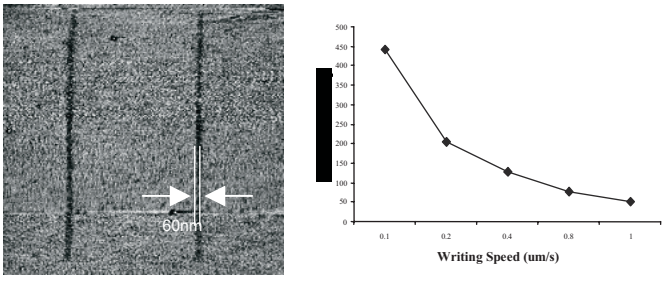

(b)

Figure 6. *Characterization of local thermal vapor inking chip (a) dots array writing (3.58 μm by 3.58 μm scanning size) and (b) lines writing (3.3 μm by 3.3 μm scanning size) at 25 ºC and relative humidity 30 %*

CONLUSION

In this paper, we report a novel method to ink scanning probes for nanolithgraphy based on local thermal vapor ink transfer method. This method can finish low loss and parallel inking scanning probes within several minutes. At the same time, the special design ink reservoir can accommodate probe tip into individual reservoir to limit the possible ink contamination. Moreover, the different ink channels can be loaded different inks so this chip has multiple inking capabilities.

ACKNOWLEDGEMENT

The authors thank DARPA Advanced Lithography program and NSF Center for Nanoscale Science and Engineering (Northwestern University) for support.

REFERENCES

[1] L. Demers, D. Ginger, S. Park, S. Chung and C. Mirkin, “Direct Patterning of Modified Oligonucleotides on Metals and Insulators by Dip-Pen Nanolithography”, *Science*, Vol. 296, pp. 1836-1838 (2002)

[2] K. Lee, J. Lim and C. Mirkin, “Protein, Nanosturctures Formed Via Direct-Write Dip-Pen Nanolithography” *Am. Chem. Soc*, Vol.125, pp.5588-5589, 2003

[3] H. Zhang, Z. Li and C. Mirkin, ”Dip-Pen Nanolithography-Based Methodology for Preparing Arrays of Nanosturctures Functionalized with Oligonucleotides” *Adv. Mater.* Vol. 16, pp.1480-1484, 2002

[4] J. Jang, S. Hong, G. Schatz and M. Ratner, “Self-assembly of Ink Molecules in Dip-Pen Nanolithography: A Diffusion Model”, *Journal of Chemical Physics*, Vol. 115, pp. 2721-2729, 2001

[5] B.L. Weeks, A. Noy, A. E. Miller and J. J. DeYoeo, *Physical Review Letters*, Vol. 88, pp. 255505-1 to 255505-4 (2002)

[6] D. Banerjee, ”Next Generation Microfluidic Ink Delivery Systems for Dip-Pen Nanolithography Application in Biotechnology” *ASME Biomedicine Miniaturization*, Irvine, CA, 2005

[7] K. Ryu, X. Wang, K. Shaikh, D. Bullen and E. Goluch, “Integrated Microfluidic Inking Chip for Scanning Probe Nanolithography” *Applied Physics Letter*, Vol. 85 pp. 136-138, 2004

[8] X. Wang, PhD Dissertation, “Microelectromechanical and Microfluidic Systems for Scanning Probe Lithography”, *University of Illinois at Urbana and Champaign*, 2005

A PNEUMATICALLY-ACTUATED MICROVALVE FOR SPATIALLY-SELECTIVE CHEMICAL DELIVERY

Kyusuk Baek, Yang Li, Mayurachat Gulari, and Kensall D. Wise

Engineering Research Center for Wireless Integrated MicroSystems
The University of Michigan, Ann Arbor, MI 48109-2122

ABSTRACT

This paper reports a drug-delivery probe (Figure 1) with on-chip normally-open microvalves that are used in blocking mode, preventing flow to non-selected orifices and allowing drugs to be injected into spatially-localized areas of the brain to modify cellular activity. The present valves are driven pneumatically to allow detailed studies of valve operation, but will be used with on-chip thermo-pneumatic actuators that operate from low voltage, produce negligible tissue heating, and have several microns of throw while holding off drive pressures as high as 50kPa. For a valve having a diaphragm radius of 200μm, the fully-open pressure drop at a flow rate of 513pL/sec is only 7.4kPa. For diaphragm radii of 180, 200, and 220μm, leak rates of 32, 21, and 15pL/sec, respectively, are measured at an actuation pressure of 35kPa.

INTRODUCTION

Silicon microelectrode arrays have become widely used in neurophysiological research over the past decade. Micro-electrode arrays capable of stimulating or recording from the nervous system are one of the principal tools used today for studying the central nervous system at the cellular level. They are also the basis for a number of neuroprosthetic devices being developed to address neurological disorders such deafness, blindness, epilepsy, paralysis and Parkinson's disease. To understand the cell function in an electrochemical system, there is growing interest in combining multi-site stimulating/ recording probes with the ability to deliver drugs to the nervous system with high spatial specificity, both for basic research in neuropharmacology and for possible use in neuro-prosthetics [1, 2]. For such probes, used for multi-site, multi-chemical injection, there must be a way to select the desired chemical and route it to the proper site in order to minimize the fluidic lead count. In this way, if two chemicals are to be used, there only three lines are needed for the implant: the first chemical, the second chemical, and perhaps a saline flushing solution. By being able to direct the fluid flow, any of the chemicals can be routed down any number of channels to the respective site. Without these capabilities, only the chemical in a particular line can be injected down that line to a single associated site. A separate line would be needed for each individual site, making multi-delivery site devices excessively tethered by external tubing coming off the back end. The solution to this situation requires on-chip multiplexers (Figure 2), which are an integral part of every chemical delivery system in the macro world.

REQUIREMENTS FOR MICROVALVES

The integrated microvalves on a neural probe must be compatible with probe fabrication technology [1] without adding excessive complexity. They should also be robust and compatible with chronic use in-vivo. Due to the difficulty of replacing a chronic device, any such device needs long-term reliability (>5 years) and packaging that is able to withstand the extracellular environment. The valves reported here will be used with the on-chip thermo-pneumatic actuators in Figure 3. For thermo-pneumatic actuation, the use of high voltages within any living organism difficult due to the risk of electrical leakage and shock. In order to avoid damaging the neural system, a low actuation voltage (<10V) is required. Any temperature rise in the tissue must be no more than 2°C to avoid neural damage. Moreover, the entire delivery system must be kept small enough to avoid excessive tissue displacement and disruption of the cellular system.

Figure 1. *A drug delivery probe with integrated microvalves*

Pressure ejection is the method used on the Michigan drug delivery probe. In operation, nitrogen pressure is applied at the back end of polyimide tubing, and the fluid in the channel moves in the direction of the pressure gradient. The flow rate is determined by the liquid properties, the applied pressure, and the channel cross-sectional area. A typical cortical neuron can be recorded electrically over a distance of roughly 50-100μm. In order to effectively alter the neuronal environment, the minimum amount of injected chemical can arbitrarily be taken at about 10% of a 100μm-diameter sphere, which is equivalent to about 50pL. This amount of chemical is generally injected into the tissue in 100mSec, resulting in a typical flow rate of 500pL/Sec, or 30nL/min. Drugs have previously been delivered to tissue using a 1-2Psi pressure pulse having a duration of 100msec [2]. Recently, it has been observed that fast chemical injection can mechanically damage or even kill cells, so the trend is to deliver drugs over longer pulse-durations (5nl for 10Sec) or to deliver smaller volumes of liquid with higher drug concentrations [3]. The minimum acceptable leak rate varies greatly among target

diseases. A negligible amount of injected chemical can arbitrarily

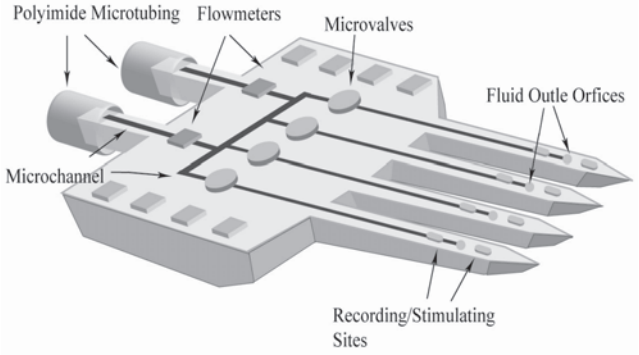

Figure 2. *The probe with multi-shanks and microvalves*

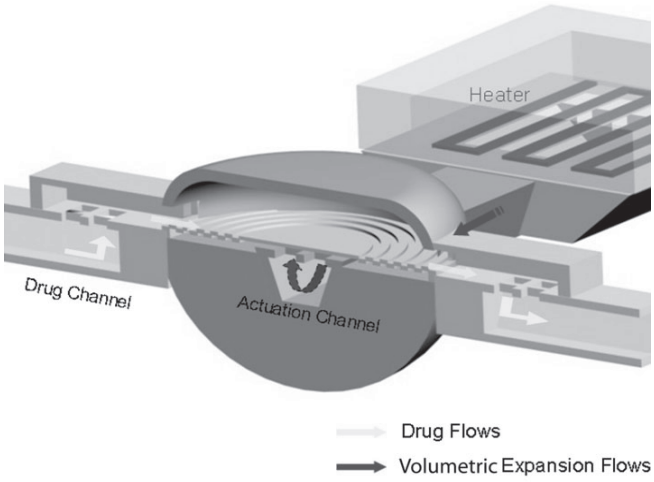

Figure 3. *A diagram of the thermopneumatic microvalve*

be taken at about 0.5% of a 100µm-diameter sphere, which is equivalent to about 2.5pL. For example, for a 100mSec pulse duration, the leak rate should be less than 25pL/Sec.

FABRICATION

Fabrication should be compatible with a standard buried-channel probe process that allows electrical recording and stimulation as well as integrated flowmeters [4] on the same structure. The basic microvalve structure used is shown in Figure 3 and is realized using a 13-mask process. Fabrication of the microvalve takes only two masks in addition to the normal probe with microchannels [5]. The process begins with blank (100) silicon wafers. The first step is to define the probe shape using a patterned a 1.2µm-thick silicon dioxide layer grown over the entire wafer in about 3 hours at a temperature of 1100^{o}C. The second step forms the buried channels. Screen masking structures with 2µm openings are patterned along the <110> direction in the silicon. 4µm openings are used for the output port of the actuation channel, which delivers driving pressure to the corrugated diaphragm. 4µm-deep trenches for the channels and corrugations of the valve diaphragm are etched with a deep reactive ion etcher (DRIE), which selectively etches silicon anisotropically by creating a chemically-reactive RF plasma and a DC bias. This etching process needs to penetrate through the shallow boron layer and into the lightly-doped silicon beneath. Once formed, the trenches are connected by undercutting the undoped silicon between the trenches to form channels using 50 minutes in ethylenediamene pyrocatchol (EDP) at 110 ^{o}C (Figure 4 a,b). An unsealed 20~25µm-deep channel is formed with shallow boron ribs on the ceiling spaced by the trench areas. Then, low-pressure chemical vapor deposited (LPCVD) 1.2µm thick-SiO_2/Si_3N_4/SiO_2, which normally isolates the electrodes from the substrate, also seals the channel by filling in the trench gaps (Figure 4c). Wider openings not fully sealed by stacked dielectrics still have enough space to deliver actuation pressure. Following the formation of the microchannels in the probe substrate, the space between the substrate and the valve diaphragm is formed using a 3µm-thick CVD sacrificial polysilicon layer. Stress-compensated 1µm-thick silicon oxide/silicon nitride/silicon oxide dielectrics are then deposited to form the corrugated diaphragm itself (Figure 4d). Etch access holes are formed around the perimeter of the diaphragm to allow removal of this first sacrificial polysilicon layer. The sacrificial layer is removed using a 3-hour tetramethyl ammonium hydroxide (TMAH) etch (Figure 5). After diaphragm release, the etch holes are filled by depositing additional silicon nitride/silicon dioxide dielectric. A 3µm-thick sacrificial

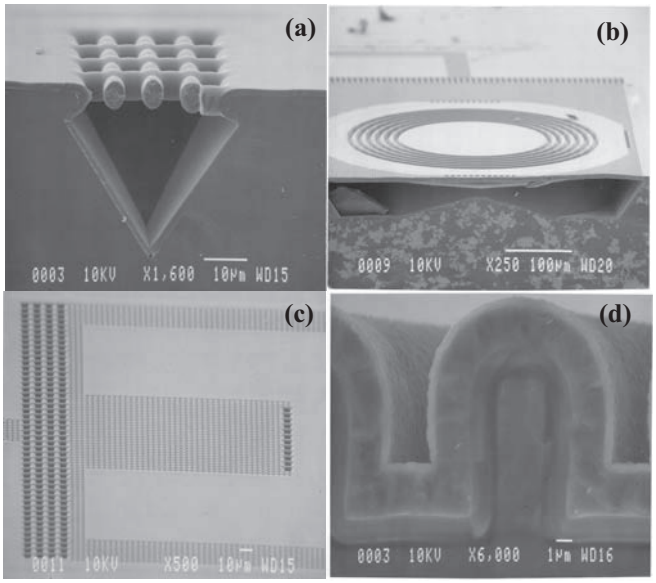

Figure 4. *(a) Drug-delivery microchannel after EDP etching, (b) Actuation channels after EDP (c) Top view of actuation channel after filling in trench gaps through stacked dielectrics (d) Cross-section view of corrugation diaphragm after covering CVD polysilicon by stacked dielectrics*

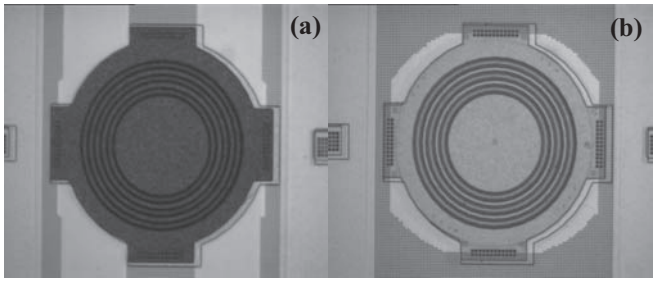

Figure 5*. (a) Dark circular shape in diaphragm area is the CVD sacrificial polysilicon. (b) After diaphragm release, fully etched out cavity is shown through the transparent diaphragm made of silicon dioxide/ silicon nitride/ silicon dioxide. The cavity is connected to actuation channel through wider openings*

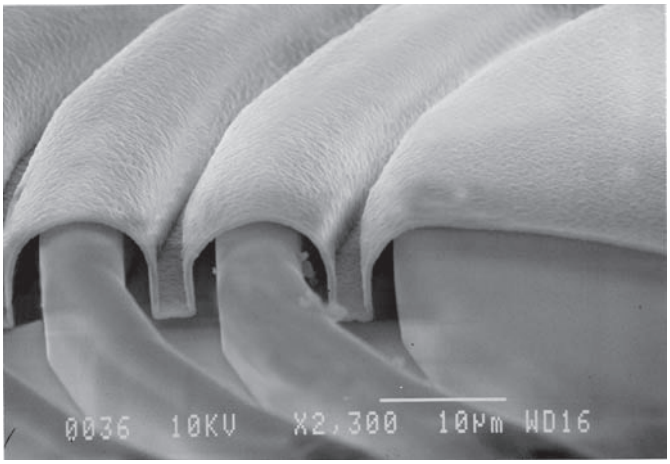

Figure 6. *A corrugated diaphragm after the second polysilicon sacrificial layer is removed.*

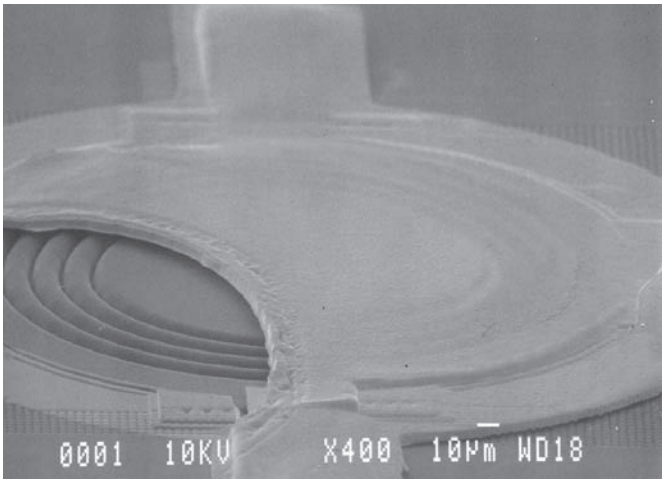

Figure 7. *A pneumatically-driven microvalve with corrugated diaphragm after release in EDP.*

polysilicon layer is now deposited to form the flow path through the valve and is beveled along 20µm of its outer edge to improve the ability of the diaphragm to seal to the valve cap. The second etch access holes are patterned to allow removal of this second sacrificial polysilicon layer (Figure 6). After the second sacrificial layer is etched by a 4 hour TMAH, a 7µm-thick stress-balanced silicon dioxide/ silicon nitride/ silicon dioxide stack is now deposited and patterned to form the cap. (Figure 7) The thick cap is to maximize the deflection of diaphragm.

RESULTS

To confirm that the fabricated microvalve is suitable for a chronic drug-delivery device, it is necessary to measure the flow hydraulic resistance across system and the leak rate at certain pressure range. To measure the hydraulic flow resistance and leak rate across the drug-delivery system, the flow testing tools were set up as shown in Figure 8. The flow is driven using a volume flow controlled syringe pump (WPI UltraMicroPump) and a micro syringe (Hamilton 0.5µL). Pressure is measured with a differential pressure transducer (Omega P26). The fluid is filtered through a 0.2µm in-line filter (Corning, Inc.) to remove trace particulates. Complete saturation of the flow system is ensured by using the procedure [3]: the testing device (Figure 9) is first back-filled with fluid using a vacuum pump system; then a flexible polyimide tube

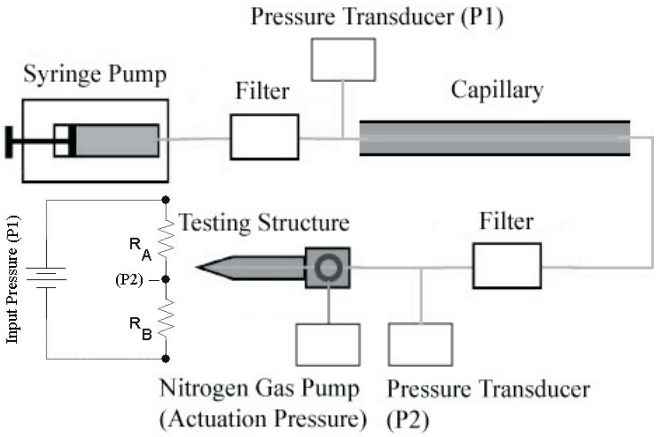

Figure 8. *Schematic diagram of the flow testing tools illustrating pneumatic microvalve characterization. A small diagram shows a pressure-equivalent circuit. R_A is a hydraulic flow resistance of a capillary and R_B is a hydraulic flow resistance of a drug-delivery probe.*

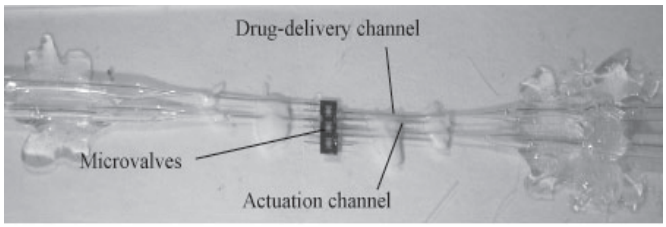

Figure 9. *A picture of testing device. Each device has three pneumatic microvalves. Each microvalve has two actuation channels and one drug-delivery channel.*

(WPI MicroFil) is inserted into the glass capillary; and finally a syringe assembly provides the required flow through the device. The seal between the syringe and the glass capillary of the device assembly is maintained with biocompatible epoxy.

PRESSURE DROP MEASUREMENTS

The pressure difference across the microvalve and its series microchannel has been analyzed to understand the drug delivery rate as a function of drive pressure. A pneumatic microvalve is composed of two channels. One is for drug-delivery and the other is for actuation (Figure 9). A first experiment was performed to measure the pressure variation (P2) across the system for water for different input pressures (P1) as shown in Figure 8. No pressure is applied to the actuation channel to make the valve open. A 30µm-ID, 10cm-long capillary (Polymicro Inc.) with a hydraulic resistance of $5x10^{15}$ Pa•s•m^{-3} and a diaphragm radius of 200µm was used. As shown in Figure 10 and 11, the total hydraulic resistance of the entire testing system was around $19.5x10^{15}$ Pa•s•m^{-3} at an input pressure of 10kPa, which shows that the hydraulic resistance of the open-microvalve is $14.5x10^{15}$ Pa•s•m^{-3}. At a flow rate of 513pL/sec (Figure 11), the pressure drop across the system is 7438.5Pa, which is slightly lower than the simulated result of 8410Pa using FLUENT. The difference results from the fact that the size of a fabricated microvalve is larger than that of the simulated one. As the input pressure (P1) increases, the cross-sectional area of liquid-path in microvalve increases due to the liquid pressure to a flexible diaphragm for a microvalve and consequently the hydraulic flow resistance decreases. It results in

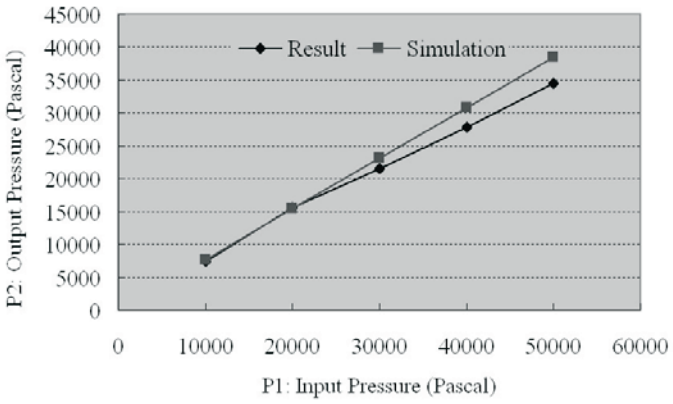

Figure 10. *A pressure variation across the testing device as a function of input pressure (P1)*

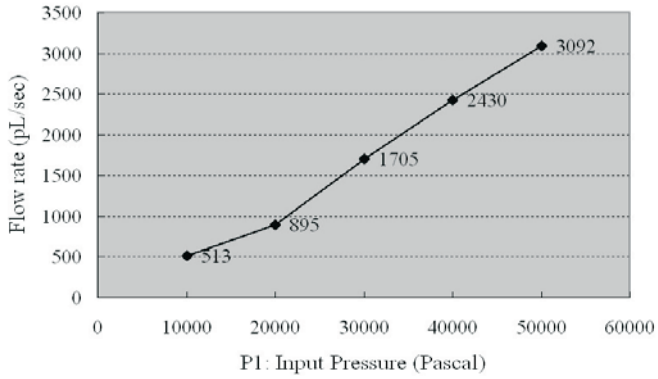

Figure 11. *An open-flow rate variation as a function of input pressure (P1)*

the nonlinearity of the flow rate (Figure 11) as the input pressure (P1) increases.

LEAK RATE MEASUREMENT

The pressure difference across the microvalve has been measured (Figure 12) to understand the leak rate (Figure 13) as a function of drive actuation pressure at the fixed input pressure of 10kPa. A 10cm-long capillary with an inner diameter of 15µm (Polymicro Inc.) and a hydraulic resistance of $80x10^{15}$ Pa•s•m^{-3} was used with diaphragm radii of 180, 200, and 220µm. The corresponding measured leak rates are 32, 21, and 15pL/sec, respectively, at an actuation pressure of 35kPa (Figure 13). These experiments show that the closed leak rate for a diaphragm radius of 200µm at 10kPa input pressure (P1) is 21pL/Sec and the open flow rate is 513pL/Sec at the same pressure.

CONCLUSIONS

The pneumatically-actuated on-chip microvalve is completely compatible with the existing process for recording and stimulating probes and with the use of on-chip circuitry. It requires only two masks in addition to those for the standard probe process. As discussed earlier, the minimum effective flow rate of injected chemical is estimated at 500pL/Sec and the amount of injected chemical that can be considered negligible can be taken at about 0.5% of a 100µm- diameter sphere, corresponding to 25pL/Sec for a 100mSec pulse-duration. Therefore, this valve structure fulfills

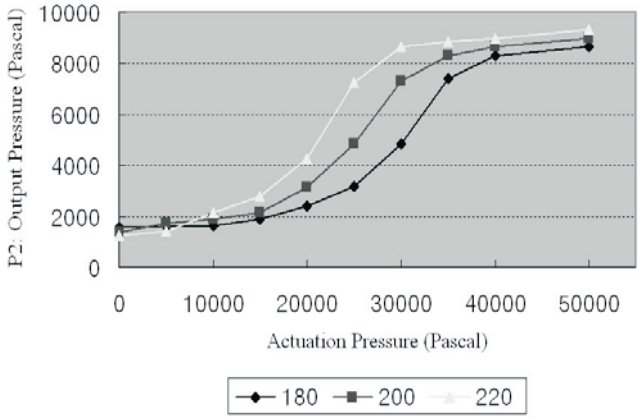

Figure 12. *The pressure (P2) variation across the testing device as a function of actuation pressure at an input pressure (P1) of 10kPa.*

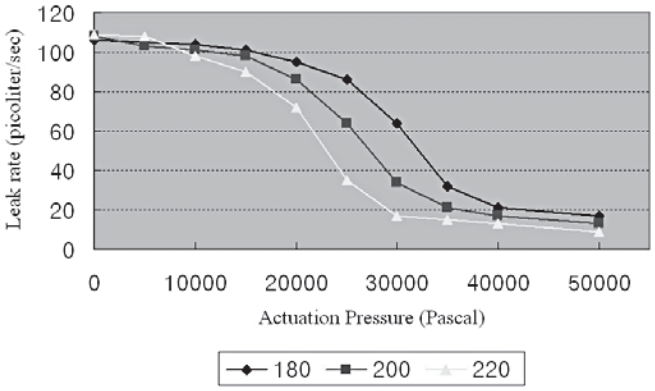

Figure 13. *The leak rate measured as a function of actuation pressure at an input pressure (P1) of 10kPa.*

the requirements of leak rate (<25pL/Sec) and minimum open flow rate (>500pL/Sec) at 10kPa input pressure (P1).

REFERENCES

[1] K. D. Wise, D. J. Anderson, J. F. Hetke, D. R. Kipke, and K. Najafi, "Wireless Implantable Microsystems: Electronic Interfaces to the Nervous System," (Invited), *Proc. IEEE*, pp. 76-97, January 2003.

[2] J. Chen, K. D. Wise, J. F. Hetke, and S. C. Bledsoe, Jr.," A Multichannel Neural Probe for Selective Chemical Delivery at the Cellular Level," *IEEE Trans. Biomed. Engr.*, 44, pp. 760-769, August 1997.

[3] R. Rathanasingham, D. R. Kipke, S. C. Bledsoe, and J. D. McLaren, "Characterization of Implantable Microfabricated Fluid Delivery Devices," *IEEE Trans. Biomed. Engr.*, v 51, n 1, pp.138-145, January 2004.

[4] Y. Li, K. Baek, M. Gulari, K. D. Wise, "An In-Line Thermal Flowmeter with Vacuum-Based Thermal Isolation Chamber for In-Vivo Drug Delivery", *IEEE Sensors 05*, Los Angeles, November 2005.

[5] K. Baek, Y. Li, M. N. Gulari and K. D. Wise, "A Chronic Drug-Delivery Probe With Integrated Pneumatic Microvalves", *7th Int. Conf. on Miniaturized Chemical and BioChemical Analysis Systems (µTAS'05),* Boston, October 2005.

CHARACTERIZATION AND DESIGN OF DIGITIZING PROCESSES FOR UNIFORM AND CONTROLLABLE DROPLET VOLUME IN EWOD DIGITAL MICROFLUIDICS

Jian Gong and Chang-Jin "CJ" Kim
Mechanical and Aerospace Engineering Department, University of California, Los Angeles (UCLA)
Los Angeles, CA, USA

ABSTRACT

We report characterization and precise control of droplet volume for digital microfluidics under electrowetting-on-dielectric (EWOD) actuation both in air and oil environments. By using multi-layer printed circuit board (PCB) as an EWOD chip and custom-making an automatic control board, the restrictions on the electrode pattern design and driving signal are eliminated, empowering us to run various electrode sequences and electric signals. Reading droplet volumes optically or electrically, we characterize and optimize the droplet creation and cutting processes. The results lead to more uniform and repeatable droplet volume, which is essential for a precision instrumentation application. The tunable droplet volume is also available by changing the digitizing parameters.

INTRODUCTION

Digital microfluidics fulfill fluidic operations by manipulating droplets through various mechanisms such as thermal, chemical, surface wave, dielectrophoresis (DEP), or electrowetting-on-dielectric (EWOD), the last currently being the most prominent. In digital microfluidics, droplet volume uniformity and accuracy (digital unit) are two essential factors for many applications such as drug discovery or quantitative analysis. Although the digitizing processes (e.g., creating droplets from bulk liquid) are already included in the device design, the results are further affected by the liquid dynamics. Externally controlled pumps and valves are usually used for droplet dispersion in micro-channel or parallel-plate configuration [1][2], which requires extra setup and compromises the simplicity digital microfluidics can bring about for the final systems.

Using EWOD [3], which allows for local modulation of surface wettablity through embedded electrodes, the process of droplet creation, moving, mixing and cutting has been studied in [4]. The droplet creation integrated into the microfluidic chip free of external setup has significantly simplified the system development and device package [5]. The next question is how accurate and precise the volume of such droplets can be. Since the droplet digitization on EWOD chip is affected by details of operation procedures and parameters as well as electrode sizes and shapes, a systematic study has been difficult. Helped by the recent development of a multi-layer EWOD chip and a custom-built electrical control board, which make parametric studies practical, we report the first results of such a study.

EWOD CHIP AND EXPERIMENT SETUP

Recently we have developed a new EWOD chip fabrication technology by taking advantage of the multi-layer printed circuit board (PCB) that allows direct and independent electrical access to each electrode [6], as shown in Fig. 1. This multilayer electrical connection eliminates the limitation on electrode pattern design and the side connection wires which disturb the droplet digitizing process in the single electrode layer EWOD chip [5].

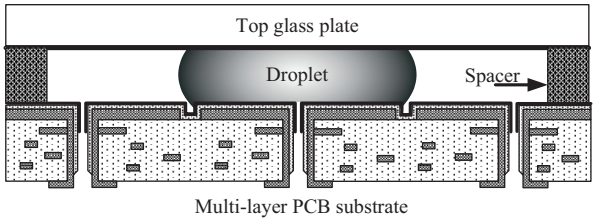

Figure 1. *Direct-referencing EWOD chip fabricated with four-layer printed circuit board (PCB) technology [6].*

In Fig. 1, the EWOD chip is made of a PCB substrate and a glass plate. A 4-layer PCB is lapped, polished, and then 8000Å Parylene C is deposited as dielectric layer and 2000Å Teflon® as hydrophobic coating. The top glass is coated with 2000Å transparent ITO as a ground electrode and 2000Å Teflon® as hydrophobic coating. Droplets are then sandwiched between the PCB and the glass by spacers. The device is either exposed to air or filled with oil. In this paper, the EWOD chip has 1.5 mm x1.5 mm electrode pads and a 100 μm-thick spacer between the parallel plates.

Our experiments are performed using the setup shown in Fig. 2, which measures the droplet volume on chip and controls the EWOD driving voltages by high voltage relay array. Different droplet digitizing processes are tested, and the optical images and electrical signals of the droplet footprint are recorded.

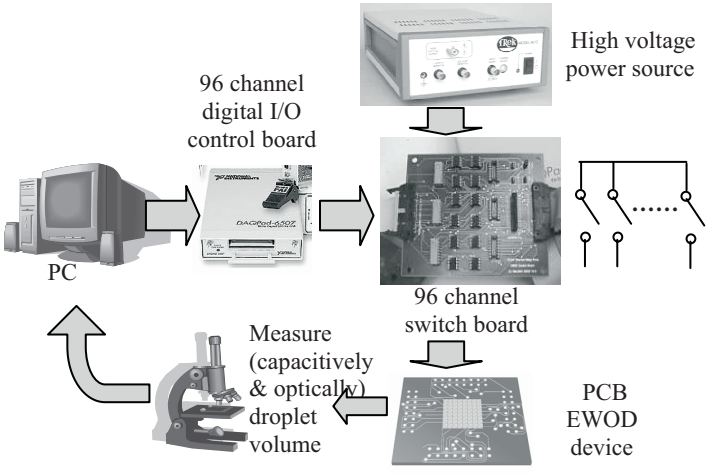

Figure 2. *Experiment setup to measure the droplet volume on chip and control the driving signals.*

To provide designed electrical signal sequences to the EWOD device, we have custom-built a dedicated automatic electrical control board. In this control board, one 96-channel relay switch

board is controlled by a National Instruments (NI) DAQPAD-6507 96-channel digital I/O control board. We also developed control program in the upstream PC, which can design, store and send the high voltage switch sequence to the I/O board through a USB port. The resulting control board can switch the high voltage up to 500 V and simultaneously control the 96 channels as fast as 1 ms.

The droplet volume is calculated by multiplying the measured droplet footprint area with the spacer size. Since the electrodes are much larger than the spacer in the current EWOD chip (15:1) and liquid contact angle is typically near 90°, the error is expected to be less than 1%. We measure the droplet footprint by two different methods. One is by capturing droplet optical images and having their areas read and calculated by Scion Image®. We also determine the footprint electrically by measuring the capacitance between the electrodes on the top and bottom plates [5]. Because the droplets are quite flat, i.e., the contribution of the fringe-field is relatively small, a linear relationship is expected between the capacitance and the footprint area. Fig. 3 shows the measured capacitance vs. the optically-measured droplet size. A linear relationship is confirmed, and the calibration between the capacitance and droplet volume can be obtained.

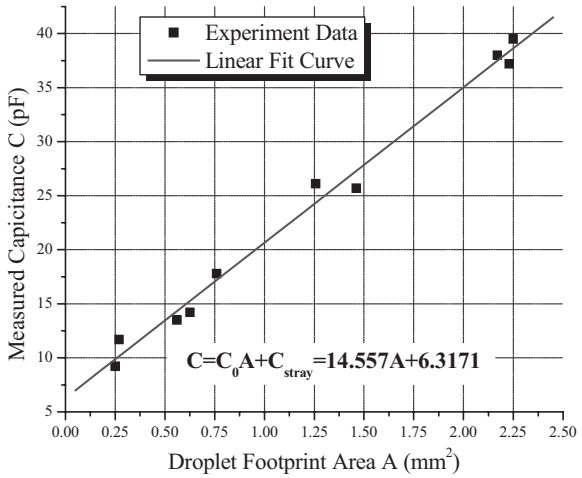

Figure 3. *Capacitance measurement vs. droplet footprint area.*

EXPERIMENTAL RESULTS

For droplet creation, the typical method and electrode pattern are shown in Fig. 4 as Creation Procedure I. In this configuration, we design one big electrode (9 x bigger than normal size) as the liquid reservoir and two normal size electrodes for pulling and creation sites. To create one droplet from the reservoir, the liquid is first pulled out by the pulling electrode. A droplet is created by activating both the reservoir and creation electrodes but not the pulling electrode. For each step, the turned-on electrodes are activated with $80V_{AC@1kHz}$ for 500ms. Using this method, we can create droplets until the reservoir has less than one droplet volume left. The reservoir is initially filled 70-80% to ensure enough space for the liquid to be pulled back during the first creation. Overall, 5-6 droplets can be generated without replenishing during one creation cycle. The results of Creation Procedure I are summarized in Fig. 5, which shows 25 creations over 5 cycles with overall volume variation of ±5%. It is worth noting that the variation was several times worse when the creation procedure was operated manually. The electronic operation was possible only after the custom-built control board became available. Fig. 5 also shows that the volume of generated droplets increases as the liquid left in the reservoir decreases. This is most probably due to the dynamic droplet necking involving competition between two liquid movements at the same time. Because the remaining liquid volume in the reservoir becomes smaller and the resulting pulling back force from the reservoir decreases, more liquid would drift into the creation electrode, generating a bigger droplet.

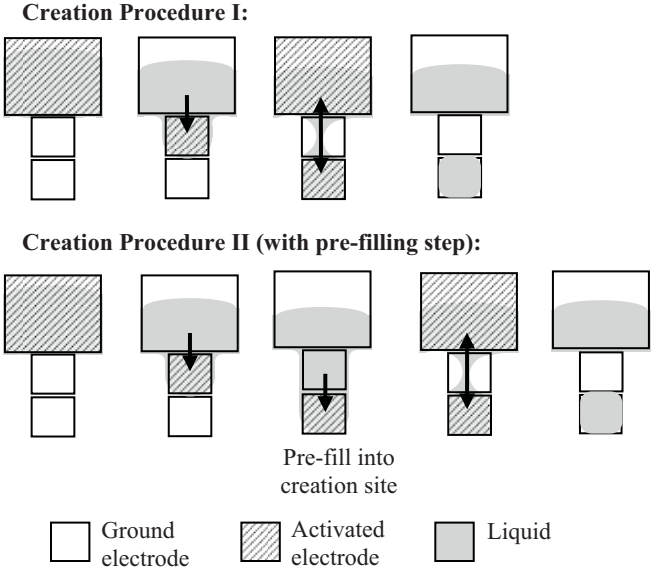

Figure 4. *Two different types of droplet creation procedures. Arrows show the droplet movement direction.*

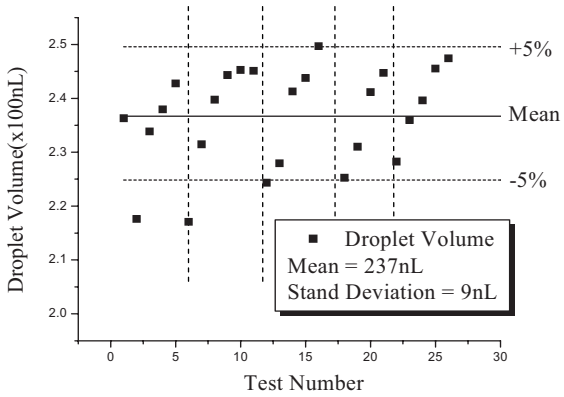

Figure 5. *Droplet volume distribution for Creation Procedure I at $80V_{AC@1kHz}$. Dotted vertical lines separate different creation cycles. Droplet volume increases within a cycle as creation repeats.*

To reduce the dynamic competition between the two movements, we designed the Creation Procedure-II shown in Fig. 4, which adds an extra step of pre-filling the creation electrode. Since the creation electrode is pre-filled, during droplet necking, there's just one main liquid movement – pulling back by the reservoir. The liquid already in the creation electrode is held there and its volume is maintained during the droplet necking. Then the droplet volume in the creation site is well defined, and the dynamic effect is minimized. The droplet volume is only determined by where the neck would break. As shown in Figs. 6 and 7(a), the droplet volume distribution by Creation Procedure II is more uniform (±2%) than that by Creation Procedure I (±5%) and not affected by the volume of liquid remaining in the reservoir. Creation Procedure II was also tested in silicone oil (5cs, Clearco® product), which is another common environmental fluid for EWOD digital microfluidics. Water droplets immersed in oil have much smaller contact angle hysteresis than those in air. Smaller

hysteresis means the contact lines move with less resistance and so do the droplets. The small resistance makes the EWOD actuation easier, allowing for lower driving voltage, although it in turn reduces the stability of droplets (e.g., against gravity and disturbances). The use of oil also raises such concerns as oil contamination and packaging but helps preventing evaporation of water droplets. Requiring only 30V in oil (vs. 80V for in-air operation), Creation Procedure II produced droplets with increased volume, as shown in Fig. 7(b).

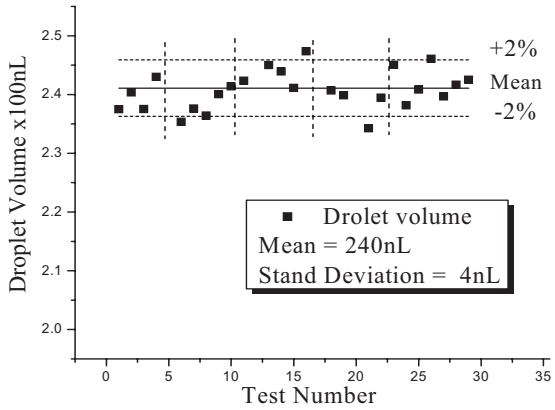

Figure 6. *Droplet volume distribution during Creation Procedure II with 80$V_{AC@1kHz}$. Dotted vertical lines separate different creation cycles (24 creations over 5 cycles). There is no apparent trend of droplet volume changes within one cycle.*

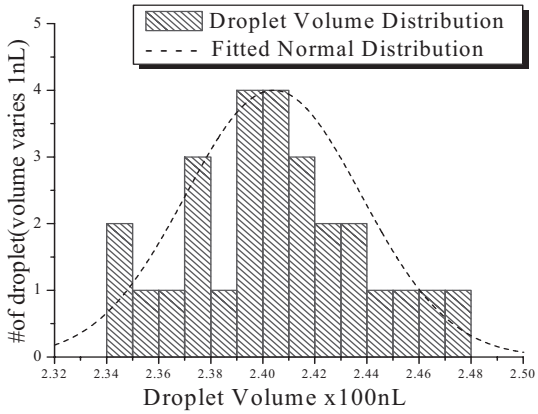

(a) In air. Creation voltage of 80 $V_{AC@1kHz}$ was used.

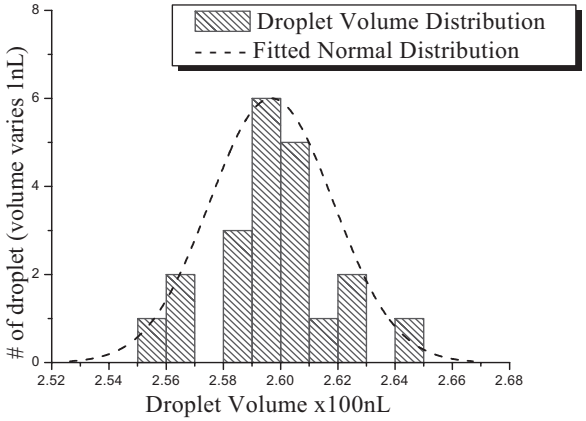

(b) In oil. Creation voltage of 30 $V_{AC@1kHz}$ was used.

Figure 7. *Volume distribution of droplets made by Creation Procedure II on EWOD PCB device in air and oil.*

The ability to tune the droplet volume is also desirable for a more powerful system. As noticed in the experiments, droplet volume changes with various signal parameters such as driving voltage and signal duration. Using Creation Procedure II, we conducted a series of experiments by varying the voltage applied to creation site. As shown in Fig. 8, we can control the droplet volume from 225 nL to 245 nL (10%) by changing the creation voltage from 70 V to 95 V with ±2% accuracy at every voltage level.

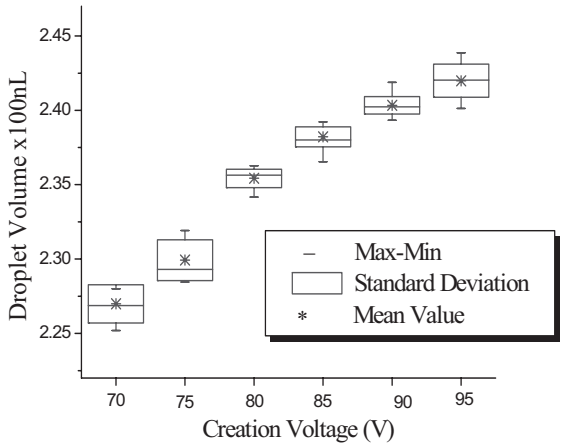

Figure 8. *Volume of droplets made by Creation Procedure II for varying voltages (1 kHz RMS value).*

Dividing a big droplet into two of exactly the same size is more difficult since any asymmetric condition before or during the cutting would lead to an uneven division. As shown in Fig. 9(a) as an example, when a big droplet moves from right to left, its tail would cover more adjacent electrode than its head. If we apply voltage to the two adjacent electrodes on the path of droplet movement to divide the droplet, more liquid would stay in the tail side during the droplet necking, causing the new droplet on the tail side to be bigger than the one on the head side. We may apply a short pulse voltage to the head side electrode to pull the droplet toward the middle, but consistent results are not expected without automatic feedback control. Realizing that the symmetry is maintained perpendicular to the direction of droplet moving, a solution is to cut the droplet perpendicularly, as shown in Fig. 9(b). As shown in Fig. 10, size distribution of the cut droplets is also uniform (±2%), and the average cutting ratio (1:0.988) is close to 1:1.

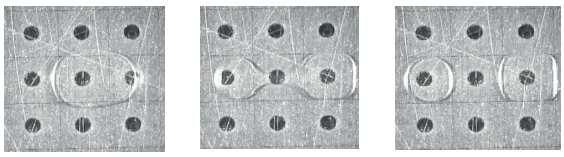

(a) Droplet cutting with asymmetric initial position.

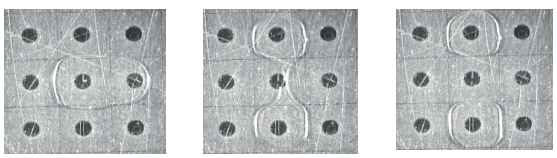

(b) Droplet cutting with symmetric initial position.

Figure 9. *Droplet cutting affected by the initial position. Droplet initially moves from right to left.*

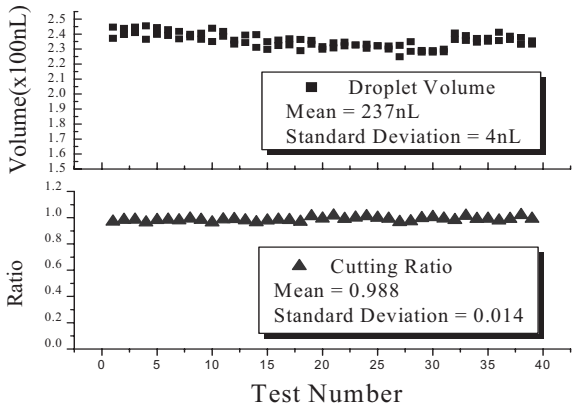

Figure 10. *Droplet volume and cutting ratio in the even (1:1) droplet cutting process with* $80V_{AC@1kHz}$.

DISCUSSIONS

As we have observed and shown in this paper, droplet creation and cutting are very sensitive processes affected by many factors. By precisely controlled signals and properly designed digitizing procedures, we have alleviated the uncertainties including dynamic effect and improved the uniformity and repeatability of droplet volumes. Although we can control the electrical signal well, the variation among fabricated chips and environmental conditions during operation are unavoidable, such as surface hydrophobicity deteriorating over a long cycle. In a well-controlled lab environment, we can continue monitoring the device performance and tuning the driving signals to compensate for the variations, such as tuning the droplet volume by changing the creation voltage. This means feedback control is desirable for fully automatic digital microfluidics systems. Fast electronic reading of droplet volume is essential for closed-loop feedback control systems, for which the capacitive measurement confirmed in this paper is a good candidate. Currently, the capacitive measurement of droplet volume is being added to the control system board and different feedback algorithms are being investigated to achieve more uniform and tunable droplet volume for digital microfluidics system.

CONCLUSIONS

We have designed and characterized droplet digitizing processes using the PCB EWOD chip and dedicated electrical control board. Uniform droplet volume distribution (±2%) has been achieved for both creation and cutting by a properly designed digitizing procedure and precise electrical control. Tunable droplet volume by changing a control signal parameter suggests that droplet volumes may be prescribed in digital microfluidics system with real-time feedback control.

ACKNOWLEDGEMENT

This work was supported by the NASA Institute for Cell Mimetic Space Exploration (CMISE) the Jonsson Comprehensive Cancer Center both at UCLA.

REFERENCES

[1] H. Ren, V. Srinivasan, and R. B. Fair, "Design and Testing of an Interpolating Mixing Architecture for Electrowetting-Based Droplet On-Chip Chemical Dilution," *Technical Digest of the 12th International Conference on Solid-Sate Sensors, Actuators and Microsystems (Transducers '03)*, Boston, USA, (2003), pp. 619-622.

[2] Q. Xu and M. Nakajima, "The generation of highly monodisperse droplets through the breakup of hydrodynamically focused microthread in a microfluidic device", *Apply Physics Lett*er, Vol 85, No.17, pp 3726-3728, (2004).

[3] J. Lee, H. Moon, J. Fowler, C.-J. Kim, and T. Schoellhammer, "Addressable Micro Liquid Handling by Electric Control of Surface Tension", *Technical Digest of the 14th International Conference on Micro Electro Mechanical Systems (MEMS '01)*, Interlaken, Switzerland, (2001), pp. 499-502.

[4] S.K. Cho, H. Moon, and C.-J. Kim, "Creating, Transporting, Cutting, and Merging Liquid Droplets by Electrowetting-Based Actuation for Digital Microfluidic Circuits", *Journal of Microelectromechanical. System.,* Vol. 12, No. 1, pp. 70-80, (2003).

[5] J. Gong, S.-K. Fan, and C.-J. Kim, "Portable Digital Microfluidics Platform with Active but Disposable Lab-On-Chip", *Technical Digest of the 17th International Conference on Micro Electro Mechanical Systems (MEMS '04)*, Masstricht, The Netherlands, (2004), pp. 355-358.

[6] J. Gong and C.-J. Kim, "Two-Dimensional Digital Microfludic System by Multi-Layer Printed Circuit Board", *Technical Digest of the 18th International Conference on Micro Electro Mechanical Systems (MEMS '05),* Miami, USA, (2005), pp. 726-729.

DEVELOPMENT OF A WATER MONITORING SYSTEM BASED ON INTEGRATED POLYMER MICROFLUIDICS

L. Zhu[1], D. Meier[2], Z. Boger[2,3], C. Montgomery[2], S. Semancik[2], D.L. DeVoe[1]

[1]Department of Mechanical Engineering, University of Maryland, College Park, MD 20742 USA
[2]National Institute of Standards and Technology, Gaithersburg, MD 20899 USA
[3]OPTIMAL – Industrial Neural Systems Ltd., Be'er Sheva, 84243 ISRAEL

ABSTRACT

A polymer microfluidic system for monitoring of volatile organic compounds diluted in water is presented. The sensor platform employs silicon-based microhotplate gas sensors as active detection elements, using a silicon-in-plastic microfabrication technology to enable integration of individual sensor chips into a larger polymer microfluidic substrate. The fabrication process provides seamless fluidic and electrical interconnects between the silicon and polymer substrates. The chemical monitoring system is designed to sample a water source, extract solvent present within the aqueous sample into the vapor phase, and direct the solvent vapor past the integrated gas sensor for analysis. Design, fabrication, and characterization of a prototype system is described, and results from illustrative measurements performed using methanol, toluene, and 1,2-dichloroethane in water are presented.

INTRODUCTION

There is growing concern regarding the quality of water supplies, which are susceptible to both natural and man-made chemical contamination. Contamination by volatile organic compounds (VOCs) is of particular concern because many VOCs produce serious health effects, such as liver or nervous system problems, reproductive difficulties, and increased risk of cancer [1]. The U.S. Environmental Protection Agency (EPA) currently sets maximum contaminant levels for safe drinking water on 53 VOC contaminants. A variety of detection methods have been employed for water analysis, such as LC/MS and GC/MS [2]. However, these methods generally rely on labor-intensive sample collection and laboratory-based analysis, which limit the quality, quantity, and frequency of data collected. These factors have led to a need to develop new technology for in-situ VOC monitoring system which is sensitive, selective, and compact, and which involves low power consumption for use in long-term monitoring applications.

Reports from the U.S. EPA have suggested that polymer-absorption and metal-oxide-semiconductor sensors are viable candidates for use in such a sensing system based on their simplicity and robustness [3], and several efforts have addressed the development of such sensing systems. For example, researchers at Sandia National Laboratories have developed an in-situ polymer-based chemiresistor sensing system for real-time detection of VOCs in soil and groundwater [4]. Ho et al. reported a surface acoustic wave sensor for in-situ monitoring of VOCs which consists of a chemically adsorbent polymer film on a piezoelectric substrate [5], and a microscale gas chromatography system for biomedical and environmental monitoring applications was recently reported [6]. However, these devices rely on passive transport of gas from a water source, and do not support higher levels of integration for water delivery or vapor pressure control. Furthermore, the performance of these devices was impacted by environmental temperature fluctuations.

In the present work, we report the application of silicon-in-plastic microfabrication technology to the development of an integrated microfluidic gas sensor for the monitoring of VOCs in water supplies. The silicon-in-plastic microfabrication method provides the ability to use no more than the necessary high cost silicon area, and thereby offers the potential to substantially reduce overall system fabrication costs. The microfluidic system provides the required fluid routing, while offering several advantages for efficient solvent extraction such as large specific interface area, large ratio between interface area and channel volume, and short diffusion distance and time [7]. Furthermore, microfluidic systems can readily support integrated microheaters to control the liquid and vapor temperature, and thereby enhance the solvent concentration delivered to the gas sensor chip.

FABRICATION

The fabrication process developed for integration of bare gas sensor chips into a polymer microfluidic substrate is depicted in Figure 1. A round hole 3 mm in diameter is first milled through a 1.5 mm thick polycarbonate (PC) substrate. A microhotplate gas sensor chip is next placed face-down on a flat layer of partially cured polydimethylsiloxane (PDMS, Sylgard 184; Dow Corning, Midland, MI). The PC substrate is aligned over the chip and placed onto the PDMS with the chip centered inside the milled hole. The assembly is placed in a vacuum chamber and the milled hole is filled with epoxy (353ND; Epoxy Technology, Billerica, MA). After the epoxy is cured for 12 hr at room temperature, followed by 12 hr at 50 °C, the PDMS layer is removed. The epoxy serves to secure the chip within the PC substrate, while leveling the chip surface to within 1 μm of the PC surface. But small gaps can form at the silicon/epoxy/PC interfaces due to thermal mismatch and epoxy shrinkage during curing. These gaps, which are typically on the order of several microns deep, can cause several problems when forming metal interconnects between the PC substrate and on-chip bond pads. To overcome these problems, a 6 μm layer of parylene C is deposited to passivate the sidewalls and bridge small gaps prior to metal deposition. Parylene C covering the bondpads and microhotplates of the gas sensor is removed by oxygen plasma etching using a Cr/Au mask. After the parylene layer is patterned, the mask metals are stripped, and new Cr (20 nm) and Au (500 nm) layers are deposited and patterned to provide interconnections from the bondpads on the gas sensor to connection pads on the PC substrate. Finally, conductive epoxy was applied at the connection pads to provide electrical access to the system. A photograph of a typical substrate fabricated using this approach is shown in Figure 2.

The integrated sensor array platforms used in this work are 4-element microhotplate gas sensor chips designed by NIST researchers [8] and fabricated at MIT Lincoln Laboratory. Each chip is 1.6 mm square. After integrating the silicon chip, a XeF_2 isotropic silicon etch is used to remove silicon from beneath the hotplate, allowing final release of the suspended microhotplates in-situ. After release, semiconducting metal oxides are grown on the

microhotplate elements to provide the required sensor films by chemical vapor deposition.

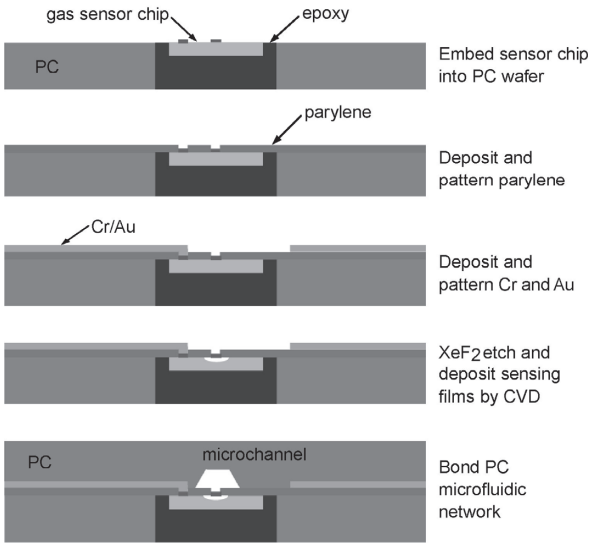

Figure 1. *Fabrication process for the integrated microfluidic gas sensing system.*

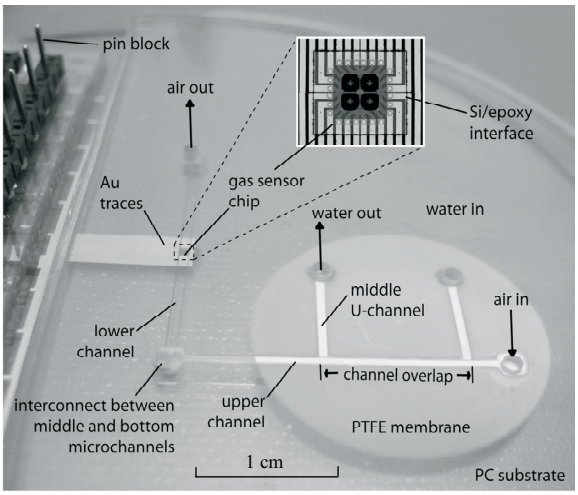

Figure 2. *Photograph of a fabricated microfluidic substrate with integrated microhotplate gas sensor chip.*

Gas-phase solvent extraction from the aqueous phase is a key requirement for the water monitoring system, since solvent sensing is ultimately performed in the gas-phase. The solvent extraction subsystem was fabricated using polymer microfluidic technology. The design consists of two microchannels separated by a porous hydrophobic membrane. The microchannels are trapezoidal in cross-section and 100 µm deep with a width at half-depth of 640 µm, and were fabricated by hot embossing using a bulk-etched silicon template. A 50 µm thick polytetrafluoroethylene (PTFE) membrane with 70% porosity and 0.22 µm average pore size was thermally bonded between the upper (straight microchannel) and middle (U-shape microchannel) PC layers, creating a porous interface where the channels overlap. Next, a bottom PC layer was bonded to the composite structure using solvent bonding. The bottom PC layer contains a microchannel on the exposed side, which is in fluid connection with the straight channel in the upper PC layer by aligned two 1.5 mm diameter holes premilled at the end of the middle and bottom microchannels before bonding. This microchannel is used to deliver gas to the microhotplate sensor chip. The 3-layer PC microfluidic assembly was fixed to the bottom substrate containing the silicon sensor chip by mechanical clamping, with the microchannel in the bottom of the 3-layer structure aligned over the sensor elements. In the final assembly, the middle U-shaped channel delivers a continuous stream of water which passes over the middle microchannel with the PTFE membrane preventing the aqueous solution from entering the upper channel. Due to its native vapor pressure, solvent within the water passes through the membrane in the gas phase. A continuous flow of dry air is supplied to one end of the upper channel, which delivers the solvent to the gas sensor through the channels in the upper and bottom PC layers.

VAPOR TRANSPORT MODEL

In order to optimize the design of the air-liquid two-phase flow system, a model for vapor transport across the porous membrane was employed. TeGrotenhuis et al. previously reported a model for a solvent extraction system having two immiscible fluids flowing through rectangular microchannels separated by a porous plate [9]. This model can be readily modified for the case where the water channel contains a liquid phase, while the membrane and the air channel support a gas phase. As described in the TeGrotenhuis model, the boundary condition governing analyte flux between the liquid phase within the water channel and gas phase within the membrane is given by,

$$D_l \frac{\partial C_l}{\partial y} = k\left(C_m - m_a C_l\right) \tag{1}$$

where D_l is the diffusion coefficient of the solvent in liquid, and C_l and C_m are the solvent concentrations within the liquid and membrane, respectively, at the liquid/membrane interface. The parameter m_a is the equilibrium distribution coefficient which is defined by the ratio of the equilibrium analyte concentration in the air channel to analyte concentration in the liquid channel at the liquid/membrane interface. This parameter is equivalent to the Henry's law constant for the solvent. The parameter k is an overall gas phase mass transfer coefficient defined by the mass transfer resistance across the liquid/air interface. For the present case, k was assumed to be 0.1 cm/sec based on the mass transfer coefficient of six organic compounds provided by Guo and Roache [10]. Beyond these modifications, the original TeGrotenhuis model was used to predict solvent effluent concentration within the air microchannel.

A numerical simulation of effluent concentration was performed over a range of air and liquid flow rates for the case of methanol. Air and liquid diffusion coefficients of $D_a = 0.159$ cm^2/s and $D_l = 1.9\times10^{-5}$ cm^2/s [11] were used. The diffusion constant for methanol within the membrane, D_m, was estimated analytically using a model for gas diffusion in porous media [12],

$$D_m = D_a \varepsilon^{\frac{4}{3}} \tag{2}$$

where ε is the membrane porosity. Using this model with $\varepsilon = 0.7$ yields $D_m = 0.079$ cm^2/s. A 1 cm long, 100 µm deep intersection region was defined between the liquid and air microchannels. The results were normalized to the saturated vapor concentration of the liquid analyte as determined from the Henry's law constant for methanol, given on a mole fraction basis as 0.29 at 25 ^{o}C [11]. As can be seen from Figure 3, the effluent concentration may be increased by raising the liquid flow rate and reducing the air flow rate. This result is reasonable, since higher liquid flow rates will rapidly replenish analyte in the water as gas-phase analyte is delivered across the membrane. Similarly, lower air flow rates will allow gas-phase analyte to accumulate in the microchannel, leading to higher effluent concentrations.

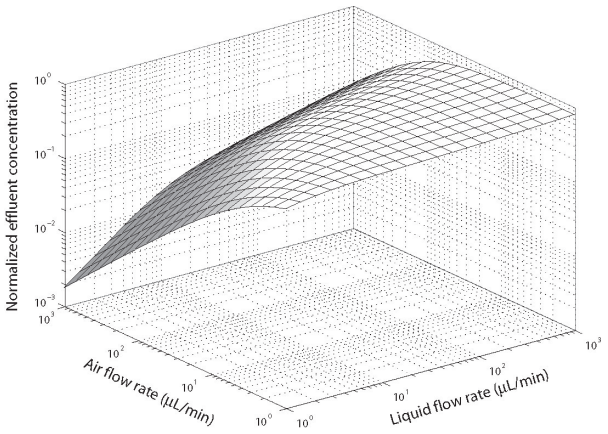

Figure 3. *Numerical results of methanol effluent concentration with different air and liquid flow rates.*

EXPERIMENTAL RESULTS AND DISCUSSION

While the equilibrium responses of the metal oxide films have been employed for various detection and monitoring applications, it has been shown that the transient (or kinetic) responses can be particularly useful to distinguish between various analytes. The imposed temperature change in a hotplate element results in a transient response in the sensor film conductance which provides a basis for achieving gas identification as well as measuring concentration by employing a temperature programmed sensing methodology [13,14]. The TPS program used in this work alternates the sensor temperature between a ramp value (from 60 °C to 480 °C in 29 equal steps) and a base value (200 °C) every 500 ms. In this way, 58 data points (conductance of the sensing film, 29 corresponding to the ramp temperature and 29 to the base temperature) are collected for each sensor in 14.5 sec. After 5 sec at the base temperature, this temperature sequence is repeated throughout the analyte delivery program.

A microfluidic water monitoring system with an integrated microhotplate gas sensor was fabricated with a 1 cm overlap region between the liquid and air channels to evaluate the performance of the water monitoring sensor platform. A syringe pump was used to deliver a precise flow of water/solvent mixture in the liquid channel, and a mass flow controller was used to deliver dry air flow in the gas channel. A laptop computer provided temperature control and monitoring of conductometric response for the integrated gas sensor elements. Based on the model results, the flow rate of dry air was set to the minimum value supported by the mass flow controller of 500 μL/min, and the flow rate of liquid was set to a relatively high value of 20 μL/min. While higher liquid flow rates are desirable to enhance the solvent concentration in the air channel, flow rates above 20 μL/min were often observed to produce leakage in the microfluidic system. At the start of each experiment, air and liquid were pumped to their channels for several minutes to stabilize the air/liquid interface. After stabilization, the TPS program was started. Measurements were performed using 3 different VOC analytes: methanol (0, 1, 10, and 100 ppm), toluene (0, 10, and 100 ppm), and 1,2-dichloroethane (0, 10, 100, and 1000 ppm). Measurements of sensor response for toluene and 1,2-dichloroethane were not performed at 1 ppm due to the relatively low signal observed at 10 ppm. All reagents were procured from Fisher Scientific (Fair Lawn, New Jersey).

Conductance measurements over two TPS cycles from a single microhotplate for different concentrations of methanol are shown in Figure 4. This data has been filtered using a running normalization approach, in which the initial conductance measurement for each cycle is normalized by the final value measured in the previous cycle, thereby limiting the effects of baseline signal drift. As can be seen from Figure 4, the characteristics of the TPS response vary as a function of concentration, and these features may be used as signatures for analyte identification and quantification. Artificial neural networks (ANNs) offer an efficient and rapid means of recognition and classification of analytical data, and have recently been applied to the problem of analyte identification and quantification from microhotplate gas sensor data [15].

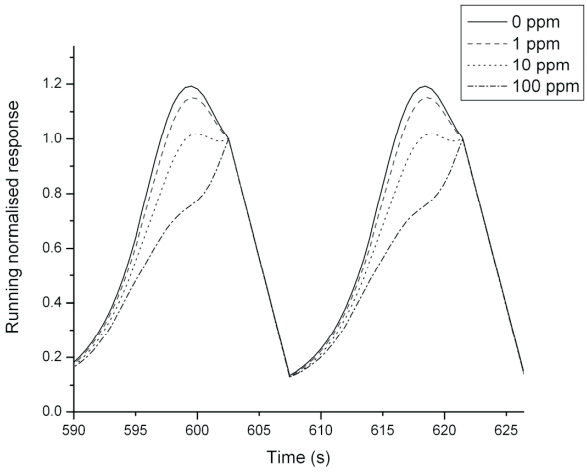

Figure 4. *Example response over two TPS cycles to methanol at constant concentration levels from 0 ppm to 100 ppm.*

In this work, the Guterman-Boger ANN modeling approach was applied to the methanol, toluene, and 1,2-dichloroethane TPS data measured using the integrated microfluidic platform. The data from a minimum of 25 TPS cycles for each analyte and analyte concentration were presented to the ANN as a 116-input vector (29 temperature steps on four sensors). The ANN was trained using 2/3 of the sensor data selected randomly, and the remaining 1/3 of the data was reserved as a validation data set. The random training and validation selection measures the consistency of the data within each analyte concentration value test. The resulting ANN model was applied to both the training and validation data sets. The estimated concentrations for each analyte are shown in Figure 5(a)-(c). Because the sensing films generally take about 1 min to reach equilibrium after being exposed to a new analyte concentration, the first 3 TPS cycles were removed from the these plots.

The average estimated concentrations are given in Figure 6 as a function of the known concentrations. The error bars in this figure represent +/- σ for the estimations at each concentration level. Due to the logarithmic axis, any non-positive concentration estimates are not shown in this figure. A summary of the estimated concentration error and standard deviation relative to the known concentrations is provided in Table 1. Predictions for methanol concentrations down to 10 ppm are quite good, with the concentration underestimated by 8%. When reducing the methanol concentration to 1 ppm, the estimation error increases to 40%, but with minimum deviation in the estimations. In contrast, the toluene estimation error is -3.6% at 10 ppm, but with a large standard deviation equal to 28.5% of the actual concentration level. The estimation error for 1,2-dichloroethane is even larger, with -62.2% error at 10 ppm and high variance in the data. Based on the measured data, approximate detection limits for the fabricated system are 1 ppm for methanol, 10 ppm for toluene, and 100 ppm for 1,2-dichloroethane.

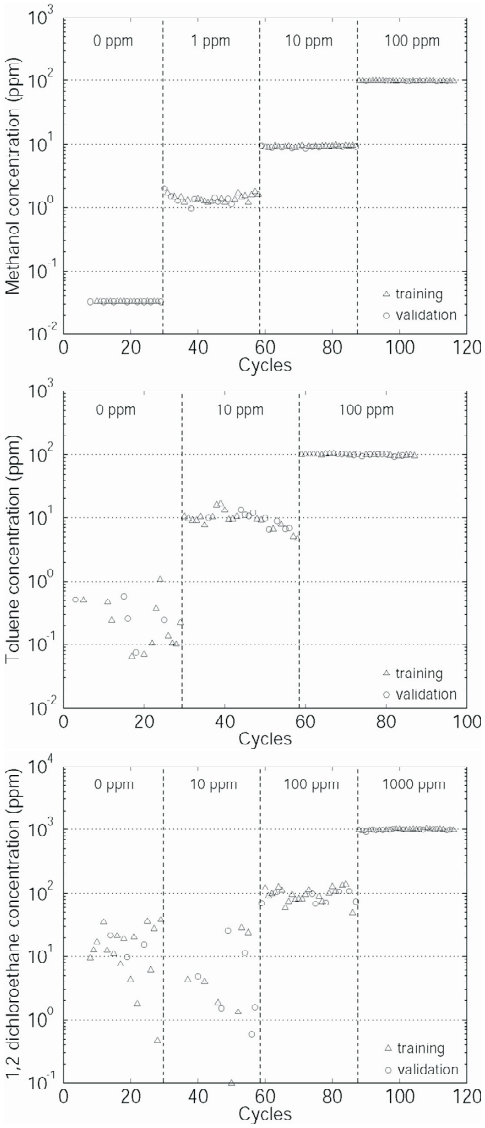

Figure 5. *Experimental measurements of VOC concentration by ANN for methanol, toluene, and 1,2-dichloroethane.*

CONCLUSIONS

The demonstrated water monitoring platform combines a silicon-based microhotplate sensor chip capable of conductometric measurement of organic solvents in the gas phase with a microfluidic 2-phase flow network for effective solvent extraction. This study has primarily focused on evaluating the sensitivity of the system to a suite of VOCs diluted in water, with results indicating approximate detection limits of 1 ppm for methanol, 10 ppm for toluene, and 100 ppm for 1,2-dichloroethane. Although the sensitivity is lower than that required for effective monitoring of drinking water supplies, the system in its current form could be amenable to monitoring point source contaminant emissions where higher concentrations are present.

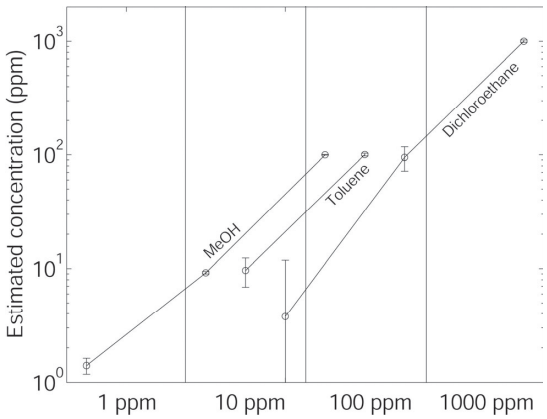

Figure 6. *Summary of sensor performance for each VOC analyte. Error bars indicate standard deviations for the ANN data provided in Figure 5.*

REFERENCES

[1] A. Szczurek, P. M. Szecowka, B. W. Licznerski, Sensors and Actuators B, 58 (1999), pp. 427-432.

[2] S. D. Richardson, Anal. Chem., 73 (2001), pp. 2719-2734.

[3] C. K. Ho, M. T. Itamura, M. Kelley, R. C. Hughes, Review of chemical sensors for in-situ monitoring of volatile contaminants, SAND2001-0643, Sandia National Laboratories, Albuquerque, N.M (2001).

[4] C. K. Ho, R. C. Hughes, Sensors, 2 (2002), pp. 23-34.

[5] C. K. Ho, E. R. Lindgren, K. S. Rawlinson, L. K. McGrath, J. L. Wright, Sensors, 3 (2003), pp. 236-247.

[6] C. Lu, W. Tian, W. H. Steinecker, A. Guyon, M. Agah, M. C. Oborny, R. D. Sacks, K. D. Wise, S. W. Pang, E.T. Zellers, Proc. Micro Total Analysis Systems, Squaw Valley, CA (2003), pp. 411-414,.

[7] M. Tokeshi, T. Minagawa, T. Kitamori, Anal. Chem., 72 (2000), pp. 1711-1714.

[8] S. Semancik, R. E. Cavicchi, M. C. Wheeler, J. E. Tiffany, G. E. Poirier, R. M. Walton, J. S. Suehle, B. Panchapakesan, D. L. DeVoe, Sensors and Actuators B, 77 (2001), pp. 579-591.

[9] W. E. TeGrotenhuis, R. J. Cameron, M. G. Butcher, P. M. Martin, R. S. Wegeng, Separation Science and Technology, 34 (1999), pp. 951-974.

[10] Z. Guo, N. F. Roache, Annals of Occupational Hygiene, 47 (2003), pp. 279-286.

[11] C. L. Yaws, Handbook of transport property data: viscosity, thermal conductivity, and diffusion coefficients of liquids and gases, Gulf Publishing, Houston, TX, 1995.

[12] R. J. Millington, Science, 130 (1959), pp. 100-102.

[13] R. E. Cavicchi, J. S. Suehle, K. G. Kreider, M. Gaitan, P. Chaparala, IEEE Electron Device Letters, 16 (1995), pp. 286-288.

[14] S. Semancik, R. Cavicchi, Accounts of Chemical Research, 31 (1998), pp. 279-287.

[15] Z. Boger, D. C. Meier, R. E. Cavicchi, S. Semancik, Sensor Letters, 1 (2003), pp. 86-92.

	1 ppm		10 ppm		100 ppm		1000 ppm	
	Δ	σ	Δ	σ	Δ	σ	Δ	σ
Methanol	40.1%	15.7%	-8.0%	2.4%	-0.4%	0.6%	n/a	n/a
Toluene	n/a	n/a	-3.6%	28.5%	0.3%	2.9%	n/a	n/a
1,2-dichloroethane	n/a	n/a	-62.2%	214%	05.4%	24.2%	0.2%	2.4%

Table 1. *Summary of estimated concentration average error (Δ) and standard deviation (σ) relative to the known concentration.*

EXPERIMENTAL CHARACTERIZATION OF FREQUENCY DEPENDENT ELECTROSTATIC ACTUATOR FOR AQUEOUS MEDIA

Vikram Mukundan and Beth L. Pruitt
Mechanical Engineering, Stanford University
Stanford, CA, USA

ABSTRACT

We have designed and fabricated an electrostatic actuator for operation in ionic media. The device was designed to mechanically stimulate cells and to study their mechanical properties. The frequency dependence of the device has been characterized for different media. A simple lumped capacitor circuit model for the device agrees fairly well with the experimental results. Surface treatment techniques to avoid stiction in the device have also been studied.

INTRODUCTION

Mechanical stress is known to affect cell life **[1]** and the role of forces acting on a cell is an important field of study. Initial work utilized soft-lithographic techniques to study the interaction between cell and substrate **[2]**. A number of biophysical techniques have also been developed to study the properties of cellular and sub-cellular components **[3, 4]**. Some of these techniques include optical tweezers, atomic force microscopy (AFM), micropipette aspiration and shear flow chambers. Optical tweezers and AFM provide high force resolution but are limited to low force ranges. Micropipette aspiration is a technique that has been successfully applied to study the properties of cell membranes and non-adherent cells. However, these techniques do not interact through the focal adhesions of a cell on a substrate. Other single cell manipulations have been demonstrated using off chip actuators. For example, Lin et al measured the forces in cardiac myocyte contraction with microfabricated polysilicon cantilevers **[5]**. Saif et al **[6]** and Yang et al **[7]** employed a functionalized micro-cantilever with an external piezoelectric actuator to measure the mechanical properties of fibroblasts. For on chip actuation, Chronis and Lee developed an electrothermally actuated SU-8 microgripper for cell manipulation without control of the loading profile[8]. Most similar to our design, the dual comb electromechancial nano-material testing devices developed by Zhu and Espinosa are used in air or vaccum for characterizing carbon nanotubes **[9]**.

The device presented here will enable simultaneous stimulation and measurement of mechanical properties. We have incorporated two pairs of comb-drives to enable drive and sensing functions for force-displacement, strain rate and cyclic loading characterization of cells patterned and cultured on the devices. The actuator is designed with thin-film gold islands to be functionalized with molecules suitable for cell adhesion. Ionic shielding effects are circumvented by operating the device at high frequency. The system response is estimated from lumped model capacitor models for the electrodes, which can be related to the properties of the electrolyte using the theory of diffuse charges.

THEORY

The comb-drive actuator comprises interdigitated pairs of electrodes, with one suspended and free to move. When a voltage V is applied across the electrodes, the electrostatic force is balanced by the stiffness in the suspension **[10]**. The force displacement relation is given by

$$F = kx = \frac{N\varepsilon b}{d}V^2 \tag{1}$$

Where k is the suspension stiffness, ε is the permittivity of the medium. N is the number of fingers, d is the gap length and b is the thickness of the device. However, this relation holds only for a dielectric medium in the gaps. The cells also need to be kept away from the regions of fringing electric fields. A FEMLAB (now COMSOL Multiphysics) model was used to estimate the field distribution in such a system. Figure 1 shows that the field is practically zero at locations more than 200 μm above the right electrode. Moreover, the moving electrode will be grounded along with the substrate, so that the cell binding substrate is well shielded from the electric field effects.

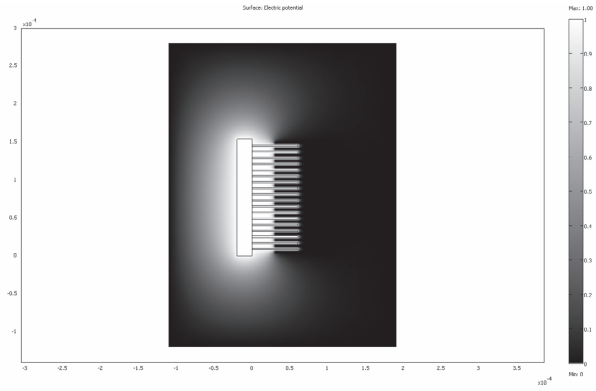

***Fig 1**. Electrostatic field distribution for a pair of comb-drive electrodes*

Electrostatic actuation in ionic media was demonstrated by Sounart et al. **[11]** and Pachawagh et al **[12]**. They demonstrated that the ionic screening of the electrodes can be avoided by using a high frequency signal that modulates the required actuation signal. The frequency is such that the polarity of the field changes at a rate faster than the ions can respond to and the shielding of the field is avoided.

Bazant et al **[13]** argued that the charging dynamics of an electrode-electrolyte system is governed by the RC time constant of the system. When a solid surface is immersed in an electrolyte,

there is spontaneous accumulation of ions near the electrodes due to surface potential at the interface. The same occurs when an external potential is applied at the electrode. The linearized expression for the double layer capacitance per unit area is given by,

$$c_{EDL} = \frac{\varepsilon}{\lambda_D} \tag{2}$$

where λ_D is the Debye length of the double layer. Its dependence on the electrolyte properties in terms of the ionic charge valence *z*, average solute concentration *C*, Boltzmann constant k_b and temperature *T* is given in terms of as follows **[13]**.

$$\lambda_D = \sqrt{\frac{\varepsilon k_b T}{2z^2 e^2 C}} \tag{3}$$

The conductivity of a symmetric electrolyte with ions of charge *z* can be expressed as follows.

$$\sigma = \frac{2(ze)^2 CD}{k_b T} \tag{4}$$

where *D* is the diffusivity of the ions. For an electrode pair of spacing d immersed in a symmetric electrolyte of charge *z*, the effective time constant is as follows.

$$\tau_C = \frac{\lambda_D d}{D} \tag{5}$$

The electrode pair (Figure 2) is silicon with native oxide of thickness t~2 nm. The gap of length d is filled with the electrolyte medium. The circuit model for this is shown in Figure 3 where, C_{ox}, C_{EDL} and C_W are the capacitances of the oxide, double layer and the actuator respectively. R_W is the resistance of the medium between the electrode, which is derived from the electrolyte conductivity relation above. The term R_{Si} is not part of the electrode system, but arises due to the resistivity of the substrate through which the signal propagates. Specifically in this case, it is the resistance of the beam suspensions through which the shuttle is grounded.

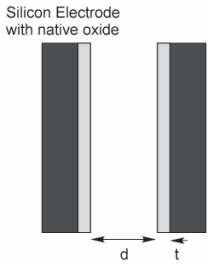

***Fig 2**. The electrodes are modeled as capacitors with gap d, and series capacitance of the dielectric native oxide.*

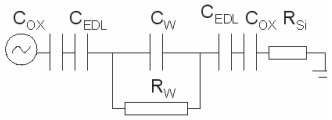

***Fig 3**. Lumped parameter circuit of the system. The resistance of the silicon, R_{Si} is currently the limiting term in performance.*

The dominant time constant of this circuit is evaluated as follows.

$$\tau_c = RC_{eff} = \frac{\varepsilon_{ox}\varepsilon_o d}{2\sigma t}\left[\frac{1}{1+\frac{\varepsilon_{ox}\lambda_D}{\varepsilon_w t}}\right] \tag{6}$$

where, ε_{ox} and ε_w refer to the relative permittivity of the oxide and water respectively.

FABRICATION

The devices are fabricated on a Silicon-On-Insulator (SOI) wafer; a fabrication schematic is shown in Figure 4. The silicon electrodes and suspension beams are etched into the device layer by Deep Reactive Ion Etching (DRIE) process. The metal lines comprising of Chromium/Platinum/Gold are patterned by a lift-off process. The wafer saw is used to obtain single dies before the sacrificial layer release etch. The devices are released by a timed wet-etch of the underlying oxide. The devices are then dried in a liquid CO_2 critical point dryer (CPD) to avoid stiction. Figure 5 is a Scanning Electron Micrograph of a released device.

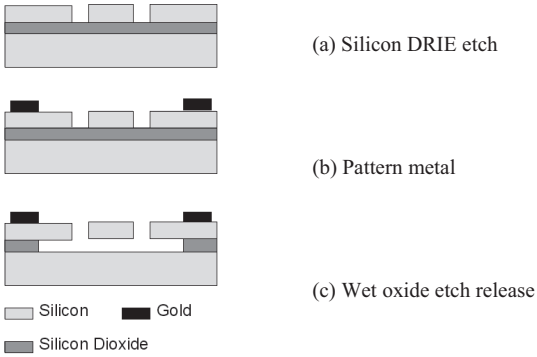

***Fig 4**. Schematic of fabrication steps*

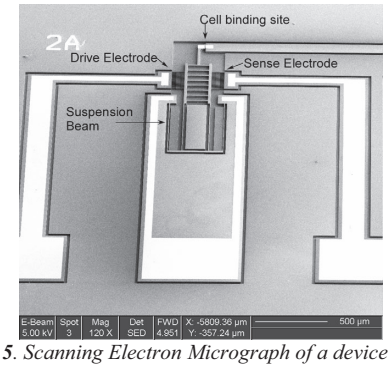

***Fig 5**. Scanning Electron Micrograph of a device*

The device design consists of a drive electrode to actuate, a sense electrode to measure displacement by change in capacitance and a cell binding substrate with gold islands to adhere cells to. The beam suspension is designed as a folded fixed-guided beam. The stiffness of the cell and that of the beam would be in parallel, necessitating the beams to be as compliant as possible to extract stiffness properties of the cells. For fibroblasts, the average stiffness has been reported as 0.001 N/m with a maximum elongation of about 15 µm **[6]**. The suspension in the devices has stiffness of *k* = 0.24, 0.58 or 1.46 N/m. The maximum displacement of these devices is about 20 µm, which is set by the onset of side instability.

EXPERIMENTAL DETAILS

The device was packaged on a ceramic Dual Inline Package (DIP) as shown in Figure 6. The actuation voltage was applied between the electrodes, with the substrate grounded. The actuator requires tens of volts for actuation in air, while it needs less than ten for actuation in water or ionic media. The DC signal was supplied through Kepco power amplifier. The AC signal was applied from an Agilent 33120A function generator. The actuator displacement was measured optically by a CCD camera attached to an upright microscope.

The package cavity was filled with the fluid for measurement. The device with the leads was setup under the microscope as shown in the Figure 7. The displacement between the two gold pads as shown in figure was measured by a code written in MATLAB. Pixel resolution of the camera enables a measurement with an accuracy of about 200 nm in displacement. Image processing techniques to improve resolution are under investigation as are improved signal conditioning circuits for using the sense electrodes signal for feedback control.

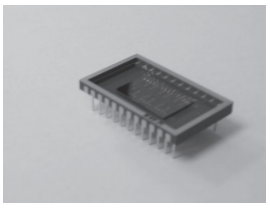

***Fig 6**. A chip with 6 devices is mounted and bonded in a leaded chip carrier. The carrier creates a natural well for cell culture media.*

***Fig 7**. Experimental setup with a Leica DMRXA2 upright microscope, and Leica 350fx CCD camera.*

RESULTS

DISPLACEMENT CHARACTERIZATION

Displacement as a function of frequency and amplitude of applied voltage was evaluated in air, de-ionized water, and ionic media. The displacement was found to be linear with the square of voltage. Two different tests were conducted for the same device in DI water. The first test is to measure the voltage-displacement curve and the second is to measure the frequency response of the displacement. The results are plotted in Figures 8 and 9 respectively. The theoretical estimate of the displacement is also shown.

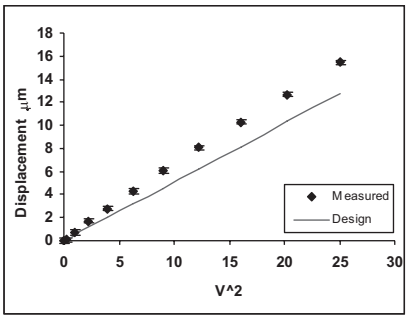

***Fig 8**. Actuator displacement vs. square of applied voltage for a device immersed in DI water, operated at 1 MHz.*

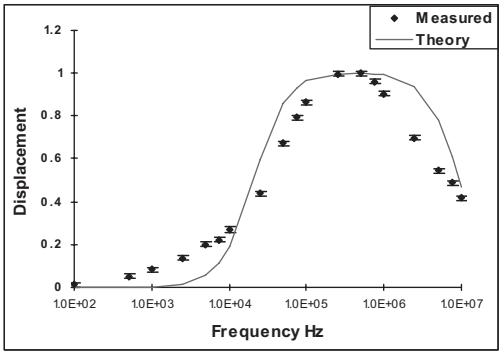

***Fig 9**. Actuator displacement vs. signal frequency for a constant amplitude of 3.5 V. The plots are normalized to the maximum displacement. The model predicts the square of the voltage across the actuator for different frequencies, which is proportional to the displacement.*

The frequency response does not flatten out at higher frequencies but rolls off due to substrate losses that were larger than anticipated. The path resistance due to the long suspended beams of about 0.02 Ω-cm is 2.67 kΩ. This causes a low-pass effect as the resistive component dominates at higher frequencies.

In order to stimulate cells, the device needs to operate in ionic media. The device displacement was characterized in different concentrations of Potassium Chloride (KCl) solution and Dulbecco's Modified Eagle Medium (DMEM). The results of the tests are plotted in Figures 10 and 11. The theoretical predictions according to the lumped capacitor model are also indicated on the graph.

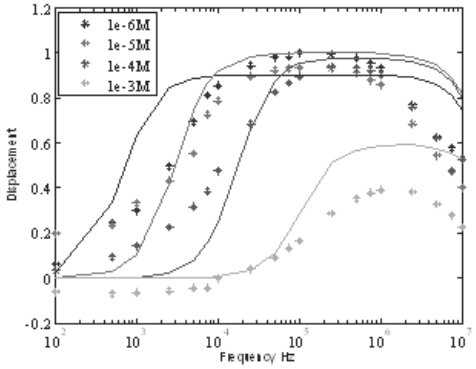

***Fig 10**. Normalized actuator displacement in varying concentration of KCl solutions. Solid lines represent theory and symbols represent data.*

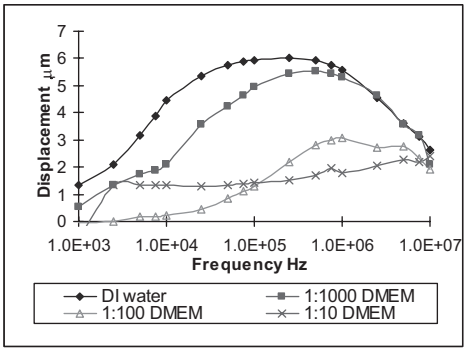

***Fig 11.** Actuator displacement at 5 V in different dilutions of DMEM, a common cell culture media. Isotonic solutions for cells require 100% DMEM.*

The curves show an increase in transition frequency with media concentration. However, there is little difference between the curves for 1 μM KCl and 10 μM KCl, which is thought to be due to the presence of impurities in the solution and at the die surface. The effective conductivity of the medium is increased by these impurities. The effect of dissolved impurities would be lower in the case of higher concentrations of KCl. It was not possible to achieve actuation for concentrations higher than 10 mM in the case of KCl and less than 1:100 dilution in the case of DMEM. Applying signals of amplitudes greater than 5V also caused electrolysis at the electrodes, accompanied by the release of gas bubbles.

SURFACE TREATMENT

The devices need to be released in a CPD to avoid stiction of the suspended structures. This limits the reusability of the devices as they cannot be dried and cleaned before reuse. This becomes important in the case of biological samples, where the substrates need to be cleaned between subsequent experiments. Anti-stiction self-assembled monolayer (SAM) coatings for MEMS may improve the reliability of these devices **[14]**. We coated the devices with 1, 1, 2, 2-Perfluorodecyltrichlorosilane (FDTS) in water vapor plasma. The contact angle after treatment was measured to be 104 ± 3^0. However, the increased surface energy made it difficult to displace air from the narrow gaps in the devices as shown in figure 12. Moreover, the highly hydrophobic surfaces likely collapsed when immersed in water as no actuation was observed in these devices. When the devices were dried and tested in air, they did not show any actuation. Further work is required to tune the surface energy to an optimum level.

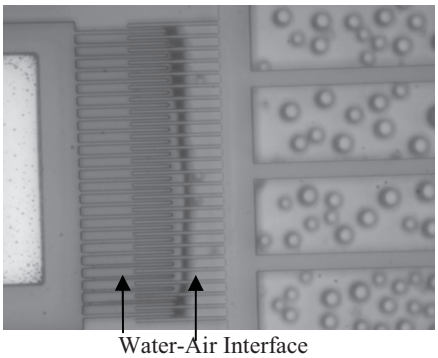

***Fig 12**. Image of a FDTS coated device immersed in water*

CONCLUSIONS

We have designed and fabricated an electrostatic actuator for stimulating cells in ionic media. The displacement characteristics of the device have been measured in media of different concentrations. Two limitations will be addressed in the future designs. First is the potential drop across the path resistance at higher frequency. High path resistance prevents the use of the device at frequencies required by cell culture media. It will be reduced by using a higher doped substrate or by plating the conducting path with metal lines. The second limitation of these devices is their re-usability. Once immersed in media, the devices cannot be dried in air without stiction problems nor returned to the CPD in a clean room. In order to mitigate this, silane surface treatment was investigated. However, the highly hydrophobic surface causes stiction when immersed in water. Moreover the surface tension causes air bubbles to be trapped between narrow gaps in the device. Tuning the surface energy to an intermediate value may solve both the problems.

ACKNOWLEDGEMENTS

VM is supported by the Stanford Graduate Fellowship (2003-06). Fabrication work was performed in part at the Stanford Nanofabrication Facility (a member of the National Nanotechnology Infrastructure Network) which is supported by the National Science Foundation under Grant ECS-9731293, its lab members, and the industrial members of the Stanford Center for Integrated Systems. This work was supported by NSF CAREER Award ECS-0449400. The authors would like to thank Prof. Roya Maboudian and Brian Bush for their discussions and help with the surface treatment experiments. Travel support was generously provided by the Transducers Research Foundation.

REFERENCES

1. J. L. Tan, J.Tien, D. M. Pirone, D. S. Gray, K. Bhadriraju, C. S. Chen, "*Cells Lying on a bed of microneedles: An approach to isolate mechanical forces"*. Proceedings of the National Academy of Sciences, 2003. **100**(4): p. 1484-1489.

2. A. D. Bershadsky, N. Q. Balaban., B. Geiger, "*Adhesion Dependent cell Mechanosensitivity"*. Annual REview of Cell Development, 2003. **19**: p. 677-695.

3. K. J. Van Vliet, G.Bao., S. Suresh, "*The biomechanics toolbox: experimental approaches for living cells and biomolecules"*. Acta Materalia, 2003. **51**: p. 5881-5905.

4. G. Bao, S.Suresh., "*Cell and molecular mechanics of biological materials"*. Nature Materials, 2003. **2**: p. 715-725.

5. G. Lin, K. S. J. Pister, K. P. Roos, "*Micromachined Polysilicon Heart Cell force Transducer"*. Journal of Microelectromechanical Sytems, 2000. **9**(1): p. 9-17.

6. M. T. A. Saif, C. R. Sager., S. Coyer, "*Functionalized BioMicroelectromechanical Systems Sensors for Force Response study at Local Adhesion sites of Single livling cells on substrates"*. Annals of Biomedical Engineering, 2003. **31**: p. 950-961.

7. S. Yang, T.Saif., "*Reversible and repeatable linear local cell force response under large stretches"*. Experimental Cell Research, 2004. **305**: p. 42-50.

8. N. Chronis, L. P. Lee, "Electrothermally activated SU-8 microgripper for cell manipulation in solution", Journal of Microelectromechanical Systems, 2005, **14**(4): p857-863

9. Y. Zhu, H. D. Espinosa., "*An electromechanical material testing system for in situ electron microscopy and applications"*. Proceedings of the National Academy of Sciences, 2005. **102**(41): p. 14503-14508.

10. W. C. Tang, M. G. Lim, R. T. Howe, "*Electrostatic Comb Drive Levitation and Control Method"., *Journal of Microelectromechanical Sytems, 1992. **1**(4).

11. T. L. Sounart, T. A. Michalske., K. R. Zavadil, "*Frequency-Dependent Electrostatic Actuation in Microfluidic MEMS"*. Journal of Microelectromechanical Sytems, 2005. **14**(1): p. 125-133.

12. H. V. Panchawagh, D. Serrel, D. S. Finch, T. Oreskovic, and R. L. Mahajan. "*Design and Characterization of a BioMEMS device for invitro mechanical simulation of single adherent cells"*. in *ASME International Mechanical Engineering Congress and Expedition*. 2005. Orlando.

13. M. Z. Bazant, K.Thornton, Armand Ajdari, "*Diffuse-charge Dynamics in Electrochemical Systems"*. Physical Review E, 2004. **70**: p. 021506-1-23.

14. R. Maboudian, C. Carraro, "*Surface Chemistry and Tribology of MEMS",.* Annual Review of physical Chemisty, 2004. **55**: p. 35-54.

LAB-ON-A-CARD ASSAY FOR ENTERIC PATHOGENS

B. H. Weigl (1)*, J. Gerdes (2), P. Tarr (4), P. Yager (3), L. Dillman (1), J. Gerlach (1), M. Steele (1), R. Peck (1), S. Ramachandran (3), M. Lemba (3), D. Hoekstra (2), M. Kokoris (2), M. Nabavi (2), F. Battrell (2), D. M. Denno (3), E. J. Klein (3)

(1) Program for Appropriate Technology in Health (PATH), 1455 NW Leary Way, Seattle, WA 98107, Telephone (206) 285-3500, FAX (206) 285-6619; (2) Micronics, Inc., Redmond, WA; (3) University of Washington, Seattle, WA; and (4) Washington University, St. Louis, MO.

ABSTRACT

We describe the functional elements of a diagnostic instrument and disposable enteric card (DEC) system under development that rapidly identifies and differentiates *Shigella dysenteriae* serotype 1, *Escherichia coli* O157:H7, *Campylobacter jejuni*, and *Salmonella* and *Shigella* species in stool samples. These elements, currently realized as microfluidic subcircuits on individual cards, are (1) whole pathogen immunocapture, (2) nucleic acid extraction, (3) on-chip rapid PCR, and (4) lateral flow detection of amplicons. The system utilizes a low-cost disposable lab-on-a-card platform designed to identify enteric bacterial pathogens in patients with acute diarrhea. Special emphasis is placed on the utility of the device to diagnose both intentionally released enteric biothreat agents as well as to provide a platform to identify infections that are common worldwide. All reagents are stored in dry form on the card.

In this paper we report on the design and validation of individual subcircuits, identification and validation of capture antibodies and strategy for organism immunocapture, and identification and validation of specific PCR primer sequences for over 200 clinical isolates of enteric pathogens as well as spiked and pathogenic stool samples.

INTRODUCTION

Bioterrorist use of enteric pathogens is a significant potential threat, and naturally occurring enteric infections already burden global health. Enteric disease can result from bacterial, viral, or protozoal contamination of food and water, and infectious diarrhea is the second leading cause of morbidity and mortality worldwide–accounting for an estimated 3,100,000 deaths annually. In the United States, the rate of infectious diarrhea is lower than in developing countries, but it is estimated that 375,000,000 cases of diarrhea occur in the U.S. annually resulting in 73,000,000 physician consultations, 1,800,000 hospitalizations, and 3,100 deaths **[1-3]**. The cost of medical care and lost productivity from infectious diarrhea in the U.S. is estimated at $6 to $23 billion.

The intentional contamination of a salad bar with *Salmonella* **[4]** and a laboratory coworker's food with *Shigella* stolen from the laboratory **[5]** are two examples of bioterrorism on US soil. In both cases, an enteric pathogen was effectively being used as a biothreat agent.

Diagnosing the pathogen that causes diarrhea is a nontrivial undertaking under the best conditions, and not feasible when resources are extremely limited as in resource-poor countries, or if developed systems are stressed during a biothreat crisis. Syndromic management of diarrhea without any laboratory information for the patient and/or health care worker is not ideal, yet it is a reality in many settings. Where available, culture methods are used to detect and identify organisms that may be present, but the application of these methods is sporadic, time consuming, expensive, and lacks specificity. Technology in clinical laboratory identification of enteric pathogens has changed little since the early 1900s, and utilizes a series of culture plates with selective media to isolate and culture target organisms (Figure 1). This process is consumes time, requires skilled labor, and is costly. *C. jejuni* and *E. coli* O157:H7 require typically 1 to 2 days from receipt of specimen to result, while *Salmonella* and *Shigella* require between 2 and 4 days.

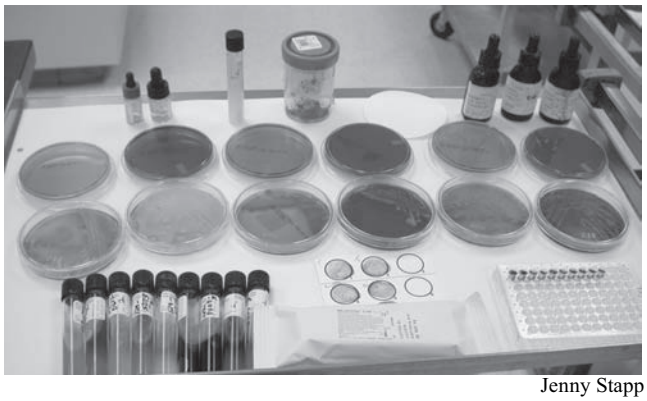

Jenny Stapp

Figure 1. *Culture plates representing a thorough clinical workup including Aeromonas, Campylobacte, E. coli O157:H, non-O157:H7 STEC, Plesiomonas, Salmonellae, Shigellae, Vibrios, Yersiniae, at a cost of ~ US$199.*

Culture methods to detect *E. coli* O157:H7 generally utilize selective media based upon the observation that *E. coli* O157:H7 do not ferment sorbitol. However, other enteric bacteria can share this phenotype, and there are reports of sorbitol-fermenting, toxigenic and pathogenic E. coli O157 that are fairly common in Europe **[6]**. Screening that is based solely on the sorbitol phenotype may therefore result in falsely negative results. Furthermore, confirmatory testing is required for sorbitol nonfermentors utilizing additional resources and time. Excellent results can be obtained retrospectively with complete bacteriological characterization, but it is a technology that is too slow for practical use in response to an outbreak or in clinical situations.

Other identification techniques include enzyme immunoassays (EIAs) that detect organism antigens or their toxins and genotyping. Tu et al. **[7]** reported an EIA that detects *E. coli* O157:H7. Recently, a triplex PCR assay for the detection of *Campylobacter jejuni*, *Salmonella* spp., and *Escherichia coli* O157:H7 was reported **[8]** that used genomic identification of the bacteria but was not specific to virulence factors associated with these pathogens.

The importance of all four of these agents (*Shigella dysenteriae* type 1 (Sd1), STEC, *C. jejuni*, and *Salmonella* spp.) is demonstrated by their classification as Category B priority pathogens based on NIAID Biodefense Research **[9].** In addition, with the possible exception of *E. coli* 0157:H7, these agents are common pathogens in many developing settings.

Sd1 is an especially virulent pathogen that causes regional outbreaks of dysentery. Symptoms of cramps, diarrhea, blood or pus in the stool, fever, and/or vomiting can begin in as few as 12 hours after ingestion. Sd1 is a plausible bioterrorism agent because of its virulence, highly infectious nature, and hardiness in the

environment. An infectious dose can be as few as 10 organisms. During infection, Sd1 invades and destroys the cells that line the large intestine and is very prolific–shedding one million to one hundred million organisms per gram of stool. Without prompt and effective treatment, the fatality rate of Sd1 can be as high as 15%.

E. coli O157:H7 produces one or more toxins similar to Sd1, which often leads to hemorrhagic colitis. Like Sd1, STEC disproportionately affect the young and elderly. Symptoms include crampy abdominal pain, vomiting, and watery diarrhea, which usually progresses to bloody diarrhea. While STEC infections are self-limiting, up to 10% of patients will develop hemolytic uremic syndrome (HUS) **[10].** It is estimated that there is an overall mortality rate of 1 to 35 percent among patients infected with STEC. *E. coli* O157:H7 is the most commonly occurring STEC and in 2001, 3,478 cases of STEC were reported in the U.S. alone.

Campylobacter jejuni is the leading cause of bacterial diarrhea in the U.S. with an estimated number of cases exceeding four million annually **[10**]. Symptoms include fever, nausea, muscle pain, and watery diarrhea that may contain blood. Most infections are self-limiting, but complications, especially in susceptible populations, may include reactive arthritis, septicemia, and Guillain-Barré Syndrome.

Salmonella species are responsible for two to four million cases of diarrhea in the U.S. each year **[11].** *Salmonella* has previously been used as a bioterrorism agent. In 1984, a religious cult in Oregon poisoned salad bars with *Salmonella* causing disease in 751 people **[4]**.

THEORY

The multiplex DEC test we are developing (see schematic in Figure 2) will be an automated, easy-to-use, point-of-care platform to detect simultaneously and rapidly, multiple different enteric

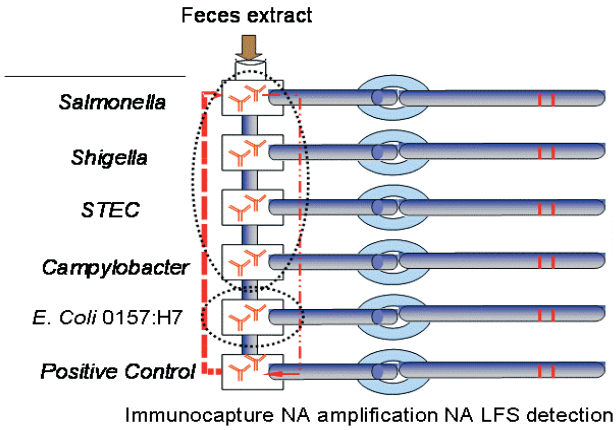

Figure 2. Schematic of DEC approach. *Showing a combination of whole pathogen immunocapture (immunocapture agents for Salmonella, Shigella, and Campylobacter are grouped together), nucleic acid extraction, PCR, and lateral flow detection of amplicons.*

pathogens that cause disease with similar symptoms, ie. diarrhea. The method is unique in that it seeks the bacterial agent using a orthogonal approach via antigen capture and the amplification of specific virulence genes for precise identification of the specific etiological agent. It will provide a mechanism for accurate, point-of-care diagnosis with a rapid turn-around time for results. The method is based on microfluidic lab card technology developed at Micronics and the University of Washington. This technology has been used in many different applications ranging from diffusion-based separation and detection **[12-17]** to projects involving cytometry on a chip **[18-21]** and nucleic acid-based amplification and detection techniques **[22].**

EXPERIMENTAL DETAILS

Presently, we have implemented each of the four elements of the DEC as microfluidic subcircuits on individual cards before embarking on full integration of the disposable device. Fluid transfer between the subcircuits occurs by pipette. The subcircuits are (1) whole pathogen immunocapture, (2) nucleic acid extraction, (3) on-card rapid PCR, and (4) lateral flow detection of amplicons, and are described below. In addition, we have demonstrated the feasibility of drying and resuspending all reagents needed for the DEC, thus allowing the possibility of storage at ambient temperature.

(1) Immunocapture of whole organisms: Our approach to capture pathogens on the DEC is based on antibodies coupled to magnetic beads. Figure 3 shows the current immunocapture subcircuit.

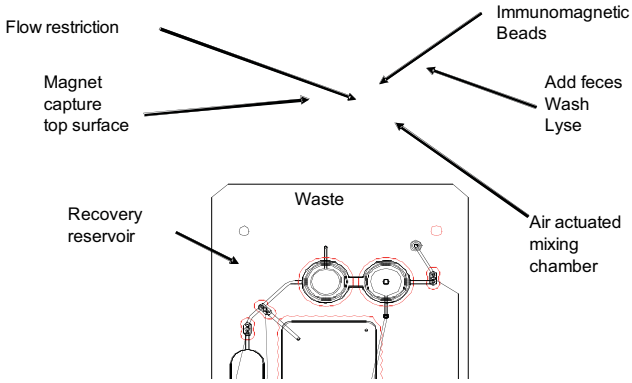

Figure 3. *Whole pathogen immunomagnetic bead capture subcircuit.*

One (or more in most cases) antibody suitable for whole organism capture has been identified for each target pathogens and validated using EIA plates, a magnetic bead-based capture system, or both. Organism capture has been validated from spiked stool for *E. coli* O157:H7, *Salmonella*, and *C. jejuni.* In addition, freshly shed stools containing *E. coli* O157:H7 have also been tested and were positive. Further, *E. coli* O157:H7 is especially difficult to identify by nonmultiplexed PCR. Therefore, we cultured and tested 14 confounder organisms (selected on a phylogenetic basis, to increase the validity of the results) with the selected antibody to determine that only pathogenic strains are captured. Additionally, three microfluidic subcircuits (the nucleic acid extraction, PCR amplification, and a qualitative lateral flow detection subcircuit), have been completed and tested. PCR primers were designed for all organisms and their specificity confirmed. 200 clinical isolates were cultured and tested with PCR to validate primer specificity. In addition a fourth subcircuit, the antibody capture subcircuit, has been validated for feces in a tube format and is currently being adapted to a lab card.

One significant technical accomplishment of this program is its validation of the selectivity of antibody for whole organism for direct capture from both frozen and fresh naturally infected human

stool, and spiked normal stools. It was unclear at the beginning of this project if sufficient selectivity could be achieved in such a microbially complex milieu and if the target organisms of interest reliably express the critical surface antigens during infection. However for all spiked and fresh stool samples so far tested, the capture methodology was concordant with the EIA and culture results. Another significant finding relates to the combined selectivity approach provided by immunocapture and PCR. After completing primer design and validation for all organisms, and selecting and validating capture antibodies, we found that primers for all target organisms except for *E. coli* O157:H7 are sufficiently specific to amplify the target sequence in the presence of other organisms. On the other hand, we found that the capture antibody for *E. coli* O157:H7 is quite specific in the presence of other target organisms, as well as in fresh and spiked stool samples. Thus, antibodies can be used to partially purify *E. coli* O157:H7 from generic *E. coli* and other flora in stool.

(2) Nucleic acid (NA) extraction on microfluidic card: A card that can purify RNA from lysed leukocytes or bacteria (Figure 4) is loaded with specimen in a lysis solution which contains a chaotropic buffer that allows RNA from the sample to bind to silica. On-card silica filter and microfluidic valves for fluid control and automate RNA binding, washing, drying, and elution. The card was initially validated in experiments in which we processed 10^6 white blood cells using commercial kits or suspended in lysis buffer, before applying samples to the port on the lab card. LightCycler assays determined that the microfluidic card solutions had a slightly lower crossing point (25.3) than the control RNeasy solutions (27.1). This card also has been validated for lysis and detection of Gram-negative bacteria in feces.

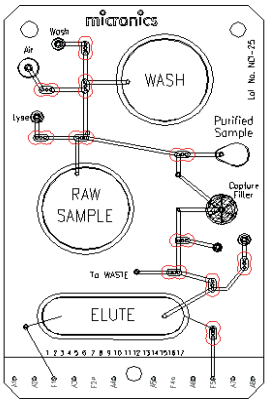

Figure 4. Schematic of nucleic acid extraction subcircuit. *The operational steps currently are:*
(1) sample injected
(2) nucleic acids captured on silica membrane
(3) wash
(4) dry membrane
(5) elute
(6) eluent taken for analysis
The purification of nucleic acid on the card is completed in < 5 minutes and is under complete software control.

3) PCR subcircuit: Micronics has developed a prototype thermal control unit (TCU) for extremely rapid temperature ramps (Figure 5). This TCU thermocycles the amplification chamber of a disposable microfluidic card. For efficient thermal transfer, a simple laminate card was designed with an amplification chamber capped by one layer of 0.004" Mylar, permitting the capping layer of the chamber to touch the TCU. The 16-second cycle time (longest in tests) can be diminished considerably with heat sinks, TCUs, and efficient thermal interface material. Even at 16 seconds, 30 full cycles requires only 8 minutes.

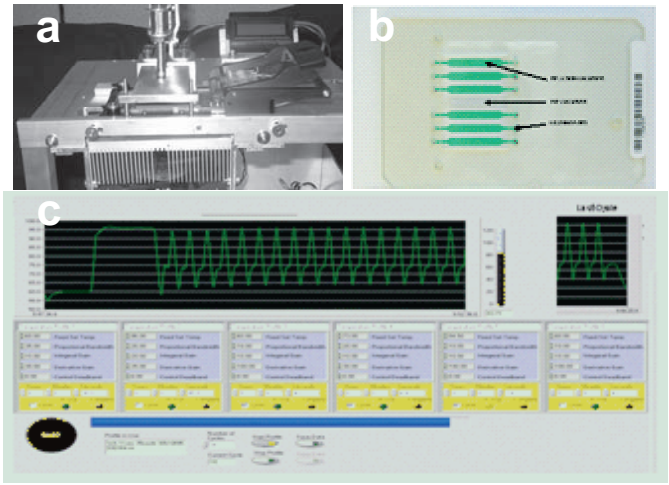

Figure 5. 5A Micronics-developed TCU. 5B *PCR amplification lab card capable of performing six amplifications simultaneously,* ***5C*** *and software interface with thermal couple trace showing 60 second 60ºC reverse transcription followed by 16-second PCR cycles.*

Figure 6 demonstrates the fluid control system that operates both on-card valves (using a small air pump) and fluid control (using positive displacement pumps).

Figure 6. DEC Instrument and disposable interface*–current prototype (shown without thermocycler attachment).*

Figure 7 exemplifies the products of PCR subcircuit, with a gel showing the products of extracted and purified *Salmonella*. Similar results have been obtained with all target organisms. In the case *E. coli* 0157:H7, we have applied this system to human stool from children infected with this pathogen.

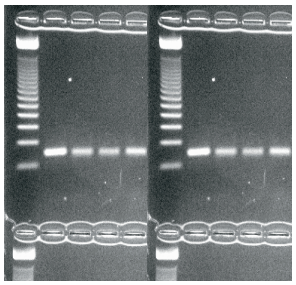

Figure 7. Ethidium bromide stained DNA in agarose gel of salmonella amplified with the DEC PCR subcircuit*. The left lane for the upper and lower gel is a MW marker; lane 1 for each gel is the result from a standard thermal cycler; the other 16 lanes are results for the DEC PCR subcircuit run for 15 minute and 34 cycles.*

(4) Lateral flow (LF) detection of amplicons: For this project, we are adapting an existing endpoint detection system using a LF amplicon detection method. This technique allows non-electrophoretic detection of PCR products, and obviates the use of gels or sophisticated optics to measure dye-coupled amplicons.

Figure 8 illustrates the components in the LF strips and how the reactions are created. In brief, amplicons (the bar with 5' and 3' ends) bind to dried capture probes to create detection probes nested within the amplicon. One capture probe has a biotin label and the other has a fluorescein (FITC) label (used here as a hapten). As the solution wicks along the strip, streptavidin-coated microparticles move with the solution, and a streptavidin/biotin association is formed between microparticles and the amplicon/capture duplex. As they migrate through the LF strip, the microparticles with detection probes bind to a previously deposited line of anti-FITC antibodies through the FITC hapten on the other capture probe. As the chromogenic particles accumulate on the antibody stripe, a blue line becomes apparent, indicating successful NA amplification and the presence of target. Procedural control lines have been included, and results are available in a few minutes.

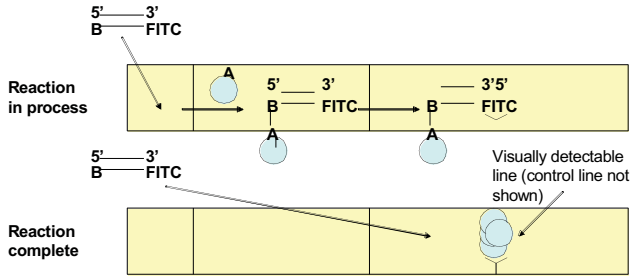

Figure 8: Schematic of amplicon detection using lateral flow strips. *The strips operate by simple wicking (no incubations or washes are needed) and will be integrated on the DEC.*

Figure 9 demonstrates amplicons with the lateral flow strip, showing PCR products from the amplified *Salmonella* DNA.

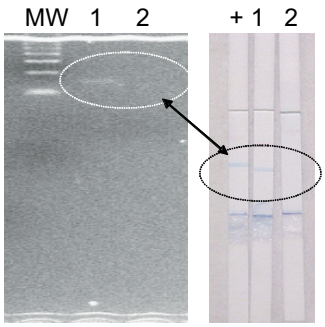

Figure 9: Gel and strip detection of Salmonella amplicon *(MW = Molecular weight control; 1 = amplified on card template, 2 = on card no template control, + = thermocycler template control.*

5) Dry Reagent Storage: On-card dry reagent storage will enable the use of the DEC system without refrigeration for reagents and disposables. In addition, it will remove the need for external, bulky, liquid reagents (except for stable aqueous resuspension and driving fluid resevoirs). To determine the feasibility of the reagent drydown and resuspension process, three different reagent classes have been studied: 1) antibody coated magnetic beads for pathogen capture, 2) lysis buffer for extraction of nucleic acids from the pathogens, and 3) amplification of DNA by polymerase chain reaction (PCR).

Several methods to stabilize proteins already exist and are widely used in industry. These methods use trehalose, a non-reducing disaccharide, which forms a glassy state above room temperature. The protein is protected against degradation and crystallization because low molecular mobility in the glassy state **[23]**. The native state of the protein is thought to be maintained largely because of the substitution of the waters of hydration of protein by sugar molecules during drying **[24]**. However all these methods use freezedrying. A novel method to control dissolution of preserved biomolecules in a microfluidic device has been previously studied in which enzyme is preserved in a trehalose-dextran matrix at elevated temperatures.

The preservation method has been tested for the reagents for immunocapture, lysis, and for the PCR master mix.

Bead preservation: Tosyl-activated magnetic beads of 1 µm diameter (Dynal Biotech LLC) were covalently linked with antibodies to *E. coli* (Abcam) according to the supplier's instructions. The beads were suspended in buffer containing varying concentrations of trehalose (5-20% w/v) and trehalose-dextran (1:1). Ca. 0.1 mg of beads in 20 µL of volume were spotted on a Mylar membrane and dried in an oven at 37 ° C under 15-18% humidity conditions. Resuspension was studied in a flow channel constructed with Mylar around the bead spot. Antibody-coated magnetic beads retained their ability to capture *E. coli* after resuspension from dehydrated state. The beads aggregated as is evidenced by SYTO 9 staining of the bacteria (Figure 10).

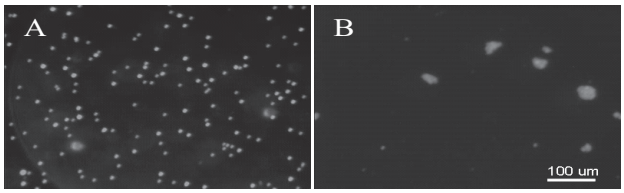

Figure 10. 10a *shows magnetic beads after resuspension from dehydrated state.* ***10b*** *shows SYTO 9-stained E. coli captured by the magnetic beads.*

Lysis buffer preservation: The buffer reagent for lysis of the pathogens as part of the nucleic acid extraction subcircuit does not contain molecules that need protection from harsh conditions. However, in the dry form the lysis buffer crystallizes, which may be undesirable for incorporation into small channels of a microfluidic device. The addition of trehalose formed a matrix; but only 40% trehalose concentration produced a nearly complete glassy matrix (Figure 11).

Lysis buffer containing 4.5 M guanidinium thiocyanate, 50 mM MES, pH 5.5, 20 mM EDTA, 1 % N lauroyl sarcosine and 5 % Triton X100 were prepared containing varying amount of trehalose (0-40% w/v). About 10 µl of buffer were spotted on to Mylar membrane and dried (37 ºC, 15-18% humidity).

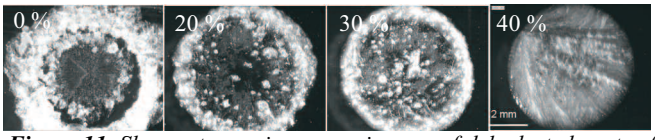

Figure 11. *Shows stereomicroscope images of dehydrated spots of lysis buffer in varying concentration of trehalose (w/v).*

Resuspension of the dehydrated buffer demonstrated no difference in the presence or absence of trehalose. The crystals readily re-solubilize, and the buffer successfully lysed the bacteria. No colony-forming units were detected on agar plates.

PCR master-mix preservation: PCR master mix (ThermoScript™ Plus Platinum Taq mix from Invitrogen) containing dNTPs, polymerase enzyme, *Salmonella* Primer mix (Vanilla) and buffer were prepared and dissolved in equal volume of varying concentration of trehalose to give a final concentration of 0, 10, 15 and 20% (w/v). The master mix was pipetted into polystyrene wells of a 96-well plate and dried (37ºC, 15% humidity) for varying intervals. After drying, the master mix was rehydrated with water. Ca. 1 x 10^5 CFU/µL DNA template (*Salmonella*) was added and the sample loaded on to the PCR subcircuit card. PCR was performed using the TEC prototype. After an initial denaturation at 90ºC for 1.0 min, 35 cycles of amplification were performed with denaturation (90ºC 8s), annealing (50ºC for 10s) and elongation (6 ºC for 12s). Amplified DNA was electrophoresed in 3% agarose, ethidium-stained, and viewed under UV illumination.

The PCR master mixes retained their activity after storage in a trehalose matrix (Figure 11). A 70 bp amplicon was detected after PCR of the resuspended samples. Absence of trehalose resulted in loss of enzyme activity within 24h and formation of primer-dimers. The functionality of the master mix could be preserved even after 28 days.

Figure 12. Ethidium bromide-stained DNA in agarose gel after PCR of trehalose preserved master-mix. 12A *shows a 70 bp amplicon in lane 2 (positive control) and corresponding amplicon in lane 4-5 of samples preserved in 10, 15 and 20% trehalose respectively for 24h. Lane 7: sample without trehalose during dehydration and shows primer-dimer formation. Lane 1: 50 bp DNA ladder, and lane 3 is negative control (no DNA template).* ***12B*** *shows 70 bp amplified product after 28 days of dry preservation (lanes 4-6 corresponding to 10, 15 and 20 % trehalose respectively). Lane 3 is positive control.*

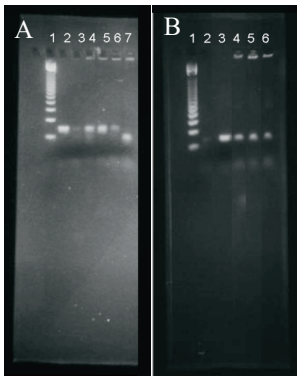

CONCLUSIONS

We have demonstrated the functionality of each subcomponent of the DEC system. We have demonstrated selective antibody capture for all target organisms directly from stool. We have shown pathogen lysis and nucleic acid extraction and capture on microfluidic cards. We have demonstrated PCR at the required sensitivity on microfluidic cards rapidly (8 minutes). We have shown that reagents needed for immunocapture, lysis, and DNA amplification by PCR for pathogen detection can be stored in trehalose matrix in dry form and retain their activity upon reconstitution. In the future all of these components will be incorporated into a microfluidic platform, an on-chip device, for point-of care diagnostic systems. Finally, we have shown detection of amplification products on lateral flow strips. Current work is directed towards integration and field validation.

REFERENCES

[1] R. A. Guerrant, T. Van Gilder, T. S. Steiner, N. M. Thielman, L. Slutsker, R. V. Tauxe, T. Hennessy, P. M. Griffin, H. DuPont, R. B. Sack, P. Tarr, M. Neill, I. Nachamkin, L. B. Reller, M. T. Osterhol, M. L. Bennish, L. K. "Pickering. Infectious Disease Society of America Guidelines. Practice Guidelines for the Management of Infectious Diarrhea", *Clinical Infectious Diseases,* 32, 3 (2001) pp. 331-351.

[2] United States Food and Drug Administration Center for Food Safety and Applied Nutrition. *Foodborne Pathogenic Microorganisms and Natural Toxins Handbook,* January 2002.

[3] World Health Organization. "Guidelines for the Control of Epidemics due to *Shigella dysenteriae* type 1", WHO/CDR/95.1.

[4] T. J. Torok, R. V. Tauxe, R. P. Wise, J. R. Livengood, R. Sokolow, S. Mauvais, K. A. Birness, M. R. Skeels, J. R. Horan, L. R. Foster. "A large community outbreak of salmonellosis caused by intentional contamination of restaurant salad bars", *Journal of American Medical Association,* 278, 5 (1997) pp. 389-395.

[5] S. A. Kolavic, A. Kimura, S. L. Simons, L. Slutsker, S. Barth, C. E. Haley. "An outbreak of *Shigella dysenteriae* type 2 among laboratory workers due to intentional food contamination", *Journal of American Medical Association,* 278, 5 (1997) pp. 396-398.

[6] H. Karch, M. Bielaszewska. "Sorbitol-fermenting Shiga toxin-producing Escherichia coli O157:H(-) strains: epidemiology, phenotypic and molecular characteristics, and microbiological diagnosis", *J Clin Microbiol.* Review, 39, 6 (2001) pp. 2043-9.

[7] S. I. Tu, D. Patterson, C. Briggs, P. Irwin, L. Yu. "Detection of immunomagnetically captured *Escherichia coli* O157:H7 by antibody-conjugated alkaline phosphatase", *Journal of Industrial Microbiology & Biotechnology,* 26, 6 (2001) pp. 345-349.

[8] C. Gilbert, D. Winters, A. O'Leary, M. Slavik. "Development of a triplex PCR assay for the specific detection of *Campylobacter jejuni*, *Salmonella* spp., and *Escherichia coli* O157:H7", *Molecular and Cellular Probes,* 17, 4 (2003) pp. 135-138.

[9] NIAID Category A, B & C Priority Pathogens. http://www.niaid.nih.gov/biodefense/bandc_priority.htm (accessed October 2003).

[10] Centers for Disease Control and Prevention. Summary of Notifiable Diseases-United States, (2001). *Morbidity and Mortality Weekly Report,* published May 2, 2003 for 2001/Vol. 50/No. 53.

[11] Centers for Disease Control and Prevention. "Outbreaks of *Escherichia coli* O157:H7 Infection and Cryptosporidiosis Associated with Drinking Unpasteurized Apple Cider-Connecticut and New York", October 1996. *Morbidity and Mortality Weekly Report,* 46, 01 (1997) pp. 4-8.

[12] A. Hatch, A. E. Kamholz, K. R. Hawkins, M. S. Munson, E. A. Schilling, B. H. Weigl, P. Yager. "A rapid diffusion immunoassay in a T-sensor", *Nature Biotechnology,* (invited review article), 19, 461 (2001).

[13] B. H. Weigl, P. Yager, "Microfluidic diffusion-based separation and detection", *Science*, 15, (1999) pp. 346-347.

[14] K. J. Halle, J. J. Li, M. S. Munson, J. Monteith, E. Guzman, S. Feather, J. Verba, Q. Porter, V. Kenning, A. E. Kamholz, B. H. Weigl, P. Saltsman, R. Bardell, P. Yager. "Capture and release concentration of bacteria using free-flow-zone electrophoresis." In: Harrison DJ and van den Berg A. eds. *Micro Total Analysis Systems*, Dordrecht: Kluwer Academic Publishers (2003).

[15] B. H. Weigl, C. J. Morris, N. Kesler, C. F. Battrell, R. L. Bardell. "Standard and high-throughput microfluidic disposables based on laminar fluid diffusion interfaces", In: Bornhop DJ, Dunn DA, Mariella DP Jr., et al, eds. *Biomedical Nanotechnology Architectures and Applications,* [Proceedings of SPIE v 4626] (2002) pp. 421-428.

[16] P. Jandik, B. H. Weigl, N. Kessler, J. Cheng, C. J. Morris, T. Schulte, N. Avdalovic. "Initial study of using laminar fluid diffusion interface for sample preparation in HPLC", *Journal of Chromatography A.* 954 (2002) pp. 33-40.

[17] B. H. Weigl, R. L. Bardell, T. H. Schulte, C. F. Battrell, J. Hayenga. "Design and rapid prototyping of thin-film laminate-based microfluidic devices", *Biomedical Microdevices,* 3, 4 (2001) pp. 267-274.

[18] B. H. Weigl. "New assays and separations based on laminar fluid diffusion interfaces—results from field trials for cell analysis, HTP screening, and medical diagnostics." In: Harrison DJ, van den Berg A, eds. *Micro Total Analysis Systems*, Dordrecht: Kluwer Academic Publishers (2002).

[19] C. F. Battrell, J. Hayenga, R. Bardell, C. Morris, P. Graham, N. Kesler, C. Lancaster, T. Schulte, B. H. Weigl, P. Saltsman, M. Shen. "Cell lysing and cytometry in an integrated microfluidic card system." In: Harrison DJ, van den Berg A, eds. *Micro Total Analysis Systems,* Dordrecht: Kluwer Academic Publishers (2002).

[20] T. H. Schulte, R. L. Bardell, B. H. Weigl. "Microfluidic technologies in clinical diagnostics", [invited review article]. *Clinica Chimica Acta.* 321, 1-2 (2002) pp. 1-10.

[21] B. H. Weigl, R. L. Bardell, C. R. Cabrera. "Lab-on-a-chip for drug development", [invited review article]. *Advanced Drug Delivery Reviews*, 55, 3 (2003) pp. 349-377.

[22] J. C. Gerdes. "Self-contained cartridge integrating nucleic acid extraction, amplification and lateral flow detection", *J Clinical Ligand Assay*, 20 (1997) pp. 70-72.

[23] K. Izutsu, S. Yoshioka, T. Terao. "Effect of mannitol crystallinity on the stabilization of enzymes during freeze-drying", *Chem Pharm Bull,* (Tokyo). 42, 1, (1994) pp. 5-8.

[24] J. H. Crowe, L. M. Crowe, J. F. Carpenter and C. Aurell Wistrom. "Stabilization of dry phospholipid bilayers and proteins by sugars", *Biochem J,* 242 (1987) pp. 1-10

IMPEDANCE BASED BIOSENSOR WITH DIELECTROPHORESIS CONCENTRATION FOR CARDIAC MYOCYTE HYPERTROPHY SENSING

Mo Yang[1], Chee Chew Lim[1], Ronglih Liao[2] and Xin Zhang[1]
[1]Boston University and [2]Brigham and Women's Hospital, Harvard Medical School, Boston, MA, USA

ABSTRACT

Cardiac hypertrophy is an established and independent risk factor for the development of heart failure and sudden cardiac death that may be regulated by growth factor such as Endothelin-1 (ET-1). The majority of existing techniques to monitor hypertrophy *in vitro* is based on florescence probes designed to show morphological and biochemical alterations indicative of cardiomyocyte hypertrophy [1]. In this paper, a new cardiomyocyte-based impedance sensing system with the assistance of dielectrophoresis (DEP) cell concentration is developed to monitor the dynamics process of ET-1 induced cardiomyocyte hypertrophy. This device can increase the sensitivity of the impedance system and also has the potential to reduce the time for detection by a significant factor.

INTRODUCTION

Cardiac hypertrophy is an established and independent risk factor for the development of heart failure and sudden cardiac death [2] [3]. At the level of individual cardiac myocytes, the cell morphology alters (increase in cell size and myofibrillar re-organization) and protein synthesis is activated [4] [5]. Since cardiac hypertrophy plays such a crucial role in many diseases such as myocardial infarction and arrhythmia, a new bio-analytical assay is expected to monitor hypertrophy in cultured cardiac myocytes non-invasively and in real time.

Using microfluidic chip to perform cellular studies on cardiac myocytes is currently a major interest due to its desirable characteristics. Werdich *et al*. reported a method to study single cardiac myocytes by recording the extracellular potential using planar microelectrodes in sub-nanoliter volume [6]. Klauke *et al*. developed a PDMS microfluidic chip to study the contraction of a single cardiomyocyte by electrical stimulation [7].

In this paper, a new cardiomyocyte-based impedance sensing system with the assistance of dielectrophoresis (DEP) cell concentration is developed to monitor the dynamic process of Endothelin-1 (ET-1) induced cardiomyocyte hypertrophy. A DEP microfluidic device is fabricated capable of concentrating cells from a dilute sample to form the cell monolayer with tight junctions. This device can increase the sensitivity of the impedance system and also has the potential to reduce the time for detection by a significant factor. Studies herein are carried out to examine the feasibility of this impedance sensing system for ET-1 induced cardiac myocyte hypertrophy. An equivalent circuit model is introduced to fit the impedance spectrum to fully understand the impedance sensing system.

DESIGN AND FABRICATION

In this task, glass microscope slides (2 in × 3 in, Fisher Scientific) were covered with a layer of positive photoresist (AZ 5214) by means of a spin-coater with 4000 rpm; the resist was then hardened at 100°C for 6 min on a hot plate. After baking, the photoresist was patterned with a mask aligner using an exposure dose of 10 mW for 20s, and subsequently developed by AZ 400 MIF developer (1:3) for 35s. After this step, the glass slides were cleaned by DI water and dried by nitrogen. The first metal layer for the DEP electrodes was deposited by sputtering of aluminum and patterned by lift-off to create the DEP electrodes. Then a thick layer of silicon dioxide was deposited by plasma enhanced chemical vapor deposition (PECVD) to completely isolate the DEP electrodes. Windows were defined in the PECVD oxide layer using conventional lithography and opened by reactive-ion-etching to access the bond pads on the first metal layer. Subsequently, the second metal layer, which serves as measurement electrodes, was deposited by sputtering 800 Å over a chromium adhesion layer and patterned by lift-off. The glass slide with microelectrodes was sealed with a custom made silicone chamber which has inlet and outlet tubes. An HP 33120A arbitrary waveform generator was used as the ac signal source to produce sinusoidal signal with a frequency specified at 2 MHz. Images were collected using a Nikon microscope with and without fluorescence filters and recorded by a charge-coupled device (CCD) digital camera (Pixera Penguin 600 CL, Pixera Corp., Los Gatos, CA). Figure 1 shows the cross section of the packaged device and the bioprocessor.

EXPERIMENTAL DETAILS

All fluids were injected into the chips using motor-driven micropump. The flow rate in the main channel of the bioprocessor was controlled by adjusting the pressure applied at the injector. The flow rate through the incubation chamber was controlled by applying a back-pressure at the chamber output using pressurized nitrogen. In this biochip, external valves at the input and output tubes were used to isolate the chip from the injection system during incubation. While in the bioprocessor, all the microbore tubes leading into and out of the chip were manually pinched to achieve isolation.

Experiments with this biochip were performed with it mounted onto a custom-made heated platform with a built-in RTD temperature sensor. Electrical connections to the chips were established by using probes mounted on micromanipulators attached to the heated platform. Experiments with the bioprocessor were done with the chip carrier mounted on the stage of a Nikon Eclipse E600 epi-florescence microscope (Nikon USA Corp., Melville, NY). During all the experiments, a computer controlled the temperature of the chips to be within ±0.2°C or better using the readings from the off RTD sensors, depending on the chip being used, to adjust the power delivered to the heaters on which the chips were mounted. The chip stages were completely enclosed to keep air drafts from disturbing the temperature.

The impedance of the electrodes in the chip was measured with an Agilent 4284A LCR meter (Agilent Technologies Inc., CA) connected to the chip through an Agilent 16048A BNC test fixture. All of these instruments were connected to a computer through a GPIB interface. The impedance measurement process was controlled by Labview (National Instruments Corp.) virtual instruments. The impedance of interdigitated electrodes was measured at 52 frequencies logarithmically spaced between 100 Hz and 1 MHz. with a 50-mV voltage excitation. Sinusoidal DEP signals were generated by an Agilent 33120A function generator.

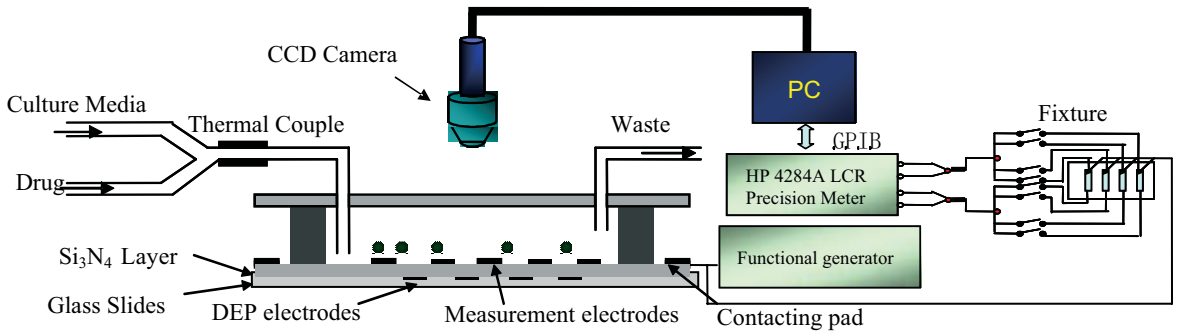

Figure 1. *Simplified cross section of impedance based biosensor system with dielectrophoresis concentration.*

All the experiments were performed with the bioprocessor heated to (37±0.1) °C. The cells suspended in PC-1 serum free media were injected at an input flow rate of ~ 1.4 µL/min, with the capture electrodes excited with a 2 V_{pp} sinusoidal signal at 2MHz (conductivity adjusted to 5 mS/m by addition of DI water). During injection, the flow rate in the incubation chamber was manually controlled to be between 4 and 10 nL/min. Flow rate control was performed manually by adjusting the pressure applied to the bioprocessor based on the observed velocity of the cells in the channels. After the whole 40 µL of sample had been forced through the bioprocessor the flow was stopped, the DEP capture electrodes were turned off, and a solution of DMEM-M199 (4:1) was injected at a flow rate of less than 0.5 µL/min. As the meida in the chamber was replaced by DMEM-M199 (4:1), the excitation voltage on the capture electrodes was increased to 3.5 V_{pp} and the frequency to 3MHz to maximize the DEP forces acting on the cells. After pinching the tubes, the impedance measurement process was started and the cells were incubated for a minimum of 24h. When a reference measurement was desired, cells were injected only into one of the two devices in a bioprocessor, where the other device received DMEM-M199 (4:1) only. The device with DMEM-M199 (4:1) provided baseline impedance in the absence of any metabolic activity.

RESULTS AND DISCUSSION

The impedance spectrum of this system can be represented by an equivalent circuit shown in Fig. 2. In this circuit, the resistor R_s is mainly due to the conductivity of the bulk solution and the wire connection whereas the Z_{CPE} represents the dielectric properties of the electrode/electrolyte and surface morphological information. R and C are the resistance and the capacitance of the layer of the absorbed proteins. R_c and C_c are elements related to the cell layer. The model presented here is derived from a physical analysis of the simplest electrochemical processes taking place at the interface and is thus bound to better represent the phenomena being measured [7]. In addition, fitting the model to impedance values at a large number of frequencies over a large range makes the measurement more sensitive. Such fitting essentially concentrates small changes in the impedance at each frequency point into larger changes in a small number of parameters that might have some physical relevance.

The impedance spectra derived from equivalent circuits composed of ideal elements, like capacitors and resistors, do not fit the measured spectra in a satisfactory way because of the inhomogeneity of the surface. To overcome this problem, it is possible to replace the ideal elements by constant-phase elements (CPEs) Z_{CPE} which account for the nonlinearities and the frequency of the elements. This is the simplest model that would properly fit the measured data over the whole frequency range and at all times during incubation.

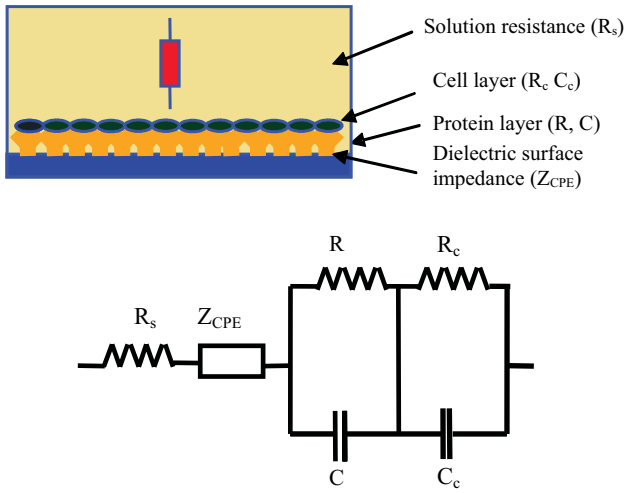

Figure 2*. Equivalent circuit for analysis. R_s is mainly due to the conductivity of the bulk solution and the wire connection whereas Z_{CPE} represents dielectric properties of the electrode/electrolyte and surface morphological information. R and C are the resistor and the capacity of the layer of the absorbed proteins. R_c and C_c are elements related to the cell layer.*

The first biochip was used to perform preliminary tests of the impedance technique with live cells incubated inside the chip. Suspensions of different concentrations of cardiac myocytes were injected into the chip and incubated in an on-chip temperature around 37°C for more than 24 hours.

Figure 3 compares the first and last impedance spectrum recorded in this experiment in two-dimensional representation. The open circle (o) represents the frequency dependant impedance spectrum before the cardiomyocyte monolayer was exposed to 100 nM ET-1 addition (t= 0h) whereas the square (□) corresponds to the impedance spectrum of the same electrode after the cells were exposed to the 100 nM ET-1 and experienced the ET-1 induced cell morphology change (t= 4h). As apparent from Fig. 2 the difference in the total impedance between vital and hypertrophy cells passes a maximum at roughly 4 kHz indicating that impedance readings at this frequency are most sensitive to the associated changes in cell morphology.

Figure 4 shows the change in impedance over time using DEP concentration method for the two cardiomyocyte cases: 4.6×10^3 cfu/mL and 5.3×10^4 cfu/mL. It clearly shows that DEP method dramatically increases the impedance amplitude which is related to the increased cell numbers on the impedance microelectrodes.

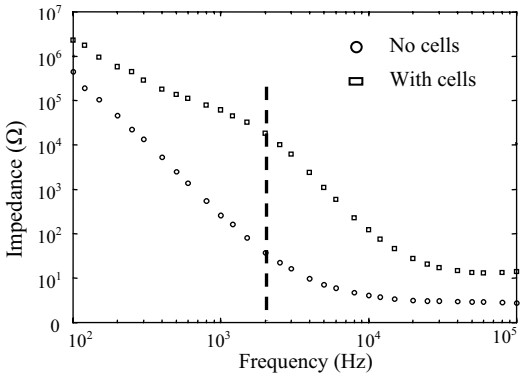

Figure 3. *The first and last impedance spectrum recorded in this experiment in two-dimensional representation.*

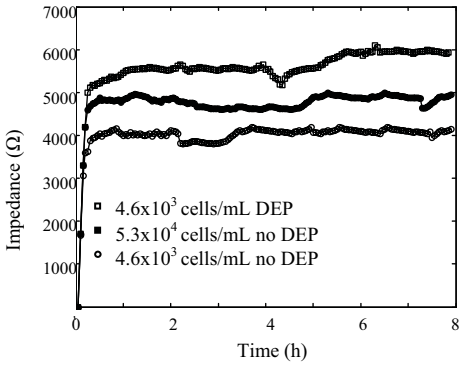

Figure 4. *DEP assisted cell concentration. As can be seen, DEP method dramatically increases the impedance amplitude.*

To assess the effects of ET-1 on the extent of cell-substrate adhesion, we monitored changes in cell-substrate resistance after the addition of ET-1. Typical results are shown in Fig. 5a. The extent of cell-substrate adhesion is expressed as "normalized" resistance, which was defined as a ratio of the resistance to the initial value before addition of ET-1. The addition of 100 nM induces a rapid increase in impedance after an initial lag phase of around 0.3h. Within 3 hours the impedance magnitude approaches the saturation value. To get a quantitative measure for the dynamics of ET-1 induced changes we determined the time necessary for half-maximum reduction of the impedance at 4 kHz (t_{Z50}). The analysis shows that the mean value of 20 similar time courses is around 1.7 ± 0.2 h. ET-1 induced a significant increase in normalized resistance, indicating strengthening of the cell-substrate adhesion at 4 h after addition of ET-1 (Fig. 5b).

Since focal adhesion kinase (FAK) has been reported to play an important role in ET-induced hypertrophy such as promoting sarcomere assembly, we compared the time course of the impedance change with the time course of FAK activation upon ET-1 exposure. Fig. 5c traces the activity of FAK before and several hours after exposing the cells to 100 nM CHX. Comparing with Fig. 5a, we can see that that even very small and clearly sub-maximum levels of FAK activity is with large changes in impedance. After 2h of ET-1 exposure FAK activity amounts to less than 55% of its final value while the impedance of the cell layer at 4 kHz has already increased for more than 80% of its total change indicative of more sensitivity of our impedance assay.

The effect of DEP concentration on the impedance spectrum with the addition of ET-1 is also explored for two cases: 4.6×10^3 cfu/mL and 5.3×10^4 cfu/mL (Fig. 6). The impedance spectrum on the concentration of 5.3×10^4 cfu/mL is treated as the baseline. The sample at concentration of 5.3×10^4 cfu/mL injected without the

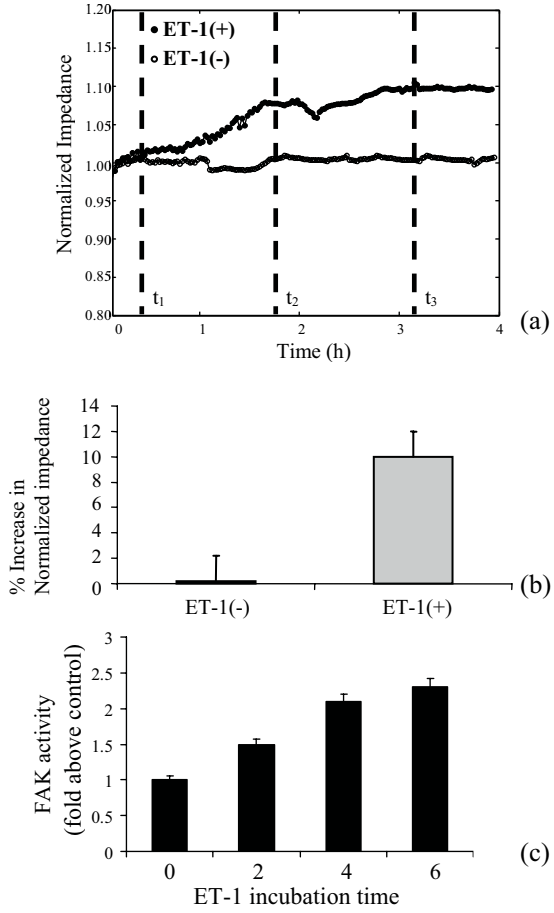

Figure 5. *Effects of ET on adhesion of cardiac myocytes to the Extracellular Matrix (ECM). After starvation for 12 hours, they were stimulated with ET-1 (nM). (a) Typical tracing representative of four replicate experiments. In all these experiments, initial resistance of cardiac myocytes was within the range of 3000 to 5000 Ω. To simplify the comparison, ordinate represents normalized. (b) Comparison of percentage increase in normalized resistance at 4 hours after addition of ET-1, ET(+), with control ET(-). Results shown are mean ± SD from four independent experiments. (c). Focal adhesion kinase (FAK) activity as function of ET-1 incubation time.*

DEP-based concentration system active increased the impedance amplitude by 10% corresponding to a cell size increase due to ET-1 addition. On the other hand, for the sample at relatively low concentration of 4.6×10^3 cfu/mL injected with the concentration system active, a very strong hypertrophy signal with the impedance amplitude increase of 18% was visible during the first hour of incubation. The DEP cell concentration method clearly increased the cell number on the impedance detection microelectrodes, the sensitivity of hypertrophy detection and made the low concentration sensing possible for very dilute cell suspensions.

To correlate this variation of impedance to cardiac myocyte behavior, the fitting procedure with the previous equivalent circuit, defined without ET-1, is applied to impedance variation as a function of ET-1 concentration. Values of R_s, Z_{CPE}, R and C remain constant in the equivalent circuit while values of R_c and C_c components vary as a function of ET-1 concentration as shown in Fig. 7. The error bars include the experimental error on impedance

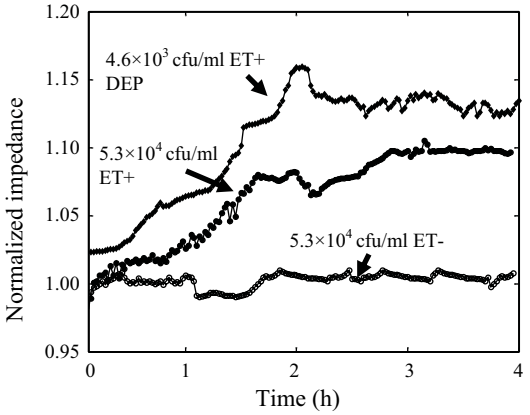

Figure 6. *Normalized impedance of cardiac myocytes injected into the bioprocessor at various concentrations, with and without the DEP-based concentration system active, plus sterile KB. Values at t=0 are defined as 100%.*

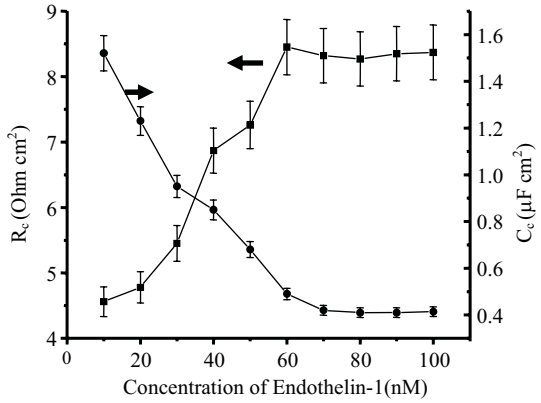

Figure 7. *Equivalent circuit parameter shows the correlation of variation of impedance to cardiomyocyte behavior. Here, R_c and C_c are parameters related to the cell layer.*

measurements and the discrepancy of experimental values related to the equivalent circuit model. As shown in Fig. 4, the cell layer resistance R_c changes from 4.52 Ω cm^2 to 8.43 Ω cm^2 due to cardiac myocyte hypertrophy, with an increase by 86.50% and the capacitance C_c change from 1.52 μF cm^2 to 0.41 μF cm^2. The general evolution of R_c and C_c is indicative of the effect of ET-1 on cardiomyocyte morphology and a saturation effect is observed for both components for concentration higher than 60 nM which corresponds to the saturation effect on the experimental curve.

CONCLUSIONS

In this paper, a new cardiaomyocyte-based impedance sensing system with the assistance of dielectrophoresis cell concentration was developed to monitor the dynamics process of Endothelin-1 induced cardiomyocyte hypertrophy. When cultured *in vitro* cardiac myocytes are up to 20×100 μm in size and can form close contacts to the substrate. Both of these characteristics are favorable for the development of high seal resistances. Thus, they make an excellent choice for impedance studies where a large cellular size compared to the extracellular electrode diameter is desirable. Furthermore, when cultured at the appropriate densities, cardiac myocytes develop cytoplasmic bridges (gap junctions) between cells to form moncellolayers in culture. These tight junctions help inhibit cell movement, thereby deceasing the mobility of cardiac myocytes *in vitro.* For this purpose, a dielectrophoresis microfluidic device is fabricated capable of concentrating cells from a dilute sample to form a cell monolayer with tight junctions. This device can increase the sensitivity of the impedance system and also has the potential to reduce the time for detection by a significant factor. Studies herein were carried out to examine the feasibility of this impedance sensing system for ET-1 induced cardiac myocyte hypertrophy. An equivalent circuit model is introduced to fit the impedance spectrum to fully understand the impedance sensing system.

ACKNOWLEDGEMENTS

This work is supported in part by the National Science Foundation CAREER Award (DMI-0239163). The authors would like to thank all the other members at the Boston University Laboratory for Microsystems Technology and the Cardiovascular Institute at Boston University School of Medicine and Brigham and Women's Hospital, especially Dr. Douglas B. Sawyer for his technical advice.

REFERENCES

[1] Y. Fukuda, Y. Hirata, S. Taketani, T. Kojima, S. Oikawa, H. Nakazato, and Y. Kobayashi, "Endothelin stimulates accumulations of cellular atrial natriuretic peptide and its messenger RNA in rat cardiocytes," *Biochem. Biophys. Res. Commun.*, 164, 1431–1436 (1989).

[2] D. Levy, R. J. Garrison, D. D. Savage, W. B. Kannel, and W. P. Castelli, "Prognostic implications of echocardiographically determined left ventricular mass in the Framingham Heart Study," *N. Engl. J. Med.*, 322, 1561–1566 (1990).

[3] H. Ruskoaho, "Atrial natriuretic peptide: synthesis, release and metabolism," *Pharmacological Reviews,* 44, 479-602 (1992).

[4] B. H. Lorell, B.A. Carabello, "Left ventricular hypertrophy. Pathogenesis, detection, and prognosis," *Circulation*, 102, 470–479 (2000).

[5] M. E. Diane, B. S. James, G. Geetha, L. Jueren, L. B. Kenneth, and M. S. Allen, "Endothelin-induced cardiac myocyte hypertrophy: role for focal adhesion kinase," *Am. J. Pysol. Heart Circ. Physiol.*, 278, H1695–H1707 (2000).

[6] A. A.Werdich, E. A. Lima, B. Ivanov, I. Ges, M. E. Anderson, J. P. Wikswo, and F. J. Baudenbacher, "A microfluidic device to confine a single cardiac myocyte in a sub-nanoliter volume on planar microelectrodes for extracellular potential recordings," *Lab on a chip*, 4, 357–262 (2004).

[7] C. Tlili, K. Reybier, A. Geloen, L. Ponsonnet, C. Martelet, H. B. Ouada, M. Lagarde, and N. Jaffrezic-Renault, "Fibroblast cells: a sensing bioelement for glucose detection by impedance spectroscopy," *Anal. Chem.*, 75(14), 3340–3344 (2003).

IN-DROPLET PARTICLE SEPARATION BY TRAVELLING WAVE DIELECTROPHORESIS (twDEP) AND EWOD

Yuejun Zhao[a], Ui-Chong Yi[b], and Sung Kwon Cho[a*]
[a]Department of Mechanical Engineering, University of Pittsburgh
Pittsburgh, PA 15261, USA
[b]Core Microsolutions Inc.
Los Angeles, CA 90024, USA

ABSTRACT

This paper describes successful particle separations within a droplet by traveling wave dielectrophoresis (twDEP) and consecutive droplet splitting by electrowetting-on-dielectric (EWOD). This in-droplet method will provide a new functionality of separation and concentration for digital (droplet-based) microfluidics [**1**], thereby possibly eliminating the necessity of adopting the conventional microchannel-based separation methods.

INTRODUCTION

There are currently high demands for means to efficiently manipulate and discriminate bio entities in microfluidics [**2**, **3**]. To date, numerous systems have been developed to meet these demands. However, most of them are based on continuous flows which basically require complicated micro channel networks, consequently raising the cost of design and fabrication and lowering the reliability of operation. Recently, in the mean time, digital (droplet-based) microfluidics [**1**] (in particular operated by electrowetting-on-dielectric (EWOD)) successfully demonstrated various fluidic operations, obviating the above drawbacks. A large number of individual minute droplets carrying bio samples can be manipulated (created, transported, split, and mixed) in parallel on a two-dimensional (2-D) surface, with no need to build any micro channel structures. Furthermore, all of these operations can be accomplished under digital control from a programmable controller, promising tremendous potential for chemical and biologic analysis [**4**].

However, the implementation of bio sample concentration and separation in digital microfluidics is still challenging since most of the previously developed concentration and separation methods essentially rely on long micro channels (e.g. micro capillary electrophoresis). Therefore, simply adopting the conventional concentration and separation methods into digital microfluidics requires constructing microchannel networks, as a result deteriorating the original strength of digital microfluidics. Most recently, with a motivation to realize concentration and separation in digital microfluidics without microchannels, Cho and Kim [**5**] presented an in-droplet particle separation and concentration control by using electrophoresis in a droplet configuration. However, this technique exclusively works only with electrically charged particles, limiting its application for non or weakly charged particles.

On the contrary, dielectrophoresis (DEP) [**6**] accesses a wide range of particle characteristics by changing the frequency of the applied electric field and by using different suspending media. In DEP particle separations, particles to be separated need no charge treatments. In particular, traveling wave dielectrophoresis (twDEP), originally described by Masuda *et al* [**7**, **8**], that uses a traveling electric field with numerous electrodes allows long distance transportations of various particles. Therefore, this principle has currently been developed into a comprehensive technique for manipulating and separating various particles and cells [**9**-**12**]. To our knowledge, however, dielectrophoretic particle separations have rarely or never been successfully implemented in digital (droplet-based) microfluidics. Hence, in this paper, we implement twDEP particle separations within a droplet and furthermore integrate them with follow-up EWOD droplet splitting, thereby eliminating any possibility of particle dispersion posterior to separation.

CONCEPT

Figure 1 illustrates sequential procedures of the proposed in-droplet particle separation: (1) initial state with a droplet containing mixed particles (Fig. 1(a)); (2) transportation of target particles (shown as black) into the right edge of the droplet by twDEP (Fig. 1(b)); (3) droplet splitting by EWOD (Fig. 1(c)); (4) final state (Fig. 1(d)). For twDEP particle separation, four spiral electrodes (Fig. 4(a)) placed on the bottom plate are used to generate a traveling electric field. Then they are switched for grounding when EWOD is on for droplet splitting (Fig. 1(c)). Meanwhile, three transparent electrodes placed on the top plate are used for the EWOD droplet splitting. The left and right electrodes (except the middle one) are activated to elongate and split the droplet (Fig. 1(c)). For improved separation precision, multiple droplets with the same particle type can be re-joined and may go through further separation in the next stage.

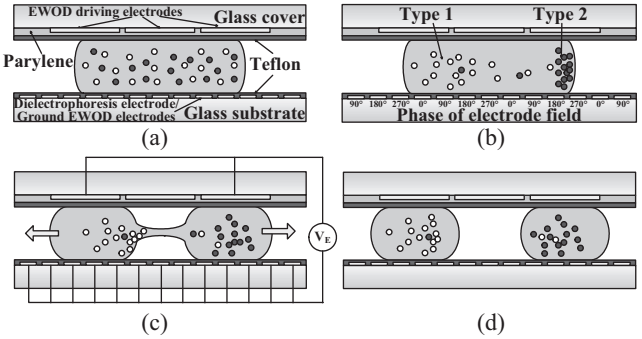

Figure 1. *The schematic of particle separation procedures in a droplet: (a) A droplet containing mixed particles is placed between two parallel plates; (b) under the traveling wave dielectrophoresis (twDEP) generated by the bottom electrodes, target particles (type 2, black) are transported and concentrated on the right side; (c) under the electrowetting-on-dielectric (EWOD) force generated by the top electrodes, the droplet is split into two daughter droplets; (d) finally two types of particles are separated into respective two daughter droplets.*

FABRICATION OF TESTING DEVICES

The testing devices that mainly consist of two parallel plates (top and bottom) were fabricated using standard lithographic micro

fabrication technology. The bottom plate fabrication includes two steps: metallization and patterning of twDEP electrodes and deposition of the hydrophobic layer. For the twDEP electrodes, a

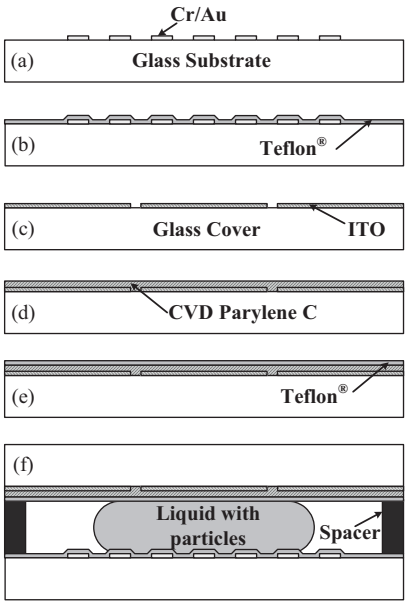

Figure 2. *Fabrication process flow of testing devices: (a) deposition and patterning of electrodes (Cr/Au) on bottom glass; (b) spin-coating of Teflon® AF; (c) Top glass cover with patterned ITO layer; (d) Deposition of parylene layer by CVD and patterning; (e) Spin-coating of Teflon® AF layer; (f) Putting the droplet containing particles and integration of the top and bottom plates with a spacer in between.*

chromium layer of 100 Å in thickness as an adhesion layer and a gold layer of 1000 Å in thickness were sequentially deposited on a glass wafer by sputtering and then patterned by wet etching into parallel electrodes of 10 μm width and 10 μm spacing. The bottom plate was finally coated with a hydrophobic Teflon layer. Spin-coating of 2% Teflon solution (Teflon AF 1600® + Fluorocarbon solvent) resulted in a 2000 Å thick Teflon layer. The main fabrication process on the top plate consists of three steps: patterning of EWOD electrodes, deposition and patterning of the dielectric layer, and deposition of the hydrophobic layer. For the driving electrodes, an ITO (Indium Tin Oxide) layer was patterned by wet etching. Then, a 2 μm parylene layer as a dielectric layer was deposited using a vapor deposition method (Specialty Coating Systems: PDS-2010 LABCOTER® 2), followed by opening of the parylene layer on electrode pads by physical scratching in order to transmit activation signals to each driving electrode. Finally, the top plate was also spin-coated with the hydrophobic Teflon layer.

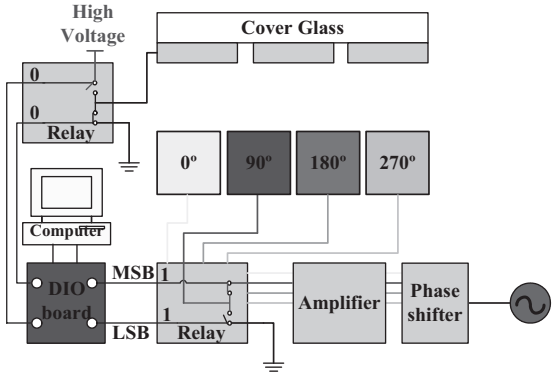

Figure 3. *Schematic of activation signal flows.*

The last step of the fabrication process is to integrate the two plates (Fig. 2(f)). After putting a droplet containing particles on the bottom plate, the top cover plate was gently pressed against the spacers that were already placed on the bottom plate. The clean room tape was used for the spacers, making the channel gap at 70 μm that allows successful droplet splitting based on the design rule [**1**].

Figure 3 illustrates how to generate EWOD/twDEP signals. The whole system consists of a personal computer, a digital output board (DAQPad-6507, National Instrument), a custom-made phase shifter, amplifier and interface circuit mainly containing photo-coupled relays (PhotoMos®, AQW614EH, Aromat Co.). A PC-based program generates control signals transmitted through a digital I/O board. The control signals switch the relays through which a 90˚ shift traveling wave is transmitted to the bottom plate electrodes and EWOD activation voltages to the top plate electrodes on the testing devices.

EXPERIMENT RESULTS

As a first step, we tested particle transportation and concentration in a droplet using a single type of particle (5-μm aldehyde sulfate (AS) beads). A traveling wave of 90º phase shift to the adjacent electrodes is generated with a four spiral electrodes design. To avoid multi-layer wiring, a spiral type was used, as shown in Fig. 4(a). Note that the droplet is largely placed on the area of parallel electrodes, not touching the center of the spiral electrodes. Before twDEP actuation, 5-μm aldehyde sulfate (AS) beads (seen as white dots) are initially uniformly suspended in the droplet; under the twDEP wave (10 kHz, 10 Vp-p) almost all the particles move to the right region of the droplet (Figs. 4(b) and (c)).

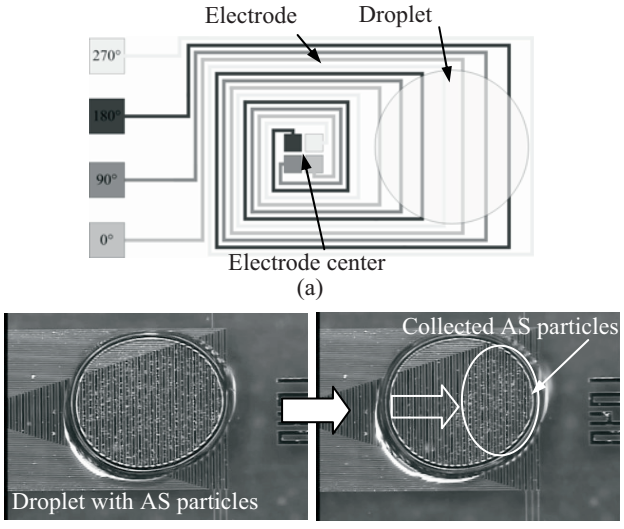

Figure 4. *Top views of transportation of particle of single type into the right side of the droplet: (a) Electrodes design; (b) Before twDEP actuation, 5 μm aldehyde sulfate (AS) beads are uniformly suspended in the droplet; (c) Almost all the particles move to the right region of the droplet under the twDEP wave (10 kHz, 10 Vp-p).*

Next, twDEP particle separations are performed in the following three different mixture cases: (case 1, Fig. 5) 8-μm glass beads and 5-μm AS beads; (case 2, Fig. 6) 8-μm glass beads and ground pine spores (GPS); (case 3, Fig. 7) 5-μm AS beads and 10-μm CML beads.

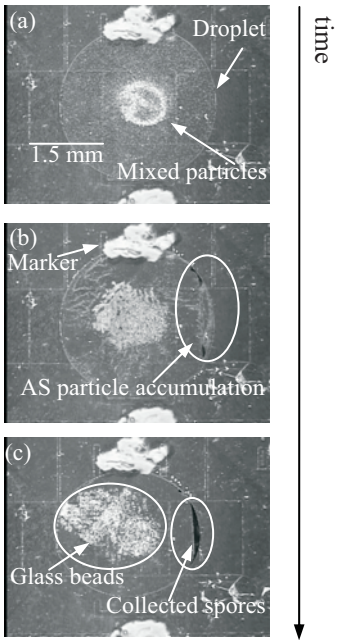

Figure 5. *Sequentially captured pictures of particle separation (case 1). 8-μm glass bead (seen as white) and 5-μm blue-dyed aldehyde sulfate (AS) beads (seen as black) are initially mixed (a) and then separated under a twDEP wave of 800 kHz and 15 Vp-p (b, c).*

Figure 5 shows the sequentially captured pictures of particle separation for case 1. Initially 8-μm glass beads (seen as white) and 5-μm blue-dyed aldehyde sulfate (AS) beads (seen as black) are mixed in the droplet as shown in Fig. 5(a). The AS particles are moving to the right edge of the droplet under 800 kHz and 15 Vp-p while the glass beads are circulating and overall a little bit pushed to the left; After several minutes almost all the AS (seen as black) particles are collected in the right edge of the droplet as shown in Figs. 5 (b) and (c). Note that the white makers were intentionally placed to help to position the droplet.

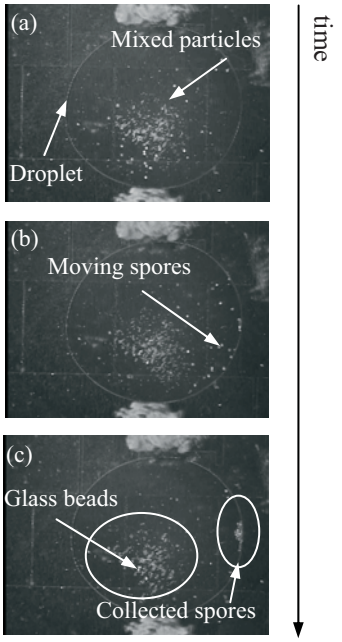

Figure 6. *Sequentially captured pictures of particle separation (case 2). Lycopodium powder (Ground Pine Spores or GPS seen as big white dots) and glass beads (seen as small white dots) are mixed (a) and then separated under a traveling wave of 800 kHz and 20 Vp-p (b, c).*

Figure 6 shows the sequential pictures of spore separation for case 2. Similar to case 1, successful separation was achieved. Before separation, Lycopodium powder (Ground Pine Spores or GPS seen as big white dots) and glass beads (seen as small white dots) are mixed in the droplet as shown in Fig. 6(a). The spores are moved to the right under 800 kHz and 20 Vp-p while the glass beads are a little bit pushed to the left; After several minutes the spores are collected at the right edge of the droplet as shown in Figs. 6 (b) and (c).

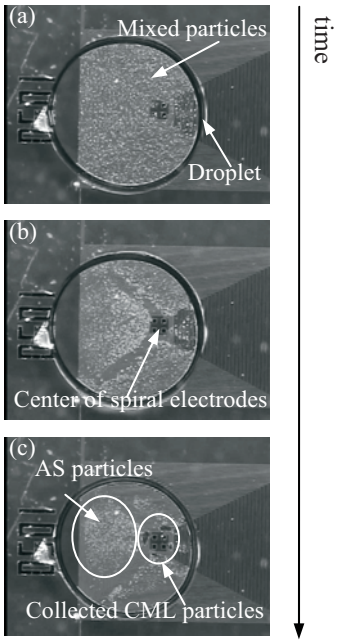

Figure 7. *Sequentially captured pictures of particle separation (case 3). 5-μm aldehyde sulfate (AS) beads (seen as white) and 10-μm CML (seen as black) particles are mixed.*

Figure 7 shows the sequentially captured pictures of particle separation for case 3. Initially 5-μm aldehyde sulfate (AS) beads (seen as white) and 10-μm CML (seen as black) particles are mixed in the droplet as shown in Fig. 7(a). The CML (black) particles are moving to right region (the center of the spiral electrodes) under 50 kHz and 4 Vp-p while the AS beads (white) are circulating as shown in Fig. 7(b). After several minutes CML (black) particles are collected in the right area while the AS beads (white) suspends in the left region as shown in Fig. 7(c). Note that the droplet is positioned such that the center of the spiral electrodes is placed inside the droplet contour, differently from the cases in Figs. 4, 5, and 6. As a consequence, the CML beads (black) are collected near the center of the spiral electrodes while cases 1 and 2 show target particle collections in the right edge of the droplet since the droplet largely covers the area of parallel electrode pattern (not the center of the electrodes). This means that the target particle collection region can be controllably positioned within a droplet depending on where the droplet is placed on the spiral electrodes.

Lastly, figure 8 shows particle separation and subsequent droplet splitting. Initially 8-μm glass beads (seen as big white dots) and 5-μm blue-dyed aldehyde sulfate (AS) beads are mixed in the mother droplet as shown in Fig. 8(a). AS particles (seen as small

white dots) are moving to the right side of the droplet under 800 kHz and 15 Vp-p while the glass beads are circulating and overall a little bit pushed to the left as shown in Fig. 8(b). Splitting function by EWOD (1 kHz and 150Vp-p) makes the droplet physically divided into two daughter droplets. After splitting, the left droplet is glass beads rich while the right one is AS beads rich as shown in Figs. 8(c) and (d). This splitting step enables to eliminate particle dispersion problems after completing the separation.

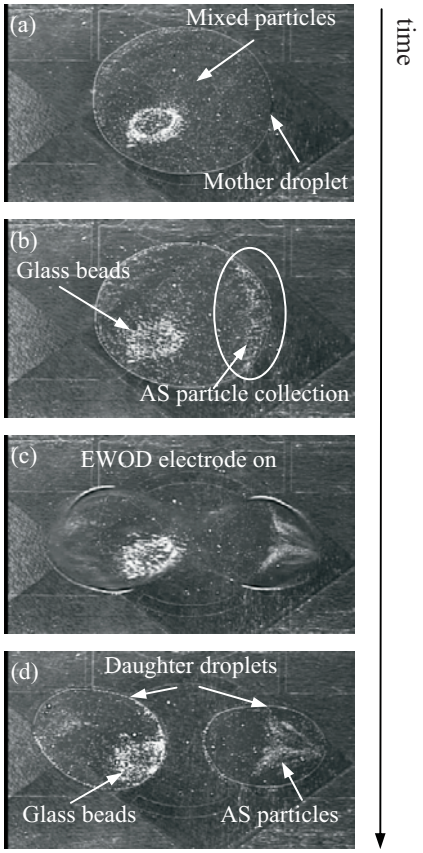

Figure 8. *Sequentially captured pictures of particle separation and droplet splitting. 8-μm glass beads (seen as big white dots) and 5-μm blue-dyed aldehyde sulfate (AS) beads (seen as small white dots) are mixed, then separated by twDEP (800 kHz and 15 Vp-p), and finally secured in each daughter droplet produced by EWOD splitting process.*

CONCLUSIONS

This paper describes successful twDEP (traveling wave dielectrophoresis) particle separations in droplet configurations and subsequent droplet splitting. 5 different cases of particle combinations have been examined and their successful concentration and separation have been experimentally demonstrated. Furthermore, subsequent EWOD droplet splitting was successfully integrated, securing separated particles in each produced daughter droplet. This splitting step enables to essentially avoid particle dispersion problems that otherwise would deteriorate the separation efficiency posterior to the separation. This integrated in-droplet separation method will provide a new functionality of separation and concentration for digital (droplet-based) microfluidics, thereby possibly eliminating the necessity of adopting the conventional microchannel-based separation methods.

REFERENCES

[1] S. K. Cho, H. Moon, and C.-J. Kim, "Creating, Transporting, Cutting and Merging of Liquid Droplets by Electrowetting-Based Actuation for Digital Microfluidic Circuits," *Journal of Microelectromechanical Systems*, *12*, 1, pp. 70 - 80 (2003).

[2] P. R. C. Gascoyne, and J. V. Vykoukal, "Particle Separation by Dielectrophoresis," *Electrophoresis, 23,* pp. 1973 - 1983 (2002).

[3] C. H. Kua, Y. C. Lam, C. Yang, and K. Youcef-Toumi, "Review of Bio-particle Manipulation Using Dielectrophoresis," *Innovation in Manufacturing Systems and Technology*, (2005). http://hdl.handle.net/1721.1/7464

[4] P. R. C. Gascoyne, and J. V. Vykoukal, "Dielectrophoresis-Based Sample Handling in General-Purpose Programmable Diagnostic Instruments," *Proceedings of the IEEE*, *92*, 1, pp. 22 - 42 (2004).

[5] S. K. Cho, and C.-J. Kim, "Particle Separation and Concentration Control for Digital Microfluidics Systems", *MEMS 2003 Conference*, Kyoto, Japan (2003), pp. 686 - 689.

[6] H. A. Pohl, *Dielectrophoresis: The behavior of neutral matter in nonuniform electric fields*, Cambridge University Press, Cambridge, New York (1978).

[7] S. Masuda, M. Washizu, and M. Iwadare, "Separation of Small Particles Suspended in Liquid by Non-uniform Travelling Field," *IEEE Transactions on Industry Applications, 23*, pp. 474 - 480 (1987).

[8] S. Masuda, M. Washizu, and I. Kawabata, "Movement of Blood Cells in Liquid by Non-uniform Travelling Field," *IEEE Transactions on Industry Applications, 24*, pp. 217 - 222 (1988).

[9] M. P. Hughes, R. Pethig, and X. B. Wang, "Dielectrophoretic Forces on Particles in Travelling Electric Fields," *Journal of Physics D: Applied Physics*, *29,* pp. 474 - 482 (1996).

[10] H. Morgan, N. G. Green, M. P. Hughes, W. Monaghan, and T. C. Tan, "Large-area Travelling-wave Dielectrophoresis Particle Separator," *Journal of Micromechanics and Microengineering, 7,* pp. 65 - 70 (1997).

[11] P. R. C. Gascoyne, C. Mahidol, M. Ruchirawat, J. Satayavivad, P. Watcharasit, and F. F. Becker, "Microsample Preparation by Dielectrophoresis_Isolation of Malaria," *Lab Chip, 2,* pp. 70 - 75 (2002).

[12] L. M. Fu, G. B. Lee, Y. H. Lin, and R. J. Yang, "Manipulation of Microparticles Using New Modes of Traveling-Wave-Dielectrophoretic Forces: Numerical Simulation and Experiments," *IEEE /ASME Transactions on Mechatronics, 9,* 2, pp. 377 - 383 (2004).

METAL-CORED CARBON MICROPOSTS FOR THREE-DIMENSIONAL LI$^+$ MICROBATTERY

Fardad Chamran, Ui-Chong Yi, and Chang-Jin "CJ" Kim
Mechanical and Aerospace Engineering Department, University of California, Los Angeles

ABSTRACT

We have designed, fabricated and tested a novel carbon electrode for three-dimensional (3D) lithium-ion microbattery applications. This structure consists of an array of high-aspect-ratio carbon posts (> 15:1) with nickel metal embedded in their core. Carbon was prepared by pyrolyzing parylene precursor in an inert environment at high temperature. Proper reversible capacity was observed during charge and discharge of lithium ion in a half-cell battery setup. The initial results suggest that this half cell battery can be post-processed to form a full 3D lithium ion battery with high energy density at high discharge rates.

INTRODUCTION

Microbatteries based on 3D architecture offer the opportunity to overcome the energy and power deficiencies of conventional thin-film batteries when limited to small foot-print areas [**1,2**]. Different types of 3-D architectures including nano-scale aerogel electrodes and micron size post electrodes have recently been reviewed [**2**]. Full secondary (rechargeable) 3D nickel-zinc [**3**] as well as lithium-ion [**4**] microbatteries have already been demonstrated. Lithium ion batteries have drawn serious attractions in the past few years due to their high energy densities. Different types of carbonaceous materials have been extensively used as anodes in commercial lithium ion batteries [**5**]. Recently, electrode post arrays of carbon have been fabricated by molding them in silicon template [**6**] or by pyrolysis of photoresist [**7,8**] to be used as the anode electrode in 3D Li-ion batteries. The main drawback of these carbon rods, however, is the loss of energy density at high discharge rates [**2,7**] due to the semi-conducting behavior of the carbon and high ohmic potential losses along the length of the post. The novel electrode structure that we introduce here circumvents this effect by placing a metal core (nickel in this report) inside the active carbon material (Fig. 1).

DESIGN

To provide enough active carbon and increase the energy density of the electrode on a given footprint area, it is necessary to increase the aspect ratio of the post structure. On the other hand, this high energy is inaccessible at high discharge rates due to the excessive ohmic losses in the high aspect ratio post array [**2**]. Our 3D electrode structure presented here is designed in a way that minimizes the overall internal resistance of the carbon post structures. Fig. 2a schematically depicts the previously introduced carbon post [**7**], and Fig. 2b is the structure introduced here for the first time. The nickel post inside each rod effectively extends the current collector into the carbon. Any point on the high surface area anode directly communicates to the nickel current collector without having to go through a large volume of the carbon and minimizes the overall ohmic potential drop at high discharge rates. Parylene has been previously used as the precursor for making carbon and the mechanical and electrical properties of pyrolyzed parylene have been measured [**9**]. The intercalation and deintercalation of lithium ion in pyrolyzed parylene is investigated in this report for the first time. Its benzene rich structure and conformal deposition on surfaces with high topographical variations makes it a suitable choice of polymer precursor to fabricated carbon for our design.

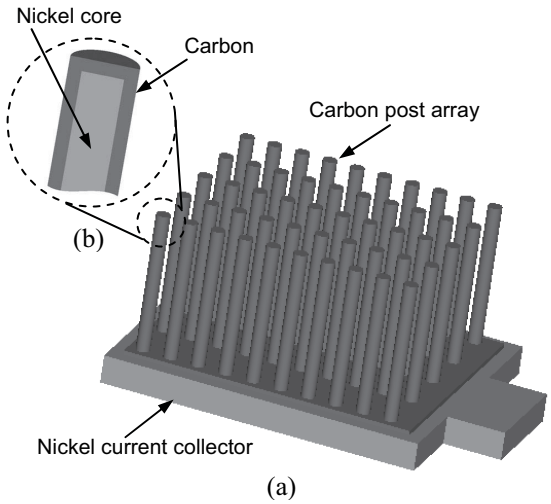

Fig. 1 Schematic of carbon post electrode array with metal in its core. (a): overall, (b): cross-section of a post

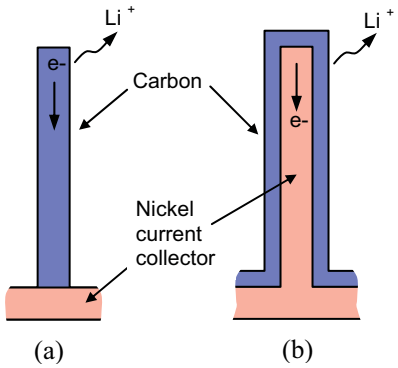

Fig. 2 Schematic of deintercalation of Li-ion in carbon post anode during discharge. (a): Previously reported carbon post suffers from the high potential drop along the slender carbon post at high discharge rates. (b): Our design of carbon post has minimized potential drop through its metal core, while maintaining the carbon as the anodic material

FABRICATION

Two types of samples were fabricated. The first type was flat and representing a conventional 2D thin film carbon electrode. Thermal oxide was first grown on silicon substrate as the passivation layer. Parylene-C was then deposited on the sample using CVD and pyrolyzed at 1000°C in the furnace during argon gas

flow to form the carbon. The second type of the samples was fabricated by conformal deposition of parylene over nickel post array and subsequent pyrolysis to form carbon. Fig. 3 shows the detailed fabrication process. Silicon was etched in step 1, using the method of either DRIE or photo-assisted anodic etching, to form an array of high-aspect-ratio holes as the electroplating mold [**6**]. In step 2 the backside was etched using RIE to make the through holes. It was followed by thermal oxidation to passivate the silicon for the following metallization steps.

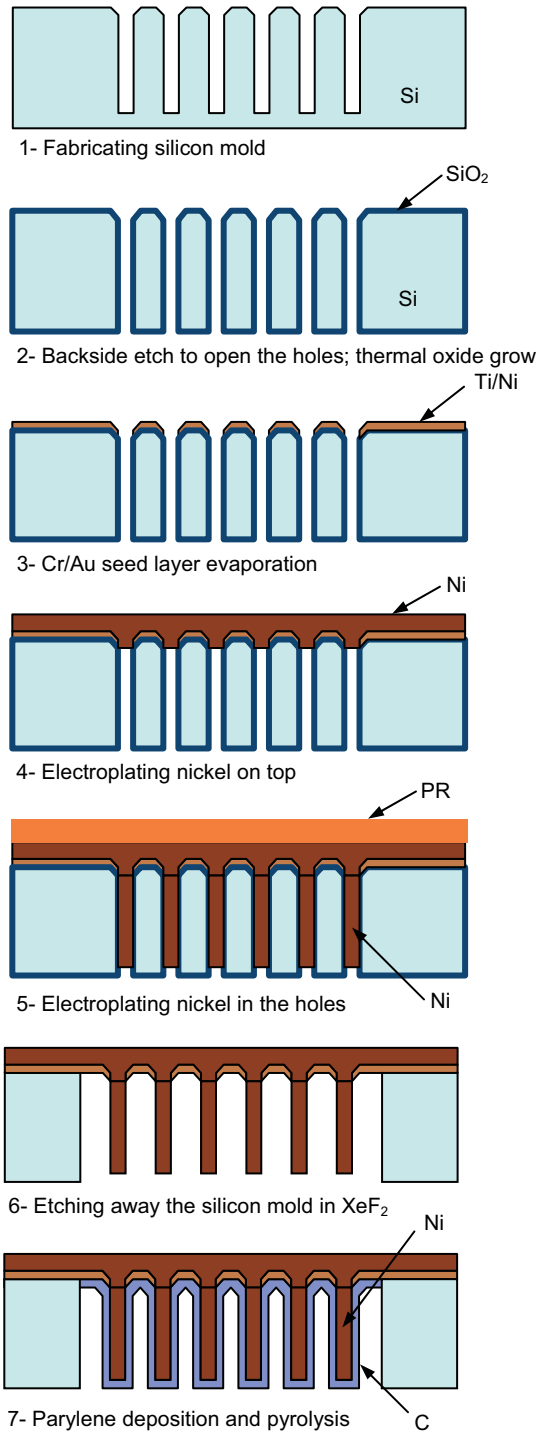

Fig. 3 Fabrication of carbon-coated nickel micropost array

In step 3, Ti/Ni (100/1000Å) seed layer was evaporated. Ni was electroplated at 10mAh/cm^2 in step 4 using nickel sulfate electroplating solution to seal the holes at the top side of the substrate. In step 5, nickel was electroplated in the holes using the top-side nickel as the seed layer. Nickel was electroplated at constant current density of 5 mA/cm^2. Photoresist was applied to passivate the top side from being electroplated during this step. In step 6, the oxide and silicon were etched away using BOE and XeF_2, respectively, to expose the nickel post array. In step 7, parylene-C was conformally deposited on the nickel posts using CVD. As the final step it was pyrolyzed into carbon in the furnace and during argon gas flow at 1000°C. Temperature increase and cooling down rate was set to 1°C /min.

Fig. 4 is the SEM image of a silicon mold fabricated by anodic etching of n-type silicon in 5% HF during backside illumination. Fig. 5 corresponds to step 6 of the process, showing the nickel posts before parylene deposition. The nickel posts are 10 µm in diameter and 170 µm tall. 5 µm of parylene-C was conformally deposited on the nickel posts. Fig. 6 is the SEM image of the final carbon posts. The thickness of the carbon is 1 µm. Fig. 7 is the SEM image of a sample prepared by using DRIE etched mold. 11.5 µm of parylene was deposited on the nickel posts. The diameter of each post is 60 µm and the height is 400 µm. The parylene pyrolyzed to 3.2 µm of carbon.

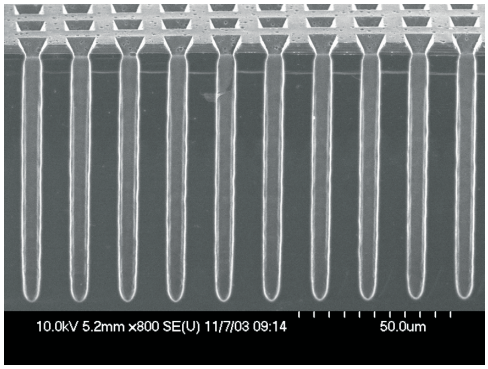

Fig. 4 Array of high aspect ratio holes in silicon, fabricated by anodic etching in HF during backside illumination

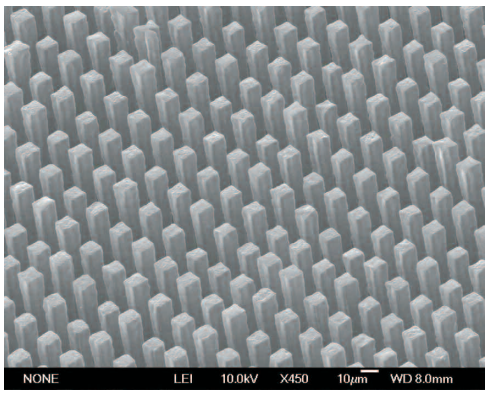

Fig. 5 Nickel post array before parylene deposition, corresponding to step 6 of the process

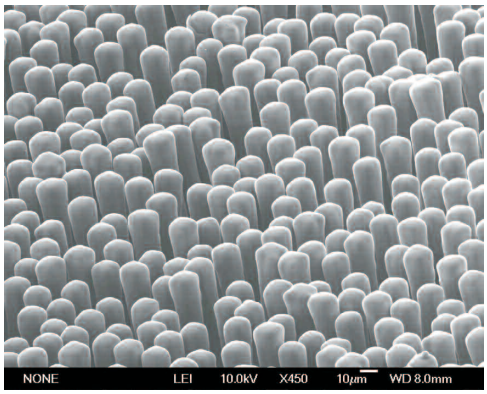

Fig. 6 Fabricated sample using anodic-etched silicon mold. Nickel posts are 10 μm in diameter and 170 μm tall, covered with 1 μm carbon

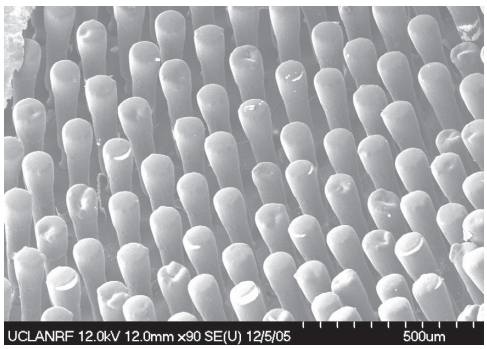

Fig. 7 Fabricated sample using DRIE-etched silicon mold. Nickel posts are 60 μm in diameter and 400 μm tall, covered with 3.2 μm carbon

EXPERIMENT

Resistivity of parylene-pyrolyzed carbon was measured at 0.015 Ω-cm on the flat sample using four-point probe. Electrochemical measurements were carried out for both type of flat and post array electrode. The electrolyte was 1 M $LiClO_4$ in a 1:1 volume mixture of ethylene carbonate (EC) and dimethyl carbonate (DMC). Two different types of cyclic voltammetry and galvanostatic charge-discharge tests were performed on the samples in an argon-filled glove box. Three-electrode system setup with lithium metals as the counter and reference electrodes was used for testing. As the first step, lithium ion was intercalated at 0.1 mA/cm^2 in a flat sheet of carbonized parylene. The thickness and area of the sample were 1 μm and 1 cm^2, respectively. The sample was electrically connected using an alligator clip at one corner. The results exhibited reversible intercalation/deintercalation of lithium with an areal capacity of 0.047 mAh/cm^2. This translates to gravimetric capacity of 235 mAh/g, which is in the range of reversible capacities reported for pyrolyzed SU-8 [**7**]. The micropost structures were tested in the subsequent experiments. Fig. 8 is the cyclic voltammetry of post array of Fig. 6, with 10 μm diameter and 170 μm high on 0.5 cm^2 footprint area. The electrode was cycled at 1 mV/s between 0.01 V and 2 V. The graph shows proper intercalation/deintercalation of lithium. Charge-discharge behavior of this structure was tested during galvanostatic test at two different discharge rates. Fig. 9 shows the galvanostatic charge-discharge measurements at 0.1 mA/cm^2 (the first cycle is not shown here due to its irreversible capacity). The lithium capacity of 0.75 mAh/cm^2 was observed at this discharge rate. Fig. 10 is the galvanostatic charge-discharge at 1 mA/cm^2 for the same structure. At this higher discharge rate a lower capacity of 0.16 mAh/cm^2 was observed. The lower aspect ratio structure of Fig. 7 was also tested for charge-discharge behavior. Fig. 11 shows the expected irreversible capacity loss on the first discharge. For the second and succeeding three cycles, the lithium capacity of 0.55 mAh/cm^2 was observed at discharge rate of 0.1 mA/cm^2.

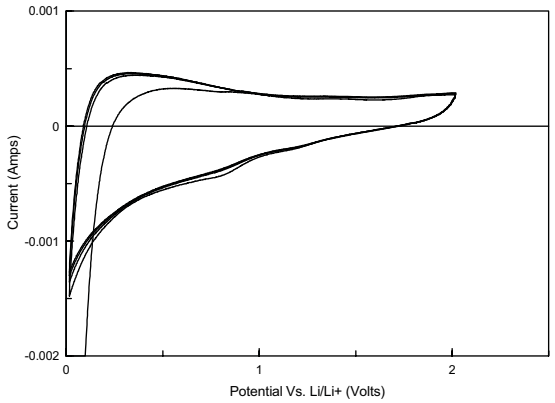

Fig. 8 Cyclic voltammetry scan curves at 1 mV/s for carbon post array of Fig. 6

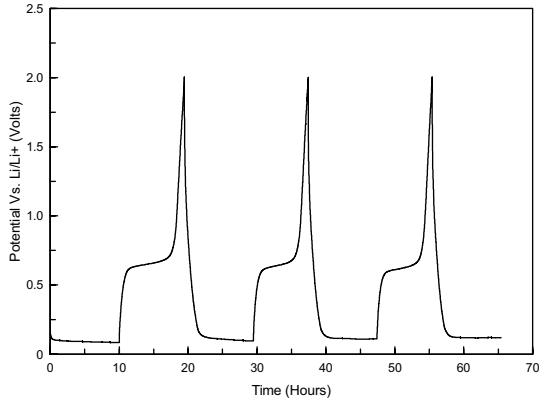

Fig. 9 Galvanostatic charge-discharge curves at 0.1 mA/cm^2 for carbon post array of Fig. 6

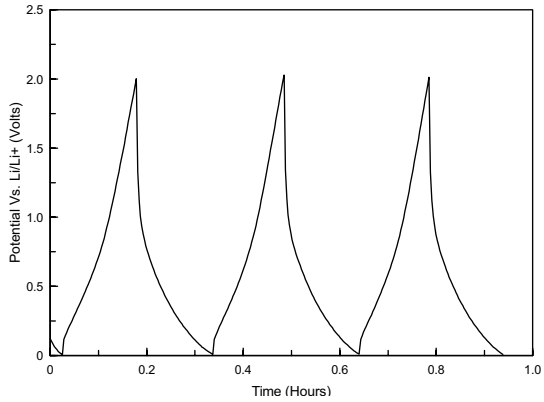

Fig. 10 Galvanostatic charge-discharge curves at 1 mA/cm^2 for carbon post array of Fig. 6

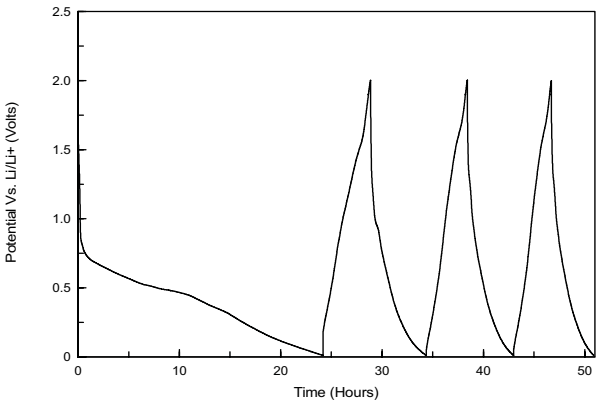

Fig. 11 Galvanostatic charge-discharge curves at 0.1 mA/cm^2 for carbon post array of Fig. 7

DISCUSIONS

It was observed that pyrolyzed parylene reversibly intercalates lithium ion and can be used as the anode material for rechargeable batteries. Comparing the lithium capacities for the flat sample and the post structure, high increase of stored energy was observed for the post structures. This is due to the increase in the surface area and the large volume of the active carbon material. The effect of the discharge rate on the lithium capacity was also tested for the post structures. By increasing the discharge rate from 0.1 mA/cm^2 to 1 mA/cm^2, only 1/5 of the capacity was accessed. This is suspected to be due the geometrical configuration of the half cell testing setup and not the ohmic potential losses. During our measurements, the 3D carbon electrode was placed in the electrolyte in front of a lithium sheet counter electrode, causing a high electric field concentration at the tip of the posts and much lower field at the bottom area of the posts. Due to this effect most of the insertion of lithium ions takes place at tip area, and lowers the active volume of the carbon. This effect will be eliminated when a full battery is made out of this half cell, by conformal deposition of thin electrolyte and the counter electrode. In this case, the electric field will be more uniform along the long post and high energy density lithium battery may be fabricated.

ACKNOWLEDGEMENTS

This work was supported by PowerMEMS Inc. and the Office of Naval Research (MURI grant N00014-01-1-0757). The authors appreciate the help and advice of Mr. Yuting Yeh and Prof. Bruce Dunn during electrochemical measurements.

REFERENCES

1. R. W. Hart, H. White, B. Dunn, and D. Rolison, "3-D Microbatteries", *Electrochemistry Communications*, **5** (2003), pp. 120-123.
2. J. W. Long, B. Dunn, D. Rolison, and H. S. White, "Three-Dimensional Battery Architectures," *Chemical Reviews,* **104** (2004), pp. 4463-4492.
3. F. Chamran, H.-S. Min, B. Dunn and C.-J. "CJ" Kim, "Three-Dimensional Nickel-Zinc Microbatteries," *Proceedings of IEEE International Conference on Micro Electro Mechanical Systems (MEMS'06)*, Istanbul, Turkey, Jan. 2006, pp. 950-953.
4. M. Nathan, D. Golodnitsky, V. Yufit, E. Strauss, T. Ripenbein, I. Shechtman, S. Menkin and E. Peled, "Three-Dimensional Thin-Film Li-Ion Microbatteries for Autonomous MEMS," *J. Electromechanical Systems*, **14, 5** (2005), pp. 879-885.
5. J. R. Dahn, T. Zheng, Y. Liu and J. S. Xue, "Mechanisms for Lithium Insertion in Carbonaceous Materials," *Sience*, **270** (1995), pp. 590-593**.**
6. F. Chamran, Y. Yeh, B. Dunn and C.-J. Kim, "Three Dimensional Electrodes for Microbatteries," *Proc. ASME Int. Mechanical Eng. Congress*, Anaheim, California, Nov. 2004, CD Vol. 2, IMECE2004-61925.
7. C. Wang, L.Taherabadi, G. Jia, M. Madou, Y. Yeh, and B. Dunn, "C-MEMS for the Manufacture of 3D Microbatteries," *Electrochemical and Solid State Letters*, **7** (2004), pp. A435-A438.
8. C. Wang, G. Jia, L. Taherabadi and M. Madou, "A Novel Method for the Fabrication of High-Aspect Ratio C-MEMS Structures," *J. Microelectromechanical Systems*, **14, 2** (2005), pp. 348-358.
9. S. Konishi, M. Liger, T. Harder and Y.-C. Tai, "Parylene-Pyrolyzed Carbon for MEMS Applications," *Proceedings of IEEE International Conference on MEMS (MEMS'04),* Maastricht, Netherlands. Jan. 2004, pp. 161-164.

MICRO-MRI VELOCIMETRY IN MICROCHANNEL NETWORKS

L. Guy Raguin, Dimitris C. Karampinos, and Sharon L. Honecker
Mechanical & Industrial Engineering Dept., University of Illinois
Urbana, Illinois USA

John G. Georgiadis
Mechanical & Industrial Engineering Dept. and the Beckman Institute, University of Illinois
Urbana, Illinois USA

ABSTRACT

We report here the first use of microscopic Magnetic Resonance Imaging (micro-MRI) velocimetry to quantify both the interstitial topology and the pressure-driven flow of water through an engineered microchannel network made from polydimethylsiloxane (PDMS) using a standard volume radio-frequency coil (7.6 cm ID). The multilayered PDMS microchannel network consists of two identical non-communicating capillary networks, each featuring 1.9-mm-deep and 0.9-mm-wide staggered channels forming a 10×8 periodic array. A multi-slice spin-echo sequence with 117 μm×156 μm in-plane resolution is employed to reconstruct the interstitial geometry of the network. The superiority of phase contrast micro-MRI velocimetry is demonstrated first in simpler microchannels, and then used to extract the two-dimensional velocity field in the complex microchannel network. The micro-MRI velocity measurements have a spatial resolution of 195 μm×254 μm and are accurate in terms of overall mass conservation to within 3% of the imposed flow rate.

INTRODUCTION

Given the complexity of the underlying physicochemical phenomena, the fabrication of microfluidic systems [**1-3**] needs be coordinated with the in-situ characterization of the function of their components. The majority of quantitative methods used to probe flow in microchannels rely on visible light, such as particle tracking techniques (e.g. micro-PIV [**4**]), infrared light (e.g. optical coherence tomography [**5**], or infrared PIV [**6**]). Despite the excellent spatial resolution, the ability to measure fluid velocity in topologically complex geometries remains limited, since such methods rely on optical penetration, matching the index of refraction in the field of view, and the introduction of tracer particles. Refraction index matching is impossible for non-planar or multiphase fluidic systems such as those found in endothelialized microvascular networks [**3**]. The seeding of particles in flows where multiple force fields are present, such as in electrokinetic flows, presents an additional challenge since these particles tend to become charged and diverge from streamlines, producing the so-called electrophoretic drift [**7**]). In addition, the extraction of the full velocity field in complex microflows via PIV requires high numerical aperture optics, which limits the depth of focus [**8**] and consequently decreases the optical penetration depth.

We propose the use of Magnetic Resonance Imaging (MRI) to characterize complex microfluidic devices fabricated with polymeric materials. There have been earlier successful attempts to measure velocity in single microchannels with MRI [**9-10**] but they required specialized radiofrequency (RF) micro-coils, wrapped around the individual microchannel. The present work marks the first time that MRI employing standard volume RF coils, not integrated to the sample, is used to characterize single-phase flow through complex microchannel networks.

The closest systems to the microchannel network are 3-D lattices of packed particles with the interstitial space fully saturated with a liquid. One of the first systematic applications of MRI to characterize pressure-driven flow through such systems was reported by Shattuck et al. [**11-12**]. A number of average flow velocities comparisons between MRI velocimetry results and flowmeter measurements have been since reported for packed beds constructed by packing randomly spherical beads in a tube. Using pulsed-field-gradient MRI sequences and glass sphere beds, Deurer et al. [**13**] reported that MRI overpredicts the average velocity by 50%, while Ren et al. [**14**] reported that MRI overpredicts by 27% for 0.6-mm-spheres. Using phase-encoding MRI velocimetry, Bijeljic et al. [**15**] reported 2-D measurements in Stokes flow across aligned and staggered rows of millimeter-sized cylinders confined inside a Hele-Shaw cell but only qualitative statements about the interstitial velocity field were made. Moser [**16**] used phase contrast MRI to measure axial interstitial velocities in a packed bed made by randomly packing 3.175-mm-diameter spherical acrylic beads. Overall, the computed mass flow rate in each slice agreed with the flowmeter reading to within 5.3% -6.4% depending on the flowrate.

Since there are large discrepancies in the literature in terms of the accuracy of the various MRI velocimetry protocols, the search for the best protocol is conducted in simple microchannels, before we turn our attention to the complex microchannel network.

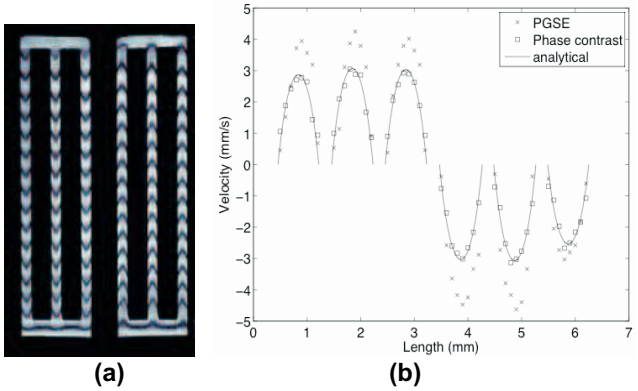

Figure 1. *Comparison of axial velocity profiles obtained from three micro-MRI velocimetry protocols. (a) Spin-tagging spin-echo marks flow in the simpler microchannel network; (b) pulsed-gradient spin-echo (PGSE) and phase contrast spin echo, in six parallel microchannels, for which an analytical solution is known.*

MRI VELOCIMETRY PROTOCOLS

Using stereolithography, a simple microchannel network was built featuring six parallel channels, each with a rectangular cross-section of approx. 750 μm × 850 μm. Water doped with copper

sulfate (T1/T2 = 0.25/0.22 s) flows in one direction inside three microchannels, and returns through the other three, cf. Figure 1(a). The fluid interconnects between the two sets of co-current flow channels are outside the slice shown in Figure 1(a). An analytical solution is available for the velocity profile of fully-developed channel flow [**17**]. MRI experiments were conducted using a wide-bore 14.1 Tesla vertical imaging system (Oxford Instruments, Abingdon, UK) with a gradient set (Resonance Research, Billerica, MA) capable of up to 90 G/cm in 0.1 ms, resulting in a clear bore of 46 mm. Three MRI velocimetry protocols are investigated: phase contrast spin-echo (PC-MRI [**18**]), pulsed-gradient spin-echo (PGSE [**19**]), and spin-tagging spin-echo (STSE [**20**]). For all three protocols, we used a field of view (FOV) of 1.6 cm × 2 cm with uniform in-plane resolution of 100 μm, and slice thickness of 1.2 mm.

Velocity fields were acquired flows with Re < 5. (Typically, Reynolds numbers are based on the channel width.) Figure 1(a) shows the STSE results (Re = 4), which provides a qualitative image of the flow. Figure 1(b) compares the velocity profiles inside the six channels measured using PGSE and PC-MRI (Re = 3.3) to the analytical solution averaged over the depth of the channels. Our preliminary results [**21**] indicate that for MRI velocimetry in microchannels, STSE provides good qualitative results but lacks in resolution, PGSE produces biased estimates because the velocity distribution is not symmetrical for the voxels at low resolution compared to the channel size, while the velocity measurements via PC-MRI provide the best agreement with the analytical solution.

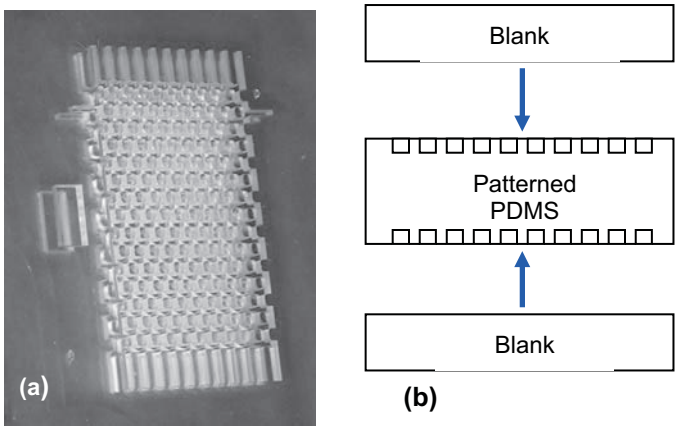

Figure 2. *Fabrication of the microchannel network: (a) Patterned central PDMS layer with capillary bed relief on both sides. (b)Flat layers bonded to form the microchannel network.*

MICROCHANNEL NETWORK

Figure 2 describes the fabrication of the test section consisting of two identical non-communicating capillary networks, each with two side ports to perform future infusion studies. Each capillary network features inter-connecting staggered channels forming a 10×8 periodic array. The PDMS layers were fabricated using variations of replica molding which involves pouring the PDMS prepolymer mixture (Sylgard 184, Dow Corning) over a master and curing it at 75°C for 12 hours. A novel two-sided mold was used to create the central patterned layer and the two blank layers were fabricated to a precise thickness using the molding process proposed by Jo et al. [**22**]. The two blank PDMS layers are bonded to the patterned PDMS layer after reactive ion etching pretreatment and the microchannels are connected via mm-sized tubes to fluid supply plenums fed by syringe pumps. Ultrasound waves were used to eliminate air bubbles from the network.

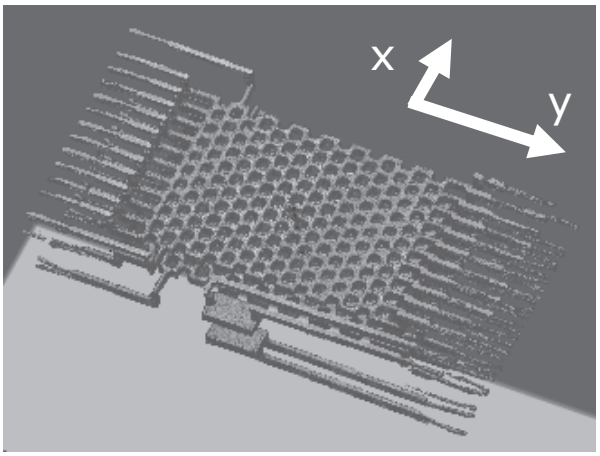

Figure 3. *Volumetric rendering of the water-filled spaces in the microchannel network via spin density MRI protocol. The signal corresponds to the local water density and therefore delineates the interstitial space occupied by water. The mean flow is along the y-axis. The x-axis corresponds to the phase-encoding, and the y-axis to the read-out directions for MRI.*

Figure 3 illustrates the use of micro-MRI to determine the critical (internal) dimensions of the microfluidic network. MRI experiments were conducted using a Varian 4.7 Tesla horizontal imaging spectrometer with Oxford ASG-26 gradients capable of up to 6.5 G/cm in 0.5 ms. The spatial resolution of the velocity measurement is 195 μm × 254 μm. This is the result of a compromise between imaging time and field of view (5 cm × 6.5 cm), given the RF coil inner diameter (7.6 cm) and maximum gradient strength available. For comparison, Zhang and Webb [**10**] achieved a resolution of 15.6 μm × 15.6 μm with their 3.2-mm-long RF coil wrapped around a single microchannel (800 μm OD).

MRI VELOCIMETRY

The microchannel network was fully flooded with a aqueous solution of copper sulfate to lower the relaxation time T1 to 1 s (instead of 3 s for deionized water), hence allowing for shorter repetition times (TR) and reducing the overall image acquisition time. Two sets of micro-MRI phase contrast velocimetry experiments were performed: the first to illustrate the advantages of correcting for partial volume effects, and the second to assess the quality of the velocity measurements by checking mass conservation along the mean flow direction of the microchannel network.

A 2-D velocity data set was acquired for a Reynolds number Re = 1 (volumetric flow rate Q = 54.8 ml/hr, average axial velocity in the axial channels of the network Uavg = 0.8 mm/s, with Re based on the single channel hydraulic diameter and Uavg) with a high spatial resolution: 256 data points are collected in both read-out and phase-encoding direction for a 5 cm × 6.5 cm FOV and a 3.25-mm slice thickness. This yields a spatial resolution of 195 μm in the phase-encoding direction (x-axis) and 254 μm in the read-out direction (y-axis). The data matrix is then zero-padded to 512 × 512. The bipolar gradients parameters are Gflow = 6.4 G/cm, tflow = 6 ms, resulting in a velocity sensitivity of K = 1.56 s/mm (maximum velocity encoded without inducing phase

wrapping Vmax=2mm/s). Using TE/TR = 44.7/3000 ms, the total acquisition time is 12 min 48 s per velocity component (Vx, Vy). A FORTRAN code was written to obtain a "virtual mask" for the velocity reconstruction and in order to study the partial volume effect due to the imaging method. The experimental data determine the FOV, the resolution and orientation of the microchannel network, and the code outputs a simulated amplitude image where each pixel takes a value from 0 to 1 representing the theoretical water content of the pixel. Since the microchannel network has an average porosity (or liquid volume fraction) of approximately 61.5%, we expect to observe a significant effect of the water/PDMS interface on the signal quality. A close-up of the velocity vectors is shown using an experimental mask (obtained by thresholding an experimental amplitude image) in Figure 4(a), and the same field processed by using our virtual mask are shown in Figure 4(b). The importance of the virtual mask is manifested when computing volumetric flow rates because of the experimental noise and inaccuracies introduced in the experimental mask caused by binary thresholding.

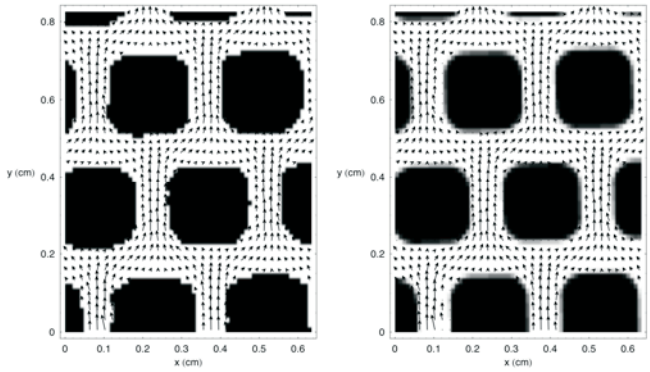

Figure 4. *Close-up of velocity vectors in the microchannel network obtained for Re = 1, using (left panel) an experimental mask (obtained by thresholding an experimental amplitude image), and (right panel) a numerically-obtained ``virtual'' mask.*

Given the spatial heterogeneity of the inlet flow, a readily available validation test of the MRI measurements is to verify that the amount of fluid circulated through the microchannel network is equal to that imposed by the syringe pump, i.e. to check the mass balance throughout the microchannel array. Both microchannel networks of the phantom are flooded and the two-dimensional velocity field is measured for Re = 1.5 (Q = 82.2 ml/hr, Uavg = 0.6 mm/s) with a high spatial resolution: 256 data points are collected in both read-out and phase-encoding direction. The 5 cm x 6.5 cm FOV is carefully chosen so that both networks are lined up one on top of the other and an 11-mm-thick slice is used to capture both networks in a single slice. Again, the data matrix is zero-padded to 512 × 512. The bipolar gradients parameters are Gflow = 5 G/cm, tflow = 7 ms, resulting in a velocity sensitivity of K = 1.61 s/mm (or a maximum velocity encoded without phase wrapping Vmax = 1.96 mm/s). Using TE/TR = 49/4000 ms, the total acquisition time is 17 min 4 s per velocity component (Vx, Vy). A virtual mask was computed based on the MRI amplitude images and applied to extract the velocity field inside the combined microchannel networks. The corrected volumetric flow rate, Qexp, normal to the (axial) y-direction is computed for each y location, as well as for each repeated cell in the periodic microchannel arrays in the axial direction. We find that Qexp then overestimates the volumetric flow rate (Q = 82.2 ml/hr) imposed by the syringe pump by 1% on average. Some deviations occur in regions of the microchannel networks where the flow direction varies from axial (y) to transverse (x) and the cross-sectional area expands by a factor of three. The volumetric flow rate averaged over each repeated cell of the microchannel networks is relatively constant (standard deviation < 3% of Q) indicating that the velocity measurements are self-consistent in that mass is conserved from cell to cell in the axial direction.

CONCLUSIONS

We report here the first use of MRI for the quantitative visualization of flow through arrays of interconnected microchannels, which are the standard elements in continuous-flow microfluidic devices **[1-3**]. This was accomplished by employing a regular sized volume RF coil, and choosing the phase contrast spin echo MRI protocol (PC-MRI). A systematic comparison of PC-MRI with other available MRI velocimetry techniques revealed the superiority of the former.

The present work supports the view that are several advantages inherent to the use of micro-MRI velocimetry to probe microfluidics. The use of a single platform and experimental setup for the extraction of both topological and velocimetry data is unique to MRI. It is also evident that flow measurements are completely non-invasive (no tracer particles or dyes are required), and that slice selection and penetration into the opaque device by MRI are unconstrained. This is not limited to PDMS, and it simply requires that the magnetic susceptibility gradients between the fluid and the solid material be minimized. MRI-compatible materials include the whole gamut of materials used in the fabrication of complex, multilayered, microfluidic networks [**1-3**]. In contrast to velocimetry techniques using optical microscopy, the field-of-view afforded by MRI can be arbitrarily oriented in 3-D space and it can encompass the full device, so no microscope stage repositioning is necessary during the imaging. Finally, it is worth mentioning that, by a simple change of imaging protocol, the same MRI set-up can be used to image quantitatively mass transport [**23**] in microfluidic devices or phantoms of biomedical significance.

ACKNOWLEDGEMENTS

The authors gratefully acknowledge the financial support by the NSF Center for Nanoscale Chemical-Electrical-Mechanical-Manufacturing Systems (Nano-CEMMS, award DMI-0328162), and the NSF Science and Technology Center of Advanced Materials for Purification of Water with Systems (The WaterCAMPWS, award CTS-0120978) in the University of Illinois at Urbana-Champaign (UIUC).

REFERENCES

[1] D. J. Beebe, G. A. Mensing, and G. M. Walker, "Physics and applications of microfluidics in biology," *Annu. Rev. Biomed. Eng.*, 4:261–286 (2002).

[2] H. A. Stone, A. D. Stroock, and A. Ajdari, "Engineering flows in small devices: microfluidics toward a lab-on-a-chip," *Annu. Rev. Fluid Mech.*, 36:381–411 (2004).

[3] M. Shin, K. Matsuda, O. Ishii, H. Terai, M. Kaazempur-Mofrad, J. Borenstein, M. Detmar, and J. P. Vacanti, "Endothelialized networks with a vascular geometry in microfabricated poly(dimethyl siloxane)," *Biomed. Microdev.*, 6:269–278 (2004).

[4] J. G. Santiago, S. T. Wereley, C. D. Meinhart, D. J. Beebe, and R. J. Adrian, "A particle image velocimetry system for microfluidics," *Expts. Fluids*, 25:316–319 (1998).

[5] C. W. Xi, D. L. Marks, D. S. Parikh, L. Raskin, and S. A. Boppart, "Structural and functional imaging of 3D microfluidic mixers using optical coherence tomography," *Proc. Natl Acad. Sci. USA*, 101:7516–7521 (2004).

[6] D. Liu, S. V. Garimella, and S. T. Wereley, "Infrared micro-particle image velocimetry in silicon-based microdevices," *Expts. Fluids*, 38:385–392 (2005).

[7] S. Devasenathipathy, J. G. Santiago, and K. Takehara, "Particle tracking techniques for electrokinetic microchannel flows," *Anal. Chem.*, 74:3704–3713 (2002).

[8] D. Sinton, "Microscale flow visualization," *Microfluid. Nanofluid.*, 1:2–21 (2004).

[9] U. Tallarek, T. W. J. Scheenen, P. A. de Jager, and H. Van As, "Using NMR displacement imaging to characterize electroosmotic flow in porous media," *Magn. Reson. Imaging*, 19:453–456 (2001).

[10] X. Zhang and A. G. Webb, "Magnetic resonance microimaging and numerical simulations of velocity fields inside enlarged flow cells used for coupled NMR microseparations," *Anal. Chem.*, 77:1338–1344 (2005).

[11] M. D. Shattuck, R. P. Behringer, G. A. Johnson, and J. G. Georgiadis, "Magnetic resonance imaging of interstitial velocity distributions in porous media," *ASME FED*, 125:39-45 (1991).

[12] M. D. Shattuck, R. P. Behringer, G. A. Johnson, and J. G. Georgiadis,, "Convection and flow in porous media. 1. Visualization by magnetic resonance imaging," *J. Fluid Mech.*, 332: 215–245 (1997).

[13] M. Deurer, I. Vogeler, A. Khrapitchev, and D. Scotter, "Imaging of water flow in porous media my magnetic resonance imaging microscopy," *J. Environ. Quality*, 31: 487–493 (2002)

[14] X. Ren, S. Staph, and B. Bl¨umich, "NMR velocimetry of flow in model fixed-bed reactors of low aspect ratio," *AIChE J.*, 51: 392–405 (2005).

[15] B. Bijeljic, M. D. Mantle, A. J. Sederman, L. F. Gladden, and T. D. Papathanasiou, "Slow flow across macroscopically rectangular fiber lattices and an open region: visualization by magnetic resonance imaging," *Phys. Fluids*, 13:3652–3663 (2001).

[16] K. W. Moser, "Quantitative measurement of velocity and dispersion via Magnetic Resonance Imaging," Ph.D. dissertation, University of Illinois at Urbana–Champaign (2001).

[17] C. Pozrikidis, *Introduction to Theoretical and Computational Fluid Dynamics*, Oxford, NY, Oxford Univ. Press (1997).

[18] K. W. Moser, E. C. Kutter, J. G. Georgiadis, R. O. Buckius, H. D. Morris, and J. R. Torczynski, "Velocity measurements of flow through a step stenosis using Magnetic Resonance Imaging," *Expts. Fluids*, 29:438–447 (2000).

[19] J.D. Seymour, B. Manz, P. T. Callaghan, "Pulsed gradient spin echo nuclear magnetic resonance measurements of hydrodynamic instabilities with coherent structure: Taylor vortices," *Phys. Fluids,* 11:1104-1113 (1999).

[20] T. J. Mosher and M.B. Smith, "A DANTE tagging sequence for the evaluation of translational sample motion". *Magn. Reson. Med*. 15: 334-339 (1990).

[21] L. G. Raguin, D. Karampinos, J. G. Georgiadis, and L. Ciobanu, "Comparison of MR Velocimetry Protocols for Microchannels", *47th Experimental Nuclear Magnetic Resonance Conference (ENC)*, Pacific Grove, CA, USA, April 23 – 28 (2006).

[22] B. H. Jo, L. M. Van Lerberghe, K. M. Motsegood, and D. J. Beebe, "Three-dimensional microchannel fabrication in polydimethylsiloxane (PDMS) elastomer," *J. Microelectromech. Syst.*, 9:76–81 (2000).

[23] L. G. Raguin, D. Hernando, D. Karampinos, L. Ciobanu, B. P. Sutton, Z.-P. Liang, and J. G. Georgiadis, "Quantitative analysis of q-space data," in *Proceedings of the IFMBE,* 3rd *European Medical & Biological Engineering Conference, Prague*, vol. 11, (2005).

MICROFLUIDIC MIXERS FOR THE INVESTIGATION OF PROTEIN FOLDING USING SYNCHROTRON RADIATION CIRCULAR DICHROISM SPECTROSCOPY

A.S. Kane[1,2], D. Hertzog[1], P. Baumgartel[3], J. Lengefeld[3], D. Horsley[4], B. Schuler[5], O. Bakajin[1]

[1] BioSecurity and Nanosciences Laboratory, Lawrence Livermore National Laboratory, Livermore, CA; [2]Department of Electrical & Computer Engineering, University of California, Davis; [3] Department of Physical Biochemistry, University of Potsdam, Germany; [4] Department of Mechanical & Aeronautical Engineering, University of California, Davis; [5] Department of Biochemistry, University of Zurich, Switzerland;

ABSTRACT

The purpose of this study is to design, fabricate and optimize microfluidic mixers to investigate the kinetics of protein secondary structure formation with Synchrotron Radiation Circular Dichroism (SRCD) spectroscopy. The mixers are designed to rapidly initiate protein folding reaction through the dilution of denaturant. The devices are fabricated out of fused silica, so that they are transparent in the UV. We present characterization of mixing in the fabricated devices, as well as the initial SRCD data on proteins inside the mixers.

INTRODUCTION

An improved understanding of how proteins fold into their secondary structure may have a significant impact in the prevention and treatment of various diseases. Use of microfluidic mixers with a variety of spectroscopic techniques such as single molecule [1], and ensemble FRET [2], SAX [3,4], FTIR [5] has improved the time resolution and greatly reduced sample consumption over more conventional stopped flow mixing methods. Circular dichroism (CD) is a spectroscopic technique commonly used for studies of protein folding that so far has not been used with microfluidic devices. In CD spectroscopy, linearly polarized light is incident on an optically active protein. Linearly polarized light consists of both left and right circularly polarized light of equal magnitude and phase. An optically active material preferentially absorbs one of these circularly polarized components of light. The measured CD signal is this difference in absorption between left and right circularly polarized light as a function of wavelength. Protein structures such as alpha helices and beta sheets can be distinguished in the CD signal. SRCD allows us to use wavelengths below 220 nm where differences between the CD spectra of random coil and the various secondary structure types are most pronounced. Microfluidic mixing allows a fast initiation of the protein folding reaction. By combining microfluidic initiation of the folding reaction with observations using SRCD, we will be able to measure structure formation during the early events of protein folding (sub ms). Our research will clarify an intense debate in the protein folding community as to when, in the process of folding, the secondary structure content forms.

EXPERIMENTAL DETAILS

We designed, fabricated and characterized mixing in the microfluidic device prototype. A photograph of a device prototype is presented in Fig. 1. Since at high concentrations, guanidinium hydrochloride denaturant (GuHCl) prevents proteins from folding, one of the most common ways to initiate folding is through rapid dilution of denaturant with buffer. In our device, protein solution with high denaturant concentration is injected into one channel and buffer solution is injected into another channel as shown in Fig. 2. The solutions meet at a serpentine-shaped region depicted in Fig. 3. The serpentine-shaped region performs mixing in the laminar flow regime by virtue of diffusion and chaotic advection [6]. Once the solutions are mixed and the denaturant is diluted, the folding reaction is initiated. The spectroscopic measurements are performed in the "observation channel" downstream.

To allow for transparency in the UV range where CD measurements are performed, the mixers are fabricated out of fused silica (Corning 7980, 0F grade). The channels are etched to

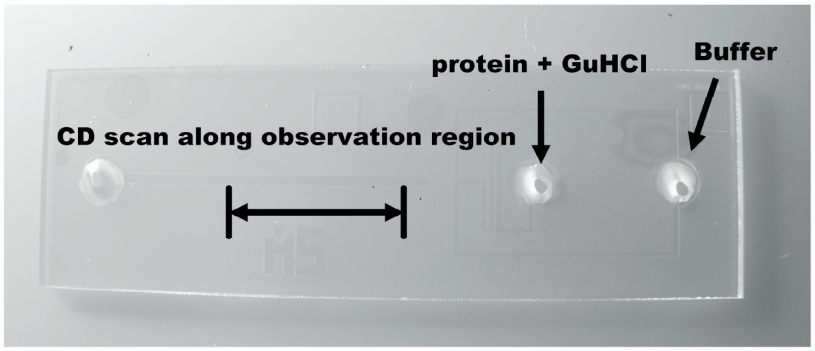

Figure 1: *Photograph of fabricated mixer with sandblasted inlet / exit holes.*

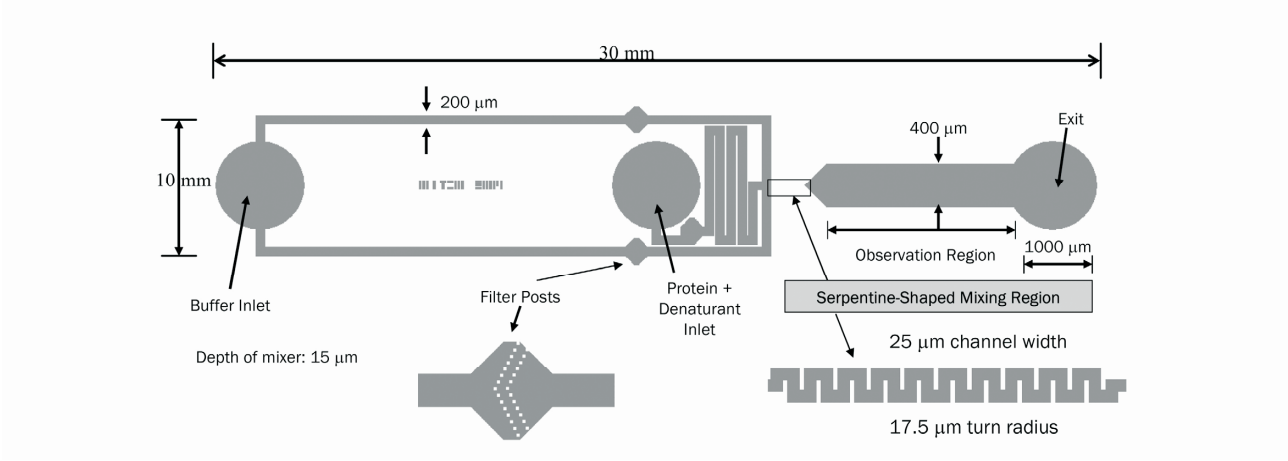

Figure 2: Schematic of the design of SRCD Mixer.

a depth of 14.5 μm using deep reactive ion etching with nearly vertical sidewalls. Etching is performed with an STS Advanced Oxide Etcher with a selectivity of approximately 17:1 using an undoped polysilicon mask. The inlet holes are fabricated by micro-sand blasting. Sealing of microfluidic mixers is accomplished by direct fusion wafer bonding to another fused silica substrate. Both the etched and unetched wafers were first thoroughly cleaned using piranha solution (sulfuric acid + hydrogen peroxide) and reverse RCA cleaning procedure. Following the piranha etch, substrates were cleaned for 10 minutes in 5:1:1 H_2O:HCl:H_2O_2 solution at a temperature of 75° C. The final step is to clean the substrates for 20 minutes in 5:1:1 H_2O:NH_4OH:H_2O_2 solution at a temperature of 72° C. After drying, the substrates were first pre-bonded and then fused at 1100C.

RESULTS

Mixing is observed at various flow rates by measuring the fluorescence intensity of fluorescein dye mixed with buffer. We mounted the mixer chips on a plastic holder that allows us easy connection to a syringe pump (Harvard Apparatus Infusion Syringe Pump 22, Model 55-2222). The fluorescein dye and the buffer were mixed in the ratio 1:1. To quantify the mixing process, we defined a mixing metric, M, based on the standard deviation of the fluorescence intensity as

$$M = 1 - 2\sqrt{\sum_{i=1}^{N} \frac{\left(I_{norm,i} - I_{avg}\right)^2}{N}}\,.$$

Value of mixing metric M=0 corresponds to a completely unmixed state, while M=1 corresponds to a completely mixed state. Intensity scans were taken at various flow rates to measure M as shown in Fig. 4A-4D. Our experiments demonstrate that, as expected, at progressively higher flow rates, Dean and Corner vortices interact to stretch and fold streamlines, thus enhancing mixing (Figure 4E).

Figures of merit for the performance of the mixers for protein folding measurements are: 1) mixing metric M; 2) mixing time, 3) time resolution & 4) sample consumption. The mixing time corresponds to the time it takes for the solution to traverse the serpentine mixing region. The time resolution is determined as the time the protein solution spends in the beam. That time is calculated as the ratio of the width of the beam spot (~50μm) and the average flow velocity in the observation region. A plot of the mixing metric M, mixing time and time resolution as a function of the total flow rate is shown in Fig. 5. With the current device design, the fastest mixing time obtained was 50 μs at a flow rate of 400 μl/min. This indicates that we will be able to observe folding events that happen at time scales >50 μs.

Initial evaluation of the microfabricated mixers at the BESSY II synchrotron beam (Berlin, Germany) has determined that the mixers are suitable for measurements of protein folding kinetics. The SRCD data presented in Fig. 6 is of the filtered lysozyme protein solution inside the microfluidic device. The data shows an acceptable signal-to-noise ratio, which confirms that the developed etch process results in a smooth enough fused silica surface that does not interfere with the polarization of the CD signal.

Figure 3: *Scanning electron micrograph of the mixing region.*

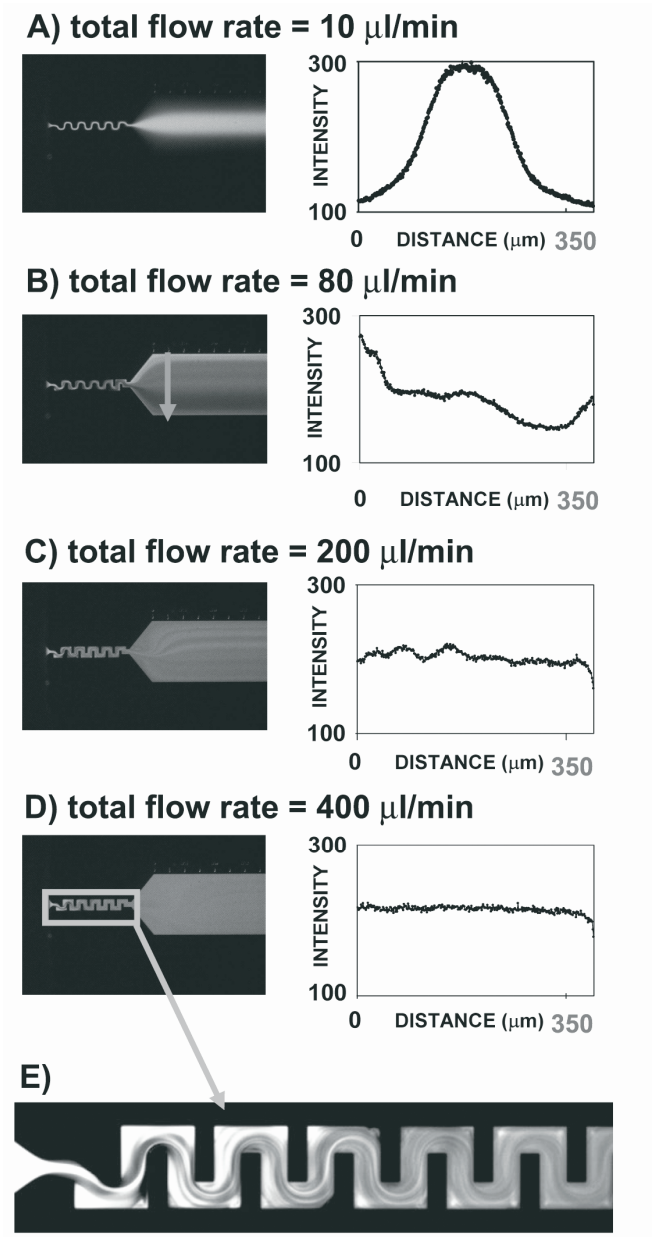

Figure 4: *A-D: Fluorescence images of mixing as a function of flow rate. Intensity scans are performed perpendicular to the direction of flow, across the entire width of the observation channel, as indicated by the gray arrow in Fig. 4B. E: Zoom of the mixing region.*

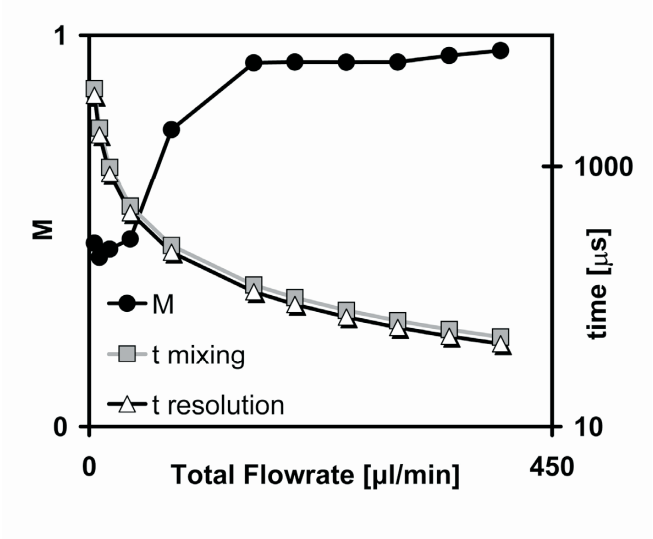

Figure 5: *Plot of the mixing metric, mixing time and time resolution as a function of total flow rate.*

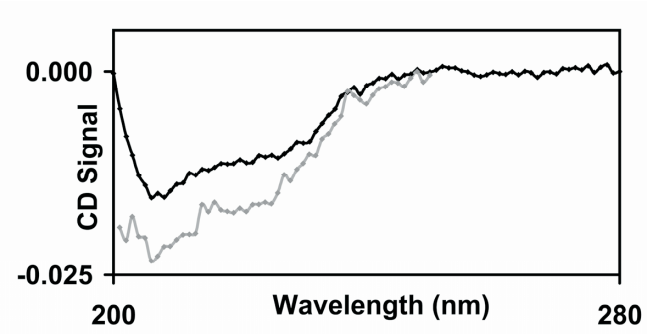

Figure 6: *SRCD data of filtered lysozyme protein solution inside microfluidic device. Black curve shows the reference data of lysozyme in water while the gray curve shows the data taken with the lyzozyme and 0.6M GuHCl in the mixer. The measurements in the presence of 0.6M GuHCl are limited to about 199 nm because of GuHCl absorption.*

CONCLUSIONS AND FUTURE DIRECTIONS

We described the design, fabrication and characterization of the microfluidic devices for measurement of protein folding kinetics using SRCD. We presented the data demonstrating the feasibility of the kinetic experiments with our devices.

Further SRCD measurements will be performed to analyze the kinetics of formation of the protein secondary structure while performing mixing of the protein + GuHCl solution with buffer. The current microfluidic mixers will be optimized in order to achieve low mixing times together with lower sample consumption. Introducing a microfluidic mixer for synchrotron-based spectroscopy opens up additional avenues for research in the biological sciences.

ACKNOWLEDGEMENTS

This work was supported by Human Frontiers Science Program. The work of Olgica Bakajin, Avinash Kane and David Hertzog was performed under the auspices of the U.S. Department of Energy by University of California Lawrence Livermore National Laboratory under contract No. W-7405-Eng-48 and partially supported by funding from the Center for Biophotonics, an NSF Science and Technology Center, managed by the University of California, Davis, under Cooperative Agreement No. PHY 0120999. A. Kane was also supported by the SEGRF Program at LLNL.

REFERENCES

[1] E. Lipman, B. Schuler, O. Bakajin, W.A. Eaton, "Single-molecule measurement of protein folding kinetics",*Science*, *301*, 1233 (2003)

[2] D.E. Hertzog, X., Michalet, M. Jager, X.X. Kong, J.G. Santiago, S. Weiss & O. Bakajin, "Femtomole Mixer for Microsecond Kinetic Studies of Protein Folding", *Analytical Chemistry, 76,* 7169 (2004)

[3] L. Pollack, M.W. Tate, N.C. Darnton, J. B. Knight, S. M. Gruner, W.A. Eaton, R. H. Austin, "Compactness of the denatured state of a fast-folding protein measured by submillisecond small-angle x-ray scattering", *Proc. Natl. Acad. Sci. U.S.A*., 96,10115 (1999)

[4] S. Akiyama, S. Takahashi, T. Kimura, K. Ishimori, I. Morishima, Y. Nishikawa, & T. Fujisawa, "Conformational Landscape of cytochrome c folding studied by microsecond-resolved small angle x-ray scattering", Proc. Natl. Acad. Sci. U.S.A., 99, 1329 (2002)

[5] E. Kauffmann, N.C. Darnton, R.H. Austin, C. Batt, K. Gerwert , "Lifetimes of intermediates in the beta-sheet to alpha-helix transition of beta-lactoglobulin by using a diffusional IR mixer", *Proc. Nat. Acad. Sci. USA*, 98 (12), 6646-6649 (2001)

[6] P. Chamarthy, S. Werely, "Mixing Characteristics in a Serpentine Microchannel", *ASME International Mechanical Engineering Congress and Exposition,* Anaheim, CA (2004)

MULTILAYERED POLYMER MICROFLUIDIC CHIP WITH NANOFLUIDIC INTERCONNECTS FOR MOLECULAR MANIPULATION

Bruce R. Flachsbart[1,2], Kachuen Wong[1], Jamie M. Iannacone[2,3], Edward N. Abante[1], Robert L. Vlach[1], Peter A. Rauchfuss[1], Paul W. Bohn[2,3], Jonathan V. Sweedler[2,3], and Mark A. Shannon[1,2]

[1]Department of Mechanical & Industrial Engineering, University of Illinois at Urbana-Champaign
[2]Beckman Institute for Advanced Science and Technology, University of Illinois at Urbana-Champaign
[3]Department of Chemistry, University of Illinois at Urbana-Champaign
Urbana, Illinois USA

ABSTRACT

The design, fabrication, and preliminary testing is presented for a polymer multilayered hybrid micro-nanofluidic chip that consists of poly(methylmethacrylate) (PMMA) layers containing microfluidic channels separated in the vertical direction by polycarbonate (PC) nanocapillary array membranes (NCAMs). This design architecture enables nanofluidic interconnections to be placed in the vertical direction between microfluidic channels. Such an architecture combines microfluidic manipulations (separation, injection, collection, etc.) with nanofluidic molecular capabilities (molecular sizing and affinity reactions, channel isolation, enhanced mixing, etc.) on a single chip. Recent polymeric microfabrication advances have made this scalable construct possible: 1) processing thin polymer layers on releasable and compliant carriers, and 2) the high resolution contact-printing of a strong thermal adhesive. Bond strength was demonstrated by pressurizing channels with 90 psi nitrogen without failure. Devices were characterized in terms of measuring resistivity and electroosmotic flow (EOF) along the channels at different pH values. The functionality of the chip is demonstrated by filling a cross channel with 1 μM green-fluorescent protein (GFP) and electrokinetically transporting analyte plugs through the NCAM and down the separation channel while performing laser induced fluorescence (LIF) analysis. The development of this new type of hybrid micro-nanofluidic device potentially will allow unprecedented molecular manipulations for chemical and biological sensing applications.

INTRODUCTION

Three dimensional (multilayered) microfluidic devices have been pursued in order to increase the functionality and complexity of the sequential biochemical manipulations possible within a device [1-4]. A proposed approach to further increase the functionality of this class of device is integrating microfluidics with nanofluidics in a hybrid approach that can exploit the physical dimensions of the nanoscale through the incorporation of nanocapillary array membranes (NCAMs) within the device [5]. This approach has been demonstrated in polydimethylsiloxane (PDMS) based microfluidic devices and has been shown to facilitate a variety of sample manipulations, including: nanofluidic gated injection of an analyte and the electrophoretic separation of that analyte [6], the mixing and reaction an analyte and a reagent [7], the collection of a specific electrophoretically separated band [8], and the separation of an analyte based on mass (or molecular size) [9]. Here, we demonstrate this hybrid approach within a PMMA microfluidic device in a scalable construct incorporating multiple NCAMs.

Multilayered polymer microfluidic chips with nanofluidic interconnects, such as those shown in Fig. 1, were fabricated by sequentially bonding microfluidic layers separated in the vertical direction by NCAM layers. An expanded view of a device is given in Fig. 2 showing the individual layers, their function, and the bond order. In Fig. 2, layer 2 is first bonded to layer 1, and then layer 3 is added, and so on, in a top-down fabrication approach. The routing of the microfluidic channels between the reservoirs is depicted in Fig. 3 along with a cross-sectional view of a channel intersection region showing the nanofluidic interconnects between the crossing microfluidic channels. Both ends of the chips are symmetric, containing two sets of cross-channel nanofluidic interconnects for the purpose of injecting and collecting analyte bands to and from the 28 mm separation channel in the middle. All optically transparent materials, including the adhesive, were used, thus allowing both visible and near UV inspection and interrogation of all the channel layers.

The fabrication process involved two recent advances in polymeric microfabrication: processing thin (< 40 μm), labile polymer layers on a compliant carrier that is released after bonding, and contact-printing a high resolution (< 100 μm) custom adhesive. Thin microfluidic layers are fragile and by supporting them on carrier substrates, extensive further processing becomes possible (metallization, etch, deposition, patterning, etc.). The compliance of this construct (layer plus carrier) is an important issue when bonding multi-layered structures. Bonds must accommodate both local non-uniformities (defects, submicron debris, etc.), and global non-uniformities (surface warpage, curvature, etc.), with the later tending to be additive with each layer. PMMA and PC have moduli 2-3 orders of magnitude greater than PDMS, and to achieve good bond quality a combination of adhesive layer compliance, for local non-uniformities, and layer carrier compliance, for global non-uniformities, was used. The second fabrication advance incorporated the contact printing of an adhesive layer using a flat

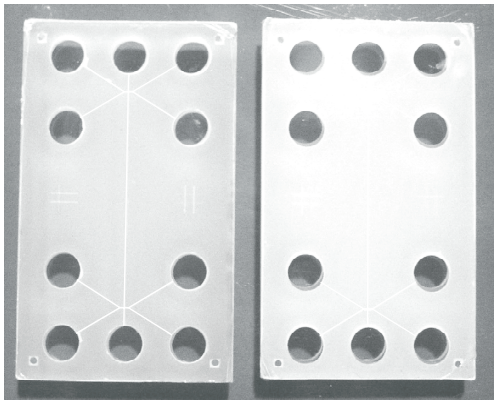

Figure 1 *A multilayer device (eight layers in total) containing three microfluidic channel layers separated vertically by two nanocapillary array membranes (NCAMs). The NCAMs within each device are 10 and 100 nm for the left sample, and 10 and 220 nm for the right sample. Chips are 24 x 40 mm (~1.6 mm thick).*

Layer	Description
1	Polycarbonate reservoir layer with ten 4 mm diameter reservoirs
2	PMMA via layer which couple reservoirs to the microfluidic channels
3	PMMA channel layer for sample introduction or collection
4	NCAM
5	PMMA separation channel layer
6	NCAM
7	PMMA channel layer for sample introduction or collection
8	PMMA bottom layer

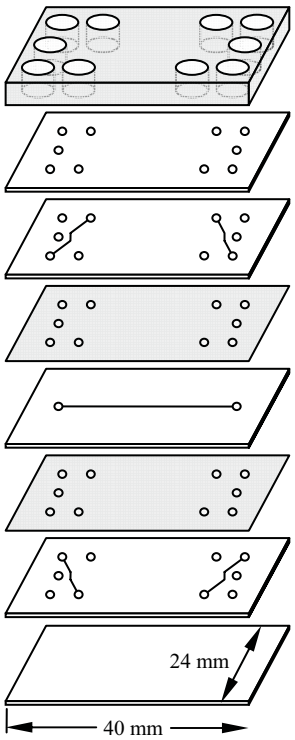

Figure 2 *Diagram depicting the individual layers of the 8-layer devices shown in Fig. 1. PMMA and NCAMs range in thickness from 5 to 40 μm and 6 to 10 μm respectively.*

disk-shaped PDMS stamp. While elastomeric stamps have been used to contact print monolayer inks [10], thin metal films [11], and liquid polymers [12], the use of contact printing in microelectromechanical system (MEMS) fabrication to pattern layers as thick as 1 μm, as in the adhesive layer printing of benzocyclobutene for wafer level bonding [13], is relatively recent. PDMS is commonly used for contact printing primarily due to its ability to conform to a surface without trapping bubbles at the interface [14].

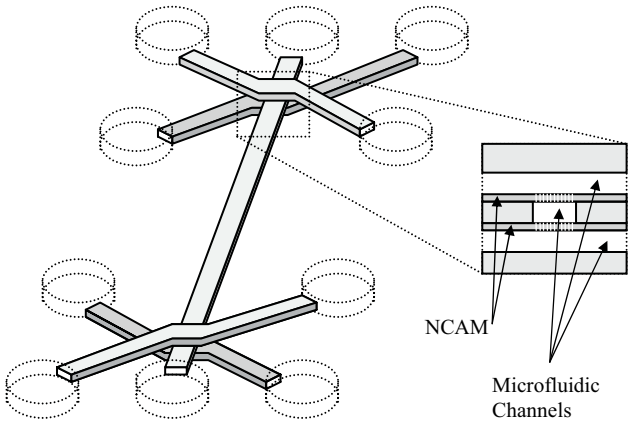

Figure 3 *Relief schematic of an eight layer device showing the routing scheme for the microfluidic channels relative to each other and the reservoirs. On the right is a cross-section of the intersection region where nanofluidic interconnects is formed between the microfluidic layers via NCAMs.*

DEVICE FABRICATION

The assembly of the layers into the device in Fig. 1 consisted of the sequential operations of contact printing adhesive layers, bonding, and releasing the bonded PMMA layers from their temporary carriers. The overall fabrication scheme of the multilayer device is shown in Fig. 2 and consisted of: (a) a semi-rigid PC reservoir layer on which to build the device; (b) individually processing each distinct labile polymer layer on a separate carrier, including if necessary spinning and curing the polymer layer, patterning, etching, and applying the adhesive; (c) transferring, aligning, and bonding the labile polymer layer to the device; (d) releasing the carrier; and (e) repeating with subsequent layers to form a multilayer chip. First, adhesive was contact printed onto the top surface of PMMA layer #2 in Fig. 2, which was then bonded to the PC top piece (layer #1 in Fig. 2) at 130ºC and 5.2 MPa of applied pressure under vacuum for 10 minutes. PMMA layer #2 was processed while affixed to a temporary coverglass carrier (No. 2 thickness), which, after bonding, was released by submersion in a hot water bath at approximately 50ºC for 5 min. Layer compliance was achieved using an elastomeric polymer to press the coverglass to the sample stack with 5.2 MPa of force at 130°C. The next PMMA layer #3 was bonded to the device stack in the same way that layer #2 was bonded (i.e. the top surface of PMMA layer #3 was coated with an adhesive, whereby it was bonded to the device stack, and its temporary carrier released using a hot water bath). Bonding NCAM layers required a slightly different approach since adhesive could not be applied to the NCAM layer without plugging the nanoscale pores. Thus the adhesive was applied to each of the layers facing the NCAM layer. Accordingly, the bottom surface of PMMA layer #3 and the top surface of the PMMA layer #5 were coated with adhesive. An NCAM layer #4 was placed between them, aligned and bonded together. After the bonding process, the coverglass carrier for PMMA layer #5 was released. The process was repeated for the second NCAM layer #6 and the PMMA layer #7. The final, unpatterned PMMA layer #8 was bonded to the device after coating the bottom of PMMA layer #7. The final step was a 12 hr. vacuum-oven cure at 130ºC at a temperature and time sufficient to fully crosslink all the epoxy adhesive layers without allowing remaining solvents or curing byproducts to coalesce.

The PMMA layers were formed by spincoating PMMA dissolved in propylene glycol monomethyl ether acetate (PGMEA) and anisole (all from Sigma Aldrich) onto a coverglass (Fisher Scientific, 35 x 50 mm, #2 thickness) that acted as the carrier plate for the PMMA layer. The PMMA on the coverglass was then cured to 180ºC in an oven for 6 to 24 hours depending on layer thickness. After curing, the PMMA layer was sputter coated with a layer of aluminum (~100 nm), and patterned using standard photolithographic procedures. The development of the positive photoresist etched the aluminum layer, thereby transfering the mask pattern to the aluminum layer. The PMMA channels and vias were then formed by reactive ion etching (RIE) using an oxygen and argon plasma (Axic RIE – 600 Watts). A straight side-wall profile created during this etch step was important for high resolution adhesive transfer. The final step in the preparation of the PMMA layers was the removal of the aluminum layer with photoresist developer, which also removed any remaining photoresist residue.

NCAM layers are commercially available from GE Osmonics Labstore and can be obtained with nominal pore diameters ranging from 10 nm to 400 nm. NCAMs are temporarily mounted onto PDMS disks using methanol, so that they lie flat when being

aligned and transferred to the device. Figure 4 shows a 47 mm diameter NCAM layer after bonding showing complete coverage of the underlying 24 x 40 mm device. The NCAM layer would then be trimmed and openings the size of the reservoirs made using RIE and a silicon shadow mask.

Figure 4 *Device after first NCAM layer bonded, showing the complete overlap of the 24 x 40 mm device by the 47 mm diameter NCAM. The excess NCAM would then be trimmed before bonding the next layer to the device.*

ADHESIVE CONTACT PRINTING

The transfer process consisted of spincoating a PDMS substrate (disk) with adhesive, which was then transferred by pressing the adhesive onto the desired layer to be bonded. The epoxy adhesive was a mixture of Dow Corning solid epoxy novalac-modified resin with curing agent in a 2.5:1 mass ratio, and various solvents (2-methoxyethanol 15 to 50% by mass range, anisole 15 to 50% by mass range, and PGMEA 0 to 10% by mass range, the exact amounts depend upon the adhesive layer thickness desired). Most often, the solvents were selected to modify the viscosity of the adhesive in order to achieve a thickness of ~1 μm via spincoating in order to achieve sharp transfer interfaces.

Optical microscope inspection after contact printing was used to monitor the degree to which the pattern was resolved during the contact printing procedure. Figure 5 depicts a PDMS substrate after contact printing to layer #7, and both the PDMS substrate and the device are utilized for quality control. Ultimate printing resolution was determined by the smallest dimension that could be printed consistently without "bridging" and/or seeping of the adhesive into the channel. Figure 6 shows some examples of common contact printing errors. If a printed layer had errors, the PMMA surface could be reprinted with adhesive after removing the previous layer with methanol. Features smaller than 100 μm can be resolved using an adhesive layer approximately 1 μm thick.

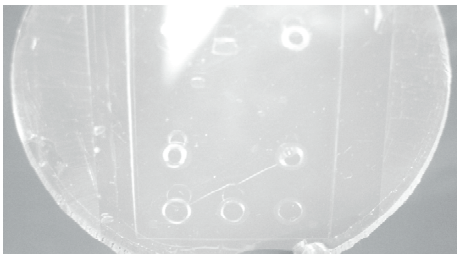

Figure 5 *A photograph of a PDMS substrate after contact printing an adhesive layer onto a PMMA microfluidic channel layer. The adhesive pattern that is left on the PDMS can be monitor to verify the quality of the transfer process.*

Thinner adhesive layers generally achieve better transfer resolution, but also tend to be harder to release from the PDMS substrate and do not accommodate local non-uniformities as well.

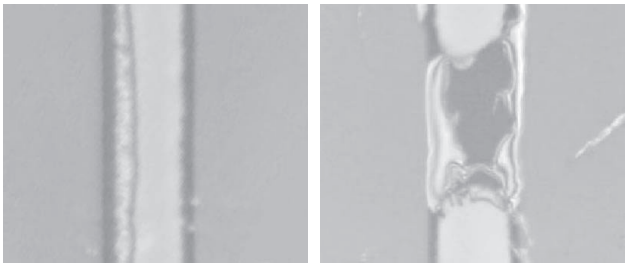

(a) (b)

Figure 6 *Optical images of microfluidic channels showing contact printing errors where (a) the adhesive has seeped into the channel, and (b) the adhesive has "bridged" the microchannel.*

Another factor that affected contact printing resolution was the temperature of the adhesive carrier. PDMS has a greater affinity to the adhesive layer when it is cold, and the affinity decreases with increasing temperature. Heating the PDMS carrier and adhesive to 50ºC for 3 min improved the transfer of adhesive to the areas in contact with the PMMA surface. The chip and adhesive carrier could then be cooled to improve the adhesion of the adhesive that was not in contact with the surface. This heating and cooling of the adhesive carrier substantially improved the yield of the process in addition to significantly improving the contact printing resolution.

DEVICE TESTING

Devices were tested physically, electrically, and functionally. The physical strength of the bonding process was tested by threading reservoirs to accommodate pressure hose fittings in a modified device as shown in Figure 7. Channels were then filled with a fluorescent solution and both ends pressurized with nitrogen while inspecting the channels for delamination. Reservoir bottom rupturing was the primary failure mechanism, generally occurring above 6 atm (90 psi). Electrical characterization consisted of 1) measuring microfluidic channel resistivity and 2) determining the electroosmotic flow (EOF) coefficients along the channels at different pH values. Linear I-V plots ($R^2 > 0.995$) using 10 mM phosphate buffer (PB) (pH 7.4) were obtained yielding a mean of 26.7 ± 0.4 *MΩ/cm* along the longer microfluidic channel (Δl = 2.80 cm) and 37.6 ± 0.4 *MΩ/cm* along the shorter cross-channels (Δl = 1.23 cm). Measurements were stable and reproducible over a

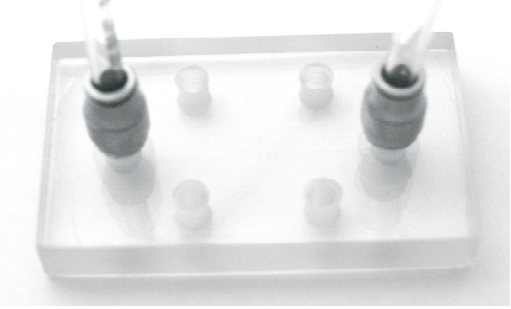

Figure 7 *A chip modified to accommodate threaded high-pressure hose connections used for pressure testing layer bond strength. The device was vacuum filled with fluorescent solution, then pressurized with nitrogen, while continuously inspecting the channel for delamination. Reservoir bottom rupturing was the primary failure mechanism above 90 psi.*

week. No measurable leakage current was observed through the chip itself, indicating no discernable fluid leaks between levels. Electroosmotic flow (EOF) mobilities versus solution pH, given in Table 1, were measured using the current monitoring method using 5 mM and 10 mM PB solutions at 100 V. These EOF values are within a factor of two of published EOF values for PMMA microfluidic channels, which are noted to vary with processing method [15]. Transport through the nanofluidic interconnects (across the NCAM membrane) was demonstrated by filling a cross channel with 1 μM of green-fluorescent protein (GFP) and electrokinetically transporting analyte plugs (with 600 V pulses 2 seconds in duration) into the middle separation channel. A 488 nm Ar+ laser was focused on the receiving channel away from the intersection and a detector was used to produce the laser induced fluorescence (LIF) graph shown in Figure 8. Plug injections were confined and reproducible.

Table 1 *Electroosmotic coefficients {$cm^2/V{\cdot}s$} for phosphate buffer solution versus pH measured using the current monitoring method.*

	Cross Channel Ave.	**Separation Channel**
pH 8.8	$2.7 \pm 0.6 \times 10^{-4}$	$2.2 \pm 0.3 \times 10^{-4}$
pH 7.3	$2.8 \pm 0.5 \times 10^{-4}$	$3.5 \pm 0.7 \times 10^{-4}$
pH 4.4	$2.5 \pm 0.9 \times 10^{-4}$	$2.2 \pm 0.3 \times 10^{-4}$

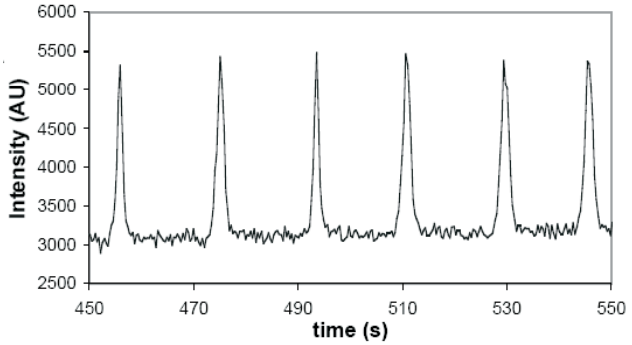

Figure 8 *Laser-induced fluorescence (LIF) detection of 1 μM GFP in 10 mM PB injected for 2 s at 600 V from one microfluidic channel, across a NCAM, and into a second microfluidic channel containing the PB solution only.*

CONCLUSIONS

The fabrication and preliminary testing of a hybrid micro-nanofluidic device using multiple NCAMs and PMMA microfluidic layers was detailed. This construct produced a high quality device that has the potential to be scaled beyond the eight layer devices presented and tested. The interconnection of five separate microfluidic channels with four nanofluidic interconnects seeks to increase the functionality and sophistication of the sequential biochemical manipulations possible within a device.

ACKNOWLEDGEMENTS

This work was partially supported by National Science Foundation's *The WaterCAMPWS*, a Science and Technology Center of Advanced Materials for the Purification of Water with Systems under the agreement number CTS-0120978, the Center for Nano-Chemical-Electrical-Mechanical Manufacturing Systems under DMI-032-28162, and by Strategic Environmental Research and Development Program under Army W9132T-05-2-0028.

REFERENCES

[1] T. Thorsen, S. J. Maerki, and S. R. Quake, "Microfluidic large-scale integration," *Science*, **298**, p. 580-4, 2002.

[2] J. R. Anderson, D. T. Chiu, R. J. Jackman, O. Cherniavskaya, J. C. McDonald, H. Wu, S. H. Whitesides, and G. M. Whitesides, "Fabrication of topologically complex three-dimensional microfluidic systems in PDMS by rapid prototyping," *Analytical Chemistry*, **72**, p. 3158-3164, 2000.

[3] G. Mensing, T. Pearce, and D. J. Beebe, "An ultrarapid method of creating 3D channels and microstructures," *JALA - Journal of the Association for Laboratory Automation*, **10**, p. 24-28, 2005.

[4] B. H. Weigl, R. Bardell, T. Schulte, F. Battrell, and J. Hayenga, "Design and rapid prototyping of thin-film laminate-based microfluidic devices," *Biomedical Microdevices*, **3**, p. 267-74, 2001.

[5] T.-C. Kuo, D. M. Cannon Jr, M. A. Shannon, P. W. Bohn, and J. V. Sweedler, "Hybrid three-dimensional nanofluidic/microfluidic devices using molecular gates," *Sensors and Actuators, A: Physical*, **102**, p. 223-233, 2003.

[6] D. M. Cannon Jr, T.-C. Kuo, P. W. Bohn, and J. V. Sweedler, "Nanocapillary array interconnects for gated analyte injections and electrophoretic separations in multilayer microfluidic architectures," *Analytical Chemistry*, **75**, p. 2224-2230, 2003.

[7] T.-C. Kuo, H.-K. Kim, D. M. Cannon Jr, M. A. Shannon, J. V. Sweedler, and P. W. Bohn, "Nanocapillary arrays effect mixing and reaction in multilayer fluidic structures," *Angewandte Chemie - International Edition*, **43**, p. 1862-1865, 2004.

[8] J. J. Tulock, M. A. Shannon, P. W. Bohn, and J. V. Sweedler, "Microfluidic separation and gateable fraction collection for mass-limited samples," *Analytical Chemistry*, **76**, p. 6419-6425, 2004.

[9] T.-C. Kuo, D. M. Cannon Jr, Y. Chen, J. J. Tulock, M. A. Shannon, J. V. Sweedler, and P. W. Bohn, "Gateable nanofluidic interconnects for multilayered microfluidic separation systems," *Analytical Chemistry*, **75**, p. 1861-1867, 2003.

[10] L. H. Dubois and R. G. Nuzzo, "Synthesis, structure, and properties of model organic surfaces," *Annual Review of Physical Chemistry*, **43**, p. 437-463, 1992.

[11] L. Yueh-Lin, R. L. Willett, K. W. Baldwin, and J. A. Rogers, "Additive, nanoscale patterning of metal films with a stamp and a surface chemistry mediated transfer process: applications in plastic electronics," *Applied Physics Letters*, **81**, p. 562-4, 2002.

[12] M. Wang, H. G. Braun, T. Kratzmuller, and E. Meyer, "Patterning polymers by micro-fluid-contact printing," *Advanced Materials*, **13**, p. 1312-1317, 2001.

[13] J. Oberhammer and G. Stemme, "BCB contact printing for patterned adhesive full-wafer bonded 0-level packages," *Journal of Microelectromechanical Systems*, **14**, p. 419-425, 2005.

[14] Y. Xia and G. M. Whitesides, "Soft Lithography," *Annual Review of Physical Chemistry*, **28**, p. 153-184, 1998.

[15] Z. Chen, Y. Gao, R. Su, C. Li, and J. Lin, "Fabrication and characterization of poly(methyl methacrylate) microchannels by *in situ* polymerization with a novel metal template," *Electrophoresis*, **24**, p. 3246-3252, 2003.

NANO SELF-ASSEMBLED ION-SENSITIVE FIELD-EFFECT TRANSISTORS FOR ACETYLCHOLINE BIOSENSING

Yi Liu, Arthur G. Erdman, and Tianhong Cui*
Department of Mechanical Engineering, University of Minnesota
Minneapolis, MN 55455, USA
Tel: 612-626-1636 Fax: 612-625-6069 E-mail: tcui@me.umn.edu

ABSTRACT

In this paper, the fabrication and characterization of acetylcholine biosensors based on nano self-assembled ion-sensitive field-effect transistors (ISFETs) are demonstrated. The fabrication is implemented with a very low-cost layer-by-layer nano self-assembly technique. A self-assembled polyaniline thin film works as the semiconducting channel material, while a SiO_2 nanoparticle thin film serves as the gate dielectric material. A typical polyaniline ISFET operates at a low-voltage range and has a mobility of 1.49 cm^2/Vs. Acetylcholine in a concentration as low as 1 μM could be detected with this sensor. The results presented herein suggest a route to inexpensive ion-sensitive field-effect transistors for biosensing applications.

INTRODUCTION

Acetylcholine (Ach) is a chemical transmitter in both the peripheral nervous system and central nervous system of many organisms including humans. Acetylcholine neurotransmission is considered to play a critical role in human during the processes such as behavioral activity, arousal, attention, learning, memory, etc. An abnormally short supply of acetylcholine is associated with Alzheimer's disease, which ranks the fourth in the causes of death among adults. Therefore, the sensing of acetylcholine concentration is important and of great interest. Some methods can be used to detect the concentration of acetylcholine, for example, electrospray ionization mass spectrometry (EIMS) [1] and biosensors [2]. However, both the EIMS and the silicon-based biosensors are relatively expensive because the EIMS is a bulky instrument and the fabrication of silicon-based biosensors is complicated and costly. Polymers and nanoparticles are alternatives to silicon for making low-cost electronic devices and systems. In this report, polymer- and nanoparticle-based field-effect transistors are fabricated and characterized for acetylcholine biosensing.

Biosensors are analytical devices incorporating a biological material with a physical transducer or transducing microsystem. The transduction mechanism may be optical, electrical, thermal, piezoelectric, magnetic, etc. One of the most popular biosensors is based on the ion-sensitive field-effect transistor (ISFET), which was first introduced by Bergveld in 1972 [3]. The advantages of ISFET based biosensors include high sensitivity, real-time, and label-free detection of a wide range of chemical and biological species. Since ISFET biosensors can be produced by the integrated circuit production method, they could be reduced in size and mass-produced. They are not only known as one of the most important miniaturized biosensors, but also as devices to bridge the gap between microelectronics and biotechnology.

Recently, layer-by-layer (LBL) nano self-assembly technique has attracted much attention since the introduction by G. Decher et al. [4] The LBL process involves alternating immersion of a substrate into aqueous solutions of polycations and polyanions. With each immersion, a polyion layer is deposited and the surface ionization of the substrate is reversed, allowing a subsequent layer with opposite charge to be deposited. Multilayer thin films made of interesting charged materials such as nanoparticles, conjugated polymers, DNA, and proteins, etc. can be formed with controlled thickness in nanometer scale. Using LBL self-assembly, it is very simple and inexpensive to produce organized films similar to the ones obtained with the sophisticated and expensive molecular beam epitaxy technology. The versatility, relative ease of preparation, ultra low cost, and potential for scale-up have made LbL self-assembly a viable chemical approach for the fabrication of nanostructure devices. There are several self-assembly techniques, such as langmuir-blodgett (LB) films, self-assembly of monolayers (SAM), and LBL self-assembly. Compared to LB technique and SAM technique, the LBL films exhibit a much larger thermal and mechanical stability, and can be prepared up to hundreds of layers. LBL self-assembly is proving to be a useful and versatile technique for the formation of multilayered thin films with a wide range of electrical, optical, and biological properties. It can find applications including optical diode [5], biosensor [6], etc.

Previously, we have reported the fabrication of LBL self-assembled nanoparticle thin films as building blocks for a field-effect transistor [7]. In this paper, the LBL self-assembly technique is extended to form thin films of polymer, nanoparticle and enzyme for the fabrication of ISFET based acetylcholine-sensitive biosensor. Conjugated polymer, polyaniline (PANI), has been self-assembled as the semiconductor channel material. Figure 1 shows the schematic diagram of the acetylcholine-sensitive ISFET. The sensing principle of the acetylcholine ISFET biosensor is based on the

biocatalyzed hydrolysis of acetylcholine in the presence of acetylcholine esterase (AchE), as shown in Eq. (1). The hydrolysis results in acetic acid that changes the PH of the solution, and can be detected by the ISFET.

$$(CH_3)_3N^+CH_2CH_2OCOCH_3 + H_2O \xrightarrow{AchE} (CH_3)_3N^+CH_2CH_2OH + HOCOCH_3 \quad (1)$$

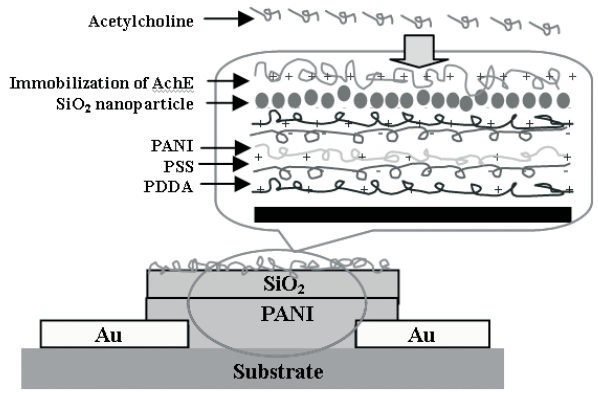

Figure 1. *The schematic diagram of the Ach-sensitive ISFET*

EXPERIMENT

The polyions involved in the fabrication process were positively charged poly(dimethyldiallyl-ammonium chloride) (PDDA) and negatively charged poly(styrenesulfonate) (PSS). Polyaniline doped with sulfuric acid was used as the channel material. SiO_2 nanoparticles 40~60 nm in diameter were used as the gate dielectric material. The acetylcholine esterase from electric eel and acetylcholine chloride were prepared from de-ionized (DI) water. All the above materials were purchased from Sigma-Aldrich Corporation, except that the SiO_2 nanoparticle dispersion was from Nissan Chemical Corporation.

The nano self-assembled ISFETs were built on a standard 4-inch silicon wafer with a layer of SiO_2 300 nm thick. First, two layers of chrome (100 nm) and gold (200 nm) were deposited on the wafer with e-beam evaporation, and then patterned by optical lithography to form the source/drain electrodes. Next, photoresist was spin-coated on the wafers and patterned to open windows directly above the channel region. Prior to the layer-by-layer self-assembly, the wafer were put into the O_2 plasma for 30 seconds to clean the photoresist residue inside the opening window. The wafer were then alternately immersed in aqueous PDDA and PSS solutions, in a sequence of [PDDA (10 min) + PSS (10 min)]$_3$. These three bi-layers of PDDA/PSS served as the precursor layers that helped to enhance the subsequent adsorption of conjugated polymers and nanoparticles. PDDA and PSS also worked as the sandwich layers between two neighboring nanoparticle, polymer, or AchE layers, depending on the charge polarization of the solution. Between two immersions of the wafer into solutions, there was intermediate rinsing using DI water for 1 minute to remove the residue on the previous layer from the surface. Following the precursor layers, five layers of PANI polymer thin films were coated on the entire wafer surface in the sequence of [PANI (10 min) + PSS (10 min)]$_5$. Next, the SiO_2 nanoparticle dispersion were coated in the sequence of [PDDA (10 min) + SiO_2 (4 min)]$_6$ to produce a gate dielectric thin film. Before immobilizing AchE on the top surface of SiO_2 nanoparticle thin film, the wafer was soaked in an acetone solution with ultrasonic agitation to lift off the self-assembled materials not in the target window. Finally, AchE was immobilized on the top of the SiO_2 film in the sequence of {PDDA (10 min) + [PSS (10 min) +AchE (10 min)]$_3$}. Scanning electron microscopy (SEM) was used to investigate the self-assembled nanoparticle and AchE thin films. Figures 2a and 2b show images of self-assembled SiO_2 nanoparticle thin films and AchE enzyme on the top of channel region.

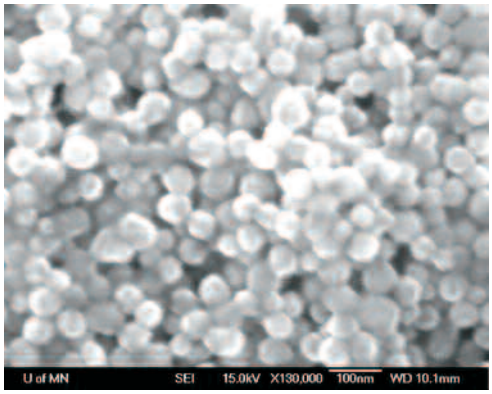

(2a)

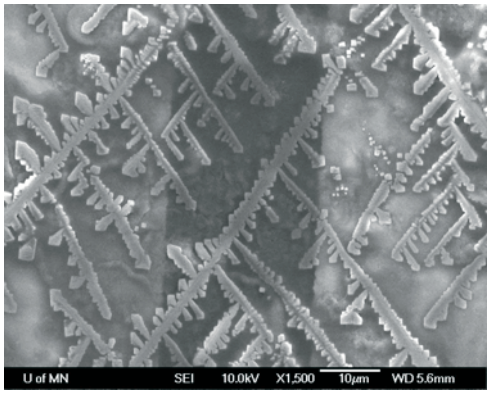

(2b)

Figure 2. *The SEM images of (2a) SiO_2 nanoparticle thin film, and (2b) AchE enzyme on the top of channel region.*

RESULTS AND DISCUSSIONS

A HP 4156B semiconductor parameter analyzer is used to characterize the electrical behaviors of the fabricated ISFETs. Ag/AgCl is used as the reference gate electrode. Figure 3a shows the output characteristic of a typical PANI ISFET at an acetylcholine solution with a concentration of 10 mM. This ISFET behaves like a traditional metal oxide semiconductor field-effect transistor (MOSFET). At higher positive gate

voltage, the drain current is higher, which indicates that the LBL self-assembled PANI ISFET is functional as an n-type transistor. It is at the "normal-on" state at zero gate voltage, and then works at depletion mode with a negative bias. Electron polarons and bipolarons are the main charge carriers in the n-type PANI semiconductor thin films. This is different from the spin-coated PANI transistor that work as a p-type transistor [8][9]. These two different charge carrier mechanisms are due to the difference between the layer-by-layer self-assembled PANI thin film and the spin-coated PANI thin film. In the spin-coated PANI thin film, only the PANI solution was deposited on the channel region between the source and the drain electrodes. However, in the layer-by-layer self-assembled PANI, the PANI was sandwiched into the PSS polyelectrolyte by electrostatic force. The network of mixed PANI and PSS results in strong electron-hole asymmetry in PANI thin film. This n-type asymmetry with respect to polaronic effects, which has been predicted by J. Libert et al [10], can contribute to the n-type field-effect characteristics. The n-type field-effect in LBL self-assembled PANI thin films has also been observed by J. Paloheimo et al. [11]

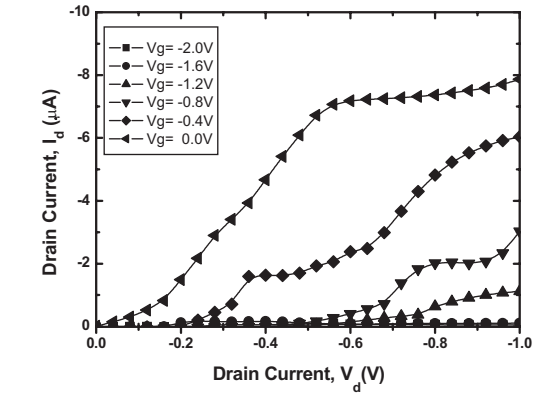

(a)

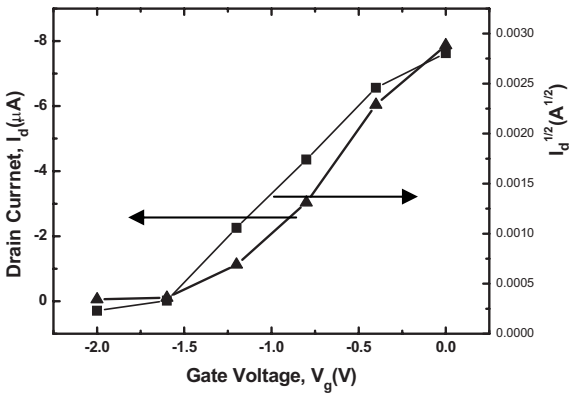

(b)

Figure 3. *(a) The output characteristic and (b) transfer characteristic of the PANI ISFET in an acetylcholine solution with a concentration of 10 mM.*

Figure 3b shows the transfer characteristic of the same PANI ISFET in the acetylcholine solution (10 mM). The extracted threshold voltage is -1.8 V. The calculated mobility based on the traditional MOSFET theory is 1.49 cm^2/Vs. There are 40 ISFETs fabricated on one wafer. The characterized mobility of these devices is within the range from 1 to 5 cm^2/Vs. It is noticed that the general polyaniline mobility is within the range from 10^{-5} to 10^{-4} cm^2/Vs [11]. Our PANI based ISFET has a higher mobility, and were investigated carefully.

It is observed that the gate current is higher when the gate voltage is zero, but reduces rapidly when the gate voltage negatively increases. This implies that there are hydrogen ions passing through the gate dielectric layer and participating in the charge transport at zero or low negative gate bias. Since the diameter of the hydrogen ion is less than 0.3 nm, it can easily penetrate the small spaces among the SiO_2 nanoparticles. Since polyions (PDDA and PSS) within the multilayer films are also conductive in solution, the total charge carriers in the channel should include hydrogen ions, electron polarons from the gate-affected PANI semiconductor thin films and the polyions between the PANI thin films. These carriers greatly increase the channel's conductivity as well as the charge transport ability. Therefore, the calculated mobility should be an "equivalent mobility" that takes into account all the charge carriers. The equivalent mobility could be much higher than a similar transistor in atmosphere ambient. Similar behavior is also observed by Sandberg, et al. in an all-polymer field-effect transistor, which has a high mobility (>100 cm^2/Vs) in a humid environment, about 4~5 orders higher than a typical polymer transistor using poly(3-hexylthiophene) as channel material [12].

Figure 4 shows the sensitivity of a typical PANI ISFET for different concentrations of acetylcholine when the gate voltage is 0 V and the drain voltage is -1 V. At lower concentration of acetylcholine, the drain current is also smaller. This is because lower concentration of hydrogen ions can be generated during the reaction between acetylcholine and acetylcholine esterase when the concentration of acetylcholine is lower. This has also demonstrated how the device can be effectively used as a biosensor. The ISFET could detect a concentration change of acetylcholine down to 1 μM.

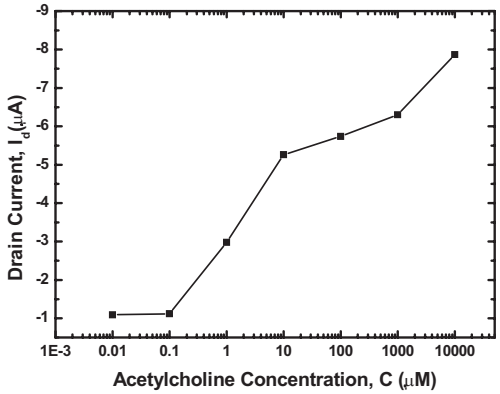

Figure 4. *The sensitivity of the PANI ISFET for sensing acetylcholine concentration.*

Figure 5 shows the response time of the PANI ISFET with respect to the open circuit potential change for differrent concentrations of acetylcholine. The voltage between drain electrode and the Ag/AgCl reference electrode escalated with an increased acetylcholine concentration. When the concentration of acetylcholine was changed from 10 nM to 100 nM, the change of gate potential was negligible. However, when the concentration of acetylcholine was 1 μM, the increase of the gate potential was obvious. Further increases in the concentration of acetylcholine also greatly increased the gate potential. Since a change of the gate voltage will affect the channel conductivity, it is obvious that the ISFET could detect variations of acetylcholine concentration larger than 1 μM.

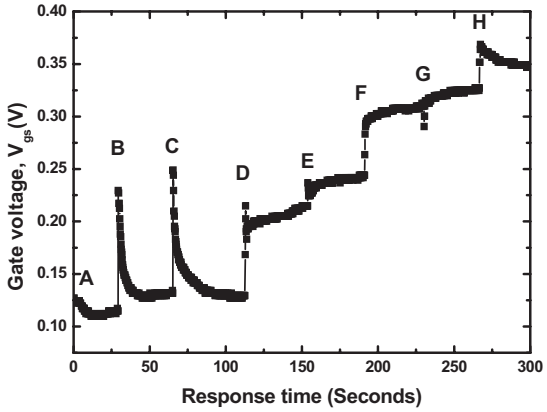

Figure 5. *The response time of the PANI ISFET at different concentration of acetylcholine (A: DI water, B: 10 nM, C: 100 nM, D: 1 μM, E: 10 μM, F: 100 μM, G: 1 mM, H: 10 mM).*

CONCLUSIONS

In this paper, polyaniline ISFET based on the low-cost layer-by-layer nano self-assembly was successfully fabricated and used for the acetylcholine biosensing. Acetylcholine concentration down to 1 μM could be detected use the self-assembled biosensors. The ISFET exhibited high performance, operating at very low voltages with a high mobility. The results show promise for a large scale logic circuit integration of biosensors and biomedical systems. Further work is ongoing to improve the sensitivity of the ISFET for acetylcholine sensing such that it could detect acetylcholine down to 10 nM.

ACKNOWLEDGEMENT

The authors would like to thank Prof. David Redish from Department of Neuroscience at the University of Minnesota for his helpful discussion.

REFERENCES

[1]. R. Dunphy and D.J.Burinsky, "Detection of choline and acetylcholine in a pharmaceutical preparation using high-performance liquid chromatography/electrospray ionization mass spectrometry", *Journal of Pharmaceutical and Biomedical Analysis*, *31*, 905 (2003).

[2]. A.B. Kharitonov, M. Zayats, A. Lichtenstein, E. Katz, and I. Willner, "Enzyme monolayer-funcitionalized field-effect transistors for biosensor applications", *Sensors and Actuators B*, *70*, 222, (2000).

[3]. P. Bergveld, "Development, operation and application of the ion sensitive field-effect transistor as a tool for electrophysiology", *IEEE Trans. Biomed. Eng. BME-19*, 342, (1972).

[4]. G. Decher, "Fuzzy Nanoassemblies: Toward layered polymeric multicomposites", *Science*, *277*, 1232 (1997).

[5]. A. A. Mamedov, A. Belov, M. Giersig, N. N. Mamedova, and N. A. Kotov, "Nanorainbows: Graded Semiconductor Films from Quantum Dots", *J. Am. Chem. Soc.*, *123*, 7738, (2001).

[6]. Q. Chen, J. Han, H. Shi, B. Wu, X. Xu, and T. Osa, "Use of Chitosan for developing layer-by-layer multilayer thin films containing glucose oxidase for biosensor applications", *Sensor Letters*, *1*, 102, (2004).

[7]. T. Cui, Y. Liu, and M. Zhu, "Field-Effect Transistors with Layer-by-Layer Self-Assembled Nanoparticle Thin Films as Channel and Gate Dielectric", *Applied Physics Letters*, *87*, 183105, (2005).

[8]. C. Kuo, S. Chen, G. Hwang, H. Kuo, "Field-effect transistor with the water-soluble self-acid-doped polyaniline thin films as semiconductor," *Synthetic Metals*, *93*, 155, (1998).

[9]. C. Kuo, S. Weng, R. Huang, "Field-effect transistor with polyaniline and poly(2-alkylaniline) thin film as semiconductor," *Synthetic metals, 88*, 101, (1997).

[10]. J. Libert, J. L. Bredas, and A.J. Epstein, "Theoretical study of p- and n-type doping of the leucoemeraldine base form of polyaniline: Evolution of the geometric and electronic structure", *Phys. Rev. B*. *51*, 5711, (1995).

[11]. J. Paloheimo, K. Laakso, H.Isotalo, H. Stubb, "Conductivity, thermoelectric power and field-effect mobility in self-assembled films of polyaniline and oligoanilines", *Synthetic metals*, *68*, 249, (1995).

[12]. H. Sandberg, T.G. Backlund, R.Osterbacka, and H. Stubb, "High-performance all-polymer transistor utilizing a hygroscopic insulator", *Advanced Materials*, *16*, 1112, (2004).

SURFACE-MICROMACHINED IN-CHANNEL PARYLENE DUAL VALVES FOR UNPOWERED MICROFLOW REGULATION

Po-Jui Chen[1], Damien C. Rodger[1,2], Ellis Meng[3], Mark S. Humayun[2], and Yu-Chong Tai[1]
[1]California Institute of Technology, Pasadena, CA 91125 USA
[2]Keck School of Medicine, University of Southern California, Los Angeles, CA 90033 USA
[3]University of Southern California, Los Angeles, CA 90089 USA

ABSTRACT

This paper presents the world's first in-channel parylene dual-valved microfluidic system for unpowered microflow regulation. Incorporating a normally-closed and a normally-open passive check valve in a back-to-back configuration inside a microchannel, the dual-valved system has successfully regulated the pressure/flow rate of air or liquid without power consumption or electronic/magnetic/thermal transduction. By exclusively using parylene C as the structural material, the fabricated valves have higher flexibility to shunt flows in comparison with other conventional thin-film valves. In addition, the parylene-based devices are completely biocompatible/implantable, and provide an economical paradigm for fluidic control in integrated lab-on-a-chip systems. Testing results have successfully demonstrated that the microflow regulation of the dual-valved system can achieve mmHg pressure – mL/min flow rates for air and mmHg pressure – μL/min flow rates for water. This regulation range is suitable for controlling biological conditions in human healthcare, such as regulating elevated intraocular pressure (IOP) in glaucoma patients.

INTRODUCTION

Micro-electro-mechanical systems (MEMS) is an enabling technology to build various microfluidic devices (e.g., channels, valves, pumps, mixers, etc.) for micro-total-analysis systems (μTAS) and lab-on-a-chip applications [**1**][**2**]. Among such devices microvalves are the key component to systematically control microflow for reliable operation. Microvalves are designed to be active or passive, with passive valves (check valves) having advantages of simple operation, zero power consumption, and ease of integration. Based on their actuation mechanism, micromachined check valves are categorized as normally-open (Fig. 1(a), fluidic channel is always open unless there is sufficient backward pressure) [**3**] or normally-closed (Fig. 1(b), fluidic channel is blocked until pressure is above cracking pressure) [**4**][**5**] valves. However, both types of check valves are not ideal. For normally-open valves the cracking pressure to conduct forward flow is minimal, while there is always a leakage problem when backflow is applied. For normally-closed valves the backflow leakage can be reduced, but the cracking pressure turns out to be so large that reasonable flow rate is not achievable with low pressure loading. These problems are inevitable using current MEMS fabrication technologies.

Even though micromachined check valves are not ideal, different design schemes can be implemented to realize different fluidic behaviors from those in a single valve. In this work, a novel dual-valve configuration has been developed to achieve passive microflow regulation by incorporating a normally-closed check valve and a normally-open check valve together inside a microchannel. This configuration inherently regulates pressure and flow rate of fluids without any power consumption. In addition to implementing similar design concepts from previous work [**3**][**4**], both the design and fabrication of normally-closed and normally-open check valves have been modified and improved so that the in-channel dual-valved system is capable of controlling flows in the mmHg pressure – μL/min flow rate range, further controlling biological conditions in human healthcare. For example, a dual-valved device can be implanted in a glaucoma patient's eye to facilitate regulation of his or her elevated IOP. Such a configuration can also be integrated in lab-on-a-chip systems for refined flow regulation in life science research.

DESIGN

In order to realize flow regulation, the back-to-back dual-valved configuration illustrated in Fig. 1(c) was developed. By placing a normally-closed valve in forward flow operation at the inlet and placing a normally-open valve in backward flow operation at the outlet of a microchannel, the overall fluidic behavior combines the dashed regions of Fig. 1(a) and Fig. 1(b), resulting in the curve shown in Fig. 1(c). In this configuration, the normally-closed check valve dominates the fluidic control in terms of conducting flows through the channel at pressures higher than the threshold point. The normally-open check valve works in reverse leakage mode so that it serves as a fluid stopper, in which flow at pressures higher than the cut-off point is blocked. If the individual check valves are well-tuned, this passive in-channel dual-valved microsystem is able to spontaneously regulate pressure/flow rate in the designated range of forward flows without active actuation. Additionally, this configuration is leak-proof to backward flows due to the normally-closed valve at channel inlet. Because the dual valves are required to be integrated in-channel for this back-to-back operation, they were designed to be surface-micromachined for fabrication convenience.

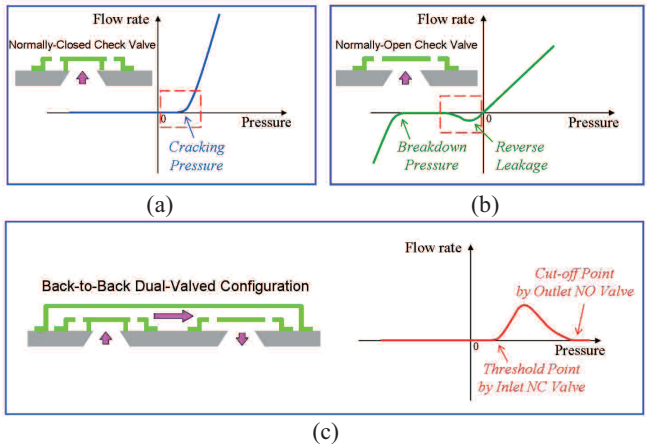

Figure 1. *Concept of dual-valved microflow regulation. Combining the single valve behavior shown in the dashed regions of (a) and (b) in a "back-to-back" configuration results in the passive pressure/flow rate regulation shown in (c).*

Fig. 2 shows the designs of micro check valves. A free-standing membrane suspended by tethers acts as the normally-open check valve, in which forward flow can be easily achieved while reserve leakage happens in backflow [**3**]. As for the normally-closed valve, it needs a pre-stressing force to block the inlet orifice so forward flow can not pass through without sufficient pressure loading. Accordingly, a vacuum-collapsed sealing method [**4**] is implemented. As a chamber is collapsed by a pressure difference between the chamber pressure and the ambient pressure, the diaphragm connected to the chamber is snapped downward and pressed against the valve seat, resulting in the dynamic behavior of a normally-closed check valve. To ensure that the cracking pressure of the normally-closed valve is well controlled, its mechanical design was verified by iterative FEMLAB™ (now called COMSOL Multiphysics™) simulations (Fig. 3) to estimate the valve performance. Depending on the use of straight-armed or twisted-armed tethers to suspend the membrane, single check valves can have different structural rigidities and their fluidic behaviors (flow resistance, cracking pressure, etc.) are correspondingly altered. Parylene C (poly-para-xylylene C) was selected as the structural material because of its mechanical flexibility (Young's modulus ~ 4 GPa), chemical inertness, biocompatibility (USP Class VI grade), and CMOS/MEMS process compatibility. Furthermore, conformal parylene deposition takes place at room temperature in a vacuum (~ 22 mTorr), which facilitates the vacuum-collapsed sealing of the normally-closed check valve.

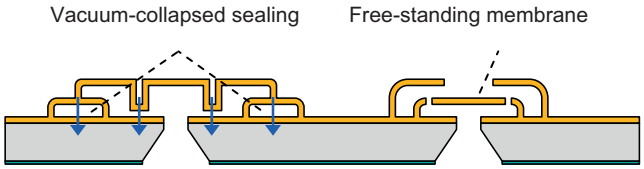

Figure 2. *Cross-section of normally-closed (left) and normally-open (right) micro check valves. Arrows in normally-closed valve denote the dragging direction when the chamber is collapsed by vacuum sealing.*

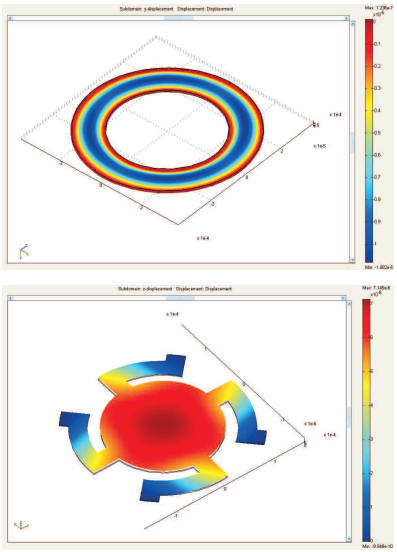

Figure 3. *FEMLAB™ simulations to estimate pre-stressing force of the vacuum-collapsed chamber (top) and resultant threshold pressure applied to valve membrane (bottom) to shunt fluids. By coupling these simulations the dynamic behavior of a complete normally-closed check valve was determined.*

FABRICATION

The fabrication process illustrated in Fig. 4 started with growing a 2 µm wet oxide on a standard silicon wafer. The backside of wafer was then bulk-etched by KOH, leaving 25 µm membranes for fluidic coupling ports. Afterwards, a multi-layer surface-micromachining technology was utilized to build frontside structures including a series of photoresist and parylene C layers. The sacrificial photoresist layers were hard-baked at 120 °C for edge-smoothening and degassing. All parylene C layers were roughened by oxygen plasma treatment to reduce stiction in the fabricated devices. Using this process, valve seats, check valves, and a integrated microchannel were fabricated. After etching away the backside silicon membrane to open through holes and stripping photoresist with acetone, an additional frontside parylene C coating was finally applied to accomplish the vacuum-collapsed sealing of the normally-closed valve.

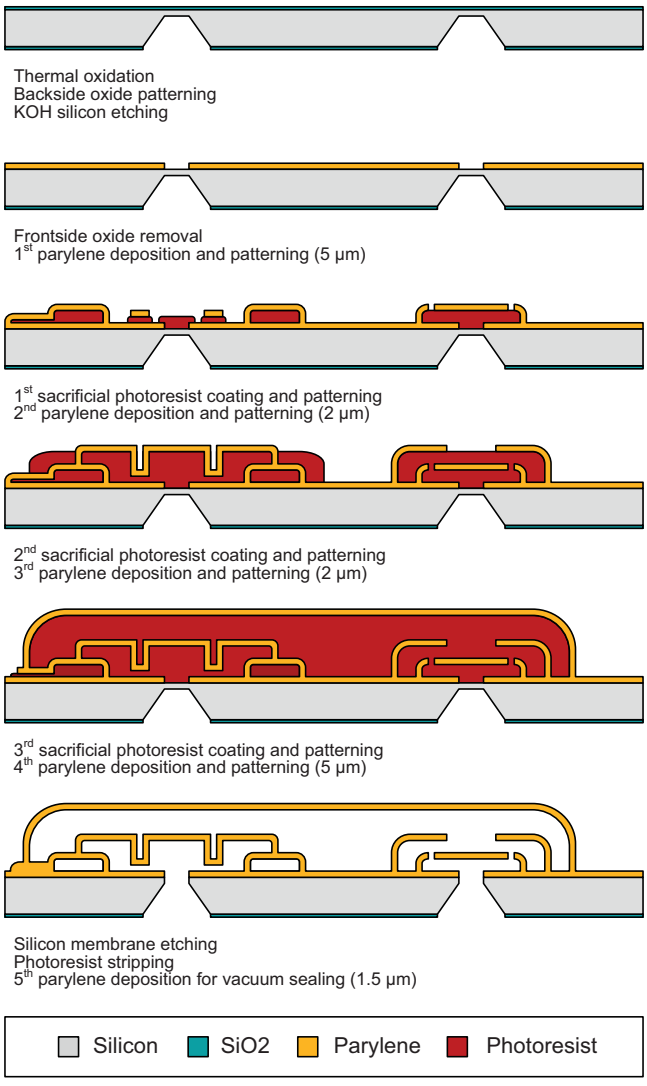

Figure 4. *Fabrication process flow.*

During fabrication the normally-closed valve was the most complex component. A three-step partial exposure lithography was applied to a single sacrificial photoresist layer in order to construct a three-level base featuring a vacuum-collapsed chamber, a valve-seat contact, and a etching/sealing channel of a normally-

closed valve (Fig. 5). A 7-µm-high chamber was connected to a 2-µm-high channel in order to realize final photoresist stripping and 1.5-µm-thick parylene vacuum sealing through that channel. A 5 µm photoresist spacer between the valve and the valve seat was made to control the pre-stressing force and threshold pressure of the fabricated valve by its height difference to the chamber. Planarization by spin-coating thick photoresist over the three-level structure was then needed to create a flat valve membrane for uniform device performance. Fig. 6 shows the fabricated in-channel parylene dual valves.

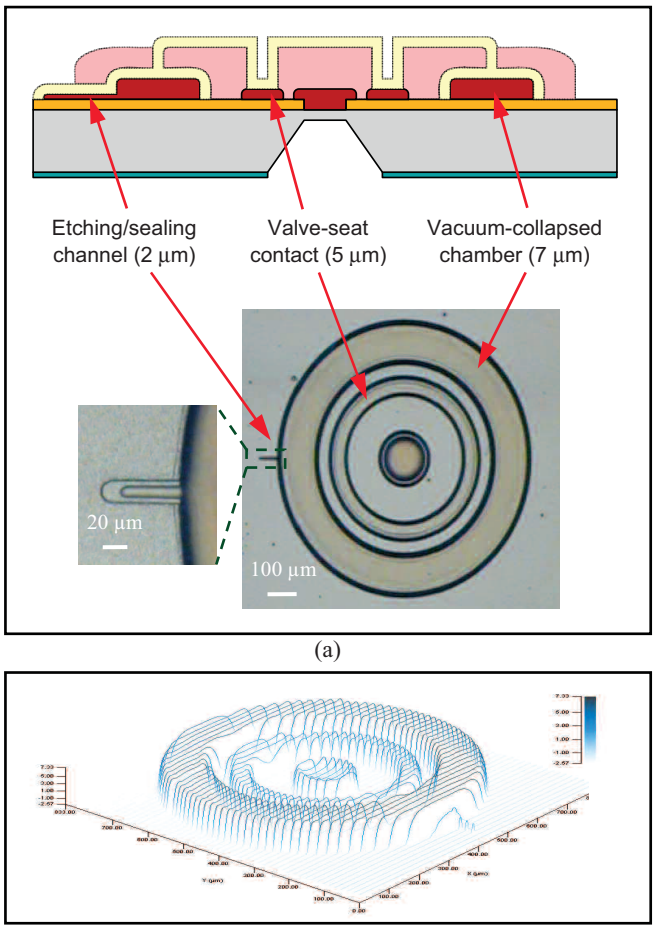

Figure 5. *Three-level sacrificial photoresist layer coating using three-step partial exposure lithography: (a) Cross-section schematic and top-view micrographs of the fabricated structure; (b) 3-D profile scan of (a).*

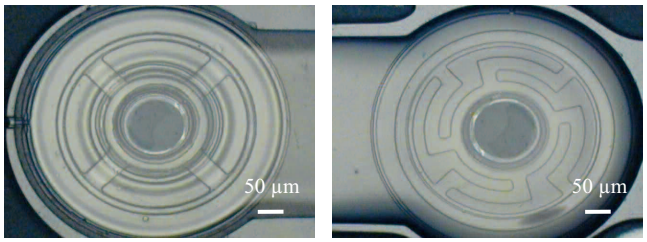

Figure 6. *Micrographs of the fabricated in-channel parylene dual valves (top view). (left) Normally-closed micro check valve. (right) Normally-open micro check valve. The diaphragm tethers can be designed as straight arms or twisted arms depending on performance requirements.*

TESTING AND DISCUSSION

Microfabricated in-channel single valves and dual valves were tested using the fluidic setup illustrated in Fig. 7. A customized testing jig was used to provide a macroscale/microscale fluidic interface with diced chips so that microflows could be introduced to the devices through their backside fluidic ports. Compressed air or water served as the fluid source. On the front end of the jig, a pressure regulator and a pressure gauge were connected to control the injection pressure of the fluids. The tuning resolution was up to 0.01 psi (~ 0.5 mmHg) even without using hydrostatic pressure generated by height difference of liquid column. Flow rate measurement and fluid collection was done on the back end of the jig. Based on the different viscosities of the fluids, flow rate measurement was performed via different methods. Air flow rate was measured with a flow meter due to its large value (mL/min range), while water flow rate was measured by recording the marching velocity of the water column front in the capillary due to its relatively small flow rates (on the order of µL/min). Using these techniques, the pressure/flow rate behavior of the devices for the different fluids could be accurately monitored.

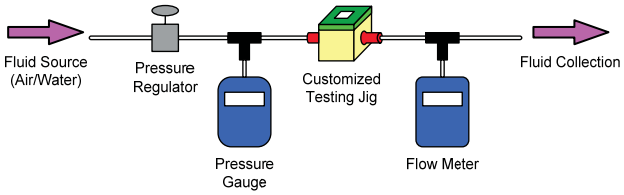

Figure 7. *Schematic of fluidic interface setup for device testing.*

Pressure/flow rate testing results are shown in Fig. 8 and Fig. 9 using air and water as the working fluids, respectively. The tested valves were of the twisted-arm tether type in order to have a more compliant mechanical response. In single valve operation, the fabricated normally-closed check valve demonstrated a remarkably low cracking pressure around 0.2 psi (~ 10 mmHg), which was in good agreement with FEMLAB™ simulations. This was a result of the fluidic pressure being applied on central area of the flexible membrane, thus effectively overcoming the pre-stressing force of the vacuum-collapsed chamber and shunting the fluids to the channel. Furthermore, there was no backflow leakage to the normally-closed valve. For the normally-open check valve, the cracking pressure was not obviously observed and the forward flow resistance was significantly lower compared to the normally-closed valve, providing a higher flow rate with the same degree of pressure loading. In terms of reverse leakage, the backward flow rate peaked at more than 2 mL/min for air and 2 µL/min for water. This leak rate started to decrease when the pressure loading was higher than 0.6 psi and was greatly suppressed with pressure loading higher than 1 psi, which implies that the valve membrane was in firm contact with valve seat. The breakdown pressure was confirmed at more than 25 psi with no obvious leak rate within this range of pressure operation. Microfluidic pressure/flow rate regulation was successfully performed in dual valve operation. Combining the single check valve behaviors, the dual-valved microsystem was able to regulate pressure in a range of 0-1 psi (~ 0-50 mmHg) with measured flow rates of up to 0.7 mL/min for air and 1.3 µL/min for water. These small flow rates were due to a large fluidic resistance obtained by the dual check valves with a microchannel in the test configuration. As expected, no reverse leakage was observed with pressure loading greater than 25 psi.

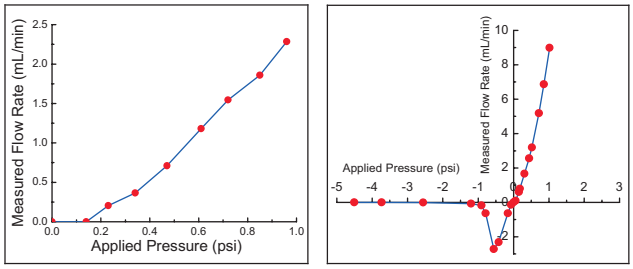

(a) (b)

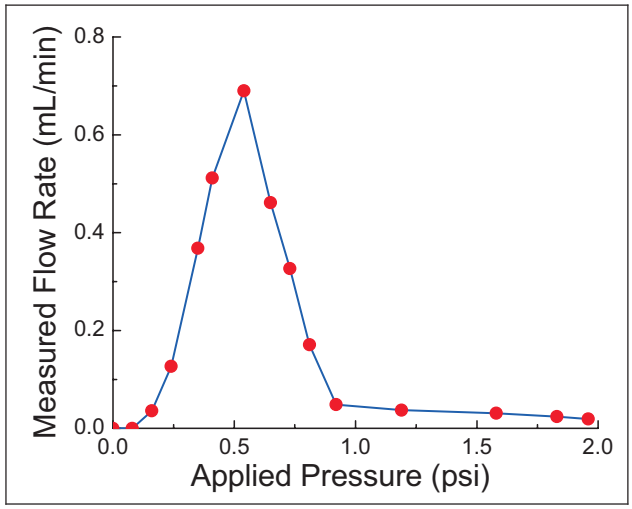

(c)

Figure 8. *Device testing with air as the working fluid: (a) Single normally-closed check valve; (b) Single normally-open check valve; (c) Dual valve operation for microflow regulation.*

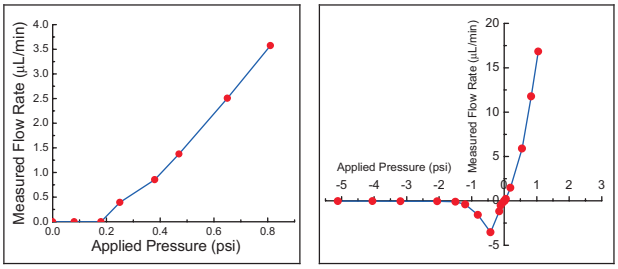

(a) (b)

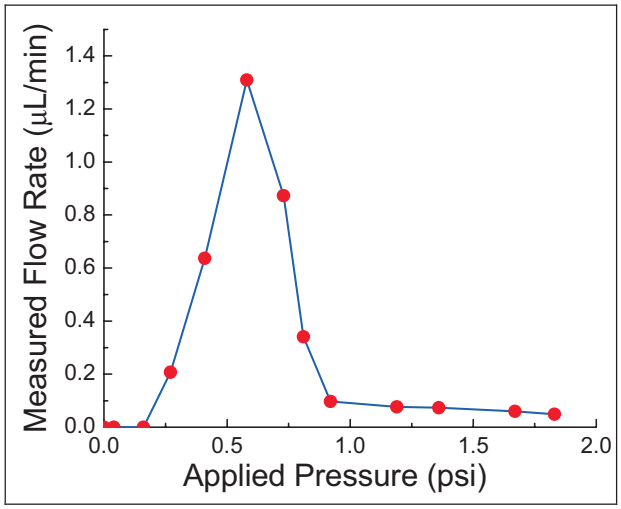

(c)

Figure 9. *Device testing with water as the working fluid: (a) Single normally-closed check valve; (b) Single normally-open check valve; (c) Dual valve operation for microflow regulation.*

CONCLUSION

A parylene-based unpowered dual-valved microflow regulation system has been successfully developed. By incorporating a normally-closed and a normally-open check valve in back-to-back configuration inside a microchannel, fluid pressure/flow rate can be systematically controlled. Because of passive operation in check valves, only mechanical elements were involved and no power consumption/transduction was required. A multi-layer surface-micromachining technology was used to construct the integrated dual-valved channels. Fabrication and characterization of single check valves and dual valves have been demonstrated. In single valve testing, both normally-closed and normally-open check valves achieved fluidic behaviors in good agreement with design and simulation. Excellent pressure/flow rate regulation was obtained in dual valve testing. Flow rates of 0.7 mL/min for air and 1.3 µL/min for water were obtained within a 0-50 mmHg pressure range. With this unique microflow regulation performance, our biocompatible/implantable dual-valved system can be exploited to conduct life science research and control biological conditions such as regulating elevated IOP of glaucoma patients.

ACKNOWLEDGEMENTS

This work was supported in part by the Engineering Research Centers Program of the National Science Foundation under NSF Award Number EEC-0310723. The authors especially thank Mr. Trevor Roper for his fabrication assistance.

REFERENCES

[1] A. van den Berg and T. S. J. Lammerink, "Micro Total Analysis Systems: Microfluidic Aspects, Integration Concept and Applications," *Topics in Current Chemistry*, vol. 194, pp. 21-50, 1997.

[2] S. Shoji, "Fluids for Sensor Systems," *Topics in Current Chemistry*, vol. 194, pp. 163-188, 1998.

[3] X. Q. Wang, Q. Lin, and Y.-C. Tai, "A Parylene Micro Check Valve," *Technical Digest*, *The 12th IEEE International Conference on MicroElectroMechanical Systems (MEMS 1999)*, Orlando, FL, USA, Jan. 17-21, 1999, pp. 177-182.

[4] X. Q. Wang and Y.-C. Tai, "A Normally-Closed In-Channel Micro Check Valve," *Technical Digest*, *The 13th IEEE International Conference on MicroElectroMechanical Systems (MEMS 2000)*, Miyazakli, JAPAN, Jan. 23-27, 2000, pp. 68-71.

[5] J. Xie, X. Yang, X. Q. Wang, and Y.-C. Tai, "Surface Micromachined Leakage Proof Parylene Check Valve," *Technical Digest*, *The 14th IEEE International Conference on MicroElectroMechanical Systems (MEMS 2001)*, Interlaken, Switzerland, Jan. 21-25, 2001, pp. 539-542.

SURGICALLY IMPLANTED MICRO-PLATFORMS IN *MANDUCA SEXTA* MOTHS

Ayesa Paul[1], Alper Bozkurt[2], John Ewer[3], Bernd Blossey[1] and Amit Lal[2]
[1]Dept. of Natural Resources, [2]*Sonic*MEMS Laboratory, School of Electrical and Computer Engineering,
[3]Dept. of Entomology. Cornell University, USA.

ABSTRACT

We demonstrate for the first time *surgically* implanted platforms and substrates for attachment of microsystems in insects without adverse effect to adult lifespan. The technology demonstrates the insertion of biocompatible balsa-titanium anchor in the late pupal stage of a moth, *Manduca sexta*, resulting in a permanently anchored base in the adult. We also present results on inserting silicon chips (4mm X 2mm X0.5mm) in the late pupal stage. The inserted substrates become permanently incorporated into the resulting adult moth as the wound is healed and the anchor site reinforced during the process of metamorphosis. This technology could open a wide venue to use insects with surgically incorporated MEMS devices as flying machines, to deploy payloads at a target of interest.

INTRODUCTION

Over the past four decades, tremendous interest has developed in creating cm-scale autonomous micro aerial vehicles (MAV) for applications ranging from reconnaissance in the battlefield to environmental monitoring. Significant advances made by microfabrication technology have made it possible to realize mm-scale low-power microsystems capable of carrying out a wide array of sensing and actuation tasks. However, the power sources for the flight of a mechanical MAV have not scaled down well. Hence attempts by aerodynamic and robotic engineers to create mechanical MAVs have only met with limited success.

In this paper, we employ nature's best flyers, insects, to realize "biobot" MAVs. Insects are autonomous flying machines and have much better aerodynamic performance than any existing mechanical flying machine. Insects also exist in diverse shapes and sizes. Large insects like the hawkmoth, *Manduca sexta*, have powerful flight muscles and can be equipped to carry telemetric payloads weighing up to 1 gram. Insects provide models for robotics as "*biobots"* [1] [2], where an intact biological system is harnessed using applied artifacts like MEMS.

Several research groups have successfully glued telemetric and electronic devices onto insects to track the insect's movement and migratory path [3] and attached miniature "backpacks" for environmental monitoring [4] [5], wireless communication or biobotic manipulation of behavior [6]. However, attaching backpacks at the adult stage leads to unreliable connections and displacement of the payload, and leads to trauma for the insect as it perceives the load as foreign weight (Table 1). Glued-on telemetric devices are temporary attachments and have been reported to fall off when the insect is in confined spaces or when foraging in vegetation. Moreover, handling a mobile and active adult to attach payloads is difficult for mass production. And with the typical adult lifespan of 2-3 weeks, delivery to the site of deployment at the correct time is challenging.

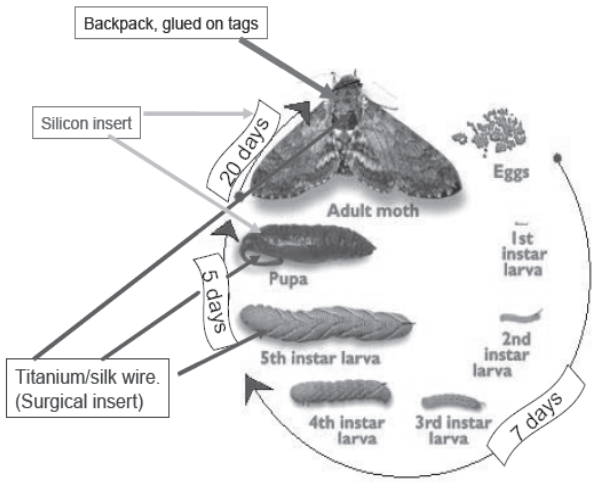

Figure 1. *Schematic illustration of the working principle on surgical insertion of the micro-platform at different stages during the life cycle of the moth.*

With the increasing interest in developing biobots that can be harnessed as MAVs with MEMS sensors and actuators, we present a Hybrid Insect with micro cargo platform surgically implanted at different life stages in *Manduca sexta*, without adverse effect to the insects life span or flight capacity. We take advantage of the metamorphosis process during the growth of the insects, when they transform from a feeding and foraging larva to an adult, to successfully implant platforms for microsystems without traumatizing the adult insects.

THEORY

Insects survive extreme surgery and this has been proved by parabiosis experiments [7], where anatomical and physiological union of a thorax with head to an abdomen from two individual silk moths has been demonstrated. These experiments were performed on silk moths at the pupal stage of development. This encouraged us to attempt to permanently attach a payload to the insect by (a) surgically inserting the micro-system into the insect for permanent attachment and (b) using the pupa, a relatively immobile stage of development. Insects grow by regenerating their outer exoskeleton (cuticle) with every molt. Hence, it is feasible to incorporate biocompatible foreign material in a life stage before emergence as adult, therefore allowing healing of the wound around the inserted material during the development of the new cuticle that occurs during the molt. This new tissue interface may ensure permanent attachment of the insert to the insect. This resource could eventually be tapped to develop devices that could be integrated into the insect tissue system like muscles or nerves to control the insect's behavior (movement). It is known that insects respond to pheromones, changes in wavelength of light,

and to various frequencies of ultrasound by altering their movement pattern either away or towards the source of stimuli. Hence one can potentially control the insects' flight path by utilizing the intrinsic natural responses to various stimuli like light, ultrasound and micro-discharge of pheromone from microsystems attached in addition to the payload.

METHODS

The moths, *Manduca sexta*, larvae and pupae were purchased from Carolina Biological Supply Company (Burlington, NC) and were reared at 26^0C, 80% relative humidity and a 12:12h light and dark photoperiod. Upon emergence, adults were transferred to a larger wire cage for proper expansion of the wings. We used the 5^{th} instar larva, pupa and adult stage (Fig 1) of *Manduca sexta* (moths) to develop the surgical protocol.

The experiments were aimed at evaluating (a) mortality rates (b) successful integration of the insert at adult emergence and (c) longevity of the adult compared to an unaltered control adult after the surgical procedure was performed at various stages of the life cycle of the moth. The first experiments involved insertion of surgical thread into the three stages of development (last instar larvae, pupal, and adult). The second experiment involved insertion of biocompatible titanium wire as anchors into these three life stages. The titanium wire post design was later modified to support a balsa wood block as the platform before the wire was inserted into the abdomen of the insect. The third experiment comprised of silicon chip surgically inserted into the larva, pupa, and adult on the ventral side of the abdominal body cavity. SEM photographs were taken to observe any tissue growth forming an interface between the titanium wires and the silicon insert, reinforcing the implants.

Table 1: *List of advantages and disadvantages of using robotic MAV and insects as payload carriers.*

		Advantage	Disadvantage
MAV manual robotics		**1.** Manipulation of flight is possible. **2.** Loss of MAV not due to external natural stimuli (pheromone, ultrasound)	**1.** Expensive to design and manufacture versatile models. **2.** Useful load disappears with decrease in MAV size.
Insect as payload carriers	**Superficial Attachment**	**1.** Versatile MAV models. **2.** Can carry a load of half its muscle weight	**1.** Lack of control of flight direction. **2.** Unreliable and prone to dislodge. **3.** Light weight power source not available.
	Surgical Attachment	**1.** Permanent structure for attachment of payload. **2.** Versatile MAV models. **3.** Can carry a load of half its muscle weight. **4.** Acclimatization to the extra load is easier when load is attached at a pre-adult stage.	**1.** Lack of control of flight direction. **2.** Light weight power source not available

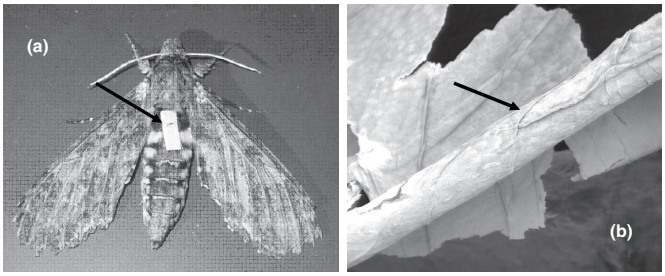

Figure 2. *Micro-cargo platform on adult Manduca sexta (a) photograph showing the balsa- titanium platform surgically inserted on the abdomen, (b) SEM photograph shows tissue growth on the titanium wire inside the abdomen resulting in a stronger and reliable attachment due to tissue support.*

Light was the stimuli/ method that was used for the control of locomotion or direction of flight. A miniature LED-based optical cue generator (0.7cm X 1.8cm, 0.5g) was designed (Fig 5) to manipulate flight direction. The device was designed to turn the LED on either the left or right side of the moth to bias flight either towards or away from the light stimulus. The experiment was designed to be conducted in a wind tunnel under red light.

RESULTS AND DISCUSSION

The results for the first set of experiments with silk tethers inserted in the late pupa showed successful adult emergence and no significant change in survival rates, mobility or behavior (Table 2) when compared to controls. The silk inserts in the larval stage (late 5^{th} instar) showed only partial success: When the silk thread was inserted just below the surface it was sometimes shed during the molt to the pupa, whereas deep insertions sometimes fatally punctured the insect's gut.

In the second set of experiments, titanium wires to be used as anchors were inserted into the abdominal cavity. Insertion of wires into the larval stage was not successful as the larvae failed to molt. However, insertion in the late pupal stage resulted in successful emergence of the adult with firmly anchored titanium wire posts (Fig 2 a,b). The healed wound around the wire anchors showed tissue growth when analyzed under a scanning electron microscope.

In the third set of experiments, silicon chips (4mm X 4mm) inserted in ventral abdominal cavity of the late pupal stage allowed for the successful emergence of the adult (Fig 3) with the chip firmly embedded in the body cavity. Prying the chip out of the body cavity caused the removal of a large piece of body wall, demonstrating the permanent attachment of the insert (Fig 5). Inserts into the pupae caused the formation of a tissue interface, thereby anchoring the insert firmly inside the body cavity. Initial test with the LED device mounted on the moth showed no direct response to light stimuli. These tests were not done in a wind tunnel.

The technology demonstrated here opens up the possibility to integrate either MEMS sensors and actuators (or rigid platforms to attach the Microsystems) in the various life stages in an insect's lifecycle. The cm^3 scale microsystems are a near perfect fit to the cm-dimensions of flying insects such as moths and butterflies. This method of implanting not only creates a venue to use the different life stages of an insect, it also results in healing of the insect around the insert forming a permanent

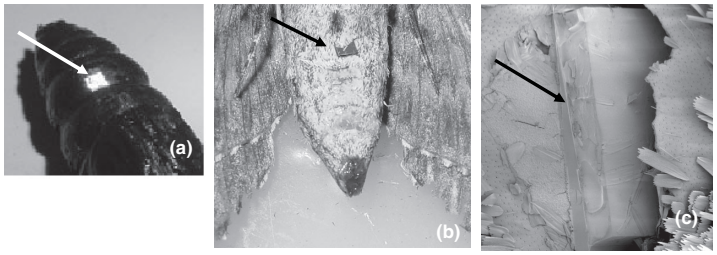

Figure 3*. Silicon chip inserted into (a) late pupal stage resulting in (b) emergence of adult with the silicon insert and (c) a SEM photograph of the silicon in the adult body.*

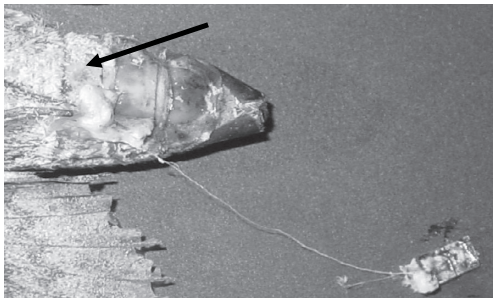

Figure 4*. Integration of the silicon chip within the abdominal cavity is demonstrated by the tissue loss while prying the insert out of the body cavity of the adult. This is due to tissue growth around the silicon chip.*

Figure 5*. Circuit board with a miniature LED based device to regulate direction of flight in the adult moth.*

Table 2. *Survival rates of Manduca sexta with inserts at all the developmental life stages (larvae, pupae and adult).*

Procedure	Life-stage (insert)	Number of replicates	Survived life stages with the insert.			Total% survived.
			Larva	Pupa	Adult	
	Larvae	20	0	0	0	0
Silk thread	Pupae	10	NA	8	8	80
(CS insert)	Adult	5	NA	NA	5	100
	Larvae	20	19	18	18	90
Silk thread	Pupae	10	NA	10	9	90
(LS insert)	Adult	5	NA	NA	5	100
	Larvae	10	0	0	0	0
Titanium	Pupae	30	NA	30	30	100
Wire	Adult	15	NA	NA	14	93.33
	Larvae	5	0	0	0	0
Silicon	Pupae	8	NA	7	7	87.5
chip	Adult	5	NA	NA	3	60
Total = 153						

structure yielding a more reliable bio-microsystem interface between the insect and the inserts. Once the platforms are integrated into the physiological system of the insect body at a stage earlier than the adult, the foreign load can be perceived as the insect's own body weight on emergence. This could result in higher payload carrying capacity of the insect. Moreover, the possibility of integrating the payload at the (relatively) immobile pupal life stage of an insect, whose emergence time into the adult stage can be manipulated (lengthened) with temperature and/or other environmental stimuli, opens the possibility of mass producing hybrid insect biobots and on time deployment of the insect at the target site, respectively.

Additionally, the tissue growth around the microsystems in the insect body could eventually present a bio-electromechanical interface that could be used to control locomotion by stimulating nerves and/or muscles to bias insect behavior like flight. Locomotion could also be controlled by manipulating the sensory organs to external stimulus like ultrasound, pheromones, and light wavelength and patterns. These external stimuli, if generated from a MEMS sized actuator, can be positioned on/in the insect. This might override the insect's instinctive behavior and result in more accurate control of its locomotion towards the target.

ACKNOWLEDGEMENT

The authors would like to thank Rajesh Duggirala for innovative ideas on the experimental design and Siva Prasad for technical assistance. This work was partially supported by a Cornell Ithaca & Weill Medical School Collaboration grant, NSF, and DARPA-MTO. The facilities used for this research include the *Sonic*MEMS laboratory and the Duffield Research laboratory at Cornell University.

REFERENCES

[1] S. B. Crary, Moore,T.E., Conklin, T.A., Sukardi,F., and Kotiditschek, D.E., "*Insect Biorobotics: Electro-neural control of cockroach walking.*," *Abstr. IEEE Int. Conf. Robotics and Automation, Workshop WT3, Bio-Mechanics*, pp. 42-54, 1996.

[2] C. Louden, "*"Insect morphology above the molecular level: biomechanics.""* *Ann. entomol. Soc. Am.*, vol. 88, pp. 1-4, 1995.

[3] J. R. Riley, "*The flight paths of honeybees recruited by waggle dance.*," *Nature*, vol. 435, pp. 205-207, 2005.

[4] Y. Kuwana, Ando,N., Kanzaki, R., and Shimoyama, I., "*A radio telemetry system for muscle potential recordings from freely flying insects.*," *Proceedings of IEEEBEMS/EMBS conf., Atlanta, GA, Oct.1999*, pp. 846, 1999.

[5] W. Kutsch, "Transmission of muscle potentials during free flight of locusts," *Computers and electronics in Agriculture*, vol. 35, pp. 181-199, 2002.

[6] P. Mohseni, Nagarajan, K., , "*An ultralight biotelemetry backpack for recording EMG signals in Moths*," *IEEE Transactions on Biomedical Engineering*, vol. 48, pp. 734-737, 2001.

[7] C. M. Williams, "*Physiology of insect diapause: the role of the brain in the production and termination of pupal dormancy in the giant silkworm Platysemia cecropia.*," *Biological Bulletin*, vol. 90, pp. 234- 243, 1946.

WIRELESS CHEMICAL SENSORS FOR HIGH TEMPERATURE ENVIRONMENTS

Edward Birdsell and Mark G. Allen
School of Mechanical Engineering, Georgia Institute of Technology, Atlanta, GA USA
School of Electrical and Computer Engineering, Georgia Institute of Technology, Atlanta, GA USA

ABSTRACT

This work reports wireless ceramic chemical sensors operating in high temperature environments. The sensors utilize a passive wireless resonant telemetry scheme to eliminate the need for onboard power and exposed interconnects. An inductor-capacitor (LC) resonator circuit forms the basis for the wireless platform. The sensor inductor is fabricated from electroplated nickel and the capacitor portion of the circuit is fabricated using mixed-oxide ceramic dielectrics. These dielectrics are found to exhibit variations in electrical properties with exposure to differing concentrations of CO_2 and NO_x. Dual sensing schemes are presented that utilize the two observed electrical responses in these materials; conductivity changes for CO_2 detection and permittivity changes for NO_x detection. CO_2 sensors have been fabricated that are able to function up to 675ºC. NO_x sensors capable of operating at up to 600ºC, while detecting NO concentrations below 5ppm, are also presented.

INTRODUCTION

Developing sensors for operation in high temperature environments, such as those found in internal combustion and turbine engines, presents a number of materials related challenges. Previous work, utilizing multilayer ceramic laminated technology from the ceramic packaging industry, has successfully demonstrated devices fabricated from low-temperature co-fireable ceramic (LTCC). In particular, a wireless pressure sensor operating at temperatures up to 450°C **[1,2]** was demonstrated. Temperature limitations of these LTCC devices are due to the glass frit component of the material. While the frit allows for a lower curing temperature, it also introduces a material with a more rapidly increasing conductivity than the pure ceramic. Later work has replaced the LTCC with high purity Al_2O_3 to eliminate the frit component and extend the temperature range of the devices. Wireless sensing platforms have been developed that have demonstrated wireless temperature measurement above 1000°C **[3]**. In this work, the high purity alumina sensing platform has been adapted to quantitatively measure chemical concentrations of CO_2 and NO.

Typically, a potentiometric approach using solid electrolytes is used for high temperature chemical sensing. However, this approach is difficult to adapt to a passive sensing scheme. Work by Ishihara **[4-6]** has shown that certain mixed-oxide compositions demonstrate electrical response to various gases at high temperature. In particular, a number of $BaTiO_3$ based mixed-oxides exhibit electrical response to CO_2 exposure and ZnO based mixed-oxides to NO exposure. Two specific dielectric compositions have been identified that exhibit electrical responses that are readily employed in a passive sensing approach. An equalmolar mixture of $BaTiO_3$-La_2O_3 has been found to vary in conductivity with exposure to CO_2. Similarly, a mixture (1:1 mole ratio) of ZnO-WO_3 has been found to vary in permittivity with exposure to NO. By incorporating these chemically sensitive dielectrics into the capacitor structure of the LC circuit, a chemical sensor can be constructed.

CHEMICAL SENSOR DESIGN

The equivalent electrical circuit model of the chemical sensor, with a coupled measurement antenna, is illustrated in Figure 1. L_a, L_s, and L_m refer to the antenna inductance, sensor coil inductance, and the mutual inductance, respectively. R_s is the series resistance of the inductive sensor coil and R_p is the parallel resistance, due to leakage, across the sensor capacitor, C_s. The input impedance, Z_a, of the antenna can be modeled from this circuit using Equations 1, 2, 3, and 4 (derivation of these equations can be found in prior publications **[1]**). The results from these equations show that both C_s and R_p influence the measured antenna impedance, Z_a. This allows two approaches to sensor design; sensors based on changing material conductivity, and sensors based on changing material permittivity.

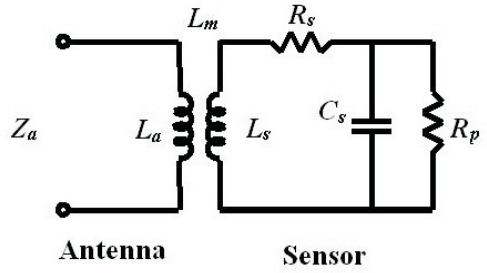

Figure 1. *Equivalent circuit of wireless sensor and measurement antenna.*

$$Z_a = \left[\frac{\omega^2 k^2 L_s L_a A}{A^2 + B^2} + j\left(\omega L_a - \frac{\omega^2 k^2 L_s L_s B}{A^2 + B^2} \right) \right] \tag{1}$$

$$A = R_s + \frac{R_p}{1 + \omega^2 C_s^2 R_p^2} \tag{2}$$

$$B = \omega L_s - \frac{\omega C_s R_p^2}{1 + \omega^2 C_s^2 R_p^2} \qquad k^2 = \frac{L_m^2}{L_a L_s} \tag{3,4}$$

Previous high temperature wireless pressure and temperature sensors have used a parallel plate configuration for the capacitor structure. In these chemical sensors it is necessary to maximize the exposed surface area of the dielectric material. The approach taken here is to replace the parallel plate electrodes with an interdigitated electrode structure. After the electrodes are deposited, the

chemically sensitive dielectric is added. This significantly simplifies fabrication and enables the deposition of the dielectric as a final step. Figure 2 shows details of the sensor layout.

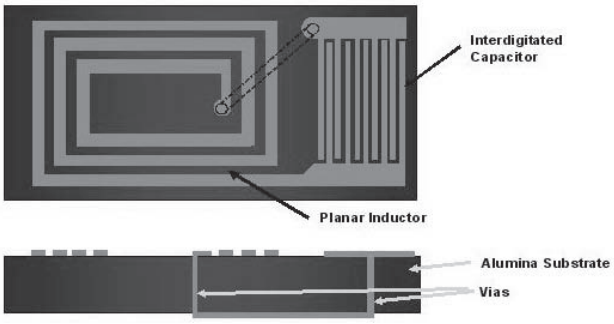

Figure 2. *Diagram of wireless sensing platform.*

The concern in this case, with a capacitor structure utilizing interdigitated electrodes, is that the underlying and unresponsive dielectric of the sensor body will contribute significantly to the overall capacitance of the LC circuit, thereby lowering the sensitivity. However, due in part to the high dielectric constant of the chemically-sensitive material, modeling shows that the induced electrical energy is concentrated in the chemically sensitive dielectric layer (Figure 3). As a result, changes in this layer dominate the response of the sensor.

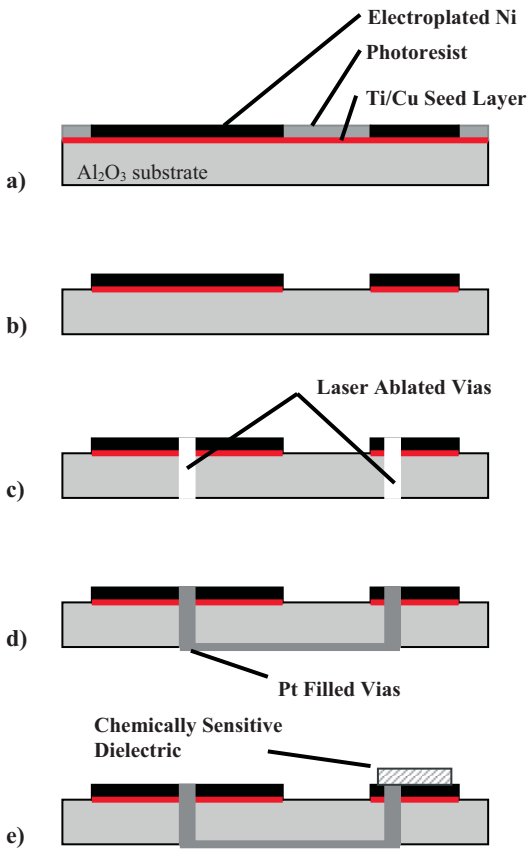

Figure 4*. Process flow for sensor fabrication.*

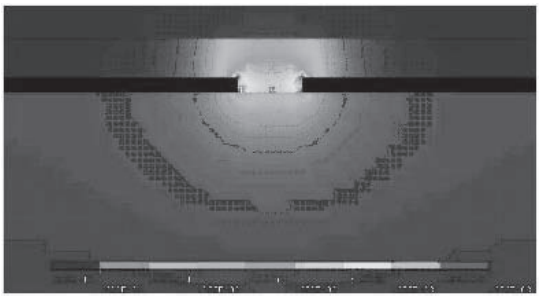

Figure 3. *Modeling results indicate electric field lines are localized in chemically- sensitive material.*

CHEMICAL SENSOR FABRICATION

The fabrication process for the chemical sensors is divided into two parts. First, the wireless sensing platform is formed by electroplating the inductor and capacitor electrode structure. Second, the chemically responsive mixed-oxide dielectric is prepared and deposited using stencil printing.

A. Ni electroplated inductive coil and interdigitated capacitor electrode structures

A metal seed layer consisting of 30 nm of Ti and 400 nm Cu is DC sputtered on 50.8 mm x 50.8 mm x 0.66 mm high-purity alumina (99.6%) thin-film substrates obtained from Coors Ceramics Company (Superstrate 996). These substrates have a non-polished (as-fired) surface finish. Next, a 30 micron layer of thick photoresist (Futurrex NR9-8000) is deposited. This layer is photo-lithographically patterned to form molds for electroplating the inductor and capacitor electrode structures. 10 microns of Ni is next electroplated using a nickel sulfamate bath at a current density of 5 $mA \cdot cm^{-2}$. The deposition rate was measured to be 0.32 $um \cdot min^{-1}$ (Figure 4a). After electroplating, the photoresist and seed layer are removed (Figure 4b). Two interconnect vias are drilled through the alumina substrate using a Nd:YLF laser (Figure 4c). A platinum ink (Dupont 9141) electrical trace is screen printed on the back side of the substrate to complete the LC circuit (Figure 4d). The ink is dried at 100°C for one hour to drive off solvents. Afterwards the ink is heated to 1000°C in an air atmosphere at a ramp rate of $10°C \cdot min^{-1}$ and held for 30 minutes to cure before cooling to room temperature at a rate of $10°C \cdot min^{-1}$.

B. Mixed-oxide dielectric material

The preparation of the chemically sensitive dielectric material is identical for both mixed oxide compositions ($BaTiO_3$-La_2O_3 for CO_2 detection and ZnO-WO_3 for NO_x detection) and uses traditional powder processing techniques. Commercially available powders of high purity, fine grained $BaTiO_3$ and La_2O_3 or ZnO and WO_3 are combined to form a 1:1 mole ratio. The powder batch is ball milled with water in a 250mL Nalgene bottle for 24-48 hours at 60 rpm. Alumina cylinders, 12.7 mm diameter x 12.7 mm length, are used as grinding media. This milling process serves to break up any powder conglomerates, mix the components, and reduce the overall grain size of the material. The resulting mixture is highly uniform in particle size and composition. After milling, the liquid slurry is poured into a 20 mm x 150 mm Pyrex® Petri dish. The slurry is baked at 90ºC for 6 hours to completely remove the water. Once dry, the powder is used to create a screen-printable ink. The mixed-oxide is combined with glycerin and mixed using a mortar and pestle. A weight ratio

of glycerin to powder of approximately 0.1:1 produces ink with an acceptable consistency and viscosity for screen or stencil printing.

The dielectric ink is then stencil printed, using a 10mm x 14mm stencil opening, on to the surface of the interdigitated capacitor electrodes (Figure 4e). The entire sensor is then heated at a rate of 3°C°·min^{-1} to 700°C and held for a duration of five hours before cooling to room temperature at 10°C·min^{-1}. This process serves two functions. First, it removes the glycerin used in the ink formation (290°C decomposition temperature). Second, the five hour dwell calcines the mixed oxide mixture. An insignificant amount of sintering occurs during the calcining and the resulting mixture remains porous upon cooling to room temperature. Previous x-ray diffraction work with this material indicates that it remains a simple mixture of the beginning mixed-oxide powders after the calcining process. Figure 5 shows an image of a fabricated sensor. The outside dimensions of the sensor are 25 mm x 40 mm.

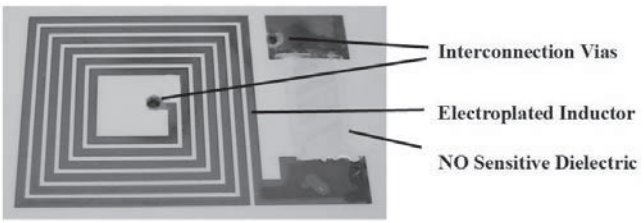

Figure 5. *Fabricated sensor with electroplated nickel inductive coil. NO sensitive dielectric stencil printed over capacitor electrodes.*

CHEMICAL SENSOR TESTING

Measurements for the chemical sensors are conducted using a Lindberg box furnace (Model BF51848) that has a maximum temperature of 1100°C. The furnace is fitted with a feed-through to pass a loop antenna inside the heated chamber. The antenna is constructed from a 50 cm length of 1 mm diameter Nickel-Chromium wire sheathed in a protective alumina multi-bore tube (AluSik–99 ZA or equivalent). The sensor is placed within the plane of the antenna loop and the impedance, *Z*, of the antenna is measured as a function of frequency using an HP4194A impedance analyzer. The furnace is ramped to each measurement temperature point and allowed to equilibrate for 30 minutes before data is taken. A K-type thermocouple located directly adjacent the sensor serves to monitor localized temperature and confirm accuracy. In order to control the atmosphere within the furnace, a 1 mm I.D. stainless tube is inserted through the furnace floor. This tube is connected to the output of two MKS Instruments mass flow controllers used to mix the incoming gas. The controllers supply a constant flow of dry air at a rate of 163 smL·min^{-1}. This flow is sufficient to create a positive pressure within the furnace and allow control of atmospheric conditions within the test chamber. Varying concentrations of the test gases are metered into the constant flow to alter the chamber atmosphere.

A. CO_2 wireless sensor – variable conductivity dielectric

The sensor is placed in the test chamber, heated to 675°C at 5°C·min^{-1}, and allowed to stabilize for 6 hours. Once stabilized, baseline measurements are taken. Various concentrations of CO_2 are next fed into the chamber. Each concentration of CO_2 is exposed to the sensor for a period of five minutes prior to measurement. Between CO_2 exposures, the chamber is purged with dry air for 30 minutes. Figure 6 shows the response of the sensor to varying CO_2 concentrations. $BaTiO_3$-La_2O_3 has been shown to have a reduced conductivity when exposed to CO_2 [**3**]. As a result, equation 1 predicts a lowering of the impedance phase angle measured at the antenna. This is observed experimentally as shown in Figures 6 and 7. The response is also dependent on concentration enabling the quantitative measurement of CO_2.

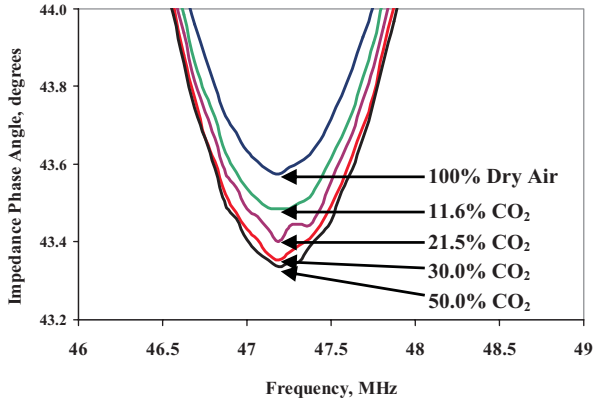

Figure 6. *CO_2 sensor ($BaTiO_3$-La_2O_3) at 675°C demonstrates variation in magnitude of impedance phase angle with exposure to CO_2.*

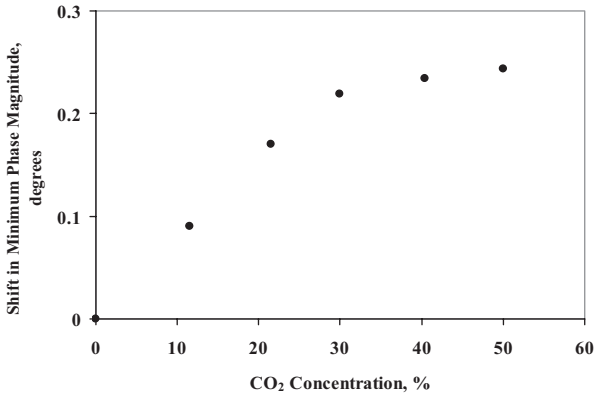

Figure 7. *Sensor response dependence on to gas concentration enabling quantitative measurements of CO_2.*

B. NO wireless sensor – variable permittivity dielectric

The NO sensor was tested over two concentration ranges (above and below 40 ppm NO). For high NO concentrations the sensor is placed in the test chamber and heated to 400°C at 5°C·min^{-1} and allowed to stabilize for 6 hours. Once stabilized, baseline measurements are taken and the sensor is exposed to NO concentrations ranging from 40-1400 ppm. The atmosphere is controlled by combining dry air with a 10,000 ppm certified concentration (±2%) of NO in a nitrogen carrier gas. As with the CO_2 sensors, the chamber is purged with dry air for 30 minutes between measurements. The sensor is exposed to each concentration of NO for a period of five minutes prior to measurement. The ZnO-WO_3 mixed oxide dielectric exhibits a change in permittivity as opposed to the change in conductivity

observed in $BaTiO_3$-La_2O_3. As a result, shifts in the resonant frequency of the sensor are expected. Figure 8 shows the response of the sensor for NO concentrations greater than 40 ppm. Above approximately 500 ppm, this response plateaus and is thought to be the result of saturation. However, for applications involving the monitoring of exhaust gases, NO concentrations in the tens of ppm and below are of most interest.

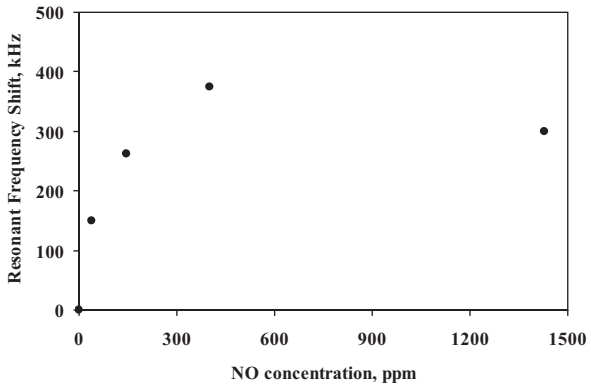

Figure 8. *NO sensor (ZnO-WO_3) exhibits saturation effects above 500ppm at 400°C.*

Testing of the sensor with lower NO concentrations follows a similar procedure as outlined above for the higher concentrations. To obtain accurate atmospheric concentrations below 40 ppm NO, a dry air flow was combined with a certified NO concentration of 1000 ppm (±2%) in a nitrogen carrier gas. In these tests the test chamber is heated to 600°C in order to explore the temperature limitation of the sensing material. The sample is heated to the target temperature at the same $5°C \cdot min^{-1}$ and allowed to stabilize for 6 hours. Once stabilized, baseline measurements are taken. Figure 9 shows the response of the sensor to NO concentrations below 40 ppm. The sensor exhibits a measurable shift in resonant frequency even below the 5 ppm level where the average response is 30 $kHz \cdot ppm^{-1}$. Response of the sensor is proportional to NO concentration and demonstrates quantitative passive wireless measurement of NO below 5 ppm at 600°C.

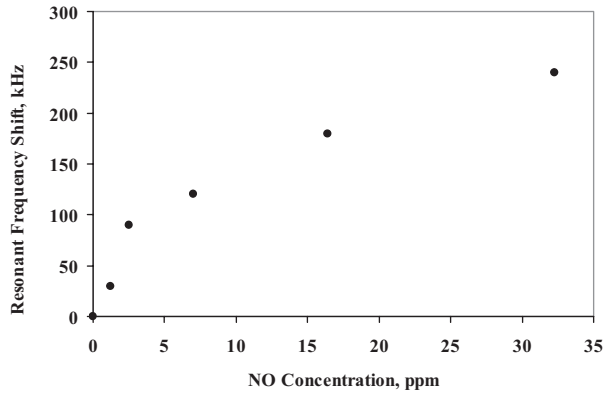

Figure 9. *NO sensor exhibits measurable shifts in resonant frequency in response to concentrations below 40ppm at 600°C.*

ZnO-WO_3 characterization by Ishihara [5] has previously shown permittivity reductions exceeding 50% for NO exposure in similar ranges. However, this characterization was preformed at a significantly lower frequency (50 kHz) than the typical 40-60 MHz operating regime of these sensors. Observed permittivity reduction in ZnO-WO_3, based on resonant frequency shift, is approximately 3% (at 35 ppm). It is believed that the notable difference between the previously characterized bulk material and the 'as-fabricated' material is due, at least in part, to this difference in operating frequency.

CONCLUSIONS

Two passive wireless chemical sensors have been presented. A CO_2 sensor based on the conductivity changes in $BaTiO_3$-La_2O_3 has been demonstrated to quantitatively measure CO_2 concentrations at 675°C. An NO sensor based on permittivity changes in ZnO-WO_3 has successfully measured NO concentrations below 5ppm at 600°C. The wireless sensing platform developed for these sensors can be readily adapted to sense a variety of other gases and even other phenomena by incorporating a dielectric that produces an electrical response to the property of interest.

ACKNOWLEDGEMENTS

This project was supported in part by NASA and DoD under the URETI program on Aeropropulsion and Power Technology. The authors would like to thank Dr. Jin-Woo Park for valuable technical discussions.

REFERENCES

[1] M.A. Fonseca, J.M. English, M. von Arx, M.G. Allen, "Wireless Micromachined Ceramic Pressure Sensor for High-Temperature Applications", *Journal of Microelectromechanical Systems*, Vol. 22, No. 4, Aug. 2002

[2] J.M. English, M.G. Allen, "Wireless Micromachined Ceramic Pressure Sensors", *Proceedings IEEE MEMS '99*, pp. 511-516, 1999

[3] E.D. Birdsell, J. Park, M.G. Allen, "Wireless Ceramic Sensors Operating in High Temperature Environments", *40th AIAA/ASME/SAE/ASEE Joint Propulsion Conference*, Fort Lauderdale, FL, July 2004

[4] T. Ishihara, K. Kometani, M. Hashida, Y. Takita, "Applications of Mixed Oxide Capacitor to the Selective Carbon Dioxide Sensor", *Journal Electrochemical Society*, Vol. 138, No. 1, Jan. 1991

[5] T. Ishihara, S. Sato, Y. Takita, "Capacitive-Type Sensors for the Selective Detection of Nitrogen Oxides", *Sensors and Actuators B*, Vol. 24-25, pp. 392-395, 1995

[6] T. Ishihara, S. Sato, Y. Takita, "Sensitive Detection of Nitrogen Oxides Based Upon Capacitance Changes in Binary Oxide Mixture", *Sensors and Actuators B*, Vol. 30, pp. 43-45, 1996

ARRAYS OF COUPLED NANOMECHANICAL RESONATORS

Maxim K. Zalalutdinov
SFA Inc.
Crofton, MD USA

Jeffrey W. Baldwin, Martin H. Marcus, and Brian H. Houston
Naval Research Laboratory
Washington, DC USA

Robert B. Reichenbach, Jeevak M. Parpia
Cornell University
Ithaca, NY USA

ABSTRACT

Arrays of coupled radio-frequency (RF) nanomechanical resonators were fabricated using ultra-thin SOI wafers, e-beam lithography and a combination of a dry and wet etch. Wide-scale propagation of the collective modes of the elastic excitations through the arrays has been demonstrated experimentally by utilizing an optical setup with a laser-driven thermoelastic excitation and an interferometry-based detection of the mechanical motion. We show the acoustic band formation in our arrays and provide an estimate of the density of states as well as the localization length of the extended modes. We envision applications in sensing and RF signal processing that would employ arrays of coupled resonators operated as delay lines, which motivates our ongoing study of the propagation of the elastic waves through the resonator arrays. The presence of a third, independently positioned laser beam in our setup allows us to simulate the loading of the array, by introducing a heat-induced stress, and thus detuning the resonators at chosen locations. We present experimental data regarding group velocity, phase shift relations, dispersion, and a brief discussion of practical implementations of devices based on such arrays.

INTRODUCTION

The collective behavior of coupled nanoelectromechanical resonators can be seen as a tool for breaking scaling laws that limit the performance of microminiaturized high frequency devices [**1,2,3,4**]. By expanding the number of high frequency, high quality factor resonators that are coupled into arrays, one can create a new media - an artificial crystal with extended acoustic bands formed by splitting and overlapping of the mechanical resonances of the individual devices. Direct control over the geometry of the resonators and coupling strength provides the ability to engineer the frequency response of the arrays (including some nonlinearities). Numerous wave-based phenomena from crystalline solids, microwaves, and optics can be simulated in realm of the elastic waves in nanoresonator array (NRA). For example, the presence of the bandgaps in the acoustic spectra of NRA opens an opportunity to operate with acoustic excitations in terms of defect-induced impurity levels, borrowing the ideology from doped semiconductors and photonic crystals. Controlled dispersion and nonlinear effects may allow the acoustic waves to exhibit solitons, intrinsic localized modes (ILM), waves scattering, *etc*.

For sensing applications (*i.e.* added mass sensing, vapor sensing, *etc.*) the resonator array can be considered as an ultimate flexural plate wave (FPW) device [**5**]. For a NRA the extra sensitivity to mass-loading is gained by decreasing the mass of the resonators, increasing the frequency of operation, and lowering phase velocity (*i.e.* shrinking the wavelength) of the elastic waves that are used to probe the loading. The NRA features well-controlled acoustic bands in the radio frequency range that can be used to design a variety of novel RF devices dedicated for frequency domain signal processing. Broadband filters, traveling wave amplifiers, dispersion-based spectrum analyzer, *etc.* can be designed to operate with broadband excitations implemented as elastic waves propagating through the array.

In this paper we present results of the fabrication and experimental study of 2D arrays of coupled plate-type nanomechanical resonators (Fig. 1). Each resonator is comprised of a silicon square plate supported by a square SiO_2 pillar at the center. Coupling between neighbors is provided by narrow beams connecting the centers of the square sides (Fig. 1).

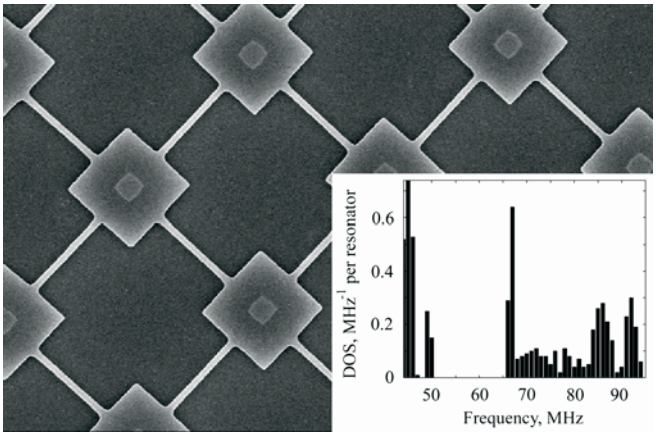

Figure 1. *SEM image showing part of the paddle resonator array. The dimensions of the silicon square paddles are 2x2 μm, thickness 45nm. The SiO_2 pillar supporting the center of the paddle has a cross section 0.54x0.54μm and is 150nm tall. The connecting bars are 2 μm long and 200nm wide. Inset shows the results of finite element analysis for the density of states in the 10x10 paddle array. DOS was calculated by direct counting of the number of modes (deduced from FEM modal analysis) per frequency interval.*

We use modal analysis based on numerical simulations that employ finite elements methods (FEM) to predict the response of our arrays. Shell-type elements were used to model the resonators as plates, free on outside and clamped on the pillars' edges. Direct counting of the number of the normal modes of the array per frequency interval provides us with the density of states (DOS) for our "artificial crystals". The inset of Fig. 1 demonstrates the DOS for a 10x10 array of the plate resonators shown in the SEM image. The DOS plot shows the presence of two distinct acoustic bands (45-50 MHz and 65-95MHz) separated by a pronounced bandap. Inspection of the mode shapes of the array and cross-referencing

with the modes of a single paddle resonator indicate that the low frequency band of the array's DOS is being populated by the "bridge-type" modes produced by the motion of the connecting arms, while the upper band is filled with a variety of modes stemming from the square plate itself. Experimental observation of the predicted band structure in our microfabricated resonator arrays, estimation of the localization range for the collective modes, and evaluation of the disorder effects were the initial research goals. We present our recent results and discuss the broader topic related to propagation of the broadband elastic excitation through the resonator arrays.

FABRICATION

Commercially available SOI wafers with the silicon layer thickness 45nm and buffered oxide (BOx) 150nm were used in the fabrication. Direct e-beam writing in 50nm-thick hydrogen silsesquioxance resist (HSQ, Dow Corning) spun over SOI wafer was used to create a mask for subsequent dry etch through the Si layer. We utilized a cryogenic plasma etch (T=100 K) in a SF_6 and O_2 gas mix (SF_6 serves as a source of fluorine radicals for the etching and oxygen provides passivation of the sidewalls) [**6**]. This process, implemented in an inductively coupled plasma (ICP) chamber, is known to provide very high selectivity towards the etching of Si with respect to a SiO_2 mask. Ion-induced damage is also minimized in the ICP process. This prevents additional ion implantation, and thus does not adversely affect the internal friction for these resonators. A subsequent wet etch in concentrated HF (48%) is timed to partially undercut the BOx layer, releasing the periphery of the Si square plates, while leaving a SiO_2 supporting pillar at the center of the resonator.

EXPERIMENTAL DETAILS

Optical transduction was used to study the vibratory response of the array. A long working distance glass corrected objective lens was used to focus three laser beams each into micron-sized spots on the NRA located in a vacuum chamber (P~10^{-8} Torr). The optical path of one of the lasers (blue, wavelength 412nm) was fixed and its focused spot was positioned within the NRA using a microstep stage moving the entire vacuum chamber. The other two laser beams (red HeNe 633nm and green YaG 512nm) were equipped with steering mirrors, which allowed us to position their spots independently within 60x60 μm^2 image area provided by CCD camera (Fig. 2). A point-type thermoelastic excitation was provided by modulating the intensity of the blue diode laser (412 nm) focused on a single paddle resonator within the array. The amplitude of the laser power modulation delivered to the sample was adjusted to ~50 microWatts. The time-variable local heating induced by the focused laser beam in our structures generated a modulated stress due to thermal expansion and thus provided the driving force. The resulting motion of the suspended structures was detected interferometrically, by focusing another laser (red CW HeNe, 633 nm) at a different point in the array and measuring the modulation of the reflectivity [**7**]. This modulation originates in the motion-induced variation of the gap in a Fabry-Perot interferometer created by the resonator plate (acting as a semitransparent mirror) and the underlying substrate.

Independent positioning of the blue (drive) and red (detect) lasers provides the flexibility that is necessary to detect propagation of the elastic waves through the array "from point A to point B". However, the response at "point B" is a result of the interference of numerous elastic waves taking different paths through the array. In order to study the propagation pattern we have introduced a third laser (green YAG, 512nm) in our setup. This laser delivers up to 2mW of CW power to a chosen resonator "C" located somewhere in between "A" and "B" and causes significant detuning of that resonator "C" due to heat-induced stress. The presence of the green laser upgrades our NRA to a "three-port" device allowing us to introduce well-controlled local perturbations into the dynamics of the array.

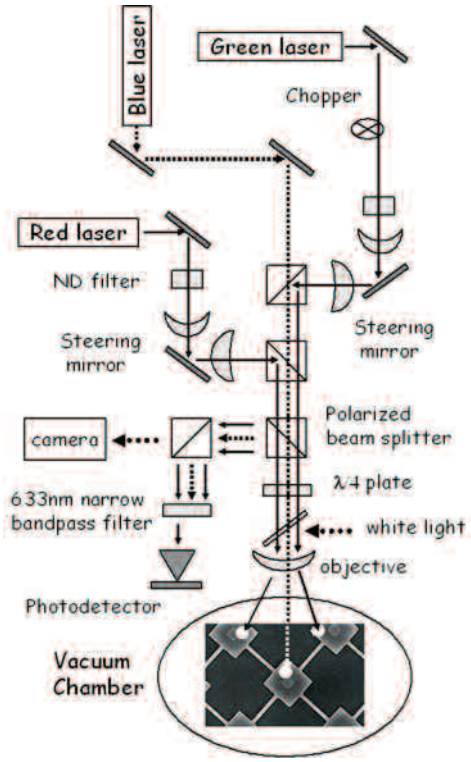

Figure 2. *Schematic diagram of the experimental setup. RF modulated blue diode laser (412nm wavelength) was used to excite the NRA. The red laser (HeNe 633nm) provides interferometric detection of the mechanical motion. An independently positioned green laser was employed to introduce local perturbations in the array.*

RESULTS AND DISCUSSION

Fig. 3 shows the frequency response of a 20x20 NRA with 2μm-long connecting arms. Instead of a few distinct peaks corresponding to normal modes of a single resonator, the system exhibits hundreds of peaks arranged in two wide-spread bands: the low-frequency band (45-55MHz) and upper band (70-105MHz). The positions of the bands are in very good agreement with the results of the numerical calculations shown in Fig. 1. The direct counting of the number of peaks in the lower band (Fig. 3) provides an estimation of 12 MHz^{-1} for the DOS. This number is almost an order of magnitude lower than the value expected from FEM analysis. We attribute this discrepancy to the fact that only a limited number of resonators surrounding the driving point is participating in the collective modes. We suggest that the propagation of the elastic waves over the array is limited by the Anderson's localization [**8**] and is determined by "disorder," *i.e.* mistune of the resonators forming our "artificial crystal" [**9**]. Inset in Fig. 4 shows the spatial decay of the band-averaged elastic energy (calculated by integrating the square of the amplitude of the motion over the frequency band). By moving the detecting red

laser away from the driving point we observe that the amplitude of the motion is nearly vanished at a distance of 5 unit cells. We conclude that the array has an effective size of approximately 10x10 which leads to a theoretical prediction of the DOS that is in good agreement with the experimental value.

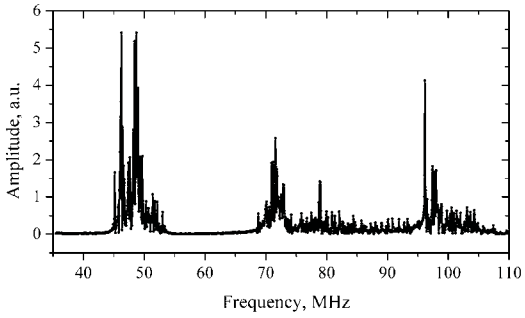

Figure 3. *Frequency response of 20x20 paddle array with 2μm-long connecting arm. Data acquired by driving a paddle at the center of the array and detecting the vibrations at the next paddle.*

Lines 1-5 in Fig. 4 show unwrapped phase-frequency dependences acquired for separations from 1 to 5 unit cells between the driving and detecting beams. The slope $d\varphi/d\omega$ of these curves provides an estimate for a group delay for the elastic waves propagating through the array. Given the separation distance, the group velocity v_{gr}~3 m/s can be calculated. This number is few orders of magnitude slower than typical value for group velocity used in FPW devices.

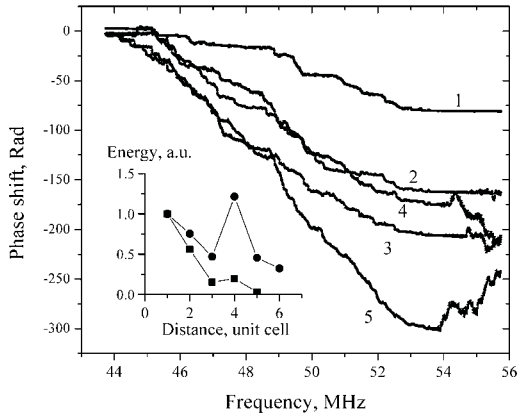

Figure 4. *Phase delay for the low-frequency band of 20x20 paddle array with 2μm-long connecting arm. Numbers 1-5 next to curves correspond to separation (in unit cells) between driving and detecting beams. Inset shows spatial decay of the acoustic energy averaged over the low band (squares) and upper band (circles).*

In order to demonstrate control over the band diagram of our array we increase the coupling between paddle resonators by reducing the length of the connecting arms down to 1μm without modifying the size of the paddles or the width of the undercut (Fig. 5). This modification shifts the lower band in Fig. 3 up in frequency and makes it merge with the upper band, eliminating the bandgap. Numerical simulations based on a model of an ideal 10x10 paddle array (no disorder) confirm the presence of a single band comprised of a few merging sub-bands that originate from different modes of vibrations (inset in Fig. 5). After introducing disorder, implemented in our model as random mistune of the resonators, (*df/f*~3% according to experimental data) the FEM calculations predict much more "homogenized" DOS within the band, due to the spread and interpenetration of different sub-bands and the creation of somewhat exotic collective modes that exhibit different types of normal modes at different nodes of the array.

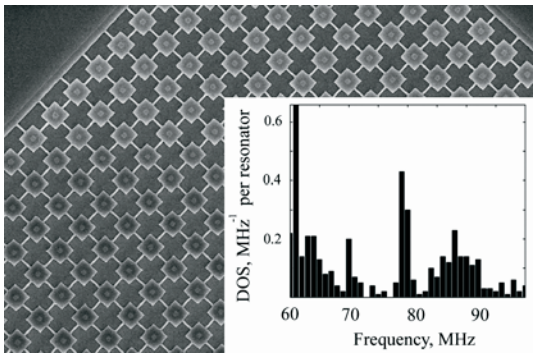

Figure 5. *Resonator array with stronger coupling (i.e. 1μm connecting arms). Part of the frame is shown. The inset shows the results of FEM simulations for the density of states of 10x10 array.*

Figure 6 shows the vibrational spectrum of a 40x40 NRA with 1μm arms. The single band is observed in accordance with FEM calculations. Peak counting provides an estimated 12 MHz^{-1} for the density of states and the phase slope corresponds to the group velocity v_{gr}~4 m/s. By stepping the red laser and measuring the amplitudes of vibrations at different separations from the driving point we demonstrate that at least a 20x20 area of our 40x40 paddle array is participating in the collective modes.

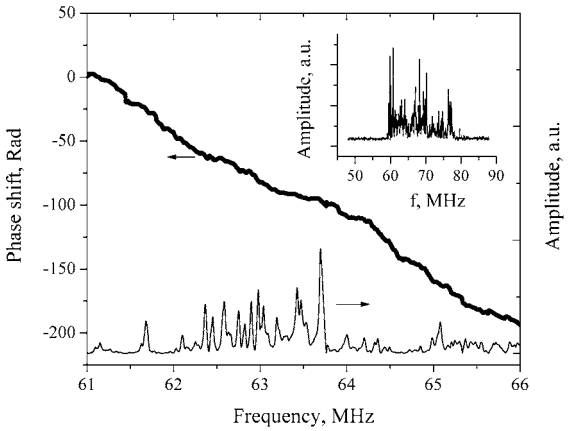

Figure 6. *Part of the vibration spectrum for the 40x40 paddle array with 1μm-long connecting arm. Data acquired by driving a paddle at the center of the array and detecting the vibrations 24μm (8 unit cells) away. The inset shows the full band of the array.*

The effective size of the 40x40 array is large enough to start pursuing the major questions of interest: the pattern of the energy flow through the array and the contribution of a particular resonator to the extended modes of the array. In order to evaluate the involvement of a single resonator in the collective modes of vibrations we focus our third, green laser (512nm, 2mW CW power) on that chosen resonator. The resulting local heat-induced stress is sufficient to provide frequency shifts for the fundamental

modes an isolated resonator far in excess of their half-widths. When the affected resonator is a part of the array, the entire band can be modified. To highlight such alterations of the array's response we modulate the intensity of the green laser at a very low frequency (mechanical chopper with f_{mod} ~10Hz is utilized in our setup) while acquiring the vibrational spectrum with our usual blue laser drive and red laser pickup. The resulting "telegraphic noise" due to bouncing between the non-perturbed spectrum and the one modified by the green laser is illustrated in Fig. 7.

The fact that the influence of the green laser can be detected at a remote location, and is well-pronounced over a wide spectral range, confirms the extended nature of elastic excitations in our arrays. In sensing applications, for example, a similar local perturbation can be caused by a modified mass loading due to absorption of some analyte to one of the resonators. For RF signal processing the NRA can be considered as a multiport device where each port (*i.e.* node of the array) can control delay and dispersion in a wide frequency range or can also be used to alter the flow pattern of the signal through the array.

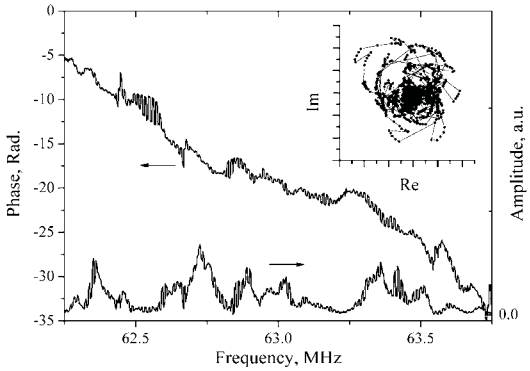

Figure 7. *Vibration spectrum of the 40x40 array (1μm connecting arms) modulated by the chopped green laser. Blue laser (drive) is positioned at the center (origin), red laser (pickup) is shifted 5unit cells North and the coordinates for the green laser spot are 2 North, 2 West. The inset is a Nyquist plot of this data.*

Practical implementations of the NRA-based devices may include a thermal actuator fabricated as resistive heater (similar to one described in [**10**]) located on the frame of the array. An optical setup with micro-packaged VCSEL lasers and integrated photo detectors could be used for the pick-up. One can also envision a magnetomotive detection sytem with the conducting wire running over series of resonators. Other transduction methods based on ferroelectricity, piezoresistivity, *etc*. can be considered but would probably be limited to the cases when the detection is implemented on a resonator next to the frame. External perturbations for the three-port devices could be introduced either thermally or by applying mechanical stress (with low frequency electrostatic comb-type actuators for example).

CONCLUSIONS

The presence of extended modes of vibrations in microfabricated 2D arrays of coupled nanomechanical plate-type RF resonators has been demonstrated. The vibrational spectra of the array exhibit wide acoustic bands separated by bandgaps that can be tuned by tailoring the geometry of the array. We show that the number of the resonators involved in the collective modes in our arrays can exceed 400 (20x20 effective size) and give an estimate of 12 MHz^{-1} for the density of states. By operating the array as a delay line an estimate has been obtained of group velocity V_{gr}~4m/s for the elastic excitations propagating through the array. We demonstrate that a local perturbation introduced at a given point in the array can cause alterations to the response of the array that are extended both in space and frequency. We anticipate that nano-resonator arrays may ultimately have a range of applications in sensing and RF signal processing.

ACKNOWLEDGMENTS

The authors gratefully acknowledge Dr. J. Vignola and Dr. D. M. Photiadis for helpful discussions. The authors would also like to thank the member of technical staff of the Institute for Nanoscience at NRL, D. R. King for assistance. This work was supported by the Office of Naval Research and Cornell Center for Material Research (CCMR, NSF IDMR-0079992).

REFERENCES

[1] U. Demirci, M. A. Abdelmoneum, and C. T.-C. Nguyen, "Mechanically corner-coupled square microresonator array for reduced series motional resistance," *Dig. of Tech. Papers*, the 12th Int. Conf. on Solid-State Sensors & Actuators (Transducers'03), Boston, MA, June 2003, pp. 955-958.

[2] S. Lee and C. T.-C. Nguyen "Mechanically-coupled micro-mechanical arrays for improved phase noise" *Proceedings*, IEEE Int. Ultrasonics, Ferroelectrics, and Frequency Control 50th Anniv. Joint Conf., Montreal, Canada, August 2004, pp. 280-286.

[3] S. A. Bhave, Di Gao, R. Maboudian and R. T. Howe "Fully –Differential Poly_SiC Lame-Mode Resonator and Checkerboard filter" 18th IRRR International Conference on Micro Electro Mechanical Systems (MEMS 2005), Miami, Florida, January 2005, pp. 223.

[4] E. Buks and M. Roukes "Electrically Tunable Collective Response in a Coupled Micromechanical Array" JMEMS Vol. 11 pp. 802 (2002).

[5] D.S. Ballantine, R.M. White, S.J. Martib, A.J. Ricco, E.T. Zellers, G.C. Frye, H. Wohltjen "Acoustic Wave Sensors Theory, Design and Physico-Chemical Applications" Academic Press (San Diego, London, Boston, New York, Sydney, Tokyo, Toronto) 1997, pp. 111-145.

[6] R. Dussart, M. Boufnichel, G. Marcos, P. Lefaucheux, A. Basillais, R. Benoit, T. Tillocher, X. Mellhaoui, H. Estrade-Szwarckopf and P. Ranson "Passivation mechanisms in cryogenic SF_6/O_2 etching process" J. Micromech. Microeng. 14 pp, 190-196 (2004), http://www.oxfordplasma.de/process/si_needl.htm

[7] D.W. Carr and H.G. Craighead "Fabrication of Nanoelectromechanical Systems in Single Crystal Silicon using SOI Substrates and Electron Beam Lithography" J. Vac. Sci. Technol. B **15**, 2760 (1997).

[8] P.W. Anderson "Absence of Diffusion in Certain Random Lattices" Phys. Rev. **109**, 1494 (1958), R. L. Weaver "Anderson Localization in the time domain: Numerical Studies of waves in two-dimensional disordered media" Phys. Rev. B 49, 5881 (1994), A. MacKinnon, B. Kramer "The Scaling Theory of Electrons in Disordered Solids: Additional Numerical Results" Z. Phys. B – Condensed Matter **53**, 1 (1983).

[9] M. Zalalutdinov, J. Baldwin, M. Marcus, R. Reichenbach, J. Parpia and B. Houston "2-Dimensional Array of Coupled Nanomechanical Resonators" submitted to Appl. Phys. Lett.

[10] M. Zalalutdinov, K.L. Aubin, R.B. Reichenbach, A.T. Zehnder, B.H. Houston, J.M. Parpia, and H.G. Craighead "Shell-type micromechanical actuator and resonator" Appl. Phys. Lett. **83**, pp. 3815 (2003).

A 2-AXIS QUASI-PASSIVE PLATFORM FOR NANOSCALE PHOTONIC ASSEMBLY

Biao Li, Marco Pietrusky, Andre Sharon
Fraunhofer USA Center for Manufacturing Innovation
15 St. Mary's St., Brookline, MA 02446, USA

ABSTRACT

As the need for communication bandwidth continues to increase and devices move from multi-mode to single-mode technology, optical alignment requirements are becoming more stringent, approaching the nanometer level. We previously reported a 1-axis quasi-passive platform with nanoscale alignment tolerance **[1]**. This paper presents our research on a 2-axis positioning platform capable of four degrees-of-freedom in-plane motion. Particularly, a modified design has been adapted for rapid device production. In addition, a focused ion beam (FIB) technique has been utilized for in-situ stress element trimming and nanoscale motion characterization. Furthermore, an automated program has been implemented for light coupling experiment. Finally, the reliability of the 2-axis platforms has been evaluated.

INTRODUCTION

Currently, active alignment remains as the only viable means for low-loss optical coupling with the required alignment tolerance (<100 nm) **[2]**. The problems associated with this costly process are well known to those in photonic packaging including complex fiber handling and post-alignment shift. Silicon optical bench (SiOB) technology emerged as a means to passively align and integrate optical components on an optical breadboard **[3]**. However, progress in the development of SiOB technology has been slow due to the difficulties in aligning the optical path to nanometer-scale tolerance often required. Using purely passive locating features, one can position components on a micro-optical bench to desired locations relative to one another within a tolerance of at best 1 μm. This is an order of magnitude worse than what is needed for efficiency coupling between devices and/or fibers.

Inspired by resistor trimming in microelectronics, we developed a quasi-passive integration technique capable of nanometer-scale positioning tolerances. The concept capitalizes on inherent residual tensile stresses in MEMs thin films, and comprises a platform suspended by stressed flexure elements on either side. These thin film flexures, made of highly stressed materials such as silicon nitride, can support in-plane tensile stresses up to ~1 GPa. By selectively trimming stress elements, the equilibrium position of the platform can be biased to one side or another, enabling high resolution relative motion between the suspended platform and the base. The movement of the platform can be directed toward the light path using techniques of active alignment but without necessitating any micro-handling of the components or fibers, and without necessitating subsequent immobilization. The scale of this adjustment is well suited to the alignment task, yielding nanometer-scale resolution with sufficient range for typical applications.

As a proof of concept, we previously reported a 1-axis quasi-passive platform capable of sub-micron alignment optimization **[1]**. This paper presents our research on a 2-axis positioning platform with emphasis on stress element design, nanoscale motion characterization, laser trimming automation, and robustness enhancement.

FINITE ELEMENT MODELING

Figure 1 shows the finite element modeling (FEM) of the platform displacement in response to trimming the stress elements. The 2-axis platform enables four in-plane degrees-of-freedom — two in translation, and two in angular rotation. Translation can be achieved by cutting pairs of stress elements symmetrically; while angular motion can be achieved by asymmetrically trimming the stress element. The effect of cutting a stress element on one side of the platform is identical to that of pulling the corresponding one on the other side. FEM also indicates that more stress elements facilitate higher resolution motion; while fewer stress elements facilitate larger displacement. Nanometer-scale platform movement is reachable with a large number of short stress elements.

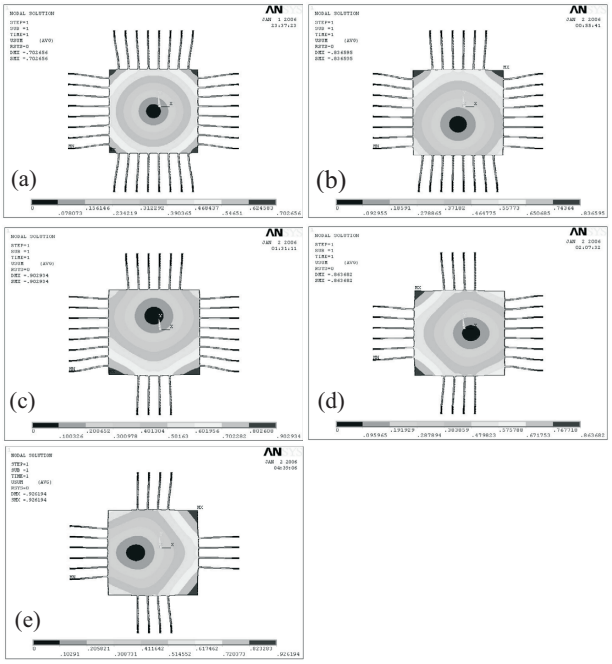

***Figure 1**: Finite element simulation of the nanoscale platform motion in response to trimming the stress element. (a) Initial position; (b) downward motion; (c) upward motion; (d) rightward motion; and (e) leftward motion.*

EXPERIMENTAL DETAILS

I. Rapid production of 2-axis platform. We have manufactured 2-axis devices using standard microfabrication technology. The process started with polished [100] orientation silicon (Si) wafers. Prior to low-pressure chemical vapor deposition (LPCVD), standard wafer cleaning was applied. A 200 nm thick stoichiometric Si_3N_4 thin film was grown from 30 sccm dichlorosilane (DCS) and 90 sccm ammonia at 825 ^oC under a pressure of 300 mTorr. This resulted in an inherent tensile stress of approximately 1 GPa in the film. The platform and stress element

patterns were formed after selectively reactive ion etching the frontside Si_3N_4 film. Consequently, etching windows were created after selectively etching backside Si_3N_4 film. Finally, the patterned wafers were put into a potassium hydroxide (KOH) bath to release the Si_3N_4 from the surrounding Si structure.

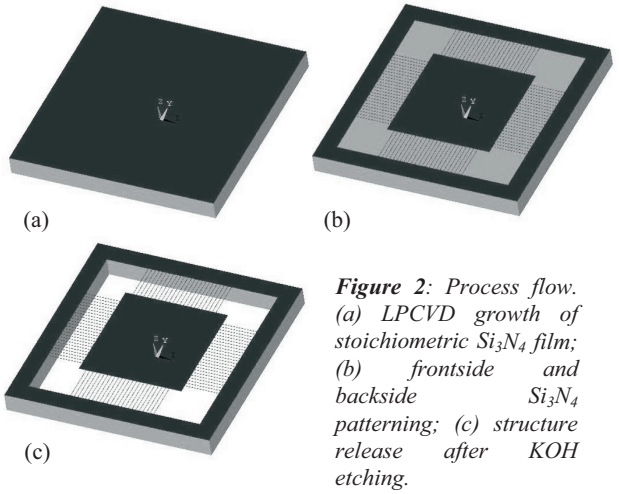

***Figure 2**: Process flow. (a) LPCVD growth of stoichiometric Si_3N_4 film; (b) frontside and backside Si_3N_4 patterning; (c) structure release after KOH etching.*

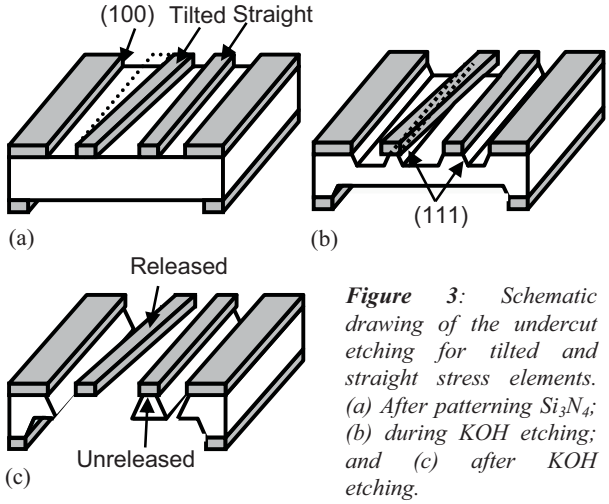

***Figure 3**: Schematic drawing of the undercut etching for tilted and straight stress elements. (a) After patterning Si_3N_4; (b) during KOH etching; and (c) after KOH etching.*

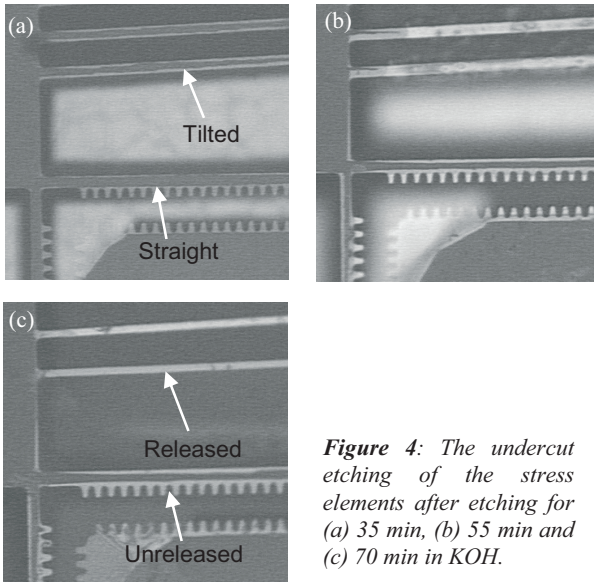

***Figure 4**: The undercut etching of the stress elements after etching for (a) 35 min, (b) 55 min and (c) 70 min in KOH.*

To activate the stressed-element, all Si underneath the Si_3N_4 film must be completely removed. It is found that the release of Si_3N_4 always took a great deal of time for a straight configuration where all stress elements were oriented along the (100) direction of the Si wafer (Figures 3&4). As such, the free-suspended structures were often destroyed during the long-term aggressive etching process. On the other hand, a tilted configuration where stress elements were misoriented from the (100) orientation of Si wafers would be subjected to severe undercut etching. We exploited this characteristic for rapid production of a 2-axis platform. Figure 5 illustrates a micro-machined 2-axis platform. The tilted stress elements were completely released due to quick undercut etching.

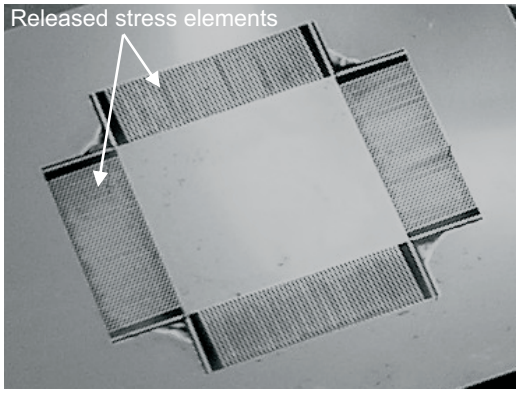

***Figure 5**: Optical photograph of a micro-machined 2-axis platform with completely released stress elements.*

II. Focused ion beam trimming and characterization. A focused ion beam (FIB) technique **[4]** was utilized for in-situ stress element trimming and nanoscale motion characterization. The experiment was conducted in an FEI FIB 200 system. As shown in Figure 6a, the 2-axis platform was first epoxy glued on a polished Si piece before transported into vacuum chamber. The Si piece provided not only a conductive substrate for effective charge neutralization but also a clear background for nanoscale imaging. A focused ion beam ejected from a liquid Gallium (Ga) ion source, with a spot size of less than 10 nm, is scanned across the sample with 30 kV kinetic energy. At a beam current of 70 pA and with a magnification of 2000, individual stress element could be selectively etched within one minute. Figure 6b shows a FIB trimmed stress element.

To evaluate the platform motion with respect to stress element trimming, we created several trenches on the underlying Si piece using FIB milling. Prior to FIB processing, patterning geometry of 10 μm × 1 μm × 1 μm was defined at the location of 10 μm away from the platform edge. Using a beam current of 70 pA and a magnification of 6500, trenches were generated on Si. Figure 6c illustrates a FIB milled trench that is close to the upper midpoint of the platform. Images were recorded using secondary electron contrast with a magnification of 6500 (corresponding to a pixel spacing of 11 nm).

Figure 6d illustrates the platform movement after symmetrically cutting four stress elements on the upper side. With more stress elements pulling below the platform, the FEM predicted a net movement of 195 nm downwards. To determine the true position shift of the platform after trimming the stress elements, we attempted to align the trench at different images to the same horizontal level (guideline 1). The positions of platform were then identified by guidelines 2 and 3. The FEI 200 system

provides the ability of fine-tuning the magnification (±1×). Thus, imaging distortion during different scans is neglected. Using a 10 μm scale bar as a reference, the distance between guidelines 2 and 3 was measured as -206 nm. Since the measurement error for each guideline is one pixel size, ±11 nm, the total error of the measurement is ±33 nm. This indicated that the platform behaved as modeled, resulting in a net movement of approximately 206 nm (±33 nm) downwards.

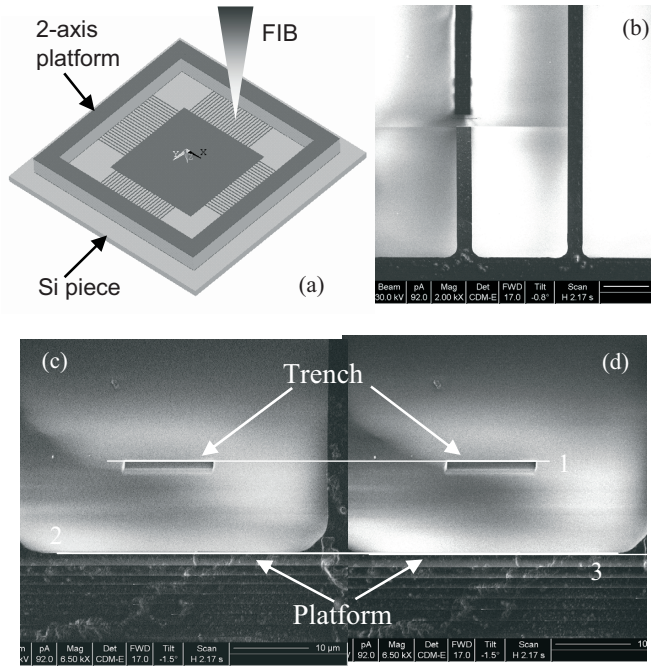

***Figure 6**: Nanoscale motion characterization. (a) A 2-axis platform is placed on a polished Si piece for FIB trimming and imaging; (b) A stress element is FIB cut; (c) A maker is FIB machined on the underneath Si piece. (d) Downward platform motion after FIB trimming four stress elements.*

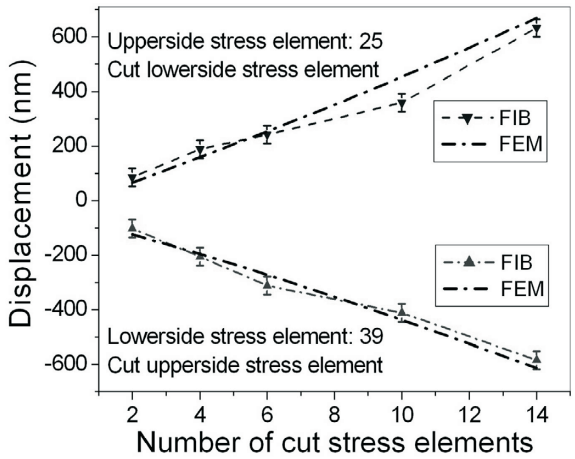

***Figure 7**: Platform motion with respect to trimming stress elements. The measured data (error bar: ±33nm) agrees well with the finite element simulation results.*

Figure 7 exhibits the platform motion as the result of removing the stress elements at the upper- and lower-side of the platform, respectively. The dots-dashed-lines represent the experimental data derived from FIB measurement, while the solid lines refer to the FEM results. The measured displacement agrees well with the finite element modeling, validating this as a predictable device for nanoscale motion management. In addition, the translation is almost linear and reversible with respect to the number of cut stress elements. With 39 stress elements on the lower side, trimming one stress element on the upper side of the platform generates approximately 38 nm downward motion. The upward motion is realized by cutting the stress elements on the lower side of the platform. The average upward motion step, 42 nm, is slightly larger than the downward motion step because only 25 stress elements exists on the opposite side.

III. Automated fiber coupling experiment. We tested the two-axis device in a real functional application, namely the alignment of two single-mode optical fibers to one-another. In our prior work **[1]**, a scanning laser system was employed for characterizing the 1-axis platform, in which SU-8 grooves were patterned for single-mode fiber attachment. Since a ~4 μm thick ProTEK protection layer was necessary to maintain SU-8 intact during KOH etching, the subsequent removal of this layer would always break the stress elements. In the current approach, we utilized two x-y-z-θ stages to manipulate two single-mode fibers attaching respectively to the suspended platform and the stationary base of the 2-axis device. After pre-alignment, the fibers were epoxy glued for light coupling characterization (Figure 8a).

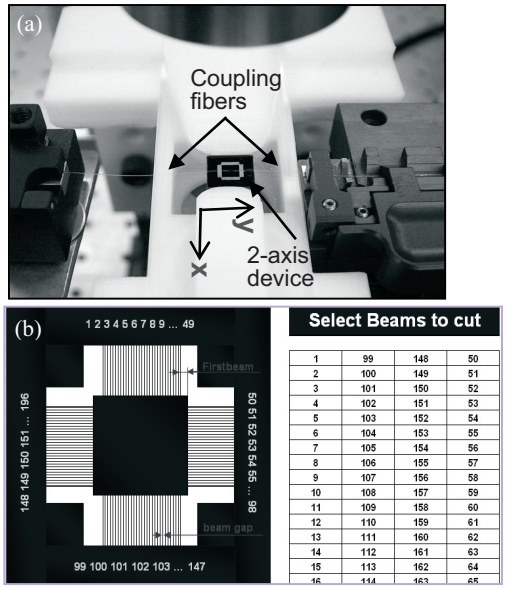

1	99	148	50
2	100	149	51
3	101	150	52
4	102	151	53
5	103	152	54
6	104	153	55
7	105	154	56
8	106	155	57
9	107	156	58
10	108	157	59
11	109	158	60
12	110	159	61
13	111	160	62
14	112	161	63
15	113	162	64
16	114	163	65

***Figure 8**: (a) Fiber coupling experiment. The opposite end of a single-mode fiber attached to a laser diode is mounted on the suspended platform, while the opposing end of a fiber attached to a power meter is mounted on the stationary base of the substrate. Selective laser trimming of the stress elements enables nanoscale motion between the two fibers. (b) Interface of laser trimming system.*

We developed an automated program for laser trimming. As shown in Figure-8, the computer interface allows the selection of any stress element. A visual-basic program translates the code into ScanWare for the actual firing of laser pulse. This enables rapid, flexible, and straightforward command of platform position. In our experiment, the fibers were placed in parallel to the y-axis stress elements. Selective laser trimming of the stress elements enabled 2-axis nanoscale motion between the two fibers.

Figure 9 displays an alignment process resulting from selectively trimming the 2-axis stress elements using programmed laser pulsing. The experiment was performed by cutting the stress elements in x-axis and y-axis, respectively, which led to lateral and axial positioning of the aligned fiber. The resulting light passing from one fiber to the other was then measured. The relative position steps were not actually measured, but determined from finite element simulation. Obviously, the alignment of the two fibers can be optimized for maximum coupling. In addition, the coupling efficiency is more sensitive to the shift of lateral position (x-axis) than axial position (y-axis).

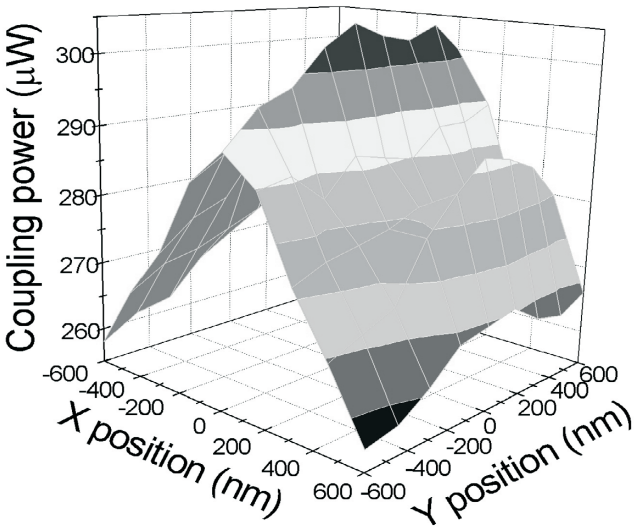

***Figure 9**: Fiber coupling improvement resulting from selectively trimming 2-axis stress elements. The coupling power is more sensitive to lateral (x-displacement) than axial (y-displacement) changes.*

IV. Reliability evaluation of the 2-axis platform. Finally, we performed finite element modeling to evaluate the reliability of the 2-axis platform based on Telcordia standards. To analyze if the device was robust enough against external unexpected shocks, we derived von Mises equivalent stresses with ANSYS modeling, and then solved for the acceleration level necessary to reach a given level of fracture strength (~7 GPa for SiN_x **[5]**) for various stress element length and number. It is seen from Figure 10a that long stress elements require large shock levels to achieve the fracture stress. From Figure 11a it is also clear that a large number of stress elements require a high level of shock to achieve the fracture stress. The simulation predicts that the 2-axis platform is able to survive under a 3000 g shock.

The thermal stability of the 2-axis platform was also analyzed. Shown in Figure 10b and Figure 11b is the displacement of the platform center at two typical temperature extremes for thermal cycling, -40 °C and +80 °C, respectively. The temperature variation modifies the positioning characteristics only approximately a few nanometers. The remarkable thermal stability of the 2-axis platform is attributed to the tensile constraint from the 2-axis stress elements.

We further calculated the resonant frequency of the 2-axis platform with different configurations. As shown in Figure 10c and Figure 11c, the resonant frequency raises with the increasing number and the decreasing length of stress elements. The overall frequency is more than 10 KHz. This is far above typical vibration frequency ranges (20 Hz to 2000 Hz). All this validates the potential of the 2-axis platform for nanoscale photonic packaging.

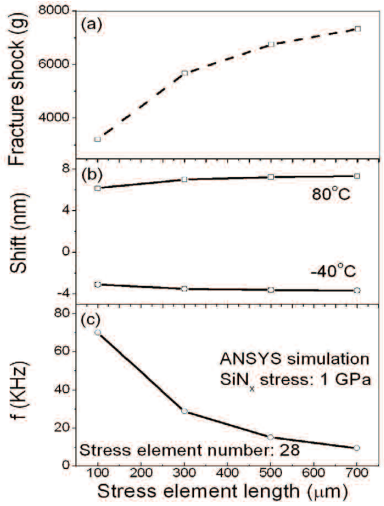

***Figure 10:** Dependence of (a) shock resistance, (b) thermal stability and (c) resonant frequency on stress element length.*

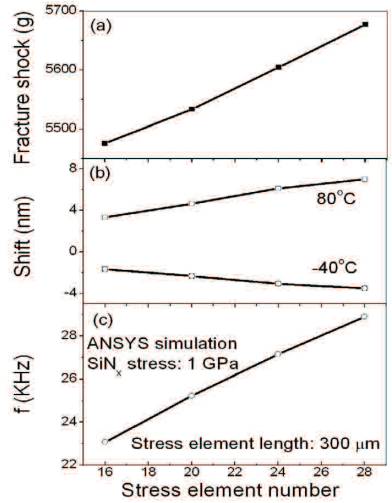

***Figure 11**: Dependence of (a) shock resistance, (b) thermal stability, and (c) resonant frequency on stress element number.*

REFERENCES

[1] B. Li, J. Menger, T. Walsh, H. Wirz, A. Sharon, "Development of quasi-passive optical substrates for photonic packaging", *Proceeding of the 18th IEEE International Conference on Micro Electro Mechanical Systems* (MEMS '05), Miami Beach, FL, USA, 01/30-02/03, (2005), pp. 104-107

[2] A. Goding, "Active alignment is here to stay", *Photonics Spectra*, pp. 110-112 (2002)

[3] W. Shakespeare, R. Pearson, J. Grenestedt, P. Hutapea, V. Gupta, "MEMS integrated submount alignment for optoelectronics", *Journal of Lightwave Technology*, **23**, 504(2005)

[4] B. Li, H. Xie, B. Xu, R. Geer, J. Castracane, "Investigation of strain in microstructures by a novel moiré method", *Journal of Microelectromechanical Systems*, **11**,829(2002)

[5] Wen-Hsien Chuang Luger, T. Fettig, R.K. Ghodssi, R. "Mechanical property characterization of LPCVD silicon nitride thin films at cryogenic temperatures", *Journal of Microelectromechanical Systems*, 13, 870 (2004)

A MONOLITHIC CMOS-MEMS 3-AXIS ACCELEROMETER WITH A LOW-NOISE, LOW-POWER DUAL-CHOPPER AMPLIFIER

Hongwei Qu, Deyou Fang and Huikai Xie
Department of Electrical & Computer Engineering, University of Florida
Gainesville, Florida 32611-6200, USA

ABSTRACT

This paper reports the process development, interface circuit design and device characterization of a monolithically integrated 3-axis capacitive accelerometer with a single proof mass. An improved DRIE post-CMOS MEMS process has been developed, which provides robust single-crystal silicon structures in all three axes and greatly reduces undercut of comb fingers in dry release. A low-noise, low-power, dual–chopper amplifier is designed for each axis, which consumes only 1 mW power. With a 40dB on-chip amplification, the measured sensitivities of the lateral- and z-axis accelerometers are 560 mV/g and 320 mV/g, respectively, which can be decreased by simply decreasing the amplitude of the modulation signal. The over-all noise floors of the lateral- and z-axis are 12 μg/√Hz and 110 μg/√Hz, respectively when tested around 200 Hz.

INTRODUCTION

Assembling single-axis accelerometers for 3-dimensional acceleration sensing drastically increases the packaging size and cost. Thus monolithic 3-axis accelerometers have drawn interests from both industry and universities **[1-7]**. Analog Devices, Inc. (ADI), Bosch, Freescale and ST Microelectronics have all launched their 3-axis accelerometers **[1-4]**. These commercially available 3-axis accelerometers are all based on thin-film microstructures and majority of them use hybrid packages, whose performances are normally limited by the structure thickness, residual stress and parasitics. The noise floors of most of these devices are on the order of a few hundreds μg/√Hz. Some bulk micromachined 3-axis accelerometers were demonstrated with higher resolutions **[6, 7]**, but the micro-g resolutions were achieved at an expense of large device sizes. Furthermore, the wet etch based fabrication processes used in these bulk accelerometers require double-side alignment **[6]** and/or wafer bonding **[7]**, resulting in high fabrication cost.

In order to achieve high resolution, small size and low cost simultaneously, a single-crystal silicon (SCS) based CMOS-MEMS 3-axis accelerometer with a single proof mass was developed **[8]**. But it has two drawbacks. First, although most of the sensing structure is made of single-crystal-silicon (SCS), the z-axis sensing employs Al/SiO_2 thin-film spring beams, which has poor temperature performance. Second, the silicon undercut for electrical isolation of substrate silicon also undercuts the silicon underneath comb fingers, which increases the comb-finger gap and in turn reduces the sensitivity and resolution. Recently, a new sensor design and fabrication process were proposed by Qu et al **[9]** to overcome the drawbacks in **[8]**. Better temperature performance was achieved by employing a torsional SCS-based z-axis spring; and the comb-finger undercut problem was much alleviated by performing the electrical isolation formation and the sensing structures etching separately.

However, there are still two significant issues in **[9]**. First, the overheating during the dry release step severely undercuts the sensing comb fingers and springs, increasing the comb-finger gaps and even causing device failure. Second, the circuit noise still dominates the overall noise of the device.

In this paper, a further modified CMOS-MEMS process and a new amplifier design are used to resolve these two issues. The detailed characterization of fabricated 3-axis accelerometers is presented.

3-AXIS ACCELEROMETER AND CIRCUIT DESIGN

The 3-axis CMOS-MEMS accelerometer reported in this paper features a single proof mass for triple axes sensing, in which an imbalanced torsional z-axis sensing element is embedded in the lateral proof mass, as shown schematically in the 3-D model in Fig. 1. The lateral proof mass, along which the rotor comb-fingers are attached, is anchored to the substrate through two pairs of symmetric crab-leg SCS springs. The symmetric springs are flexible in both x- and y-axis, allowing the dual-axis in-plane sensing by two separate groups of orthogonally-oriented SCS comb-fingers. The differential capacitive sensing in z-axis is achieved by using the sidewall capacitance formed by the multiple metal layers in the thin-film portion of comb fingers **[10]**. The TSMC 4-metal 0.35μm CMOS technology is used for CMOS fabrication through MOSIS. Three metal layers are used to form the z-sensing capacitors. By dividing the z-axis sensing capacitors into four groups and swapping the connections of the capacitors in upper and lower metal layers, fully differential sensing and offset cancellation can be realized **[9]**. Note that SCS is incorporated in both the torsional z-axis springs and sensing fingers for robust structures. The SCS in the z-axis sensing comb-fingers is purely for the purpose of mechanical support. In contrast, the SCS in the lateral-axes comb-fingers is used as both mechanical support and capacitor electrodes.

A SEM micrograph of a fabricated 3-axis accelerometer is shown with insets in Fig. 2, where the dimensions of the lateral and z-axis sensing elements are also given. The thickness of all the structures is 35μm and the gap for all the comb-fingers is 2.1μm. The length of the lateral- and z- axis sensing comb-fingers are 85 μm and 55 μm, respectively, both having the same width of 4.8 μm. The length and width of z-axis torsional mechanical springs are 400 μm and 4 μm, respectively. The crag-leg springs for lateral axes have the same length and width of 320 μm and 5 μm in both directions.

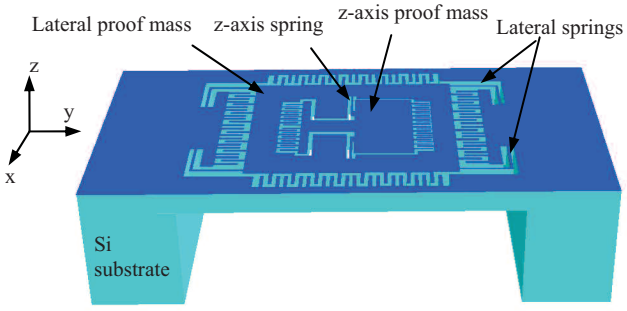

***Figure 1**. Schematic 3-D model of the 3-axis accelerometer. Electrical isolation structures are not shown.*

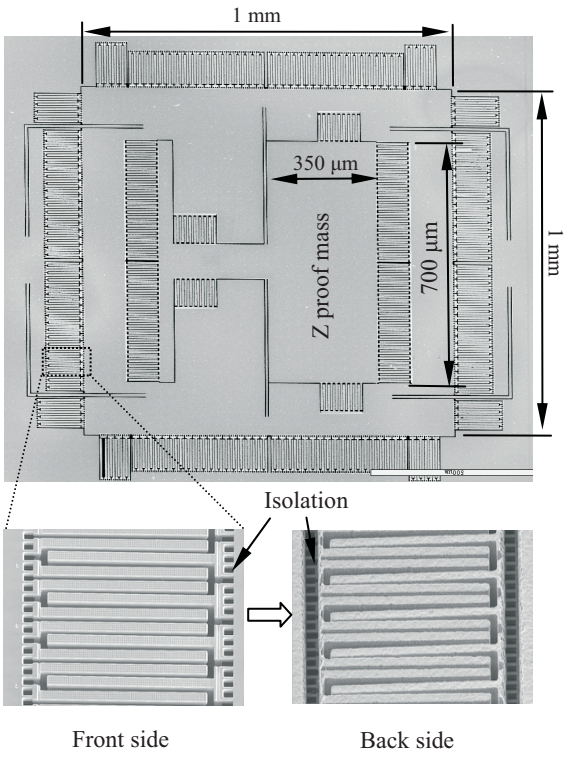

***Figure 2**. SEM photograph of the sensing element of the fabricated CMOS-MEMS 3-axis accelerometer. The insets show front and backside of the electrical isolation structures.*

With the above design parameters, the calculated sensitivity of the lateral axes and z-axis are 4.5 mV/g and 2.3 mV/g, respectively with a 1.5 V modulation.

A two-stage dual-chopper amplifier (DCA) is integrated with the 3-axis accelerometer for each axis as the continuous-time readout circuit. A total gain of 40dB is designed. Fig. 3 shows the DCA architecture which employs two modulation clocks (1 MHz and 20 kHz respectively) to achieve low noise and low power consumption simultaneously **[11]**.

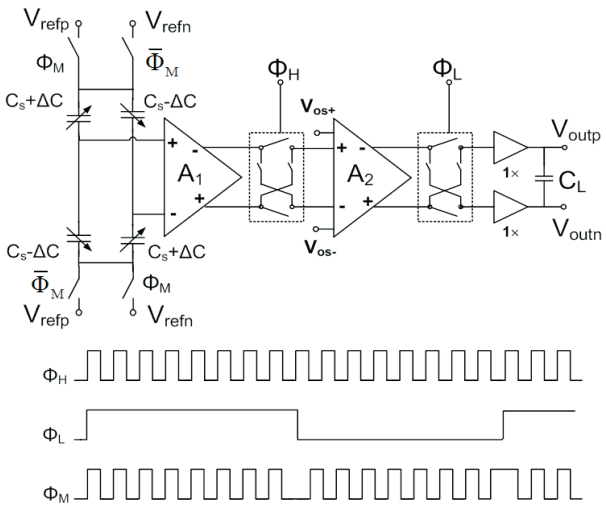

***Figure 3**. Diagram of the interface circuit.*

FABRICATION PROCESS

The post-CMOS microfabrication reported in **[9]** improves the device performance by reducing the undercut on comb fingers and mechanical springs. This is accomplished by performing the electrical isolation etch and the final release of comb fingers and mechanical springs separately. Top metal layer (M4) is only used to pattern the electrical isolation structures. After the electrical isolation trenches are formed, as shown in the insets of Fig. 2, M4 is removed by wet or plasma aluminum etch to expose the patterns of other structures of the accelerometer.

Some negative effects caused by the two-step etch process were observed. The most significant one is the rapid silicon undercut of comb fingers and mechanical springs due to the overheating of these fine structures during the plasma etch. This undercut happens even within a very short over-etch after the accelerometer is released. The reason for the severe undercut is the reduced thermal conductance from the comb fingers to the substrate. The heat generated from chemical reaction and ion bombardment in silicon DRIE can not be dissipated effectively, which consequently raises the temperature of the suspended microstructures. This positive feedback eventually leads to high etching rate and the comb fingers will be undercut very quickly. The same effect was also observed on the z-axis sensing element where the heat can only be transferred through the two long torsional springs.

Precise etching end-point detection is an effective method to avoid the over etch **[12]**. However, this requires additional sophisticated instruments on the current DRIE system and the detection accuracy is limited due to a wide range of structure complexities and opening sizes. In this work, we demonstrated a modified process, which effectively solves the thermally related comb-finger undercut.

The process flow is illustrated in Fig. 4. There is only one slight modification to the CMOS-MEMS process used in **[9]**. After the backside etch that produces a silicon membrane and defines the structure thickness (Fig. 4(a)), a thick sacrificial photoresist layer (~50µm) is applied on the back of the silicon membrane (Fig. 4(b)). After the isolation etching is completed (Fig. 4(c)-4(d)), this

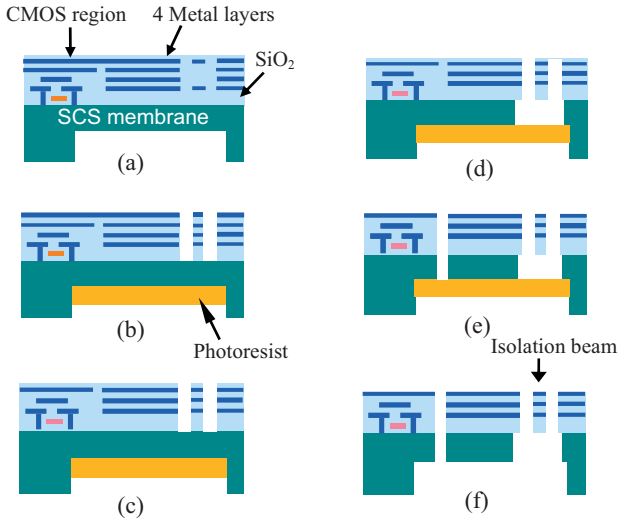

***Figure 4**. Post-CMOS microfabrication process flow. (a) Backside etch. (b) Backside photoresist coating followed by front side anisotropic SiO_2 etch. (c) Top Al etch. (d) Deep Si etch and undercut to form isolation structures. (e) Anisotropic SiO_2 etch and DRIE Si etch for comb fingers and mechanical springs. (f) Photoresist ashing for final release.*

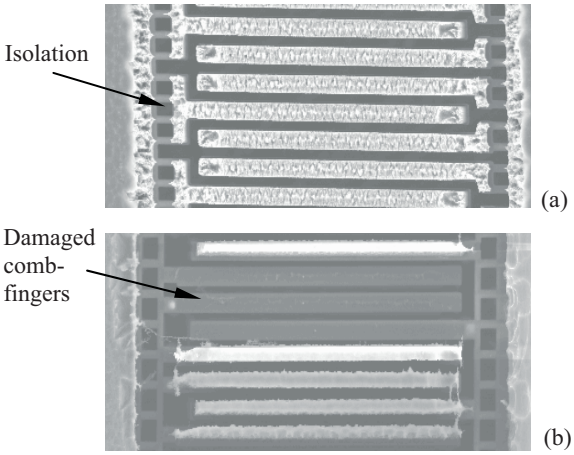

Figure 5. *(a) By using backside photoresist coating, the release of the sensing fingers are well controlled with slight footing effect. (b)Without backside photoresist coating, some comb fingers are etched away in a similar release etch.*

photoresist layer functions as a thermal path during the DRIE silicon etch that forms the entire microstructure (Fig. 4(e)). Finally, the photoresist is removed by oxygen plasma ashing to release the device (Fig. 4(f)). In Fig. 5, a comparison is made between sensing comb fingers fabricated with and without backside photoresist coating. The undercut of the silicon on comb fingers is greatly reduced and the finger damage is completely avoided by using the modified process (Fig. 5(a)). Furthermore, the photoresist layer helps reducing the backside contamination caused by back scattering. In contrast, without the photoresist layer as thermal path, electrical isolation trenches greatly reduce thermal flow from comb fingers to substrate. Consequently comb fingers are over heated and seriously undercut (Fig. 5(b)).

It should be pointed out that the thermal effect and the modified process described above are valid to many other MEMS devices with structures similar to this 3-axis accelerometer. A proper device design also helps in reducing the thermal problem described above. By considering the aspect-ratio dependent etching effect (ARDE), we can design the device in such a way that the etch-through sequence for different structures can be well controlled.

EXPERIMENTAL RESULTS

Fig. 6 is the photograph of a wire bonded die showing the locations of the 3-axis sensor and interface circuits. A dummy on-chip interface circuit was tested with an overall gain of 40 dB and a 16 nV/√Hz electronic noise floor was measured.

The sensitivities in the lateral axes and z axis were measured as 560 mV/g and 320 mV/g, respectively, at a 1.5 V modulation signal using a Piezotronics shaker which provides standard 1-g acceleration at 159.1 Hz. An impulse response test showed that the resonant frequencies for the lateral axes and z axis are 1.5 kHz and 450 Hz, respectively. These frequencies are about 15% lower than the simulated results, reflecting a remaining slight undercut to the mechanical springs in the plasma etch process. Due to the asymmetry of the z-axis proof mass, the z-axis sensing element has relatively high cross-axis sensitivities which were measured to be 2.1% from the x-axis and 4.7% from the y-axis, as shown in Fig. 7. The noise measurement was conducted using a LDS shake table and SRS network spectrum analyzer. The spectral response of the z-axis output at a 200 Hz, 0.5-g external

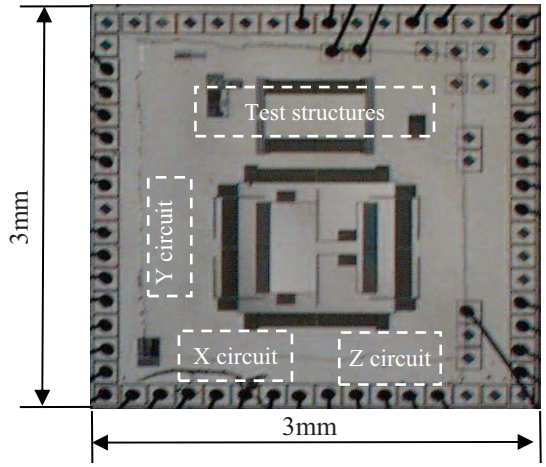

Figure 6. *Photograph of the wire bonded die.*

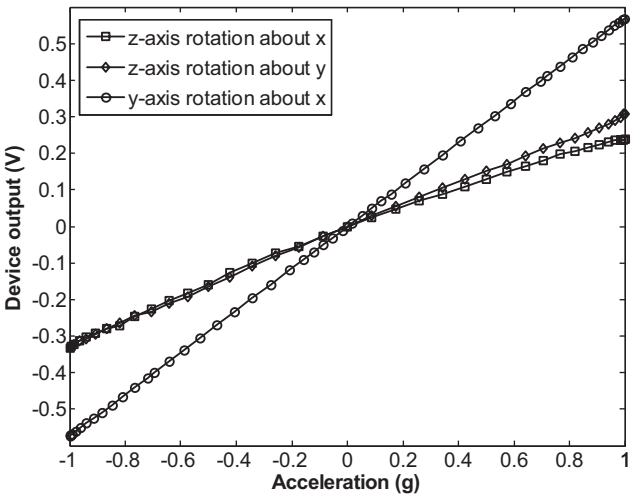

Figure 7. *Static test results of the z- and y- axis using a precision rotary stage.*

acceleration is shown in Fig. 8. The overall noise floor of the z element is 110 μg/√Hz. Although both x- and y-axis have the same number of identical sensing comb-fingers, there is a slight sensitivity difference between these two lateral axes due to the arrangement of the mechanical springs. The spectrum of y-axis output under a 200 Hz, 0.05-g acceleration is shown in Fig. 9. An overall noise floor of 12 μg/√Hz is demonstrated.

The temperature coefficient of sensing capacitance originates from the thermal-induced curling of the thin-film electrical isolation beams, in which aluminum and SiO_2 have different temperature coefficient of expansion. Therefore, by measuring the temperature coefficient of the comb finger curling, the temperature performance of the sensor can be extrapolated. In experiment, the PLCC-52 sensor package was heated by a band heater taped on the back of the package, and the sensor temperature was measured by a spot thermocouple. The vertical curling of the sensing comb fingers was measured in a temperature range from room temperature to 96°C, using a Wyko surface optical profilometer. A maximum net negative 0.533 μm curling at the free end of the comb-fingers was measured in the above temperature range. Since the sensor structure thickness is 35 μm, the corresponding change of the electrode engaged area is approximately 0.23%. Based on these measurements, a positive 3.04×10^{-4}/°C temperature coefficient of sensitivity (TCS) of the lateral sensor was extrapolated. Due to the complete SCS structure,

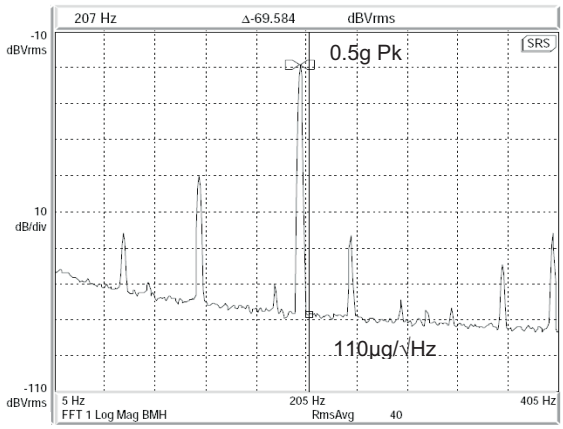

***Figure 8**. The spectrum of the z-axis output under 0.5g at 200 Hz (RBW = 1Hz).*

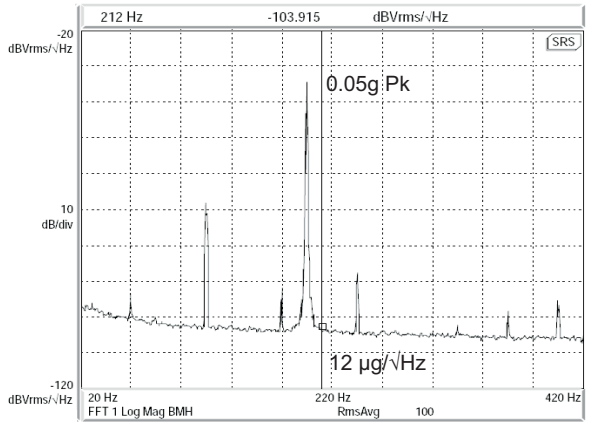

***Figure 9**. The spectrum of the y-axis output under 0.05g at 200 Hz (RBW = 1Hz).*

no apparent temperature-induced structure curling was observed on the z-axis sensing element. An overall sensor TCS of approximately 0.285%/°C was measured, which is mainly caused by the gain drifting of the first open-loop amplification stage of the on-chip amplifier. This is verified by circuit simulation, and a temperature insensitive amplifier is under design.

The measured performance is further summarized in Table 1. As a comparison, the performance of ADXL330, a 3-axis accelerometer from ADI, is included.

***Table 1**. Performance summary of the reported device and a comparison with ADXL330 from ADI **[1]**.*

Parameters	Measured Values	
	This work	ADXL330
Chip size (mm × mm)	3×3	4×4 (package)
Lateral axes sensitivity (mV/g)	560	300
Z axis sensitivity (mV/g)	320	300
Circuit noise floor (nV/√Hz)	16	-
Power consumption of each axis (mW)	1	0.64~1.15
Lateral axes noise floor (µg/√Hz)	12	170
Z axis noise floor (µg/√Hz)	110	350

CONCLUSION

A 3-axis CMOS-MEMS accelerometer with a single proof mass has been demonstrated in this work. The single-crystal silicon incorporated in the device ensures robust sensor structures and high resolution. Low-power consumption (1 mW for each sensing axis) and low-noise floors in all three axes are achieved simultaneously with a compact device size. Compared to the previous processes, this modified post-CMOS microfabrication process has much larger process tolerances by providing additional thermal path to the suspended microstructures in plasma etching processes. Though only photoresist was used in this work, there exist many other more suitable materials for the additional heat dissipation. This method can be widely used in the micromachining of MEMS devices with similar suspended structures. Due to its small size, low power consumption and high resolution, this 3-axis accelerometer has a variety of applications including health monitoring, video games and infrastructure securities.

ACKNOWLEDGEMENT

This project is partially supported by the UCF-UF Space Research Initiative and University of Florida Startup Fund. The CMOS chip fabrication was supported by MOSIS through its Educational Program.

REFERENCES

[1] Analog Devices, Inc., "ADXL330 low-power, iMEMS 3-axis accelerometer", Datasheet Rev. PrA., Oct. 2005.

[2] Bosch Sensortech, "SMB360 triaxial acceleration sensor", Datasheet Rev. 1, Nov. 2005.

[3] Freescale Semiconductor, "MMA7260Q 3-axis accelerometer", Datasheet Rev. 2, Feb. 2006.

[4] ST Microelectronics, "LIS3L02AQ3 MEMS linear inertial sensor", Datasheet Rev. 2, May 2005.

[5] M. Lemkin and B. E. Boser, "A three-axis micromachined accelerometer with a CMOS position-sense interface and digital offset-trim electronics," *IEEE J. of Solid-State Circuits,* vol. **34**, No. **4**, pp. 456-468, 1999.

[6] J. Chae, H. Kulah and K. Najafi, "A monolithic three-axis micro-g micromachined silicon capacitive accelerometer," *J. of MEMS*, vol. **14**, pp. 235-242, 2005.

[7] H. Takao, H. Fukumoto and M. Ishida, "A CMOS integrated three-axis accelerometer fabricated with commercial submicrometer CMOS technology and bulk-micromachining," *IEEE Trans.on Elec. Devices,* vol. **48**, pp. 1961-1968, 2001.

[8] H. Xie, Z. Pan, W. Frey, and G. Fedder, "Design and Fabrication of an Integrated CMOS-MEMS 3-Axis Accelerometer," *The 2003 Nanotechnology Conference*, 2003.

[9] H. Qu, D. Fang, and H. Xie, "A single-crystal silicon 3-axis CMOS-MEMS accelerometer," *Proceedings of IEEE Sensors 2004*, vol. **2**, pp.661-664, Oct. 24-27, 2004, Vienna, Austria.

[10] H. Xie, and G.K. Fedder, "Vertical Comb-finger Capacitive Actuation and Sensing for CMOS-MEMS," *Sensors & Actuators, A*, Vol. **95** (2002), pp. 212-221.

[11] D. Fang, H. Qu and H. Xie, "A 1mW dual-chopper amplifier for a 50 µg/√Hz monolithic CMOS-MEMS capacitive accelerometer", to be presented at the *2006 Symp. on VLSI Circuit*, Jun. 15-17, 2006, Honolulu, Hawaii.

[12] Z. Wan, J. Liu, and H. H. Lamb, "Electron cyclotron resonance plasma reactor for SiO2 etching: Process diagnostics, end-point detection, and surface characterization," *J. of Vacc. Sci. & Tech.: A*, vol. **13**, pp. 2035-2043, 1995.

A COMBUSTIBLE/ELECTRONEGATIVE GAS DETECTOR UTILIZING URANIUM DOPED CAST CERAMIC MICROCHANNELS

John D. Olivier and Chester G. Wilson
Institute for Micromanufacturing, Louisiana Tech. University

ABSTRACT

This paper reports on an on-chip radioactive microdevice constructed from a lost mold ceramic casting process. Uranium acetate nanoparticles are imbedded into this room temperature curing ceramic process. This cast microchannel provides a robust, on chip beta particle (fast electron) source, which is used for electronegative gas collection, and gas mobility determination. These are both standard macroscale techniques for combustible gas identification. It can either serve to ionize the local gas, which is being measured, or it can be captured by local electronegative gas. The beta source is biased to ground, and a separate current collection electrode is biased positively or negatively. This measures local ion/electron generation, and provides mobility information. As these mobilities and ionization constants are unique to particular gas species, different gas conditions provide different current collection signatures. Air, helium, alcohol and carbon dioxide are characterized with this device.

I. INTRODUCTION

Explosive gas detection is important to security and industrial applications. Tin-oxide gas detectors are probably the most common combustible gas detector; the measured gas interacts with absorbed oxygen, resulting in a conductivity change. While array-based detectors of this type have improved performance dramatically, these devices have limitations in determining the exact type of gas; both propane and carbon dioxide result in a resitivity change [1,2]. Several micro-gas chromatographs have been developed, but these are highly complex devices, and fabrication is costly [3,4]. Small scale plasma spectroscopic devices have been developed, but these devices require hundreds of volts to operate. [6,7]. Several small scale devices that rely on ion-mobility measurements have also been developed, and would further be improved with the use of tunable on-chip radioactive sources [8,9]. Electroplated nickel isotope microdevices have been constructed for on-chip power sources, but not for gas detection [10]. Electronegative gas absorption is a common technique in analytical chemistry; this uses a large low energy beta particle emitting source, which ionizes a carrier gas, and certain gas types absorb electrons, changing measured current.

The technology described here allows: 1) a wide variety of radioactive materials that could not be electroplated to be cast in ceramic at room temperature, 2) high energy particle sources that serve to ionize both carrier gasses and the gas to be measured, and 3) on chip electrodes that can collect the created ions and electrons, which are characteristic of the measured gas (Fig. 1).

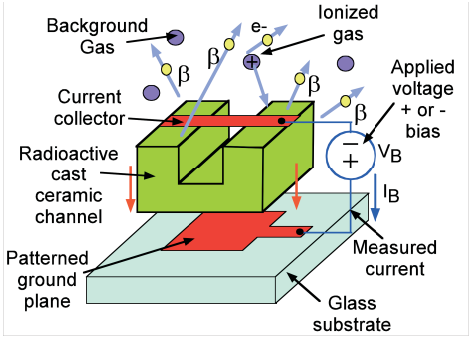

Fig. 1 Uranium particles embedded in the ceramic micro-channel emit high energy beta partcles, which ionize proximal gasses. The ionization constant and mobilities can be measured using patterned electrodes.

II. RADIOACTIVE MICROCASTINGS

The uranium-doped ceramic microcastings are manufactured with a room temperature lost-mold process (Fig. 2). The undoped ceramic castings are created using a two part, dry and wet, compound. The first component is an alumina ceramic powder, and the wet activator is a nanoparticle colloid.

The inexpensive fabrication process allows an on-chip 0.543 MeV beta particle source (Fig. 3). A uranium-doped microchannel is fabricated, and then imbedded into a microsandblasted glass cavity, where electrodes have been patterned (Fig. 4). This high-

energy source liberates secondary electrons in the ceramic, and it either ionizes or it is captured by the background gas. The source activity can be tailored by changing the dopant levels (Fig. 5). Several mm thick polymer coatings only attenuate about 50% of the beta emission, so the source can be encapsulated (Fig. 6). As the radioactive castings are small, the emitted flux falls off quickly with distance, mitigating safety problems (Fig. 7).

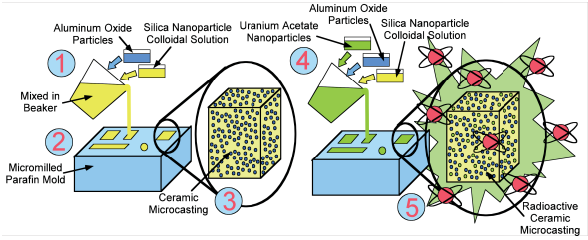

Fig. 2 Using room temperature curing ceramics composed of aluminum oxide particles with a silica nanoparticle colloidal activator (1) Micro-castings of varying geometries are created (2). This solution hardens to a 10^9 ohm-cm ceramic at room temp. (3). When uranium particles are added (4), an on-chip radioactive source is created (5). Flux and radioactive loading can be tuned.

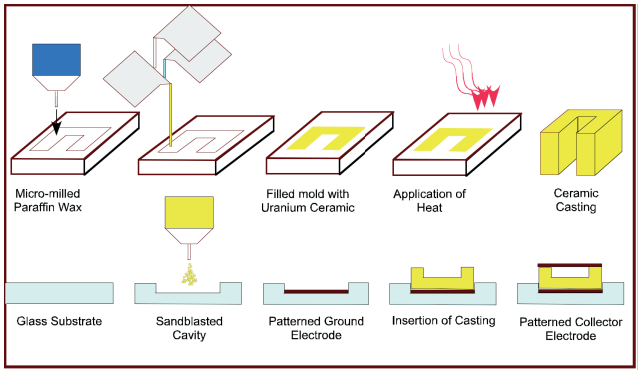

Fig. 3 Ceramic radioactive castings are made with a lost wax process, these castings are imbedded into a cavity sandblasted in glass, with a patterned ground plane and collector. An optional polymer coating can be applied over ceramic casting to protect the source.

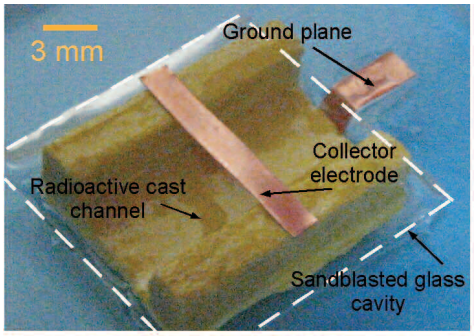

Fig. 4 Uranium microdevice is yellow, and imbedded in microsandblasted glass cavity.

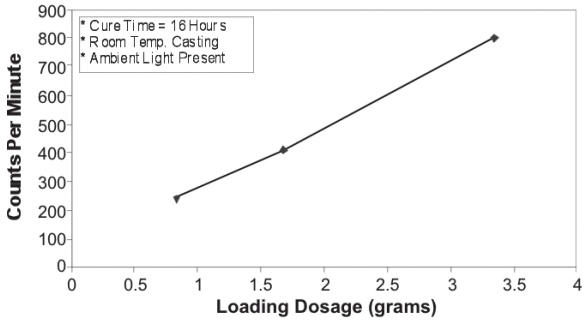

Fig. 5 Radioactivity, and particle flux is linear with uranium loading into ceramic. Counts per minute are higher than that caused by beta emission of uranium alone; secondary emissions are produced from aluminum oxide particles.

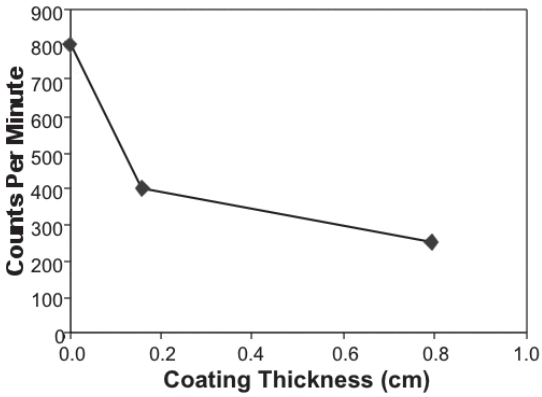

Fig. 6 Coating the nuclear ceramic material with polymer films causes a minor decrease in beta emission. This is desirable because emission can be finely tuned using very inexpensive methods.

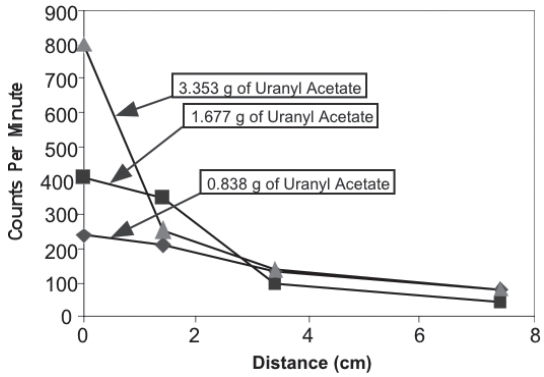

Fig. 7 As the distance of three distinctively doped ceramic micro-castings increases from a beta detector, the counts emitted per minute of the micro-casting falls off very rapidly. This results in only locally ionized gas, and increases safety.

III. EXPERIMENTAL RESULTS

To characterize these devices, initial testing was done in dried air, where the biasing electrode is fed into a current collecting 38 pF ceramic capacitor (Fig. 8). Current collection in air is substantially increased above background with the addition of the nuclear source, allowing larger charge capture (Fig. 9). As the background atmosphere is heated, current collection is considerably increased, as moisture is reduced, and ionization probabilities increased. When the biasing electrode is positive, electrons are captured, along with negative ions. Negative biasing collects positive ions, due to the large difference in mobilities, the currents of the two species vary several fold (Fig. 10). Increasing the collector bias voltage increases the species currents differently, until they become equal at saturation (Fig. 11). The current collected is insensitive to electrode area; several fold increases in capture area result in only incremental increases in current (Fig. 12). Helium, a frequent carrier gas was tested; noble gases do not capture electrons, and the ion/electron mobility difference is found considerably higher (Fig. 13). With helium, electron current collection occurs much faster than with less mobile ion collection.

This device was tested with alcohol vapors and in the presence of a carbon dioxide ambient. Carbon dioxide, an electronegative gas which captures electrons, provides a greater current when the electrode is biased positively (Fig. 14).

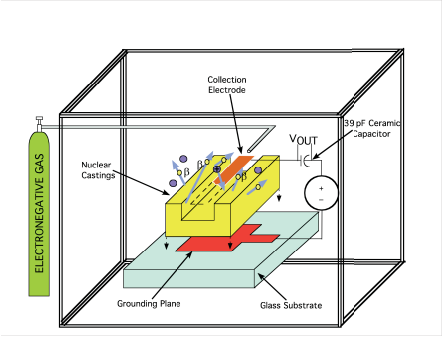

Fig. 8 Testing was implemented in a controlled chamber. Charge is collected on a ceramic capacitor, over seconds, resulting in mV signals.

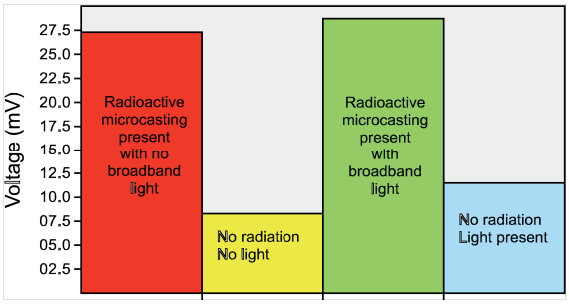

Fig. 9 The radioactive source increases ionization of background gas several-fold.

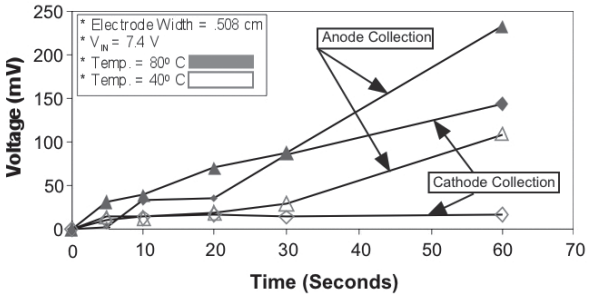

Fig. 10 Elevated temperatures substantially increase collected currents in air.

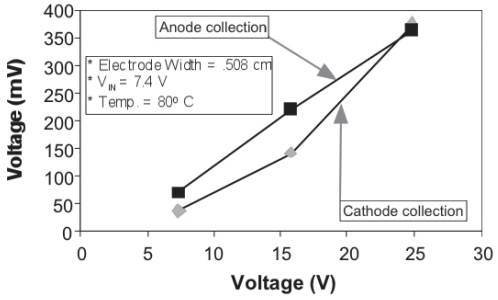

Fig. 11 As the collector bias is increased, anode and cathode current increases, until they match.

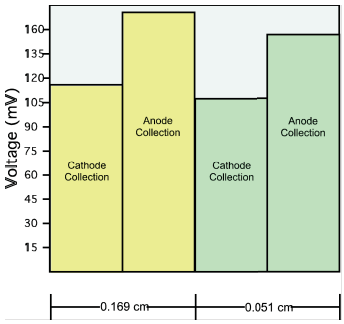

Fig. 12 Anode and cathode current collection is fairly insensitive to electrode sizes. As electrode size decreases little signal attenuation is observed for both cathode and anode collection.

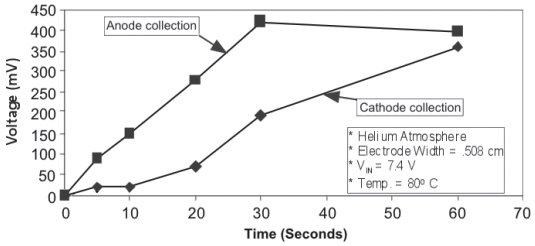

Fig. 13: Helium, a noble gas with a small ionization potential captures no electrons, so larger anode currents are seen initially. After sufficient time, collection currents become equal.

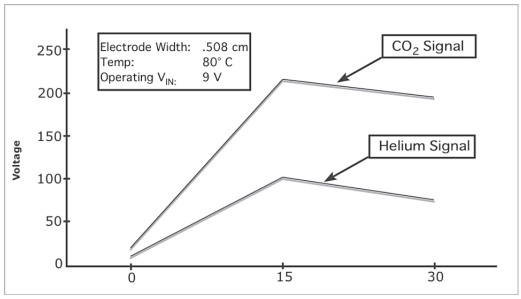

Fig. 14: Carbon dioxide, which captures electrons, provides higher anode current than alcohol vapors.

IV. CONCLUSIONS

A new fabrication technique to produce uranium doped ceramic microcastings is presented. Unique to the fabrication process is the ability to controllably dope the ceramic castings with varying types of radiating nuclear isotopes. The device presented here utilizes a cast ceramic microchannel doped with uranyl acetate, which provides an ionization source that has been tested for use in gas mobility measurements. An on-chip electrode serves to collect positive/negative ions and electrons. Beta emission from these sources serves a two-part role in the device functionality, they ionize the background gas to be tested, and they provide a source of electrons that are captured by the gas. The device has been characterized in air, helium, alcohol vapors, and carbon dioxide, resulting in different voltage-current characteristics.

ACKNOWLEDGEMENTS

This material is based upon work in part supported by the DARPA and SPAWAR SC under award # N66001-05-1-8903. This work was also funded in part by the Louisiana Board of Regents Research Competitiveness Subprogram.

REFERENCES

[1] R. Cavicchi, et. al., "Microhotplate Gas Sensor Arrays", *Proc. of SPIE*, 1999, pp. 38-49

[2] B. Panchapakesan, D.L. Devoe, R.E. Cavicchi, R.M. Walton, and S. Semancik, "Micromachined Array Studies of Tin Oxide Films: Nucleation, Structure, and Gas Sensing Characteristics" *MRS Symposium Proc,*, 574, 1999, pp. 213-218

[3] L.C. Chia-Jung, J. Whiting, R.D. Sacks, and E.T. Zellers, "Portable Gas Chromatograph with Tunable Retention and Sensor Array Detection for Determination of Complex Vapor Mixtures," *Analytical Chemistry*, (75)6, Mar. 2003, pp. 1400-1409

[4] Y. Kawamura, S. Konishi, M. Nishi, "Development of a Micro Gas Chromatograph for the Analysis of Hydrogen Isotope Gas Mixtures in the Fusion Fuel Cycle," Fusion Engineering and Design, v58-59, Nov 2001, pp. 389-394

[6] J.C.T. Eijkel, H. Stoeri, A. Manz, "A dc microplasma on a chip employed as an optical emission detector for gas chromatography," *Anal. Chem.* 72, 6/00, pp. 2547-2552

[7] C. G. Wilson, Y. B. Gianchandani, "LEd-SpEC: Spectroscopic detection of water contaminants using glow discharge from liquid electrodes," *IEEE Transactions on Electron Devices,* 49/12, Dec 2002, pp. 2317-2322

[8] R. A. Miller, E. G. Nazarov, G. A. Eiceman, and A. King, "A MEMS radi-frequency ion mobility spectrometer for chemical vapor detection," Sensors and Actuators, (91)3, 2001, pp. 301-312

[9] W. Chambers, J. Phelan, et. al., "Explosive ordinance detection in land and water environments with solid phase extraction/ion mobility spectrometry," *Proc. of SPIE*, v 3710, n I, 1999, pp 290-298

[10] H. Li, A. Lal, et. al., "Self-Reciprocating Radioisotope-Powered Cantilever", Jour. Appl. Phys., 2001, pp. 1122.

A DIGITAL MEMS OPTICAL SWITCH

Roman C. Gutierrez, Tony K.Tang, Robert Calvet, Darrell Harrington, Stephen Vargo, Indrani Chakraborty*

Siimpel Corporation, 400 East Live Oak Ave., Arcadia, CA, USA
*Bain & Company, Inc. 1901 Avenue of the Stars, Los Angeles, CA, USA

ABSTRACT

This paper summarizes the work done in the development of a commercial three dimensional digital MEMS optical switch and its unique reliability challenges. The paper describes the design, fabrication, and testing of the three-dimensional steering MEMS mirror for the digital optical switch.

INTRODUCTION

Optical switches based on microelectromechanical systems (MEMS) have been the subject of substantial development over the past ten years [1-4]. Due to the requirements for small size and low cost systems, there has been a widely acknowledged need for using digitally controlled mirrors in the optical switch. Digital control eliminates the need for closed loop control in the positioning of each mirror in an optical switch. This is achieved using optical elements made from precise MEMS structures that "snap" into a multitude of predefined positions. This paper presents the design, fabrication and test of a highly reliable digital MEMS mirror with up to 32 positions.

This work was partially funded by the Advanced Technology Program, managed by NIST. We would also like to acknowledge Professor Roger Howe for his support on understanding the reliability issues of these devices.

OPTICAL SWITCH OVERVIEW

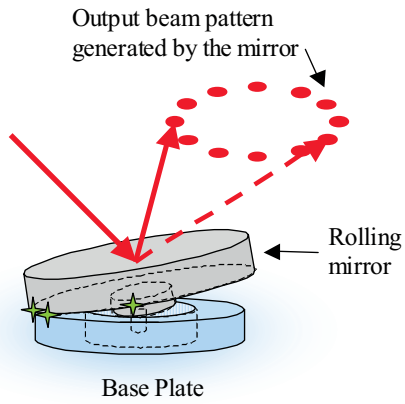

Figure 1. *The digital MEMS mirror uses simple mechanical features that allow the mirror to point in precise, predefined positions every time.*

Figure 1 illustrates the MEMS mirror of this digital optical switch. This design allows the mirror to "snap-down" to a number of precisely predefined positions. These positions are defined with submicron accuracy using a photolithographic process. In this approach, the mirror is in contact with the baseplate and rolls about a central pivot. The pivot allows the mirror to access N different snap-down positions distributed in a circle around the central pivot. The plane of the mirror is precisely defined kinematically by three points of contact: one on the central pivot and two on the perimeter of the circle. An electrode is used to electrostatically attract the mirror to this position. A beam of light reflecting from this mirror traces out a cone as the mirror rolls to its N different positions.

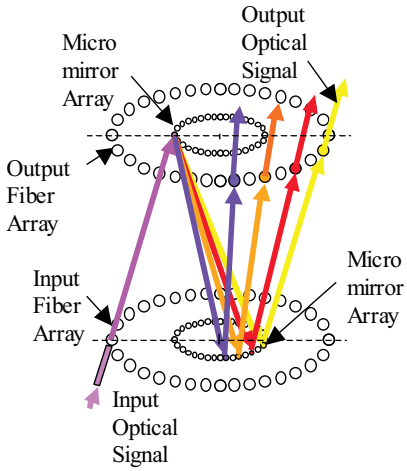

Figure 2. *The optical design for a switch based on one-stage digital MEMS mirrors.*

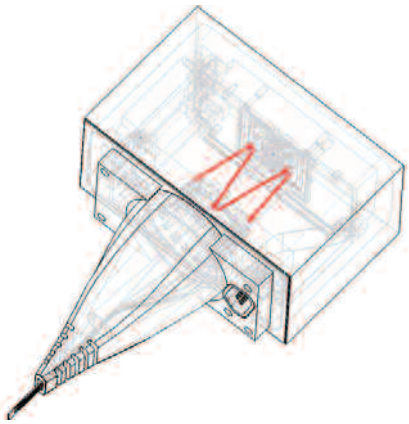

Figure 3. *Schematic of an 8x8 digital MEMS optical switch shows the path of light within the switch.*

Figure 2 illustrates how an NxN digital MEMS optical switch works using this type of MEMS mirror. The light enters the switch through an optical fiber and is collimated by a lens. The combined fiber and lens is referred to as a collimator. Since the one-stage digital MEMS

mirror can direct light to points on a circle, the mirrors and fibers are arranged in circles. The mirror array circle is concentric with the fiber array circle. The collimated beams are pointed such that the light hits the mirrors on the opposite side. Each fiber, therefore, has its corresponding mirror. Using this structure, light from any input fiber can be directed to any output fiber with less than 3 dB of optical loss.

Figure 3 illustrates the layout of an 8x8 optical switch using this type of digital MEMS mirror. A ribbon fiber with 16 individual single mode fibers is fed into a circular collimator array. Directly opposing this collimator array is a circular array of 16 MEMS mirrors, where each mirror has 8 digitally controlled positions. The red arrows illustrates how the light travels from one collimator to another, by bouncing off a first MEMS mirror, a fixed mirror, and a second MEMS mirror. The 8x8 optical switch includes all of the drive electronics within the hermetically sealed package.

MEMS MIRROR FABRICATION

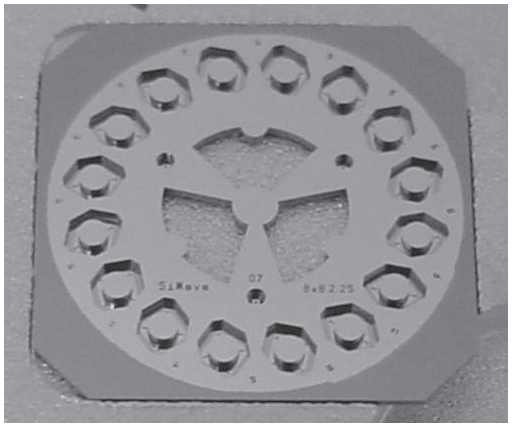

Figure 4. *Photographs of the MEMS mirror (left) and baseplate (right) for a digital MEMS optical switch.*

Figure 5. *Photographs of the MEMS mirror (left) and baseplate (right) for a digital MEMS optical switch.*

The digital MEMS mirrors require three dimensional structures built using inherently planar photolithographic and etch processes. The digital MEMS mirror is composed of two components that are separately fabricated and then assembled together: the MEMS mirror and the baseplate. Figures 5 and 6 show photographs of the MEMS mirror and baseplate structures for the 8x8 optical switch.

SOI (Silicon on Insulator) wafers are used to make these structures, and the process is outlined in Figure 6. The mirror is made by first patterning and etching the suspension and pivot on the silicon epilayer and then cutting out the mirror on the substrate. Deep Reactive Ion Etching (DRIE) is used to etch both the epilayer and the substrate. The last step consists in depositing a Ti/Pt/Au layer to increase the reflectivity of the mirror in the near infrared.

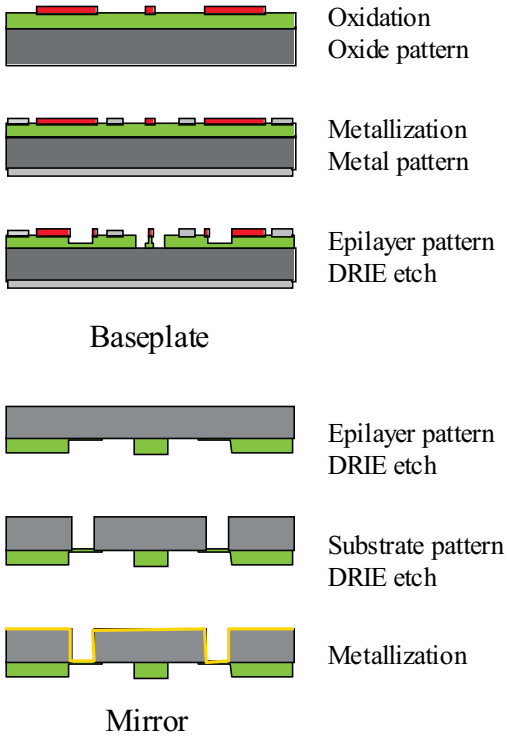

Figure 6. *Process sequence to fabricate MEMS base-plates and mirrors using single SOI wafers.*

The baseplate fabrication consists of a double DRIE etch on the epilayer. This is achieved by using a double patterning of oxide and photoresist, similar to the embedded masking process described by Mita et al. [5]. The metal paterning is used to electrically contact the epilayer, since the silicon is used to carry the electrical signals for electrostatic actuation.

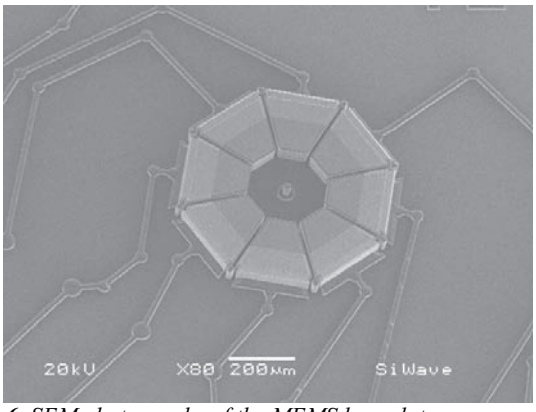

Figure 6. *SEM photographs of the MEMS baseplate.*

In order to set the pointing angle of the mirror accurately, all of the kinematic points that set the digital positions of the mirror must be defined in one mask layer. This is done during the first oxidation patterning allowing the highest possible accuracy. Figures 6 and 7 show SEMs of the finished baseplate for one mirror in a 8x8 switch mirror array. In these pictures, the wedges are the electrodes, and between the electrodes on the outer perimeter are the kinematic points on which the mirror rests when it is actuated. Each electrode has a silicon trace to electrically contact it to a pad that is on the rim of the chip.

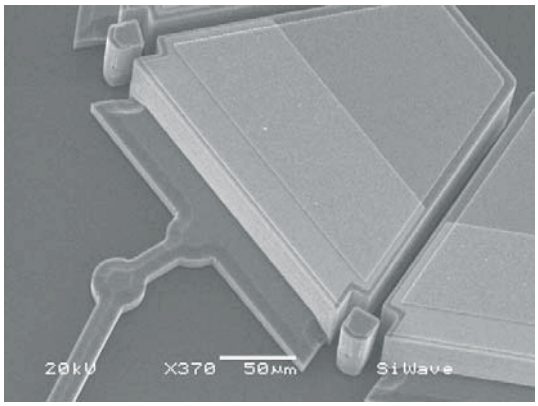

Figure 7. *SEM photographs of the MEMS baseplate.*

FUNCTIONAL AND RELIABILITY TESTS

This type of MEMS mirror relies on contacting surfaces, and the reliability of such contact was a significant issue, in contrast to the situation for conventional "macro" machines. A comparison of the surface-to-volume ratio of MEMS and their macroscopic counterparts explains the underlying physical reason for the predominance of surface phenomena in determining MEMS performance. Because surface forces dominate over body forces as the size of a mechanical component is scaled down in size, the control of these forces becomes very important in MEMS design.

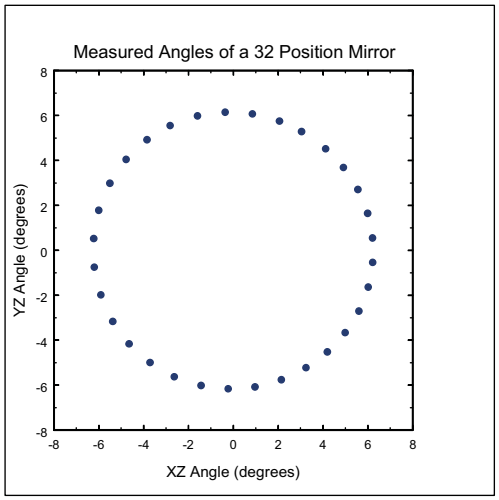

Figure 8. *Data of the mirror during 250,000 cycles around all 32 positions. Repeatability in pointing angle is 0.003 degrees.*

Previous MEMS research has demonstrated repeatedly that contacting surfaces can easily adhere in the microscale [6-8], a phenomenon called "stiction," and that they may also exhibit very high friction coefficients and be subject to significant wear. The forces involved in contacting surfaces on the micro scale have been the subject of substantial research over the past twenty years. The relative magnitude of surface forces is: capillary (adsorbed water) >> electrostatic >> van der Waals. In the case of oxidized silicon surfaces in room air, the work of adhesion (the energy needed to separate contacting surfaces) due to capillary forces can exceed that due to van der Waals attraction by a factor of 10^4. The optimal surface coating for minimizing stiction and wear would be both hydrophobic (eliminating capillary forces) and hard; ideally, contact would occur over as small an area as possible.

This MEMS switch technology has several features that make the problem of contacting surfaces tractable. For example, mirror-baseplate contact occurs at lithographically defined "kinematic points." The material and contacting edge shape of the kinematic point is engineered to reduce local shear loads and stiction forces. A second important feature is that the basic mirror motion during actuation is rolling, rather than sliding. As a result, wear at the kinematic points is greatly reduced.

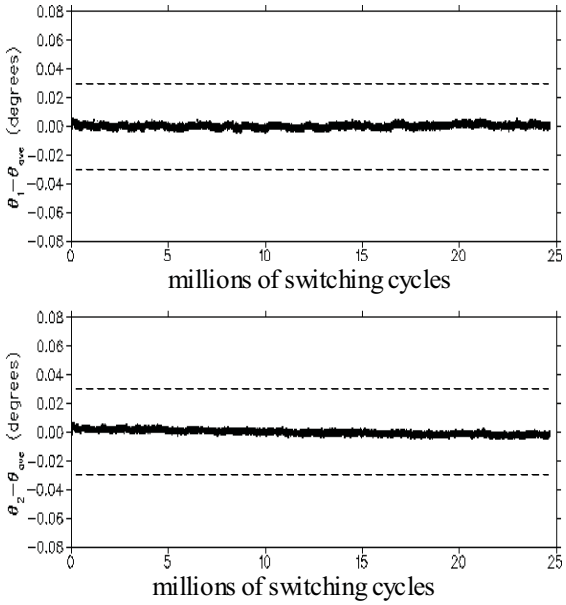

Figure 9. *A plot of the change in elevation angle for two positions during a 25 million cycle wear experiment in 7% RH. The dotted lines contain the allowable change in elevation angle for 0.5 dB insertion loss repeatability.*

A MEMS mirror with 32 positions was tested over 25 million cycles inside a dry box at 7% RH and a temperature of ~ 25 Celsius. The mirror pointing angle was monitored optically with a resolution of 0.003 degrees. The mirror was first actuated around all 32 positions for 250,000 cycles, and all angles measured every 32,000 points. The data is shown in Figure 8. This test demonstrates that the MEMS mirror is capable of switching to all 32 states, and that the repeatability in angle is ~ 0.003 degrees, which is substantially better than 0.06 degrees required for 0.5 dB repeatability in insertion loss in a 32x32 optical switch. The mirror was then switched between two adjacent states for nearly 25 million cycles without interruption. The mirror pointing angle was measured optically with a resolution of 0.003 degrees. The data from the test is shown in Figure 9.

Many of the same design features of the digital MEMS switch that minimize its vulnerability to wear also tend to minimize the probability of failure due to stiction. In comparison to other MEMS switches, the mirror structure is much larger and the ratio of kinetic energy to the surface forces from contact at the small kinematic points is much greater. The electrostatic actuation forces are also much larger than for conventional MEMS, which makes overcoming stiction easier.

We have calculated the forces that act on the digital MEMS micromirror to understand and predict the stiction of the mirror under different relative humidity (RH) conditions. Below is a list of the forces for the micromirrors being tested.

1. Springs provide a separation force of 6 micro-Newtons
2. Electrostatic rolling separation force is 50 micro-Newtons at 100 Volts
3. Capillary adhesion force
    - 52% RH (lab environment) ~100 micro-Newtons
    - 7% RH (dry box) ~ 14 micro-Newtons

Based on these results, it was expected that the capillary adhesion force would exceed both the spring separation force and the electrostatic rolling force at 52% RH. This matched experiments carried out on the micromirrors in lab environment. Stiction was only overcome by the rolling force when using 200-300 Volts. In addition, it was expected that the electrostatic rolling force (100 Volts) would exceed the capillary adhesion force at 7% RH. This also matched experiments carried out on the micromirrors in a dry box environment with a measured RH of 7%. Furthermore, there was no stiction during wear testing of the micromirror devices which underwent 25 million cycles, which indicates that there is no appreciable change in capillary adhesion forces over this many cycles.

CONCLUSION

We have demonstrated digital MEMS mirrors with up to 32 accurate mechanically prescribed positions. We have discussed the efforts taken to make these devices extremely reliable, and demonstrated mirrors with no measurable degradation after 25 million cycles. These digital MEMS mirrors enable, among other things, three dimensional digital optical switches that are smaller and lower cost than competing approaches.

REFERENCES

1. Marxer, C., et al., “Vertical Mirrors Fabriated by Deep Reactive Ion Etching for Fiber-Optic Switching Application“, *Journal of Microelectromechanical systems*, Vol. 6, No. 3: 277-285, (1997).
2. Miller, R.A., et al., “An Electromagnetic MEMS 2x2 Fiber Optic Bypass Switch” ,Transducers ’97, Vol.1., (1997)
3. A. Neukermans, et al., “MEMS Technology for Optical Networking Applications”, *IEEE Communications Magazine*, pp. 62-69, January, (2001); and references therein.
4. P. Dobbelaere, et al, “Digital MEMS for Optical Switching,” *IEEE Communications Magazine*, vol. 40, no. 3, pp. 88-95, Mar. (2002)
5. M. Mita et al, “Multiple-height Microstructures Fabricated by ICP-RIE and Embedded Masking Layers,” Trans. IEE Japan, Vol. 120-E, No. 11, 2000, pp.493-497.
6. W. Robert Ashurst, et al., “Alkene based monolayer films as anti-stiction coatings for polysilicon MEMS“, *Sensors and Actuators* A 91, 239-248 (2001).
7. R. Maboudian and R.T. Howe, “Critical review: Adhesion in surface micromechanical structures*,” J. Vac. Sci. Technol. B,* vol. 15, pp.1-20, (1997); and references therein.
8. N. Tas, et al., “Stiction in surface micromachining”, J. Micromech. Microeng., vol.6, pp. 385-397, (1996); and references therein.

A MAGNETICALLY ENHANCED WIRELESS MICRO-GEIGER COUNTER

Christine K. Eun[1], Ranjit Gharpurey[2] and Yogesh B. Gianchandani[1]
[1]*Department of Electrical Engineering and Computer Science, University of Michigan, Ann Arbor*
[2]*Department of Electrical and Computer Engineering, University of Texas, Austin*

ABSTRACT

This paper reports a micromachined Geiger counter with integrated permanent magnets that enhance the RF transmission from the discharges initiated by incident beta particles. With the intent of wireless sensing within the ultra wideband (UWB) spectrum, the transmission in the 2.0-2.8 GHz frequency range is investigated. The device consists of a 1x2 cm^2 micromachined glass/Si cavity sandwiched between two miniaturized NdFeB rare earth magnets. Several different magnet orientations as well as two different shapes of magnets (square and ring) are investigated. The square and ring magnets have a maximum flux density of 2.40 and 0.91 kG, respectively. Preliminary results show that the RF spectra in the presence of ^{90}Sr and ^{204}Tl sources of 0.1-1.0 μCi increased by ~8 relative dBμV (compared to non-magnetic devices) at a distance of 5 cm from the device. The radiation pattern emitted by the microdischarges is measured in the plane of the device. Wireless spectra from electrostatic discharges are also reported.

I. INTRODUCTION

Past work on lithographically microfabricated radiation sensors has included solid-state and gas-based X-ray detectors [1-5]. It has been shown that a micromachined Geiger counter generating gas microdischarges created by the passage of a beta particle transmits radio-wave signals potentially suitable for sensor networking [6,7]. These RF transmissions produced by the microGeiger were controlled by bias circuitry components.

Gas discharges across relatively large gaps (on the order of cm) have been employed in the past with spark gap transmitters for communication applications dating back to Guglielmo Marconi in the mid-1890's [8]. In 1901, Bose reported utilizing discharges within waveguides in order to generate microwaves, and more recent activity has also been reported [9].

Networked radiation sensors are envisioned for monitoring public buildings with high pedestrian traffic such as train stations, football stadiums and shopping malls. Wireless communication between sensors can enable rapid and low cost deployment or reconfiguration of networks. Wireless networks can also be employed for monitoring environmental hazards and inaccessible terrains. The prospect of not only utilizing the inherent RF transmissions from discharge-based sensors, but also to have the ability to control and influence the wireless signal output is very attractive from a viewpoint of implementing a wireless network.

Employing large permanent magnets in plasma magnetron systems for micromachining have found widespread use with sputtering deposition systems. Traditionally, plasma magnetrons made use of powerful magnets to increase plasma density and consequently increase sputtering efficiency. The mean free path is relatively large (on the order of a few cm) due to operation at lower pressures (on the order of 5-10 mTorr of pressure) [10]. Miniaturized permanent magnets have been utilized in the past to enhance and confine dc microplasmas to enable localized, maskless etching of silicon with SF_6 gas [11].

This paper presents a magnetically enhanced micromachined Geiger counter for β-particle detection, which uses permanent magnets along with glass/Si structures to produce wireless transmission in the ultra wideband (UWB) window. In Section II, device concepts such as basic wireless Geiger operation as well as the magnet configuration used to achieve RF field strength enhancement is discussed. Section III presents the recent experimental results including field enhancement data and emission pattern plots. Section IV concludes with a discussion of possible applications.

II. DEVICE CONCEPTS AND OPERATION

Basic Wireless Geiger Operation

The basic device includes a lithographically micromachined component which is a glass-Si-glass sandwich in which a central Si post forms the cathode and a peripheral Si ring forms the anode. This component measures 1x2 cm^2 and contains 6 different detection cavities that share a common anode on each die. The region proximal to the cathode has a weak field and is called the drift region, whereas that adjacent to the anode is the higher field amplification region. Discharges can be either electrostatically initiated (exceeding gas breakdown voltage) or beta particle-initiated. As beta particles pass through the glass window, they ionize the surrounding gas atoms, resulting in an avalanche current pulse and consequent RF transmission. The micro-Geiger device inherently operates as a UWB transmitter along the guidelines specified in [12].

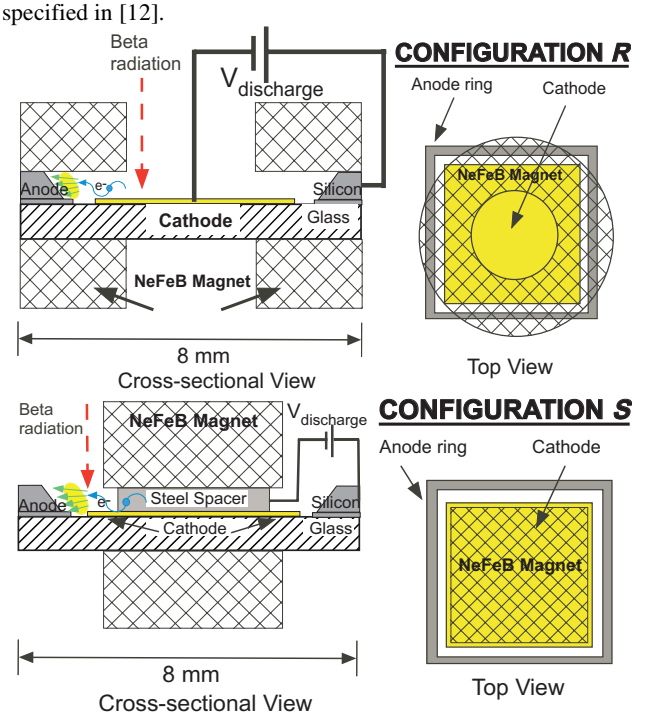

Fig. 1: (a) Cross-section of device in ring magnet configuration (Configuration *R*). (b) Cross-section of device in square magnet configuration (Configuration *S*).

Magnetic Enhancement Configuration

Configuration *R* (Fig. 1a) and Configuration *S* (Fig. 1b) show the cross-section of the device in the different configurations tested.

They utilize strong magnetic fields provided by miniaturized neodymium-iron-boron (NdFeB) rare earth magnets. Ring-shaped as well as square-shaped magnets were used to construct the sandwich structures. Each square magnet measured 6x6x6 mm^3. A steel spacer was utilized as the cathode electrode contact to avoid passing large amounts of current through the permanent magnets and consequently damaging the upper permanent magnet. Each ring magnet measured 6 mm outer radius and a 2.5 mm inner radius. Figure 2 shows a photograph of the micro-Geiger device assembled in Configuration *R*. The electrical contact for the cathode passes through the opening of the top ring-shaped magnet. The structure is stabilized by the second magnet located below the micromachined Geiger counter. The magnetic field lines were aimed to be positioned perpendicular to the discharge path.

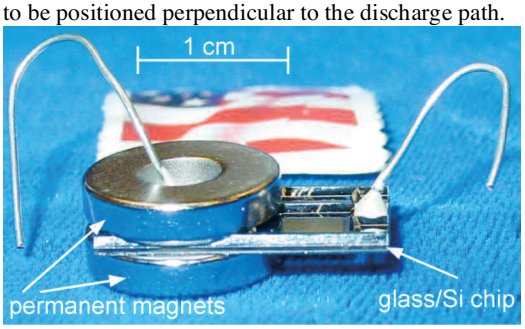

Fig. 2: Photograph of micro-Geiger device in the ring magnet arrangement (Configuration *R*).

A particle that is moving in the presence of both an electric field and an orthogonal magnetic field, B_0, which is also consequently perpendicular to the discharge path, will give rise to a drift velocity, v_F, perpendicular to both fields:

$$v_F = \frac{(\mathbf{F}_\perp / q) \times \mathbf{B}}{B_0^2} \qquad (1)$$

$F_\perp$ represents the transverse force due to the electric field acting on the particle. **B** is the component of the magnetic field that is orthogonal to the electric field and *q* represents the charge. The particle velocity is directly proportional to the applied magnetic field. The particle will experience a gyrating motion, much like a spiral coil course, around this new, elongated discharge path [13]. Since each accelerating particle emits electromagnetic radiation, increasing the number of excited atoms can generate a stronger overall signal. In essence, this new discharge path provides an opportunity for more ion-to-neutral gas atom collisions and thereby creates more ionized particles that can participate in the wireless transmission.

III. EXPERIMENTAL RESULTS

Magnetic field strength measurements of each magnet (square and ring) were taken in the X and Z direction with a Hall sensor and the results are shown in Fig. 3a and Fig. 3b, respectively. The magnetic flux density in the Z direction of each square magnet ranged from 0.17 to 2.40 kG measured at a distance from 2 to 12 mm. The strength of the ring magnet in the Z direction varied from a flux density of 0.11 to 0.91 kG measured at a distance of 3 to 16 mm. In the X direction, the strength varied between 0.05 to 0.50 kG and 0.05 to 0.90 kG for the square and ring magnet, respectively. The X distances ranged between 5 to 21 mm. The strength of the square magnet in the Z direction was greater than the ring magnet but was measured to be weaker in the X direction. The measured magnetic field strength dropped off exponentially as expected.

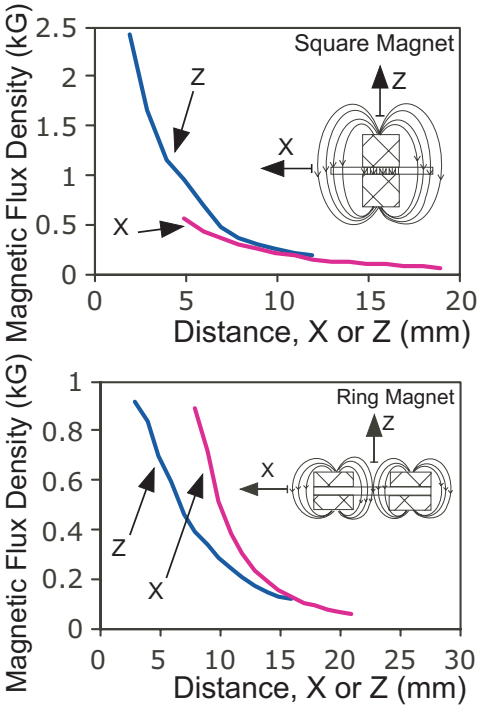

Fig. 3: (a) Magnetic flux density of a square magnet with respect to axial distance measured with a Hall probe (Bell Hall Generator: BH-205). (b) Magnetic flux density of a ring magnet with respect to axial distance.

The antenna of an RF field strength analyzer was positioned 91.5 cm away from the device while the source to detector distance was fixed at 5 cm. Frequency scans were taken in narrow-band frequency modulation (NBFM) reception mode spanning the frequency range from 2.0 GHz to 2.8 GHz in 5 MHz steps. All measurements were taken in a Ne/air gas environment with the various magnetic arrangements summarized in Table I. (A compass was used to determine the pole direction on the magnet.) For beta-initiated discharges, the pure beta emitters, ^{90}Sr and ^{204}Tl, were used with strengths 0.1 and 1.0 μCi, respectively.

Figure 4 shows the resulting spectrum using the square magnet assembly (Configuration *S*) during electrostatic breakdown. Electrostatic breakdown occurs when the applied voltage exceeds the gas breakdown potential. A significant increase in signal strength (~7 rel. dBμV) was observed around 2.3 and 2.6 GHz compared to the control measurement. The control measurement for Configuration *S* was taken without magnets present but with the steel spacer providing electrical contact to the cathode. Figure 5 shows the same configuration but this time with beta-initiated discharges using the radioisotope, ^{204}Tl. The resulting spectra showed a dramatic improvement in field strength (~8 dBμV) between 2.0 and 2.8 GHz with the exception of 2.2 to 2.3 GHz.

Table I: Magnet shape and pole orientation for each configuration.

Configuration	Magnet shape	Pole orientation
SN	Square	North up
SS	Square	South up
RN	Ring	North up
RS	Ring	South up

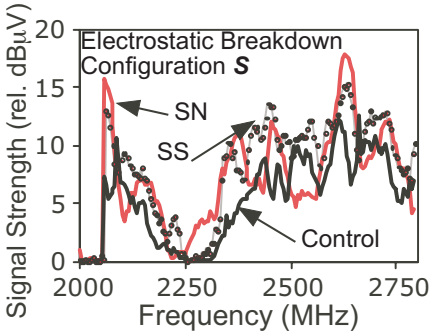

Fig. 4: Discharge spectra of electrostatic breakdown measured using an RF field strength analyzer (Protek, Inc., #3290). The control was taken in the absence of magnets with steel spacer providing electrical contact to cathode. Configuration *SN* and *SS* are also shown. Spectral strength increases in the presence of the magnetic field. Tests were conducted in a Ne/air environment.

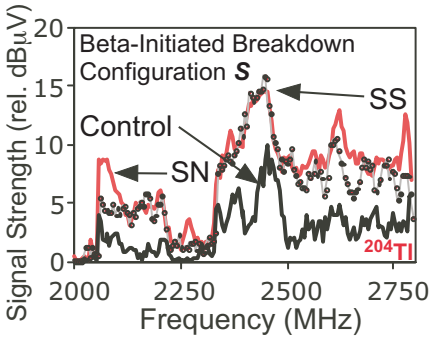

Fig. 5: Discharge spectra of beta-initiated breakdown using ^{204}Tl as the radioactive source. Configuration *SN* and *SS* are shown along with the control measurement.

Figures 6 and 7 illustrate the same series of measurements but this time using the dual ring-shaped assemblage (Configuration *R*). Both plots show significant increase in signal strength measured when compared to the control measurement. Figure 8 compares the resulting spectra when the electrode roles are reversed (anode becomes cathode, cathode becomes anode): this decreased spectral strength.

A measurement was performed to determine the directionality of the transmitted RF spectra. The experimental set-up is illustrated in Fig. 9, whereas the emitted radiation pattern of the RF transmissions from the microdischarges received as a function of in-plane rotation angle has been plotted in Fig. 10. The applied bias voltage was kept constant at 900 V in the presence of ^{90}Sr while the sensor and source were rotated at various angles relative to the RF field strength analyzer. Figure 10(a-top) shows the control measurement of the RF transmission characteristics in the absence of the permanent magnets spanning from 0° to 180°, measured at 15° intervals, at a constant radius of 91.5 cm. The tested frequencies spanned 2.0 to 2.8 GHz in NBFM reception mode. Electrical contact was made directly to the central cathode. The plot shows fairly uniform spectra spanning the perimeter of the circle. Figure 10(b-bottom) shows the same transmission characteristics, this time in the presence of the applied magnetic field in Configuration *RN*. A fairly uniform enhancement in the spectrum in the presence of the magnets compared to the absence was observed.

These results show a clear magnetic enhancement of spectral strength observed while operating in both Configuration *S* and Configuration *R*. Experimental results have also demonstrated that the microdischarges are relatively uniform and thereby independent of rotation angle. This supports the idea that magnetic enhancement of the RF transmission is taking place rather than magnetic shaping of the spectra.

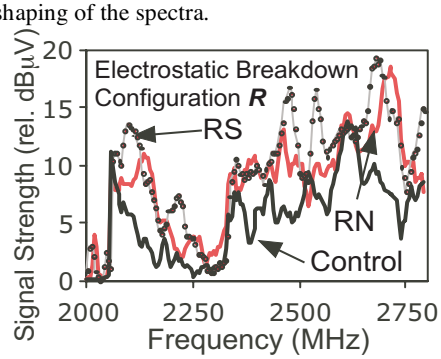

Fig. 6: Discharge spectra of electrostatic breakdown. The control was taken in the absence of magnets. Configuration *RN* and *RS* are also shown. A significant peak increases in signal strength can be seen around 2.1, 2.5 and 2.7 GHz.

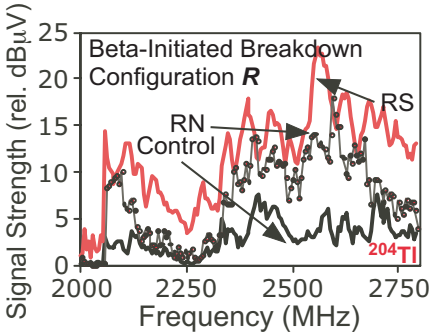

Fig. 7: Discharge spectra of beta-initiated breakdown using ^{204}Tl as the radioactive source. Significant spectral enhancement was achieved spanning the entire 800 MHz (2.0-2.8 GHz) bandwidth in the presence of the magnetic field.

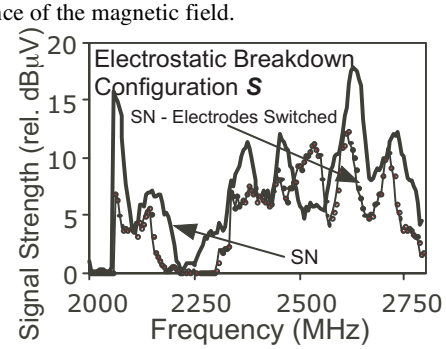

Fig. 8: Discharge spectra of electrostatic breakdown. Electrodes were switched (anode became cathode, cathode became anode) with Configuration *SN*. Switching of electrodes decreased the spectral strength measured.

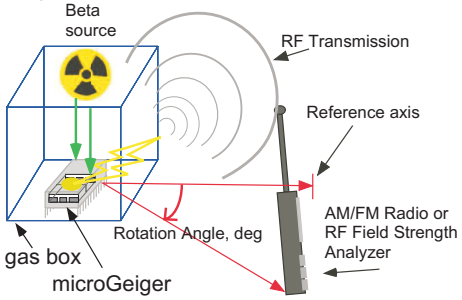

Fig. 9: Schematic illustrating rotation angle used to plot radiation pattern. The reference axis defined the 0° measurement and all subsequent angles were measured from this. Measurements ranged from 0° to 180° in 15° intervals.

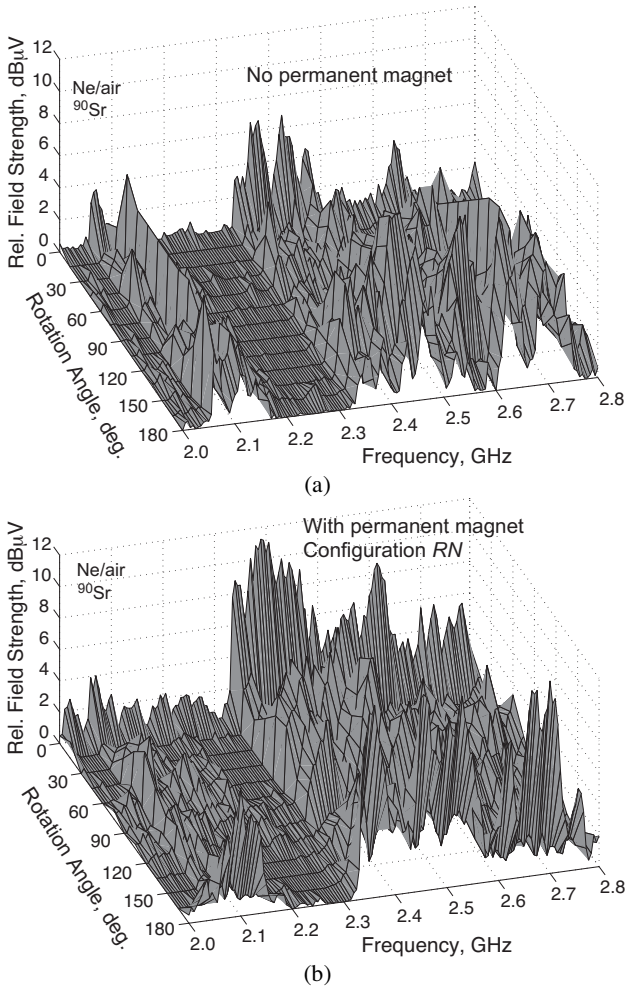

Fig. 10: Radiation pattern plots for the microGeiger discharges spanning from 0° to 180° around the perimeter of a circle with a radius of 91.4 cm. (a-top) Taken in the absence of an external magnetic field. (b-bottom) Taken in the presence of an external magnetic field, Configuration *RN*. The 2.0-2.8 GHz radiation patterns are fairly uniform around the circle.

IV. CONCLUSIONS

With the fast emergence of wireless sensor applications along with new wireless standards, developing distributed wireless sensing networks is very attractive. Utilizing miniaturized magnets to considerably increase the inherent emission characteristics of discharge-based transducers that do not require additional electronics would be a significant step in wireless sensor networking. The presence of the magnetic field induces a drift velocity of the electrons and ions that is perpendicular to the discharge path. This additional velocity force results in a change in the current discharge behavior that is realized during operation of the microGeiger. The device integrated a 1x2 cm^2 micromachined glass/Si cavity between two miniaturized NdFeB rare earth magnets. Experiments involved several different magnet orientations as well as two different shapes of magnets (square and ring) were investigated. Weak radioactive sources with strengths ranging from 0.1-1.0 μCi were used. Each square and ring magnet had a maximum flux density of 2.40 and 0.91 kG, respectively. Preliminary results show that in the presence of miniaturized magnets, the RF spectra emitted by the gas discharges in the 2.0 to 2.8 GHz frequency range showed consistent increase in the field strength intensity. The significant change in the received RF spectrum shows the influence of the magnets on the plasma resistance even at atmospheric pressure. Increasing field strength can offer a larger transmission distances and a potentially wider sensing area. Experimental results have also demonstrated that the microdischarges are relatively independent of rotation angle.

It is noteworthy that discharges are observed in other contexts in the micro-domain. Microdischarge-based chemical sensors used for vapor and liquids are known to produce optical spectra that are characteristic of chemical species [14]. Additionally, microdischarges are generated unintentionally in electrostatic transducers [15]. The findings presented here could potentially extend to these other contexts.

ACKNOWLEDGEMENTS

This work was supported primarily by the Engineering Research Centers Program of the National Science Foundation under Award Number EEC-9986866. The facilities used for this research include the Michigan Nanofabrication Facility (MNF) at the University of Michigan. The authors would like to thank Tze-Ching (Richard) Fung for his assistance with the test setup and measurement advice in this effort.

REFERENCES

[1] S. A. Audet, E. M. Schooneveld, S. E. Wouters and M. H. Kim, "High-Purity Silicon Soft X-Ray Imaging Sensor," *Sensors and Actuators*, (A22), nos. 1-3, Mar. 1990, pp. 482-486.

[2] G. Charpak, J. Derre, Y. Giomataris, P. Rebourgeard, "Micromegas, a multipurpose gaseous detector," *Nuclear Instruments & Methods in Physics Research,* (A478), nos. 1-2, Feb. 2002, pp 26-36.

[3] J. A. Kemmer, "Silicon detectors for nuclear radiation," *IEEE Transducers,* 1987 A478, pp. 252-257.

[4] M. Wada, J. Suzuki, and Y. Ozaki, "Cadmium telluride ß-ray detector," *IEEE Transducers*, 1987 A478, pp. 258-261.

[5] R. Wunstorf, "Radiation hardness of silicon detectors: current status," *IEEE Transactions on Nuclear Science,* 44(3), Jun. 1997 pp. 806-14.

[6] C. K. Eun, R. Gharpurey, and Y. B. Gianchandani, "Broadband wireless sensing of radioactive chemicals utilizing inherent RF transmissions from pulse discharges," *IEEE Intl. Conf. on Sensors*, Nov. 2005.

[7] C. K. Eun, R. Gharpurey, and Y. B. Gianchandani, "Controlling Ultra Wide Band Transmissions from a Wireless Micromachined Geiger counter," *IEEE Intl. Conf. on Micro Electro Mechanical Systems*, Jan. 2006.

[8] J. E. Brittain, "Electrical engineering Hall of Fame: Guglielmo Marconi," *Proceedings of the IEEE*, 92(9), Aug 2004, pp 1501-4.

[9] A. G. Heaton and J. H. Reeves, "Microwave radiation from discharges," *3rd Intl. Conf. on Gas Discharges*, Sept. 1974, pp 73-77.

[10] C. H. Shon, J. K. Lee, H. J. Lee, Y. Yang, and T. H. Chung, "Velocity Distributions in Magnetron Sputter," *IEEE Transactions on Plasma Science*, 26(26), Dec. 1998, pp 1635-1644.

[11] C. G. Wilson and Y. B. Gianchandani, "Miniaturized Magnetic Nitrogen DC Microplasmas", *IEEE Transactions on Plasma Science*, 32(1), Fe. 2004 pp. 282-287.

[12] FCC 02-48, First Report and Order, "Revision of Part 15 of the Commission's Rules Regarding Ultra-Wideband Transmission Systems," Feb 14, 2002: http://hraunfoss.fcc.gov/edocs_public/attachmatch/FCC-02-48A1.pdf.

[13] M. A. Lieberman and A. J. Lichtenberg, *Principles of Plasma Discharges and Materials Processing*, John Wiley and Sons, Inc. 2nd Edition,2005.

[14] B. Mitra and Y. B. Gianchandani , "The micromachined flashFET: a low-power, three-terminal device for high speed detection of vapors at atmospheric pressure,"*IEEE Intl. Conf. on Micro-Electro- Mechanical Systems*, Jan. 2005, p 794-7.

[15] T. Ono, Y. Dong, M. Esashi, "Microdischarge and electric breakdown in a micro-gap," *Journal of Micromechanics and Microengineering*, 10(3) 9/00, pp. 445-51.

A MICROASSEMBLED LARGE-DEFLECTION TIP/TILT MICROMIRROR FROM A SINGLE-MASK DRIE PROCESS

Matthew E. Last, V. Subramaniam, and Kristofer S.J. Pister
Berkeley Sensor and Actuator Center, University of California Berkeley
Berkeley, California USA

ABSTRACT

An electrostatically-actuated micromirror optimized for large static pointing angles is designed, fabricated, and tested. A single-mask SOI process is used to create the actuators, mechanisms, and microassembly tools described in this paper. Two pick-and-place microassembly steps are used to (a) attach a mechanism that converts the actuators' in-plane motion into rotational motion, and (b) attach a mirror face sheet to the rotation mechanism. We report the largest static range of deflection angles for a micromirror: 0-28.2^o and 0-14.9^o at 50V for each axis. Compared to the previous record [1], this corresponds to a 27% improvement in one axis but a 12% reduction in the other axis. Moreover, we use a single-mask process as opposed to the seven-mask process in [1]. Other new accomplishments reported here include a microfabricated tweezer that grabs and simultaneously rotates parts out of plane, a flexurally-suspended Zero Insertion Force (ZIF) socket for the assembled part, and a new tether design that holds the part while the tether is being broken.

INTRODUCTION

Complex actuated micromechanical systems capable of out-of-plane motion have numerous applications in fields like optics and micro-robotics. Such systems can be built in complex multi-layer MEMS processes as demonstrated in [2, 3]. There is however a tradeoff available between process complexity (difficulty of wafer-level fabrication) and post-process complexity (chip-level operations); microassembly techniques can be used to shift this complexity from the fabrication to the post-process. Microassembly of MEMS structures using serial pick and place or various parallel directed assembly techniques has been used to integrate electronics with micromechanisms [4] and to construct electromechanical structures [5, 6].

Serial pick and place microassembly of surface-micromachined parts using specially designed robotic arms with passive grippers has been demonstrated [7]. Complex assembled SOI structures for applications such as miniaturized scanning electron microscopes and variable optical attenuators [8, 9] have also been demonstrated. However, neither of the groups mentioned here have quantified the mechanical stability of their connectors against actuation forces. The functionality of the micromirror presented here hinges on advances made in our lab in mechanically rigid sockets. Rotation stages are fabricated in a single mask SOI process, then picked up and assembled into sockets attached to electrostatic actuators (fig 1). Linear motion of the actuators is converted to out-of-plane two-axis motion of the rotation stage. A mirror face-plate is then assembled on the rotation stage. Thus we demonstrate the use of pick and place assembly to create a high performance two-axis micromirror.

FABRICATION

The process used here and in [10] consists of a single-mask, high-aspect-ratio, deep reactive ion etch (DRIE) through the device layer of a custom-made SOI wafer. The wafer consists of a 20μm thick device layer, a 5μm buried oxide layer, and a 300μm handle wafer. A timed HF acid etch and critical point drying step release the parts from the handle wafer. A self assembled monolayer of an organosilane (FDTS) is deposited using a molecular vapor deposition system from Applied Microstructures. This serves to make the exposed silicon surfaces hydrophobic and reduces stiction between parts. An entire design cycle consisting of design changes, mask fabrication, part fabrication and assembly has been demonstrated in as little as 30 hours.

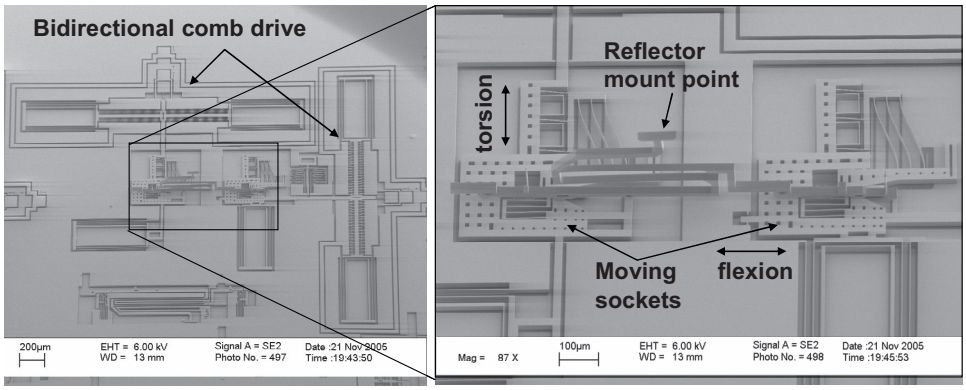

Figure 1: *2-axis rotation stage. Left: electron micrograph shows a birds-eye view of comb drive actuators, moving clamps, and assembled rotation stage. Right: SEM shows a zoomed perspective*

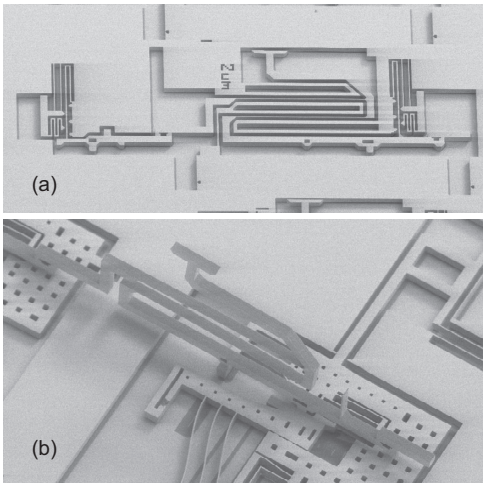

Figure 2: *Rotation stage. (a) As fabricated (b) As assembled*

MICROASSEMBLY

Pick and place microassembly builds complex out-of-plane mechanisms by picking up planar micro-parts, rotating them 90° out-of-plane, and permanently affixing them to the SOI device layer using microfabricated sockets (fig 2). This process, along with the design of the microparts and tooling required, is described in [10]. Some modifications to the process which enabled the two-axis micromirror are presented below.

The assembly process requires a tool that can reliably grasp a part, perform the out-of-plane rotation, and let go of it. A new spring-loaded rotation stage, the sidewall-gripping "ortho-gripper", is presented here (fig 3). Fabricated using the same single-mask process, it consists of two single degree-of-freedom fingers that grasp a part and rotate it exactly 90°. The two fingers can each move orthogonally to one another with one degree of freedom. This tool differs from previous versions of the ortho-gripper [10] in that it grips the sidewalls of the parts to be assembled instead of their top and bottom surfaces, thus SOI wafers with arbitrary buried oxide thicknesses can now be used. The analysis and design of spring-loaded ortho-grippers are shown in [11]. Operation of the sidewall-gripping version of the tool is presented here for the first time.

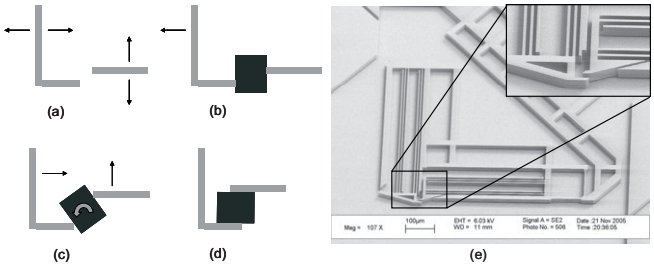

Figure 3: *Ortho-gripper Principle of Operation: The fingers are shown initially grasping a part (b), in the process of rotating the part (c), and after rotation is complete (d). SEM image of sidewall-gripping Ortho-gripper (e). Detail of gripper fingers (inset)*

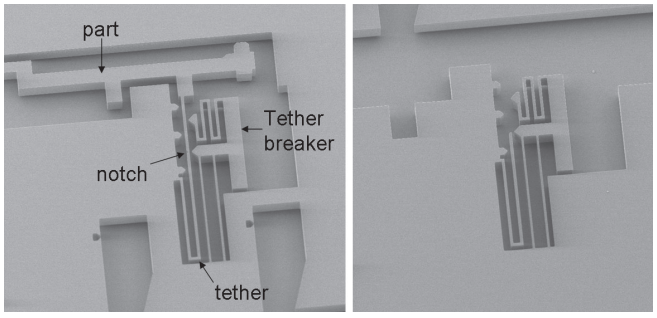

Figure 4: *Tether with integrated tether-breaker*

The ability of the rotation stage to reliably rotate microparts depends on the predictable breakage of the tethers that hold the part to the wafer during fabrication. A new tether design with an integrated tether-cleaving tool is presented (fig 4). This tool holds the part in place while the tether is broken, preventing the part from being flung away as the strain energy stored in the tether is released. To break the tether, the tether breaker is pushed with a probe tip. The tip of the breaker and the tip at the end of the serpentine spring touch the tether at the same time. The spring-loaded tip holds the part in place while the tether is being broken and prevents the part from flying away.

Finally, a fully-suspended ZIF socket with a friction-based clamping mechanism that robustly secures the assembled part is presented (fig 5). Interferometer data shows that no part of the socket comes into contact with the substrate even when experiencing reaction forces from the assembled structure. This socket provides a rigid coupling between the assembled mechanism and in-plane actuators and suspensions, without the use of sliding contacts. In addition, rigid sockets improve assembly yield by securing the part to the device layer with approximately 4 orders of magnitude more force than the ortho-gripper can exert. This is important because reliable ungrasping of the part after assembly depends on this ratio of forces. This rigidity is also useful for ensuring the shock tolerance of the assembled structure.

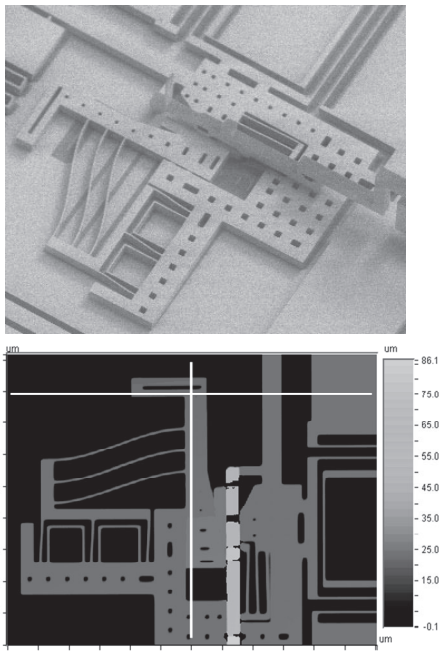

Figure 5: *SEM and optical surface profile (from intereferometer) of part inserted into moving socket*

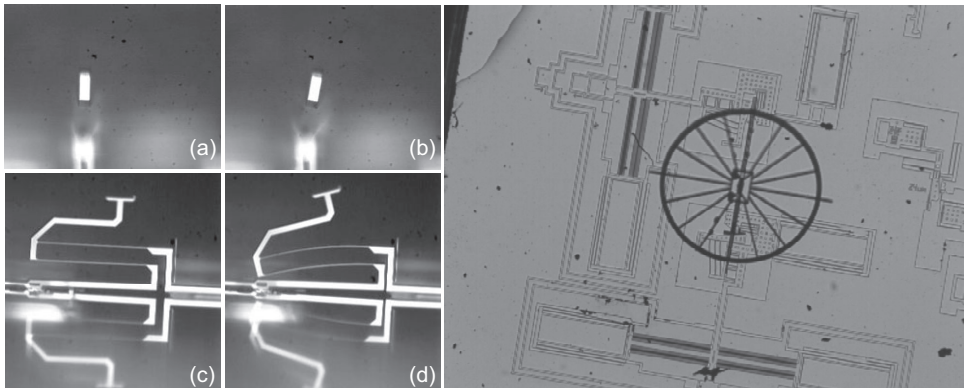

Figure 6: *Left: Photomicrographs show an end-on view of motion about the torsion axis (a,b) and a side view of motion about the flexion axis (c,d) Right: Optical micrograph showing assembled dummy mirror*

A pull-out force >12mN in each axis is required to dislodge the assembled part, corresponding to an acceleration of over 40,000g's.

MICROMIRROR

The micromirror is composed of three sub-parts: the actuators, the assembled rotation mechanism, and the assembled mirror face sheet. Two bi-directional electrostatic comb drive actuators are oriented orthogonally to one another and move in the plane of the chip. These actuators each apply 21μN at 55V and provide displacements up to 17μm. At high voltages, one direction of the comb drive actuator short-circuits to the substrate so only one quarter of the full range of motion of the micromirror was tested. Each actuator is attached to a flexurally-suspended socket, into which the rotation mechanism is assembled. This rotation mechanism consists of two thin parallel flexures connected at one end with a rigid beam (fig 7) which is attached to the mounting point for the mirror face sheet. The other ends of the flexures are attached to the actuators (fig 1). When actuated, the flexures either bend (flexion) or twist (torsion), resulting in the two axes of motion (figs 6). The assembled rotation mechanism thus eliminates the additional structural layers from the wafer-level fabrication process that are typically required for 2-axis rotation stages. The two-axis rotation stage is designed to maximize DC deflection while ensuring that the stress developed on the beams is below the stress limit of silicon. A simplified rotation stage was also simulated in ANSYS (fig 7) using its non-linear modeling capabilities to yield the maximum stresses generated and the maximum angle of deflection.

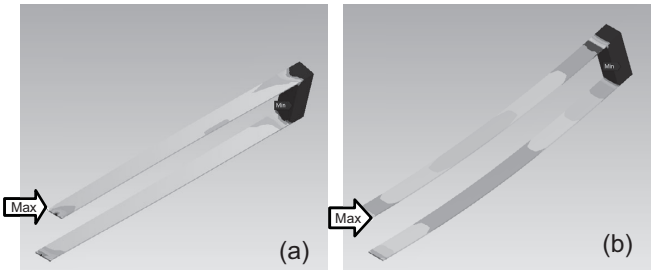

Figure 7: *Simulations of 2-axis rotation stage. Von Mises stress obtained at maximum deflection in (a) torsion mode, (b) flexion mode. Maximum Stress = 200MPa in (a) and 100MPa in (b)*

Optical deflection angle of a laser beam bounced off of the top of the rotation stage was measured to quantify the DC rotation of the devices. Mechanical rotation angle is half the optical angle shown here. Two devices were tested: Device one had two functional actuators (pull-mode about torsion and flex axes) and was tested by bouncing the laser beam off of the top of the device. The second device had only one functional axis (torsion) and was tested using a video camera (as in fig 6). This was done by using an optical microscope to look through a 45° mirror placed next to the chip. Maximum DC deflections of 28° (torsion) and 22° (flexion) were obtained from two separate devices (fig 8).

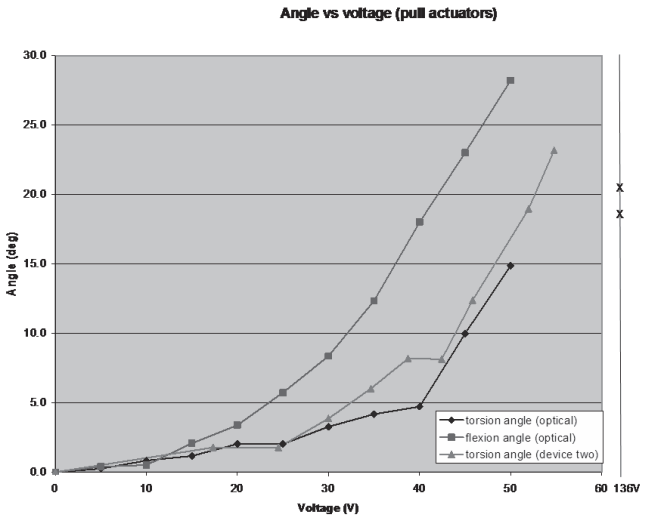

Figure 8: *Experimental test data. For comparison, the best quadrant of operation of the highest-performing large tip/tilt mirror is shown (X's at 136V) from [1]. This rotation stage achieves larger static deflection angles at lower voltages.*

Since the current process is not ideal for creating mirror face sheets, an assembled face sheet shown in (fig 6) is used which serves merely as an assembly technology demonstrator. This face sheet was affixed to the mirror mount of the two-axis rotation stage using epoxy. A low inertia mirror can be fabricated by sacrificing some process complexity as demonstrated in [3, 12]. Fabrication of such a mirror would require at least one additional mask. The mirror face sheet and mechanisms can be built in different processes and optimized separately without requiring the

compromise in performance or increase in process complexity that monolithic integration would require.

CONCLUSIONS

Microassembly provides an attractive option for fabricating complex MEMS structures using a simple fabrication process. This simplicity translates into fast design cycles and high fabrication yield. Microassembly yield increases with the improved tooling presented in this paper: tethers that break gently and predictably, grippers that rotate parts by exactly 90^{o}, and robust sockets. This paper demonstrates that in addition to the speed and yield benefits, a single-mask microassembly-based process can be used to create high performance devices. The electrostatically-actuated tip/tilt micromirror described here sets a new record for DC deflection angle in one of the two axes of rotation.

REFERENCES

[1] Milanovic V., D.T. McCormick, and G.A. Matus, *Gimbal-less Monolithic Silicon Actuators for Tip-Tilt-Piston Micromirror Applications.* IEEE Journal of Select Topics in Quantum Electronics, 2004. **10**(3): p. 462-471.

[2] Hollar S., A. Flynn, C. Bellew, and K.S.J. Pister. "Solar powered 10 mg silicon robot". *Proceedings IEEE Sixteenth Annual International Conference on Micro Electro Mechanical Systems. Kyoto, Japan. 19-23 Jan. 2003.* (2003)

[3] Milanovic V., M. Last, and K.S.J. Pister, *Laterally actuated torsional micromirrors for large static deflection.* IEEE Photonics Technology Letters, 2003. **15**(2): p. 245-7.

[4] Cohn M.B., *Assembly Techniques for Microelectromechanical Systems*, in *Engineering -- Electrical Engineering and Computer Sciences*. 1997, University of California, Berkeley: Berkeley. p. 150.

[5] Guckel H., T. Christenson, and K. Skrobis, *Metal micromechanisms via deep X-ray lithography, electroplating and assembly.* Journal of Micromechanics & Microengineering, 1992. **2**(4): p. 225-8.

[6] Fischer K. and H. Guckel, *Long throw linear magnetic actuators stackable to one millimeter of structural height.* Microsystem Technologies, 1998. **4**(4): p. 180-3.

[7] Dechev N., W.L. Cleghorn, and J.K. Mills. "Tether and joint design for microcomponents used in microassembly of 3D microstructures". *MEMS/MOEMS Components and their Applications. San Jose, CA,USA. 26-27 Jan. 2004.* (2004)

[8] Tsui K., A.A. Geisberger, M. Ellis, and G.D. Skidmore, *Micromachined end-effector and techniques for directed MEMS assembly.* Journal of Micromechanics & Microengineering, 2004. **14**(4): p. 542-9.

[9] Saini R., A. Geisberger, K. Tsui, C. Nistorica, M. Ellis, and G. Skidmore. "Assembled MEMS VOA". *2003 IEEE/LEOS International Conference on Optical MEMS. Waikoloa, HI*. 18-21 Aug., (2003)

[10] Last M., V. Subramaniam, and K.S.J. Pister. "Out of plane motion of assembled microstructures using a single-mask SOI process". *TRANSDUCERS '05. The 13th International Conference on Solid-State Sensors, Actuators and Microsystems. Digest of Technical Papers.* Seoul, South Korea, 5-9 June 2005., Korean Sensors Society. (2005)

[11] Last M., *Silicon on Insulator Pick and Place Microassembly*, in *Engineering - Electrical Engineering and Computer Science*. 2005, University of California, Berkeley: Berkeley. p. 168.

A NANOMECHANICAL PROTEIN CONCENTRATION DETECTOR USING A NANO-GAP SQUEEZING ACTUATOR WITH COMPENSATED DISPLACEMENT MONITORING ELECTRODES

Won Chul Lee[1,2], Young-Ho Cho[1], and Albert P. Pisano[2]
[1]Digital Nanolocomotion Center, Korea Advanced Institute of Science and Technology
Daejeon REPUBLIC OF KOREA
[2]Berkeley Sensor and Actuator Center, University of California at Berkeley
Berkeley, California USA

ABSTRACT

We present a new class of the protein *concentration* detector based on the mechanical stiffness measurement of protein-receptor layers in a squeezed nano-gap. Compared to the previous protein size detector, the present device reduces the distortion and uncertainty in the displacement measurement by adding an actuated nano-gap and reference electrodes. Compared to the conventional protein detectors based on electrochemical, optical, and optomechnical principles, the present device also offers simple, inexpensive, and high-precision protein detection. We design and fabricate the protein concentration detector using an electrothermal actuator and two nano-gaps with reference electrodes. In experimental study, we verify that the present protein detector measures the size of the proteins, streptaividin and m-antibiotin, as 12.1±2.3nm and 13.2±3.3nm at the measurement uncertainty of ±1.1nm, respectively, while showing the concentration detection sensitivity of 2.88N/m/nM in the m-antibiotin concentration range of 5~10nM.

INTRODUCTION

High-precision protein detectors are actively studied for diagnosis and prognosis. [**1**] Previously, we presented the nanomechanical detection principle [**2**], where the actuator squeezes the protein-receptor layers in the nano-gap through a mechanical spring(k_1). This nanomechanical principle offers simple, inexpensive, and high-precision protein detection [**2**] compared to electrochemical [**3**], optical [**4,5**], optomechancial [**6**], and mechanical [**7,8**] principles.

From the nanomechanical principle, we presented the protein *size* detector(Fig.1a) [**2**] based on the squeezed displacement measurement of $x_2(t)$ in Fig.2a. The previous device [**2**], however, was unable to measure the protein *concentration* due to a couple of problems: 1) the distortion in the time-dependent squeezed displacement($x_2(t)$ in Fig.2a) that should be corrected by the time-dependent actuated displacement of $x_1(t)$; 2) the displacement measurement uncertainty of ±7.4nm [**2**] caused by signal drift and noise.

In this work, we succeed to measure the protein concentration by solving the above-mentioned problems as follows: 1) We add an actuated nano-gap(Fig.1b) to measure $x_1(t)$ in addition to $x_2(t)$. We synchronize $x_1(t)$ and $x_2(t)$ to obtain the directed correlation(Fig.2b) between x_1 and x_2, thus eliminating the distortion included in $x_1(t)$ and $x_2(t)$; 2) We use reference electrodes (Fig. 3) in both actuated and squeezed nano-gaps to compensate the signal drift and noise, thus reducing the displacement measurement uncertainty from ±7.4nm to ±1.1nm. We also experimentally verify the selectivity, repeatability, and sensitivity of the protein concentration detector.

Figure 2b illustrates the protein detection principle of the device, where the mechanical stiffness of protein-receptor layers is measured by x_1 - x_2 relationship. When the squeezing electrode touches the receptor-protein layers on the nano-gap surfaces (Fig.3), the layers provide added stiffness (k_{rp} in Fig.1) to the mechanical spring(k_1). The added stiffness changes the slope of the modulation lines on x_1 - x_2 plane(Fig.2b). We measure the protein concentration from the slope(s) of the modulation line, while detecting the protein presence and size from the ordinate shift(Fig.2a) of the slope changing point(P).

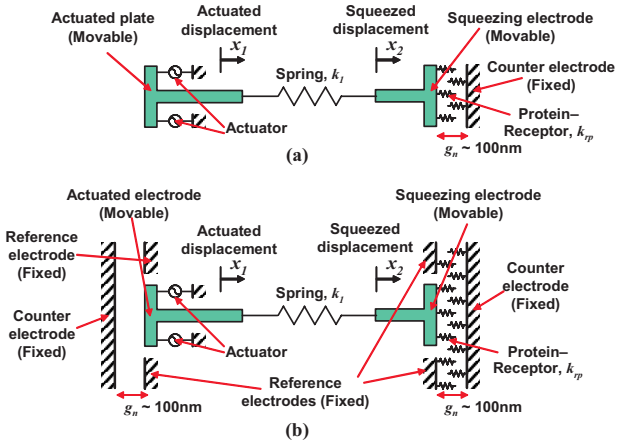

Figure 1. *Comparison of the nanomechanical protein detectors: (a) the previous protein presence detector [2]; (b) the present protein concentration detector, measuring the actuated and squeezed displacements using compensated displacement monitoring electrodes.*

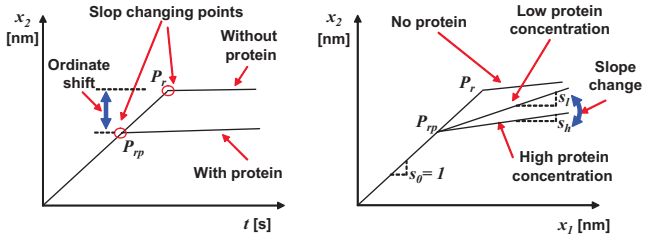

(a) (b)

Figure 2. *Working principle of the nanomechanical protein detectors: (a) the previous protein presence detection [2] using the relationship between the actuation time, t, and the squeezed displacement, x_2; (b) the present protein concentration detection using the relationship between the actuated and squeezed displacements, x_1 and x_2.*

DESIGN AND FABRICATION

We design the nanomechanical protein detector as shown in Figure 4 and Table 1. We use an electrothermal actuator and the nano-gaps for the operation in a buffer solution. The nano-gap, g_n, is formed from a fabricated initial gap, g_i. We obtain the nano-scale distance between the squeezing electrode and the counter electrode after attaching the counter electrode to stoppers.

Figure 4 contains a top view of the electrothermal actuator. The currents though heating bars generate heat, elongating them and deforming the hinges. Thus, the output port (m_1) of the electrothermal actuator moves in the x_1-direction. From 2-dimensional electrothermal and thermomechanical analysis, we obtain the electrothermal actuation of 699nm at the temperature change of 29.6°C. We can verify that the displacement of the electrothermal actuator is large enough to cover the nano-gap of 100nm.

We can detect the squeezed motion, x_2, using an impedance change of the nano-gap. The squeezed motion changes the impedance of the buffer solution between the squeezing electrode and the counter electrode. In order to reduce the displacement measurement uncertainty, we use reference electrodes (Fig. 3) in both actuated and squeezed nano-gaps to compensate the signal drift and noise.

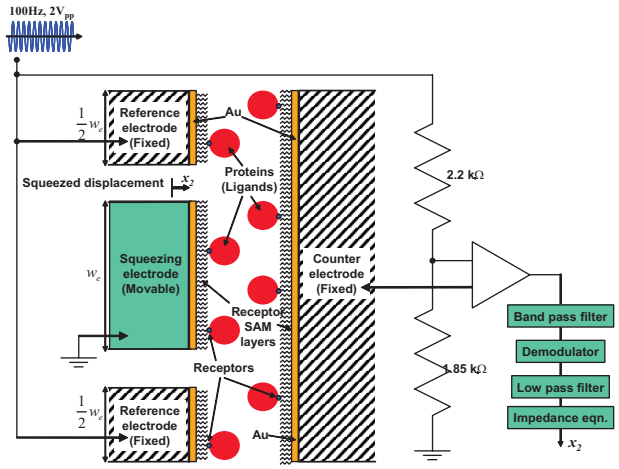

Figure 3. Squeezed and reference nano-gaps and compensated displacement monitoring methods in the protein concentration detector.

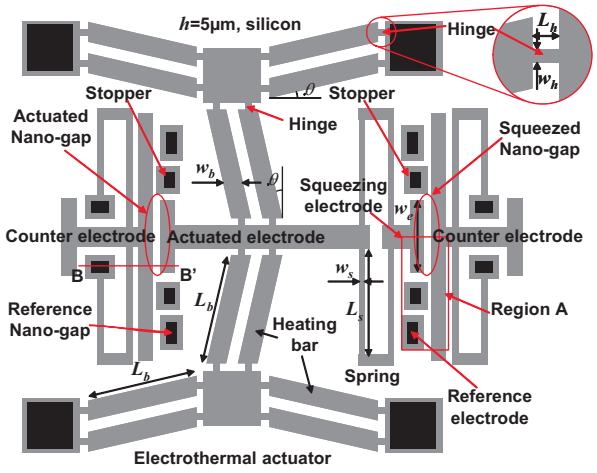

Figure 4. Top view of the protein concentration detector.

Table 1. Measured dimensions of the fabricated devices

Structures*	Dimensions
Structure thickness, h	5 μm
Bar length, L_b, × Bar width, w_b	220 μm × 28 μm
Bar angle, θ_b	6°
Hinge length, L_h, × Hinge width, w_h	10.0 μm × 4.0 μm
Spring length, L_s, × Spring width, w_s	200 μm × 3.2 μm
Electrode width, w_e	52.0 μm
Initial gap, g_i	10.0 μm
Nano-gap, g_n	100 nm

*The structures are shown in Figs.3 and 4.

The designed protein concentration detector is fabricated (Fig.5) as shown in Fig.6, followed by the process of receptor immobilization. The two-mask microfabrication process is shown in Figure 5, representing the cross section along B-B' in Fig.4. Nano-gap surface has been smoothed by oxidation(Fig.5b) and oxide-etching(Fig.5c) during the fabrication process.

Biotin, the receptor, is immobilized on the gold surface of the nano-gap electrodes using SAM (Self Assemble Monolayer). We deposit the mixed SAM layer, composed of 11-mercaptoundecanol and 16-mercaptohexa-decanoic acid. Then, the gold surface is biotinylated using biotinamidohexanoic acid hydrazide. Figure 7 shows the fluorescent image, which indicates that the biotin is immobilized on the nano-gap electrodes.

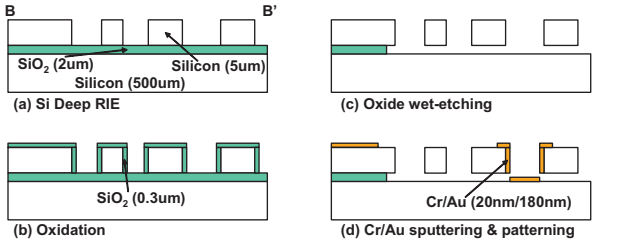

Figure 5. Microfabrication process showing the cross section along B-B' in Fig.4.

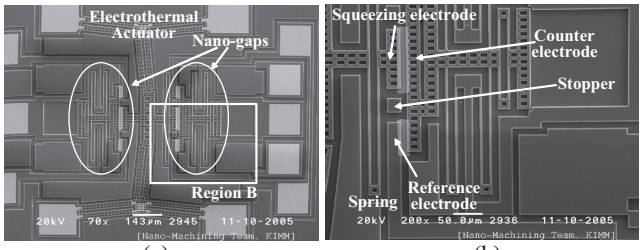

(a) (b)

Figure 6. SEM photographs of the protein concentration detector: (a) overall structure; (b) an enlarged view of the Region B in (a).

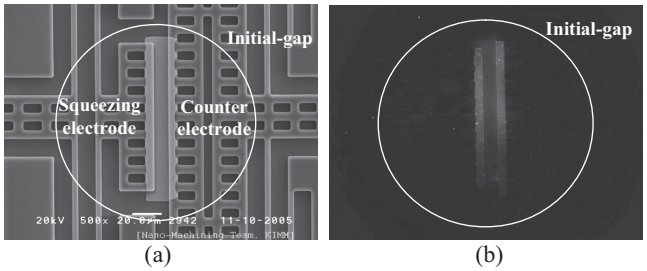

(a) (b)

Figure 7. Microscope images of the initial-gap in the protein concentration detector with FITC tagged streptavidin: (a) SEM image; (b) fluorescent microscope image.

EXPERIMENTAL RESULTS

In experimental study(Table 2), we characterize 1) the distortion in the time-dependent squeezed displacement, 2) the displacement measurement uncertainty, 3) the selectivity, 4) the repeatability, and 5) the sensitivity of the protein concentration detector. 1) The distortion, expressed by the t - x_2 nonlinearity(3.0%) in Fig.8, is eliminated by the time-dependent actuated displacement of $x_1(t)$ in Fig.8a. 2) The displacement measurement uncertainty are reduced to ±1.1nm(Fig.8) due to the compensated displacement monitoring electrodes. 3) The protein detection selectivity is verified by Fig.9 and Table 3: The detector generates the size detection signal (12.1±2.3nm) for receptor-active protein and the null detection signal for receptor-inactive protein. 4) The detection repeatability is demonstrated by Fig.10 and Table 4: The detector measures the protein size(13.2±3.3nm). After the protein removal, the size detection signal returns to the initial state (null signal) indicating no protein.

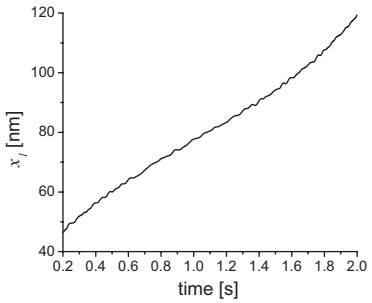

(a)

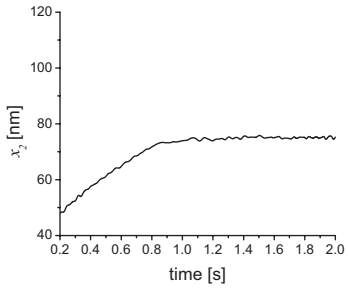

(b)

Figure 8. *Measured displacements of the protein concentration detector: (a) the actuated displacement, x_1; (b) the squeezed displacement, x_2.*

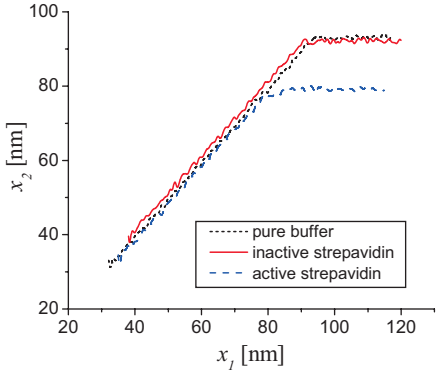

Figure 9. *Experimental squeezed displacement, x_2, for the actuated displacement, x_1, in the selectivity verification using receptor-active and receptor-inactive proteins.*

Table 2. *Receptors and proteins used in the experiments for the performance verification*

Verified performance	Receptor	Protein
Selectivity	Biotin	Streptavidin
Repeatability	Biotin	M-antibiotin
Sensitivity	Biotin	M-antibiotin

Table 3. *Experimental ordinate shifts* of the slope changing points for the selectivity verification using 3 devices, each from different dice*

Device #	Inactive streptavidin**	Active streptavidin
A	2.3±2.1nm	12.1±2.4nm
B	-0.3±2.9nm	10.9±2.9nm
C	1.1±2.9nm	13.2±3.1nm
Average	1.0±2.6nm	12.1±2.3nm

*The ordinate shifts, obtained from the five repeated measurements of the slope changing points, are indicated in the forms of (average ± 2σ).
**0.5uM streptavidin solution is inactivated by the pre-incubation with 2.0uM d-biotin solution.

Table 4. *Experimental ordinate shifts* of the slope changing points for the repeatability verification using 3 devices, each from different dice*

Device #	M-antibiotin addition	M-antibiotin removal
A	13.9±3.2nm	-2.3±3.0nm
B	14.3±2.7nm	0.1±2.5nm
C	11.3±1.2nm	1.0±1.3nm
Average	13.2±3.3nm	-0.4±3.4nm

*The ordinate shifts, obtained from the five repeated measurements of the slope changing points, are indicated in the forms of (average ± 2σ).

Table 5. *Experimental slopes and receptor-protein stiffness for different concentrations of m-antibiotin solution*

Concen-tration	Slope, s				Stiffness of receptor-protein layers, $n \cdot k_{rp}$
	Device A	Device B	Device C	Ave.±2σ	
1nM	N/A	N/A	N/A	N/A	N/A
3nM	N/A	N/A	N/A	N/A	N/A
5nM	0.228	0.171	0.240	0.213±0.074	9.6±4.6 N/m
7nM	0.128	0.151	0.137	0.139±0.023	15.8±3.0 N/m
10nM	0.104	0.095	0.088	0.096±0.016	24.1±4.5 N/m
20nM	0.095	0.100	0.109	0.101±0.015	22.6±3.5 N/m
500nM	0.101	0.083	0.107	0.097±0.025	23.8±7.2 N/m

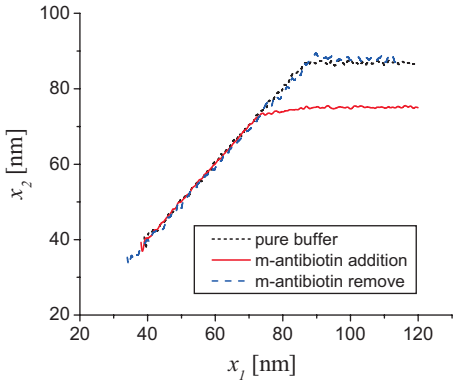

Figure 10. *Experimental squeezed displacement, x_2, for the actuated displacement, x_1, in the repeatability verification using m- antibiotin.*

5) We verify the sensitivity of the fabricated device from Table 5, where the slope and the stiffness are obtained from the modulation lines (Fig.11) for protein-receptor layers in the protein concentration range of 1~500nM. For the protein concentration of 5~10nM (Fig.12), the stiffness($n \cdot k_{rp}$) is measured in the range of 9.6~24.1N/m at the sensitivity of 2.88N/m/nM. The stiffness is saturated over 10nM concentration, indicating the protein-receptor binding saturation.

It is experimentally verified that the present protein detector measures the size of the proteins, streptaividin and m-antibiotin, as 12.1±2.3nm and 13.2±3.3nm at the measurement uncertainty of ±1.1nm, respectively, while showing the concentration detection sensitivity of 2.88N/m/nM in the m-antibiotin concentration range of 5~10nM.

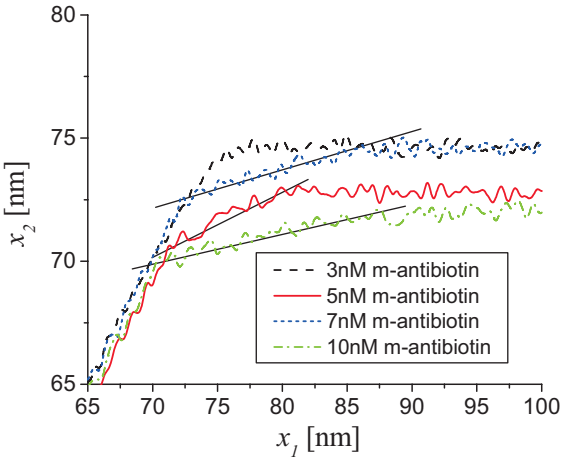

Figure 11. *Experimental squeezed displacement, x_2, for the actuated displacement, x_1, in various m-antibiotin concentrations.*

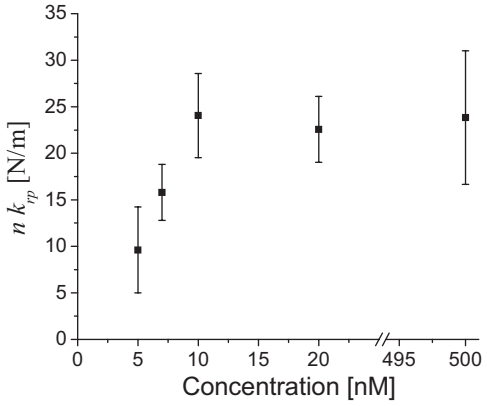

Figure 12. *Experimental stiffness of receptor-protein layers, $n \cdot k_{rp}$, in various m-antibiotin concentrations.*

CONCLUSIONS

We presented a new class of the protein *concentration* detector based on the mechanical stiffness measurement of protein-receptor layers in a squeezed nano-gap. Compared to the previous protein *size* detector based on the squeezed displacement measurement, we added the actuated nano-gap and reference electrodes. Thus, the present device compensated the distortion in the time-dependent squeezed displacement and reduced the displacement measurement uncertainty of ±7.4nm caused by signal drift and noise. We designed and fabricated the protein concentration detector using the electrothermal actuator and two nano-gaps with reference electrodes. In experimental study, we verified that the present protein detector measured the size of the proteins, streptaividin and m-antibiotin, as 12.1±2.3nm and 13.2±3.3nm at the measurement uncertainty of ±1.1nm, respectively, while showing the concentration detection sensitivity of 2.88N/m/nM in the m-antibiotin concentration range of 5~10nM.

ACKNOWLEDGEMENTS

This work has been supported by the National Creative Research Initiative Program of the Ministry of Science and Technology (MOST) under the project title of "Realization of Bio-Inspired Digital Nanoactuators."

REFERENCES

[1] S. Hanash, "Disease Proteomics," *Nature*, Vol.422 (2003), pp.226-232.
[2] W. C. Lee and Y.-H. Cho, "Nanomechanical Protein Detectors Using Electrothermal Nano-gap Actuators," *MEMS'04* (2004), pp.629-632.
[3] M. Lambrechts and W. Sansen, *Biosensors: Microelectrochemical Devices*, IOP Publishing Ltd., Philadelphia and New York, 1992.
[4] R.P. Ekins, "Ligand Assays: from Electrophoresis to Miniaturized Microarrays," *Clinical Chemistry*, Vol.44, No.9 (1998), pp.2015-2030.
[5] J. Homola, S.S. Yee and G. Gauglitz, "Surface Plasmon Resonance Sensors: Review," *Sensors and Actuators*, Vol.B54 (1999), pp.3-15.
[6] J. Fritz, M. K. Baller, H. P. Lang, H. Rothuizen, P. Vettiger, E. Meyer, H.-J. Güntherodt, Ch. Gerber, and J. K. Gimzewski, "Translating Biomolecular Recognition into Nanomechanics," *Science*, Vol.288, No.5464 (Apr. 14, 2000), pp.316-318.
[7] J. Zhang and E.S. Kim, "Vapor and Liquid Mass Sensing by Micromachined Acoustic Resonator," *Proc. 16th IEEE Inter. Conf. Micro Electro Mechanical Systems (MEMS 2003),* Kyoto Inter. Conference Hall, Kyoto, Japan (Jan. 19-23, 2003), pp.470-473.
[8] J. Rickert, A. Brecht and W. Gopel, "QCM Operation in Liquids: Constant Sensitivity during Formation of Extended Protein Multilayers by Affinity," *Analytical Chemistry*, Vol.69, No.7 (1997) pp.1441-1448.

A PIEZOELECTRICALLY ACTUATED CERAMIC-SI-GLASS MICROVALVE FOR DISTRIBUTED COOLING SYSTEMS

Jong M. Park[1], Ryan P. Taylor[2], Allan T. Evans[1], Tyler R. Brosten[2], Gregory F. Nellis[2], Sanford A. Klein[2], Jeffrey R. Feller[3], Louis Salerno[3], and Yogesh B. Gianchandani[1]
[1]Department of Electrical Engineering and Computer Science, University of Michigan, Ann Arbor
[2]Department of Mechanical Engineering, University of Wisconsin, Madison
[3]NASA Ames Research Center, Moffett Field, CA 94035

ABSTRACT

This paper describes a normally-open, self-encapsulated, valve for modulating refrigerant flow in a cryogenic cooling system. The valve consists of a micromachined die fabricated from a silicon-on-insulator wafer and a glass wafer, a commercially available piezoelectric stack actuator, and Macor ceramic encapsulation that has overall dimensions of 1×1×1 cm^3. A perimeter augmentation scheme for the valve seat has been implemented to provide high flow modulation. In tests performed at room temperature the flow was modulated from 980 mL/min. with the valve fully open (0 V), to 0 mL/min. with 60 V actuation voltage, at an inlet pressure of 55 kPa. Preliminary test results obtained at 80 K demonstrate that higher actuation voltages (≈ 120 V) are required to close the valve. However, it shows consistent modulation capability regardless of inlet pressure up to approximately 1 atm.

I. INTRODUCTION

Future space missions will require cooling of large systems such as optical assemblies or propellant depot stations with a high degree of temperature stability and small gradients. One solution is to create a distributed cooling network that uses actively controlled, micro-scale valves that are integrated with heat exchangers and sensors. More specifically, multiple cooling elements, each of which consists of actively controlled valves integrated with heat exchangers and temperature sensors, are positioned across the structure to be cooled. With each cooling element working independently in response to local sensors, temperature can be controlled efficiently. Figure 1 illustrates how each cooling element can be realized: (a) a flow of cryogenic fluid at the load temperature through exchangers positioned across the structure to be cooled, or (b) a flow of cryogenic fluid at a higher temperature and pressure through recuperative heat exchanger, taking advantage of Joule-Thompson refrigeration. Either way, having valves that work reliably at cryogenic temperatures with large flow modulation capability is essential. This paper reports the development and preliminary test results of piezoelectric valves fabricated from Si, glass, and ceramic.

II. DEVICE CONCEPTS AND OPERATION

The general approach utilized for this valve is to push a bulk Si micromachined plate against a glass substrate that has the inlet and outlet holes in it. Out-of-plane actuation was chosen to reduce the likelihood of friction between the actuated part and the substrate. The valve requires high forces to displace the Si against inlet pressure that can exceed 1 atm. for some cases. Piezoelectric actuation is attractive because it can provide high forces and consumes negligible DC power. Macor® (machinable glass ceramic) is chosen for encapsulation material because of low thermal expansion at low temperature. In addition, it is machinable, capable of holding tight tolerances, and exhibits no outgassing and zero porosity.

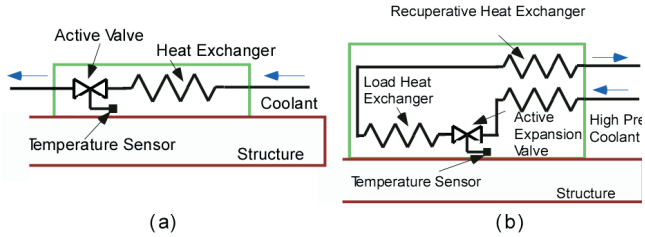

Fig. 1: Proposed application of actively controlled valve. Microvalves can (a) modulate flow of coolant in distributed heat exchangers, or (b) be used as expansion valves in Joule-Thompson cryocoolers.

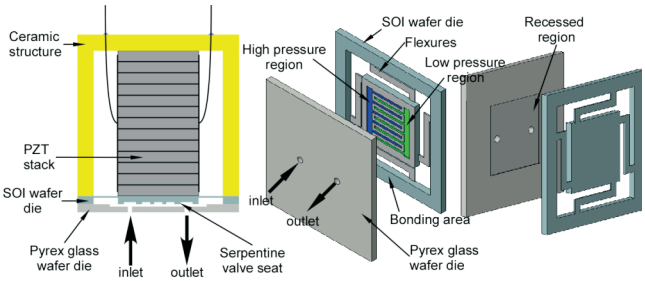

Fig. 2: Microvalve concepts: valve cross-section, ceramic-PZT-Si-glass structure is shown on the far left. Micro groove patterns to increase flow area are shown in the middle. The recessed glass along with the top view of Si piece is shown on the right.

Out-of-plane, stacked PZT actuation has been used widely in valves [1-4]. However, as each valve is constructed for different application, the performance goals are different. In our case, a normally open valve is desirable because the open condition is a safe failure mode, so that flow of the refrigerant is not blocked. For the same reason, an extremely tight seal is not essential. Instead, we need valves working at cryogenic temperatures, able to withstand several atm. of inlet pressure, and able to provide large flow modulation (0-1000 mL/min).

The main challenge comes from the small displacement of PZT actuation, leading to modest flow modulation. Furthermore, the piezoelectric coefficient of PZT is substantially degraded at cryogenic temperatures [5], further reducing the displacement. We overcame this limited displacement by using perimeter augmentation. The flow area for an out-of-plane valve (A_{valve}) is given by the product of the valve stroke (δ) and the perimeter of the valve seat (p).

$$A_{valve} = \delta \cdot p \quad (1)$$

Thus, by increasing the perimeter of the valve seat, flow area can be increased substantially, which results in large flow modulation. Serpentine grooves are fabricated on the valve plate (5×5 mm^2) as shown schematically in Fig. 2, so that the perimeter measures about 127 mm. Each groove measures 50 μm wide and 120 μm deep. The valve plate is suspended by four flexures of 500 μm

beam width. The valve has total foot print of 1×1 cm^2. (A picture of the grooves from fabricated device is shown in Fig. 6.)

III. DEVICE FABRICATION

To ensure control of material properties, the final device is comprised of only bulk materials; deposited thin films are not used for any structural layer, although they are used in intermediate steps. The fabrication process uses two wafers: a silicon-on-insulator (SOI) wafer which has device layer, buried oxide layer, and carrier wafer thicknesses of 50 μm, 0.5 μm, and 450 μm, respectively, and a 500 μm thick Pyrex glass wafer. The fabrication processes for SOI and glass wafers are illustrated in Fig. 3 and Fig. 4, respectively.

The use of the SOI wafer in the fabrication process permits the buried oxide layer to provide an etch stop for deep reactive ion etching (DRIE), while the epitaxial layer provides a well-controlled flexure thickness and bulk Si properties. The first DRIE process step etches down to the buried oxide layer from the top, and defines the flexure structures. Then the bottom side is patterned with Al and photoresist. The photoresist pattern acts as etch mask for the second DRIE step that is approximately 400 μm deep. Next, the photoresist is removed and Al is used as an etch mask for the final DRIE step, which engraves serpentine grooves for perimeter augmentation. The Al layer is then removed and the wafer is prepared for bonding.

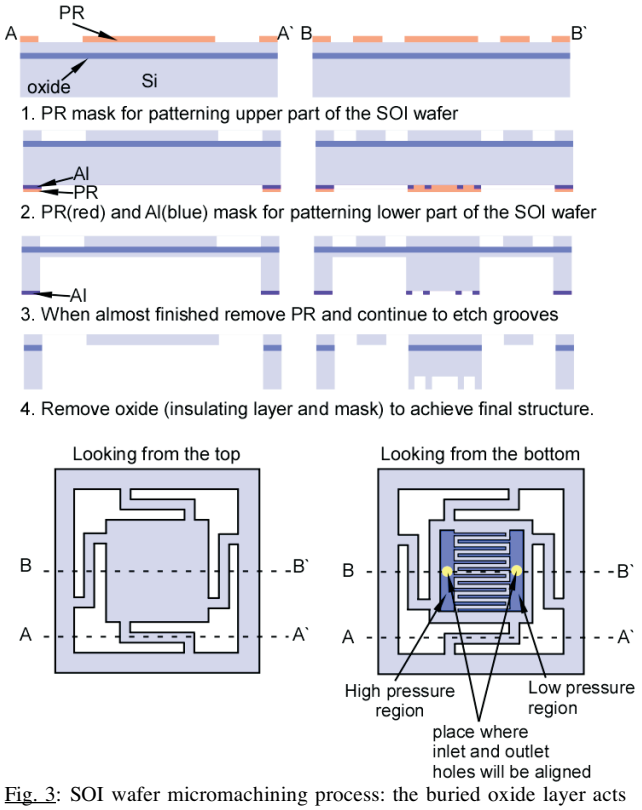

Fig. 3: SOI wafer micromachining process: the buried oxide layer acts as an etch stop for DRIE. A three step DRIE process is illustrated for the SOI wafer.

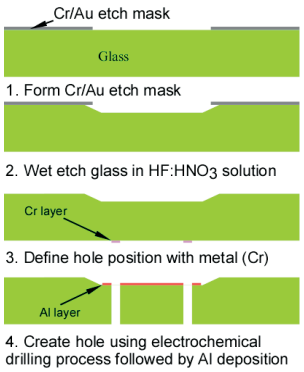

Fig. 4: Glass wafer micromachining process: A glass wafer undergoes a wet etch process and a electrochemical discharge machining process for inlet and outlet hole creation. Finally Al metal layer is deposited and patterned in preparation for anodic bonding to prevent bonding of the valve seat to the glass substrate.

A recess of 2 μm is wet etched into the glass wafer in order to accommodate the PZT displacement (Fig. 4). A thin Cr layer (100 nm) is patterned to define the position of inlet and outlet holes that are formed using electrochemical discharge machining (ECDM) [6]. ECDM of glass is a rapid, low cost method that provides a near-vertical profile and is suitable for hole formation. The procedure is performed in 40% NaOH solution at room temperature, and the glass is machined using approximately 300 μm diameter tungsten cathode and 37 V bias. After the holes are formed, the residual Cr layer is removed.

A thin layer of Al must be deposited into the glass recess to prevent inadvertent bonding of the valve seat to the glass substrate due to shallow recess depth and very compliant flexures. Anodic bonding is performed at 400˚C and 800 V, after which the Al layer on SOI wafer is dissolved. The bonded wafers are then diced and prepared for assembly with the ceramic structure and PZT.

The final step is to attach the PZT stack and ceramic cap by

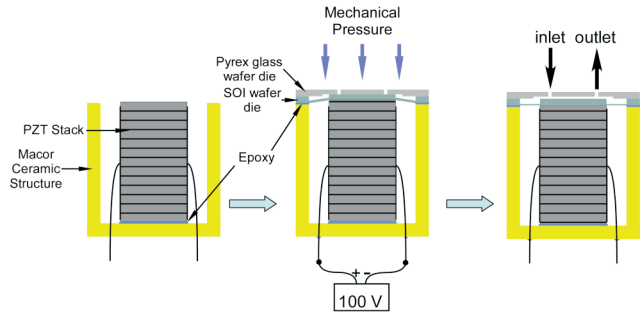

Fig. 5: Prestressed microvalve assembly procedure: (a) First, PZT stack is attached to the Macor ceramic structure using epoxy. (b) Then diced Si-glass die is bonded at the end of PZT and Macor structure by epoxy joint. During this procedure, the PZT stack is actuated until the epoxy is fully cured which results in a normally open valve (c).

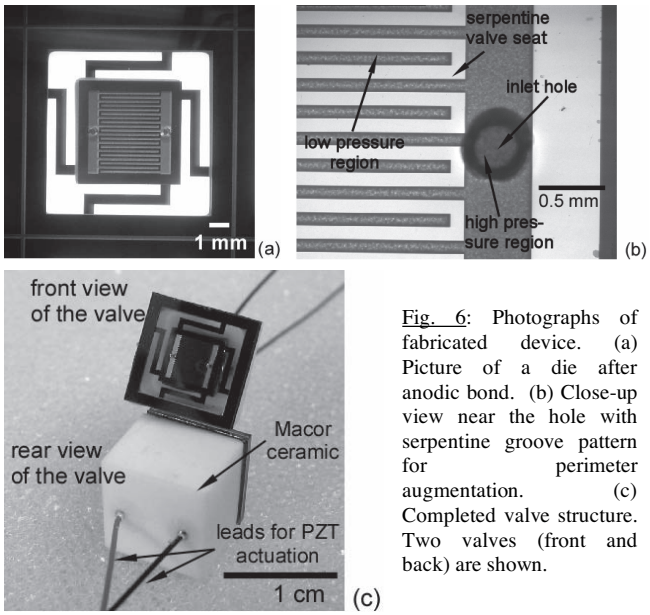

Fig. 6: Photographs of fabricated device. (a) Picture of a die after anodic bond. (b) Close-up view near the hole with serpentine groove pattern for perimeter augmentation. (c) Completed valve structure. Two valves (front and back) are shown.

epoxy. The first prototype valve that was tested in room temperature was assembled using regular Devcon 2-part epoxy. However, Devcon epoxy is only rated down to -40°C, so for cryogenic testing, Stycast 2850 FT epoxy is used. To create a normally-open valve, the PZT stack is energized at 100 V during the assembly process, so that it shortens after assembly (Fig. 5). Note that the PZT need not be bonded to the Si – this would accommodate variations in its height caused by expansion mismatch between the PZT and the Macor, and also relieve any stress on flexures caused by large temperature variation. The completed valve structure is pictured in Fig. 6. The valve has dimensions of 1×1×1cm^3.

IV. EXPERIMENTAL AND MODELING RESULTS

Preliminary tests were performed at room temperature with He gas flow. A schematic of the test is shown in Fig. 7. An in-line thermoplastic filter is placed upstream of the device to trap any particles or moisture. Pressure gauges are mounted so that inlet and outlet pressure can be monitored. Copper piping (6.35 mm ø) is connected to 0.4 mm holes in glass through an aluminum header. A ball valve is added at the end so that the outlet pressure can be controlled, if necessary.

In the first set of tests, the inlet pressure was regulated (21-55 kPa), and the outlet was maintained at atmosphere, while the flow rate was measured over 0-60 V actuation. As shown in Fig. 8, as actuation voltage increases, the PZT expands, the clearance between silicon valve seat and glass substrate decreases, thus flow rate decreases. With 55 kPa of inlet pressure, flow rate could be modulated from 0 to 980 mL/min. At 60 V, the valve leakage was below the measurement limit (< 0.1 mL/min.).

These test results were compared with prediction from numerical flow model (Fig. 9). The model used a combination of reduced Navier Stokes 2-d equations and empirical formulations. The flow through the grooves was simplified by assuming that the fluid is incompressible, laminar, constant viscosity, and hydrodynamically fully developed. In this limit, the pressure gradient in the groove is related to the local mass flow rate ($\dot{m}$) according to:

$$\frac{dp}{dx} = -\frac{K\mu per_g^2}{32\rho A_{c,g}^3}\dot{m} \tag{2}$$

where p is the local pressure, μ and ρ are the viscosity and density of the fluid, respectively, both of which are assumed to be constant, per_g and $A_{c,g}$ are the perimeter and cross-sectional area of the groove. The parameter K is a constant that depends on the groove aspect ratio. Flow through the land region was assumed to be governed by a reduced form of the 2-d Navier Stokes equations shown in Eqn. (3).

$$\frac{\partial u_m}{\partial x} + \frac{\partial v_m}{\partial y} = 0 \tag{3}$$

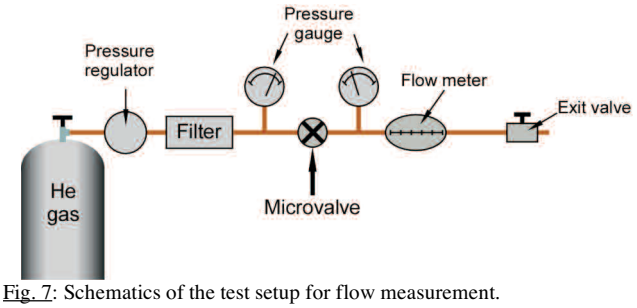

Fig. 7: Schematics of the test setup for flow measurement.

where u_m and v_m are the average local x and y velocities through the land, related to the pressure gradient by:

$$u_m = -\frac{h^2}{12\mu}\frac{\partial p}{\partial x} \tag{4}$$

$$v_m = -\frac{h^2}{12\mu}\frac{\partial p}{\partial y} \tag{5}$$

where h is the valve seat clearance. The above set of equations were discretized in a single land and groove then solved using sparse matrix decomposition in the Matlab© environment. The results of the model were characterized using a set of non-dimensional numbers governing the flow through a single land and groove. Using the derived non-dimensional relations, a second full valve model was developed and implemented using Engineering Equation Solver (EES) in order to determine the simulated flow rate.

The Fig. 9 was obtained by assuming that the hole diameters for inlet and outlet are 350 μm and displacement of PZT at 60V is 4 μm. In addition, a linear relationship between PZT displacement and voltage was assumed. Thus, seat clearance from the glass substrate can be expressed as in Eqn. (6).

$$Clearance\ (\mu m) = 4 - Voltage(\mathrm{V}) \cdot 0.067 \tag{6}$$

The flow rates from the model tend to fall slightly faster than the experimental results, but in general they match reasonably well. The main discrepancy comes from uncertainties in seat clearance and inaccurate inlet and outlet hole size used in the model. Compressibility of He gas and hysteretic behavior of PZT also contribute to the difference between the model and experimental data.

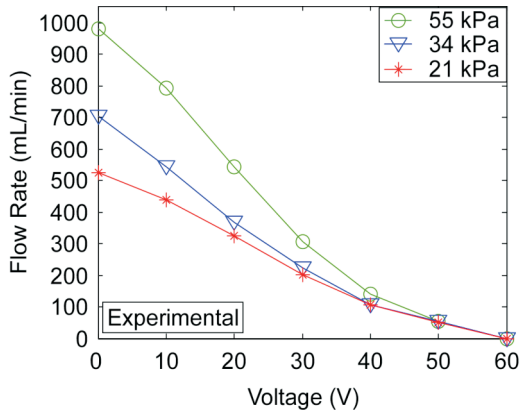

Fig. 8: Flow rates as a function of voltage are plotted. As the actuation voltage increases, the valve is closed which results in a decrease in flow rate.

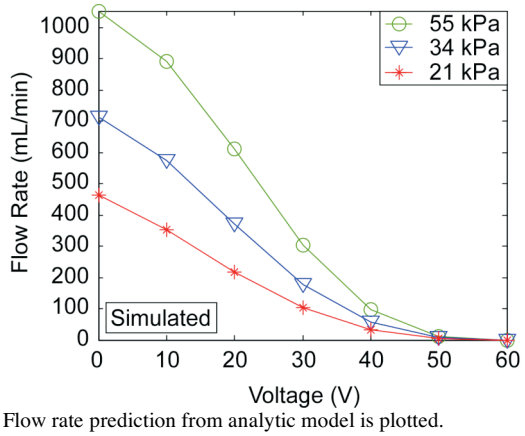

Fig. 9: Flow rate prediction from analytic model is plotted.

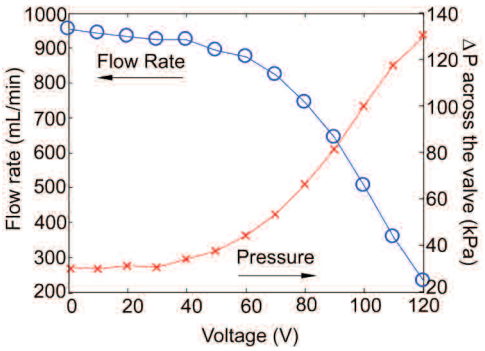

Fig. 10: Flow rate and inlet to outlet pressure differential as the valve with an inlet pressure of 145 kPa goes from being wide open (0V) to completely closed (120V).

In a separate experiment, a pressure drop across the valve was recorded along with the flow rate as the actuation voltage was varied from 0 to 120 V (Fig. 10). At 145 kPa inlet pressure, 28 kPa pressure drop across the valve was obtained by partially closing the exit valve, and flow rate of 950 mL/min. was recorded. As the actuation voltage was increased, the valve restricted more flow while sustaining larger pressure drop across the valve. At 120V, it sustained a pressure drop of 130 kPa.

In order to verify the operations of the valve at cryogenic temperatures, another set of experiment was performed near liquid nitrogen temperature (80 K). (For this valve Stycast epoxy was used, and the PZT was not bonded to the Si valve plate.) The test setup is schematically shown in Fig. 11. The He gas was cooled by passing it through liquid nitrogen heat exchanger. Inlet and outlet pressure were monitored. In addition, thermocouples were used to probe inlet and outlet gas temperature. The gas was then passed through another heat exchanger to bring it back to room temperature and exhausted to atmosphere, while the flow rate was measured. The valve performance is shown in Fig. 12 for inlet pressures 35 kPa, 70 kPa, and 104 kPa. Compared to the room temperature results, higher voltages were needed to completely close the valve. This is likely the result of degraded piezoelectric coefficient at cryogenic temperatures [5]. The normalized flow rate (NFR) is presented in Fig. 13. This is defined as:

$$NFR = \frac{flow\ rate\ at\ corresponding\ voltage}{flow\ rate\ at\ 0V} \qquad (7)$$

In Fig. 13, the three curves obtained at different inlet pressures look very similar to each other. This illustrates consistent modulation of the valve over the range of inlet pressures tested.

V. CONCLUSIONS

This effort has resulted in the successful fabrication of a piezoelectrically actuated ceramic-Si-glass microvalve for distributed cooling application. A perimeter augmentation scheme was used to overcome limited displacement of PZT and provide large flow modulation. At room temperature, flow rate of 980 mL/min. was measure with inlet pressure of 55 kPa. At cryogenic temperatures, it required higher voltage to completely close the valve due to degraded piezoelectric coefficient, but it showed consistent modulation capability.

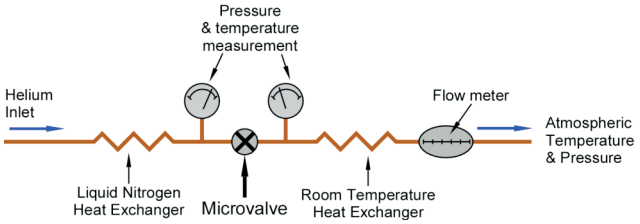

Fig. 11: Schematics of the test setup for cryogenic flow measurement.

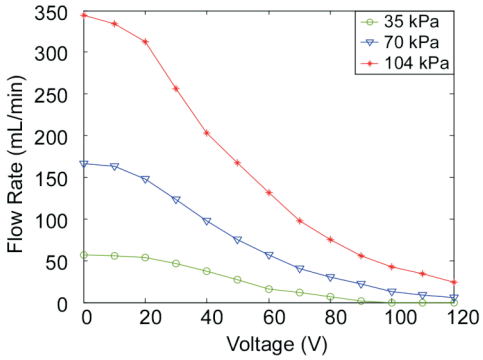

Fig. 12: Flow rates as a function of voltage at cryogenic temperature.

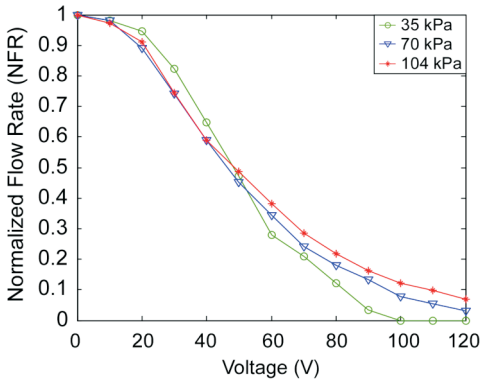

Fig. 13: Normalized flow rate vs. actuation voltage obtained at cryogenic temperature.

ACKNOWLEDGEMENTS

The authors are grateful to the Michigan Nanofabrication Facility at the University of Michigan. The authors also appreciate Daniel Hoch at University of Wisconsin for valuable discussion. This work is supported primarily by NASA under award NNA05CP85G.

REFERENCES

[1] I. Chakraborty, W.C. Tang, D.P. Bame, T.K. Tang, "MEMS Micro-valve for Space Applications," *Sensors and Actuators*, V. 83, pp. 188-193, 2000

[2] M. Esashi, S. Shoji, A. Nakano, "Normally Closed Microvalve and Micropump Fabricated on a Silicon Wafer," *Sensors and Actutors*, V. 20, pp. 163-169, 1989

[3] S. Shoji, B. Schoot, N. Rooij, M. Esashi, "Smallest Dead Volume Microvalves for Integrated Chemical Analyzing Systems," *Transducers '91*, pp. 1052-1055, 1991

[4] C. Lee, E.H. Yang, "A Piezoelectric Liquid-Compatible Microvalve for Integrated Micropropulsion," *Technical Digest of the 2004 Solid-State Sensor and Actuator Workshop*, Hilton Head Isl., SC, 6/6-10/04, pp. 160-163, 2004

[5] R.P. Taylor, G.F. Nellis, S.A. Klein, D.W. Hoch, J. Fellers, P. Roach, J.M. Park, Y. Gianchandani, "Measurements of the Material Properties of a Laminated Piezoelectric Stack at Cryogenic Temperatures," *International Cryogenic Materials Conference*, 2005, in press.

[6] V. Fascio, R. Wuthrich, D. Viquerat, H. Langen, "3D Microstructuring of Glass Using Electrochemical Discharge Machining (ECDM)," *International Symposium on Micromechatronics and Human Science*, pp. 179-183, 1999

A RESONANT SISO SENSOR BASED ON A COUPLED ARRAY OF MICROELECTROMECHANICAL OSCILLATORS

Barry E. DeMartini[1], Jeffrey F. Rhoads[2], Steven W. Shaw[2], and Kimberly L. Turner[1]
[1]Department of Mechanical and Environmental Engineering, University of California – Santa Barbara
Santa Barbara, California USA
[2]Department of Mechanical Engineering, Michigan State University
East Lansing, Michigan USA

ABSTRACT

This work details the preliminary development and testing of a novel, single input – single output (SISO) resonant microsensor, which exploits vibration localization in a coupled-oscillator architecture to allow for the detection of multiple analytes with a single platform. The work includes a brief description of a preliminary sensor design and its operating principles, an outline of a lumped mass analog that proves convenient for analysis and predictive design, and preliminary experimental results, recently obtained from a first-generation device, which verify the sensor's feasibility.

INTRODUCTION

Chemical and biological sensors based on microresonators are considered viable alternatives to modern sensing systems since they consume less power and space than their macroscale counterparts **[1-3]**. Traditionally, these systems track resonance shifts in essentially single-degree-of-freedom oscillators induced by mass or stiffness changes. As these changes are caused by local bonding, stress stiffening, or a similar chemical-mechanical process, the resonance shifts, in turn, indicate the presence of a given analyte. Existing sensors require the measurement of the response of an individual resonator for the detection of a specific compound, or a class of compounds. Large sensor arrays composed of isolated microresonators can be used to broaden detection capabilities **[4]**, but the addition of the attendant electronics (arising from a larger number of system outputs) adds to the complexity of such sensors.

The present work introduces a sensor design that is intended to couple the inherent benefits of a sensor array with those of a SISO system. The system is realized by coupling an array of simple microbeam resonators with slightly different natural frequencies to a common shuttle mass, which is used for both actuation and sensing (see Fig. 1). The benefit of this architecture is that, due to vibration localization in the set of mistuned beams and their coupling to the shuttle mass, frequency shifts of any of the individual oscillators can be tracked through the response of the shuttle mass **[5]**. This, in turn, allows for the detection and identification of multiple analytes with a single platform.

The next section provides a brief description of a representative sensor, the formulation of a lumped mass model, and an analysis of the system response. This is followed by a description of the results obtained from a preliminary experimental investigation. The paper concludes with a brief discussion of design and integration issues and a summary of planned work.

THEORY

Though the sensor described herein can be implemented in a variety of geometrical forms, the translational design depicted in Fig. 1 was selected as the focus of this work. This relatively simple sensor geometry consists of a shuttle mass (SM) that is connected to ground by folded beam supports (S) and excited by interdigitated electrostatic comb drives (CD). Attached to the shuttle mass are four microbeams (M), each of slightly different length to allow for ample separation of the system's natural frequencies.

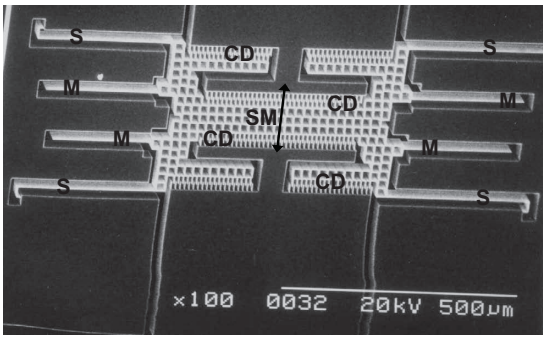

Figure 1. *A scanning electron micrograph of the sensor. The device's shuttle mass is labeled SM, the individual microbeams M, the electrostatic comb drives CD, and the folded beam supports S. The dominant direction of motion is indicated by the arrow.*

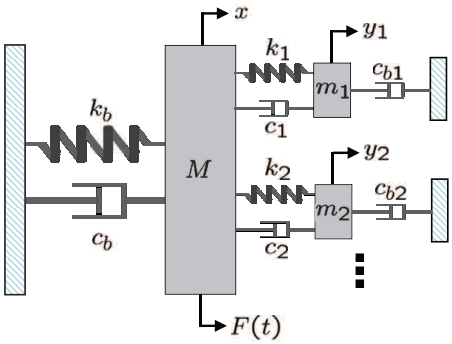

Figure 2. *Mass-spring-dashpot analog of the sensor depicted in Fig. 1. Note that the comparatively larger mass M is used to represent the shuttle mass and the smaller masses m_i represent the microbeams.*

For ease of analysis it proves convenient to represent the device depicted in Fig. 1 as an equivalent mass-spring-dashpot system, as depicted in Fig. 2, where the shuttle mass is represented by mass M and the microbeams by the smaller masses m_1, m_2, etc. From this linear analog the system's equations of motion are easily determined to be

$$M\ddot{x} + \sum_i m_i\left(\ddot{x} + \ddot{z}_i\right) + \sum_i c_{bi}\left(\dot{x} + \dot{z}_i\right) + c_b\dot{x} + k_b x = F(t) \tag{1}$$

$$m_i\left(\ddot{x} + \ddot{z}_i\right) + c_{bi}\left(\dot{x} + \dot{z}_i\right) + c_i\dot{z}_i + k_i z_i = 0, \qquad i = 1,\ldots,N \tag{2}$$

where z_i is the relative displacement of the ith subsystem given by

$$z_i = y_i - x, \qquad i = 1,\ldots,N, \tag{3}$$

c_b, c_i, and c_{bi} represent equivalent linear damping coefficients arising from various dissipation effects, and $F(t)$ represents the applied electrostatic force generated by the comb drives. Assuming harmonic voltage excitation and ample device thickness, $F(t)$ can be approximated by

$$F(t) = \frac{\varepsilon_0 n h V_A^2}{2g}\left(1 + \cos 2\omega t\right), \tag{4}$$

where ε_0 represents the free space permittivity, n the number of comb fingers, g the gap between adjacent comb fingers, h the device thickness, and V_A the amplitude of the applied AC voltage. Nondimensionalizing Eqs. (1) and (2) and redefining by translation the dynamic variable x to remove the explicit appearance of a DC equilibrium shift (see Eq. 4), allows the equations of motion to be compiled into a standard matrix form given by

$$MX'' + CX' + KX = \Gamma(\tau), \tag{5}$$

where X represents the compiled state vector, M the effective mass matrix (incorporating inertial coupling terms), C the effective damping matrix (incorporating dissipative coupling terms), K the effective stiffness matrix, and $\Gamma(\tau)$ the effective forcing vector, which is sparse except for the first element. The sensor's response can be determined using this matrix equation through a number of standard techniques (e.g., the impedance approach adopted in **[6]**).

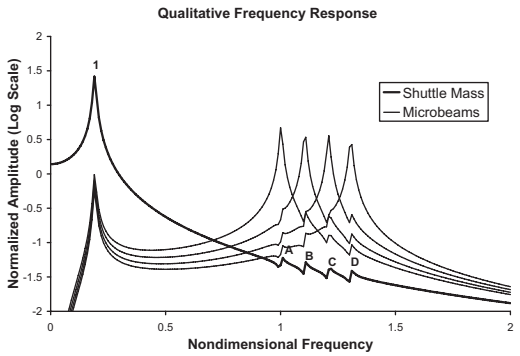

Figure 3. *Qualitative frequency response for the sensor. Note that the labeled resonances correspond to the following modes: (1) A translational in-plane mode, (A, B, C, and D) modes where energy is localized in one of the system's microbeams.*

A desirable form of the system frequency response, recovered using an approach similar to that outlined in **[6],** is shown in Fig. 3. As evident, the shuttle mass' response features a dominant low-frequency resonance, labeled (1), corresponding to a bulk, in-plane translational mode, and four comparatively higher-frequency (and lower-amplitude) resonances, labeled (A), (B), (C), and (D), corresponding to in-plane modes where the system's energy is largely confined to, that is, localized in, a single microbeam (as evident from the relative resonant amplitudes of the microbeams). Sweeping the system's excitation frequency through the region that contains resonances (A), (B), (C), and (D) allows for the detection of resonance shifts, induced by mass and/or stiffness changes in any of the individual microbeams, using solely the measured response of the shuttle mass.

As noted above, the qualitative frequency response shown in Fig. 3 depicts a desirable form of the system's frequency response. This, however, is not the qualitative response that is recovered for arbitrarily selected system parameters. To recover the response shown in Fig. 3, and thus to ensure proper sensor operation, system parameters must be carefully selected. Due to the relative simplicity of the sensor geometry presented herein, the only system parameters pertinent for design are the system inertia ratios (defined as the ratio between a given microbeam's effective modal mass and that of the shuttle), the system frequency ratios (defined as the ratio between the fundamental natural frequency of a given isolated microbeam and the first natural frequency of the shuttle mass), and the amplitude of the AC voltage excitation applied to the electrostatic comb drives. This driving amplitude is used primarily to control the amplitude of the shuttle mass response, so that the resonance peaks of interest are measurable, and the system response remains linear.

Selection of the frequency ratios is used primarily to ensure ample separation between resonances (A), (B), (C), and (D) and all other system resonances, including those related to both in-plane and out-of-plane modes. If these four resonances are placed too close to the resonance corresponding to the bulk, in-plane mode they become saturated and shifts in a given resonance become difficult to detect. Similarly, if the resonances are too close to a resonance corresponding to an out-of-plane mode, the resonant amplitudes decrease and it becomes quite difficult to detect resonance shifts using solely the shuttle mass' amplitude response. There must also be ample separation between each of the four resonances, as placing the resonances too close to one another leads to the elimination of the distinct resonance peaks, and thus undermines detection.

Selection of the inertia ratios is used primarily to manipulate the coupling strength, and thus, is used in conjunction with the frequency ratios, to control the extent of localization in the microbeams **[7]**. For sensing, sufficient localization is essential for the identification of the source of a resonance shift. Since the microbeams are coupled to the shuttle mass, mass or stiffness changes in a single oscillator induce shifts in all of the coupled system natural frequencies. However, if the response of the microbeams is sufficiently localized, mass or stiffness changes in a single oscillator induce markedly larger shifts in the resonance associated with that particular oscillator. This allows for not only the detection of resonance shifts using the shuttle mass response, but also the identification of the source of the resonance shift (in this case, the specific microbeam that induced it). By providing selective surface chemistry on the microbeams this should allow for rapid, and potentially automated, identification of a target analyte or group of analytes.

EXPERIMENTAL RESULTS

The device depicted in Fig. 1 was fabricated using a standard SOI process flow. In order to validate the feasibility of the sensor design, mass detection was simulated by comparing the response of the shuttle mass before and after the deposition of a small amount of mass on the shortest (highest frequency) microbeam. The device was placed in partial vacuum and the shuttle mass frequency response was obtained through the use of a laser vibrometer **[8]**. As shown in Fig. 4, the sensor exhibited a baseline frequency response qualitatively compatible with that predicted in Fig. 3, which was produced using approximate system parameters. In particular, the experimental frequency response displayed the predicted low-frequency resonance (1) corresponding to the bulk, in-plane mode, two resonances (2, 3) corresponding to out-of-

plane modes, and four predicted higher-frequency resonances (A, B, C, and D) corresponding to the localized microbeam modes. The localized nature of these vibration modes was verified using a stroboscopic in-plane measurement system and video imaging. While the resonances corresponding to the out-of-plane modes (2, 3) were not predicted using the lumped mass model developed in the previous section, which describes only in-plane modes, it is worth noting that these resonances had been predicted by modal simulations performed using a commercial finite element package. Additionally, the separation between resonance (3) and (A) was smaller than desired, and may render resonance (A) as not useful for sensing (These issues can be easily addressed in future designs.).

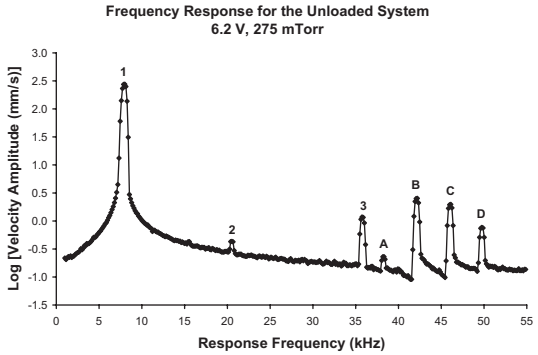

Figure 4. *Experimentally-obtained frequency response for the sensor actuated with a 6.2 V AC signal in 275 mTorr pressure. Note that the labeled resonances correspond to the following modes: (1) Bulk in-plane mode, (2, 3) out-of-plane modes, (A, B, C, and D) modes where energy is localized in one of the system's microbeams.*

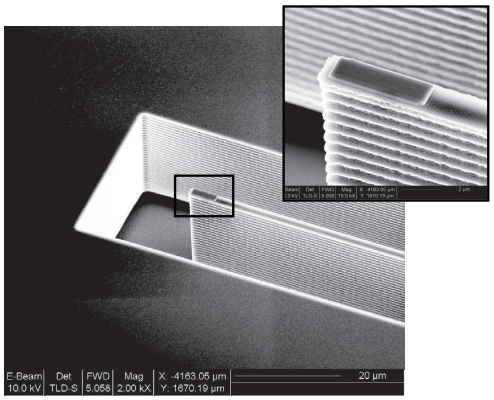

Figure 5. *A scanning electron micrograph of the platinum patch added to the shortest microbeam. The inset, which was used for measurement purposes, shows a closer view. The patch is approximately 1.57 x 5.10 x 0.22 µm in size and has a mass of about 38 pg.*

Once the baseline frequency response was obtained, a Focused Ion Beam (FIB) was used to deposit a 1.57 x 5.10 x 0.22 µm platinum patch on the desired microbeam, as shown in Fig. 5. This resulted in an approximate mass change, computed by volume, of 38 pg. The frequency response diagrams obtained for the sensor shuttle mass with and without the platinum mass addition are shown in Figs. 6-8. As predicted, the mass addition induced shifts in all of the system's resonances. However, due to vibration localization, the shift in resonance (D) was about 40 times that of the other peaks. Specifically, resonance (D) shifted by approximately 124 Hz as compared to the next largest resonance shift, which occurred in resonance (C), which was approximately 3 Hz (see Figs. 6-8). This indicates an experimental mass resolution of approximately 3.3 Hz/pg a value comparable to alternative multi-analyte sensor designs **[4]**.

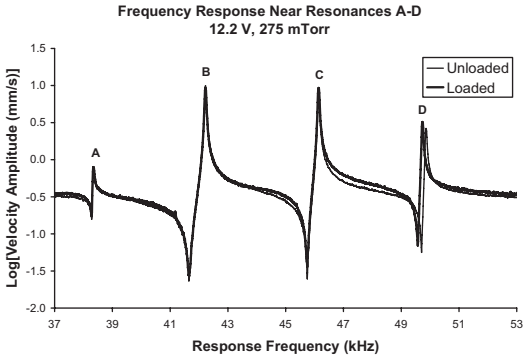

Figure 6. *Experimentally-obtained frequency response for the sensor actuated with a 12.2 V AC signal in 275 mTorr pressure. Note that the added-mass loading introduces resonance shifts, the largest of which occurs in resonance (D), which corresponds to the localized mode of the corresponding beam. Here, and in Figs. 7 and 8, individual data points have been removed for clarity.*

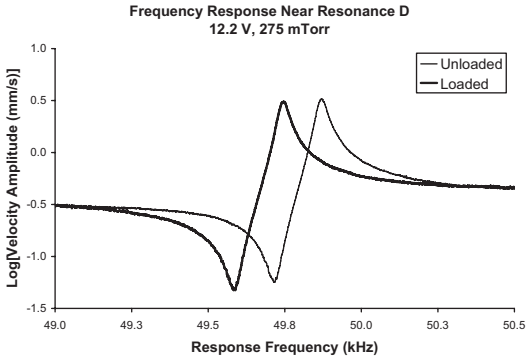

Figure 7. *Experimentally-obtained frequency response near resonance (D) for the sensor actuated with a 12.2 V AC signal in 275 mTorr pressure. Note that mass loading introduces a resonance shift of 124 Hz.*

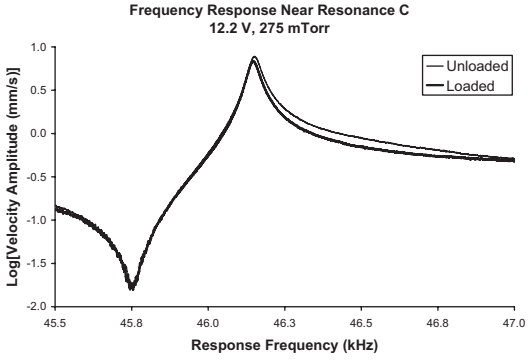

Figure 8. *Experimentally-obtained frequency response near resonance (C) for the sensor actuated with a 12.2 V AC signal in 275 mTorr pressure. Note that mass loading introduces a resonance shift of about 3 Hz.*

DESIGN AND INTEGRATION

While the preceding sections include brief descriptions of some of the issues that must be considered in the course of sensor development, it is important to briefly discuss a few others relating to both design and integration. Foremost amongst these are sensor metrics, in particular, mass resolution. The sensor described herein was designed with proof of concept and not maximum metrics in mind. A mass resolution of approximately 3.3 Hz/pg was measured, and while this value compares favorably to other reported values for multi-analyte resonant sensors **[4]**, it is less than those reported for sensors based on isolated microresonators **[2]**. Device scaling will help to improve mass resolution, but physical sensing limits and the fact that shifts in the shuttle mass frequency response are measured, rather than shifts in isolated microbeam resonances, dictate that the maximum attainable mass resolution will generally be less than those of its uncoupled counterparts **[9, 10]**.

Another important issue to be considered in the course of development is the method of response measurement. In this preliminary study measurement was a secondary concern, as it had been predetermined that a laser vibrometer would be employed to obtain the system frequency response. The electrostatic comb banks that were included in the original device design could be used in conjunction with an external or integrated circuit for measurement purposes, but the effective capacitance change the drives yield near resonance (approximately 0.4 fF) is not of sufficient magnitude, even if increased slightly by drive reconfiguration, to be measured with a high degree of accuracy. As such, future designs would likely benefit from the inclusion of piezoelectric or magnetomotive drive and/or sensing mechanisms, as the voltage signals induced from material strain or emf effects should be easier to measure using standard external or integrated circuitry.

Another issue that must be considered in the course of design and development is the actual sensor environment. As detailed in the preceding section, all of the experimental results described herein were obtained for a device in partial vacuum. This was done since the resonances were not sufficiently prominent at 1 atm, due to the small Q values associated with the resonance peaks of interest. While a low pressure environment may be suitable for some sensing activities, the vast majority will require that the device operate in ambient pressure conditions. Geometrical reconfiguration of the in-plane device and device scaling may well be sufficient to allow for this, as fluid pumping between the microbeams and the sidewalls of the substrate is believed to be a large source of dissipation in the present design. Alternative geometries (e.g. in-plane torsional geometries) and phase response analysis, two issues currently being explored, may also aid sensing at 1 atm.

CONCLUSION

This work details a novel, single input – single output (SISO) resonant microsensor that exploits vibration localization in a coupled array of microbeams to allow for the detection of multiple analytes with a single device. It was shown that a linear lumped mass model for the sensor proves sufficient for both analysis and predictive design. A preliminary device design based on these ideas was fabricated and tested using a simulated added mass. The device was experimentally determined to have a mass resolution of approximately 3.3 Hz/pg, a value comparable to those reported for other multi-analyte resonant microsensors, yet less than those values reported for sensors based on isolated microresonators. While the results of this preliminary study are believed to be a positive indication of the sensor's feasibility, a number of issues still must be considered, most notably, improving the sensor mass resolution, introducing a more robust measurement method, integrating the sensor with a circuit capable of measuring shifts in each of the shuttle mass resonances, and determining configurations that result in higher Q values. These issues, along with a number of others pertinent to development, are currently under consideration.

ACKNOWLEDGEMENTS

This work was graciously supported by the National Science Foundation under contract NSF-ECS-0428916.

REFERENCES

[1] J. R. Vig, R. L. Filler, and Y. Kim, "Chemical Sensor Based on Quartz Microresonators", *Journal of Microelectromechanical Systems, 5,* 138 (1996).

[2] B. Ilic, D. Czaplewski, M. Zalalutdinov, H. G. Craighead, P. Neuzil, C. Campagnolo, C. Batt, "Single Cell Detection with Micromechanical Oscillators", *Journal of Vacuum Science and Technology B, 19,* 2825 (2001).

[3] T. Thundat, P. I. Oden, and R. J. Warmack, "Microcantilever Sensors", *Microscale Thermophysical Engineering, 1,* 185 (1997).

[4] H. P. Lang, M. Hegner, and C. Gerber, "Cantilever Array Sensors", *Materials Today, 8,* 30 (2005).

[5] A. Alsuwaiyan and S. W. Shaw, "Localization of Free Vibration Modes in Systems of Nearly Identical Vibration Absorbers", *Journal of Sound and Vibration, 228,* 703 (1999).

[6] L. Meirovitch, *Elements of Vibration Analysis* (1986).

[7] C. Pierre and E. H. Dowell, "Localization of Vibrations by Structural Irregularity", *Journal of Sound and Vibration, 114,* 549 (1987).

[8] K. L. Turner, P. G. Hartwell, and N. C. MacDonald, "Multi-Dimensional MEMS Motion Characterization Using Laser Vibrometry", *Proceedings of Transducers '99: The 10th International Conference on Solid State Sensors and Actuators,* Sendai, Japan, 6/7-10/99 (1999), pp. 1144-1147.

[9] G. Abadal, Z. J. Davis, B. Helbo, X. Borrise, R. Ruiz, A. Boisen, F. Campabadal, J. Esteve, E. Figueras, F. Perez-Murano, and N. Barniol, "Electromechanical Model of a Resonating Nano-Cantilever-Based Sensor for High-Resolution and High-Sensitivity Mass Detection", *Nanotechnology, 12,* 100 (2001).

[10] K. L. Ekinci, Y. T. Tang, and M. L. Roukes, "Ultimate Limits to Inertial Mass Sensing Based Upon Nanoelectro-mechanical Systems", *Journal of Applied Physics, 95,* 2682 (2004).

A VARIABLE FOCUS MICROLENS USING EWOD ON A TAPERED SU-8 STRUCTURE

Yuan-Jen Chang, and Victor M. Bright
Department of Mechanical Engineering, University of Colorado
Boulder, CO, USA

Ethan Schonbrun
Department of Electrical and Computer Engineering
University of Colorado
Boulder, CO USA

Kamran Mohseni
Department of Aerospace Engineering Science
University of Colorado
Boulder, CO USA

ABSTRACT

Electrowetting on dielectric is a promising technology for variable focus liquid microlens. When an electrical field is applied across a liquid droplet and a dielectric layer, the contact angle of the liquid can be tuned with different applied voltages. Therefore, the focal length of a microlens would vary by simply applying an electrical field without any moving mechanical components. In this paper, we demonstrate that the dielectric structure of the lens can be made of SU-8. The tapered SU-8 structure, obtained by UV overexposure, confines the droplet and provides the droplet-centering mechanism. SU-8 has high dielectric constant and is suitable as a dielectric layer in electrowetting. The measured contact angle change of the water droplet matches the Lippmann-Young equation. It is shown that by choosing two similar-density liquids, the effect of gravity and mechanical vibration can be minimized. The working microlens is demonstrated using the images of numbers and laser beam focusing.

INTRODUCTION

Tunable microlenses, with variable focal length, have attracted significant interest in optical and biomedical applications [**1-6**]. Such microlenses do not require any mechanical moving parts. An attractive technology for tunable microlenses is Electrowetting on Dielectric (EWOD). In EWOD, the surface energy of a liquid droplet on a dielectric layer is modified by application of an electric field. Consequently, the droplet's contact angle can change, which results in droplet shape change, and therefore change of focal length. Microlenses using EWOD with metal or glass structure have been applied in the design of miniaturized optical systems, such as mini-cameras for portable electronic devices [**7-9**]. However, such technologies are not easily integrated into microsystems. Electrowetting microlenses have also been microfabricated on silicon substrates [**10**]. Due to the square shape of etched silicon holes, however, the optical performance of such microlenses is limited.

SU-8 is a photosensitive material commonly used to form thick, high aspect ratio polymeric microstructures with vertical sidewalls. Due to the thickness of a SU-8 layer, the exposure dosages are different at the top and at the bottom of the layer [**11**]. A SU-8 structure with a smooth sidewall at a certain angle can be achieved by UV overexposure. Since SU-8 is an epoxy-based negative-tone photoresist, the hole developed after exposure tends to be smaller at the top than at the bottom. SU-8 has favorable mechanical properties, high thermal stability, and high dielectric constant. Therefore, SU-8 is not only suitable as the structure but also as a dielectric material in the liquid lens using EWOD.

In this paper, we demonstrate a variable focus microlens consisting of two immiscible liquids on a tapered SU-8 structure. The densities of the liquids are chosen to be close to each other. The light-weight, tapered SU-8 structure provides the confining and centering mechanism for the liquids. We use images of numbers positioned under the microlens and the focusing of a laser beam at different applied voltages to demonstrate operation of the microlens.

PRINCIPLE OF OPERATION

The contact angle of a liquid droplet on a planar solid substrate can be expressed by Young's equation:

$$\gamma_{LG}\cos(\theta) = \gamma_{SG} - \gamma_{SL}, \tag{1}$$

where γ denotes the interfacial energy between two media, S denotes the substrate, L denotes the droplet, and G denotes the surrounding medium. θ is the contact angle of the droplet on the substrate.

The relationship between the applied voltage and the surface tension of a droplet on a dielectric surface can be expressed by the Lippmann equation,

$$\gamma_{SL} = \gamma_0 - \frac{1}{2}\frac{\varepsilon\varepsilon_0}{d}V^2, \tag{2}$$

where γ_0 is the surface tension of the solid-liquid surface interface at zero voltage, ε and ε_0 are the permittivities of the dielectric layer and vacuum respectively, d is the thickness of dielectric layer, and V is the voltage applied across the dielectric layer. Consequently, Young's equation is extended, resulting in the Lippmann-Young equation where the contact angle change is then given by

$$\cos(\theta) = \cos(\theta_0) - \frac{\varepsilon\varepsilon_0}{\gamma_{LG}d}V^2. \tag{3}$$

The contact angle of a droplet without application of a voltage is given by θ_0. From the Lippmann-Young equation, it is obvious that a lower voltage is needed to change contact angle with a thinner dielectric layer. It should be noted that the saturation of contact angle is not considered in the equations.

CHARACTERIZATION OF SU-8 LAYER

SU-8 (2000 series, Microchem Corp., USA) is an epoxy-based photoresist suitable for making high aspect ratio structures and is a dielectric material. We test the dielectric properties of SU-8 by measuring the contact angle of a water droplet. First, a 5μm thick SU-8 layer is spin-coated on a gold-plated substrate. After pre-baking at 65°C and 95°C for one minute each, UV

exposure is performed for 50 seconds (3.0 mW/cm^2 at 365nm). Then the SU-8 layer is post-baked on a hotplate at 65°C and 95°C for one minute each and cooled down on the hotplate to room temperature. A 300nm thick Teflon layer (AF1601S, Dupont) is coated on top of the SU-8 by spinning and serves as a hydrophobic layer. A drop (~ 5μL) of de-ionized (DI) water (resisitivity ~ 17 MΩ-cm) is placed on the hydrophobic surface. A DC voltage is applied with micro-probes between the bottom gold electrode and the liquid. Figure 1.(a) shows the water contact angle without the application of voltage, while Figure 1.(b) shows the change of contact angle at 140 V.

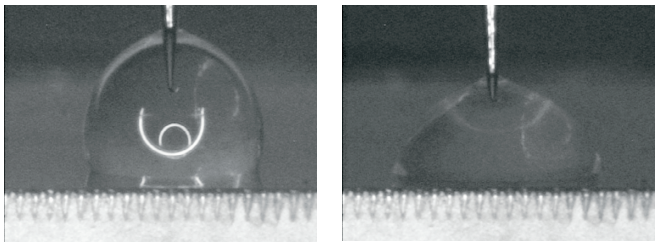

(a) *0 V* ***(b)*** *140 V*

Figure 1. *Change of the contact angle of water on SU-8 substrate.*

The contact angle is measured by taking a picture of the droplet using a CCD camera through a microscope. The initial contact angle of 115° with 0 V is measured. Figure 2 shows the contact angle change with various applied voltages. Saturation of contact angle is observed after 160 V, which is not shown in Figure 2. The dielectric constants of SU-8 and Teflon used in the calculation are 3 and 1.9, respectively. The solid line is the theoretical calculation based on the Lippmann-Young Equation. The black dots are the experimental measurements. SU-8 photoresist is a defect-free dielectric material layer.

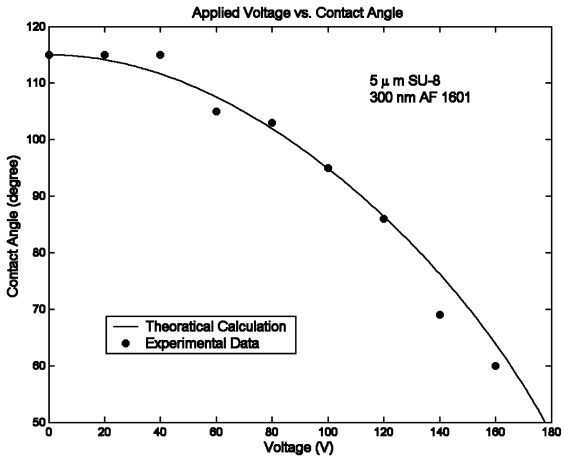

Figure 2. *Voltage vs. Contact angle*

DESIGN OF MICROLENS

The schematic view of the variable focus lens is illustrated in Figure 3. The SU-8 structure is patterned on a glass substrate to form the cavity of the microlens. The angular sidewall provides the drop-centering confining mechanism to keep the optical axis in position. Meanwhile, the angular sidewall is needed for the follow-on metal deposition and spin-coating steps. The metal layer is deposited on top of the SU-8 structure as an electrode in EWOD. The metal on the bottom of the glass is removed to open a window for light to pass through. Another SU-8 and Teflon layer are spin-coated as the dielectric and hydrophobic layer for EWOD, respectively. The lens consists of a non-polar liquid, silicone oil (T11, Gelest, Inc.), and water. The density of silicone oil is 0.94 g/cm^3 and the index of refraction is 1.4. The densities of the two liquids are chosen to be close to each other in order to minimize the effects of gravity or mechanical vibrations. The cover glass with an indium tin oxide (ITO) electrode is coated by a layer of Teflon, and positioned over the bottom substrate structure filled with oil and water. The ITO layer is used as the counter-electrode in electrowetting. Non-conductive epoxy is then manually applied around the perimeter of the substrate stack to seal off the liquid lens.

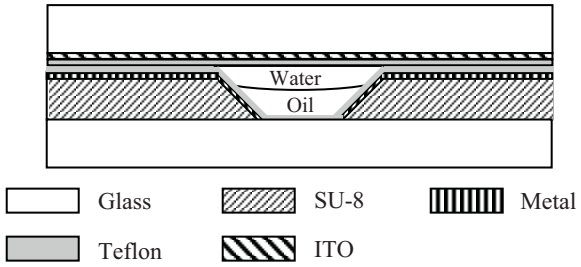

Figure 3. *Schematic view of the variable focus microlens.*

EFFECTS OF UV OVEREXPOSURE

A smooth sidewall on the SU-8 structure is needed for the follow-on thin dielectric SU-8 and hydrophobic Teflon coatings by spinning. We use backside exposure of a double-layered SU-8 through a 1mm thick glass microslide to form angular SU-8 sidewalls. The tapered SU-8 structure is achieved by over-exposure with conventional UV mask and contact printing technology. The mask pattern is a ring with inner diameter of 3mm and outer diameter of 8mm. The UV exposure is performed with a broadband UV system. A layer of 2-micrometer thick SU-8 is first spun on a glass microslide as the adhesive layer for the follow-on thick SU-8 layer. 700-micrometer thickness is obtained by spinning two layers of SU-8 2100. The baking process is described in the following section. Different exposure times are performed and the fabrication results after 20-minute development are shown in Figure 4.

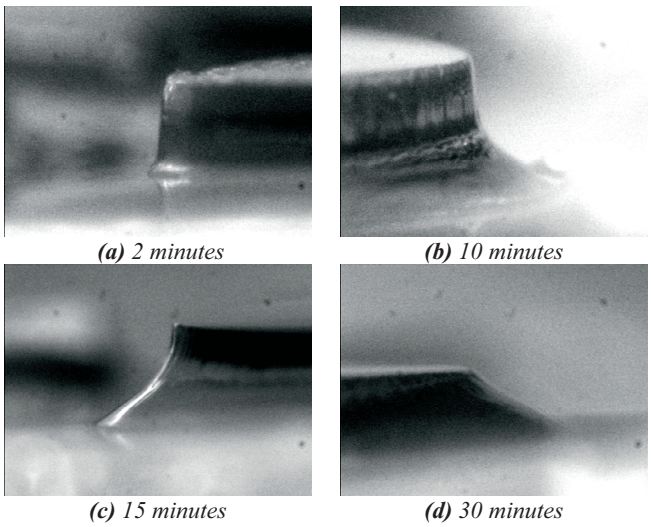

(a) *2 minutes* ***(b)*** *10 minutes*

(c) *15 minutes* ***(d)*** *30 minutes*

Figure 4. *Profile of SU-8 sidewall with different exposure times.*

The SU-8 structure with 2-minute exposure time shows a vertical sidewall profile, while it shows a smooth angular sidewall with 30-minute exposure time. Longer exposure time results in a smoother sidewall. Therefore, 30-minute exposure time with our broadband UV system is chosen for all microlens fabrication in order to get smooth sidewalls on SU-8 structures.

FABRICATION

Microlens fabrication starts with the fabrication of the bottom substrate which is capped by a glass with an ITO electrode after filling with two immiscible liquids. The fabrication process of the bottom substrate is illustrated in Figure 5. First, a 2-micrometer thick SU-8 layer is spun on a 1mm thick glass substrate to form an adhesive layer for the follow-on thick SU-8 coating. The thin SU-8 layer is pre-baked at 65°C and 95°C for one minute each and cooled down to room temperature on a hotplate. A 550-micrometer thick SU-8 layer is achieved by spinning two SU-8 layers. Both layers are pre-baked at 65°C for 30 minutes and at 95°C for 4 hours on a hotplate separately. In all follow-on steps, a slow heating and cooling processes are required to avoid cracking of the thick SU-8 layer. A broadband UV system is used to over-expose the SU-8 from the backside of the glass for 30 minutes (5220 mJ / cm^2 at 365nm). The whole substrate is then post-baked at 65°C and 95°C for 30 minutes and 1 hour, respectively. A SU-8 structure with smooth angular sidewalls is created after development for 20 minutes in the SU-8 developer (PGMEA, Microchem Corp. USA).

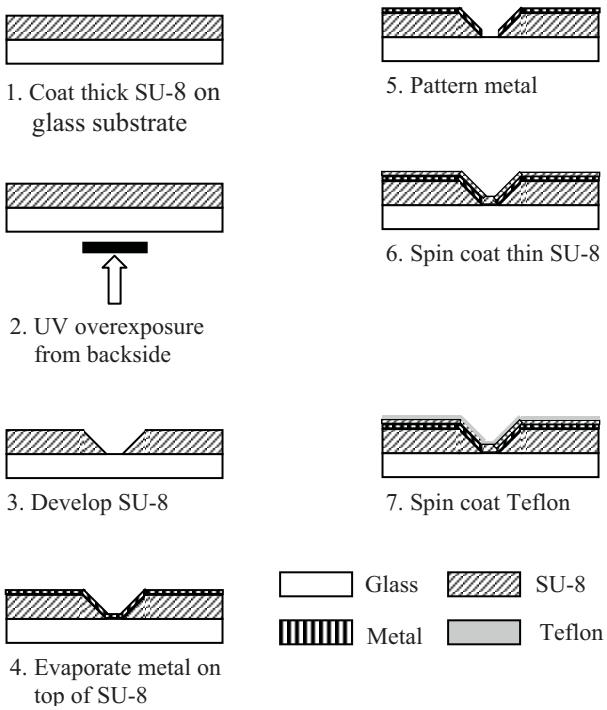

Figure 5. *Fabrication process of bottom substrate.*

10nm thick titanium and 200nm thick gold layers are then deposited by electron beam evaporation. The temperature of the substrates during electron beam evaporation is around 66°C. The metallic layers are then patterned to open a window on top of the glass substrate. Another 2-micrometer thick SU-8 layer is spun on top of the metallic layers as a dielectric layer. The pre-bake process takes place at 65°C for 1 minute and 95°C for 5 minutes in an oven. The dielectric SU-8 layer is cross-linked by UV exposure for 50 seconds. The post-bake is performed at 65°C for 1 minute and 95°C for 5 minutes. Finally, a 300nm hydrophobic Teflon layer is applied. The Teflon layer is baked at 90°C for one hour and cooled down to room temperature in an oven. This completes the formation of the bottom substrate structure. The tapered SU-8 structure is shown in Figure 6. The outer diameter of the SU-8 structure is 8 mm at the top while the diameter at the bottom is 9.5 mm. The inner diameter of SU-8 cavity is 3 mm at the top and 1.5 mm at the bottom. The diameter of aperture of the lens is 1 mm. The angle of the sidewall is measured as 36 degrees, and is shown in Figure 7. A top cover glass plate with ITO electrode is spin-coated with a 300nm Teflon layer. Silicone oil and DI water are the two liquids used for the lens and are manually placed inside the SU-8 cavity. After filling the liquids in the cavity, the device is sealed around its perimeter by epoxy.

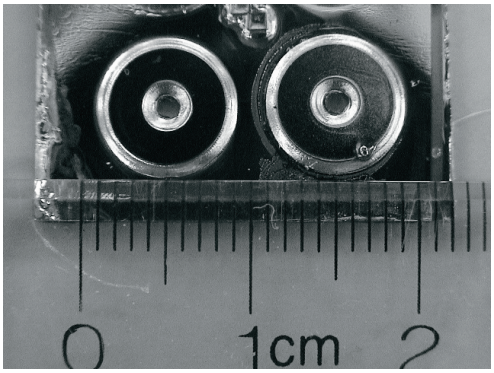

Figure 6. *Tapered SU-8 structure*

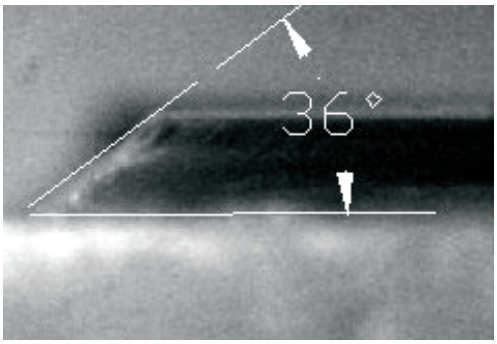

Figure 7. *Angle of sidewall of the SU-8 structure*

MICROLENS DEMONSTRATION

The demonstration of the working microlens is performed by taking the image of numbers (‘3’ and ‘4’) printed on paper and positioned under the device. The images are captured through a microscope. The microscope is first focused on the numbers under the device with no applied voltage. Then different voltages are applied to the microlens device and the images of the numbers are captured with the microscope camera. In Figure 8, the images of numbers at 0 V and 60 V are shown. From the images with 60 V applied, the defocused numbers can be clearly observed.

Another demonstration of the working device is performed by taking the image of a laser beam. A collimated He-Ne laser beam is passed through a pin hole of 1mm in diameter. The laser beam then passes through the microlens from the water side. A reflective surface is placed at the focal plane of the microlens when the

applied voltage is zero and the image is taken by a camera. Images are then taken when the different voltages are applied. The images of the laser beam at 0 V and 60 V are shown in Figure 9. It is observed that the laser beam expands uniformly across the beam width when the voltage is applied to the microlens, thus proving uniformity of the lens shape.

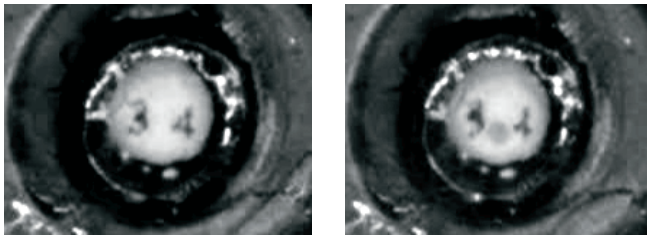

0 Volt 60 Volts

Figure 8. *Images (number '3' and '4') captured at 0 V and 60 V applied to the microlens.*

0 Volt 60 Volts

Figure 9*. Images of a laser beam passing through the microlens with 0 V and 60 V applied.*

CONCLUSIONS

A variable focus microlens based on EWOD on a tapered SU-8 structure has been demonstrated. Images of printed numbers positioned under the microlens and the focusing of a laser beam passing through the microlens at different applied voltage levels successfully demonstrate a working device. Using SU-8 photoresist as a structural material, a wide range of sizes of microlenses can be fabricated. In addition, the SU-8 structures are easily integrated into other microsystems.

ACKNOWLEDGEMENTS

The authors would like to thank Lung-Hao Hu in the MEMS group at University of Colorado at Boulder for helping with SU-8 fabrication. The authors would also like to thank personnel of the Microchem Corp. for valuable discussions.

REFERENCES

1. L.G. Commander, S.E. Day, D.R. Selviah, "Variable Focal Length Microlenses," *Optics Communications, 177*, 157, (2000)
2. D. Y. Zhang, V. Lien, Y. Berdichevsky, J. Choi, ad Y. H. Lo, "Fluidic adaptive lens with high focal length tunability," *Applied Physics Letters, 82*, 3171, (2003)
3. D.Y. Zhang, N. Justis, and Y. H. Lo, "Integrated Fluidic Adaptive Zoom Lens," *Optics Letters, 29*, 2855, (2004)
4. W. Wang, J. Fang, and K. Varahramyan, "Compact Variable-Focusing Microlens with Integrated Thermal Actuator and Sensor," *IEEE Photonics Technology Letters, 17*, 2643, (2005)
5. S. Kwon, L. P. Lee, "Focal Length Control by Microfabricated Planar Electrodes-based Liquid Lens (μPELL)," *The 11th International Conference on Solid-State Sensors and Actuators,* Munich, Germany, 6/10-14/01, (2001), Transducer '01.
6. T. Krupenkin, S. Yang, and P. Mach, "Tunable liquid microlens," *Applied Physics Letters*, 82, 316, (2003).
7. B. Berge, J. Peseux, "Variable focal lens controlled by an external voltage: An application of electrowetting" *European Physical Journal E, 3*, 159, (2000).
8. C. Gabay, B. Berge, G. Dovillaire, S. Bucourt, "Dynamic Study of a Varioptic Variable Focal Lens," *Proceedings of SPIE*, Vol. 4767, 2002, pp. 159-165.
9. S. Kulper, and B.H.W. Hendriks, "Variable-focus liquid lens for miniature cameras," *Applied Physics Letters, 85*, 1128, (2004).
10. F. Krogmann, W. Moench, and H. Zappe, "Tunable Liquid Micro-Lens System," *the 13th international Conference on Solid-State, Actuators and Microsystems,* Seoul, Korea, 6/5-9/2005, pp.1014-1017.
11. K. Kim, D. S. Park, H. M. Lu, W. Che, K. Kim, J.-B. Lee, and C. H. Ahn, "A tapered hollow metallic microneedle array using backside exposure of SU-8", *Journal of Micromechanics and Microengineering, 14*, 597, (2004).

ABSORPTION FILTERS FOR WAVELENGTH TUNING AND FINESSE SWITCHING OF LONG WAVE INFRARED THERMAL DETECTORS

Yuyan Wang, Benjamin J. Potter, Michael Sutton, and Joseph J. Talghader
University of Minnesota, Department of Electrical and Computer Engineering
Minneapolis, Minnesota 55455

ABSTRACT

A resonant long-wavelength infrared (LWIR) absorption filter for thermal detectors is proposed and demonstrated. The filter operates not by transmitting light like a typical Fabry-Perot, but rather by coupling light in a small wavelength region into one mirror where it dissipates and heats the thermal detector plate. The top plate, or mirror, is movable and can be continuously tuned to have a resonance from 8.7 to 11.1μm using electrostatic actuation with 0-42V applied voltage. Since LWIR features are often very course compared to those in the visible, the widths of the tuned resonances are about 1.5μm. At an actuation voltage of 45V, the filter switches into a broadband mode with an absorption width of 2.83μm to enhance sensitivity for scenes with few photons and little spectral information. The switching time between the modes is about 100μsec and the settling time about 400-700μsec. Both times are readily compatible with standard microbolometer frame times.

INTRODUCTION

Microfabricated optical cavities are used in a variety of spectrally sensitive devices in the visible, ultraviolet, and near-IR. Currently, telecommunications is probably the biggest application areas, where they are used for resonant cavity-enhanced (RCE) photodetectors [**1**, **2**], micro machined tunable detectors [**3**, **4**], and wavelength-division multiplexing systems (WDM) [**5**, **6**], among others. In the middle wavelength infrared (MWIR) and LWIR regions, the fabrication of Fabry-Perot filters are more complex because the optical materials must be infrared-compatible and the layer thicknesses must be larger **[7-10]**.

Despite these successes, it is very difficult to build filters for uncooled LWIR thermal detectors, which has limited previous researchers to demonstrations of discretely tunable 2- or 3-color thermal detectors **[11-13]**, rather than continuously tunable ones. The problem originates with the thermal isolation of the uncooled detector itself. Integrating a tunable Fabry-Perot cavity above a detector will create three air gaps, or 2 air gaps if one places the thermal detector layer inside the cavity. Multiple air gaps mean that there are multiple optical cavities, which may couple together to cause unwanted spectral artifacts and limited tuning.

To negate these problems, we present a single air-gap coupled absorption filter for thermal detectors using a micromachined weakly absorbing top mirror. Instead of filtering in transmission as a standard Fabry-Perot, these devices couple incident radiation into their own top plate, which serves as mirror, absorber, and thermistor all at once. The devices can be continuously tuned, and a tuning range from 8.7 to 11.1μm with 0-42V of actuation voltage is demonstrated in this work. Additionally, the devices can also be actuated to a broadband mode at 45V where the resonance width is increased to 2.83μm. This mode is used to enhance its sensitivity in presence of low-light signals with less spectral information. Experiments have shown that the devices have switching times of about 100μsec and settling times of about 400-700μsec, making them compatible with focal plane array frame rates.

DESIGN

The concepts in this paper apply to all thermal detectors, but in this work, they are demonstrated using a microbolometer. Figure 1 shows a diagram of the microbolometer cavity. The IR absorbing material is deposited on the top of the upper plate of germanium (Ge). A thin layer of chromium (Cr) is chosen as the absorber because it is convenient for deposition and it has the most desirable optical constants of common metals. A key characteristic of Cr is that it produces a reasonably symmetric resonance with respect to wavelength. The bottom mirror is a modified quarter-wave distributed Bragg reflector (DBR), composed of Ge and zinc sulfide (ZnS) on the top of an evaporated gold/chromium (Au/Cr) reflector with reflectivity centered around 10μm.

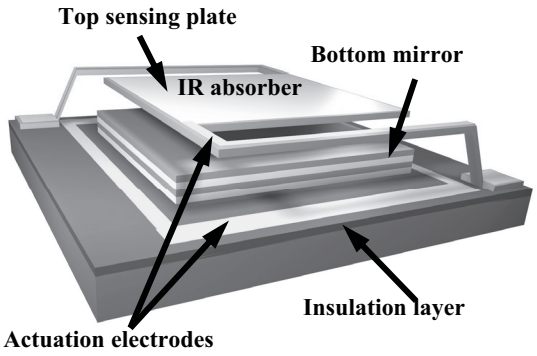

Figure 1. *Conceptual diagram of a tunable absorption filter for LWIR microbolometers. The primary actuation electrodes are on the support beams and substrate to delay snap-through and enhance tuning range.*

The filter works in two modes. One is broadband IR reflection/absorption detection mode that is designed to maximize the thermal light absorbed. In this mode, a 45V actuation voltage pulls the top plate near the bottom mirror, creating a very small gap ($<< \lambda/10$). The top mirror itself does not touch the DBR mirror but instead the beam supports make contact so as not to thermally short the device. Although the contact area has not been measured in these devices yet, it is desirable to design the top movable structure such that the contact area is small enough to not affect the thermal performance [**14**].

The other mode is a reflection/absorption narrowband detection mode, achieved by using 0-42V actuation voltage to electronically control the air-gap over a distance of 4.3 to 6.4μm. The position of the absorption resonance is continuously tuned, and a sharper resonance is obtained with the non-zero air gap. This mode can be used to recognize objects with subtle differences in

emissivity spectrum, which are difficult to identify using standard bolometers [**15**]. Although this paper only describes single devices, the design is compatible for use with a read-out integrated circuit (ROIC) beneath the bottom mirror, which would have the ability to control individual pixels in an array.

The top mirror is designed to have low thermal mass so that the thermal response time is small in the final detector. The resonance width (about 1.5μm in proposed device) matches many coarse spectral features in LWIR. An optimization program based on transmission matrix simulations [**16**] is used to optimize the layer structure. The optimized results are listed in Table 1.

Table.1 *Layer structure of the experimental devices in this study. (The optical constants of these materials have been taken from Palik [**17**].)*

Material	Thickness	n	k
Cr	18 Å	11.8	29.8
Ge	0.6292 μm	4	0
Air gap	3.7-6.8 μm	1	0
Ge	0.1480 μm	4	0
ZnS	0.5557 μm	2.2	0
Ge	0.2456 μm	4	0
ZnS	0.5597 μm	2.2	0
Au	0.50 μm	12.24	54.7
Cr	300 Å	11.8	29.8
Si substrate	…	3.42	…

EXPERIMENTAL DETAILS

The fabrication of LWIR absorption filters differs from many micromachining processes because of the unusual IR optical materials. The fabrication procedure is illustrated in Figure 2.

First, a silicon nitride layer is deposited with low-pressure chemical vapor (LPCVD) on a four inch n-type (100) silicon wafer. To enhance the bottom mirror reflectivity, a layer of Au with a seed layer of Cr is then evaporated on the nitride open areas, followed by two Ge/ZnS quarter-wave pairs (for λ~10μm) deposited via RF magnetron sputtering. The quarter-wave layers are patterned to form bottom mirrors. The deposition properties of the Ge and ZnS are adjusted to get consistently low-stress films and acceptably fast deposition rates. CF_4 and H_2 plasma are used to dry etch the Ge and ZnS layers respectively. After completing the substrate reflector, Au and Cr layers are deposited to form the electrode lines that surround the bottom mirrors. A sacrificial layer of SiO_2 with nominal thickness of 6.8μm is then deposited, which will later form the air gap. A polyimide sacrificial etch was originally attempted and abandoned later because it required a pure-oxygen etch-release that caused too many defects in the optical films. After patterning the anchor holes for the supports, the top-plate structural Ge layer is sputtered, followed by a thin evaporated Cr metal (patterned using lift-off) for absorption. Next, Au and Cr films are evaporated along the supporting beams and bonding pads to provide electrical contacts to the top plate for actuation. Finally, the devices are released in a diluted buffered oxide etchant and dried with a critical point dryer to prevent stiction.

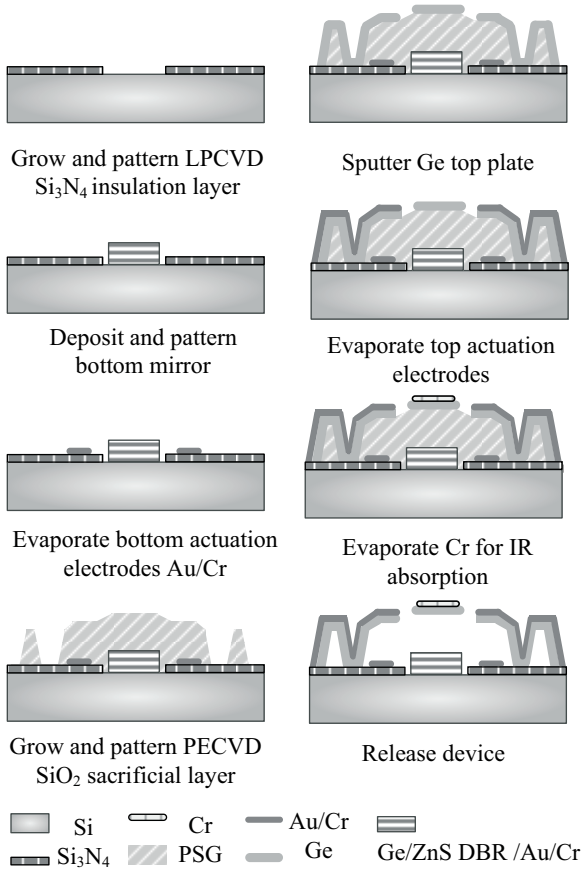

Figure2. *Process flow for the LWIR wavelength tunable microbolometer filter.*

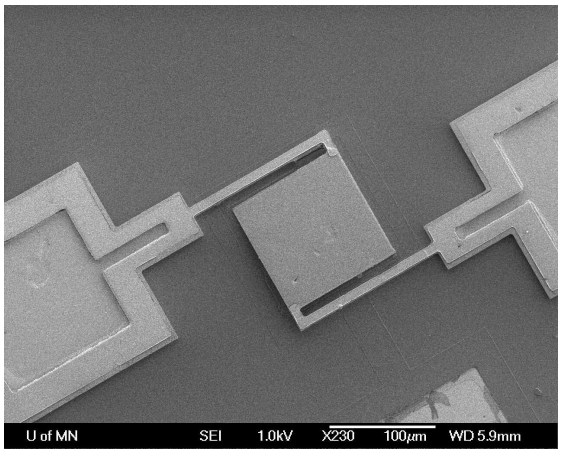

Figure 3. *SEM image of a device after etch release. The top plate is 100 by 100μm and is supported by two 150 by 5μm beams. Au/Cr has been evaporated on the beams and anchors for actuation. The two structures to the left and right are bonding pads for later testing.*

Figure 3 shows a SEM micrograph of a typical finished filter pixel. The top plate flatness deviation is less than λ/16 of the design wavelength (λ~10μm). The temperature during fabrication (after finishing the initial silicon nitride insulation layer) does not exceed 200°C, making the process compatible with read-out integrated circuits (ROIC) beneath the bottom mirror.

MEASUREMENTS AND SIMULATION

The areas of the filters varied from 25x25μm^2 to 120x120μm^2. The measured resistance of the top plates is about 35KΩ at room temperature. The Cr/Ge plate has a temperature-sensitive resistance with a coefficient of approximately 0.07%/K.

A spectrum simulation, which incorporates the fabricated structure thickness and the mirror profile parameters measured by a Zygo interferometric microscope, has been carried out in to determine the air gap spacings that correspond to each wavelength. Figure 4 shows the evolution of the reflected peaks at different air gaps. Note that since there is no transmission, the absorption spectrum is *1-R*. Also, the simulation indicates that nearly all light absorption happens within the top Cr layer on the device, which is necessary for efficient thermal detection.

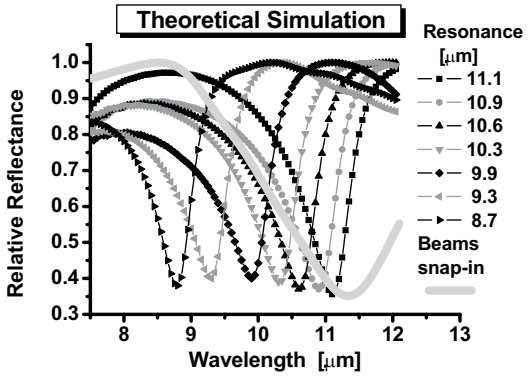

Figure 4. *Spectral simulation of the experimental devices. This simulation includes the layer structure of Table 1 and a small curvature present in the top plate that broadens the resonance*

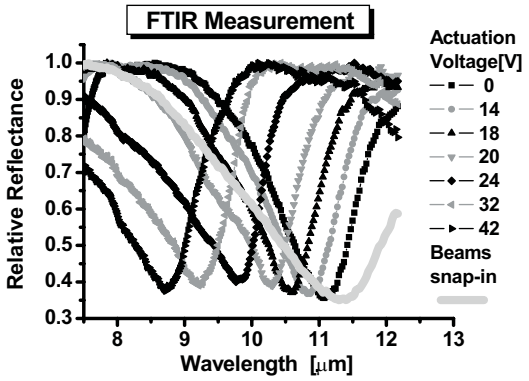

Figure 5. *FTIR measurement of the relative reflectance spectra of a 120 by 120μm square filter. As the applied voltage is varied from 0-42V, the narrowband resonance shifts from 11.1μm to 8.7μm. A broadband resonance centered at 11.3μm is created when the voltage is increased to 45V.*

The relative reflectance of the 120x120μm^2 prototype is measured using a Nicolet Magna 750 Fourier Transform Infrared Spectroscopy (FTIR) system with microscope attachment. The filter does not transmit measurable light through the substrate. During the FTIR measurement, a voltage is applied on the supporting arms and the surrounding electrodes beneath the arms using a Keithley 230 Programmable Voltage Source. Changing the voltage level shifts the interference peak, enabling continuous tuning. The voltage-wavelength relationship is stable and shows no hysteresis.

The measured spectrum matches well with simulation and clearly illustrates that the filter has wide continuous tunability. Specifically, the devices are tunable from 8.7 to 11.1μm using 0-42V of actuation voltage. A broadband absorption mode is reached at 45V, where the resonance full-width-at-half-maximum (FWHM) increases to 2.83μm, compared with approximately 1.5μm in the narrowband operation range. The switching between these two modes is emphasized in Figure 6.

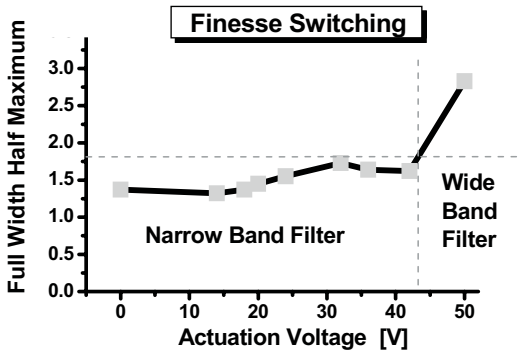

Figure 6. *The resonance FWHM versus actuation voltage for the same device tested in Figure 5. The FWHM changes by approximately 87% between the tuning and broadband modes. The switch is reversible and occurs at about 45V.*

To study the transient response of the filter at the onset of actuation, a position sensitive detector (PSD) is used to capture the movement of the top filter plate under a square-wave actuation voltage. The voltage pulse and the output of PSD are measured simultaneously using a digital oscilloscope. The slowest devices are those with the biggest plates, having dimensions of 120 by 120μm. Figure 7 shows a rise time of 110μsec with a settling time about 466μsec, and a fall time of 96μsec with a settling time of 672μsec respectively. These transients are easily compatible with microbolometer thermal time constants, which are usually in the range of 5-20ms.

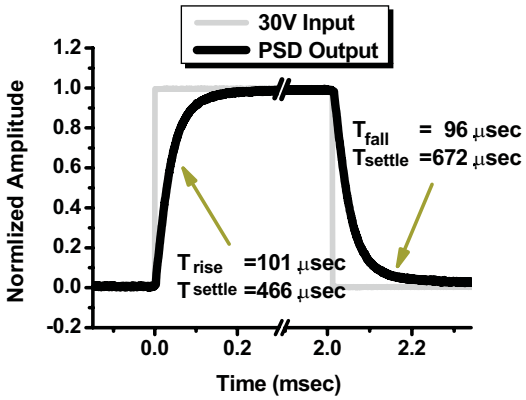

Figure 7. *A typical transient response of the devices with plates of size 120 x 120μm. The plates are supported by two beams with lateral size of 100 by 5μm and actuated by a 30V square wave voltage pulse.*

CONCLUSIONS

The electrostatic actuation and optical response of a wavelength tunable absorption filter for thermal detectors has been presented. The filter operates by coupling light over small band of wavelengths into its top mirror, which doubles as the detector plate of a microbolometer. Narrowband tuning from 8.7 to 11.1μm is obtained by varying the actuation voltage from 0 to 42V, and a broadband mode is obtained at 45V. Optical characterization has confirmed a good agreement between numerical simulations and experimental results in terms of resonances position and displacement. However, non-ideal features of the fabricated filter can be observed in the broadening and the decreasing amplitude of the reflected peaks.

ACKNOWLEDGEMENT

This project is supported by Microsystems Technology Office of DARPA and the Army Research Office under contract DAAD19-03-1-0343. The processing was performed at the Nanofabrication Center at the University of Minnesota, which is part of the NSF-sponsored NNIN.

REFERENCES

[1] R. Kuchibhotla, A Srinivasan, J. C. Campbell, C. Lei, D. G. Deppe, Y. S. He, and B. Streetman, "Low-voltage high-gain resonant-cavity avalanche photodiode," *IEEE Photon. Technol. Lett., 3,* 354 (1991).

[2] K. Kishino, S. Unlu, J.-I. Chyi, J. Reed, L. Arsenault, and H. Mo, "Resonant cavity-enhanced (RCE) photodetectors," *IEEE J. Quantum Electron., 27,* 2025 (1991).

[3] E. C. Vail, M. S. Wu, G. S. Li, W. Yuen, and C. J. Chang-Hasnain, "A Novel Widely Tunable Detector with Wavelength Tracking," Postdeadline Paper, *Proceedings of Optical Fiber Communications Conference (OFC),* Feb./26-Mar./3, San Diego, California (1995), pp18-2

[4] M. C. Larson, B. Pezeshki, and J. S. Harris, "Vertical coupled-cavity microinterferometer on GaAs with deformable-membrane top mirror", *IEEE Photon. Technol. Lett., 7,* 382 (1995).

[5] J. Peerlings, A. Dehe, A. Vogt, M. Tilsch, C. Hebeler, Langenham F, P. Meissner, H. L. Hartnagel, "Long resonator micromachined tunable GaAs-AlAs Fabry-Perot filter," *IEEE Photon. Technol. Lett., 9,* 1235 (1997).

[6] S. Irmer, J. Daleiden, V. Rangelov, C. Prott, F. Romer, M. Strassner, A. Tarraf, H. Hillmer, "Ultralow biased widely continuously tunable Fabry-Perot filter," *IEEE Photon. Technol. Lett., 15,* 434 (2003).

[7] D. Rossberg, "Silicon micromachined infrared sensor with tunable wavelength selectivity for application in infrared spectroscopy", *Sensors and Actuators A: Physical, 47,* 413 (1995).

[8] H. Alause, F. Grasdepot, J. P. Malzac, W. Knap and J. Hermann, "Micromachined optical tunable filter for domestic gas sensors", *Sensors and Actuators B: Chemical, 43,* 18 (1997).

[9] Mitsunori Saito and Hideki Furukawa, "Infrared tunable filter by the use of electrostatic force", *Appl. Phys. Lett. 79,* 4283 (2001).

[10] JT., Daly, W. A. Bodkin, W. J. Schneller, R. B. Kerr, J. Noto, R. Haren, M. T. Eismann, B. K. Karch, "Tunable narrow-band filter for LWIR hyperspectral imaging*", Proceedings of SPIE Vol 3948 Photodetectors: Materials and Devices V,* 1/26-28/00, San Jose, California (2000), pp. 104-115.

[11] S.-W. Han and D. P. Neikirk, "Design of infrared wavelength-selective microbolometers using planar multimode detectors," *Proceedings of the SPIE Vol. 5836 Smart Sensors, Actuators, and MEMS II, Microtechnologies for the New Millennium 2005,* 05/9-11/05, Seville, Spain (2005), pp. 549-557.

[12] Vladimir N. Leonov and Donald P. Butler, "Two-color thermal detector with thermal chopping for infrared focal-plane arrays", *Applied Optics, 40,* 2601, (2001).

[13] Y. Wang, B. Potter, M. Sutton, R. Supino and J. Talghader, "Step-wise Tunable Microbolometer Long-wavelength Infrared Filter", *Technical digest of the 13th International Conference on Solid-State Sensors, Actuators and Microsystems*, 6/5-9/05, Seoul, Korea (2005), pp.1006-1009.

[14] W. B. Song, M. Sutton, and J. J. Talghader, "Thermal contact conductance of actuated interfaces", *Appl. Phys. Lett. 81,* 1216 (2002).

[15] R. A. Wood, "Monolithic silicon microbolometer arrays," in Uncooled Infrared Imaging Systems and Arrays, *New York Academic*, (1997), *Semiconductors and Semimetals, 47,* ch. 3, pp. 43-121.

[16] H. A. Macleod, Thin Film Optical filters. 3rd ed. *Inst of Physics Pub Inc,* (2001).

[17] E. Palik, Handbook of optical constants. *Academic Press,* (1998).

ADHESION AND FRICTION MEASUREMENT METHOD FOR A MEMS PROBE ARRRAY

Wesley S. Smith, Peter G. Hartwell, Robert G. Walmsley
Hewlett-Packard Laboratories
Palo Alto, CA 94304

ABSTRACT

This paper presents a unique method for measuring the adhesion and friction forces between a MEMS probe tip array and a sample surface. The method includes capability to measure the dependence of stiction and friction with varying normal force, humidity, surface materials, and rest time. A differential laser Doppler vibrometer (LDV) is used to measure the relative velocity between an unconstrained sample and the probe tips (20nm radius of curvature). By removing lateral constraints, only frictional forces act in the direction of relative motion. We present preliminary results comparing the adhesion forces to the normal force and examining time dependence of adhesion. No-load adhesive forces (6-20nN per probe tip), coefficients of static friction (0.4-0.56), and trends in time dependence are compared to previous findings indicating that valid results are obtained with this method.

INTRODUCTION

Adhesion and friction forces are present any time two surfaces contact each other. Advancing technology in micro-devices has led to several applications in which the movement of one surface over another is required. Applications involving probe arrays are being investigated for use in data storage [**1**], parallel imaging [**2**], and biological analysis [**3**]. Other applications where adhesion and friction play dominant roles include scanning probe microscopy [**4**], micro-motors and gears [**5**], and contacting stops of micro-mirrors [**6**]. Several studies have shown that the adhesive and friction forces depend on the normal force between the surfaces, the contact area, and the relative humidity [**4-10**]. Understanding the effects of these conditions on micro-scale adhesion and friction can lead to increased control of movement, knowledge of forces required for actuators, and investigation of failure mechanisms such as wear.

MICRO AND NANO SCALE FRICTION

Micro devices concentrate contact to a single asperity or controlled locations of asperities. Due to high surface area to volume ratios van der Waals forces, electrostatic forces, and capillary forces dominate over inertial and gravitational forces [**8**]. At this scale, interfacial friction can be described by

$$F = S_c A + \mu N .$$

The μN term is the traditional Amontons' formulation for macro-scale friction, and the $S_c A$ term represents the dependence on the contact area between the surfaces. Here S_c is the critical shear stress between the two layers [**9**]. Other sources suggest adhesion forces are also strongly dependent on meniscus bridges that form in the presence of humidity at contacting surfaces [**7-9**].

Wear resulting from friction and adhesion is an issue for MEMS applications such as data storage [**1,11**]. Tip wear depends on the material properties of the contacting surfaces and the normal loads between them [**11**].

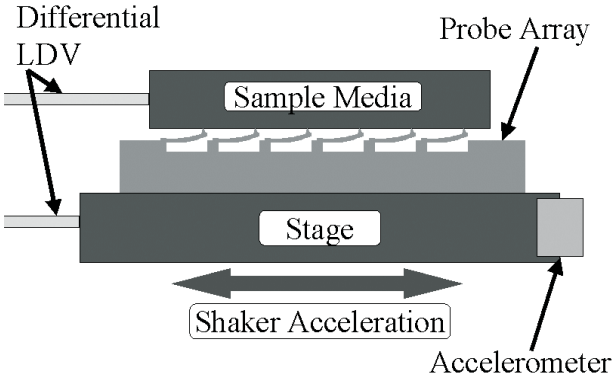

Figure 1. *Schematic of measurement setup. The unconstrained sample media sits on top of an array of probe tips that are located at the end of cantilevers. Acceleration of the stage creates lateral friction forces that act on the sample media at the probe tips.*

Methods used for measuring friction on the micro-scale generally involve a form of scanning probe microscopy including atomic force microscopy (AFM), friction force microscopy (FFM), scanning tunneling microscopy (STM) [**4**], or surface force apparatus (SFA)[**12**]. Scanning methods monitor the reactions of a cantilever as a probe tip is moved over a surface. SFA involves measuring adhesive forces by contacting a probe to a surface and measuring the force required to pull the probe from the surface. These methods have been used to characterize friction in several varying conditions including velocity, relative humidity, normal load, contact area, and behavior over asperities [**8-10**]. The results from these experimental methods depend on precise calibration of piezoelectric actuators used to provide the force for the scanning and accurate characterization of the cantilevers [**8**].

We developed a unique method to characterize the scale dependent adhesion and friction effects between a MEMS probe tip array and a sample surface. This technique provides flexibility to vary the effective normal force, ambient humidity, contact media, and time intervals between actuated motions, allowing accurate characterization of these effects on friction. The experimental setup eliminates unknown reaction forces associated with scanning a cantilever over a fixed surface and the necessary calibrations required by other friction measurement methods. The system shown in Figure 1 isolates adhesion and friction forces by reducing the forces that act on the sample to the normal force at the probe tips, the sample's weight do to gravity, and the lateral friction forces.

EXPERIMENTAL SETUP

Adhesion and friction forces are measured between an array of probe tips pointing upward and a flat sample media that is free to move on top of the tips (Figure 1). The single crystal silicon (SCS) probe tips are located at the end of silicon cantilevers. A pre-stressed nitride layer causes the cantilevers to bend upwards

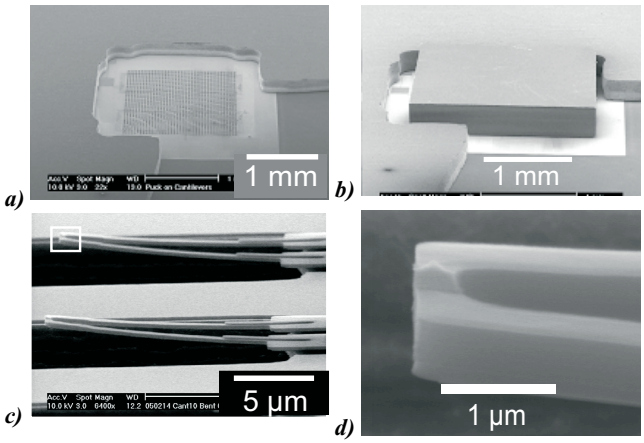

Figure 2. *(a) SEM images of probe array with stainless steel fence, (b) the 2mm x 2mm X 380µm sample media on top of the array, (c) pre-stressed cantilevers bent up 1-3µm, and (d) the oxidation sharpened probe tips (~20nm radius of curvature).*

providing a 1-3µm gap between the sample and the substrate (Figure 2a-c). Variations in the amount the cantilevers are bent up and differences in the tip heights are compensated for by the compliance of the individual cantilevers. Uniform contact between the sample surface and the probe tips is achieved as the cantilevers deflect due to the weight of the sample. At this scale, surface forces dominate over any small variations in normal force present at each probe tip. The complete array contains 1600 (40x40 array) probe tips that are oxidation sharpened to have a nominal radius of curvature of 20nm (Figure 2d). The array spans an area of 1.6mm x 1.6mm. The sample media is a SCS chip (2mm x 2mm x 380µm) that is placed on top of the probe tips (Figure 2b).

The array of cantilevers is rigidly fixed to a horizontal shaker by gluing the array to a stainless steel fence (Figure 2a,b). This fence fixes the array to the shaker stage, constrains the sample to remain above the probe array, and allows an optical path to the sample's edge for vibrometer measurements. The cantilever orientation can be set to point in the direction of acceleration (axial) or perpendicular to the acceleration (transverse). The shaker is capable of producing horizontal accelerations (> 40 m/s^2) more than sufficient to overcome the stiction forces. An accelerometer mounted to the stage shown in Figure 3 measures the motion of the shaker.

A differential laser Doppler vibrometer (LDV) focused on the shaker stage and on the edge of the silicon sample measures the relative motion of the sample and the probe array (Figure 1,3). The sample will remain fixed to the probe array until the lateral force of the shaker overcomes the stiction force. Dynamic friction governs the subsequent relative motion.

The experimental setup shown in Figure 3 includes a nozzle that is calibrated to vary the normal force between the probes and the sample and an environmental chamber to vary the ambient relative humidity. An equivalent normal force between the probe tips and the sample can be varied between 30 and 250µN using a pressure transducer to control the flow rate of nitrogen through the vertically oriented nozzle (Figure 3). The set-point pressure to equivalent mass conversion is calibrated by positioning the nozzle over a microbalance (Figure 4). An exponential equation is fit to the calibration data for finding intermediate equivalent masses. The effective normal force is the product of gravity and the sum of the sample mass and the equivalent mass. The dependence of stiction and friction on normal force is obtained by measuring the relative motion while varying the pressure applied to the top of the sample.

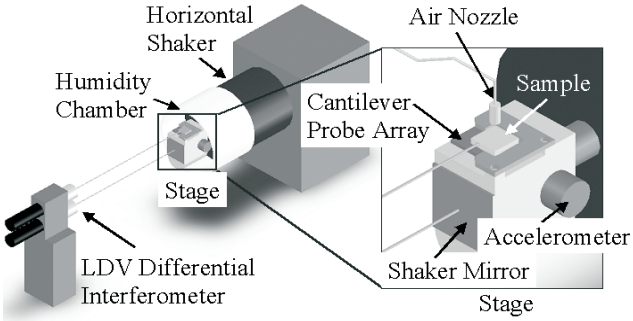

Figure 3*. Overall schematic of friction test setup. LDV lasers are focused on a mirror attached to the shaker and on the edge of the sample media resting on top of the probe tips. A nozzle is located directly above the sample media to provide a calibrated additional normal force to the sample media (30-250µN). An environmental chamber surrounds the entire setup providing relative humidity control between 0.5 and 75% RH.*

Previous studies have shown a strong dependence of friction characteristics on ambient humidity [**4-10**]. An environmental chamber encloses the shaker's stage to control the humidity at the contact points. Adjusting the flow rate of nitrogen over a water surface in a bubbler controls the relative humidity. The nozzle described above is also equipped with vacuum to lift the sample off the probe tips. This was done when humidity was changed to ensure uniform distribution of humidity between the probe tips and the sample. A hygrometer on the outlet line measures the relative humidity inside the chamber. Values of relative humidity between 0.5% and 75% were obtained using this method.

Additional flexibilities of this measurement method include the ability to quantify the time dependence of stiction and to vary the materials being examined. A custom actuation waveform was applied to the shaker to examine rest time effects (Figure 5b). By varying the time between impulse events (50-500ms) within the waveform and the time between triggering the waveform (30s – 10min), the characteristics of the time dependence can be determined. Although not performed in these experiments, the sample media can be coated with various materials including polymers or thin films to measure the friction characteristics of these materials. In addition, thin films can be grown on the probe tips for friction characterization between two desired materials.

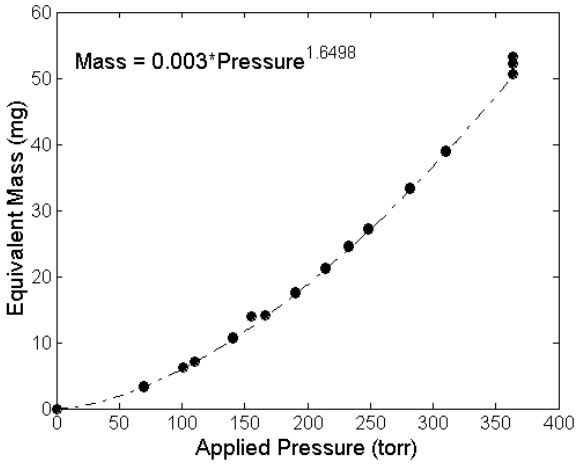

Figure 4. *Equivalent mass calibration for the pressure controlled nozzle. An exponential fit was applied to determine intermediate equivalent mass values.*

EXPERIMENTAL METHODS

Verification that the sample is in uniform contact with the probe tips is done by analyzing the vertical deflection of the sample when hit with a burst of pressure. The differential LDV measures the vertical displacement of the sample and the pressure transducer gives data on the amount of pressure applied. Comparing the force-deflection curves gives the spring constant of the array. Consistent spring constants at each of the four corners of the sample indicate that uniform tip contact has been achieved.

Two forms of shaker actuation are used in the experiments. The first method involves a continuously oscillating acceleration that steadily increases in magnitude (Figure 5a). Relative motion of the sample to the probe array occurs when the acceleration exceeds the critical force needed to overcome stiction. After this release, the dynamic friction at the probe tips governs the motion of the sample. A major disadvantage of this method is that it involves a high travel distance between the sample and the tips that contribute to wearing of the tips and changes in the behavior of friction.

The second actuation method applies several bursts of acceleration sufficient in magnitude to overcome stiction. This method removes the hysteresis effects of stiction on time by accelerating the probe array twice in the same direction (pulses 2 and 3 in Figure 5b). It also reduces the travel distance between the two surfaces to minimize wear and allows adjustment of the time between pulses to examine the time dependence of stiction.

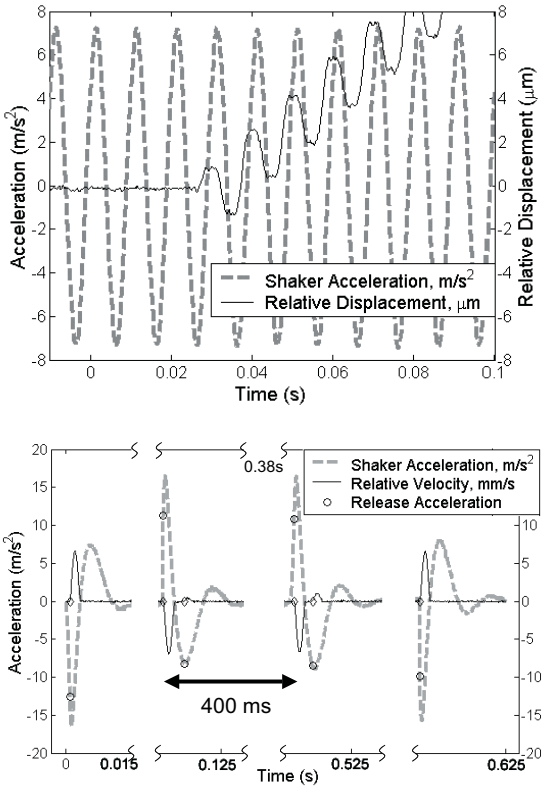

Figure 5. *Continuous (a) and pulsed (b) actuation waveforms are plotted with the characteristic output from the differential LDV. The bias of movement in (a) is due to the axial orientation of the cantilevers (cantilevers point in same direction as acceleration). This bias is removed by rotating the cantilevers 90°. A rest time of 400ms is shown in (b).*

RESULTS

Preliminary results were obtained for various samples involving a single crystal silicon (SCS) sample in contact with SCS probe tips. Figures 6 and 7 show the normal load dependence of adhesion. The results in Figure 6 compare the two different actuation methods using two different probe arrays.

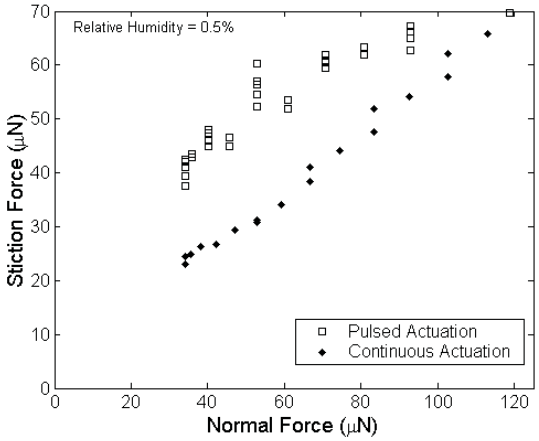

Figure 6. *Dependence of stiction on normal force. Force values represent the force over the complete array of 1600 probe tips.*

The slope of the lines in the plot above gives the coefficient of static friction. With a linear fit to the data, a static coefficient of 0.40 to 0.56 is found for the silicon surface sliding over the probe array. These values are consistent with the microscale friction coefficients of 0.45-0.50 for Si(100) reported by Tambe and Bhushan [**7**]. As the normal load approaches zero, JKR theory predicts a non-zero stiction force [**9**]. This no-load adhesive force is purely dependent on the surface area of the two contacting surfaces. Extrapolating the data shown in Figure 6 to zero normal force gives no-load adhesive forces of 6-20nN per cantilever tip (20nm radius of curvature). These values correspond well with the adhesive forces of 50nN reported for a 30-50nm radius of curvature tip [**8,10**].

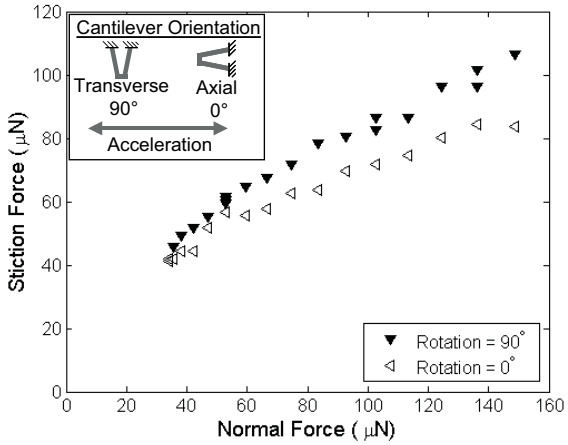

Figure 7. *Effect of orientation of cantilevers on stiction force with pulsed actuation. Rotating the cantilevers 90° produces higher friction forces at higher loads. The forces are distributed over the array of 1600 probe tips.*

Figure 7 shows the effect of the orientation of the cantilevers with respect to the direction of acceleration. When the cantilevers point in the same direction as the acceleration (axial), there is a slight bias between the stiction forces in one direction (Figure 5a). When the cantilevers are oriented perpendicular to the acceleration (transverse), this bias is removed, and the friction forces are shown to increase.

Results for the time dependence of stiction using the pulsed actuation method are shown in Figure 8. At small rest times between releases (50-500ms), the values for friction show very little dependence on time. However, at longer rest times, there is a trend for the stiction value to increase slightly. This increase is uniform for both relatively dry conditions (RH 0.5%) and ambient conditions (RH = 40%). The total increase in static friction force per cantilever is on the order of 1.5nN over a rest time of 400s. This magnitude of increase is much smaller than published single tip results where there is approximately a 30nN change over the same period [**8**].

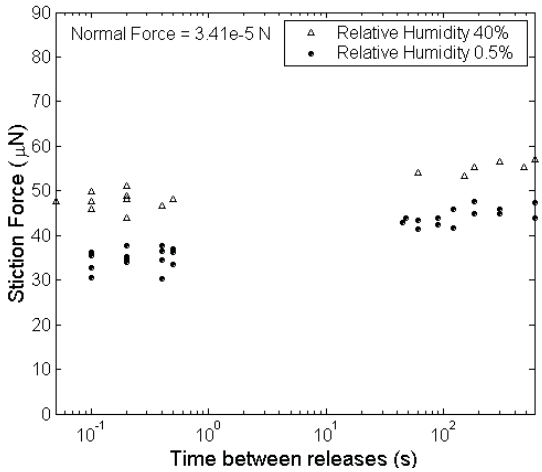

Figure 8. *Time dependence of stiction for axially oriented cantilevers. The time dependence of stiction is shown to have a slightly increasing trend toward more stiction with greater time. Although the stiction is higher for RH = 40%, the trend is similar for dry conditions. Stiction forces are shown over the 1600 probe tip array.*

CONCLUSION

The methods for measuring micro and nano-scale friction between a MEMS probe tip array and a sample surface presented in this paper produce similar results to those using scanning probe microscopy. By removing the constraints on the sample surface, lateral motion is governed solely by friction forces. This method also avoids calibration of piezo actuators needed for the force measurements of the scanning probe techniques. However, several complications to the method exist. Since friction is measured across an entire array, average values of friction forces are found. The strong dependence on surface contact area causes small fabrication variations to produce large differences in resulting forces.

The method described here is intended to serve as a platform for future studies of friction. It provides the flexibility to examine many of the main factors currently attributed to adhesion and friction. Further studies are underway to characterize the adhesion force dependence on relative humidity. The method will incorporate a vacuum chamber replacing the current environmental chamber to examine friction in dry conditions. For studies in the reliability of MEMS devices where friction and wear are issues, further investigations on the behavior of different material coatings and quantifying the wear that occurs are needed.

ACKNOWLEDGEMENTS

The authors would like to thank Hewlett-Packard Laboratories for supporting this work. Special thanks goes to Uija Yoon, now at Stanford University, for the fabrication of the probe arrays. We would also like to thank Matt Messana of Stanford University for contributing data filters for the analysis of the stiction data and Tom Kenny of Stanford University for his support in preparing this manuscript.

REFERENCES

[1] P. Vettiger,.G. Cross, M. Despont, U. Drechsler, U. Durig, B.Gotsmann, W. Haberle, M.A. Lantz, H.E. Rothuizen, R. Stutz, and G.K. Binnig, "The 'Millipede'-Nanotechnology Entering Data Storage". *IEEE Trans. On Nanotech*., 91, 1 (2002).

[2] S. C. Minne, G. Yaralioglu, S. R. Manalis, J. D. Adams, J. Zesch, A. Atalar, C. F. Quate, "Automated parallel high-speed atomic force microscopy," *App. Phys. Lttrs.* 72, 18 (1998).

[3] M. Poggi, L.A. Bottomley, and P.T. Lillehei. "Scanning Probe Microscopy" *Anal. Chem*. 74 (2002).

[4] B. Bhushan, H. Fuchs, S. Hosaka. "Micro/nanotribology studies using scanning probe microscopy," *Applied Scanning Probe Mehods*. Springer-Verlag, Berlin Heidelberg (2004), pp.171-203.

[5] D.M. Tanner. "Reliability of surface micromachined microelectromechanical actuators," *Proc. 22nd International Conference on Microelectronics,* MIEL 2000, Nis, Serbia, 14-17 May 2000, vol. 1, pp. 97-104.

[6] M.R. Douglass. "Lifetime estimates and unique failure mechanisms of the digital micromirror device (DMD)," *36th Annual Reliability Physics Symposium Proc.,* Reno, NV, 3/31-4/2/98, 1998 IEEE International (1998), pp. 9-16.

[7] M. Scherge, X. Li, J. A. Schaefer, "The effect of water on friction of MEMS," *Tribology Lttrs.,* 6 (1999).

[8] N. Tambe, and B. Bhushan, "Scale dependence of micro/nano-friction and adhesion of MEMS/NEMS materials, coatings and lubricants". *Nanotechnology*, 15 (2004).

[9] B. Bhushan, *Handbook of micro/nanotribology* 2nd ed., CRC Press, Boca Raton, FL (1999), pp. 247-272, 371-432.

[10] B. Bhushan, and C. Dandavate, "Thin-film friction and adhesion studies using atomic force microscopy," *J. App. Phys.,* 87, 3 (2000).

[11] B.D. Terris, S.A. Rishton, H.J. Mamin, R.P. Ried, D. Rugar, "Atomic force microscope-based data storage: track servo and wear study," *Appl. Phys.* A, 66 (1998).

[12] D. Tabor, and R.H.S. Winterton. "The direct measurement of normal and retarded van der Waals forces," *Proc. of the Royal Society of London, A, Math. and Phys.Sci.* 312. (1969), pp. 435-450.

DESENSITIZING METHOD FOR MEASUREMENT OF THIRD-ORDER INTERMODULATION DISTORTION IN CMOS-MEMS MICROMECHANICAL RESONATORS

Chiung-Cheng Lo[1], and G. K. Fedder[1,2]
[1]Department of Electrical and Computer Engineering and [2]The Robotics Institute
Carnegie Mellon University, Pittsburgh, PA, 15213
Email: Chiungcl@ece.cmu.edu Tel: 412-268-8194 Fax: 412-268-4594

ABSTRACT

A new desensitization method to characterize linearity of micromechanical resonator filters is introduced. The practical measuring range is larger than either the conventional 1 dB compression test or the two-tone test for RF frequencies. An analytic expression for a new 1 dB desensitizing point (DP_{1dB}) metric is directly related to the 1 dB compression point (CP_{1dB}). This method is verified on a CMOS-MEMS square-frame resonator (SFR) with resonant frequency of 5.849 MHz, quality factor of 1268 and insertion gain of -31.8 dB and -41.7 dB for input polarization voltage of 10 V and 30 V, respectively. The measured DP_{1dB} is 26.7 Vac corresponding to a CP_{1dB} of 32 dBm.

INTRODUCTION

Recent progress of microresonators as passive components in wireless communication applications achieves high quality factor (Q) and high operational frequency. For example, hollow-disk ring resonators have been demonstrated with Q> 60,000 at 24 MHz and Q>14,000 at 1.2 GHz [1]. By mechanical or electrostatic coupling, MEMS resonators yield filtering and mixing functions with miniature size [2-4]. However, in order to fulfill strict wireless communication specifications, such as the minimum total third-order input intercept point (IIP3) of -18 dBm in the signal path for the European GSM standard [5], the measurement and the modeling of the nonlinear effects of micro resonators is critical.

Nonlinear effects of microresonators are presented, and two types of linearity measurement are discussed in part 1. In part 2, a new desensitization method is introduced, the measurement set-up is illustrated, and the mechanism of this method is examined. A series of experiments are conducted and the validation of this measurement method is analyzed in part 3.

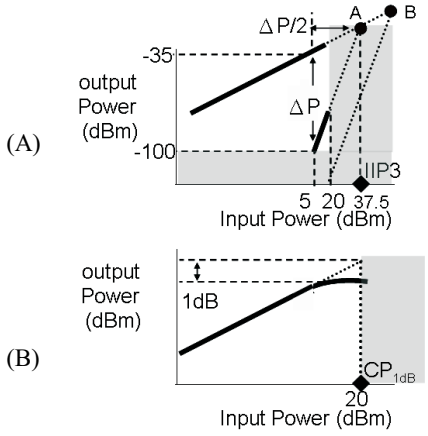

Figure 1. *Example of measured range for (A) a two-tone test and (B) a 1 dB compression test. Shaded areas are inaccessible for measurement.*

NONLINEAR MICRORESONATORS

Nonlinearity of the communication systems, especially the third-order intermodulation distortion, is critical to quantify because it usually defines the upper bound of the power handling ability. Nonlinearity occurs when out-of-band tones are modulated and results in generation of in-band components. When the input signal, V_{in}, consists of a desired signal, $V_i \cos\omega_i t$, and two out-of-band interference tones, $V_{im-1}\cos\omega_{im-1}t$ and $V_{im-2}\cos\omega_{im-2}t$, the output components after transferring through a nonlinear system are given by [6]

$$V_o = (a_1 V_i + \underbrace{\frac{3a_3 V_i^3}{4}}_{(a)} + \underbrace{\frac{3a_3 V_i V_{im-1}^2}{2}}_{(b)} + \underbrace{\frac{3a_3 V_i V_{im-2}^2}{2}}_{(c)})\cos\omega_i t \quad (d) \quad (1)$$
$$+ \underbrace{\frac{3a_3 V_{im-1}^2 V_{im-2}}{4}\cos((2\omega_{im-1}-\omega_{im-2})t}_{(e)} + \underbrace{\frac{3a_3 V_{im-1} V_{im-2}^2}{4}\cos((2\omega_{im-2}-\omega_{im-1})t}_{(f)} + \ldots$$

where component (a) is the fundamental tone and (e) and (f) are the intermodulation tone (IM). The nonlinear system in (1) is modeled as

$$V_o = a_1 V_{in} + a_2 V_{in}^2 + a_3 V_{in}^3 \ldots \quad (2)$$

In order to quantify this phenomenon, the two-tone test has been applied by other groups [7-8]. This method measures the effect of component (e) and (f) in (1). The frequencies of the two tones are selected to maximize the IM tone, given by

$$2\omega_{im-1} - \omega_{im-2} = \omega_r \quad or \quad 2\omega_{im-2} - \omega_{im-1} = \omega_r \quad (3)$$

where ω_r is the resonant frequency. By plotting the output power versus input power for the fundamental tone and IM tone, the intercept of the extrapolation of these two lines is IIP3, shown in Figure 1(A). In addition, IIP3 is given by [6]

$$IIP3_{dBm} = \frac{\Delta P_{dB}}{2} + P_{in,dBm} \quad (4)$$

Where P_{in} is the input power and ΔP is the power difference between fundamental and IM tone. However, the mechanical filtering characteristic suppresses off-resonance output signals to some degree, which degrades the accuracy of extrapolating IIP3. This problem is magnified in the case of high quality factor resonators. The measurement range of this method is a function of dynamic range of measurement instruments, testing range, and the insertion loss of the measured device. For example, in the case that the maximum output power of signal generator is 20 dBm, the noise floor of spectrum analyzer is -100 dBm, the insertion loss of the measured device is 40 dB, and the testing range is

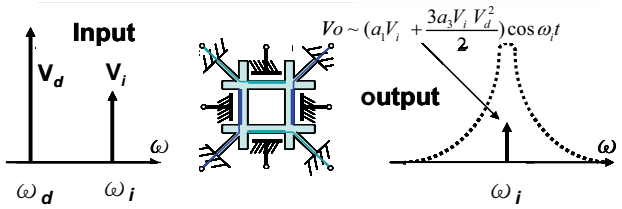

Figure 2. *Desensitization test of intermodulation in a nonlinear resonator*

15 dB, the intercept is point (A) shown in Figure 1(A), and the corresponding IIP3 is 37.5 dBm, which is approximately the upper bound of measurement range in the two-tone test. For a highly linear device with IIP3 in point (B), the IM tone is below the noise floor and IIP3 is not measurable.

Another method to determine the linearity is to measure the CP_{1dB}, which measures the effect of component (b) in (1). Nevertheless, if the nonlinear component is too weak relative to the component (a), then a high amplitude signal source is needed to cause measurable nonlinearity. This large input signal requirement limits the measurement range of this method. Given a maximum RF source power of around 20 dBm, the nonlinearity can be measured on microresonators with CP_{1dB} less than 20 dBm, as shown in Figure 1(B). The corresponding IIP3 is about 29.6 dBm, which is given by [6]

$$IIP3_{dBm} = CP_{1dB} + 9.6 \tag{5}$$

This relation is an approximation based on (2). Because of the effect of mechanical filtering, (5) might not hold for every situation, and a detailed IIP3 model for the tested device is needed.

DESENSITIZATION METHOD

As shown in Figure 2, this work introduces a desensitization method to measure the linearity of HF CMOS-MEMS square-frame resonator that consists of four free-free beams connected at the nodal points of the first flexural resonant mode [9]. While introducing a low-frequency strong desensitizing tone at ω_d with high-frequency desired signal within the filter passband at ω_i, the insertion gain will drop due to the third-order intermodulation effect, which is similar to component (c) or (d) in (1). The advantages of this method are that: first, it measures only the resonant output signal, which is not affected by the off-resonance suppression. Second, due to lower frequency, it is easy to obtain a large-magnitude signal source for the desensitizing tone. This extends the measuring range for testing highly linear devices. Third, fewer instruments are required than in the two-tone test. This method needs only a network analyzer and one low-frequency signal source, compared to two high-frequency signal sources and a spectrum analyzer for the two-tone test.

The schematic of the measurement setup is shown in Figure 3. The input signal, $V_i \cos\omega_i t$, the input polarization voltage, V_p, and the desensitizing tone, $V_d \cos\omega_d t$, are applied across the input electrodes. Fundamental force and nonlinear forces are given by

$$F = \frac{\partial C_i}{\partial x}(V_i \cos\omega_i t - V_d \cos\omega_d t - V_p)^2 + \frac{\partial C_o}{\partial x}(V_{po})^2 \tag{6}$$

where C_i and C_o are input and output capacitance, x is the mechanical displacement and V_{po} is the output polarization voltage. With the assumption that mechanical displacement is much smaller than the electrode gap, (6) can be expanded into a Taylor series. With small electrode gaps, mechanical spring nonlinearities are negligible compared to the capacitive nonlinear effect [7]. The mechanical displacement is solved from the equation of motion with perturbation techniques [10]. The output voltage components at resonant frequency are

$$V_{O,fi} = [(i\frac{4C^2 Q V_p V_{po}}{g^2 K} - i\frac{32C^4 Q^3 V_d^2 V_p^3 V_{po}}{g^6 K^3} + \frac{8C^3 Q^2 V_d^2 V_p V_{po}}{g^4 K^2})V_i \\ - i\frac{72C^4 Q^3 V_p^3 V_{po}}{g^6 K^3} V_i^3 + ...]\omega_i Z \tag{7}$$

where C_i and C_o are replaced by C with the assumption of negligible mismatch, Q is the quality factor, g is the electrode gap, K is mechanical stiffness, Z is the transimpedance of the on-chip amplifier. The second and third terms of (7) are the first two substantial nonlinear output components for the tested device with the parameters listed in the Table 1. If the second term is the largest nonlinear component, the magnitude of output the voltage will decrease with increasing desensitizing voltage. However, if the third term is largest, the magnitude of the output voltage will increase with increasing desensitizing voltage.

EXPERIMENTAL RESULTS

The SEM picture of the tested resonator is shown in Figure 4. To model this resonator, results from a series of tests of sweeping input polarization voltage are shown in Figure 5. The resonant

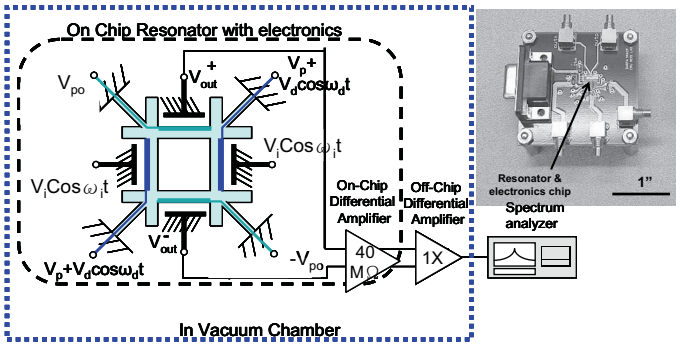

Figure 3. *The linearity measurement set-up for the desensitizing method and the perspective view of a resonator chip on a custom-designed test board.*

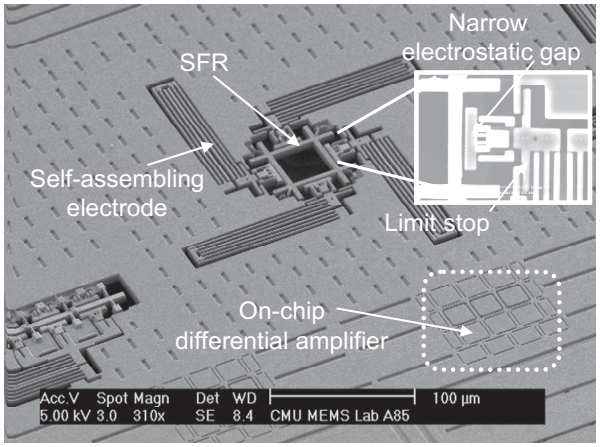

Figure 4. *The SEM picture of a SFR with self-assembling electrodes to provide small electrode gaps. [9]*

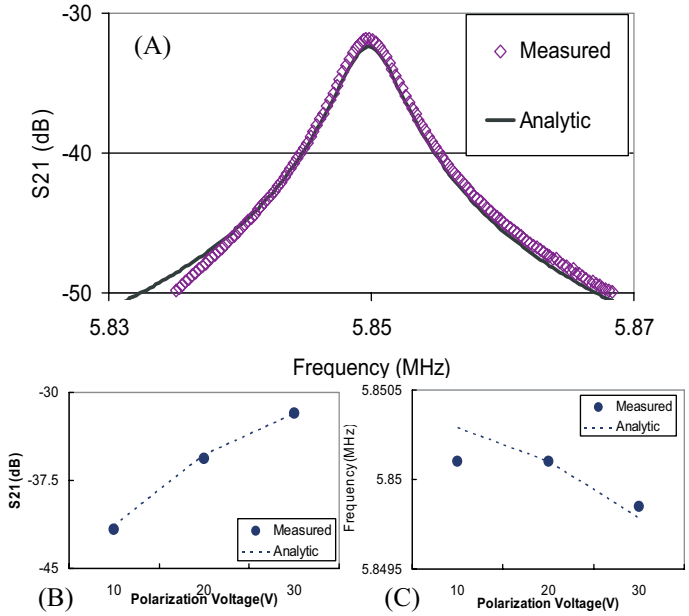

Figure 5. *(A) Measured response and analytic solution of SFR with V_p of 30 V, 20 mTorr of pressure, and V_{in} of 10 dBm for 1st flexural resonant mode. The parasitic effect is measured and subtracted. (B) and (C) are the extracted measured result and analytic solution of maximum S_{21} and resonant frequency versus V_p., respectively*

frequency is 5.849 MHz, the quality factor is 1268, and the insertion gain is -31.8 dB and -41.7 dB for V_p of 10 V and 30 V, respectively. Figure 5(A) shows the measured frequency response with the analytic solution, which is calculated from the features listed in the Table 1. The effect of input polarization voltage in the S_{21} and resonant frequency is measured and calculated, shown in Figure 5(B) and (C). The measurement result is consistent with analytic model, showing that increasing the V_p will increase S_{21} and lower the resonant frequency. The discrepancy at low V_p in the Figure 5(C) might result from the measurement error with small magnitude signal and insufficient measurement resolution.

Frequency responses with different desensitizing voltages are measured, shown in Figure 6. The measured maximum S_{21} values are extracted and plotted with the analytic solution in Figure 7. The analytic solution is modeled by (7) with the parameters listed in the Table 1 where the second component is the dominant nonlinear effect and causes S_{21} drop while increasing desensitizing voltage. With 20 Vac of desensitizing voltage, the S_{21} drops to 0.55 dB; this is slightly larger than analytic result of 0.49 dB. This measurement validates the features of tested device listed in the Table 1 and the nonlinear model based on (7).

In order to compare the linearity performance of different devices, the DP_{1dB} is defined as the magnitude of desensitizing tone to cause 1dB drop in S_{21}. Neglecting other nonlinear components except the dominant second term in (7), the DP_{1dB} is

$$DP_{1dB} = 0.116\frac{g^2K}{CV_pQ} \tag{8}$$

For the tested devices, the DP_{1dB} is 26.7 Vac. The CP_{1dB} is calculated to be 32 dBm, caused by the forth term in (7), related to DP_{1dB} by

$$CP_{1dB} = 20\log(\frac{DP_{1dB}}{0.16}) - 12.19 \tag{9}$$

This superior linearity is due to a medium size electrical gap of 0.84 μm, compared to the results in other work [7-8]. A plot of DP_{1dB}, CP_{1dB} and S_{21} versus electrode gap size is shown in Figure 8, which shows a trade-off between linearity and insertion gain in reducing electrode gap size.

The desensitization method is eventually limited by the nonlinear effects in amplifiers and the network analyzer, and by electrical breakdown on the tested device at high values of V_d. While there are strong tones along with fundamental tone in the input of amplifiers and network analyzer, the nonlinear effect of those stages blocks the fundamental tone, the mechanism of which is similar to the phenomena shown in (1). Output spectrums with

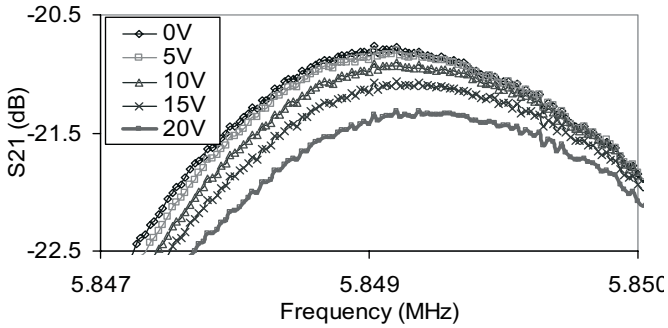

Figure 6. *Measured response of the SFR for different desensitizing voltages, V_d, with f_d = 1 kHz, V_p = 42.5 V, V_{po} = 45 V, pressure = 11 mTorr, and V_{in} = 10 dBm.*

Table 1. *Features of tested microresonators*

	Measured	Analytic
Beam Length(μm)	64.7	-
Beam Width(μm)	4.6	-
Beam Thickness(μm)	-	5.0
Input/Output Capacitor Width(μm)	-	20
Input/Output Capacitor Gap, g (μm)	-	0.84
Output Polarization Voltage,V_{po} (V) (for tests in the Figure 5)	20/-17.4	18.7
Input/output Polarization Voltage,V_p (V) (for tests in the Figure 6)	42.5/45	45.5/47
Mechanical Stiffness, K (N/m)	-	13942
Resonant Frequency(MHz)	5.849	5.849
Quality Factor, Q	1268	1268
S_{21}(dB) (for tests in the Figure 5, V_p=30V)	-31.8	-31.8
Input Power, P_{in}(dBm)	10	10
On-Chip Amp. Transimpedance, Z (MΩ)	-	40.6

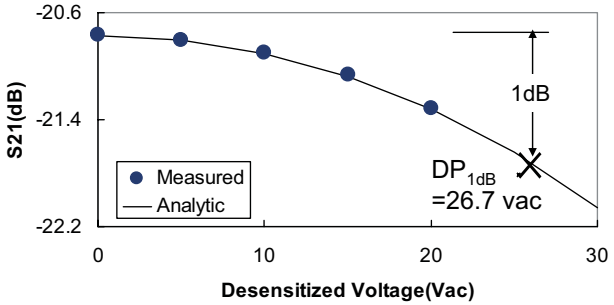

Figure 7. *Measured and analytic S_{21} versus the desensitizing voltage, V_d. The measured data is extracted from Figure 6 and the features applied in analytic model are listed in the Table 1.*

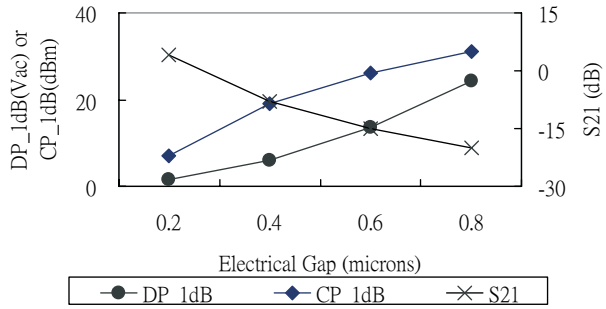

Figure 8. *Analytic results of DP_{1dB}, CP_{1dB} and S_{21} versus the electrode gap with the assumption that all the features listed in the Table 1 are constant when adjusting the electrode gap.*

different frequencies of the desensitizing tone and the magnitude difference between the fundamental tone, f_i, and the mixing tone, $(f_i–f_d)$, are shown in Figure 9. Since the magnitude of mixing tone is 12.5 dB smaller than the fundamental tone, the nonlinear effect of the amplifiers and network analyzer is insignificant.

Electrical breakdown on the tested device is the major limitation in this device. In one case, a combination of the V_d of 30 Vac at the f_d of 1 kHz with the V_p of 42.5 V has caused electrical breakdown of an input electrode on the microresonators. However, with improved layout to enhance the isolation of electrical wires, this range might be increased.

Another noticeable phenomenon is the magnitude drop with different f_d in the Figure 9, which results from the mechanical resonant shape. Even though this drop is not significant, it causes inaccuracy in the nonlinear models of (7) and the expression of DP_{1dB} of (8). A complete model is under development.

CONCLUSIONS

A new desensitization method of characterizing linearity of MEMS resonator filters is introduced. Verifications are performed on a CMOS-MEMS square-frame resonator, showing that the DP_{1dB} is 26.7 Vac and CP_{1dB} is calculated to be 32 dBm. This method is able to measure nonlinear effect of highly linear resonator filters, with a measuring range larger than that of a 1 dB compression test or a two-tone test. An analytical expression of 1 dB desensitization point was presented and verified, which can be used to balance the trade-off between linearity and signal gain in future resonator designs.

ACKNOWLEDGEMENT

This research effort was supported by the DARPA/MTO NMASP program under award DAAB07-02-C-K001.The authors would like to thank Suresh Santhanam for the developing the vacuum system and the helping with device processing.

REFERENCES

[1] Sheng-Shian Li, Yu-Wei Lin, Yuan Xie, Zeying Ren, and Nguyen C.T.-C.," Micromechanical hollow-disk ring resonators", *Technical Digest of 17th IEEE International Conference on MEMS*, Maastricht, The Netherlands(2004), pp. 821 – 824.

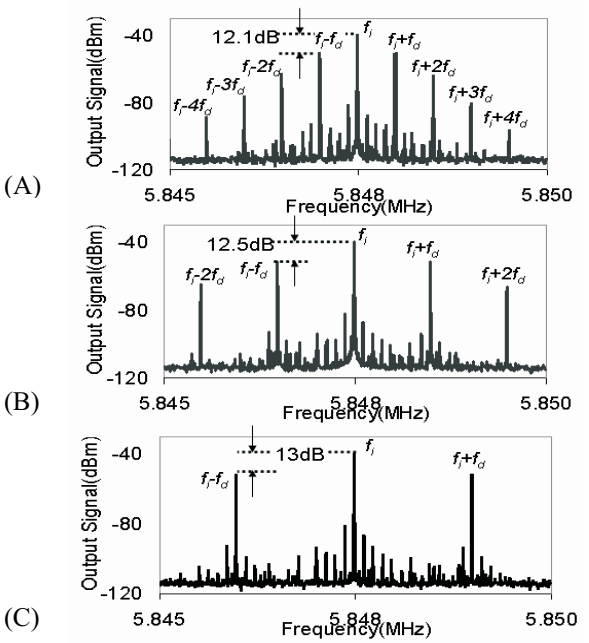

Figure 9. *Measured output spectrum of the SFR with input frequency of 5.8474 MHz along with desensitized tone of 15 Vac at different frequency, f_p,. (A) 0.5 kHz (B) 1 kHz and (C) 1.5 kHz*

[2] Ark-Chew Wong, and Nguyen C.T.-C., "Micromechanical mixer-filters ("mixlers")" *Journal of Microelectro-mechanical Systems*, V. 13, 2004, pp. 100 – 112.

[3] Liwei Lin, Howe, R.T., and Pisano, A.P., "Micro-electromechanical filters for signal processing", *Journal of Microelectromechanical Systems*, V. 7, 1998 pp. 286 – 294.

[4] Galayko, D., Kaiser, A., Buchaillot, L., Collard, D., and Combi, C., "Electrostatic coupling-spring for micro-mechanical filtering applications," *Proceedings of the 2003 International Symposium on Circuits and Systems*, Bangkok, Thailand (2003), pp. 530-533.

[5] Jacques C. Rudell, Jeffrey A. Weldon, Jia-Jiunn Ou, Li Lin, and Paul Gray, "An Integrated GSM/DECT Receiver: Design Specifications," *UCB Electronics Research Laboratory Memorandum*

[6] B. Razavi, *RF Microelectronics*, Prentice Hall, 1998

[7] Alastalo, A.T., and Kaajakari, V., "Intermodulation in Capacitively Coupled Microelectromechanical Filters," *IEEE Electron Device Letters*, VOL. 26, No.5, May 2005, pp. 289 – 291

[8] Navid, R.; Clark, J.R.; Demirci, M.; Nguyen, C.T.-C.;, "Third-order intermodulation distortion in capacitively-driven CC-beam micromechanical resonators," *Technical Digest of 14th IEEE International Conference on MEMS*, Interlaken, Switzerland (2001), , pp. 228-231.

[9] Chiung-Cheng Lo; Fang Chen; Fedder, G.K.;, "Integrated HF CMOS-MEMS Square-Frame Resonators with On-Chip Electronics and Electrothermal Narrow Gap Mechanism," *Digest of Technical Papers of The 13th International Conference on Solid-State Sensors, Actuators and Microsystems, Seoul, Korea(2005)* , pp. 2074-2077.

[10] Leonard Meirovitch, *Methods of Analytical Dynamics*, McGraw-Hill, 1970.

DESIGN & CHARACTERIZATION OF A MEMS THERMAL SWITCH

J.H. Cho[1], C.D. Richards[1], J. Jiao[2], D.F. Bahr[1], and R.F. Richards[1]
[1] School of Mechanical and Materials Engineering Washington State University, Pullman WA, USA
[2]Dept. of Physics, Portland State University, Portland OR USA

ABSTRACT

In this paper we present the design, fabrication, and characterization of a MEMS thermal switch. Three switch designs are considered: one in which the conductive material is in the form of liquid-metal micro droplets, one in which the conductive material consists of aligned carbon nanotube arrays, and one in which solid silicon contacts are used. The ratio of thermal resistance in the on and off conditions is used to characterize performance. Based on these measurements the switch incorporating liquid-metal droplets is superior to the other two switches. The liquid-metal switch has a thermal resistance off to on ratio of 168 and can provide heating rates of 905 ^{o}C/s.

INTRODUCTION

The ability to control heat transfer on small time and length scales could improve the performance of many micro devices; such as, thermoelectric micro-coolers, DNA amplification microchips, and some micro heat engines. First, it has been demonstrated that the performance of thermoelectric coolers could be nearly doubled if operated in a transient or pulsed mode [1,2]. Second, DNA amplification via PCR requires precise temperature control. The use of small sample sizes (~ 1 µl) and microfluidic devices has already dramatically reduced both the size and power needs of the equipment needed and the time required for DNA amplification [3]. Third, using waste heat to do mechanical work on the micro scale can be accomplished by controlling the flow of waste heat. For example, our group at Washington State University has demonstrated a MEMS-based micro heat engine that can harvest low-temperature heat to do mechanical work and produce electrical power [4].

To be able to control heat transfer to thermoelectric coolers, micromachined PCR devices and micro heat engines a type of thermal switch or thermal valve is required. Such a thermal switch would be able to change its effective thermal conductivity in order to turn heat transfer on and off. A figure of merit for such a device is the ratio of thermal contact resistance in the off and on positions, i.e., R_{off}/R_{on} of the switch. As shown in Fig. 1, a high thermal resistance, R_{off}, is required in the off position, so that the switch does not 'leak' heat. This off resistance is governed primarily by the thermal properties of the gap. A very low thermal resistance, R_{on}, is required in the on position, so that the heat transfer may be maximized. This on resistance depends primarily on the properties of the contacts used in the switch material.

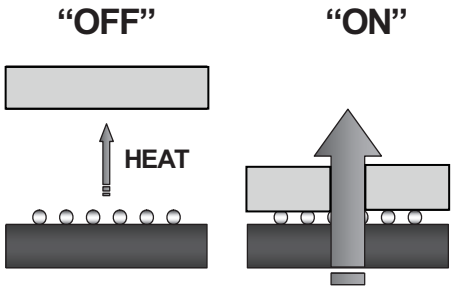

Figure 1. *Thermal switch concept.*

EXPERIMENTAL METHODS

In this paper we address the effect of the thermal contact material. The thermal resistance of thermal switches with patterned contacts of either liquid-metal micro droplets or vertically aligned carbon nanotubes are compared to the thermal resistance of thermal switches with solid silicon contacts. The speed of switching is assessed by measuring the transient temperature history of the switch under dynamic operation.

We have used two types of patterned arrays of contacts for thermal switches: liquid-metal micro droplets and vertically aligned carbon nanotubes (VACNT). The liquid-metal droplet arrays consist of a 40 x 40 grid of 1600 mercury, 30-µm diameter, micro droplets deposited via selective vapor deposition. The vertically aligned carbon nanotube arrays consist of bundles of multiwall carbon nanotubes patterned in the same grid and with the same diameter as the micro droplets. Arrays of liquid-metal micro droplets, Fig. 2, and arrays of VACNT's, Fig.3, are fabricated on a silicon die. A second silicon die is used to make and break contact

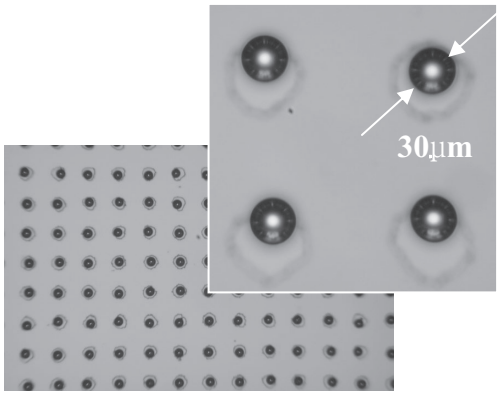

Figure 2. *Liquid-metal micro droplets.*

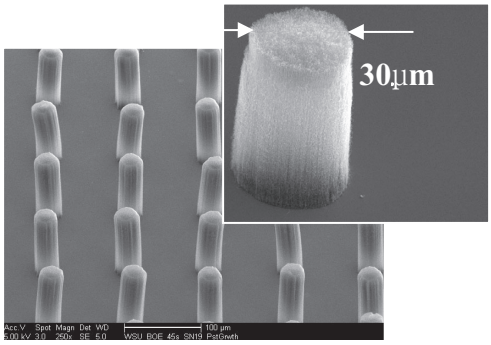

Figure 3. *Vertically aligned carbon nanotube arrays.*

with the micro-droplet or VACNT array. When the die is mechanically actuated to make contact, squeezing the thermal contact array between them, the thermal switch is in its "on" state. When the die breaks contact, creating a gas gap between the die, the thermal switch is in its "off" state.

Liquid-metal micro-droplet arrays are fabricated by preferentially condensing mercury vapor on gold targets patterned on the silicon die. First, wet oxidation is used to grow 100-nm thick silicon dioxide layers on both sides of a (100), 3-inch diameter silicon wafer. On the back side of the wafer, a 12-nm layer of titanium and a 175-nm thick layer of platinum are deposited using DC magnetron sputtering. Platinum Resistance Thermometers (PRT's) and heaters are fabricated by defining serpentine traces using a platinum-liftoff method. These PRT's and heaters are used to characterize the thermal switch. The front side of the wafer is sputtered with a 5-nm adhesion layer of titanium/tungsten followed by a 300-nm layer of gold. The gold is then patterned via photolithography to produce a 4 mm square, 40 x 40 pattern of 1600 20-μm diameter circular gold targets. The gold targets are subsequently covered with a 1.5-μm thick layer of photoresist. The photoresist is then etched around the gold targets as shown in Fig. 2. The 40 x 40 grids of circular gold targets on the front of the wafer are aligned directly opposite the resistance heaters and PRT's defined on the back of the wafer [5].

CNT growth is accomplished via a chemical vapor deposition (CVD) method. An iron nitrate sol gel catalyst is spun onto a wafer followed by photoresist and then patterned. A (100) silicon wafer is prepared for sol gel spin coating by etching in buffered oxide etchant (BOE) to remove the native oxide layer. Next, the sol gel solution is spun onto the silicon wafer. After cleaning, the iron containing silicon dioxide catalyst is patterned. A traditional photolithographic process is used to pattern the sol gel catalyst. Next, the wafer is exposed to UV light masked with a 1600 dot array identical to that used for the mercury droplet array. The photoresist is developed, and the wafer rinsed and dried. The wafer is then etched in BOE. After etching the photoresist is stripped, the wafer is cleaned, and then diced.

Multi-walled carbon nanotube growth is accomplished through the use of the CVD reactor. The sol gel patterned dies are placed in a ceramic boat in the center of a quartz tube, which is in turn inserted into a horizontal tube furnace. The tube is evacuated to 120 milliTorr and a three stage process follows: catalyst calcinations, catalyst activation, and MWCNT growth with an admixture of H_2 and C_2H_2. After the growth period, the tube is evacuated and allowed to cool to room temperature [7].

The MEMS thermal switches are first characterized under steady state conditions. The apparatus is shown in Fig 4. The test facility enables the control of the applied force squeezing the contacts (silicon surfaces, liquid-metal micro-droplet arrays or VACNT arrays) when the thermal switch is on, the thickness of the gas gap when the thermal switch is off, and the gas pressure in the gap. The silicon die, on which the thermal switch contacts are fabricated, the contact die, makes up the bottom half of the thermal switch. That contact die is mounted on the aluminum carrier shown in Fig. 4. A guard-heated calorimeter, used to measure heat transfer across the thermal switch, makes up the top half of the thermal switch [6]. The guard-heated calorimeter, also shown in Fig 4, consists of a silicon heater die, a heat flux sensor and a guard heater, all mounted on a rigid aluminum plate. In order to make thermal resistance measurements, the heat flux sensor is zeroed by controlling power delivered to the guard heater. Under this condition, all the electrical power dissipated in the silicon heater die is transferred as heat down through the thermal switch to the bottom contact die. The heat transfer rate across the switch is thus equal to the input power to the silicon heater die and is determined from the current supplied and the voltage drop across the heater. The temperature difference across the thermal switch is measured with PRT's micromachined on the top silicon heater die and the bottom contact die. The thermal resistance across the thermal switch is taken to be the ratio of the temperature difference across the thermal switch over the heat transfer rate across the thermal switch.

To characterize the dynamic behavior of the switch a radial heat flux sensor, shown in Fig. 5, has been designed and micromachined in silicon. The heat flux sensor consists of a 2-μm thick, 1.2-mm square membrane etched into a silicon wafer. Two concentric, annular platinum resistance thermometers (100-nm thick) are fabricated on the membrane at radii of 4.25-mm, and 5.5-mm respectively. A third PRT is defined in a square pattern at the center of the membrane. Measurements are made by periodically bringing the thermal switch contact die into and out of contact with the center of the membrane heat flux sensor. As the thermal switch contacts make and break contact with the membrane, the temperature of the contact die, T_1, the temperature at the center of the membrane heat flux sensor, T_2 , and the temperatures at the two concentric annular PRT's: T_3 at a radius of r_3 = 4.25-mm, and T_4 at a radius of r_4 = 5.5-mm are recorded. The heat transfer rate across the thermal switch can be determined from the temperature difference across the two annular PRT's [8]:

$$q = \frac{2\pi Lk(T_3 - T_4)}{\ln(r_4 / r_3)} \quad (1)$$

where L is the membrane thickness of the radial heat flux sensor , k is the thermal conductivity of the silicon membrane, and r_3 and r_4 are the respective radii of the temperature measurements.

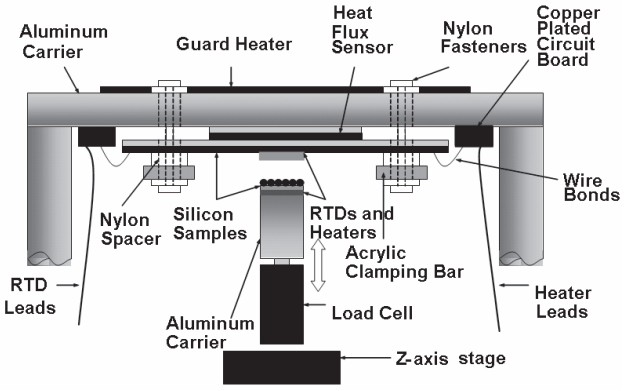

Figure 4. *Schematic of steady state heat transfer experiments.*

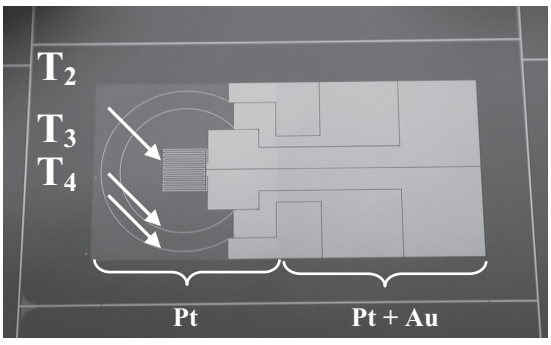

Figure 5. *Radial heat flux sensor.*

The temperature difference across the thermal switch is the difference between the temperature of the contact die, T_1, and the temperature at the center of the membrane heat flux sensor, T_2. The thermal resistance across the thermal switch is once again taken to be the ratio of the temperature difference across the thermal switch over the heat transfer rate across the thermal switch.

The movement of the contact die into and out of contact with the membrane heat flux sensor is controlled by a piezo stack actuator. The displacement of the thermal switch contact die is measured with laser vibrometer. The load applied as the contact die comes into contact with the membrane heat flux sensor is measured with a *S* type load cell which is attached between the piezo stack actuator and the thermal switch contact die.

RESULTS

Three switch conductor materials were tested, polished silicon surfaces, Hg micro droplets, and VACNT's. All measurements for steady state conditions were obtained in a reduced pressure atmosphere of air at 0.45 Torr. The results for the three switches in the off state are shown in Fig. 6. The thermal resistance of the "off" condition is characterized with respect to the gap thickness between the top and bottom dies. In the off position, the three switches have essentially the same thermal resistance. The thermal resistances for the three contact dies are seen to increase from 130 ^{o}C/W when the gas gap thickness is 20 microns, to 150 ^{o}C/W when the gas gap thickness is 100 microns, close to the mean free path length of 126-μm for these conditions.

The thermal resistance of the "on" condition switch is characterized as a function of the applied load squeezing the switch closed. These data are shown in Fig. 7. For the closed, switch "on", condition, the thermal resistance of the contacts controls the heat transfer. For the Hg micro-droplet array the thermal resistance varies from 1.2 ^{o}C/W at an applied load of 0.1 N to 0.6 ^{o}C/W at 1 N. The thermal resistance of the VACNT array varies from 32 ^{o}C/W at an applied load of 0.1 N to 15 ^{o}C/W at 1 N. The silicon die contacts have a thermal resistance that varies for varies from 49 ^{o}C/W at an applied load of 0.1 N to 34 ^{o}C/W at 1 N. In the on position, the Hg micro droplets have the lowest thermal resistance. The relatively high values of the VACNT and silicon switches are due to contact resistance. The mechanisms for the contact resistance in the two switches are different. In the silicon to silicon switch the presence of asperities, contaminants, or other imperfections in the two mating surfaces can lead to a condition in which the actual contact area is severely reduced. Heat transfer then occurs primarily by conduction through the gas gap. In the case of the VACNT structures the contact resistance is governed by much more complex interface phenomena that are currently an active area of research.

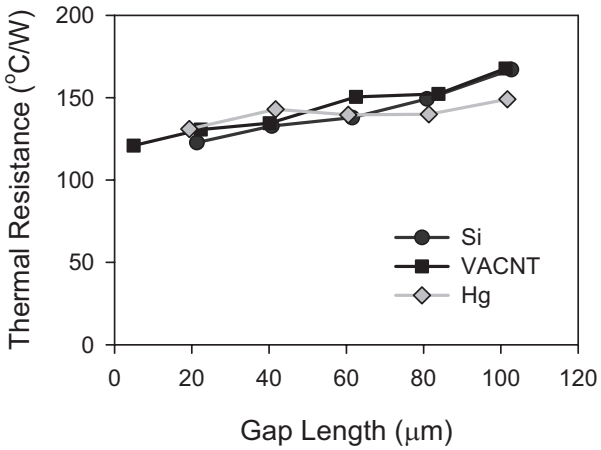

Figure 6. *Thermal resistance for switch off.*

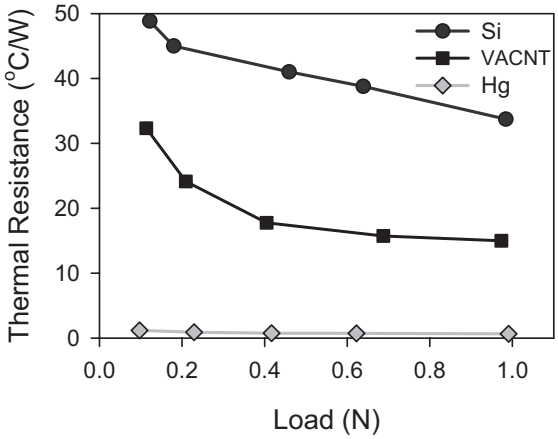

Figure 7. *Thermal resistance for switch on.*

The performance of the thermal switches may be characterized by the nondimensional ratio of the "off" state thermal resistance to the "on" state thermal resistance: R_{off}/R_{on}. For the Hg micro droplet switch the thermal resistance ratio, R_{off}/R_{on}, is 168. The value of R_{off}/R_{on} for the VACNT switch is 6.8 and for the silicon-silicon switch is 3.4. The Hg micro-droplet switch is clearly superior.

The dynamic response of a liquid-metal switch is shown in Fig. 8. The test was performed in a reduced pressure atmosphere of air at 0.1 Torr. The time history of four temperatures are

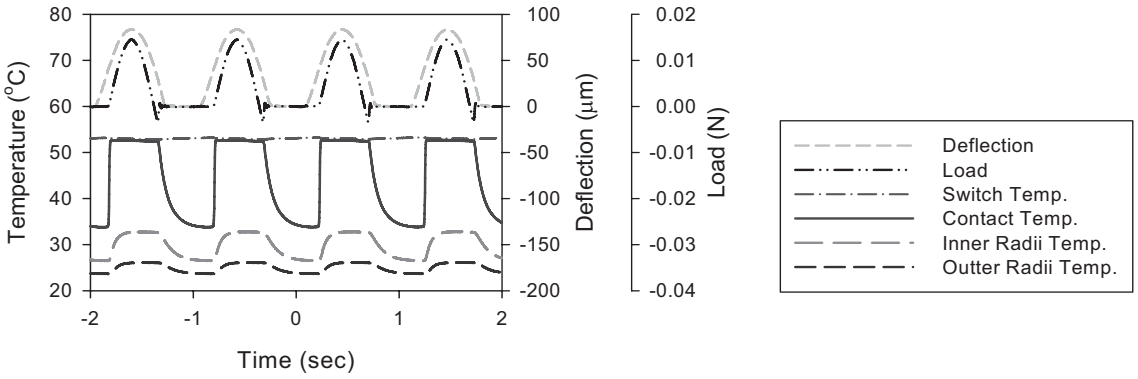

Figure 8. *Dynamic behavior of thermal switch.*

shown: the switch temperature (T_1) of the micro-droplet array die, the center contact temperature (T_2), along with the radial heat flux sensor's inner and outer radii temperatures (T_3 and T_4). The switch deflection and applied load are also shown. The location of T_2, T_3, and T_4 are shown in Fig 5.

As the lower die, with the liquid-metal micro-droplet arrays, contacts the center of the heat flux sensor (on the top die), the switch turns "on" and the temperature increases. This occurs in 0.02 seconds as seen in Fig. 9. The figure shows a 0.02 second window of one of the contact events depicted in Fig. 8. The switch turns "on" at t = 0.22 seconds and the temperature increases from 34.4 ^{o}C to 52.5 ^{o}C over a span of 0.02 seconds. The heating rate is thus 905 ^{o}C/sec. The heat transferred is determined from the radial heat flux sensor measurements of T_3 and T_4 when the switch is on. In this case T_3 and T_4 are 32.8 ^{o}C and 26.1 ^{o}C respectively which yields a heat transfer rate of 51 mW from Eqn (1).

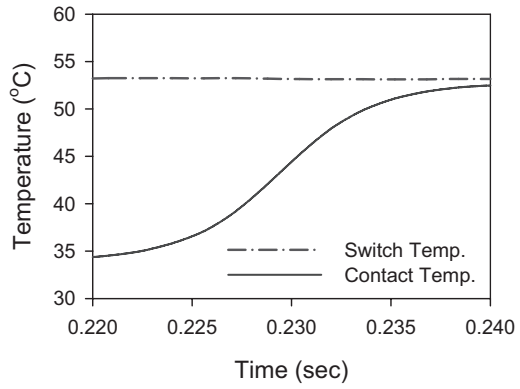

Figure 9. *The switching speed of the thermal switch.*

SUMMARY

In this work the design, fabrication and testing of a thermal switch are presented. Three switch conductor materials were tested: polished silicon surfaces, arrays of Hg micro droplets, and arrays of VACNT's. The switch performance was characterized by the ratio of thermal resistance in the switch off to on position. The on state thermal resistances of the VACNT switch and the silicon contact switch showed relatively high values of contact resistance. The liquid-metal micro-droplet switch showed a much smaller contact resistance at the same applied load. As a result, the liquid-metal micro-droplet switch had the best performance of the three switches tested with an off to on thermal resistance ratio of 168. The switching speed of the Hg micro-droplet switch was shown to be on the order of 0.02 seconds, realizing heating rates of 905 ^{o}C/sec.

REFERENCES

[1] A. Miner, A. Majumdar and U. Ghoshal, "Thermomechanical refrigeration based on transient thermoelectric effects," *Applied Physics Letters*, 75, 1176-1178, (1999)

[2] G. J. Snyder, J-P. Fleurial, T. Caillat, R. Yang and G.Chen, "Supercooling of Peltier cooler using a current pulse," *Journal of Applied Physics*, 92, 1564-1569, (2002)

[3] C.T. Wittwer, G.C. Fillmore and D.J. Garling, "Minimizing the time required for DNA amplification by efficient heat transfer to small samples," *Anal. Biochem*., 186, 328-331, (1990)

[4] S. Whalen, M. Thompson, D. Bahr, C. Richards and R. Richards, "Design fabrication and testing of the P3 micro heat engine" *Sensors & Actuators: A. Physical*, 104, 200-208 (2003).

[5] J.H. Cho, T. Wiser, C.D. Richards, D.F. Bahr and R.F. Richards, "Fabrication and Characterization of a Thermal Switch," *Sensors and Actuators,* in press.

[6] T. Wiser, "Steady State Heat Transfer Characterization of a Liquid Metal Thermal Switch," MS Thesis, WSU, 2005

[7] C. M. McCarter, D.F. Bahr, R.F. Richards, C.D. Richards, D. McClain, and J. Jiao, "Integration of Carbon Nanotubes with MEMS through Standard Photolithographic Techniques, *MS&T 2005, Nanomaterials Symposia*, Pittsburgh, PA, September, 2005.

[8] Frank P. Incropera and David P. DeWitt, Introduction to Heat Transfer, Fourth Edition, John Wiley & Sons, Inc., 104-107, (2002).

DESIGN, FABRICATION, AND CHARACTERIZATION OF A MICROTURBOPUMP FOR A RANKINE CYCLE MICRO POWER GENERATOR

Changgu Lee[1] , Mokhtar Liamini[2], Luc G. Fréchette[1, 2]

[1] Columbia University, Department of Mechanical Engineering
220 Mudd bldg, MC 4703, New York, NY 10027, USA
[2] Université de Sherbrooke, Department of Mechanical Engineering
2500 boul. Universite, Sherbrooke, QC, J1K 2R1, Canada

ABSTRACT

A microfabricated turbopump has been designed, fabricated and experimentally characterized as the core component of a micro steam turbine power-plant-on-a-chip, which aims to implement the Rankine thermal cycle for micro power generation. The device consists of a four-stage radial planar type turbine and a spiral groove viscous pump supported on gas-lubricated bearings. The device is composed of five wafers: one glass wafer, one SOI wafer, and three silicon wafers. The silicon and SOI wafers are patterned using shallow and deep reactive ion etching (total of 14 masks), while the Pyrex glass wafer are ultrasonically drilled. Anodic bonding, fusion bonding and manual assembly with alignment structures were then used to complete the device and enclose the 4 mm diameter rotor. In a test using compressed air to drive the turbine, the rotor was spun up to 116,000 rpm, which corresponds to 25m/s in tip speed producing 0.073 W of mechanical power, and the pump pressurized water by 88kPa with a flow rate of 4mg/s. The pump performance chart was also completely characterized for speeds up to 120,000 rpm. A 1-D pump model based on lubrication theory has shown close agreement with the data and predicted 7.2% of maximum pump efficiency over the range of operating speeds.

INTRODUCTION

As high-tech products such as portable electronics, distributed sensors, small scale actuators, and micro vehicles are being developed and improve in functionality, the demand is increasing for compact power sources with high energy and power per unit volume that could replace batteries with relatively low power density. MEMS heat engines have the potential for these applications, providing the benefits of high power production per unit volume from the small size, and low production cost from batch fabrication technology.

Among the heat engines, a micro Rankine cycle steam turbine is a good candidate for micro power generations, leveraging the technology developed for micro gas turbines [1]. The Rankine vapor cycle is similar to the Brayton gas cycle implemented in gas turbine engines in that they use turbines to convert fluid energy to mechanical energy. But, the critical difference is in the pressurization process, for which the gas cycle uses the air compressor, while the vapor cycle uses a liquid pump. Even though the gas cycle is typically able to achieve high efficiency by increasing the turbine inlet temperature, the viscous effect which dominates the efficiency of the compressor at small scales reduces the efficiency of the system as a whole. In contrast, the pump work in the vapor cycle is significantly small compared to the energy produced by the turbine such that it does not affect the overall efficiency of the system substantially, even at small scales. Therefore, the micro Rankine cycle steam turbine has the characteristics necessary to become an alternative to batteries in high power density applications due to its acceptable efficiency and low cost when incorporated with MEMS technology [2].

In order to demonstrate the concept of the micro Rankine power generation system, a microturbopump has been developed using silicon microfabrication techniques, such as deep etching and multiple wafer bonding. This device consists of a steam turbine and a viscous pump supported on a gas-lubricated bearing system, forming the core energy conversion component of the Rankine system. This paper presents our recent accomplishments in the development of this rotating subsystem for a Rankine power MEMS, complementing the turbine characterization previously reported [3].

DEVICE LAYOUT AND DESIGN APPROACH

The turbopump converts thermal-fluidic energy of flow through the turbine into mechanical energy to drive a pump and other loads acting on the rotor. The components of the device include a turbine, pump, main thrust bearing, auxiliary thrust bearing, journal bearing, and seals as illustrated in Figure 1. Pressurized gas comes into the inner radial position from the top side and flows radially outward through the blade rows of the turbine, spinning the rotor. Simultaneously, water is drawn from the bottom side by the pump with spiral groove patterns and is discharged to the center of the bottom side of the device. In order to prevent flooding in undesired areas, a seal with partial grooves is installed on the bottom side of the rotor surrounding the pump. A hydrostatic thrust bearing with small circular nozzles keeps the rotor axially balanced by supplying force from the bottom side against the pressure force acting on the turbine side. A hydrostatic journal bearing, which surrounds the rotor as a circular gap, helps keep lateral balance by providing a restoring force as described in previous work [4].

Among the components, the turbine and thrust bearing (TB) have novel configurations, different from the previous MEMS gas turbomachinery [1],[4]. The turbine has a multi-stage configuration to potentially achieve high pressure ratio for reasonable efficiency of the whole Rankine thermal system, and the thrust bearing system is designed to exert the thrust force only from one-side with the goal of developing a self-supporting bearing system. The pump and seal have spiral groove patterns on the surface to draw and pressurize the fluids using viscous drag. Especially, the dynamic pressurization of the seal due to the spiral patterns was necessary in order to ensure the successful performance of the pump by confining the liquid flow in the center area. The journal bearing (JB) was directly inspired from previous work at MIT [4].

Low order models have been developed and used for component and system-level design [5], including: 1) a turbine

model based on mean line analysis with loss correlations extracted from CFD ; 2) a flow resistance model for the thrust bearing; 3) models based on lubrication theory for the pump and seal. They were combined to design a micro turbopump system with desired performance levels while satisfying power balance (production versus consumption), as well as rotor axial position balance. The device was designed to produce 4.7W of mechanical power from steam with 200°C and 3 atm of turbine inlet conditions and to pump water pressurizing 4.5 atm at rotor tip speed of 260 m/s. The turbine, whose diameter is 4 mm, has approximately 1200 blades with 100 um of chord length and 50 um of height, and the viscous pump has 16 grooves with 6 um of depth (Figure 2). The journal bearing is 380 um deep and 10 um wide when the rotor is centered. The thrust bearing consists of 34 nozzles with 10 um of width and 85 um of depth [5].

FABRICATION

The complete device is made of five wafers as shown in Figure 1: one Pyrex glass wafer (wafer A), one silicon-on-insulator (SOI) wafer (wafer B), and three silicon wafers (wafers C, D, and E). The glass wafer is mechanically machined using ultrasonic drilling, and the others are fabricated using photo-lithography, reactive ion etching (RIE), and deep reactive ion etching (DRIE). The processing of each wafer is illustrated in Figure **3** and goes as follows:

Wafer A: The holes are formed by ultrasonic drilling.

Wafer B: Using nested masks, the top side is deep etched twice to reach the oxide layer, and the other side is patterned and also etched to the oxide layer. Then, the oxide layer is removed by buffered oxide etchant (BOE) to complete through-wafer holes.

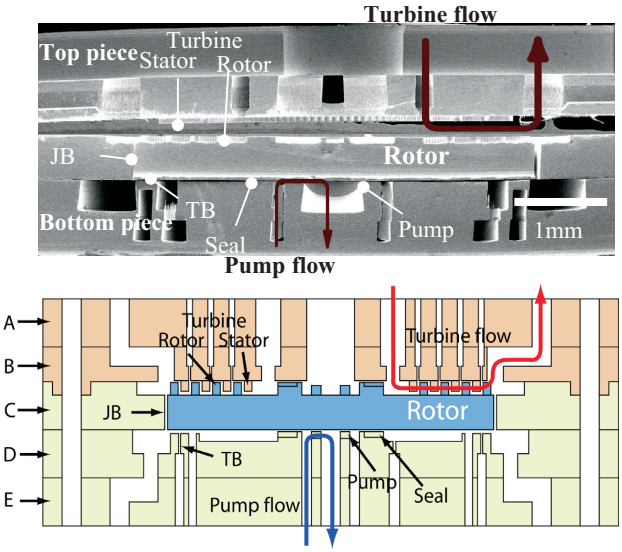

Figure 1. *SEM image (top) and schematic (bottom) of the cross-section of a device. The letters (A to E) identify the 5 wafers.*

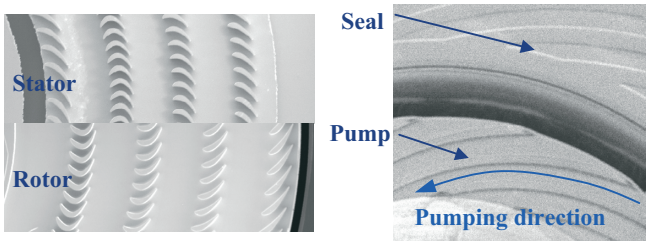

Figure 2. *SEM images of turbine (left) and pump (right). The length of turbine blades is about 100um. The outer radius of the pump is 550um.*

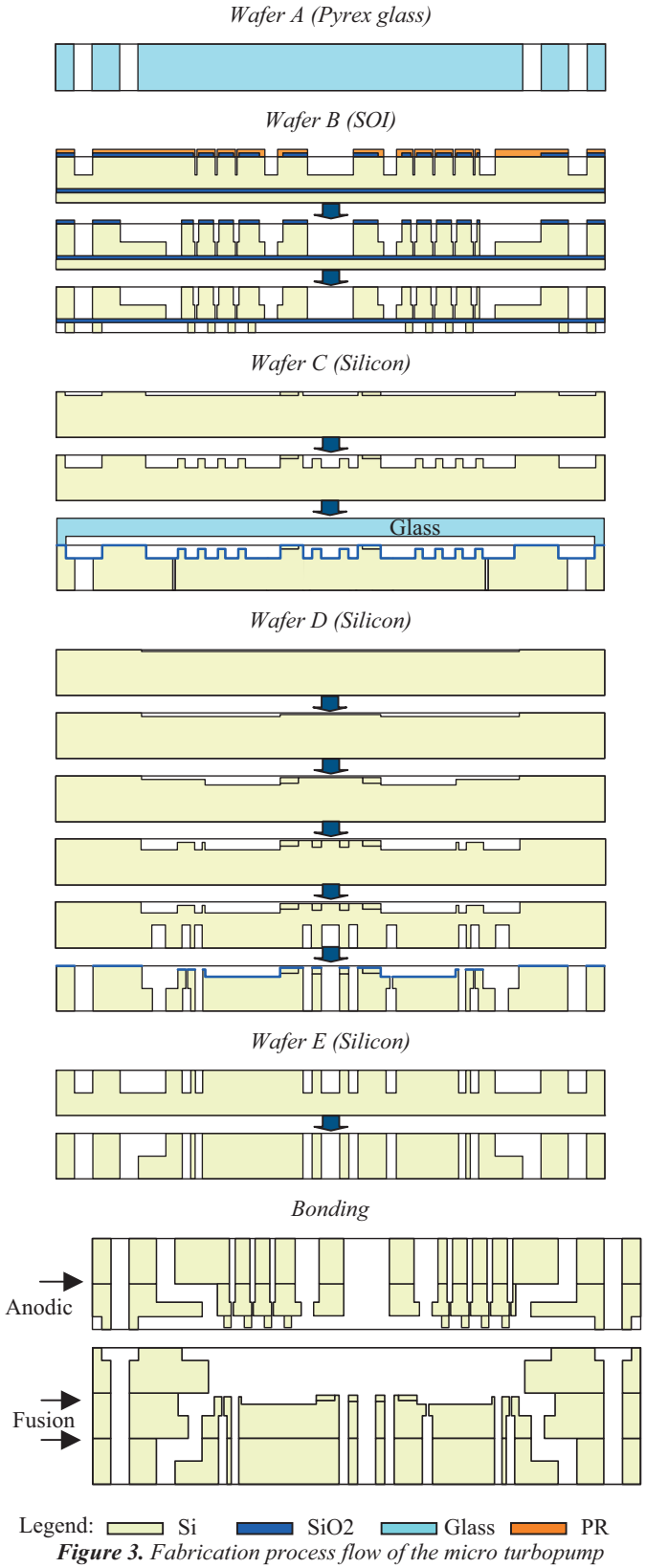

Figure 3. *Fabrication process flow of the micro turbopump*

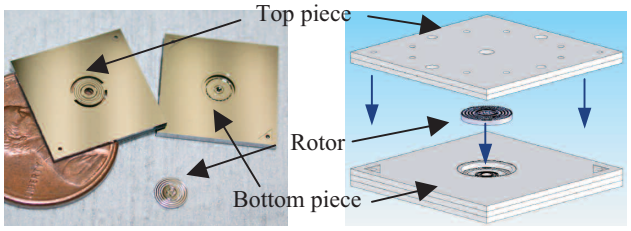

Figure 4. *Micro turbopump device (left) and assembly process (right). The dimension of the assembled device is 15×15×2.3mm^3.*

Wafer C: The top side receives a shallow etch at first, and a deep etch to form the rotor blades. Then, the oxide is deposited by plasma-enhanced chemical vapor deposition (PECVD) to protect the surface during the through etch from the other side. The journal bearing is created by a deep etch from the bottom side, defining the rotor. A glass handle wafer was attached to prevent the rotor from falling in the chamber when it is cut out. It is removed and kept separately from the wafer after clearing the oxide layer.

Wafer D: At first, the top side receives four shallow etches. Subsequently, the bottom side is etched half way through with the top side covered by an oxide layer for surface protection. Finally, the top side is patterned and etched until through holes are formed.

Wafer E: The wafer is etched half way through from both sides to create channels and holes.

Overall 14 photomasks were used, and 4 shallow silicon etching, 10 deep silicon etching, and 3 PECVD oxide deposition steps were performed. After the wafers are completed, they go through the cleaning processes such as oxide removal using buffered oxide etchant (BOE) and MOS (or RCA) clean. Then, the wafers are aligned and contacted. The glass wafer and SOI wafer are pressed with a slight force of 25N and remain in contact for 10 minutes in vacuum at 350 °C, with 1000 Volts applied for anodic bonding. The other wafers are pressed with a force of 1700N for 30 seconds in vacuum. They are then annealed at 1000 °C for 1 hour in the nitrogen environment for strong fusion bonding.

After completing the fabrication process, the device has three pieces as shown in Figure 4. The top piece is the stack of wafers A and B, and the bottom piece the stack of wafers C, D, and E. The device is assembled by inserting the rotor into the center hole of the bottom piece and aligning the top piece to the bottom piece using alignment features in the corners of the mating surfaces, which consist of triangular holes and circular pins.

DEVICE CHARACTERIZATION

The assembled device is placed in a test package, which is made of flexiglass. The channels in the device are connected to the package through rubber o-rings to allow supply and discharge of the working fluids (gas and liquid). Compressed air was supplied to operate the bearing system and drive the turbine. The gap between the rotor and the surface of the pump grooves was kept almost constant during the tests by regulating the thrust bearing flow rate, and was assumed to be 1μm in the modeling. Turbine and bearing operation have previously been characterized up to 300,000 rpm [3].

To characterize the pump, water is introduced at its inlet with the flow controlled by a downstream valve and its flow rate is measured using a digital mass flow meter. Using this approach, the pump performance chart was completely characterized for speeds up to 120,000rpm (Figure 5). The pump valve was regulated to vary the flow rate from zero to maximum for a fixed rotor speed. A maximum pressure rise of 240 kPa (valve closed) and maximum flow rate of 9 mg/s (valve fully open) were achieved at a speed of 120,000 rpm. The pump model has shown close agreement with the data and predicted 7.2% of maximum pump efficiency over the range of operating speeds, which is at least one order of magnitude superior to other MEMS pumps, with efficiencies typically less than 0.1%.

The overall turbopump performance was characterized by keeping the valve opening fixed and measuring inlet and outlet conditions of the turbine and pump (Figure 6). In this test, the rotor was spun up to 116,000 rpm, which corresponds to 25m/s in tip speed, with 41kPa of turbine differential pressure and 24mg/s of turbine flow rate, while the pump pressurized water by 88kPa with a flow rate of 4mg/s. The pump model suggests that the pump efficiency remains constant at its maximum over the operating range, and the calculation result agrees well with the data (Figure 7). At the maximum speed achieved, the turbine model predicts 0.073 W of mechanical power production and an isentropic efficiency of 16% with Re=186.

Based on the system model calculation, out of the total power produced by the turbine, 10% was consumed by the viscous pump, while the rest was dissipated by other components through viscous drag (Figure 8). In the calculation, the ungrooved part of the seal was assumed to be wet. In Figure 8, the chart was obtained for the maximum speed, but the distribution was similar for other speeds. Turbine bar indicates power production, while the others represent consumption or dissipation. The thrust bearing (TB) and seal were intentionally designed for high drag in order to mimic the load of a generator that would be integrated on the rotor for a Rankine cycle micro power generator. These results suggest that up to 75% of the turbine mechanical power could be available for power generation with redesigned seals and thrust bearing.

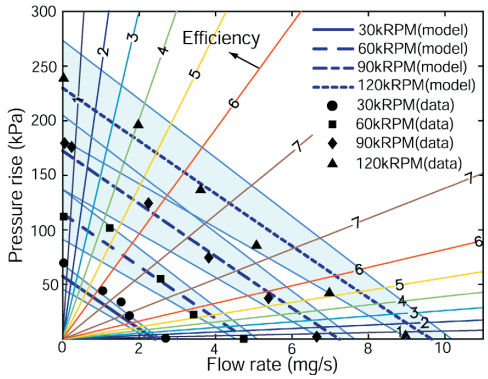

Figure 5. *Pump performance chart (pressure rise versus flow rate) for various rotor speeds. Shaded areas represent uncertainty of the gap between the rotor and the pump in modeling, which is 1+/-0.25um. Contours of pump efficiency (in percent) are also shown, emanating from the origin.*

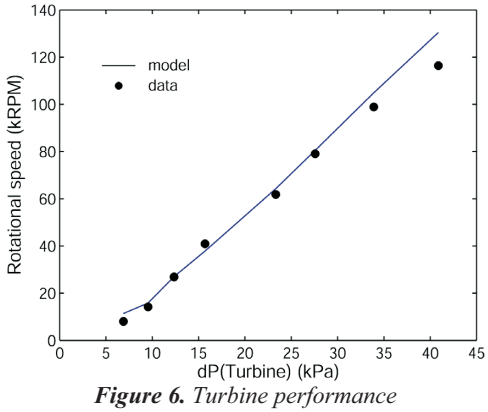

Figure 6. *Turbine performance*

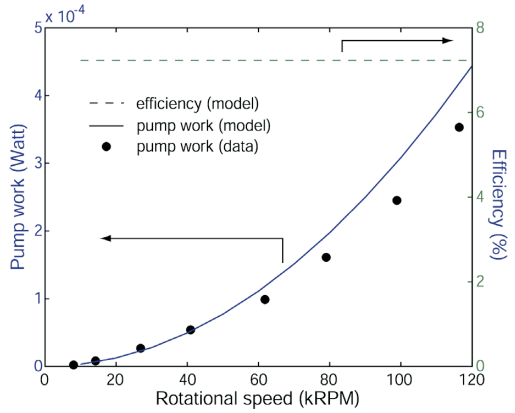

Figure 7. Pump performance. The pump work is defined as the product of the pressurization and the volumetric flow rate, which were individually measured, and the pump efficiency as the ratio of pump work to consumed power by viscous drag in the pump.

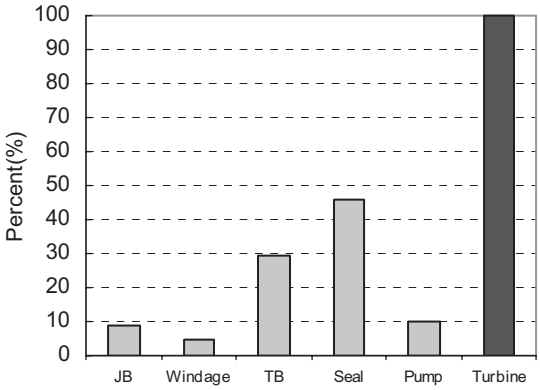

Figure 8. *Power consumption budget of the turbopump (model)*

PROJECTED PERFORMANCE OF A MICRO RANKINE POWER GENERATOR

The measured performance, especially the rotor speed, is still far lower than designed. However, these and previous results [3] validate our component and system models. Based on the model predictions at the design speed, the turbine would have 70% of isentropic efficiency and the pump 7%. This estimation of the efficiencies is close to the assumptions of Mueller and Fréchette [6], which suggest that the whole micro Rankine power generation system could produce several watts of electric power with 1-12 % of thermal efficiency, depending on the heat addition and discharge conditions, for a similar size device as the current one.

As expected, the pump efficiency is relatively low compared to the MIT micro compressor (50-70 % in optimum operations [1]), which is part of the Brayton cycle micro gas turbine. However, the power consumed by the pump is almost trivial compared to the turbine power available. In contrast, the micro compressor inherently consumes a large portion of the turbine-generated power, which results in poor thermal efficiency for a micro gas turbine of about 2-3 % [7].

CONCLUSION

A micro turbopump device with a multi-stage turbine and viscous pump supported on gas-lubricated bearings has been developed and demonstrated. The device was designed using analytical models supported by CFD, and was made of five bonded wafers, which went through 14 photolithography and etching processes. The 4 mm diameter rotor was spun up to 116,000 rpm pumping water at the rate of 4mg/s with 88kPa of pressurization. At the maximum speed reached, the turbine produced 0.073W of mechanical power, of which 10% was consumed by the viscous pump. The pump performance chart was also completely characterized for speeds up to 120,000rpm, and has shown 7.2% of maximum efficiency over the range of operating speeds. The rotational speed was limited by axial balance limitations and work is on-going to increase the operating range. Based on the test results, the improvement in operating speed is expected to lead to reasonable thermal efficiency of the whole Rankine power generation system.

This work proves the concept of the rotating subsystem for a micro Rankine power system and provides a validated design basis for future development. The technology demonstrated herein will also contribute to the development of other types of power MEMS, such as gas turbines, coolers, and pumps.

ACKNOWLEDGEMENTS

This work was supported by the NASA Glenn Research Center, Alternate Fuels Foundation Technologies program (contracts NAS3-02118 and NAS3-03105), monitored by Dr. Glenn Beheim. The authors gratefully acknowledge this support.

The fabrication work was performed in part at the Cornell NanoScale Science and Technology Facility (CNF), a member of the National Nanotechnology Infrastructure Network, which is supported by the National Science Foundation (Grant ECS 03-35765).

REFERENCES

[1] A. H. Epstein, "Millimeter-Scale, Micro-Electro-Mechanical Systems Gas Turbine Engines," Journal of Engineering for Gas Turbines and Power, Vol. 126, pp205-226, April 2004.

[2] L. G. Fréchette, C. Lee, S. Arslan, Y. C. Liu, "Design of a Microfabricated Rankine Cycle Steam Turbine for Power Generation," Proc. ASME Int'l Mech. Eng. Congress and Expo. (IMECE'03), Washington, D.C., November 16-21, 2003.

[3] C. Lee, and L. G. Fréchette, "Demonstration and characterization of a Multi-Stage Silicon Microturbine," Proc. ASME Int'l Mech. Eng. Congress & Expo., Orlando, FL, November 5-11, 2005, Paper IMECE2005-81435

[4] L. G. Fréchette, , S. A. Jacobson, K. S. Breuer, F.F. Ehrich, R. Ghodssi, R. Khanna, C.W. Wong, X. Zhang, M.A. Schmidt, A.H. Epstein, "High-Speed Microfabricated Silicon Turbomachinery and Fluid Film Bearings," *IEEE/ASME J. of MEMS*, Vol. 14, No.1, 2005.

[5] C. Lee, "Development of a microfabricated turbopump for a Rankine vapor power cycle," Ph.D Thesis, Columbia University, February 2006.

[6] N. Mueller, and L. G. Fréchette, "Performance Analysis of Brayton and Rankine Cycle Microsystems for Portable Power Generation," Proc. ASME Int'l Mech. Eng. Congress & Expo., New Orleans, Louisiana, Nov. 17-22, 2002.

[7] J. M. Protz, "An Assessement of the Aerodynamic, Thermodynamic, and Manufacturing Issues for the Design, Development, and Microfabrication of a Demonstration Micro Engine," Ph.D Thesis, Massachusetts Institute of Technology, September 2000.

DEVELOPMENT AND CHARACTERIZATION OF HIGH-SENSITIVITY BIOINSPIRED ARTIFICIAL HAIRCELL SENSOR

Nannan Chen, Jack Chen, Jonathan Engel, Saunvit Pandya, Craig Tucker, and Chang Liu
Micro Actuators, Sensors, and Systems Group, University of Illinois at Urbana-Champaign
Urbana, IL, USA

ABSTRACT

We report the development of a high sensitivity artificial haircell (AHC) sensor that employs high aspect-ratio cilium (up to 700μm tall) made of SU-8 epoxy and silicon piezoresistive strain sensors. In this work, we demonstrate the application of the artificial haircell for underwater flow sensing. For device characterization, we have performed deflection testing, resonant frequency testing, sensitivity threshold testing and preliminary dipole field response experiments. We have demonstrated a flow rate sensitivity of 2mm/s.

INTRODUCTION

In numerous biological species, the hair cell sensor serves as the building block to fill a variety of sensing needs, including sensing vibration, flow, and touch [**1-2**]. Figure 1 shows the example of a spider's flow receptor hair cell sensor. It is based on organic materials but can detect sub-nm dendritic displacement and the slight breezes caused by nearby predators or prey. The functions of hair cells have been very closely studied by biologists over the years, but only in recent years, with the development of micromachining techniques have researchers started to mimic the stimulus-transmission mechanism of biological sensing system [**3-5**]. Existing haircell sensors are based on various sensing methods, but the sensors are either not sensitive enough to detect very low flow speed (on the order of several mm/s) or they require parallel arrays of sensors to achieve such sensitivity. In this work, we present the design of an AHC sensor that is both highly sensitive and efficient, that is we are able to detect very low flow speed using a single sensor.

DEVICE DESIGN

The device mimics the structure of a biological hair cell sensor. It consists of a cilium-like hair sitting on a paddle-shaped cantilever with doped silicon strain gauges at the base. A schematic drawing of the AHC is shown in Figure 2. Figure 3 shows an SEM of an actual device.

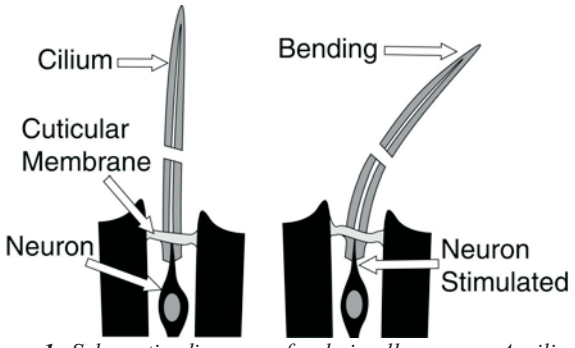

Figure 1. *Schematic diagram of a haircell sensor. A cilium is attached to a neuron. When the cilium is displaced by mechanical stimulus (originating from vibration, flow impingement, contact, etc), the neuron provides electrical output.*

For the cantilever-cilium configuration, the drag force acting on the cilium is completely transferred to the distal end of the cantilever. The system can then be simplified to a moment loaded cantilever:

$$\varepsilon = \frac{6M}{Ewt^2}$$

where ε is the strain, M is the moment, E is the Young's modulus for silicon, w is the cantilever width and t is the cantilever thickness. The thickness is chosen to be 2μm for fabrication feasibility and good sensitivity. Based on existing signal processing circuitry and achievable piezoresistive gauge factors, we assume the minimum strain the system can detect is 2.5 micro-strain. Given a desired minimum detectable flow speed of 1mm/s, M is now a function of the cilium height and diameter. Figure 4 is a 3-D map that shows what cantilever width design will satisfy these requirements as a function of cilium height and diameter.

For single spin SU-8 process, 600μm height and 80μm diameter are reasonable values for cilium dimensions. Based on these cilium dimensions, the cantilever width is determined to be 40μm. The length of the cantilever is chosen so that the resonant frequency is on the order of several KHz.

The strain gauges are achieved by ion implantation. The ion implantation is performed on very lightly doped n-type sample with boron as dopant. To optimize the performance of the stain gauge, we have chosen the ion implantation parameters so that the doping depth is approximately 1/3 of the total beam thickness and the doping concentration is on the order of $1x10^{20}cm^{-3}$ [**6**]. The effective gauge factor is experimentally determined to be 33.6, which includes all contact and parasitic resistances. The output of the sensor is read out using a Wheatstone bridge. All resistors of the Wheatstone bridge are defined on chip during ion implantation to minimize the thermal noise of the flow sensor.

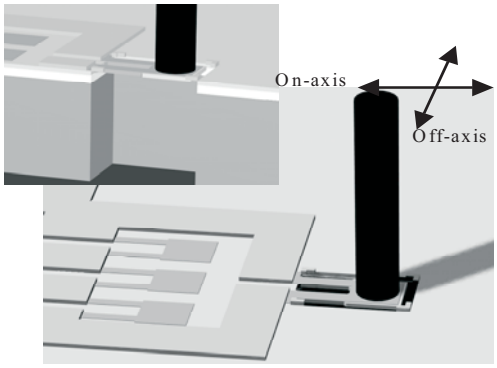

Figure 2*. Perspective side view of an artificial haircell (AHC) sensor. A high aspect ratio hair is located at the distal end of a silicon paddle.*

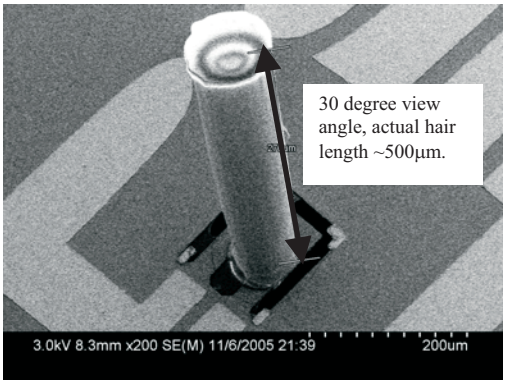

***Figure 3**. SEM of a single released AHC sensor.*

DEVICE FABRICATION

The devices are fabricated on the SOI wafers with 2µm device thickness, 2µm oxide, and 300µm handle thickness. The cilia are made of high aspect ratio SU-8 structures with 80µm diameter and 500-700µm height. SU-8 is chosen for its ability to form rigid high aspect ratio structures using common lithography tools. The process flow is demonstrated in the Figure 5.

First, we send out the SOI wafer for ion implantation (Fig. 5(a)). After getting the wafer back, a short drive-in is performed and at the same time a thin layer of oxide is formed to serve as the insulation layer. Then we open the contact windows to the doped silicon (Fig. 5(b)). Electrical connection is formed using gold on titanium deposition and lift-off (Fig. 5(c)). The paddle-like cantilevers are then defined by front side DRIE (Fig. 5(d)). Following that the bulk backside etching is also performed using DRIE to get the cantilevers ready for release (Fig. 5(e)). A single layer of SU-8 2075 is then spun to achieve thickness of approximately 700µm (Fig. 5(f)). For pre-exposure bake, the samples are ramped up to 105^{o}C at 150 ^{o}C/hr ramp rate and soaked at 105^{o}C. After a total bake time of 13 hours the samples are then ambient cooled to room temperature. The photolithography is done using a Karl Suss contact aligner at 365nm. A high-wavelength pass optical filter with cutoff frequency of 300nm is used during exposure to eliminate the "T-topping" effect of the SU-8 structures (Fig. 6). The exposure dose is 3000mJ/cm^2. For post-exposure bake, the samples are again ramped up to 105^{o}C at 150 ^{o}C/hr ramp rate and soaked at 105^{o}C for half an hour. The samples are then ramped down to room temperature at a controlled rate of 15 ^{o}C/hr. The development is done using designated SU-8 developer with IPA as the end point indicator. After the cilia assembly, the devices are released in BHF to free the cilium-on-cantilever structures (Fig. 5(g)).

Most of the processing steps are standard, expect for the SU-8 step. SU-8 is very sensitive to processing parameters, but once the processing recipe is established, the process is very repeatable and able to achieve high device yield. One of the benefits of using SU-8 is that the process minimizes manual handling of the devices during the assembly of the cilia hence improves the device yield and makes batch fabrication of the devices possible. This is contrast to previous devices that required manual wire-bonding of individual cilia. The presented devices are fabricated in pairs oriented at 90˚ angles to each other to allow 2-axis flow measurement.

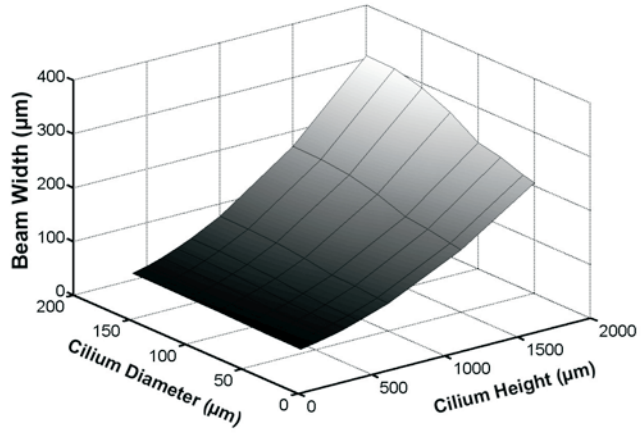

***Figure 4.** 3-D map shows the possible combinations of cilium height, diameter and cantilever width that satisfy our design scenario assumptions.*

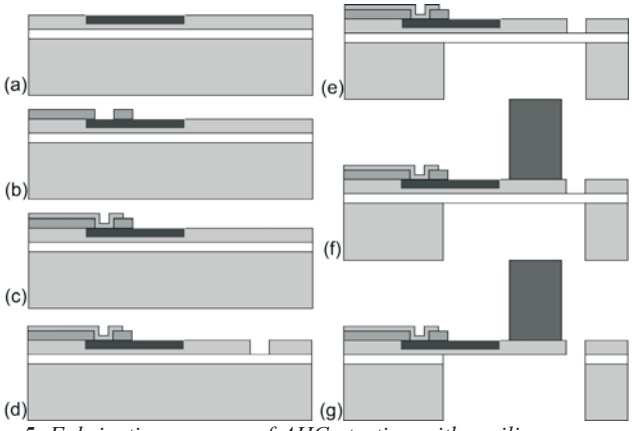

***Figure 5.** Fabrication process of AHC starting with a silicon-on-insulator (SOI) wafer.*

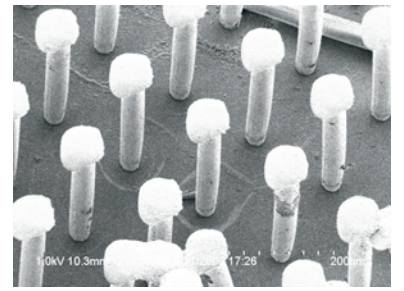

(a)

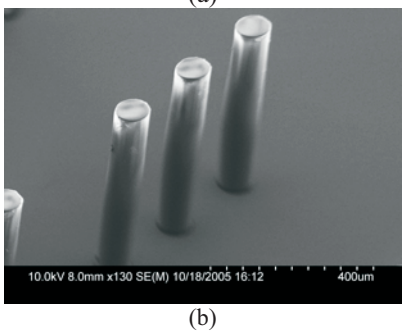

(b)

***Figure 6.** (a) SEM of SU-8 structures obtained without using optical filter showing the "T-Topping" effect. (b) SU-8 structures obtained using optical filter. "T-topping" effect is eliminated.*

EXPERIMENT AND RESULT

A series of experiments are done to characterize the AHC device performance and demonstrate its preliminary application as an underwater flow sensor.

Tip Deflection Test

The tip deflection test is done using the probe station. The resistance change of the strain gauge is recorded while the tip of the cilium is transversely deflected in a controlled manner. We assume that the vertical deflection of the cantilever is close to the deflection of the cilium under small angle assumption. See Figure 7 for the results of both on and off-axis deflection tests. Off-axis is defined as deflection orthogonal to the on-axis designed direction as shown in Figure 2.

Along the on-axis, the device shows very linear and sensitive response under very small defections. This is very important in our application which requires good sensitivity at very slow flow speeds. Based on the deflection response, the gauge factor is determined to be 33.6, which includes all contact and parasitic resistances. It was found that contact resistances dominated, and that an additional polyimide layer served to protect the contact areas between the metal wiring and semiconductor strain gauges during BHF release. The device has also demonstrated a very directional response with almost no response due to off-axis deflection. This is desirable in order to accurately determine flow direction as well as velocity.

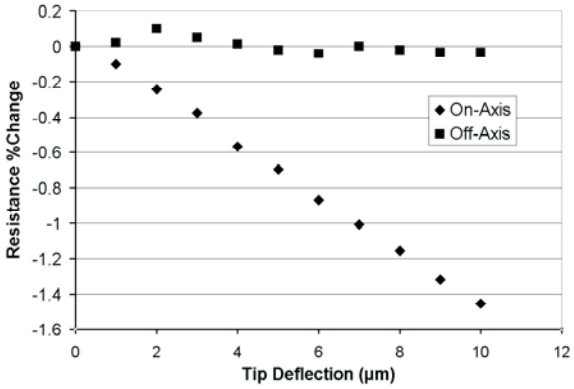

Figure 7. *Tip-deflection test shows very directional response of the AHC sensor. A high rejection ratio of off-axis input is observed.*

Resonant Frequency Test

The resonant frequency test is done using the AFM under Non Contact Mode. The sample is first sputtered with metal. The smooth top surface of the cilium makes it reflective to the laser beam. See Figure 8 for a typical output of the AFM. A resonant frequency of 3.07 KHz is observed for that particular device. This agrees with our design for the resonant frequency range. This lower resonant frequency is mainly due to the cantilever structures. A resonant frequency that is orders of magnitude higher is also observed. The higher resonant frequency is mainly contributed by the rigid SU-8 cilium structure.

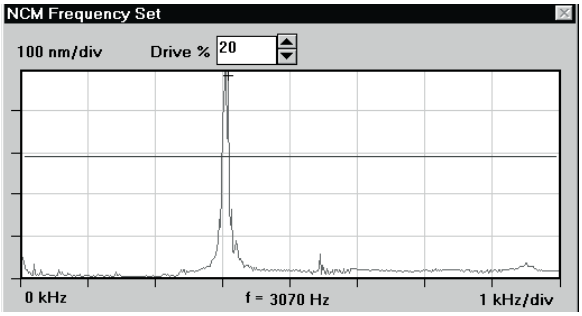

Figure 8*. An AFM operated under non-contact mode is used to test the resonant frequency of AHC structure. Shown here is a typical AFM output of resonant frequency test.*

Sensitivity Threshold Test

The sensitivity threshold test is done under the controlled flow condition generated by a dipole source. A dipole source is a vibrating sphere that generates mainly local, incompressible flow in the near field. Shown in Figure 9 is the sensor output vs. dipole acceleration sweep. This test is controlled by a LabVIEW program in order to quickly vary the dipole output while measuring the AHC response. The sensor output hits the noise floor around 45m/s^2 of dipole acceleration. Based on the simplified near field dipole model calculation, this acceleration is translated to approximately 2mm/s flow speed [**7**]. This has demonstrated the sensor's capability of performing accurate low flow speed detection.

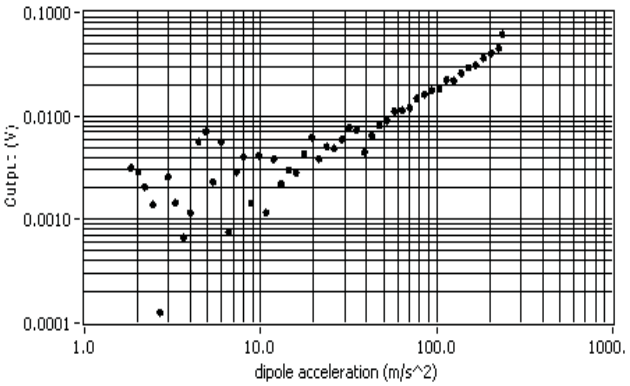

Figure 9. *Sensor output vs. dipole acceleration shows the noise floor around 45m/s^2, which translates to 2mm/s flow speed.*

Preliminary Dipole Localization Experiment

The localization experiment is done with the vibrating dipole source sweeping across the position of the sensor. The dipole source is attached to a computer controlled motorized linear stage allowing accurate positioning of the dipole relative to the sensor. See Figure 10 for the sensor output vs. the position of the dipole source. A peak is observed when the dipole source is directly above the position of the sensor as expected by the dipole model. With further calibration and more sophisticated signal processing, the AHC sensors can be utilized in the precise localization and tracking of a moving object.

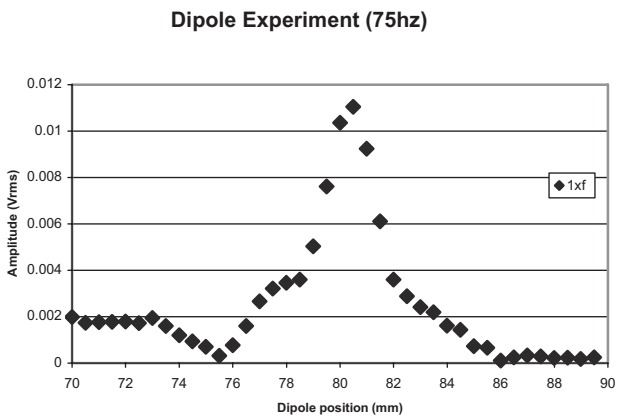

Figure 10*. The sensor was used to "visualize" the velocity field created by an oscillating dipole source.*

DISCUSSION AND CONCLUSION

Even though the device fabrication process is well established, there are still several challenges we are facing that can affect the output and performance of the devices.

During the photolithography of the cilia, since we are trying to focus over the range of several hundred microns, misalignment is inevitable. Usually, we are able to get the cilium close to the center of the paddle. For example in Figure 3, the cilium is partially offset on the cantilever, this has shortened the effective length of the cantilever, but since the length of the cantilever is not a determinant factor in the sensitivity of the sensor, it should not affect the sensitivity too much. However the misalignment may contribute to the asymmetric moment loading of the cantilevers, which may lead to lower sensitivity and asymmetry of the sensor response.

The high sensitivity of the sensor is achieved at the compromise of device robustness. To improve the robustness, new packaging schemes and protection features are being developed, as well as new materials for the hair structure. Our current work also involves using a pair of AHC sensors oriented orthogonal to each other to allow flow angle detection with precision as high as 1 degree (Fig. 11). Bio-inspired approaches such as covering the cilia in a gelatinous cupula are also being explored.

We have developed a high sensitivity artificial hair cell sensor that is able to detect flow speed down to the order of several mm/s. This will make the sensor a very valuable candidate in the study of the biological world and in creating bio-inspired artificial sensing organs such as an artificial lateral line.

Figure 11. *A pair of AHC sensors oriented orthogonally for resolving angular flow information.*

ACKNOWLEDGMENT

Special thanks to DARPA BioSenSE and AFOSR Bioinspired Concept programs.

REFERENCES

[1] J. T. Albert, O. C. Friedrich, H.-E. Denchant, and F. G. Barth, "Arthropod Touch Reception: Spider Hair Sensilla as Rapid Touch Detectors," *Journal of Comparative Physiology A*, vol. 187, pp. 303-312, 2001.

[2] F. G. Barth, "Spider Mechanoreceptors," *Current Opinion inNeurobiology*, vol. 14, pp. 415-422, 2004.

[3] Y. Ozaki, T. Ohyama, T. Yasuda, and I. Shimoyama, "Air flow sensor modeled on wind receptor hairs of insects," presented at IEEE International Conference On MEMS, 2000.

[4] J. v. Baar, M. Dijkstra, R. Wiegerink, T. Lammerink, R. d. Boer, and G. Krijnen, "Arrays of cricket-inspired sensory hairs with capacitive motion detection," presented at IEEE Inernational Conference on MEMS, Miami Beach, FL, 2005.

[5] J. Engel, J. Chen, N. Chen, and C. Liu, "Development and Characterization of an Artificial Hair Cell Based on Polyurethane Elastomer and Force Sensitive Resistors," The 4th IEEE International Conference on Sensors, Irvine, California, 31 Oct- 1 Nov, 2005.

[6] J. A. Harley and T. W. Kenny, "1/f Noise Consideration for the Design and Process Optimization of Piezoresistive Cantilevers," *JMEMS*, vol 9, no. 2, June 2000.

[7] J. Chen, J. Engel, N. Chen, S. Pandya, S. Coombs, and C. Liu, "Artificial Lateral Line and Hydrodynamic Object Tracking," MEMS 2006 Conference, Istanbul, Turkey , January 22 - 26, 2006

HIGH FREQUENCY LOW IMPEDANCE CAPACITIVE SILICON BAR STRUCTURES

Siavash Pourkamali and Farrokh Ayazi
School of Electrical and Computer Engineering
Georgia Institute of Technology, Atlanta, GA 30332
E-mail: siavash@ece.gatech.edu, Tel: (404)385-6693, Fax: (404)385-6650

ABSTRACT

This paper presents high frequency high-Q micromachined capacitive silicon bulk acoustic resonators (SiBAR) with impedances well within the required range for electronic applications. Resonator motional resistances as low as 200Ω and quality factors as high as 90,000 are demonstrated for clamped-clamped silicon BARs in the VHF range. The same resonators have been operated in their higher width extensional modes up to the fifth mode demonstrating frequencies as high as 765MHz with comparatively low motional resistances. Temperature characteristics and thermal temperature compensation techniques for such resonators are investigated. Thermal frequency tuning of >1% is demonstrated for the high frequency resonators. Several structural variations of ultra-long silicon BARs for maximized electromechanical coupling are demonstrated and discussed as well.

I. INTRODUCTION

Development of silicon micromachined devices for frequency referencing is a fast growing technology with strong potential for a wide range of applications in electronics. High frequency capacitive silicon resonators have shown great capability for implementation of highly stable integrated frequency references [1,2]. Temperature compensated bulk micromachined single crystal silicon I-BARs operating in a few MHz range with quality factors in excess of 100,000 have been previously demonstrated [1].

For frequencies in the 100MHz and higher, capacitive electromechanical transduction may quickly become inefficient to provide satisfactory motional resistances. In addition, as the frequency increases, parasitic capacitances become a more serious issue and lower resistances are desired to alleviate excessive signal loss.

Thick capacitive bulk acoustic wave silicon resonators known as "SiBAR" were introduced in [3] for the first time. With their large transduction area and HARPSS-enabled deep-submicron capacitive gaps [4,5], such resonators demonstrated much lower equivalent motional resistances (~5.0kΩ) in the VHF range compared to disk resonators [4,5]. In this work, more efficient designs of SiBAR structures have enabled reduction of resonator impedances by another order of magnitude compared to values presented in [5]. Resulting motional resistances easily satisfy the requirements for low power VHF oscillators without the need for brute force pushing of the fabrication limits.

A large tuning range can be achieved by heating the high frequency SiBARs. Accordingly, a self compensating strategy can be developed that uses the resonator as a heater and a temperature sensor simultaneously.

Finally, several structural variations of SiBARs can be deployed to maximize their effective length and further increase the electromechanical coupling. Long SiBARs need to be supported at several locations along their structure to maintain reasonable structural stiffness.

II. LOW IMPEDANCE CLAMPED-CLAMPED SiBARs

HARPSS-on-SOI process that has previously been used for fabrication of thick disk resonators [4,5] was used for fabrication of the resonators in this work. Figure 1 shows the SEM view of a fabricated 20μm thick, 40μm wide, 150μm long clamped-clamped SiBAR with 170nm capacitive gaps. The resonators are expected to operate in their first width extensional modes, and the operating frequencies are determined by their width.

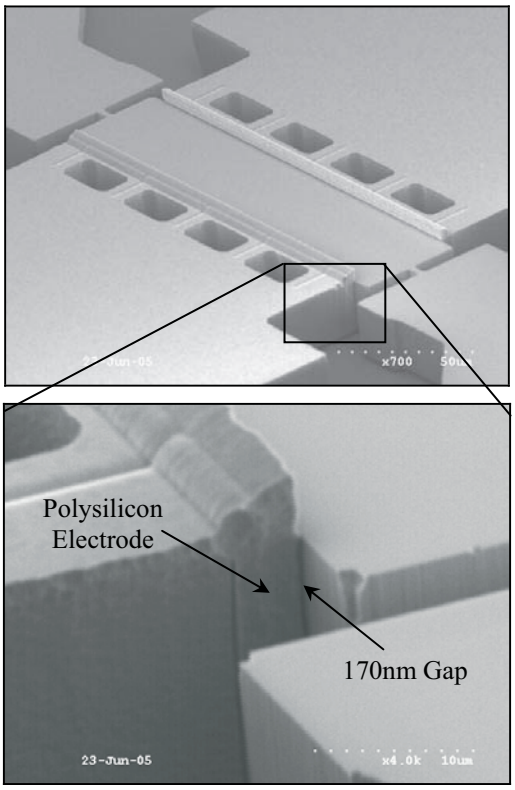

Figure 1. SEM view of a 40μm wide, 150μm long, 20μm thick clamped-clamped SiBAR and the close up of its electrode showing the 170nm capacitive gap.

In the previous demonstration of SiBARs, the support lengths were set to the quarter wavelength at the operating frequency (half of the resonator width). This was assuming that such support dimension would minimize flow of energy from the supports to the substrate and maximize the quality factor of the resonator. However, it is shown here that the support length does not have a significant effect on the Q of the clamped-clamped SiBARs and very high quality factors in the same range can be obtained for devices with much shorter supports. The support length for the resonator in Figure 1 is only 4μm making the structure much stiffer and capable of tolerating much larger polarization voltages without getting pulled-in. As a result, over one order of magnitude lower equivalent electrical impedances are achieved for such resonators.

Figure 2 shows the measured frequency response for the resonator of Figure 1 operating in its first width extensional mode at 107MHz. As shown in Figure 2a, the quality factor of the resonator is 49,600 when biased at a low V_p. However, it gradually drops to 13,200 as the V_p increases to 90V (Figure 2b). This is due to the existence of an unexpected loading resistance in the resonator structure. The measured impedance with V_p of 90V is 1050Ω. The real motional resistance of the resonator can be back calculated using the unloaded Q value measured at low V_p (before the Q loading starts) and the following equations:

$$R_{meas} = R_m + R_{load}, \text{ and } \frac{Q_{loaded}}{Q_{unloaded}} = \frac{R_m}{R_{meas}} \quad (1,2)$$

Where R_m is the motional resistance of the resonator, R_{meas} is the resistance measured by the network analyzer, and R_{load} is the loading resistor. Motional resistance of **280Ω** is extracted from the resonator responses in Figure 2.

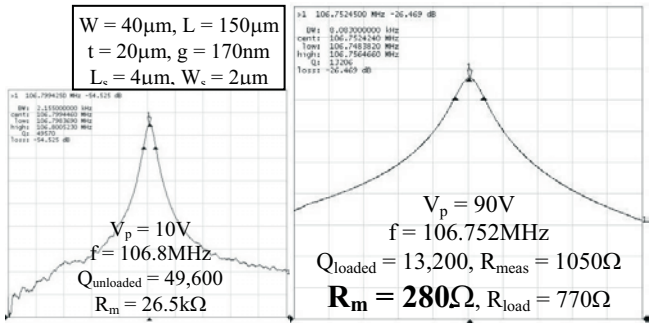

Figure 2. Measured frequency response of the SiBAR of Figure 1 showing Q loading due to extremely low resonator motional resistance.

Figure 3 shows a similar set of measured frequency responses for a 50µm wide, 300µm long SiBAR fabricated on the same substrate. The extracted motional resistance for this resonator is **200Ω**.

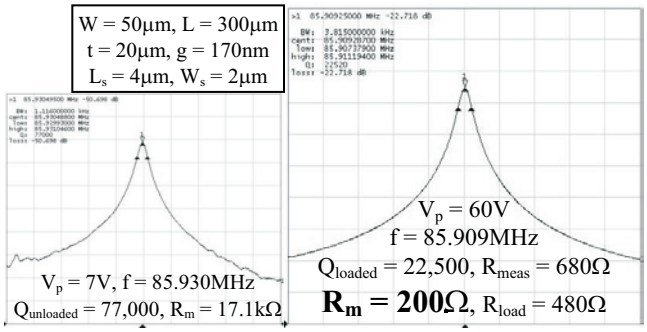

Figure 3. Measured frequency response of a 50µm wide, 300µm long SiBAR with motional resistance as low as 200Ω.

The measured static resistances between the two polarization voltage pads on the two sides of the resonators are close to the extracted loading resistor values. Therefore, the resistivity of the silicon substrate in the V_p path is suspected to be responsible for Q loading.

The starting SOI substrate for the resonators in Figures 2 and 3 had a device layer resistivity of 0.015Ω.cm. To further investigate the effect of substrate resistivity on Q loading, another batch of resonators were fabricated on a SOI substrate with lower device layer resistivity (0.002Ω.cm). Figure 4 shows the frequency response and extracted resistance values for a 20µm thick, 40µm wide, 150µm long SiBAR with 125nm capacitive gaps (Gap aspect ratio = 160) fabricated on the lower resistivity substrate. The extracted loading resistance for this resonator is only 120Ω which is over 6 times lower than the loading resistor for the same device on the previous higher resistivity substrate.

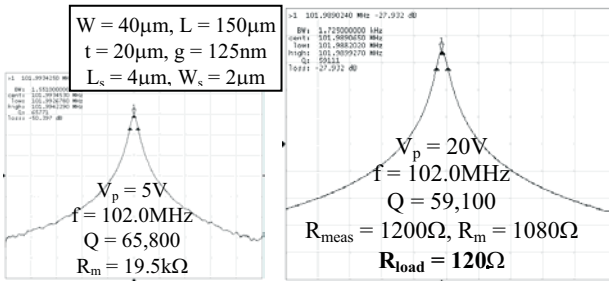

Figure 4. Frequency response of a SiBAR with similar dimensions as the resonator of Figure 2, fabricated on a lower resistivity substrate showing a much lower loading resistance of 120Ω.

Frequency Tuning and Temperature Compensation:

One of the remaining major bottlenecks limiting the capability of silicon resonators is their much larger temperature coefficient of frequency compared to quartz resonators. This results from larger temperature coefficient of young's modulus of silicon. Figure 5 shows the measured frequency response as well as temperature dependant frequency drift graph for a 50µm wide, 540µm long SiBAR. The measured frequency drift of -27.8ppm/ºC is in good compliance with previously reported values for single crystal silicon resonators [4]. At lower frequencies electrostatic frequency tuning of the capacitive resonators can be large enough for temperature compensation over a >150ºC range [1]. However for frequencies in the 100MHz and above, the electrostatic tuning is not large enough for temperature compensation unless extremely narrow (sub-100nm) capacitive gaps are realized and/or comparatively large polarization voltages are applied.

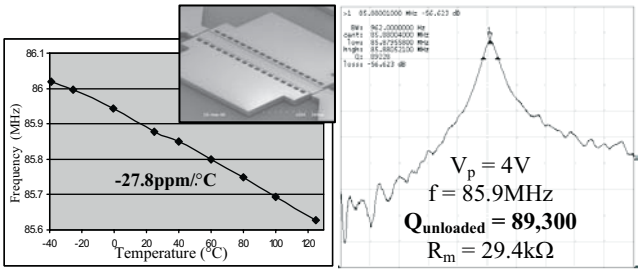

Figure 5. SEM view, frequency response and temperature induced frequency drift data for a 20µm thick, 50µm wide, 540µm long SiBAR with 170nm gaps.

The alternative frequency tuning approach evaluated in this work is using the large temperature drift of the resonator for its tuning as well as temperature compensation at the cost of burning extra power. Conductivity of the body of the resonators and availability of two pads on the two end of the device make it very convenient to use the resonator itself as a heater. Figure 6 shows a frequency tuning of more than 1MHz (1.2%) achieved for the 86MHz resonator of Figure 5 by passing a DC current through its body. This is done by applying slightly different bias voltages to the two V_p pads of the resonator. According to the measured temperature induced frequency drift (Fig. 5), this is equivalent to

an elevated temperature of ~450°C for the resonator (neglecting second order effects). It is worth noting that the resonator was operating flawlessly with no degradation of the quality factor at high temperature. A temperature dependant current source can be used to keep the temperature of the resonator elevated (e.g. at 125°C) independent of the temperature of the surrounding environment and avoid the temperature drift. In this case, the unpackaged resonator on a 1.2×1.2cm^2 silicon substrate with no thermal isolation from the test setup, 85mW of power was required at room temperature to keep the temperature of the resonator elevated at125°C. This can be reduced to a few mW or even below mW for a single resonator inside a thermally isolated package.

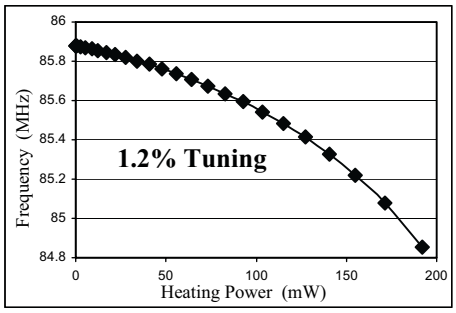

Figure 6. Measured frequency tuning characteristic of the resonator of Figure 5 resulting from heating current passed through the resonator.

Furthermore, one can take advantage of temperature dependency of the resistance of the resonator and use it as a simultaneous in-situ temperature sensor. Incorporation of an active feedback mechanism around such device can result in a highly stable temperature characteristics.

Higher resonance modes:

Figure 7 shows the measured resonance frequency of a 5µm thick, 30µm wide, 150µm long, SiBAR with 135nm capacitive gaps operating in its fundamental and higher modes up to the 5th mode.

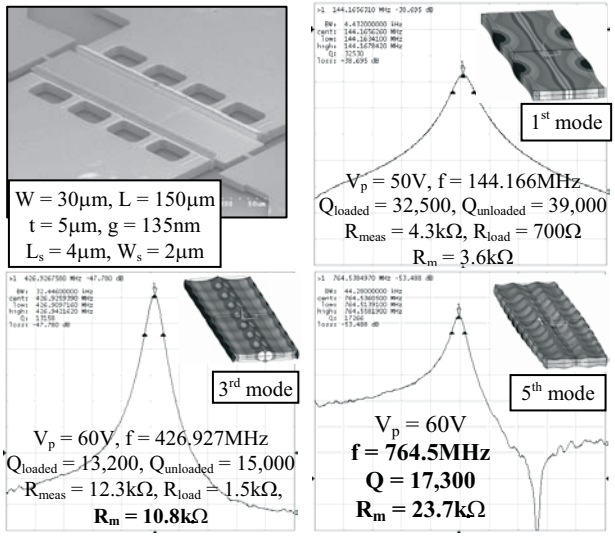

Fig. 7. SEM view and measured frequency response of a 30µm wide, 150µm long, 5µm thick SiBAR at its first and higher odd width extensional modes up to the fifth mode.

The supports for the resonators are in the middle of their width, which is a resonance node for odd higher width extensional modes. Therefore, they can be operated in such higher modes with high quality factors and much higher resonance frequencies.

Quality factors of 15,000 and 17,300 are measured for the 3rd and 5th width extensional modes of this resonator at 427MHz and 765MHz respectively. Measured motional resistance of 11kΩ and 23kΩ for these modes are close to one order of magnitude lower than the impedances reported for surface micromachined capacitive resonators at similar frequencies [6].

III. ULTRA-LONG SiBARs

For oscillator applications resonator Q as high as possible is desired to minimize the close to carrier phase noise. However in most of the filter applications, a comparatively small (<1000) filter Q is targeted and very high resonator Q can help slightly reduce filter insertion loss, however is not a necessity; instead very low resonator motional resistances are required to avoid the need for large terminating resistors and resulting problems caused by parasitic input and output capacitance of the resonators [7]. In other words, low resonator impedance has to be resulting from strong electromechanical coupling not its high quality factor. In addition to increasing V_p and reducing the gap size, electromechanical coupling can also be maximized by increasing the length of the resonator. However, elongation of the regular clamped-clamped SiBAR will eventually result in excessive compliance of its structure and consequently stiction and early pull-in issues. To maintain the resonator stiffness while increasing its length, perpendicular support beams are added at several locations along the length of the ultra-long SiBARs (Figure 8).

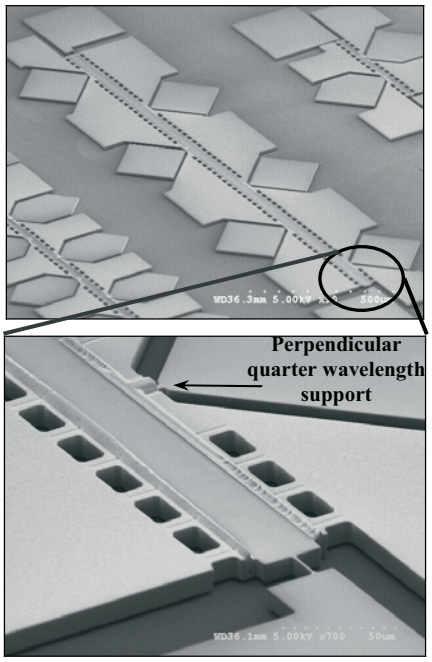

Fig. 8. SEM view of an ultra-long (30µm wide, 1800µm long) SiBAR with perpendicular supports along its length.

As expected, the added supports reduce the resonator quality factor significantly (Figure 9a). Adding notches to the resonating body at the support interconnects helps increase its quality factor to some extent [6] (Figure 9b). However the Q is still much lower than the regular clamped-clamped SiBAR. Such large structures are very susceptible to having unwanted spurious modes close to their main

mode (Figure 9). Therefore, precautions need to be taken in their design to suppress the undesired modes as much as possible.

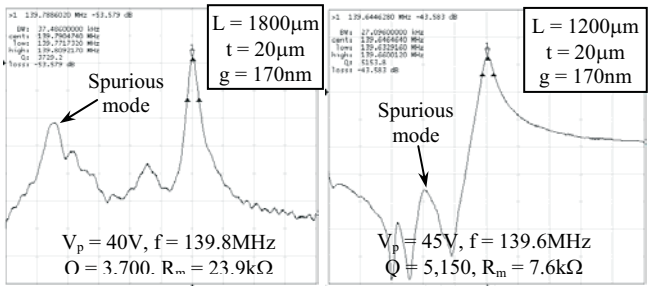

Figure 9. Measured frequency response of ultra-long 20µm thick 30µm wide SiBARs with perpendicular support beams along their length, (a) solid (un-notched) BAR, (b) notched BAR.

IV. SQUARE SILICON BARS

Corner supported square structures are an alternative approach explored in this work to increase the effective resonator length. Figure 10 shows the SEM view and frequency response of a single square SiBAR supported at its four corners. Polysilicon interconnects bridging over the resonator [4] provide electrical connection between different sections of the electrodes for the square SiBARs.

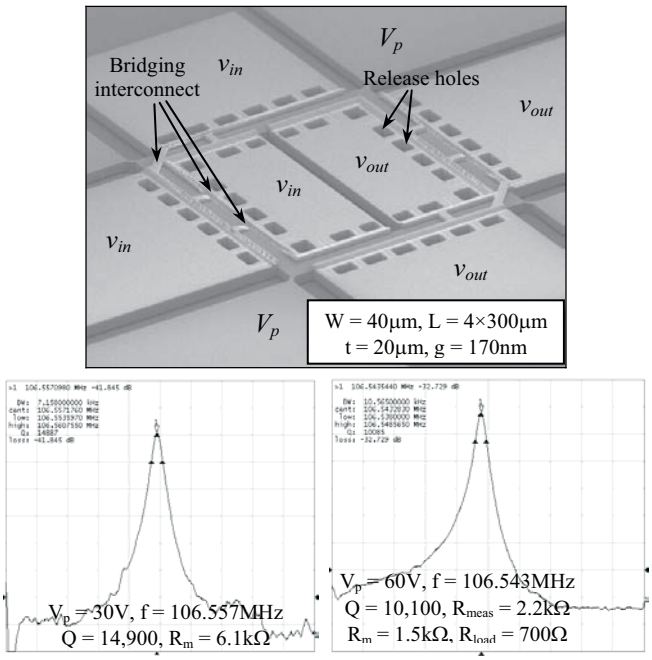

Figure 10. SEM view of a 20µm thick 40µm wide corner-supported square silicon BAR and its measured frequency response under low and high polarization voltages.

In the square resonator of Figure 11 the length maximization is taken another step further. This resonator consists of a network of four squares sharing common sides with each other. Square SiBARs have larger quality factors compared to the linear ultra-long SiBARs. However their quality factor is much lower than that of the regular clamped-clamped SiBARs. Extensive finite element analysis and measurements are required for complete characterization and insightful design of the ultra-long linear BARs and the square BARs.

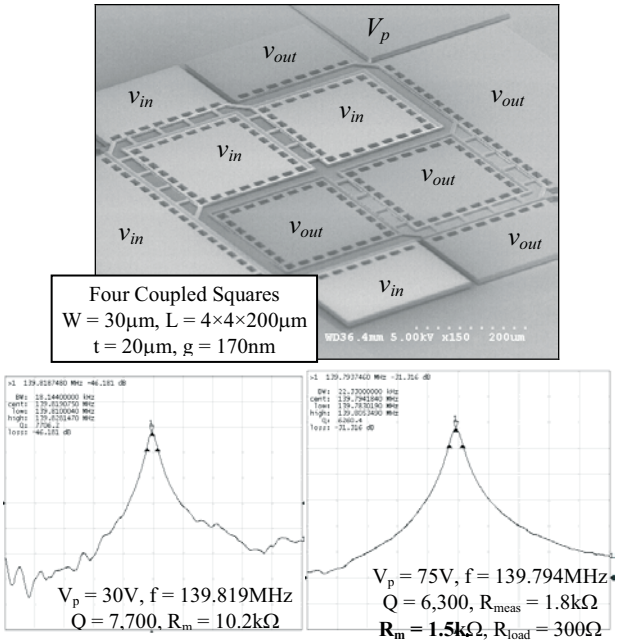

Figure 11. SEM view of a 4-square network silicon BAR and its measured frequency response with different polarization voltages.

CONCLUSIONS

In conclusion, low impedance high frequency capacitive resonators with great potential for implementation of highly stable low phase noise oscillators are presented. Quality factors as high as a few tens of thousand and motional resistance well below 1kΩ are simply achievable for SiBARs in the VHF range without the need for ultra-thin (sub-100nm capacitive gaps).

Poor temperature stability of silicon resonators compared to quartz crystals is the major drawback for employment of such resonators in wide range applications. By passing current through the conductive body of the clamped-clamped SiBARs they can be used as self-heaters as well as temperature sensors simultaneously. An active feedback mechanism along with optimal packaging for thermal isolation enables realization of low power highly temperature-compensated silicon frequency reference.

A variety of ultra-long SiBAR structure can be deployed for improved electromechanical coupling at the cost of reducing the resonator quality factors.

Acknowledgements

This work is supported under the DARPA NMASP program.

References:

[1] G.K. Ho, et al, "Temperature compensated IBAR reference oscillators," Proceedings MEMS'06, pp. 910-913.

[2] Y.-W. Lin, et al, "60-MHz wine glass micromechanical disk reference oscillator," *Digest of Technical Papers*, ISSCC 2004, pp. 322-323

[3] S. Pourkamali, G. K. Ho and F. Ayazi, "Vertical capacitive SiBARs," MEMS'05, pp. 211-214.

[4] S. Pourkamali, et al, "VHF single crystal silicon side supported disk resonators-Part II: implementation and characterization," JMEMS, Vol. 13, Issue 6, December 2004, pp. 1054-1062.

[5] S. Pourkamali and F. Ayazi, "High frequency capacitive micromechanical resonators with reduced motional resistance using the HARPSS technology," proceedings, 5th Silicon RF topical meeting 2004, pp. 147-150.

[6] S.-S. Li, Y.-W. Lin, Y. Xie, Z. Ren, and Clark T.-C. Nguyen, "Micromechanical hollow-disk ring resonators," MEMS'04, pp. 821-824.

[7] S. Pourkamali and F. Ayazi, "Electrically coupled MEMS bandpass filters-Part I: with coupling element," Journal of Sensors and Actuators A 122, 2005, pp. 307-316.

FLOW-STRUCTURE INSTABILITY PREVENTION IN A MEMS HIGH FLOW GAS VALVE

Aaron J. Knobloch[1], Charles E. Seeley[2], Amol Mulay[3], Richard J. Saia[1]

[1]Micro and Nano Structures Technologies
[2]Energy and Propulsion Technologies
General Electric Global Research Center
Niskayuna, NY USA

[3]John F. Welch Technology Centre
Bangalore, India

ABSTRACT

This paper presents an innovative method of preventing structural resonance due to a fluid-structure interaction for a MEMS high flow rate gas valve. This normally closed gate valve design consists of a pair of slender electrothermal beam actuators that move a slider with rectangular slits to modulate the flow of gas through a series of flow channels below the actuator. Under certain flow and voltage conditions, the slider structure enters a resonance condition first identified by an audible noise and an undesirable flow output. Visual inspection of the slider and electrothermal beams during resonance indicated that the in-plane displacements of the normally quasi-static beams oscillate wildly such that the beams buckle. A computational fluid dynamic (CFD) analysis in combination with a mechanical model of the electrothermal beams showed that forces on the walls of the slots tend to close the actuator but are insufficient on their own to cause beam buckling. The design of the valve, with its "floating" slider mechanism, has no sliding contact points to create friction that could also create damping. Therefore, this structure has a high Q factor which can amplify the resonant oscillating displacement. Based on viscoelastic properties of RTV silicone, a small, precisely controlled amount of silicone was dispensed using a computer controlled dispense system to create two damping "straps" between the slider mechanism and the rigid supporting structure around the valve. Subsequent testing indicated that the instability could not be induced under normal operating conditions once the silicone dampers were installed.

INTRODUCTION

Many MEMS devices are based on oscillating microstructures such as comb drives, quartz crystal resonators and cantilever beams. These devices with size scales from nanometers up to hundreds of microns are able to achieve high actuation strokes due to a minimal amount of damping inherent in their design [1-2]. When used as sensors, an important factor to improving the sensitivity of these devices is to maximize the sharpness of resonance, or Q-factor. The Q-factor is heavily influenced by the ambient environment [3-4] since typically Q scales with viscosity of the fluid surrounding the MEMS device. In some cases, this necessitates vacuum operation for minimal viscous damping of the structure. While numerous studies of the effects of damping of MEMS oscillatory sensors and actuators have been presented, the majority of these have focused on increasing Q for better performance. Few studies have examined reducing Q to increase damping on MEMS devices [5].

Extensive prior research on the design and microfabrication of MEMS devices for flow control of gases and liquids is available. One design that is ameable to high flow rate gas modulation is a gate valve structure [6]. Since a gate valve design actuates perpendicular to the direction of flow, a gate valve is easily integrated with planar electrothermal or electrostatic actuation schemes and does not require a high force actuator to work against the flow to close the valve. This paper examines a high flow rate gate microvalve that exhibits a flow-induced resonance from a coupled interaction of the fluid and structure (FSI) that adversely affects the valve performance. A novel method for adding damping to the microvalve is presented that mitigates the undesirable resonance from the fluid structure interaction.

VALVE DESIGN AND OPERATION

The objective of the microvalve design in this effort was to develop the capability of modulating airflow rates of 5000-10000 sccm. In order to minimize valve power consumption and maximize flow area, a gate valve design was utilized that operates by moving a set of fingers across a series of slots as shown in Figure 1. The required flow rates and die size constraints necessitate slot sizes on the order of 120 μm in width [7]. Therefore, an actuation system was required to produce at least this amount of stroke within the geometric constraints of the die. A bent beam electrothermal actuator (Vbeam actuator) was chosen based on a survey of competing actuation concepts and prior experience with this design [8].

Figure 2 shows a top view of the microvalve structure. While the focus of this paper is on the flow induced instability and prevention rather than the fabrication, the following is a brief description of the microvalve design and process flow. The slider is composed of 30 slots 120 μm wide and 2990 μm long. The electrothermal actuator is a bent beam 35 μm wide, 6900 μm long. The actuator is fabricated on a 385 μm thick highly doped (0.015-0.02 ohm-cm) silicon wafer with a two sided deep reactive ion

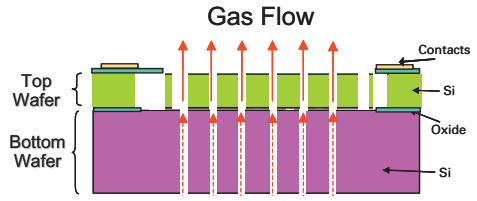

Figure 1. *Cross-sectional view of the MEMS gas valve where the middle slider composed of an array of 135 μm wide fingers uncovering the slots of bottom wafer.*

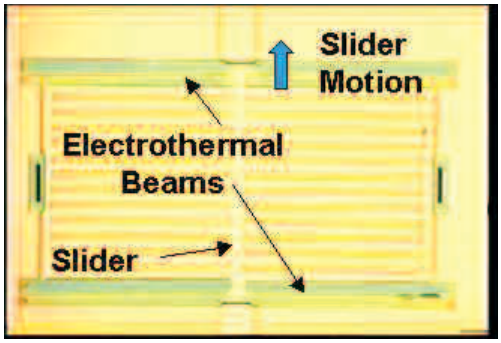

Figure 2. *Top view of the early generation MEMS gas valve showing an array of slots actuated by a pair of electrothermal actuators.*

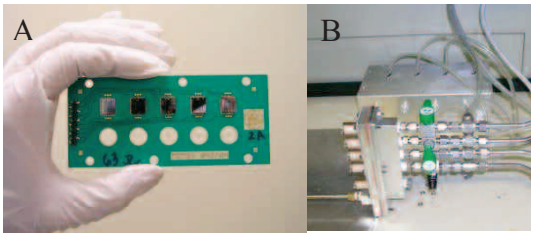

Figure 3. *A, picture of the microvalve assembled on an aluminum board. B, microvalve test manifold with individual solenoids controlling each channel (orifice not shown).*

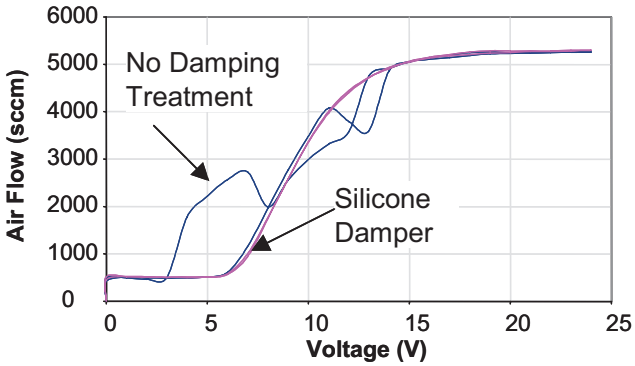

Figure 4. *Comparison between undamped and damped gas valve operation.*

etch. The actuator wafer is silicon fusion bonded to another wafer etched with 30 120 µm wide slots such that the slots are covered in the non-energized position. A short etch in the actuator and slot regions prevents a fusion bond between the slider or actuator and the lower wafer.

Since the microvalve is thermally actuated, a Thermal Clad® circuit board with an aluminum substrate and dielectric clad top from The Bergquist Company was chosen as a test vehicle due to its heat dissipation properties (See Figure 3). The die are mounted over open slots in the board using standard die pick and place equipment and are then wire bonded to make electrical connections. Each die is adhered to the board using GE RTV116 high temperature silicone. This compliant material with good thermal conductivity maintains its mechanical properties at elevated temperature (die temperatures can reach upwards of 100ºC). A populated board is inserted into a two part metal manifold with machined flow passages and solenoid shutoff valves for each microvalve. The manifold is part of a fluidic test rig (Figure 3) with integrated flow meters and an upstream pressure regulator (1245 Pa) for microvalve characterization. Pressure is measured in the flow circuit just upstream to the set of microvalves at the manifold inlet and just downstream of each microvalve with a differential pressure sensor to determine the pressure drop across each valve. Following the downstream pressure sensor is a restrictive 4.9 mm diameter orifice.

In order to characterize the flow response of the microvalve, the input voltage to the valve was ramped up from 0 V to 24 V DC and back down to 0 V in increments of 1 V. Once the voltage was set, a time delay of four seconds was imposed for the flow to stabilize before pressure and flow measurements were taken. A software-controlled procedure was used to ramp the voltage, open/close the solenoid shutoff valves and record the data as needed. Figure 4 shows the flow response of a typical microvalve without damping treatment along side the desired response. The instability seen in Figure 4 is not consistent valve to valve and a very small percentage (<10%) of valves exhibited no audible noise

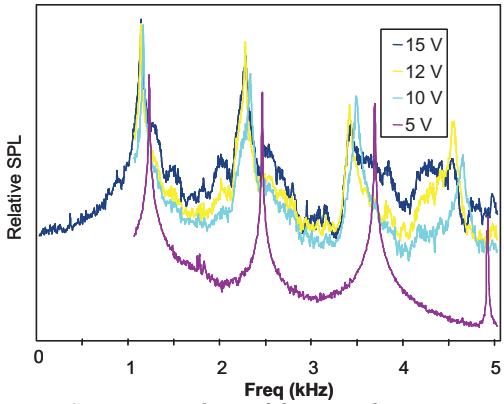

Figure 5. *Spectrum analysis of the gas valve noise at a variety of voltages.*

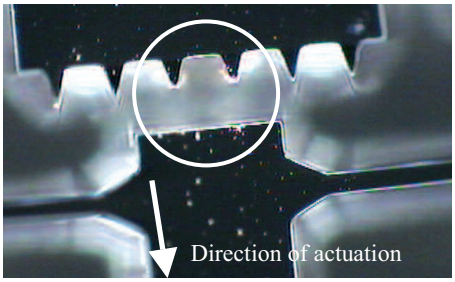

Figure 6. *Close up view of valve and reverse stop after operation of unstable valve. The silicon chips and divots on the actuator along with the blunted points indicate actuation of the valve opposite to the intended direction.*

or flow disturbance. The flow instability was especially noticeable in the range of voltage from ~5 V to 14 V. Audibly, the noise was characterized by single frequency flute like tone with an extra "harshness" and a mechanical sounding vibration. A typical spectrum of the tone is shown in Figure 5. The tone was recorded by placing a microphone near the valve and calculating the autospectrum of the frequency content of the acoustic signal. Although the amplitude is strictly relative in this figure, the total RMS level of the sound is estimated at 80-90 dB SPL. The acoustic spectrum indicates a fundamental frequency at approximately 1.2 kHz, and a number of N multiple harmonics. This is consistent with the expected fluid structure interaction. A resonance condition is created where the motion of the fluid excites the slider structure in a periodic manner causing the valve to open and close at a rapid pace. A pressure wave is created with each opening and closing as the fluid varies in velocity. This pressure wave creates the tone observed by the listener. The pressure wave is also "chopped" by the motion of the slider, so it is not a pure sine wave and creates the N multiple harmonics that give the harsh tone. The mechanical vibration noise is most likely the slider contacting the sides of the MEMS device.

Inspection of the valves after operation (Figure 6) revealed noticeable damage that would require bending of the beams in the opposite direction as is intended. Video of the valve's operation was taken with the backend of the manifold removed from the assembly. This video confirmed a resonance in the structure at valve positions corresponding to the audible noise. The oscillation amplitude is observed to vary from the maximum beam displacement at a particular input voltage to a negative displacement causing contact with the reverse stop. This reverse displacement causes the two beams to have an S-shape implying beam buckling. This resonance behavior was observed on more

than 30 devices from a multitude wafers and wafer lots eliminating process variability as a root cause.

FLUIDIC AND STRUCTURAL MODELING

Analysis of the conditions causing the electrothermal beams to lose stiffness and become susceptible to the destructive FSI is composed of two parts: a fluidic model of the forces acting on the actuator and a mechanical model of the forces required to buckle the beam. A computational fluid dynamics (CFD) model was constructed using the software package FLUENT to determine the forces created by the flow conditions through the valve. The initial single slot two-dimensional (2D) models were expanded to three-dimensional (3D) models to include the actual slot wall depth. Several parametric variations of the slot geometry, corresponding to various actuator voltages, were investigated. A mass flow rate inlet boundary condition was defined based on the experimentally measured flow rate for a given slot opening. With outlet pressure defined to be atmospheric pressure, a steady state solution was obtained for each valve position. Figure 7 shows the predicted velocity distribution of flow at three different openings. The velocity distribution shows that there is a recirculation zone that forms downstream of the constriction that changes with valve position. The fluidic forces on actuator walls were obtained by integrating pressure values on actuator wall areas. Figure 8 shows the forces on the left wall, right wall and the net force on the actuator. The figure indicates that the forces on the walls of the slots tend to close the actuator, similar to what is observed in the visual observations of the valve oscillation. These forces tend to peak at 14 V.

A Finite Element Model was created to investigate the force-deflection behavior of the electrothermal beam and understand the

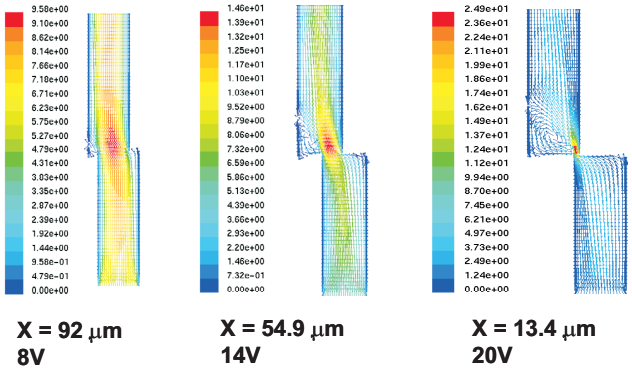

Figure 7. *Velocity (m/s) flow patterns within a single slot at a variety of openings (X) showing a recirculation zone on the left wall.*

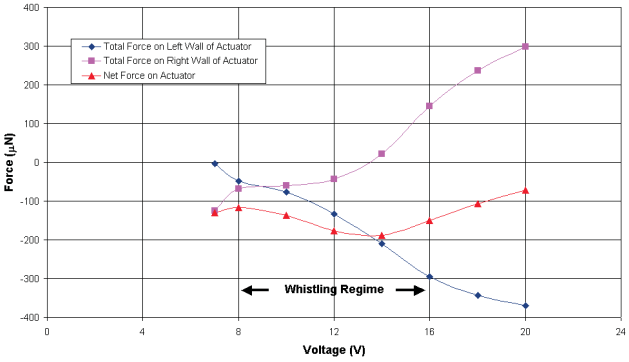

Figure 8. *Summary of results from the CFD analysis of a single gas valve slot showing maximum force acting to close the valve at 14 V.*

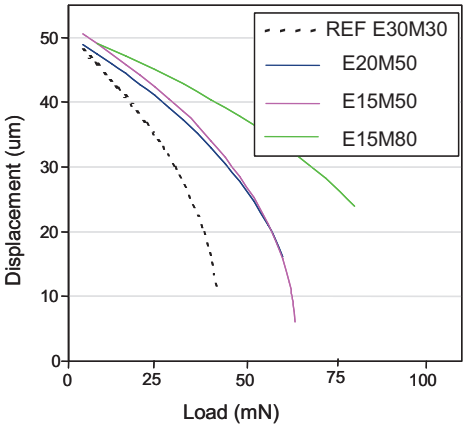

Figure 9. *Buckling results for electrothermal beam.*

effects of the loads from the fluid flow. The large deflection and snap-through buckling characteristics of the beam required a non-linear analysis. Since this increased the computational effort, a symmetric, 2D model of the beam was used to reduce simulation time. This facilitated the investigation of many different parametric variations to optimize the characteristics of the electrothermal beam. The beam was simulated by applying an elevated temperature resulting in a net free displacement, similar to the actual electrothermal behavior when electrical current is applied. Next, an opposing force, representing the forces from the fluid flow, is applied that reduces the total displacement of the actuator. The stiffness of the beam is calculated once the displacement and forces are known. The opposing force is then increased until snap-though buckling occurs as the stiffness goes to zero. An example of the force-deflection and buckling characteristics of various electrothermal beams are shown in Figure 9. Here, the legend indicates a parametric investigation of different electrothermal beam widths at the ends "E" and middle "M" in microns. Clearly, the beam can be designed to higher load carrying capability and stiffness while keeping the length constant. A similar 3D model was constructed to investigate variations in the out of plane geometry. For example, variability in fabrication of the beam, especially due to undercutting during the etching process, created beams with an hourglass cross-section. The 3D model showed that the loss of material due to undercutting led to a significant reduction in stiffness of the beam that exacerbated issues related to fluid structure interaction.

SILCONE DAMPING SOLUTION

Once it was determined that the undesirable excitation, flow instability and noise was due to the FSI, several concepts were explored to increase damping, or reduce the Q-factor of the microvalve. Many of these concepts involved springs attached to slider structure in order to dissipate energy from the motion of the valve. However, a classical solution of an integrated silicon spring attached to the slider would require a very low stiffness in order not to artificially limit the deflection of the actuator and increase the power consumption of the valve. Another possibility not explored here would be to decrease the gap (5 μm) between the slots underneath the slider and the slider itself. A smaller gap would increase damping on the device. A similar effect could be accomplished by adding a third wafer with either a corresponding set of slots on top of the actuator [9].

A less risky and more cost effective approach was to attach an elastic, flexible viscoelastic spring to the slider after assembly. Another Finite Element Model was created using ANSYS to investigate the mechanical behavior of the viscoelastic silicone straps used to increase damping of the structure. The geometry of

the strap used in the model included portions that are bonded to the slider and die edge, and also the region of the strap that is stretched when the slider moves. Static displacement constraints were imposed on the slider, and the opposing force from the strap was determined from the model. This enabled a calculation of an effective spring constant for various sizes and numbers of straps. This spring constant was subsequently introduced into the electrothermal beam actuator model and facilitated sizing of the straps such that the effect on the slider displacement due to the opposing forces of the straps was less than 5%. The stresses experienced by the strap were found to be small enough to avoid issues related to fatigue such as relaxation or debonding. The model and example stress results are shown in Figure 10. The elastic modulus for the family of silicones considered for the straps is characterized by a storage modulus (real part) and loss modulus (imaginary part). Although the loss modulus is ignored for static deflection, it increases significantly at high frequency such that at the resonant frequency of the valve, it is nearly the same magnitude as the storage modulus. Calculations based on the strap model showed that the viscous forces due to the strap could easily exceed the elastic forces. This finding gave a good indication that the viscoelastic properties of the silicone provided the damping force needed to eliminate the undesirable FSI.

A GE RTV106 paste was used and dispensed on the microvalve on two opposite locations as seen in Figure 11. RTV106 was chosen due to high temperature capability and its viscosity to prevent flow down into the slots of the microvalve. The RTV106 was dispensed using a MRSI 170G auto dispense system after the valves were attached to the boards. This tool used vision recognition to accurately apply the two straps. The final straps were 300 μm wide and extended approximately 800-1000 μm in length. Valves with silicone straps were tested as part of the flow manifold to determine the effect of these straps on the valve's reliability. The valves were actuated from a closed to open position at a frequency of 1 hz. Tests of 5 devices indicated no failure when cycling up to 10,000 cycles.

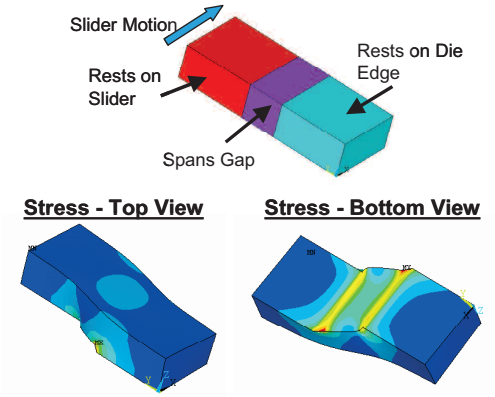

Figure 10. *Stress and design analysis of silicone strap used for damping.*

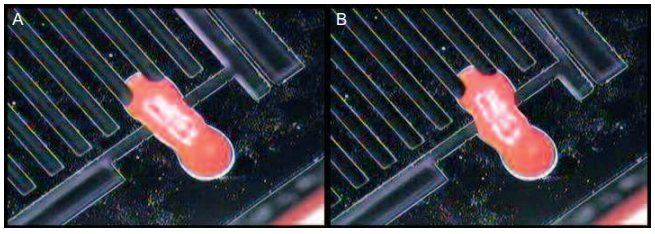

Figure 11. *Optical photographs of silcone "strap" used to dampen the flow induced oscillation of the gas valve. A, shows the valve at 0V and B shows the valve 24V.*

CONCLUSIONS

A high flow rate gas valve was designed, fabricated, and tested. Initial testing of the silicon valve indicated a flow-induced resonance which caused unstable motion of the electrothermal actuators in the plane of the wafer. This resonance of the electrothermal beams caused undesirable and inconsistent flow/voltage response of the valve. In order to understand the origin of the resonance, a CFD model of an individual slot at various positions indicated that flow forces act to close the valve. An analysis of the forces necessary to buckle the thermal beams revealed that the flow forces are insufficient on their own to cause the deflections seen experimentally. However, due to the low damping of the slider and electrothermal beams, these small flow induced oscillations are amplified into large deflections. In order to prevent the resonance of the structure, damping was added through the addition of a pair of silicone springs to the slider. Testing of these devices indicated that the resonance of the structure was removed with the addition of the silicone dampers. Limited testing of the reliability indicated that these dampers were reliable up to 10,000 cycles.

ACKNOWLEDGMENTS

The authors would like to acknowledge the support and hard work of the team at GE-Infrastructure Sensing including George Wu, Sisira Gamage, Terry Cookson and Sam Wong who fabricated the microvalve devices. The authors would like to thank Jason Castle for microvalve testing and Don Lester for work in die attach and RTV dispense. The authors also wish to acknowledge the support of Todd Graves, Dave Najewicz, and Nick Okruch.

REFERENCES

[1] R.E. Mihailovich, et. al., "Dissipation measurements in vacuum-operated single-crystal silicon microresonators", *Sensors & Actuators A*, vol. 50, pp. 199-207, (1995).

[2] K.Y. Yasumura, et al., "Quality factors in micron- and submicron-thick cantilevers", *Journal of MEMS*, vol. 9, no. 1, pp. 117-125, (2000).

[3] Y.H. Cho, et al., "Viscous Energy Dissipation in Laterally Oscillating Planar Microstructures: A Theoretical and Experimental Study", *Proc. of IEEE MEMS,* Ft. Lauderdale, FL, (1993).

[4] F.R. Blom, et al., "Dependence of the quality factor of micromachined silicon beam resonators on pressure and geometry", *J. Vac. Sci. Technol.,* B10, 1, pp. 19-26, (1992).

[5] K. Y. Yasumura, J. D. Grade, and H. Jerman, "Fluid Damping of an Electrostatic Actuator for Optical Switching Applications," *Proc. of the 2002 Solid State Sensor and Actuator Workshop*, Hilton Head, SC, pp. 358-61, (2002).

[6] M. Walters, et. al., "A silicon micromachined gate valve," presented at the *1998 Solid State Sensors and Actuators Workshop*, Hilton Head, SC, (1998).

[7] A. Knobloch, et. al., "Experimental Study of Entrance Effects on Laminar Gas Flow through Silicon Orifices", *Proc. of 2005 ASME International Mechanical Engineering Congress and Exposition (IMECE)*, Orlando, November 5-11, (2005).

[8] K. R. Williams, et. al., "A Silicon Microvalve for the Proportional Control of Fluids," *Digest of the 10th International Conference on Solid-State Sensors and Actuators (Transducers '99)*, Sendai, Japan, pp. 1804-1807, (1999).

[9] K. Y. Yasumura and H. Jerman, "Pressure Enhanced Air Damping in Enclosed Laterally Oscillating Microstructures," submitted to the *2006 Solid State Sensor and Actuator Workshop*, Hilton Head, SC, (2006).

INTEGRATED PERISTALTIC 18-STAGE ELECTROSTATIC GAS MICRO PUMP WITH ACTIVE MICROVALVES

Hanseup Kim, Aaron A. Astle, Khalil Najafi, Luis P. Bernal, and Peter D. Washabaugh

Center for Wireless Integrated MicroSystems (WIMS)
University of Michigan, Ann Arbor, MI 48109-2122, USA

ABSTRACT

We report the design, fabrication, and testing of a fully integrated peristaltic 18-stage electrostatic gas micro pump with active microvalves. It consists of nine 2-stage pump units and 19 microvalves that are serially-connected and individually-controlled. It utilizes a number of techniques to achieve high-pressure and high flow-rate performance: 1) multi-stage (18-stage) configuration to distribute the total pressure across individual stages thus allowing each stage to operate at low pressure to accommodate the weak forces available in the micro scale; 2) a fluidic resonance-based operation to achieve high mass flow rate despite the small volume displacement of an individual membrane; 3) active timing control of microvalves to regulate pump operation for either high flow or high pressure; and 4) several new designs, such as checkerboard microvalves, dual-electrodes, and dual-chambers to achieve efficient electrostatic pumping. The fabricated 18-statge pump produced the highest air flow rate of ~4.0 sccm and maximum pressure difference of ~17.5 kPa with a total power of only ~57 mW. It has a total package volume of 25.1 × 19.1 × 1 mm^3.

Key Words: Electrostatic pump, Micro gas pump, Peristlatic pump, Active microvalves.

INTRODUCTION

Recent literature has increasingly reported the importance of miniaturizing conventional 'bulk' chemical analysis or monitoring instruments in reducing analysis time, amount of target samples, cost, as well as in increasing analysis resolution, and portability. The miniaturization efforts cover numerous fields from environmental and health monitoring to bio- and pharmaceutical research, such as gas or water monitoring, blood or saliva analysis, cell or tissue handling, lab-on-a-chip, drug delivery, and drug tests. In spite of active miniaturization efforts and their recent success in sensing technology in the micro domain, micro-analysis devices still depend on conventional 'meso-scale' fluid delivery systems, such as large gas tanks or syringe pumps, to obtain high pressures and high flow rates [1]. The dependence on such 'bulky' fluidic systems prevents both a true miniaturization of the systems and precise control of small doses of chemicals and bio-subjects.

Similar challenges exist to the development of a micro gas chromatography (μGC) system under development at the Center for Wireless Integrated MicroSystems (WIMS) at the University of Michigan [2]. The WIMS μGC is a highly complex microsystem and requires high-flow rate and a high-pressure gas flow to support the operation of other micro components such as a pre-concentrator, micro columns, and micro sensors. Previous gas micropumps have shown only limited capabilities, such as low flow-rate, low pressure, and large volume, thus failing to meet the requirements of the WIMS μGC. Generally, flow rate is limited by the small deflections of a pumping membrane, while pressure is limited by the small actuation forces available in the micro domain. Additionally, micro pumping becomes unpredictable due to gas compressibility above a certain frequency.

Theoretical studies have shown that a high flow rate, high pressure, low power, and small gas micro pump could be realized by 'pressure accumulation' through a low-compression multi-stage configuration and 'high-speed volume displacement' through a high-frequency resonant operation of a pumping membrane in an electrostatic micro pump [3].

In this paper, we report the fully integrated peristaltic 18-stage electrostatic gas micro pump with active microvalves that achieves high-pressure and high flow rates by such 'pressure-accumulation' and 'high-speed volume displacement'. We also report the operation of checkerboard-shape microvalves and their influences on pumping.

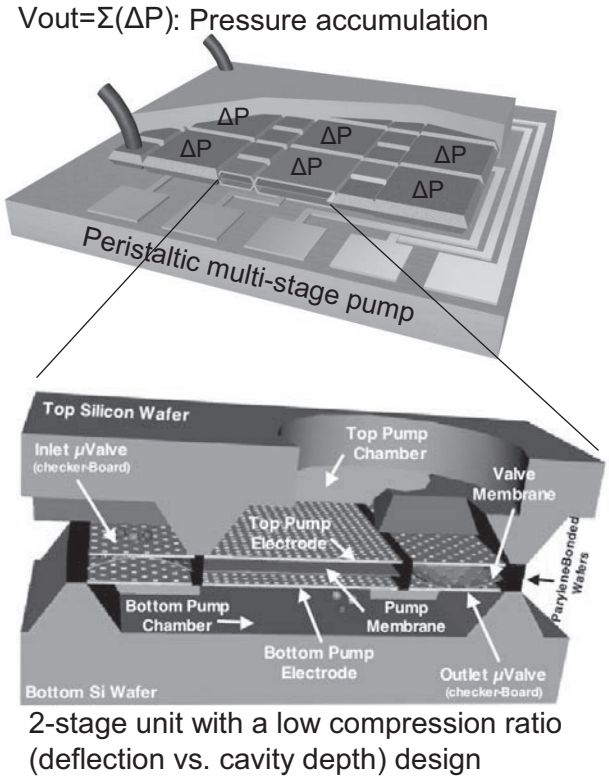

Figure 1: Illustration of (top) an integrated multi-stage (18-stage) micropump for high-pressure generation and (bottom) the detailed structure of a single pump unit (2-stage) formed by two bonded-wafers.

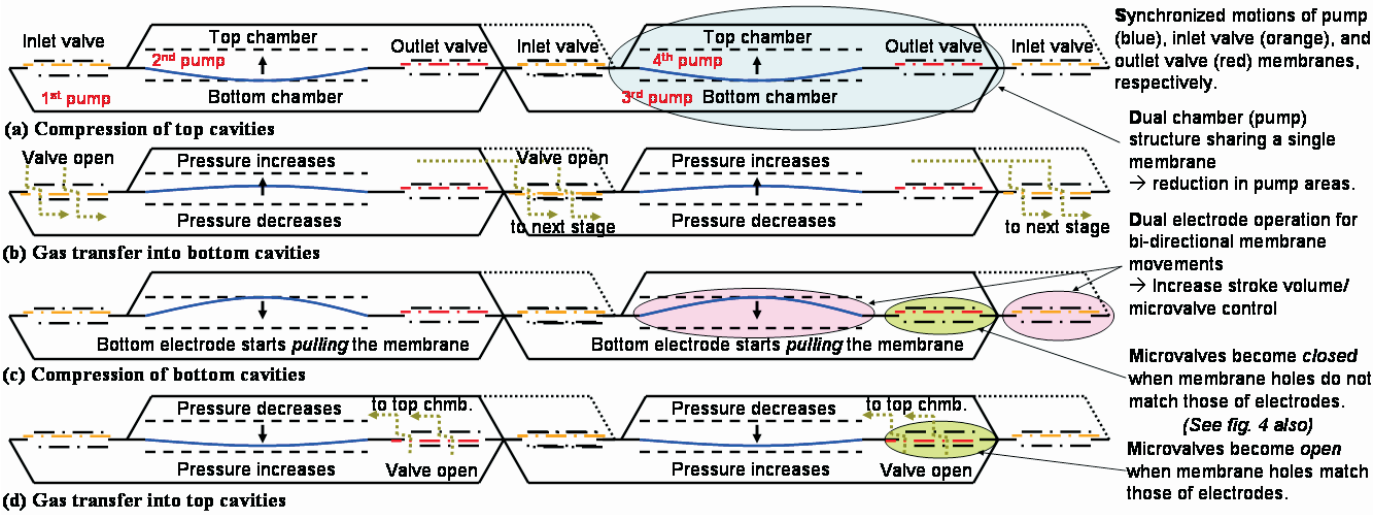

Figure 2: Operation principle of the reported multi-stage micropump. Respectively synchronized membrane movements generate peristaltic air-flows to adjacent pump stages. Air-flows come into the 1st pump chamber at bottom during a gas transfer period (b), then move out into the 2nd pump chamber on top during the next gas transfer period (d). This process repeats to next-stages.

OPERATION

The 18-stage pump distributes the overall pressure uniformly across individual stages and accumulates it for a high pressure difference across the whole pump (Figure 1-(top)). It is notable that such pressure-accumulation becomes possible through a low-compression design, where the volume compressed by a membrane is small compared to the overall pumping chamber volume [3]. In contrast, a simple cascade of several micro pumps generally leads to performance degradation due to non-uniform pressure distribution and thus pressure overloading in the last few stages [4, 5].

The 18-stage pump utilizes pumping membranes that are actuated at a high-frequency fluidic resonance and generates a high mass flow rate. The pumping membranes are made from flexible polymer films and are electrostatically-actuated by dual electrodes in two directions. The use of 'large-deflection' flexible polymer and 'pull-pull' dual-electrodes maximizes the gas flow rate.

The 18-stage pump consists of nine serially-connected 2-stage units (Figure 1-(bottom)). Each 2-stage unit includes two (dual) pumping chambers formed in the top and bottom wafers and inlet and outlet (transfer) microvalves formed between the two bonded-wafers. Dual-pumping chambers reduce the overall size of the pump by stacking two chambers on top of each other and sharing a single pumping membrane. Inlet and outlet microvalves consist of one polymer valve membrane and two silicon electrodes, all of which contain checkerboard-type array of holes. The microvalve opens or closes gas flow depending on the match or mismatch of holes between the valve membrane and one of the dual electrodes.

Figure 2 shows the peristaltic operation of the 18-stage micro pump. In this peristaltic pump, gases progress according to pressure changes in adjacent pumping chambers. As the main pumping membrane moves up and expands the bottom chamber with all the microvalves closed, the pressure in the first (bottom) chamber becomes lower (Figure 2 (a)). When the pressure in the first (bottom) chamber becomes low enough to introduce atmospheric gases into the chamber, the inlet "checkerboard" microvalve opens by a separate control signal and gases are introduced into the micro pump (Figure 2 (b)). When the pumping membranes reach the top, all the valves are closed and the next cycle begins. In the next cycle, the pressure in the first (bottom) chamber increases, as the main pumping membrane moves down and compresses the bottom chamber with all the microvalves closed (Figure 2 (c)). When the pressure in the first (bottom) chamber becomes higher than the adjacent second (top) chamber, the outlet valve opens and gases transfer from the bottom to the top chamber (Figure 2 (d)). The same process repeats through the rest of the stages. Please note that as the pumping membrane moves down (*up*), it not only compresses (*expands*) the bottom chamber into high (*low*) pressure, but also expands (*compresses*) the top chamber into low (*high*) pressure simultaneously. Also please note that an outlet valve of the previous stage is an inlet valve of the next adjacent stage.

Figure 3 shows the timing control of integrated microvalves. The timing control over the valve opening duration determines the flow rate and pressure rise of the pump. When the opening duration is long (close to half the cycle: 0.5T), the pump flow rate is maximized and the pressure rise is very small because most of the gas just transfers because it was being confined and compressed. In this case the pump operates in the high-flow rate timing mode (HFT). On the other hand, when the opening duration is short (0.25T), the duration of the membrane compression is increased and, therefore, the pressure increases and the flow rate decreases, which is defined as the high-pressure timing mode (HPT).

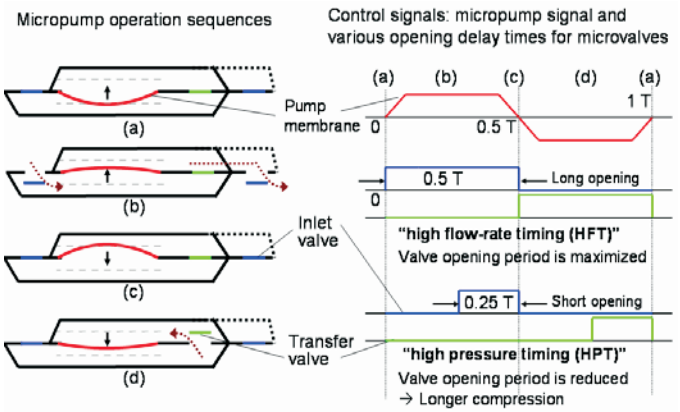

Figure 3: Microvalve timing control: HFT for high flow rate and HPT for high pressure pumping.

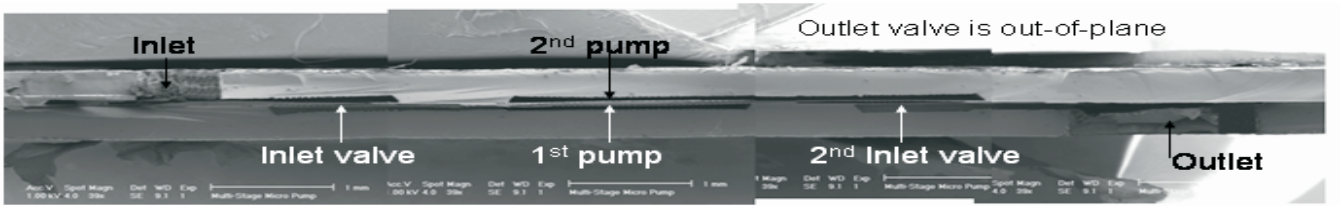

Figure 5: SEM of the cross-section of a fabricated two-stage micropump. A multi-stage micropump simply has a repeated form of such a structure.

FABRICATION

Figure 4 describes the microfabrication process for the multi-stage micro pump [6]. Fabrication consists of wafer bonding and membrane transfer among three wafers. First, a Parylene membrane is transferred from a carrier wafer onto a device wafer that contains pumping chambers, fluidic channels, and electrostatic electrodes. The transfer is performed at a wafer-level and constructs a thin (~1.5 μm thick) membrane that is suspended over the perforated electrode (~2000 μm) by a small gap (~ 5 μm) [7]. Then, a second device wafer is bonded to the first at a low temperature (~230°C) [8], thus sandwiching the pump and microvalve membranes between two electrodes and closing off the pump chamber.

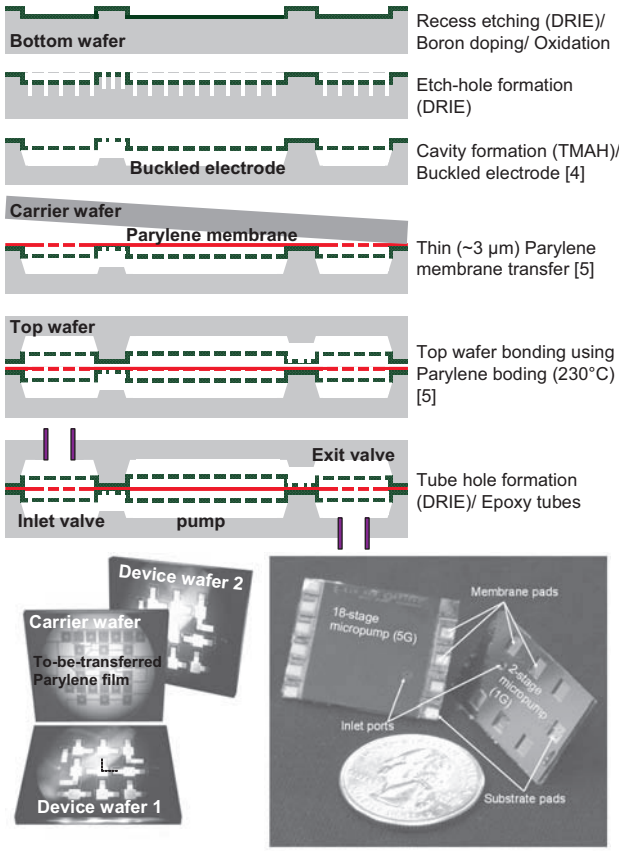

Figure 4: Microfabrication process flow [6].

TEST RESULTS AND DISCUSSION

The fabricated 18-stage micro pump as well as 4-stage and 2-stage pumps were operated at different voltages, frequencies, and microvalve timing, while being monitored using electronic mass flow meters and pressure transducers. First, the 18-stage pump is operated at different frequencies using a square wave voltage signal of ±100V to determine fluidic resonant frequency where highest flow rate or high pressure is generated. This test was performed under high flow timing (HFT) and high pressure timing (HPT), respectively. Then, at each resonance frequency, the fabricated micro pumps were operated under different load conditions to obtain the flow-vs.-pressure performance plot. Finally, they were used to pump air to move liquid droplets and columns in order to visualize and quantify performance.

Flow rate vs. operation frequency

Fabricated 18-, 4-, and 2-stage micropumps generated highest air flow rates of ~4.0, 3.0, and 2.1sccm under the high flow rate timing (HFT), as shown in Figure 6. They consumed 57.0, 15.1, and 9.1 mW. The 18-stage micropump has a resonance frequency at 17 kHz, while 4-stage and 2-stage pumps have resonance peaks at 14 kHz. Note that these measured flow rates are achieved by actuating membranes that are only 2 × 2 mm^2. When a pumping efficiency is defined by the flow rate to the membrane stroke volume, this result shows the highest efficiency by any membrane-based MEMS micro pump.

Pressure vs. operation frequency

Fabricated 18-, 4-, and 2-stage micro pumps produced maximum pressure differences of ~17.5, 7.0, and 2.5kPa under the high pressure timing (HPT), as shown in Figure 7. These maximum pressure differences were obtained at an operation frequency of ~15 kHz. Please note that the maximum pressure differences were obtained at different operation frequencies compared to the highest flow rates. The maximum pressure difference increases as the number of stages in the micro pump increases. The measured maximum pressure of 17.5 kPa is the highest pressure generated by any electrostatic MEMS micro gas pump. Additionally, such pressure-accumulation through the multiple stages is realized for the first time by any MEMS pump.

Pressure vs. flow rate for different microvalve timing

Fabricated 18-, 4-, and 2-stage micro pumps demonstrated (1) that the micro pump has multiple performance lines (HFT and HPT) depending on the microvalve timing and (2) that the micro pump performance is easily controlled by varying the microvalve timing, and (3) that a higher pressure is achieved by using HPT, and a higher flow rate is achieved by using HFT, as shown in Figure 8. As shown, each fabricated micro pump has at least two different performance lines (HFT and HPT). For example, an 18-stage micro pump generates a higher maximum pressure (17.5 kPa) using HPT than using HFT (12.8 kPa). Similarly, the pump produces a higher maximum flow rate (4.0 sccm) using HFT than using HPT (2.6 sccm).

Visualization

Finally, the fabricated micro pumps were operated to visualize the gas pumping capability by pumping liquid droplets from one end to the other end of a tube. Figure 9 shows a sequence of photos illustrating the movement of a liquid droplet by air being pumped behind the droplet by a 4-stage pump. The droplet is ethanol, and the tube has a diameter of 1.56 mm.

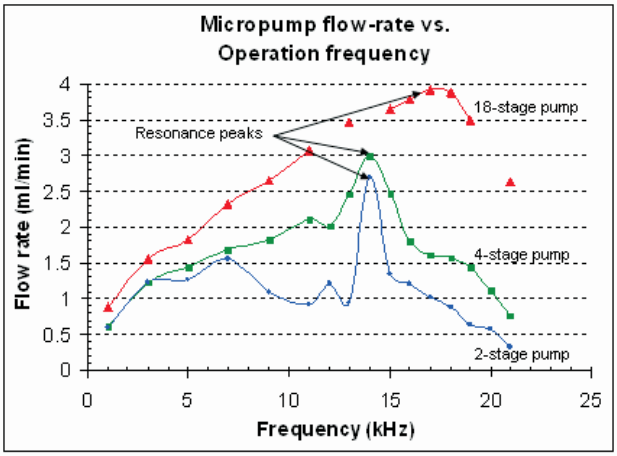

Figure 6: Mass (gas) flow rate result measured using electronic flow meters (Omega FM1600 series) over a wide range of frequencies. An 18-stage micropump has a resonance frequency at 17 kHz, while 4-stage and 2-stage pumps have resonant peaks at 14 kHz.

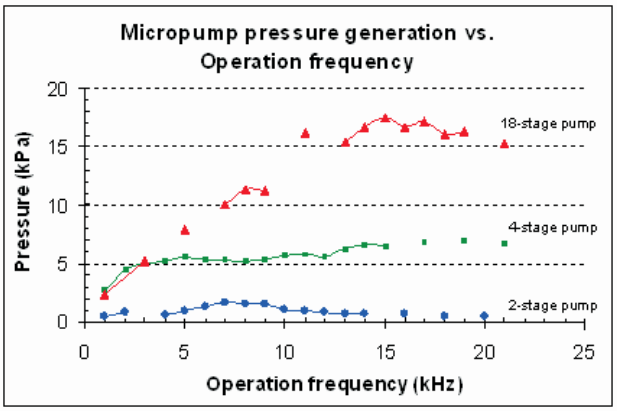

Figure 7: Measured pressure difference over a wide range of operation frequency. The pressure was measured using electronic pressure transducers (Validyne DP-45).

CONCLUSIONS

We have developed fully integrated 18-, 4-, and 2-stage peristaltic electrostatic micro gas pumps with active microvalves. The microfabricated pumps 1) achieve high pressure (17.5 kPa) by accumulating pressure differences across multiple stages, 2) obtain high flow rate (4.0 sccm) by operating at a high fluidic resonance frequency (~15 kHz) despite a small membrane size (2×2 mm^2), while consuming only small power (~57 mW), 3) have demonstrated pumping control (high flow rate or high pressure generation) by adjusting the microvalve opening duration (HFT or HPT); and 4) successfully implemented new designs, such as checkerboard microvalves, dual-electrodes, and dual-chambers to achieve efficient electrostatic pumping.

ACKNOWLEDGEMENT

This project is funded by the Engineering Research Centers Program of the National Science Foundation under Award Number EEC-9986866.

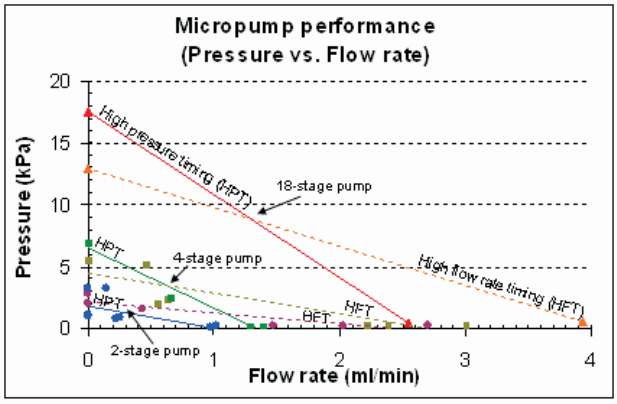

Figure 8: Pressure versus flow rate measurement results of different number of stage micropumps.

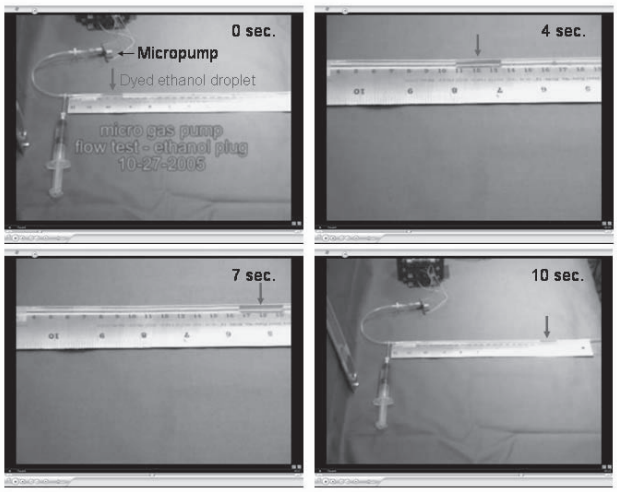

Figure 9: Visualization: ethanol drop is pumped through a thin tube (flow rate: 1.1 sccm) using air being pumped by a gas micro pump.

REFERENCES

[1] G. C. Frye-Mason et. al, "Microfabricated gas phase chemical analysis systems," *Microprocesses and Nanotechnology Conference*, pp. 60-61, 1999.

[2] E. Zellers et.al., "A versatile MEMS gas chromatograph for determinations of environmental vapor mixtures," *Hilton Head '04*, Hilton Head Island, SC, pp. 61-66, 2004.

[3] A. Astle, A. Paige, L. P. Bernal, J. Munfakh, H. Kim, and K. Najafi, "Analysis and design of multistage electrostatically-actuated micro vacuum pumps," *ASME IMECE*, 2002-39308.

[4] R. Zengerle, A. Richter, and H. Sandmaier, "A micro membrane pump with electrostatic actuation," *MEMS '92*, Travemunde, Germany, pp. 19-24, 1992.

[5] M. Stehr, H. Gruhler, H. Straatmann, S. Messner, H. Sandmaier, and R. Zengerle, "The selfpriming VAMP," *Transducers '97*, Chicago, pp. 351-352, 1997.

[6] H. Kim, K. Najafi, A. Astle, L. Bernal, and P. Washabaugh, "Fabrication and performance of a dual-eledctrode electrostatic peristaltic gas micropump," *μTAS '05*, pp. 1173-1176, pp. 2005.

[7] H. Kim and K. Najafi, "Wafer bonding using Parylene and wafer-level transfer of free-standing Parylene membranes," *Transducers '03*, Boston, MA, USA, pp. 790-793, 2003.

[8] H. Kim and K. Najafi, "Characterization of a low-temperature wafer bonding using thin film Parylene," *IEEE Journal of Microelectromechanical Systems (JMEMS)*, vol. 14, no. 6, pp. 1347-1355, 2005.

LOW POWER ELECTROSTATIC HELMHOLTZ-RESONANCE MICROJET GENERATOR FOR PROPULSION AND COOLING

Hanseup Kim[1], Abel H. Jauregui[2], Christian Morrison[1], Khalil Najafi[1], Luis P. Bernal[1], and Peter D. Washabaugh[1]

[1]Center for Wireless Integrated MicroSystems (WIMS ERC), University of Michigan, Ann Arbor, MI
[2]Center for Wireless Integrated MicroSystems, New Mexico Institute of Mining and Technology, Socorro, NM

ABSTRACT

This paper presents the fabrication and test results of an electrostatic Helmholtz-resonance micro-acoustic actuator for high-velocity air jet generation. It incorporates a curved-electrode electrostatic actuator (~8.8 μm deep) to provide twice better performance than previously reported devices that used a flat-electrode design. The out-of-plane curved electrode is formed on a silicon wafer through the buckling of stressed thin films forming the electrode.

The fabricated device has a footprint of 1.6 × 1.6 cm^2 and contains 25 acoustic micro thrusters. It operates using a 140 V and 70 kHz sinusoidal signal and produces: 1) thrust of 55.6 μN, 2) maximum air velocity of 1.2 m/s, and 3) average velocity of 1.0 m/s across the whole chip. The average power consumption of the 25 micro thruster array is 3.11 mW. The generated jet was visualized by pumping ethanol clouds into a vertical gas stream up to 12 cm. In addition, the fabricated microjets successfully cooled a heated (~ 51°C) aluminum plate (1.6 × 1.6 cm^2) down by ~10°C, which corresponds to a cooling power of 1138 W/m^2 per unit area at a temperature difference of 100°C.

Key Words: Buckled Electrode, Electrostatic actuator, Helmholtz resonance, Micro jet and propulsion.

INTRODUCTION

Microjets are useful in many applications, including chip cooling, gas pumping, and air-breathing micro thrusters for propulsion. To achieve high air velocity (and therefore high thrust), high-frequency and large-volume displacement of an actuation membrane at Helmholtz resonance is desirable (Figure 2) [1]. However, in electrostatic actuators, large-volume displacement is limited by the small gap between a diaphragm and an electrode. The small gap is necessary to keep the operation voltage low enough for practical electrostatic actuation. Such limitation can be overcome by using a curved electrode electrostatic actuator [2]. The curved electrode keeps the gap small between a membrane and a diaphragm around the peripheral, but allows a large deflection at the center. Thus, it achieves a large volume displacement at a low voltage.

Out-of-plane curved electrode structures can be easily microfabricated by engineering the buckling of stressed thin films [3]. This buckling method is simpler, cheaper, and more uniform than other methods, such as DRIE lag [4] and gray-scale photo-mask sets [5].

In this paper, we report a Helmholtz-resonance microjet generator with large-volume displacement and low power consumption, using a buckled curved electrode design. Its jetting and propulsion performance as well as cooling capability are also reported.

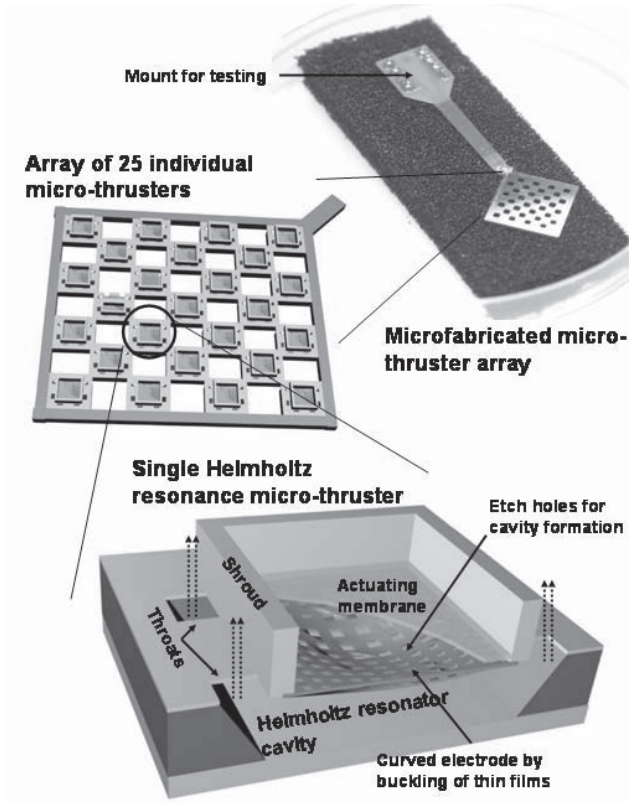

Figure 1. Conceptual illustration of a single micro-thruster with a curved electrode (bottom), array of 25 micro-acoustic-thrusters (center), and the fabricated micro-thruster array that is mounted on a PC board (top).

LOW-POWER HELMHOLTZ MICROJET

Helmholtz resonance microject

Figure 2 shows the operation of a Helmholtz-resonance microjet generator. When a membrane is deflected by a buckled electrode to compress the air inside a Helmholtz-resonance cavity, a directional air jet is ejected from the cavity (Figure 2. (a)). Since the ejected jet is directional, it transfers a large momentum out in the vertical direction. When the membrane returns to its original position due to its restoring force, the cavity volume is expanded and air is pulled into it from outside (Figure 2. (b)). The inhaled air comes from all directions and thus produces only a small momentum vertically into the cavity. Such single deflection and restoration of the membrane completes a cycle, and repeats at a high-frequency resulting in a net momentum generated and zero mass transfer per cycle. The operation frequency is determined by the geometry of the cavity.

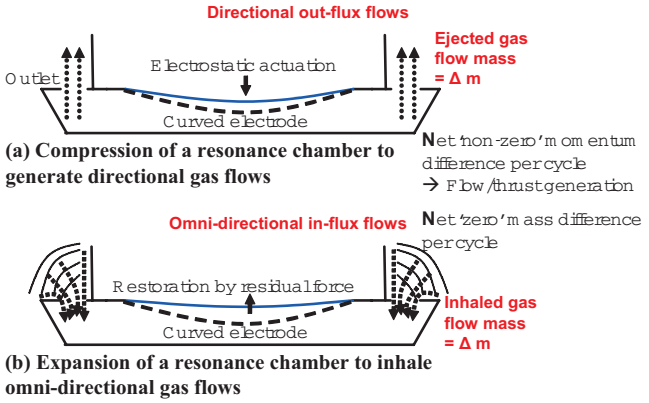

(a) Compression of a resonance chamber to generate directional gas flows

(b) Expansion of a resonance chamber to inhale omni-directional gas flows

Figure 2. Operation principle of the electrostatic acoustic microjet generator.

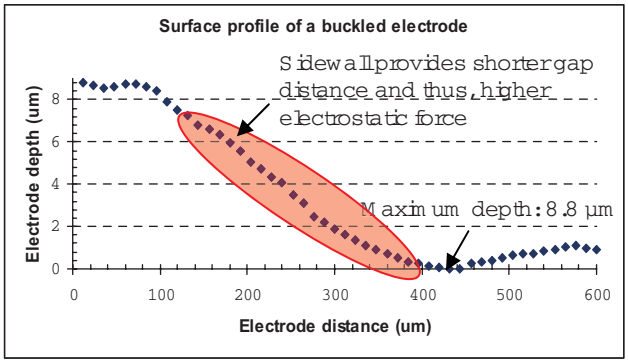

Figure 3. Surface profile of the fabricated curved electrode over half the whole electrode. This curvature enables low-voltage electrostatic operation by reducing the gap distance around the periphery while maintaining a large separation in the center of the actuator [3].

Buckled electrode electrostatic actuator

Curved electrodes are built by utilizing the intrinsic stress in thin films. Thin films are deposited on a substrate and then released from the substrate to form a suspended diaphragm. The built-in compressive stress in these thin films causes buckling out of the plane of the wafer, thus forming a naturally0curved diaphragm, which can be used a s curved electrode., as shown in Figure 3 [3]. The buckled electrode provides a smooth curvature around the periphery, which is necessary for low-voltage operation. In addition, it also provides high structural strength, preventing the movement of electrodes during electrostatic attraction [3].

FABRICATION

Figure 4 shows a simplified microfabrication process flow. First, layers of compressively stressed thermally grown silicon oxide (0.5-μm) and LPCVD polysilicon (3.8-μm) were deposited. Then, the polysilicon layer was doped with boron to provide high resistance against the TMAH wet etching during the cavity formation. On top of the doped polysilicon, a layer of tensile silicon nitride (0.1-μm) was deposited to induce the electrode to buckle downwards [6]. The composite layers were patterned with perforation holes using DRIE etching. These perforation holes were used to wet-etch the silicon substrate (un-doped) under the composite membrane and also to reduce

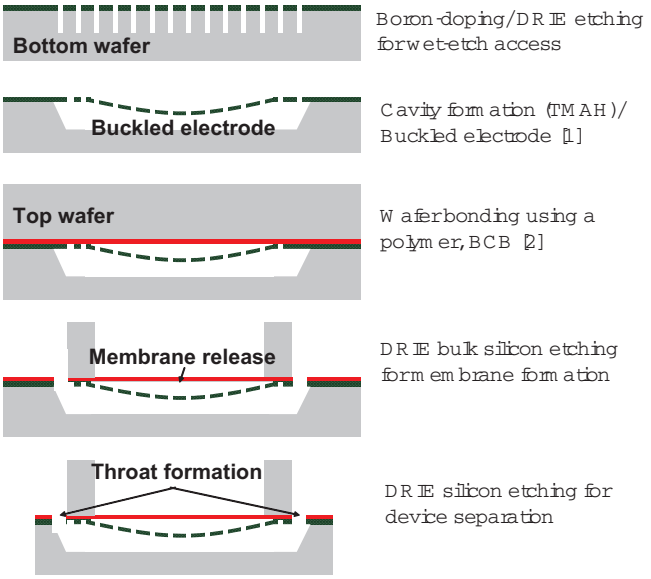

Figure 4. Simplified microfabrication process

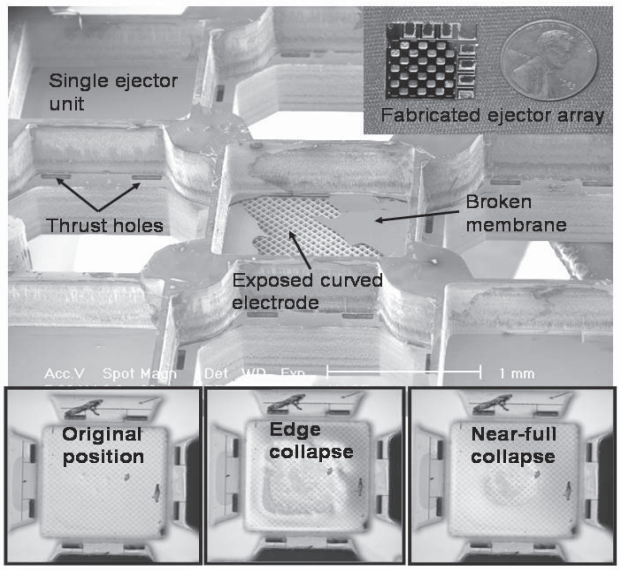

Figure 5. (Top) SEM view of a fabricated micro actuator array. Individual units have two holes per side (total eight thrust holes per device). (Bottom) Sequential photos of membrane collapse by a curved electrode.

damping during membrane actuation. When the silicon substrate was etched, the composite layers were buckled due to the intrinsic compressive stress. Then, a second wafer deposited with several films forming a moveable diaphragm was bonded using BCB [1]. Finally, the second wafer DRIE etched to release the moveable diaphragm, and to form microjet throats (holes).

The fabricated device contains 25 individual microjet generators in a chess-board array, as shown in Figure 5. Each individual microjet generator has an actuation membrane at the center and eight throats on four sides. Under the membrane, a perforated curved electrode is located over a Helmholtz-resonance cavity. The curved electrode gradually deflects the membrane down from the edges toward the center, as shown in Figure 5.

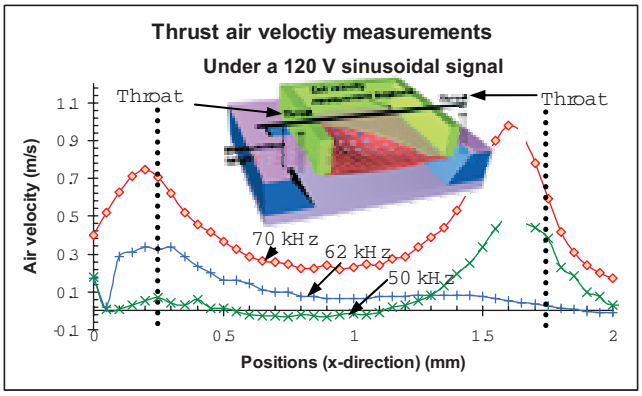

Fig 6. Air velocity measurements across an individual micro-thruster (refer to the 3D drawing) at different frequencies. Thrust values are highest over the thrust holes (throats). Thrust generation shows a maximum value at a resonance frequency of 70 kHz.

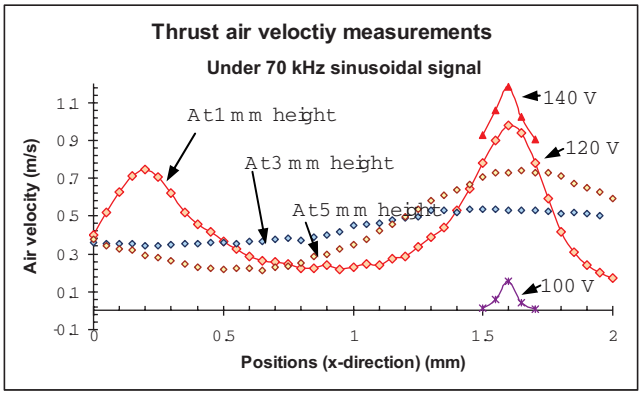

Fig 7. Air velocity measurements across an individual micro-thruster at different heights and voltages.

TEST RESULTS

The fabricated microjet generators (Figure 5) were first tested to determine the resonant frequency using a microphone located 2-cm above the chip. Peaks in the acoustic spectrum identify the resonant frequencies. Next, the air flow velocity produced by the micro-thrusters, actuated by a 140V sinusoidal signal at 70kHz, was measured using a hot-wire anemometer, which was placed at various heights above the chip and scanned across the whole chip to determine the variation in flow velocity. The jet flow was visualized with ethanol droplets formed by a commercial nebulizer. The thrust was also measured directly using a pendulum balance. Finally, cooling capability was verified by measuring temperature variations of a target surface when cooled using generated air jet.

Hot-wire anemometry test (microjet measurement)

The hot-wire anemometry tests were performed to directly measure the velocity from a microjet. A hot-wire (TSI model 1210 T1.5) was attached to a micro-manipulator with three-axis freedom and then placed on various locations across an individual microjet generator, while its resistance variation is monitored. The specific hot-wire test setup was calibrated through a series of wind-tunnel test to attune the relationship

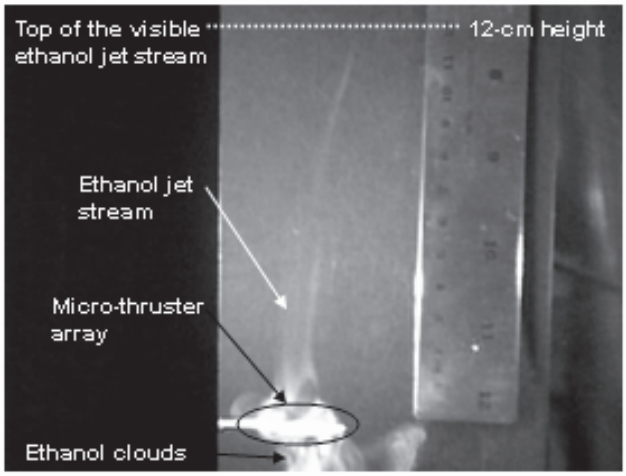

Fig 8. Visualization of thrust generation (video clips): Ethanol jetting test results show that an ethanol column was generated vertically more than 12 cm above the chip and ethanol clouds.

between resistance variation and air velocity. The hot-wire test was also performed under various operation voltages and at different heights.

Test results (Figures 6, 7) show that the fabricated individual microjet generator produced a maximum air velocity of ~1.2 m/s, and an average velocity of ~1.0 m/s across the device, when the velocity is measured at 1-mm above the throat. The measured air velocity is maximized at a resonance frequency of 72 kHz, a voltage of 140 V, and a location close to the throat (1-mm high).

Jetting test (microjet visualization)

To visualize the jetting performance, a fabricated device was actuated to jet an ethanol cloud. The ethanol cloud was formed using a commercial nebulizer under a microjet generator array, and then jetted through the thruster when it was turned on. The jetting tests (Figure 8) show that the microjet generators can pump an ethanol aerosol into a column up to 12 cm.

Thrust performance

To measure the thrust generated by a microjet array, the microjet generator array (total mass 2.0 g including mounts) was attached to a 1.8-m long string balance and operated at 70 kHz with a 140V sinusoidal driving signal. Then, the moving distance was measured to calculate the generated thrust.

Test results (Figure 10, bottom) show that the microjet array (25 devices) traveled over a distance of 4.5 mm, which corresponds to a thrust of 55.6 μN. This measured thrust value corresponds to 2.2 μN per microjet generator. The measured thrust is at least twice higher than the thrust of 1.08 μN from the previous microjet generators with flat electrodes [1].

To further illustrate thrust performance, the microjet device was operated in the pendulum balance at the same driving signal of 140 V, 70 kHz and modulated at 0.43 Hz, the resonant frequency of the pendulum. The resulting oscillatory motion is illustrated in Figure 10. The maximum displacement amplitude was 8.3 cm.

Cooling performance

Finally, cooling capability was measured with the device generating air jets toward a target (heated) plate at a distance of 4mm. The target consists of an aluminum plate (25 × 25 × 0.5 mm^3) attached to a heating element (Omega model KHLV-101/10) with the

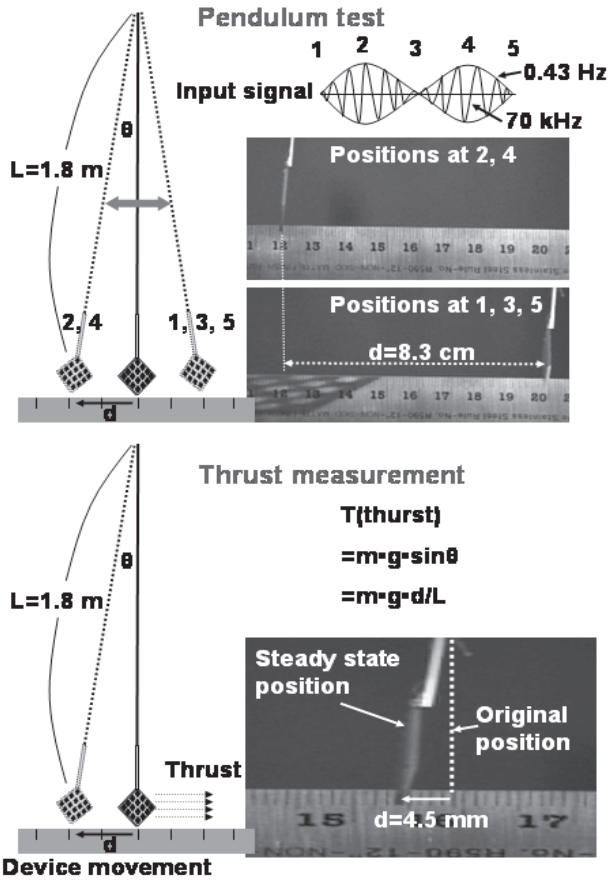

Fig 10. Visualization of thrust generation (video clips): (Top) Pendulum test show the micro device travels ~8.3-cm distance back and forth by a 0.43-Hz amplitude modulation of the sinusoidal 70 kHz driving signal under 140 V. (Bottom) Thrust measurement show the device moved ~4.5-mm under the continuous application of a 140V, 70kHz ac drive signal, this deflection corresponds to a thrust of 55 μN.

same size. The temperature variations over the heating element were measured at three different locations by using three type-K thermocouples (Omega SC-GG-K-30-36-PP) and a digital thermometer (Omega HH501DK).

Figure 9 summarizes the temperature difference from ambient and cooling power per unit area when the array is on and off. As can be seen, a heated aluminum plate was cooled down from ~51°C to ~41°C. This cooling power can be estimated to 1138 W/m^2 per unit area at a temperature difference of 100°C, which is higher than the cooling power of 600 W/m^2 from the previous flat-electrode design [7].

DISCUSSIONS AND CONCLUSIONS

The fabricated microjet generator with a buckled electrode has demonstrated that it can achieve a higher performance at lower-power consumption than the previous flat-electrode design, as summarized in Table 1. It improved the microjet thrust by 107% and the cooling power by 90%, while operation voltage is increased from 120 V to 140 V.

A few notable observations were also made during testing. First, the curved electrode was not able to deflect the membrane completely at the center. This inability came from the relationship between the increasing restoration force of a stretched membrane and the decreasing attractive force from a

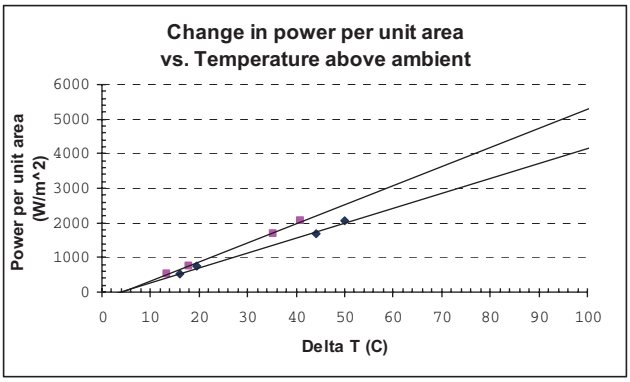

Fig 9. Cooling test results show that the generated air jet can be used to cool down a heated surface. The jet is directed toward the target surface.(pink square: after cooling, blue diamond: before cooling).

Table 1: Performance summary.

Specification	**Curved electrode micro ejector**	Flat electrode micro ejector [1]
Diaphragm deflection	**8.8 μm**	4 μm
Thrust	**55.6 μN**	26.9 μN
Max. velocity	1.2 m/s	0.80 m/s
Average velocity	1.0 m/s	0.35 m/s
Dimension (cm^3)	1.6 × 1.6 × 0.1	1.6 × 1.6 × 0.1
Voltage	140 V	120 V

reduced electrode area. This implies that another type of a curved electrode could be more efficient. Second, a higher applied voltage still could generate a higher performance. To protect the fabricated device, voltages higher than 140 V were not applied.

ACKNOWLEDGEMENT

The authors thank Fernando Cheng for his help on the hot-wire measurement testing set-up. This project is partially funded by the Engineering Research Centers Program of the National Science Foundation under Award Number EEC-9986866.

REFERENCES

[1] T.-K. A. Chou, K. Najafi, M. O. Muller, L. P. Bernal, and P. D. Washabaugh, "High-density micromachined acoustic ejector array for micro propulsion," *Transducers '01*, pp. 890-893, 2001.

[2] Legtenberg-R, Gilbert-J, Senturia-SD, and Elwenspoek-M, "Electrostatic curved electrode actuators," *Journal-of-Microelectromechanical-Systems*, vol. 6, no.3, pp.257-265, 1997.

[3] H. Kim, K. Najafi, P. D. Washabaugh, and L. P. Bernal, "Large-deflection out-of-plane electrostatic buckled-electrode actuator," *Transducers '03*, pp. 794-797, 2003.

[4] Chou-T-KA and Najafi-K, "Fabrication of out-of-plane curved surfaces in Si by utilizing RIE lag," *MEMS '02*, pp.145-8, 2002.

[5] Gimkiewicz-C, Hagedorn-D, Jahns-J, Kley-E-B, and Thoma-F, "Fabrication of microprisms for planar optical interconnections by use of analog gray-scale lithography with high-energy-beam-sensitive glass," *Applied-Optics*, vol.38, no.14, pp.2986-90, 1999.

[6] L.-S. Fan, R. S. Muller, W. Yun, R. T. Howe, and J. Huang, "Spiral microstructures for the measurement of average straingradients in thin films," *MEMS '90*, pp. 177-181, 1990.

[7] T.-K. A. Chou, K. Najafi, M. O. Muller, L. P. Bernal, P. D. Washabaugh, and B. A. Parviz, "Micromachined e-jet for IC chip cooling," *ISSCC '02*, pp. 356-357, 2002.

MEASUREMENT OF INSECT FLIGHT FORCES USING A MEMS BASED PHYSICAL SENSOR

Mansoor Nasir [a], Michael Dickinson [b] and Dorian Liepmann [a]
[a] Dept. of Bioengineering, Berkeley Sensors and Actuator Center, University of California at Berkeley, USA
[b] Bioengineering, California Institute of Technology, Pasadena, CA ,USA

ABSTRACT

In this paper we discuss the development of a force sensor for investigation of flight forces in flying insects. The proposed sensor uses piezoresistive sensing techniques to quantitatively measure changes in flight forces of a tethered insect. The sensor is fabricated on a wafer-level using standard MEMS technology. The goal of the research is the development of a sensor that allows for the measurement of forces with more than one degree of freedom (DOF). Direct measurement of rotational and translational forces will be very useful in elucidating complex aerodynamics mechanisms due to rapidly rotating and flapping wings, the understanding of which is critical in the development of micro-flying robotic insects.

INTRODUCTION

Flying insects are able to perform remarkable maneuvers and flying acrobats by a deceptively simple process of beating their wings. However, a closer look at insect flight reveals a highly complex and sophisticated mechanism based on unsteady aerodynamics. These mechanisms include principles like rotational circulation, delayed stall and wake capture which allow the insects to generate flight forces responsible for keeping them aloft. Not only do insects have more independent force controls than fixed wing aircrafts but the flight forces vary both in frequency and amplitude. Adding to the complexity is the fact that there is a huge diversity of flying insects with different wing morphologies. The study of insect flight is therefore a challenging problem from both, engineering and biological perspectives.

Biologists have generally focused on a selected few biologically significant flying insects to study insect flight. Of these fruit flies (*Drosphila melanogaster)* is probably one of the most frequently used model **[1]**. House flies (*Musca domestica*) and hawkmoth (*Manduca sexta*) have also been used for scientific research **[2], [3]**. These represent superb models for elucidating general principles that are critical in the realization of any biomemtics inspired flying microrobotic systems.

By far the most important tool for understanding flight mechanisms thus far has been high speed videography. By breaking down the rapidly beating wing motion into separate frames and then applying image processing tools, changes in wing orientation and wingbeat frequency and amplitude can be studied. Since the insects are small and hard to observe in free-flight, Dickenson et. al. developed a virtual reality flight arena where they study tethered simulation of insect flight. A wing beat analyzer uses optical tracking of tethered fruit flies to deduce changes in wing beat frequency and amplitude and this method has been successfully used to make yaw force measurements **[4]**. However, optical tracking methods require elaborate setups and it is very difficult to simultaneously measure rotational and translational forces in real time. Therefore, quantitative force measurements can greatly assist scientist in understanding insect flight both from neurophysiological and engineering standpoints.

MEMS sensors are being increasingly used in biological investigations because they combine the advantages of integrated circuit microfabrication techniques with robust macroscopic design and instrumentation principles, thus allowing an easier interface with biological environments ranging anywhere from single-cell manipulation to wafer-level drug delivery systems.

Consequently, MEMS force sensor are ideal for measuring insect flight forces which requires a design robust enough to support the insect weight but at the same time is sensitive enough to measure forces in mN—μN range. Forces can be measured using pieozoresistive, capacitive, optical and piezoelectric sensing techniques, with each having its advantages and drawbacks. However because of the aforementioned requirements, piezoresistive sensing is most suitable for measuring multidirectional forces as it provides ease of design, fabrication and needs simpler backend electronics. It should be mentioned however that capacitive force sensing has been successfully shown to accurately measure lift forces in fruit flies **[5]**. Still multi DOF force measurement remains a challenging problem yet to be solved with any kind of sensing mechanism.

The proposed force sensor uses piezoresistive sensing techniques to measure instantaneous flight force. Concurrent research on a multi DOF is also being conducted and the initial results have been reported **[6]**. Recently other biological applications of MEMS strain gauge force sensors have been reported in literature as well **[7]**.

FORCE MICROSENSOR DESIGN

Piezoresistivity is the change in resistance of the material when it is under stress. By tactically placing strain gauges at high stress areas of a structure, force can be measured. Semiconductors strain gauges are not only well-suited for bulk fabrication but are up to two orders more sensitive than metal counterparts. Since the underlining theory is well understood and the sensing mechanism is inherently mechanical, novel designs can be used measure multidirectional forces with increased sensitivity.

In developing a microsensor for measurement of flight forces, a number of requirements need to be satisfied. The sensor has to balance the material strength needed to support the weight of the flying insect while at the same time remain compliant enough to measure forces in the desired range. The design needs to be able to allow easy tethering of the fly and placement inside the virtual flight arena. Sensor reusability is important for reliable and repeatable experimental test results. Fig. 1 shows a solid model of the force sensor that replaces the current tether.

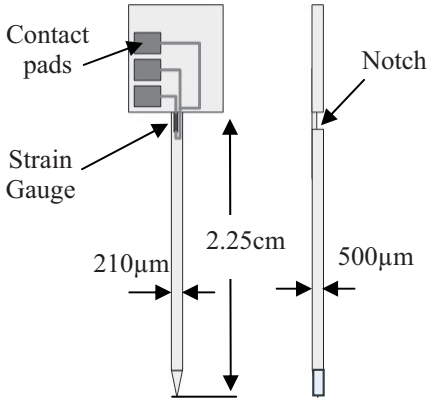

FIGURE 1*: A model of force sensor. The fly is tethered at the tapered end of the sensor.*

This design has only one strain gauge and therefore it cannot resolve force into its components. The wider section is glued to a printed circuit board and the contact pads are used for electrical interface with the PCB. Linear beam theory implies that the maximum strain is near the base of the cantilever and so placing a strain gauge in this area provides higher force sensitivity. In addition to this the substrate under the strain gauge is thinner than the rest of beam. Since most of the beam bending is restricted to this section it acts like a stress-riser and further increases our force sensitivity. Sensor sensitivity is controllable via fabrication techniques allowing for a wide range of forces and frequencies to be measurements.

Strain gauges are most commonly used in Wheatstone bridge configurations. The bridge is initially balanced with the strain gauges in the circuitry without any force applied. Once acted upon by a force, gauge resistance changes and the unbalanced bridge results in an output voltage which can then be amplified and filtered.

ANALYTICAL MODEL

Linear beam theory can be used to find the governing equations defining the relation between the force acting at the tip of the sensor and resulting strain across each strain gauges. The base of the sensor is essentially an anchor and therefore the forces only deform the beam.

FIGURE 2*: Side view of the sensor with 'L' being the length between the point where force F is applied and the anchor.*

If the strain gauge is located on the top surface of the thinner section of the beam then the stress is given by

$$\sigma = \frac{M}{I}c \qquad \text{where} \qquad I = \frac{bh^3}{12} \qquad (1)$$

where c is the distance from neutral fiber. I, which is the moment of inertia, depends on the thickness of the beam h, at the point where strain gauge is located. Using the Hook's law the change in resistance of the strain gauge can be related to the force being applied at the tip of the beam.

$$\sigma = \varepsilon.E \qquad \text{and} \qquad \varepsilon = \frac{1}{G}\frac{\Delta R}{R}$$

$$\therefore \frac{\Delta R}{R} = G\frac{L.F.c}{bh^3/12}$$

where E, the Young's Modulus and G, the gauge factor are material properties for the strain gauge. We can see that by decreasing h the stress in the thinner section can be greatly increased. Thus the change in resistance due to piezoresistive effect is magnified as seen in finite element simulation shown in Fig. 3. Also the stiffer the beam, the higher is the resonant frequency which is an important factor for testing insects with higher wingbeat frequencies.

This simple analytical model is only shown for the one force. Forces in other directions contribute to the overall change of resistance of the strain gauge but since there is only one strain gauge in this case, there is no way to resolve for these components in this design.

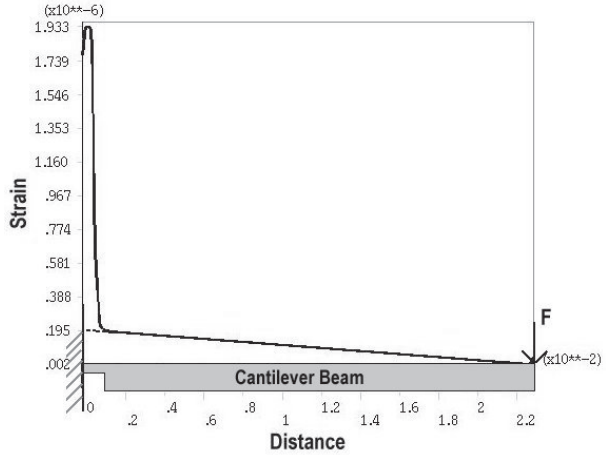

FIGURE 3: *Simulation shows that by making a section of the beam near the anchor thinner, 160µm as opposed to 500µm, strain was magnified nearly10-fold.*

FABRICATION

Standard bulk micromachining was used to fabricate the force sensor. The fabrication process has been standardized and requires only four masks.

A single p-doped polysilicon strain gauge is microfabricated near the base of the cantilever beam with Al leads for measuring the voltages across it. This sensor has three wires coming off the strain gauge to allow the strain gauge to be hooked up in a three-wire ¼ Wheatstone bridge which provides better temperature compensation. Lead-gauge overlap helps reduce the contact resistance. Low temperature oxide (LTO) deposited over the Al leads not only protects them from getting scratched but also acts as a mask for the final etch done from the top side (Fig. 4, 5).

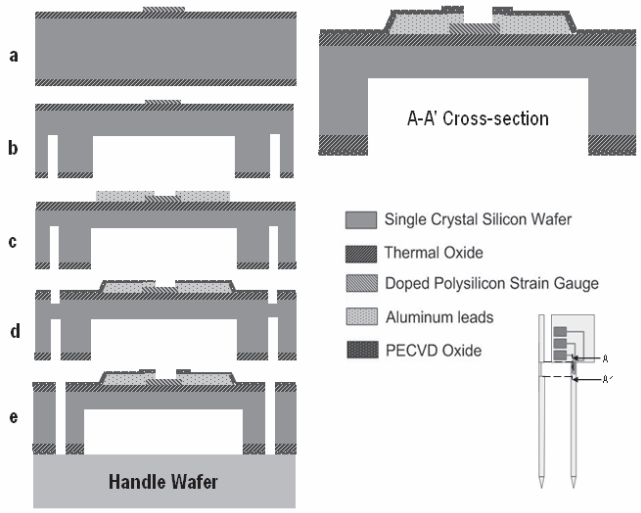

FIGURE 4*: (a) A oxide passivation layer (<1µm) is grown on a P-type single crystal Si wafer followed by deposition, annealing and pattering of N-doped polysilicon layer (~400Å (b) DRIE etch is used to etch from the back side to thin the substrate under the strain gauge and also in the trenches for through-etch (c) Aluminum (Al) (~1.2µm) is sputtered and then patterned using wet etch.(d) A thin layer of LTO (0.5µm) is deposited over the Al leads for protection. This oxide layer is etched in a RIE-etcher to open holes for through-etch (e) After putting on a handle wafer, a final DRIE-etch is done from the front side to release the sensors from the Si wafer.*

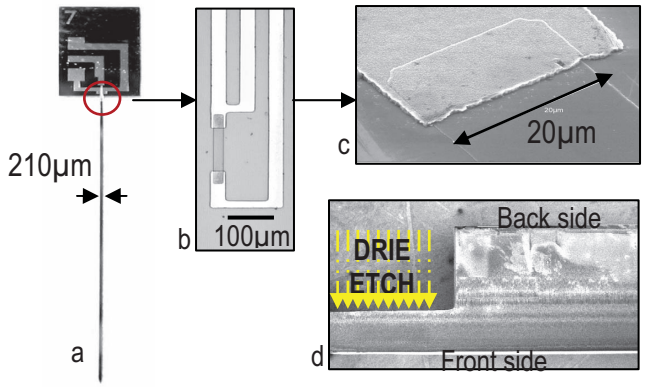

FIGURE 5*: (a) Microfabricated force sensor with one strain gauge. (b) Magnified image shows the doped poly strain gauge and the Al leads. (c) SEM of the strain gauge and Al lead overlapping it (d) Side view SEM of the sensor shows the notch made by DRIE etching from the backside.*

The electrical interface for the sensor is very simple and is made by gluing the sensor to the PCB and then using ultrasonic wirebonder to connect the pads to PCB connects.

SENSOR CALIBRATION

The force sensor was calibrated for both static and dynamic loads. The strain gauge is connected in a three-wire quarter Wheatstone bridge. The output is amplified, filtered (1kHz cutoff) and digitized to be recorded by software. For static loading, dead weights were used to apply force at the tip of the sensor. The bridge is first balanced sensor with no weight and then once loaded the change in voltage is recorded. By loading the sensor with different weights a relationship between force and voltage can be found (Fig. 6)

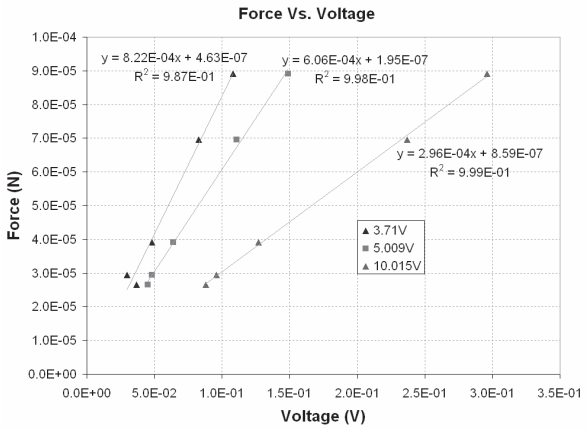

FIGURE 6*: At different bridge input voltages the strain gauge voltage follows different curves due to self-heating effects in strain gauge which becomes more prominent with higher currents (i.e. bridge input voltage). However the relationship to force is still linear in each case.*

A nanoindenter machine was used to find the spring constant of the sensor and it was within reasonable error of the values predicted by FEM simulations. Since flying insects are beating their wings during flight, the sensor must be tested under dynamic loading conditions as well (Fig. 7).

The resonant frequency was found by looking at the impulse response of the beam. It was verified that the resonant frequency of the beam is higher than the wingbeat frequencies of commonly studied insect, which are typically in 100—200Hz range **[8]**. This way aliasing effects due to under sampling can be avoided.

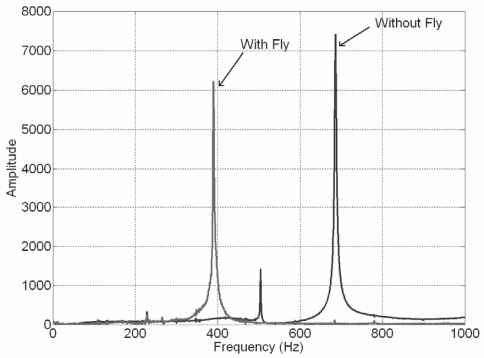

FIGURE 7*: Even when the beam is weighed down with a tethered house fly, the resonant frequency is still higher than the wingbeat frequency of the fly, reported to be around 190Hz* ***[9]****.*

INSTANTANEOUS FLIGHT FORCE MEASUREMENT

Once calibrated, flight forces in simulated flight can be found by tethering the insect to the end of the force sensor. The results shown are recorded for force measurements with tethered house flies. In order to tether the fly, it is temporarily sedated by refrigeration for 5 minutes. While sedated, the beam is glued to the fly in the thorax region. The flies are glued at a slight angle to the horizontal to mimic the body orientation in free-flight. As the body temperature of the fly returns to normal it 'wakes' up and is ready for force tests. If the fly is given a small piece of paper then it 'lands' on the paper and when pried away from the flying insect, it starts to fly again. (Fig. 8)

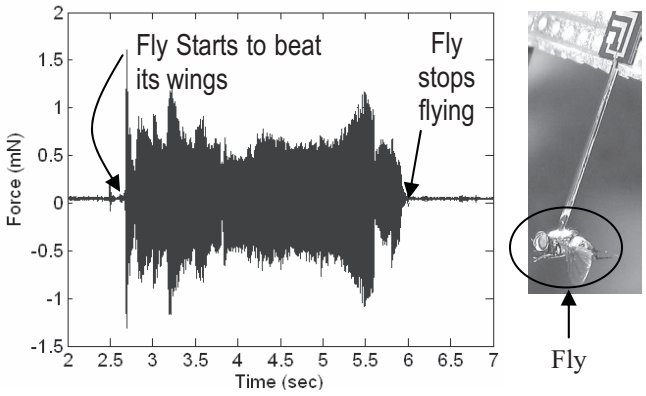

FIGURE 8*: As the house fly beats its wings, the oscillating voltage across the strain gauge can be translated into the instantaneous forces using the calibration curves.*

By taking the FFT of the signal we can look at the frequency content. The fundamental frequency for house flies is around 170Hz in tethered flight. The reported wingbeat frequency of free-flying house flies is around 190Hz (Fig. 9). The discrepancy between the two was also noted for free-flying and tethered locust and is probably a consequence of tethering **[10]**. Wingbeat frequency of many flying insects tends to deviate only slightly because beating wings at resonance minimizes the expended energy **[8]**.

Using a stiffer force sensor (i.e. higher spring constant), insects with higher resonant frequencies and harmonics can also be detected. The force sensor can therefore be a very useful tool for measurement of flight forces in insects which beat their wings at a

high enough frequency that it is very difficult to use high speed videography as there aren't enough frames per wingbeat.

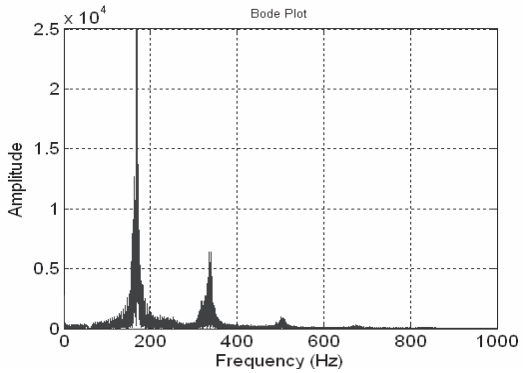

FIGURE 9: *The frequency content of the time series flight force data reveals that for a house fly the fundamental mode is around 170Hz and the first harmonic at roughly twice the fundamental mode*.

The magnitude of forces applied by the fly change significantly over time and this shows that the fly is constantly modulating flight forces to make different maneuvers. The advance ratio per wingbeat is going to be smaller then estimated solely on the basis of instantaneous forces being measured since the fly experiences drag forces during upstroke.

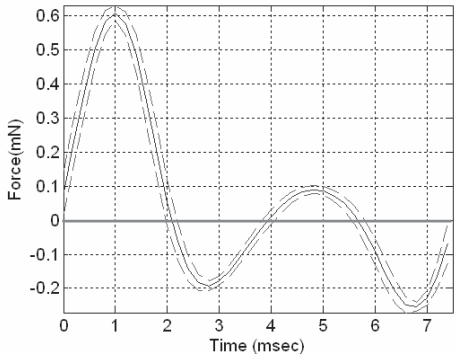

FIGURE 10: *High resolution force response over one cycle shows the forces during down and up strokes. Data from 10 cycles has been averaged. The first force peak is due to the downstroke motion of the wings.*

More importantly, tests with tethered flies have also been conducted to find forces generated during one upstroke—downstroke cycle (Fig. 10). Since the tethered insect produces flight forces in both horizontal and vertical directions, it is not possible to find out the relative contribution of lift, thrust and sideslip components with only one strain gauge. However, preliminary tests done in our lab using high speed videography of house flies tethered to the force sensor indicate that sideslip is not being actively controlled and therefore does not contribute significantly to instantaneous force measurement.

The force pattern like the one shown in fig. 10 varies widely depending on the kind of maneuver being performed by the fly. However, it can still be inferred that measured force is increasing during the downstroke which is responsible for most of the generated lift, while upstroke when the voltage is decreasing is associated with most of the forward thrust. The fact that force variation is not just a simple sinusoid clearly indicates the presence of complex mechanisms associated with unsteady aerodynamics.

CONCLUSION

A force sensor has been developed. The design of the sensor allows for measurement of instantaneous forces in tethered simulation of flight. The microfabricated sensor was calibrated for static and dynamic loads. Initial tests with tethered house flies have allowed measurement of instantaneous flight forces. Concurrent research on a multidirectional version of this force sensor will allow measurement of flight forces with more than one DOF. These quantitative force measurements when used in conjunction with high speed videography, will allow a better understanding of complex mechanisms underlining unsteady aerodynamics. In addition this tool will also allow for comparative biomechanical analysis of flight mechanism in different flying insects.

REFERENCES

[1] Vogel, S. "Flight in Drosophila II. Variations in stroke parameters and wing contour" *J. exp. Biol. 46*: pp:383-392 (1967)

[2] Wagner H. "Flight performance and visual control of flight of the freeflying housefly (Musca domestica)" *Phil. Trans. R. Soc. Lond. B, 312*: 581-595 (1983)

[3] D'Abrera, B. "Sphingidae mundi. Hawk moths of the world*." Faringdon, U.K.: E.W. Classey Ltd.* (1986)

[4] Dickinson, M. H. and Lighton, J. R. B. "Muscle Efficiency and Elastic Storage in the Flight Motor of Drosophila" *Science, Vol. 268*, p. 87—90 (1995)

[5] Potassek DP, Sun Y, Fry SN and Nelson BJ. "Characterizing fruit fly flight behavior using a micro force sensor with a new comb drive configuration." *J. of MEMS,Vol. 14*, p 4—11. (2005)

[6] Nasir, M., Dickinson, M.,Bartsch and Liepmann, D., "Multidirectional Force and Torque Sensor for Insect Flight Research" *Proc. of Transducers*, p. 555—558 (2005)

[7] Bartsch, M. S., Partridge, A., Pruitt, B. L., Full. R. J. and Kenny, T. W. "A Three-Axis Piezoresistive Micromachined Force Sensor for Studying Cockroach Biomechanics." *MEMS, ASME, Vol. 2*, p. 443—448 (2000)

[8] Dudley, R "Biomechanics of Insect Flight" *Princeton University Press, Princeton NJ*, pp. 89-90, (2000).

[9] M Rockstein and PL Bhatnagar, "Duration and frequency of wing beat in the aging house fly, Musca domestica L", *Biol Bull, Vol. 131*: 479-486 (1966)

[10] Baker P.S., Gewecke M. and Cooter R.J., "The natural flight of the migratory locust, Locusta migratoria L. III. Wing-beat frequency, flight speed and attidude." *J. comp Physiol A*, *Vol. 141,* pp:233-237 (1981)

ACKNOWLEDGEMENT

The researchers would like to thank Packard Foundation for the funding of this project and Jae-Hyung Lim for help with data acquisition software.

MEMS FILTER WITH VOLTAGE TUNABLE CENTER FREQUENCY AND BANDWIDTH

Lih Feng Cheow, Hengky Chandrahalim, and Sunil A. Bhave
OxideMEMS Lab, 102 Phillips Hall, Cornell University, Ithaca, NY 14853, USA

ABSTRACT

This paper reports on the design of a reconfigurable ladder filter using RF MEMS resonators with voltage-tunable series and parallel resonance frequencies. The ladder filter consists of one shunt and two series resonators operating in the half-wave thickness shear vibration mode. It demonstrates a center frequency tuning range of 8 MHz at 817 MHz and an adjustable bandwidth from 600 kHz to 2.8 MHz, while maintaining an insertion loss < 4 dB, stop-band rejection > 30 dB and pass-band ripple < 2 dB. This voltage tunable design enables channel agility and reconfigurability, substantially reducing the filter count in channel-select radio receiver architectures. Finally, a simple algorithm is provided to facilitate dynamic tuning of filter center frequency and bandwidth.

INTRODUCTION

Multi-band, multi-standard radio receivers require a large array of channel-select filters connected in parallel. The input capacitance of the filter array will 'load' individual filters, deteriorating their stop-band rejection. For reconfigurable radios the front-end filters must also handle encoded waveforms with different bandwidth requirements. A filter with dynamically tunable center frequency and bandwidth will not only overcome fabrication tolerances and thermal drift, but will also reduce capacitive loading at the filter input, enable handling of multiple waveforms, and substantially decrease the number of filters in next-generation receivers.

Low frequency filters comprised of electrostatically-coupled resonators have been demonstrated with 10× bandwidth tunability **[1]**. However, it is challenging to implement electrostatic coupling springs at GHz frequencies even with 100 nm air-gaps. Galayko *et al* presented a tunable bandwidth filter using clamped-clamped beam resonators in a ladder configuration **[2]**. The first transmission zero (and hence filter bandwidth) was tuned by controlling the series resonance frequency of the shunt resonator, though large parasitic capacitance prevented implementation and tunability of the second transmission zero of the filter.

In a typical ladder filter configuration, $\omega_{parallel}$ of the shunt resonator, which defines the filter center frequency f_c, is matched to ω_{series} of the series resonators. Filter bandwidth (BW) is determined by notches on either side of the pass-band and is 2× the pole-zero separation of the series and shunt resonators. The key to tunable ladder filters is the ability to change f_c and to dynamically tune the pole-zero separation $\omega_{parallel}$ - ω_{series} of the resonators. We have previously demonstrated channel-select ladder filters with 600 kHz bandwidth, 25 dB stop-band rejection, excellent shape factor, and low insertion loss (IL) using dielectrically-transduced thickness shear mode resonators **[3]**. In this paper, we introduce a voltage biasing scheme capable of independently tuning the series resonance and pole-zero separation of the filter's constituent resonators. Coupled with orthogonal frequency tuning **[4]**, we can configure the filter with desired pass-band characteristic in real time.

ORTHOGONAL FREQUENCY TUNING

The series resonance of low frequency resonators can be tuned by electrostatic spring tuning. However, the stiffness of high frequency resonators is quite large (a 1 GHz bulk-mode resonator has stiffness on the order of 1 MN/m in the resonant direction) and would require considerable electrostatic force to tune the stiffness and the series resonance frequency.

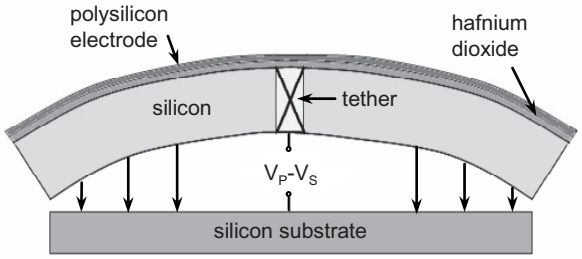

Figure 1. *Longitudinal cross-section of a half-wave thickness shear mode resonator. The tuning voltage V_p-V_s generates a vertical force and bends the silicon bar in the vertical direction, thereby changing the effective stiffness of the resonator.*

In contrast, orthogonal frequency tuning deforms the resonator in a direction perpendicular to the direction of vibration. The resonators are generally less stiff in the orthogonal direction and can be deformed with substantially less force. The symmetric half-wave thickness shear mode resonator exhibits a small-amplitude flexure mode coupled to the shear mode **[3]**. The Southwell-Dunkerley formula approximates the combined shear-flexure frequency as

$$\frac{1}{f_{total}^2} = \frac{1}{f_{shear}^2} + \frac{1}{f_{flexure}^2} .$$

When a polarization voltage V_p is applied to the resonator and a voltage V_s is applied to the substrate, the tuning voltage V_p-V_s generates an electrostatic force that deflects the structure towards the substrate, as illustrated in Figure 1. Bending the structure softens the flexural mode stiffness, lowering the series resonance frequency.

POLE-ZERO SEPARATION TUNING

A dielectrically transduced MEMS resonator can be represented by an equivalent series LCR circuit in parallel with a feedthrough capacitance C_{ft}, as shown in Figure 2. For a given transduction efficiency $\eta \equiv V_p \partial C/\partial x$, $R_X = b/\eta^2$, $C_X = \eta^2/K$, and $L_X = M/\eta^2$, where b, K and M denote the damping constant, effective spring stiffness and effective mass of the resonator. The feedthrough capacitance in a two-port resonator originates from electric field coupling from the input electrode to the output electrode and is a function of electrode geometry. The series resonance frequency is given by

$$\omega_{series} = \frac{1}{\sqrt{L_x C_x}} = \sqrt{\frac{K}{M}} .$$

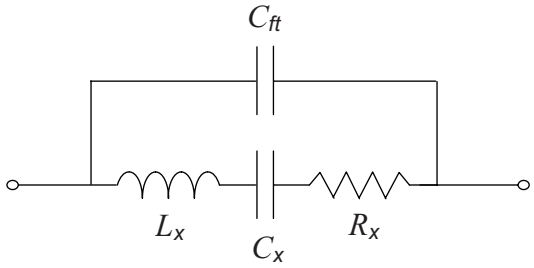

Figure 2. *Equivalent circuit of a dielectrically transduced MEMS resonator.*

An expression for the parallel resonance frequency is obtained through a first-order Taylor's expansion

$$\omega_{parallel} = \frac{1}{\sqrt{L_x \frac{C_x C_{ft}}{C_x + C_{ft}}}} = \omega_{series}\sqrt{1+\frac{C_x}{C_{ft}}} \approx \omega_{series}\left(1+\frac{C_x}{2C_{ft}}\right)$$

$$\omega_{parallel} - \omega_{series} \approx \omega_{series}\frac{C_x}{2C_{ft}}$$

$$\frac{\Delta\left(\omega_{parallel} - \omega_{series}\right)}{\Delta\omega_{series}} \approx \frac{C_x}{2C_{ft}}.$$

For electrostatic transduction, the ratio of C_X to C_{ft} is very small (10^{-4} – 10^{-2}). Therefore, the separation between the series and parallel resonances is largely independent of the series resonance frequency shifts due to changes in the spring constant *K*. The pole-zero separation can be modeled as a function of structure bias voltage V_p

$$\omega_{parallel} - \omega_{series} = \left(\frac{\varepsilon^2 A^2}{2d^4 C_{ft}\sqrt{KM}}\right) V_p^{\,2}.$$

In other words, the parallel resonance frequency is simply a voltage-controlled offset from the series resonance frequency.

FILTER TUNING ALGORITHM

A ladder filter consists of a shunt resonator and two series resonators. For minimum insertion loss and pass-band ripple, the parallel resonance frequency of the shunt resonator is matched to the series resonance frequency of the series resonators. Ladder filters can be cascaded to provide higher stop-band rejection at the expense of insertion loss. To achieve the desired center frequency and bandwidth, we use the following filter synthesis method:

1. Fix V_p and change V_s for the series and shunt resonators such that the desired series resonance frequencies are obtained (orthogonal frequency tuning).

2. Tune V_p - V_s separately for each resonator to obtain the desired pole-zero offset. Since V_p - V_s remains constant, the bending of the resonators does not change so the series resonance frequency remains fixed.

FABRICATION PROCESS

Filter T-sections consisting of one shunt and two series resonators shown in Figure 3 were fabricated on an SOI wafer with a 3 µm heavily doped device layer and 0.5 µm buried oxide. The resonators are 310 µm (and 300 µm) × 100 µm × 3.1 µm released

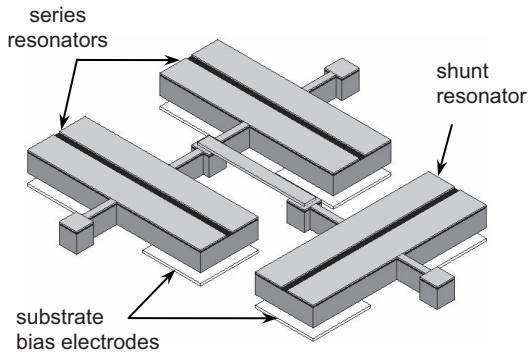

Figure 3. *3D model of tunable ladder filter.*

silicon bars with 20 nm of hafnium dioxide and 50 nm of polysilicon layers on top for dielectric transduction. Orthogonal frequency tuning was achieved by applying a substrate bias voltage to bend the resonators in the vertical direction. A back-side etch was added to the fabrication process in **[3]** to create substrate islands for independent tuning of the resonators. A front-side trench etch allowed isolated DC bias voltages to be applied to the resonators (Figure 4). Process limitations prevented polysilicon connections between the series and shunt resonators, so a small gold bondwire was implemented as seen in Figure 5.

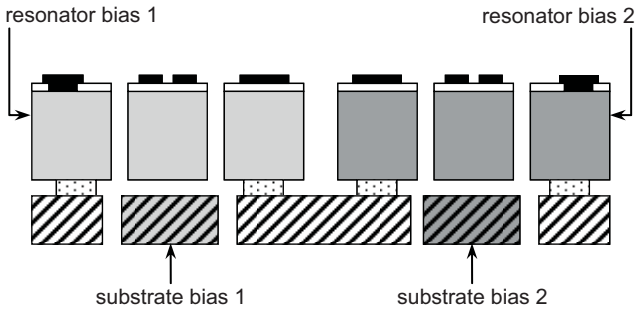

Figure 4. *Device cross-section with isolated resonator and substrate for applying independent tuning voltages.*

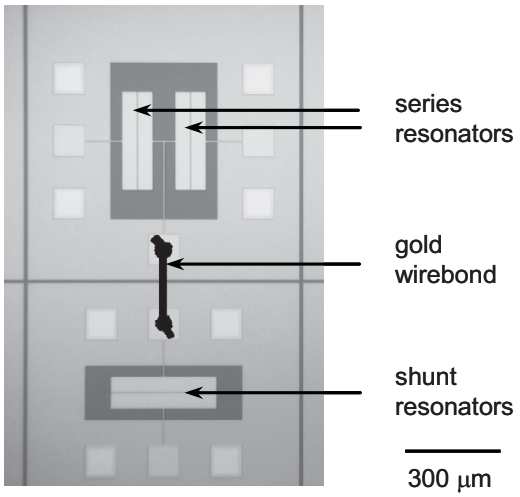

Figure 5. *Microphotograph of tunable ladder filter with a gold wirebond bridge. Care must be taken to ensure that the wirebond does not damage the oxide under the pads and short the devices.*

EXPERIMENTAL RESULTS

The resonators and filters were characterized using a DesertCryo microwave probe station. The resonator proof-mass was grounded and a DC bias V_p was applied to both the drive and sense electrodes with MiniCircuits bias-Ts. Quality factor characterization and S_{21} transmission measurements were performed using an Agilent 8722ES Network Analyzer. The resonators and filters were terminated with 50 Ω and 500 Ω impedances, respectively.

Measurement results demonstrating orthogonal frequency tuning are shown in Figure 6. Keeping V_p constant at 5V and varying the substrate bias V_s from 5V to 17V, we can tune the series resonance frequency of a single resonator from 816 MHz to 802 MHz, while maintaining a quality factor Q > 7000. The parallel and series resonance separation does not change during orthogonal frequency tuning.

Figure 7 shows that the pole-zero separation of the resonator varies from 0.6 MHz to 1.6 MHz when V_p is changed from 5V to 12V. The substrate bias V_s was held at V_p during this measurement to prevent orthogonal forces acting on the resonator.

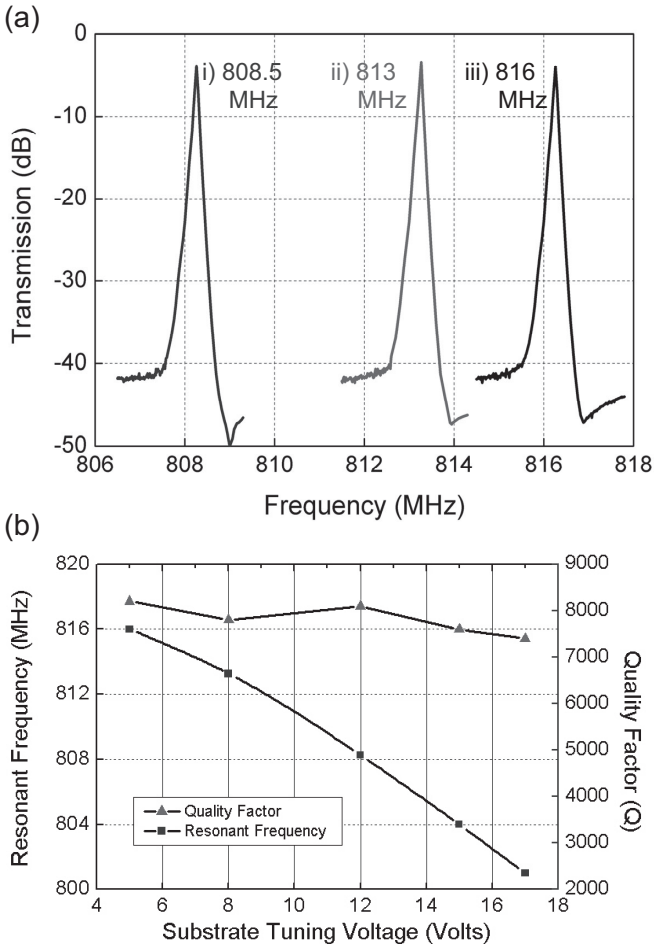

Figure 6. *(a) Measured series resonance tuning for V_s = 5V and V_s = (i) 12 V, (ii) 8 V, and (iii) 5 V. Orthogonal frequency tuning shifts series and parallel resonances by equal amount. (b) Resonant frequency tuning vs. substrate voltage. A tuning range of 15 MHz is observed while maintaining Q > 7000.*

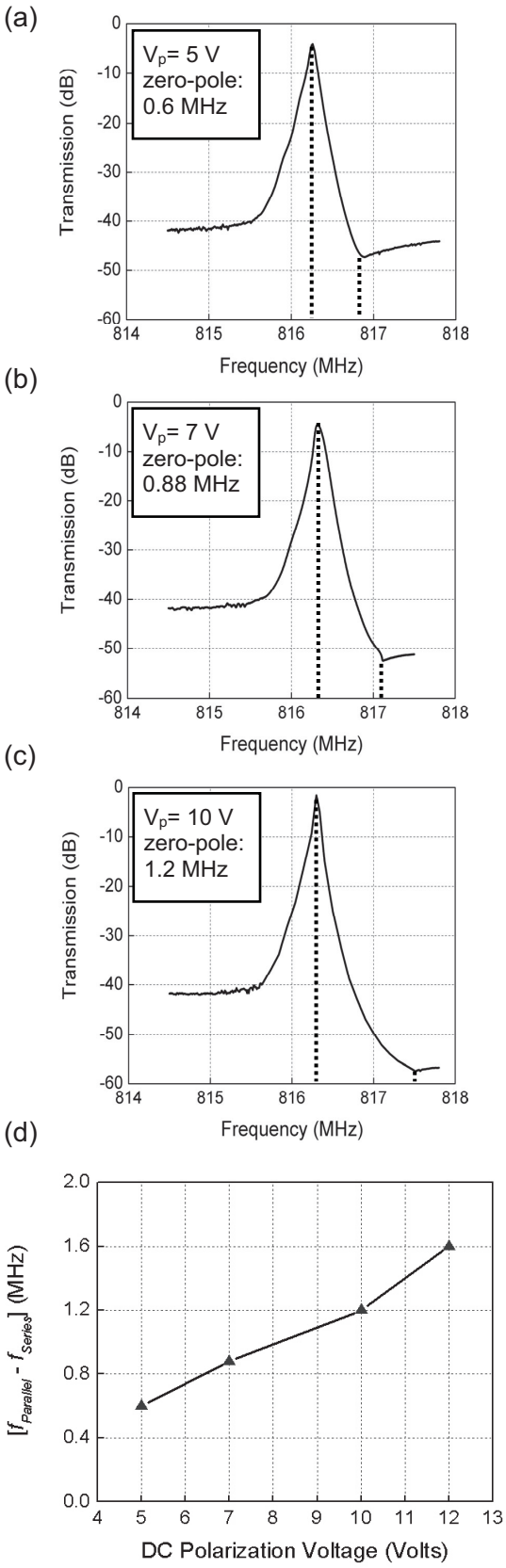

Figure 7. *(a,b,c) Measured transmission response demonstrating pole-zero separation of a thickness shear mode resonator as DC bias V_p increases from 5V to 10V. (d) Measured pole-zero separation vs. DC bias voltage of the resonator.*

A bias voltage V_p = 5 V yields a pass-band with f_c = 817.2 MHz, 0.6 MHz bandwidth, and IL of 3.2 dB (Figure 8). By applying V_s = 12 V and 15 V to the shunt and series resonators respectively, the center frequency is tuned from 817 MHz to 809 MHz without degradation in IL (3.5 dB) and shape factor (1.3), as shown in Figure 9.

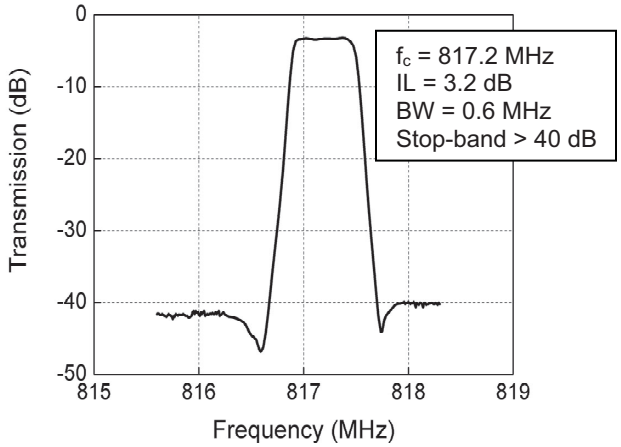

Figure 8. *Measured transfer function of ladder filter with no tuning. Resonator and substrate bias voltages are at 5V.*

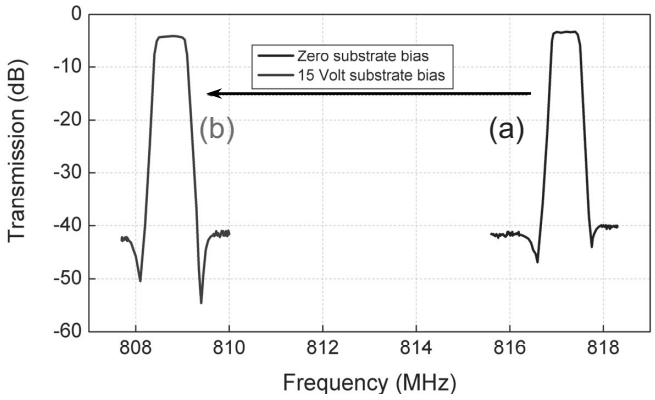

Figure 9. *Measured transmission of ladder filter with center frequency tuning from 817 MHz to 809 MHz with (a) no tuning, and (b) series resonator: V_p=5V, V_s=15V; shunt resonator: V_p=5V, V_s=12V.*

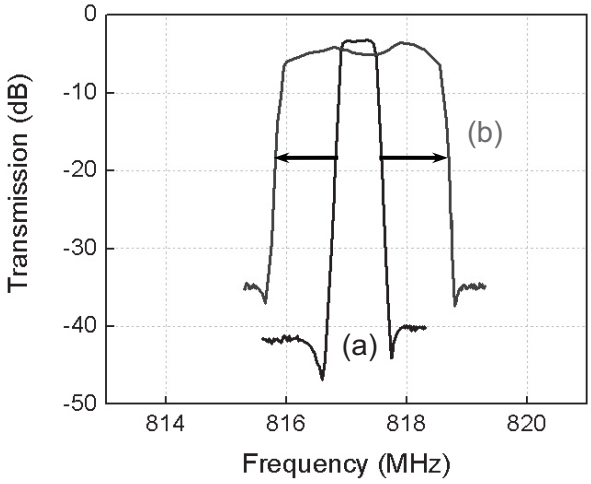

Figure 10. *Measured transmission of ladder filter with bandwidth tuning from 0.6 MHz to 2.8 MHz with (a) no tuning, (b) series resonator: V_p=12V, V_s=12V; shunt resonator: V_p=13V, V_s=16V.*

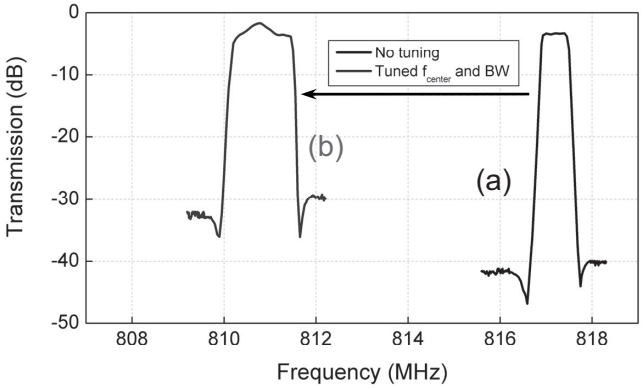

Figure 11. *Measured transfer function of ladder filter with bandwidth tuning from 0.6 MHz to 1.4 MHz and center frequency tuning from 817 MHz to 811 MHz with (a) no tuning, and (b) series resonator: V_p=10V, V_s=19V; shunt resonator: V_p=9V, V_s=17V.*

Figure 10 shows the bandwidth tuning from 0.6 MHz to 2.8 MHz while maintaining a constant center frequency at 817.2 MHz. However, the pass-band ripple increased from 0.4 dB to 1.8 dB. Finally, a combination of bandwidth and center frequency tuning is shown in Figure 11. A pass-band with f_c = 811 MHz and 1.4 MHz bandwidth is obtained.

CONCLUSIONS

Voltage tunability is more versatile than one-time modifications like laser trimming and mass loading, and enables us to overcome process tolerance and temperature variation frequency shifts. We have demonstrated bandwidth and center frequency tunability in an RF MEMS filter with IL < 4 dB and stop-band rejection > 30 dB. With process tolerance and temperature variation frequency shifts of ±1.2MHz and -14ppm/ºC, respectively, this tuning capability not only overcomes these variations, but also enables channel agility and adaptability in multi-mode radio receivers.

ACKNOWLEDGEMENTS

The authors wish to thank the Cornell Center for Nanoscale Systems and RF Micro Devices, whose generous grant made this research possible, and the Cornell Nanofabrication Facility for device fabrication.

REFERENCES

[1] S. Pourkamali *et al*, "Electrostatically coupled micromechanical beam filters," *MEMS 2004*, Maastricht, The Netherlands, January 25-29, 2004, pp. 584-587.

[2] D. Galayko *et al*, "Tunable passband T-filter with electrostatically-driven polysilicon micromechanical resonators," *Sensors and Actuators A: Physical*, vol. 117, issue 1, January 3, 2005, pp.115-120.

[3] H. Chandrahalim *et al*, "Channel-select micromechanical filters using high-K dielectrically transduced MEMS resonators," *MEMS 2006*, Istanbul, Turkey, January 22-26, 2006, pp. 894-897.

[4] H. Chandrahalim *et al*, "Thickness shear mode vibrations in silicon bar resonators," *Ultrasonics 2005*, Rotterdam, The Netherlands, September 18-21, 2005, pp. 898-901.

MICROFABRICATED PROBES FOR LABORATORY PLASMAS

Janet A. Stillman[1], Franklin C. Chiang[1], Patrick A. Pribyl[2], Mio Nakamoto[2], Walter Gekelman[2], and Jack W. Judy[1]

Departments of Electrical Engineering[1] and Physics[2], University of California at Los Angeles, Los Angeles, California, 90095, USA

ABSTRACT

We present the first of a series of microfabricated sensors for directly measuring fundamental plasma parameters with unprecedented resolution in typical laboratory plasmas. Microfabricated probes hold the promise of significantly advancing basic plasma physics by enabling the measurement of some fundamental plasma processes under controlled conditions at the relatively high plasma densities typically of interest. Our first probes are arrays of micrometer-scale electric-field sensors for directly measuring fluctuating electric fields in the Large Plasma Device (LAPD) at UCLA. They are made of polyimide, chrome, and gold, have tip widths ranging from 8 μm to 20 μm, are 22 μm thick, and spaced 40 μm apart. The fabricated tips are wirebonded to a preamplifier PCB with commercial amplifiers, and everything is inserted inside a plasma chamber. The frequency response of the detectors extends to 1 GHz.

I. INTRODUCTION

Plasma, or ionized matter, supports a variety of collective modes and makes up a very large fraction (perhaps 99%) of the observable universe. As the "fourth state of matter", plasmas also play a critical role in our economy, from the plasma processing of semiconductor wafers to the use of thermonuclear plasmas in energy research. In addition, low-temperature plasmas are already used in lighting, plasma-screen televisions, and in medicine for sterilization and dental procedures. However, despite the broad interest, utility, and widespread presence of plasmas, there are a great many fundamental unknowns about plasmas. This lack of fundamental plasma-science knowledge limits our ability to understand plasma behavior and to use it optimally for a wide range of economically significant applications (e.g., IC and MEMS manufacturing, etc.). Specifically, we need diagnostic tools and technologies that can operate at the smallest scales of import in plasmas.

One fundamental plasma parameter is the Debye length. Since a plasma is a collection of charged particles, introducing a charged object into the plasma causes plasma particles to move in response, with oppositely charged particles being attracted to the object. The net effect is that any electric fields from the object are shielded out of the bulk of the plasma by the plasma itself. The characteristic physical scale on which this happens is the Debye length, and beneath this size scale, a material object does not disturb the macroscopic plasma. The Debye length is given by

$$\lambda_D = \sqrt{\frac{\varepsilon_o \cdot k_b \cdot T_e}{n_e \cdot q_e^2}} \quad , \qquad (1)$$

with permittivity of free space ε_o, Boltzmann's constant k_b, electron temperature T_e, density of electrons n_e, and electron charge q_e. A plot of the Debye length as a function of the density of electrons in a plasma is given in Fig. 1 for a range of electron temperatures, and approximate parameter values are indicated for a variety of natural and human-made plasmas. An important observation from Fig. 1 is that the Debye length of human-made plasma systems is generally less than 1 mm, whereas it is considerably larger than 1 mm for natural plasmas.

Much work has been done in using probes to diagnose plasmas. In space, where the Debye length can be meters, it is easy to construct probes of the right size, but it is extremely difficult to control experimental conditions. The situation is reversed for almost all terrestrial plasmas of interest, such as those used in the semiconductor and microfabrication industry or in basic laboratory research, with the physical dimensions of probes being larger than a Debye length, which is typically 30 to 100 μm in these plasmas. Objects larger than these dimensions, when introduced into the plasma, result in a sheath in the local plasma potential surrounding them, and the physics of this sheath must be taken into account when attempting to deduce plasma properties from probe signals [**1**]. The presence of this sheath is particularly troublesome when attempting to measure fluctuating plasma electric fields. Such problems can sometimes be bypassed using non-invasive optical techniques [**2**, **3**], but these techniques lack 3-D spatial resolution, are time consuming, and are very expensive. A better solution is to use appropriately small direct-measurement tools.

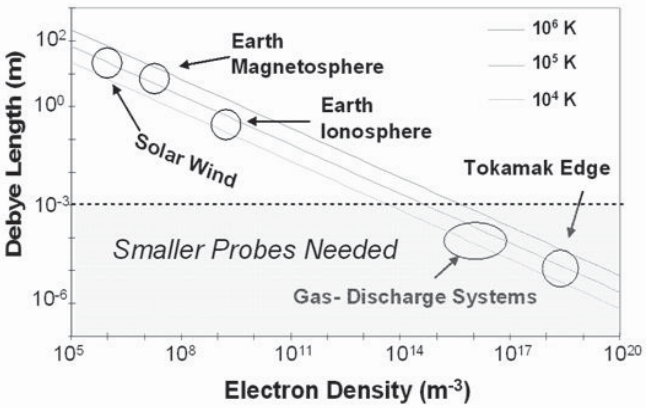

Fig. 1. *Plot of the Debye length in a plasma as a function of the density of electrons for a range of electron temperatures.*

Integration of microfabrication techniques with plasma research have already begun. Researchers, hoping to improve process control for the semiconductor industry, have successfully measured ion-flux distributions in plasma-etching reactors [**4**] and have begun integrating sensors into wafers for localized temperature measurements within plasma chambers [**5**]. However, all prior work used devices that were larger than the Debye length in the plasma being studied, which means there may be effects that have not been taken into account in the results.

Micromachining techniques have also been used to create microplasmas for localized etching and deposition [**6**]. Conventional machining techniques have yielded electric-field microprobes that showed promise in observing micron-scale fundamental phenomenon within plasmas [**7**], but were limited by the non-uniform spacing and angles between individual probe tips. The micromachined probes presented here overcome these shortcomings.

II. MOTIVATION

With the advent of micromachining and micro-electromechanical-systems (MEMS) technologies, a variety of microscale sensors can be fabricated to measure high-density terrestrial plasmas without disturbing the plasma itself. These plasma-measurement devices could bring about a sea change in our

ability to measure fundamental plasma parameters. The ultimate goal of this work is to further the understanding of plasma physics and plasma interactions in high-density plasma-processing tools. We will do this by creating a variety of microsensor systems (e.g., electric-field detectors and ion-energy analyzers).

III. DESIGN

Microscale measurement of the electric field requires differential wire tips sized on the order of the Debye length. Since the Debye length in the LAPD is typically 20 to 100 μm, we designed probe tip widths ranging from 8 μm to 20 μm and the two tips of a single pair spaced from 20 μm to 52 μm apart (Fig. 2). Tips of adjacent pairs are separated by 40 μm to 108 μm, giving us the ability to track traversing signals.

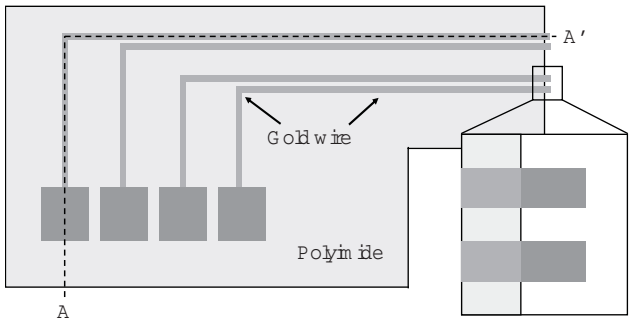

Fig. 2. *Top view of the micromachined electric-field probe.*

We arrayed several sets of differential pairs in a line in order to measure the electric field at several points along the magnetic field. We also interspersed probe-tip pairs with wire pairs lacking exposed tips, allowing us the opportunity to compare signals from the tips to signals from the wiring or other sources. Most of the probes are designed to measure the electric field along the magnetic field of the chamber, but we also included pairs for measuring the electric field perpendicular to the magnetic field.

We first tried using a high-deposition-rate PECVD oxide for mechanical support and insulation. However, after encountering many problems with intrinsic stress, we instead embedded the probes and wires in a 23-μm-thick cantilever of HD Microsystems PI-2600 low-stress polyimide. This polyimide has an advertised glass-transition temperature of 350 °C and does not begin to physically degrade until 620 °C. It is also mechanically stiff for a polyimide, with an elastic modulus of 8.5 GPa. In our process and handling we have found it nearly indestructible, and our yield was close to 100%. With a mass density of about 1.4 kg/m^3, our cantilever/probe structure in vacuum had an estimated resonance frequency of about 4.8 kHz, well below the frequencies of interest.

With a relative permittivity of 2.9, a 10-μm-thick layer of this polyimide is sufficient to yield a capacitance coupling of the 1-cm-long, 32-μm-wide probe wire to the ambient plasma of less than 3 pF. This significantly reduces the coupling of the wires to the plasma as compared to the probe tips, and is still sufficiently thin relative to a Debye length.

We selected gold as the material for the electrodes, as it is easily wirebonded to. In addition, unlike aluminum, gold forms no significant oxide layer and so would be easier to model in the future. Gold also has a low magnetic permeability, is ductile, and has a low enough resistivity that we can achieve a sufficiently low resistance in 1-cm-long, 0.5-μm thick, and 20- to 32-μm-wide wires. We found that we could not wirebond to a thin layer of gold with our available wedge wirebonder, because the wirebonder tip punctured the gold pad on the flexible polyimide base without bonding to it. Our final process, therefore, involved evaporating a thin seed layer of gold and electroplating additional gold to a thickness of 2.5 μm.

IV. FABRICATION

A. Pre-amplification Circuitry and Housing

We fabricated the preamplification circuitry with a custom 4-layer PCB using a 1.8-GHz commercial amplifier (Texas Instruments THS4303). The plasma normally has a potential of several tens of volts, so we capacitively couple the probe signal through a simple one-pole high-pass RC filter with a 3-dB frequency of about 5 MHz. We attempted to minimize the parasitic capacitance of the input circuit of this amplifier, with a target of less than 5 pF, and a resistance of less than 25 Ω.

A small custom-built copper box protects the electronics from the plasma. For cooling purposes, a copper tube with a hairpin turn is inserted into the feedthrough shaft to a point near the copper box and pressurized air is forced through the tube. The copper box has a screw-on lid and small holes on the front and back sides. Signal wires enter the box from the shaft through the hole on the back end, where they are soldered onto the PCB. We glued the probe chip onto the opposite end of the PCB, so that it stuck out through the front hole into the plasma. We then wirebonded the probe connections to the PCB.

The dimensions of the custom-built copper box are 7 cm × 5 cm × 0.5 cm, which are large enough to cause a local disturbance to the plasma. We extended the probe tips as far as possible from the box to minimize these effects; for the initial test that distance was only 0.5 cm (about 200 times the Debye length); the next iteration will be a centimeter or more.

B. Microprobe Fabrication

The two-mask fabrication process for the probe tips begins with a silicon wafer whose only purpose is to provide a platform for the probe fabrication. As seen above in Fig. 3(a), a 10-μm-thick film of polyimide (HD Microsystems PI-2600 LX) is deposited to form the lower insulator and the base of the mechanical support for the probe tips. A seed layer consisting of chrome (10 nm) and gold (30 nm) is then evaporated onto the wafer, followed by the deposition and patterning of a 6.5-μm-thick photoresist film (Microposit SJR 5740). The photoresist acts as a mold for electroplating a 2.5-μm-thick layer of gold that will serve as the electrodes and wiring (Fig. 3(b)). We electroplate with a commercial solution, Technic AR 434, at room temperature and 1 mA/cm^2. After stripping away the photoresist, the unplated regions of the seed layer is etched to electrically separate all the chips on the wafer by first dipping the wafer in a gold etchant followed by a quick dip in chrome etchant (Fig. 3(c)).

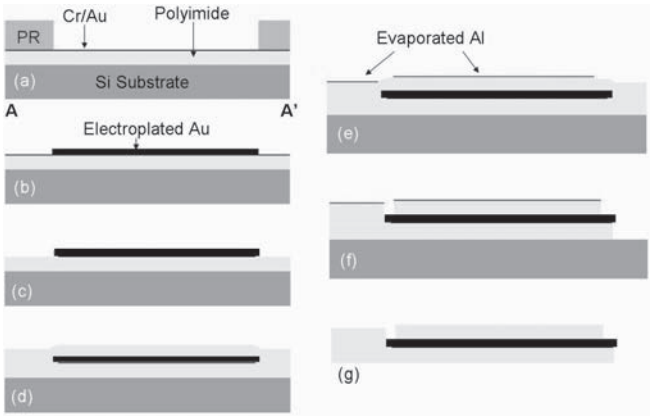

Fig. 3. *Process flow for a micromachined electric-field probe.*

We then spin on the second layer of polyimide, forming a sandwich of gold wires between two insulating polyimide layers (Fig. 3(d)). The second layer of polyimide is 13 μm thick, in order

to compensate for the topology of the wires and to guarantee good electrical insulation. We then mask the polyimide for an etch to expose the bondpads and tips on each probe as well as physically separate all the probe chips on the wafer from one another. The mask is a 50-nm-thick evaporated aluminum film, which was patterned by lift-off (Fig. 3(e)). We etch the unmasked polyimide in a 100% oxygen plasma at 0.2 Torr in a reactive ion etcher (Oxford Instruments, Bristol, UK). The gold bondpads protect the layer of polyimide beneath them (Fig. 3(f)). Although we observe a little undercut of the probe tips, the majority of the polyimide beneath the exposed wire tips remains. This makes the probes one-sided, that is, the electrodes face upwards and thus will only be able to measure the plasma on "top".

Finally, we peel the polyimide and gold "chips" off of the silicon substrate (Fig. 3(g)), and glue and wirebond them to the preamplification PCB. Figure 4 shows a probe chip mounted in the copper housing. To peel the polyimide structures off the wafer without damaging them, the adhesion promoter that we used (HD Microsystems VM-652) had to be applied in a particular pattern. If no promoter was used, the layer of polyimide would not adhere well to the wafer throughout the whole process. If too much promoter was used, the probes were impossible to remove without damaging them. Therefore, the solution we used was to apply the adhesion promoter to only the edges of the wafer before the first layer of polyimide was spun on. We did this by spinning the wafer at 300 rpm and gently touching the wafer edge with a clean-wipe moistened with the adhesion promoter, resulting in ring of adhesion promoter on only the outer 5 mm or so of the wafer (Fig. 5) As long as no air bubbles got trapped underneath the polyimide layer after it had cured, the entire layer of polyimide would remain well attached to the wafer during the whole fabrication process. However, no adhesion promoter would be present to hold down the polyimide structures after the release etch.

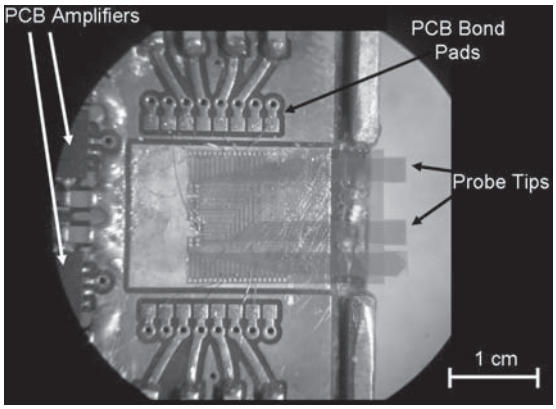

Fig. 4. *Mounted probe housed in copper box.*

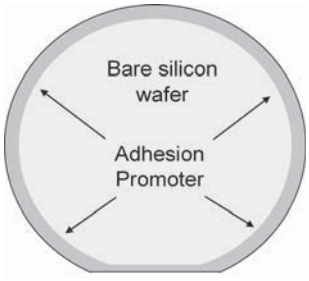

Fig. 5. *Pattern of adhesion-promoter application*

V. EXPERIMENTAL RESULTS

A. Physical Properties

The physical properties of the probe tips were investigated using a scanning electron microscope (Hitachi S4700 SEM). We found that after the oxygen plasma etch, some polyimide residue remained on the exposed gold pads and tips. This "microlace" made wirebonding difficult. To clean off the pads and tips, we etched the probe tips for five minutes in 15% CF_4 and 85% O_2, at the expense of a few hundred nanometers of gold. Figure 6 shows an SEM image of a released probe tip, and Fig. 7 shows an SEM of a set of 20-µm-wide wire tips separated by 20 µm.

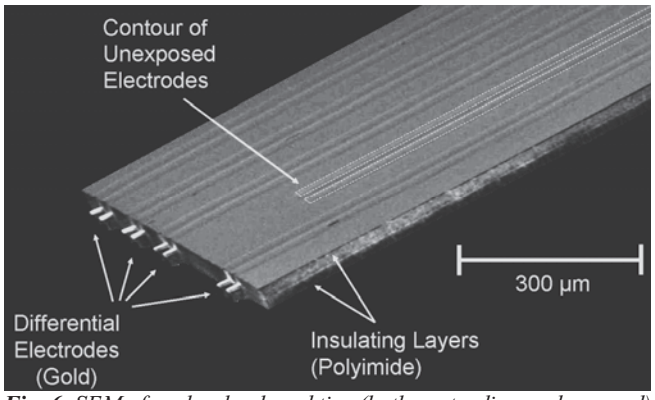

Fig. 6. *SEM of probe shank and tips (both protruding and covered).*

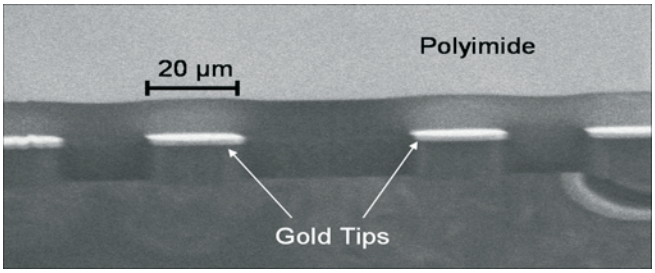

Fig. 7. *SEM of protruding probe tips.*

B. Electrical Properties

The measured tip-to-pad resistance was 22 Ω for an 8-µm-wide tip and a 32-µm-wide wire. We characterized the frequency response of an assembled probe system (six functional probe tips, mounted on the PCB, and wired through the probe shaft to an external amplifier) by placing a short piece of wire protruding from a terminated 50-Ω cable attached to a network analyzer (HP 8753D) near the probe tip array and capacitively coupling it to the probe tips; the results are shown in Fig. 8.

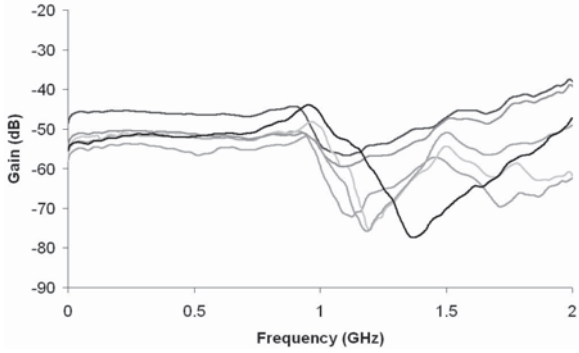

Fig. 8*. Frequency-response plot for six protruding probe tips on a single probe shank.*

The frequency response of the exposed probe tips have a relatively flat frequency response up to 1 GHz. Beyond 1 GHz, all probes display large fluctuations in the gain. This could be due to the inductance of the wire bonds and/or inadequate high-frequency printed-circuit-board layout, but is not associated with the probe tips themselves. For example, an interconnect inductance of 5 nH with a circuit input capacitance of 5 pF has a resonant frequency of

about 1 GHz. We can conclude, therefore, that the stray capacitance is not too large.

Figure 9 shows the FFT of the smallest detectable signal magnitude by the complete system, found by connecting the device directly to a digital oscilloscope (LeCroy LT584) in a non-plasma environment. As can be seen, the electronics noise is far less than the detected signals with a peak amplitude of about -20 dBm.

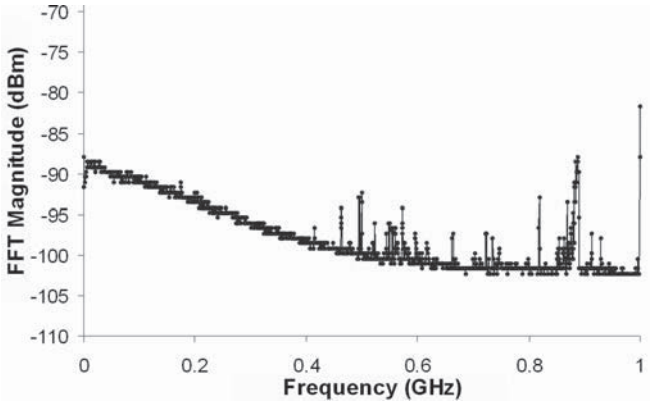

Fig. 9. *Minimum detectable signal magnitude of complete system.*

C. Testing in Plasma Environment

Initial testing of the probe in a plasma environment was done by inserting the assembled probe system (Fig. 10) into the LAPD. In one experiment, the tips are placed into a narrow current channel induced in the plasma. The results both demonstrate the functionality of the probes and reveal never-before-observed phenomena [**7**]. The physics behind the phenomena will be published separately in the future.

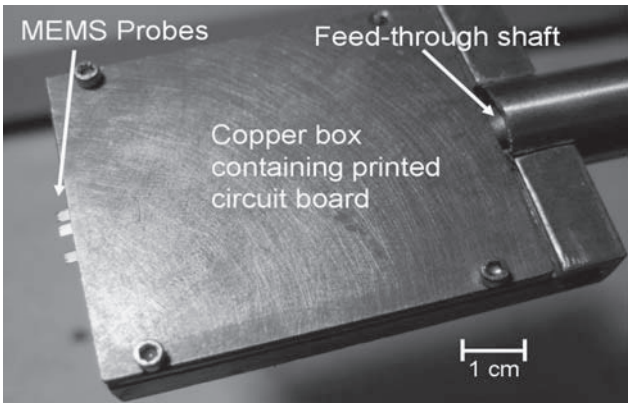

Fig. 10. *Assembled probe system.*

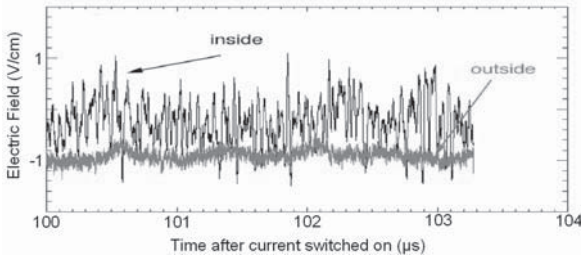

Fig. 11. *Observed perpendicular electric-field activity inside and outside of the induced current sheet as a function of time.*

Figure 11 plots the perpendicular electric field observed from both inside and outside of the current layer 100 μs after the current is switched on. The frequency spectrum of the signals plotted in Fig. 11 is shown in Fig. 12. Note the wave electric field is quite large, on the order of 1 V/cm, with the probes being small enough and close enough together to make this number believable.

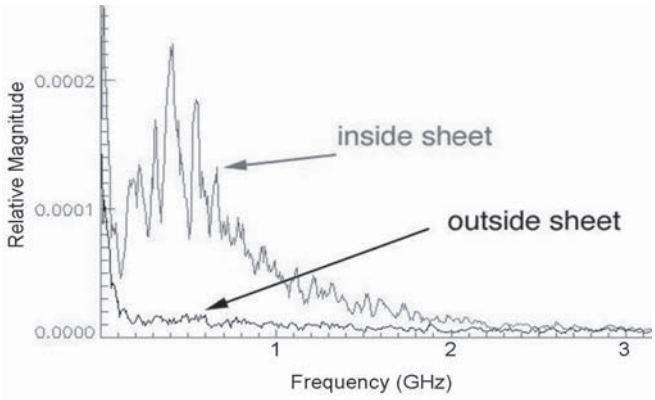

Fig. 12. *Spectrum of perpendicular electric-field activity inside and outside of the induced current sheet.*

VI. CONCLUSION

We believe that there is great value in combining the controlled environment of laboratory-created plasma with the sophistication and precision of microprobes to further our understanding of fundamental plasma physics. We have demonstrated a first-generation microfabricated plasma probe that can take local measurements of the electric field in a magnetoplasma. It is clear from the initial tests done at the LAPD that there are many previously unobserved phenomena waiting to be characterized and explained. We are now working on improvements to these microprobes, as well as other types of diagnostics, such as a micrometer-scale ion-energy analyzer to measure ion-distribution functions. The ion-energy-analyzer design will be similar to that used by other researchers [**8**, **9**], but scaled down in size. It will consist of three conductive grids biased in such a way that ions are filtered and collected based on their energies. Eventually, all of these plasma probes should incorporate on-chip amplifiers to convert the sub-picocoulomb charge levels to 50-Ω signals.

VII. REFERENCES

[1] I. H. Hutchinson, *Principles of Plasma Diagnostics*, 2nd ed., 2002, Cambridge University Press.

[2] Bachet et al., "Laser-Induced Fluorescence Observation of Self-Organized Ion Structures Induced by Electrostatic Perturbations," *Phys. Rev. Lett.* vol. 80, no. 15, pp. 3260-3263 (1998).

[3] Sadeghi et al., "Transport of Argon Ions in an Inductively Coupled High-Density Plasma Reactor," *Appl. Phys. Lett.,* vol. 70, no. 7, pp. 835-837 (1997).

[4] Kim et al., "An On-Wafer Probe Array for Measuring Two Dimensional Ion Flux Distributions in Plasma Reactors," *Rev. Sci. Instr.*, vol. 73, no. 10, pp. 3494-3499 (2002).

[5] Freed et al., "Autonomous On-Wafer Sensors for Process Modeling, Diagnosis, and Control," *IEEE Trans. Semicond. Manuf.*, vol. 14, no. 3, pp. 255-264 (2001).

[6] Wilson et al., "Silicon Micromachining using *In Situ* DC Microplasmas," *J. Microelectromech. Syst.*, vol. 10, no. 1, pp. 50-54 (2001).

[7] Pribyl et al., "Debye-size Microprobes for Electric-Field Measurements in Laboratory Plasmas," *Rev. Sci. Instr.*, (submitted Sept. 2005).

[8] Stone et al., "Instrument for Differential Ion Flux Vector Measurements On Spacelab 2," *Rev. Sci. Instrum.*, vol. 56, no. 10, pp. 1897-1902 (1985).

[9] Blain et al., "High-Resolution Submicron Retarding Field Energy Analyzer for Low-Temperature Plasma Analysis," *Appl. Phys. Lett.*, vol. 75, no. 25, pp. 3923-3925 (1999).

MICROMECHANICAL TIME DELAY MECHANISMS FOR ORDNANCE FUSING

Jing Liu and Don L. DeVoe
Center for Micro Engineering, University of Maryland
College Park, MD USA

Lawrence Fan
Naval Surface Warfare Center
Indian Head, MD

ABSTRACT

Micromechanical SOI/DRIE time delay mechanisms have been developed as part of a larger fuzing system for rifled munitions, in which a passive timing mechanism triggers at a predetermined rotational speed, followed by a desired delay time before the next element of the munition fuzing train is activated. Mechanism arrays designed to initiate at centrifugal accelerations up to 263 g are simulated and characterized using a high-speed camera, with delay times of between 0.67 and 0.95 ms achieved for single array elements.

INTRODUCTION

Mechanical time delay mechanisms for munition applications typically initiate after a specific launch condition is met (e.g. threshold barrel velocity). Arming of the munition occuring once the set delay time has passed, ensuring that the munition is sufficiently far from the barrel to prevent premature detonation during the launch cycle [1]. Using a purely mechanical delay mechanism provides several advantages over electronic timers, including robustness to electronic interference and jamming, and passive operation without the need for external power. Microfabrication technology offers important benefits for time delay mechanisms, including small size, light weight, and low per-unit cost. Microfabricated inertial switches have been used in fuzing applications [2,3], but these devices are designed to trigger instantaneously upon reaching a threshold acceleration rather than providing a post-threshold delay.

A range of timing mechanisms which release stored spring energy have been reported, including runaway escapements [4-6]], gearless runaway escapements [7,8], and tuned escapements [9-11]. A microfabricated escapement mechanism for fuzing applications was recently described using both SOI/DRIE and LIGA methods [12] based on a pre-tensioned spring to store energy prior to releasing a slotted peg. In contrast to these designs which use stored potential energy to drive the mechanisms, a different design based on a rotary sequential-leaf mechanism [1,13] is used here. This design consists of an array of identical elements that pivot around their individual rotation centers. Each element is constrained from rotating until the previous element in the array has rotated past a critical angle. The first element in the chain is designed to rotate through the critical angle only after a linear acceleration threshold has been reached. When the first device element reaches its critical angle, the second element is allowed to move. The dynamics of the second element defines a time period during which the element travels from its initial position through its own critical angle, and so on until all elements of the array have switched. The total delay time provided by the mechanism is the summation of individual delay times for each element in the chain.

The sequential-leaf design is particularly attractive for miniaturization. Unlike other types of time delay mechanisms, the leaf mechanism can be realized using an array of identical structures, each consisting of a simple mass and rotational suspension spring. Fabrication is compatible with single-layer SOI/DRIE processing. Since the design does not rely on stored energy, no post-fabrication assembly is required.

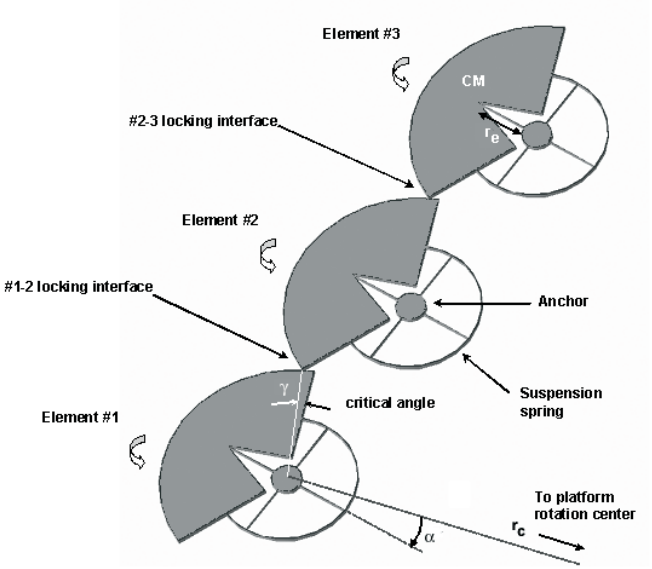

Fig. 1 Schematic of a 3-element rotary sequential-leaf time delay mechanism.

While macro-scale leaf mechanisms have been designed to respond to linear accelerations [14,15], the concept is extended in this paper to work with centrifugal acceleration. A schematic layout of a 3-element design is shown in Fig. 1. Each element consists of a fan-shaped seismic mass suspended above the substrate by a rotational spring composed of a rigid ring structure and four beams which share a common anchor point. The center of mass is designed to coincide with the apex of the v-notch where one of the quad-symmetric anchor beams connects to the mass.

THEORY

Consider a single leaf element as part of the 3-element mechanism shown in Fig. 1. The mechanism is secured to a platform rotating at a constant angular velocity of Ω, with each leaf possessing an anchor point located a distance r_c from the rotational center of the platform. When the platform rotates, centrifugal force creates a moment which induces a rotation of the first leaf about its anchor. The nonlinear equation of motion for a single leaf element is readily derived using a Lagrangian approach as,

$$\ddot{\theta}(mr_e^2 + I) - \Omega^2 m r_c r_e \sin(\theta + \alpha) + k(\theta)\theta + T(\theta, \dot{\theta}) = 0 \qquad (1)$$

where θ is the element rotation from its initial equilibrium position, m is the mass of the mechanism element, I is the element's moment of inertia about its center of mass, and k is the

torsional spring constant. The distance from the rotation center to center of mass is defined by r_e, and α defines the angle between the line connecting the center of mass and the platform rotation center, and the line connecting the center of mass and the anchor point. The displacement- and velocity-dependent torque $T(\theta, d\theta/dt)$ results from damping due to a combination of frictional contact between adjacent elements and air damping. For fabricated devices, each beam in the quad-symmetric torsional anchor was 853 μm long, 5 μm wide, and 20 μm deep. Following previous analyses of torsional anchors [16-18], the nonlinear suspension spring constant was calculated through 2-D finite element analysis with ANSYS. The resulting torque-deflection relationship for the spring is accurately described by a third-order polynomial up to a maximum rotation angle of 7°, leading to a nonlinear spring constant described by,

$$k(\theta) = 21820 + 2307\theta + 1185\theta^2 \quad (2)$$

The damping coefficient c_{air} of the element was derived according to the shape of the element [19]. For the designs explored in this work, the damping coefficient is given by,

$$\boldsymbol{c_{air}} = \frac{3\pi}{16}\frac{\mu(\boldsymbol{R_2}^4 - \boldsymbol{R_1}^4)}{\boldsymbol{h}} \quad (3)$$

where μ is the viscosity of air, h is the substrate gap, R_2 is the outer radius of the leaf element, and R_1 is an effective inner radius used to account for the notch removed from the leaf to provide connection to the spring. Note that the leading $3\pi/16$ factor results from the use of a leaf design which consists of a partial disk covering an angular range of $3\pi/4$ rad. Damping due to the spring beams and connection ring was assumed to be negligible compared to the leaf element. Using this expression, an estimated damping coefficient of 85 pN·m·s/rad was calculated and used for dynamic modeling. To model interfacital friction between adjacent leaf elements, a static friction coefficient of 0.4 and dynamic friction coefficient of 0.3 were found to provide a reasonable match between simulated and experimental results.

Theoretical values of switching times were determined using three methods. First, an analytic approximation was derived by assuming a constant angular velocity during a switching event, so that the direction and magnitude of the frictional contact force remains constant. Under zero initial conditions for leaf displacement and velocity, and assuming a constant angular velocity ω_c during the switching event, Eqn. (1) may be linearized and solved for delay time as,

$$t_{delay} = \frac{1}{\omega_n}\cos^{-1}\left[1 + \frac{k - \Omega^2 m r_c r_e \cos\alpha}{T - \Omega^2 m r_c r_e \sin\alpha}\gamma\right] \quad (4)$$

where γ is defined as the critical angle through which the leaf element must rotate before the next element becomes free to move (see Fig. 1), and ω_n is the resonant frequency given by,

$$\omega_n = \sqrt{\frac{k - \Omega^2 m r_c r_e \cos\alpha}{m r_e^2 + I}} \quad , \quad (-\cos\alpha) > 0 \quad (5)$$

and where the linear spring constant k in Eqns. (4) and (5) can be determined by taking the average value of $k(\theta)$ given by Eqn. (2), i.e.

$$k = \frac{1}{\gamma}\int_0^{\gamma} k(\theta)\,d\theta \quad (6)$$

While Eqn. (4) provides a simple estimate for the switching time, it ignores significant nonlinearities inherent in the torsional spring and damping parameters. For a more accurate simulation, the full nonlinear equation of motion was solved numerically using Matlab to determine device dynamics.

Finally, while the analytic and numerical solutions provide insight into single-element switching times, the full time delay mechanism involves multiple elements with interfaces which undergo dynamic collisions during a switching event, and thus experience mechanical interactions beyond friction alone. To simulate multi-element dynamic behavior including interfacial impact events, element contact was included in numerical dynamic simulations using ADAMS software. The nonlinear springs were modeled by connecting each element to the chip carrier by a revolute joint, with a non-linear torque applied to each element. Contact constraints were applied between the first and second elements, and between the second and third elements. As discussed previously, friction was included to simulate interfacial damping between mechanism elements.

EXPERIMENTAL DETAILS

Micro time delay mechanisms were fabricated using a single mask SOI/DRIE process with a 20 μm thick device layer and 2 μm buried oxide layer. Minimum resolution after DRIE processing was better than 3 μm for both lines and spaces, allowing the gap between adjacent mechanism elements to be on the order of 2-3 μm. A maximum sidewall roughness of R_a = 0.01 μm was measured parallel to the wafer surface. Following HF release and supercritical drying, devices were stored in ambient laboratory conditions for several weeks prior to testing. Electron micrographs of a single leaf and a closeup of the locking interface between adjacent leafs from a typical fabricated device are shown in Fig. 2.

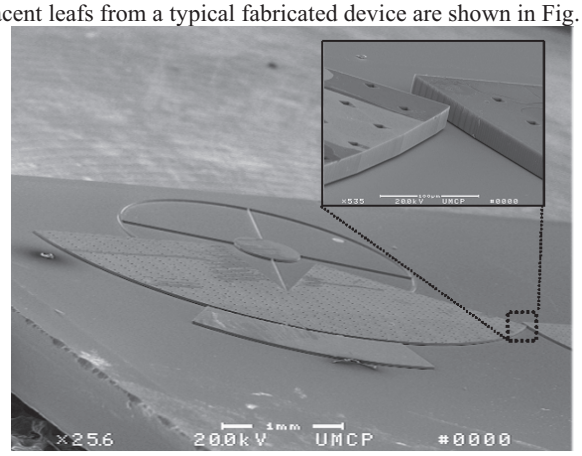

Fig. 2 Electron micrograph showing a released leaf element. Inset details locking interface between adjacent elements.

Devices were designed with 1.1 mm radius leaf elements positioned with centers of mass located 28 mm from the center of munition rotation, and to initiate switching at angular speeds ranging from 20 rps (46 g) to 50 rps (285 g). System parameters for each of the four designs are provided in Table 1, including predicted time delays based on multi-body dynamics modeling.

Table 1. Summary of designed critical angles for the first and second elements in fabricated 3-element mechanisms.

Design:	#1	#2	#3	#4
critical angle, 1st element (deg)	1.9	3.1	5.1	5.6
critical angle, 2nd element (deg)	1.2	1.8	3.8	4.3
theoretical switching accel. (g)	34	72	184	223
theoretical delay time (ms)	1.0	0.9	0.7	0.6

Devices were characterized using an experimental consisting of a chip carrier attached to a computer-controlled rotation platform based on a modified photoresist spinner capable of accelerating the chip carrier to speeds of 5000 rpm. A rhomboid prism was positioned with one end over the chip, and the other end centered on the rotation axis of the carrier. The rhomboid prism projected the mechanism image to the chip carrier rotation center through two total internal reflections from the end faces of the prism, thereby displacing the chip image by a radial distance defined by the length of the rhomboid prism. Using this approach, a camera positioned over the rotation axis was able to image the chip regardless of the rotation angle of the carrier, enabling long exposure times and eliminating the need for synchronizing image capture from a static camera located at the same radial distance as the chip. A high-speed Phantom v4.0 camera (Vision Research Inc., Wayne, NJ) enabled 3700 frames per second capture with a 0.27 ms frame interval. Imaging optics were based on a 6.5:1 ratio zoom lens (Zoom 6000, Navitar, Rochester, NY) and a 150W fiber optic light source (ACE® DDL, Schott Fostec, Auburn, NY) for coaxial illumination.

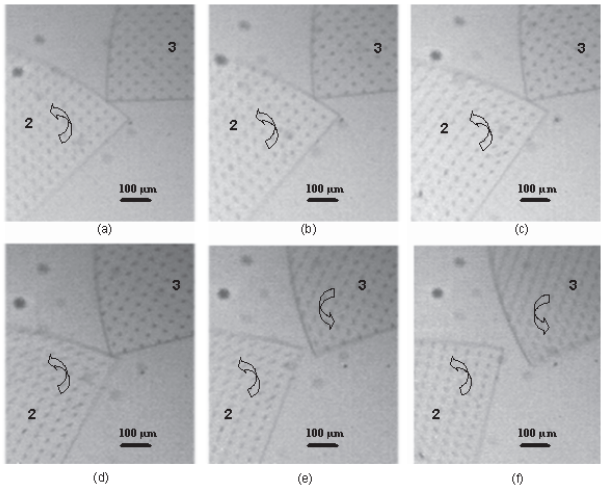

Fig. 3 Switching event between the 2nd and 3rd leaf of a fabricated mechanism. Leaf 3 is constrained from moving in frames (a-d), and released in frames (e-f) after leaf 2 reaches its critical angle.

Fig. 3 shows eight successive images during a typical switching event, revealing the progressive increase in rotation angle for element #2, and finally the unlocking of element #3 once the critical angle is reached. Rotation angles were measured using image processing software provided with the camera. Angle measurement tolerance was approximately 0.2°.

Measured centrifugal switching accelerations for each design are shown in Fig. 4, along with the theoretical predictions provided by both analytical modeling and dynamics simulations conducted with ADAMS multi-body dynamics software. Note that while measured variations in switching speed were generally independent of rotation rate, variations in the switching acceleration tended to be proportional to the square of the rotation rate, as shown by the error bars which represent +/-1σ for the experimental data. Although the device designed to switch at the highest rotation speed exhibited slightly lower variability in measured switching acceleration compared to the second-highest speed device, this overall trend remains valid within expected experimental variability. Theoretical predictions are also shown for numerical solutions to the full nonlinear equations of motion, and results of dynamics simulations using ADAMS software. A comparison of experimental and theoretical time delay measurements is shown in Fig. 5. This plot also includes the predicted values from the linearized time delay expression given by Eqn. (4). Error bars reflect the experimental time-measurement resolution for a single camera frame of +/- 0.135 ms. Each experiment was repeated using 3 different devices, with no observed variability in switching time for any of the designs. Overall, the experimental results provide reasonable agreement to the nonlinear analytic model and dynamics simulations for all tested designs. For designs with larger critical angles, the linear analytic model of Eqn. (4) agrees well with experimental results, suggesting that this simple model is suitable for further design optimization without relying on complex numerical solutions or time consuming dynamics simulations.

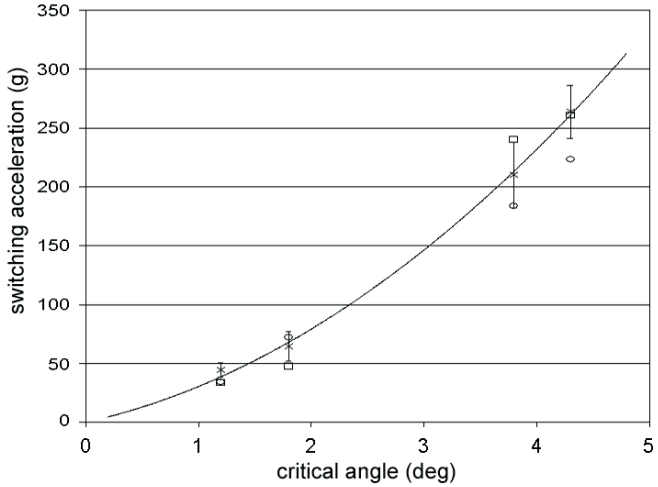

Fig. 4 Comparison of experimental (×) switching accelerations with nonlinear analytic (o) and dynamics simulation (□) analyses.

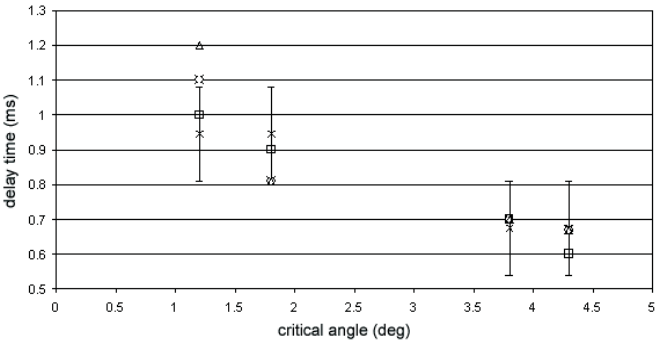

Fig. 5 Comparison of experimental (×), nonlinear numerical (o), linear analytic (△), and dynamics simulation (□) analyses.

Overall, reasonable agreement was obtained between experimental results and both analytic and dynamics simulation models, within the constraints imposed by the experimental setup. Discrepancies between the different models are reasonable, especially for devices with larger critical angles. Furthermore, such discrepancies are not surprising. The dynamics simulations involved multiple elements with interfaces undergoing dynamic collisions during a switching event. In contrast, interfacial impact was not considered in the analytic models. More importantly, the dynamics simulations used a friction model based on a piecewise continuous relationship between velocity and friction coefficient, while the nonlinear analytic model was simulated using a simpler friction model with discrete static and dynamic friction

coefficients. Friction is a critical parameter in defining the dynamics of the mechanically-interacting leaf elements, and so the observed discrepancies are not unexpected. Furthermore, despite these discrepancies, agreement between dynamics simulations and nonlinear analytic model results provides confidence that the model captures the key physics of the mechanisms, and is suitable for further use as an analytic tool without relying on the difficult and time consuming dynamics simulations. Additionally, the linearized analytic model converges well with the full nonlinear model for larger critical angles, and provides an accurate prediction of delay time using a simple expression which is suitable as a design tool.

While the sequential-leaf time delay mechanisms fabricated in this work provide up to 0.67 ms delay per element for a mechanism rotating with a centrifugal acceleration of 263 g, higher switching accelerations are required for many fuzing applications. From the theoretical model, the switching speed can be increased by increasing the stiffness of the suspension spring for the first mechanism element, thereby setting a higher rotation speed threshold required to rotate the first element beyond its critical angle and unlock the remainder of the train. For example, if the spring constant of design #1 (see Table 1) were increased by a factor of 4, the switching speed would increase from 263 g to 902 g. It is also desirable to increase the delay time of each element. Delay time is increased by reducing the resonance frequency of the elements, e.g. by reducing the spring constant. Both switching speed and time delay improvements can be realized simultaneously by reducing the spring constants for all mechanism elements, with the exception of the first element, whose suspension spring is stiffened to define a higher initial release acceleration.

CONCLUSIONS

Leaf-type micro-scale time delay mechanisms have been designed, fabricated, and tested. Delay times as high as 0.95 ms were realized for single elements within 3-element mechanisms operating at relatively low rotational speeds (20 rps, with a centrifugal acceleration of 44 g). At higher speeds (50 rps, 263 g) delay time for devices which differed only in their critical rotation angles exhibited delay times of 0.67 ms per element. This study was conducted to evaluate the basic functionality of microfabricated sequential-leaf time delay mechanisms for application to fuzing systems. Higher rotation speeds of 200-250 rps and associated centrifugal accelerations of several thousand g are required for many munitions applications, with total delay times from tens to hundreds of ms. While the demonstrated time delays and switching accelerations for 3-element mechanisms are not yet sufficient for such applications, both the concept and the analytical model have been validated experimentally in this work, and the models suggests that modified designs are within reach for meeting required application goals.

REFERENCES

1. MIL-HDBK-757(AR), *Fuzes* (1994).
2. S. Michaelis, H.-J. Timme, M. Wycisk, and J. Binder, "Additive electroplating technology as a post-CMOS process for the production of MEMS acceleration-critical Switches for transportation applications", *J. Micromech. Microeng.*, *10*, 120-123 (2000).
3. T. Tonnesen, O. Ludtke, J. Noetzel, J. Binder, and G. Mader, "Simulation, design and fabrication of electroplated acceleration switches",*J. Micromech. Microeng.*, *7*, 237-239 (1997).
4. M. E. Anderson, "An analysis of the runaway escapement as a mechanical acceleration-integrator", M.S. thesis, University of California, Los Angeles, CA (1966).
5. G. Lowen, and F. Tepper, "Dynamics of the pin pallet runaway escapement", Tech. Rep. ADB0289355, Army Armament Research and Development Command, Dover, NJ (1978).
6. A. C. Wang, and T. W. Lee, "On the dynamics of intermittent-motion mechanisms—Part2: geneva mechanisms, ratchets, and escapements", *J. Mechanisms, Transmissions, and Automation in Design*, *150*, 541-551 (1983).
7. L. P. Farace, "A gearless safe and arming device for artillery firing (program summary and mathematical analysis)", Tech. Rep. ADA0412981, Frankford Arsenal, Philadelphia, PA (1975).
8. M. Kenig, "Failure analysis of gearless safety and arming device", Tech. Rep. AD7800147, Frankford Arsenal, Philadelphia, PA (1973).
9. N. Czajkowski, "Theoretical and experimental analysis of the dynamics of Junghan's escapement", M.S. thesis, University of Maryland, College Park (1955).
10. K. Schulgasser, and C. Dock, "Development of the dock escapement", in *Proc. of the Timers for Ordnance Symposium*, *1*, 15-34 (1966).
11. D. Popovitch, "Timing escapement mechanism", U.S. Patent 3 168 833 (1965).
12. C. H. Robinson, R. H. Wood, and T. Q. Hoang, "Development of inexpensive, ultra-miniature MEMS-based safety and arming (S&A) device for small-caliber munition fuzes", *Proc. 23rd Army Science Conference*, CO-02 (2002).
13. W. E. Ryan, "Rotary-type setback leaf S&A mechanisms, analysis and design", Tech. Rep. HDL TR1190 (U-149244), Harry Diamond Laboratory, Adelphi, MD (1964).
14. R. W. Baker, "Analysis of a rotary-type, multiple leaf, setback sensor for a safety and arming mechanism", M.S. thesis, University of Rhode Island, RI (1977).
15. A. Hausner, "An analysis of friction in a T293 setback leaf system", Tech. Rep. AD602624, Harry Diamond Labs, Washington D. C. (1960).
16. S. M. Barnes, S. L. Miller, M. S. Rodgers, and F. Bitsie, "Torsional ratcheting actuating system", *Proc. MSM*, 273-276 (2000).
17. W. Davis, A.P. Pisano, "On the vibrations of a MEMS gyroscope", *Proc. MSM*, 557-562 (1998).
18. W. Davis, "Mechanical analysis and design of vibratory micromachined gyroscopes", Ph.D. dissertation, University of California, Berkeley, CA (2001).
19. A. Padmanabhan, "Silicon micromachined sensors and sensor arrays for shear-stress measurements in aerodynamic flows", Ph.D. dissertation, Massachusetts Institute of Technology, Cambridge, MA (1997).

MULTI-LAYER EMBEDMENT OF CONDUCTIVE AND NON-CONDUCTIVE PDMS FOR ALL-ELASTOMER MEMS

Jonathan M. Engel, Nannan Chen, Kee Ryu, Saunvit Pandya, Craig Tucker, Yingchen Yang, Chang Liu
Micro Actuators, Sensors, and Systems Group, University of Illinois at Urbana-Champaign
Urbana, IL USA

ABSTRACT

PDMS (polydimethylsiloxane) elastomer is widely used in MEMS. However, PDMS is non-conductive and as a result is used in mostly structural applications. We report methods for monolithic integration of conductive and non-conductive PDMS for realizing wholly polymer-based devices with embedded elastomer wires, electrodes, heaters, and sensors. In this work we demonstrate elastomer strain gauges, capacitive pressure sensors, as well as microfluidic channels with integrated heaters and sensors. The process uses a series of PDMS patterning, micromolding, and bonding techniques with conductive PDMS features made by mixing with multiwall carbon nanotubes (MWNT).

INTRODUCTION

Traditionally, elastomers such as PDMS have played a large but mainly structural role in MEMS, serving as protective layers, encapsulants, valve diaphragms, fluidic channel structures, and so forth. However, a number of "active" devices have been made using modified elastomers, including organic vapor sensors [1], liquid sensors [2], force sensitive resistors [3], and ultrasonic emitters [4]. These devices use elastomers mixed with solid fillers, such as carbon black, MWNT, or metallic powders to give the resulting composite material the desired properties. Researchers have also captured metal films in PDMS layers to create elastomer tactile sensors [5]. Most recently, work has been done to capture in-situ grown MWNT in PDMS to create strain gauges and field emission devices [6].

The goal of our work is to create devices that can be handled directly, take advantage of the unique characteristics of composite elastomers, and enable applications that require conformal and robust materials. To develop a general new class of processes and structures to meet this goal, we take advantage of a process for precision patterning of thin film elastomers [7]. By combining patterning technique spin casting and molding, we have realized a number of all-elastomer devices with embedded conductors and sensors such as shown in Figure 1.

DESIGN AND FABRICATION

In order to realize functional regions of conductive PDMS in concert with structural insulating PDMS, we have developed a fabrication process as shown in Figure 2. The process begins with the vapor coating of chlorotrimethylsiloxane (CTMS) on the substrate to assist in the release of the final elastomer assembly (Figure 2a). Next, photoresist (PR) is spun and patterned to define the molds for the conductive PDMS (Figure 2b). PDMS is then mixed with multiwalled carbon nanotubes (MWNT) in order to make a conductive composite. The ratio of MWNT to PDMS elastomer is chosen depending on the desired application and performance of the device. In the case of simple conductors for capacitive sensors or resistive heaters, a large amount of MWNT may be added to increase the conductivity of the composite. In the case of strain or force sensitive devices, a lower loading of MWNT is desired to increase sensitivity. Details of the conductivity of PDMS and MWNT composites can be found in [8]. For the devices presented here, 10% by weight MWNT is mixed with Sylgard-184 PDMS.

Once the MWNT and PDMS have been mixed, the composite is applied to the PR mold and patterned as detailed in [7]. The patterned elastomer is cured at 90˚C for 10 minutes, and the PR mold removed in acetone (Figure 2d). The conductive PDMS structures are then captured by either spin or pour casting unmodified PDMS around them as shown in Figure 2e. The resulting assembly is cured at 90˚C for 30 minutes in a leveled oven before being peeled from the substrate (Figure 2f).

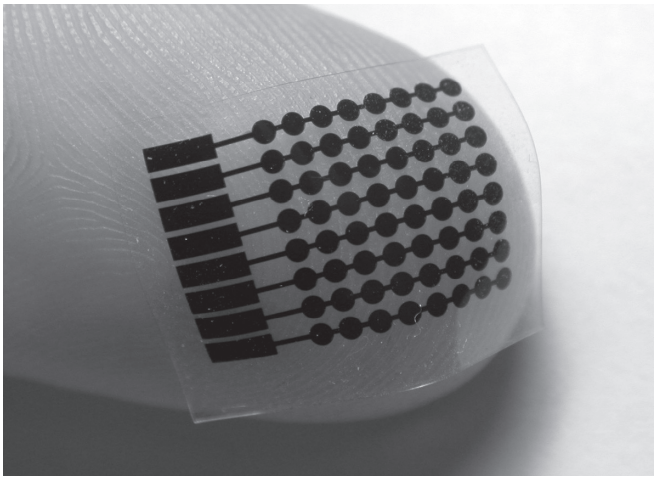

(a)

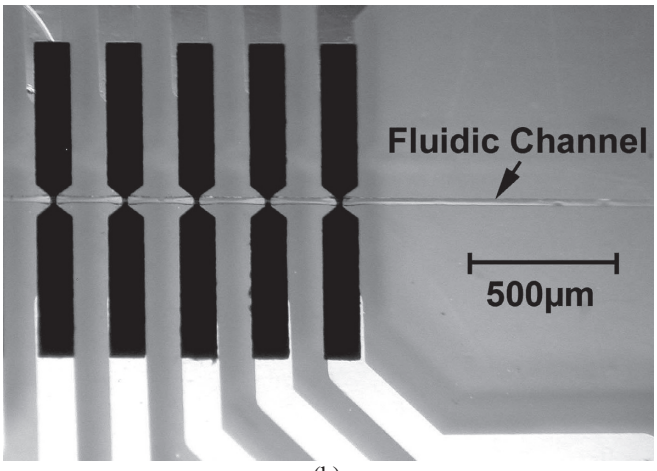

(b)

***Figure 1**: a) Photo of PDMS tactile sensor sheet. Black parts are made of conductive PDMS and embedded in transparent, non-conductive PDMS skin. b) Micrograph of PDMS microfluidic channel with embedded conductive elastomer devices that cross the channel (running horizontally).*

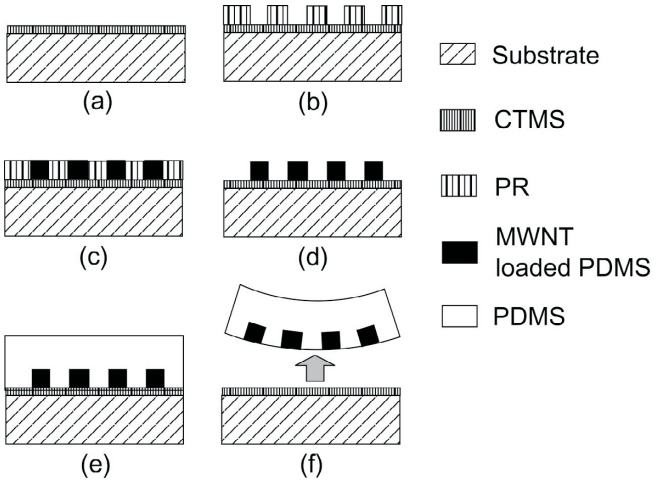

Figure 2: *Schematic diagram of a single-layer general fabrication process: a) vapor coating substrate with CTMS (chlorotrimethylsiloxane), a chemical agent to facilitate later release in step f, b) patterning photoresist (PR) mold, c) applying MWNT loaded PDMS and removing excess using a blade, d) removing PR mold, leaving precision patterned functional PDMS behind, e) spin casting unmodified PDMS, f) and finally peeling the PDMS with embedded sensors.*

This process can be combined with other traditional elastomer patterning techniques such as used for defining micro-fluidic or pneumatic channels (Figure 1b). Multiple layers can also be combined to create complex devices such as capacitive pressure sensors. We have applied this approach to produce a number of new devices – elastomer strain gauges, channels with embedded flow-rate sensors, and a soft capacitive tactile sensor are demonstrated.

RESULTS AND DISCUSSION

In simplest form, a strip of conductive elastomer is embedded as a strain gauge in unmodified PDMS (Figure 3a). Applied strain alters the average spacing between conductive particles and therefore the resistance reading (Figure 3b). In contrast to existing semiconductor and metal strain gauges, our all-elastomer strain gauge can repeatably measure large strains (>1%). Embedded in the insulating elastomer, the gauge undergoes the same strain as the bulk PDMS, surviving large deformations typical of elastomers. Figure 3b shows the principle of operation of conductive elastomer strain gauges, where variation in conductive particle spacing is transduced as a change in resistance. In general, tensile strain causes increased resistance while compressive strain decreases mean particle spacing and decreases resistance. Figure 3c shows sample data collected with an Agilent 34401A multimeter from an elastomer strain gauge undergoing large (~25%) strain while being manually stretched.

Currently, a rigid substrate is required in order to bring heaters or sensors into close proximity to microfluidic channels and reaction chambers. Compliant total analysis systems such as required for implantation or use with wearable labs cannot be easily implemented in this way. In order to overcome these limitations, we have embedded conductive elastomer sensors along with microfluidic channels to allow detection of liquids, flow, organic solvents, as well as localized heating (Figure 1b and Figure 4). To demonstrate this potential, we arranged an embedded sensor array along a channel (Figure 4a). The conductive portion serves as both a heater and sensor. The operating principle is basically that of a heated film flow meter as schematically represented in Figure 4b. When the sensor is heated above ambient and the resistance monitored, a change in output signifies a change in heat lost to the environment. With an excitation voltage of 6V, and only 1μW input power, a large (~10%) change in output voltage is measured when water is introduced into the channel (Figure 4c). This change is due to heat loss to the fluid. Measurements are made using an Agilent 34401A multimeter. This can be used to detect fluid fronts or analyte plugs as commonly used in micro total analysis systems.

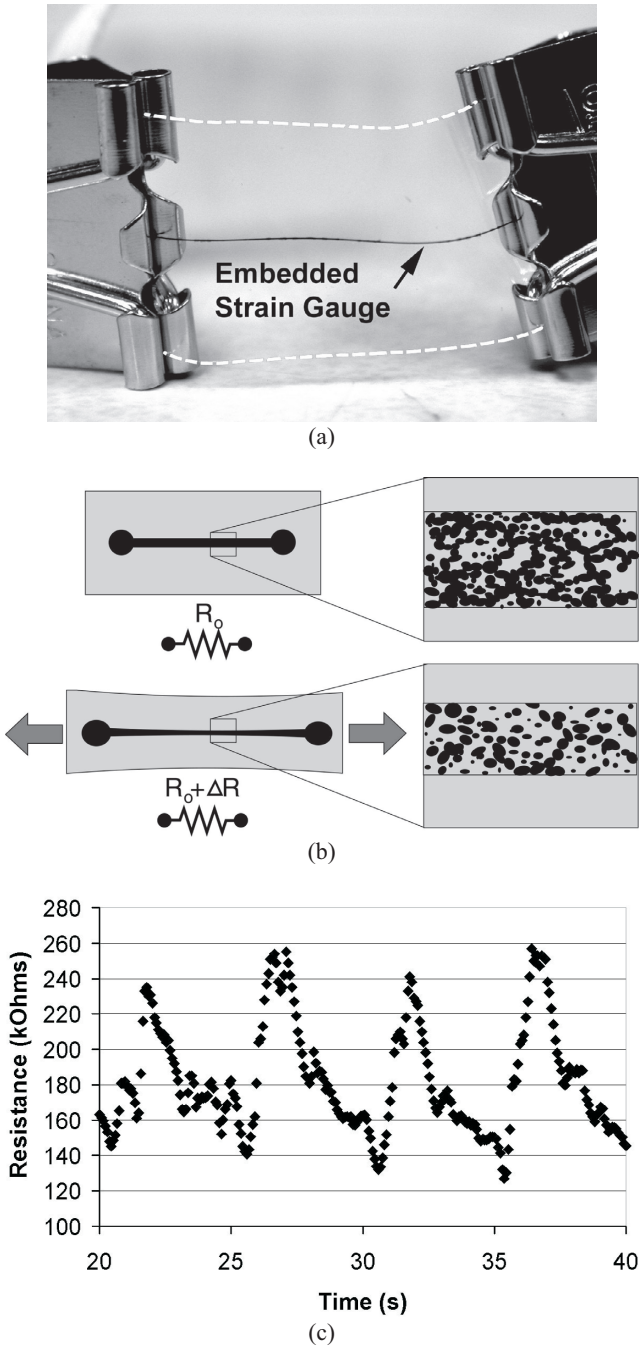

Figure 3*: a) Photo of PDMS sheet with embedded strain gauge. Dashed white lines indicate perimeter of clear PDMS strip. b) Schematic showing operation of elastomer strain gauge operation. c) Sample data of MWNT strain gauge undergoing large (~25%) strain.*

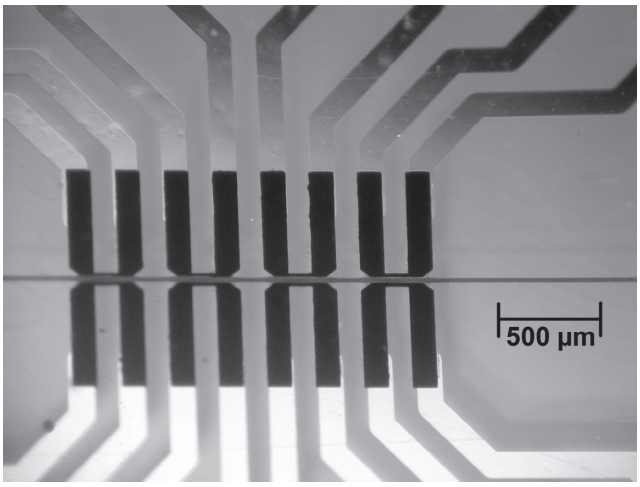

(a)

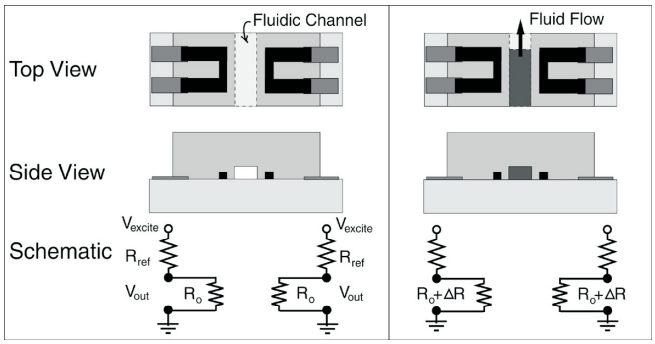

(b)

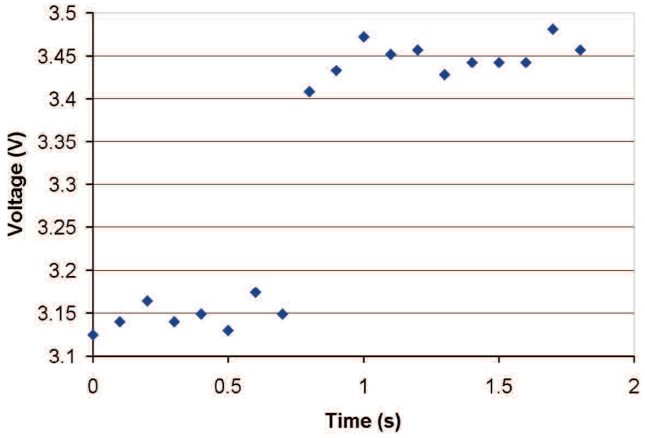

(c)

***Figure 4**: a) Micrograph of embedded flow sensors next to channel filled with red dye. b) Schematic showing operation of embedded flow sensors. An external reference resistor (R_{ref}) is connected in series with the PDMS sensor (R_o) and a current heats the sensor above ambient. When fluid flows in the channel heat is lost to the fluid, changing the sensor resistance and the output voltage. c) Chart showing change in output voltage (6V excitation) when fluid flows into channel.*

By using multiple layers, more complex devices are also realized. For example, by combining two layers of elastomer with embedded electrodes (Figure 1) and orienting them orthogonal to each other a matrix of capacitive pressure sensors is created as shown in Figure 6a. The capacitance of a flat plate capacitor is

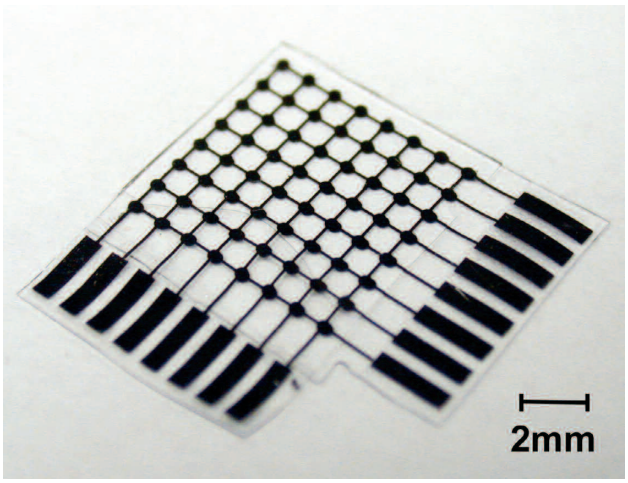

(a)

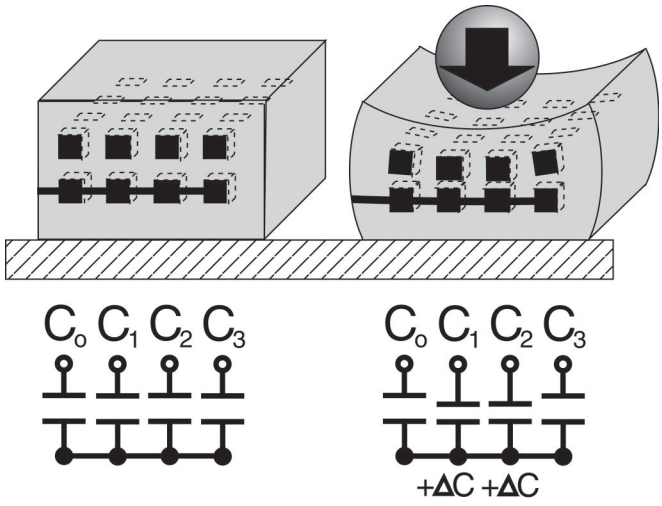

(b)

***Figure 5**: a) Photo of orthogonal embedded PDMS electrode layers, which results in an array of capacitive pressure sensors. b) Schematic showing operating principle of capacitive array.*

proportional to electrode area and inversely proportional to electrode gap. Thus large area and small gap are desired, but using soft materials like PDMS presents a significant challenge for maintaining a small electrode gap. Previous efforts to make collapsible capacitive PDMS devices require larger gaps, numerous bonding steps, and subsequent large area. The presented device uses a PDMS filled capacitive gap of 4µm which gives it high stiffness compared to air-gap capacitive devices. However, the filled gap gives increased robustness to stiction, particles, and mechanical overload as well as increasing the baseline capacitance of the sensors. Air gap capacitors are possible using similar techniques to those used to create microfluidic channels (Figure 4).

Testing reveals that interrogating the row and column capacitance of the array allows imaging of contact with other objects. For example, when loaded by a 3mm spherical indenter under a 500g load and the capacitance measured with an Agilent 4263B LCR meter, the array changes capacitance as shown in Figure 6. Additionally, the negative-valued artifacts observed in Figure 6 can be eliminated by using electronics designed to interrogate multiplexed capacitive arrays. These circuits switch non-interrogated rows and columns to ground to minimize parasitic parallel capacitances.

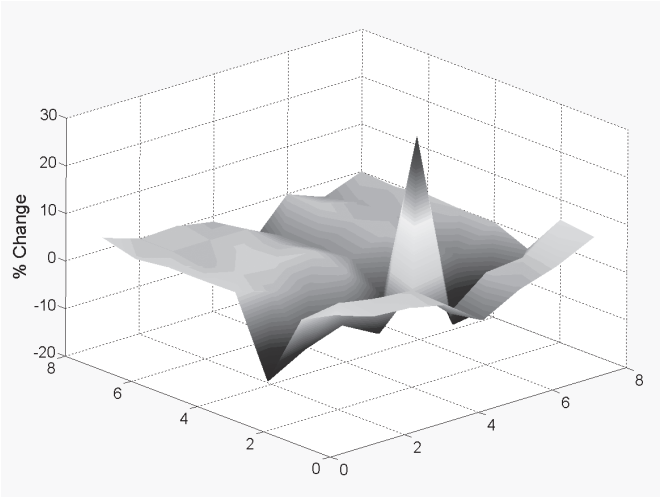

Figure 6*: Graph of change in capacitance of array when loaded by a 3mm spherical indenter. X and Y axes are the row and columns of the capacitive array.*

CONCLUSIONS

We have demonstrated a new fabrication technique and approach to realizing all-elastomer MEMS devices. This is accomplished by combining micro patterning of conductive elastomer features with traditional spin casting and molding of insulating elastomers. Conductive elastomers are made functional by mixing with multi-walled carbon nanotubes. In this way we have created several new devices, including all-elastomer strain gauges, microfluidic systems with embedded elastomer sensors and heaters, and robust stretchable capacitive elastomer tactile sensors. The presented technique has further promise for soft biomedical applications, such as interocular pressure measurements, large strain measurements for smart-prosthetics and robotics, and compliant pathogen detection systems for wearable deployment.

ACKNOWLEDGMENTS

This work was funded by the Air Force Office of Scientific Research (AFOSR) Bio-Inspired Concept program and the Defense Advanced Research Projects Agency (DARPA) BioSenSE program.

REFERENCES

[1] J. Chen and N. Tsubokawa, "Novel Gas Sensor from Polymer-Grafted Carbon Black: Vapor Response of Electric Resistance of Conducting Composites Prepared from Poly(ethylene-block-ethylene-oxide)-Grafted Carbon Black," *Journal of Applied Polymer Science*, vol. 77, pp. 2437-2447, 1999.

[2] E. Segal, R. Tchoudakov, M. Narkis, and A. Siegmann, "Sensing of liquids by electrically conductive immiscible polypropylene / thermoplastic polyurethane blends containing carbon black," *Journal of Polymer Science: B*, vol. 41, pp. 1428-40, 2003.

[3] J. M. Engel, J. Chen, D. Bullen, and C. Liu, "Polyurethane Rubber as a MEMS Material: Characterization and Demonstration of an All-Polymer Two-Axis Artificial Haircell Flow Sensor," presented at IEEE International Conference on MEMS, 2005.

[4] T. Buma, M. Spisar, and M. O'Donnell, "A high frequency ultrasound array element using thermoelastic expansion in PDMS," presented at IEEE Ultrasonics Symposium, 2001.

[5] H. K. Lee, S. I. Chang, K. H. Kim, S. J. Kim, K. S. Yun, and E. Yoon, "A Modular Expandable Tactile Sensor Using Flexible Polymer," presented at IEEE International Conference on MEMS, 2005.

[6] Y. J. Jung, S. Kar, S. Talapatra, C. Soldano, G. Viswanathan, X. Li, Z. Yao, F. S. Ou, A. Avadhanula, R. Vajtai, S. Curran, O. Nalamasu, and P. M. Ajayan, "Aligned Carbon Nanotube-Polymer Hybrid Architectures for Diverse Flexible Electronic Applications," *Nano Letters*, vol. 6, pp. 413-418, 2006.

[7] K. Ryu, X. Wang, K. Shaikh, and C. Liu, "A method for precision patterning of silicone elastomer and its applications," *Journal of Microelectromechanical Systems*, vol. 13, pp. 568-575, 2004.

[8] J. M. Engel, J. Chen, N. Chen, S. Pandya, and C. Liu, "Multi-Walled Carbon Nanotube Filled Conductive Elastomers: Materials and Application to Micro Transducers," presented at IEEE International Conference on MEMS, 2006.

PRESSURE ENHANCED AIR DAMPING IN ENCLOSED LATERALLY OSCILLATING MICROSTRUCTURES

Kevin Y. Yasumura
Mechanical Engineering Group, Product Design Division
FormFactor Inc., Livermore, CA

Hal Jerman
Advanced Research Group
Coherent Inc., Santa Clara, CA

ABSTRACT

High aspect ratio MEMS devices have been enabled by the development of deep reactive ion etchers. These devices have found use in lateral accelerometers [1], microengines [2], and optical applications [3]. While resonant sensors or scanners may require high-Q operation, closed-loop control of actuators is improved by having the device close to critically damped. Analysis and modeling of the damping for laterally resonant devices have traditionally focused on a Couette or Stokes-based fluid model [4], [5]. For DRIE devices of typical geometry, the damping from these mechanisms may result in a Q of $>$50, perhaps suitable for a resonant device, but inadequate for damping a closed-loop actuator. We have developed a technique that uses a cap over the device producing a small air gap between the top and bottom surfaces of the moving part of the actuator to act as a fluid resistor. When air is 'pumped' through this gap by lateral motion of the device, the flow resistance of this air channel provides the needed damping for the system.

INTRODUCTION

One measure of an actuator's performance is its response to externally applied shocks and vibrations. This is especially important for actuators used for optical applications. Sub-micron motion of the actuator or optical element can produce large changes in the optical performance. One method to reduce an actuator's sensitivity to external accelerations is to damp the modes of motion. While closed loop control of the actuator motion is often used, passive damping techniques can also be used to obtain significant improvement in device performance. By damping the motion of the actuator, the response to resonant excitation can be reduced as the Q of the actuator.

For actuators fabricated from single-crystal silicon we can ignore intrinsic sources of mechanical dissipation and focus instead on the external damping caused by the surrounding fluid medium (air) [6]. Figure 1 shows a photograph of the DRIE actuator used in this work. It features two banks of comb drives connected by two orthogonal beams. These beams are attached to two flexures that form the attachment to the surrounding substrate wafer. Details of the fabrication process can be found in previous work [7].

The actuator shown in Fig. 1 will have a number of sources of fluid damping. These sources can be generalized into three terms: damping beneath the motor, damping above the motor, and damping between the comb fingers. Assuming these sources of mechanical energy loss are independent, the total dissipation can be expressed as

$$\frac{1}{Q_{total}} = \sum_i \frac{1}{Q_i} = \frac{1}{Q_{bottom}} + \frac{1}{Q_{top}} + \frac{1}{Q_{comb}}. \qquad (1)$$

Depending upon the specific actuator dimensions and geometry, each of the terms in Eq. 1 will contribute different amounts to the mechanical damping in the system. The usual method of quantifying each of the damping terms is to use either a Couette or Stokes-based flow model between the actuator and its nearby surfaces via the intermediary fluid medium. In most cases the intermediary fluid is air. However, some applications may take advantage of the increased viscosity and dielectric constant of other fluids [8]. In this work, when we discuss fluids, it will be assumed to be air. The equations, however, are general and can be applied to systems involving more viscous materials. Because this work focuses on laterally oscillating structures that have full-deflection ranges of 10's of μm, contributions from squeeze film damping will not contribute large amounts to the system dissipation [9].

Actuator encapsulation is often used as a means to seal an actuator in vacuum for improved quality factor or for improved packaging and handling. In this work we demonstrate that placing a cap over the motor can have an additional damping benefit. Figure 2 shows a diagram of an actuator with a flow-restricting cap placed above it. Without the cap, air is free to move into and out of the motor surroundings as it oscillates. With the cap, however, air is now blocked from entering and leaving the motor area. If the motor has a large enough cross sectional area in the direction that it oscillates, air will now be forced to flow above (between the motor and cap) and beneath the motor (between the motor and underetch cavity). The motor will now act like a piston driving air across its surface. This piston-like effect is what will produce the damping enhancement.

COUETTE AND STOKES-BASED AIR DAMPING

For the actuator shown in Figs. 1 & 2 air flow between the motor and substrate wafer (or cap) can be described using the one dimensional Navier-Stokes equation. Taking the surrounding air to be an incompressible fluid without pressure gradients, the Navier-Stokes equation is reduced to the one dimensional diffusion equation given by

$$\frac{\partial u(y,t)}{\partial t} = \frac{\mu}{\rho}\frac{\partial^2 u(y,t)}{\partial y^2} \qquad (2)$$

where $u(y,t)$ is the flow velocity field, μ is the fluid absolute viscosity, and ρ is the fluid mass density. The fluid velocity flow field, $u(y,t)$, is a function of both the distance between the moving motor

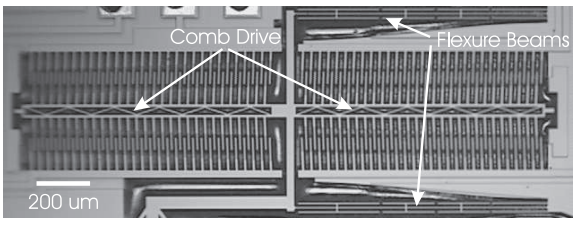

Fig. 1. Photograph of one of the electrostatic comb drive actuators used in this work. This actuator features two sets of comb drives anchored to the substrate with flexure beams. The actuator is 85 μm thick.

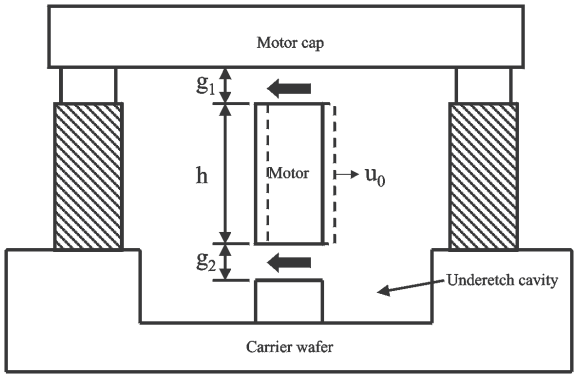

Fig. 2. Diagram of a capped micromachined motor. The motor has a height h, width w (into the paper), and moves with a velocity amplitude of u_0. The gap above the motor between the motor and cap is g_1 and the gap between the motor and underetch cavity is g_2.

and stationary surface and of time. The motor is assumed to move with small amplitude motion that varies as $sin(\omega t)$. Typical Reynolds numbers, Re, of ~0.15 are obtained for our actuators ensuring that the fluid flow will be laminar.

For Couette-based flow, the left hand term in Eq. 2 is taken to be 0 (slowly varying flow) such that the velocity flow field is a linear function of the gap between the motor and stationary surface. However, a more general solution takes into account that the fluid has finite mass and thus will not respond instantaneously to the motion of the actuator. This produces the Stokes-based flow condition described by Cho for a laterally oscillating surface micromachined electrostatic actuator [5]. We can therefore consider Couette flow to be a limiting case of Stokes flow. For the actuators used in this work and those of Tang and Cho [4], [5], it will be shown that there is little difference between the damping forces generated by the two flow conditions.

Whether, the fluid flow is assumed to be Couette or Stokes-like, the quality factor is defined as

$$Q = \frac{2\pi W}{\Delta W} \tag{3}$$

where W is the total energy stored in the oscillator and ΔW is the energy lost per radian. The energy lost is equal to AD where A is the surface area over which the dissipation occurs and D is the energy loss per radian per unit surface area. This dissipation is caused by the fluid shear force on the actuator. Thus, the amount of mechanical dissipation is dependent upon the total shear force on the actuator as it moves in the fluid medium. More specifically, the dissipation per cycle per unit area is given by

$$D = -\int_0^{2\pi/\omega} \tau(y,t)u(y,t)dt \tag{4}$$

where the shear force for a given flow-field is

$$\tau(y,t) = -\mu \left.\frac{\partial u(y,t)}{\partial y}\right|_{y=0}. \tag{5}$$

Solving for the quality factor of an oscillator with either Couette or Stokes-based flow produces a Q of the same form. For both flow conditions, the quality factor is given by

$$Q(g_{eff}) = \frac{g_{eff}}{\mu A}\sqrt{km} \tag{6}$$

where g_{eff} is the effective gap between the moving plates, A is the plate overlap area, k is the actuator stiffness, and m is the motional mass of the actuator. For actuators moving in air, the viscosity, μ, is 180 uP. For Couette-flow the effective gap is simply the distance, d, between the moving motor and stationary plate. Thus, for Couette-based air flow $g_{eff,c} = d$. For Stokes-flow, however, there are two possible effective gaps. For air flow between the moving motor and a stationary surface, the effective gap is given by

$$g_{eff,s} = \frac{1}{\beta}\left(\frac{sinh2\beta d + sin2\beta d}{cosh2\beta d - cos2\beta d}\right)^{-1} \tag{7}$$

where $\beta = \sqrt{\rho\omega/2\mu}$, and d is the physical separation between the two surfaces. From this equation for the effective Stokes gap we can identify $\delta = 1/\beta$ as a characteristic length scale for Stokes-based flow [5]. For air flow above an uncapped motor the effective gap is simply the characteristic length scale δ. Therefore, the effective gap above the motor is given by $g_{eff,\infty} = \delta$. For an actuator with a 5 μm gap operating at 1 kHz, the effective gap ratio, $d/g_{eff,s}$, is 1.00023. This shows that for the actuators we typically use, there is little difference between the Couette and Stokes-based flow models. Therefore, for the remainder of this work, we will use the real physical gap distance when discussing motor gaps.

Eqs. 1 & 6 now provide a means to calculate quality factors in laterally oscillating actuators. The results of these calculations are shown in Table I for two motor styles. Both motors have the same comb drive region as shown in Fig. 1. They do, however, differ in the additional actuator elements attached to the comb drive. This, along with process variation, results in two motors with different damping surface areas, masses, spring constants, and resonance frequencies. These two motors also differ in the motor gap beneath the moving actuator. Motor 1 has a 15 μm gap while Motor 2 has a 5 μm gap. For Motor 1 the measured Q of 10.2 is much lower than the Stokes-based calculation of 44.9. Motor 2's measured Q is also much lower than the Stokes-calculated value of 23.8. In order to explain the measured Q's we introduce the pressure-driven flow model for laterally oscillating micromachined actuators.

Pressure Enhanced Damping

For most micromachined actuators, it is assumed that there are no pressure gradients acting upon the actuator. This includes external pressure gradients or gradients produced by the motion of the actuator device. With this assumption, the Navier-Stokes equation becomes the diffusion equation (Eq. 2). For our high aspect ratio structures, however (tall with respect to the gap distances), we may not be able to neglect the $-1/\rho(dp/dx)$ term in the Navier-Stokes equation.

In Fig. 2 a motor of height h moves with velocity amplitude u_0. This actuator has a cap placed upon it that restricts air flow around the actuator. Without the cap, air would be free to enter and leave the regions surrounding the actuator as it oscillates. With the cap, however, the surrounding air must now be displaced. Because the fluid flow around our actuators is treated as incompressible, the displaced air must travel across the top and bottom of the capped actuator to the region on the left. This piston-like effect produces a combination of pressure driven and Stokes-based flow across the surface of the actuator with the result that the total shear damping force is increased depending upon the geometry of the actuator and gaps above and below the motor. With these assumptions, let us now calculate the amount of expected damping force enhancement due to the pressure-driven flow effect.

First, the Stokes shear force on a plate moving with velocity amplitude u_0 will be calculated. For a capped actuator, the total Stokes shear force acting on it will be the sum of the shear force

Motor Parameter	Motor 1	Motor 2
Motional mass m	8.22 $\times$ 10^{-8} kg	5.26 $\times$ 10^{-8} kg
Spring constant k	1.0 N/m	1.5 N/m
Resonance frequency f_0	555 Hz	850 Hz
Cap gap g_{top}	5 μm	5 μm
Motor gap g_{bottom}	15 μm	5 μm
$\Delta(h, g_1, g_2)$	11.9	52.0
Stokes Q	44.9	23.8
Pressure Q	9.7	1.5
Measured Q	10.2	1.4

TABLE I

TABLE OF MOTOR PARAMETERS FOR THE TWO STYLES OF MOTORS PRESENTED IN THIS WORK. THE COMB DRIVE REGIONS WERE IDENTICAL, HOWEVER, ADDITIONAL STRUCTURES WERE USED TO CHANGE THE RESONANCE FREQUENCY AND AMOUNT OF MOTIONAL MASS. MOTOR 2'S MOTOR GAP, g_{bottom}, WAS FABRICATED AT 5 μm TO VERIFY THAT THE Q WOULD FOLLOW THE PRESSURE ENHANCED AIR-DAMPING THEORY.

above and below the plate. With a gap g_1 above the motor and a gap g_2 below the motor, the total shear force is

$$\tau_{s,g_1,g_2} = \frac{\mu u_0}{g_1} + \frac{\mu u_0}{g_2} = \frac{\mu u_0 (g_1 + g_2)}{g_1 g_2}. \tag{8}$$

For pressure driven flow, the velocity field is given by

$$u(y,g)_p = -\frac{1}{2\mu}\frac{dp}{dx}(gy - y^2) \tag{9}$$

where g is the gap through which the air flows (g_1 or g_2) and dp/dx is the pressure gradient formed across the motor as it oscillates. From Eq. 5, the pressure driven shear force on one side of the motor will be

$$\tau_{p,g} = -\frac{1}{2}\frac{dp}{dx}(g - 2y)\Big|_{y=0}. \tag{10}$$

We therefore need to determine the pressure gradient as a function of actuator and gap dimensions in order to calculate the pressure-driven shear force on the moving actuator. The simplest method to determine the pressure gradient for an incompressible fluid is to use a mass-flow calculation to equate the amount of displaced fluid to the fluid flow across the gaps above and below the motor. This flow will be considered to be one dimensional and will ignore edge effects even though the motor has a finite physical depth of w. This mass flow equality can be written as

$$\rho h w u_0 = \int_0^w\int_0^{g_1} \rho u(y,g_1)dydw + \int_0^w\int_0^{g_2} \rho u(y,g_2)dydw \tag{11}$$

where on the left side we have the displaced fluid due to the actuator of height h and width w. The right side of Eq. 11 shows the sum of the fluid flow above and below the motor. Using Eq. 9 in Eq. 11 and solving for the pressure gradient gives

$$\frac{dp}{dx} = -\frac{12\mu h u_0}{g_1^3 + g_2^3}. \tag{12}$$

From this expression for the pressure gradient , the total pressure-driven (Poiseuille) shear force can be calculated as the sum of the shear force above and below the motor:

$$\tau_{p,g_1,g_2} = \tau_{p,g_1} + \tau_{p,g_2} = \frac{6h\mu u_0 (g_1 + g_2)}{g_1^3 + g_2^3}. \tag{13}$$

We now have an expression for the shear force acting on the actuator due to pressure-driven flow across the motor surfaces. Eq. 13 can be reexpressed as

$$\tau_{p,g_1,g_2} = \kappa(h, g_1, g_2)\mu u_0 \tag{14}$$

where

$$\kappa(h, g_1, g_2) = \frac{6h(g_1 + g_2)}{g_1^3 + g_1^3}. \tag{15}$$

Eq. 15 gives an absolute magnitude for the pressure-based shear force in terms of the motor height, cap gap, motor gap, fluid viscosity, and actuator velocity. This is shown in Fig. 3 where $\kappa(h, g_1, g_2)\mu$ has been plotted for three different motor gap values of 5 μm, 10 μm, and 15 μm. For all three gap values, the motor height is 85 μm. Fig. 3 shows that as the motor gap is reduced, the amount of damping shear force enhancement increases. In addition, for a given motor gap distance, decreasing the cap gap will further increase the amount of damping force enhancement. There is a point, however, at which further reduction in the cap gap will actually reduce the amount of damping force enhancement. From Eq. 15 it can be shown that for a given motor gap, the maximum shear force is obtained when the corresponding cap gap is $1/2$ the motor gap value (*i.e.*, when $g_1 = g_2/2$). This reduction in the damping shear force enhancement with further reduction of the cap gap is caused by the motor and cap gap-height asymmetry. This asymmetry produces two competing effects when calculating the shear force: a reduction of the gap heights increases the pressure drop, dp/dx, across the moving actuator while also reducing the total shear force, τ, for that pressure drop. Removing the broken gap symmetry (*i.e.*, forcing $g_1 = g_2 = g$), the κ function will no longer have a local maxima and is now proportional to $1/g^2$. This will produce a continuous increase in shear force as the gap distances are decreased simultaneously. This argument is valid as long as the fluid prefers to flow instead of compress. For a real system, there will be a point at which the shear-flow induced damping begins to be limited by fluid compression.

In order to obtain a reproducible amount of enhanced mechanical damping in a capped actuator, the motor and cap heights must be controlled. For a 5 μm motor underetch cavity depth, cap gaps within the range of 1.1 to 3.9 μm (2.5 $\pm$ 1.4 μm) will produce at least 90% of the optimal damping value. This is a large acceptance range and allows for less stringent fabrication tolerances.

In order to use the pressure-based damping theory to make quality factor predictions, let us recast Eq. 13 into a different form. Using Eq. 8, Eq. 13 can be rewritten as

$$\tau_{p,g_1,g_2} = \frac{6hg_1g_2}{g_1^3 + g_2^3}\tau_{s,g_1,g_2}. \tag{16}$$

where we are now expressing the total shear force as a multiple of the corresponding Stokes-based shear force. Because the total shear force acting on the motor can be approximated as the sum of the

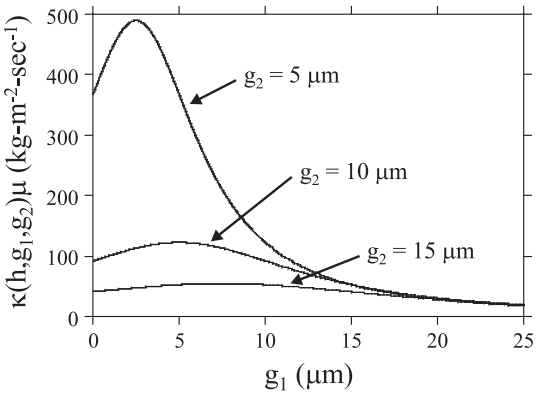

Fig. 3. Plot of $\kappa(h, g_1, g_2)\mu$ for 85 μm-tall motors with motor gaps, g_2, of 5, 10, and 15 μm. The cap gap, g_1, is varied from 0 to 25 μm. For a given motor gap value g_2, the maximum amount of damping shear force is obtained when $g_1 = g_2/2$.

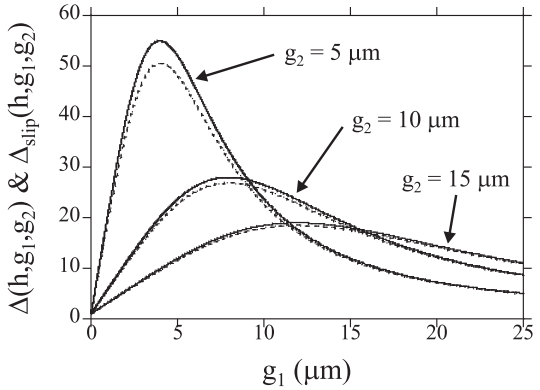

Fig. 4. Plot of $\Delta(h, g_1, g_2)$ (solid lines) and $\Delta_{slip}(h, g_1, g_2)$ (dotted lines) for motor gaps, g_2, of 5, 10, and 15 μm. For each of these motor gap values, the cap gap, g_1, is varied from 0 to 25 μm. For each of these cases the motor height, h, is 85 μm.

Stokes and Poiseuille terms, we can now write the total shear force acting on the motor as

$$\tau_{t,g_1,g_2} = \tau_{s,g_1,g_2} + \tau_{p,g_1,g_2} = \Delta(h, g_1, g_2)\tau_{s,g_1,g_2} \tag{17}$$

where the damping enhancement function, $\Delta(h, g_1, g_2)$, is given by

$$\Delta(h, g_1, g_2) = \frac{6hg_1g_2}{g_1^3 + g_2^3} + 1 \tag{18}$$

A more accurate calculation will also take into account slip effects at the boundary walls. Using the Maxwell slip theory with an accommodation coefficient of 1, the $\kappa(h, g_1, g_2)$ function (Eq. 15) can be reexpressed as

$$\kappa_{slip}(h, g_1, g_2) = \frac{6h(g_1 + g_2)}{g_1^3 + g_2^3 + 6g_1^2\lambda + 6g_2^2\lambda} \tag{19}$$

producing the slip-adjusted Δ function

$$\Delta_{slip}(h, g_1, g_2) = \frac{6hg_1g_2}{g_1^3 + g_2^3 + 6g_1^2\lambda + 6g_2^2\lambda} + 1 \tag{20}$$

where λ is the mean free path of air ($\sim$69 nm at STP).

Figure 4 shows a plot of $\Delta(h, g_1, g_2)$ and $\Delta_{slip}(h, g_1, g_2)$ for 85 μm-tall actuators with motor gaps, g_2, of 5, 10, and 15 μm. Note that at smaller motor gaps, the boundary slip term becomes more important. Figure 4 shows that for an 85 μm-tall actuator with a 5 μm motor gap, a damping correction factor (with respect to the equivalent Stokes-based shear force) of $>$50 can be obtained.

The Q calculations shown in Table I are in excellent agreement with the measured values. Motor 2's measured Q of 1.4 is in excellent agreement with the value calculated using the pressured enhanced damping theory. This shows that the pressure-driven flow model presented in this work can produce the large amount of additional damping required to obtain large amounts of Q reduction. For Motor design 2, with a 5 μm motor gap and a 5 μm cap gap, a damping correction factor of $\sim$50 is obtained through the pressure enhanced damping theory. This amount of additional damping is difficult to produce by other passive means. Methods such as increasing the comb overlap area are not as space efficient as the pressure-flow method. The reason for this is that adding damping combs adds additional mass to the actuator and takes up more surface area on the die. To-date, thousands of actuators demonstrating enhanced pressured-based damping have been fabricated and shipped as part of a tunable laser or tunable filter product.

CONCLUSIONS

The development of DRIE actuators allows for the fabrication of actuators with surrounding sidewalls. When an enclosed cavity is formed through placement of a capping structure, pressure-enhanced damping occurs. This damping mechanism can be described using the Δ function that quantifies the amount of additional shear force on the actuator with respect to the equivalent Couette force. Additionally, the amount of damping can be increased by minimizing the gaps above and below the motor. For a given motor gap (under the motor), the damping can be optimized by selecting the cap gap to be $1/2$ of the motor gap. Finally, quality factors approaching unity have been obtained for laterally oscillating structures with motor and cap gaps of 5 μm.

ACKNOWLEDGEMENTS

The authors would like to thank Dan Laser for helpful discussions, Kathy Jackson for help with sample preparation, and Sam Wong at GE Infrastructure Sensing for assistance with device fabrication.

REFERENCES

[1] A. Partridge, *et al.* A high-performance planar piezoresistive accelerometer. *J. Microelectromech. Syst.*, 9(1):58–66, 2000.

[2] A.H. Epstein, *et al.* Power MEMS and Microengines. *Proc. IEEE Tranducers '97*, pages 753–756, 1997.

[3] H. Jerman and J.D. Grade. A mechanically-balanced, drie rotary actuator for a high-power tunable laser. *Proc. Solid-State Sensor, Actuator, and Microsystems Workshop, Hilton Head Island, South Carolina*, pages 7–10, 2002.

[4] W.C. Tang, T.-C. H. Nguyen, and R.T. Howe. Laterally driven polysilicon resonant microstructures. *Proc. IEEE Workshop on Microelectromech. Syst., Salt Lake City, UT, Feb 1989*, pages 53–59, 1989.

[5] Y.-H. Cho, A.P. Pisano, and R.T. Howe. Viscous damping model for laterally oscillating microstructures. *J. Microelectromech. Syst.*, 3(2):81–87, 1994.

[6] K.Y. Yasumura, *et al.* Quality factors in micron- and submicron-thick cantilevers. *J. Microelectromech. Syst.*, 9(1):117–125, 2000.

[7] J.D. Grade, H. Jerman, and T.W. Kenny. A large-deflection electrostatic actuator for optical switching applications. *Proc. Solid-State Sensor, Actuator, and Microsystems Workshop, Hilton Head Island, South Carolina*, pages 97–100, 2000.

[8] K.Y. Yasumura, J.D. Grade, and H. Jerman. Fluid damping of an electrostatic actuator for optical switching applications. *Proc. Solid-State Sensor, Actuator, and Microsystems Workshop, Hilton Head Island, South Carolina*, pages 358–361, 2002.

[9] P.W. Kwok, M.S. Weinberg, and K.S. Breuer. Fluid effects in vibrating micromachined structures. *J. Microelectromech. Syst.*, 14(4):770–781, 2005.

SELF-POWERED HUMIDITY SENSOR POWERED BY NICKEL-63 RADIOISOTOPE

Rajesh Duggirala, Amit Lal and Clifford Pollock
*Sonic*MEMS Laboratory,School of Electrical and Computer Engineering, Cornell University, Ithaca, NY USA
Michael Kranz
Morgan Research Corporation, Huntsville, Alabama USA

ABSTRACT

We demonstrate a self-powered humidity sensor that can significantly extend the operating lifetime of battery powered wireless sensor suites. The self-powered sensor employs a radioisotope powered humidity sensitive polymer capacitor, which modulates the conductance of a MOSFET. The current modulation of the MOSFET is enough to wake-up a circuit in power-sleep mode. We demonstrate two capacitor biasing architectures. One is based on changes in the leakage resistance of the polymer capacitor, and the other on changes in the capacitance of the polymer capacitor. We present results on the testing and characterization of prototype assemblies of the microfabricated polymer capacitor chiplet, the MOSFET chiplet, and the radioisotope thin-film source. The polymer capacitor was measured to have a humidity sensitivity of 0.33pF/%RH and a capacitance decay time constant of ~50 seconds. The humidity sensitivity of the output current of the self-powered sensor was measured to be ~10uA/%RH @ 5V bias.

INTRODUCTION

Wireless sensor suites deployed in remote and inaccessible areas need long operating lifetimes as battery monitoring and replacement is often cost-prohibitive. Such applications include long-term health monitoring of tactical missiles, industrial equipment, buildings [1], etc. In addition to efforts on increasing the lifetime of the conventional electrochemical batteries currently in use, work is being done on alternative power solutions. These approaches include powering the sensor suite using energy scavenged from ambient vibrations [2], solar [3], tidal energy 4], etc. Additionally, alternative fuel-based power sources such as fuel cells [5] and radioisotope power generators [6] have also been proposed. All these solutions look promising, but are yet to be adopted widely.

An alternate approach to increasing the lifetime of battery powered sensor suites employs zero-power sensors, which can be passive or self-powered. Such self-powered sensors can wake-up the rest of the sensor node ("mote") when required, conserving the battery power for emergency computations and communications. Self-powered sensors based on passive fiber-optics [7] have been demonstrated previously. However, fiber-optic based approaches can require complicated signal processing for conversion of optical signals to electrical. In this paper, we address the need for a self-powered sensor with an electronic readout that can be processed easily by the mote electronics.

We demonstrate a radioisotope powered humidity sensor based on a water sensitive polymer capacitor which modulates the conductance of a MOSFET. The novel radioisotope-biased-MOSFET circuit gives out a self-powered amplified electronic readout, making signal conditioning easy for the electronics. Moreover, the demonstrated sensor topology can be readily adapted to sensing other physical phenomena including temperature, shock, chemical concentrations. Our sensor consumes zero-battery-power and can potentially extend the lifetime of condition monitoring sensor suites to multiple decades. These zero-battery-power sensors allow event-based power management of unattended sensor systems and orders of magnitude reduction in average power consumption.

We use Nickel-63, a safe radioisotope, whose power output is nearly independent of the ambient conditions, and can have several decades of useful life as the half-life is 100.2 years. The 2-milliCurie Nickel-63 thin-film emits low energy (average energy = 17keV) β-particles with penetration depths < 10 μm in solids. As a result, it can be deployed safely without substantial shielding or concerns about security.

THEORY

Radioisotope Biasing

An electrically isolated β-particle emitting radioisotope thin-film always develops a voltage bias because of the continuous emission of electrons. The voltage bias level depends on the balance between the voltage dependant charge leakages from the film into ambient air and the electron current output from the source. Hence, weak sources with low current output (e.g. 1-millicurie outputs ~5.9pA) need to be placed in vacuum (~1-1000mtorr) to achieve voltage biases in the 1-20V range. Such biases have been used previously to drive electrostatic resonators [8]. We use it here for the first time to bias sensors and electronics.

We use the voltage bias on the radioisotope thin-film to bias the gate of a MOSFET, via a humidity sensitive polymer capacitor, which modulates the bias. We demonstrate two architectures, to be used depending on the leakage resistance R_{PC} of the capacitors. Since the current output from the source is just 10.2pA, anything connected across the radioisotope-collector should have impedance greater than or equal to 100GΩ. Capacitors with R_{PC}>>1000GΩ can be placed in a series stack as shown in Figure 1(b), with the capacitor ratio in the stack controlling the gate voltage V_{gs} of the MOSFET as follows:

$$V_{gs} = V_{Ni} \frac{C_{PC}}{(C_{PC} + C_{bias})}, \text{ for } R_{PC}>>1000\text{G}\Omega.$$

For capacitors with R_{PC} ~1000GΩ, the capacitor divider architecture cannot be used as the leakage resistance of the polymer capacitor starts to dominate. The ratio of the leakage resistances of C_{PC} and C_{bias} starts controlling V_{gs}, and since the leakage resistance of the on-chip capacitor R_{bias}>>1000GΩ, any variation in resistance due to humidity doesn't alter V_{gs} significantly. In such cases, the polymer capacitors can be connected directly across the gate and source of the MOSFET as shown in Figure 1(d). Since V_{gs} is then given by

$$V_{gs} = I_s R_{PC}, \text{ for } R_{Ni}>>R_{PC}.$$

Any change in the humidity that alters the leakage resistance in the capacitor will change V_{gs}, and hence the conductance of the MOSFET. The MOSFET amplifies the change in the capacitor current, making the signal processing easy.

Humidity Sensitive Polymer Capacitor

In a humidity sensitive capacitor, a polymer or other porous dielectric layer absorbs water from the atmosphere. The large

polarizability of the absorbed water molecules alters the capacitance between the electrodes on either side of the material. That final capacitance can be calculated by modeling the moist polymer as a composite material, as follows

$$C = \frac{\varepsilon_o A}{d} * (\varepsilon_p + f_w * (\varepsilon_w - \varepsilon_p)) .$$

Here, C is the capacitance of the structure, A is the electrode area, ε_p is the relative dielectric constant of the polymer dielectric, ε_w is the relative dielectric constant of water, and f_w is the volume fraction of water within the polymer. The capacitance of the structure depends primarily on the geometry, but the sensitivity and transient response of the structure depend on f_w, which can be controlled by varying the electrode mesh size on the top electrode.

In addition to the capacitance, the leakage resistance of the layer stack is also a critical parameter. Nominally, this leakage resistance is extremely high, meaning that the conductivity of the polymer dielectric is low, as would be expected. However, as water is absorbed, ionic groups within the material are disassociated, thereby increasing the conductivity between the electrodes. The resistance of the structure can also be modeled by treating the moist polymer as a composite material, as follows

$$R^{-1} = (\frac{L}{A}\rho_p)^{-1} + (\frac{L}{A} f_w \rho_w)^{-1} .$$

Here, R is the resistance of the capacitor, L is the thickness of the dielectric, A is the capacitor's electrode area, ρ_p is the conductivity of the polymer, ρ_w is the conductivity of the water and disassociated ionic species, and f_w is the volume fraction of water absorbed within the dielectric. The resistance depends primarily on the material processing and the existence of impurities within the material. Leakage resistances ranging from 10GΩ to >10TΩ have been demonstrated. Furthermore, at these large levels of resistance, other charge leakage mechanisms, including the removal of charge directly from the electrode surface through interactions with the external gas, become significant percentages of total current through the circuit. These mechanisms must be mitigated through careful attention to packaging, interconnect lengths, and electrical isolation.

FABRICATION

The goal of this work was to demonstrate radioisotope biasing of the humidity sensitive polymer capacitor and the MOSFET. Discrete components were used for the radioisotope source, the humidity sensitive capacitor chip and the MOSFET chip, with the goal of a hybrid chip solution to integration in mind. A 1milliCurie Nickel-63 thin-film electro-less deposited on a 10mm x 10mm X 0.1mm Ni foil was used in all the experiments. The MOSFETs were fabricated in the AMI-AMS 1.5um technology available through MOSIS, and the humidity sensor was designed and microfabricated at Morgan Research Corporation. The components were finally assembled in a 6"x6"x6" vacuum chamber with electrical and gas feed-throughs.

The humidity sensor was microfabricated using a simple surface micromachined process. An initial layer of aluminum was first electron beam evaporated onto an SOI wafer, and then patterned to form a bottom electrode and wire bond pad. An SOI substrate was used because it allows the fabrication of other MEMS devices on the same chip. Subsequently, a layer of HD Microsystems PI2723 polyamide was spin cast on the Aluminum electrodes, and then patterned to realize a capacitor dielectric layer. Then, a second aluminum layer was evaporated onto the structure, and patterned into a mesh. Finally, the structure was encapsulated with nitride to protect it during subsequent process steps. A final nitride strip exposed the humidity sensor materials to the external environment.

TESTING

The discrete components were first characterized individually, and then assembled in a vacuum chamber to test the system for functionality.

Radioisotope Voltage Source

The radioisotope thin-film source was enclosed in a 2" X 2" X 1" aluminum box, which serves as a collector for the electrons emitted. The voltage bias build-up on the thin-film depends on the collector material, the source-collector geometry and placement, and the pressure in the vacuum chamber. The aluminum box collector was chosen for the proof-of-concept experiments and may be further optimized.

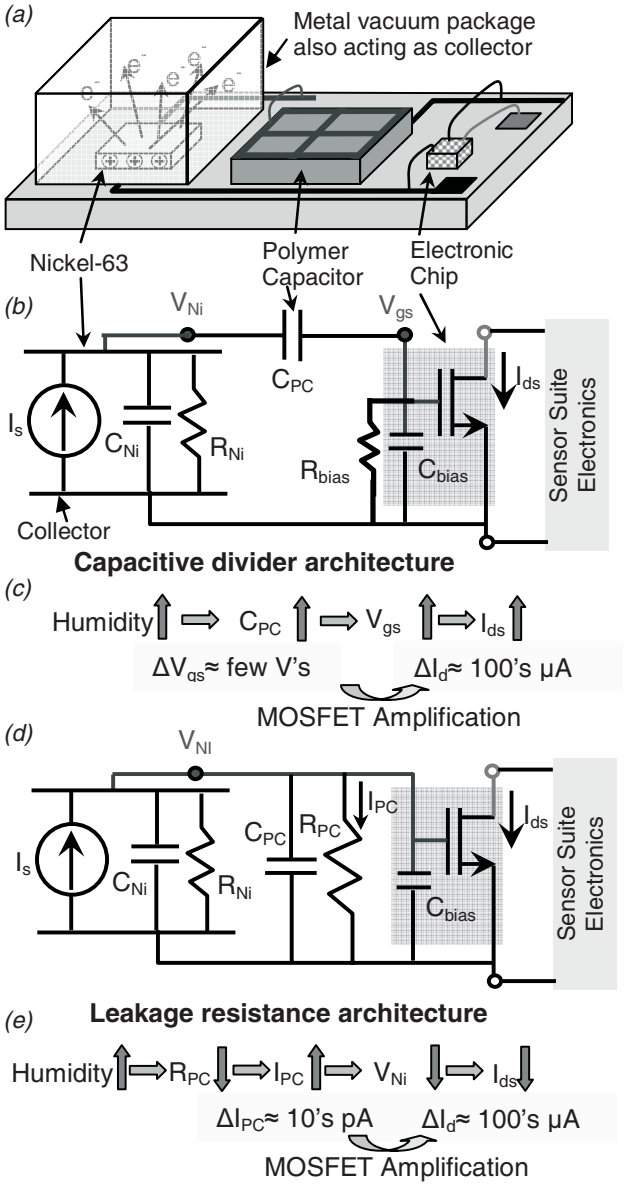

***Figure 1**. (a) Schematic the hybrid on-chip radioisotope powered humidity sensor concept. (b) Electrical equivalent circuit and (c) schematic illustrating the working principle of the sensor system with the capacitive divider architecture. (d) Electrical equivalent circuit and (e) schematic illustrating the working principle of the sensor system with the leakage resistance architecture.*

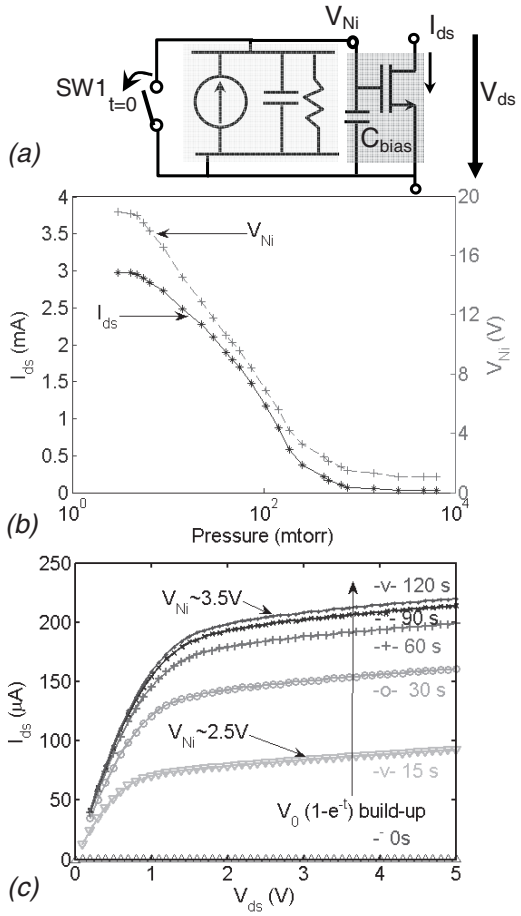

Figure 2. *(a) Schematic of radioisotope bias generation test circuit. On-chip C_{bias} was designed to be 5.9pF. (b) Plot of measured I_{ds} vs. pressure @ V_{ds}=5V, with switch SW1 open. The equivalent V_{gs} was calculated from the MOSFET characteristics of the N-MOSFET (AMI-AMS 1.5μm technology, W/L=2.5) (c) Measured shift in MOSFET (poly1-N-MOSFET with W/L=2.5) I_{ds}-V_{ds} characteristics with exponential build-up of radioisotope bias after opening the switch SW1.*

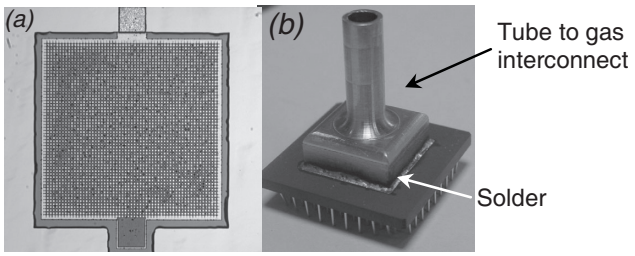

Figure 3. *(a) Photograph of the polymer capacitor (b) Photograph of the polymer capacitor package used for testing.*

The radioisotope source-collector can be modeled electrically as shown in Figure 1(b). The flux of electrons is modeled by the current source I_s, the leakage resistance by R_{Ni} and the air gap capacitance by C_{Ni}. In order to characterize the radioisotope source-collector system, the aluminum box with the source inside was placed in a vacuum chamber (~1millitorr) and the short circuit current output of the source measured using a Keithley Parametric Analyzer. The measured current value of 10.2pA was found consistent with the 2milliCurie (=11.2pA current output) activity of the source. R_{NI} was calculated to be ~7TΩ @1millitorr from the slope of the I-V curve of the source-collector terminals. A capacitance meter measured C_{Ni} to be ~2pF.

The radioisotope source-collector were then connected across the gate-source of an N-MOSFET as shown in Figure 2 (a). The chamber was then pumped down and the I_{ds} at V_{ds}=5V monitored (Figure 2(b)) during pump-down. This was used to characterize the bias generation with respect to pressure. The corresponding V_{gs} was calculated from the I_{ds}-V_{gs} curve measured for the MOSFET. As expected, lower pressure results in fewer particles getting ionized, or lower charge leakages, and hence higher voltage bias generated. Measurements show that moderate levels of vacuum (~100millitorr) are sufficient for the operation of the bias generation. At atmospheric pressure, a drain current of 26μA was measured for an applied drain voltage of 5V, indicating a build-up of 1.05V on the radioisotope source. To further confirm that it indeed is the radioisotope source generating the bias, the radioisotope source-collector capacitor was shorted using switch SW1, and then opened. The I_{ds}-V_{ds} for the MOSFET was measured at periodic intervals to illustrate exponential build-up of thin-film voltage due to the constant emission of electrons from Nickel-63.

Humidity Sensitive Polymer Capacitor

The devices were characterized at the die level and suitable devices epoxy attached in a ceramic pin grid array package. A copper lid with a ¼" pipe fitting was then soldered onto the package. This was for the interface with the gas feed-through in the vacuum chamber which would expose the sensor capacitor to the external atmosphere. The package was placed inside a controlled environmental chamber for testing at various levels of humidity. One electrode of the sensor element was excited with a $1V_{p-p}$ sinusoidal voltage at 0.2 Hz. The other electrode of the sensor was connected to the input of a trans-impedance amplifier with a $1x10^9$ gain. The current through the sensor element due to the slow sinusoid was then measured and the capacitance calculated at various levels of humidity (Figure 4). For 2mmX2mm devices with 20% of the top electrode exposed to the atmosphere, a sensitivity of 0.33pF/%RH was measured with a capacitance delay time constant of approximately 50s (Figure 5).

Self-powered Humidity Sensor

For the self-powered humidity sensor demonstration, the radioisotope source-collector, the humidity sensor package and the MOSFET chip were assembled in the vacuum chamber. The humidity sensor was exposed to atmosphere through a gas feed through. The opening of the gas feed through was exposed to a solution of sodium chloride to achieve 75%RH at thermal equilibrium. Leaving the gas feed-through exposed to ambient resulted in an estimated 30%RH. Two types of sensors were tested. One type was designed to have polymer capacitors with R_{PC}>>1TΩ, and the other with R_{PC}~1TΩ.

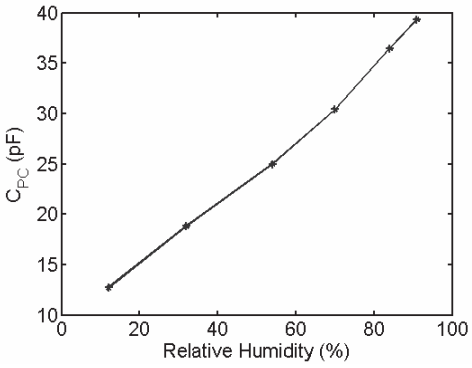

Figure 4. *Capacitance vs. RH for a 22pF@ 45RH polymer capacitor.*

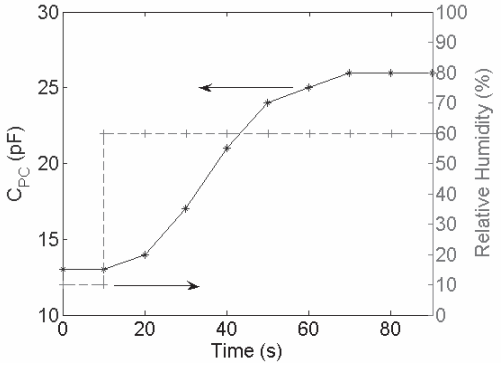

Figure 5. *Plot illustrating the transient response of the polymer capacitor in an environmental chamber when subjected to a step increase in relative humidity from 0%RH to 60%RH*

For the sensor using high R_{PC} polymer capacitor, the components were connected in the capacitive divider architecture (Figure 1(b)) and the chamber pumped down with the sensor feed-through exposed to ambient. The I_{ds} at V_{ds}=5V was measured to be 1.65mA when the pressure settled at ~1millitorr. This was compared to the final I_{ds} of 2.95mA reached without the polymer capacitor, and it was estimated that the final V_{gs} dropped from 18.9V to 9.25V as expected due to voltage division in the capacitor stack. Based on the value of C_{bias} and the measured parasitic capacitances (~7pF in parallel with C_{bias}) in the system, C_{PC} was estimated to be ~12pF in ambient conditions. The MOSFET I_{ds}-V_{ds} was measured at two different values of humidity and an expected upward shift (Figure 6) observed at elevated humidity levels. As the humidity increases, the capacitance of the sensor increases, raising the voltage bias on the gate of the MOSFET, and that consequently modulates drain current. From measured I_{ds}, C_{PC} was estimated to be ~28pF. Both the calculated values were close to the measurements made on the polymer capacitor.

For the sensor using R_{PC}~1TΩ polymer capacitor, the components were connected in the leakage resistance architecture (Figure 1(d)). Comparison of measured I_{ds} at ~1millitorr (sensor exposed to ambient) with that measured without the polymer capacitor revealed estimation for the leakage resistance R_{PC} of 1.05TΩ. The MOSFET I_d-V_{ds} was measured at two different values of humidity and an expected downward shift (Figure 7) observed at elevated humidity levels. As the humidity increases, the leakage in the capacitor increases, pulling the voltage bias down and hence reducing the drain current.

CONCLUSIONS

Two different architectures for long half-life radioisotope biasing of sensor elements were presented. The resulting self-powered sensors output easily readable amplified electronic signals through a unique MOSFET biasing scheme. Such zero-battery-power-consuming sensors can greatly extend the operating lifetime of the battery powered sensors, by using the battery only in the case of an event. Future work will involve realization of a hybrid on-chip platform for the self-powered sensor and charactering the sensitivity of the polymer capacitors. The sensitivity can be increased to completely switch the MOSFETs ON or OFF, which could be used to digitally wake up a mote.

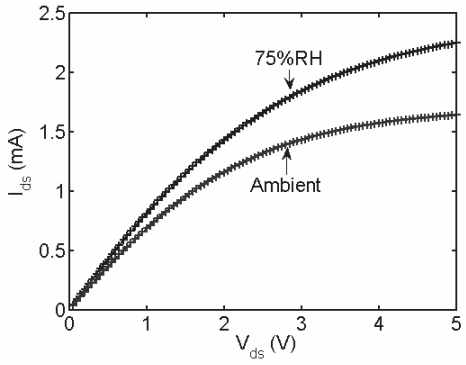

Figure 6. *Measured shift in the capacitive divider architecture sensor's I-V characteristics with relative humidity increase. A poly1-N-MOSFET in the AMI-AMS 1.5um process with W/L=2.5 was used for the experiments.*

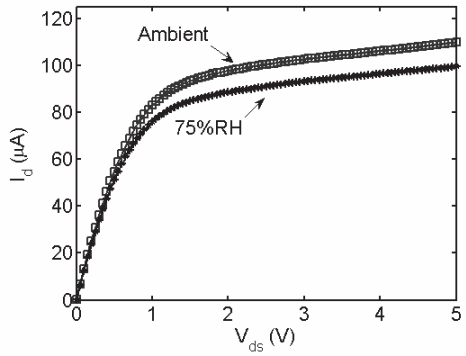

Figure 7. *Measured shift in the leakage resistance architecture sensor's I-V characteristics with relative humidity increase. A poly1-N-MOSFET in the AMI-AMS 1.5um process with W/L=2.5 was used for the experiments.*

ACKNOWLEDGEMENTS

This work was supported by DARPA-MTO under the RIMS program, and contracted under the U. S. AMRDEC.

REFERENCES

[1] N. A. Tanner, "Structural health monitoring using modular wireless sensors", *Journal of Intelligent Material Systems and Structures*, v 14, n 1, Jan. 2003, p 43-56.

[2] S. Roundy, "A study of low level vibrations as a power source for wireless sensor nodes", *Computer Communications*, v 26, n 11, 1 July 2003, p 1131-44.

[3] B. A. Warneke, "An autonomous 16 mm^3 solar-powered node for distributed wireless sensor networks", *Proceedings of IEEE Sensors 2002*, pt. 2, vol.2, p 1510-15.

[4] G. W. Taylor, "The Energy Harvesting Eel: a small subsurface ocean/river power generator", *IEEE Journal of Oceanic Engineering*, v 26, n 4, Oct. 2001, p 539-47.

[5] J. Pavio et al., "LTCC fuel cell system for portable wireless electronics", *Advancing Microelectronics*, v 29, n 5, Sept. 2002, p 8-11.

[6] A. Lal, R. Duggirala, H. Li, "Pervasive power: a radioisotope-powered piezoelectric generator", *IEEE Pervasive Computing*, v 4, n 1, Jan.-March 2005, p 53-61.

[7] F. J. Arregui et al., "Optical fiber-based sensor of harmful gas fabricated using the electronic self-assembly monolayer process", *Proceedings of the SPIE - The International Society for Optical Engineering*, v 4253, 2001, p 84-91.

[8] S. Kan and A. Lal, "Self-powered IC-compatible DC bias for electrostatic resonators", *Technical digest of IEEE MEMS 2004*, Maastricht, 2004, pp 817-820.

SINGLE-WALLED CARBON NANOTUBE MICROPATTERNS AND CANTILEVER ARRAY FABRICATED WITH ELECTROSTATIC LAYER-BY-LAYER NANO SELF-ASSEMBLY AND LITHOGRAPHY

Wei Xue and Tianhong Cui*
Department of Mechanical Engineering, University of Minnesota
111 Church Street SE, Minneapolis, MN 55455, USA
Tel: 612-626-1636 Fax: 612-625-6069 E-mail: tcui@me.umn.edu

ABSTRACT

A simple and effective approach is presented for patterning single-walled carbon nanotube (SWNT) microstructures by combining electrostatic layer-by-layer (LbL) nano self-assembly, lithography, and lift-off. This technique provides a simple, low-cost, and low-temperature fabrication method with a short processing time. SWNT micropatterns with feature sizes as small as 5 μm were fabricated and characterized. The thickness of a (PDDA/SWNT) bi-layer was measured approximately as 76 Å. To investigate the potential applications of SWNTs, magnetic cantilever arrays consist of SWNTs, iron oxide (Fe_2O_3) nanoparticles, and polyelectrolytes were developed. Due to the outstanding mechanical properties of the SWNTs, the fabricated cantilever arrays are strong and flexible. The cantilever arrays can be used in applications such as biosensors and microvalves.

INTRODUCTION

Since the discovery in 1991, carbon nanotubes (CNTs) have been investigated extensively due to their unique structural, electrical, chemical, and mechanical properties [1]. CNTs are promising materials in nanotechnology and can be used in a wide range of applications including chemical sensors, biosensors, stress/strain sensors, scanning probes, field emission displays, nanoelectronics devices, and nanoelectromechanical systems (NEMS) [2-5]. In their natural forms, CNTs are highly sensitive to molecules such as NO_2 and NH_3 [2]. With rational chemical and/or physical modification, CNTs are capable of detecting more types of molecules (e.g., H_2, CO, glucose, and DNA) [6]. The controllable deposition of CNTs, either individually or as a bulk material, is an essential step in building practical devices.

Current deposition approaches include chemical vapor deposition (CVD), selective electrophoresis deposition, Langmuir-Blodgett method, and nano-manipulation using atomic force microscope tips [7-8]. However, commercialization of CNT-based devices demands faster, less expensive, and more convenient deposition techniques. Electrostatic layer-by-layer (LbL) nano self-assembly was introduced to produce films in micro- and nanoscale. LbL nano self-assembly is an effective and economic approach to build well-organized multilayers in nanometer scale. LbL self-assembled thin films can be deposited on the surface of almost any materials with any topography [9]. With this technique, SWNT thin films have been fabricated and investigated by several groups. Compared with other SWNT/polymer matrices, LbL self-assembled SWNT thin films show enhanced mechanical properties [10]. In addition, the thin films fabricated with LbL self-assembly usually retain the electrochemical catalytic activities of the CNTs [11].

In this paper, we report a simple, effective, and versatile technique to fabricate SWNT microstructures through a combination of electrostatic LbL nano self-assembly and conventional lithography. This technique provides a simple, low-cost, and low-temperature fabrication method with a short processing time. The SWNT films and micropatterns were built with alternating layers of poly(dimethyldiallylammonium chloride) (PDDA) and SWNTs. The enhanced mechanical properties of SWNT thin films can be utilized in a variety of applications. To investigate the potential applications of SWNT thin films, magnetic cantilever arrays composed of PDDA, SWNTs, and Fe_2O_3 nanoparticles were fabricated.

MATERIALS

SWNTs (1.1 nm in diameter, 50 μm in length) were purchased from Chengdu Organic Chemicals Co. Ltd. The polyelectrolytes, including PDDA (polycation, molecular weight MW 200,000 to 350,000, 3 mg/ml, 0.5 M NaCl) and poly(sodium 4-styrenesulfonate) (PSS) (polyanion, MW 70,000, 3 mg/ml, 0.5 M NaCl) were obtained from Sigma-Aldrich. Magnetic iron oxide nanoparticles (Fe_2O_3, 50 nm in diameter, surface covered with hydrophilic PSS, concentration: 2 mg/ml) were obtained from Chemicell GmbH. The Fe_2O_3 nanoparticles are negatively charged due to the surface coverage of PSS. All materials were diluted in deionized (DI) water.

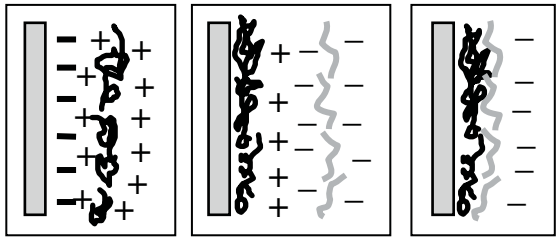

(a) $\{Polycation/SWNTs\}_m$

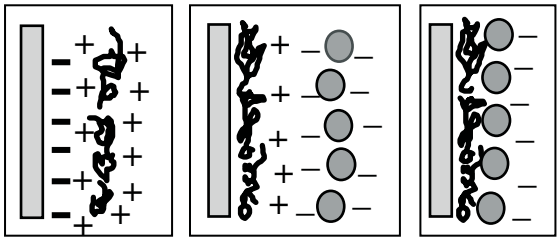

(b) $\{Polycation/Fe_2O_3\ Nanoparticles\}_n$

Figure 1. *Schemes of layer-by-layer alternate assembly of (a) polycation/SWNTs and (b) polycation/Fe_2O_3 nanoparticles.*

It is well known that pristine SWNTs suffer from poor solubility in water and other chemicals. The hybrid polymer/SWNT composites often have problems such as poor polymer-SWNT connectivity, phase segregation, and structural inhomogeneities [10]. LbL self-assembly is a good approach to

overcome these problems because it is a solution-based technique. SWNTs with rational treatment can be dispersed in DI water and uniformly deposited on the substrate. Highly homogenous polymer/SWNT thin films with enhanced mechanical properties can be fabricated. The schemes of self-assembled thin films through alternate adsorption of oppositely charged polyelectrolytes, SWNTs, and Fe_2O_3 nanoparticles are shown in Fig. 1.

To increase the solubility in DI water, the SWNTs were chemically functionalized by a mixture of nitric and sulfuric acid (1:3 HNO_3:H_2SO_4) at 110ºC for 45 min. The mixture of acids cut the SWNTs into short tubes with openings at both ends. Carboxylic (-COOH) functional groups were covalently attached to the open ends and sidewalls. Next, the SWNT dispersion was diluted with DI water and filtered with a PVDF membrane (with pore diameter of 0.22 µm). The SWNTs were then rinsed with DI water to remove the residual acids. The treated SWNTs were dispersed in DI water. The SWNT dispersion was ultrasonically vibrated for 1 hour. The final step was to remove the excessive SWNTs by centrifuging the SWNT dispersion at 5000 rpm for 15 min. After the chemical funcationalization, the SWNTs were negatively charged and uniformly dispersed in DI water with a concentration of 1 mg/ml.

SWNT MICROPATTERNS

In previous reports, we presented the patterning of nanoparticle-based structures with the technique that combines the LbL self-assembly, lithography, and lift-off [12]. The same approach can be used to pattern SWNT thin films, as shown in Fig. 2. We have successfully fabricated micro-scale patterns on both silicon and polymer substrates.

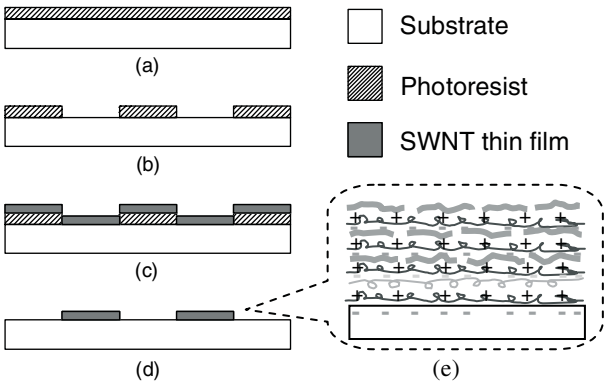

Figure 2. *Fabrication process of the SWNT micropatterns by LbL self-assembly, lithography, and lift-off.*

The patterning of the SWNT thin films starts by depositing a 1.5 µm layer of photoresist (PR1813) on a substrate (Fig. 2a). Conventional lithography is used to pattern the photoresist layer (Fig. 2b). The next step is to deposit the SWNT multilayer with LbL self-assembly (Fig. 2c). The substrate is soaked into different solutions, and the sequence of the immersion is: [PDDA (10 min) + PSS (10 min)]$_2$ + [PDDA (10 min) + SWNTs (15 min)]$_n$, where n represents the number of (PDDA/SWNT) bi-layers. The coating of the first two (PDDA/PSS) bi-layers is to prepare a smooth base for the subsequent coating. Intermediate rinsing with DI water and drying with a nitrogen flow are required to remove the excessive polyelectrolytes and SWNTs. Figure 1e shows the detailed construction of the SWNT multilayer. The final step is to dissolve the photoresist and remove the SWNT multilayer with the lift-off technique (Fig. 1d). The substrate is soaked in acetone for 1 min with the assistance of ultrasonic vibration. The self-assembled SWNT multilayer is permeable for acetone. Acetone molecules penetrated through the SWNT thin film can dissolve the photoresist and strip off the SWNT multilayer in those areas. Only the SWNT multilayer directly assembled on the substrate remains.

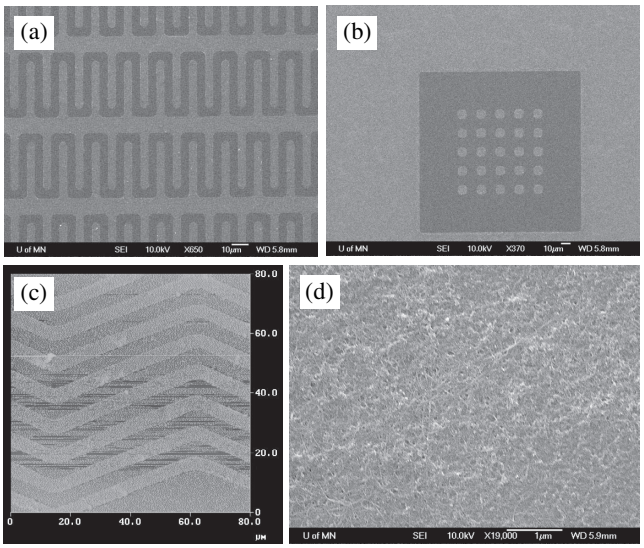

Figure 3. *Images of (PDDA/SWNT)$_6$ micropatterns. SEM images of (a) micro-springs with linewidth of 5 µm and (b) micro-squares with dimensions of 10 µm × 10 µm. (c) AFM image of micro-springs with linewidth of 5 µm. The scanning area is 80 µm × 80 µm. (d) Close inspection of the assembled SWNTs on the substrate with SEM.*

Scanning electron microscopy (SEM, JEOL 6500) and atomic force microscopy (AFM, Digital Instruments Dimension 3000, tapping mode) were used to inspect the SWNT micropatterns created with the fabrication technique described above. Figure 3 shows the SEM and AFM images of SWNT micropatterns and self-assembled SWNTs on the substrate. The samples used for microscopy inspection are (PDDA/SWNT)$_6$ micropatterns. The SWNT thin film is formed by a dense network of SWNTs. The SWNTs are randomly deposited on the surface. The length of the SWNTs is in the range of 1 – 2 µm which is due to the chemical treatment. However, as shown in the figure, the diameters of most SWNTs are much larger than pristine SWNTs (1.1 nm). The reason for this discrepancy is that during the self-assembly process, several SWNTs are wrapped together due to their extremely high aspect ratios. Therefore, the assembled SWNTs are mainly in the form of nanotube bundles which are approximately 5 – 10 nm in diameter and 1 – 2 µm in length.

To estimate the thickness of the SWNT multilayer, a group of 50 µm lines composed of (PDDA/SWNT)$_6$ multilayer was fabricated on a silicon substrate using the method described above. Surface profiler (Dektak, Model IIA) was used to measure the vertical profile of the SWNT lines. The average thickness of the (PDDA/SWNT)$_6$ structure was measured approximately as 400 Å. The surface profiler obtains its measurement data by moving a diamond tip stylus over the patterns during the scan. It usually gives relatively accurate results on hard substrates. However, when used on soft thin films, the scanning is destructive and may give inaccurate results. In order to verify the measured results from the surface profiler, an ellipsometer

(Gaertner Scientific Co.) was used to detect the thin film thickness. Ellipsometer provides a non-destructive method and gives more accurate results once the rough thickness of the film is known. The measured thickness of the $(PDDA/SWNT)_6$ multilayer was 455.4 ± 5% Å. Therefore, the average thickness of a (PDDA/SWNT) bi-layer is approximately 76 Å.

SWNT-BASED MAGNETIC CANTILEVER ARRAY

The mechanical properties of the LbL self-assembled SWNT thin film were studied and reported. The Young's modulus of the SWNT film was measured as 17 – 35 GPa, and the ultimate tensile strength was measured as 180 – 325 MPa [10]. Compared with strong polymers which are commonly used for MEMS devices such as polymethyl methacrylate (PMMA, Young's modulus: 2 GPa, ultimate tensile strength: 50 MPa), SWNT thin films are several times stronger. SWNT films also have enough flexibility due to its composite essence. In general, the SWNT thin films have the mechanical properties between those of silicon and polymers. The SWNT thin films can serve as structural components in MEMS devices to provide both flexibility and strength. In addition, the "bottom-up" LbL self-assembly technique has the ability to control the film thickness in nanometer scale. Therefore, the SWNT cantilever array may have the potential to be used in a variety of applications.

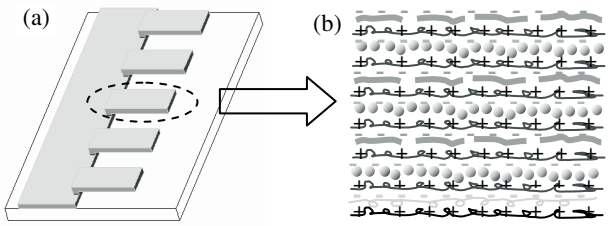

Figure 4. *(a) Scheme diagram of the cantilever array fabricated on silicon substrate. (b)Illustration of the SWNT-based magnetic cantilever multilayer. The multilayer consists of PDDA (+), PSS (-), Fe_2O_3 nanoparticles (-), and SWNTs (-).*

To investigate the potential applications of SWNT thin films, especially in biosensing, SWNT-based magnetic cantilever arrays were designed and fabricated. The schematic diagram of the SWNT cantilever array is illustrated in Fig. 4. Both the roots and the beams are composed of SWNT multilayer. Iron oxide nanoparticles are integrated in the multilayer as magnetically sensitive material, which makes the measurement convenient. The cantilever array can be used in detecting biomolecules such as proteins, enzymes, and DNAs. A number of biomolecules are naturally charged and can be assembled in alternation with polyelectrolytes based on LbL self-assembly technique. Because the cantilevers are self-assembled multilayers, the surfaces of the cantilevers are charged. The biomolecules can be readily adsorbed onto the cantilevers. The resonant frequency shift caused by the mass increase of the cantilever can be detected by an optical interferometer. Another possible application is to use the cantilever beams as magnetically driven microvalves.

The fabrication process of the cantilever array is shown in Fig. 5. A layer of photoresist PR1813 is spin coated on the substrate (Fig. 5a). A window for the cantilever root is opened using ultraviolet (UV) lithograph (Fig. 5b). Second UV lithography is executed with part of the PR1813 layer protected. The protected PR1813 is used as the sacrificial layer which is underneath the cantilever beam (Fig. 5c). The PDDA/PSS/SWNT/Fe_2O_3 multilayer is self-assembled on the substrate (Fig. 5d). The immersion sequence is [PDDA (10 min) + PSS (10 min)]$_2$ + {PDDA (10 min) + Fe_2O_3 (15 min) + [PDDA (10 min) + SWNTs (15 min)]$_2$ + PDDA (10 min) + Fe_2O_3 (15 min) + PDDA (10 min) + SWNTs (15 min)}$_3$. Nine layers of SWNTs are used to strengthen the cantilever structure. Six layers of Fe_2O_3 nanoparticles make the cantilever magnetically sensitive. The growth of the multilayer was monitored by a quartz crystal microbalance (QCM). The effective surface coverage of the Fe_2O_3 nanoparticles was measured approximately as 30%. The effective thickness of the multilayer was calculated approximately as 200 nm. The exposed PR1813 is dissolved by 351 developer with the lift-off technique. In order to remove the multilayer coated on the exposed PR1813, the lift-off process is implemented with ultrasonic vibration (Fig. 5e). The freestanding cantilever beam is released by stripping off the PR1813 sacrificial layer with acetone (Fig. 5f).

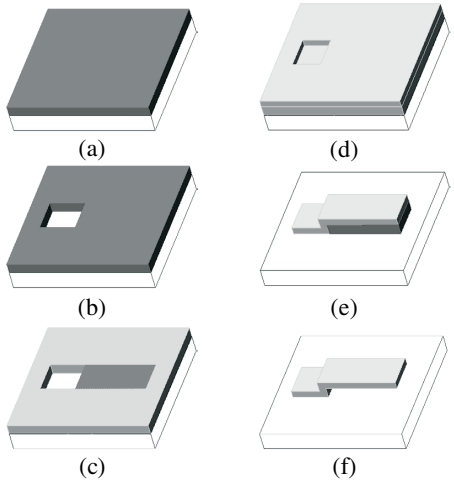

Figure 5. *Fabrication process of the self-assembled cantilever.*

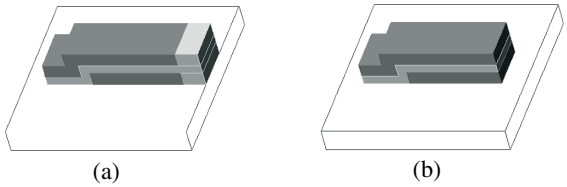

Figure 6. *Modified lift-off process with a "sandwich" structure. (a) Before lift-off. (b) After lift-off with 351 developer.*

The micropatterns fabricated with conventional lift-off processes usually have step profiles. The stripper molecules can easily attack the underlying photoresist layer and remove the unwanted top layer. However, as shown in Fig. 5d, the self-assembled multilayer covers the whole surface of the device and is almost at the same height. During the lift-off process, ultrasonic vibration is required to break the multilayer. It takes 8 – 10 min to remove the unwanted parts of the thin film due to its high mechanical strength. The long-time ultrasonic bath severely weakens and damages the cantilever structures, especially the joints between the roots and the beams. The weakening of the structures may cause detachment of the beams from the roots. Therefore, a modified lift-off process was developed to replace the lift-off step shown in Fig. 5e. A "sandwich" structure provides additional protection for the cantilever roots and beams. As shown in Fig. 6, a top photoresist layer is coated to cover the surface of the multilayer. It should be noted that only part of the

multilayer is shown in the figure for visibility. The whole surface is actually covered by photoresist. The parts of the photoresist that cover the cantilever roots and beams are protected by photomask while other parts of the photoresist are exposed under UV light. Based on the modified lift-off process, the ultrasonic bath time can be greatly reduced to 2 min. Both the cantilever roots and beams are well protected by the top photoresist layer.

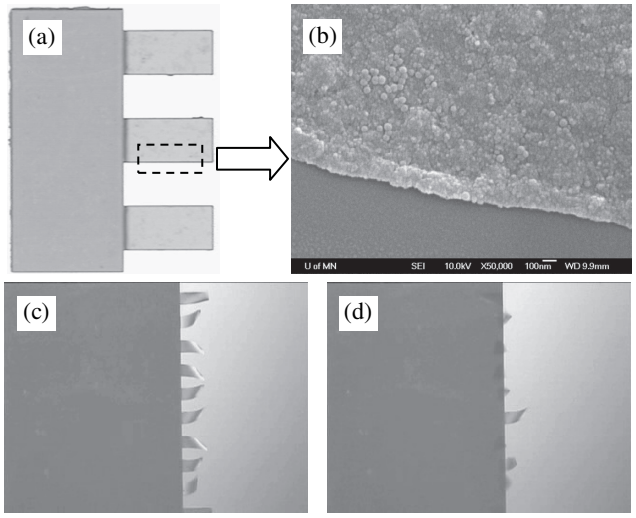

Figure 7. *Images of the LbL self-assembled cantilever array. (a) Optical image of the cantilever array. The length and the width of the beams are 300 μm and 150 μm, respectively. (b) SEM inspection of the edge of the cantilever. (c) Cantilever array in acetone solution without external magnetic field. (d) Flexed cantilever array under the influence of external magnetic field. The beams are 150 μm in length and 50 μm in width.*

The images of the fabricated cantilever array are shown in Fig. 7. Figure 7a shows an optical image of a cantilever array consists of three beams. Figure 7b shows the SEM inspection of the edge of the beam. The Fe_2O_3 nanoparticles can be clearly seen from the figure. To strip off the top protecting and the bottom sacrificial photoresist layers, the device is submerged in acetone. The beams float in the solution when there is no external magnetic field (Fig. 7c). When an external magnetic field is applied by holding a permanent magnet 1 cm above the device, the beams are deflected (Fig. 7d). The deflection angles can exceed 90 degrees in the presence of the magnetic field. The beams restore rapidly after moving the magnet away from the device. There is no observable structural failure or damage after repeated deflections (more than 100 times). The SWNT multilayer is proven to be very flexible and strong. However, the internal stress inside the SWNT multilayer is not neglectable. The free ends of the cantilever beams are curled in the acetone solution. This may cause measurement problems when optical method is used. Further studies will be conducted to solve the problem. Possible solutions include increasing the multilayer thickness, trimming the corners of the beams, increasing the number of SWNT layers, etc.

CONCLUSIONS

We have presented an effective, simple, low-cost, and low-temperature approach to fabricate SWNT thin films and micropatterns using LbL nano self-assembly and UV lithography. SWNT micropatterns with features as small as 5 μm have been produced. It is believed that the patterned feature size can be downscaled to submicron or even nanoscale if high-resolution lithography techniques such as electron-beam lithography are used. The assembled SWNTs are mainly in the form of nanotube bundles which are approximately 5 – 10 nm in diameter and 1 – 2 μm in length. The thickness of a (PDDA/SWNT) bi-layer is approximately 76 Å. LbL self-assembled cantilever array composed of polyions/SWNTs/nanoparticles multilayer has been fabricated. A modified lift-off process provides additional protection for the cantilever structures. The strength and thickness of the cantilever can be adjusted in a wide range. The cantilever beams can be easily deflected to over 90º. The fabricated cantilever array can be used as magnetically driven microvalves. It can also be used in biosensing applications for biomolecules adsorption and detection because a number of biomolecules can be easily adsorbed on the self-assembled multilayer.

REFERENCES

[1] S. Iijima, "Helical Microtubules of Graphitic Carbon", *Nature, 354,* 56 (1991).
[2] J. Kong, N.R. Franklin, C. Zhou, M.G. Chapline, S. Peng, K. Cho, H. Dai, "Nanotube Molecular Wires as Chemical Sensors", *Science, 287,* 622 (2000).
[3] K.A. Williams, P.T.M. Veenhuizen, B.G. de la Torre, R. Eritja, C. Dekker, "Carbon Nanotubes with DNA recognition", *Nature, 420,* 761 (2002).
[4] W.B. Choi, D.S. Chung, J.H. Kang, H.Y. Kim, Y.W. Jin, I.T. Han, Y.H. Lee, J.E. Jung, N.S. Lee, G.S. Park, J.M. Kim, "Fully Sealed, High-Brightness Carbon-Nanotube Field-Emission Display", *Applied Physics Letters, 75,* 3129 (1999).
[5] M. Penza, F. Antolini, M.V. Antisari, "Carbon Nanotubes as SAW Chemical Sensors Materials", *Sensors and Actuators, B: Chemical, 100,* 47 (2004).
[6] J. Kong, M. G. Chapline, H. Dai, "Functionalized Carbon Nanotubes for Molecular Hydrogen Sensors", *Advanced Materials, 13,* 1384 (2001).
[7] L. Valentini, C. Catalini, I. Armentano, J.M. Kenny, L. Lozzi, S. Santucci, "Highly Sensitive and Selective Sensors Based on Carbon Nanotubes Thin Films for Molecular Detection", *Diamond and Related Materials, 13,* 1301 (2004).
[8] Y. Jang, S. Moon, J. Ahn, Y. Lee, B. Ju, "A Simple Approach in Fabricating Chemical Sensor using Laterally Grown Multi-Walled Carbon Nanotubes", *Sensors and Actuators, B: Chemical, 99,* 118 (2004).
[9] Younan Xia, George M. Whitesides, "Soft Lithography", *Annual Review of Materials Science, 28,* 153, (1998).
[10 A.A. Mamedov, N.A. Kotov, M. Prato, D.M. Guldi, J.P. Wicksted, A. Hirsch, "Molecular Design of Strong Single-Wall Carbon Nanotube/Polyelectrolyte Multilayer Composites", *Nature Materials, 1,* 190 (2001).
[11] M. Zhang, K. Gong, H. Zhang, L. Mao, "Layer-by-Layer Assembled Carbon Nanotubes for Selective Determine of Dopamine in the Presence of Ascorbic Acid", *Biosensors and Bioelectronics, 20,* 1270 (2005).
[12] F. Hua, T. Cui, Y. Lvov, "Ultrathin cantilevers based on polymer-ceramic nanocomposite assembled through layer-by-layer adsorption", *Nano Letters, 4,* 823, (2004).

TEMPERATURE STABLE, POST-PROCESS TUNABLE, HIGH Q HBARS AT 3~5 GHZ

Hongyu Yu, Hao Zhang, Wei Pang, and Eun Sok Kim
Department of Electrical Engineering
University of Southern California
Los Angeles, CA 90089-0271, U.S.A.

ABSTRACT

This paper describes a temperature-compensated High-overtone Bulk Acoustic Resonator (HBAR) with a loaded quality factor (Q) of 801 and 545 at 3.427 GHz and 4.597GHz, respectively. The HBAR is composed of an Al/ZnO/Al resonator on a SiO_2/Si/SiO_2 diaphragm where a thermally grown SiO_2 with positive temperature-coefficient-of-frequency (TCF) compensates the negative TCF of the rest of the resonator layers. The HBAR's TCF reaches zero at a specific temperature, and is lower than 1ppm/°C over a 30°C temperature span, where the TCF is about 100 times better than the value obtainable with an un-compensated Al/ZnO/Al Film Bulk Acoustic Resonator (FBAR). Also, the resonant frequency of the HBAR as well as its TCF is shown to be tunable by adding additional SiN and/or SiO_2 layer after fabrication.

INTRODUCTION

There are three types of Bulk Acoustic Wave (BAW) resonators based on piezoelectric film: micromachined Film Bulk Acoustic Resonator (FBAR), Solidly Mounted Resonator (SMR) and High-overtone Bulk Acoustic Resonator (HBAR) [1~4]. Most BAW resonators are composed of metal/piezofilm/metal on top of a thin diaphragm or a thick substrate, and have shown a quality (Q) factor greater than hundreds (even tens of thousands in case of HBAR) at a resonant frequency of 0.5 to 10 GHz. The resonant frequency is predominantly determined by the thickness of the piezoelectric film. With their inherently high Q, BAW resonators are ideally suited for filters and oscillators at GHz, since the Q determines the insertion loss and phase noise for filters and oscillators, respectively.

Since Agilent mass-produced FBAR-based duplexer filters for mobile phones in 2000, FBARs are widely used for RF front-end filters for mobile phones. Similar filters based on SMR recently have joined the mobile phone market. On the other hand, HBAR remains to be used only for niche oscillator applications, though its Q can be made much higher than FBAR and SMR, mainly due to its multiple resonances and low electromechanical coupling coefficients.

Chip-Scale Atomic Clock (CSAC) enables miniature (and low power consuming) time reference for high security communication and jam-resistant global-positioning-system receiver. Since CSAC requires a very high Q resonator for its local oscillator, HBAR-based voltage controlled oscillators (VCO) is ideally suited for CSAC, where the oscillation frequency of particular interest is 3.4GHz or 4.6GHz for different system design topologies.

However, for HBAR-based VCO to be used for CSAC's local oscillator, the resonator must be very stable in temperature. For example, the resonant frequency shift of the resonator should not exceed 20ppm over 60 to 80°C, which means the temperature coefficient of frequency (TCF) of the resonator should be less than 1 ppm/°C (a conventional Al/ZnO/Al stand-alone resonator has a TCF of about -70 ppm/°C [5]).

To reduce HBAR's TCF, the following techniques have been explored and reported. A heater was embedded into an HBAR [6] to tune the resonant frequency to compensate the TCF. But this approach consumes large power and lacks repeatability. Another technique for HBAR is to use a capacitor (having a temperature coefficient in opposite sign to that of the HBAR's clamped capacitance) in series with the HBAR. The achievable TCF of an HBAR with this approach is limited by available capacitor.

The most promising technique for temperature compensation of a bulk acoustic resonator is to use a support layer (e.g., SiO_2 or Elinvar) that has TCF opposite to that of the piezoelectric layer for FBAR [7, 8]. No literature is found on temperature compensating HBAR with this method of incorporating a temperature-compensating layer. This paper describes HBAR with temperature-compensating SiO_2 layer, particularly their measured TCF's, timing stabilities and the post tuning ability.

THEORY

The resonant frequencies of a HBAR resonator is predominantly determined by acoustic-wave traveling time in the resonator, and are

$$f_r \approx \frac{N}{2(d_{piezo}/V_{piezo} + d_{elec}/V_{elec} + d_{substrate}/V_{substrate})^{-1}}$$

where d_{piezo}, d_{elec}, $d_{substrate}$ are the thicknesses of the piezomaterial (ZnO), electrodes (Al), and diaphragm (SiO_2) (or substrate (SiO_2/Si/SiO_2)), respectively, while V_{piezo}, V_{elec} *and* $V_{substrate}$ are the acoustic velocities in the piezomaterial, electrodes, and diaphragm (or substrate), respectively. The dependence of the resonant frequency on temperature mainly comes from the acoustic velocity's dependence on temperature. The acoustic velocity is equal to $\sqrt{E/\rho}$ where E and ρ are Young's modulus and mass density, respectively. For most materials (such as Al, Si and ZnO) Young's modulus decreases as temperature increases, causing negative TCF for a BAW resonator.

However, due to the unique crystalline structure, the Young's modulus of SiO_2 increases as temperature increases, resulting in a positive TCF. Thus, SiO_2 layer can be used for compensating a negative TCF of Al/ZnO/Al/Si HBAR.

We build an HBAR with Al/ZnO/Al on SiO_2/Si/SiO_2 substrate (which is actually a diaphragm). Most of the resonator's acoustic energy is stored in the relatively thick single crystalline Si layer where the acoustic loss is much less than ZnO or Al. Hence, the resonator's Q is mostly determined by the single crystalline Si, and can be much higher than FBAR. The thermally grown SiO_2 layers below and above the Si layer are to compensate the negative TCF's of ZnO, Al and Si. Due to the complicated structure and acoustic energy distribution in the HBAR, there has not been an effective model to accurately predict the TCF of the HBAR, and

we have fabricated HBARs with various multilayer thickness ratios to obtain optimum TCF experimentally.

FABRICATION AND TESTING

The temperature compensated HBARs are fabricated on a Silicon-on-Insulator (SOI) wafer with the fabrication steps shown in Fig. 1. After obtaining a silicon diaphragm (out of the silicon device layer of SOI) by TMAH, XeF_2 and buffered HF etching (in that order) on an SOI wafer, we thermally grow wet SiO_2 on the device silicon layer to form $SiO_2/Si/SiO_2$ diaphragm. Then bottom 0.1μm Al is evaporated on the SiO_2 layer and patterned, followed by deposition of 0.68μm thick ZnO in a RF sputtering system with 10mTorr Argon and Oxygen gas mixture (50%/50%) at 300°C and 300W. After patterning the ZnO, 0.1μm thick top Al electrode is evaporated and patterned. The bottom Al, ZnO, and top Al on top of the diaphragm form the wave-generating layers of an HBAR.

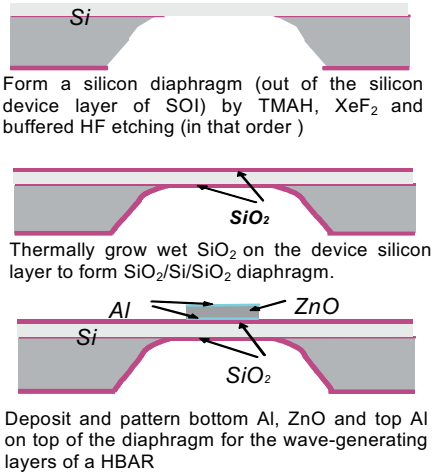

Figure 1 Brief fabrication process for the temperature compensated HBAR

The fabricated resonators are characterized with HP8753D network analyzer with Cascade microwave micropositioner and probes (for impedance measurement) and Instec's hot/cold chuck (for temperature variation). We have developed a Labview program to acquire data from the network analyzer and analyze it by curve fitting to monitor HBAR's resonant frequencies. The noise floor of this method is around 0.5ppm, which is good enough for measuring the dependence of the HBAR's resonant frequency on temperature.

RESULTS AND DISCUSSION

HBARs with various top-view shapes and sizes (Fig. 2) along with various thickness ratios have been fabricated and tested. The testing results show little difference among different top-view shapes, but the top-view dimension of the HBAR affects the Q much. The HBAR with 100 μm long sides is measured to have the highest Q at 3 to 5 GHz.

Figure 2 Top-view photos of the fabricated HBARs on SiO_2/Silicon/SiO_2

The TCF of the HBAR is directly related to the thickness ratios among various structure layers. Figure 3 shows the measured TCF's at about 80°C for different thickness ratios for the $SiO_2/Si/SiO_2$ multi-layers for the HBAR with Al/ZnO/Al having thicknesses of 0.1μm/0.68μm/0.1μm (for 3.4 GHz) and 0.1μm/0.48μm/0.1μm (for 4.6 GHz), respectively. The measured TCFs depend linearly on the thickness ratio between the positive TCF layer (SiO_2) and the effective negative TCF layer (obtained by converting the Al, ZnO and Si layers to an equivalent Si layer). The ratios of 0.28 and 0.35 produce zero TCF's for the 4.6 and 3.4GHz HBARs, respectively.

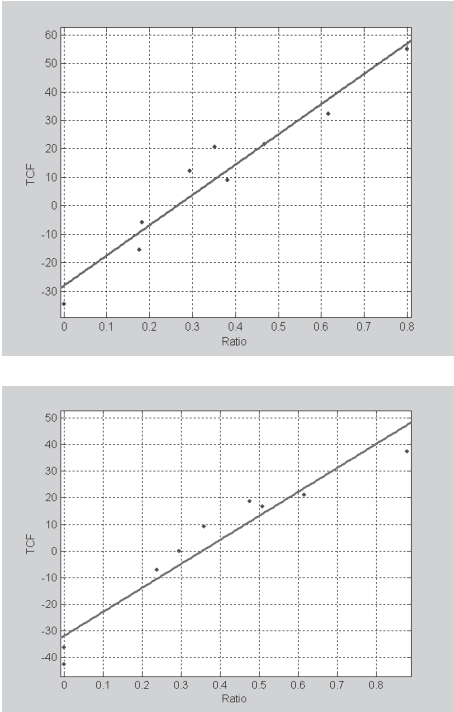

Figure 3 Measured TCF (ppm/°C) at 4.6GHz(top) and 3.4GHz (bottom) vs. the ratio of the +TCF layer thickness to the –TCF layer thickness.

The zero TCF HBAR with Al/ZnO/Al/SiO_2/Si/SiO_2 (0.1μm/0.68μm/0.1μm/1.7μm/9.9μm/1.7μm) is measured to have eight resonant frequencies between 3 and 5 GHz (Fig.2). The HBAR has different TCF's at these frequencies, which are shown in the Table 2. The reason for the different TCF's is the different acoustic energy distribution along the HBAR thickness. The more acoustic standing wave energy in the positive TCF layer (SiO_2), the more positive of the whole HBAR's TCF.

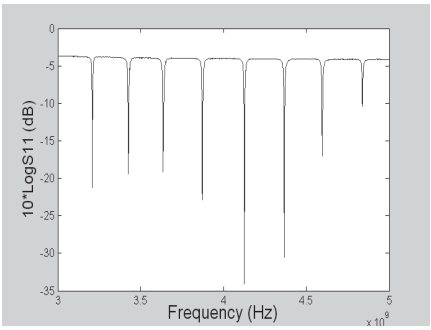

Figure 4 Measured S_{11} vs. frequency of the HBAR.

Table 1 TCFs at five different resonant frequencies of the HBAR on SiO_2/SI/SiO_2

Resonant Frequency (GHz)	3.208	3.427	3.636	3.873	4.124	4.366	4.597
TCF (ppm/°C) at 72.5°C	-1.87	0	-3.95	-10.1	-10.7	-6.5	-1.84

The HBAR is measured to have impedance variation from 3.416 to 3.428GHz as shown in Fig. 5. The highest loaded Q's at the parallel resonant frequency (3.4271 GHz) and series resonant frequency (3.4215 GHz) are measured to be 801 and 660, respectively. The electromechanical coupling coefficient (K_t^2) is 0.41%. If the series resistance is de-embedded [9], the unloaded Q's are 821 and 1045 at the parallel and series resonant frequencies, respectively.

At the parallel and series resonant frequencies near 3.4 GHz, the HBAR is measured to have a TCF of 1.0 to –0.8 ppm/°C between 60 and 90°C, where the zero TCF point is at 72.5°C. The parallel resonant frequency vs. temperature (from room temperature to 125°C) is shown in Fig. 6. The total parallel resonant frequency change between 53 and 90°C (over 37°C range) is 36.6kHz, mere 10.7ppm. And from room temperature (27°C) to 120 °C, the total resonant frequency change is 312kHz, which is 91ppm.

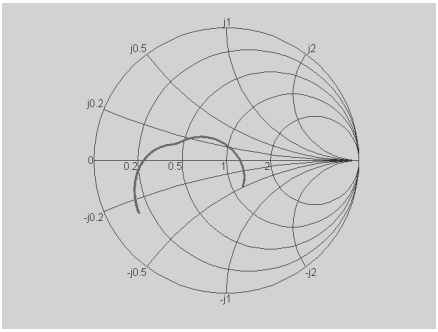

Figure 5 Measured Smith-chart impedance from 3.416 to 3.428GHz.

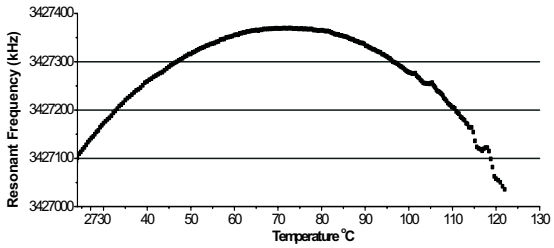

Figure 6 Measured resonant frequency vs. temperature for the HBAR at 3.427GHz.

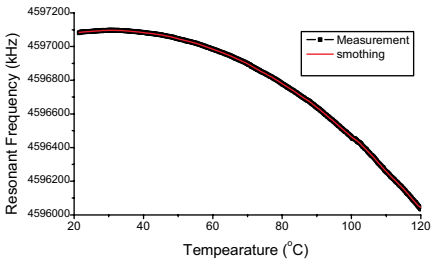

Figure 7 Measured resonant frequency vs. temperature for the HBAR at 4.597GHz

The same HBAR yields a zero TCF at 32.8°C (Fig. 7) with a loaded parallel Q of 545 for a parallel resonant frequency of 4.597 GHz. The HBAR's parallel resonant frequency varies a total of 228ppm at 4.597 GHz over a wide temperature span of 24 to 125°C. Note that the resonant frequency of a typical silicon-supported ZnO HBAR varies about 3,700ppm over 24 – 125°C.

The TCFs at the parallel and series resonant frequencies of the HBAR are measured to vary with temperature as shown in Fig 8. The measurement shows that the TCF changes linearly from 4ppm/°C at 23°C to around -4ppm/°C at 122°C, with a slope of -0.079ppm/°C/°C. With this linear variation of the TCF, we cannot obtain a very low TCF from –50°C to 120°C. Thus, in an effort to obtain an "S-shape" in the resonant frequency vs. temperature curve, we have applied a DC voltage to piezoelectrically stiffen the HBAR to see if the voltage can affect the TCF vs. temperature curve. As can be seen in Fig. 9, the DC voltage is measured to change the resonant frequency of the HBAR. However, we have observed no change in the TCF curve by an applied DC voltage.

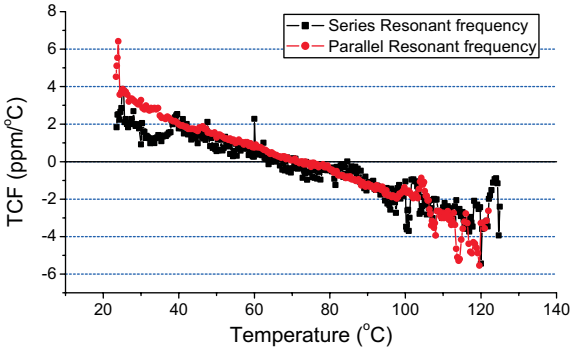

Figure 8 Measured TCF at parallel resonant frequency (*gray*) and series resonant frequency (*black*) vs. temperature of the HBAR.

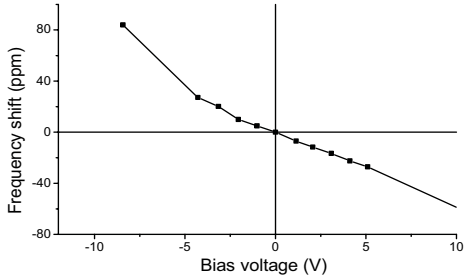

Figure 9 Measured HBAR's resonant frequency vs. applied DC voltage.

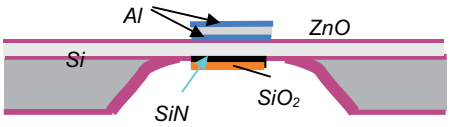

Figure 10 Post-process tuning by additional layers of PECVD SiN and SiO_2 on the backside of HBAR

Due to the sensitivity of HBAR's resonant frequency and TCF to the structure's multilayer thicknesses, the fabrication process needs to be controlled critically to meet the frequency and TCF demand for the devices. Thus, we have developed a post-process, frequency and TCF tuning method by depositing PECVD SiN and SiO_2 layers on the backside of the HBAR (Fig. 10). The measured data show that the additional layers change the HBAR's resonant frequency and TCF at a different rate. Thus, any desired resonant frequency and TCF can be obtained by combining different thicknesses of the SiN and SiO_2. For example, an

additional 0.6μm thick SiN and 0.4μm thick SiO_2 on Al/ZnO/Al/SiO_2/Si/SiO_2(0.1μm/0.68μm/0.1μm/1.7μm/3.9μm/1.7μm) HBAR makes the HBAR have a 3.427GHz resonant frequency and zero TCF at 75°C with a same high Q (a fine tuning from a resonant frequency of 3.601GHz and TCF of 13.9ppm/°C).

For CSAC, an HBAR-based voltage controlled oscillator (VCO) can be used for keeping a short-term stability of the clock, while the atomic emission unit keeps the long-term stability. Nevertheless, the long-term (as well as short-term) stability is still very important for HBARs. For testing the short-term stability, we keep the temperature compensated HBAR at 72.5°C, where the TCF of HBAR is 0, to minimize the effect from the temperature fluctuation. Figure 11 shows that the parallel frequency fluctuation is measured to be about 3.3ppm and 6.7ppm within 90 minutes and 8 hours, respectively.

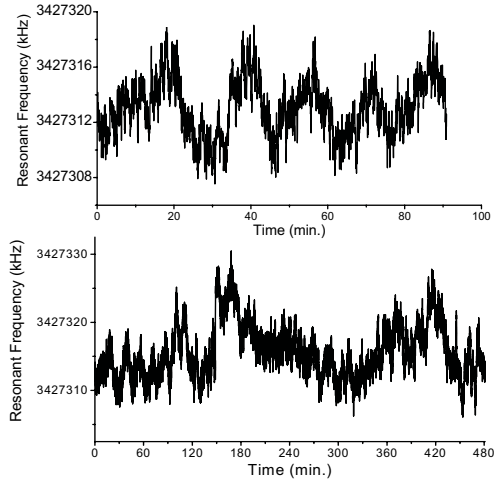

Figure 11 Measured short-term stability of the temperature compensated HBAR.

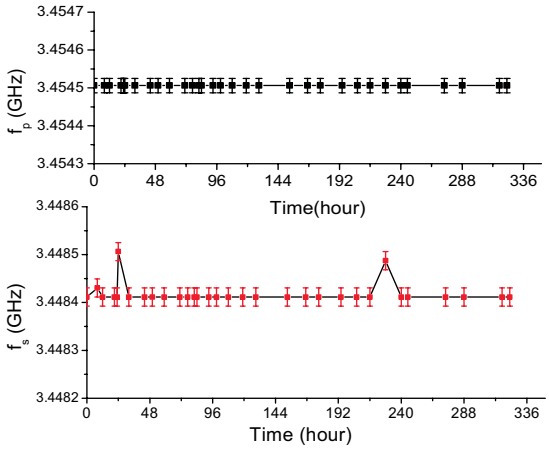

Figure 12 Measured long-term stability of the temperature compensated HBAR.

To test the long-term stability we place the HBAR on a printed circuit board (PCB), and connect it to the network analyzer through an SMA connector. The network analyzer applies a constant power of –3.8dBm to the HBAR to obtain the S_{11}. Though the HBARs used for the short-term and long-term stability tests are from the same wafer and have similar TCF parameters, their resonant frequencies are different. Figure 12 shows that the parallel resonant frequency remains constant (within the measurement error of 11ppm) over 330 hours, but the series resonant frequency varies about 33ppm over the same period of time. The reason for the fluctuation of the series resonant frequency is that there is a spurious resonance very near the series resonant frequency, which may have much higher TCF than the series resonant frequency.

CONCLUSION

In this paper we describe the experimental verification that using SiO_2 layer to compensate the HBAR's TCF is effective. A single HBAR supported on a SiO_2/Si/SiO_2 substrate/diaphragm (made on an SOI wafer) possesses a very low TCF and a high Q of about 800 and 545 at 3.4 GHz and 4.6GHz, respectively. Also the post-process tuning method is shown to be effective in meeting the frequency and TCF specifications without having to optimize the complicated thickness ratios for mass production. Therefore, using SiO_2 to compensate the HBAR's TCF is a very promising method to obtain a low TCF and high Q resonator at 3 - 5 GHz. Thus temperature-compensated HBAR is particularly suited for a voltage controlled oscillator for a local oscillator of a chip-scale atomic clock.

ACKNOWLEDGEMENT

This material is based on work supported by Defense Advanced Research Projects Agency (DARPA) under contract # N66001-02-1-8918.

REFERENCES

[1] T. W. Grudkowski, J. F. Black, T. M. Reeder, D. E. Cullen, and R. A. Wagner, "Fundamental-mode VHF/UHF minature acoustic resonators and filters on silicon," *Appl. Phys. Lett.,* vol. 37, pp. 993-995, 1980.

[2] K.M. Lakin and J.S. Wang, "Acoustic Wave bulk composite resonators," *Appl. Phys. Lett.,* vol. 38, pp. 125-127, 1981.

[3] K. Nakamura, H. Sasaki, and H. Shimizu, "ZnO/SiO2 diaphragm composite resonator on a silicon wafer," *Electron. Lett.,* vol. 17, pp. 507-509, 1981.

[4] J.T. Haynes, M. S. Buchalter, R. A. Moore, H. L. Salvo, S. G. Shepherd, B. R. McAvoy, " Stable Microwave Source Using High Overtone Bulk Resonators," Microwave Symposium Digest, MTT-S International Volume 85, Issue 1, June 1985, pp. 243 – 246

[5] H. Yu,W. Pang, H. Zhang, and E. S. Kim, "Film bulk acoustic resonator at 4.4 GHz with ultra low temperature coefficient of resonant frequency," IEEE International Micro Electro Mechanical Systems Conference, Miami, Florida, January 30 – February 3, 2005, pp. 28-31.

[6] S. P. Caldwell, M. M. Driscoll, S. D. Stansberry, D. S. Bailey and H. L. Salvo "High-overtone, bulk acoustic resonator frequency stability improvements" Frequency Control Symposium, 1993. 47th., Proceedings of the 1993 IEEE International 2-4 June 1993 pp.744 – 748

[7] S.L. Pinkett, W.D. Hunt, B.P. Barber, and P.L. Gammel, "Determination of ZnO temperature coefficients using thin film bulk acoustic wave resonators," IEEE Trans. Ultra. Ferro. and Freq., vol. 49, no. 11, pp. 1491-1496, 2004.

[8] Y. Yoshino, M. Takeuchi, K. Inoue, T. Makino, S. Arai and T. Hata, "Control of temperature coefficient of frequency in zinc oxide thin film bulk acoustic wave resonators at various frequency ranges." Vacuum (2002), 66(3-4), pp. 467-472

[9] R. Ruby and P. Merchant, "Micromachined Thin Film Bulk Acoustic Resonators," IEEE International Frequency Control Symposium, 1994, pp. 135-139

THERMAL AND MECHANICAL CHARACTERIZATION AND CALIBRATION OF HEATED MICROCANTILEVERS

Jungchul Lee, Thomas Beechem, Keunhan Park, Zhuomin Zhang, Samuel Graham, and William P. King
Woodruff School of Mechanical Engineering, Georiga Institute of Technology
Atlanta, GA USA

ABSTRACT

This paper reports the thermal and mechanical characterization and calibration of heated atomic force microscope (AFM) cantilevers. The cantilevers are characterized during steady-state, pulsed, and periodic heating. Using a laser Raman technique, it is possible to measure local temperature and temperature distribution in the silicon cantilever with a resolution of 1 °C and 1 μm while providing local surface stress measurements. This work provides improved understanding of thermal, electrical, and mechanical behaviors of silicon heated AFM cantilevers thereby enabling new applications for the device.

INTRODUCTION

Heated microcantilevers were originally developed for thermomechanical data storage **[1,2]** however these cantilevers are additionally useful for highly sensitive metrology **[3]**, nanometer-scale manufacturing **[4]**, and sensing heat flows < 1 nW. These applications beyond data storage demand strict requirements for device characterization and in particular temperature calibration well beyond what is required for data storage.

This paper reports advancements in characterization and calibration of these heated microcantilevers with temperature precision of 5 °C between room temperature and 800 °C, in both time domain and frequency domain operation from steady-state to > 1 MHz. For this research, we have developed a novel laser Raman technique that can simultaneously measure temperature and intrinsic stress in the cantilever with 1 μm resolution.

MICROFABRICATED CANTILEVERS

The silicon microcantilever-heaters were fabricated in our group at the Georgia Institute of Technology using a standard silicon-on-insulator process for cantilever fabrication. The fabrication processes were adopted from previously published reports on heated microcantilever fabrication **[1]** but modified to accommodate our microfabrication facility. The cantilever tip was formed using an oxidation sharpening process **[5]** and had a radius of curvature near 20 nm. The cantilever was made electrically active through two phosphorous doping steps: Two parallel cantilever legs and heater region near the free end were doped to $1x10^{20}$ and $1x10^{17}$ cm^{-3}, respectively. Therefore, the heater region was more highly resistive than the rest of the cantilever. Figure 1 shows scanning electron microscope (SEM) and infrared (IR) microscope images of a 'U' shape heated microcantilever, indicating atomically sharp tip, low intrinsic stress, and substantial heating only near the free end of the cantilever, respectively. The development of an all-silicon heated AFM cantilever was a significant advancement over previous work as silicon composed cantilevers having integrated heaters can reach higher temperatures, heat more quickly, and have reduced thermally-induced bending. However, detailed investigations showed that thermally-induced bending was not entirely suppressed.

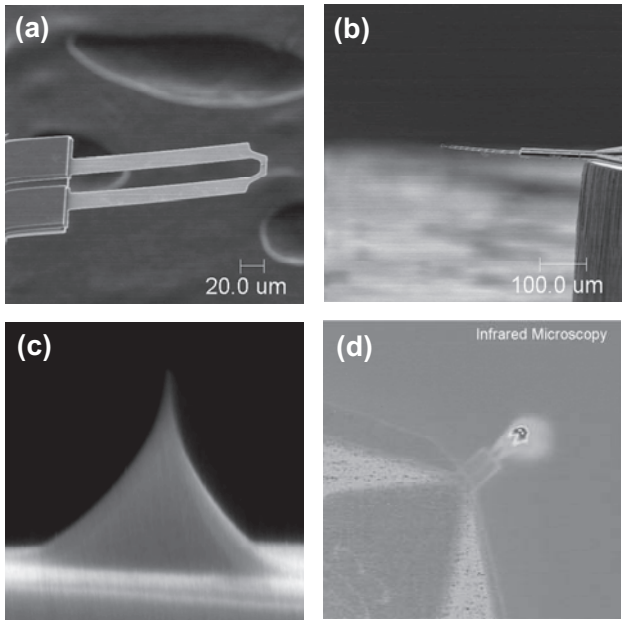

Figure 1. *(a)-(c) SEM images of a microcantilever heater, side view showing low intrinsic stress, and cantilever tip. (d) IR microscope image of the heater cantilever during steady electrical excitation. The IR image is approximately 0.5 mm square. The doped silicon cantilever is fabricated in a 'U' shape such that it forms a continuous electrical path. The region near the cantilever free end is a highly resistive heater and the legs have lower electrical resistance such that they carry electricity. The IR image confirms substantial heating near only the free end of the cantilever.*

For heated AFM cantilevers, the characterization of temperature and stress are important to assess the operational bounds of the device while ensuring reliability. In the operation of these devices, temperature measurements are often performed without regard for simultaneous stress evolution due to the difficulty in performing such measurements concurrently. In general, the measurement of temperature and stress in these devices is not trivial due to their size scale and the temperature range over which they operate.

ELECTRICAL CHARACTERIZATION

To characterize cantilever heating, the cantilever electrical response was examined with DC, square pulse, and AC excitation; shown in Figs. 2-4. In both DC mode (Fig. 2a,b) and during short pulses (Fig. 2c,d), the cantilever exhibits highly nonlinear temperature coefficient of electrical resistance (TCR) and thermal runaway **[6]** where the TCR changes from positive to negative. The nonlinear behavior coupled with the cantilever thermal time constant near 100 μs significantly complicates the cantilever AC response, which depends upon both frequency and excitation voltage (Fig. 3). Low frequency oscilloscope traces in Fig. 3a-c

show that the cantilever resistance is linear when the input voltage is low but becomes nonlinear as voltage is increased. All *I-V* curves intersect with the origin, indicating that the electric power is totally dissipated by Joule heating. In Fig. 3d, voltage and current traces are plotted for 5 V-rms and 1 MHz as an example of high frequency response. The most apparent difference from the low frequency region is the large phase difference between the voltage and current. This phase difference suggests that the impedance plays an important role in the cantilever electric response.

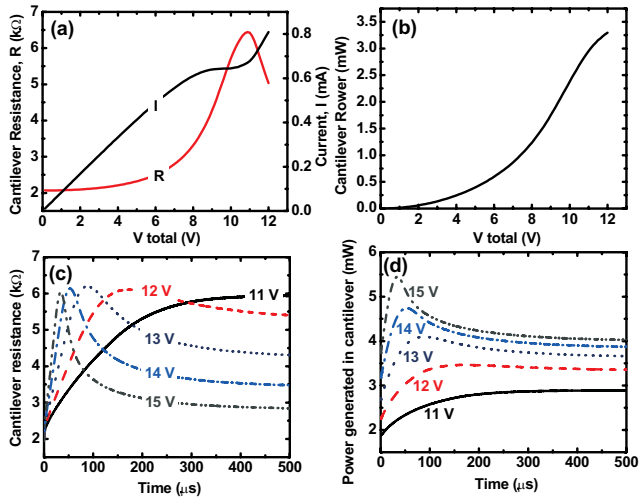

Figure 2. *DC response of a heated AFM cantilever as a function of excitation voltage: (a) cantilever resistance and current (b) cantilever power. Square pulse response as a function of time at five different voltage settings: (c) Cantilever resistance (d) cantilever power.*

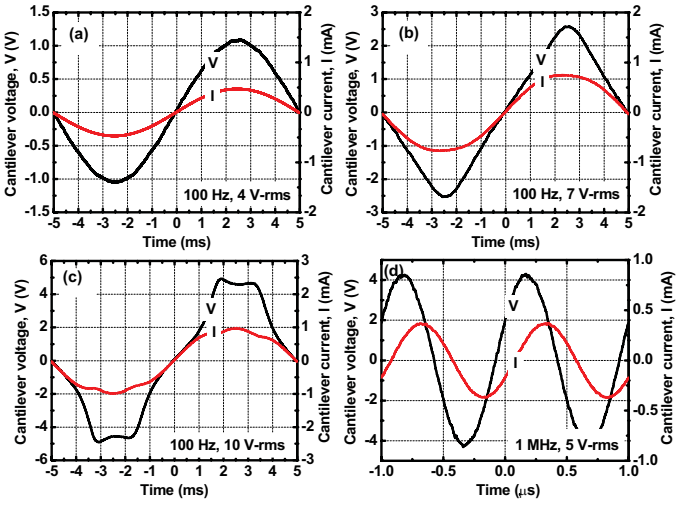

Figure 3. *AC response of a heated AFM cantilever as a function of time at (a) low frequency and low voltage: 100 Hz & 4 V-rms (b) low frequency and intermediate voltage: 100 Hz & 7 V-rms (c) low frequency and high voltage: 100 Hz & 10 V-rms (d) high frequency: 1MHz & 5 V-rms.*

Frequency domain characterization (Figs. 4,5) enables frequency modulated experiments which are desirable for measuring heat flows < 1 nW, as these experiments have increased signal to noise ratio and suppression of 1/f noise. When the heated

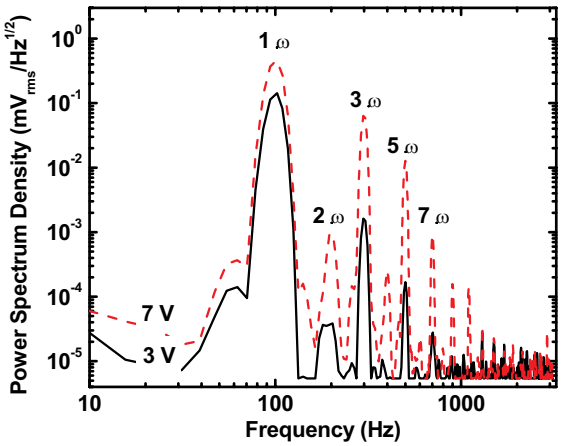

Figure 4. *Spectrum analysis compares the magnitude of high order harmonics at two AC excitation voltages where the driving frequency is 100 Hz. As excitation voltage increases, 3ω and 5ω components become significant such that they result in highly complex nonlinearity in the cantilever resistance.*

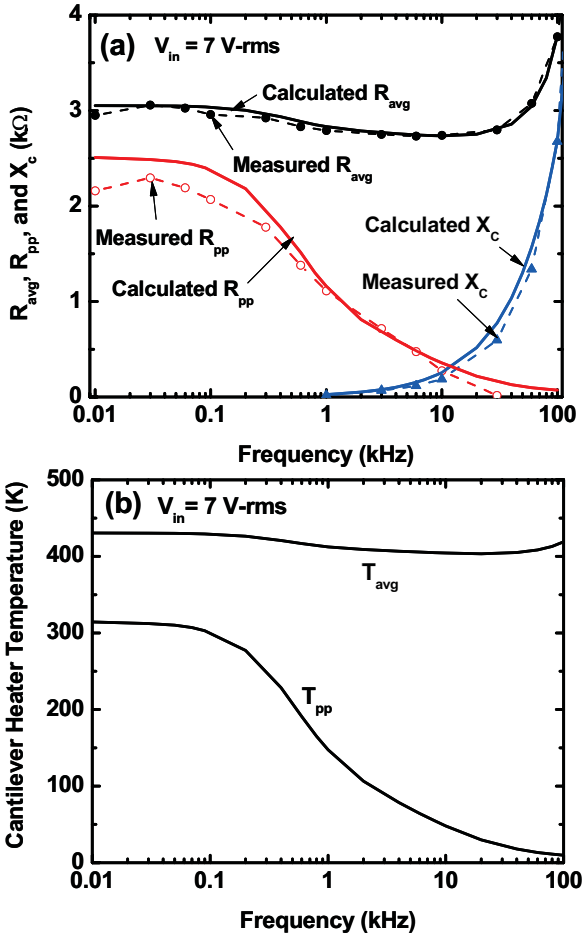

Figure 5*. Transient heat transfer simulation was performed and results are compared with experiments. (a) comparison of the cantilever impedances that are experimentally obtained and simulated when excitation voltage is 7 V-rms. R_{avg}, R_{pp}, and X_c are average resistance, peak-to-peak resistance, and reactance, respectively. (b) Calculated cantilever heater temperature for the same case as (a). T_{avg} and T_{pp} are average and peak-to-peak heater temperature, respectively.*

cantilever is operated with oscillatory electrical excitation having frequency ω, the power dissipation in the cantilever will oscillate at frequency 2ω and cantilever temperature/resistance will follow the power oscillation. The generated 2ω resistance will generate 3ω voltage oscillation in conjunction with 1ω current input and higher overtones will be cascaded in a similar fashion. Fig. 4 shows power spectrum density of the heated cantilever with 100 Hz AC excitation. As AC voltage increases, more high order overtones become detectable due to highly nonlinear cantilever resistance and thermal runaway. In general, the amplitude of these harmonic overtones increases with increasing driving voltage amplitude and decreasing driving frequency.

Combined measurements and 1D numerical modeling allow estimates of both steady and oscillatory heating in the cantilever (Fig. 5). Fig. 5a shows frequency-dependent cantilever resistance and reactance when the input voltage is fixed at 7 V-rms. The calculated values match well with the experimental data: only the simulated peak-to-peak resistance overestimates the measured data by 7.4% at low frequencies. This deviation could be attributed to an underestimate of the volumetric heat capacity of the cantilever or the variation of the effective heat transfer coefficient. The cantilever heater temperature in Fig. 5b shows a similar trend as the resistance. The peak-to-peak values of cantilever resistance and heater temperature maintain their magnitudes until around 100 Hz and then decrease to become negligibly small.

MECHANICAL CHARACTERIZATION

In AFM operation, the interaction between the cantilever tip and the underlying substrate is of great importance and requires precise knowledge of the mechanical properties such as spring constant and resonance frequency. For mechanical characterization, thermal noise spectrum of the heated cantilever was measured using an Asylum MFP-3D AFM. Resonance frequency and Q factor were directly obtained from the measured spectral noise density shown in Fig. 6. To convert

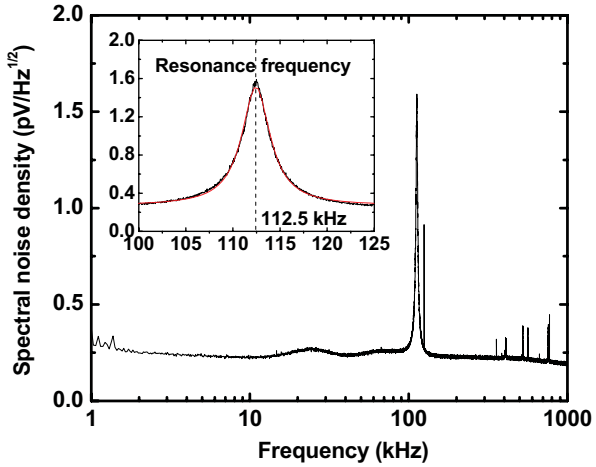

Figure 6. *Cantilever mechanical spectral noise density using thermal noise spectrum. The tested cantilever has a resonance frequency of 112.5 kHz as shown in the inset.*

a photodiode voltage into an actual displacement, the deflection sensitivity of the photodiode was obtained by taking a force-displacement curve on the AFM. By applying equipartition theorem **[7]** and deflection sensitivity, the spring constant of the cantilever was extracted.

Finite element analysis (FEA) was performed to compare measured mechanical properties with simulation and to investigate high order vibration modes as well. FEMLAB^{TM} eigen-frequency analysis was used herein. The simulated resonance frequency was 109.2 kHz and showed good agreement with the measurement. FEA results also show several fundamental vibration modes of the 'U'-shaped heated cantilever. High order vibration modes correspond to higher frequency resonance peaks in the thermal noise spectrum (Fig. 6). However, simulated 2nd and 3rd resonant modes were not observed considerably in the thermal noise spectrum partly due to the low sensitivity of photodiode.

Raman spectroscopy is an optical measurement technique well suited for the temperature and stress measurements in microelectromechanical systems (MEMS) devices, especially those made from silicon due to its strong scattering cross-section **[8]**. Raman Spectroscopy measures the inelastic scattering of light from materials which results from changes in the polarizability of the atoms. Thus, any effect which may change the lattice spacing and polarizability of nonmetallic solids will result in changes in the Raman signature. Raman scattering has been used to determine temperature distribution with micron spatial resolution in crystalline and polycrystalline nonmetallic materials.

Based on our calibration experiments, the position of the Raman Stokes peak is sensitive to both temperature and stress but the line width (FWHM) of the Stokes peak only depends upon the temperature. Differences between the temperatures calculated by the Stokes peak position and line width method should then reveal the effect of stress in devices. Therefore, an analysis of the Stokes spectra will allow the simultaneous determination of temperature and stress.

A novel Raman spectroscopy technique measured local temperature (Fig. 7) and stress (Fig. 8) in a backscattering mode on either side of the cantilever utilizing a specially designed stage that ensured similar conditions for measurements on either side. The cantilever temperature decays roughly exponentially from the tip to the base, indicating a significant amount of heat dissipation into the nearby gas. In addition, the temperature gradient also increases as the excitation voltage increases. The low doped heater shows more significant increases in both temperature and temperature gradient compared to the highly doped legs.

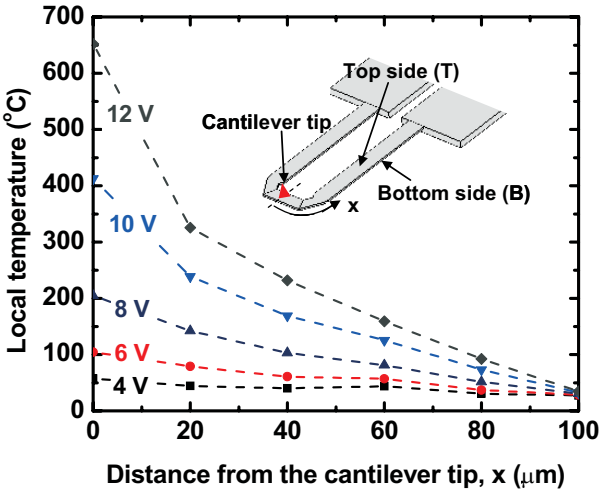

Figure 7. *Local temperatures at various locations are measured using Raman spectroscopy. The temperature distribution decays roughly exponentially from the tip to the base, indicating a significant amount of heat dissipation into the nearby gas.*

Figure 8 shows that stress diverges on either side of the cantilever, having elevated stress with increasing temperature on the bottom side and corresponding reduction on the top side. These results confirm that the heated cantilever experiences thermally induced bending which may be caused as a result of the top side doping process. These findings regarding temperature and stress significantly improve upon previously published assumptions regarding the heated cantilever that neglect thermally induced stress and corresponding deflection.

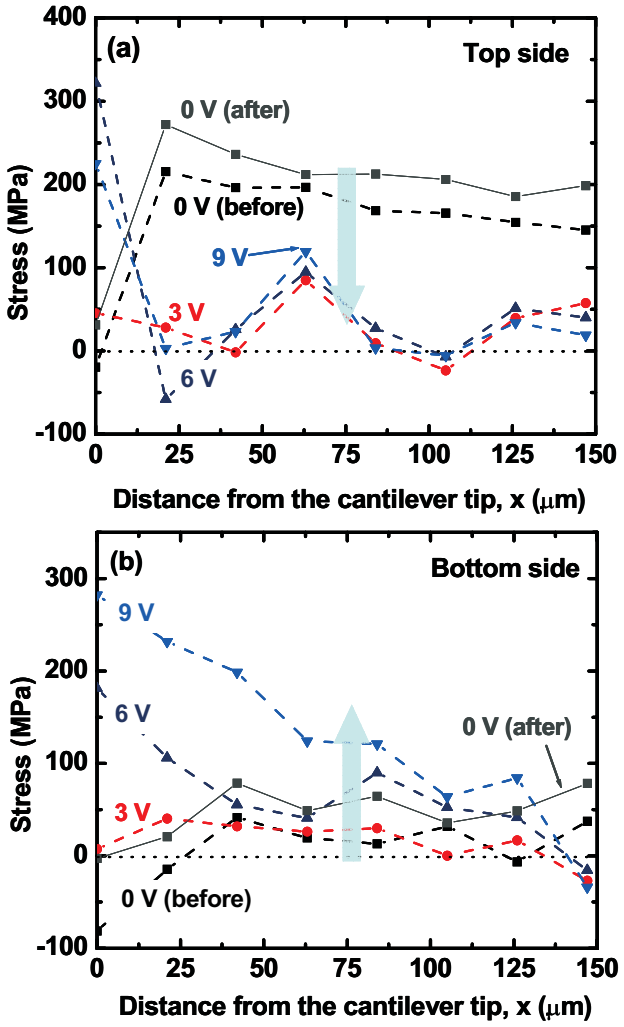

Figure 8. *Measured stresses of the heated cantilever using Raman spectroscopy on top and bottom sides. As cantilever power or temperature increases, stress of top side tends to decrease but stress of bottom side seems to increase. The arrows represent changes in stress level as temperature increases. The heated cantilever experiences bending due to nonuniform heating and intrinsic stress. Data near the tip show no trend due to its complex loading state.*

CONCLUSIONS

This paper reports advancements in the characterization and calibration of heated microcantilevers. These measurements help elucidate complex temperature-dependent electrical characteristics of the heated cantilever and suggest how to operate them with DC, pulse, and AC excitation. This first report of frequency-domain operation of heated microcantilevers opens new opportunities for cantilever sensors.

Using Raman spectroscopy, localized temperature and stress are simultaneously examined with μm resolution. Precise temperature calibration was performed with improved precision by >10× over previous reports and can extend the use of the heated cantilever beyond data storage. Thermally induced stresses were qualitatively examined from differences in temperature measured by Stokes peak position and line width methods. Mechanical characterization was performed using thermal noise spectrum and mechanical properties such as resonance frequency, Q factor, and spring constant were examined.

This work facilitates new applications of the heated cantilever such as micro/nano calorimeter, mass detection, and nanolithography while a novel laser Raman technique exploited in this work improves design and characterization for other thermal MEMS devices as well.

REFERENCES

[1] B.W. Chui, T.D. Stowe, Y.S. Ju, K.E. Goodson, T.W. Kenny, H.J. Mamin, B.D. Terris, and R.P. Ried, "Low-stiffness silicon cantilever with integrated heaters and piezoresistive sensors for high-density data storage," *Journal of Microelectromechanical Systems*, 7, (2002), pp. 69-78.

[2] W.P. King, T.W. Kenny, K.E. Goodson, M. Despont, U. Duerig, M. Lantz, H. Rothuizen, G. Binnig, and P. Vettiger, "Microcantilevers for thermal nanoimaging and thermomechanical surface modification," *Technical Digest of the 2002 Solid-State Sensor and Actuator Workshop*, Hilton Head, SC (2002).

[3] W.P. King, T.W. Kenny, and K.E. Goodson, "Comparison of thermal and piezoresistive sensing approaches for atomic force microscopy topography measurements," *Applied Physics Letters*, 85, (2004), pp. 2086-2088.

[4] P.E. Sheehan, L.J. Whitman, W.P. King, and B.A. Nelson, "Nanoscale deposition of solid inks via thermal dip pen nanolithography," *Applied Physics Letters*, 85, (2004), pp. 1589-1591.

[5] T. S. Ravi, R. B. Marcus, and D. Liu, "Oxidation sharpening of silicon tips," *Journal of Vacuum Science & Technology, B*, 9, (1991), pp. 2733-2737.

[6] B. W. Chui, M. Asheghi, Y. S. Ju, K. E. Goodson, T. W. Kenny, and H. J. Mamin, "Intrinsic-carrier thermal runaway in silicon microcantilevers," *Microscale Thermophysical Engineering*, 3, (1999), pp. 217-228.

[7] J. L. Hutter and J. Bechhoefer, "Calibration of atomic-force microscope tips," *Review of Scientific Instruments*, 64, (1993), pp. 1869-1873.

[8] M. R. Abel, T. L. Wright, W. P. King, and S. Graham, "Thermal metrology of silicon micro-structures using Raman spectroscopy," *IEEE Transactions Component & Packaging Techchnology*, to be published.

WIDE DYNAMIC RANGE MICROELECTROMECHANICAL VISCOSITY SENSOR

Robert L. Borwick III, Philip A. Stupar, and Jeffrey F. DeNatale
Rockwell Scientific Company
Thousand Oaks, CA, USA

ABSTRACT

A novel MEMS device has been designed to directly measure the viscosity of a fluid. The device, which incorporates both actuation and position sensing, is submerged in a fluid and measures the resistance to motion due to the viscous drag forces of the fluid. When this device is operated in the intended over-damped ($\xi >>1$) regime, it has a response time that is linear with viscosity. Using our design, a single device is capable of measuring viscosity from 0.5cP to over 1000cP while maintaining a highly linear response. This same device also has good sensitivity; it can to detect viscosity changes on the order of ±0.5%.

INTRODUCTION

MicroElectromechanical (MEM) devices offer numerous advantages in the field of sensors. Their mechanical operation is inherently suited to the measurement of physical properties. Their compact size and portability can enable in-situ monitoring in both laboratory and field environments, providing valuable real-time information on system environment and health. One application that effectively exploits these benefits is a MEMS-based viscosity sensor **[1-3]**.

The ability to accurately and efficiently assess the health and remaining useful life of lubricating fluids represents a critical element in implementing optimal condition based maintenance of machinery. Chemical and physical properties such as total acid number (TAN), pH, water concentration, anti-oxidant concentration, particle size, and viscosity are among some of the properties used to evaluate the remaining useful life of lubricating fluids. Considerable effort over the years has been put into the development of chemical diagnostics for lubricating fluids, although sensors to provide a direct measure of fluid viscosity are less well developed. This paper presents the design, fabrication and experimental results of a MEMS viscosity sensor with high measurement linearity and wide dynamic range.

THEORY OF OPERATION

The sensor operates submerged in a fluid and senses the resistance to actuation due to the viscous drag forces of the fluid. The device is actuated and the time response of motion measured to directly determine the viscosity. We have designed the device to be over-damped when actuated in fluids of interest. Solving the equation of motion for an over-damped system **[4]**, and assuming that we are sufficiently over-damped, the position as a function of time is given by:

$$x(t) = x(o)e^{((\zeta^2-1)^{1/2}-\zeta)\omega_n t} \qquad (1)$$

where t is time, ζ is the damping coefficient, and ω_n is the resonant frequency. This expression defines the final resting position as zero and the initial position as $x(0)$. If we define the response time as the time required to move a constant percentage of the initial displacement, we can divide equation 1 by the initial displacement and solve for the response time:

$$t = C((\zeta^2 - 1)^{1/2} + \zeta) \qquad (2)$$

Where C is a constant that is a function of the displacement percentage and resonant frequency of the device. When this device is operated in the intended over-damped ($\zeta >>1$) regime, the response time reduces to $t=2C\zeta$ and is linear with the damping coefficient ζ.

Additionally, the device has been designed to place a predominantly shear force on the fluid, and minimize the contributions of compressive interactions. Inter-digitated comb fingers on the device provide the shear on the fluid (fig. 1). Because the spacing between the comb fingers is small compared to the height and length, we can assume a linear velocity distribution in the liquid between the comb fingers, and therefore, the damping coefficient will be linearly proportional to the absolute viscosity of the fluid. These comb fingers are also used to capacitively measure the time response of the device motion.

All the measurements presented here were made on Newtonian fluids. However, this device is capable of measuring the viscosity of non-Newtonian fluids at different shear rates. Because the response time is not a function of total displacement, only the percentage of the initial displacement, different shear rates can be applied by changing the initial displacement. Therefore, we can measure the shear rate dependence of the viscosity of non-Newtonian fluids.

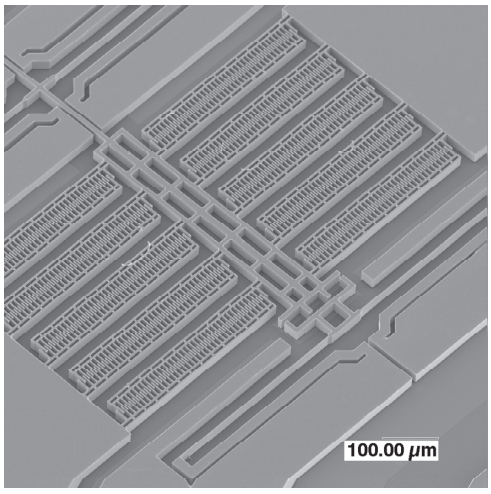

Figure 1. *Micrograph of MEMS viscosity sensor. The comb fingers are long relative to their displacement to minimize fluid compression.*

DESIGN AND FABRICATION

We have designed and fabricated two device types that are over-damped in a fluid that has a viscosity greater that 0.5cp. Each device has an actuator and a capacitor for position sensing. These

components are electrically isolated, but mechanically coupled using a SiO_2 bridge. The primary difference between two device designs is the actuator. The two actuation methods that were explored offer distinct trade-offs in device operation. The actuation methods utilize a Lorentz force or an electrostatic force.

The Lorentz-force actuator utilizes the passing of a current, in the presence of a permanent magnetic field. For the present experiments, these are nominally 10mA and 0.2 T, respectively. This actuation method has the advantage of supplying a force that is independent of the dielectric properties of the fluid in which the viscosity sensor is submerged. This is a distinct advantage over an electrostatic drive, since the force applied will not change when measuring fluids with different dielectric constants nor will polar fluids affect it. However, having a permanent magnet in the package may be undesirable. Since many of the systems that would benefit from continuous monitoring of the viscosity have motors, there may be an abundance of ferrous particulates that would be attracted to the permanent magnet and may clog the sensor. However, utilizing a filter or device lid with a second permanent magnet to preferentially attract any ferrous particulates could mitigate this problem.

Electrostatic-force actuation does not require a permanent magnet to be present in the package, and a force comparable to the Lorentz force actuator is obtained with DC voltages on the order of 10 volts in a fluid with a dielectric constant of 2. Simply adjusting the drive voltage can compensate for the issue of measuring multiple fluids with dramatically different dielectric constants. Because the response time is independent of the total displacement, small changes in the actuation force do not affect the device performance. However, the actuation voltage would need to be adjusted for a large dielectric change to ensure that the actuator does not hit the built in mechanical stops. Solving the issue of operation in polar fluids is more difficult and requires more complexity in the actuation method. By using an AC drive voltage that is faster than the response time of the polar fluid it is possible to use electrostatic actuation to measure viscosities of polar fluids **[5]**.

The final required component of the device is the ability to sense position with respect to time. When a force is applied to the device, the position of the differential comb capacitor is measured using a commercially available capacitive sensing ASIC. This chip uses a 100kHz clock frequency to measure capacitance. This frequency has proven to be high enough to measure viscosities of polar fluids, including alcohols such as isopropanol. The inter-digitated comb fingers used to capacitively measure the time response of the device motion also provide the shear on the fluid.

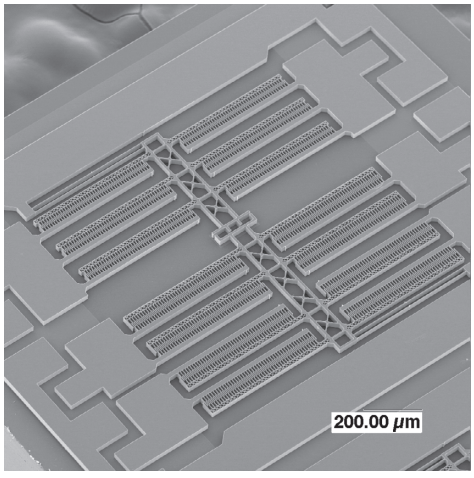

Figure 2. *Micrograph of the electrostatic MEMS viscosity sensor.*

The device is fabricated using the Rockwell Scientific aMEMS process **[6]**, an SOI device layer transfer process. It consists of a 20µm silicon device layer that is patterned using DRIE to create the capacitive sensing comb structures and the device suspension. For the Lorentz-force actuator (fig. 1), the suspension doubles as the current carrying beam creating a force that results in a lateral deflection of the suspension. Coupled differential comb finger banks are used to create the capacitance change. In the case of the electrostatic actuator (fig. 2), the suspension provides a path to charge one half of the capacitor banks, while the other half is used for sensing the capacitance change. Here again the DRIE is used to form the drive capacitor bank.

EXPERIMENT AND RESULTS

Using both the Lorentz-force and electrostatic actuated devices, several measurements have been made. The majority of the results presented here will focus on the Lorentz-force actuator, however the functionality and linearity of the electrostatic drive has been verified. The following experimental results show the response time versus viscosity performance, the broad sensing range with excellent linearity, the device resolution and sensitivity, and finally a demonstration of the ability to distinguish fresh lubricant from degraded lubricant.

Before the sensors were tested, each one was affixed to a 12-pin package with an inner cavity of 3.8mm x 4.8mm and depth of 1.3mm. The actuator and sense capacitors were wire bonded, and the package was then mounted to a test board (fig. 3). The test board is shaped like a T to accommodate the signal I/Os and the capacitive sensing ASIC at one end, and the viscosity sensor at the opposing end. This configuration allows for a single drop of fluid to be placed in the package for testing, as well as completely submerging the sensor end of the board in a beaker of fluid. The single drop volume required to make a measurement is on the order of 20µL. When the test board is submerged in a beaker of lubricant, a stir bar is used to circulate the fluid. The fluid flow in the beaker appears to have no measurable affect on the response time.

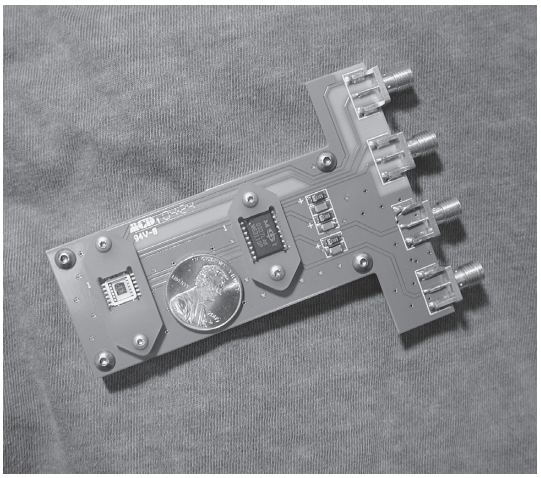

Figure 3. *MEMS viscosity sensor mounted to a test board with capacitive sensing ASIC.*

Calibrated viscosity standards were used to evaluate the viscosity sensor. These standards are silicone based and were chosen to have a range from 5 to 500cp. Once a calibration factor was obtained from the viscosity standards, additional laboratory fluids were tested. These fluids included alcohols, such as

propanol, octanol and decanol and alkanes such as heptane. Heptane was also used to clean the sensor in between tests. The silicone based viscosity standards are soluble in heptane and were easily removed by a light rinse. Once a device was cleaned it could be placed in a new fluid. There were no stiction problems observed if the device dried out completely. The only issue noted was that high viscosity fluids would take a little longer to re-wet a dry device. Re-wetting with heptane prior to a new measurement alleviates this issue.

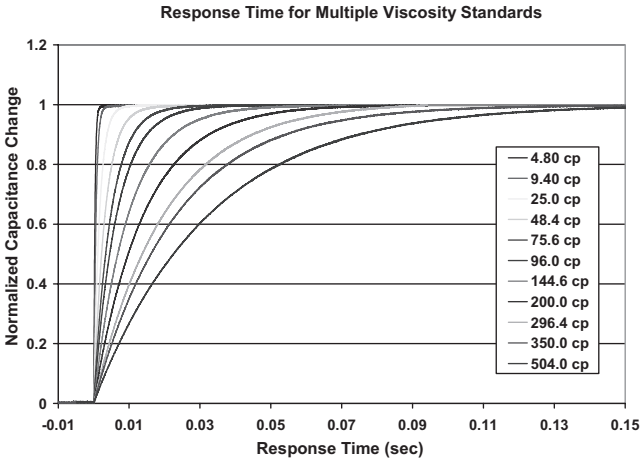

Figure 4. *Response time traces for multiple calibrated viscosity standards.*

By measuring the capacitance versus time for a step input current, the response time of the device, defined as the time required to move from 10% to 90% of the resting location, can be determined. As the viscosity of the fluid increases, the response time of the device also increases (fig. 4). The lower viscosity fluids (0.5cp) had a response time of less than one millisecond while the higher viscosity fluids (1000cp) required up to 200ms. The response time is related to the resonant frequency of the device and can be adjusted to suit the particular viscosity range that is being measured. A device designed to monitor a lubricant over a smaller viscosity range can be designed to have a sub millisecond response time, thereby allowing over 1000 measurements a second to be taken and averaged for noise reduction. Plotting the measured response time versus the viscosity of the fluid shows the highly linear response of the device over a wide range of viscosities spanning greater than three orders of magnitude (fig. 5). Resonant type viscosity sensors tend to have a limited linear range, and cannot resolve high viscosity fluids because the under-damped condition no longer holds **[1]**. Using our design, a single device is capable of measuring viscosity from 0.5cP to over 1000cP while maintaining a highly linear response.

The viscosity sensor also has good sensitivity, being able to detect viscosity changes on the order of 2%. To test the sensitivity of the device, viscosity standards were mixed together to produce four solutions with 1% increments in viscosity (93-96cp). Multiple measurements were made in each of the four solutions (fig. 6). As shown, only one measurement point intersected with a neighboring viscosity measurement and viscosity changes of 2% are easily resolvable. This performance is comparable to large, rotary style viscometers such as those available from Brookfield Engineering **[7]**.

After establishing the device linearity and resolution, a continuous measurement of viscosity was made to acquire repeatability and short-term reliability data. An overnight test in Castrol 5050 was conducted, and a change of approximately 5% was observed. This change was a larger than expected and did not appear to be random. We speculated that the change may have been temperature related, and remade the measurement over a 19 hour period while simultaneously observing the temperature of the fluid. The results of this experiment are seen in figure 7. The observed drift in viscosity was not due to sensor error, but was correlated with temperature changes of the fluid due to small variations in ambient temperature. For less than a 2 degree centigrade change, the fluid had a 5% viscosity change.

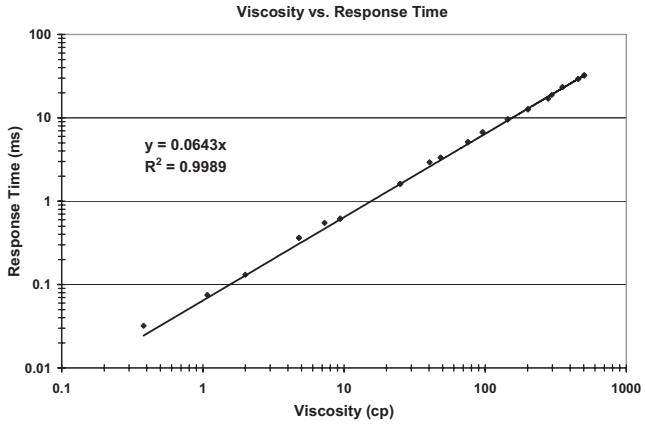

Figure 5. *Viscosities of known fluids and viscosity standards plotted against measured response times.*

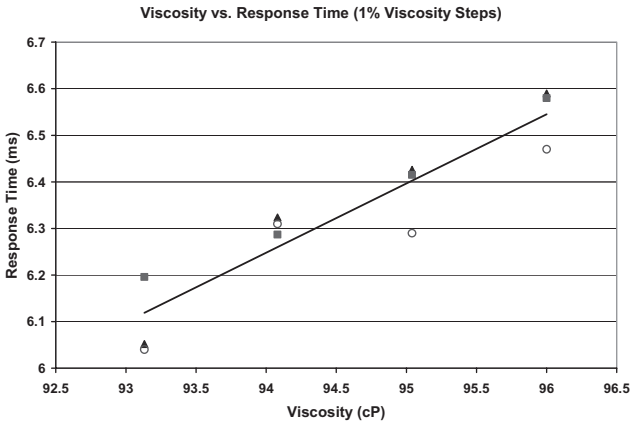

Figure 6. *Three measurements made at 1% viscosity change intervals, showing the resolution is on the order of 2%.*

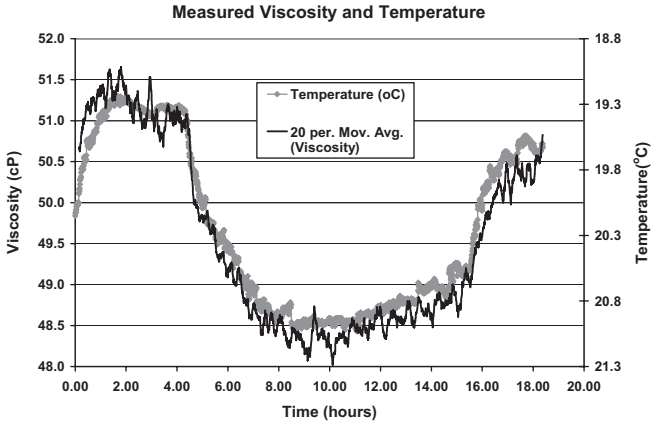

Figure 7. *Viscosity and Temperature overnight monitoring.*

This change is consistent with the measured viscosity temperature dependence for the oil, which is approximately 2% per degree Celsius at 20°C. This data indicates that the sensitivity of the device is better than the measured 2% for controlled temperature conditions, with values of ±0.5% more representative.

Viscosity is a very important parameter used in the evaluation of lubricating fluids. As a lubricant degrades during operation, the viscosity monotonically increases. In order for the MEMS viscosity sensor to be viable for evaluation of degraded lubricants, it must be sensitive enough to distinguish between the viscosity of a fresh and degraded sample. To test this, a sample of Castrol 5050 was thermally degraded on a hot plate set at 250°C for 4 hours. The viscosity of both the fresh sample and the thermally degraded sample was then tested using the same device. As shown in figure 8, the device is sensitive enough to easily resolve the viscosity change associated with thermally degraded oil. During our experiment, the viscosity of the thermally degraded oil increased by approximately 10%. Oil that degrades during machine use would likely have a larger viscosity change. Previous work has shown that the viscosity of automobile engine oil increases by approximately 40% as it degrades over useful life **[8]**.

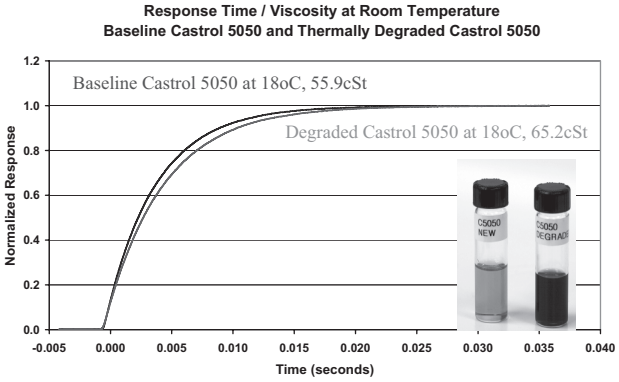

Figure 8. *Response times for fresh oil and thermally degraded oil.*

Most of the experiments described here were performed using fresh, clean samples with no particulates. Although the device does have moving parts with small clearances (2μm), the sensor has proven to be relatively immune to most contaminants. Many experiments in degraded oils saturated with visible particulates have been unaffected by the contaminants. However, we have seen occasional device failures when small particulates on the order of the size of the comb finger spacing have become stuck between comb teeth. Sensors deployed in dirty environments will likely need to either be placed near the in line filter or packaged with lids with integrated filters. Mesh screens with small openings (~1um) and large open area (~50%) are commercially available.

CONCLUSIONS

A MEMS viscosity sensor was designed and fabricated. The measured performance of this device indicates that it is capable of measuring a very wide range of viscosities (>1000x) with a single device. In addition, the excellent linearity and sensitivity of the device shows that it performs comparable to large scale, commercially available viscometers. A viscosity sensor of this type facilitates real time, in-situ viscosity measurements. This is essential for applications such as lubrication health monitoring for condition-based maintenance of motorized vehicles, automation equipment, and other rotary equipment. Due to its small size (2 x 2mm) and limited fluid sampling requirement (20μL), the device can easily be mounted inside a lubrication reservoir of any piece of equipment to monitor viscosity degradation during operation.

Future work will concentrate on characterizing the temperature performance and reliability of the device. Many of the in-situ applications would require the device to operate at elevated temperatures up to 150°C. Although the preliminary data looks promising, long-term reliability data needs to be collected to fully characterize the device. In addition, the effects of particulate contamination will be characterized, along with mitigation techniques such as using in line filters and adjusting the comb finger spacing.

ACKNOWLEDGEMENTS

This research was sponsored by Rockwell Automation. The authors thank Fred Discenzo of Rockwell Automation for his technical support on this program. Additionally, the authors thank Martin Kendig for insightful conversations regarding lubricant health monitoring. Finally, the authors thank Kathleen Garrett for all her support in fabrication of the viscosity sensors.

REFERENCES

[1] O. Brand, J M. English, S. A. Bidstrup, M. G. Allen, "Micromachined Viscosity Sensor for Real-Time Polymerization Monitoring", *Technical Digest of the 1997 International Conference on Solid-State Sensors and Actuators*, Chicago, IL, June 16-19, (1997), pp. 121-124.

[2] M. K. Jain, C. A. Grimes, "Effect of Surface Roughness on Liquid Property Measurements Using Mechanically Oscillating Sensors", Sensors and Actuators A, 100, (2002), pp. 63-69.

[3] B. Jakoby, M. Scherer, M. Buskies, H. Eisenschmid, "Microacoustic Viscosity Sensor for Automotive Applications", *Technical Digest of the 2002 IEEE International Conference on Sensors*, Orlando, FL, June 12-14, (2002), pp. 1587-1590.

[4] L. Meirovitch, "Principles and Techniques of Vibrations", Prentice-Hall, Inc., Upper Saddle River, New Jersey, NJ, (1997), pp. 110.

[5] T. L. Sounart, T. A. Michalske, K. R. Zavadil, "Frequency-Dependent Electrostatic Actuation in Microfluidic MEMS", Journal of Microelectromechanical Systems, 14, 1, (2005), pp. 125-133.

[6] R. Borwick, P. Stupar, J. DeNatale, R. Anderson, C. Tsai, K. Garrett, R. Erlandson, "A High Q, Large Tuning Range MEMS Capacitor for RF Filter Systems", Sensors and Actuators A, 103, (2003), p. 33.

[7] www.brookfieldengineering.com

[8] A. Basu, A. Berndorfer, C. Buelna, J. Campbell, K. Ismail, Y. Lin, L. Rodriguez, S. Wang, "Smart Sensing of Oil Degradation and Oil Level Measurements in Gasoline Engines", Technical Digest of SAE 2000 World Congress, Detroit, MI, March 6-9, (2000), pp. 1-7.

WIREBONDER ASSEMBLY OF HINGELESS 90° OUT-OF-PLANE MICROSTRUCTURES

S. H. Tsang, D. Sameoto, I. Foulds, A.M. Leung, M. Parameswaran,
Institute of Micromachine and Microfabrication Research
School of Engineering Science
Simon Fraser University
Burnaby, BC, CANADA, V5A 1S6

ABSTRACT

A novel design and analysis for the assembly of 90° out-of-plane microstructures using a standard microelectronics wirebonder is presented. The microstructures can be assembled by a single point actuation and use a selectively compliant spring system that converts an in-plane motion to an out-of-plane rotation. The single point actuation can be provided by a standard microelectronics wirebonder. A wirebonder is a common piece of equipment for microelectronics packaging and therefore the assembly method described here introduces a practical and economical approach. The microstructure designs were fabricated using either PolyMUMPs or a prototyping process developed at Simon Fraser University that uses SU-8 as a structural layer. The designs were modeled using the Finite Element Analysis (FEA) software ANSYS, and tested for positional repeatability and reliability verifying the proof of concept.

INTRODUCTION

Out-of-plane components have numerous applications for on-chip optics [1] and RF systems [2]. These components must be fabricated in-plane and assembled afterwards to achieve out-of-plane orientation. The current methods for assembly can be integrated on-chip using electrostatic [3] or thermal actuators [4] to produce the motions necessary for assembly, but these actuators require a large sacrifice of chip area. External systems, such as robotic pick-and-place [5] are also currently in use but require a significant investment in specialized equipment. More recently, there has been development in thermal kinetic assembly [6] and centripetal assembly [7] of micro devices, but both methods require the use of hinges to allow the structures to rotate out-of-plane. Because the creation of hinges requires the use of multiple structural layers, hinges cannot be used when processes are limited to a single structural layer. Furthermore, hinges are susceptible to friction and mechanical jamming, which reduces the yield of assembled structures. Other assembly methods proposed employ the surface tension of solder-ball reflow [8] or residual stress mismatch between epitaxial layers [9] to lift and assemble micromachined flaps. However, these systems require special processing to accomplish the required reflow or materials incompatible with standard integrated circuits to achieve enough stress mismatches to make these systems viable for system integration.

We present a design for a novel method of assembling hingeless 90° out-of-plane microstructures using a single lateral push provided by a wirebonder tip. The out-of-plane rotation is accomplished by constraining the lateral displacement of the microstructure using a serpentine spring such that the lateral motion causes the microstructure to flip upwards into a 90° out-of-plane orientation. Once assembled, the devices are held in place by frictional force [10], which is further increased by the downward restoring force of the serpentine springs.

THEORY

Out-of-plane rotation can be accomplished by constraining the lateral displacement of the microstructure with a spring such that a lateral push will cause the microstructure to flip upwards 90° out-of-plane. The intermediate steps and force balancing that causes the rotation is shown in Figure 1. The lateral assembly force combined with the restoring force of the springs produces a torque out-of-plane when the base of the microstructure contacts the substrate (Figure 1B). As the bottom lip slides forward, the rotational torque increases until the structure becomes upright.

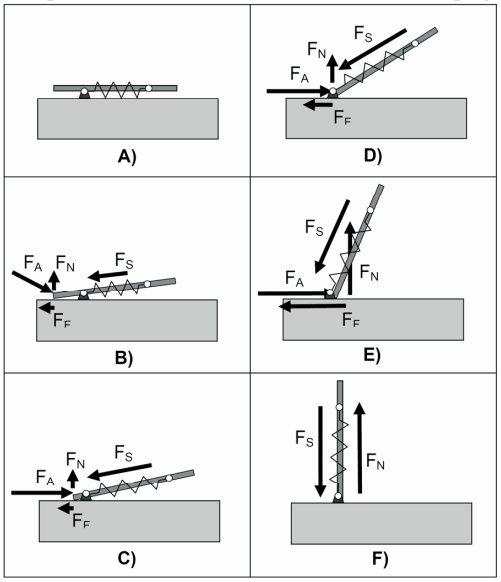

Figure 1. *Sequence A-F shows the force diagram for the concept of assembling hingeless microstructures to 90° out-of-plane, using a single lateral push. F_A denotes assembly force, F_S denotes the restoring force of the spring, F_N denotes the normal force and F_F denotes the frictional force.*

Once assembled, any lateral perturbations must overcome the force of friction and the restoring force of the spring in order to dislodge the upright structure. The assembled position of the structure is a state of local stability allowing the structure to remain assembled after the assembly force is removed.

Designs have been fabricated using the commercially available PolyMUMPs [11] process as well as an SU-8 prototyping process developed at Simon Fraser University [12]. One PolyMUMPs design that was fabricated, assembled and simulated is shown in Figures 2 through 4.

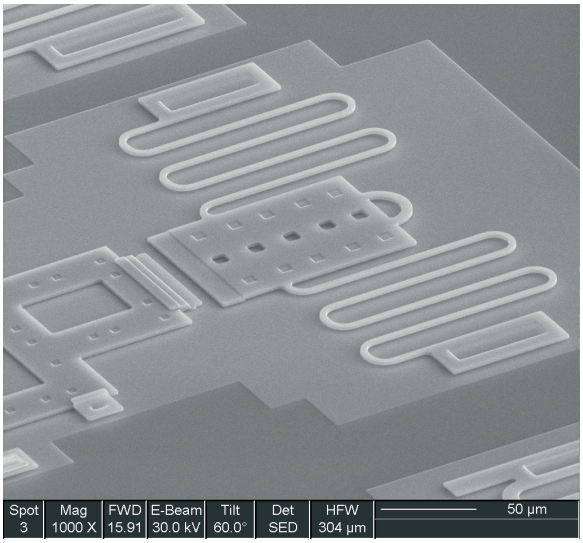

Figure 2. *Scanning electron micrograph of an out-of-plane microstructure fabricated in PolyMUMPs. The serpentine springs are 130µm in length, with a 1:2 (height to width) aspect ratio.*

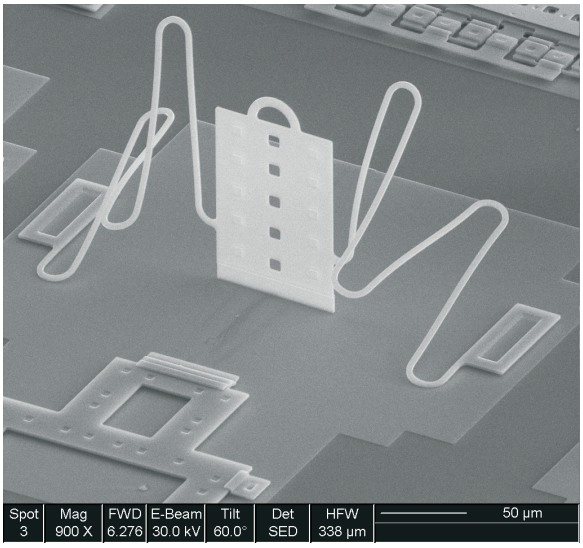

Figure 3. *Scanning electron micrograph of the 90° hingeless out-of-plane microstructure shown in Figure 2 assembled out-of-plane.*

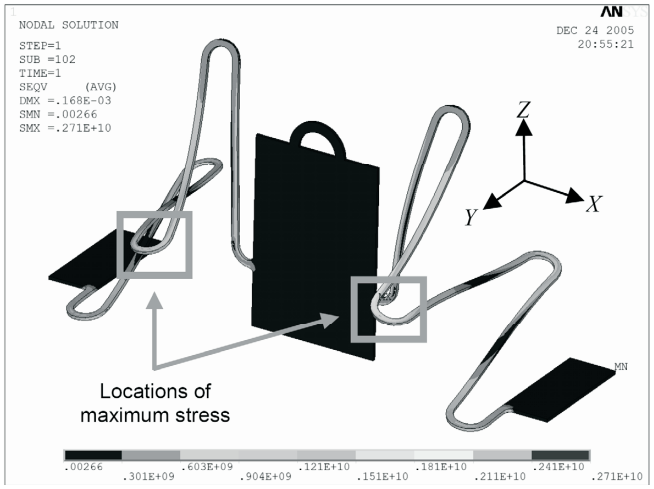

Figure 4. *Finite element solution of the 90° hingeless out-of-plane microstructure fabricated using the PolyMUMPs process*

DEVICE MODELING

The bending of the spring system is heavily non-linear, therefore, finite element models were necessary to solve for the spring deflection and stress concentrations. Using Young's modulus (158 GPa) and Poisson's ratio (0.22) for PolyMUMPs, the assembled model is generated and shown in Figure 4. The boxed off areas of Figure 4 indicate the locations of maximum stress which is also indicative of the expected location of structural failure. Furthermore, the model determined that the restoring force of the spring produces a downward (-*Z* direction) component of 0.159mN and a lateral (-*Y* direction) component of 0.366µN at the bottom lip of the assembled device where contact with the substrate occurs. Because the force of gravity can be neglected for micro-scale devices, the resultant frictional force is given by

$$F_f = \mu F_N = \mu F_{Z_{Spring}}, \qquad \text{Eq. 1}$$

and using a value of 4.9 for μ (static coefficient of polysilicon on polysilicon)[10], a maximum frictional force of 0.779mN is generated at the base of the structure. The force of friction is three orders of magnitude greater than the restoring lateral force and allows the structure to remain assembled in place. Furthermore, because of the strong force of friction, and the downward restoring force of the spring the assembled structures are highly resistant to shock. The amount of shock that the assembled structure can survive without collapsing can be derived by examining the maximum acceleration required to dislodge the bottom lip of the assembled device. The assembled structure is most vulnerable to shock in the *Z*-direction since reducing the Z force component by F_{Shock} reduces the frictional force by $4.9 \times F_{Shock}$. To solve for the shock force that causes the assembled structure to collapse, we use the following equation:

$$F_{Shock} = ma = F_Z = \rho V a, \qquad \text{Eq. 2}$$

where ρ is the density of silicon (2.33×10^3 Kg/m^3), and *V*, the volume of the device (3.66×10^{-14} m^3). Therefore, solving for the maximum acceleration, gives a value of 2.63×10^6 m/s^2 which is equivalent to exposing the structure to approximately 270,000 Gs. As illustrated by the device model, the structures are highly resistant to shock and will remain assembled once the assembly force is removed.

EXPERIMENTAL DETAILS

The lateral force that the can be obtained from a wirebonder tip is much greater than necessary for assembly. Therefore, the only important control variable is the lateral displacement required for the compliant spring system to fully assemble. The wirebonder assembly of the structure is performed by lowering the bonding tip until it touches the substrate adjacent to the bottom lip of the microstructure. Because the substrate is significantly stronger than any microstructure that can be produced, using the substrate as a physical limit for the wirebonder tip to adjust the *Z* position easily allows this assembly method to position the tip at the correct height above the substrate. By sliding the X-Y table in the lateral direction while the tip is down, the tip pushes the structure causing it to rotate and lock into place. Figure 5 shows a sequence of photomicrographs illustrating the motion of assembly for the SU-8 fabricated structures. Figure 6 shows the SEM of the same device after assembly. Figure 7 shows rotation angle vs. lateral displacement of the microstructures. The time required to assemble the structure using a manual wirebonder (Mech-El Industries NU-829) is approximately 1 second. Using a fully automated wirebonding system, the assembly time can be significantly reduced.

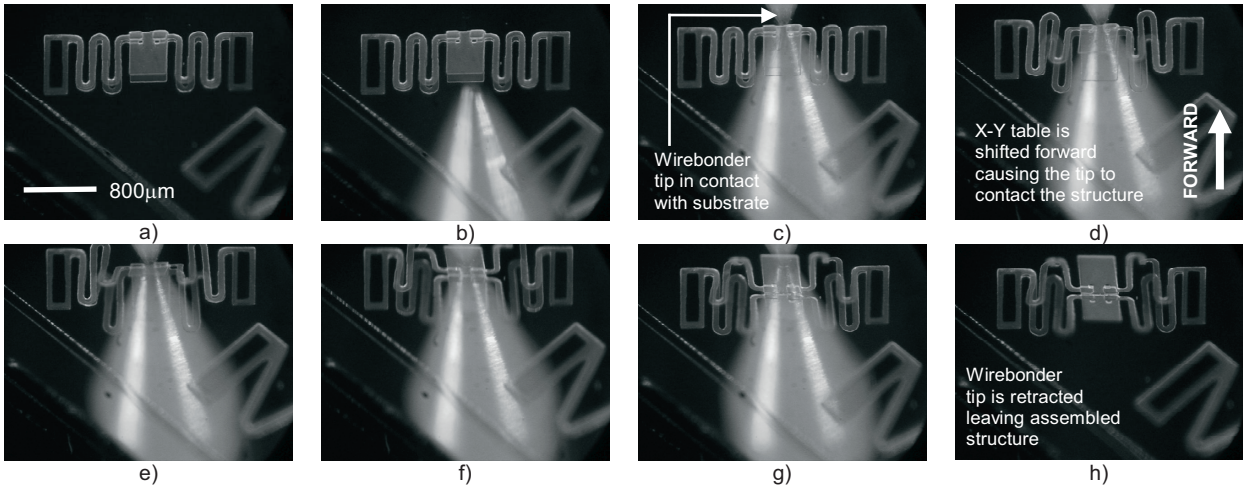

Figure 5. *Sequence showing the wirebonder assembly of a hingeless microstructure fabricated using an SU-8 prototyping process. The out-of-focus secondary image is the reflection of the wirebonder tip off of the substrate. The serpentine spring system for this structure is 20μm thick and 60μm wide, with 700μm long segments.*

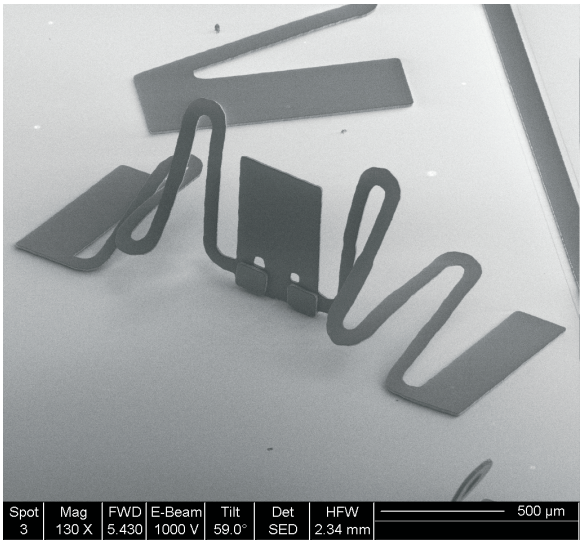

Figure 6. *Scanning electron micrograph of the wirebonder assembled structure. Device fabricated using an SU-8 prototyping*

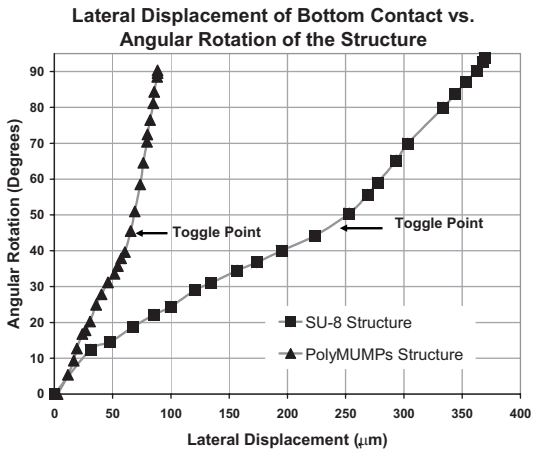

Figure 7. *Relationship between the lateral displacement versus angular rotation of the devices created in SU-8 and PolyMUMPs. After the toggle point, the structures will remain assembled when the assembly force is removed.*

REALIABILITY AND POSITIONAL REPEATABILITY

Because we are unable to access a fully automated wirebonder, the reliability and positional repeatability for the assembly of the microstructures were tested using a fully automated system by mounting three computer controlled Zaber Technologies T-LS28-M microstages together to provide the *X-Y-Z* degrees of freedom. Using the open-loop computer controlled microstages, several chips, each containing 31 out-of-plane SU-8 devices, were assembled and disassembled 6 times with 100% success (total of 186 successful assemblies). In addition, a single randomly selected device was cycled through assembly and disassembly 220 times without failure. Devices that are free from fabrication defects achieved 100% successful assemblies. The yield for successful assembly is highly process dependent rather than device dependent. If the devices are defect free, successful assembly is expected. By capturing photomicrographs of the assembled devices and using the National Instruments Vision Builder for analysis, we are also able to determine the positional repeatability of the system. Figure 8 illustrates a single frame of the photomicrographs that was used to determine the positional repeatability.

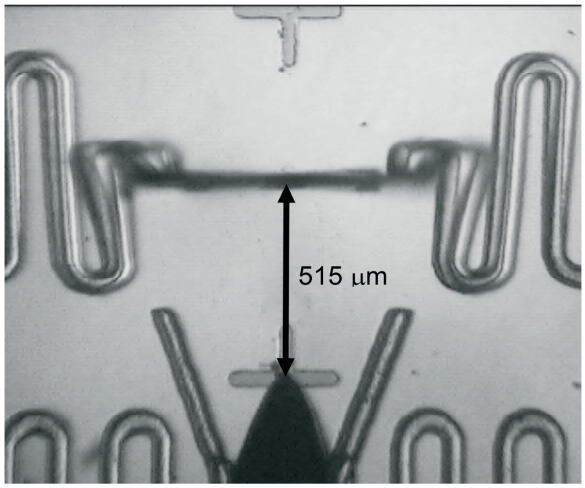

Figure 8. *Photomicrograph of one frame of the automatically assembled microstructure fabricated in SU-8.*

With the open-loop system, we are able to achieve an average 515.48μm of displacement over 60 cycles with a standard deviation of 1.24μm. The average angular accuracy achieved by cycling the single device is 89.98° with a standard deviation of 0.24°. By comparing the angle of the assembled devices and the displacement of the microstages, the positional repeatability is shown to be primarily dependent on the external assembly system and not on the microstructures. Therefore, by moving towards an industrial closed-loop automated wirebonding system for assembly, a high degree of repeatability is expected.

APPLICATIONS

Because the design of the out-of-plane microstructures do not require hinges, a reliable electrical connection to the out-of-plane devices can be made. Applications such as thermal accelerometers, micro-inductors, micro-antennas, and micro-grippers can easily be fabricated and assembled out-of-plane using this method. Figure 10 illustrates an assortment of devices that have been prototyped and assembled using the open-loop automated assembly method.

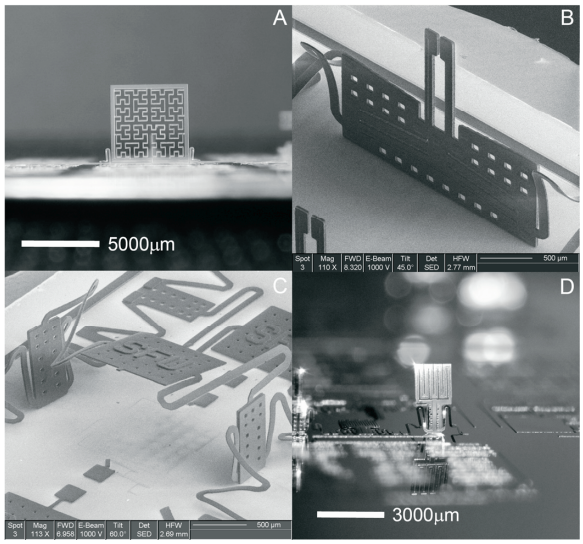

Figure 10. An *assortment of out-of-plane devices: A) Fractal Antenna B) Microgripper C) Thermal Isolation Platform D) Meander Inductor*

CONCLUSION

Out-of-plane assembly for microdevices has typically involved complex post processing or integrated actuators. Both methods can be costly in time and money and frequently result in poor yield. The design described here can use a standard microelectronics wirebonder or low cost micro-stages for assembly. Because wirebonding is already an integrated step for packaging commercial MEMs devices our assembly design has the potential to produce commercially viable 3-dimensional assembled devices. The work presented here provides a method for implementing the wirebonder for assembly to reduce cost and complexity for manufacturing out-of-plane microstructures. The devices have been analyzed, fabricated and tested in two distinct micromachining technologies, indicating its viability for many micromachining processes. The designs are highly resistant to shock, and have shown high yield. The main criterion for assembly is good control of lateral position for the single point actuation which can be programmed using automated wirebonding for the assembly of out-of-plane devices.

REFERENCES

[1] L. Y. Lin, S. S. Lee, M. C. Wu, and K. S. J. Pister, "Micromachined integrated optics for free-space interconnections," presented at Micro Electro Mechanical Systems, 1995, MEMS '95, Proceedings. IEEE, 1995.

[2] D. J. Young, V. Malba, J.-J. Ou, A. F. Bernhardt, and B. E. Boser, "Monolithic high-performance three-dimensional coil inductors for wireless communication applications," presented at Electron Devices Meeting, 1997. Technical Digest., International, 1997.

[3] N. C. Tien, O. Solgaard, M.-H. Kiang, M. Daneman, K. Y. Lau, and R. S. Muller, "Surface-micromachined mirrors for laser-beam positioning," *Sensors and Actuators A: Physical*, vol. 52, pp. 76-80, 1996.

[4] J. R. Reid, V. M. Bright, and J. H. Comtois, "Automated assembly of flip-up micromirrors," presented at Solid State Sensors and Actuators, 1997. TRANSDUCERS '97 Chicago., 1997 International Conference on, 1997.

[5] K. Tsui, A. A. Geisberger, M. Ellis, and G. D. Skidmore, "Micromachined end-effector and techniques for directed MEMS assembly," *Journal of Micromechanics and Microengineering*, vol. 14, pp. 542, 2004.

[6] V. Kaajakari and A. Lal, "Thermokinetic actuation for batch assembly of microscale hinged structures," *Microelectromechanical Systems, Journal of*, vol. 12, pp. 425-432, 2003.

[7] K. W. C. Lai, A. P. Hui, and W. J. Li, "Non-contact batch micro-assembly by centrifugal force," presented at Micro Electro Mechanical Systems, 2002. The Fifteenth IEEE International Conference on, 2002.

[8] R. R. A. Syms, E. M. Yeatman, V. M. Bright, and G. M. Whitesides, "Surface tension-powered self-assembly of microstructures - the state-of-the-art," *Microelectromechanical Systems, Journal of*, vol. 12, pp. 387-417, 2003.

[9] J. M. Z. Ocampo, P. O. Vaccaro, T. Fleischmann, T.-S. Wang, K. Kubota, T. Aida, T. Ohnishi, A. Sugimura, R. Izumoto, M. Hosoda, and S. Nashima, "Optical actuation of micromirrors fabricated by the micro-origami technique," *Applied Physics Letters*, vol. 83, pp. 3647-9, 2003.

[10] M. G. Lim, J. C. Chang, D. P. Schultz, R. T. Howe, and R. M. White, "Polysilicon microstructures to characterize static friction," presented at Micro Electro Mechanical Systems, 1990. 'Proceedings, An Investigation of Micro Structures, Sensors, Actuators, Machines and Robots'. , IEEE, 1990.

[11] A. C. David Koester, Ramaswamy Mahadevan, Mark Stonefield, and Busbee Hardy, "PolyMUMPs Design Handbook," MEMSCAP 2003.

[12] H. Lorenz, M. Despont, N. Fahrni, N. LaBianca, and P. Renaud, "SU-8: a low-cost negative resist for MEMS," *J. Micromech. Microeng.*, vol. 7, pp. 121-124, 1997.

3-D PATTERNED MICROSTRUCTURES USING INCLINED UV EXPOSURE AND METAL TRANSFER MICROMOLDING

Seong-O Choi[1], Swaminathan Rajaraman[1], Yong-Kyu Yoon[1], Xiaosong Wu[2] and Mark. G. Allen[1]

School of Electrical and Computer Engineering[1], School of Polymer, Textile and Fiber Engineering[2],
Georgia Institute of Technology,
Atlanta, GA, 30332, USA

ABSTRACT

We report a fabrication approach for three-dimensional (3-D) microstructures having functional metal patterns by using inclined UV lithography and 3-D metal transfer micromolding. Inclined rotational UV exposure using SU-8 has been exploited to simultaneously generate gradually varying 3-D structures with different heights in a single mask. For 3-D metal patterning, a metal transfer micromolding process has been utilized, where pre-patterned metal electrodes are formed on a polydimethylsiloxane (PDMS) mold prior to transfer, and these patterned metal structures are transferred to the molded 3-D microstructures during the micromolding process. Two approaches for metal pre-patterning have been utilized: one is selective metal removal by planar pattern transfer on an uneven surface and the other is pattern transfer using a shadow mask. Two test vehicles of 3-D patterned microstructures implemented by this process are demonstrated: an electroporation microneedle array and a 3-D microelectode array (MEA). Insertion tests on pig skin using the fabricated microneedle array with different heights have been successfully performed, showing different penetration depths by fluorescent imaging.

INTRODUCTION

Recent advances in micromolding have enabled rapid progress in the cost-effective fabrication of three-dimensional (3-D) microstructures [1]. In general, the micromolding process consists of master structure fabrication, negative mold fabrication, and casting and separation. The fabrication of master structures often relies on advanced UV lithography using SU-8 for its complex 3-D structure capability [2]. As a mold material, PDMS has been widely utilized because of its mechanical compliance and faithful feature reproduction. In the conventional molding process, direct casting of a variety of polymers into the mold is performed to complete the process. In the case of *patterning* of metals on the three-dimensional surface to functionalize or enable other applications such as microelectrode arrays (MEAs) or an electrically active microneedle array for electroporation, either complex lithographic approaches [3], electrodeposited resists [4] or serial direct laser patterning [5] needs to be applied to the molded 3-D structures.

Alternatively, the 3-D micro electrodes can be formed during the molding process. The so-called *3-D metal transfer micromolding process* performs metallization and subsequent patterning on the PDMS mold prior to casting polymer, and these patterned metal structures are transferred to the molded 3-D microstructures during the molding process as shown in Figure 1**.** This process can be thought of as a three-dimensional extension of 2-D metal transfer processes used in nanoprinting [6], which exploits the difference in surface energy between PDMS and the microstructure material to enable metal transfer.

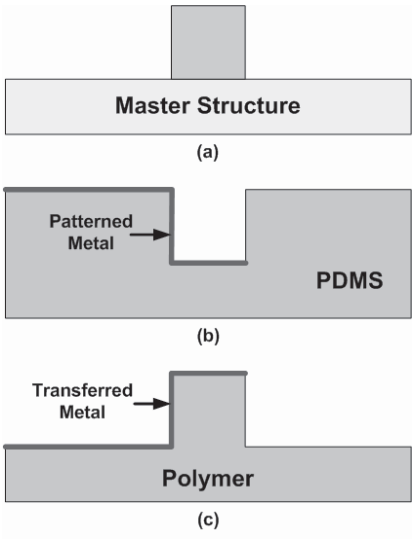

Figure 1. *Concept of 3-D metal transfer micromolding: (a) Fabrication of a master structure, (b) Fabrication of PDMS mold from the master followed by metal deposition and patterning, (c) Formation of 3-D metal-patterned polymeric microstructure.*

The process has several advantages. First, since metallization and metal patterning is performed on the mold structure, which is a negative form of the master structure, the process has an additional degree of freedom in 3-D metal patterning for the structures otherwise metal patterning may not be convenient with. Secondly, the pre-deposited or patterned metal layers contribute to enhancing moldability by increasing wettability on the mold surface for liquid polymer casting [7]. Third, the transferred metal does not necessarily require an intermediate adhesion layer as in conventional physical vapor deposition, further simplifying the process.

This paper consists of 3-D microfabrication using inclined UV lithography and micromolding for master structure fabrication, and subsequent 3-D metal transfer molding in which two metal patterning processes are demonstrated. The process is illustrated through two sample structures; one of the structures, an array of microneedles of varying heights, is tested for its insertion capabilities.

3-D MICROSTRUCTURE FABRICATION

A rigid SU-8 mold is fabricated using inclined UV lithography [8-10] to form negative concave shapes of various depths as shown in Figure 2a, b. Both mask dimensions as well as the incident angle of UV light determine the depth of the mold. This rigid mold is used to produce a mold master (Figure 2c) from

PDMS or other suitable material (such as Ni in the case of electroplating). The mold master is then used to create a flexible replica (Figure 2d) of the original rigid mold; this flexible mold should be made from PDMS due to both its low modulus and low surface energy. This flexible mold is then optionally metallized and patterned as described below. Polymer microstructures with various heights are then fabricated from the flexible mold (Figure 2e, f).

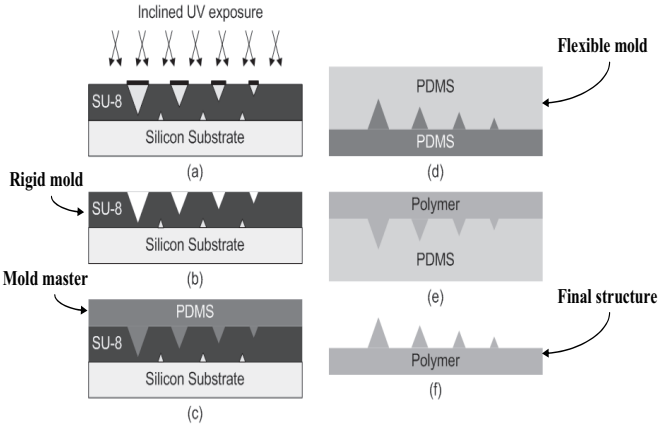

Figure 2. *Fabrication steps for 3-D microstructure.*

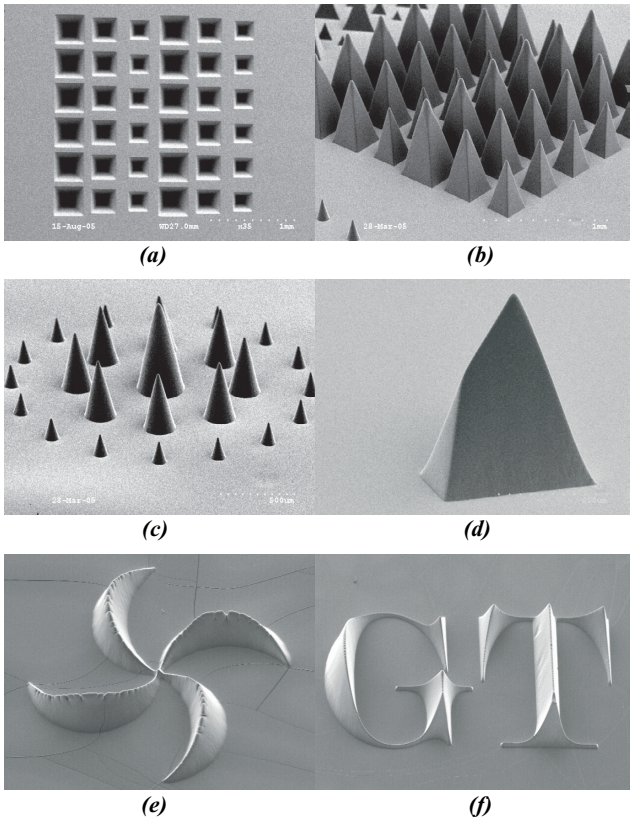

Figure 3. *Fabricated structures: (a) rigid SU-8 mold, (b) variable height microneedle array cast from a flexible mold, (c) cone-shape microneedle, (d) beveled-tip microneedle, (e) vane-shape structure, (f) GT logo*

Figure 3 shows various structures fabricated from inclined rotational exposure combined with the subsequent molding process. With differing mask shapes and inclination angles, molded copies of gradually-varying complex 3-D structures have been achieved. One application of interest for this technology is 3-D microneedle array fabrication. Advantages of this process include (1) easy control of the height and the tip angle of the microneedle by control of inclination angle; (2) simultaneous fabrication of microneedles of various heights by controlling the mask footprint; (3) no need for subsequent wet or dry etching for sharp tip fabrication.

3-D METAL TRANSFER MICROMOLDING

In 3-D metal transfer micromolding, metallization is performed on the negative form of the master made of PDMS. Two metallization schemes and subsequent 3-D metal transfer micromolding have been demonstrated. One scheme is to use selective metal removal from an intentionally formed non-planar mold surface using a 2-D metal transfer process. The other is to use selective metal deposition onto and into mold features using a shadow mask.

High Surface Energy Plate Approach: Figure 4 shows the fabrication steps using a selective metal removal process for an electrically functionalized molded electroporation microneedle array, which requires conductive microneedles and electrical isolations between needle rows. The PDMS mold is fabricated by a two-step SU-8 process and subsequent PDMS molding to form a protruding feature which will ultimately electrically isolate each row (a, b). After depositing Au on the mold (c), the Au layer on the protruding structure is removed by bringing a high surface energy plate in contact with the mold (d), transferring the metal on the protruding surface to the plate in a 2-D metal transfer scheme. UV-curable resin is then cast into the mold and optically cured (e). The pre-patterned Au layer is then transferred during the demolding process (f), resulting in the formation of a polymeric microneedle array with electrical isolations between needle rows (Figure 5). This process avoids the issues associated with conventional metal patterning, since conventional approaches will experience difficulties in patterning of the isolation layer on the bottom of the substrate due to the protruding needle structures.

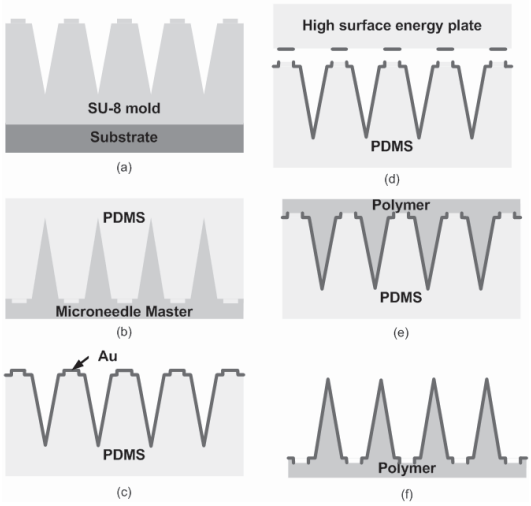

Figure 4. *Fabrication steps for metal transfer onto a 3-D structure using a high surface energy plate*

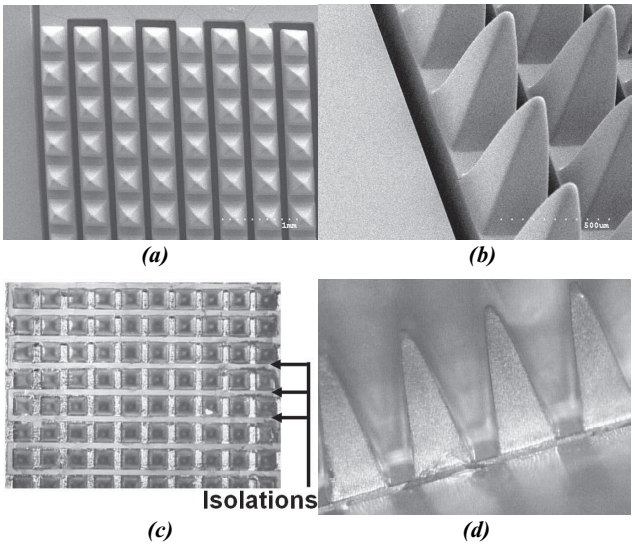

Figure 5. *Fabricated microneedle arrays with applications in electroporation: (a ,b) SEM of the mold master, (c,d) Optical photomicrograph of metal patterned structures.*

Shadow Mask Approach: Metal can be patterned on the three-dimensional molds using a shadow mask approach. The shadow mask used in this paper was made from 125-150µm thick Kapton sheets using excimer laser ablation. The ablation is achieved at 250mJ energy (20% attenuation) at the rate of 50-60µm per cut. Feature sizes as small as 20µm can be achieved using these parameters. This mask is then aligned with the PDMS mold (refer to section on 3-D Microstructures). Alignment marks are cut on the shadow mask to aid this process. The mask is held in position (proximity contact). This substrate is then loaded into a filament evaporator and Au/Cr (1µm/100Å) is evaporated. We have experimented with Au/Cr evaporation instead of just Au, because theoretically the adhesion force between Cr and cast polymer is higher than that between Au and polymer. However, it turned out that in both cases adhesion between the metal and polymer passes the Scotch tape test. SU-8 is then cast into this mold baked and blanket exposed. The SU-8 tower array is carefully peeled off from the PDMS mold after post-exposure baking. The Au/Cr metal layer is transferred from PDMS to SU-8 and becomes Cr/Au on the SU-8 structure in the case of both Au and Cr being evaporated. Due to the usage of shadow masks the towers have metal lines at various heights on them satisfying the 3-D metallization needed for improved MEA performance [11]. Also address lines to contact these electrodes are achieved to the end of the chip. The chip could potentially be mounted and wirebonded for use in MEA experiments. Figure 6 details the process steps and Figure 7 shows optical micrographs of the fabricated structures.

APPLICATIONS AND DISCUSSION

One application of interest for this technology is an electrically functional 3-D active microneedle array. The negative mold master has been fabricated using inclined rotational UV exposure with SU-8 as described in the previous section. Combined with the 3-D metal transfer molding process, cost-effective, mass-producible electrically active 3-D microstructures can be fabricated. These microneedles could be utilized as an electroporation microneedle array for either gene delivery through skin or electrochemotherapy of highly-localized solid tumors. Other applications of interest include simultaneous local and systemic delivery of drug to blood vessels; drug delivery system through a cornea, which is not flat in nature; simultaneous measurement of biopotentials such as action potential at different sites (3-D MEA); and measurement of electrical properties of skin as a function of depth.

For these active microneedle applications, the strength of the needles and the ability to penetrate tissue has been tested. An array of microneedles with various heights that was made from biodegradable polymer, polylactic acid (PLA) has been used for pig skin *in vitro*. Red dye was spread on the pig skin, and a microneedle array was inserted with a force of approximately 10 N. After removing the microneedle array, the red dye on the surface was removed with deionized water. Cryosection microscopy was used to examine the cross-section of the pig skin (Figure 8), and showed that the microneedle array was successfully inserted with different penetration depths. The tip diameter of the microneedle array was less than 20µm.

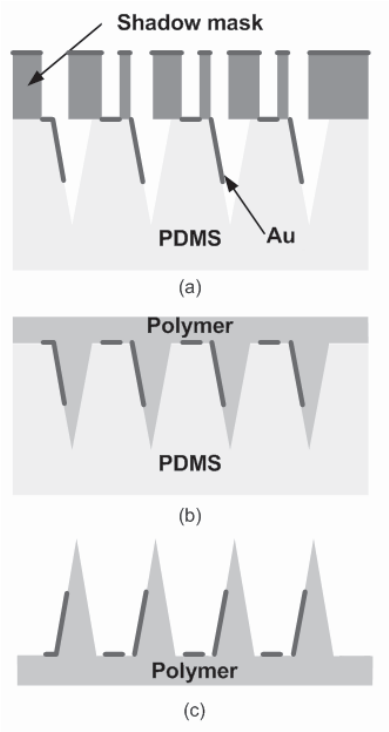

Figure 6. *Fabrication steps for metal transfer onto a 3-D structure using a shadow mask*

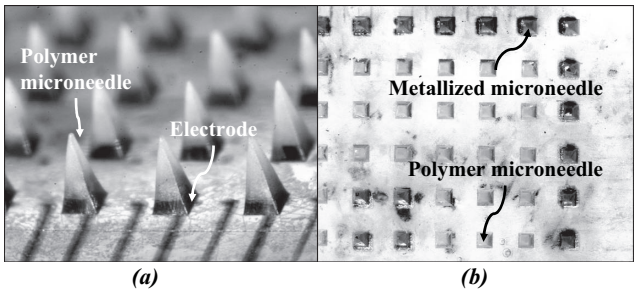

Figure 7. *Fabricated micro-tower arrays: (a) electrodes with address lines and metal lines at various heights, (b) top view of the selectively metallized micro-towers*

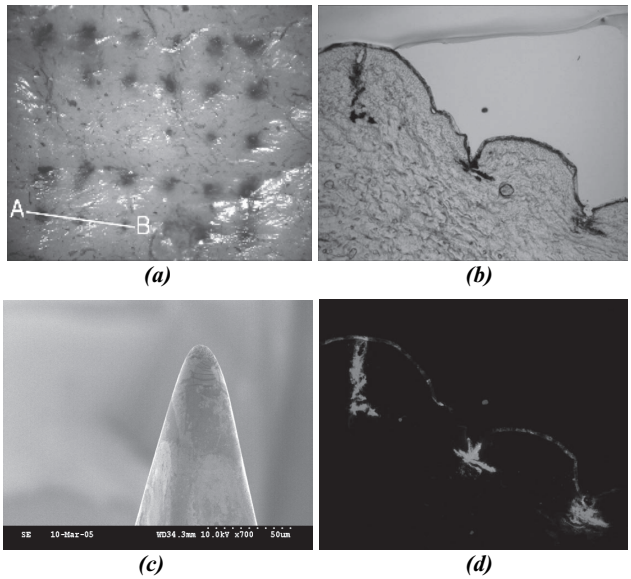

Figure 8. *Optical photomicrograph of pig skin after insertion test with microneedle array of various heights: (a) visible light image (left: plan view; right: cross-section of A-B), (c) SEM micrograph of microneedle tip (scale bar indicates 50μm), (d) fluorescent light image of the cross-section showing 3 different penetration depths.*

CONCLUSIONS

We have developed a technology for the fabrication of 3-D microstructures bearing metal patterns by combining inclined UV exposure and metal transfer micromolding. We have demonstrated two separate techniques for selective metal definition on the final structures: one using a high surface energy plate and the other using a shadow mask. In both these techniques metal has been selectively defined on the master mold and then transferred to the final structure during molding. This technology is potentially applicable to fabricate an electrically active microneedle array for either gene therapy or electrochemotherapy, 3-D microelectrode array for neural stimulation/recording, and so on.

ACKNOWLEDGEMENTS

We wish to acknowledge Mr. Richard H. Shafer for valuable technical discussions. Also we would like to thank Mr. Gary Spinner and the staff of Microelectronics Research Center (MiRC) at Georgia Tech for their efforts in running the cleanroom efficiently. We also appreciate the efforts of Dr. Jung-Hwan Park, Mr. Jungwoo Lee, and Prof. Mark Prausnitz for their assistance with the microneedle insertion tests into pig skin.

REFERENCES

[1] G. Vozzia, C. Flaimb, A. Ahluwaliaa, and S. Bhatiab, "Fabrication of PLGA scaffolds using soft lithography and microsyringe deposition", *Biomaterials*, 24 (2003), pp. 2533-2540

[2] Y.-K. Yoon, J.-H. Park, and M. G. Allen, "Muldirectional UV Lithography for Complex 3-D MEMS Structures", *J. MEMS* (2006), in press

[3] N. P. Pham, E. Boellaard, J. N. Burghartz, and P. M. Sarro, "Photoresist Coating Methods for the Integration of Novel 3-D RF Microstructures", *J. MEMS*, 13 (2004), pp. 491-499.

[4] S. Linder, H. Baltes, F. Gneadinger and E. Doering, "Photolithograhy in Anisotropically Etched Grooves", *Proceedings of the IEEE MEMS Conference (MEMS'96) ,* San Diego, CA, 2/11-15/96, IEEE (1996), pp. 38-43.

[5] Y. Choi, S. Choi, R. H. Shafer, and M. G. Allen, "Highly Inclined Electrodeposited Metal Lines Using an Excimer Laser Patterning Technique" , *Technical Digest of the 13th International Conference on Solid-state Sensors, Actuators and Microsystems (Transducers'05)*, Seoul, Korea, 6/6-9/05, IEEE (2005), pp. 1469-1472.

[6] S. Hur, D. Khang, C. Kocabas, and J. A. Rogers, "Nanotransfer Printing by use of Noncovalent Surface Forces: Applications to Thin-film Transistors that use Single-Walled Carbon Nanotube Networks and Semiconducting Polymers", *Appl. Phys. Lett.*, 85 (2004), pp. 5730-5732

[7] X. Wu, Y. Zhao, Y. K. Yoon, S. O. Choi, J. H. Park, and M. G. Allen, "Wafer-scale Micromolding of Unitary Polymeric Microstructures with Simultaneously Formed Functional Metal Surface", *Proceedings of μTAS 2005 conference*, Boston, MA, 10/09-13/2005, Transducers Research Foundation (2005), pp.205-207

[8] M. Han, W. Lee, S.-K. Lee, and S. S. Lee, "3-D Microfabrication using Inclined/Rotated UV Lithography", *Sensors and Actuators A*, 111 (2004), pp. 14-20.

[9] H. Sato, T. Kakinuma, J. S. Go, and S. Shoji, "In-channel 3-D Micromesh Structures using Maskless Multi-Angle Exposures and their Microfilter Application", *Sensors and Actuators A*, 111 (2004), pp. 87-92.

[10] Y.-K. Yoon, J.-H. Park, F. Cros, and M. G. Allen, "Integrated Vertical Screen Microfilter System using Inclined SU-8 Structures", *Proceedings of the IEEE MEMS Conference (MEMS'03),* Kyoto, Japan, 1/19-23/2003, IEEE (2003), pp. 227-230.

[11] M.O. Heuschkel, M. Fejtl, M. Raggenbass, D. Bertrand, P. Renaud, "A Three Dimensional Multi-Electrode Array for Multi-Site Stimulation and Recording in Acute Brain Slices", *J. Neuroscience Methods*, 114 (2002), pp. 135-148.

BACKSIDE RESISTIVE LOCALIZED HEATING FOR LOW TEMPERATURE WAFER-LEVEL BONDING AND PACKAGING

Jay Mitchell, and Khalil Najafi
Center for Wireless Integrated Microsystems (WIMS)
University of Michigan, Ann Arbor, MI 48109-2122, USA

ABSTRACT

A new method has been developed for localized heating of a bond region when bonding two wafers, while maintaining a low temperature where sensitive devices are located. Using this technique, access is only required to the backsides of the two wafers, thus making the process easier and wafer-level compatible. In this "differential" heating method, one of the two wafers to be bonded is heated from the backside, and the other is cooled from the backside. Heat flows through the bond areas where the two wafers are in contact, thus heating these regions more than other. Integrated temperature sensors were used to measure the temperature at different distances from the bond region while making a Au-Si eutectic bond between silicon and glass wafers. When bond regions reached ~410-475ºC, the sensitive device regions 600 µm and 50 µm away from the bond were measured to reach only 92 and 250ºC, respectively. Simulations using ANSYS were performed and used for the design of the wafer bonding setup and for predicting the needed input power and heater temperatures.

INTRODUCTION

Vacuum/hermetic sealing is required for a wide range of micro-systems. Current wafer-level encapsulation techniques such as frit bonding (~450ºC), Au-Si eutectic bonding (~390 ºC) [1], and thin film encapsulation (~600 ºC) [2] require relatively high temperatures that often preclude their use in some applications. For this reason, researchers have investigated lower temperature bonding methods using polymers and solders at lower temperatures. Another option is to use a well established high temperature bonding method and use *localized heating* to heat the bond region to a high temperature, while maintaining a low temperature where devices that are to be encapsulated are located.

A number of localized heating methods have been reported in the literature using lasers, microwaves, resistive elements and induction. In *laser assisted* localized heating, a laser wavelength is chosen that is transparent to the substrate but heats the material at the bond region. Laser assisted bonding has been applied in solder and anodic bonds [3, 4]. In a similar manner *microwaves* have been used to fuse two Au surfaces to achieve silicon to silicon bonds [5]. Using *resistive heating*, substrates have been bonded through plastic, PSG, solder, fusion and eutectic bonding [6]. In this case, the resistor had to be fabricated on the front surface of one of the wafers, and then accessed electrically for heating. Therefore, using this technique at the wafer level is challenging. *Inductive heating* is a related technique in which an inductive coil creates a magnetic field, causing large eddy currents in a bond ring made out of a ferromagnetic material. This technique has been applied for silicon to silicon and silicon to glass wafer bonds [7]. The main draw back of this technique is that it limits the range of materials that can be processed on the bonded wafers.

We report a localized heating method in which heat is applied to the backside of one of the two wafers to be bonded (e.g., the *"cap" wafer* used to encapsulate the device), and removed from the backside of the second wafer (e.g., the *"device" wafer*) as illustrated in Fig. 1. Because most of the heat is drawn towards the heat sink in Fig. 1, the device region is heated less than the bond region. This method is attractive because it can be applied on a wide range of materials and at wafer level. The heating of the cap wafer mentioned above could be achieved using a variety of techniques, including using a heater substrate with on-chip resistive heaters, as reported in this paper.

MODELLING AND DESIGN

A 3-D thermal model was constructed with the layers shown in Fig. 1 to aid in the design of the wafer bonding setup. The complete system consists of several substrates: a Cogetherm™ insulator plate (10.5 mm thick), a glass heater substrate with on-chip resistive heaters (550µm), a silicon *cap wafer* (550µm), a *device wafer* (modeled as either silicon or glass, 550µm) a copper plate heat sink substrate on top of the device wafer (3.1 mm thick), and a steel plate providing the bond force (modeled as 14 mm thick).

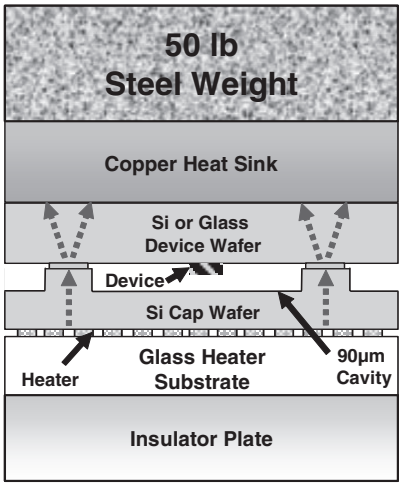

Figure 1: *A schematic showing that using the differential heating method, most of the heat flows toward the heat sink as supposed to laterally, towards the device.*

Figure 2 shows the structure of the to-scale 3-D model used for predicting necessary input powers and the resulting temperature distributions. In this model, there is symmetry along the planes perpendicular to the x and y axes so that the model represents a quarter of the actual assembly. As with the eventual test setup, arrays of heaters were used to heat up 4 bond rings at a time on a relatively small portion of the wafer. The picture of the assembly in Fig. 2 was made transparent to allow a view of a quarter of one of these 0.75x10500x13300 µm heaters which encompasse 4 full bond rings (that is 1 bond ring in this quarter symmetry model). As also shown in Fig. 2, adjacent bond brings were incorporated into the final model. It was found with successive 3-D models, the addition of more and more detail (such as added assembly width and adjacent bond rings) resulted in lower predicted temperatures for a given input power and in results that more closely matched those seen in initial tests.

In simulating the model, a steady state solution was found by applying a uniform power density across the heater, while the top

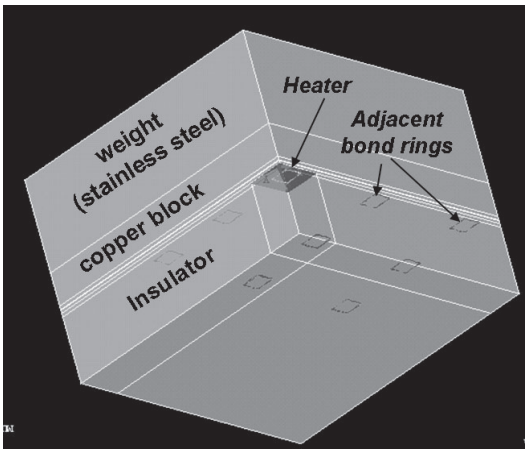

Figure 2: *The structure of the model used for simulation.*

of the steel plate and the bottom of the insulator plate were held at 23ºC. Figure 3 shows the results of a model for the case where a 110 W power is applied to the heater for a bond to a *glass* device wafer. As shown in Fig. 3b, temperature profiles were produced across different planes sliced through different portions of the assembly in order to analyze the results. The device cavities were 90 µm deep (Fig. 1 and 3d), each bond ring was 2.3x2.3mm square (Fig. 3e), and the bond ring widths were 100, 50 or 25µm (Fig. 3e).

As shown in Figs. 3a and 3c, the temperature drops very quickly across the glass *device wafer*, and approaches room temperature at the copper heat sink. Furthermore as illustrated in Fig. 3a, due to lateral heat spreading, there is a large lateral temperature gradient across the assembly. As shown in Figs. 3c and 3e, this leads to a temperature gradient across the heater of 375 to 514 ºC and across the bond ring of 410 to 473 ºC. Figure 2e illustrates the effectiveness of this localized heating method, with the temperatures dropping to 250 ºC and 99 ºC at 100 and 600 µm from the bond ring.

Table 1 shows the power needed to heat the entire bond ring to above 410ºC, the temperature at the heater, and the temperature 600 µm from the bond ring for bonds to glass and silicon *device wafers.* As shown, when silicon is used as the *device wafer,* the

Table 1: *ANSYS Predicted power need to achieve a bond ring temperature of greater than 410ºC, and the temperature at the heater and at a 600 µm distance away from the bond ring .*

Device wafer Material	Power	Heater Temp.	Temp. 600 µm away
Glass			
Bond ring width:**100 µm**	110 W	Ave: 453 ºC Max:514 ºC	99 ºC
Silicon			
bond ring width:**100 µm** SiO_2 thickness: **none**	1900W	Ave: 932ºC Max:1291ºC	330 ºC
bond ring width:**100 µm** SiO_2 thickness:**6 µm**	600 W	Ave: 630ºC Max: 881ºC	118 ºC
bond ring width:**50 µm** SiO_2 thickness:**6 µm**	450 W	Ave: 605ºC Max: 802ºC	91 ºC

model predicts a necessary power of 1800W, and a maximum heater temperature of 1291ºC to achieve a bond ring temperature above 410 ºC. Material selection for such a high power, high-temperature heater would be challenging. The higher necessary power and maximum heater temperature is due to the larger thermal conductivity of single crystal silicon (141 W/m·K) as compared to glass (1.4 W/m·K). In other words, silicon draws heat away from the heater more efficiently.

Figure 4 shows a simple 1-D representation of the heat flow, q, from the heater, through the bond ring, to the heat sink. When bonding to a glass *device wafer*, the thermal resistance directly above the bond ring, $R_{bond\ ring}$, is extremely large compared to the other thermal resistances because of: 1) the relatively small cross sectional area at the bond ring, A, and 2) the small thermal conductivity, k, of glass. This large thermal resistance leads to a large temperature drop directly above the bond ring (Fig. 2c) and therefore a relatively small necessary input power and maximum heater temperature. When bonding to a silicon *device wafer*, $R_{bond\ ring}$ can be increased by either using a dielectric layer (decreasing k) or decreasing the bond ring width (decreasing A). As shown in Table 1, using a 6 µm SiO_2 layer brings the necessary power down to 600W and the maximum heater temperature down to 881ºC. This thickness of SiO_2 was chosen to approximate the combined

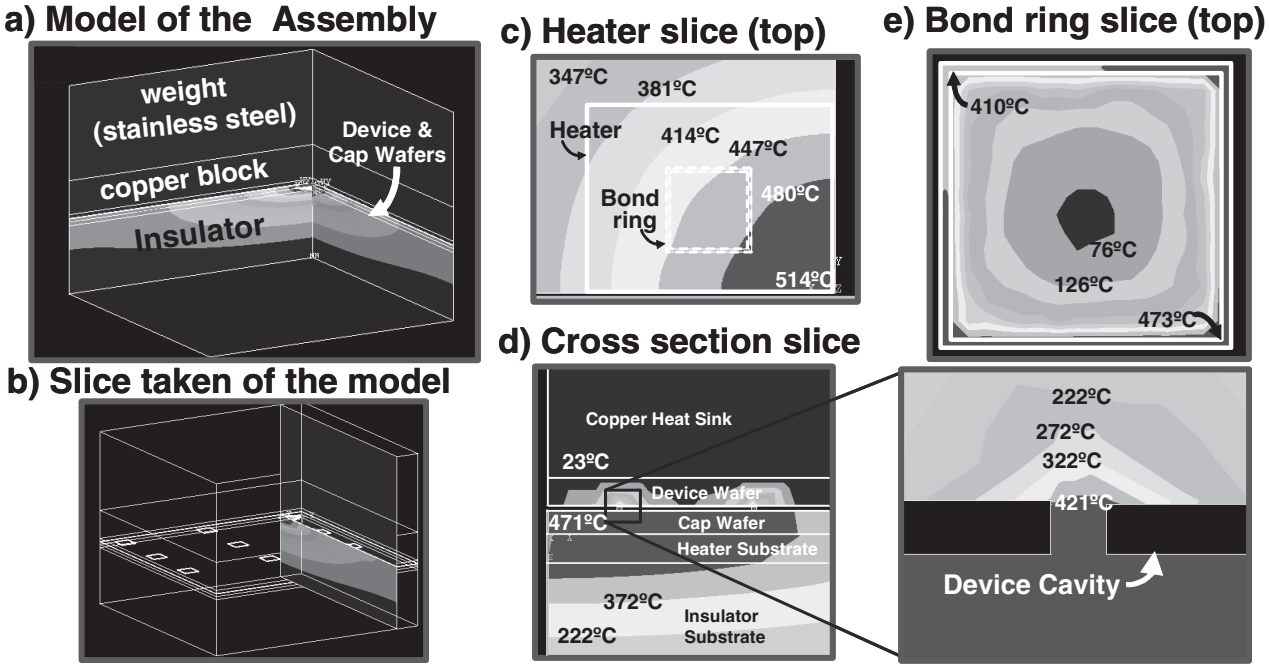

Figure 3: *a) A parametric view for the model of the differential heating test setup, b) an illustration of a slice taken out of the model, c) a slice showing a cross section of the heater and bond ring, d) a slice of the heater and e) a slice of the bond ring.*

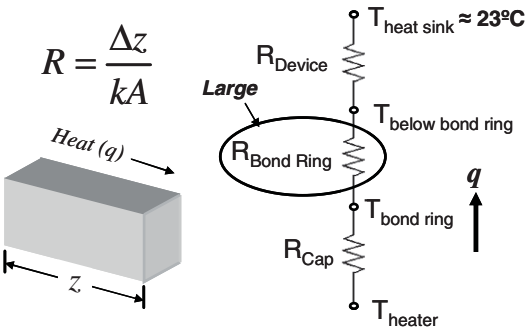

Figure 4: *A schematic of heat flow in the bonder test setup.*

thermal conductivity of the thin film stack in a CMOS wafer. As also shown in Table 1, reducing the bond width to 50 µm also reduces the necessary input power and the maximum heater temperature.

TESTING & RESULTS

In the first round of testing, bonds were made using differential heating to achieve a Au-Si eutectic bond. A Au-Si eutectic layer on the silicon *cap wafer* was bonded to a 5000 Å layer of gold on a glass *device wafer*. In Au-Si eutectic bonding, the temperature is raised to above the Au-Si eutectic temperature (363ºC), causing silicon to diffuse into the Au bond ring. It then melts and can mate to either a polysilicon or a gold thin film [1].

In fabrication of the glass *device wafer*, a 1000 Å platinum layer was first deposited and patterned to form temperature sensors. A 5000 Å layer of plasma enhanced chemical vapor deposited (PECVD) Si_xN_y was then deposited for electrical insulation. Finally a 5000 Å gold layer (which would later get bonded to) was evaporated and patterned over the top of the Si_xN_y. On the *cap wafer,* 96 gold bond rings were electroplated onto a Cr/Au seed layer with a thickness of 4 µm. Each bond ring was 2.3x2.3 mm square, encompassing a 90 µm deep reactive ion etched (DRIE) cavity and had a 100 µm width—as in the case modeled. Furthermore, part of the *cap wafer* was diced away. Once the *cap* and *device wafers* were aligned, this allowed access to leads that were connected to the temperature sensors (Fig. 5b).

Figure 1 showed a cross-section of the wafer-level bonding test set up, where a 50 lb weight applies a 1 MPa pressure across the 96 bond rings arrayed across the wafer. After alignment of the wafers in a SUSS BA6 aligner, the two wafers were clamped with 4 small clips, placed on a copper heat sink, and wire bonded to two PCB as shown in Fig. 5a—thus providing connectivity to the temperature sensors.

According to the modeling results, bonding a silicon *cap wafer* with 96 bond rings to a *device wafer* made of either glass or silicon (with a 6 µm thick oxide) would require 2640 or 14400 Watts, respectively. Because of the large required heating power, an array of heaters was used, with each heater requiring a fraction of the total heating power to generate the required temperatures across the wafer. The heater array also allows heating of the different parts of a wafer to different temperatures. Figure 5c shows the heater arrays, laid out to heat 4 bond rings each. Heater arrays were fabricated by first evaporating a 0.75 µm film of Au onto a glass substrate. This thin film was patterned to form a 3x4 array of heaters on each wafer. Each heater consisted of a 100 µm wide, 700mm long, winding coil that encompassed a 10.5 x 13.3 mm area (as in the model). the heater substrate was diced into a 70 by 76 mm rectangle where two leads per heater ran out to bond pads at the periphery. In this manner, two heater substrates could encompass a 4" diameter wafer as in Fig. 5c.

The heaters and temperature sensors used in these experiments are essentially thin-film metal resistors that can

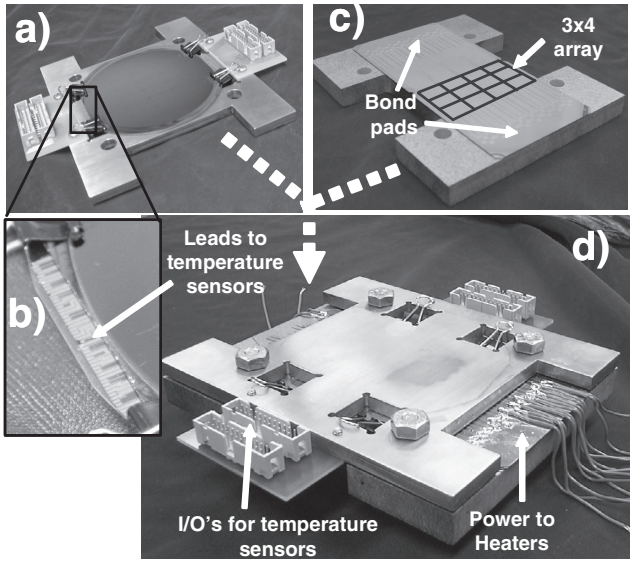

Figure 5: *A picture of a) the leads which connect to the temperature sensors, b) the wafers sitting on the copper heat sink, c) two heater substrates sitting on top of the Cogetherm™ insulator plate, and d) the total assembly.*

measure temperature, and that can heat up with a large input power. Before testing, the temperature coefficient of resistance (TCR) was measured for each of the heater and temperature sensor resistors. Figure 6 shows a view from the backside of the glass *device wafer* that was aligned to and clamped to the *cap wafer.* Each of the three temperature sensors in Figure 6 forms a 4-point probe, where the temperature is measured by applying a specified current across two of the leads and the voltage drop is measured across the other two. Given the measured TCR (where ΔT = [Δ resistance]/[initial resistance *TCR]) the temperature could be measured with a resolution of better than 1ºC for the temperature sensors and heaters.

As illustrated in Fig. 6, there is a roughly 100µm misalignment in the y-axis resulting in distances of 50, 100 and 600µm between the temperature sensors and the bond ring. Figure 7 shows that for heater temperatures from 50 to 390°C, the temperatures measured at 50, 100 and 600µm from the bond ring agree very well with those predicted from the model (the dashed lines in Fig. 7). Figure 8 shows temperature vs. time for the heater and at 50, 100 and 600µm away from the bond ring. As demonstrated, it takes roughly 20 seconds to approach the steady state temperature and 5 second for the substrate to cool back down to room temperature.

To demonstrate that a bond could be achieved, two heaters were taken to approximately 110W with heater 1, achieving 446ºC,

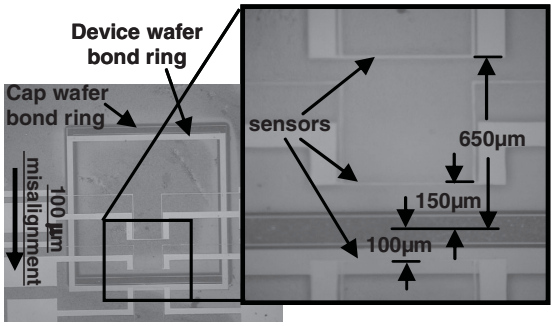

Figure 6: *A view through the backside of the glass device wafer which was clamped to the Si cap wafer showing the 100 µm misalignment and temperature sensors at different distances from the bond ring.*

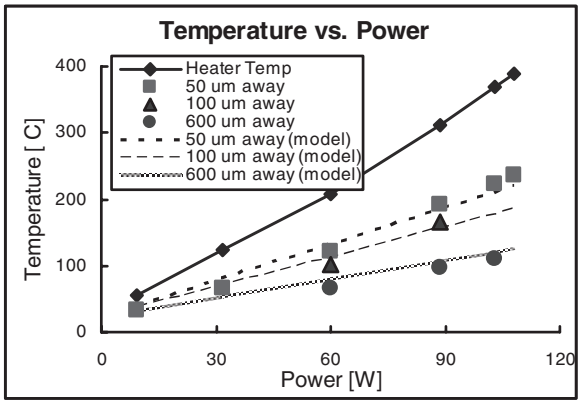

Figure 7: *A graph of the temperatures measured and predicted at the heater at 50, 100 and 600 µm from the bond ring where the dotted lines represent the predicted modeling results.*

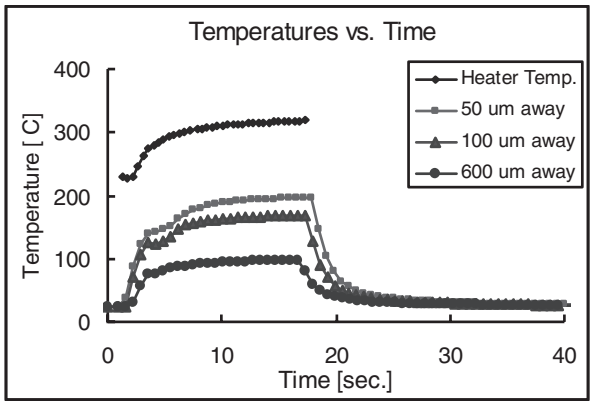

Figure 8: *Temperature vs. time for the heater, and temperature sensors 50, 100 and 600 µm from the bond ring.*

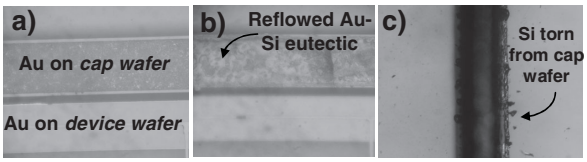

Figure 9: *a) Misaligned Au on the cap and device wafers before bonding, b) after bonding. c) Silicon torn from the cap wafer, adhering to the device wafer via a Au-Si eutectic bond.*

and heater 2, achieving 390 ºC (this variation in temperatures could be due to a number of factors such as different contact resistances or their relative location near the center or periphery of the wafer). These temperatures were within 1% and 15% of the power predicted in the model (Table 1). After forcibly pulling the wafers apart, the bond rings were inspected. Figure 9 shows a bond ring before the bond experiment (Fig 9a); part of the horizontal *misaligned* portion, where the solder melted but had nothing to bond to (Fig. 9b); and part of the vertical *aligned* portion that mated with the gold and created a strong bond (Fig. 9c). Similar to Au-Si eutectic bonds in [1], Fig. 9c shows that when the wafers were pulled apart, silicon tore from the *cap wafer* and stuck to the *device wafer* via the Au eutectic layer—thus indicating a strong bond.

For the average temperatures of 446 and 390ºC seen on heaters 1 and 2, the model predicts bond ring temperatures ranging from 410 to 474 ºC and 353 to 407 ºC. Therefore, all of the bond rings encompassed by heater 1 should melt/bond and only parts of the bond rings encompassed by heater 2 should melt/bond. This was confirmed in that under heater 1, 100% of the 4 bond rings melted and glass either transferred to the silicon wafer or silicon to the glass wafer in the *aligned* regions, whereas, under heater 2 roughly 80% of the 4 bond rings melted and either glass or silicon transfer was observed in the *aligned* regions. More extensive bonding tests will be conducted in the future.

CONCLUSION

A new method for localized heating of a bond region has been developed for bonding two wafers, while maintaining a low temperature where sensitive devices are located. In application of this technique, access is only required to the back sides of the two wafers, thus eliminating the need for access to wafer front side, as is sometimes needed in localized wafer bonding techniques. Integrated temperature sensors were used to measure temperatures at different distances from the bond region while making a Au-Si eutectic bond between silicon and glass wafers. Using a 3D ANSYS thermal model, the needed input power and temperature distributions were predicted for silicon to glass and silicon to silicon bonds. Using a heater array (10.5x13.3mm per cell), bonds were made on individual portions of the wafer using 110 Watts per heater to heat 4 bond rings at a time. When heating the bond ring to an estimated 410 to 475ºC, the temperature 600 and 50 µm away from the bond region was measured and extrapolated to be 92 and 250ºC respectively.

In future work, investigations will be made for silicon to silicon bonds using this bonding method. As illustrated from the simulations, an oxide of around 6 µm (equivalent to the thermal resistance of some CMOS stacks) helps reduce the maximum heater temperature and the power necessary to achieve bond temperatures. Furthermore, this localized heating method may also be applied to other lower temperature solders.

ACKNOWLEDGMENTS

This work was supported primarily by the Engineering Research Centers Program of the National Science Foundation under Award Number EEC-9986866.

REFERENCES

[1] J. Mitchell, G. R. Lahiji, and K. Najafi, “Encapsulation of vacuum sensors in a wafer level package using a gold-silicon eutectic,” *Tech Digest, Transducers’05*, Seoul, Korea, 928-931 (2005).

[2] R.N. Candler, W.T Park, M. Hopcroft, B. Kim, T.W. Kenny, “Hydrogen diffusion and pressure control of encapsulated MEMS resonators,” *Tech Digest, Transducers’05*, Seoul, Korea, 920-923 (2005).

[3] R. Witte, H. Herfurth and S. Heinemann, "Laser joining of glass with silicon," *Proc. of the International Society for Optical Engineering*, vol. 4637, 487-95, (2002).

[4] Y. Tao, A.P. Malshe and W.D. Brown, "Selective bonding and encapsulation for wafer-level vacuum packaging of MEMS and related micro systems," *Microelectronics Reliability*, 44, 251-258, (2004).

[5] N.K. Budraa, H.W. Jackson, M. Barmatz, W.T. Pike and J.D. Mai, "Low pressure and low temperature hermetic wafer bonding using microwave heating," *Proc. of IEEE MEMS Conf.*, 490-492 (1999).

[6] Y.T. Cheng, L. Lin and K. Najafi, "Localized silicon fusion and eutectic bonding for MEMS fabrication and packaging," *IEEE J. Microelectromech Syst.,* 9, 3-8, (2000).

[7] H. Yang, M. Wu and W. Fang, "Localized induction heating solder bonding for wafer level MEMS packaging," *J Micromech. & Microengineering*, 15, 394-399, (2005).

EFFECT OF THE NONLINEAR ELECTROSTATIC ACTUATION FORCE ON THERMOELASTIC DAMPING/QUALITY FACTOR IN MEMS

Sudipto K. De and N. R. Aluru
Department of Mechanical & Industrial Engineering
Beckman Institute for Advanced Science and Technology
University of Illinois at Urbana-Champaign, IL

ABSTRACT

MEMS (microelectromechanical systems) with very high quality factors are essential for several applications like ultra-fast and high precision actuators and sensors. Thermoelastic damping is a fundamental dissipation mechanism that always imposes an upper limit on the quality factor of these devices and needs to be understood properly for the accurate prediction of the quality factor. The general theory of thermoelastic damping developed by Zener [**1**] and later modified by Lifshitz and Roukes [**2**] has been used extensively for studying thermoelastic damping in MEMS. The general theory is applicable for MEMS beams undergoing simple harmonic oscillations in the flexural mode. However, under electrostatic actuation, which is the most popular mode of actuation in MEMS, the nature of the thermoelastic damping in MEMS can be significantly different from that predicted by the general theory of thermoelastic damping. This is due to the nonlinear coupling between the electrostatic force and the displacement of the microstructure giving rise to complex oscillations. The general theory of thermoelastic damping is modified in this paper for predicting thermoelastic damping in MEMS under arbitrary electrostatic actuation forces.

INTRODUCTION

MEMS devices are being developed for a variety of applications like accelerometers [**3**], inertial sensors [**4**], chemical sensors [**5**] and RF filters/oscillators [**6**]. In most of these applications, having a high quality factor results in reduced readout errors, lower power requirements, improved stability and increased sensitivity. Thermoelastic damping (TED) [**1**] is one of the fundamental dissipation mechanisms that is inherent to the system (cannot be completely eliminated by improved design or fabrication) and is found to impose an upper limit on the quality factor of MEMS devices [**2**]. The effect of thermoelastic damping on the quality factor of MEMS devices has been studied extensively using both the general theory of thermoelastic damping [**1, 2**] for simple MEMS structures like microbeams [**7**] and also using finite element based physical level (thermomechanical) models for MEMS devices with complex geometries like gyroscopes [**8**], where the general theory (applicable for beams) is not accurate. In this paper, thermoelastic damping in MEMS under electrostatic actuation (the most commonly used mode of actuation in MEMS) is studied. The nonlinear electrostatic force can give rise to complex (non-simple harmonic) oscillations under normal operating conditions [**9**] for which cases thermoelastic damping cannot be predicted correctly using the general theory of TED. The general theory of TED is modified in this paper for the accurate prediction of thermoelastic damping/quality factor in MEMS under arbitrary electrostatic actuation. This modified theory can be conveniently (fast and accurate) used in the design and analysis of MEMS devices.

GENERAL THEORY OF THERMOELASTIC DAMPING

The general theory of thermoelastic damping developed by Zener [**1**] and later modified by Lifshitz and Roukes [**2**], has been used extensively to study the effect of TED on the quality factor of MEMS beams and is found to give good agreement with experimental results for simple harmonic oscillations in the flexural mode of the MEMS beams [**7**], [**10**]. According to the Zener's theory the quality factor due to thermoelastic damping of a beam undergoing simple harmonic motion in the flexural mode, Q_{TED} , is given by [**1**]

$$Q_{TED} = \frac{\hat{C}_p}{E\alpha^2 T_0}\frac{1+(\omega\tau_z)^2}{\omega\tau_z} \tag{1}$$

where E is the Young's modulus, α is the coefficient of thermal expansion, T_0 is the absolute temperature; $\hat{C}_p$ is the specific heat under constant pressure of the beam material and ω is the angular frequency of excitation. τ_z is the relaxation time of the first mode of vibration given by $\tau_z = b^2/(\pi^2\kappa)$ [**1**], where κ is the thermal diffusivity of the beam material and b is the beam thickness. Thus the expression $1/Q_{TED}$ (measure of the amount of energy dissipated) has a maximum value of $E\alpha^2 T_0/(2\hat{C}_p)$ when $\omega\tau_z = 1$. Zener's theory (Eq. 1) was made more accurate in [**2**] by Lifshitz and Roukes using the 1-D beam theory and 1-D heat conduction equation. The equation of motion for a beam under thermoelastic damping is given by [**2**]

$$\rho A\frac{\partial^2 U}{\partial t^2} + \frac{\partial^2}{\partial x^2}\left(EI\frac{\partial^2 U}{\partial x^2} + E\alpha I_T\right) = 0 \tag{3}$$

where ρ is the density of the beam material, A and I are the cross-sectional area and the mechanical contribution to the moment of inertia of the beam, respectively and U is the displacement of the beam in the y-direction. x axis is defined along the length of the beam and y and z axes are along the thickness and width direction of the beam, respectively. The term I_T (the thermal contribution to the moment of inertia) is given by

$$I_T = \int_A y\theta\, dy dz \tag{4}$$

where $\theta = T - T_0$ is the change in the temperature from the equilibrium temperature T_0. The linearized heat equation (assuming $\theta \ll T_0$) along the y-direction (temperature gradients along the other directions are assumed to be negligible) is given by [**2**]

$$\frac{\partial\theta}{\partial t} = \kappa\frac{\partial^2\theta}{\partial y^2} + y\frac{E\alpha T_0}{\hat{C}_p}\frac{\partial}{\partial t}\left(\frac{\partial^2 U}{\partial x^2}\right) \tag{5}$$

The coupled thermoelastic equations (Eqs. 3-5) are solved by assuming simple harmonic motion and substituting

$$U(x,t) = U_1(x)e^{i\omega t} \quad \text{and} \quad \theta(x,y,t) = \theta_1(x,y)e^{i\omega t} \tag{6}$$

into Eq. 5 and getting the temperature profile along the beam $\theta_1(x,y)$. The expression for the temperature profile is next substituted into Eq. 3 and a frequency dependent Young's modulus E_ω is obtained. The quality factor can be computed from the real and the imaginary parts of the E_ω (see [**2**] for details) as

$$Q_{TED} = \frac{\hat{C}_p}{E\alpha^2 T_0}\left(\frac{6}{\xi^2} - \frac{6}{\xi^3}\frac{\sinh\xi + \sin\xi}{\cosh\xi + \cos\xi}\right)^{-1} \tag{7}$$

where $\xi = b[\omega/(2\kappa)]^{1/2}$. Both these theories (the Zener's theory and the Lifshitz and Roukes's theory) are based on the assumption that the motion of the beam is simple harmonic and would fail to predict accurately the thermoelastic damping in beams under complex oscillations (non simple harmonic motions) which can be present under electrostatic actuation.

THERMOELASTIC DAMPING UNDER ELECTROSTATIC ACTUATION: MODIFIED THEORY

Electrostatic actuation in MEMS is realized by applying a potential difference (combination of a dc and an ac voltage) between the microstructure (for example, a micro-beam) and the ground plane. The electrostatic force generated is nonlinear in nature and can give rise to complex nonlinear oscillations of the microstructure [**9**], [**11**]. A modified theory is presented here to study the effect of these complex oscillations on thermoelastic damping/quality factor in MEMS under electrostatic actuation. The modified theory solves the coupled thermoelastic equations (Eqs. 3-5) by assuming

$$\begin{aligned} U(x,t) &= \sum_{N=0}^{NT} U_N(x) e^{iN\omega t} \\ \theta(x,y,t) &= \sum_{N=0}^{NT} \theta_N(x,y) e^{iN\omega t} \end{aligned} \tag{12}$$

where NT is the number of harmonics considered. The modified theory replaces Eq. 6 in the general theory by Eq. 12 for the expressions for the displacement $U(x,t)$ and the temperature profiles $\theta(x,y,t)$ in the beam. Substituting Eq. 12 into Eq. 5 gives

$$\theta_N(x,y) = \frac{\Delta_E}{\alpha}\frac{\partial^2 U_N(x)}{\partial x^2}\left[y - \frac{\sin(k_N y)}{k_N \cos(bk_N/2)}\right] \tag{13}$$

for $N > 0$, where $k_N = (iN\omega/\kappa)^{1/2}$, $\Delta_E = E\alpha^2 T_0/\hat{C}_p$ and $\theta_0(x,y) = 0$. I_T can be computed from Eqs. 4 and 13 as

$$I_T = \sum_{N=1}^{NT} \frac{I\Delta_E}{\alpha}\left[1 + f(N\omega)\right]\frac{\partial^2 U_N(x)}{\partial x^2} e^{iN\omega t} \tag{14}$$

which is substituted into Eq. 3 to obtain a frequency dependent Young's modulus $E_{N\omega}$ for each of the harmonics $N > 0$ as

$$E_{N\omega} = E\left[1 + \Delta_E\{1 + f(N\omega)\}\right] \tag{15}$$

and $E_{0\omega} = E.f(N\omega)$ in Eqs. 14 and 15 is given by

$$f(N\omega) = \frac{24}{b^3 k_N^3}\left[\frac{bk_N}{2} - \tan\left(\frac{bk_N}{2}\right)\right] \tag{16}$$

The stiffness and the damping constant of each of the harmonics K_N and C_N can be computed from the real and the imaginary part of the corresponding $E_{N\omega}$, respectively, using

$$K_N + iN\omega C_N = pE_{N\omega} \tag{17}$$

where p is a constant that depends on the type of beam (for example $p = 8EI/l^3$ for a cantilever beam of length l [**12**]). While the value of K_N is found to be negligibly affected by the thermoelastic effects and can be assumed to be equal to $K_N = K = pE$ (for example $8EI/l^3$ for a cantilever beam) for all values of N, the value of C_N is found to be

$$C_N = \frac{K\Delta_E}{N\omega}\left(\frac{6}{\xi_N^{\,2}} - \frac{6}{\xi_N^{\,3}}\frac{\sinh\xi_N + \sin\xi_N}{\cosh\xi_N + \cos\xi_N}\right) \tag{18}$$

for $N > 0$ and where $\xi_N = b[N\omega/(2\kappa)]^{1/2}$ (Note that $C_0 = 0$). At this point, a mass-spring-damper (MSD) model of MEMS is introduced into the modified theory (to compute the overall damping constant and quality factor) and is given by

$$M\ddot{u} + C\dot{u} + Ku = F_e = \frac{\varepsilon A V^2}{2(g-u)^2} \tag{19}$$

where M is the mass of the beam, C and K are the overall damping and stiffness constants of the beam, respectively, and F_e is the electrostatic force that depends on the undeformed gap g, the area A of the micro-beam facing the ground electrode, the displacement u, the permittivity of vacuum ε and the applied voltage V. A voltage of the form $V = V_{dc} + V_{ac}e^{i\omega t}$ is considered, where the real and the imaginary parts of $e^{i\omega t}$ corresponds to a cosine or sinusoidal ac excitation, respectively. Harmonic balance analysis [**13**] of Eq. 19 is done by substituting the expression

$$u = \sum_{N=0}^{NT} u_N e^{iN\omega t} \tag{20}$$

into Eq. 19 and the closed form expressions for u_N are obtained by equating the coefficients of $e^{iN\omega t}$ for $N = 0,1,2,\ldots,NT$ to zero. While M and K are known in the left hand side of Eq. 19, the thermoelastic damping force can be expressed in terms of C_N as

$$C\dot{u} = \sum_{N=0}^{NT} iN\omega C_N u_N e^{iN\omega t} \tag{21}$$

The closed form expression for u_N for $N > 2$ is given by

$$\begin{aligned} u_N = -[&-M\omega^2 \sum_{I=1}^{R} u_I^2 u_{P-2I}(P-2I)^2 \\ &- 2M\omega^2 \sum_{I=1}^{P-1} u_{P-I}(P-I)^2 \mathrm{T}(I) \\ &+ i\omega \sum_{I=1}^{R} C_{P-2I} u_I^2 u_{P-2I}(P-2I) \\ &+ i2\omega \sum_{I=1}^{P-1} C_{P-I} u_{P-I} \mathrm{T}(I) + K\sum_{I=1}^{R} u_I^2 u_{P-2I} \\ &+ 2K\sum_{I=1}^{P-1} u_I \mathrm{T}(P-I) - 2Kg\Gamma(P) - LKgu_{P/2}^{\,2}] \\ &\times [Mu_0^2\omega^2 P^2 - iC_P\omega u_0^2 P - 3Ku_0^2 + 2Kgu_0]^{-1} \end{aligned} \tag{22}$$

where $R = P/2-1$ and $L = 1$ when P is even and $R = (P-1)/2$ and $L = 0$ when P is odd. $T(I)$ is the summation of the combination of all possible pairs $u_J u_K$ for $J + K = I$ and $J < K$. u_0 is obtained in a closed form from the solution of the equation

$$(g-u_0)^3 - g(g-u_0)^2 + \frac{\varepsilon A V_{dc}^2}{2K} = 0 \tag{23}$$

and u_1 and u_2 are obtained as

$$\begin{aligned} u_1 &= -\frac{\varepsilon A V_{dc} V_{ac}}{(Mu_0^2\omega^2 - 3Ku_0^2 + 2Kgu_0 - iC_1 u_0^2\omega)} \\ u_2 &= \frac{2Mu_0u_1^2\omega^2 - 3Ku_1^2u_0 + Kgu_1^2 - \varepsilon AV_{ac}^2/2}{(4Mu_0^2\omega^2 - 3Ku_0^2 + 2Kgu_0 - i2C_2u_0^2\omega)} \end{aligned} \tag{24}$$

The overall damping coefficient can be computed from the total amount of energy dissipated per period ΔE using C and the values of C_N for $N = 0$ to NT, and equating them as

$$C = \sum_{N=0}^{NT} C_N \bar{u}_N^2 N^2 \left[\sum_{N=0}^{NT} \bar{u}_N^2 N^2 \right]^{-1} \tag{25}$$

where $\bar{u}_N$ is the absolute value of u_N. The quality factor of the system can be computed using the relation

$$Q_{TED} = \frac{2\pi E_{\max}}{\Delta E} = \frac{K\bar{u}_{\max}^2}{\omega \sum_{N=0}^{NT} C_N \bar{u}_N^2 N^2} \tag{26}$$

where $\bar{u}_{max}$ is the maximum absolute value of u in a period, computed from Eq. 20.

RESULTS

A silicon cantilever beam of dimensions: length = 200 μm, thickness = 5 μm and width = 10 μm, is considered and the effect of electrostatic actuation on the thermoelastic damping coefficient and quality factor of the beam is studied here by comparing the results obtained from the general theory and the modified theory. The material properties used for the beam are given in [7]. The resonant frequency of the beam is found to be 138 KHz and the dynamic pull-in voltage is 44.5 V from the MSD model. Considering the expression for the electrostatic force F_e given in Eq. 19, when the applied voltages are small (far off from pull-in), F_e can be written as

$$F_e \approx \frac{\varepsilon A}{2g^2}\left[V_{dc}^2 + \frac{V_{ac}^2}{2} + 2V_{dc}V_{ac}\sin(\omega t) - \frac{V_{ac}^2\cos(2\omega t)}{2} \right]$$

for sinusoidal excitation as $u \ll g$. Defining $r = V_{ac}/(V_{dc}+V_{ac})$, when the dc bias is dominant (dc operation) $r \rightarrow 0$ and when the ac voltage is dominant and the dc bias is zero (ac operation), r = 1. Fig. 1 shows the variation in QTED with the excitation frequency for (a) dc operation and (b) ac operation in the MEMS cantilever beam. Zener's model evaluated at $f = \omega/(2\pi)$ (the excitation frequency) matches with the modified theory for dc operation (where the motion is simple harmonic). For ac operation, Zener's model evaluated at $2f$ matches with the modified theory as the oscillations are still simple harmonic but at twice the excitation frequency.

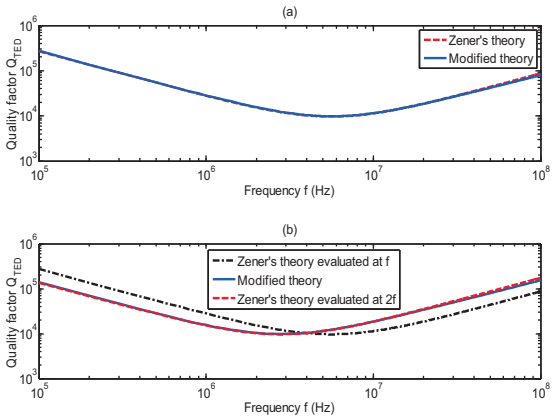

***Figure 1**. Comparison between the general and the modified theories under small applied voltages for (a) dc operation ($r \rightarrow 0$) and (b) ac operation (r=1).*

However, for intermediate values of r between 0 and 1, the electrostatic force F_e contains both the first and the second harmonic components of the excitation frequency. As a result, the oscillations also have both these two components in them giving rise to non simple harmonic oscillations for which case, the general theory of TED is expected to fail. The actual thermoelastic damping constant C and quality factor Q_{TED} in that case can be predicted by the modified theory as shown in Fig. 2.

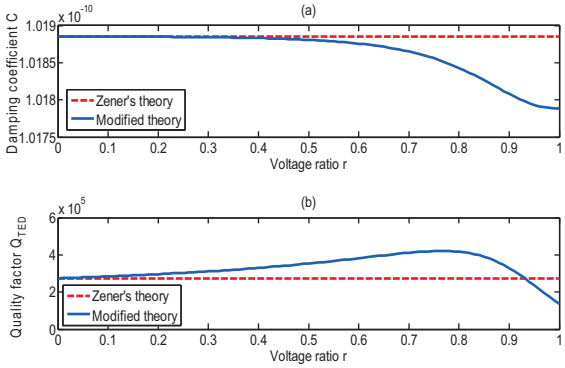

***Figure 2.** Variation in thermoelastic damping coefficient C and Q_{TED} in the MEMS beam at f = 100 KHz with r predicted by the general and the modified theories .r is varied by simultaneously increasing V_{ac} (.001 to 1) and decreasing V_{dc} (1 to 0) linearly.*

When the applied voltages are large (close to pull-in), the nonlinearity in the electrostatic force due to $F_e \propto 1/(g-u)^2$ becomes important and can give rise to complex oscillation [11]. These complex oscillations can significantly alter the values of the damping coefficient and quality factor as shown in Fig. 3 for the MEMS beam. The modified theory shows several spikes in the value of C and Q_{TED} as it varies with f at 42 V dc and 2.8 V ac. This is due to the presence of higher order harmonics (see Fig. 4) in the oscillations introduced by the $F_e \propto 1/(g-u)^2$ nonlinearity at these large voltages. Zener's model does not capture any of these spikes.

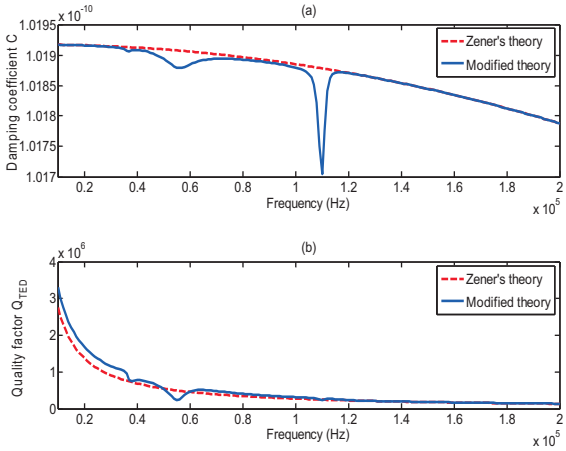

***Figure 3.** Variation in thermoelastic damping coefficient C and Q_{TED} in the MEMS beam with the ac excitation frequency f at a large dc bias of 42 V (near pull-in) and a large ac voltage of 2.8 V (near ac pull-in).*

Fig. 4(a) shows the harmonic balance analysis of the MSD model indicating the presence of several higher order harmonics in the oscillations of the MEMS beam at 42 V dc and 2.8 V ac. The

N-th harmonic is found to spike at the N-th superharmonic frequency other than at the resonant frequency (110 KHz at 42 V dc). As the different harmonics have different damping coefficients C_N (which are evaluated in the modified theory and shown in Fig. 4(b)), the overall damping coefficient/quality factor changes with the variation in the relative strengths of the different harmonics (the first ten harmonics were considered in our analysis).

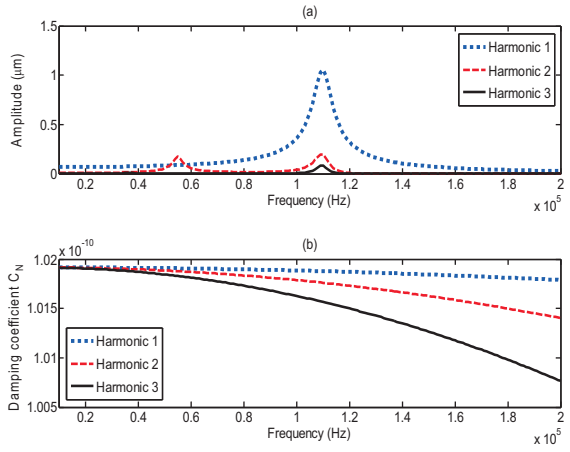

Figure 4. Variation in (a) strength of the harmonics with the excitation frequency from the harmonic balance analysis of the MSD model and (b) CN with the excitation frequency obtained from the modified theory.

As the ac voltage is gradually increased (from 0.001 V ac to 2.5 V ac) under the 42 V dc bias, the difference between the two theories start to become significant as shown in Fig. 5. In fact at 0.001 V ac, the modified theory and the general theory gives the same values of C as the higher order harmonics are not significant at such small ac voltages. As the ac voltage increases, the higher order harmonics become stronger and the modified theory deviates from the general theory of Zener/Lifshitz and Roukes (spikes are formed at the superharmonics of the excitation frequency).

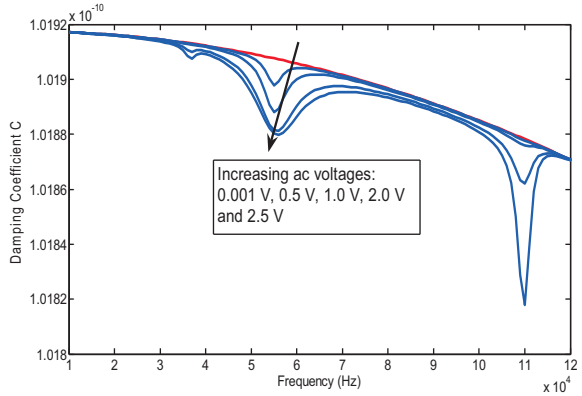

Figure 5. *Deviation of the modified theory from the general theory as the ac voltage increases at 42 V dc in the MEMS cantilever beam. As the ac voltage increases, the higher order harmonics in the oscillations become stronger forming the spikes in variation of C with the excitation frequency f.*

CONCLUSIONS

The general theory of thermoelastic damping is modified in this paper for application to electrostatic MEMS. The nonlinear electrostatic force present under electrostatic actuation can give rise to complex oscillations in the system which cannot be accounted for by the general theory (based on simple harmonic oscillations). The modified theory takes into account these higher order harmonics present in the oscillations due to nonlinear electrostatic force to compute the overall damping coefficient and quality factor accurately.

This work is supported by the National Science Foundation under Grant numbers 0121616, 0217986 and 0228390.

REFERENCES

[1] C. Zener, "Internal Friction in Solids I: Theory of Internal Friction in Reeds", *Physical Review*, *53*, 90 (1938).

[2] R. Lifshitz and M. L. Roukes, "Thermoelastic Damping in Micro- and Nanomechanical Systems", *Physical Review B*, *61(8)*, 5600 (2000).

[3] H. Luo, G. K. Fedder, and R. Carley, "A 1 mG Lateral CMOS-MEMS Accelerometer", *13th Annual Intl. Conf. on Micro Electro Mechanical Systems, MEMS 2000*, Miyazaki, Japan, 01/23-27/00, IEEE, New York (2000), pp. 502 - 507.

[4] N. Yazdi, F. Ayazi, and K. Najafi, "Micromachined Inertial Sensors", *Proc. of the IEEE*, *86(8)*, 1640 (1998).

[5] M. S. Weinberg, B. T. Cunningham and C. W. Clapp, "Modeling Flexural Plate Wave Devices", *J. of Microelectromechanical Systems*, *9(3)*, 370 (2000).

[6] C. T. -C. Nguyen, "Micromechanical Resonators for Oscillators and Filters", *Proc. of the 1995 Ultrasonics Symposium*, Seattle, WA, 11/07-10/95, IEEE, New York (1995), pp. 489 - 499.

[7] T. V. Roszhart, "The Effect of Thermoelastic Internal Friction on the *Q* of Micromachined Silicon Resonators", *Technical Digest of the 1990 Solid-State Sensor and Actuator Workshop,* Hilton Head Isl., SC, 06/04-07/90, IEEE New York (1990), pp. 13 - 16.

[8] A. Duwel, J. Gorman, M. Weinstein, J. Borenstein and P. Ward, "Experimental Study of Thermoelastic Damping in MEMS Gyros", *Sensors and Actuators A*, *103*, 70 (2003).

[9] S. K. De and N. R. Aluru, "Full-Lagrangian Schemes for Dynamic Analysis of Electrostatic MEMS", *J. of Microelectromechanical Systems*, *13(5)*, 737 (2004).

[10] K. Y. Yasumura, T. D. Stowe, E. M. Chow, T. Pfafman, T. W. Kenny, B. C. Stipe and D. Rugar, "Quality Factor in Micron- and Submicron-Thick Cantilevers", *J. of Microelectromechanical Systems*, *9(1)*, 117 (2000).

[11] S. K. De and N. R. Aluru, "Complex Oscillations and Chaos in Electrostatic MEMS Under Superharmonic Excitations", *Physical Review Letters*, *94*, 200401 (2005).

[12] E. G. Popov, "Engineering Mechanics of Solids", Prentice-Hall (1997).

[13] A. T. Nayfeh and D. T. Mook, "Nonlinear Oscillations", John Wiley & Sons (1979).

EVALUATION OF O_2 PLASMA AND XeF_2 VAPOR ETCH RELEASE PROCESSES FOR RF-MEMS SWITCHES FABRICATED USING CMOS INTERCONNECT TECHNOLOGY

Christopher V. Jahnes, Nils Hoivik, John M. Cotte, Minhua Lu, and John H. Magerlein
IBM T. J. Watson Research Center
Yorktown Heights, NY 10598

ABSTRACT

This paper evaluates two commercially available dry etch processes for releasing integrated RF MEMS devices. The first is an oxygen microwave plasma removal of a Diamond-Like Carbon (DLC) sacrificial layer and the second is a XeF_2 vapor phase removal of an amorphous silicon (a-Si) sacrificial layer. The studied techniques were selected for compatibility in fabricating monolithically integrated RF-MEMS devices within the interconnect levels of CMOS and Bi-CMOS technologies. To determine the etch rate of the sacrificial release layer, test wafers were fabricated using a simple 1-mask lithography level that allows direct observation of the release etch through a dielectric membrane. Effects relating to changes in the release etch rate are documented and discussed. Additionally, the ability of XeF_2 to extract sacrificial layers through small via holes, and bulk vs. thin-film etching of a-Si for MEMS release etches are presented. The results of this study demonstrate that both oxygen microwave plasma removal of DLC and XeF_2 vapor phase etch of a-Si can be used to manufacture RF-MEMS devices using high volume CMOS interconnect manufacturing processes.

INTRODUCTION

A common process element in the fabrication of MEMS devices is the removal of a sacrificial layer to release the micromechanical device from a substrate. Ideally the release process removes the sacrificial layer quickly and cleanly without altering the micromechanical element. In a more specific application, such as integrating RF-MEMS devices in CMOS interconnect levels [1-2], the release process must also not degrade the existing structure or devices. While many processes exist to remove sacrificial layers [3], we have studied XeF_2 etching of Si sacrificial layers and O_2 microwave plasma etching of Diamond-Like-Carbon (DLC) sacrificial layers. Both of these techniques work well in the aforementioned application where the sacrificial layer is typically less than 1.0 μm thick and the micromechanical beam is primarily SiO_2. In addition, Si and DLC are compatible with CMOS fabrication lines and can be deposited by many different techniques. The commercially available process tools used to perform the release etch are an Applied Materials APS + chamber for the O_2 microwave plasma process and a Xactix X3 Xetch ® system.

The efficiency of the release etch can be influenced by geometric relationships that evolve as micromechanical structures are being released. Even small displacements of the micromechanical beams during the release etch can have significant effects. In this report we have fabricated structures to facilitate evaluation of both XeF_2 and O_2 microwave plasma release etching processes. The test devices were made identical to compare the two processes and gain a general understanding of the etch behavior. Structures to evaluate release etching of a sacrificial layer through via holes and of bulk Si sacrificial layer etching were also explored. For demonstration purposes, fully integrated RF-MEMS CMOS integrated switches were fabricated and tested to verify compatibility of these processes with interconnect structures. Both techniques resulted in MEMS switches with insertion loss < 0.5 dB.

EXPERIMENTAL DETAILS

The test samples used to evaluate the two release etch processes are shown in Figure 1 with optical photographs of an example device before and after the release etch. The fabrication process for these samples is as follows: for the a-Si release samples, the Si wafer is first thermally oxidized to form a 100 nm thick SiO_2 layer to protect the Si wafer from being etched in the XeF_2 process. For the DLC samples the thermal oxide layer was not required. The next step is to form the sacrificial layer which for DLC was deposited by PECVD with post 400 °C annealing and the a-Si samples were deposited by DC sputtering. After the sacrificial layer deposition, the dielectric membrane was deposited. For the a-Si release structures a single layer of PECVD SiO_2 1000 nm thick was deposited at 400°C. In the case of the DLC a sandwich structure of SiN 35 nm/SiO_2 1000 nm/SiN 35 nm was deposited by PECVD at 400°C. SiN is required to gain good adhesion between the DLC and SiO_2. To minimize stress distortion a top layer of SiN was added to "balance" the stress gradient of the structure. Lastly, the samples are coated and patterned with photoresist, etched with RIE to open the dielectric stack down to the release layer and the resist is then stripped in-situ with an O_2 plasma. The O_2 resist strip process does remove the DLC in the open areas but is timed such that no detectable undercut occurs.

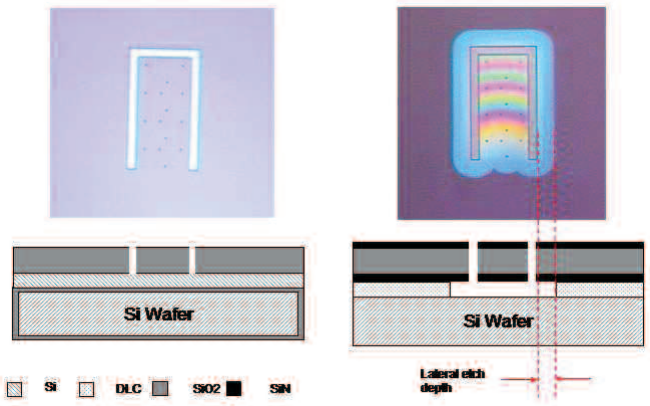

Figure 1. *Top: Optical photos of structures prior to release (left) and after release (right). Bottom: Schematic view of silicon test vehicle (left) and DLC release (right).*

O_2 MICROWAVE PLASMA RELEASE ETCH

An Applied Materials APS+ microwave strip chamber was used to perform the O_2 microwave plasma release etches. The chamber uses IR lamps to directly heat the wafer which is placed slightly downstream of the waveguide that introduces the microwave into the chamber [4]. Key advantages to this platform for etching are the lack of ion bombardment to minimize sputtering effects and the application of heat to enhance the etch rate of the DLC. In these experiments wafer pieces were used and placed on a 200 mm wafer to allow for simultaneous processing on different structures. In all cases the gas chemistry was kept constant (O_2 3000 sccm and N_2 200 sccm) at a total pressure of 2 Torr.

Two sets of samples were fabricated to optimize the O_2 microwave plasma release process. The first set was made with a 300 nm DLC sacrificial layer. After release, the membrane was under slight tensile stress, and had very little stress related distortion. In the second set of samples, a range of DLC thicknesses was deposited (100 nm. 200 nm, 400 nm and 800 nm) to evaluate the release etch rate as a function of sacrificial layer thickness. However, the dielectric membrane for these samples was deposited using a different PECVD reactor and upon release were found to have highly distorted membranes. This was later determined to be from a temperature variation during the PECVD SiO_2 deposition that increased the compressive stress of the dielectric membrane and added a negative stress gradient within the SiO_2 layer.

As a result, upon release the membrane deflected downward towards the substrate, as shown for the device in Figure 2A. This deformation effectively narrows the release gap and causes an uneven removal of the sacrificial layer. High temperature annealing (450 ^oC) was used to minimize the stress magnitude and gradient to the point where the etch front was uniform. The stress effects were still apparent however as shown in Figure 2B. For comparison the device shown in Figure 2C is from the first sample set with a 3000 nm DLC sacrificial layer, and with a slightly tensile membrane and no stress gradient. White light interferometric measurements were used to measure the membrane deflection at mid length of the cantilever for samples after 10 min O_2 microwave plasma etch. A deflection of 10 nm to 50 nm towards the substrate was observed for the set of samples with stress related distortions, and no deflection was detected for the sample that was free of stress related distortions.

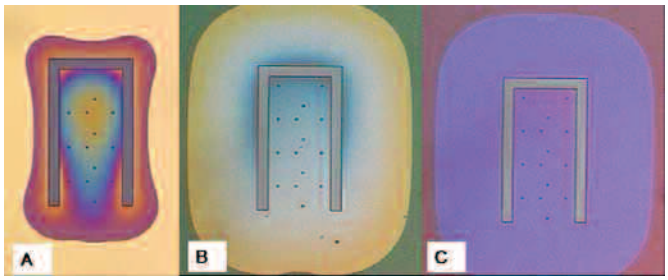

Figure 2. *Optical photograph of released test samples (cantilever 27 μm x 60 μm). Deformations in A shows a highly stressed membrane with uneven release front in as-deposited membrane. After annealing, sample B (with a 400 nm DLC sacrificial layer) demonstrates a reduced compressive stressed membrane. Sample C has a 300 nm DLC sacrificial layer, tensile membrane with no stress gradient and no stress related distortion.*

To optimize the O_2 microwave release process, wafer temperature and microwave power were varied. Shown in Figure 3 is a plot of the lateral undercut depth as a function of wafer temperature. As expected, the etch rate increases rapidly with increasing temperature, reaching rates as high as 6 μm/min. All the samples appear to have equal release etch rates until temperatures above 250 ^oC. The difference in lateral etch rate at higher temperatures may be due to diffusion limiting effects. In addition, deflection in the released membrane, which is larger for these deep undercuts, may play a significant role.

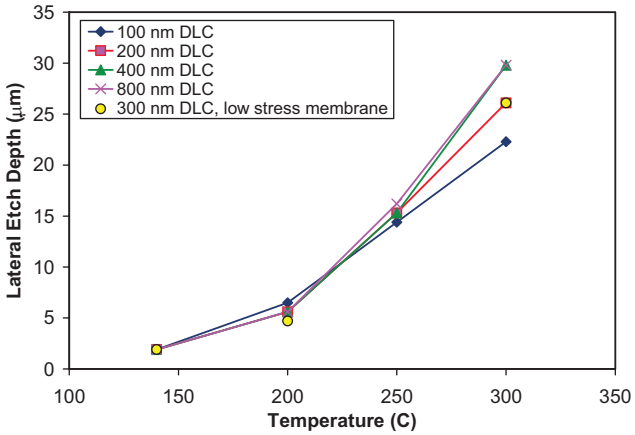

Figure 3. *Plot of lateral etch depth vs. wafer temperature during O_2 plasma microwave release at 1400 W for a 5 min. release etch.*

The effect of microwave power on the release etch rate is shown in Figure 4. A near linear increase in rate was observed up to 500 W, after which the release etch rate slowed and eventually remained constant. At this point the plasma may be at a critical density and not increase [5]. Another possible explanation for the release rate to level off would be if physical sputtering were occurring, acting as to mask the release layer. However no SiO_2 loss was observed for a 25 min 1400 W etch.

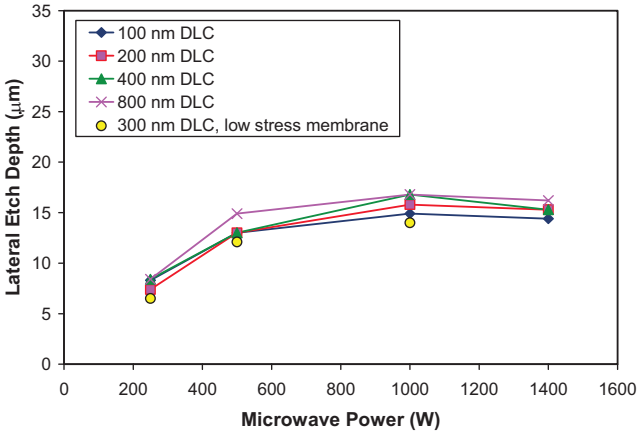

Figure 4. *Plot of release etch vs. microwave power for O_2 microwave plasma etch at 250 ^oC for 5 min.*

XeF_2 RELEASE ETCH

All Si etching experiments were performed using an X3 Series XeF_2 etching system manufactured by Xactix [6]. The XeF_2 etching is a gas phase process with no plasma and is performed at room temperature (although the Si etching process is exothermic in nature [7]). The XeF_2 release etch is a cyclical process where XeF_2 gas is introduced into a process chamber, allowed to react for a pre-determined dwell time, and pumped out. Gas pressure is established in a separate expansion chamber prior to introduction into the process chamber. The process chamber pressure is 3.4 times lower than the pressure reported here which is measured in the expansion chamber. The amount of Si etched can be controlled by the number of pulses, as well as XeF_2 pressure and concentration using N_2 as a dilutant. The samples etched for each experiment had Si exposed over 1.6% of the top surface dielectric area, and were 2x2 cm chips with the Si wafer edge exposed (a total of 0.66 μm^2). The a-Si sacrificial layers were 100, 200, 400, 600, 800 or 1000 nm thick. These samples were also annealed at 450 ^oC prior to release to reduce the as-deposited stress gradient. After release, the deflection for a 60 µm long cantilever was ~ 1 µm.

Due to the large selectivity between Si and SiO_2, all samples were etched in DHF (100:1) for 15 sec followed by a DI water rinse to remove any native oxide from the Si layer. Samples which did not receive this pre-processing step required an additional 20-30 cycles of XeF_2 in order to break through the native oxide before any etch could be observed [7]. The etch rate of thermal SiO_2 was measured to be ~60A for 20 cycles with 1.5T XeF_2 and 10T N2.

To study the effect of XeF_2 concentration on the release etch rate, two sets of samples were run at 1.5 and 3.0 Torr. A higher XeF_2 concentration is expected to lead to a faster etch rate as illustrated in Figure 5. However the release etch rate increased far more than expected. It is known that the XeF_2 etch is not 100 % efficient [7] and this data suggests the efficiency is pressure dependent. The decrease in release rate at high pressure for thinner sacrificial layers is likely diffusion related. Similar dependencies on aperture vs. lateral etch depth for thin film etching were reported for 3 Torr XeF_2 etches [7].

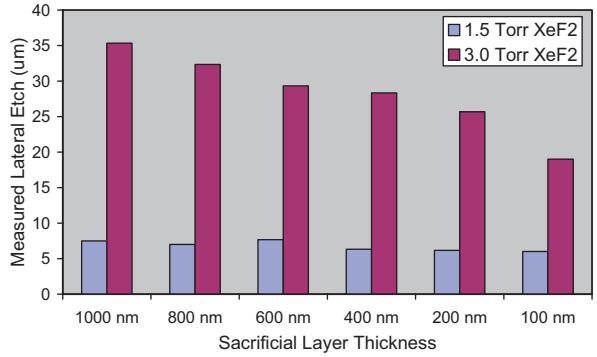

Figure 5. *Measured lateral etch rate with varying XeF_2 pressure. Both sets were run for 10 cycles, each 30 sec.*

Lateral etch rate was also measured as a function of dwell time by varying the dwell time from 5 to 60 sec for three sacrificial layer thicknesses. As seen in Figure 6, the amount of etching is relatively independent of dwell time. From this experiment is evident that the etch process happens in the first few seconds upon exposure of Si to XeF_2. The independence of exposure time was also observed for samples etched with 3.0 Torr XeF_2. This observation contradicts earlier reports on an increase in lateral etch of poly-Si with increasing pulse duration [7]. Furthermore, no pressure increase was observed in the process chamber during the etch process. As presented, this data supports a self-limiting effect or a reactant limited etch process. More experiments are in progress to determine this more accurately.

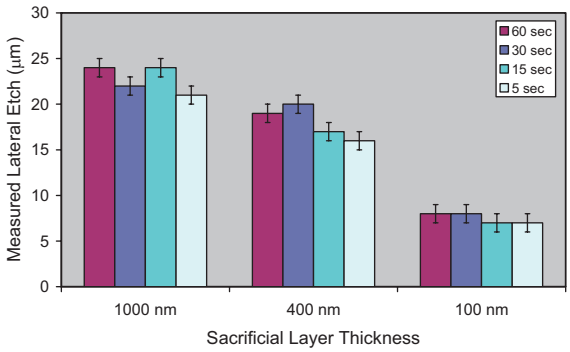

Figure 6. *Measurement on effect of cycle time on lateral etch rate. The cycle time was varied between 5 – 60 sec. for 40 cycles 1.5 Torr XeF_2.*

Adding nitrogen to raise the process pressure resulted in an increase in overall release etch rate with a maximum observed for 10 Torr N_2 and 1.5 Torr XeF_2 as shown in Figure 7. The additional nitrogen pressure increased the reaction rate of the physisorbed XeF_2 by as much as a factor of 3 while it also enhanced limited reactions.

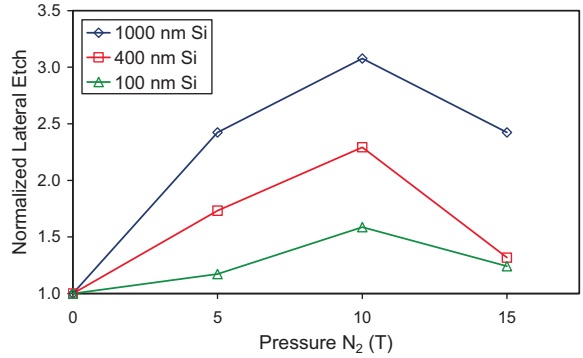

Figure 7. *Measured normalized effect of N_2 pressure on lateral etch rate. Maximum etch rate is obtained for with N_2 pressure of 10 Torr (10 cycles, 30 sec 1.5 Torr XeF_2)*

To compare bulk Si etching, samples were prepared with a single layer of patterned thermal SiO_2. Figure 8 shows a comparison between lateral etch rate for a thin film and bulk sacrificial layer. The lower undercut rate for a bulk release is not unexpected since more material is being removed, and should be factored in when releasing MEMS devices from a bulk Si-substrate. Thus, devices which depend on dielectrics and metals with low etch selectivity to Si should utilize a thin film over bulk release process as to minimize the exposure to XeF_2.

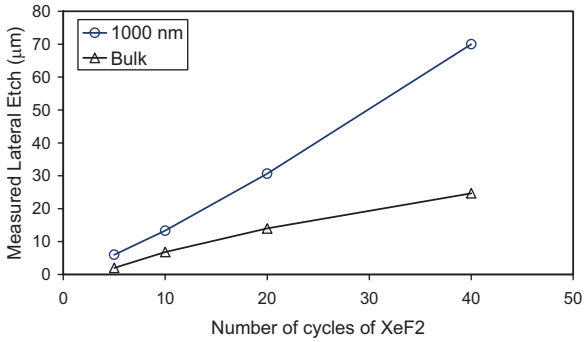

Figure 8. *Comparison of lateral etch rate of a thin-film to a bulk release process. 30 sec pulses, 1.5 Torr XeF_2 – 10 Torr N2*

COMPARISON OF RELEASE PROCESSES

Figure 9 shows a comparison between the O_2 and XeF_2 release process. For the O_2 release process, the effective etch rate decreases with lateral etch depth. This is caused by the effective surface area increase of DLC as the release etch depth increases. The flux of excited O_2 species entering the release area is determined by the geometry of the membrane cutout, which remains constant. Both release processes show a decrease in etch rate for a thin sacrificial layer, due to diffusion limitations and stress related deformation of the structural layer. It is important to note that most RF-MEMS devices typically need about 10 μm to 20 μm of a lateral etch to fully release all devices.

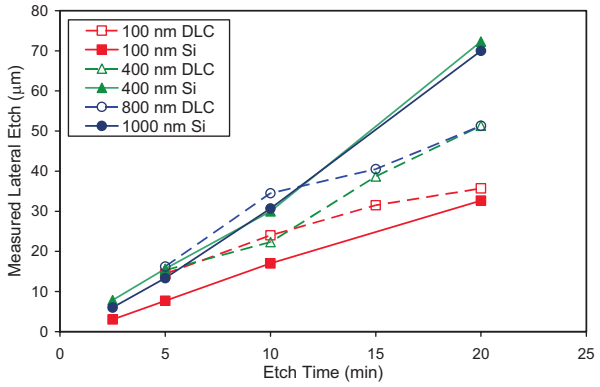

Figure 9. *Comparison of lateral etch depth vs. etch time for a 250 °C 1400 W O_2 microwave plasma and 30 sec pulsed 1.5 Torr XeF_2 – 10 Torr N_2 Si release process.*

Release can also be carried out through a dielectric film with small holes, which may subsequently be pinched off for wafer-level packaging by thin-film encapsulation. This was previously described in detail for the DLC process using the O_2 plasma release process [1]. Figure 10 shows SEM pictures of a sacrificial layer removal using XeF_2 dry etch to extract a 300 nm thick a-Si film through 0.25 μm diameter x 1.0 μm tall holes in a 1 μm thick SiO_2 film.

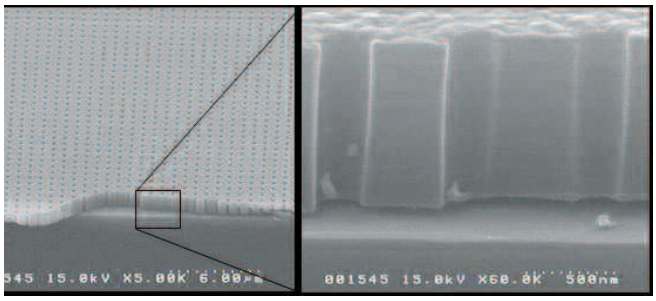

Figure 10. *SEM image of cleaved sample of hole grid pattern for XeF_2 a-Si release through a top dielectric layer with 0.25-um wide holes 1.0 μm tall. The nominal gap is 300 nm.*

SUMMARY

The results of this study demonstrate that both O_2 plasma removal of DLC and XeF_2 vapor phase etch of a-Si can be used to manufacture RF-MEMS devices using high volume CMOS interconnect manufacturing processes. Both techniques can extract a sacrificial release layer through small vias, which is a requirement for thin-film encapsulation packaging of RF-MEMS devices at wafer level. For large lateral undercuts (>20 μm), XeF_2 is superior as compared to microwave plasma etching as the release rate decrease is less pronounced. Measured RF performance of ohmic switches fabricated both with DLC and Si release layers have demonstrated excellent RF characteristics.

ACKNOWLEDGEMENTS

The authors wish to thank Roy Carruthers and Blake Lin for sample preparation, and Kyle Lebouitz from Xactix Inc. and Glenn Laliberte from Applied Materials Corporation for their technical assistance with the commercial release etch process tools used for this study.

REFERENCES

[1] Jennifer L. Lund et al. "A Low Temperature Bi CMOS Compatible Process for MEMS rf Resonators and Filters", *Solid-State Sensor, Actuator and Microsystems Workshop, Hilton Head Island*, June 2-6, 2002.

[2] C. V. Jahnes et al. "Simultaneous Fabrication of RF MEMS Switches and Resonators using Copper-based CMOS Interconnect Manufacturing Methods", *MEMS 2004 Technical Digest, Jan 25-29,* pp 789 – 792.

[3] Micromachined Transducers Sourcebook, 1 Edition 1998, Gregory T. Kovacs.

[4] www.appliedmaterials.com

[5] Thin Film Processes II, 1991, edited by John L. Vossen, Werner Kern.

[6] www.xactix.com

[7] Patrick B. Chu et al. "Controlled Pulse-Etching with Xenon Difluoride", Transducers 1997, Chicago June 16-19, pp 665 – 668.

FORCE-DISTANCE SPECTROSCOPY: A GENERIC METHOD TO DETERMINE THE YOUNG'S MODULUS OF FREESTANDING NANOSTRUCTURES

N. Duarte[1], Q. Xiong[2,3], S. Tadigadapa[1], P.C. Eklund[2,3]
[1]Department of Electrical Engineering, [2]Department of Physics, [3]Department of Materials Science and Engineering
The Pennsylvania State University, University Park, PA16802 United States

Abstract:

We report here the determination of Young's modulus of bottom-up synthesized nanowires. AFM force-distance spectroscopy was performed at the mid-point of nanowire bridges fabricated using microfabrication techniques. The deflection per unit force was calculated from the difference in slope of the force distance curve on the nanowire bridge and a non-deformable surface. Young's modulus of the nanowires was subsequently deduced from the solution of the first mode of the Euler-Bernoulli beam equation with fixed-fixed boundary condition and a concentrated point load at the mid-point. The dimensions of the bridge were determined from atomic force microscopy (thickness) and field-emission scanning electron microscopy (length and width). We believe this method provides significant improvements on previously reported methods and can be used in any other nano-beam systems to measure their mechanical properties.

Introduction:

Understanding of mechanical properties of nanoscale materials, such as nanotubes or nanowires (NWs/NTs) is essential for their applications in nanomechanics [1], NEMS devices [2], sensors [3], and nano- electronic [4, 5]. Unfortunately many macroscopic techniques for measuring mechanical properties, e.g., tensile test, cannot be done routinely at nanoscale. As a result, nanomechanical measurements still remain a challenge and advances in reliable methods to perform these measurements are currently needed.

Atomic force microscopy (AFM) based techniques play a key role in such measurements. Wong et al. [6] first reported elegant utilization of lateral force microscopy (LFM) to determine Young's modulus of single clamped non-suspended silicon carbide nanorods and multiwall carbon nanotubes (MWNTs). Song et al. [7] also used LFM to measure the elastic modulus of vertically aligned ZnO nanowires. Due to the uncertainty in the lateral dimensions, length, and cross-section of the nanowires intrinsic to this method, the measured values of Young's modulus showed fairly large variation [7]. However, for vertically aligned nanostructures with short length and low density, this method can be a convenient approach. Salvetat et al. showed that bending of MWNTs [8] or single-walled carbon nanotubes (SWNTs) ropes [9] could be measured under contact-mode AFM, allowing the extrapolation of both elastic and shear moduli.

Recently, nanoindentation has emerged as an alternative technique to measure the Young's modulus and hardness of materials such as ZnS nanobelts [10] and silver nanowires [11]. Nanoindentation is basically an AFM-based method, in which a diamond cantilever is used first as an imaging probe to locate the NWs, and then is used to indent the NWs in-situ. Force-displacement curves can be obtained for both load and unload situations and the morphology of the indent can be scanned sequentially. The hardness is given by analysis of the indentation and the Young's modulus is obtained from the unloading force-displacement curve [11]. The main benefits of this technique are that it does not require clamping on the ends of NWs and gives a quantitative measurement of hardness at nanoscale. In general however, it is not a satisfactory technique due to its destructive nature and the uncertainty in relating the sort of deformation (dislocation or plastic) occurring in the nanomaterials to the Young's modulus and hardness.

In this paper, we report a generic, AFM-based method to measure the Young's modulus of nanowires, using ZnS nanowires as an example. We have successfully fabricated clamped-clamped suspended nanobridges on Si substrates by standard microfabrication techniques. AFM was then used to locate the nanobridge and force-distance (FD) spectroscopy was performed at the middle point of the nanobridge. The slope of the FD curve obtained on the nanowire bridge can be compared with that obtained on non-deformable substrates to obtain the Young's modulus. The interaction between the nanobridge and the AFM tip was modeled by the Euler-Bernoulli beam equation with a fixed-fixed boundary condition and a concentrated point load. The Young's modulus of the nanowire was then deduced after an accurate determination of the bridge dimensions using AFM (thickness) and field-emission scanning electron microscopy (FESEM) (length and width). For the example of ZnS nanowires, the measured Young's modulus ranged from 45-65 GPa, which is about 10-20% smaller than that of the bulk. We believe this method can be used for any other nano-beam systems to measure their mechanical properties. ZnS nanowires were chosen as our study material because, as they have electroluminescent properties, they promise to be important in creating nanoeletronic and nano-optic devices [13].

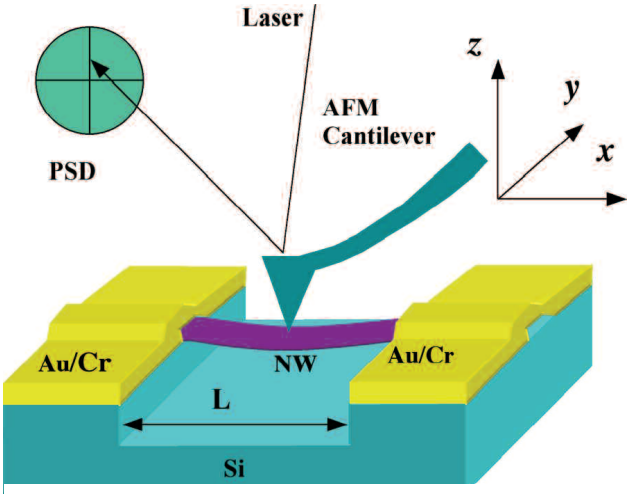

Figure 1: Schematic diagram of force-distance spectroscopy on a nanobridge. The nanobridge, which is fixed by Au/Cr thin films at both ends. is across a trench in Si substrates.

Fabrication:

Nanowire nanobridges, shown schematically in Figure 1, were fabricated by dispensing bottom-up synthesized nanowires on a silicon wafer, followed by definition of end-clamping pads by microfabrication and a final vapor phase XeF_2 vapor phase release. The ZnS nanowires were grown by pulsed laser vaporization method [12] and exhibit wurtzite structure with a rectangular cross section and lengths of more than ten microns.

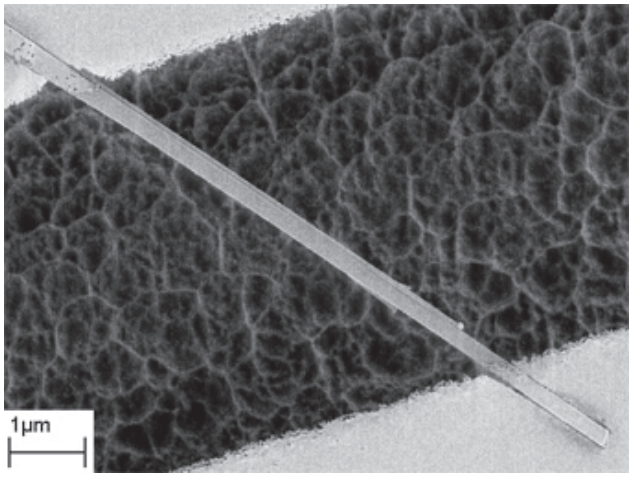

Figure 2: FE-SEM of an actual nanobridge

Details about growth and characterization of these nanowires with SEM, high-resolution TEM, and selective-area electron diffraction can be found elsewhere [13, 14]. The as grown nanowires were then dispersed into ethanol by ultrasonication to obtain a metastable suspension. Several drops of this suspension were dispersed by spin coating onto a clean and native oxide removed silicon substrate. The Si substrate with ZnS nanowires was then dehydration baked for 5 minutes at 200°C on a hot plate. Lift-off photo resist LOR-1A (Microchem Corp.) was applied to the substrate and spun for 1 minute at 2,000 RPM, resulting in about 150 nm in thickness. A soft bake at 180°C for 5 minutes on the hot plate followed. Subsequently, photo resist SPR-3012 was applied to the substrate and spun for 1 minute at 4,000 RPM, resulting in a thickness of about 1,200 nm. The wafer was soft baked at 100°C for 1 minute. After exposure and development, in MF-CD-26, the samples were transferred into an e-beam evaporator where 10 nm Cr and 40 nm Au films were deposited sequentially. Lift-off was carried out in 60°C bath of Remover PG (Microchem Corp.). Finally, XeF_2 etching was carried out to release the nanowire and a trench with a depth of ~ 500 nm in Si substrate was achieved. Figure 2 shows an FESEM (Leo 1530) image of the resulting nanobridge. The image shows that the etched surface in the trench is locally uniform and the bridge is clear of other materials. The depth of the trench is important since if the trench is too deep, the nanobridge may become unclamped. If the trench is too shallow, there might be some residual supporting pillars underneath the nanobridge, which will result in erroneous FD spectroscopy measurements. From our experiments, we believe 500 - 1000 nm depth is sufficient. Our device structure looks similar to a recent report on mechanical properties of Au nanowires [15], however it should be noted that report used focused ion beam milling to define the trench, followed by deposition of the nanowires, AFM manipulation to position the nanowires, and e-beam induced deposition of platinum clamping pads. Our method is significantly simpler and provides higher yield as there is no risk of nanowires falling into the trenches during manipulation.

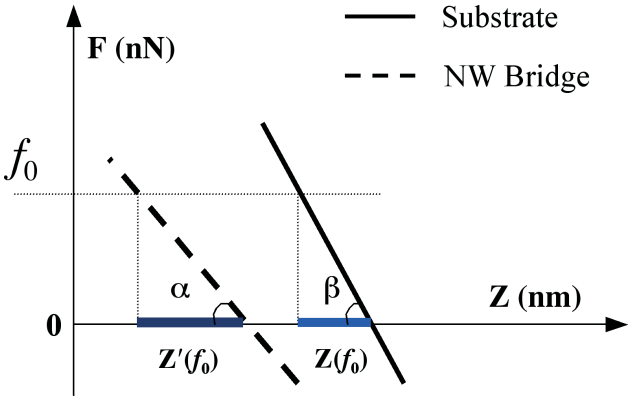

Fig.3: Ideal linear part of the force-distance (FD) spectra.

Method:

The principle of performing FD spectroscopy on a nanobridge is illustrated in Fig. 1. The nanobridge was first located under contact-mode AFM. Then the AFM cantilever, with a calibrated force constant of 0.13-0.17 N/m, was brought into contact with the middle point of the nanobridge where FD spectroscopy was performed. To avoid breaking the nanobridge, the amount of total force and Z-scanner range was limited.

Typical FD curves show the approaching (non-contact), jumping to contact due to van der Waals forces or capillary forces (snap-on), contact, adhesion and pull-off characteristic regimes [16]. For a hard and non-deformable sample, the slope of the FD curve in the contact regime gives the spring constant of the AFM cantilever. Figure 3 shows a schematic diagram of the linear part of FD curves obtained on a non-deformable substrate (solid line) and a deformable substrate, e.g., the nanobridge. The deflection of the nanobridge at a certain force is given by, $\Delta Z = Z'(f_0) - Z(f_0)$ indicated on the horizontal axis.

For the nanobridge, due to its elastic compliance, the *Z*-scanner moves further for the same applied force. As a result, the FD curves obtained from a deformable substrate have smaller apparent slope, as indicated by dashed line. The deflection of the nanobridge at a certain force f_0 is given by:

$$\Delta Z = Z'(f_0) - Z(f_0) = \frac{f_0}{\tan\alpha} - \frac{f_0}{\tan\beta} \quad (1)$$

where $\tan\alpha$ and $\tan\beta$ are the slopes of the FD curves in the linear contact regime. The force per unit deflection is:

$$\frac{f_0}{\Delta Z} = \frac{\tan\alpha \tan\beta}{\tan\beta - \tan\alpha} \quad (2)$$

The out-of-plane displacement Z of the nanowire bridge, upon the application of the point load due to the AFM cantilever tip, can be characterized by the Euler-Bernoulli beam equation [17]:

$$EI\frac{d^4Z}{dx^4} = f\delta(x - x_0) \quad (3)$$

where E is the Young's modulus, I is the area moment of inertia and x_0 is the position of the load. The coordinates have been defined in Figure 1. The assumption made is that E and I do not change along the length of the beam. The area moment of inertia, I, is $\pi d^4/64$ for a cylindrical beam with a diameter of d, whereas for a rectangular beam with a width w and a height h $I = wh^3/12$ [18]. Using the fixed-fixed boundary condition, the solution to Eq. (3) is given by [17]:

$$Z = -\frac{fx^2}{48EL}(3L - 4x), (0 \le x \le L/2) \quad (4)$$

where L is the total length of the nanobridge, which can be measured from AFM and FESEM. The negative sign means the deflection is downwards. At $x=L/2$, the deflection ΔZ will be

$$\Delta Z = \frac{fL^3}{192EI} \quad (5)$$

Then the Young' modulus E can be expressed as:

$$E = \frac{f}{\Delta Z} \bullet \frac{L^3}{192I} \quad (6)$$

The first term in this formula is the force per unit deflection, measured by FD spectroscopy; while the second term is a geometrical factor associated with the dimension (i.e., length and the area moment of inertia) of the nanobridge. The geometrical factor can be determined by AFM and FESEM with good accuracy. For ZnS nanobridges with a rectangular cross section, eq. (6) can be specifically written as:

$$E = \frac{f}{\Delta Z} \bullet \frac{L^3}{16wh^3} = \frac{\tan\alpha \tan\beta}{\tan\beta - \tan\alpha} \bullet \frac{L^3}{16wh^3} \quad (7)$$

Results:

Figure 4 shows an AFM image taken at contact mode. Clear contrast of the trench and the nanobridge is observed. Figure 5 shows two typical FD curves obtained on substrate (blue curve) and the middle point of the nanobridge (red curve).

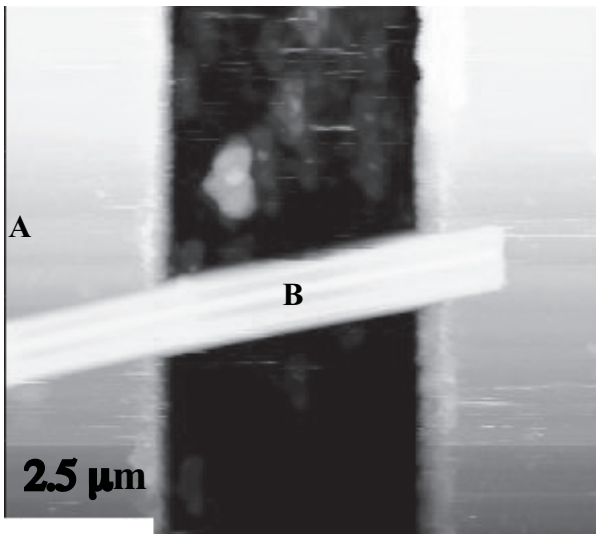

Fig.4: Contact mode AFM image of a ZnS nanobridge.

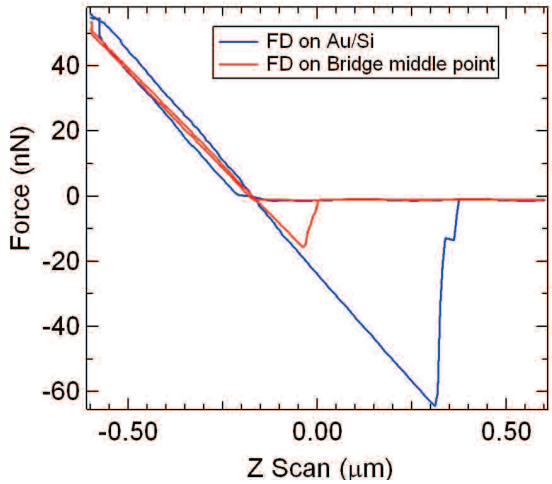

Fig.5: Force-distance curves obtained on the substrate for calibration (blue) and at the middle of the nanobridge (red).

Sample ID	Geometric Factor (1/m)	tanβ (nN/µm)	tanα (nN/ µm)	$f/\Delta Z$ (N/m)	Young's Modulus (GPa)
A03	5.76E+10	144	125	0.94	54.2
A11	5.40E+10	137	119	0.93	50.4
C1_02	1.70E+11	148	106	0.38	64.1
C2_01	2.30E+12	143	20	0.03	51.8
E1_01	5.81E+10	155	129	0.77	44.9
E2_01	3.84E+10	162	142	1.13	43.2

Table1: Tabulated results for several nanobridges. The geometric factor is from the second term in Eqn.(7).

The nanowire appears large in the AFM scan because of the tip size, as evidenced by the repeated structures in the trench. It is consistent with our above analysis on FD spectroscopy that the slope of the linear regime of the FD curve obtained on the nanobridge is lower in comparison with that obtained on the substrate. Least-square fitting was performed to extract the slope for both FD curves. Nanobridges with variable lengths (~ 2-10 µm) and different cross sectional dimensions have been measured. Table 1 lists all the results including the geometrical factor determined from AFM and FESEM, slopes for nanobridges and substrates, the calculated $f/\Delta Z$, and the calculated Young's modulus according to Eqn.(7). From Table 1, we can see the measured Young's modulus is reasonably consistent. The overall average value is about 54.0 ± 5.5 GPa, which is about 25% less than the bulk value of 75 GPa. This error value also indicates that our method more precise than previously reported methods which consistently have errors of 8 GPa or greater [6,7]. The only methods with better reported precision are nanoindentation [10] (0.2-3.5 GPa) and lateral AFM bending [10] (1.1-11 GPa), both of which are destructive methods.

It is worthwhile to point out that the adhesion force between Au film and Si is about 60 nN, much stronger than that between AFM cantilever and ZnS nanobridge. The adhesion forces between the AFM cantilever and the Au film are quite consistent while the adhesion forces between Si cantilever and the ZnS nanobridges varies from sample to sample ~ 0-15 nN. In fact, some of the nanobridges even show negligible adhesion forces. This variation is probably due to the fact that the surface varies from wire to wire. HRTEM has shown that these ZnS nanowires have a very thin amorphous layer with unknown composition [13, 19]. The small adhesion forces between AFM cantilever and ZnS nanobridge provide us two advantages: (i) The nanobridge will not be broken during approach of the AFM cantilever into contact with the bridge (snap-on), so FD spectroscopy can be non-destructively repeated; and (ii) The FD spectroscopy is still performed in the linear regime for the nanobridge. However, we do want to emphasize that the nanobridges are fragile and can be easily broken due to any carelessness during AFM operations. Slow scan rate and a slow scanning direction perpendicular to the nanobridge are required to minimize such accidental damage.

Discussion:

In contrast to our assumption of uniform cross-section for the nanowires, several reports have reported a modulation of the cross-sectional dimensions along the length of the nanowire axis [14, 20]. This modulation actually leads to a symmetry breaking of the surface potential and therefore surface optic

phonons are activated in Raman scattering [14, 20]. Microscopically, in our FESEM and AFM images we have observed that the cross section (width in FESEM and height in AFM) of the nanobridge has some variations. Additionally we have observed a 5% variation from wire to wire. We think that this variation in width can explain the dispersion of the values of final Young's modulus. Additionally we are in the process of testing the precision of these measurements with multiple measurements on the same wires. With improvement of the geometrical factor, the accuracy of the Young's modulus measurement using this method can be improved.

It is still a matter of speculation whether the Young's modulus at nanoscale is different than that of bulk material, or at what scale the Young's modulus will be substantially different. It has been reported recently that the Young's modulus of Au nanowires (40-250 nm) is independent of diameter while the yield strength is diameter-dependent and is 100 times larger than that of the bulk materials [15]. On the other hand, it has also been reported that 1D Al and Au nanostructures show a decrease in the Young's modulus in comparison with bulk state [21]. In semiconducting nanowires, the measured Young's modulus in LFM [7] and nanoindentation [10] both show a reduction compared with that of the bulk materials. Our measured values of Young's modulus for ZnS nanowires are consistent with other reports on reduction of Young's modulus in the nanoscale [7, 10], showing a 10-20% reduction as compared to bulk values.

Conclusion:

We have used force-distance spectroscopy to study the mechanical properties of ZnS nanobridges, fabricated by standard microfabrication method. The interaction between the concentration forces exerted by AFM cantilevers and the nanobridge was modeled by the Euler- Bernoulli beam equation with a fix-end boundary condition. The Young's modulus was determined by a geometrical factor, which can be measured by AFM and FESEM, and a term of force per unit deflection, measured by force-distance spectroscopy. For ZnS nanowires, we measured the Young's modulus to be 51.5±7.5 GPa, which is a 30% decrease compared with bulk ZnS. We believe this method based on force-distance spectroscopy and the model analysis can be used for other one-dimensional nano-beams down to 10 nm regime with the help of several steps of microfabrication.

Acknowledgements:

We thank Prof. E. Manias for discussion of force-distance spectroscopy. The financial support was provided by NSF-NIRT (Nanotechnology and Interdisciplinary Research Initiative), Grant DMR-0304178.

References:

1. Kim, P.; Lieber, C. M., Nanotube nanotweezers. *Science* **1999,** 286, (5447), 2148-2150.
2. Sazonova, V.; Yaish, Y.; Ustunel, H.; Roundy, D.; Arias, T. A.; McEuen, P. L., A tunable carbon nanotube electromechanical oscillator. *Nature* **2004,** 431, (7006), 284-287.
3. Cui, Y.; Wei, Q. Q.; Park, H. K.; Lieber, C. M., Nanowire nanosensors for highly sensitive and selective detection of biological and chemical species. *Science* **2001,** 293, (5533), 1289-1292.
4. Lieber, C. M., The incredible shrinking circuit - Researchers have built nanotransistors and nanowires. Now they just need to find a way to put them all together. *Scientific American* **2001,** 285, (3), 58-64.
5. Samuelson, L., Self-forming nanoscale devices. *Materials Today* **2003,** 6, (10), 22-31.
6. Wong, E. W.; Sheehan, P. E.; Lieber, C. M., Nanobeam mechanics: Elasticity, strength, and toughness of nanorods and nanotubes. *Science* **1997,** 277, (5334), 1971-1975.
7. Song, J. H.; Wang, X. D.; Riedo, E.; Wang, Z. L., Elastic property of vertically aligned nanowires. *Nano Letters* **2005,** 5, (10), 1954-1958.
8. Salvetat, J. P.; Kulik, A. J.; Bonard, J. M.; Briggs, G. A. D.; Stockli, T.; Metenier, K.; Bonnamy, S.; Beguin, F.; Burnham, N. A.; Forro, L., Elastic modulus of ordered and disordered multiwalled carbon nanotubes. *Advanced Materials* **1999,** 11, (2), 161-165.
9. Salvetat, J. P.; Briggs, G. A. D.; Bonard, J. M.; Bacsa, R. R.; Kulik, A. J.; Stockli, T.; Burnham, N. A.; Forro, L., Elastic and shear moduli of single-walled carbon nanotube ropes. *Physical Review Letters* **1999,** 82, (5), 944-947.
10. Li, X. D.; Wang, X. N.; Xiong, Q.; Eklund, P. C., Mechanical properties of ZnS nanobelts. *Nano Letters* **2005,** 5, (10), 1982-1986.
11. Li, X. D.; Hao, H. S.; Murphy, C. J.; Caswell, K. K., Nanoindentation of silver nanowires. *Nano Letters* **2003,** 3, (11), 1495-1498.
12. Morales, A. M.; Lieber, C. M., A laser ablation method for the synthesis of crystalline semiconductor nanowires. *Science* **1998,** 279, (5348), 208-211.
13. Xiong, Q.; Chen, G.; Accord, J. D.; Liu, X.; Gutierrez, H.; Redwing, J. M.; Lew Yan Voon, L. C.; Lassen, B.; Eklund, P. C., Optical properties of rectangular cross-sectional ZnS nanowires. *Nano Letters* **2004,** 4, (9), 1663-1668.
14. Xiong, Q.; Wang, J. G.; Reese, O.; Voon, L. C. L. Y.; Eklund, P. C., Raman scattering from surface phonons in rectangular cross-sectional w-ZnS nanowires. *Nano Letters* **2004,** 4, (10), 1991-1996.
15. Wu, B.; Heidelberg, A.; Boland, J. J., Mechanical properties of ultrahigh-strength gold nanowires. *Nature Materials* **2005,** 4, (7), 525-529.
16. Prater, C. B.; Maivald, P. G.; Kjoller, K. J.; Heaton, M. G., Probing nano-scale forces with the atomic force microscope. *Veeco Metrology Group*.
17. Gere, J. M.; Timoshenko, S. P., *Mechanics of materials*. 4th ed.; PWS Pub Co.: Boston, 1997; p xvi, 912.
18. Young, W. C.; Budynas, R. G., *Roark's formulas for stress and strain*. 7th ed.; McGraw-Hill: 2000.
19. Xiong, Q.; Gupta, R.; Adu, K. W.; Dickey, E. C.; Lian, G. D.; Tham, D.; Fischer, J. E.; Eklund, P. C., Raman spectroscopy and structure of crystalline gallium phosphide nanowires. *Journal of Nanoscience and Nanotechnology* **2003,** 3, (4), 335-339.
20. Gupta, R.; Xiong, Q.; Mahan, G. D.; Eklund, P. C., Surface optical phonons in gallium phosphide nanowires. *Nano Letters* **2003,** 3, (12), 1745-1750.
21. Haque, M. A.; Saif, M. T. A., Deformation mechanisms in free-standing nanoscale thin films: A quantitative in situ transmission electron microscope study. *Proceedings of the National Academy of Sciences of the United States of America* **2004,** 101, (17), 6335-6340.
22. Read, A. J. N., R. J.; Nash, K. J.; Canham, L. T.; Calcott, P. D.; A. Qteish, First-principle calculation of the electronic properties of the silicon quantum wires. *Physical Review Letters* **1992,** 69, (8), 1232-1235.

HIGH SPEED ANISOTROPIC ETCHING OF GLASS AND PIEZOCERAMICS FOR MICROSYSTEM APPLICATIONS

Abhijat Goyal, Srimath S. Subasinghe, Vincent Hood, and Srinivas Tadigadapa
Department of Electrical Engineering, Penn State University, University Park, PA – 16802

ABSTRACT

In this article, we present an inductively coupled plasma (ICP) based dry anisotropic dielectric etching process. The reactive ion etching system employed SF_6/Ar based chemistry and was used to define high aspect ratio features in materials such as glass (Pyrex® 7740), single crystal AT and Y cut quartz, and piezoceramics. An etch rate of 0.536 µm/min at a rms surface roughness of 1.97 nm was obtained for Pyrex samples using an optimized recipe comprising of SF_6 flow rate of 5 sccm, Ar flow rate of 50 sccm, 2000 W of ICP power, 475 W of substrate power, substrate holder temperature of 20°C, and distance of substrate holder from ICP source to be 120 mm. Use of a similar recipe to etch bulk lead zirconate titanate (PZT) resulted in an etch rate of 0.32 µm/min. We used Design of Experiment (DOE) methodology to optimize the etching process with respect to etch rate and rms surface roughness. Regression using least square fit was used to define an arbitrary etch rate number (W_{etch}) and an rms surface roughness number (W_{rms}) as a function of eight correlated process parameters, namely ICP power (W_{ICP}), substrate power (W_{sub}), flow rate of gases (Q_{SF6}, Q_{Ar}), operating pressure ($P_{process}$), temperature of substrate (T_{sub}), and the distance of the substrate from the source (D). The etching process, its optimization and quantification techniques presented in this article present very useful tool for MEMS fabrication and packaging applications.

INTRODUCTION

Future innovations and improvements in navigational grade inertial microsensors, optical waveguides, high frequency crystal oscillators and filters, microactuators, and nano air vehicles etc. are going to increasingly rely on the successful micromachining of materials such as glass, quartz, piezoelectric ceramics etc. A high speed, anisotropic, etch process is required for defining high aspect ratio features to realize resonators, actuators, and passive structural elements in a microsystems. In this study, we used an inductively coupled plasma based reactive ion etching system employing SF_6/Ar chemistry to accomplish high speed anisotropic etching of quartz, Pyrex, bulk PZT, etc. We present results on process optimization to achieve high etch rate along with minimum rms surface roughness of the etched features. Control over the properties of etched surfaces is important for MEMS devices given their large surface area to volume ratio. Surface imperfections results in creation of loss channels in active components, and structural defects in passive components, resulting in loss of microsystem functionality and reliability.

Pyrex substrates were used for optimizing the etch process for quartz, glass, etc. For the etch process optimization for piezoceramics, PZT-4 substrates were used. The 4" Pyrex® 7740 wafers (double sided polished) were cleaned thoroughly with Acetone/Isopropyl Alcohol (IPA) followed by piranha clean (1:1 H_2SO_4:H_2O_2) for one hour. A seed layer, consisting of 200 nm of gold with 20 nm of chromium as an adhesion layer, was subsequently e-beam evaporated on the cleaned glass (Pyrex® 7740) surface. The etch patterns were then delineated on the seed layer using standard lithography and wet etching steps [1]. The patterned 4" wafers were diced into individual 1" dies. A thick layer (5-10µm) of nickel was then electroplated onto the seed layer on the 1" dies. A standard run time of one hour was used for all the samples.

In the case of PZT substrates, finely lapped PZT-4 substrates were cleaned using acetone/isopropyl alcohol (IPA) followed by descumming in oxygen plasma. A 100 nm chromium (Cr) adhesion layer and 350 nm gold (Au) seed layers were deposited via electron beam evaporation on the cleaned PZT substrates. A thick Ni layer (2-5µm) was then electroplated on the Au seed layer. The electroplated PZT substrates were thereafter diced into smaller 1 cm square dies. The PZT dies were mounted onto an aluminum substrate using Fomblin™ oil. After the etching step, the Ni hard mask was stripped using isotropic wet etching of the gold seed layer. The details of the fabrication sequence can be found

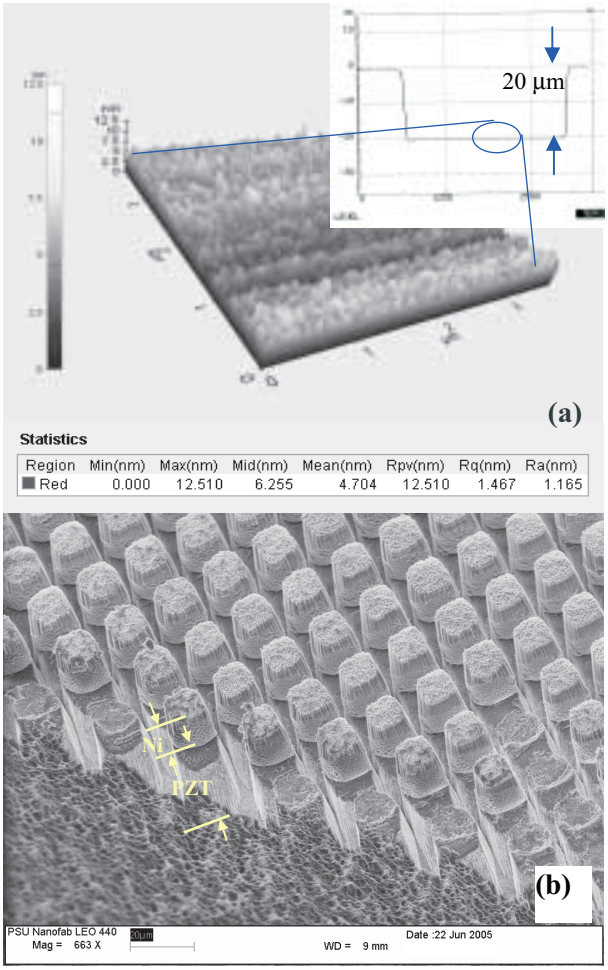

Figure 1: *(a)Alpha-step and AFM image of the surface obtained after 1 hour (20.3 µm) etching of Pyrex (b) SEM image of the etched feature in bulk PZT for minimum feature size of 3 µm. Almost vertical sidewalls were obtained. Also can be seen is the electroplated nickel on the top of the pillars acting as a hard mask during the etching process.*

elsewhere [2-4].

For both the samples, the etch rate was determined from the step height of the etched feature. The rms surface roughness (only for the etched Pyrex substrates) along with step height (for both the substrates) was measured using a stylus profilometer. Additionally, atomic force microscope (AFM) and scanning electron microscope (SEM) was used to characterize the properties of the sidewalls and for accessing the quality of the etched features in terms of their rms surface roughness.

DESIGN OF EXPERIMENT (DOE)

One of the primary problems with the optimization of etching process is the large number of process variables and the complex interaction between them. It typically requires an impractically large number of runs to come up with the optimized process to obtain the desired etch rates and the rms surface roughness. Use of scientific process optimization methods such as Design of Experiment (DOE) can traditionally reduce the number of runs required. However, even then the number of runs can be too large to be practical. For example, in one of the related studies, we used a combination of $SF_6/C_4F_8/Ar/O_2/CH_4$ based chemistry for etching Pyrex [3]. Optimization of the etching process with such a large number of variables, 10 in that case will typically require 2^{10} (1024) sample runs. In such as a case, the process space can be divided into subspaces to further reduce the number of runs.

A. Etching of Pyrex

For the Pyrex wafers, a standard DOE methodology employing two factorial design was used to study the variation of etch rate and rms surface roughness as a function of the process parameters. We optimized the process conditions to obtain the highest etch rate with minimum possible surface roughness. Four process parameters, ICP power (500 W - 2000 W), substrate power (100 W – 475 W), SF_6 flow rate (5 sccm – 50 sccm) and Ar flow rate (5 sccm – 50 sccm) were optimized as part of DOE. It was possible to obtain an etch rate of 0.536 µm/min and rms surface roughness of 1.97 nm at an ICP power of 2000 W, substrate power of 475 W, SF_6 flow rate of 5 sccm, and Ar flow rate of 50 sccm [5]. The other process parameters were distance of the substrate holder from the source which was fixed to be 120 mm, temperature of substrate holder which was fixed at 20ºC. The pumping system was operated at full capacity so that the pressure during etching was between 1-2 mTorr. Figure 1 (a) shows the AFM image of the surface generated after the etch step. Also shown in inset of Figure 1 (a) is the side view of the etch profile. Almost vertical side walls were obtained. The apparent non-vertical angle of the sidewall in the stylus profile is due to finite dimension of the tip of the profilometer and hence is not a true measure of the sidewall angle.

The etch rate and rms surface roughness were found to improve with increasing ICP power, substrate power, and Ar flow rate (Figure 2 (a), (b), and (c)). However, for increasing flow rate of SF_6, the etch rate increased whereas rms surface roughness decreased (Figure 2(d)). For increasing operating pressure (Figure 2(e)) and distance of substrate from source (Figure 2(f)), both the etch rate and rms surface roughness deteriorated.

B. Etching of bulk PZT

In this case, we optimized the process conditions to get the best etch rate, and we did not consider the rms surface roughness of the etched features. The focus was on achieving maximum anisotropic profile of the etched features. An SF_6/Ar based process, similar to the one used for etching Pyrex, was used to etch PZT. A high etch rate of 0.32 µm/min was achieved. Figure 1(b) shows 3 micron by 3 micron pillars etched into bulk PZT ceramic substrates using optimized SF_6/Ar based chemistry. As in the case of Pyrex etching, the etch rate increased with increasing ICP power, substrate power, and increasing flow rates of Argon and SF_6 (Figure 3 (a), (b) and (c)).

Given the same recipe that was used to etch Pyrex worked for etching of PZT, the authors believe that the optimized process is similar to ion milling [6, 7], with addition of SF_6 providing the chemistry and enhancing the etching process. Without the chemistry provided by fluorine ions and radicals, the etching process in ion milling primarily relies on eroding the surface using incident energetic ion beam. In the present case, the fluorine ions and radicals react with atoms on the surface of the sample (Pyrex or PZT), forms reaction products and the incident beam of energetic ions aids in the desorption of the reaction products from the surface of the sample. Also, the incident ions help in deeper penetration of fluorine based ions and radicals into the surface of

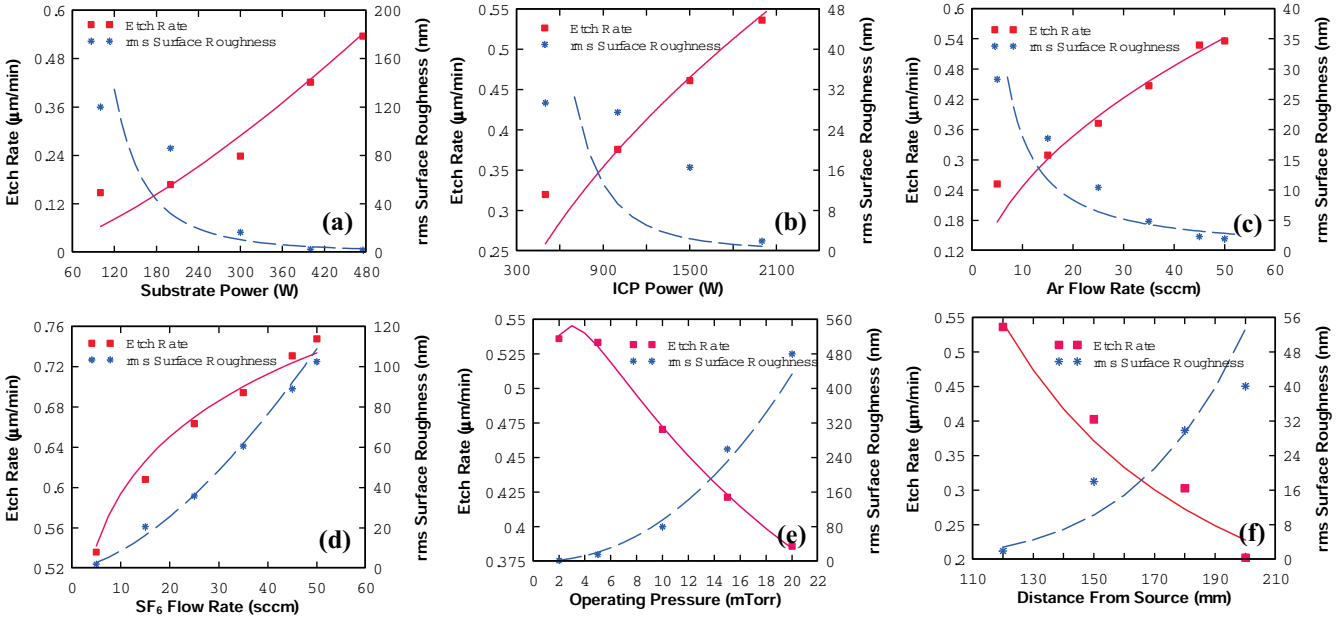

Figure 2: *Variation of etch rate and rms surface roughness with (a) Substrate Power, (b) ICP power, (c) Ar flow rate, (d) SF_6 flow rate, (e) operating Pressure and (f) Distance from source for etching of Pyrex. The lines in the graphs are fit to the data and are given by equations 1-6 in the text.*

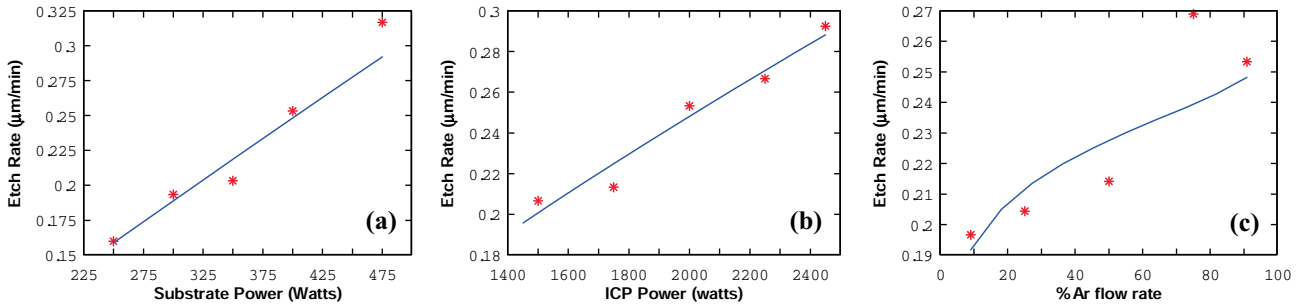

Figure 3: *Variation of etch rate as a function of (a) Substrate Power, (b) ICP Power, and (c) Ar and SF_6 flow rate for bulk PZT substrate. The solid lines are fits to the data according to equations 7 and 8, as given in the text.*

the sample, thereby accelerating the etching process.

REGRESSION FOR PROCESS QUANTIZATION

For the quantification of the etch process, it is useful to define a quantitative measure of the etch rate and rms surface roughness in terms of process parameters. Etch characteristics which vary monotonically with respect to the process parameters can be easily modeled using power law. Use of such power law metrics, for parameters which do not vary monotonically with process parameters, results in significant errors in the quantization process. However such errors can be significantly reduced by use of additional higher order terms in the quantization metric. For the quantization process, the data was arranged in a *m* by (*n*+1) matrix, where *m* are the total number of runs and *n* is the total number of process parameters used in the quantization process. The last column in the matrix consists of value of the etch parameter, i.e. rms surface roughness or etch rate, that is being quantized. This is followed by using a computer program such as Mathematica® to regressively fit a nonlinear power law equation by minimizing the least square error. The fitting equation can be expressed as –

$$\ln(W) = \ln(a_0) + \sum_{i=1}^{n} a_i \ln(PP_i) + \sum_{k=2}^{3} \sum_{j=1}^{n} a_j \ln(PP_j^k) \qquad (1)$$

where, W is the arbitrary number relating etch characteristics to the process parameters, a_i and a_j are the fitting parameters, PP_j are the process parameters whose effect on the etch characteristics are being quantized. Rewriting the equation by taking exponentials on both sides –

$$W = a_0 \left(\prod_{i=1}^{n} PP_i^{a_i}\right) \exp\left[\sum_{k=2}^{3} \sum_{j=1}^{n} a_j \ln(PP_j^k)\right] \qquad (2)$$

which is the form of equation that is being used in this paper to express the etch parameters in terms of process parameters. The higher order terms, given by the third term in equation (1) are required only when the variation of etch characteristics with respect to process parameters is not monotonic. We can call these terms as "correction factors" to the power law model used for the quantization process. The correction terms are a result of interaction between different components of the process space or where the change in etch parameters as a function of process parameters is not monotonic. Without the correction factors the spread of data is significant and hence the description in terms of the reduced etch parameters becomes less meaningful.

(a) For SF_6/Ar based Pyrex etching: From the least square fit to the data in our experiments, an etch rate number (W_{etch}) was defined, as

$$W_{etch} = \frac{W_{ICP}^{0.52} W_{sub}^{1.36} Q_{SF_6}^{0.135} Q_{Ar}^{0.48} T_{sub}^{0.065} P_{process}^{0.2}}{D^{1.67}} \exp(-0.094(\ln P_{process})^2) \quad (3)$$

where W_{ICP} is the ICP power in Watts, W_{sub} is the substrate power in Watts, Q_{SF6} is the flow rate of SF_6 in sccm, Q_{Ar} is the flow rate of Ar in sccm, T_{sub} is the substrate temperature during the process in ºC, $P_{process}$ is the ambient pressure during the process in mTorr, and D is the distance from the ICP source of the substrate holder in mm. The etch rate can now be defined as -

$$R_{etch} = aW_{etch} \text{ or } \ln(R_{etch}) = \ln(a) + \ln(W_{etch}) \qquad (4)$$

where R_{etch} is the etch rate in µm/min and "a" is a proportionality constant that relates etch rate to the etch rate number. The parameter a and the powers of the process parameters in equation (3) were determined using least square fit to the data. The value of $\ln(a)$ from the least square fit from the data was obtained to be -3.2. Expression of the data in this form results in the plot of $\ln(R_{etch})$ with respect to $\ln(W_{etch})$ to be a straight line with a slope of unity as shown in Figure 4 (a). A surface roughness number (W_{rough}) was defined in a similar way as

$$W_{rough} = \frac{Q_{SF_6}^{1.58} P_{process}^{2.18} D^{5.726} T_{sub}^{0.197}}{W_{ICP}^{3.173} W_{sub}^{2.8} Q_{Ar}^{1.172}} \qquad (5)$$

where the parameters are defined as in equation (3). The rms

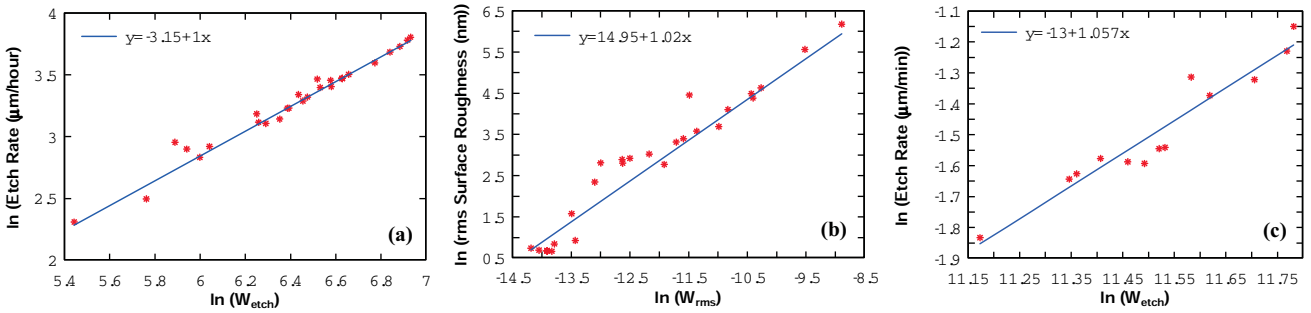

Figure 4: *Plot of natural logarithms of etch rate number and the etch rate, and natural logarithms of rms surface roughness number and the rms surface roughness for SF_6/Ar chemistry (a) and (b) Pyrex, and (c) for PZT.*

surface roughness can now be defined as –

$$R_{rough} = bW_{rough} \text{ or } \ln(R_{rough}) = \ln(b) + \ln(W_{rough}) \quad (6)$$

The parameter "*b*" and the powers of the process parameters in equation (5) were determined using least square fit to the data. The value of ln(*b*) from the least square fit from the current data was obtained to be 14.95. The plot of ln(R_{rough}) to ln(W_{rough}) lie along a straight line with a slope of unity as shown in Figure 4 (b). Once etch rate and rms surface roughness numbers are defined for a given etch tool and a given material, it can be used to predict the expected etch rate for any given set of process parameters.

(b) For SF_6/Ar based PZT etching: An etch rate number (W_{etch}) was similarly defined as a function of the above four correlated process parameters for bulk PZT samples. The etch rate number was defined as follows –

$$W_{etch} = \frac{W_{icp}^{0.74} W_{sub}^{0.95} Q_{Ar}^{0.09}}{Q_{SF_6}^{0.018}} \quad (7)$$

where W_{icp} is the top ICP power in watts, W_{sub} is the substrate power in Watts, Q_{Ar} is the flow rate of Ar and Q_{SF6} is the flow rate of SF_6 in sccm. The etch rate can now be defined as –

$$R_{etch} = cW_{etch} \quad (8)$$

where R_{etch} is the etch rate in µm/min. As in the case of Pyrex, the constant "*c*" and the exponents of the process parameters in equation (1) were obtained the fit of the etch data. As expected, expression of the etch data in this form results in graph of natural logarithm of R_{etch} against the natural logarithm of W_{etch} to be a straight line as shown in Figure 4(c). An R^2 value of 0.96 is obtained from the fit which indicates a good fit to the data with low spread of data points along the straight line. The value of constant "*c*" was obtained to be 2.3×10^{-6}.

CONCLUSIONS

We have demonstrated a high speed dielectric etch process while maintaining control over the rms surface roughness of the etched features which is important for MEMS applications. We used an ICP-RIE system lined with magnets for generating high density plasma at minimum operating pressures (1-2 mTorr). By optimizing process conditions, we were able to obtain an etch rate of 0.536 µm/min and an rms surface roughness of ~1.97 nm for Pyrex samples. At the same time, an etch rate of 0.32 µm/min was obtained for bulk PZT substrates. Using a standard factorial design of experiment methodology, we were able to ascertain effect of various process parameters on etch rate and rms surface roughness. Additionally quantitative metrics called etch rate number and rms surface roughness number were defined by least square fitting the etch data to a function dependent entirely on the process parameters. The demonstrated process can be used for rapid and controlled anisotropic etching of dielectrics for MEMS fabrication and packaging applications.

ACKNOWLEDMENTS

This work is supported by an NSF-NIRT grant, MCE 0096097.

REFERENCES

1. Madou, M.J., *Fundamentals of Microfabrication: The Science of Miniaturization*. 2nd Edition ed. 2002, Boca Raton, Florida: CRC Press.
2. Goyal, A., V. Hood, and S. Tadigadapa, *High speed anisotropic etching of Pyrex(R) for microsystems applications.* Journal of Non-Crystalline Solids. **In Press, Corrected Proof**.
3. Subasinghe, S.S., A. Goyal, and S.A. Tadigadapa. *High aspect ratio plasma etching of bulk lead zirconate titanate*. in *Micromachining and Microfabrication Process Technology XI*. 2006: SPIE.
4. Goyal, A., V. Hood, and S. Tadigadapa. *High-speed anisotropic etching of quartz using SF[sub 6]/C[sub 4]F[sub 8]/Ar/O[sub 2] based chemistry in inductively coupled plasma reactive ion etching system*. in *Reliability, Packaging, Testing, and Characterization of MEMS/MOEMS V*. 2006: SPIE.
5. Montgomery, D.C., *Design and analysis of experiments*. 6 ed. 2004: John Wiley and Sons.
6. Petit, D., et al., *Nanometer scale patterning using focused ion beam milling.* Review of Scientific Instruments, 2005. **76**(2): p. 26105-1.
7. Fu, Y., Z. Shen, and N.K.A. Bryan, *A novel harmless trimming for micro-device with defects and particles in arbitrary geometry by fine milling of focused ion beam.* Microelectronics Journal, 2004. **35**(2): p. 111-15.

LATERAL LAMINATION APPROACH FOR MULTILAYER PIEZOELECTRIC MICROACTUATOR

Xiaosong Wu[1], Guang Yuan[2], Seong-O Choi[2], Yanzhu Zhao[2], Seong-Hyok Kim[2], Yong-Kyu Yoon[2] and Mark G. Allen[2]
Schools of Polymer, Textile and Fiber Engineering[1] and Electrical and Computer Engineering[2]
791 Atlantic Drive, N.W., Georgia Institute of Technology
Atlanta, GA, 30332, USA

ABSTRACT

This paper reports a simple lateral lamination scheme for the fabrication of multilayer piezoelectric actuators. The fabrication scheme consists of dicing of a high-d_{33} piezoelectric coefficient lead zirconate titanate (PZT) material, photolithographic high-aspect-ratio SU-8 definition of electrical isolation, and micromolding of conductive polymer electrodes. Backside and inclined UV exposure has been exploited to secure the 1mm-thick SU-8 pillar definition of internal electrodes and to prevent the formation of a tapered SU-8 pillar shape that allows electrical short paths. An electrically conductive polymer composite (ECPC, silver-PMMA: 40 vol% Ag) has been utilized for making moldable electrodes. In fabrication and actuation, it is advantageous to have the isolation structures and the electrodes to be both made with polymeric materials so that they have similar thermal and mechanical properties. An 8-layer device is successfully fabricated and tested. A displacement of 0.63 micron is achieved at 100V driving voltage, which agrees well with finite element simulation results.

INTRODUCTION

Piezoelectric actuators are used in a number of applications such as precision positioners for metrology and interferometry, ultrasonic transducers, and scanning microscopes [1-3]. The miniaturization of these and other piezoelectric components is important for the development of compact, low-driving voltage, and cost-effective devices. In order to have reasonable displacement at low voltage, often a multilayer piezoelectric scheme is utilized. Compared to their single layer counterparts, multilayer piezoelectric actuators offer several advantages such as low driving voltages while maintaining high electric fields necessary for actuation, rapid response time, and high electromechanical coupling [4]. A typical lamination scheme (Fig 1a) relies on a vertical stack of alternating layers of electrodes and piezoelectric layers, where each lamination step requires electrodes to be deposited and patterned or aligned [2, 3]. Alternatively, a planar fabrication method can be utilized to form a lateral multilayer piezoelectric actuator, in which a series of vertical grooves are cut into a PZT crystal and metallized with appropriate isolation to form a lateral multilayer structure. Such a structure was demonstrated using electroplating of electrodes followed by laser-assisted etching of PZT and electrodes [5]. However, process challenges of electroplating in deep grooves as well as issues with the laser assisted etching were also reported.

To avoid these difficulties, we propose an alternative, simple, and cost-effective lateral lamination scheme (Fig 1b) for a multilayered piezoelectric actuator. The process involves PZT dicing, photolithographic definition of high-aspect-ratio SU-8 pillars for electrical isolation, and micromolding of ECPC electrodes. This approach overcomes the reported process difficulties of [5], while simultaneously maintaining the advantages of multilayer piezoelectric actuators.

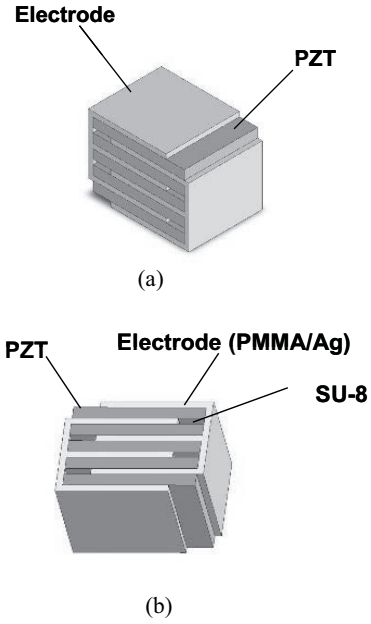

Figure 1. *Lamination architectures for multilayer piezoelectric actuator: (a) conventional vertical stack lamination, (b) proposed lateral lamination*

In this study, an effective photolithographic patterning scheme for the 1mm-thick isolation structure has been demonstrated. Specific advantages associated with the molding of internal electrodes include: (1) the ECPC casting through high-aspect-ratio trench is time-effective, compared to the long processing time of an electroplating approach; (2) the ECPC electrodes alleviate void formation issues which may occur during the plating through the deep trenches; (3) the silver-PMMA composite has mechanical and thermal properties similar to those of the isolation SU-8, which increases the stability of the actuator. Using these schemes, the PZT actuator has been designed, tested and characterized.

FABRICATION

Figure 2 illustrates the fabrication process of PZT multilayer actuators. The 1mm-thick PZT plate used in this study is a commercialized high-d_{33} piezoelectric coefficient, hard ceramic plate (PZT 855, APC International Ltd.). A proven fast and economical approach, dicing, is used to fabricate freestanding PZT fins. Because no high-temperature process is involved, there is no thermal stress or shrinkage as might be present in more traditional

processes such as sol-gel or sintering. A 20 x 20 x 1mm PZT plate (2a) is mounted on a glass substrate using adhesive and diced into 150 micron-wide 'fins' with a spacing of 165 micron defined by the thickness of the diamond blade used (2b). The diced PZT plate is transferred to a second PDMS-coated glass slide and remains on the glass slide for the rest of process. A thick epoxy-based negative photoresist SU-8 (SU-8 2025, Microchem Co.) is then cast over the diced PZT plate. SU-8 pillars for electrical isolation are formed between the fins in alternating gaps by photolithography (2c). The pillar-to-pillar separation distance is 3.5mm. A double-layer (50nm-thick titanium and 2 micron-thick copper) is deposited on the PZT structures as well as the SU-8 isolation pillars. The thickness of the copper layer on the sidewall ranges from approximately 100nm to 2 micron due to the non-uniform coating of the sputtered metal in the deep trenches. A silver-PMMA (40 vol% Ag) ECPC blend is prepared and cast into the gaps between the PZT fins, and then vacuum-cured at 65ºC (2d). After the excess polymer and metal on top of the PZT are polished away, the sample is diced into separate devices with any desired number of layers (2e). Multilayer devices, e.g, 10-layer devices with a dimension of 4 x 3 x 1mm are then released from the substrate. Electrical leads are applied on both the left and right sidewalls. The devices are then poled by applying a 2 kV/mm electric field in the transverse direction of the layer (2f) at room temperature.

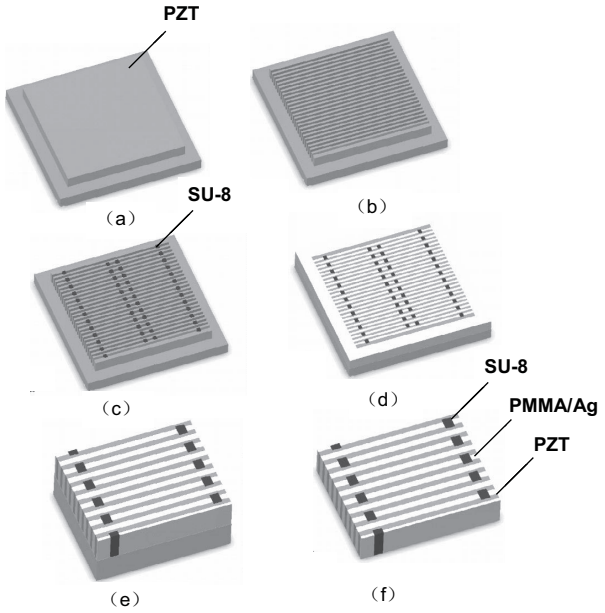

Figure 2. *Fabrication process*

SEM micrographs of diced PZT fins with SU-8 pillars are shown in Figure 3. The top view shows the uniform cuts with a PZT width of 150 micron and a spacing of 165 micron. Viewed from an angle, the SU-8 connects are found to be quite well-leveled with the PZT fins, with a tolerance of approximately 2 % over the 1mm-tall SU-8 pillar.

However, the SU-8 pillars are tapered down from the top to the bottom as shown in Figure 3(b) and Figure 4(a). It is attributed in part to non-uniform SU-8 crosslinking over the high-aspect-ratio pillars (1:7) resulting from residual solvent gradient in the thick pillar and optical dose variation between the top and bottom portions. Because the optical exposure is from the top side, the top layer is overexposed and the bottom layer is relatively underexposed, which results in the variation of the lateral dimensions of the developed SU-8 structures. The same situation applies to the back-side exposure as illustrated in Figure 4(b). The undesired gaps between SU-8 and PZT could lead to electrode shorting.

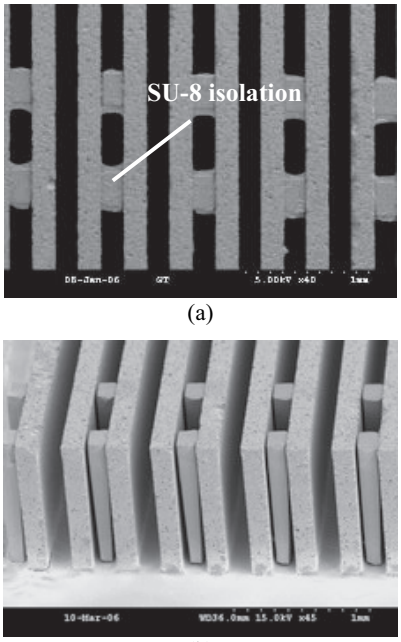

Figure 3. *SEM images of diced PZT fins with SU-8 pillars for electrode isolation: (a) top view, (b) oblique view*

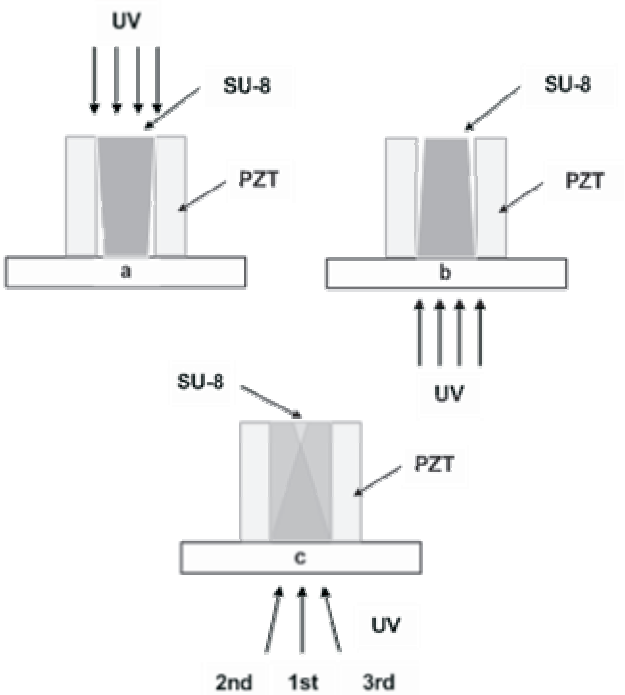

Figure 4. *(a)Tapered SU-8 pillar formed from front-side exposure, (b) tapered SU-8 pillar formed from back-side exposure and (c) back-side inclined exposure scheme for fabrication SU-8 isolation pillars with conformal contact*

An improved method of photo-patterning SU-8 electrical isolation pillar structures is through back-side inclined exposure as shown in Figure 4(c) [6]. Schematic views of the process itself as well as the comparison with front-side and back-side exposures are shown in Figure 4. The experiment is started with deposition and patterning of 50nm-thick titanium and 200nm-thick copper on top of a glass substrate. The metal pre-patterning is utilized for pillar definition using back-side exposure. A layer of 20 micron-thick SU-8 2010 is spin-coated as an adhesive layer and baked at 65ºC for 5 min and then at 95ºC for 15 min on a hotplate. A PZT plate 20 x 20 x 1mm in size is mounted on the prebaked SU-8 layer, and baked at 150ºC for 6 hours to bond two pieces together through thermally crosslinking SU-8. The PZT plate is diced into 150 micron wide 'fins' with a spacing of 165 microns in alignment with the pre-patterned substrate. This substrate is subsequently exposed from the back vertically (i.e. at an incident angle of 90º from the substrate), then exposed at 95° and 85º incident angles. SEM micrographs of diced PZT fins with SU-8 pillars formed by back-side exposure are shown in Figure 5. The magnified image in Figure 5 shows the desired conformal contact between SU-8 pillars and the sidewall of PZT layer.

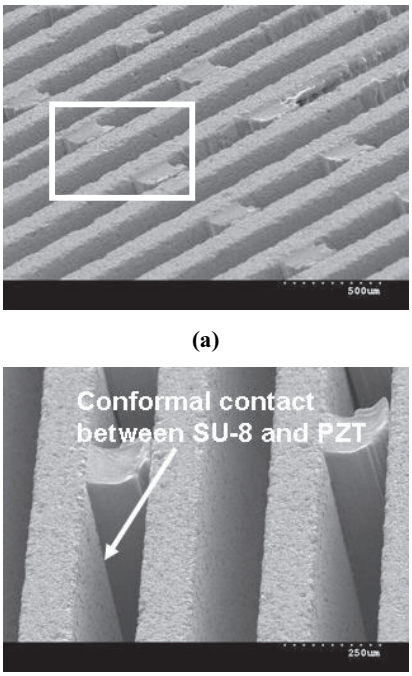

(a)

(b)

Figure 5. *(a) SEM images of diced PZT fins with SU-8 pillars formed by back-side inclined exposure, (b) magnified image of two SU-8 pillars*

CHARACTERIZATION

Before the testing of the multilayer piezoelectric actuators, the conductive polymer composite is first tested for its effectiveness as an electrode material for the PZT actuator. Thin slabs of PZT with a thickness of 150 micron and a lateral dimension of 20 mm x 1 mm are prepared. Silver-PMMA ECPC (40 vol% Ag) blend is applied on both sides of a single slab of PZT. For comparison purposes, PZT thin slabs with sputtered metal electrodes and with ECPC electrodes on top of sputtered metal electrodes are prepared as well. The property of ferroelectric polarization versus electric field (P-E) of each type is measured at 0.1 Hz using a Sawyer-Tower circuit [7] at room temperature. The P-E property is measured under an unpoled condition in all three cases.

Figure 6 shows the P-E hysteresis loops of a single PZT slab with different electrodes. For a desired remanent polarization value (P_r) of 0.25 C/m^2, the electric fields required for ECPC-only, ECPC on sputtered metal, and sputtered metal-only electrodes are 3.7kV/mm, 2kV/mm, and 1.35kV/mm, respectively. The sputtered metal structures help reduce the required electric field and are favorable for low voltage applications. Accordingly, a sputtering step should be added before the molding the ECPC electrodes in the multilayer fabrication process.

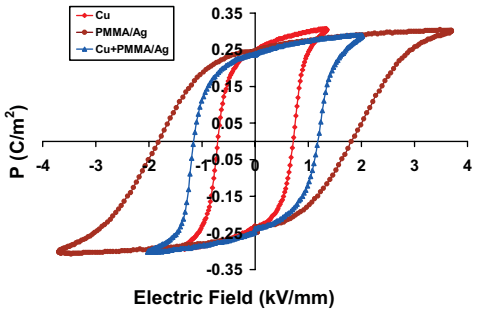

Figure 6. *P-E hysteresis loop for a single PZT layer with three types of electrodes*

Laterally-stacked actuators with 8 and 10 layers have been successfully fabricated. Fig. 7(a) and 7(b) show a 10-layer and a part of an 8-layer stack actuator, respectively. Figure 8 shows the P-E hysteresis loops of a single PZT slab and of an 8-layer actuator with the same type of electrodes.

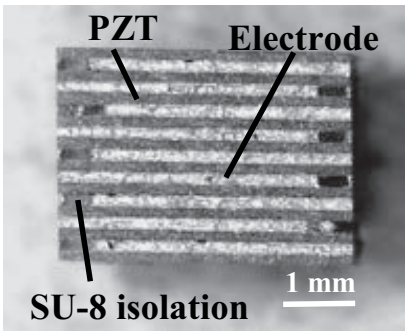

(a)

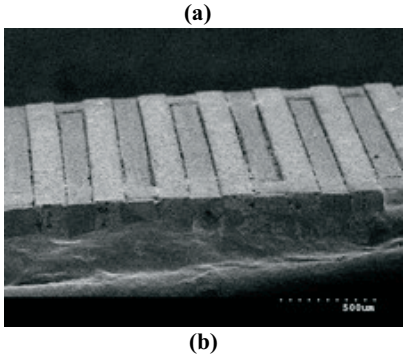

(b)

Figure 7. *(a) Optical microscopy image of a 10-layer PZT actuator with conductive polymer electrode, (b) SEM image of an 8-layer PZT actuator (Note a probe wire has been attached)*

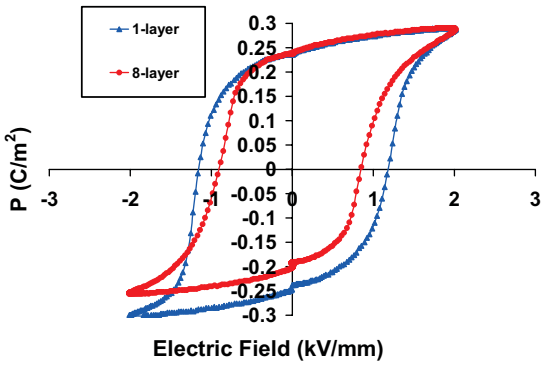

Figure 8. *P-E hysteresis loop for a single PZT layer and an 8-layer actuator*

As shown in Figures 8, the multilayer PZT actuator has a hysterisis loop similar in shape to that of a single layer structure, with the former having a lower coercive field value (0.84 kV/mm) than the latter (1.17 kV/mm), which indicates better polymer electrode coverage on the sidewall of the multilayer actuator. The multilayer PZT actuator also exhibits a slightly asymmetric hysteresis behavior.

Finite element simulation is carried out to obtain the displacement of an 8-layer actuator as a function of applied electric field using ANSYS. The simulated displacement result for an 8-layer actuator at a driving voltage of 100V is 0.505 micron as shown in Figure 9. Experimental results for actuator displacement are measured using a laser displacement sensor (LK-G32, Kenyence Co.) under quasistatic conditions (0.5Hz). Figure 10 illustrates the FEM results and experimental results of the top layer displacement of the actuator as a function of electric field for an 8-layer device. The experimental results for displacement exhibit obvious linearity and agree reasonably well with the simulation result. The discrepancy may have resulted from the difference between the d_{33} used in the simulation, which is a manufacturer-specified d_{33} value of 630×10^{-12} m/V, and the actual d_{33} value of the PZT layer after repoling the PZT in a transverse direction from the original polarization. The calculated d_{33} value from the displacement measurement is 787×10^{-12} m/V.

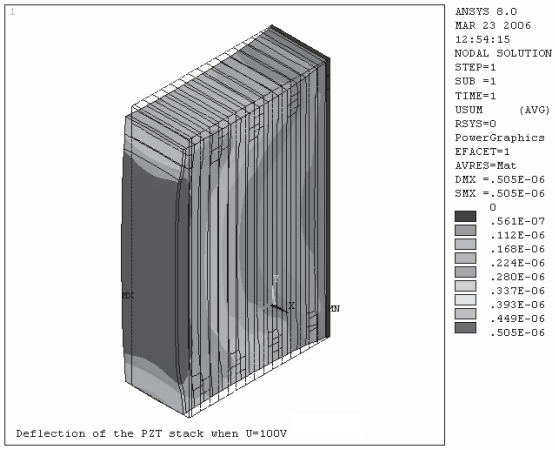

Figure 9. *FEM simulation result for an 8-layer actuator at a driving voltage of 100V*

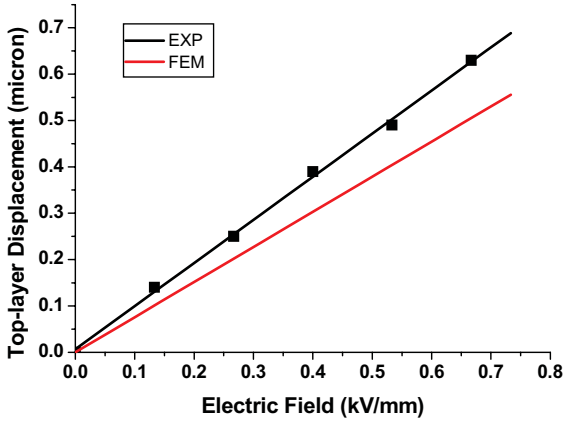

Figure 10. *Top layer displacement of an 8-layer actuator as a function of applied electric field (maximum field of 0.66 kV/mm achieved at a voltage of 100V)*

CONCLUSIONS

Laterally-stacked multilayer PZT actuators have been fabricated using diced PZT multilayer, high aspect ratio SU-8 photolithography and molding of electrically conductive polymer composite electrodes. This fabrication process is simple and straightforward compared to previous lateral lamination approaches. An 8-layer device has shown a displacement of 0.63 micron at 100V driving voltage, agreeing reasonably well with simulation results. The results indicate that the fabrication process of lateral lamination provides a valuable alternative for making compact, low-voltage multilayer piezoelectric micro-actuators. The fabricated PZT structures may be suitable for applications in microfluidics (as a microvalve or micropump actuator) and in optical zooming of camera lens.

REFERENCES

[1] S.Kawakita, T.Isogai, "Multi-layered piezoelectric bimorph actuator", *1997 International Symposium on Micromechanics and Human Science*, 1997, pp. 73-78

[2] K. Yao, K.Uchino, et al., "Compact Piezoelectric Stacked Actuators for High Power Applications" *IEEE Transactions on Ultrasonics, Ferroelectrics and Frequency Control*, 47(4), July 2000, pp.819 - 825

[3] T. Lilliehorn and S. Johansson, "Fabrication of multilayer 2D ultrasonic transducer microarrays by green machining" *J. icromech. Microeng.* 14 (2004), pp.702-709

[4] W. Zhu, K. Yao, Z. Zhang, "Design and fabrication of a novel piezoelectric multilayer actuator by thick-film screen printing technology", *Sensors and Actuators,* 86 (2000), pp.149-153

[5] G. Suzuki and M. Esashi, "Planer Fabrication of Multilayer Piezoelectric actuator by groove cutting and electroplating",*Proc. MEMS* 2000, pp. 46-51

[6] Y.-K. Yoon, J.-H. Park, and M.G. Allen, "Multidirectional UV lithography for complex 3-D MEMS structures," *J. MEMS*, 2006 (in press)

[7] C. B. Sawer and C. H. Tower, "Rochelle salt as a dielectric", *Physical review,* 35(1930), pp.269-273

LONG-TERM RELIABILITY, BURN-IN AND ANALYSIS OF OUTGASSING IN AU-SI EUTECTIC WAFER-LEVEL VACUUM PACKAGES

Jay Mitchell, G.R. Lahiji, and Khalil Najafi
Center for Wireless Integrated Microsystems (WIMS)
University of Michigan, Ann Arbor, MI 48109-2122, USA

ABSTRACT

An investigation on outgassing is presented in micro-vacuum packages fabricated using Au-Si eutectic bonding. Without getters, package pressures ranging from 2 to 12 Torr were observed—it was shown that these relatively higher micro-vacuum pressures are consistent with outgassing theory. Using Nangetters™, pressures ranging from 1 to 16 mTorr were achieved. Fourteen devices were kept in a controlled environment and tested for 437 days with ≤±2 mTorr variation in pressure. Five devices from this lot were taken out of the controlled environment and incidentally exposed to 40ºC temperatures and low frequency vibration resulting in wide fluctuations in pressure. Exposing these devices to 150 ºC up to 21 hours served as a "burn-in" step, stabilizing pressures at just above 10 mTorr. Pressures varied by no more than ±1 mTorr for the remainder of the 100 hours at 150°C and for 50 thermal cycles from -65 to 150°C.

INTRODUCTION

Low-cost, simple, reproducible, stable hermetic/vacuum packaging technologies are required for many micro-devices such as inertial sensors (~100 mTorr), infrared sensor arrays (10 mTorr) and micromechanical resonators used in RF applications (10 μTorr to 760 Torr). As a result, generic technologies for vacuum/hermetic packaging are needed for these and many other applications.

Vacuum/hermetic packaging of devices has been investigated using a number of approaches including thin film encapsulation, anodic bonding, glass frit bonding and various solder bonding techniques, demonstrating pressures ranging from 1 mTorr to 1 Torr [1-4]. These studies do a very good job of explaining the fabrication process but report very little on reliability testing. A number of companies have also developed vacuum packages and some have reported good long term testing results. Most notably, Raytheon reported stable long term testing results for 940 days at 4 mTorr [4].

Throughout the vacuum science literature, much work has been reported on developing and improving macro-scale vacuum systems and on the study of the effects of outgassing [5, 6]. Here an effort is made to apply some of this theory to micro-cavities ($1x10^{-9}$ to $1x10^{-6}$ liters), in particular focusing on outgassing effects. In [1] we presented a wafer-level packaging technique based on Au-Si eutectic wafer bonding, for achieving pressures below 10 mTorr with a yield of 80% using thin-film Nanogetters™[7] (Figure 1). Here, we report on the long-term testing and characterization, outgassing mechanisms, and an essential burn-in technique for maintaining pressures in the milliTorr (0.1 Pa) range in micro vacuum packages fabricated using Au-Si eutectic bonding. Outgassing was determined as the main obstacle for sustaining low vacuum pressures. Our burn-in technique appears to eliminate outgassing effects, allowing for ±1 mTorr pressure stability even after 100 hours at 150°C and 50 thermal cycles from -65 to 150°C.

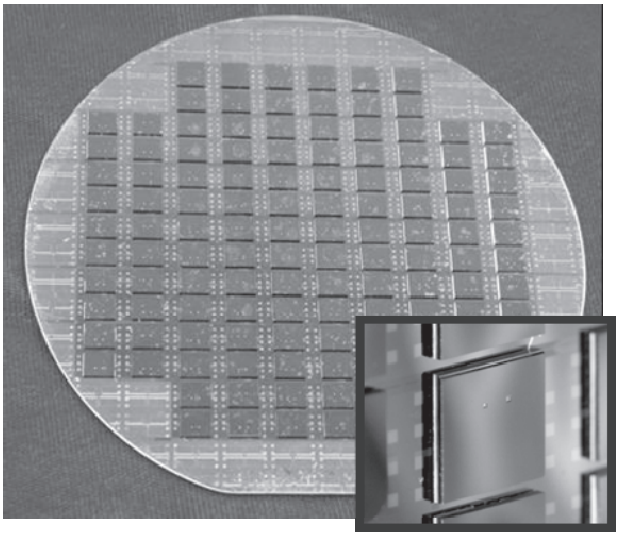

Fig. 1: *A wafer with 124 vacuum packaged device and a close up view of one of the packages.*

BACKGROUND AND THEORY

Outgassing involves desorption of materials (such as H_2O, H_2, N, O and CO_2 and hydrocarbons) from the inside surface and bulk of vacuum chambers (Figs. 2a and 2b). Extensive investigations have been conducted to determine how to remove these atoms from vacuum systems in order to lower pressures. Typically H_2O is the dominant outgassing molecule [5, 6]. In humid environments (such as a cleanroom), hundreds of monolayers of H_2O can form on the surface of a wafer.

In standard vacuum systems the pressure, p, can be calculated as a function of time:

$$p(t) = \left(p_0 - \frac{\dot{Q}_{in}}{S} \right) \cdot \exp\left(-\frac{S}{V} t \right) + \frac{\dot{Q}_{in}}{S} \tag{1}$$

where p_0 is the pressure at the pump, S is the pump speed, V is the volume of the chamber, and $\dot{Q}_{in}$ is the flow rate into the vacuum chamber. This flow rate is generally dominated by outgassing, $\dot{Q}_{outg}$:

$$\dot{Q}_{outg} = \frac{a_{1h} \cdot A}{\left(\frac{t}{1h} \right)^{\alpha}} \tag{2}$$

where A is a geometrical factor, and a_{1h} and α are fitting parameters.

In the case of a sealed micro-cavity there is only the net flow into the cavity, $\dot{Q}_{in}$. Assuming no physical leak path, the pressure, p, can be determined as:

$$p(t) = \int_0 \frac{\dot{Q}_{outg}}{V} dt \tag{3}$$

Considering Eqs. 1 and 3 the pressure inside a sealed micro-cavity will be significantly higher than the vacuum chamber it was

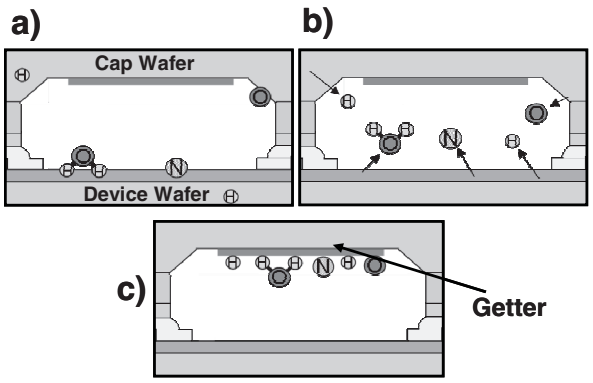

Figure 2: *An illustration of **a)** molecules which have adsorbed on the surface or into the bulk of the micro-vacuum chamber, **b)** molecules that desorb off of the chamber walls to increase the pressure and **c)** these molecules reacting with the getter to lower the package pressure.*

sealed in for two reasons: 1) the micro-cavity is not continuously pumped as in the case for Eq. 1, and 2) Eq. 3 shows that for a given surface area, smaller volumes will cause higher pressures—thus the larger surface to volume ratio of micro-cavities causes higher pressures.

As a result, without the use of getters, pressures no lower than 1 Torr have been reported using anodic, solder or frit bonding. Getters are used in macro-scale vacuum systems to aid in achieving lower pressures. They are particularly useful for micro-scale vacuum packages. Getters work on the principle that metals and alloys such as Ba, Al, Ti, Zr, V and Fe react with hydrogen, oxygen, nitrogen and hydrocarbons through oxide and hydride formation [7]. In this manner, as illustrated in Fig. 2c atoms are removed from the vacuum chamber and the pressure is lowered. Getters generally require an "activation step" at an elevated temperature at which the native oxide is dissolved away. For our application, the getter was deposited onto the inside surface of the cap wafer [1], as shown in Fig. 2. Nanogetters™ [7], provided by ISYSS Corporation, were used in this work.

ANALYSIS OF VACUUM PACKAGING RESULTS

In the Au-Si eutectic vacuum encapsulation process detailed in [1], *cap wafers* with Au bond rings were aligned and bonded to ***device wafers*** with integrate Pirani (vacuum) gauges at 390ºC. Si diffuses into the Au layer at above 363 ºC and the Au-Si eutectic forms, melts and adheres to the surface of the *device wafer*. In a final step, part of the cap wafer is diced away resulting in an array of packages across the wafer (Fig. 1). It is important to note that directly before bonding, the wafers are solvent cleaned and rinsed in water. They then go directly from the 35-40% humidity of the cleanroom into the SUSS SB6 vacuum bonding chamber. As mentioned earlier, such high exposures to moisture should result in 100s of monolayers of H_2O [6].

Figure 3 shows the bonding sequence. The chamber is first pumped down to 10 µTorr. The wafers are held apart using 100 µm spacers at 345ºC for 1 hour in order to allow for outgassing. (Nanogetters™ activate around 300ºC, but, because the chamber pressure is only 10 µTorr, there is very little reaction between the gettering material and the atoms outassing from the wafers and/or chamber). Next the wafers are brought together with 133 kPa of pressure (1000 N of force). The wafers are then heated to 390 ºC and held at this temperature for 40 minutes.

One set of packages was fabricated without evaporated getters. Initial pressures ranging from 2 to 12 Torr were observed

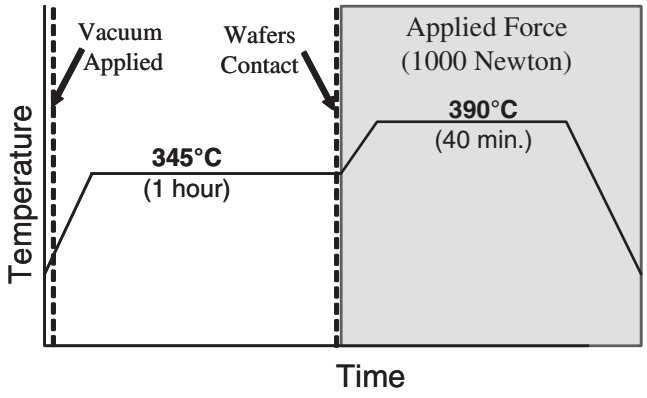

Figure 3: *The bonding process used for vacuum packaging.*

across the wafer [1] with only a handful of packages showing significant changes in pressure over time. At first glance, it is not intuitive that micropackages sealed in a 10 µTorr vacuum chamber would have pressures in this range. Considering the exponential relation between the outgassing rate and temperature [5], it is likely that most of the pressure increase happened in the 1 hour the wafers spent heating to, holding at and cooling down from 390 ºC (Fig. 3). The 2 to 12 Torr pressures would correspond to an average outgassing rate per unit area ($\dot{Q}_{outg}/A$) of $3\text{x}10^{-9}$ to $2\text{x}10^{-8}$ *liters-T/cm²-s* during that 1 hour. Considering this outgassing rate, the wafer dimensions, and the speed of the Varion TriScroll Turbo Pump (estimated at 140 cm^3/s) in Eq. 1, this level of wafer outgassing should account for, at most, a 1 µTorr partial pressure. (the rest of the pressure can be accounted for by outgasssing of all of the other surfaces in the bonding chamber).

Figure 4 shows data for packages which showed the largest change in pressure over time, where the pressure was converted to units of outgassing rate (liters•Torr/[s•cm²]) and graphed verses time. These packaged pressures went from 10 to 14 Torr and 12 to 27 Torr over a 235 day period. The graphs in Fig. 4 exhibit the power law decay typical for outgassing (Eq. 2). The observed n=1.5 behavior was shown to indicate a high exposure to humidity by M. Li et al. [6]. Furthermore, it should be noted, that the outgassing rates in Fig. 4 are significantly smaller than those in a typical macro-scale vacuum chamber. In M. Li et al. [6], for example, it took 200 hours of pumping at room temperature, to reach a $\dot{Q}_{outg}/A$ of $5\text{x}10^{-11}$ liters-T/cm²-s for a 16 liter chamber exposed to various levels of humidity.

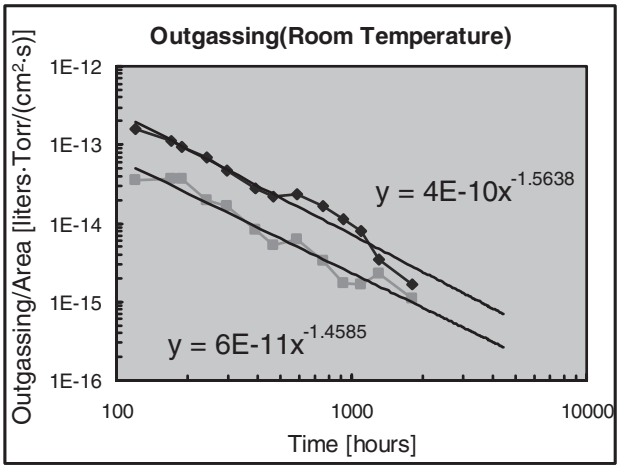

Figure 4: *A graph illustrating the outgassing rates for two packages which were packaged without getters. These packages went from 10 to 14 Torr and 12 to 27 Torr in a 235 day period.*

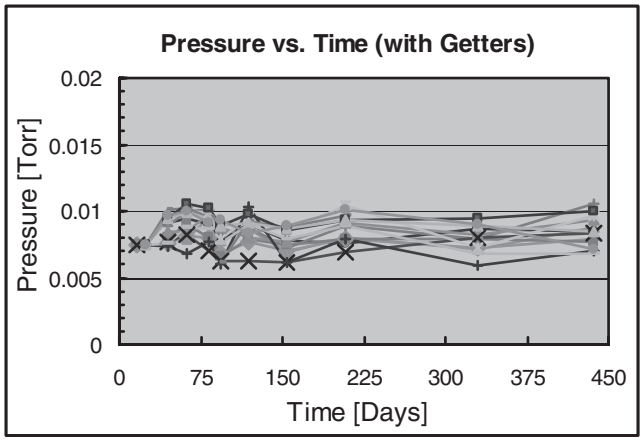

Figure 5: *Data for fourteen packages which were tested in a controlled environment (minimal vibration and temperature fluctuation) resulting in less than ±2 mTorr pressure fluctuation.*

In another set of packaged devices, pressures from 1 to 16 mTorr were achieved by encapsulating Nanogetters™ inside each of the micropackages. This is nearly a 10^3 times decrease in pressure with the addition of Nanogetters™. Figure 5 shows data for 14 devices in which testing continued for an additional 437 days after packaging in a controlled environment (i.e. limited vibration/shock, temperatures of 23±2 °C, etc.). Less than ± 2 mTorr pressure fluctuation was observed.

Figure 6 shows data from 5 packages (packages 1-5) that were taken out of the controlled environment after 200 days of testing. These devices were exposed to low frequency vibration and temperatures up to 40°C due to transit. Increases in pressure were almost certainly due to outgassing (desorbtion of gasses from cavity walls) and subsequent decreases in pressure were likely due to gettering (reaction of trapped gasses with the getter).

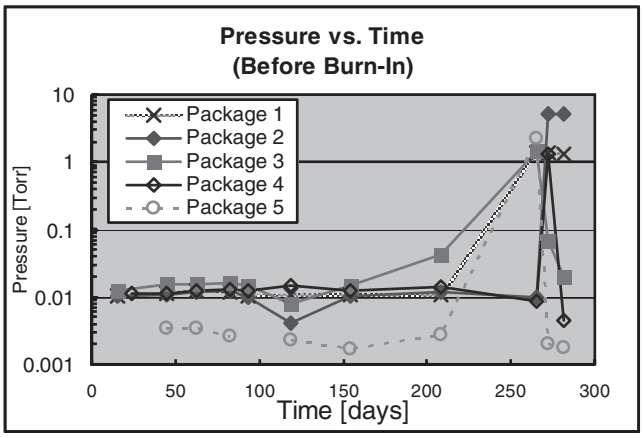

Figure 6: *Five packages which were taken* ***out of the controlled environment*** *(after 200 days). Large pressure fluctuations were observed due to outgassing and gettering.*

TEMPERATURE RAMPING AND BURN IN

Temperature ramping tests were conducted inside of a Tenney Temperature Benchtop oven/refrigeration system. A schematic of the test setup is shown in Fig. 7. Individual packages (as shown in the inset of Figure 1) were diced, mounted and wire bonded to dual-inline packages (DIPs). During testing, these DIPs were plugged into high temperature PC board which sat inside of the oven. Leads from the PC board ran to a switch box, which allowed for individual testing of each of 9 vacuum packages. Vacuum pressures were determined using a computer controlled program to direct currents across the Pirani gauges while measuring the voltage drop across them. From this data, the thermal impedance was measured and a calibration curve was used to convert thermal impedances into pressures. The test methodology for our Pirani gauges are detailed elsewhere [8].

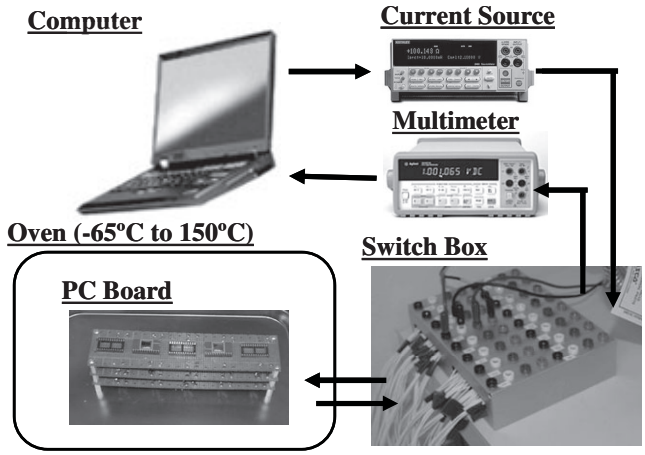

Figure 7: *Packaged vacuum sensors were tested inside of an oven using a labview program, a current source, a multimeter and a switch box to test each sensor during and ever ramping cycles.*

Temperature ramping and cycling tests were conducted on the 5 devices from Fig. 6, along with 4 packages without getters (a control sample). Temperatures were first raised to 50, 75, 100 and 125°C and held for 1 to 2 hours. As shown in Figures 8 and 9, the temperature was then raised to 150°C for 100 hours, then to -65°C for 7.5 hours and then thermal cycled from -65 to 150°C for 50 thermal cycles (well exceeding the requirements for MIL-SPEC-883F Method 1010.8 for thermal cycling). Packages 1, 3, 4 and 5 stabilized during the 50°C and 125°C bakes, whereas package 2 stabilized after 21 hours in the 150°C bake, all at just above 10 mTorr. As shown in Fig. 8, for the remainder of the 100 hour at 150°C, the 7.5 hours at -65°C and the 50 thermal cycles from -65 to 150°C, pressure fluctuations of smaller than ±1 mTorr were measured. On the other hand, Fig. 9 shows that for the packages without getters (packages 6-9) pressures only continue to increase with time.

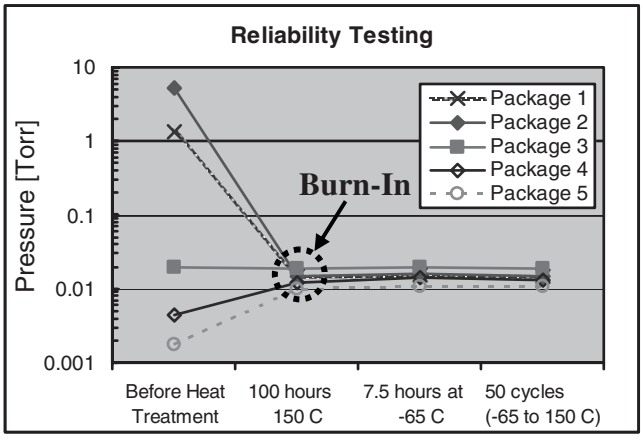

Figure 8: *After heat treatment, pressures stabilized in the packages from Figure 6. Pressures continued to be stable even after 100 hours at 150°C and thermal cycles from -65 to 150 °C.*

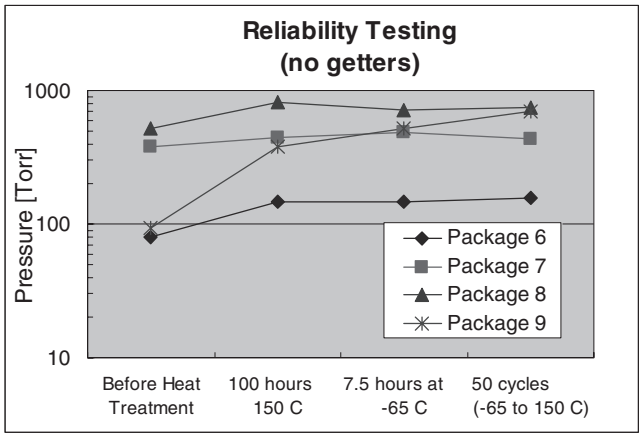

Figure 9: *The pressures in packages without getters continue to rise with temperature treatment.*

In all of the packages, elevated temperatures likely drove out atoms from the surface and bulk of the package cavities (i.e. causing outgassing as illustrated Fig. 2b) causing the increases in pressure seen in Figs. 6, 8 and 9. This increase in temperature should also provided extra energy for chemisorption of gases into the getter (i.e. gettering as illustrated in Fig. 2c), causing the pressure to fall in packages with getters. These competing effects explain the fluctuations seen in Figs. 6 and 8. Holding packages 1-5 at an elevated temperature for an extended period in Fig. 8 appears to have caused a majority of the adsorbed atoms to desorb from the inside cavity surface and then react with the getter—thus stabilizing the package pressure. Such temperature treatment could serve as a "burn-in," step in order to guarantee future pressure stability.

Figure 10 shows temperature ramping data for two of the packages that were packaged without getters. In this graph, the pressures are corrected for the ideal gas law (PV=nRT). As shown, temperatures from 50°C to 150°C caused packages without getters to permanently increase in pressure—thus implying outgassing. Cooling to -65°C on the other hand, caused a temporary reduction in pressure, suggesting condensation of outgassed molecules.

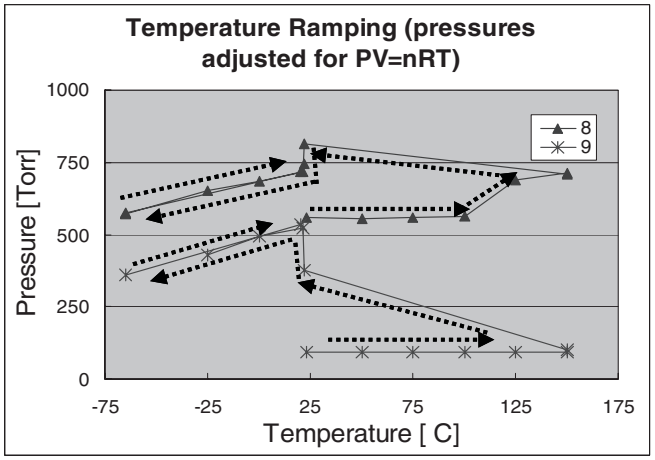

Figure 10: Temperature ramping data for two devices packaged without getters, from Figure 4, illustrating irreversible pressure increase (outgassing) from 50 to 150 °C, and reversible pressure change (condensation) from 0 to -65°C.

CONCLUSION

An investigation on outgassing was conducted on micro-vacuum packages fabricated using Au-Si eutectic bonding. Packages without getters, sealed at 10 µTorr, ended up with pressures ranging from 2 to12 Torr. It was shown that these higher micro-vacuum pressures are consistent with outgassing theory. Using Nangetters™, pressures ranging from 1 to 16 mTorr were achieved—a roughly 10^3 times reduction in pressure. Fourteen devices from the same lot were kept in a controlled environment, demonstrating pressure fluctuations of ≤±2 mTorr in 437 days of testing. Five devices from this lot were exposed to 40ºC temperatures and low frequency vibration, in transit, thereafter showing wide fluctuations in pressure. Exposing these packages to 150 ºC for up to 21 hours, all of the package pressures stabilized at just above 10 mTorr and remained stable for the remainder of the 100 hours at 150°C and for 50 thermal cycles from -65 to 150°C. It is suggested that such heat treatment could be used as a "burn-in" step in order to drive out surface molecules in micro-vacuum packages and provide extra energy for chemisorption of these molecules into the getter. Further study of these phenomena though is required.

ACKNOWLEDGMENTS

This work was supported in part by the Engineering Research Centers Program of the National Science Foundation under Award Number EEC-9986866, and in part by DARPA's HERMIT program under contract number W31P4Q-04-1-R001. We thank Sandia National Laboratories and Dr. Bernie Jokiel for the use of environmental chambers. Nanogetters™ were deposited by Integrated Sensing Systems (ISSYS).

REFERENCES

[1] J. Mitchell, G. R. Lahiji, and K. Najafi, "Encapsulation of vacuum sensors in a wafer level package using a gold-silicon eutectic," *Tech Digest, Transducers'05, Seoul, Korea,* 928-931 (2005).

[2] R.N. Candler, W.T Park, M. Hopcroft, B. Kim, T.W. Kenny, "Hydrogen diffusion and pressure control of encapsulated mems resonators," *Tech Digest, Transducers'05*, *Seoul, Korea*, 920-923 (2005).

[3] B.H. Stark and K. Najafi, "A low-temperature thin-film electroplated metal vacuum package," *J. Microelectromech Syst, 13,* 147-157 (2004).

[4] R. Gooch and T. Schimert, "Low-cost wafer-level vacuum packaging for MEMS," *MRS Bulletin, 28*, 55-59 (2003).

[5] J. M. Lafferty, Vacuum Science and Technology, John Wiley & Sons, Inc., 507-546, 1998.

[6] M. Li and H.F. Dylla, "Model for the outgassing of water from metal surfaces," *J. Vac. Sci. Technol. A*, Vol. 11, No. 4, 1702-1707 (1993).

[7] D.R. Sparks, N. Najafi and S. Massoud-Ansari, "Chip-Level Vacuum Packaging of Micromachines Using Nanogetters," *IEEE Transactions on Advanced Packaging, 26*, 277-282 (2003).

[8] J.S. Mitchell, G.R. Lahiji and K. Najafi, "An Improved Performance Poly Si Pirani Vacuum Gauge Using Heat Distributing Structural Supports," *Proc. of IEEE MEMS Conf.* 291-294 (2005).

MEMS CANTILEVER BEAM ELECTROSTATIC PULL-IN MODEL

G. J. O'Brien [1], D. J. Monk [2] and L. Lin [3]
[1] Arizona State University, Department of Electrical Engineering, Tempe, AZ 85287
[2] Freescale Semiconductor, Sensor and Analog Products Division, Tempe, AZ 85284
[3] University of California at Berkeley, Department of Mechanical Engineering, Berkeley, CA 94720

ABSTRACT

This paper describes a cantilever beam pull-in voltage model in terms of beam length, thickness, initial dielectric gap, and beam material Young's modulus. A closed form beam deflection model is described for use with voltage actuated MEMS cantilever beams via an underlying mechanically fixed electrode. Electrostatic force is summed over the deflected cantilever beam using a function integrated over beam length evaluated from anchor to beam tip. The net electrostatic moment is applied normal to the cantilever beam tip as a function of the deformed beam displacement angle. The proposed model consistently predicted pull-in voltage with less error, when compared to empirical and simulated results, than previously reported theoretical models without the use of empirical correction factors. Pull-in voltage model prediction was improved by over 12% when compared to a previously described theoretical model using polysilicon cantilever beam latch measurements as a reference.

INTRODUCTION

Multiple electrostatic pull-in models have been previously developed over the past decade for use in high-end MEMS software simulation tools [1,2]. Typically, these software simulation tools are based on finite element analysis (FEA) techniques requiring multiple solution iterations distributed amongst a plethora of nodes before converging to desired solution resolution values. Finite element analysis simulation provides a critical step towards MEMS design optimization and verification prior to device fabrication and characterization phases. However, FEA based model solution is not easily implemented via manual calculation techniques and can be difficult to include in high-level system transfer functions generated during early project definition phases.

MEMS system designers typically desire a more generic pull-in relationship [3] between critical beam layout dimensions and operational device voltage ranges during early phases of project transfer function specification using compact manual equation calculations and techniques without the use of empirical correction factors [4,5]. This first pass design feasibility approach allows the MEMS designer to identify and estimate critical device operation parameters to be optimized via computer based simulation techniques during subsequent project phases. Additionally, these compact models are useful to demonstrate generic system input/output parameter trends while training junior designers and engineering students. This is analogous to manually derived high-level transfer function approximations typically used by CMOS integrated circuit designers to model analog circuit blocks prior to system optimization and verification using high-end SPICE software tools.

Numerous MEMS applications incorporate singly clamped cantilever and/or doubly clamped beams as an integral part of their design. A brief application list includes resonators [6-9], vapor/pressure sensors [10-12], accelerometers [13,14], high-Q electronic filters [15-16], and micro relay switches [5,17,18].

Surface micromachined polysilicon cantilever beams suspended above an isolated electrode are common throughout MEMS commercial applications [13,14].

ELECTROSTATIC PULL-IN MODEL

The cantilever beam is defined in term of length, width, and thickness as shown in Figure 1.

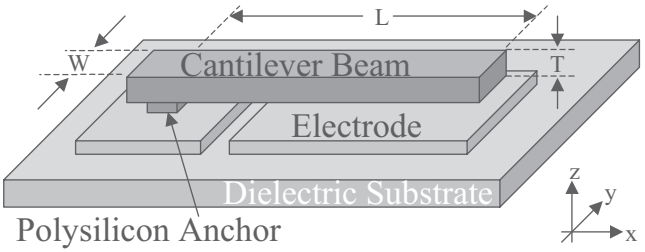

***Figure 1**. Polysilicon cantilever beam dimensions.*

The electrostatic moment M_1 (1) applied at the beam tip is described in terms of the beam displacement v along the x-axis in the z-direction [19], where E is the Young's modulus (150GPa), and I is the moment of inertia (2), as shown in Figure 2.

$$M_1 = -EI\frac{d^2v}{dx^2} \tag{1}$$

$$I = \frac{WT^3}{12} \tag{2}$$

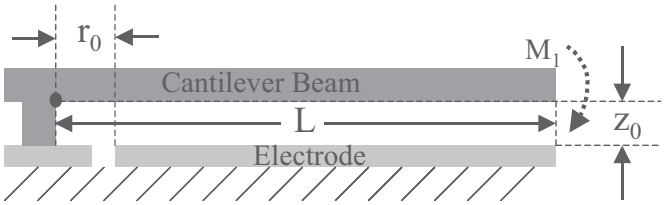

***Figure 2**. Cantilever Beam w/Moment Applied at Free End.*

The beam displacement v along the x-axis in the z-direction [19] is given in (3).

$$v = \frac{M_1x^2}{2EI} \tag{3}$$

The electrostatic moment M_1 applied at the beam tip (4) represents the summed electrostatic force F_M along the beam (5) multiplied by the resulting beam tip deflection Δ_z (6) using beam displacement v (3), where Δ_z and Z_{tip} are defined at $x=L$ as measured from the fixed electrode reference. Note that the magnitude of F_M also represents the beam mechanical restoring force magnitude.

$$M_1 = F_M L \tag{4}$$

$$\left|F_M\right| = K_Z \Delta_z \tag{5}$$

$$\Delta_Z = z_0 - z_{tip} \tag{6}$$

The z-axis cantilever beam mechanical spring constant for a tip applied moment (7) is given by (8).

$$K_Z = \left|\frac{F_M}{v(x=L)}\right| \tag{7}$$

$$K_z = \frac{EWT^3}{6L^3} \tag{8}$$

The capacitance between the deflected beam and fixed electrode is defined by (9) with substitution shown in (10) and simplification shown in (11).

$$C_{beam} = \int_{r_0}^{L} \frac{\varepsilon_o W}{z_o - v} dx \tag{9}$$

$$C_{beam} = \int_{r_0}^{L} \frac{\varepsilon_o W}{z_o - \dfrac{K_z(z_0 - z_{tip})Lx^2}{2EI}} dx \tag{10}$$

$$C_{beam} = \int_{r_0}^{L} \frac{\varepsilon_o W}{z_o - \Delta_z \dfrac{x^2}{L^2}} dx \tag{11}$$

The indefinite integral is shown for this function in (12).

$$C_{beam} = \frac{\varepsilon_0 LW}{\sqrt{z_0 \Delta_z}} a\tanh\left(\frac{x\Delta_z}{L\sqrt{z_0\Delta_z}}\right) \tag{12}$$

Model Simplification is possible by setting the electrode length equal to the beam length such that $r_0=0$ in (11) and (12) as shown in (13).

$$C_{beam} = \frac{\varepsilon_0 LW}{\sqrt{z_0 \Delta_z}} a\tanh\left(\frac{\Delta_z}{\sqrt{z_0\Delta_z}}\right) \tag{13}$$

The summed electrostatic force is defined by (13) for static electromechanical equilibrium where V_M represents the applied voltage between the beam and fixed electrode. Note that F_M represents the system mechanical restoring force (5) and Z_{tip} is the distance measured from the fixed electrode to the displaced beam defined by (6).

$$F_M = -\frac{1}{2}\frac{dC_{beam}}{d(z_{tip})} V_M{}^2 \tag{13}$$

The applied beam voltage parameter listed in (13) is rearranged in (14) with solution given in (15).

$$V_M = \sqrt{\frac{2K_z(z_o - z_{tip})}{-\dfrac{dC_{beam}}{d(z_{tip})}}} \tag{14}$$

$$V_M = \sqrt{\frac{2K_z(z_o - z_{tip})z_0 z_{tip}}{\varepsilon_0 LW\left(z_0^2 - z_0 z_{tip} + z_{tip}\left(\sqrt{z_0(z_0 - z_{tip})}\right) a\tanh\left(\dfrac{z_{tip} - z_0}{\sqrt{z_0(z_0 - z_{tip})}}\right)\right)}} \tag{15}$$

The pull-in voltage V_{MPI} [20] given by (16) represents the peak voltage (15) satisfying electromechanical static equilibrium swept over the beam tip displacement range $0<z<z_0$ as shown in Figure 3.

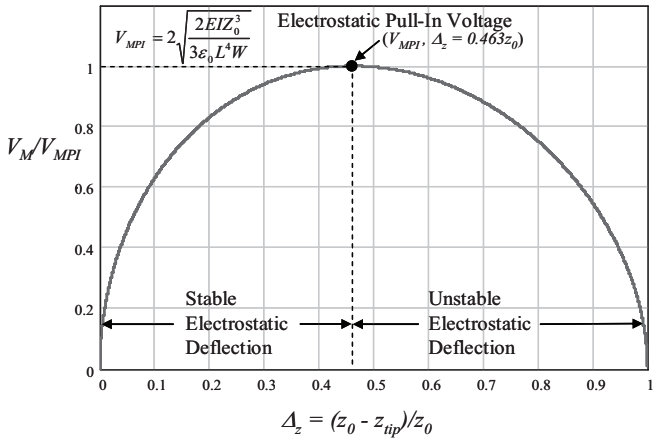

***Figure 3**. Normalized actuation voltage versus normalized beam tip displacement.*

$$V_{MPI} = 2\sqrt{\frac{2EIz_0^3}{3\varepsilon_0 L^4 W}} \tag{16}$$

The moment of inertia (2) is substituted into (16) and simplified as given by (17) in terms of beam length L, beam thickness T, initial dielectric beam gap z_0, and the material dependent Young's modulus E.

$$V_{MPI} = \frac{1}{3}\sqrt{\frac{2ET^3 z_0^3}{\varepsilon_0 L^4}} \tag{17}$$

THEORETICAL PULL-IN MODEL COMPARISON

Cantilever beam pull-in voltage has been previously described using a novel beam theory model [3] by parameter V_{th} and a parallel plate model [21] by parameter V_{PI} as shown in Figure 4. The parallel plate model parameter V_{PI} estimates the pull-in voltage to be approximately ½ that predicted by V_{th}. Typically, V_{PI} underestimates pull-in voltage. Similarly, V_{th} typically overestimates pull-in voltage. As beams width is increased, V_{th} typically predicts pull-in voltage with less error than V_{PI}. Maximum beam tip displacement, which has been previously measured using a confocal microscope as 0.46μm [22], is more

accurately described by V_{th} when compared to V_{PI} regarding model predicted maximum tip displacement prior to pull-in.

Comparing pull-in voltage magnitudes and beam tip displacements we note that V_{th} and V_{MPI} predict similar maximum stable beam tip displacements as $0.45z_0$ and $0.463z_0$ respectively. This small difference in maximum stable displacement is attributed to the similar deflected beam shape functions utilized by these models as shown in Figure 5. Note that the previous model directs electrostatic force exclusively along the z-axis, while the proposed model applies electrostatic force normal to the beam tip. The tip moment applied electrostatic force presented in this paper is analogous to the electric field boundary condition regarding field lines terminating normal to electrically conductive surfaces, such as the deflected beam and fixed electrode surfaces.

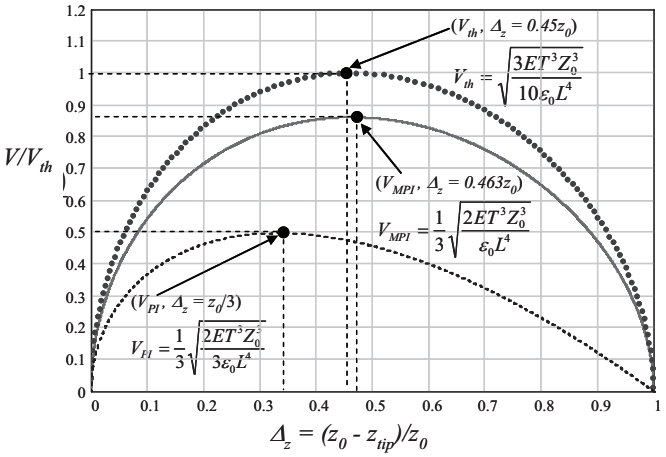

***Figure 4**. Normalized actuation voltage versus normalized beam tip displacement.*

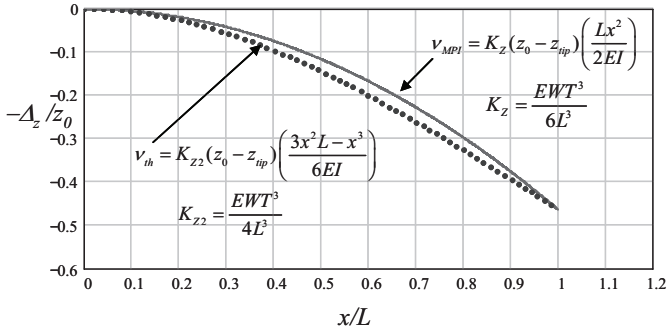

***Figure 5**. Normalized beam displacement contour versus beam length normalized from anchor to (beam tip = 0.463zo)*

EXPERIMENTAL RESULTS

Polysilicon cantilever beam arrays were fabricated on Si_3N_4 passivated silicon wafers as shown in Figure 6. The characterized polysilicon beam arrays were 160µm long and 2µm thick. Beam widths were varied at 2µm, 4µm, and 6µm. The initial dielectric gap was fixed at 2µm for all beam arrays. A typical polysilicon beam array with 160µm by 6µm by 2µm dimensions is shown in Figure 7.

Capacitance-Voltage (C-V) measurements [22] were performed using an HP-4284A LCR meter controlled via LabView software. Electrostatic actuation was accomplished by increasing the LCR meter DC bias voltage between the cantilever beam and underlying electrode in discrete 50mV increments. The pull-in voltage models are compared to empirical results in Table 1.

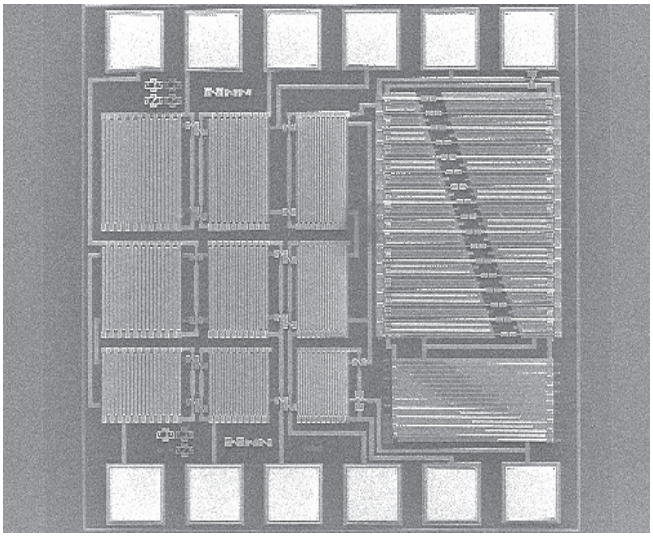

***Figure 6**. Polysilicon cantilever beam arrays with substrate fixed actuation electrodes.*

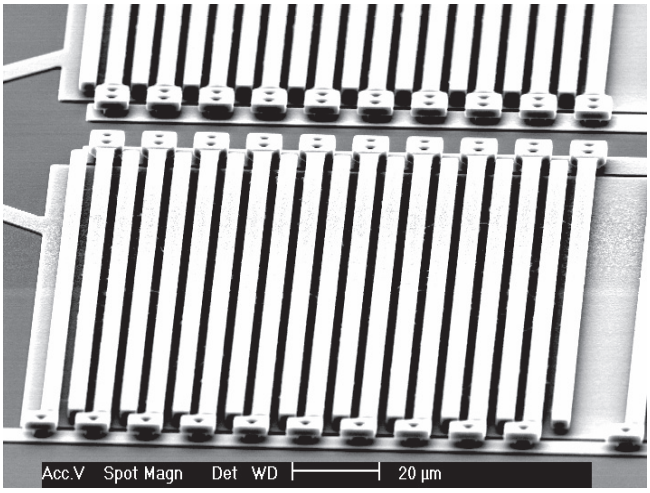

***Figure 7**. Typical polysilicon cantilever beam array (160µm long, 6µm wide, and 2µm thick) with underlying actuation electrode 2µm dielectric gap.*

***Table 1**. Polysilicon cantilever beam electrostatic pull-in voltage model prediction values compared to empirical results.*

Beam Array ID #	L = 160u T = 2u Width [u]	Empirical Pull-in [V]	Fig. 5 Vth [V]	Fig. 5 Vpi [V]	Eq (17) Vmpi [V]	Fig. 5 Vth % Error	Fig. 5 Vpi % Error	Eq (17) Vmpi % Error
1	2	14.20	22.28	11.07	19.18	36.3	-28.3	26.0
2	2	14.35	22.28	11.07	19.18	35.6	-29.6	25.2
3	2	14.15	22.28	11.07	19.18	36.5	-27.8	26.2
4	4	15.80	22.28	11.07	19.18	29.1	-42.7	17.6
5	4	16.30	22.28	11.07	19.18	26.8	-47.2	15.0
6	4	15.90	22.28	11.07	19.18	28.6	-43.6	17.1
7	6	17.85	22.28	11.07	19.18	19.9	-61.2	6.9
8	6	17.35	22.28	11.07	19.18	22.1	-56.7	9.5
9	6	17.60	22.28	11.07	19.18	21.0	-59.0	8.2

Multiple polysilicon cantilever beams were observed to remain latched [23] to the underlying polysilicon electrode post pull-in voltage excitation as shown in Figure 8. Beams were easily released from the underlying electrode using micromanipulator probes with no visual electrical current damage or welding observed.

ANSYS finite element analysis (FEA) software was used to simulate cantilever beam pull-in voltage with simulation results compared to theoretical model prediction and empirical results in

Table 2. The 3D solid 122 Ansys element type prediction yielded results with less than 0.6% Error when compared to empirical pull-in data.

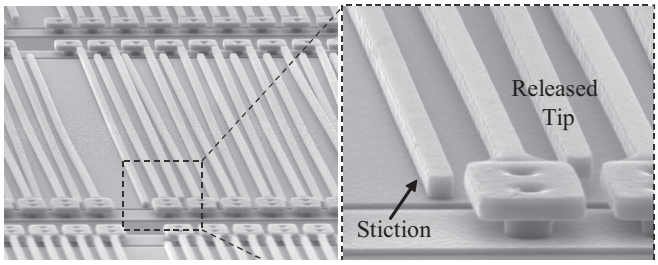

***Figure 8**. Post electrostatic voltage actuated polysilicon cantilever beam tip to fixed electrode stiction.*

***Table 2**. Pull-in voltage simulation results compared to model prediction values and average empirical result (6μm wide beams).*

ANSYS Element Dimension	Ansys Element Type	Simulated Pull-In [V]	Empirical Pull-In Avg [V]	Fig. 5 Vth [V]	Fig. 5 Vpi [V]	Eq. (17) Vmpi [V]
2D	Plane82 with plane strain	22.3	17.6	22.28	19.18	18.50
2D	Plane82 with plane stress	18.5	17.6	22.28	19.18	18.50
3D	Solid122, W=6um	17.5	17.6	22.28	19.18	18.50

CONCLUSIONS

We have presented a closed form algebraic model describing MEMS cantilever beam electrostatic actuation and pull-in. Maximum displacement of the beam tip is predicted to occur at 46.3% of the initial dielectric gap just prior to electrostatic pull-in. This model accounts for beam deflection applicable to cantilever beam and micro-relay electromechanical systems where the underlying electrode fully extends to the cantilever beam tip. The proposed beam theory model %Error was compared to empirical pull-in voltage measurements for the 2μm, 4μm, and 6μm wide beams as 25.8% (σ = 0.5%), 16.6% (σ = 1.4%), and 8.2% (σ = 1.3%), respectively. Pull-in voltage model prediction was improved by 12.8% when compared to a previously described model using polysilicon cantilever beam latch measurements as a reference. We attribute the observed improvement in model performance to the tip applied beam moment to represent electrostatic force distributed along the beam underside in this paper. Applying the summed electrostatic force under the deflected beam normal to the beam tip as a moment reduced the system defined spring constant K_z by 33.3%. Reduction of this spring constant was attributed to better pull-in model prediction.

REFERENCES

[1] E. S. Hung and S. D. Senturia, "Generating Efficient Dynamical Models for *Micromechanical* Systems from a few finite-element analysis Runs", J. Micromechanical Systems, vol 8, pp. 280-289, 1999.

[2] L. D. Gabbay, J. H. Mehner, and S. D. Senturia, and S. D. Senturia, "Computer Aided generation of non-linear Reduced-Order Dynamic Macromodels", J. Micro-mechanical Systems, vol 9, pp. 262-269, 2000.

[3] K. E. Petersen, "Dynamic Micromechanics on Silicon, Techniques and Devices", IEEE Transaction on Electron Devices, vol. ED-25, no. 10, pp 1241-1250, 1978.

[4] P. M. Osterberg and S. D. Senturia, "M-Test: A Test Chip for MEMS Mechanical Property Measurement Using Electrostatically Actuated Test Structures", J. Micromechanical Systems, vol 6, pp. 107-118, 1997

[5] P. M. Zavracky, S. Majumder, and N. E. McGruer, "Micromechanical Switches Fabricated Using Nickel Surface Micromachining", Journal of Micro-electromechanical Systems, vol. 6, pp 3-9, 1997.

[6] H. C. Nathanson, W. E. Newel, R. A. Wickstrom, and J. R. Davis, "The Resonant Gate Transistor", IEEE Transactions on Electron Devices, vol. ED-14, no. 3, pp. 117-133, 1967.

[7] K. E. Petersen, "Dynamic Micromechanics on Silicon, Techniques and Devices", IEEE Transaction on Electron Devices, vol. ED-25, no. 10, pp 1241-1250, 1978.

[8] R. T. Howe, "Applications of Silicon Micromachining to Resonator Fabrication", IEEE International Frequency Control Symposium, pp. 2-7, 1994.

[9] W. C. Tang, C. T. Nguyen, M. Judy, and R. T. Howe, "Electrostatic Comb Drive of Lateral Polysilicon Resonators", Sensors and Actuators, vol. A21, pp. 328-331, 1990.

[10] R. T. Howe, and R. S. Muller, "Resonant Microbridge Vapor Sensor", IEEE Trans. Electron Devices, ED-33, pp. 499-506, 1986.

[11] C. H. Masrangelo, and R. S. Muller, "Fabrication and Performance of a Fully Integrated μ-Pirani Pressure gauge with Digital Readout", IEEE Solid State Sensors and Actuators, Transducers 91, pp. 245-248, 1991.

[12] R. K. Gupta, and S. Senturia, "Pull–In Dynamics as a Measure of Absolute Pressure", IEEE MEMS 97, pp. 290-294, 1997.

[13] L. J. Ristic, R. Gutteridge, B. Dunn, D. Mietus, and P. Bennett, "Surface Micromachined Polysilicon Accelerometer", IEEE Solid State Sensors and Actuators, Hilton Head, p. 118, 1992.

[14] S. J. Sherman, W. K. Tsang, T. A. Core, R. S. Payne, D. E. Quinn, K. H. Chau, J. A. Farash, and S. K. Baum, "A Low Cost Monolithic Accelerometer; Product/Technology Update", IEEE International Electron Devices Meeting, pp. 501-504, 1992.

[15] C. T. Nguyen, "High-Q Micromechanical Oscillators and Filters for Communications", IEEE International Symposium on Circuits and Systems, pp. 2825-2828, 1997.

[16] K. Wang, and C. T. Nguyen, "High Order Micromechanical Electronic Filters", IEEE MEMS 97, pp. 25-30, 1997.

[17] K. E. Petersen, "Micromechanical Membrane Switches on Silicon", IBM Journal of Research and Development, Vol. 23, no. 4, pp. 376-385, 1978.

[18] M. A. Gretillat, Y. J. Yang, E. S. Hung, V. Rabinovich, G. K. Ananthasuresh, N. F. de Rooij, and S. D. Senturia, "Nonlinear Electromechanical Behavior of an Electrostatic Microrelay", IEEE MEMS 97, pp. 1141-1144, 1997.

[19] R. Roark and W. Young, "Roark's Formulas for Stress and Strain, 6th Edition", McGraw-Hill, New York, NY, 1989

[20] G. O'Brien, D. J. Monk, and L. Lin, "A Stiction Study Via C-V Plot Electrostatic Actuation/Latching", ASME Microelectromechanical Systems, vol. 1, pp. 275-280, 1999.

[21] H. C. Nathanson, W. E. Newel, R. A. Wickstrom, and J. R. Davis, "The Resonant Gate Transistor", IEEE Transactions on Electron Devices, vol. ED-14, no. 3, pp. 117-133, 1967.

[22] G. O'Brien, D. J. Monk, and L. Lin, "Electrostatic Latch and Release; a Theoretical and Empirical Study", ASME Microelectromechanical Systems vol. 2, pp. 19-26, 2000.

[23] C. H. Mastrangelo and C. H. Hsu,"Mechanical Stability and Adhesion of Microstructures Under Capillary Forces –Part 1: Basic Theory", Journal of Micro-electromechanical Systems, Vol. 2, No. 1, 1993.

MICROMACHINED PMN-PT SINGLE CRYSTAL FOR ADVANCED TRANSDUCERS

Xiaoning Jiang[1], Jian R. Yuan[2], An Cheng[3], Guy Lavallee[3], Paul Rehrig[1], Kevin Snook[1], Seongtae Kwon[1], Wesley Hackenberger[1], Jeffrey Catchmark[3], John McIntosh[3] and Xuecang Geng[4]

[1] TRS Technologies, Inc., 2820 East College Ave., State College, PA 16801.
[2] Boston Scientific Corporation, IVUS Technology Center, 47900 Bayside Parkway, Fremont, CA 94538
[3] Nanofabrication Facility, The Pennsylvania State University, 188 Materials Research Institute, University Park, PA 16802-7003
[4] Blatek, Inc., 2820 East College Avenue, Suite F., State College, PA 16801

ABSTRACT

In this paper a deep reactive ion etching (DRIE) process developed for the micromachining of bulk piezoelectrics is discussed. For the first time, a PMN-PT single crystal piezoelectric micro-array was fabricated with an array post cross section size of 14 μm x 14 μm, a height of >60 μm, and a spacing between micro-posts of about 2-6 μm. The etched single crystal piezoelectrics retained high piezoelectricity (d_{33} ~2000 pC/N) and low dielectric loss (<0.01). Single crystal/epoxy 1-3 composites were fabricated using the etched micro-arrays and the electromechanical coupling coefficient of such piezoelectric composites was ~0.72, indicating promising applications such as micro-sensors, actuators and transducers.

INTRODUCTION

Thin film, thick film and bulk piezoelectric materials have been widely used for a broad range of sensors, actuators and transducers. Thin and thick piezoelectric films such as ZnO, AlN and PZT have been more popular for piezoelectric microdevices or piezo-MEMS because of the ability to use microfabrication processes. However, the piezoelectric properties of films are significantly lower compared with their bulk counterparts, for example, electromechanical coefficients of thin and thick films of PZT are inferior to those of bulk PZT by a factor of 2-5 [1], which means that the performance of piezo MEMS devices could be further improved by using piezoelectrics with advanced properties. Various film and bulk piezoelectric materials properties are compared in Table 1. Single crystal piezoelectrics based on $Pb(Zn_{1/3}Nb_{2/3})_{1-x}Ti_xO_3$ (PZN-PT) or $Pb(Mg_{1/3}Nb_{2/3})_{1-x}Ti_xO_3$ (PMN-PT) exhibit large increases in strain over conventional piezoelectric ceramics (***Figure 1***) due to the ability to orient the crystals along a preferred high strain crystallographic direction [2]. The crystals' piezoelectric strain remains nearly hysteresis free up to levels of ~0.5 to 0.6% depending on the crystal composition, which is desired for many piezoelectric actuation. Also because of the considerably higher piezoelectric coefficients and electromechanical coupling factors, single crystals are being used to fabricate ultrasound transducers (< 20 MHz) with unprecedented bandwidth (>100%) and sensitivity [3-6].

Both dry etching (plasma and RIE etching) and wet etching methods can be used to pattern piezoelectric thin films for piezo-MEMS, but precise patterning or micromachining of bulk piezoelectrics and thick PZT films has been very difficult and that's why most of the research and development efforts were directed to thin film based micro-sensor, actuator and transducers. Anisotropic dry etching of PZT has drawn a lot of attention, and some interesting results have been achieved [7-10]. In addition to the advances in PZT dry etching, some major plasma and RIE etching tool suppliers such as Tegal and Oxford Instruments have specific tools and processes aimed at the PZT etching market. Table 2 presents etching chemistry, etch rate, and sidewall profile characteristics. Recent progress on deep PZT dry etching has shown >100 μm etch with an etching side wall angle of ~76° [7,10], which may be good for most of the piezo-MEMS fabrication. The goal of this work was to further develop a dry deep etching process with a better etching profile for fabrication of a PMN-PT single crystal piezoelectric micro-array, which is necessary to fabricate advanced high frequency ultrasound transducers [11].

In this paper, a deep etching process for PMN-PT single crystal was investigated for micromachined piezoelectric sensor, actuator and transducer applications. The possible crystal degradation because of the etching damage was also investigated**.** Various single crystal /epoxy 1-3 composites were prepared and characterized for advanced high frequency transducers.

Table 1. Film and bulk piezoelectric materials properties.

Piezoelectric materials	Piezoelectric coefficient (pC/N)	Young's Modulus (GPa)	Electro-mechanical coupling
AlN (film)	d_{31} ~-2	330	k_t ~0.24
ZnO (film)	d_{31} ~-5	210	k_t ~0.27
PZT (sol-gel, sputtering)	d_{31} ~-100	40	k_{33} ~0.39
PZT (Bulk)	d_{33}, ~600 d_{31} ~-300	70	k_{31}~0.4 k_{33} ~0.7
Single crystal (bulk)	d_{33} ~2000 d_{31} ~-1000	12	k_{31}~0.85, k_{33} ~0.93

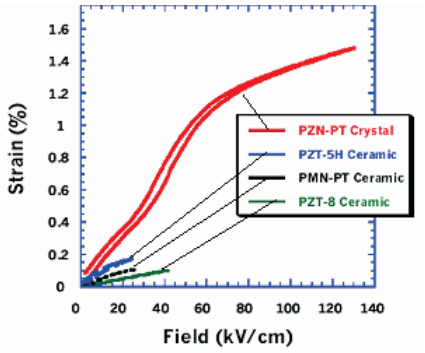

Figure 1. Piezoelectric strain response from single PZN-PT single crystal material compared to piezoelectric and electrostrictive ceramics. The crystal strain remains nearly hysteresis free up to ~0.6%. At high fields very large strains >1% can be achieved but with an increase in hysteresis.

Table 2. PZT dry etching .

Etch Chemistry	Etch Rate	Etch Depth	Side wall Angle
Cl_2/Ar, C_2F_6/Ar, Cl_2/C_2F_6/Ar, HBr/Ar	900-1300 A/min	0.25 µm	50-80°
CF_4/O_2, CF_4/N_2	~60 nm/min	-	-
Cl_2/CF_4	~90 nm/min	-	-
SF_6	300 nm/min	70 µm	~75°
SF_6	~120 nm/min	2 µm	85-90°
SF_6, SF_6/N_2, SF_6/Ar	~160 nm/min	>100 µm	~72 °

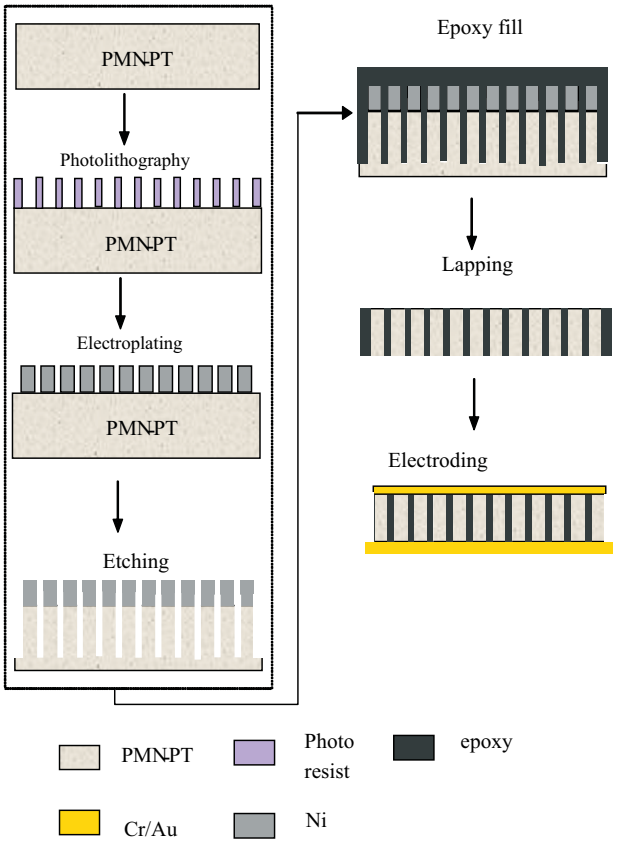

Figure 2. Schematic process flow for micromachined PMN-PT/epoxy 1-3 composites.

EXPERIMENTAL PROCEDURE AND RESULTS

PMN-PT single crystal plates with d_{33} of 1800-2200 pC/N, dielectric constant of 5000-7500, and dielectric loss <0.01 were prepared as wafers and lapped on both sides and polished on one side. For the wafer damage study, a wafer was etched without any additional wafer preparation. XRD characterization as well as d33 measurements were conducted on the damage-study wafer before and after etching. For PMN-PT micro-array fabrication, a wafer with a polished side was coated with 2000 Å Ni using an evaporator as an electroplating seed layer and then the wafer was ready for photoresist coating. A 15 µm thick photoresist (SPR-220) was coated onto the wafer and baked at 110°C for 2 minutes. A direct laser writing lithography was used in this study to pattern the photoresist. A He-Cd laser with UV energy of 50 mW and wavelength of 442 nm was used. The exposed wafers were then developed and put into a Ni electroplating bath. After electroplating the wafers were soaked in acetone to strip the photoresist, and the wafer was then ready for etching. The PMN-PT wafer with a Ni hard mask was then put into the etching chamber of the P5000 using a Cl_2 based deep etching. The etched micro-array for high frequency 1-3 composites prototyping was then ready for epoxy filling, where the spacing between posts in micro-array was filled with epoxy to form the 1-3 composites. The epoxy was cured over night at room temperature. This was followed by a precise lapping process to remove the remnant crystal at the back and the epoxy at the front until the posts were exposed from both sides and the desired thickness was achieved. Cr/Au electrodes were coated onto both sides of the composites and the composites were poled at 15 kV/cm at room temperature for a few minutes. Figure 2 shows the process flow for the micromachined high frequency 1-3 piezoelectric composite fabrication. The etching depth and the openings between posts were inspected using SEM. The impedance and phase spectrum and dielectric loss of the prototyped composites were recorded using a HP 4194A impedance analyzer, and the electromechanical coupling coefficients of the composites were then calculated using an IEEE standard [12].

The XRD pattern of the PMN-PT single crystal surface before and after Cl2 based deep etching is shown in Figure 3a and 3b, respectively. The prior and post etching patterns matched with each other closely, indicating no observable surface damage induced by the RIE processing. Figure 3c shows the strain vs. field property of the crystal after etching, which is also a typical strain-field curve for crystals without etching, meaning the piezoelectric properties were retained after etching. This experiment cleared the concern that the possible etching induced damage may affect the performance of micromachined single crystal piezoelectric devices. Laser lithography is the first step in fabrication of micromachined PMN-PT composites. Precision photoresist patterning helps define the Ni mask plated through the mold, and further affects the etching rate and depth. Figure 4a shows Ni plating through a well-defined photoresist pattern, and Figure 4b shows the Ni mask after stripping the plating and photoresist.

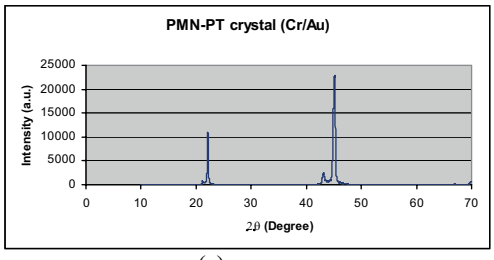

(a)

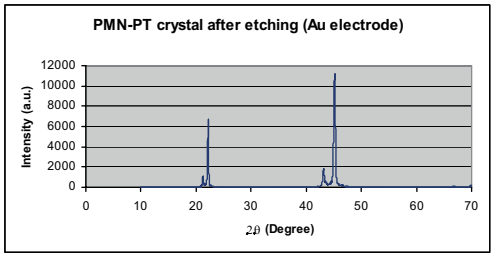

(b)

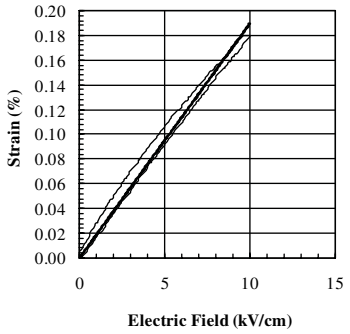

(c)

Figure 3. Experiments on the possible crystal property degradation induced by etching damage. (a) XRD pattern of crystal surface before etching. (b) XRD pattern of crystal surface after etching 9 hours . (c) Strain-field property of crystal after etching 9 hours.

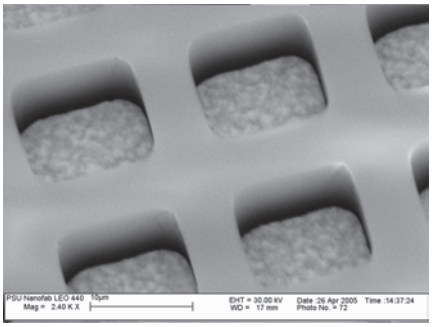

(a)

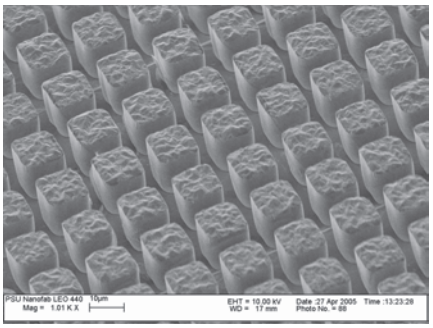

(b)

Figure 4. Photoresist and Ni pattern. (a) the photoresist pattern and plated Ni posts during plating. (b) the Ni post array after stripping the photoresist.

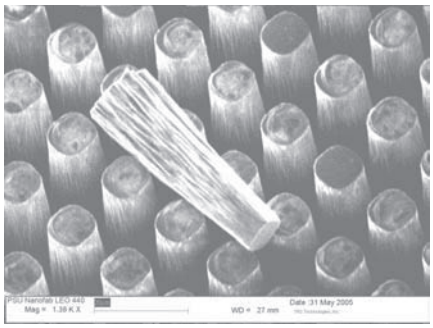

Figure 5. SEM picture of an etched PMN-PT single crystal micro-array.

The etching rate ratio of PMN-PT crystal to Ni is about more than 5 in this study. The obtained PMN-PT etching rate ranged from 2 μm/hour to 8 μm/hour depending on the pattern, exposed area, and etching conditions such as RF power, flowrate, etc [7-10]. Figure 5 shows a PMN-PT micro-array with posts of ~67 μm high, with a post height/width aspect ratio of >4. It is also noticed that the angle of etched side wall profile is >87°, which allows precise and deep etching of more closely standing PMN-PT single crystal micro-arrays comparing to the PZT etching results published by other groups [7-10]. Figure 6 shows a photograph picture of the PMN-PT/epoxy 1-3 composite ready for characterization. The thickness of the prepared piezoelectric composites ranged from 20 μm to 60 μm. To characterize the piezoelectric micro-array, an impedance analyzer was used to record the impedance and phase vs. frequency (Figure 7) and the effective electromechanical coupling of the array was calculated to be ~0.72, which is close to its bulk material property and is very promising for advanced transducers with high sensitivity and broad bandwidth [13-15]. The composite with thickness of 31 μm was used to fabricate a 40 MHz ultrasound transducer, and the transducer characterization results showed significantly improved sensitivity and bandwidth compared with PZT transducers. The results of the 40 MHz transducer characterization and animal imaging tests will be reported in another paper [16].

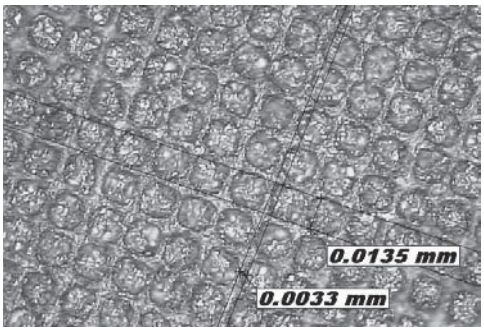

Figure 6. Photograph of a micromachined PMN-PT/epoxy 1-3 composite.

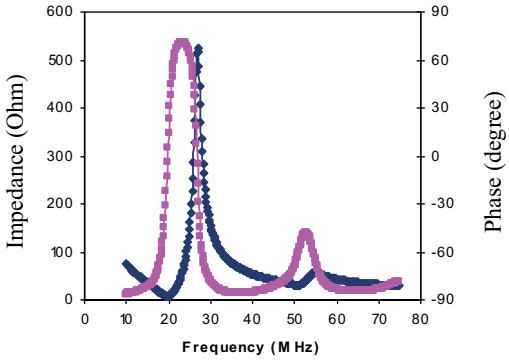

(a)

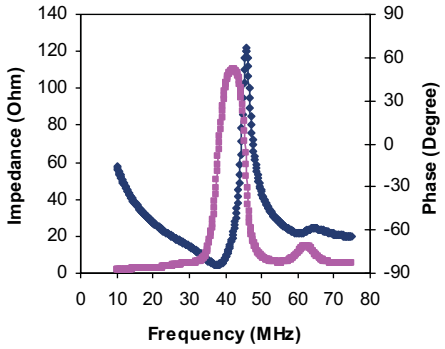

(b)

Figure 7. Resonant mode of the fabricated PMN-PT single crystal micro-array. (a) Impedance and phase vs. frequency of a 60 μm thick micro-array. (b) Impedance and phase vs. frequency of a 31 μm thick micro-array.

CONCLUSIONS

The developed deep etching process for PMN-PT single crystal shows no-noticeable etching induced damage to the crystal, the d_{33} of single crystal after etching retained its value before etching (1800-2200 pC/N). An almost vertical etching, >87° was achieved with a depth >60 μm. The PMN-PT microarray was successfully used for to prototype 1-3 piezoelectric composites. Composites with resonant frequency ranging from 20 MHz to >45 MHz showed electromechanical coupling coefficients of ~0.72, which is promising for various piezoelectric sensors and transducers applications.

REFERENCES

[1] S. Trolier-McKinstry and P. Muralt, "Thin Film Piezoelectrics for MEMS," J. Electroceram. 12 (1-2) 7-17 (2004).

[2] S.E. Park and T.R. Shrout, "Relaxor based ferroelectric single crystals for electromechanical actuators", Mat. Res. Innovat., 1, pp.20-25, 1997.

[3] T. Ritter, X.Geng, K. Shung, P.D. Lopath, S.E. Park, and T.R. Shrout, "Single Crystal PZN/PT-Polymer Composites for Ultrasound Transducer Applications", IEEE Transactions on Ultrasonics, Ferroelectrics, and Frequency Control, Vol.47, No.4, July 2000, pp. 792-800.

[4] M. Zipparo, C. Oakley, W. Hackenberger and L. Hackenberger, "Single Crystal Composites, Transducers, and Arrays", IEEE Ultrasonic Symposium 1999, pp.965-968.

[5] W. Hackenberger, X. Jiang, P. Rehrig, X. Geng, A. Winder, and F. Forsberg, "Broad Band Crystal Transducer for Contrast Agent Harmonic Imaging", 2003 IEEE Ultrasonic Symposium, pp.778-781.

[6] K.C.Cheng, H.L.W. Chan, C.L.Choy, Q.Yin, H. Luo, and Z. Yin, "Single Crystal PMN-0.33PT/Epoxy 1-3 Composites for Ultrasonic Transducer Applications", IEEE Trans. Ultrasonics, Ferroelectrics, and Frequency Control, Vol.50, No.9, Spet. 2003, pp.1177-1183.

[7] S. Wang, X. Li, K. Wakabayashi, and M. Esashi, Deep reactive ion etching of lead zirconate titanate using sulfur hexafluoride gas, J. Am. Ceram. Soc., 82(5) pp. 1339-1341, 1999.

[8] C.W. Chung, Y.H. Byun and H.I. Kim, Inductively coupled plasma etching of $Pb(Zr_xTi_{1-x})O_3$ thin films in Cl_2/C_2F_6 and HBr plasma, Proc. 200th Electrochemical Society Meeting, 2000.

[9] J.K. Jung and W.J. Lee, Dry etching characteristics of Pb(Zr, Ti)O_3 films in CF_4 and Cl_2/CF_4 inductively coupled plasmas, Jpn. J. Appl. Phys. Vol. 40(2001)pp. 1408-1419, 2001.

[10] M. Bale and R.E. Palmer, Deep plasma etching of piezoelectric PZT with SF_6, J. Vac. Sci. Technol. B 19(6), pp. 2020-2025, 2001.

[11] P.W. Rehrig, X. Jiang, W. Hackenberger, J.R. Yuan and R. Romley, "Micromachined Imaging Transducer", US Patent Application No. #11/202,674, 2005.

[12] IEEE Standard on Piezoelectricity, Std. 176-1987, IEEE, New York, 1987.

[13] J.F. Gelly, and F. Lanteri, "Comparison of Piezoelectric (thickness mode) and MEMS Transducers", 2003 IEEE Ultrasonic Symposium, pp.1965-1974.

[14] D. L. DeVoe, and A. P. Pisano, "Modeling and Optimal Design of Piezoelectric Cantilever Microactuators", J. Microelectromechanical Systems, Vol. 6, No.3, September 1997, pp.266-270.

[15] N. Ledermann, P. Muralt, J. Baborowski, M. Forster, and J.P Pellaux, "Piezoelectric $Pb(Zr_x, Ti_{1-x})O_3$ Thin Film Cantilever and Bridge Acoustic Sensors for Miniaturizaed Photoacoustic Gas Detectors", J. Micromech Microeng 14(2004) pp.1650-1658.

[16] J.R.Yuan, X.Jiang, P.W. Rehrig, et al., IEEE Ultrasonic Symposium, 2006.

MICROMANIPULATOR CONTROLLED FABRICATION OF MICRO- AND NANOSCALE POLYMER FIBERS AND APPLICATION AS SACRIFICIAL STRUCTURES IN THE PRODUCTION OF MICROCHANNELS

Scott M. Berry[1], Thomas J. Roussel[1,2], Scott D. Cambron[1,2], Steven A. Harfenist[3*], Robert W. Cohn[3], and Robert S. Keynton[1,2,3]

Departments of Mechanical Engineering[1] and Bioengineering[2], and
the ElectroOptics Research Institute and Nanotechnology Center[3]
University of Louisville, Louisville, KY, USA
* Current address for SAH is Department of Physics, California Polytechnic State University
San Luis Obispo, CA, USA

ABSTRACT

Suspended micro- and nanoscale polymer fibers were created using a new and novel technique which is performed at room temperature. This method involves drawing solvated PMMA into liquid filaments, which thin, via surface tension, as the solvent evaporates, subsequently yielding a solid fiber. The PMMA solution was drawn by two separate techniques: 1) using a stylus to extrude a solution filament between two pre-deposited pools, and 2) using a pressurized capillary loaded with solution to directly deposit filaments of solution on the substrate in a "connect-the-dots" style. Also, because both the stylus and pressurized capillary were controlled with an ultra-high precision instrument, the fibers can be precisely positioned in three dimensions. The diameters of these fibers were controlled, within the range of 450 nm to 100 μm, by varying the molecular weight of the polymer or the concentration of the PMMA solution. It was discovered that increasing either or both of these variables led to an increase in fiber diameter. Also, the effect of stylus material on fiber diameter variance was examined, with a Parylene®-coated stylus yielding the lowest overall variance. These fibers were coated with glass and Parylene® and dissolved to produce hollow microchannels suitable for electroosmotic flow. Electroosmotic channels with diameters ranging from 4 μm to 100 μm were successfully fabricated and tested.

INTRODUCTION

A new technique for fabricating micro- and nanoscale polymer fibers has been discovered and was reported in [**1, 2**]. This technique involves drawing a filament of solvated polymer at room temperature between two points and allowing surface tension forces to thin the diameter of the filament to the micro- or nanoscale before evaporation of the solvent leads to the solidification of the filament into a fiber. These structures are fabricated in three dimensions, providing an escape from the constraints of conventional planar fabrication. It has been suggested by [**1**] that fibers created with this process could be used as microoptical couplers, sacrificial backbones for microfluidic devices, or three-dimensional (3-D) electrical connectors (via applying this method to conductive polymers).

The present study describes the characterization of this process, enabling a user to control the fiber diameter by varying the experimental parameters, such as the polymer molecular weight and solvated polymer solution concentration. Additionally, this paper demonstrates the microfluidic applicability of this fabrication method by utilizing the polymer fibers as sacrificial backbone structures in the formation of suspended microchannels. Electroosmotic flow is induced in these microchannels to further validate this procedure as a viable methodology for the construction of 3-D microchannels.

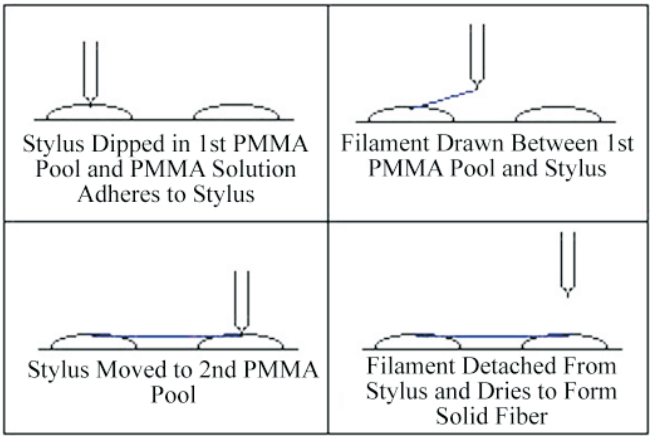

Figure 1. *Stylus-draw method of creating PMMA fibers.*

FABRICATION

Initially, fibers were drawn from reservoirs of solvated poly-methyl methacrylate (PMMA) (MicroChem) using a tungsten stylus (tip radius = 20 nm) to create a filament of solution between the two reservoirs (Fig. 1). As the solvent (chlorobenzene) evaporates, surface tension forces cause the filament to thin, resulting in the formation of a cylindrical polymer fiber with a nearly uniform cross-section Precise positioning of the fibers was accomplished by controlling the stylus with a programmable, custom-made ultra-high-precision micromilling machine (MMM) (Dover Instruments, Inc.) [3].

An alternative, direct-write, method of fiber drawing was also developed. This new technique involved loading a glass capillary (1-mm I.D.) with solvated PMMA and utilizing it to both deposit the reservoirs and draw the fibers, eliminating the need for the low-precision, manual reservoir deposition in the method previously described (Fig. 2). Manipulation of the direct-write capillary process was also controlled with the MMM, enabling nanoscale positioning resolution.

Channels were fabricated by coating the PMMA fibers with a layer of borosilicate glass (BSG) followed by Parylene®. BSG was deposited via RF sputtering (Technics 4604) to a thickness of 25 nm to establish a hydrophilic interior channel wall. A 10 μm Parylene® layer (SCS Parylene Deposition System 2010) was included to provide structural reinforcement for the fragile BSG thin wall. 500 μm-diameter holes were drilled into the coated and dried PMMA reservoirs to provide access to the PMMA and completed channels. The entire platform was submerged in acetone

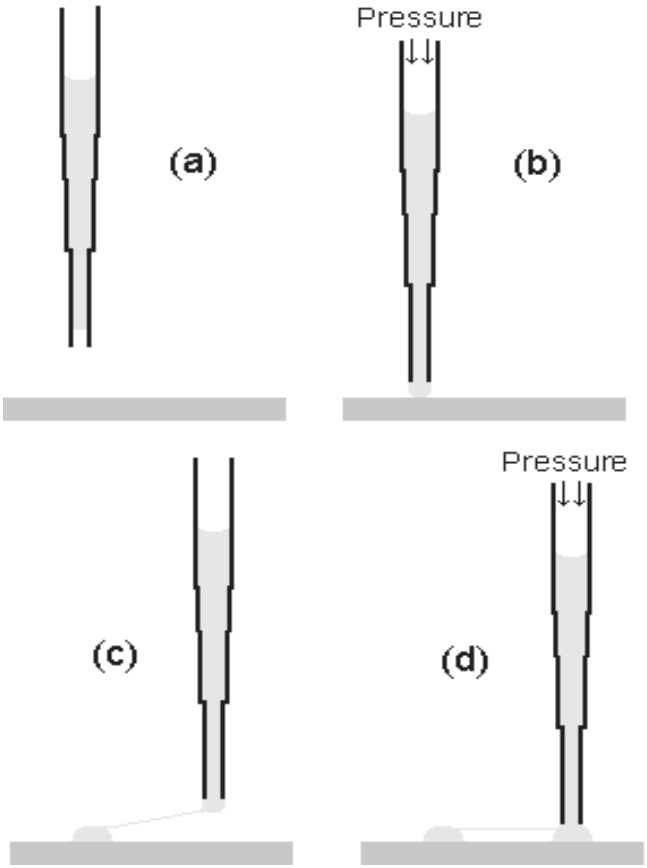

Figure 2. *Direct-write drawing of PMMA fibers, a) Load capillary with solvated PMMA, b) Pressurize capillary to expel solution into contact with substrate, c) Translate capillary to desired endpoint, d) Pressurize capillary to allow PMMA solution to contact substrate.*

for 7 days to ensure total dissolution of the shrouded PMMA matrix, leaving a hollow tube of BSG and Parylene®. Finally, the channels were dried with liquid carbon dioxide using a Samdri Critical Point Dryer (Tousimis) (Fig. 3).

All microchannel fabrication was performed on substrates containing a pair of microfabricated planar gold electrodes separated by a 1.8 mm wide trench created with a dicing saw (Disco DAD321). The channels were loaded with a phosphate buffer solution (10 mM, pH 6.1) containing 1% (by vol) of 20 nm-diameter fluorescent tracer particles (Molecular Probes) which were subsequently excited and imaged at 5 Hz using a low-light, high-resolution CCD camera (Roper Scientific) affixed to a fluorescent microscope (Olympus). The potential applied to the gold electrodes was modulated from 0 V to 1kV with the polarity being alternated between a positive and negative potential via a high voltage power supply (CZE1000PN30, Spellman High Voltage Electronics Corp.).

RESULTS

The stylus-draw method was utilized to produce fibers with diameters ranging between 450 nm to 100 µm suspended between the two reservoirs (Fig. 4a,c). In general, these fibers have a uniform cross section that tapers slightly at the fiber / reservoir interface (Fig. 4d). Fibers were drawn from concentrations ranging from 15.5% to 21.6% (by weight) for the 495k g/mol solution and 13% to 21.3% (by weight) for the 950k g/mol solution.

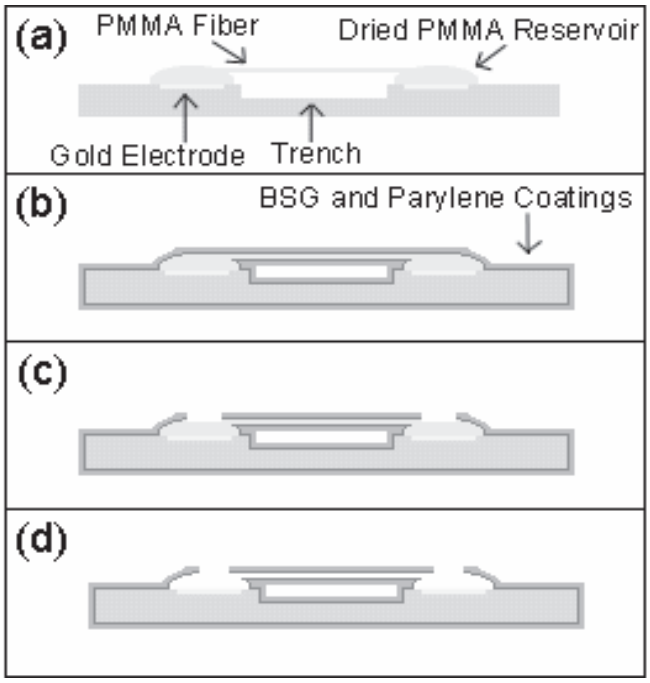

Figure 3. *Fabrication of channels from PMMA fiber, a) PMMA fiber (light blue) between two PMMA reservoirs on glass substrate (gray), b) Deposition of BSG and parylene, c) Drilling of 500 µm access holes, d) Dissolution of PMMA with acetone.*

Final diameter of the fiber was found to increase with both increasing polymer molecular weight ($P<0.025$) and increasing polymer concentration ($P<0.001$), thus providing a mechanism to control fiber diameter (Fig. 5). The large error bars in Figure 5 indicate an unwanted variance in fiber diameter believed to be caused by PMMA buildup on the stylus when several fibers are drawn in rapid succession. To alleviate this unwanted fouling of the tip, alternative stylus materials were investigated including glass, Parylene®-coated tungsten, and perfluorooctyl-trichlorosilane-coated (a nonstick material) tungsten. Table 1 summarizes this analysis, which demonstrated that a Parylene®-coated stylus yielded the best overall reduction in fiber diameter variation as evidenced by the lower standard deviation.

The direct-write method was also used to successfully draw fibers, notably in complex geometries including square "spirals," crisscrosses, and grids (Fig. 6) The primary advantage of this method is the elimination of the manual deposition of the pools at the terminal ends of each fiber (See Fig. 2). Eliminating this low-precision step increased the accuracy of fiber terminal placement as well as expedited the entire fiber fabrication process through further automation. The direct-write method also eliminated the uncontrollable stylus buildup, which was suspected of contributing to the undesired variance in fiber diameter. With the direct-write method, the maximum fiber diameter standard deviation observed was 2.70 µm with the 23% 495k g/mol solution, a value comparable to those obtained with the Parylene®-coated stylus.

Freely-suspended microchannels, as shown in figure 7, with I.D. ranging from 4 µm to 100 µm were fabricated via the procedure outlined in Figure 3. Electroosmotic flow was induced by loading the channels with buffer solution and applying a potential across the gold electrodes positioned at each end of the channel (Fig. 8). The velocity of the solution was observed to increase as the magnitude of the voltage was increased from 0 V to 1 kV. The direction of the flow reversed as the polarity of the electric field was switched, with the buffer solution moving toward the negative electrode.

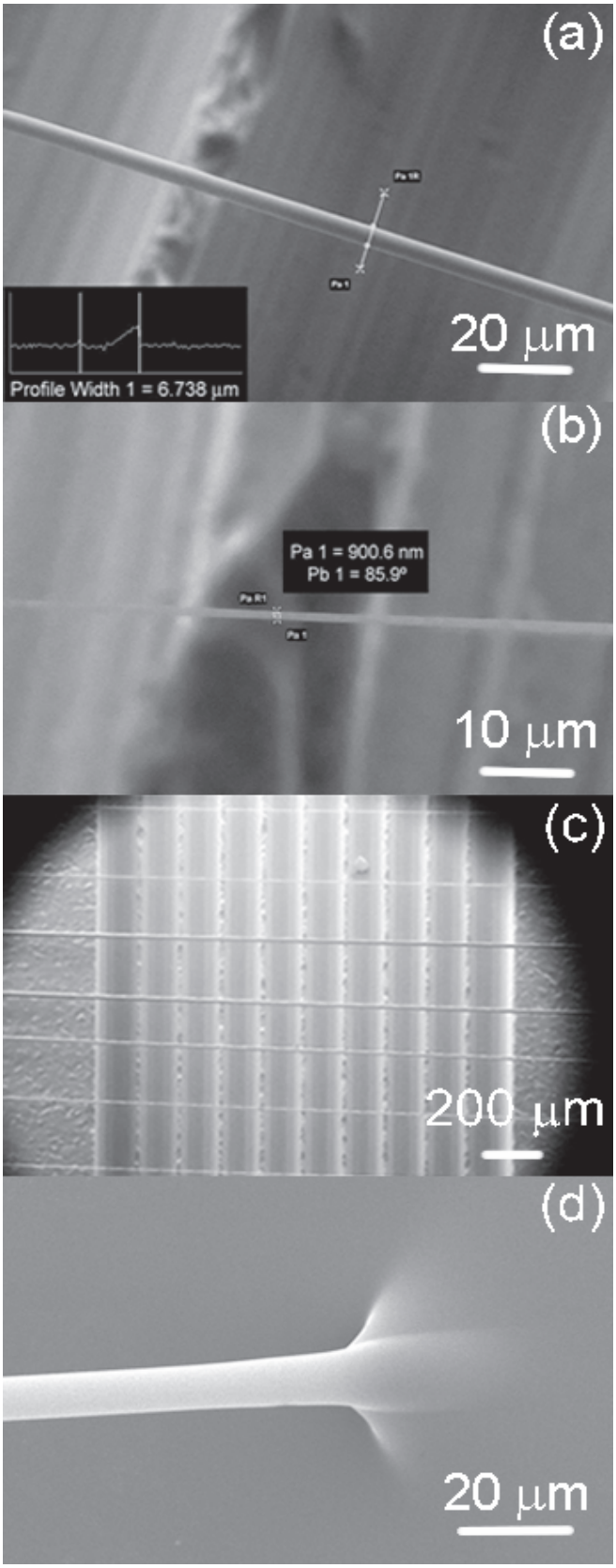

Figure 4. *SEM images of polymer fibers drawn over 1.8 mm trench. (a) Suspended fiber drawn from 15% solution of 950k g/mol PMMA. (b) Suspended fiber drawn from 13% solution of 950k g/mol PMMA. (c) Several parallel fibers drawn from 15.5% solution of 495k g/mol PMMA. (d) Tapered end of PMMA fiber.*

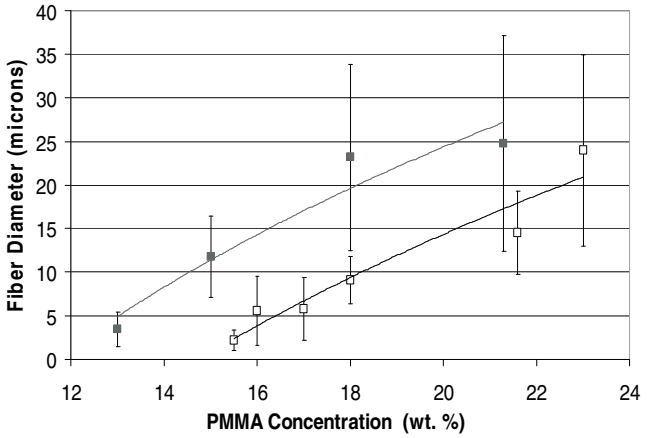

Figure 5. *Fiber diameter versus concentration. The hollow and solid data points represent the average measured diameters of the drawn fibers for the 495k g/mol data and the 950 g/mol data, respectively. The error bars represent the standard deviation of each data point.*

Conc. (wt.%)	Tungsten (µm)	Glass (µm)	Parylene (µm)	Nonstick (µm)
15.5.	2.22 ± 1.20	2.43 ± 1.09	No Data	10.81 ± 6.88
16	5.54 ± 3.95	4.38 ± 3.11	7.41 ± 2.49	8.76 ± 2.84
17	5.80 ± 3.59	4.20 ± 2.04	6.78 ± 1.38	7.92 ± 5.08
18	9.07 ± 2.68	4.84 ± 2.71	6.27 ± 3.02	4.69 ± 2.69
21.6	14.53 ± 4.82	18.37 ± 6.36	19.03 ± 1.40	15.24 ± 7.58
23	23.96 ± 11.00	17.29 ± 5.43	26.98 ± 2.03	34.80 ± 11.61

Table 1. *Fiber diameter means and standard deviations for different stylus materials.*

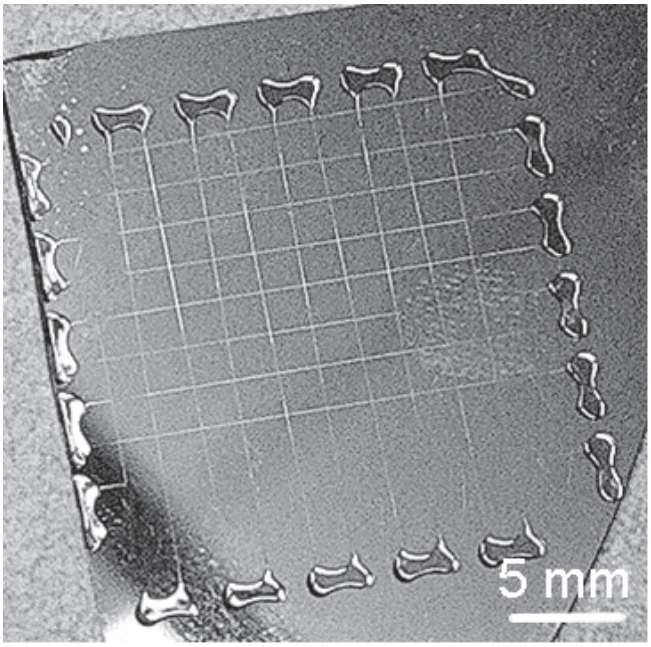

Figure 6. Pattern generated with direct-write method.

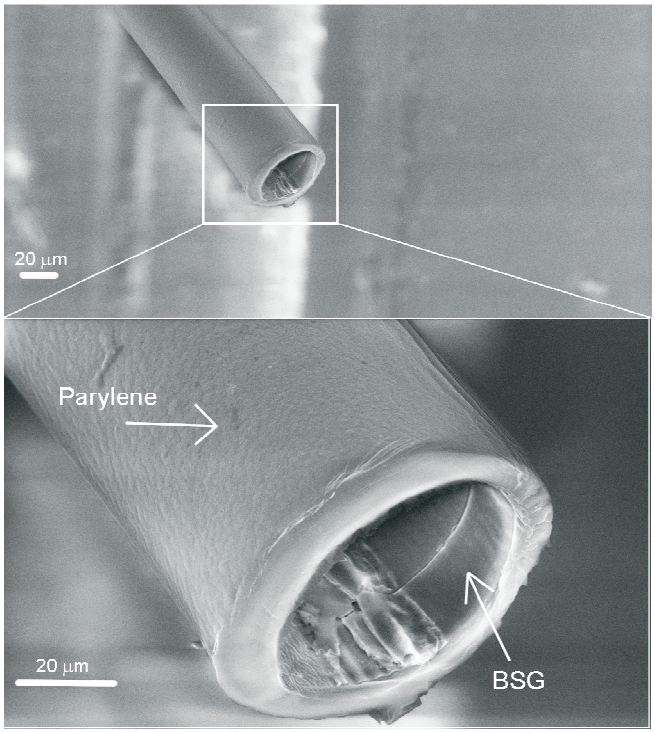

Figure 7. *SEM images of cleaved microchannel.*

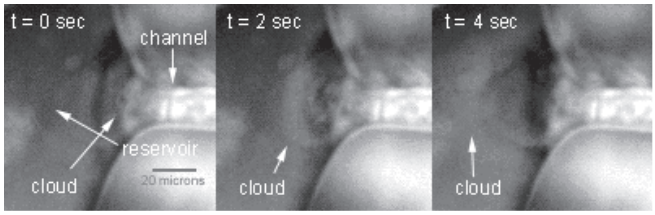

Figure 8. *Ejection of fluorescent particle "cloud" from 20 μm-diameter electroosmotic flow channel.*

CONCLUSION

Polymer micro- and nano- fibers can be drawn from a polymer solution using a stylus controlled by a custom-made ultra-high-precision micromill. PMMA fibers ranging from sub-micron diameters to 100 microns have been successfully fabricated over a 1.8 mm trench on a silicon substrate. Characterization of the process indicated that fiber diameter increased as the solid concentration of the polymer solution increased. Additionally, it was shown that increasing the molecular weight of the PMMA resulted in larger fiber diameters.

A large variance between fibers drawn under the same experimental conditions was noted. A suspected culprit of this variance was the solidification of the solution on the stylus which accumulated during the drawing process. Several different stylus materials were tested in hopes of reducing this variance, and it was discovered that the stylus material did influence the severity of this variance, with a Parylene®-coated stylus being influenced the least by accumulation. It was also demonstrated that the stylus could be entirely replaced with a pressurized glass capillary filled with polymer solution. This micromill-controlled capillary was used to direct-write complex fiber configurations with low fiber diameter variance and high yield.

Fibers created with both the stylus-draw and direct-write methods were utilized as sacrificial layers in the construction of hollow microchannels. The walls of these channels consist of a thin, inner layer of BSG to make the channels hydrophilic as well as a thicker layer of Parylene® to improve structural integrity. Unbroken, freely-suspended channels were fabricated between two electrodes, enabling electroosmotic flow to be performed, paving the way for the development of more complex microfluidic devices.

ACKNOLEDGEMENT

This work was supported by NSF grant ECS0506941, NASA Cooperative Agreement NCC5-571, NSF EPSCoR grant 6016955, DOE EPSCoR grant 46411101095, and the Commonwealth of Kentucky.

REFERENCES

[1] Harfenist, S. A., Cambron, S. D., Nelson, E. W., Berry, S. M., Isham, A. W., Crain, M. M., Walsh, K. M., Keynton, R. S., Cohn, R. W. Direct Drawing of Suspended Filamentary Micro- and Nanostructures from Liquid Polymers. Nanoletters Vol. 4 No. 10 (2004) 1931-1937.

[2] Nain, A. S., Amon, C., Sitti, M. Three-Dimensional Nanoscale Manipulation and Manufacturing using Proximal Probes: Controlled Pulling of Polymer Micro/Nanofibers. Proceedings of the IEEE International Conference on Mechatronics. 3-5 (2004) 224-230.

[3] Friedrich, C., Vasile, M. Development of the Micromilling Process for High Aspect Ratio Microstructures. Journal of Microelectromechanical Systems. Vol. 5 No. 1 (1996) 33-38.

OPTIMAL PARAMETERS FOR ArF LASER MICROMACHING OF SiC AND PZT

Jean-Philippe Desbiens and Patrice Masson
Department of Mechanical Engineering, Université de Sherbrooke
Sherbrooke, QC CANADA

ABSTRACT

The ablation process has been characterized for a number of laser sources in silicon (Si) micromachining. However, very few results can be found in the literature for excimer laser technology at 193 nm on Si and even fewer for other materials. Moreover, most of the work has previously been reported for quasi-static conditions, not taking into account the movement of the sample relative to the laser beam. In order to globally consider the relative velocity of the sample with respect to the laser beam, a metric called *Nppd* (number of laser pulses deposited per beam diameter) is first defined in this work. Experimental results are presented to evaluate the micromachining performance of the excimer laser for three different materials (Si, PZT and Pyrex). Optimal parameters are obtained and then used to micromachine silicon carbide (SiC), in addition to the previous materials.

INTRODUCTION

Laser micromachining is currently being used to complement photolithography techniques in the prototyping of a number of MEMS devices **[1]**. In particular, the 193 nm ArF excimer laser allows to micromachine materials by ablation with minimal thermal effect thanks to a short pulse width (<20 ns). The photon energy at 193 nm (6.4 eV) is in fact higher than that at higher wavelengths (5 eV with a KrF laser at 248 nm). This allows to more easily destroy the intermolecular bonds within the material. However, the power delivered by the ArF laser tends to be slightly less than that of 248 nm lasers so that the overall micromachining efficiency is reduced. Details in the order of a few microns can be fabricated using laser micromachining. New generations of MEMS integrating a number of thick layers (>5 μm) made of different materials such as glass, silicon (Si), silicon carbide (SiC) and piezoceramics (PZT) could benefit from laser micromachining techniques. These materials do not find widespread applications due to limitations in fabrication processes. Moreover, laser micromachining offers the flexibility to fabricate 3D structures **[2, 3, 4]**.

Very few quantitative results can be found in the literature on the interaction of the different parameters involved in excimer laser micromachining for workpiece dragging. Most of the references concentrate on static processes (e.g. hole drilling, mask patterning). Li **[4]** has however shown that experiment design methods can be used to optimize the parameters for Si. It appears that since considerable effort is devoted for the calibration of the parameters, very limited data is available on this. Glass (Pyrex, fused silica) and polymers are the most common materials micromachined using lasers **[2, 6, 7, 8, 9, 10]**. Ink jet printer nozzles are an example of devices manufactured by excimer laser micromachining.

It is the purpose of this work to present an experimental parametric study of ArF excimer laser micromachining of Si, PZT, Pyrex and SiC at 193 nm, taking into account the displacement of the sample.The results will help define optimal parameters for the micromachining of SiC, Pyrex and PZT which are becoming common components of MEMS.

THEORY

A. Laser-matter interaction

Two phenomena are involved in the ablation process using a laser beam : i) direct photochemical bond breaking by the absorption of photons and ii) melting of the material by thermal conduction in the material structure (photothermal process). Part of the beam energy is reflected at the surface of the sample. Following the ionisation of the material surface (photochemical process), a plasma creates an increase of the local pressure which helps vaporize solid or melted debris (Figure 1).

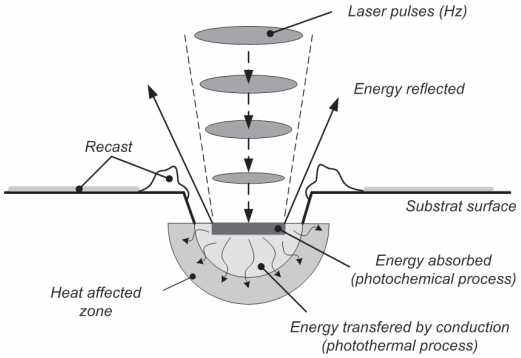

Figure 1. *Laser-matter interaction of a pulsed laser beam.*

The debris are then deposited in various shapes around the work zone. The material usinability is dependent upon their optical and mechanical properties such as reflectivity, thermal conduction, optical absorption, melting temperature,… However, laser ablation allows to micromachine any material, as opposed to standard photolithographic microfabrication techniques, even if Si and metallic materials are poor candidates. For Si, wet etching techniques or plasma techniques (DRIE) are to be preferred.

B. Parameters for pulsed laser ablation process

There are many important geometrical relations between machining parameters when using laser ablation with the workpiece dragging technique. The main following parameters are to be considered:

- linear machining velocity [V] (μm/s);
- laser repetition rate [f] (Hz);
- beam size : diameter [D] (μm);
- energy distribution over the beam area : Gaussian or uniform following homogenization;
- fluence [F] (J/cm^2);
- number of passages [N];
- beam focalization angle (3°).

From these parameters, relations can be extracted to predict the resulting micromachined geometries. (Figure 2).

From Figure 2, for a laser beam with a diameter of 15 μm pulsed at a rate of 3 Hz and travelling at 15 μm/s with respect to the sample, the depth of the micromachined trench can be predicted. Assuming an ablation rate of 5 μm/pulse, a trench of 15 μm depth is micromachined with an angle of 45°.

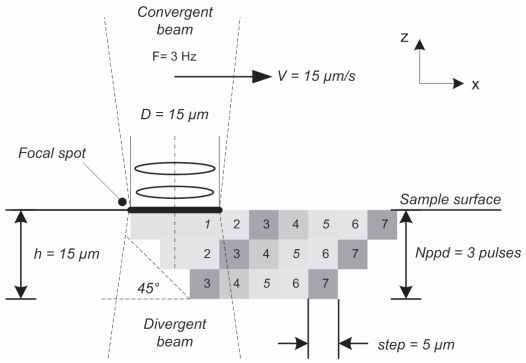

Figure 2. *Geometrical parameters for material ablation using pulsed focalized excimer laser.*

In order to globally consider the relative velocity of the sample with respect to the laser beam, it is thus possible to define a metric called *Nppd* (number of laser pulses deposited per beam diameter):

$$Nppd=N*f*D/V \qquad [shots] \tag{1}$$

By encompassing *N*, *f*, *D* and *V*, the *Nppd* parameter provides a global parameter taking into account the coupling between these parameters. The *etch rate* (µm/shot) can be determined from the *Nppd* given that one is able to measure the final depth of cut after *N* passages for constant process parameters:

$$Etch\ rate=h/Nppd \qquad [\mu m/shot] \tag{2}$$

Finally, the shape of the beam area and its energy distribution will also influence the cutting profile. For example, with a circular beam and workpiece dragging technique, the pulse overlap will be more important in the center of the trajectory. The cutting profile would then be a semi-elliptic shape. The beam focalization angle also affects slightly the cutting profile since the fluence decreases as beam area increases.

EXPERIMENTAL SETUP

A. Laser micromachining system

The four-axis (XYZR) laser micromachining system is shown in Figure 3. The system uses an X-imer 300 ArF excimer laser (MPB Communications Inc.) which generates pulses with 5 ns width. The maximum energy is around 6.5 mJ and the highest repetition rate is 300 Hz.

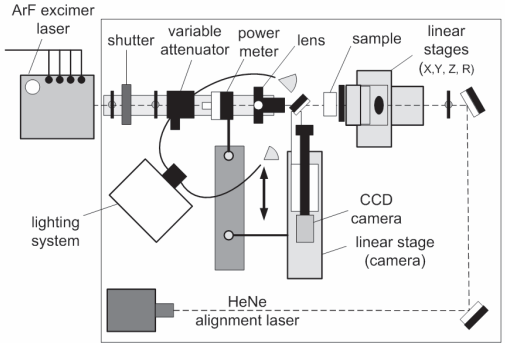

Figure 3. *Four-axis laser micromachining system.*

The 4 mm x 4 mm Gaussian beam is conditioned with a circular mask of 3 mm diameter. The beam is then collimated and focused with appropriate lenses. A variable attenuator is used to modulate beam energy. The diverging portion of the beam is used to ablate the material. By positioning adequately the sample with the Z axis, the machining tool diameter can be adjusted. Typical tool diameters can vary between 10 µm and 150 µm and the fluence used never exceed 100 J/cm^2.

B. Experimental procedure

In order to evaluate optimum parameters for laser ablation of some selected materials (Si, Pyrex, PZT and SiC), a series of seven experiments were realized, as shown in Table I.

Test	Parameter	Materials
1	Fluence, *F* (J/cm^2)	Si, Pyrex, PZT and SiC
2	Repetition rate, *f* (Hz)	Si, Pyrex, PZT
3	Velocity, *V* (µm/s)	Si, Pyrex, PZT
4	Number or passages, *N*	Si, Pyrex, PZT
5	Beam diameter, *D* (µm)	PZT
6	Focal spot displacement	Pyrex
7	Trajectory overlap for milling demonstration	Pyrex

Table I. *List of conducted tests.*

For each test and material, 16 cuts were made in order to limit the number of experimental measurements. Imaging of each laser cut is obtained using an optical microscope at 20x. Measurements for each cut are shown in Figure 4 and were estimated (±3 µm) from the image using National Instruments Vision Builder.

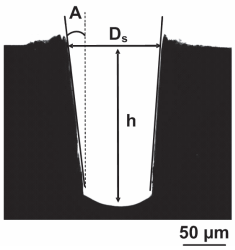

Figure 4. *Typical measurements extracted from sample image.*

Criteria for laser micromachining process optimization are:

- *ablation time* : a metric called *t* was define as the time to cut a 100 µm line with a depth of 50 µm at a particular speed (*V*) in reference with the measured ablation depth (*h*) :

$$t = 100\ \mu m * 50\ \mu m / (V * h) \qquad [s] \tag{3}$$

- *acceptable edge quality and minimum recast materials;*
- *minimum taper angle A;*
- *high value of etch rate (µm/shot).*

Each test is intended to help identify optimal values for each parameter to incrementally calibrate the process (from one test to another, cascading approach). Second order interaction between parameters was neglected. The parameters for Test 1 were fixed to known working values: *F*= 1-80 J/cm^2, *f*=50 Hz, *V*=25 µm/s, *N*=2, *D*=35 µm. Laser fluence threshold ranges from 0.5 J/cm^2 (for Pyrex) to 1 J/cm^2 (for SiC) according to preliminary observations. Pressurized air is used to clean the ablation zone.

RESULTS

Test 1 through Test 4 revealed that a proper choice of parameters can lead to better laser micromachining results (Figure 5). From these curves and visual observation of the cut profile, the optimal range identified for the process parameters are given below:

- **Fluence** (*F*) : *etch rate* rapidly increases for fluence range of 1 to 40 J/cm^2. It was observed (Figure 5a) that to avoid

thermal damage for Pyrex, fluence must be limited to 10 J/cm^2.

- **Repetition rate** (*f*) : *f* can be fixed to more than 100 Hz for Pyrex and PZT without *etch rate* reduction. The frequency is limited to 100 Hz by the laser performance which drops rapidly for higher values (Figure 5b).
- **Velocity of sample** (*V*) : velocity can be set higher than 150 µm/s since *etch rate* reach a constant value from *V*=50 µm/s as seen in Figure 5c.
- **Number of passages** (*N*) : up to 32 passages without significative reduction in e*tch rate* for Pyrex and PZT (Figure 5d).

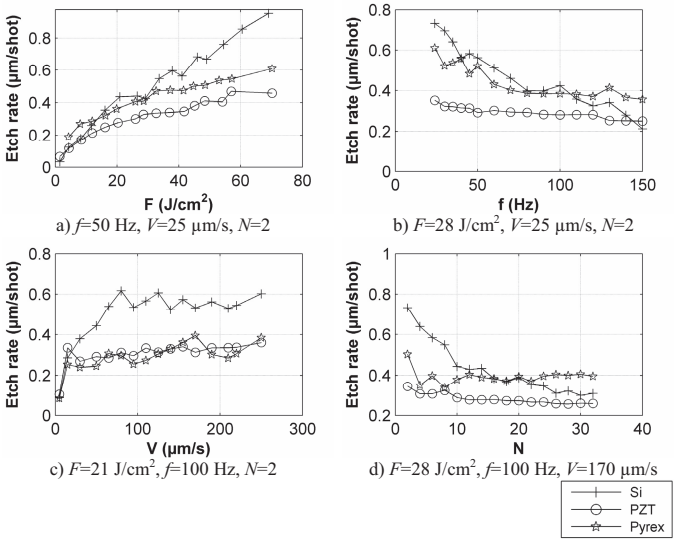

a) *f*=50 Hz, *V*=25 µm/s, *N*=2
b) *F*=28 J/cm^2, *V*=25 µm/s, *N*=2
c) *F*=21 J/cm^2, *f*=100 Hz, *N*=2
d) *F*=28 J/cm^2, *f*=100 Hz, *V*=170 µm/s

Figure 5. *Ablation rate per laser pulse for Si, PZT and Pyrex, as a function of the fluence (a), the repetition rate (b), the velocity of the sample (c) and the number of passages (d).*

Test 1 was conducted a second time with optimal parameters on all previous materials, in addition to a-SiC. As shown in Figure 6a, *etch rate* has not changed significantly after optimization even if sample velocity and repetition rate are increased. Even if *etch rate* values for SiC seem to be the lowest, the laser cut profile for amorphous SiC is clean and has a flat bottom (Figure 6c).

For an optimized process, thin layers of material are ablated at each passage. Typical ablation rate varying from 5 µm to 10 µm per passage can be achieved with fluence around 10 J/cm^2 and optimal parameters (*f*=100 Hz, *V*=170 µm/s). Ablation time *t* is typically reduced by two for all materials after calibration (see Figure 6b for Pyrex) and less recast is observed in the ablation area. It is important to note that the diameter and wall angle measurements are slightly different for each material tested. Si cut wall are also less uniform than other materials tested and recast material can be clearly see under microscope or SEM images.

Other important results arise from the complementary tests:

- **Test 5, beam diameter**: the laser beam diameter can be easily adjusted via focal point displacements. The *etch rate* is velocity and diameter dependent by the *Nppd* metric defined previously. The *etch rate* decreases with an increase in the beam diameter but not linearly as expected. Further work would be required to understand why this is not observed for PZT (Figure 6d).
- **Test 6, focal spot displacement**: by moving the focal spot in order to follow depth penetration during ablation, no *etch rate* variation is observed *for a single cut* with multiple passages.
- **Test 7, trajectory overlap**: in order to verify if laser milling leads to good geometrical results, Test 7 consisted in two laser cuts side by side with a varying overlap (0-80%). Results showed that with minimal overlap (<5%) and a circular laser beam, it is possible to ablate a cut profile with flat bottom on Pyrex. To ensure good interface between cuts, focal spot displacement was used. This result was extrapolated to laser milling of a rectangular cavity in Pyrex (Figure 7).

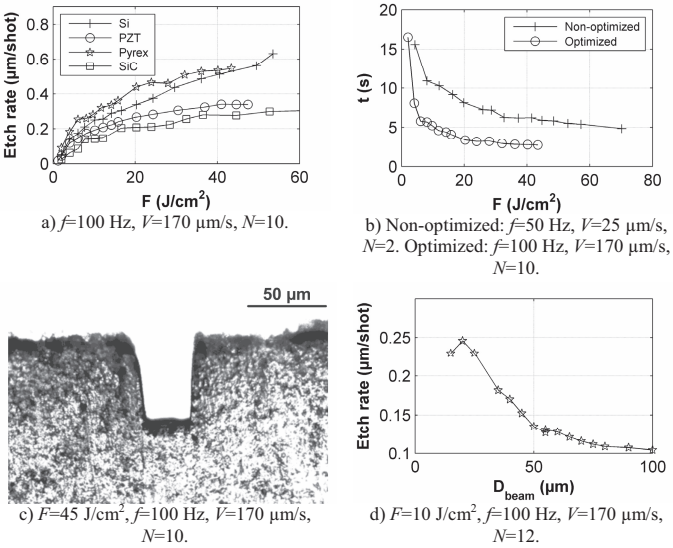

a) *f*=100 Hz, *V*=170 µm/s, *N*=10.
b) Non-optimized: *f*=50 Hz, *V*=25 µm/s, *N*=2. Optimized: *f*=100 Hz, *V*=170 µm/s, *N*=10.
c) *F*=45 J/cm^2, *f*=100 Hz, *V*=170 µm/s, *N*=10.
d) *F*=10 J/cm^2, *f*=100 Hz, *V*=170 µm/s, *N*=12.

Figure 6. *Results from optimization: ablation rate per pulse (a), ablation time for Pyrex for non-optimized and optimized processes (b), cut in a-SiC (c), ablation rate per pulse as a function of beam diameter for PZT (d).*

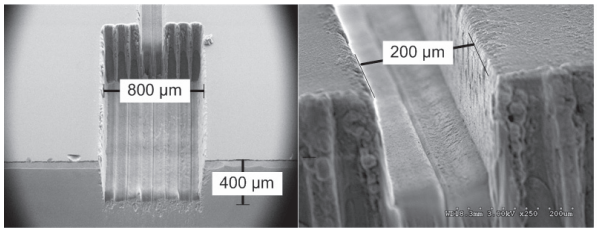

Figure 7. *Laser milling on Pyrex realized with optimal parameters and circular beam overlap strategy (F=6 J/cm^2, f=100 Hz, V=170 µm/s, N=40 x 8 for rectangular cavity, machining time: 3 hours).*

DISCUSSION

The experimental optimization process shows that optimal parameters selection is independent of material properties, except for the laser energy level (fluence) needed to ablate adequately each material (see Figure 5). Recasts were observed for Si which seems to be ablated by melting and ejection of matter. This leads to poor machining results compare to Pyrex, PZT and even SiC. However, optimal machining parameters results in cleaner ablation wall for Si because less material is processed at each passage, at higher velocity and repetition rate with moderate fluence.

Less than half of initial machining time is now necessary to ablate all materials after the optimization of the process. Si cuts are generally wider at surface and wall taper is more important. This indicates that optical or mechanical properties influence the energy absorption and thermal dissipation during laser ablation process.

The mechanical and optical properties of tested materials are shown in Table II.

	Materials				
Properties	**Si**	**SiC**	**Al**	**PZT**	**Pyrex**
ρ (kg/m^3)	2300	3200	2700	7650	2230
S_y (MPa)	2000	2100	276	80 (static)	-
E (GPa)	160	448	70	64	62.75
k (W/m.K at 300 K)	156	490	236	~1.1	1
C_p (J/kg.K)	771	750	890	350	726
$\kappa = k/\rho.C_p$ (cm^2/s)	0.88	2.04	0.98	0.0041	0.0062
$L_e = 2(\kappa t)^{1/2}$ (μm, t=5 ns)	3.25	4.95	3.43	0.22	0.27
CTE (10^{-6} /°C)	2.62	4.2	25	4-6	3.5
$T_{melting}$ (°C)	1410	3100	660	1250	820
n_R (193 nm)	3.46	4.05	0.11	-	1.543
n_I (193 nm)	2.75	1.42	2.17	-	0.077
R	**50%**	**41.1%**	**~85%**	**-**	**4.6%**
α^{-1}(10^3 cm^{-1})	1769	1000	3000	125	48.4
L_o or α^{-1}(μm)	0.0057	0.01	0.0033	0.08 **[11]**	0.21
$Ke = L_o/L_e$	**0.002**	**0.002**	**0.001**	**0.364**	**0.765**
Behavior (193 nm)	Metallic Ke<0.01			Strong absorption 0.01<Ke<10	

Table II: *Physical properties of materials for laser micromachining at 193 nm* **[11, 12, 13]**.

A metric named *Ke* is defined as the ratio of the optical penetration length (L_o) and the thermal penetration length (L_e) **[11]** and gives an evaluation of the ablation behaviour of material for a given wavelength and pulse width. The *Ke* values in Table II indicate that Si, SiC and Al exhibit metallic behaviour at 193 nm (*Ke*<0.01). Si and Al ablation mechanism is mainly a photothermal process which means that they melt and dissipate laser energy by thermal conduction. This explains why Si gives poor geometric results. On the other hand, Pyrex and PZT have strong absorption at 193 nm (0.01<*Ke*<10) and ablation tends to be more a photochemical process. Their low thermal conductivity and high absorption combined to low melting point explain this behaviour. Absorbing energy and keeping it into the exposition zone helps elevating the local temperature to melt or vaporize material. Even if SiC requires high fluence compared to Pyrex and PZT, it appears to be a good candidate for laser micromachining at 193 nm. While Si melts under the energy corresponding to 193 nm, SiC directly vaporizes when it reaches the melting point (2400-3100 °C). This leads to a slow but clean ablation.

More uniform beam energy could lead to better results for Si since the high peak energy of the Gaussian beam results in non-uniform machining depth. This aspect does not appear to be a problem for other materials that show strong absorption at 193 nm and poor thermal conductivity which leads to local machining and better depth control over the beam area.

As depicted in experimental results, typical cut widths ranging from 10 μm to 100 μm can be achieved with all materials. This is limited by optical system and laser energy. Wall angles could be at best estimated to 5° and it seems possible to get deeper than 250 μm (see Figure 4) with Pyrex, PZT and SiC. This allows high aspect ratio structures to be realized. The precision for cut width appears to be less than 5 μm. Depth precision could be as low as 0.25 μm for SiC or PZT with low fluence. The machining precision could be improved further with better and faster measurement tools.

The excimer laser machining system seems to be a good alternative for rapid machining of MEMS materials for which precision in the order of 1-5 μm is acceptable. Laser machining is faster than wet etching and DRIE for SiC and allows Pyrex, PZT and polymers machining. Among MEMS applications which can benefit from laser micromachining, bioMEMS on glass and polymers, PZT sensors and SiC high temperature sensors are good candidates. Even 3D surfaces are to be expected from laser micromachining in the next years with mask dragging techniques using excimer, high power DPSS and Copper vapor lasers **[2, 3, 6]**.

CONCLUSIONS

The optimal parameters for excimer laser micromachining of Si, Pyrex, PZT and SiC were identified from experimental data. Optimal parameters show that high repetition rate combined with high velocity workpiece dragging technique and laser fluence less than 20 J/cm^2 allow clean laser ablation at 193 nm. Thin layer ablation of material is more efficient. Pyrex, PZT and SiC appear to be good candidates for excimer laser micromachining at 193 nm as opposed to Si for which material redeposition and melting make ablation difficult.

Various 3D geometries can now be ablated in order to complete conventional microfabrication techniques for MEMS prototyping. Further investigation of parameters interaction by the use the design of experiment method may be necessary to get better machining results.

REFERENCES

[1] M. Madou, “Fundamentals of microfabrication, The science of miniaturization”, CRC Press (2002) 721 p.

[2] A. S. Holmes, “Excimer laser micromachining with half-tone masks for the fabrication of 3-D microstructures”. IEE Proc., Sci. Meas. Technol., UK, 151(2) (2004) pp. 85-92.

[3] Y.-C. Lee, C.-M. Chen, and C.-Y. Wu, “A new excimer laser micromaching method for axially symmetric 3D microstructures with continuous surface profiles”, *Sensors and Actuators*, A(117) (2005) pp. 349-55.

[4] N.H. Rizvi, P.T. Rumsby and M.C. Gower, "New developments and applications in the production of 3D microstructures by laser micromachining", *Photonic Systems and Applications in Defense and Manufacturing*, 1-3 Dec. 1999, Vol. 3898, SPIE-Int. Soc. Opt. Eng, Singapore (1999) pp. 240-9.

[5] J. Li and G. Ananthasuresh, “A quality study on the excimer laser micromachining of electro-thermal-compliant micro devices”, *Journal of Micromechanics and Microengineering*, 11(1) (2001) pp. 38-47.

[6] M. Knowles, G. Rutterford, D. Karnakis, and A. Ferguson. “Micro-machining of metals, ceramics, silicon and polymers using nanosecond lasers”, *Technical report*, Oxford Lasers Inc. (2005).

[7] B. Keiper, H. Exner, U. Löschner, and T. Kuntze, “Drilling of glass by excimer laser mask projection technique”, J.Laser Appl., 12(5) (2000) pp.189-93.

[8] P. Dyer, “Excimer laser polymer ablation : twenty years on”, *Appl. Phys. A, Mater. Sci. Process.* , A77(2) (2003) pp. 167-73.

[9] J. Jiang, C. Callender, J. Noad, R. Walker, S. Mihailov, J. Ding, and M. Day. “All-polymer photonic devices using excimer laser micromachining”, *IEEE Photonics Technol. Lett. (USA)*, 16(2) (2004) pp. 509 – 511.

[10] A.A. Tseng, Y.-T. Chen, K.-J. Ma, “Fabrication of high-aspect-ratio microstructures using excimer laser”, *Optics and Lasers in Engineering*, 41(6) (2004) pp. 827-47.

[11] Basting D., “Excimer laser technology: laser sources, optics, systems and applications”, Lambda Physik (2001) 292 p.

[12] E. Palik, “Handbook of optical constants of solids”, *Academic Press handbook series*. Academic Press (1985).

[13] K. Hellwege, H. Landolt, and R. Börnstein, “Landolt-Börnstein: Numerical Data and Functional Relationships in Science and Technology, new series: group III: crystal and solid state physics”, Springer, (1980).

SHOCK PROTECTION USING SOFT COATINGS AS SHOCK STOPS

Sang Won Yoon[1], Sangwoo Lee[1], Noel C. Perkins[2], and Khalil Najafi[1]
[1]Center for Wireless Integrated Microsystems (WIMS)
[2]Department of Mechanical Engineering
University of Michigan, Ann Arbor, MI, USA

ABSTRACT

This paper reports the modeling, fabrication and testing of shock stops formed using soft material coatings. These shock stops provide outstanding shock protection by reducing both the impulse and impact force, and by absorbing the shock energy at each impact following the applied shock. Design tradeoffs are described based on the elastic model of the thin film coated on hard shock stops. Parylene is used as the coating material due to its conformal coverage, room-temperature deposition, and chemical stability. Shock tests were performed on silicon test devices consisting of a proof mass suspended using a flexible spring, some coated with a soft coating (Parylene) and some without any coatings. These tests show that a 3μm-thick Parylene coating provides superior device survival rate (94%) compared with conventional hard stops (0%) for applied shock levels of up to 1300g.

INTRODUCTION

The performance and reliability of MEMS devices are easily impacted by external environmental disturbances including incident mechanical shocks. MEMS devices that utilize delicate mechanical structures are susceptible to these shock loads, which may ultimately damage the device or degrade its performances.

To minimize these adverse effects, two solutions are typically proposed. One solution ensures that the shock-induced stress remains less than the material fracture strength by adjusting the dimensions of the structure. The other solution employs hard wall shock stops to limit the travel of the device **[1]**. Both solutions are attractive, yet they also have shortcomings. The first method achieves improved shock resistance at the expense of device performance **[2]**. The second method only offers marginal protection since it can itself generate secondary sources of shock (e.g. subsequent impacts) that may result in fracture, debris, performance shifts, or continuous ringing of the device **[1-3]**. Effective shock protection technologies must limit these shortcomings as well as minimize device displacement.

To achieve these goals, we proposed two new shock stop concepts utilizing nonlinear springs and soft coatings **[1,2]**. The merits and demerits of each concept were analyzed using simulations and the design parameters needed to control the critical target shock amplitude were determined. These simulations revealed a significant reduction of impulse generated at 1st impact (nonlinear spring: >90%, gold soft coating: >40%) and a substantial decrease in the number of collisions (gold soft coating: >90%) compared to conventional hard wall stops.

The fabrication and testing of the nonlinear spring shock stops integrated with two MEMS devices with different sensing mechanisms and made by different processes was presented in **[3]**. Shock tests using an impact hammer demonstrated that the nonlinear spring shock stops provide outstanding device survival rate (83%) compared with hard stops (8%). Also, device fracture mechanisms under the stress developed by the induced impact force were identified.

This paper reports on the modeling, fabrication and testing of soft coating shock stops using Parylene as the coating material.

CONCEPT

Figure 1 shows the schematic view of a conventional hard shock stop and the proposed soft coating shock stop. When the device mass impact a shock stop, an impact force is generated. This force can be reduced by either 1) increasing the contact time between the mass and the stop assuming the impulse stays constant, or 2) decreasing the impulse (i.e., decreasing the momentum change) assuming the contact time stays constant. The impulse is proportional to the change in proof mass velocity **[3]**.

This goal is achieved by adding a soft coating shock stop. This concept utilizes a soft thin-film layer on an otherwise hard surface, and it relies both on the increased surface compliance and dissipation. The soft coating reduces the coefficient of restitution (COR) and thus reduces the impact force. The 'softer' coating dissipates energy during impact, and this serves to reduce both the number of impacts as well as the settling time following shock. Increasing the damping of the device mass is another means to minimize the setting time, but this method is limited by the vacuum environment required by many MEMS devices. Thus, especially in the case of vacuum packaged MEMS, absorbing the energy at the impact site becomes more attractive **[2]**.

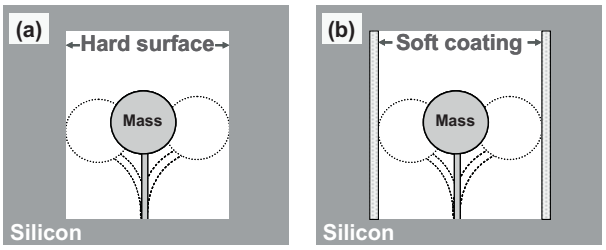

Figure 1. *Schematics of shock stop designs (a) Conventional hard shock stop, (b) Soft coating shock stop.*

Soft coating and nonlinear spring shock stops have several similarities and differences. First, both concepts utilize compliant stops to reduce the impulse (and impact force). The soft coating stop however adds considerably more dissipation and hence it also reduces the number of impacts **[2]**. Second, these two shock protection concepts require different fabrication processes. For in-plane shock protection, nonlinear spring stops can be readily fabricated with MEMS devices in a single step **[3]**, but soft coating stops need additional steps due to the need for additional material deposition. For out-of-plane protection, soft coatings may be more convenient because it is difficult to fabricate released micro-springs under a device. Finally, we can readily control our target shock amplitude for both concepts by simple design adjustments. The performance of nonlinear spring stops can be easily adjusted by changing the geometric and material properties (number, separation, stiffness) of shock springs **[3]**. The characteristics of soft coating stops are determined both by the coating material

properties and thickness, and by the design of bumpers contacting the coated surface, as described in following sections.

DESIGN

Our previous analytical results demonstrated that gold (COR≈0.22) coatings reduce the initial impulse by >40% and the number of collisions by >90% as compared to a rigid stop **[1, 2]**. But these results were calculated by considering only the reduced COR; these results could be further improved by including the elastic properties of the coating materials. Moreover, these benefits are amplified by using flexible polymers because of their viscoelastic properties, smaller Young's modulus, higher energy absorption, and greater thickness.

Yu et al. reported simple but reliable models to analyze the elasticity of a thin film layer **[4]**. This work has been experimentally proven with minor corrections or referenced by many follow-up papers **[5-7]**. These models describe the deflection (*d*) of a thin film due to a load (*p*) applied by an indenter as a function of the indenter's shape and dimensions. The film is assumed to be either perfectly bonded to or frictionless overlaying on a semi-infinite substrate (Figure 2). The equations relating *p* and *d* are given as follows for different indenter shapes:

Flat-ended indenter (Figure 2-a): $p = (\zeta_i \cdot a) \cdot d$ (1)

Conical indenter (Figure 2-b): $p = (\zeta_i \cdot \tan\alpha) \cdot d^2$ (2)

Spherical indenter (Figure 2-c): $p = (\frac{2}{3}\zeta_i \cdot \sqrt{R}) \cdot d^{3/2}$ (3)

The definition of the other variables in these equations is shown in Figure 2. ζ_i is defined to be $\zeta_i = 4E_i/(1-\nu_i)$ where E_i is Young's modulus and ν_i is Poisson's ratio. Note that a film's indentation is related to its contact area, not to its total surface area. This is observed in a similar manner both for purely elastic and elastic-plastic indentations, as reported in other papers **[5,6]**. When the film thickness approaches infinity, E_i and ν_i approach those of the thin film material (i=1). When the film thickness approaches zero, E_i and ν_i approach those of a hard substrate material (i=2). Therefore, a thicker film decreases ζ_i, and thus reduces the film's stiffness. This reduced stiffness leads to a smoother deceleration and longer contact time during impacts, and eventually decreases the impact force generated when a device collides with the shock stop **[1-3]**. But the maximum film thickness is limited by fabrication challenges and limitations.

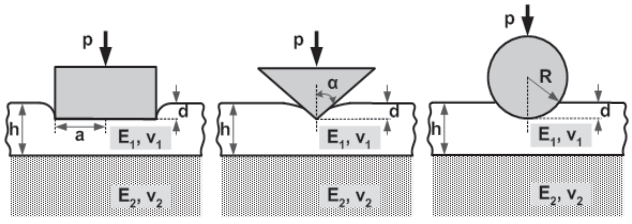

Figure 2. *A thin film layer on a semi-infinite substrate indented by (a) a rigid flat-ended indenter, (b) a conical indenter, or (c) a spherical indenter* ***[4]****.*

Figure 3 shows the elastic energy vs. deflection of the thin-film (Parylene film. ζ_i is calculated to be 20GPa from Parylene's E_i=3GPa, ν_i=0.4 **[8]**.) for a device mass that has one bumper (shaped like the indenters in Figure 2) of different shapes. Also, the energy produced by a 1000g shock applied to a device mass (0.97mg) is shown as the solid line (labeled as threshold). When the device impacts the thin film, it continues to move until the energy applied by the shock is completely converted to elastic energy stored in the thin film. The intersection points of the elastic energy plots of various indenters with the threshold shock energy show the minimum film deflections, and therefore the minimum film thickness, needed to absorb this shock. Figure 4 shows the time record of (a) the displacement of a device mass and (b) the impact force involved during this movement. In these figures, a 1000g shock is applied just before the mass (0.97mg) touches the thin film coating. From these figures, we can derive the contact time (T), which is inversely proportional to the average impact force (Figure 4-a), and the maximum involved impact force (Figure 4-b). Clearly, the shock performance of soft coating stops depends on both the coating's material properties (material selection and thickness) and the shock bumper design (shape and dimension). Consequently, the shock stop can be readily designed to accommodate a wide range of incident shock.

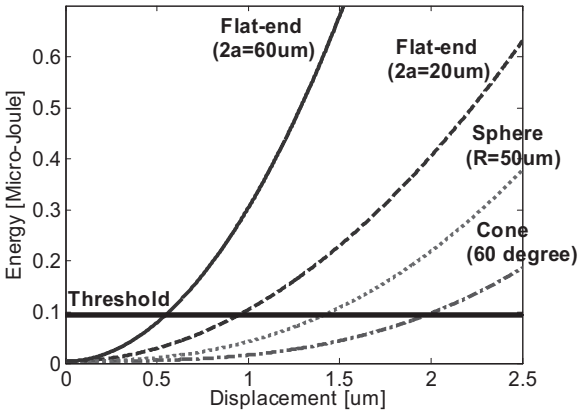

Figure 3. *Elastic energy vs. deflection of a Parylene film (ζ_i is assumed to be 20GPa) for a device mass that has one bumper (shaped like the indenters in Figure 2) of different shapes. The energy produced by a 1000g shock applied to a device mass (0.97mg) is shown as the solid line (labeled as threshold).*

FABRICATION

To demonstrate shock protection improvement using soft coating shock stops, we used the Silicon-On-Glass (SOG) process **[3]** to fabricate MEMS test structures and Parylene coated shock stops. Figure 5 shows the fabrication process flow. We first create a recess (10μm) on a Pyrex glass wafer and pattern a shield metal layer (5-a). The glass wafer is halfway diced (to form scribe lanes), and is anodically bonded to a 100μm-thick, double-polished silicon wafer. Contact pad metal is deposited and patterned (5-b), and a DRIE through wafer etch is preformed to form the device and shock stops (5-c). Finally, some samples are coated with a 3μm-thick Parylene film to form soft coating shock stops (5-d), while some samples are completed without this coating to make hard shock stops.

Parylene is selected as the coating material due to its conformal coverage and room-temperature deposition **[9, 10]**. In addition, Parylene is chemically stable **[11]**. Figure 6 is the SEM views of suspended microbeams covered with a 3μm-thick layer of Parylene, showing the excellent step coverage of Parylene.

Figure 7 shows fabricated hard (silicon) and soft coated (Parylene) shock stops and devices. For a fair comparison, both devices are selected from the same wafer and have identical dimensions. To compensate for the decrease in gap due to Parylene deposition, the gaps of devices covered with the soft coating are made larger than the gaps of hard stop devices. Because Parylene is thin with small Young's modulus, changes in the mass and stiffness due to Parylene are ignored **[12]**.

The test device consists of a silicon mass of 0.97mg (1.15mm radius, 100μm thickness, (100) silicon orientation), and a support cantilever beam with a spring constant of 79 N/m (50μm width, 1.85mm length, and 100μm thickness). These test structures were designed to be flexible enough to touch the wall, but not to suffer fracture stress before touching the wall.

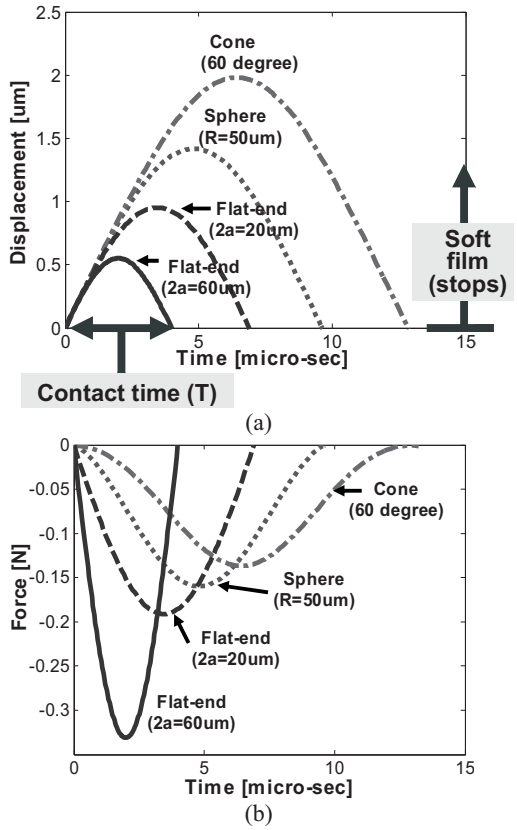

Figure 4. *The time record of (a) the displacement of a device mass and (b) the involved impact force during this movement*

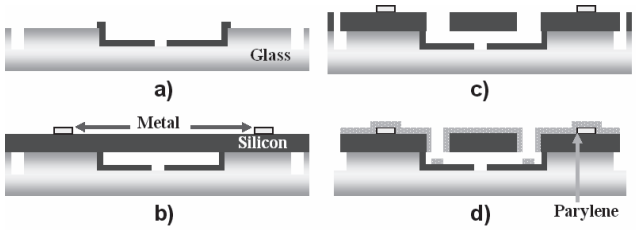

Figure 5. *Fabrication process for test devices and shock stops.*

TEST RESULTS

Fabricated devices were tested using a custom-built drop test setup, which can provide a controlled shock amplitude and direction.

In this drop test setup, samples are attached to a steel plate using epoxy and dropped from a known height (H) though guides to produce directional and repeatable shocks. For fair comparison, both hard wall and soft coating samples were mounted together, as shown in Figure 7. The steel plate collides with a steel rail at the foot of the drop test track. The small contact area between the steel plate and the steel rail decreases the contact time and generates higher shock amplitude for the same drop height. This contact time is determined by applying a 5V signal between the plate and the rail, and by measuring the time during which electrical contact is first achieved between the two. This critical contact time (*dT*) determines the maximum shock amplitude applied to the test devices. This maximum shock amplitude can be estimated based on the computed velocity change during this time interval:

$$a_{shock} = \frac{(COR+1)\cdot\sqrt{2\cdot 9.8\cdot H}}{dT} \qquad (4)$$

While this is the shock delivered to the steel plate, we assume that the test devices experience the same shock as they are firmly attached to the plate. Also, we assume that the energy losses due to friction and the epoxy layer are negligible. Based on these assumptions and the dimensions and the size of our setup, our drop tests can produce a maximum shock of 1400g when the steel plate is dropped from a height of ~8 feet.

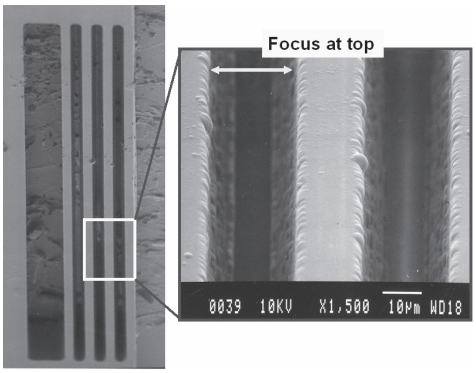

Figure 6. *SEM of the top view of suspended microbeams after Parylene deposition. It shows excellent step coverage.*

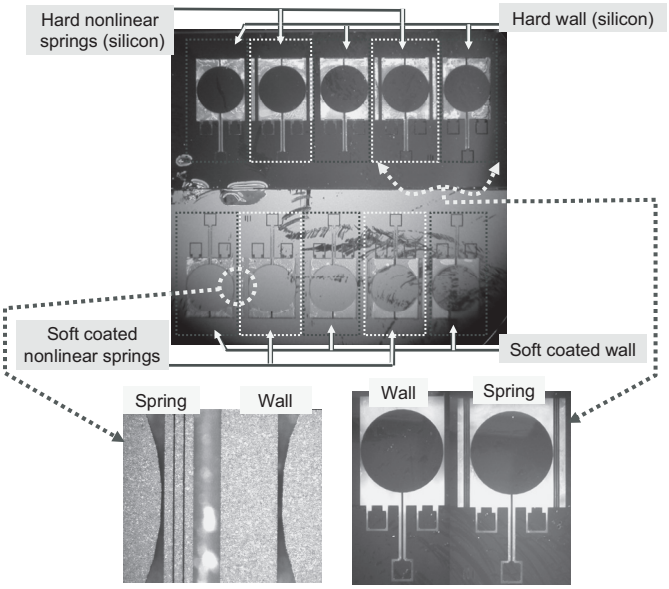

Figure 7. *Top views of the fabricated hard (silicon) and soft coated (Parylene) devices. Each sample has three wall and two nonlinear spring devices. These two samples are glued together to a steel plate for testing.*

Testing started by first applying a low level of shock to test devices and then proceeded to larger shocks by dropping the test devices from higher distances. Figure 8 shows a series of photographs of the test samples containing both hard wall and soft coating shock stops following each drop test. Shocks under ~640g produced no observable damage to either hard or soft stop devices

(8-a). When ~840g was applied, one hard stop device broke (8-b). The two remaining hard stop devices were damaged after a shock of ~940g (8-c). But, for shocks up to ~1300g, no damage was observed on any soft stop devices (8-d). We conducted this series of experiments four times using four different samples each containing several hard and soft shock stops, and the results are summarized in Table 1. The table clearly shows that soft coating shock stops provide superior shock protection providing a 94% survival rate, compared with 0% survival rate for hard stops for shocks of up to 1300g.

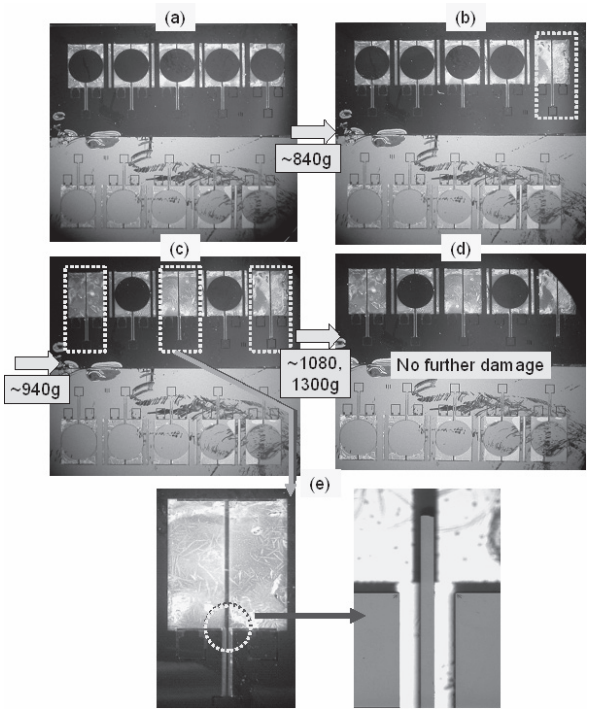

Figure 8. *A series of photographs of the test samples containing both hard wall and soft coating shock stops following each drop test (up to 1300g shock amplitude) for the device shown in Figure 7. All hard stops were damaged at the tip close to the device mass.*

Table 1. *Summary of drop test results. No hard stop devices survived, compared with 94% of Parylene coating shock stops.*

Test number	Max. applied shock [g]	Hard stop	Parylene
		Broken / Total number	Broken /Total number
1	~1300	**3/3**	**0/3**
2	~900	**3/3**	**0/3**
3	~920	**2/2**	**0/5**
4	~1080	**2/2**	**1/6**
Summary		**10/10 (100%)**	**1/17 (6%)**

Using the dimensions of our spherical device and the models in Figures 3 and 4, we derived the average impact force and the maximum impact force of both Parylene coated soft shock stops and hard silicon stops. The result shows that Parylene coated stops provide significant reduction both in average impact force (78% reduction) and in the maximum impact force (78% reduction), compared to hard silicon shock stops. This substantial impact force reduction considerably decreases the stress induced at the tip of the device beam **[3]**, and thus explains why soft coating stops produce higher device survival rate in our drop test experiments. This impact force reduction is calculated using the elasticity properties of Parylene films, whereas the impulse reduction (>40%) in **[1,2]** derived solely from the reduced COR afforded by gold coatings.

CONCLUSION

This paper describes the modeling, fabrication and testing of soft coating shock stops. This soft coating relies on both increased surface compliance and reduced coefficient of restitution, and provides better shock protection over conventional hard wall shock stops. This shock protection is determined not only by the coating material properties but also the design of bumpers attached to a device mass. As a coating material, we selected Parylene due to its conformal coverage, room-temperature deposition, and chemical stability. Using a drop test setup, we conducted multiple shock tests, and the results demonstrate that the Parylene coating provides superior device survival rate (94%) over hard stops (0%). This can be explained by the fact that Parylene coating shows substantial impact force reduction compared to hard silicon stops.

ACKNOWLEGEMENT

This work is supported by DARPA's HERMIT program (contract #: W31P4Q-04-1-R001). The authors thank Ms. A.B. Ucok & Mr. H. Kim for their help in Parylene deposition.

REFERENCES

[1] S. W. Yoon, N. Yazdi,, N.C. Perkins, and K. Najafi, "Novel integrated shock protection for MEMS", *Tech. Digest of Int. Conf. Solid-State Sensors, Actuators & Microsystems (Transducers'05),* Seoul, Korea, 396-400 (2005)

[2] S. W. Yoon, N. Yazdi, N. C. Perkins, and K. Najafi, "Micromachined integrated shock protection for MEMS", *Sensors and Actuators A: Physical* (2006)

[3] S.W. Yoon, N. Yazdi, J. Chae, N.C. Perkins, and K. Najafi, "Shock protection using integrated nonlinear spring shock stops," *Technical Digest of IEEE Int. Conf. on Micro Electro Mechanical Systems (MEMS 2006),* Istanbul, Turkey, 702-705 (2006)

[4] H. Y. Yu, S. C. Sanday and B. B. Rath, "The effect of substrate on the elastic properties of films determined by the indentation test - axisymmetric boussinesq problem"*, J. of the Mechanics and Physics of Solids*, 38, 745-64 (1990)

[5] S. M. Han, R. Saha, and W.D. Nix, "Determining hardness of thin films in elastically mismatched film-on-substrate systems using nanoindentation", *Acta Materialia*, 54, 1571-81 (2006)

[6] X. Chen and J.J. Vlassak, "Numerical study on the measurement of thin film mechanical properties by means of nanoindentation", *J. Materials Res.*, 16, 2974-82 (2001)

[7] P. M. Ramsey, H. W. Chandler and T. F. Page, "Modeling the contact response of coated systems", *Surface and Coatings Technology*, 49, 504-9, (1991)

[8] T. Harder, T.J. Yao, Q. He, C.Y. Shih and Y.C. Tai, "Residual Stress in thin-film Parylene-C", *Technical Digest IEEE Int. Conf. on Micro Electro Mechanical Systems (MEMS 2002)*, Las Vegas, USA, 435-438 (2002).

[9] L. Morisset, "Conformal Coating Through Gas Phase Polymerization", *OnBoard Technology*, 32-34 (2003)

[10] H. Kim and K. Najafi, "Characterization of low-temperature wafer bonding using thin-film parylene", *IEEE J. of Microelectromechanical Systems*, 14, 1347-55 (2005)

[11] A. Campbell and J. Scialdone, "Outgassing Data for Selecting Spacecraft Materials", *NASA Reference Publication 1124, Rev. 3* (1990)

[12] E. P. Popov, "Engineering mechanics of solids," Prentice-Hall (1990)

TESTING AND ASSEMBLY OF WIMS CUBES CONTAINING PASSIVE AND ACTIVE INTEGRATED CABLES

Asli B. Ucok, Joseph M. Giachino, and Khalil Najafi
Center for Wireless Integrated Microsystems (WIMS)
University of Michigan, Ann Arbor, MI 48109-2101

ABSTRACT

This paper presents the first assembly and electrical testing results of a packaging/assembly approach for wireless integrated microsystems (the WIMS Cube). In this assembly approach, the microsystem dice are placed inside a cube. Electrical/fluidic signal transfer between dice can be achieved in one of two ways. The first method uses rows of integrated active flexible cables that are attached to the cube walls and actuated during assembly, row-by-row, to connect to the dice. The second method uses passive flexible cables integrated with separate connector dice that are interleaved between device dice inside the cube. In both methods, flexible cables make pressure contacts to the pads and fluidic inlets of each microsystem die, thus forming a mechanical connect/disconnect system for both electrical and fluidic signals. WIMS Cube prototypes that are 5mm and 10mm on a side were fabricated. Cubes with integrated Parylene cables were tested for reliable pressure-contact electrical connections. A low contact resistance of 4.2Ω was achieved between cables and dice. Reliability was demonstrated by electrically connecting and disconnecting the passive flexible cables ~10 times. Fluidic connector cables that can eventually interface with fluidic substrates were integrated with the Cube.

INTRODUCTION

Today's packages for integrated circuits and microsystems should protect them from the external environment and allow electrical connectivity without affecting performance. Current packaging and assembly approaches do not provide the flexibility and modularity needed for a microsystem containing substrates with sensors, actuators, and circuits fabricated using different technologies. We introduced the concept of a packaging/assembly approach for wireless integrated microsystems (the WIMS Cube) [**1**], whereby multiple substrates containing circuits, sensors/actuators or instruments are stacked on top of one another in a re-workable and modular fashion inside a Cube, with interconnection between substrates provided through Cube walls and flexible cables [**2**,**3**]. The WIMS Cube concept represents a significant departure from standard 3D chip assembly and packaging approaches [**4**,**5**] in that it makes the assembly and connection reworkable, thus providing maximum flexibility when assembling/reassembling and packaging complex microsystems. In this paper, we report the first assembly and electrical testing results of a complete WIMS Cube containing multiple test substrates, the development of WIMS Cubes utilizing only "passive" cables that do not require actuation, and the successful fabrication and integration of fluidic cables that can eventually interface with fluidic substrates.

WIMS CUBE STRUCTURE AND OPERATION

Figures 1-2 illustrate WIMS Cubes with *active* and *passive* cables, respectively. The Cube can be as small as a few millimeters or as large as a few centimeters on a side and holds different dice. Electrical/fluidic signals are transferred between dice using either rows of integrated flexible cables attached to the Cube walls and actuated, row-by-row, to make pressure contacts to each die (Figure 1), or by passive cables integrated on connector dice that are interleaved between device dice (Figure 2). In case of active cables, all cables are retracted at start of assembly. After each die is "dropped" into the Cube, a row of cables is actuated/released into position. A non-conductive elastomer layer is dropped over the die, followed by another die; the process is repeated. In case of passive cables, the connector dice containing

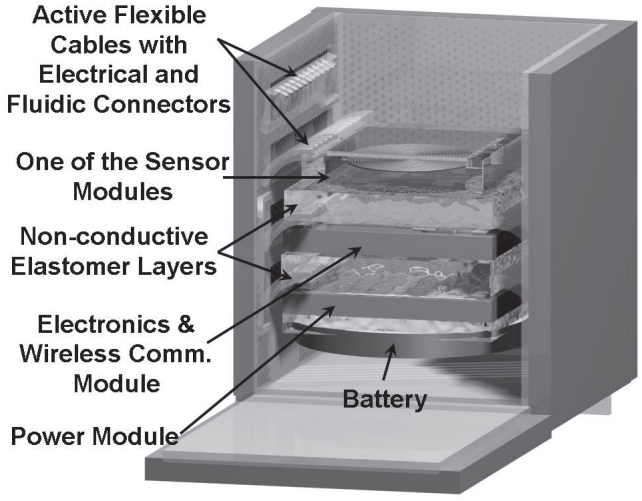

Figure 1. WIMS Cube with active flexible cables: *The flexible cables are actuated into position using on-chip actuators and make pressure contacts to pads and fluidic inlets on the dice.*

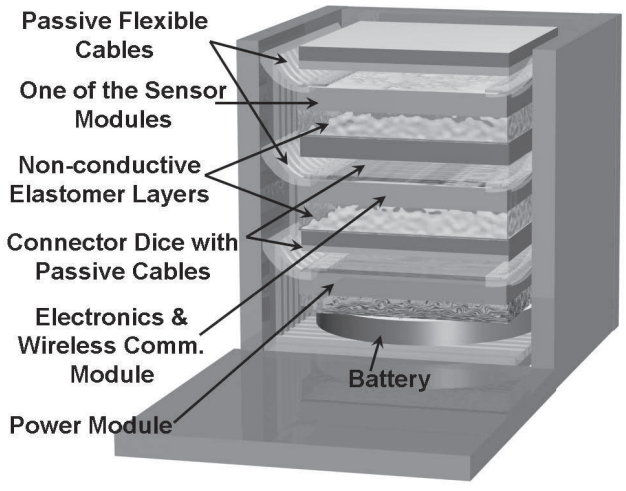

Figure 2. WIMS Cube with passive flexible cables: *WIMS Cube has connector dice with integrated passive flexible cables that make pressure contacts to system dice and cube sidewall, where routing of all signals is achieved.*

connection pads press onto their corresponding device dice to make connections. The signal is then transferred through the passive cables, which extrude at the edge of each connector die and connect to the Cube sidewall; in this case the passive cables are bent as the connector dice are dropped into the Cube. A non-conductive elastomer layer is used as a cushion between dice to accommodate local variations in pressure/distance. In both approaches, the Cube is covered by a lid, which presses against the dice and elastomers, forcing all cables into intimate contact with their substrate.

The pressure-contact connections are not permanent. This allows the microsystem to be disassembled either if one of the dice fails after assembly, or if a different microsystem with a different set of sensors or actuators is needed for another application, resulting in maximum flexibility and modularity, two critical features for microsystem applications.

ASSEMBLY OF THE WIMS CUBE

The WIMS Cube is fabricated using planar silicon technology. The bottom and the four sidewalls of the Cube are fabricated on a single substrate and are attached to each other by the flexible cable material, and a separate piece could be used as the lid of the cube. Each cube can then be handled easily and folded using a jig. The Cube sidewalls are fabricated so that the sidewalls and Cube base can be brought together like a jigsaw puzzle for good alignment as shown in Figure 3, and then glued/soldered to form the Cube.

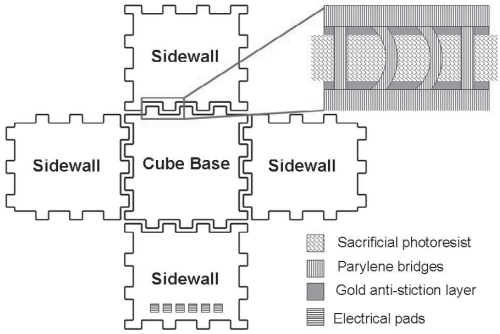

Figure 3. *Layout of the WIMS Cube*

Figure 3 shows the sidewall-to-base connector bridges that carry all the metal routing for both the actuation of each row of cables as well as the electrical connection layer. Careful handling of the Cube is necessary as these bridges may be torn, disconnecting the access to the connectors on a sidewall. These bridges should be flexible as well as rugged, and with a careful design, the probability of tear can be minimized. The bridges may be designed as multiple narrow connectors instead of a wide Parylene bridge to increase their flexibility.

Assembly platforms and a multi-tip vacuum pick for the assembly and handling of the fabricated package were also developed to improve the reliability of the handling and assembly process. The assembly platform is a jig with vacuum connections to hold the sidewalls of the Cube before it is permanently brought together, and to populate the Cube with test dice for connection tests. The jig is fabricated using silicon micromachining techniques. The assembly platform with latches and polymer hinges, shown in Figure 4, was designed to enable Cube assembly with less handling and better yield. This platform is assembled together with the Cube itself, and the latches lock the sidewalls in place during assembly.

Parylene is a very rugged material, and does not tear apart easily. However, due to bending and twisting, one can still damage the sidewall-to-base connector bridges. As a result, a special multi-tip vacuum pick was designed in order to help in handling the WIMS Cubes (Figure 5).

The following section on fabrication will present the fabrication of the WIMS Cube as well as the assembly platform and the multi-tip vacuum pick.

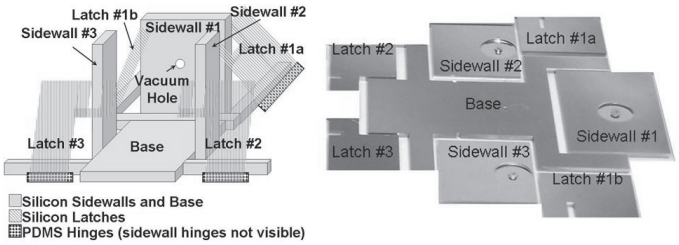

Figure 4. *Schematic of the assembly platform with latches and polymer hinges, and a fabricated assembly platform*

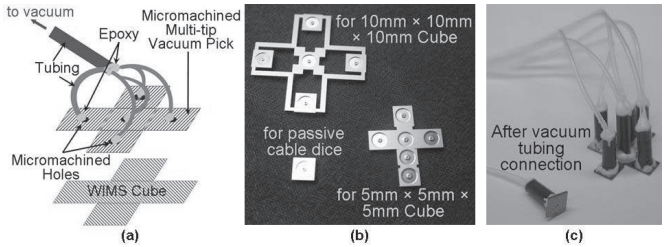

Figure 5. *(a) Schematic of the multi-tip vacuum pick, (b) various vacuum picks after fabrication, and (c) vacuum picks after the tubing connection*

FABRICATION

Figure 6 shows the 12-mask surface micromachining process for WIMS Cubes with active or passive cables with integrated electrical and fluidic connectors. The bottom cross-sectional view on the right in Figure 6 shows a connector die with electrical and fluidic connectors fabricated using the same process used for Cubes with active cables. The layers that exist for active cables, but not for passive cables, are merely removed from passive cables. Parylene is the material of choice for the cables of the WIMS Cube, since it is quite flexible, and provides sufficient chemical inertness, mechanical strength and stability [**2**,**3**].

WIMS Cube prototypes that are 5mm and 10mm on a side were fabricated. Fabrication starts with an oxidized wafer (Figure 6-a). This oxide layer is used for the insulation of pads used for actuation of rows of cables and testing the electrical connectors during cube assembly. It does not need to be too thick as long as it provides good insulation. A 3500Å-thick oxide layer is thermally grown and patterned for this process. A Cr/Au layer of 500Å/1500Å is deposited and patterned as an anti-stiction layer underneath connector bridges. Gold is a hydrophobic layer, and the probability of Parylene to stick to gold is less compared to sticking to silicon, silicon dioxide, and Parylene itself. Patterning of a sacrificial photoresist layer (1.3-1.5µm) is followed by the deposition and patterning of the first Parylene layer (~2µm). Parylene is dry-etched in O_2 plasma. The electrode metal layer (5000Å-thick gold layer), which forms the coils for thermo-magnetically actuated cables [**3**], is deposited and patterned. Although released Parylene structures do not stick to gold surfaces in a wet release process, gold film directly deposited on Parylene is found to adhere well as opposed to its adhesion problem to silicon. The soft gold layer covers the slightly rough Parylene surface well, resulting in good adhesion. By using gold alone, patterns as small as 7µm can easily be patterned. A hard-baked photoresist layer (~4µm after hard-bake) at the tips of the electrical connectors on

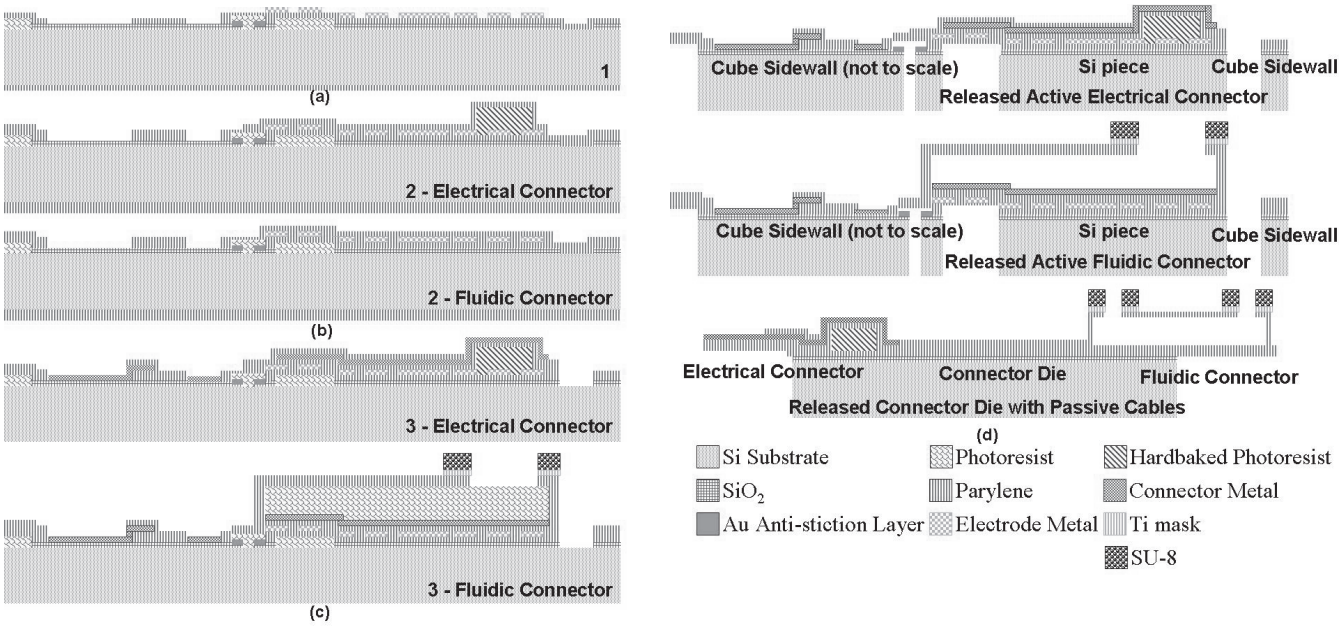

Figure 6. *Process flow of the WIMS Cubes with integrated active or passive cables with electrical and fluidic connectors*

both active and passive flexible cables forms extruding tips for pressure-contact electrical connections (Figure 6-b). Next, the second Parylene layer is deposited and patterned to open contacts on the coils. A Cr/Au layer of thickness 250Å/5000Å, is deposited to form the electrical interconnects of the cables, and the anti-stiction/anti-collapse bottom layer for the fluidic channels (Figure 6-c). The material and thickness for this metal layer is affected by many factors including the stress-compensation of the thin-film stack and the formation of low electrical routing resistances for the Cube. The sacrificial photoresist layer for the fluidic channels is then patterned. The thickness of the photoresist determines the height of the channels, and thicknesses of 8-12µm were used for this process. It is followed by the deposition of the final Parylene layer (~2µm). A 3000Å-thick Ti layer is sputtered and patterned as a mask for the final Parylene etch. The Ti layer should be sputtered and be thick enough to make sure the large step height of the fluidic channels is covered well for the final Parylene etch. Ti layers thicker than 3000Å delaminate at sharp corners, like the corners of the cables, after patterning. Ti is chosen as the mask layer, because it adheres to Parylene well, and the Ti etchant ($NH_4OH:H_2O_2:H_2O$ =1:1:4) does not damage the thin film stack of the cables during Ti mask patterning and removal. Next, a 13µm-thick SU-8 layer, which is used for forming o-ring structures at the inlets of fluidic connectors, is patterned. After etching the Parylene in order to obtain the cable structures, the Ti mask is stripped. Lastly, a backside through-wafer etch is performed to separate the Cube walls, form active flexible cables and help release passive flexible cables (Figure 6-d). WIMS Cubes are then released by removing the sacrificial photoresist layer. A novel ultrasonic agitation release/dry technique is used that combines the advantages of the gold hydrophobic layer as an anti-stiction layer and the energy provided by ultrasonic agitation.

The assembly platforms and the vacuum pick are micromachined using a 2-mask DRIE etch process for forming the cavities for vacuum tubing. The jig is one piece with PDMS hinges. The tubing is attached using epoxy.

Figures 7-8 show Cubes during assembly and testing using two different micromachined jigs. As shown in Fig. 8, Cubes with multiple test substrates containing bonding pads and interconnects have been assembled. The tests were performed using a probe station. After the three sidewalls of the Cube are folded and secured by the vacuum connections of the assembly platform, probe tips are used to access the electrical pads on the unfolded sidewall of the Cube. The test chips and non-conductive elastomer layers populating a WIMS Cube with passive flexible cables can be seen in the inset of Figure 8.

Figure 9 shows various cables after release. The silicon piece underneath the active flexible cables creates firm pressure-contact connections to the system dice during the Cube assembly. Passive flexible cables have finger-like tips for better and more reliable connection with the metal lines on the Cube sidewall.

ELECTRICAL TESTING

The fabricated WIMS Cubes with integrated Parylene cables were tested for reliable pressure-contact electrical connections. For the WIMS Cubes with passive flexible cables, the total resistance of the electrical connection system that consists of two passive cables is measured. Each of these cables makes one pressure contact to a pad on a test die and another pressure contact to the Cube sidewall. The measured resistance included the negligible resistance of the metal line between the pads (calculated to be 0.07Ω) on a test die, as well as the four pressure-contact resistances, and the resistances of the two passive flexible cables. Due to the duality of the measured components, half of the measured resistance is graphed in Figure 10 as the electrical resistance per passive electrical connector with two pressure-contact connections. A low contact resistance of 4.2Ω was achieved between cables and dice. Reliability was demonstrated by electrically connecting and disconnecting the passive flexible cables ~10 times. The variation in each measurement of Figure 10 depends on the force applied on the stack; the higher the applied force, the lower the pressure-contact resistance.

For WIMS Cubes with active cables, the Cube is designed so that four-point probe measurement of two pressure-contact connections with a negligible metal line resistance of the test dice included can be measured. Smaller than 1.9Ω resistance per two pressure-contact connections was achieved by testing active flexible cables. These cables were not actuated using the on-chip actuators but were manually pushed into position. Tests on fluidic connectors have not been performed.

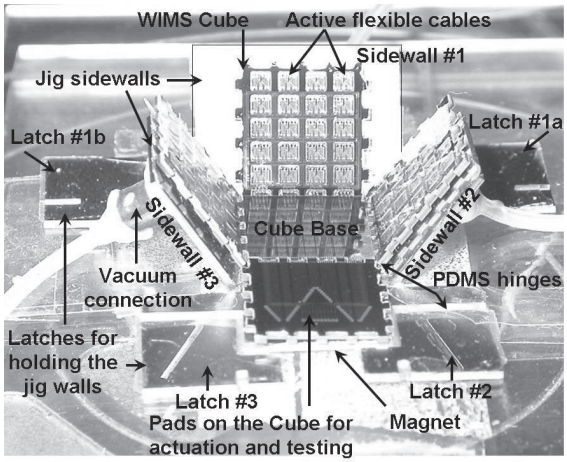

Figure 7. *A WIMS Cube with active cables during assembly. The platform is a jig with latches and PDMS hinges.*

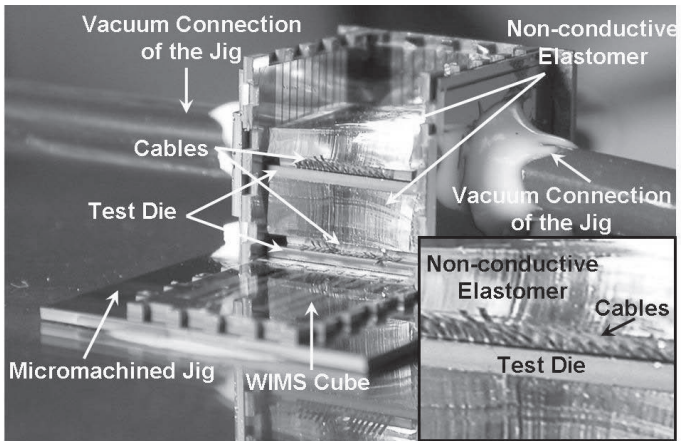

Figure 8. *A WIMS Cube with passive cables during testing. The platform is a permanently assembled jig. The Cube is dropped into the jig using a flat platform not shown in the picture.*

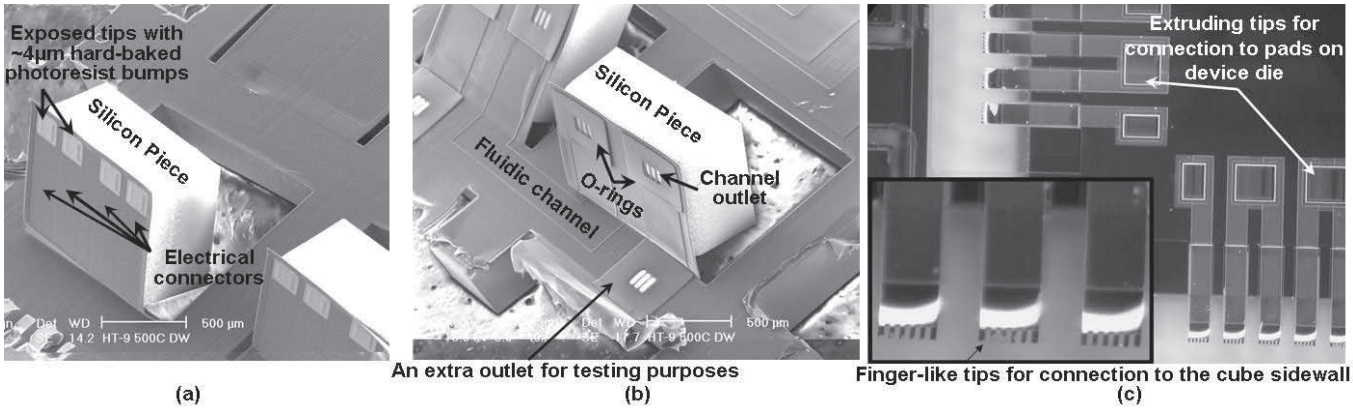

Figure 9. *Released active flexible cables (a) with four electrical connectors and (b) with fluidic connectors, and (c) Released passive electrical connectors with finger-like tips for better contact to the metal lines on the Cube sidewall*

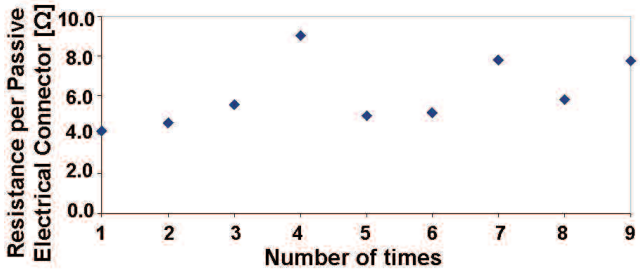

Figure 10. *Measured electrical resistance per passive electrical connector. Each passive electrical connector makes two pressure-contact connections; one to the pad on the system die and the other to the Cube sidewall.*

CONCLUSIONS

We reported the first assembly and electrical testing results of a complete WIMS Cube containing multiple test substrates, the development of WIMS Cubes utilizing only "passive" cables that do not require actuation, and the successful fabrication and integration of fluidic cables that can eventually interface with fluidic substrates. Repeated measurements of pressure-contact electrical resistance for passive cables as low as 4.2Ω were achieved. These resistances are repeatable after tens of connect-disconnect experiments (a Cube is envisioned not to undergo more than a few tens of reworking sessions). Tests on fluidic connectors have not been performed yet.

ACKNOWLEDGMENTS

The authors thank Brendan E. Casey for helpful discussions on the assembly setup. This work was supported by the Engineering Research Centers Program of the National Science Foundation under Award Number EEC-9986866.

REFERENCES

[1] A.B. Ucok, J.M. Giachino, K. Najafi, "Compact, Modular Assembly and Packaging of Multi-Substrate Microsystems," *Tech. Digest, 12th Int. Conf. Solid-State Sensors, Actuators, and Microsystems*, Boston, MA, **2**, 2003, pp.1877-1878.

[2] A.B. Ucok, J.M. Giachino, K. Najafi, "The WIMS Cube: A Microsystem Package with Actuated Flexible Connections and Re-workable Assembly," *Tech. Digest 2004 Solid-State Sensor and Actuator Workshop*, Hilton Head , SC, 2004, pp.117-120.

[3] A.B. Ucok, J.M. Giachino, K. Najafi, "Modular Assembly/Packaging of Multi-Substrate Microsystems (WIMS Cube) Using Thermo-Magnetically Actuated Cables," *Tech. Digest, 18th IEEE Int. Conf. Micro Electro Mechanical Systems*, Miami, FL, 2005, pp. 536-539.

[4] H. Goldstein, "Packages Go Vertical," *IEEE Spectrum*, **38**, No. 8, 2001, pp. 46-51.

[5] B. Murari, "Bridging the Gap between the Digital and Real Worlds: The Expanding Role of Analog Interface Technologies," *Tech. Digest, IEEE Int. Solid-State Circuits Conf.*, **1**, 2003, pp. 30-35.

WIRELESS SENSING OF DISCHARGE CHARACTERISTICS FOR QUALITY CONTROL IN BATCH MODE MICRO-ELECTRO-DISCHARGE MACHINING

Mark T. Richardson[1*], Ranjit Gharpurey[2], and Yogesh B. Gianchandani[1]
[1]Department of Electrical Engineering and Computer Science, University of Michigan, Ann Arbor, MI, USA
[2]Department of Electrical and Computer Engineering, University of Texas, Austin, TX, USA

ABSTRACT

Wireless signals are inherently generated during the spark discharges of micro-electro-discharge machining (μEDM). This work harnesses signals between 300-750 MHz for the monitoring of batch mode machining quality. In particular, the wireless spectra are used to sense incipient, debris-dominated machining that can be destructive to both the tool and the workpiece. Planar stainless steel (316L) is machined 50 μm deep in a high-density stent pattern with 30 μm features and tool fill factors ranging from 8.4% to 32.9%. In debris-dominated conditions, the 580-750 MHz frequency band shows an increased average strength over an average reference band of 410-480 MHz. The temporal evolution of the spectra permits the discharges to be monitored in a manner that is less affected by circuit parasitics than alternative electrical methods. It is amenable to real-time monitoring of large-scale production.

I. INTRODUCTION

Micro-electro-discharge machining (μEDM) is a technique that utilizes spark discharges between a tool and workpiece in a dielectric fluid to micro-machine any conductive material [1]. By finely controlling the discharge energy as well as the positioning of the tool and workpiece, any arbitrary shape can be machined. Recent applications include a cardiovascular antenna stent (stentenna) [2,3] (Fig. 1), RF switches [4], and DC-to-DC boost converters [5].

Traditionally, serial mode μEDM uses a sharpened wire as the tool, which is scrolled across the workpiece. Batch mode μEDM uses a cookie cutter type tool to machine the entire pattern in parallel. The advantages are that batch mode is lithographically

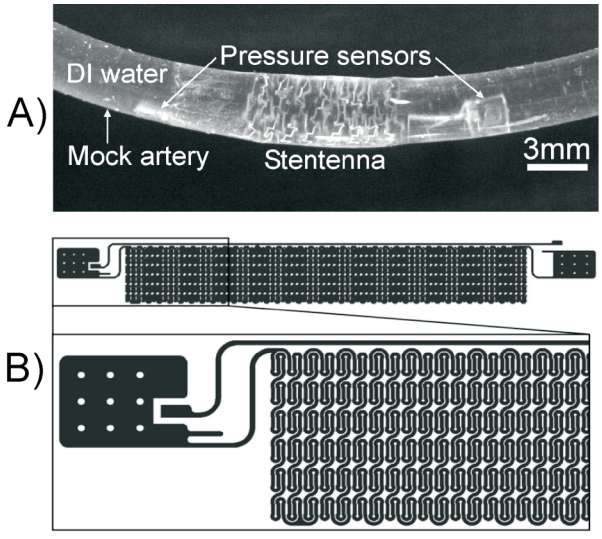

Fig. 1: (A) Low-Q flow sensing Stentenna in mock artery [2]. (B) High-Q Stentenna pattern for batch µEDM. Solid sections are pads for mounting pressure sensors [3].

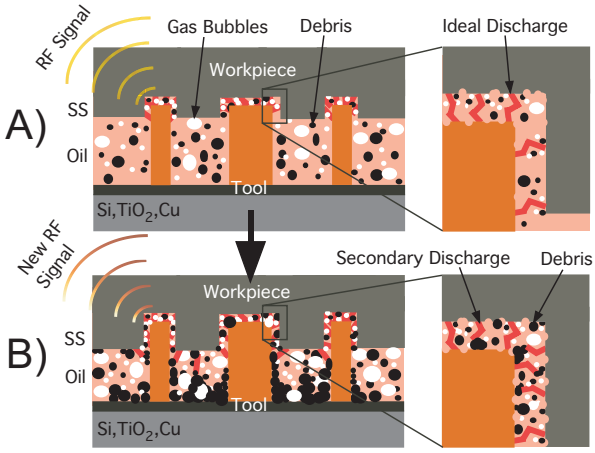

Fig. 2: (A) Ideal µEDM spark discharges produce a wireless signal that changes with secondary discharges (B) due to debris.

compatible and offers a 100x improvement in throughput over serial mode [6]. Batch mode tools can be fabricated using PMMA for X-ray or SU-8 for UV exposure in a LIGA type electroforming process. One drawback is that as feature densities increase, accumulation of trapped debris leads to spurious, secondary discharges. Without attention, this causes workpiece damage and tool recasting, eventually halting progress completely (Fig. 2) [7,8]. Damage to the workpiece consists of rough surfaces, rounded edges, and larger machining tolerances. Tool recasting is caused by secondary discharges that lead to excessive heating. The result is a tool that is wider and shorter than the original at different locations on the pattern. It would be useful to detect the change in machining conditions before this damage occurs.

Fast current spikes generate a detectable wireless signal [9-11]. Marconi first utilized spark discharges similar to those found in EDM for wireless communication in the 1890s. In the late 1970s, early work showed that it was possible to use RF transmissions to distinguish between open circuit, spark, arc, and short circuit conditions in macro-scale, serial mode EDM [12]. At the micro scale, particularly for batch mode, process monitoring is even more critical. Further, due to the smaller dimensions, tighter tolerances, electrode multiplicity and lower machining rates, the discharge characteristics are significantly different.

As debris accumulation becomes worse during machining, one would expect changes to the discharges and consequently, the wireless spectrum. In this study we explore how these characteristics can be correlated to micromachining process quality with a view toward monitoring large-scale production by μEDM.

II. EXPERIMENT DEFINITION

The test pattern used for this study was the stentenna [2,3]. Figure 1A shows a low-Q stentenna fabricated with serial µEDM that has been deployed in a mock artery. The device begins as a planar stainless steel foil that is machined into a meandering

* Corresponding Authors: 1301 Beal, Ann Arbor, MI 48109, mtrichar@umich.edu, yogesh@umich.edu

pattern. The coil is an inductor and the pressure sensors are capacitors in an LC tank. This allows wireless querying of the sensors for in-situ flow measurement in an artery by tracking the resonant frequency of the LC tank.

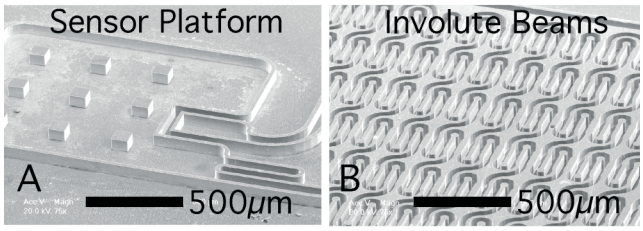

Fig. 3: 80 μm copper electroplated high-Q stentenna tool. Left: sensor platform. Right: Involute beams [3].

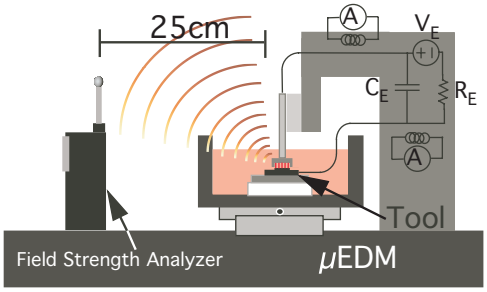

Fig. 4: Experiment setup for wireless monitoring and inductively coupled current probes.

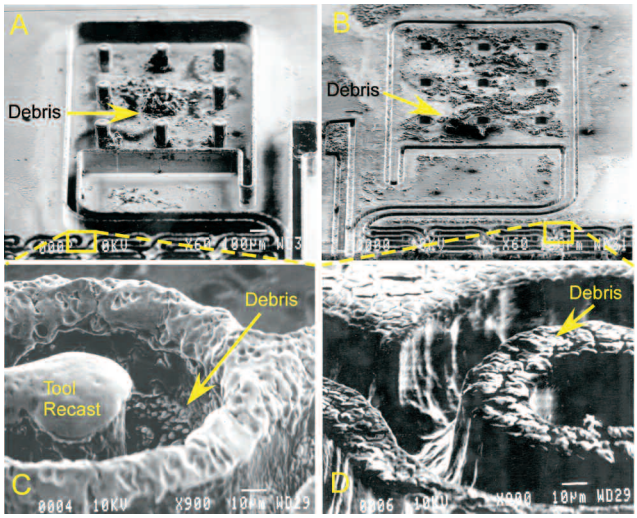

Fig. 5: A) 200 μm copper tool after machining with debris. B) Workpiece with large debris before cleaning. C) Close-up of debris, tool recast. D) Debris on workpiece top before cleaning, damaged sidewalls. E) Straight edges from non debris-dominated μEDM [8].

Table I: Machining Conditions

Tool Height	200 μm
Voltage	70 V
Capacitor	10 pF
Resistor	5 kΩ
Z-Feed	0.2 μm/s
Plunge	50 μm
Workpiece	316L Steel

While this new functionality is promising, the quality factor (Q) of the LC tank significantly limits the range and sensitivity. Three ways that the Q can be improved are to increase the inductance, decrease the parasitic resistance, or lower the nominal capacitance of the pressure sensors [3]. High-density batch mode μEDM enables the number of inductor turns to be greatly increased, giving a 16x potential improvement in inductance. This is implemented in the high-Q stentenna pattern shown in Figs. 1B and 3. The pattern is 2.5 cm long and 2.5 mm wide with 30 μm wide beams. However, due to the compact, meandering shape, this pattern is hindered by debris accumulation [3] and is a good test for the wireless monitoring technique.

The pattern can be divided into two sections, the sensor platform and the involute beams. The sensor platform (Fig. 3A) has a fill factor (tool area density) of 8.4%. The involute beams (Fig. 3B) have a fill factor of 32.9%. Copper tools were fabricated using 200 μm tall PMMA LIGA on a titanium oxide seed layer. The workpiece was a 7x7 mm^2, 100 μm thick 316L stainless steel foil, the same material as commercial stents. A small portion of the pattern was machined with minimum discharge energy to allow longer observation of the spectra as debris accumulated. In Fig. 4, which shows the machining apparatus, this translated to values of 70 V and 10 pF for V_E and C_E, respectively.

In serial mode, for which the tool is a wire tip, the tool is rapidly rotated to improve dimensional accuracy. This also helps remove debris by continuously flushing the dielectric fluid. In batch mode, since the tool is a 2-dimensionial cookie cutter, it cannot be rotated. Instead, the stage is dithered vertically by about 20 μm during machining to flush the fluid as much as possible. Machining parameters are listed in Table I. The sample was plunged 50 μm deep into the tool while recording the wireless RF field strength, plunge depth, time, and current waveform of the discharges. Note that plunge depth indicates how far the tool has advanced into the workpiece during machining. If there is appreciable tool wear, the actual machined depth may be somewhat less.

III. EXPERIMENTAL RESULTS

The SEM images in Fig. 5 show the tool and workpiece after machining. There was enough residual debris on the surface to span the full height of the tool. A significant amount of debris was left in the dielectric oil that could not be imaged. Figs. 5C and 5D show tool recasting and debris on the surfaces, indicating a large amount of debris near the machining area. Figure 5E shows a different example of high quality machining with no debris effects [8]. In Fig. 6, one can see that machining progressed steadily until 165 min. when machining became debris-dominated. Changes in discharge characteristics (and consequently the RF transmission)

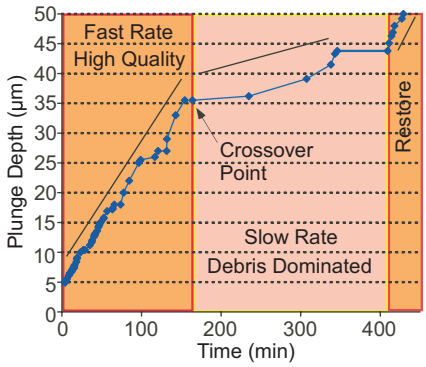

Fig. 6: Plunge rate slows around 165 min and restores around 410 min. This is because discharges are used to pulverize debris and the workpiece repeatedly retracts when it senses such events.

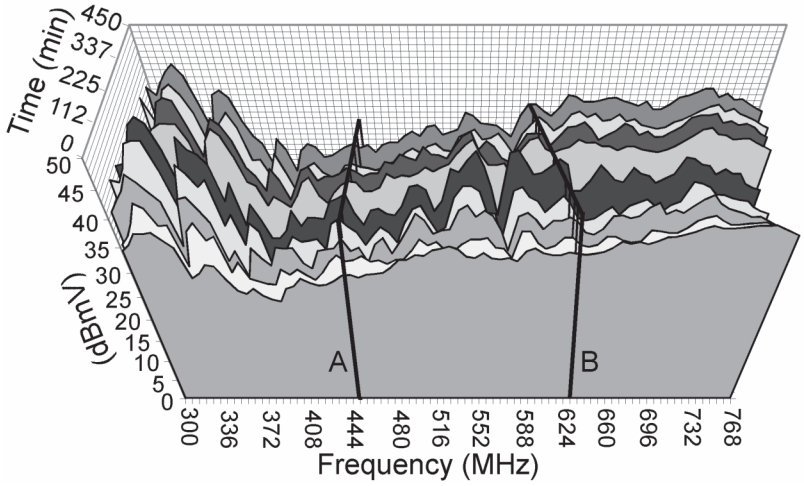

Fig. 7: Wireless signal strength at a distance of 25 cm for various times and frequencies. Each spectrum represents the average of 10 samples. Half the number of samples shown for clarity. Frequencies A and B follow different trends when normalized.

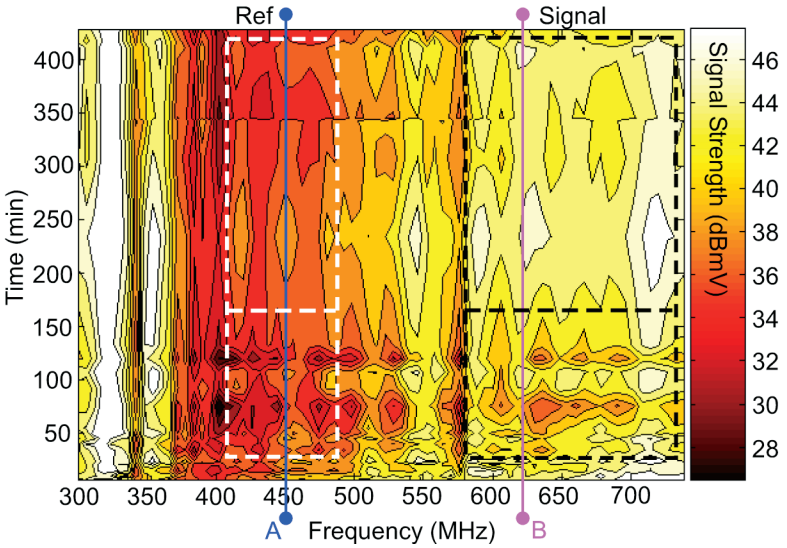

Fig. 8: Topology view (top view) of wireless signal strength over the course of machining. Each spectrum is normalized to the highest peak and plotted in Matlab. Frequencies A and B in the Ref and Signal bands change strength at different rates.

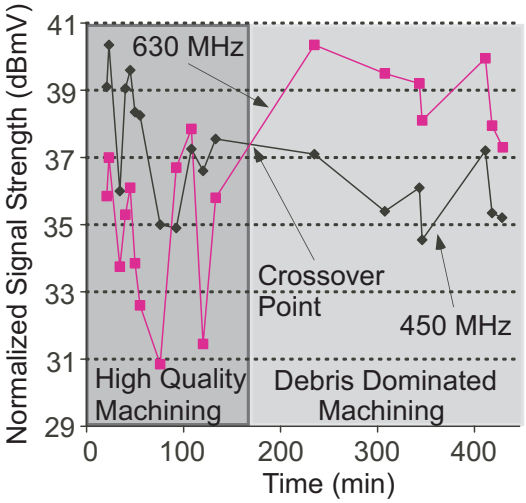

Fig. 9: The two normalized frequencies from Fig 8. A is a reference for B. Note opposing trend at ~132 min, right before the plunge rate slow down in Fig 6. Also at 100 min. First 3 data points not shown for clarity.

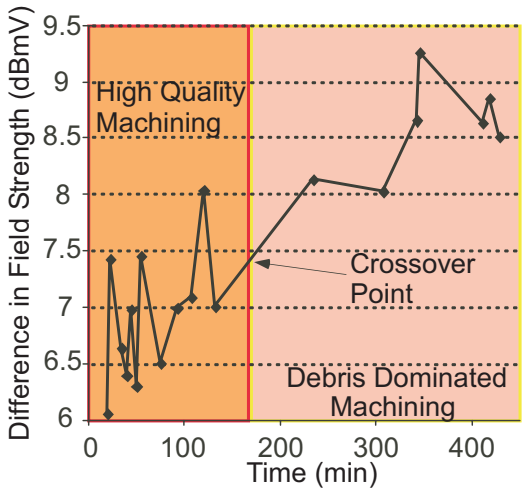

Fig. 10: The difference of the averages of the Signal and Ref bands in Fig. 8 eliminates common amplitude variations over time. Small numbers match favorable machining condition while larger numbers match poor machining according to plunge rates in Fig. 6.

are anticipated at such transition points. The potential advantage of monitoring the RF signals is that they are directly indicative of the nature of the spark. In batch mode machining, the measurable electrical characteristics of the discharge pulse are affected by a variety of parasitics. Hence, they are not always the best indicator of real-time machining quality.

Wireless measurements were taken at a distance of 25 cm using a Protek 3201 field strength analyzer (Fig. 4). The spectrum plotted in Fig. 7 was recorded over time from 300 to 750 MHz in 6 MHz steps. Data points represent the average of 10 samples and were compensated for antenna factor and background noise. The frequency range was selected to cover the upper bound of the signal and detect frequency shifts in that range. In Fig. 8, the topology view (top view) of the same data is normalized to the highest peak in each spectrum and plotted against time on the y-axis. It is a Matlab interpolation of the data points that helps distinguish trends in the signal over time. There are two regions of interest that show different trends, 'Ref' and 'Signal'. From Fig. 8 it is clear that frequencies from 580-750 MHz can be used as an averaged indicator for the crossover to debris-dominated machining. Frequency bands in the range 410-480 MHz provide a reasonable average reference for comparison.

The maximum output signal is represented by the 450 and 630 MHz signal lines and can be seen more clearly in Fig. 9. The 450 MHz line acts as a reference for the 630 MHz line. These frequencies follow the same signal strength trend until 132 min., where the 630 MHz line becomes larger ultimately crossing the 450 MHz line at 165 min. (Note that this is consistent with transition of the plunge rate (slope) in Fig. 6 where machining becomes debris-dominated at 165 min.). The maximum difference was 9.3 dBmV. Figure 10 plots the difference in the averages of the Signal and Ref. bands as a function of time. Amplitude variations that are common to both frequencies are removed, but a clear trend reflects the progressive accumulation of debris. The smaller regions track the high quality machining from Fig. 6 while larger regions track the debris-dominated machining.

Low impedance current probe traces for the cathode and workpiece in Fig. 11 gave small differences between high quality

and debris-dominated regions. As noted previously, electrical characteristics measured at the discharge electrodes in this manner are influenced by a number of electrical parasitics and are not directly indicative of the nature of the spark. Wireless measurement, therefore, promises a superior technique for real time monitoring of batch mode μEDM machining quality.

IV. DISCUSSION

During the μEDM process, as the debris accumulate; they begin to interfere with the discharge gap as diagramed in Fig. 2b. Inspection of the tool after machining shows that the amount of debris can span the distance from workpiece to tool. It has also been shown that metallic particles can transport charge from one electrode to another before discharging at much shorter distances and smaller energies [13]. These effects lead to detectable changes in the wireless field strength as the level of debris increases.

Spark discharges between two conductors in air have been modeled in the past as dipole radiation to simulate electrostatic discharge effects on circuitry [9-11]. While these models are for gas discharges and spherical electrodes, the trends are still useful to understand since a μEDM discharge still has many similarities. In [10] it was found that as the discharge gap decreased, the discharge voltage decreased, the amplitude of the electromagnetic field intensity increased, and the time rate change of the current increased. The dipole model for a square wave current pulse from $0< t < \tau_0$ is given for the magnetic flux density by:

$$B \approx -\frac{2l\sin(\theta)}{c^2 r}\frac{\partial I(t-r/c)}{\partial t} \quad (1)$$

where l is gap length, c is the speed of light in the medium, t is time, r is distance to the observation point at angle θ, and $I()$ is the current waveform [9]. The Fourier components of B are given by:

$$b = \frac{4i\sin\theta e^{i\omega[r/c+\tau_0/2-(l/c)\cos\theta]}}{cr\cos\theta}\sin\left(\frac{\omega l}{c}\cos\theta\right)\cos\left(\frac{\omega\tau_0}{2}\right) \quad (2)$$

While direct measure of these terms is not possible, it appears likely that in the context of batch mode μEDM, the accumulation of debris influences τ_0, leading to an increase in high frequency components of the radiated spectrum. Further investigation is in progress.

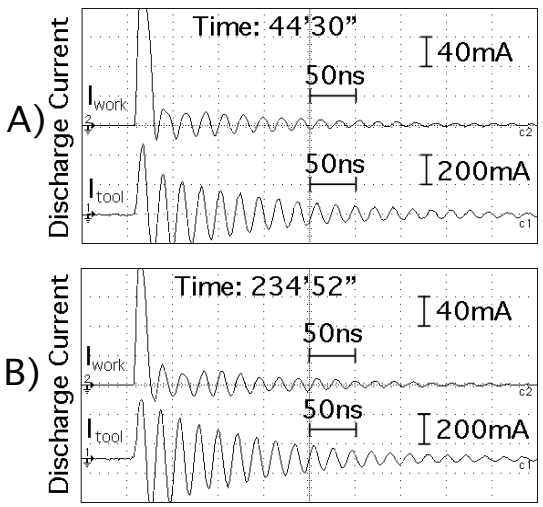

Fig. 11: Current traces for the cathode and workpiece during (A) normal machining and (B) debris-dominated regions of machining do not provide obvious indicators of decreased machining quality.

V. CONCLUSIONS

The discharges in μEDM produce detectable wireless signals. As debris accumulate in batch mode μEDM, the signal amplitude at various frequencies changes. In particular, the average transitions at frequencies >580 MHz gain in strength while others remain relatively constant over time. The difference between either two frequencies in these bands or the averages of these bands tracks the favorable and debris-dominated machining conditions. Wireless monitoring could be used to predict and prevent damage to the workpiece and tool in real time. However, frequency selection would be dependent on materials and machining conditions. Wireless monitoring could be built to interface with the control hardware of a μEDM and used in an automated production context to monitor multiple machines at once.

ACKNOWLEDGEMENTS

The authors would like to acknowledge Dr. Dawn Skala and Brandon Levey for fabrication assistance as well as Dr. Kenichi Takahata for discussions. The facilities used for this research include Sandia National Laboratories, California and the University of Michigan. Travel support has been provided by the Transducers Research Foundation.

REFERENCES

[1] T. Masaki, K. Kawata, and T. Masuzawa, "Micro electro-discharge machining and its applications," *IEEE MEMS '90*, pp. 21-26, 1990

[2] K. Takahata, A. DeHennis, K.D. Wise, Y.B. Gianchandani, "Stentenna: a micromachined antenna stent for wireless monitoring of implantable microsensors," *IEEE Conf EMBS*, 2003, pp. 3360-3

[3] K. Takahata, *Batch manufacturing technology based on micro-electro-discharge machining and application to cardiovascular stents*. University of Michigan, Electrical Eng Ph.D. Thesis, 2005

[4] K. Udeshi, M. Richardson, J.-J. Hung, L. Que, G.M. Rebeiz, Y.B. Gianchandani, "A dual-EDM reverse damascene process for RF switches and other bulk devices," *ASME IMECE*, Nov. 2005

[5] K. Udeshi, *On-chip high voltage generation using mechanical oscillators*. University of Michigan, Mech Eng Ph.D. Thesis, 2005

[6] K. Takahata, Y.B. Gianchandani, "Batch Mode Micro-Electro-Discharge Machining," *JMEMS* 11(2), pp. 102-110, 2002

[7] M.T. Richardson, Y.B. Gianchandani, "A Passivated Electrode Batch μEDM Technology for Bulk Metal Transducers and Packages," *IEEE Sensors 2005*, pp. 219-222, Nov. 2005

[8] M.T. Richardson, Y.B. Gianchandani, D.S. Skala, "A parametric study of dimensional tolerance and hydrodynamic debris removal in micro-electro-discharge machining," *IEEE MEMS 2006*, pp. 314-317, Jan. 2006

[9] A. Kadish, W. B. Maier, "Electromagnetic radiation from abrupt current changes in electrical discharges," J. Appl. Phys. 70(11), pp. 6700-11, Dec. 1, 1991

[10] H. Tomita, "Dependence of current and induced voltage due to spark discharge on gap length," *Intl Sym on Emag Compatibility*, pp. 138-141, 1999

[11] S. Ishigami, T. Iwasaki, "Evaluation of charge transition in a small gap discharge," IEICE Trans. Commun, 79B(4), pp. 474-82 Apr. 1996

[12] S.K. Bhattacharya, M.F. El-Menshawy, "Monitoring the EDM process by radio signals," *Intl J.Prod Res*, 16(5), pp. 353-63, 1978

[13] R. Tobazeon, "Electrohydrodynamic behaviour of single spherical or cylindrical conducting particles in an insulating liquid subjected to a uniform DC field," *J. Phys. D: Appl. Phys.*, 29, pp. 2595-2608, 1996

FLOW-CHAMBER MICROARRAY DETECTION OF MALARIAL ANTIGENS

Daniel J. Laser, Corwin T. Hardham, and Johann Kim
Wave 80 Biosciences, Inc.
2325 3rd St, Suite 215, San Francisco, California 94107

ABSTRACT

Detecting and quantifying circulating proteins produced by malarial parasites provides valuable information to guide diagnosis and treatment. We report on the detection and quantification of the malarial antigens HRP-II and aldolase with single-use microfluidic cartridges incorporating protein microarrays. The microarray-based cartridges are suitable for use with handheld bioassay instruments. Reagent and sample transport in the cartridges is controlled by integrated silicon electroosmotic micropumps. Applications of the flow-chamber microarrays for experimentally determining binding parameters for pairs of biological molecules are explored.

INTRODUCTION

Historically, body fluid analysis for malaria diagnosis has been through microscopic examination of blood smears for parasites, through automated analysis with laboratory PCR systems; or by card-type kits [1]. While these methods are satisfactory for many clinical settings, in some instances a fully automated (e.g. no manual dispensing/metering of reagents or skilled interpretation of assay outcomes), highly portable system for detecting and quantifying malarial antigens is desirable.

We sought to leverage protein microarrays to develop new tools and techniques for detecting and quantifying malarial antigens. Microarrays (both DNA and protein) are well established for drug discovery, but are underutilized in portable medical diagnostics. For such applications, it is convenient to locate microarrays within microscale reaction chambers linked to channel networks for delivering samples and reagents. Abundant options now exist for controlled sample/reagent delivery [2]. However, selection of geometries and operating parameters for flow-chamber microarrays requires careful study of the interplay between biochemical and microfluidic effects. The methods introduced here for developing microarray malarial antigen assays are applicable to a wide range of analytes.

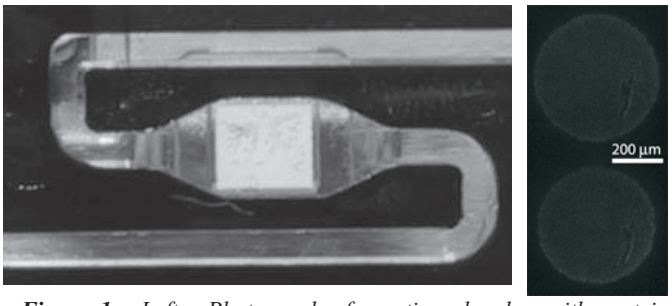

Figure 1: *Left: Photograph of reaction chamber with protein microarray. The microarray (typically eight spots) is printed on a nitrocellulose film. Right: photomicrograph of a portion of a reacted microarray.*

EXPERIMENTAL METHODS

Flow-chamber microarrays of the design shown in figure 1 were used in experiments. The microarray-containing reaction chambers are built into microfluidic cartridges; the cartridges, along with a handheld instrument, compose an automated bioassay system, a prototype of which is illustrated in figure 2. To run an assay, a small (< 50 microliters) whole blood sample, obtained through e.g. fingerstick, is allowed to wick into the cartridge sample pad (inset of figure). The sample pad is sealed by sliding closed the cartridge cover, after which the cartridge is inserted into the handheld instrument (overall size 310 cm^3, weight incl. batteries 292 g). Reagent and sample transport within the cartridge is driven by integrated slit capillary array silicon electroosmotic micropumps [3], which in turn are controlled by electrical signals from the handheld.

The reaction chamber cross-sectional dimensions are 120 µm x 3 mm. The top surface is injection molded cyclic olefin copolymer (COC); the side walls are laser-cut polymer; and the bottom surface is nitrocellulose-coated glass. Molded COC surfaces provide a smooth transition between the reaction chamber and the inlet/outlet microchannels (1 mm x 1 mm cross-section). Prior to cartridge assembly, a capture microarray (typically eight spots) is printed onto the nitrocellulose film using a modified MicroCaster handheld microarrayer (Whatman) using the manufacturer's standard arraying solutions.

For assay development and characterization, malarial reagents, including monoclonal IgG and IgM anti-*P. falciparum* and recombinant *P. falciparum* HRP-II antigen, were purchased from Immunology Consultants Laboratory, Newberg, OR.

Figure 2: *Highly portable, fully automated system for determining the composition of body fluids.*

Malarial antibodies were biotinylated according to standard protocols [4]. Biotinylated goat anti-mouse IgG (Sigma) and Cy2-streptavidin (Amersham/GE Healthcare) were used in flow-chamber microarray characterization experiments.

ASSAY CHARACTERIZATION AND MICROFLUIDICS MODELING

Sandwich immunoassays were developed for HRP-II (from *P. falciparum*) and aldolase, a pan-malarial antigen. Data from the development of the HRP-II immunoassay is plotted in figure 3. All combinations of IgG and IgM antibodies were found to yield satisfactory results except for IgM-IgM. Accordingly, HRP-II microarrays include both IgM and IgG spots; IgG is used for labeling. An assay for aldolase was developed in a similar manner. For the aldolase assay development, affinity purified polyclonal antibodies as well as monoclonal antibodies were evaluated.

A model biochemical system of solid-phase biotinylated goat anti-mouse IgG and fluid-phase Cy2-streptavidin was used to validate a method for characterizing flow-chamber microarray binding as a function of various environmental and fluid mechanical parameters. Figure 4 shows the intensity of anti-IgG spots after flowing through 20 µL of Cy2-streptavidin (5 µg mL^{-1}) at flow rates of 2, 10, and 50 µL min^{-1} (corresponding to average velocities within the reaction chamber of 0.09, 0.46, and 2.3 mm sec^{-1}, respectively) at room temperature. In all cases, the flow is fully developed in at least 99% of the reaction chamber. Analyte flux equations are easily written in terms of the analyte diffusion coefficient and bulk concentration and the one-dimensional velocity profile. The boundary condition at the film-coated surface is defined in terms of the analyte binding (association) rate constant k_a. The system is usually solved by numerical methods similar to those described by Myszka et al. [5] and others, with the added model complexity of step-function spatially variations in receptor concentration. Intensity-reading calibration permits calculation of parameters such as k_a from experimental data.

Development of the flow-chamber HRP-II and aldolase assays entailed characterization of binding for antigen capture and labeling steps. Characterization of binding processes for positive/negative control spots in the microarray permits the use of these spots to calibrate for operational uncertainties.

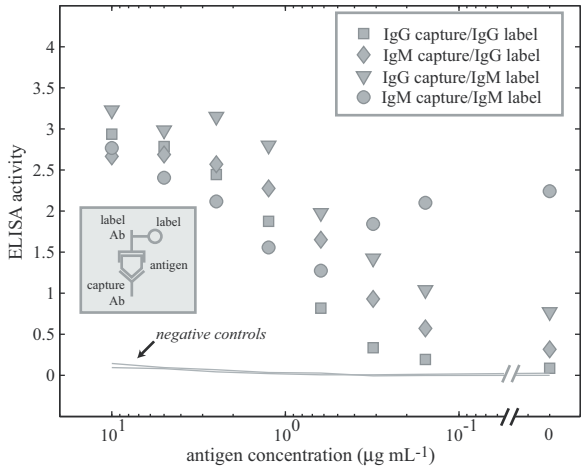

Figure 3: *Dose response for the malarial antigen HRP-II (P. falciparum) using mouse IgG and IgM monoclonal antibodies for capture and labeling. Data shown is for biotinylated label antibody, streptavidin-horseradish peroxidase secondary label. Inset illustrates schematically the principle of sandwich immunoassays.*

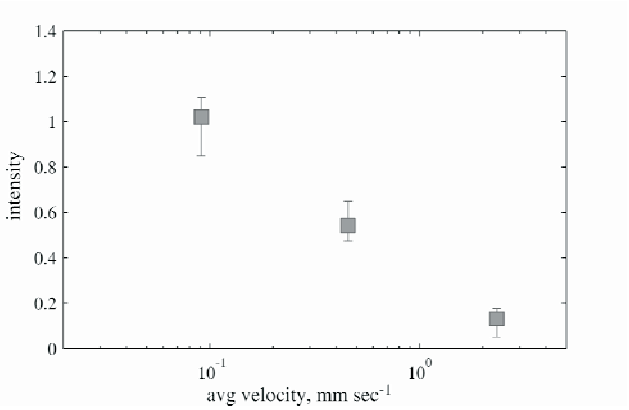

Figure 4: *Microarray capture of Cy2-streptavidin with biotinylated anti-IgG in a flow chamber. Plotted values are the mean intensities of three spots per microarray; error bars show spread. Data shown is for 20 µL of Cy2-streptavidin at 5 µg mL^{-1}; followed by 50 µL wash solution; experiments carried out at room temperature.*

CONCLUSIONS

New techniques and tools for detecting and quantifying the malarial antigens HRP-II and aldolase have been developed. Sandwich immunoassays have been developed and adapted for single-use microfluidic cartridges incorporating flow-chamber microarrays. The cartridges are designed to function as part of highly portable bioassay systems. Methods for modeling coupled microfluidic and biochemical processes and experimentally determining reaction rate constants have been developed and refined.

ACKNOWLEDGEMENTS

This work was supported in part by SBIR contract H92222-04-C-0032, U.S. Special Operations Command. It made use of National Nanofabrication Users Network facilities funded by the National Science Foundation under award ECS-9731294.

REFERENCES

[1] G. A. Farcas, K. J. Y. Zhong, F. E. Lovegrove, C. M. Graham, and K. C. Kain, "Evaluation of the Binax Now ICT Test versus Polymerase Chain Rection and Microscopy for the Detection of Malaria in Returned Travelers," *Am. J. Trop. Med. Hyg.*, vol. 69, pp. 589-592, 2003.

[2] D. J. Laser and J. G. Santiago, "A Review of Micropumps," *Journal of Micromechanics and Microengineering*, vol. 14, pp. R35-R64, 2004.

[3] D. J. Laser, K. E. Goodson, J. G. Santiago, and T. W. Kenny, "High-Frequency Actuation with Silicon Electroosmotic Micropumps," Proc. 2002 Solid-State Sensors, Actuators, and Microsystems Workshop, Hilton Head, S.C., pp. 231-234.

[4] G. T. Hermanson, *Bioconjugation Techniques*. San Diego: Academic Press, 1996.

[5] D. G. Myszka, X. He, M. Dembo, T. A. Morton, and B. Goldstein, "Extending the Range of Rate Constants Available from BIACORE: Interpreting Mass Transport-Influenced Binding Data," *Biophysical Journal*, vol. 75, pp. 583-594, 1998.

DIRECTIONAL REASSEMBLY OF MYOFIBRILS IN CULTURED CARDIAC MYOCYTES USING A THREE-DIMENSIONAL POLYMERIC SUBSTRATE

Yi Zhao, and Xin Zhang
Laboratory for Microsystems Technology
Department of Manufacturing Engineering, Boston University
Boston, MA 02215, USA

ABSTRACT

This paper presents directional reassembly of myofibrils in cardiac myocytes using a three-dimensional polymeric substrate. Such substrate modulates reorganization of dismantled myofibrils through microstructures, resembling the morphology *in vivo*. As a result, the cardiac myocytes in culture are reoriented. The mechanical forces at subcellular level are *in situ* monitored during the adhesion and redifferentiation processes using microfabricated polymeric structures, revealing evolution of the mechanical interaction between cardiac myocytes in culture and the artificial extracellular environment. This polymeric substrate has the potential to be a basis for development of *in vitro* assembled cardiac tissue.

INTRODUCTION

Heart is the most heavily worked organ in the body, pumping blood to and from all the other organs. The contractile performance of the heart heavily depends on the mechanical behavior on cellular and subcellular level. Specifically, the myofibrils within the cardiac myocytes have a directional arrangement, allowing the cells to perform large contraction and to pump as much blood as required. However, such contractile performance is somewhat deteriorated in cultured myocytes due to remodeling [1]. Many mechanical properties *in vivo* disappear because of the randomly oriented myofibrils. Therefore, there is a need to reassemble the myofibrils in a directional profile with a hope to resemble the contractile performance *in vivo*, facilitating the cardiomechanical study and cardiac tissue development.

Prior research in tissue engineering has shown that the microfabricated structures have potentials in regulation of a wide variety of cellular behaviors, such as cell growth and attachment [2, 3]. The cells cultured on such structures adapt to the artificial extracellular environment and adjust their physiologic performance accordingly. In this paper, we report the use of a polymeric substrate with three-dimensional microstructures in regulation of the reassembly of myofibrils during cell remodeling process. The cellular mechanical forces are *in situ* monitored during the adhesion and redifferentiation process to provide evidence of directional myofibrils reorganization.

FABRICATION AND SETUP

The three-dimensional substrate (**Figure 1**) is made of PDMS polymer. It consists of parallel sidewalls, embedded pillars and large polymeric posts. The distance between adjacent sidewalls is about 20 μm, in accordance with the width of a single cardiac myocyte. In the spaces between the parallel sidewalls, large polymeric posts are placed, being 100 μm to 150 μm away from one another. These posts are used to separate individual myocytes so that the cells will not interconnect. The embedded pillars are 2 μm in diameter and closely spaced, serving as mechanical sensors for force measurement. In our design, the PDMS sidewalls and the large posts are slightly higher than the embedded pillars so as to form a recessed chamber for the cells. **Figure 1c** shows the schematics of cell attachment onto the substrate.

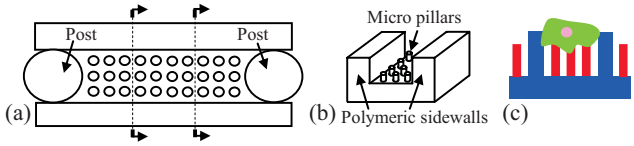

Figure 1. *The three-dimensional PDMS substrate: (a), (b) the substrate is made up of polymeric posts, parallel sidewalls and embedded pillars; (c) the cell attachment on the substrate.*

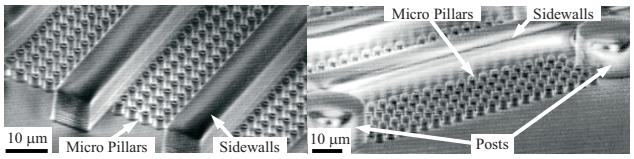

Figure 2. *SEM pictures of the three-dimensional PDMS substrate with microstructures of different heights.*

This three-dimensional polymeric substrate was fabricated using pressure-assisted micro molding technology we reported earlier [4]. The microstructures with different heights were fabricated via one replication step using single-crystal silicon template. The fabricated substrate is shown in **Figure 2**. The substrate was placed in an on-stage culture chamber and integrated with an inverted optical microscope. The fluidic and electrical connections were supplied to ensure the cells were in a preferable environment (i.e. 37 ºC and 5% CO_2/air).

MYOFIBRIL REASSEMBLY & CELL ALIGNMENT

Left ventricular myocytes were isolated from male Wistar rats according to a previously described protocol [5] and cultured on the three-dimensional substrate. The cell morphology change during the adhesion and redifferentiation processes was monitored. The cellular forces were measured from the embedded polymeric pillars.

The morphology change is illustrated in **Figure 3**. During the first 24 hours, the cells retained rod-shaped morphology as *in vivo*. In the following few days, the myofibrils were dismantled. As a result, the cells lost their striated architecture and transformed to an amorphous form. At about 72 hours, most cells were rounded. Therefore, there were no substantial cellular forces measured at this moment. As the culture continued, myofibrils reorganized and the cells stretched out pseudopodia towards the substrate. In the plain substrate, the pseudopodia proceeded in all directions so that the cells spread isotropically. The three-dimensional polymeric substrate, on the other hand, acted as scaffolds to guide the myofibrillar proteins along the longitudinal axis of the sidewalls, thus reorienting the cells.

The cell reorientation after 7 days culture is shown in **Figure 4**. It is seen from the fluorescence labeled actin filaments that the cells were well confined by the microfabricated sidewalls and being aligned by the three-dimensional structures. This is in sharp contrast to the control group where the cells were cultured on a plain polymeric substrate. A closer observation shows the myofibrils reassembly in aligned cells had a directional morphology. In the control group, however, the myofibril reassembly was randomly oriented.

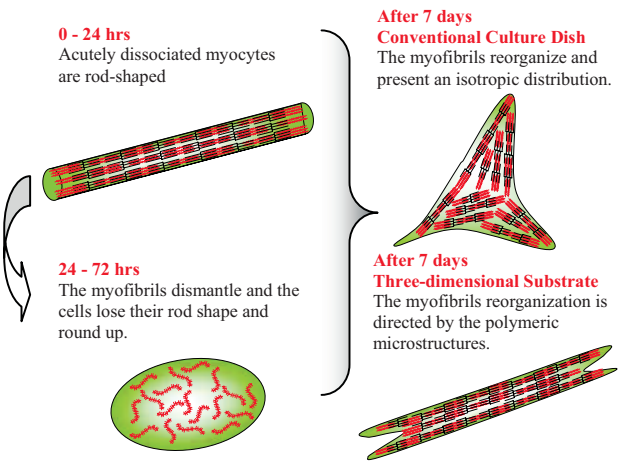

Figure 3. *Remodeling process of cardiac myocytes in long-term culture. The reassembling of myofibril adapts to the local extracellular environment.*

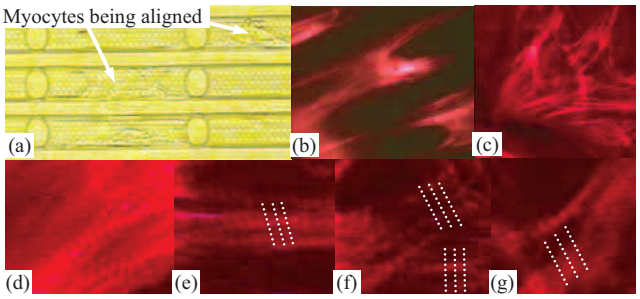

Figure 4. *The reorientation of myocytes is observed by (a) the phase contrast image and (b) fluorescence labeling of the actin filaments. (c) shows the control group cultured on plain PDMS surface. A closer observation shows the reassembling of myofibrils is directional in (d) the aligned cells and randomly oriented in (e) – (g) the control group.*

FORCES DURING REDIFFERENTIATION

With reassembly of the myofibrils and reorientation of the cells, contractile performance of the cardiac myocytes resumes. Given the fact that the large polymeric posts eliminate the physical contacts between neighboring cells, the functional gap junction is not present, as evidenced by the lack of synchronous contraction. The cell contraction is therefore driven by each cell's own pacemaker. The mechanical forces generated by the cells were determined from deformation of free ends of the micro pillars.

Figure 5 shows an aligned myocyte and the subcellular mechanical force during its contraction. The deformation of the pillars was monitored by a video camera. The force vector map was achieved by multiplying the deformation with the predetermined spring constant, showing a subcellular spatial resolution. The magnitude and direction of the cellular forces at the locations of different pillars were directly achieved from the force map. Furthermore, by assuming the cellular forces have a spatially continuous distribution, data interpolation was conducted so that the cellular forces at the locations other than the pillars were approximated. As can be seen from the force map, the major force difference between the diastolic and systolic states is along longitudinal axis of the polymeric sidewall, providing evidence of directional reassembly of the myofibrils along this direction. Therefore, the force measurement during the redifferentiation process validates this three-dimensional polymeric substrate a viable tool for reassembling the myofibrils directionally.

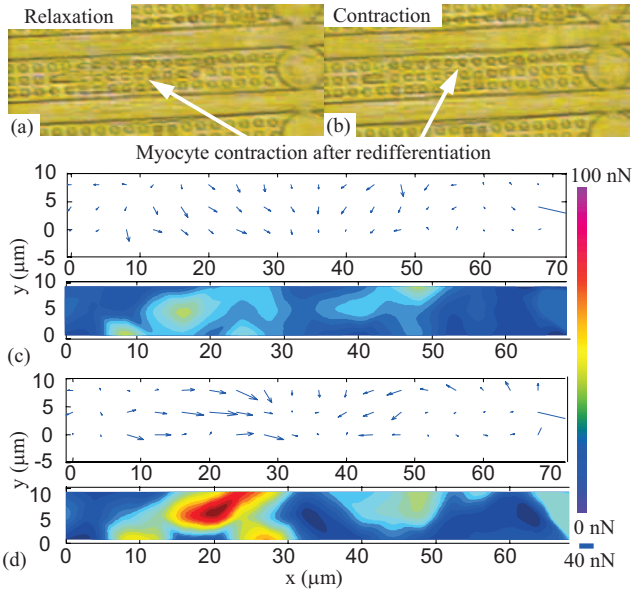

Figure 5. *(a)-(b): The contractile performance of the cells reappears when the myofibrils reassemble. The cellular forces at (c) the diastolic state and (d) the systolic state are derived from the deformation of the micro pillars.*

CONCLUSION

This study reports reorientation of myofibrils and alignment of cultured caridiac myocytes by using a polymeric substrate. The three-dimensional microstructures were built on the substrate via pressure-assisted micro molding. Long-term culture showed that the polymeric substrate can successfully modulate the reorganization of the myofibrils during the cell redifferentiation, thus aligning the myocytes along specific direction. The directional reorganization of myofibrils was confirmed by monitoring the mechanical forces developed from the aligned cells. This work promises the potential for *in vitro* assembled cardiac tissue and can lead to less sacrifice of time, cost and animal donors.

ACKNOWLEDGEMENTS

This work is supported by the NSF CAREER Award. The authors would like to thank Professor Chee Chew Lim, Professor Douglas B. Sawyer at Boston University School of Medicine, and Professor Ronglih Liao at Harvard Medical School for their technical advices.

REFERENCES

1. A.C. Nag, M.L. Lee, F.H. Sarkar, "Remodelling of adult cardiac muscle cells in culture: dynamic process of disorganization and reorganization of myofibrils", J. Muscle. Res. Cell. Motil. 17(3), 313 (1996).
2. A. Folch, S. Mezzour, M. During, O. Hurtado, M. Toner, R. Muller, "Stacks of Microfabricated Structures as Scaffolds for Cell Culture and Tissue Engineering", Biomedical Microdevices, 2(3):207, (2000).
3. S.N. Bhatia and C.S. Chen, "Tissue Engineering at the Micro-Scale", Biomedical Microdevices, 2(2):131, (1999).
4. Y. Zhao and X. Zhang, "Adaptation of flexible polymer fabrication to cellular mechanics study", Appl. Phys. Lett., 87 (14): 144101, (2005).
5. C.C. Lim, M.H. Helmes, D.B. Sawyer, M. Jain, R. Liao, "High-throughput assessment of calcium sensitivity in skinned cardiac myocytes", Am. J. Physiol. Heart Circ. Physiol. 281: H969 (2001).

AN ELASTIC MEMS DEVICE FOR CELLULAR FORCE MEASUREMENT

Yu Sun, Xinyu Liu, Wenhui Wang, Bob M. Lansdorp

Advanced Micro and Nanosystems Laboratory, University of Toronto
Toronto, Ontario, Canada

ABSTRACT

This paper presents a PDMS (polydimethylsiloxane) cell holding device and a sub-pixel visual tracking algorithm that are used together to visually resolve applied forces to a single cell at a full 30Hz with a sub-μN resolution. The computer vision microscopy based measurement technique and a further scaled-down device will provide a 0.52nN resolution, resulting in a novel platform for investigating the mechanical properties of many cell types of different sizes and for providing real-time cellular force feedback during automated microrobotic cell manipulation.

INTRODUCTION

Mechanical force plays a critical role in the interactions of biological cells with their surrounding environment. In order to understand how mechanical interactions affect the function of biological cells, cellular forces must be quantitated and their effects on the function and morphology of cells be studied. The capability of precisely measuring small forces is also important for providing force feedback during microrobotic biomanipulation where biological cells being handled are easily damaged.

Compared to cellular force measurement techniques such as optical tweezers, atomic force microscopy, magnetic beads, and micropipette aspiration, MEMS force sensors [1][2] are cost-effective and provide flexibility for system integration. However, the silicon-based devices require sophisticated equipment sets and much processing effort. Moreover, issues such as biocompatibility and operating in an aqueous environment for biological cells to survive often pose stringent challenges and intricacies in MEMS design, material selection, and microfabrication.

As microrobotic biomanipulation and single cell mechanical characterization in cellular biomechanics are always conducted under an optical microscope, it is highly desirable to simultaneously obtain high-resolution force measurements extracted from microscopy vision feedback. Thus, no distinct sensing modalities are required and a single vision sensor (CCD/CMOS camera) is capable of providing two forms of feedback (i.e., vision and force). For cellular force sensing, this concept can be implemented by visually tracking deflections of elastic, low-stiffness microstructures, and subsequently, transforming material deflections into forces.

Recently, microfabricated elastomer post/pillar structures using PDMS were constructed to visually measure traction forces generated by biological cells (smooth muscle cells [3] and cardiac myocytes [4]). PDMS-based devices are biocompatible and can be readily constructed using soft lithography without requiring intensive microfabrication efforts or sophisticated equipment sets. In [3][4], off-line image post-processing was conducted to measure PDMS post deflections. The cellular force measurement accuracy in these studies was not warranted because the small-deflection assumption in linear elasticity was not satisfied and the shear component of deflected posts not considered. Additionally, without adopting sub-pixel visual feature tracking techniques, the cellular force measurement resolution was sacrificed.

Although the PDMS devices [3][4] can be applied to measuring how much forces are generated by adherent cells at adhesion sites on top of posts, they do not allow for studying how externally applied forces affect cell responses, which is particularly true for suspended cells. A range of applications call for a new experimental platform including force-controlled microrobotic cell injection (e.g., injecting genetic materials into individual cells to treat severe infertility or to create transgenic organisms for cancer studies [5]) and cell indentation for mechanical property characterization in which forces applied by a micropipette or indenter to a cell must be measured in real time.

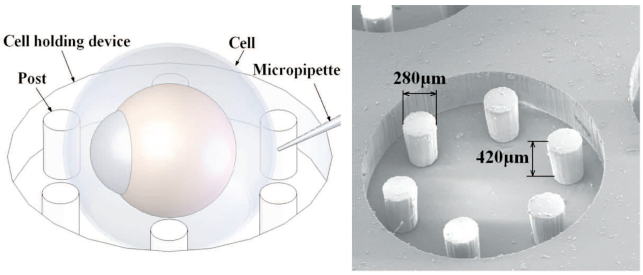

Figure 1. *SEM image of a PDMS cell holding device.*

EXPERIMENTAL SETUP

The system consists of a PDMS cell holding device, an optical microscope with a CMOS camera, and a three-degrees-of-freedom microrobot with a 40nm positioning resolution along each axis. The microrobot controls the motion of an injection micropipette to apply forces to a single biological cell that is surrounded by low-stiffness protruding posts inside a cavity. Although a single element is shown in Figure 1, there are arrays of such elements on the PDMS cell holding device. The system setup is mounted on a vibration isolation table for minimizing vibration-induced vision/force measurement errors.

The PDMS cell holding device was constructed using standard soft lithography with SU-8 2075 (MicroChem, U.S.) and a ratio of 10:1 for Sylgard 184 (Dow Corning, U.S.) and curing agent. After a molding process, the PDMS cell holding device was peeled off the SU-8 template. The depth of the cavity and protruding posts is 420μm, and the diameter of the posts is 280μm. The devices were plasma treated before use.

MATERIALS AND METHODS

The zebrafish has emerged as an important model organism for development and genetic studies. The large size of zebrafish embryos (~1.2mm including chorion that is the outside membrane in Figure 2) makes the handling and manipulation of these cells less demanding. Although zebrafish embryos were chosen in this study to demonstrate vision-based cellular force sensing, the PDMS cell holding device can be readily scaled down for studying cells of smaller sizes (e.g., mouse embryos) and the methodology is not scale or cell type dependent.

Figure 2 shows an image captured in the cell indentation experiments. An injection micropipette mounted on the microrobot is employed to exert an indentation force to a zebrafish embryo, which deflects the two supporting posts against the cell. Post deflections, measured in real time by a visual tracking algorithm, are fitted to an analytical mechanics model to obtain the injection/indentation force (F in Figure 2). A valid application of linear elasticity was guaranteed as the maximum value of the measured deflection slope of the posts' free ends is 13.7°, which satisfies $\sin\theta \approx \theta$ and thus, the small deflection assumption.

Because the ratio of post height (420μm) to diameter (280μm) in this design does not satisfy the pure bending assumption of linear elastic beams (i.e., height to diameter ratio must be greater than 5) [6], both bending and shearing must be considered to accurately map the deflection to the applied force

$$F = \sum_{i=1}^{2} \frac{\delta_{hi}}{\frac{64H^3}{3\pi ED^4} + \frac{20(1+\gamma)H}{9AE}} \quad (1)$$

where $i = 1, 2$; δ_{hi} is horizontal deflection; H and A are post height and cross sectional area; E and γ are Young's modulus and Poisson's ratio (γ=0.5 for PDMS). It is known that different processing conditions of PDMS result in large variations of Young's modulus values. In order to accurately determine the Young's modulus value, calibration experiments were conducted with a piezoresistive silicon force sensor (AE801, SensorOne, U.S.) on a PDMS cantilever beam produced under the same processing conditions. The Young's modulus value was determined to be 707.2kPa.

A sub-pixel visual tracking algorithm was developed to accurately track post deflections in real time. The task is two fold, to track image patches of the top surfaces of supporting posts as well as to accurately detect the circular center positions. A template matching algorithm with template update was used to track the motion of the supporting posts. After tracking the image patches that contain post top surfaces, the circular center positions were detected by a least squares circle detection (LSCD) algorithm. Accumulative errors caused by template updating were eliminated in the subsequent LSCD detection of circular centers.

RESULTS AND DISCUSSION

A 2.5× objective (NA 0.07) was first used in order to have both the cell and supporting posts inside the field of view. The calibrated pixel size is 4.17μm. The micropipette used for indenting cells has an outside diameter of 25μm at the tip end. The indentation speed was controlled at 600μm/sec. The sub-pixel visual tracking algorithm has a tracking resolution of 0.45 pixel and costs 22.3ms for processing each frame of image, proving the real-time capability (30Hz). Measured horizontal deflections were substituted into the mechanics model (1) to calculate indentation forces. In Figure 3, cell deformations on the micropipette side were obtained by subtracting the average horizontal deflections of the two posts from the micropipette's displacement (i.e., displacement of the microrobot). With the 2.5× objective, the vision-based force measurement resolution is 12.7μN. The force measurement resolution depends on optical conditions and is greatly improved with objectives of higher magnifications. As shown in Table I, with a 10× objective (NA 0.3), the current system is capable of visually resolving forces down to 3.7μN.

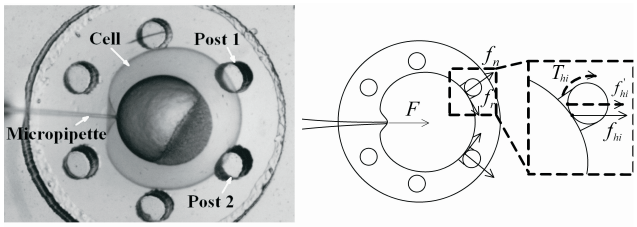

Figure 2. *Indentation forces cause two supporting posts to deflect (left) and force analysis (right).*

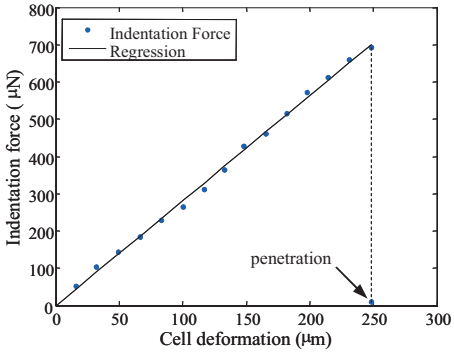

Figure 3. *Force-deformation curve of an indented zebrafish embryo.*

TABLE I. VISION-BASED CELLULAR FORCE MEASUREMENT RESOLUTION.

Objective magnification	NA	Rayleigh limit (μm)	Pixel size (μm)	Deflection resolution (pixel)	Force resolution (μN)
2.5×	0.07	3.93	4.17	0.45	12.7
4×	0.13	2.12	2.27	0.58	8.9
6.4×	0.13	2.12	1.56	0.40	4.2
10×	0.30	0.92	1.00	0.54	3.7

Besides the applicability to cellular biomechanics, the device and tracking algorithm can provide important force feedback in microrobotic cell injection. Cell membrane penetration can be precisely determined from the vision-based force measurement results for subsequent genetic material deposition (Figure 3). The abrupt position change of the supporting posts signals cell membrane penetration. Forces required to penetrate the zebrafish chorion were determined to be 692.8μN, in agreement with previously reported results [7].

Importantly, the vision-based cellular force sensing framework is not scale dependent. A cell holding device with supporting posts of 25μm in height and 5μm in diameter, based on a 0.5 pixel visual tracking resolution obtained in this study, has the capability of visually resolving forces down to 0.52nN with a 40× objective, providing an extremely cost-effective, yet powerful experimental platform for single cell studies with a sub-nN force measurement resolution.

CONCLUSION

This paper presented a method to robustly measure forces applied to single biological cells through the use of a microfabricated PDMS device and a sub-pixel computer vision tracking algorithm. The current system is capable of resolving cellular forces down to 3.7μN. A realistic estimate reveals that the methodology presented in this paper is capable of resolving forces down to 0.52nN with a scaled-down device (supporting posts of 25μm in height and 5μm in diameter). The device design and experimental technique are applicable to investigating mechanical properties of many cell types of different sizes and to providing real-time force feedback during microrobotic cell manipulation.

REFERENCES

[1] Y. Sun, K.T. Wan, B.J. Nelson, J. Bischof, and K. Roberts, "Mechanical property characterization of the mouse zona pellucida," *IEEE Trans. on NanoBioScience*, 279, 2 (2003).

[2] G. Lin, K.S. Pister, and K.P. Roos, "Surface micromachined polysilicon heart cell force transducer," *J. of MEMS*, 9, 9 (2000).

[3] J.L. Tan, J. Tien, D.M. Pirone, D.S. Gary, K. Bhadriraju, C.S. Chen, "Cells lying on a bed of microneedles: an approach to isolate mechanical force," *Proc. Natl. Acad. Sci.*, 1484, 100 (2003).

[4] Y. Zhao and X. Zhang, "Cellular mechanics study in cardiac myocytes using PDMS pillars array," *Sensors and Actuators A*, 398, 125 (2006).

[5] Y. Sun and B.J. Nelson, "Biological cell injection using an autonomous microrobotic system," *International J. of Robotics Research*, 861, 21 (2002).

[6] A.C. Ugural and S.K. Fenster, *Advanced Strength and Applied Elasticity*, Prentice Hall, 2003.

[7] D.H. Kim, Y. Sun, S. Yun, S.H. Lee, and B.K. Kim, "Investigating chorion softening of zebrafish embryos with a microrobotic force sensing system," *J. of Biomechanics*, 1359, 38 (2005).

ENVIRONMENT-ADAPTIVE VARIABLE-FOCUS LIQUID MICROLENSES

Liang Dong[1], Abhishek K. Agarwal[1], David J. Beebe[2], and Hongrui Jiang[1]
[1] Department of Electrical and Computer Engineering, University of Wisconsin-Madison, Madison, WI 53706
[2] Department of Biomedical Engineering, University of Wisconsin-Madison, Madison, WI 53706

ABSTRACT

Variable-focus microlenses have the potential for miniaturizing optical systems since they do not rely on manual positioning of the microlens. Previous variable-focus microlenses generally have small tuning range of focal lengths and/or require additional control systems. Here, inspired by human eye's lens, we realize environment-adaptive variable-focus liquid microlenses by combining the advantages of stimuli-responsive hydrogels and pinned liquid-liquid interfaces at the microscale. These microlenses have a large focal length tuning range (-∞ to +∞; divergent – convergent) and do not require additional control.

INTRODUCTION

Traditional man-made optical systems are comprised of multiple lenses where one or more of these lenses are physically displaced to realize variable focus. Nature, however, accomplishes this same function much more elegantly with an individual lens. Although advancements in miniaturization technologies have led to single microlens embodiments that are widely used in photonics, displays, and biomedical systems, these microlens technologies rely on either fixed or externally-controlled variable-focal length [**1-4**].

Instead, we look to nature for inspiration to realize smart microlenses using pinned liquid-liquid interfaces. In the human eye, ciliary muscles are controlled by the body's nervous system, thereby relaxing and contracting the shape of the lens to enable the eye to focus on different distances. Our microlenses autonomously adapt to local environmental parameters via stimuli-responsive hydrogels (e.g., pH, temperature, light, electric field, and antigen) [**5**]. Stimuli-responsive hydrogels modulate the shape and focal length of the liquid microlens (analogous to ciliary muscles) formed through a liquid-liquid interface [**6**] without the need for additional external control systems. The hydrogels simultaneously exhibit both sensing and actuating functions. The favorable scaling of ionic diffusion and fluidic surface tension can be elegantly leveraged to realize relatively short hydrogel response times [**7**] and pinned liquid-liquid interfaces, respectively. The creation of our smart liquid microlens takes advantage of these scaling properties, which allow a single microlens to have a focal length ranging from -∞ to +∞ (divergent – convergent).

In this paper, we report two types of liquid microlenses by taking advantage of the volume change of the hydrogels differently. The hydrogels used here as models to demonstrate the environment-adaptive functionality are acrylic acid (AA)-based pH-responsive and *N*-isopropylacrylamide (NIPAAm)-based temperature-responsive hydrogels [**8**].

STRUCTURE AND FABRICATION OF DEVICES

In the 'TYPE-1' liquid microlens (Fig. 1a), a set of stimuli-responsive hydrogel posts are fabricated in a microfluidic chamber. When exposed to a specific stimulus, the hydrogel posts expand and contract to bend a flexible aperture slip up and down. Consequently, the water-oil interface pinned at a hydrophilic-hydrophobic boundary bows downward and bulges upward, varying the focal length of the microlens. The 'TYPE-2' liquid microlens (Fig. 1b) has a hydrogel ring located underneath a rigid aperture. The water is enclosed by the hydrogel ring. A rigid slip is used to restrain the change in the height of the hydrogel. A changing stimulus outside the ring can cause a volume change in the inside periphery of the ring. The hydrogel ring expands and shrinks in width by absorbing and releasing water via the hydrogel network interstitials. The net volume change of water enclosed by the ring regulates the pressure difference across the water-oil interface; this induces a change in the shape of the liquid microlens, and hence the focal length.

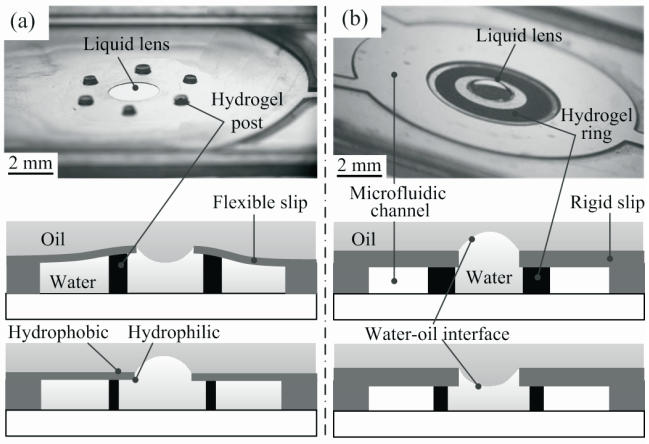

***Figure 1**. Structures and mechanisms of two types of environment-adaptive variable-focus liquid microlenses. (a) 'TYPE-1'. (b) 'TYPE-2'. In both types, microlenses are formed through curved interfaces between oil and water-based solutions which are stably pinned at a hydrophobic-hydrophilic contact line.*

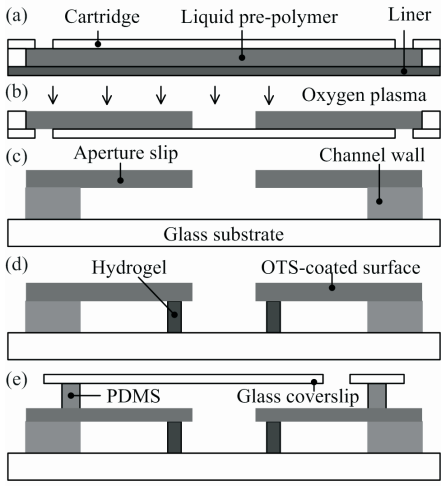

***Figure 2**. Fabrication process for both types of liquid microlenses.*

Fig. 2 shows the fabrication process of the devices. The isobornyl acrylate-based polymer (poly(IBA)) apertures of the microlenses are photopatterned (45 μm-thick for 'TYPE-1' and 125 μm for 'TYPE-2') within cartridges using liquid-phase photopolymerization (LP^3) based on UV photolithography [**7**] (Fig.

2a). After removing the liner, an oxygen plasma treatment is carried out to make the backside and sidewall of the aperture hydrophilic (Fig. 2b). The cartridge is removed and a cavity is formed by adhering the poly(IBA) aperture slip to a glass substrate. The microfluidic channels (also poly(IBA)) and hydrogel posts and rings are fabricated inside the cavity using LP^3 (Figs. 2c-d). To achieve the hydrophobic property on the top surface of the aperture slip, an octadecyltrichlorosilane (OTS) solution diluted by hexadecane (0.2 v/v %) is coated on to it (Fig. 2d). To store the oil, a poly(dimethylsiloxane) (PDMS) fence, bonded with a glass cover slip, is glued to the aperture slip (Fig. 2e).

RESULTS AND DISCUSSION

Figs. 3a-b shows the shape and focal length of a pH-sensitive liquid microlens (TYPE-1) with different pH buffers. The AA hydrogels expand in basic solutions and contract in acidic solutions with a volume transition point of pH 5.5. The transition of the microlens from divergent to convergent occurs between pH 6.0 to 8.0. The focal length can be varied from -7.6 mm to -∞ (divergent) and from 8.5 mm to +∞ (convergent). The response time of the microlens is 10-15 s. The change in environmental temperatures can vary the focal length of a liquid microlens using the temperature-sensitive hydrogel ('TYPE-1' in Figs. 3c-d). The NIPAAm hydrogels expand at low temperatures and contract at high temperatures with a lowest critical solution temperature of 32 °C. The focal length transition from positive to negative infinity occurs between 31 °C and 33 °C. The response time of this microlens is 13-20 s.

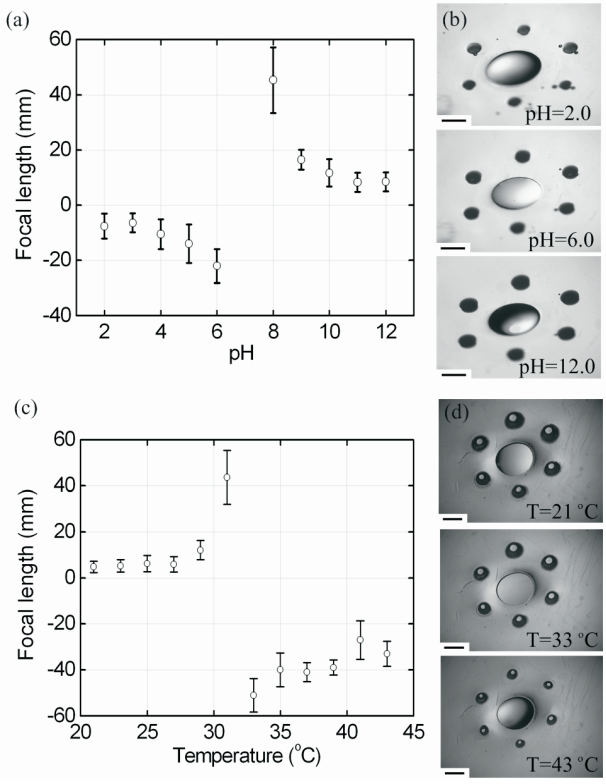

Figure 3. *(a) The focal length of the microlens (TYPE-1) using AA hydrogel as a function of pH. Syringe pumps are used to transfer buffer solutions with different pH through the input channels. (b) The shape of the liquid meniscus when varying pH. Scale bars, 1.0 mm. (c) The focal length of the microlens (TYPE-1) using NIPAAm hydrogel as a function of temperature. An external heater is used to simulate a change in environmental temperature. (d) The shape of the liquid meniscus at varying temperatures.*

The 'TYPE-2' liquid microlens (Fig. 1b) also functions to adapt to a changing temperature by using NIPAAm hydrogel. The microlens adjusts its focal length from -7.8 mm to -∞ and from 11.8 mm to +∞ as the temperature varies (Fig. 4a). The 2×4 microlens array (Fig. 4b) has a ~10% variation in focal length. Each lens pixel can be tuned individually.

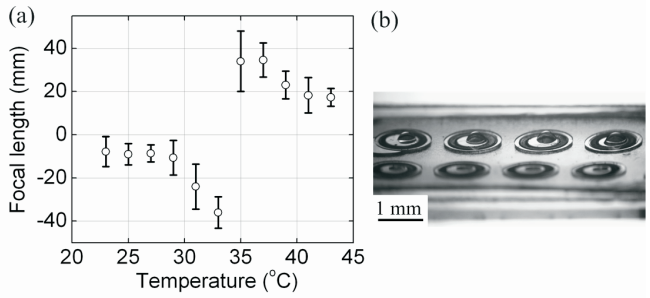

Figure 4. *(a) The focal length of a microlens (TYPE-2) as a function of temperature. (b) A liquid microlens array.*

.

CONCLUSION

A variety of stimuli-responsive hydrogels are used to implement multi-parameter, environment-adaptive smart liquid microlenses. These microlenses can potentially be integrated with other microfluidic components fabricated through a similar process [**8**] to realize functionally complex systems such as biological and chemical sensors and bio-optical microfluidic systems, and to advance lab-on-chip technologies.

ACKNOWLEDGMENTS

This work is partly supported by the U.S. Department of Homeland Security (grant number N-00014-04-1-0659) through a grant awarded to the National Center for Food Protection and Defense at the University of Minnesota, and is partly supported by the Wisconsin Alumni Research Foundation (WARF). The authors thank Dr. Jaisree Moorthy and Sudheer S. Sridharamurthy for their valuable discussions.

REFERENCES

[1] N. Chronis, G.L. Liu, K.H. Jeong, and LP Lee. "Tunable liquid-filled microlens array integrated with microfluidic network," *Optics Express* 11: 2370-2378 (2003).

[2] S. Kuiper, and B.H.W. Hendriks. "Variable-focus liquid lens for miniature cameras," *Appl. Phys. Lett*. 85: 1128-1130 (2004).

[3] C.A. Lopez, C.C. Lee, and A.H. Hirsa. "Electrochemically activated adaptive liquid lens," *Appl. Phys. Lett*. 87: 134102 (2005).

[4] H.W. Ren, Y.H. Fan, and S.T. Wu. "Liquid-crystal microlens arrays using patterned polymer networks," *Opt. Lett.* 29: 1608-1610 (2004).

[5] Y. Osada, J.P. Gong, and Y. Tanaka. "Polymer gels". *J. Macromolecular Sci.* 44: 87-112 (2004).

[6] J. Atencia, and D.J. Beebe. "Controlled microfluidic interfaces," *Nature* 437: 648-655 (2005).

[7] D.J. Beebe, J.S. Moore, J.M. Bauer, Q. Yu, R.H. Liu, C. Devadoss, and B.H. Jo. "Functional hydrogel structures for autonomous flow control inside microfluidic channels," *Nature* 404: 588-590 (2000).

[8] A.K. Agarwal, S.S. Sridharamurthy, D.J. Beebe, and H. Jiang. "Programmable autonomous micromixers and micropumps," *J. Microelectromech. Syst*. 14: 1409-1421 (2005).

TEMPERATURE REGULATED NONLINEAR MICROVALVES FOR SELF-ADAPTIVE MEMS COOLING

Matthew McCarthy[1], Nicholas Tiliakos[3,1], Vijay Modi[1], Luc Fréchette[2,1]

[1]Columbia University, Department of Mechanical Engineering, New York, NY, 10027, U.S.A.
[2]Université de Sherbrooke, Department of Mechanical Engineering, Sherbrooke, QC, J1K 2R1, Canada
[3]ATK-GASL, Ronkonkoma, NY, 11779, U.S.A.

ABSTRACT

The design and characterization of microfabricated valves for self-adaptive MEMS cooling are presented in this paper. The novel microvalves regulate the flow of a coolant using thermal buckling of eccentric nickel beams, that are solely actuated and controlled by the heat removed, without the need for external wiring or instrumentation. The adaptive microvalves have been modeled, built, and experimentally characterized. The predictions for flow rate as a function of temperature show good agreement with the data while achieving the desired nonlinear valving behavior. Increases in mass flow rate of up to $5x10^{-6}$ kg/s are achieved over temperature ranges of less than 20ºC. These results, as well as the valve fabrication process, can be used to design temperature regulated valve geometries into a distributed micro-cooling scheme.

INTRODUCTION

The current work is focused on developing a thermally adaptive microvalve for flow control in self-regulating MEMS cooling devices. An array of adaptive valves would maintain a surface below some critical temperature by locally modulating flow rate through a cooling scheme in response to changes in heat load. This creates a MEMS skin-cooling scheme similar in nature to its biological inspiration. Figure 1 shows the schematic of a single device as well as an array of devices coating a heated surface.

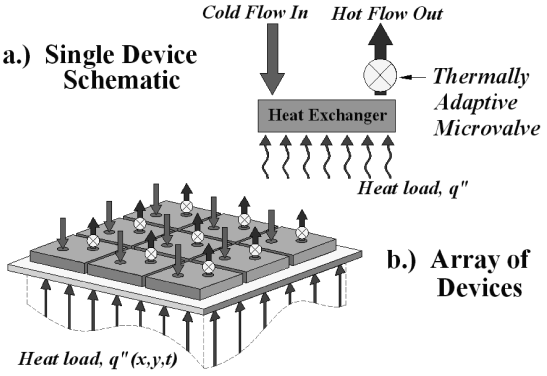

Figure 1. *Novel MEMS adaptive cooling scheme. (a) A single device and (c) an array of devices cooling a surface subject to a spatially and temporally varying heat load.*

An efficient adaptive microvalve would provide low valve actuation at moderate temperatures and relatively large valve actuation, hence large flow, at high temperatures. A highly nonlinear actuation capability over relatively small temperature ranges would prevent exceeding a critical temperature while minimizing coolant when not required.

The crucial element in this system is a microvalve that adapts to increases in temperature. By using the heat load to drive the thermal actuation, there is no need for control electronics or for resistive heating typically associated with electrothermal actuation [1]. This yields a simple, compact system that can be easily integrated into arrays of devices that need only fluidic connections for coolant.

The mechanism of buckling has been investigated as a means of achieving the nonlinear deflections needed for valve actuation.

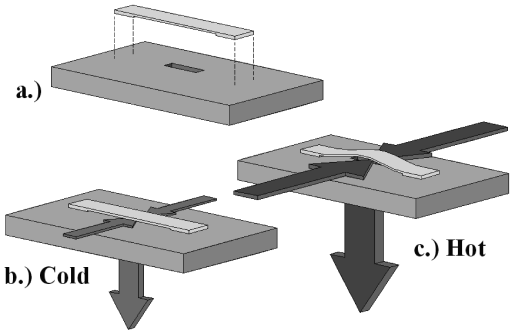

Figure 2. *Visualization of thermally adaptive valve concept. (a) Clamped beam fabricated over a slot in substrate with a pressure difference across it (b) at low temperatures, low mass flow through the thin air gap between beam and substrate (c) at high temperatures, the beam buckles, opening the air gap and allowing a large coolant flow rate.*

Figure 2 shows conceptually how buckling beam actuation can be used to increase flow rate, where the relative thermal expansion of the beam with respect to the substrate leads to a compressive load in the beam that can induce lateral deflections (buckling). Accordingly, the elastic curve and state of stress of thermally buckled beams was modeled and validated against experimental data in previous work [2]. These findings have been extended in this work to model the flow rate through the contoured beam gap as a function of temperature. This analytic model will be compared to experimental results for multiple valves under various loadings.

THEORY

The valving mechanism shown in Fig. 2 consists of a thermally buckling beam that increases the thin air gap between itself and the substrate. For small deflections relative to the beam width, the flow through this thin air gap can be modeled as flow through two infinite parallel plates. The valve mass flow rate then varies as the cube of the contoured gap, $d(x)^3$, as given by [3]:

$$\dot{m} = \frac{\Delta P}{6 w \nu} \int_a^b d(x)^3 \, dx \qquad (1)$$

where ν is the kinematic viscosity and w is the parallel plate flow distance underneath the beam. Using Eq. (1), along with the thermal buckling analysis developed in [2], yields

$$\frac{\dot{m}}{\Delta P} = \left[\frac{L}{w\nu}\right]\left(\frac{15\pi + 44}{288\pi}\right) e^3 (\sec\eta - 1)^3 \qquad (2\text{-}4)$$

$$\Delta T = \frac{1}{\alpha}\left(\frac{h}{L}\right)^2 \left[\frac{\eta^2}{3} + \left(\frac{e\pi}{4h}\right)^2 (\sec\eta - 1)^2\right] \qquad \eta \equiv \frac{L}{2}\sqrt{P/EI}$$

where η is the nondimensional axial force, e is the designed beam eccentricity, α is the difference in coefficient of thermal expansion between the beam and substrate and ΔT is the temperature rise above the zero stress state. The half-length, thickness and moment of inertia of the beam are denoted as L, h and I, respectively. Equation (2) shows the mass flow rate per unit driving pressure as a function of axial load, while Eq. (3) gives the beam temperature rise required to generate the nondimensional axial load, η. As the axial force, P, approaches the critical buckling load, η approaches $\pi/2$, and the mass flow rate per unit pressure drop blows up due to the secant term, leading to the desired non-linear valve response.

FABRICATION

Doubly clamped microfabricated beams suspended over a small air gap were fabricated using a thru mold nickel electroplating process [2]. A shallow silicon etch is previously done to create small 2-3μm eccentricities in the beam, Fig. 3(b), and a sacrificial photoresist layer is used to form the 1.5μm air gap underneath it. The beam planar dimensions are 4000μm x 700μm with thickness of 25-35μm. Deep reactive ion etching from the backside is then used to define the valve slot under the beam, as illustrated in Fig. 2.

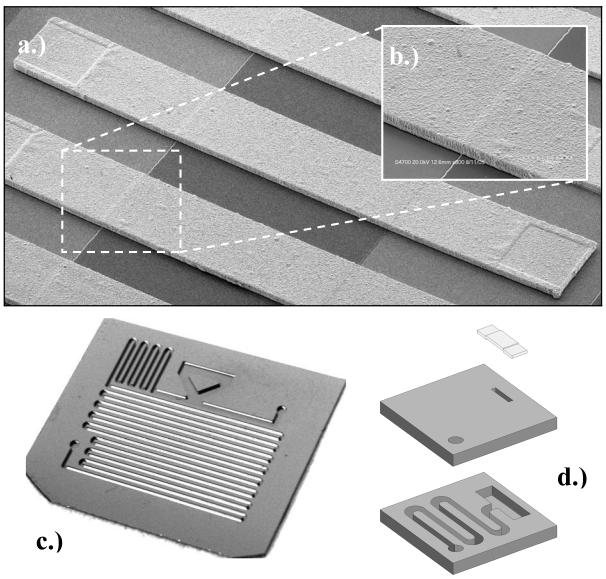

Figure 3. *(a) SEM photo of an array of eccentric clamped beams. (b) A beam eccentricity. (c) Deep etched silicon heat exchanger wafer. (d) Assembly of valve wafer and heat exchanger wafer.*

The fabricated valve wafer is bonded to another silicon wafer containing a deep reactive ion etched heat exchanger seen in Fig. 3(c). A low temperature photoresist bonding procedure is used due to the temperature sensitive nature of the valves. Figure 3(d) shows the assembly of the two wafers. The valve wafer can be inverted to change the direction of the flow through the valve and of the static pressure acting on the beam.

TESTING & RESULTS

The heat exchanger and valve assembly in Fig. 3(d) is used to heat the working fluid (air) to the wall temperature, ensuring that the valve is isothermal. A pressure port, not shown in Fig. 3(d), is fabricated in the device between the heat exchanger and the microvalve. These features allow for the simultaneous control of temperature and pressure drop across the valve during testing. Heat is added to the assembly through a thin film heater while the isothermal temperature is monitored using thermocouples. The pressure drop is maintained constant across the valve while the flow rate is measured. Each valve is tested under positive and negative pressure loadings on the beam.

Eliminating the axial load, η, Eqs. (2) and (3) are plotted against each other in Fig. 4. This shows the mass flow rate as a function of valve temperature without considering the pressure effects on the beam contour. Experimental data for two valves loaded in both pressure orientations is compared to the model.

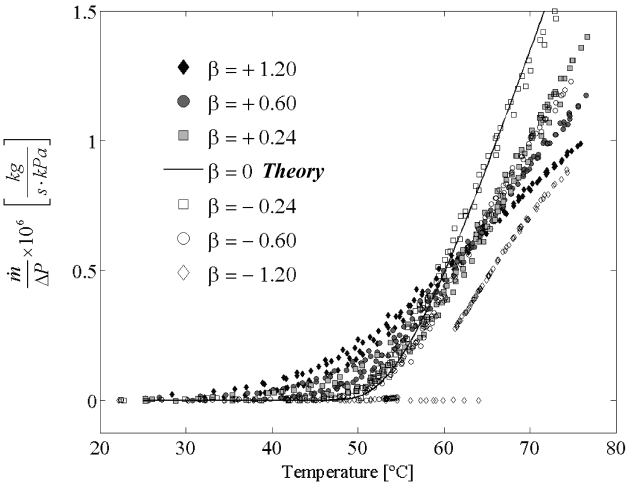

Figure 4. *Mass flow rate per unit driving pressure as a function of temperature for various pressure coefficients $\beta=(\Delta P/E)(L/h)^4$.*

Figure 4 shows that as the magnitude of the pressure coefficient, β, decreases the experimental results approach the theoretical model for beams buckling with no pressure force. The effect of pressure in the two valve orientations can also be seen. A more complex model is being developed to investigate the effects of pressure loading on the buckling beam contour. The leak rates for the valves tested here were all well below the sensitivity of the mass flow meter used. Calculations based on the valve geometry at ambient conditions suggest leak rates of $\dot{m}_{leak}/\Delta P \approx 10^{-9}$ *kg / s·kPa*, three orders of magnitude less than the maximum flow rates achieved.

CONCLUSIONS

Thermally adaptive microvalves have been modeled, built, and experimentally characterized. Order of magnitude increases in flow rate have been achieved nonlinearly over relatively small temperature ranges, and the effect of pressure can be seen. This nonlinear behavior is the key aspect needed for achieving efficient self-adaptive cooling. These results show that the modeling technique and fabrication process developed herein can be used to build thermally adaptive microvalves with the desired nonlinear actuation capabilities into a MEMS self-regulating cooling scheme.

REFERENCES

[1] D. Yan, A. Khajepour, and R. Mansour, "Modeling of Two-Hot-Arm Horizontal Thermal Actuator," Journal of Micromechanics and Microengineering, **13**, pp. 312-322. (2003)

[2] M. McCarthy, N. Tiliakos, V. Modi, and L. G. Fréchette, "Characterization and Modeling of Thermal Buckling in Eccentrically Loaded Microfabricated Nickel Beams for Adaptive Cooling", Proc. ASME Int'l Mech. Eng. Congress & Expo., Orlando, FL, Nov. 5-11, 2005, Paper IMECE2005-81415.

[3] R. W. Fox, A. T. McDonald, *Introduction to Fluid Mechanics*, John Wiley & Sons. (1998)

Authors

E

F

G

H

I

J

K

L

M

N

O

P

Q

R

S

T

U

V

W

X

Y

Z

Keywords

F

G

H

I

J

L

M

N

O

P

Q

R

S

T

U

V

W

X

Y

Z

NOTES